

COMBUSTION DYNAMICS AND HEAT TRANSFER IN AN ULTRA COMPACT COMBUSTOR

DISSERTATION

Brian T. Bohan, Major, USAF

AFIT-ENY-DS-18-S-057

DEPARTMENT OF THE AIR FORCE
AIR UNIVERSITY

AIR FORCE INSTITUTE OF TECHNOLOGY

Wright-Patterson Air Force Base, Ohio

DISTRIBUTION STATEMENT A
APPROVED FOR PUBLIC RELEASE; DISTRIBUTION UNLIMITED.

The views expressed in this document are those of the author and do not reflect the official policy or position of the United States Air Force, the United States Department of Defense or the United States Government. This material is declared a work of the U.S. Government and is not subject to copyright protection in the United States.

AFIT-ENY-DS-18-S-057

COMBUSTION DYNAMICS AND HEAT TRANSFER IN AN ULTRA COMPACT COMBUSTOR

DISSERTATION

Presented to the Faculty

Graduate School of Engineering and Management

Air Force Institute of Technology

Air University

Air Education and Training Command

in Partial Fulfillment of the Requirements for the

Degree of Doctor of Philosophy

Brian T. Bohan, B.S., M.S.

Major, USAF

August 2018

DISTRIBUTION STATEMENT A
APPROVED FOR PUBLIC RELEASE; DISTRIBUTION UNLIMITED.

AFIT-ENY-DS-18-S-057

COMBUSTION DYNAMICS AND HEAT TRANSFER IN AN ULTRA COMPACT COMBUSTOR

Brian T. Bohan, B.S., M.S.
Major, USAF

Committee Membership:

Marc D. Polanka, PhD
Chairman

Lieutenant Colonel James L. Rutledge, PhD
Member

Lieutenant Colonel Darrell S. Crowe, PhD
Member

Kevin C. Gross, PhD
Member

Andrew W. Caswell, PhD
Member

ADEDEJI B. BADIRU, PhD
Dean, Graduate School of Engineering and Management

Abstract

The Ultra Compact Combustor (UCC) is an innovative combustion system alternative to a traditional turbine engine burner with the potential to improve engine efficiency with a reduced combustor volume. The UCC shortens the axial length of the combustor, and therefore reduces engine weight, by burning in an annulus and swirling the reactants in the circumferential direction. These length and weight improvements can directly lead to an increased thrust-to-weight rating of the engine. The present research included five objectives which advanced the UCC concept on four fronts; cooling UCC turbine vanes, advanced computational modeling of UCC systems, system air split control and combustion characterization with alternate fuel injection designs, and development of a new UCC orientation to correct exit temperature profiles and fit inside an engine case.

Objective one focused on cooling of the UCC turbine vanes located radially inward from the circumferential combustor by taking advantage of the unique component configuration in this system. The leading edge of the turbine vanes were positioned axially upstream of the hot combustion gases enabling cool core flow to be ingested into the vane at the leading edge eliminating the need for compressor bleed air. Several cooling schemes were computationally analyzed that included internal and film-cooling concepts. A design was down selected, hardware was 3D printed, and this novel cooling concept was experimentally tested and validated.

Objective two demonstrated the benefits of advanced computational modeling in a UCC by incorporating conjugate heat transfer to previously used combustion and turbulent fluid analysis with adiabatic wall treatments. The addition of the conjugate model created more realistic temperature results than the adiabatic model when compared to experimental data at the exit plane of the combustor.

Objective three required the development of a variable geometry diffuser to enable dynamic UCC core-to-cavity air flow split control. The diffuser was integrated into the Version 3 UCC and the effect on combustion properties in the circumferential cavity based on flow split was fully characterized. In addition, a new cavity outer ring featuring 12 backward-facing steps was analyzed which enabled tangential air and fuel injection and an enhanced combustor operating range. The UCC with the 12-Step ring was fully characterized with respect to air and fuel flow splits, combustion heat release, acoustics, swirl velocity, and exit temperature distribution. As part of the fuel injection analysis a study of fluidic oscillators injecting propane from backward-facing steps was conducted to determine if they offered enhanced mixing compared to the baseline non-oscillating straight fuel jets. While interesting fluidic behaviors were observed, the benefits to fuel mixing from the oscillators was negligible compared to the mixing already offered by the recirculation behind the backward-facing steps.

Completion of Objectives 4 and 5 led to the development and analysis of a new UCC configuration that maintained the desired 33% axial length savings, but also fit inside an engine case and offered significant improvements in exit temperature distribution. The new combustor configuration fixed the exit temperature distribution by eliminating the need for hot gas migration across the engine core flow. With this new design the major issues that have plagued the UCC concept since inception have been addressed. After an iterative design approach the Configuration 7 combustor was selected for manufacture and experimental testing as a stand alone combustor and with rotating turbomachinery as a replacement burner in a JetCat small-scale engine. While the combustor operated with a limited range, performance properties were comparable to the stock JetCat and demonstrated the exit temperature distribution improvements, 33% axial length savings, and fitting inside of the stock JetCat casing.

Acknowledgements

Over the course of this three year program there were many people that helped me along the way. Whether the contribution was big or small, the support was appreciated and enabled me to be successful in my research. For starters I would like to thank my advisor, Dr. Marc Polanka, and the rest of my academic committee, Lt Col James Rutledge, Lt Col Darrell Crowe, Dr. Kevin Gross, and Dr. Andrew Caswell, for their guidance and help in shaping the research reported in this document. I would also like to thank my fellow COAL lab students including Lt Kevin DeMarco, Lt Tylor Rathsack, Capt Edwin Hornedo, and Maj Andrew Cottle as well as the COAL lab interns including Mr. Carl Pickl, and Mr. Nathan Clark for their valuable contributions.

My experimental research was greatly enhanced by the optical analysis support of Dr. Larry Goss of ISSI, and Mr. Michael Bischmann, Capt Brock Andrews, and Mr. Ben Hagen of AFRL. The AFIT ENY lab technicians including Mr. Jamie Smith, Mr. Josh DeWitt, Mr. Keith Long, and Mr. Mike Ranft provided a valuable service to operate, support, and enhance the existing systems in the lab as well as purchase new materials. Mr. John Hixenbaugh was instrumental in ensuring all hazardous materials I needed were made available and stored properly. My computational research was supported by Mr. Dave Doak who maintained the Linux network and quickly addressed any issues I had along the way.

Mr. Jake Wilson, a former AFIT graduate, provided me with experimental performance data on the stock JetCat, and Mr. Mateo Ugolati of the University of Cincinnati provided me with a baseline CAD model of the stock JetCat. Both of these gentlemen saved me countless hours of having to duplicate these items myself. I would also like to thank Mr. Jorge Urena from AFIT for all his help with the JetCat electrical system redesign and circuit board manufacturing.

My research required many parts to be manufactured to enable experimental testing. I would like to thank Mr. Brian Crabtree, Mr. Dan Ryan, Mr. Chris Harkless, Mr. Joe Owings, and Mr. Dean Harshman from the AFIT Model Shop for their valuable design input and all of their hard work to produce my research hardware. I would also like to thank Mr. Ben Doane and Maj Ryan O'Hara of the AFIT AniMaL lab for their support in 3D printing several components.

When I applied to this degree program I had doubts about whether I had what it took to complete it and graduate. Yet I believe that God has His hand on my life and my career and set me down this path for reasons I may never know. To paraphrase Pastor Jud Wilhite, God does not call those who feel qualified; He qualifies those He calls. There were many times throughout this program that I questioned my intelligence and abilities and wondered why I was here. However, I believe God set me down this path to succeed, and where God guides, God provides. He gave me the strength to continue each day, He qualified me to reach each successive milestone, and gave me the wisdom to see through my problems to find solutions and be successful. Now as I graduate I can fulfill my calling and take the next steps; whatever and wherever they may be.

Last but certainly not least, I would like to thank all of my friends and family, specifically my wife, daughters, and parents, for their unwavering support. They were understanding that my workload limited my availability to spend time with them, and they provided encouragement, motivation, and a listening ear if I needed to vent or talk though problems. I love you all.

Brian T. Bohan

Table of Contents

Page

Abstract iv

Acknowledgements vi

List of Figures xvi

List of Tables liii

List of Abbreviations lix

List of Symbols lxii

I. Introduction 1

1.1 Ultra-Compact Combustor 1
1.2 Turbine Film-Cooling 5
1.3 Potential for Heat Release in Film-Cooling 8
1.4 Small Turbojet Integration 9
1.5 Research Objectives 11
1.6 Uniqueness of Research 12

II. Background 13

2.1 Gas Turbine Engine Overview 13
2.1.1 Combustor Design 17
2.1.1.1 Combustion Basics 20
2.1.1.2 Flame Characteristics 22
2.1.1.3 Combustor Performance Parameters 26
2.1.2 Rayleigh Losses 31
2.1.3 Combustor Exit Temperature Profiles 32
2.1.4 Emissions 34
2.2 Compact Combustion Theory and History 39
2.2.1 Compact Combustion Cycle 40
2.2.2 Turbine Passage Burning 42
2.2.3 Trapped Vortex Combustion 44
2.2.4 High-g Combustion 54
2.2.4.1 Rayleigh-Taylor Instabilities 65
2.2.4.2 Step-Stabilized Combustion 66
2.2.4.3 Effects of Component Geometry in High-g UCC 71
2.2.4.4 High-g UCC Flow Calculations 74
2.3 High-g UCC Advancement 76
2.3.1 Sector Rigs 77

Page

2.3.2 Fighter Engine Scale Analysis . . . 80
2.3.3 UCC Turbine Vanes . . . 84
2.3.4 AFIT Full Annular Test Rig . . . 86
2.3.5 Common Flow Source Diffuser . . . 88
2.3.6 Controlling Rayleigh Losses . . . 94
2.3.7 Flow Migration Studies . . . 97
2.3.8 High-g Flame Structures and Circumferential Cavity Analysis . . . 106
2.3.9 Emissions Analysis . . . 116
2.4 Combustion Instability & Acoustics . . . 119
2.5 Secondary Flows . . . 125
2.6 Fluidic Oscillators . . . 131
2.7 Heat Transfer . . . 135
2.7.1 Conduction . . . 135
2.7.2 Radiation . . . 139
2.7.3 Convection and Film-Cooling . . . 141
2.7.3.1 Film-Cooling Flow Physics . . . 146
2.8 Secondary Combustion in Cooling Films . . . 150
2.8.1 Identification of Secondary Combustion . . . 151
2.8.2 Secondary Combustion Mitigation . . . 152
2.8.3 Cooling a Hybrid Vane . . . 155
2.9 Turbomachinery . . . 159
2.9.1 Radial Compressors . . . 160
2.9.2 Axial Turbines . . . 164
2.10 Numerical Analysis . . . 168
2.10.1 Conservation Equations of Fluid Motion . . . 169
2.10.2 Turbulence . . . 171
2.10.2.1 Reynolds Averaging . . . 172
2.10.2.2 Wall Coordinates . . . 174
2.10.3 Turbulence Models . . . 175
2.10.3.1 Wall Functions . . . 178
2.10.3.2 Turbulence Model Application . . . 178
2.10.4 Combustion Modeling . . . 180
2.10.4.1 Combustion Model Application . . . 180
2.10.5 Conjugate Heat Transfer in FLUENT . . . 182
2.11 Optical Combustor Measurement Methods . . . 184
2.11.1 Chemiluminescence . . . 185
2.11.2 Particle Streak Emission Velocimetry (PSEV) . . . 187
2.11.3 Particle Image Velocimetry (PIV) . . . 193
2.11.4 Thin-Filament Pyrometry (TFP) . . . 195
2.11.5 Infrared Thermography . . . 198
2.11.6 Schlieren Imaging . . . 199
2.12 Limitations of Previous Research . . . 203

Page

III. Facilities & Baseline Hardware . . . 205

3.1 Experimental Facilities . . . 205
3.1.1 Air Supply . . . 205
3.1.2 Fuel Supply . . . 207
3.1.3 Ventilation . . . 210
3.1.4 Control Station . . . 214
3.1.5 Instrumentation . . . 215
3.1.5.1 Hardware . . . 215
3.1.5.2 Software . . . 215
3.1.6 Optical Diagnostics . . . 216
3.1.6.1 High-Speed Imagery . . . 217
3.1.6.2 Chemiluminescence . . . 218
3.1.6.3 PSEV . . . 220
3.1.6.4 PIV . . . 222
3.1.6.5 TFP . . . 224
3.1.6.6 Infrared Thermography . . . 226
3.2 Computational Resources . . . 227
3.2.1 Software Tools . . . 227
3.2.2 High-Performance Computing Hardware . . . 228
3.3 Baseline UCC Test Rig . . . 229
3.3.1 Sealants . . . 236

IV. Objective 1: Stagnation Cooling Study . . . 238

4.1 Objective 1 Background . . . 238
4.2 CFD Case Setup . . . 240
4.3 Grid Independence Check . . . 245
4.4 Computational Settings . . . 247
4.5 Computational Results . . . 249
4.5.1 Solid Vane . . . 251
4.5.2 Hollow Vane . . . 252
4.5.3 Plugged Vanes . . . 254
4.5.4 Plugged, Film-Cooled Vanes . . . 257
4.6 Stagnation Cooled HGV Manufacturing Study . . . 264
4.6.1 Numerical Analysis of the Manufactured HGV . . . 267
4.6.1.1 Manufactured HGV Pressure Results . . . 269
4.6.1.2 Manufactured HGV Temperature Results . . . 271
4.7 Experimental Test Methodology . . . 276
4.8 Experimental Test Results . . . 279
4.9 Objective 1 Conclusions . . . 289

Page

V. Objective 2: Effect of Conjugate Heat Transfer 293

5.1 Objective 2 Background 293
5.2 CFD Case Setup 294
5.3 Grid Development 296
5.4 Computational Settings 296
5.5 Experimental Instrumentation 297
5.6 Results 300
5.6.1 Computational Flame Quenching and Metal Temperatures 300
5.6.2 Circumferential Cavity Comparison, Φ_{Cav}=0.72 302
5.6.3 Vane Passage Comparison, Φ_{Cav}=0.72 305
5.6.4 Exit Plane Comparison, Φ_{Cav}=0.72 308
5.6.5 Circumferential Cavity Comparison, Φ_{Cav}=1.1 309
5.6.6 Vane Passage Comparison, Φ_{Cav}=1.1 312
5.6.7 Exit Plane Comparison, Φ_{Cav}=1.1 314
5.7 Objective 2 Conclusions 315

VI. Objective 3: Impact of Airflow Splits and Alternate UCC Fuel Injection Schemes 317

6.1 Variable Geometry Diffuser with Baseline Fuel Injection 317
6.1.1 Diffuser Design 319
6.1.2 Diffuser Computational Analysis 324
6.1.3 Mass Flow Rate Measurements 327
6.1.4 Diffuser Characterization Test Methodology 331
6.1.5 Diffuser Characterization Experimental Test Results 333
6.1.6 Diffuser Follow-on Test Methodology 338
6.1.7 Diffuser Follow-on Experiment Test Results 339
6.1.7.1 Cavity Mass Flow Rate = 0.037 kg/s, Cavity Φ = 0.72 339
6.1.7.2 Cavity Mass Flow Rate = 0.037 kg/s, Cavity Φ = 1.1 342
6.1.7.3 74/26 Core-to-Cavity Flow Split, Cavity Φ = 0.72 345
6.1.7.4 74/26 Core-to-Cavity Flow Split, Cavity Φ = 1.1 347
6.2 6-Step Ring 351
6.2.1 6-Step Ring Computational Analysis 354
6.2.2 6-Step Ring Experimental Testing 363
6.2.2.1 6-Step Ring PIV Analysis 367
6.2.2.2 6-Step Ring with Back Wall Fuel Injection 370

Page

6.2.3 Computational Boundary Condition Study . . . 375
6.3 12-Step Ring . . . 378
6.3.1 12-Step Ring Computational Analysis . . . 380
6.3.2 12-Step Ring Experimental Testing . . . 383
6.3.2.1 12-Step Ring Comparison to Baseline Combustor . . . 384
6.3.2.2 Airflow Split Characterization at Φ_{global} = 0.36 . . . 390
6.3.2.3 Airflow Split Characterization at Φ_{global} = 0.32 and 0.28 . . . 416
6.3.2.4 Effect of Exhaust Configuration on Combustor Performance . . . 421
6.3.2.5 Effect of Fuel Injection on Combustion Stability . . . 423
6.4 Objective 3 Conclusions . . . 429

VII. Fluidic Oscillator Fuel Injectors . . . 433

7.1 Oscillator Designs and Computational Analysis . . . 433
7.2 Experimental Methodology . . . 440
7.3 Experimental Results . . . 451
7.3.1 Test Series One . . . 451
7.3.1.1 Baseline, Non-Oscillating Jets . . . 451
7.3.1.2 V2 Single Oscillator . . . 456
7.3.1.3 V2 Double Linked Oscillator . . . 459
7.3.1.4 V2 Double Separate and V3 Double Oscillator . . . 461
7.3.2 Test Series Two . . . 463
7.3.3 Fluidic Oscillator Frequencies and Spread Angles . . . 472
7.4 Fluidic Oscillator Conclusions . . . 476

VIII. Objective 4: Improving Turbine Inlet Temperature Distributions . . . 478

8.1 Objective 4 Background . . . 479
8.2 JetCat Integration Constraints . . . 482
8.3 Computational Analysis . . . 483
8.3.1 CFD Case Setup . . . 483
8.3.2 Computational Settings . . . 486
8.3.3 Grid Independence Check . . . 488
8.3.4 Design Evolution of New UCC Combustor Configurations . . . 489
8.3.4.1 Configuration 1 . . . 490
8.3.4.2 Configuration 2 . . . 493
8.3.4.3 Configuration 3 . . . 496

8.3.4.4 Configuration 4 . . . 499
8.3.4.5 Configuration 5 . . . 500
8.3.4.6 Configuration 6 . . . 505
8.3.4.7 Configuration 7 . . . 508
8.3.5 Summarized Computational Results . . . 510
8.3.5.1 Establishing Centrifugal Loading . . . 510
8.3.5.2 Step-Stabilized Combustion . . . 512
8.3.5.3 Fuel Distribution in Backward-Facing Steps . . . 513
8.3.5.4 Controlling Exit Temperature Profiles . . . 514
8.3.5.5 Additional Benefits of Dual Chamber Combustors . . . 515
8.3.5.6 Maintaining Swirl Through The Combustor . . . 518
8.3.6 Configuration 7 Detailed Computational Results . . . 520
8.4 Experimental Analysis . . . 532
8.4.1 Combustor Configuration 7 Manufacturing . . . 532
8.4.2 Experimental Methodology . . . 541
8.4.3 Experimental Results . . . 547
8.4.3.1 As-Printed Combustor . . . 548
8.4.3.2 Configuration 7 with Version 1 Shim . . . 551
8.4.3.3 Configuration 7 with Version 2 Shim . . . 558
8.4.3.4 Combustion on the JetCat Operating Line . . . 566
8.5 Objective 4 Conclusions . . . 570

IX. Objective 5: Effects of Increased Mass Flow Rates & Pressures . . . 573

9.1 Objective 5 Background . . . 573
9.2 Experimental Methodology . . . 574
9.3 Results . . . 588
9.3.1 Combustor Analysis With Rotating Hardware . . . 589
9.3.2 Self-Sustaining Engine Operation . . . 601
9.3.3 Comparison to Stock JetCat P90RXi Performance . . . 603
9.3.4 Flameout Study Results . . . 615
9.3.4.1 Fuel and Air Variation Results . . . 619
9.3.4.2 High-Speed Pressure Analysis Results . . . 628
9.3.4.3 Fuel Distribution Study Results . . . 631
9.4 Objective 5 Conclusions . . . 635

Page

X. Conclusions & Future Work 639

10.1 Objective 1 639
10.2 Objective 2 641
10.3 Objective 3 643
10.4 Objective 4 649
10.5 Objective 5 653
10.6 Overall Research Conclusion 656

Appendix A. Motion Control System Setup 657

A.1 Arduino Uno Setup 657
A.2 grblShield Setup and Installation 658
A.3 Stepper Motion Wire Pair Determination & Installation 660
A.4 Raspberry Pi Setup 661
A.5 Universal G-Code Sender 663
A.6 Position Sensors 667

Appendix B. Thermocouple Rake Actuator 672

B.1 Probe Head 673
B.2 Actuator 674
B.3 Probe Head Positioning 678
B.4 Post-Processing 680

Appendix C. 12-Step Combustor Operating Maps 688

C.1 12-Step Combustor Operating Maps, $\dot{m}_{in} = 0.06kg/s$ 688
C.2 12-Step Combustor Operating Maps, $\dot{m}_{in} = 0.108kg/s$ 694
C.3 12-Step Combustor Operating Maps, $\dot{m}_{in} = 0.120kg/s$ 700

Appendix D. JetCat Electronics, Instrumentation, and Control 706

D.1 Engine Control Module (ECM) Redesign 708
D.1.1 Starter Motor Circuit 713
D.1.2 Pump Circuit & Pulse-Width Modulation 716
D.1.3 Pass Through & Feedback Signals 719
D.1.4 ECM Pin-Outs 720
D.2 Engine Board Redesign 723
D.2.1 RPM Module 731
D.2.2 Engine Board Pin-Outs 734
D.3 Glow Plug Power Control 737
D.4 Temperature Measurements 742
D.5 Thrust Measurements 742
D.6 Pressure Measurements 745

Page

D.7 LabView Visual Interface 748
D.7.1 Warning Lights 750
D.7.2 Gauge Indicators & Lubricant Flow Control 751
D.7.3 User Controls 752
D.7.4 Calculated Performance Parameters 755
Bibliography 758

Vita 773

List of Figures

Figure		Page
1.	Traditional combustor and ultra-compact combustor	3
2.	Swirl differences between the high-g and trapped-vortex UCC variants	3
3.	Comparison of turbine inlet temperature to material limits	7
4.	Secondary combustion reactions	8
5.	Small turbine engine cutaway	10
6.	Ideal Air-standard Brayton cycle	14
7.	Traditional combustor types	18
8.	Principle features and flow pattern of a modern traditional main combustor	19
9.	Turbulent premixed combustion flame regimes	26
10.	Combustion efficiency (η_b) versus reaction rate parameter (θ)	30
11.	Rayleigh pressure loss as a function of inlet Mach number and exit to inlet stagnation temperature ratio	32
12.	Commercial engine combustor exit temperature profiles	33
13.	Equilibrium CO mole fractions in propane-air combustion at adiabatic flame temperatures and 1500K	37
14.	NO_x production in staged combustion. The path 0-1-2'-2 is ideal with instantaneous secondary air mixing, 0-1-3 indicates a path for slow mixing	38
15.	a) TVC cross section b) High-g UCC cross section and front view	39
16.	Modified Brayton cycle from Sirignano et al.	41
17.	Cycle comparisons of CTB to various numbers of ITB stages (no afterburner)	42

Figure Page

18. Temperature contours of a reacting mixing layer in a curved, converging channel 44

19. AFRL Generation 1 TVC 46

20. AFRL Current TVC a) photograph of a top view of the experimental setup; b) side view drawing, air flow path arrows are blue, fuel path is green, effusion cooling is red 47

21. Top-view chemiluminescence images of the three vane cases (top) with normalized downstream intensity profiles (bottom) 48

22. Combustion efficiency contours for varying cavity air loading and equivalence ratio; each panel represents a different cavity air driver area 49

23. Cavity injection configurations tested by Colcord and Sirignano 50

24. Flow field inside the recessed cavities using the reinforcing and parallel injection methods 51

25. Density contours with parallel injection for an inside cavity (left) and outside cavity (right) from Colcord and Sirignano 52

26. Combustion in three Reynolds number regimes for a recessed cavity in a curved channel 53

27. 2D streamline comparison in cold flow and reacting flow with and without TVC cavity wall rotation 54

28. Geometry of Jet-Swirl Combustor used by Yonezawa et al. 55

29. Combustion efficiency vs. air loading as found by Yonezawa et al. 57

30. Bubble velocity controlled flame propagation (Left) and turbulent flame speed controlled reaction (Right) 58

31. Flame propagation rate and bubble velocity as a function of g-loading 59

Figure Page

32. Flame propagation at $10g_e$ (Left), Flame propagation at $500g_e$ (Right) 61

33. 2003 Baseline UCC design used by Zelina et al. 61

34. UCC cavity equivalence ratio at blowout as a function of cavity g-loading 62

35. Instantaneous temperature contours for $1g_e$, $395g_e$, $1000g_e$, $2000g_e$, and $3000g_e$ stoichiometric propane-air premixed ame at t = 8 ms. The contour units are in Kelvin. Dimensions are in centimeters 63

36. Comparison of simulation data to Lewis' measured data 64

37. Sequenced development of Rayleigh-Taylor instabilities due to gravity 66

38. Development of a Rayleigh-Taylor instability induced spike with Kelvin-Helmholtz instabilities along the shear surface 67

39. Experimental configurations of step-stabilized flames 68

40. Flame propagation length (L) normalized by channel height and flow velocity normalized by flame speed for the three Lapsa and Dahm test cases 69

41. Effect of acceleration on blowout velocity for the three Lapsa and Dahm test cases 69

42. Chemiluminescence (left) and shadowgraph (right) for the straight channel. Top images are for U = 4 m/s, bottom images are U = 40m/s 70

43. Chemiluminescence (left) and shadowgraph (right) for the positively accelerated channel. Top images are for U = 4 m/s (+28.5 g), bottom images are U = 40m/s (+2,850 g) 70

44. Chemiluminescence (left) and shadowgraph (right) for the negatively accelerated channel. Top images are for U = 4 m/s (-28.5 g), bottom images are U = 40m/s (-2,850 g) 71

45. Test rig used by Anderson et al. 72

Figure Page

46. Angled UCC turbine vanes . . . 73

47. Angled UCC turbine vane suction surface temperature distributions . . . 75

48. Curved sector rig (left) and Infinite radius sector rig (right) . . . 77

49. High-Speed Video Image Above Radial Vane of 28 mm vane, $1000g_e$, $\phi = 2.0$ at MFR=0.05 (top), 0.1 (middle top), 0.2 (middle bottom), and 0.3 (bottom) . . . 79

50. Cross-section of the UCC section analyzed by Bohan and Polanka . . . 80

51. 2011 computational domains used by Bohan and Polanka for fighter-scale analysis . . . 81

52. Relationship of cavity inlet velocity to cavity tangential velocity and hole diameter . . . 84

53. Hybrid vane origin and orientation . . . 85

54. Hybrid vane with and without radial vane cavity . . . 86

55. Full annular test rig with tapered centerbody used by Wilson et al. . . . 87

56. Wilson et al. swirl direction study . . . 88

57. 20 hybrid vane domain with cavity inlet splitter duct . . . 89

58. Cross sectional view of the Conrad UCC with common flow source . . . 90

59. Exploded view of the Conrad diffuser . . . 90

60. Air injection panels mounted to the UCC front plate . . . 91

61. Cottle et al. restrictor plate with $\lambda = 4.6$ . . . 92

62. AFIT UCC rig used by Cottle et al. . . . 93

63. Diffuser outer channel velocity profile . . . 94

64. Layout of Johnson's low Rayleigh loss geometry . . . 95

Figure Page

65. a) Velocity contours in the LLCB b) LLCB cross-section with hybrid vane integration 96

66. Circumferentially averaged total temperatures at the combustor section exit plane using the 12-species model and ideal air inlet diameters to achieve 3,500g_e in the cavity 98

67. Measured temperature profiles for height varied probes with a) 70/30 b) 75/25 and c) 80/20 core to cavity flow splits 99

68. LLCB hybrid vane with a) original middle section and b) Gilbert et al. RVC modification 100

69. Comparison of exit temperature profiles between "Version 2" and "Version 3" of the AFIT UCC 101

70. Exit temperature profiles of simulated (dotted lines) and experimental (open circles) for hybrid vanes without a radial vane cavity (blue) and with a radial vane cavity (red) 102

71. Area-weighted average of temperature with axial position Version 2 UCC (Config 1 = without a radial vane cavity; Config 2 = with a radial vane cavity)(Rich = 1.37, Lean = 0.76) - Vertical dotted lines indicated the forward and aft walls of the circumferential cavity 103

72. Area-weighted average of temperature with axial position (Config 1 = Version 2 UCC without RVC; Config 2 = Version 2 UCC with RVC; Config 3 = Version 3 UCC without RVC; Config 4 = Version 3 UCC with RVC) - Vertical dotted lines indicated the forward and aft walls of the circumferential cavity 104

73. Combustion cavity temperature profiles (Config 1 = Version 2 UCC without RVC; Config 2 = Version 2 UCC with RVC; Config 3 = Version 3 UCC without RVC; Config 4 = Version 3 UCC with RVC) a) z/L=0.59 b) z/L=0.60 c) z/L=0.61 105

74. Other RVC designs tested by Cottle 3) Full cavity span 4) Axially extended 5) Back step only 6) Dual back steps 7) Crescent 8) Cut 106

Figure Page

75. Temperature calculations (°K) along the combustor cross section for 22% cavity air at high-g load 107

76. PLIF images from the exit plane of the curved and straight sector rig 108

77. 3D iso-surface of OH in a large-scale UCC operated at test rig conditions showing 2 modes. Surface is colored by total temperature 109

78. Flame intensities in the UCC cavity at an instantaneous measurement (top) and a 50 frame average (bottom) 109

79. Water velocity and trajectory for g-loads of $300g_e$, $1400g_e$, and $5000g_e$ at 0.7 and 1.4 MPa pressure drop 111

80. UCC Version 3, Single-point fuel injection stream traces colored by temperature (K); med-rich (top left), high-rich (top right), med-lean (bottom left), high-lean (bottom right) 112

81. Radial profiles of circumferentially-averaged tangential velocity (Version 2 UCC) 113

82. Radial profiles of circumferentially-averaged tangential velocity (Version 3 UCC) 114

83. Radial profiles of circumferentially-averaged g-loads in the circumferential cavity (Version 3 UCC) 115

84. Radial profiles of circumferentially-averaged temperatures in the circumferential cavity (Version 3 UCC) 116

85. Emission maps of high-g UCC performance at three cavity air flow splits 117

86. CO emissions index in the UCC under varying conditions 118

87. Emission maps of high-g performance in the Version 3 UCC with the LLCB and LLCB with an RVC 119

Figure Page

88. Area-weighted average of UHC with axial position (Config 1 = Version 2 UCC without RVC; Config 2 = Version 2 UCC with RVC; Config 3 = Version 3 UCC without RVC; Config 4 = Version 3 UCC with RVC) - Vertical dotted lines indicated the forward and aft walls of the circumferential cavity 120

89. Direct and indirect combustion noise sources in a traditional gas turbine combustor 121

90. Acoustic responses to relative phase shifts between pressure oscillations and heat release 122

91. Dynamic energy iso-contours as a function of acoustic frequency response and equivalence ratio recorded by an AKG microphone 123

92. Frequency spectra at an equivalence ratio of 0.62 recorded at four axial locations 124

93. Illustration of secondary flows 126

94. Symmetry plane streamlines of a horseshoe vortex system 127

95. Comparison of turbulence models to experimental LDV measurements along the stagnation plane of a turbine vane 129

96. Resulting horseshoe and passage vortices with surface trace on the vane for a fully unstructured grid 130

97. Compressor blade endwall flow field showing the flow separation process due to hub corner stall 131

98. Fluidic oscillator sequence of switching 133

99. Fluidic oscillator schematic 133

100. Fluidic oscillator frequency response to mass flow rate and a representative time-averaged spreading angle at 0.39 g/s 134

101. Linked fluidic oscillators for (a) in-phase jets, and (b) out-of-phase jets 135

Figure Page

102. Diagram of a typical film-cooling configuration with hole detail 142

103. Coolant hole exit plane vorticity and corresponding velocity vectors highlighting secondary flows 143

104. Spatial distribution of film-cooling effectiveness at various blowing ratios 148

105. Effect of injection angle on film-cooling effectiveness 149

106. Thermal profiles along coolant hole centerline for (a) attached, (b) detached then reattached and (c) fully separated coolant flow 150

107. Graphical relationship of blowing ratio to heat flux for three equivalence ratios at $x/D = 20$ 152

108. Detailed cooling hole geometry 153

109. Hole patterns used by Shewhart et al. and Lynch et al. Free stream flow was from top to bottom. 154

110. Plan view of UCC hybrid vane section with and without a core flow divider plate 156

111. The tiger claw hybrid vane variant 157

112. Interaction of hybrid guide vane film-cooling flow with UCC cavity flow 158

113. Comparison of typical engine compressor/turbine types 159

114. Radial compressor component diagram 161

115. Radial compressor velocity triangles 161

116. Axial flow turbine stage diagram and velocity triangles 164

117. Airfoil pressure distribution 167

118. Streamlines in a nozzle with pressure distribution plot. $Q = AV$ 168

119. Comparison of mean temperature fields with (top) and without (bottom) conjugate heat transfer 183

Figure Page

120. Comparison of radial profiles of the mean temperature computed at four different downstream positions (Blue=adiabatic, red=non-adiabatic) . . . 184

121. Potential energy and vibrational levels for diatomic molecules . . . 186

122. Example convolution input arrays. Left is a small image, Right is a kernel . . . 190

123. Two common kernel arrays used in Laplacian filters . . . 191

124. LoG function and kernel . . . 192

125. LoG function response at an edge . . . 193

126. Sample PSEV processing sequence . . . 194

127. Basic PIV setup . . . 195

128. PIV image post-process . . . 196

129. Arrangement for deriving the refraction angles . . . 200

130. Dual-field-lens schlieren arrangement . . . 201

131. Z-type schlieren arrangement . . . 202

132. Z-type schlieren arrangement with light ray paths . . . 202

133. COAL Lab air supply lines . . . 206

134. Ingersroll Rand H50A-SD compressor pressure relief muffler . . . 207

135. Ethylene and propane tanks in the AFIT fuel farm . . . 208

136. Propane vaporizers . . . 208

137. Propane distribution and control . . . 209

138. Ethylene fueled torch igniter . . . 210

139. Damper selector (left) and UCC and well-stirred ventilation ducts (right) . . . 211

Figure Page

140. UCC emissions control box front side (left) back side (right) . . . 212

141. CO sensor above the UCC test stand (left) and the hallway control panel (right) . . . 212

142. COAL Lab gas sensor layout . . . 213

143. COAL Lab control station . . . 214

144. Initium pressure transducer panel and thermocouple panels . . . 216

145. Custom Labview VI for UCC control . . . 217

146. Example chemiluminescence imagery . . . 219

147. High-speed IRO mated to the Phantom v16 high-speed camera . . . 219

148. High-speed IRO chemiluminescence setup . . . 221

149. Compressed air pressurized dual shaker-type SiC particle seeder . . . 222

150. Orientation of v12 high-speed camera and UCC optical access window for PSEV measurements . . . 222

151. PIV setup, camera orientation, and beam path . . . 224

152. TFP setup, camera orientations, and filament locations . . . 225

153. IR thermography setup, camera orientations, and window placements on the left, with a sample intensity count image of the HGV on the right . . . 226

154. UCC Version 3 cross-section with dimension labels . . . 229

155. UCC Version 3 . . . 231

156. UCC Version 3 diffuser exploded view (top) and middle diameter variations (bottom) . . . 232

157. UCC Version 3 air supply to diffuser adapter photo (left) cross-section (right) . . . 233

Figure Page

158. UCC Version 3 front view (with diffuser removed) showing the air driver ring plate (left) and compound hole details (right) . . . 233

159. UCC Version 3 back wall showing optical access window and cavity instrumentation blocks . . . 234

160. UCC Version 3 low-loss centerbody hybrid guide vane . . . 235

161. UCC Version 3 fuel baffle assembled (left) and installation of fuel baffle components (right three images) . . . 235

162. UCC Version 3 mechanical seals . . . 236

163. "Wet-seal" sealants used in the COAL lab . . . 237

164. Flow patterns of hot gases from the circumferential cavity interacting with the HGV . . . 240

165. Representative test domain. Solid vane is shown shaded and gridded. The boundaries of the fluid domain are outlined in black wireframe . . . 242

166. Test domain top view showing internal vane variations: a) solid vane, b) hollow vane, c) hollow with offset plug, d) hollow with offset plug closer to inlet, e) trailing edge slot . . . 243

167. Isometric view of vane c with transparent walls to view the details of the internal plug . . . 243

168. Suction surface view of the HGV with film-cooling hole placement . . . 244

169. Grid independence check results of velocity for three grid resolutions of the solid vane test case . . . 246

170. Grid independence check results of temperature for three grid resolutions of the solid vane test case . . . 247

171. Static temperature (K) contours on an adiabatic baseline solid vane suction surface. Core flow direction is labeled . . . 250

172. Static gauge pressure (Pa) contours around the baseline solid vane. . . . 251

Figure Page

173. Static temperature (K) contours on the baseline solid vane suction surface. . . . 252

174. Static temperature (K) contours on the hollow vane suction surface. . . . 253

175. Static gauge pressure (Pa) contours around the hollow vane. . . . 254

176. Static gauge pressure (Pa) comparison of variation on the plugged vanes 256

177. Velocity vectors colored by velocity magnitude (m/s) at the vane inlet for the closer plug variant. . . . 256

178. Static temperature (K) contours on the baseline plugged vane suction surface. . . . 257

179. Static temperature (K) contours on the film-cooled vane suction surface. Both film-cooled cases produced identical results 258

180. Static gauge pressure (Pa) contours through Holes 1, 2, and 3 on the ZX plane with the baseline plug, small exit area vane 259

181. Static gauge pressure (Pa) contours on the film cooled vane suction surface 260

182. Static gauge pressure (Pa) along a line on the vane surface just below Holes 1, 2, and 3 with the baseline plug, small exit area vane 260

183. Static gauge pressure (Pa) along a line of constant radius on the baseline plug, small exit area vane surface between Holes 5 and 6 261

184. Static gauge pressure (Pa) contours through Holes 1, 2, and 3 on the ZX plane with the closer plug, small exit area vane 262

185. Static gauge pressure (Pa) along a line on the vane surface just below Holes 1, 2, and 3 with the closer plug, small exit area vane 263

Figure Page

186. Velocity vectors through Hole 1 with the closer plug, small exit area vane . . . 263

187. Static gauge pressure (Pa) along a line of constant radius on the closer plug, small exit area vane surface between Holes 5 and 6 . . . 264

188. Stagnation cooled HGV 3D solid model . . . 265

189. Manufactured cooling hole locations . . . 266

190. Manufactured HGV internal support structure . . . 267

191. Static gauge pressure (Pa) along a line of constant radius on the vane suction surface for Cases 2, 3, and 4 . . . 269

192. Overall effectiveness contours for each case . . . 273

193. Case 4 overall effectiveness with contour edges shown . . . 275

194. Case 3 and 4 heat flux contours . . . 276

195. 3D printed HGV from Linear AMS with finish machining completed by the AFIT Model Shop . . . 277

196. 3D printed HGV, painted, instrumented, and installed in the UCC (Bead locations and cooling holes are highlighted with yellow dots to be visible against the black background) . . . 279

197. Vane A computational pressure distribution at 85% axial chord . . . 282

198. Computational variation of surface temperatures with iteration at the thermocouple measurement locations for both vanes . . . 285

199. IR measured surface temperatures (K) on the solid vane and Vane A from Run 1. Hardware outlines were added for clarity . . . 288

200. IR image calibration plot using embedded thermocouple measures from the solid vane and Vane A for all three runs . . . 288

201. Vane paint following Run 1 . . . 289

Figure Page

202. Computational test domain with solid walls shaded 294

203. Front view of the computational domain showing the shift in fuel injector position for the present study 295

204. UCC cavity thermocouple block and corresponding placement in computational domain 298

205. TFP filaments installed between vanes just upstream of the vane trailing edge with computational plane comparison 299

206. Computational plane at the combustor exit to compare to thermocouple rake data 300

207. Comparison of temperature contours between the adiabatic and conjugate models showing quenching at the vane surface in the conjugate domain 301

208. Comparison of computational metal surface temperatures (K) at the 0.72 equivalence ratio condition using the adiabatic and conjugate models 302

209. Temperature contours at the 1/4, 1/2, and 3/4 axial planes within the circumferential cavity, Φ_{Cav}=0.72 304

210. Experimental results at the TFP plane, Φ_{Cav}=0.72 306

211. Adiabatic computational results at the TFP plane, Φ_{Cav}=0.72 306

212. Conjugate computational results at the TFP plane, Φ_{Cav}=0.72 306

213. Experimental results at the combustor exit plane (thermocouple rake plane) at two temperature scale, Φ_{Cav}=0.72 308

214. Computational results at the combustor exit plane (thermocouple rake plane), Φ_{Cav}=0.72 309

215. Temperature contours at the 1/4, 1/2, and 3/4 axial planes within the circumferential cavity, Φ_{Cav}=1.1 311

216. Experimental results at the TFP plane, Φ_{Cav}=1.1 313

Figure Page

217. Adiabatic computational results at the TFP plane, Φ_{Cav}=1.1 313

218. Conjugate computational results at the TFP plane, Φ_{Cav}=1.1 313

219. Experimental results at the combustor exit plane (thermocouple rake plane) at two temperature scale, Φ_{Cav}=1.1 314

220. Computational results at the combustor exit plane (thermocouple rake plane), Φ_{Cav}=1.1 315

221. Turkey feather variable diffuser 319

222. Single feather shape 320

223. Cross-section of variable diffuser and actuation system (block restrictor plate and stepper motor removed for visibility) 321

224. Cross-sections of iterations of the ceramic insulator disc 322

225. Variable diffuser installed on the UCC 323

226. Variable diffuser adapter o-ring seal (left), adapter cross-section (right) 323

227. Velocity profile at a diffuser reference station with approximately equal channel heights 326

228. Gauge static pressure (Pa) distribution in a cross sectional plane of the UCC with variable diffuser at a 70/30 core-to-cavity area split 327

229. Diffuser core passage pitot/static measurement plane 328

230. Example section of a look-up table 330

231. Diffuser total/static differential pressure measurement display 331

232. Experimental results of the relationship between diffuser feather position and cavity mass flow split percentage for a cavity equivalence ratio of 0.8. Numbers along the top of the figure show the core/cavity geometric area split related to the diffuser position. 334

233. Experimental results of the relationship between diffuser feather position and average cavity tangential and radial velocities for a cavity equivalence ratio of 0.8. Numbers along the top of the figure show the core/cavity geometric area split related to the diffuser position. 334

234. Comparison of cavity temperatures with the baseline fixed position and variable diffuser at a total inlet mass flow rate of 0.108 kg/s at a 74/26 core-to-cavity mass flow split. 336

235. Experimental exit temperature profiles (K) for 0.037 kg/s constant cavity mass flow rate and cavity $\Phi = 0.72$ 341

236. Frame montage from the high-speed OH chemiluminescence video from $\dot{m} = 0.108$ kg/s, cavity $\Phi = 0.72$, showing uniform OH intensity pulsation across the entire field of view 342

237. Frame montage from the high-speed OH chemiluminescence video from $\dot{m} = 0.108$ kg/s, cavity $\Phi = 1.1$, showing flames propagating from the upper right of the field of view and traveling to the lower left. White arrow indicates the direction of air injection and bulk fluid swirl 344

238. Experimental exit temperature profiles (K) for 0.037 kg/s constant cavity mass flow rate and cavity $\Phi = 1.1$ 345

239. Chemiluminescence frequency measurements for the 74/26 core-to-cavity flow split cases at cavity $\Phi = 0.72$ 347

240. Experimental exit temperature profiles (K) for the 74/26 core-to-cavity flow split cases at cavity $\Phi = 0.72$ 348

241. Chemiluminescence frequency measurements for the 74/26 core-to-cavity flow split cases at cavity $\Phi = 1.1$ 350

Figure Page

242. Experimental exit temperature profiles (K) for the 74/26 core-to-cavity flow split cases at cavity Φ = 1.1 351

243. 6-Step Ring air and fuel injector ducting and hole pattern 352

244. Version 3 UCC with variable geometry diffuser and 6-Step Ring 353

245. Modified back plate with angled fuel injectors concept 354

246. 6-Step Ring front air driver plate hole patterns 355

247. Temperature contours (K) on the half cavity plane of the Baseline combustor and the 6-Step Ring combustor with Hole Pattern 1 at cavity Φ=0.72 357

248. Temperature contours (K) on the half cavity plane of the Baseline combustor and the 6-Step Ring combustor with Hole Pattern 2 at cavity Φ=0.72 358

249. Tangential velocity contours (m/s) on the half cavity plane of the Baseline combustor and the 6-Step Ring combustor with Hole Pattern 2 at cavity Φ=0.72 359

250. Temperature contours (K) on the half cavity plane of the 6-Step Ring combustor with Hole Pattern 2 at stoichiometric and rich cavity equivalence ratios 360

251. Fully arrayed computational domain showing back wall injectors 361

252. Temperature contours (K) on the half cavity plane of the 6-Step Ring combustor with Hole Pattern 2 with and without back wall fuel injection at a cavity equivalence ratio of 1.3 362

253. Temperature contours (K) on the half cavity plane of the 6-Step Ring combustor with Hole Pattern 2 with and without back wall fuel injection at a cavity equivalence ratio of 0.72 362

254. 3D printed 6-Step Ring hardware 364

255. Modified baseline front air driver plate to replicate Hole Pattern 2, diffuser side view 365

Figure Page

256. Redesigned cavity back plate with back wall fuel injectors 366

257. PIV seed supply location upstream of the diffuser inlet 367

258. Cold flow PIV tangential velocity contours (m/s) in the circumferential cavity 369

259. Review of CFD contours for the 6-Step Ring combustor with Hole Pattern 2 at a cavity equivalence ratio of 0.72 370

260. Average cavity temperatures (K) at increasing cavity equivalence ratios with and without back wall fuel injection at a total air flow rate of 0.06 kg/s 371

261. Average cavity temperatures (K) at increasing cavity equivalence ratios with and without back wall fuel injection at a total air flow rate of 0.09 kg/s 371

262. Experimental exit plane temperature contours (K) at 0.72 and 1.4 cavity equivalence ratios with and without back wall fuel injection at a total air flow rate of 0.06 kg/s 373

263. Experimental exit plane temperature contours (K) at 0.72 and 1.4 cavity equivalence ratios with and without back wall fuel injection at a total air flow rate of 0.09 kg/s 374

264. 6-Step Ring air injector velocity profiles using different boundary conditions 378

265. Computational temperature contours (K) and velocity magnitude contours (m/s) around a 6-Step Ring air injector with three different boundary conditions 379

266. 3D printed 12-Step Ring hardware 380

267. 12-Step Ring air and fuel injector ducting 381

268. Tangential velocity contours (m/s) on the half cavity plane of the 12-Step Ring combustor. 74/26 core-to-cavity flow split, 50/50 front wall-to-step cavity air split 382

269. Temperature contours (K) on the half cavity plane of the 12-Step Ring combustor at an equivalence ratio of 0.72 at two different air split configurations 382

Figure Page

270. Average cavity temperatures for the Baseline and 12-Step combustor as a function of cavity equivalence ratio 386

271. Experimental exit plane temperature contours (K) from the 12-Step and Baseline combustors at approximately 0.108 kg/s total air flow rate at global equivalence ratios approximating 0.20, 0.31, and 0.36 389

272. Average cavity and exit temperatures in the 12-Step combustor as a function of step fuel balance 393

273. Average exit temperature (K) operating map at $\dot{m}_{in} = 0.108kg/s$, 0% back wall fuel injection 396

274. Average exit temperature (K) operating map at $\dot{m}_{in} = 0.060kg/s$, 0% back wall fuel injection 397

275. Average exit temperature (K) operating map at $\dot{m}_{in} = 0.120kg/s$, 0% back wall fuel injection 398

276. Flooded contours of dominant audible frequency (Hz) with unfilled labeled contours of sound pressure level (dB) at $\dot{m}_{in} = 0.108kg/s$, 0% back wall fuel injection 399

278. Flooded contours of dominant audible frequency (Hz) with unfilled labeled contours of sound pressure level (dB) at $\dot{m}_{in} = 0.120kg/s$, 0% back wall fuel injection 399

277. Flooded contours of dominant audible frequency (Hz) with unfilled labeled contours of sound pressure level (dB) at $\dot{m}_{in} = 0.060kg/s$, 0% back wall fuel injection 400

279. 4D temperature operating maps of the 12-Step combustor at $\dot{m}_{in} = 0.108kg/s$ 402

280. 4D acoustic operating maps of the 12-Step combustor at $\dot{m}_{in} = 0.108kg/s$ 403

281. 4D temperature operating maps of the 12-Step combustor at $\dot{m}_{in} = 0.060kg/s$ 404

282. 4D acoustic operating maps of the 12-Step combustor at $\dot{m}_{in} = 0.060kg/s$ 405

Figure Page

283. 4D temperature operating maps of the 12-Step combustor at $\dot{m}_{in} = 0.120kg/s$ 406

284. 4D acoustic operating maps of the 12-Step combustor at $\dot{m}_{in} = 0.12kg/s$ 407

285. Average velocity (m/s) operating map at $\dot{m}_{in} = 0.060kg/s$, 0% back wall fuel injection 411

286. Average velocity (m/s) operating map at $\dot{m}_{in} = 0.108kg/s$, 0% back wall fuel injection 411

287. Average velocity (m/s) operating map at $\dot{m}_{in} = 0.120kg/s$, 0% back wall fuel injection 412

288. Average velocity (m/s) and Rayleigh loss operating map at $\dot{m}_{in} = 0.108kg/s$, 0% - 30% back wall fuel injection 414

289. Iso-surface of OH mass fraction at 1/3 maximum value, colored by tangential velocity (m/s), in the UCC configured with an 80% core split, and 66% front wall split at $\dot{m}_{in} = 0.108kg/s$, 0% back wall fuel injection 417

290. Average cavity temperature (K) operating map at $\dot{m}_{in} = 0.108kg/s$, 0% back wall fuel injection, $\Phi_{global} =$ 0.32 419

291. Average exit temperature (K) operating map at $\dot{m}_{in} = 0.108kg/s$, 0% back wall fuel injection, $\Phi_{global} =$ 0.32 419

292. Average cavity temperature (K) operating map at $\dot{m}_{in} = 0.108kg/s$, 0% back wall fuel injection, $\Phi_{global} =$ 0.28 420

293. Average exit temperature (K) operating map at $\dot{m}_{in} = 0.108kg/s$, 0% back wall fuel injection 420

294. Modified chemiluminescence setup for use with exhaust box 422

295. Flow behavior in the 12-Step combustor with no fuel injection from the stabilizing steps 425

Figure Page

296. Temperature contours (K) on the three-quarter cavity plane of the 12-Step Ring combustor. 80/20 core-to-cavity flow split, 66/33 front wall-to-step cavity air split 426

297. Air jet velocity from the fuel/air steps at $\dot{m}_{in} = 0.060kg/s$ 427

298. Air jet velocity from the fuel/air steps at $\dot{m}_{in} = 0.108kg/s$ 428

299. Air jet velocity from the fuel/air steps at $\dot{m}_{in} = 0.120kg/s$ 428

300. Fluidic oscillator Version 1 434

301. Fluidic oscillator Version 1 2D transient results showing the jet at maximum travel 435

302. Fluidic oscillator Version 2 shown in red compared to the Version 1 oscillator in black 436

303. Contours of velocity showing V2 Single oscillators at sweep extremes 437

304. Linked pairs of oscillators 438

305. Contours of velocity showing V2 Double oscillators at sweep extremes 439

306. Contours of velocity showing V3 Double oscillators at sweep extremes 439

307. Representative domain for 3D computational analysis 440

308. Comparison of the oscillator model to the 12-Step Ring 441

309. Interchangeable model upper halves shown for the V2 Single oscillator 442

310. Oscillators printed into the model base 443

311. Proof of concept schlieren setup in the AFIT COAL laboratory with light ray paths shown 445

Figure Page

312. Z-type schlieren setup in the AFRL Discovery wind tunnel facility with light ray paths shown 446

313. Model installed in wind tunnel 447

314. Pressure transducer based frequency calculation setup 447

315. Baseline non-oscillating parallel jets, time-averaged composite images at the lowest and highest CO_2 flow rates and three model and wind tunnel configurations 452

316. Secondary circulation behavior observed with the baseline non-oscillating parallel jets using a time-averaged composite image with the model in its original orientation and flipped over 453

317. Secondary circulation pattern observed behind backward-facing steps with injection 454

318. No secondary circulation behavior observed at slower wind tunnel speeds 455

319. Jet spread angle measurements for the baseline non-oscillating parallel jets using a time-averaged composite image at the lowest and highest CO_2 flow rates with 0 m/s wind tunnel speed 455

320. V2 Single oscillator, time-averaged composite images at the lowest and highest CO_2 flow rates and three model and wind tunnel configurations 456

321. V2 Single oscillator time-averaged composite image at the lowest and highest CO_2 flow rates with 0 m/s wind tunnel speed 457

322. V2 Single oscillator instantaneous maximum oscillation angles measured at the jet centerlines at the lowest and highest CO_2 flow rates with 0 m/s wind tunnel speed 458

323. V2 Double linked oscillator, time-averaged composite images at the lowest and highest CO_2 flow rates and three model and wind tunnel configurations 459

324. V2 Double linked oscillator time-averaged composite image at the lowest and highest CO_2 flow rates with 0 m/s wind tunnel speed 461

325. V2 Double linked oscillator instantaneous maximum oscillation angles measured at the jet centerlines at the lowest and highest CO_2 flow rates with 0 m/s wind tunnel speed 462

326. Baseline, non-oscillating jets, time-averaged composite images at a CO_2 flow rate of 4.75 SLPM (8.1 m/s jet velocity) with the fuel only step model 464

327. Baseline, non-oscillating jets, time-averaged composite images at a CO_2 flow rate of 7.96 SLPM (13.5 m/s jet velocity) with the fuel only step model 465

328. V2 Single oscillator, time-averaged composite images at a CO_2 flow rate of 4.75 SLPM (19.1 m/s jet velocity) with the fuel only step model 467

329. V2 Single oscillator, time-averaged composite images at a CO_2 flow rate of 2.08 SLPM (8.4 m/s jet velocity) with the fuel only step model 468

330. V2 Double linked oscillator, time-averaged composite images at a CO_2 flow rate of 4.75 SLPM (19.1 m/s jet velocity) with the fuel only step model 469

331. V2 Double linked oscillator, time-averaged composite images at a CO_2 flow rate of 2.11 SLPM (8.5 m/s jet velocity) with the fuel only step model 470

332. Correlation of jet penetration depth into the freestream relative to velocity ratio 471

333. Experimental oscillator frequency measurements taken from high-speed video files and pressure transducers plotted with CFD calculated frequency points 472

334. Correlation of oscillator frequency to a non-dimensional correlation factor 474

335. Correlation of oscillator angle to a hydraulic diameter scaled Reynold Number (RE_D) 475

Figure Page

336. Flow pattern at HGV trailing edges as shown by seeder dust. Tangent lines from the centerbody are shown to highlight the flow path. . . . 481

337. JetCat P90RXi cross-section with fluid flow path (stock combustor liner shown in orange) . . . 482

338. JetCat P90RXi cross-section with Configuration 6 combustor installed and compared to the stock combustor (shown in orange) . . . 483

339. Representative computational domain, shown for Configuration 6, with boundary conditions labeled . . . 484

340. Initial combustor design, Configuration 1, grid independence check test locations on 30° sector domain . . . 489

341. Combustor Configuration 1 . . . 492

342. Temperature contours (K) at multiple reference planes in combustor Configuration 1 . . . 493

343. Combustor Configuration 2 . . . 495

344. Fuel distribution in the stabilizing backward-facing steps (Results from C2). Colored by propane mass fraction . . . 496

345. Combustor Configuration 3 . . . 497

346. Fuel distribution in the stabilizing backward-facing steps with fences (Results from C3). Colored by propane mass fraction . . . 498

347. Combustor Configuration 4 . . . 500

348. Fuel distribution in backward-facing steps on the combustor forward wall (Results from C4). Colored by propane mass fraction . . . 501

349. Combustor Configuration 5 . . . 502

350. Comparison of single vs. dual chamber combustors . . . 503

351. Configuration 5 cross-section with secondary/dilution air inlet holes labeled by blue arrows . . . 504

Figure Page

352. Combustor Configuration 6 507

353. Combustor Configuration 7 509

354. Temperature contours (K) showing flames anchored to steps (Results from C6) 513

355. Secondary/dilution air layering. Temperature contours on periodic walls of combustor C4 515

356. Circumferentially averaged temperatures on the combustor exit plane for all configurations 516

357. Comparison of single vs. dual chamber combustors 517

358. Temperature contours (K) in dual chamber Combustor Configuration 6 518

359. Temperature contours (K) in Combustor Configuration 7 with primary zone exit diffuser and larger secondary/dilution zone volume 519

360. Contours of velocity angle (deg) on the combustor exit plane and circumferentially averaged velocity angles from Configurations 5, 6, and 7 520

361. Cavity equivalence ratio at blowout as a function of centrifugal loading with operating conditions plotted 523

362. Temperature contours (K) at approximately 66% axially in the Configuration 7 primary zone 524

363. Tangential velocity contours (m/s) at approximately 66% axially in the Configuration 7 primary zone 525

364. Configuration 7, 100K RPM operating condition circumferentially averaged combustor exit plane temperature profiles variation with iteration 526

365. Configuration 7 circumferentially averaged combustor exit plane temperature profiles at all four operating conditions for first and second order solutions 527

366. Temperature contours (K) on the Configuration 7 exit plane downstream of the nozzle guide vanes 529

Figure Page

367. Second order temperature contours (K) on the YZ plane in the Configuration 7 combustor at the 100K RPM condition . . . 531

368. Second order contours of OH mass fraction on the YZ plane in the Configuration 7 combustor at the 100K RPM condition . . . 531

369. Second order gauge total pressure contours (Pa) on the YZ plane in the Configuration 7 combustor at the 100K RPM condition . . . 532

370. Three primary components of the Configuration 7 manufactured combustor . . . 533

371. Configuration 7 manufactured hardware air inlet hole geometry modification . . . 534

372. Configuration 7 manufactured hardware ID air scoop modification . . . 535

373. Configuration 7 with stock JetCat glow plug installed through the combustor forward wall . . . 536

374. Configuration 7 with new filament glow plug installed through the combustor forward wall . . . 538

375. Configuration 7 experimental hardware fuel distribution system . . . 539

376. Configuration 7 ID and OD component hole schedule . . . 540

377. Custom and stock hardware needed for experimental validation testing . . . 542

378. Configuration 7 installed in JetCat and configured for testing with no rotating hardware . . . 543

379. Remainder of the combustor test setup with no rotating hardware . . . 544

380. Propane distribution manifold external to the engine . . . 544

381. Experimental temperature and pressure measurement locations . . . 545

Figure Page

382. Internal inspection camera 547

383. Thermocouple rake positioning at the JetCat exhaust 548

384. As printed combustor installed int he JetCat casing. A 1 mm gap is visible between the OD air inlets and the casing 549

385. 0.98 mm Version 1 OD aluminum shim. The combustor was not pushed all the way into the engine casing get a better view of the shim and how it mated to the casing and combustor. 552

386. Test Series Two results of temperature (K) at an air flow rate of 0.030 kg/s and variable fuel flow rate with the Version 1 Shim 553

387. Test Series Two results of temperature (K) at an air flow rate of 0.054 kg/s and variable fuel flow rate with the Version 1 Shim 554

388. Thermocouple rake temperature (K) measurements with radial movement. Air flow rate 0.030 kg/s, fuel flow rate 15 SLPM, circumferential position fixed at -40°. 555

389. Thermocouple rake temperature (K) measurements with radial movement. Air flow rate 0.030 kg/s, fuel flow rate 15 SLPM, circumferential position fixed at 0°. 556

390. Thermocouple rake temperature (K) measurements with radial movement. Air flow rate 0.030 kg/s, fuel flow rate 15 SLPM, circumferential position fixed at +40° 556

391. Thermocouple rake temperature (K) measurements with radial movement. Air flow rate 0.054 kg/s, fuel flow rate 22 SLPM, circumferential position fixed at 0°. 557

392. Version 2 shim installed on the Configuration 7 combustor (30% blockage) 559

393. OD blockage inserts 559

394. Version 2 shim installed with 70% blockage inserts 560

Figure Page

395. Variation in the T_{C1} combustor primary zone temperature measurement with increasing blockage at an air flow rate of 0.030 kg/s 562

396. Variation in the average T_4 combustor exit temperature measurement with increasing blockage at an air flow rate of 0.030 kg/s 563

397. Variation in the T_{C1} combustor primary zone temperature measurement with increasing blockage at an air flow rate of 0.054 kg/s 564

398. Variation in the average T_4 combustor exit temperature measurement with increasing blockage at an air flow rate of 0.054 kg/s 564

399. Variation in the P_3 pressure measurement with increasing blockage at an air flow rate of 0.030 kg/s 565

400. Variation in the P_3 pressure measurement with increasing blockage at an air flow rate of 0.054 kg/s 566

401. Cold flow pressure measurements at Stations 2, 3, and 4 with 75% blockage inserts at varied air flow rates 567

402. Configuration 7 experimentally combusting at a global equivalence ratio of 0.31 with 70% blockage 568

403. Configuration 7 experimentally derived exit temperature contours at a global equivalence ratio of 0.31 with 70% blockage 569

404. Configuration 7 experimentally derived exit temperature contours at a global equivalence ratio of 0.31 with 70% blockage repeated 569

405. Configuration 7 experimentally derived circumferentially averaged exit temperature profiles for a repeated test point at a global equivalence ratio of 0.31 with 70% blockage 570

406. Rotating hardware components installed into the JetCat (Compressor left, Turbine right) 575

407. Pump, solenoid, and fittings in the modified JetCat 576

Figure Page

408. Lubrication fittings and the redesigned electronics engine board installed on the JetCat compressor shroud 577

409. Completed engine assembly. Flow is from right to left 577

410. Lubricant pump calibration setup 578

411. Pump calibration test results 579

412. Relationship between propane flow rate and required pump duty cycle 580

413. Custom plenum to use the stock fuel lines used in pump calibration and return the fuel to the kerosene reservoir 581

414. Safety enclosure and test stand closed position 582

415. Safety enclosure and test stand opened position 582

416. Orientation of the air start nozzle to the JetCat engine cowling 584

417. Objective 5 temperature and pressure instrumentation locations 586

418. Stations 2, 5, and 7 visible temperature and pressure instrumentation 586

419. Internal engine camera left, internal safety enclosure camera right 588

420. Temperatures at all JetCat stations during a ramping test from engine start to the 1/2 idle condition 590

421. Pressures at all JetCat stations during a ramping test from engine start to the 1/2 idle condition 592

422. Calculated global equivalence ratio with the Configuration 7 combustor during all rotating tests. Non-rotating, CFD, and stock JetCat global equivalence ratios are also shown for comparison 597

423. Contact marks visible on the compressor rotor tips 598

Figure Page

424. Engine thrust with the Configuration 7 combustor during all rotating tests . . . 599

425. Calculated engine mass flow rate with the Configuration 7 combustor during all rotating tests. Non-rotating and CFD mass flow rates are also shown for comparison . . . 600

426. A reflected view up the engine nozzle during operation at 19 SLPM of propane, 19,000 RPM . . . 601

427. Time-dependent temperature and RPM data during self-sustaining operation at 14 SLPM of propane, 14,100 RPM . . . 603

428. Compressor and turbine pressure ratios from a stock JetCat P90RXi and the Configuration 7 combustor with rotating hardware . . . 604

429. Compressor and turbine temperature ratios from a stock JetCat P90RXi and the Configuration 7 combustor with rotating hardware . . . 606

430. Thrust from a stock JetCat P90RXi and the Configuration 7 combustor with rotating hardware . . . 607

431. Thrust specific fuel consumption from a stock JetCat P90RXi and the Configuration 7 combustor with rotating hardware . . . 608

432. Air mass flow rate through a stock JetCat P90RXi and the Configuration 7 combustor with rotating hardware . . . 609

433. Compressor efficiency in a stock JetCat P90RXi and the Configuration 7 combustor with rotating hardware . . . 609

434. Global equivalence ratio in a stock JetCat P90RXi and the Configuration 7 combustor with rotating hardware . . . 610

435. Turbine inlet temperature in a stock JetCat P90RXi and the Configuration 7 combustor with rotating hardware . . . 613

436. Exit temperature in a stock JetCat P90RXi and the Configuration 7 combustor with rotating hardware . . . 614

Figure Page

437. Exit velocity in a stock JetCat P90RXi and the Configuration 7 combustor with rotating hardware 615

438. Flameout study temperature and pressure instrumentation locations 616

439. Cold flow pressures at fixed 0.03 kg/s air flow rate and ramping fuel flow rate 620

440. Reacting flow pressures at fixed 0.03 kg/s air flow rate and ramping fuel flow rate 621

441. Reacting flow temperatures and pressures at a fixed 17 SLPM fuel flow rate with ramping air flow rate 622

442. Reacting flow temperatures and pressures at a fixed 18 SLPM fuel flow rate with ramping air flow rate 623

443. Reacting flow pressure differentials and calculated quantities at fixed 0.03 kg/s air flow rate and ramping fuel flow rate 625

444. Reacting flow temperatures at fixed 0.03 kg/s air flow rate and ramping fuel flow rate 626

445. Configuration 7 primary zone cross-section with flame holders and fuel injectors identified. Combustor cross-section shows the path of travel when reactions were pushed from the primary zone 627

446. Reacting flow pressure differentials at a fixed 18 SLPM fuel flow rate with ramping air flow rate 628

447. High-speed and time synced combustor data 630

448. Primary zone (T_{C1}) and turbine inlet (T_{4avg}) temperatures at variable fuel and air flow rates with ID and OD fuel injection 631

449. Primary zone (T_{C1}) and turbine inlet (T_{4avg}) temperatures at variable fuel and air flow rates with OD only fuel injection 632

450. Primary zone (T_{C1}) and turbine inlet (T_{4avg}) temperatures at variable fuel and air flow rates with ID only fuel injection 633

Figure Page

451. Temperature contours (K) of primary zone temperatures (T_{C1}) with ID and OD fuel distribution control 634

452. Temperature contours (K) of the average turbine inlet temperature (T_{4avg}) with ID and OD fuel distribution control 635

453. Electronics setup wiring diagram 658

454. Xloader screen shot 659

455. 24V power supply pin-outs 660

456. Stepper motor 661

457. Stepper motor wire diagram detail 661

458. Reverse side of a Raspberry Pi touchscreen 663

459. Raspberry Pi touchscreen setup 664

460. Universal G-code Sender screen shot 665

461. Universal G-code Sender screen shot, Machine Control tab 666

462. Position sensor power supply circuit wire diagram and hardware photo 668

463. Position sensor wire breakout 669

464. D-sub connector pin numbering 670

465. Thermocouple rake assembly 672

466. Thermocouple rake probe 673

467. Probe head dimensions and internal channels 674

468. Actuator assembly downstream view 675

469. Actuator assembly upstream view 675

470. Linear actuator detail (radial movement) 676

471. Thermocouple rake actuator gearbox 677

Figure Page

472. Actuator movement limits 678

473. Probe head positioning. Each number block represents one of the four thermocouples. Each new set of blocks represents the position after a radial movement. Upper and lower horizontal lines show the bounds of the exhaust channel. 679

474. Thermocouple rake post-process input file 681

475. Example thermal contour plots using the low loss center body vane and the dual backstep vane with the course method and 10° circumferential spacing 686

476. Thermocouple rake probe 687

477. Required Diffuser Pressure Differential (ΔP) Map, $\dot{m}_{in} = 0.060 kg/s$ 688

478. Average cavity temperature (K) operating map at $\dot{m}_{in} = 0.060 kg/s$, 0% back wall fuel injection 689

479. Average exit temperature (K) operating map at $\dot{m}_{in} = 0.060 kg/s$, 10% back wall fuel injection 689

480. Average cavity temperature (K) operating map at $\dot{m}_{in} = 0.060 kg/s$, 10% back wall fuel injection 690

481. Flooded contours of dominant audible frequency (Hz) with unfilled labeled contours of sound pressure level (dB) at $\dot{m}_{in} = 0.060 kg/s$, 10% back wall fuel injection 690

482. Average exit temperature (K) operating map at $\dot{m}_{in} = 0.060 kg/s$, 20% back wall fuel injection 691

483. Average cavity temperature (K) operating map at $\dot{m}_{in} = 0.060 kg/s$, 20% back wall fuel injection 691

484. Flooded contours of dominant audible frequency (Hz) with unfilled labeled contours of sound pressure level (dB) at $\dot{m}_{in} = 0.060 kg/s$, 20% back wall fuel injection 692

485. Average exit temperature (K) operating map at $\dot{m}_{in} = 0.060 kg/s$, 30% back wall fuel injection 692

Figure Page

486. Average cavity temperature (K) operating map at $\dot{m}_{in} = 0.060kg/s$, 30% back wall fuel injection 693

487. Flooded contours of dominant audible frequency (Hz) with unfilled labeled contours of sound pressure level (dB) at $\dot{m}_{in} = 0.060kg/s$, 30% back wall fuel injection 693

488. Required Diffuser Pressure Differential (ΔP) Map, $\dot{m}_{in} = 0.108kg/s$ 694

489. Average cavity temperature (K) operating map at $\dot{m}_{in} = 0.108kg/s$, 0% back wall fuel injection 695

490. Average exit temperature (K) operating map at $\dot{m}_{in} = 0.108kg/s$, 10% back wall fuel injection 695

491. Average cavity temperature (K) operating map at $\dot{m}_{in} = 0.108kg/s$, 10% back wall fuel injection 696

492. Flooded contours of dominant audible frequency (Hz) with unfilled labeled contours of sound pressure level (dB) at $\dot{m}_{in} = 0.108kg/s$, 10% back wall fuel injection 696

493. Average exit temperature (K) operating map at $\dot{m}_{in} = 0.108kg/s$, 20% back wall fuel injection 697

494. Average cavity temperature (K) operating map at $\dot{m}_{in} = 0.108kg/s$, 20% back wall fuel injection 697

495. Flooded contours of dominant audible frequency (Hz) with unfilled labeled contours of sound pressure level (dB) at $\dot{m}_{in} = 0.108kg/s$, 20% back wall fuel injection 698

496. Average exit temperature (K) operating map at $\dot{m}_{in} = 0.108kg/s$, 30% back wall fuel injection 698

497. Average cavity temperature (K) operating map at $\dot{m}_{in} = 0.108kg/s$, 30% back wall fuel injection 699

498. Flooded contours of dominant audible frequency (Hz) with unfilled labeled contours of sound pressure level (dB) at $\dot{m}_{in} = 0.108kg/s$, 30% back wall fuel injection 699

499. Required Diffuser Pressure Differential (ΔP) Map, $\dot{m}_{in} = 0.120kg/s$ 700

Figure Page

500. Average cavity temperature (K) operating map at $\dot{m}_{in} = 0.120kg/s$, 0% back wall fuel injection 701

501. Average exit temperature (K) operating map at $\dot{m}_{in} = 0.120kg/s$, 10% back wall fuel injection 701

502. Average cavity temperature (K) operating map at $\dot{m}_{in} = 0.120kg/s$, 10% back wall fuel injection 702

503. Flooded contours of dominant audible frequency (Hz) with unfilled labeled contours of sound pressure level (dB) at $\dot{m}_{in} = 0.120kg/s$, 10% back wall fuel injection 702

504. Average exit temperature (K) operating map at $\dot{m}_{in} = 0.120kg/s$, 20% back wall fuel injection 703

505. Average cavity temperature (K) operating map at $\dot{m}_{in} = 0.120kg/s$, 20% back wall fuel injection 703

506. Flooded contours of dominant audible frequency (Hz) with unfilled labeled contours of sound pressure level (dB) at $\dot{m}_{in} = 0.120kg/s$, 20% back wall fuel injection 704

507. Average exit temperature (K) operating map at $\dot{m}_{in} = 0.120kg/s$, 30% back wall fuel injection 704

508. Average cavity temperature (K) operating map at $\dot{m}_{in} = 0.120kg/s$, 30% back wall fuel injection 705

509. Flooded contours of dominant audible frequency (Hz) with unfilled labeled contours of sound pressure level (dB) at $\dot{m}_{in} = 0.120kg/s$, 30% back wall fuel injection 705

510. Stock Electronics 707

511. Redesigned JetCat electronics, instrumentation, and control system overview 708

512. Redesigned ECM schematic diagram, V2 Edited 710

513. Redesigned ECM board layout, V2 Edited 711

514. Redesigned ECM completed hardware layer 1, V2 Edited 711

515. Redesigned ECM completed hardware layer 16, V2 Edited 712

Figure Page

516. Fully assembled ECM 712

517. Typical connections of the DRV8871-Q1 TI motor driver 714

518. Typical connections of the LM338 TI adjustable voltage regulator 715

519. PWM duty cycle comparison 716

520. LTC6992CDCB-1 resistor requirements to achieve a 2.6kHz PWM output 717

521. PWM Gen board schematic diagram 718

522. PWM Gen board layout diagram 718

523. PWM Gen board manufactured hardware 719

524. Pin numbering for connections IO1 and IO2 721

525. Pin numbering for connections IO3 and IO4 722

526. Pin numbering for connection IO5 724

527. Redesigned Engine Board schematic diagram, V2 726

528. Redesigned Engine Board layout, V2 727

529. Redesigned Engine Board completed hardware layer 1, V2 727

530. Redesigned Engine Board completed hardware layer 16, V2 728

531. Simple inductor circuit with a flyback diode 729

532. RPM module reused from stock JetCat P90RXi 732

533. Typical application of the HAL401SF-K hall effect IC 732

534. Output voltage measurements from RPM Module outputs 1 and 2 733

535. Pin numbering for Engine Board connection IO3, IO6, and IO7 734

536. Pin numbering for connection IO8 736

Figure Page

537. Pin numbering for connections IO9 and IO10 737

538. BK Precision Model 1688B switching mode power supply (1-18V, 0-20A output) for glow plug power 738

539. BK Precision power supply remote control connector pins 739

540. Types of glow plugs used in Objectives 4 and 5 740

541. Glow plug power supply voltage feedback circuit 741

542. Glow plug power wire connectors 741

543. Dedicated JetCat thermocouple panel 742

544. Thrust sensor and pressure transducer power conditioning boards 743

545. Thrust sensor - Interface Force S-Type, Model SM-50 wiring 744

546. Engine thrust sensor calibration curve 745

547. Pressure transducer block assembly and transducer numbering 746

548. Pressure transducer calibration curves with 10V excitation 748

549. Custom JetCat LabView VI 749

List of Tables

Table		Page
1.	Pollutant types and examples	35
2.	Distribution of total emission mass quantities generated during a typical flight profile of a twin-engine transport over a 500 nautical mile range	36
3.	UCC turbine vane spacing and circumferential cavity inlet port specifications per test section	82
4.	Domain air inlet port variations	82
5.	Operating parameters used in preliminary analysis for engine condition and rig condition for complete annulus	83
6.	UCC Version 3 Dimensions	230
7.	Grid resolutions of CFD case domains	245
8.	Inlet boundary condition settings	249
9.	Mass flow rates through the plugged vane variations	255
10.	Fluid properties for cooling holes with exiting flow using the baseline plug, small exit area vane	261
11.	Fluid properties for cooling holes with exiting flow using the closer plug, small exit area vane	264
12.	Manufactured HGV cooling schemes by vane	265
13.	Manufacturing study CFD cases	268
14.	Film-cooling hole locations and computational blowing ratio results	271
15.	Minimum effectiveness and corresponding surface temperature, with point measurement values at 88% axial chord and 64% radial span	272
16.	Thermocouple bead locations in IR image coordinate system (required for calibration)	278

Table Page

17. Vane A pressure drop measurement data from the vane leading edge to the internal pressure tap at approximately 85% axial chord 280

18. Vane A pressure drop measurement data from internal vane to the external suction surface across the vane shell at approximately 85% axial chord 283

19. Average computational and experimentally measured temperatures at the 60% and 90% radial span for the solid vane and Vane A 283

20. Inlet/Exit boundary condition settings 297

21. Wall temperature boundary conditions 297

22. Adiabatic model circumferential cavity temperature results compared to experimental data, Φ_{Cav}=0.72 303

23. Conjugate model circumferential cavity temperature results compared to experimental data, Φ_{Cav}=0.72 303

24. Adiabatic model circumferential cavity temperature results compared to experimental data, Φ_{Cav}=1.1 310

25. Conjugate model circumferential cavity temperature results compared to experimental data, Φ_{Cav}=1.1 310

26. Off-the-shelf wear items on the diffuser 324

27. Temperature, velocity, dominant frequency and amplitude, and Rayleigh losses for 0.037 kg/s constant cavity mass flow rate and cavity $\Phi = 0.72$ 340

28. Temperature, velocity, dominant frequency and amplitude, and Rayleigh losses for 0.037 kg/s constant cavity mass flow rate and cavity $\Phi = 1.1$ 343

29. Temperature, velocity, g-load, dominant frequency and amplitude, and Rayleigh losses for 74/26 core-to-cavity flow splits and cavity $\Phi = 0.72$ 346

30. Temperature, velocity, g-load, dominant frequency and amplitude, and Rayleigh losses for 74/26 core-to-cavity flow splits and cavity $\Phi = 1.1$ 348

Table Page

31. 6-Step Ring Inlet/Exit boundary condition settings . . . 356

32. Heat flux boundary conditions . . . 376

33. Cool temperature boundary conditions . . . 376

34. Step injection and bulk velocities calculated for each boundary condition . . . 377

35. 12-Step Ring Comparison Test Cases . . . 385

36. 12-Step and Baseline combustor exit plane performance . . . 387

37. 12-Step Ring fuel split evaluation test points . . . 392

38. 12-Step combustor airflow split characterization test points . . . 394

39. 12-Step combustor characterization fuel distributions for Φ_{global}=0.36 . . . 395

40. 12-Step combustor velocity measurement test points . . . 410

41. 12-Step combustor acoustic comparison to chemiluminescence frequency . . . 413

42. 12-Step combustor acoustic comparison to chemiluminescence frequency . . . 415

43. Additional 12-Step combustor airflow split characterization test points . . . 418

44. Exhaust configuration test matrix . . . 422

45. Fluidic oscillator series one test matrix for each model type . . . 450

46. Grid resolutions of new UCC combustor CFD case domains . . . 485

47. Inlet/Outlet boundary condition settings for a 30° sector domain . . . 487

48. Combustor Configuration 7 detailed analysis operating conditions . . . 521

Table Page

49. Combustor Configuration 7 second order average temperatures, tangential velocities, and centrifugal loading in the primary zone 522

50. Combustor Configuration 7 second order average temperature, pattern factors, average velocity magnitude, and average velocity angle at the combustor exit plane 528

51. Combustor Configuration 7 second order gauge static and total pressures and absolute losses across the combustor, and across the combustor and nozzle guide vanes 530

52. Combustor Configuration 7 experimental instrumentation details (Temperature (T) and pressure (P) measurements were static) 546

53. Fuel flow rate limits (SLPM) to maintain combustion at each blockage level 561

54. JetCat with combustor Configuration 7 instrumentation details 587

55. Comparison of pressures from the non-rotating stand along combustor testing from Objective 4 to present rotating testing 592

56. Average temperatures and pressures at each engine station with corresponding standard deviations across all three 18 SLPM longer duration tests 593

57. Average temperatures and pressures at each engine station with corresponding standard deviations for the 19 SLPM longer duration test 594

58. Static pressure losses (%) across the combustor and combustor including present turbine components from CFD, non-rotating combustor testing, and rotating longer durations tests 599

59. Flameout study instrumentation details 617

60. Part numbers for motion control hardware components 657

Table Page

61. Programmed pulses (steps) per millimeter 667

62. Position sensor specifications 668

63. Diffuser male d-sub connector pin-outs (connected to the power supply/DAQ) 670

64. Diffuser female d-sub connector pin-outs (connected to the sensor) 670

65. Thermocouple rake male d-sub connector pin-outs (connected to the sensors) 671

66. Thermocouple rake female d-sub connector pin-outs (connected to the power supply/DAQ) 671

67. Stock JetCat P90RXi Component Electrical Limits 707

68. ECM Board Component Specifications, V2 Edited 713

69. ECM Board connector IO1 specifications 721

70. ECM Board connector IO2 specifications 722

71. ECM Board connector IO3 specifications 723

72. ECM Board connector IO4 specifications 724

73. ECM Board connector IO5 specifications 724

74. Engine Board Component Specifications, V2 728

75. Engine Board connector IO3 specifications 734

76. Engine Board connector IO6 specifications 735

77. Engine Board connector IO7 specifications 735

78. Engine Board connector IO8-lubricant pump specifications 736

79. Engine Board connector IO8-starter motor specifications 736

80. Engine Board connector IO8-internal glow plug specifications 736

81. Engine Board connector IO9 specifications 737

Table Page

82. Engine Board connector IO10 specifications 737

83. BK Precision power supply remote control connector pin specifications 739

84. Glow plug power requirements 740

85. Interface Force Sensor Model SM-50 wire specifications 744

86. Pressure transducer pressure range and wire specifications 747

List of Abbreviations

Abbreviation		Page
IGV	Inlet Guide Vane	1
UCC	Ultra Compact Combustor	2
AFRL	Air Force Research Laboratory	2
AFIT	Air Force Institute of Technology	2
OD	Outside Diameter	3
ID	Inside Diameter	4
ITB	Inter-Turbine Burner	4
CFD	Computational Fluid Dynamics	12
TSFC	Thrust Specific Fuel Consumption	15
LHV_f	Lower Heating Value of Fuel	16
CLP	Combustion Loading Parameter	27
PLF	Pressure Loss Factor	29
psi	Pounds Per Square Inch	30
TVC	Trapped Vortex Combustor	39
HGC	High-g Combustor	39
CTB	Continuous Turbine Burner	41
RQL	Rich-Burn, Quick-Quench, Lean-Burn	45
RVC	Radial Vane Cavity	47
LBO	Lean Blowout	62
PIV	Particle Image Velocimetry	77
PLIF	Planar Laser Induced Fluorescence	78
MFR	Mass Flow Ratio	78

Abbreviation		Page
VR	Velocity Ratio	78
LLCB	Low-Loss Center Body	96
FFT	Fast Fourier Transform	125
LDV	Laser Doppler Velocimetry	128
RNG	Re-Normalization Group	128
SST	Shear Stress Transport	130
NHFR	Net Heat Flux Reduction due to Film-Cooling	145
RPM	Revolutions Per Minute	163
RANS	Reynolds-averaged Navier-Stokes	173
SST	Shear Stress Transport	177
DES	Detached Eddy Simulation	177
SAS	Scale-Adaptive Simulation	177
PDF	Probability Density Function	180
PSEV	Particle Streak Emission Velocimetry	187
ISSI	Innovative Scientific Solutions, Inc.	187
SiC	Silicon Carbide	188
LoG	Laplacian of Gaussian	191
SiC	Silicon Carbide	195
IR	Infrared	198
LED	Light Emitting Diodes	202
COAL	Combustion Optical Analysis Laser	205
SLPM	Standard Liter Per Minute	208
FCR	Film-Cooling Rig	210
CO	Carbon Monoxide	211

Abbreviation		Page
H	Hydrogen	211
O	Oxygen	211
LEL	Lower Explosive Limit	211
ppm	Parts Per Million	211
CCTV	Closed Circuit Television	214
VI	Visual Interface	215
TFP	Thin-Filament Pyrometry	216
LIBS	Laser-Induced Breakdown Spectroscopy	217
IRO	Intensified Relay Optics	218
fps	Frames per Second	220
ITP	Infinite Tube Pressure	448
USB	Universal Serial Bus	657
microSD	Micro Secure Digital	662
NOOBS	New Out of the Box	662
HDMI	High-Definition Media Interface	662
Wi-Fi	Wireless Fidelity	662
CNC	Computer Numerical Control	663
EGT	Exhaust Gas Temperature	706
ECM	Engine Control Module	707
PWM	Pulse-Width Modulation	709
DC	Direct Current	716
I/O, IO	Input/Output	723

List of Symbols

Symbol		Page
T_4	Turbine Inlet Temperature	2
g_e	Gravitational Acceleration on Earth, 9.82 m/s^2	4
m/s	Meter per Second	4
T_{4max}	Turbine Inlet Temperature Maximum	6
F	Uninstalled Thrust Force	14
$\dot{m}$	Mass Flow Rate	14
V	Velocity	14
P	Pressure	14
A_{exit}	Nozzle Exit Area	14
$\dot{m}_f$	Fuel Mass Flow Rate	15
T	Installed Thrust	15
D	Drag	15
S	Uninstalled Thrust Specific Fuel Consumption	15
$\dot{Q}_{in}$	Rate of Heat Addition	16
$\dot{W}_{out}$	Work Output	16
MW	Molecular Weight	21
Φ	Equivalence Ratio	21
S_L	Laminar Flame Speed	22
δ	Laminar Flame Thickness	22
α	Thermal Diffusivity	22
ν	Mass Oxidizer-to-Fuel Ratio	22
$\bar{\dot{m}}_F'''$	Mean Volumetric Mass Production Rate of Fuel	22

Symbol		Page
ρ_u	Density of Unburned Gas	23
S_T	Turbulent Flame Speed	23
u'	Velocity Fluctuation	23
ℓ_0	Integral Length Scale	23
ℓ_K	Integral Length Scale	23
Da	Damköhler Number	24
τ_{flow}	Characteristic Flow Time	24
τ_{chem}	Characteristic Chemical Time	24
A_{exit}	Exit Area	24
V_f	Flame Propagation Velocity	24
V_{flow}	Local Flow Velocity	24
u'_{rms}	Root-Mean-Square Velocity Fluctuation	25
V_{comb}	Combustion Volume	27
Θ	Longwell Parameter	27
$k(T)$	Temperature Dependent Chemical Reaction Rate	28
E_{act}	Activation Energy	28
R	Universal Gas Constant, 8.314 J mol^{-1} K^{-1}	28
L	Combustor Length Scaling Parameter	28
q_{ref}	Reference Dynamic Pressure	29
η_b	Combustion Efficiency	30
θ	Reaction Rate Parameter	30
P_o	Stagnation Pressure	31
M	Mach Number	31
T_o	Stagnation Temperature	31

Symbol		Page
A	Cross-Sectional Area	31
PF	Pattern Factor	33
Pf	Profile Factor	34
EI	Emission Index	35
i	Species Subscript	35
χ	Mole Fraction	35
(δ_θ)	Mixing Layer Thickness at the Inlet	43
AL	Air Loading	49
τ_m	Fuel-Air Mixing Time	55
τ_c	Time for Chemical Reaction to Occur	55
τ_r	Residence Time	55
S_B	Bubble Velocity	58
r_{cavity}	Radius of Cavity	75
V_{tan}	Tangential Velocity	75
β	Tangent Angle	75
$\dot{m}_{cavity}$	Mass Flow in UCC Cavity	75
ρ_{cavity}	Density in the Circumferential Cavity	75
A_{exit}	Area of UCC Exit	75
P_T	Total Pressure	76
P	Static Pressure	76
γ	Ratio of Specific Heats	76
R	Universal Gas Constant	76
J	Joule	76
kg	Kilogram	76

Symbol		Page
K	Kelvin	76
T_T	Total Temperature	76
V	Velocity	76
ρ	Density	76
σ	Solidity	81
c	Chord	81
s	Vane Spacing	81
ϕ	Air Inlet Hole Diameter	83
$\dot{m}$	Mass Flow Rate	84
θ	Inlet Injection Angle	84
I	Number of Air Inlet Ports	84
V_{inlet}	Cavity Inlet Velocity	84
λ	Ratio of Allowable Flow Area to Total Annular Area	91
θ_t	Tangential Injection Angle	92
θ_r	Radial Injection Angle	92
$P_{T,3}$	Combustor Inlet Total Pressure	94
$P_{T,4}$	Combustor Exit Total Pressure	94
D	Hydraulic Diameter	132
W_t	Throat Width	132
H_t	Throat Height	132
W	Watt	136
α	Thermal Diffusivity	137
E	Emissive Power	139

Symbol		Page
σ	Stefan-Boltzmann constant (σ =5.67 $\times 10^{-8}$ W/(m^2·K^4))	139
ϵ	Emissivity	140
G	Irradiation	140
α	Absorptivity	140
h_f	Heat Transfer Coefficient With Film-Cooling	142
h_0	Heat Transfer Coefficient Without Film-Cooling	142
$q_0^{''}$	Convective Heat Flux Without Film-Cooling	143
T_w	Wall Temperature	143
T_{aw}	Adiabatic Wall Temperature	143
$q_f^{''}$	Convective Heat Flux With Film-Cooling	143
η	Film-Cooling (Adiabatic) Effectiveness	144
T_∞	Free Stream Temperature	144
$T_{c,exit}$	Coolant Temperature at the Film Hole Exit	144
T_r	Recovery Temperature	144
r	Recovery Factor	144
Pr	Prandtl Number	144
ϕ	Overall Effectiveness	144
$T_{c,i}$	Internal Coolant Temperature	144
M	Mass Flux Ratio, Blowing Ratio	146
ρ_c	Coolant Density	146
ρ_∞	Free Stream Density	146
U_c	Coolant Velocity	146
U_∞	Free Stream Velocity	146

Symbol		Page
$\dot{m}$	Mass Flow Rate	147
A	Cross-Sectional Area	147
$\dot{m}_{c,total}$	Total Mass Flow Rate in all Coolant Holes	147
$A_{c,total}$	Total Area of all Coolant Holes	147
A_∞	Cross-Sectional Area of the Free Stream Inlet	147
$\dot{m}_\infty$	Mass Flow Rate of the Free Stream Fluid	147
I	Momentum Flux	148
θ	Normalized Temperature	149
σ	Heat Flux Augmentation	150
$q_f^{''}$	Heat Flux Without Secondary Reactions	150
$q_r^{''}$	Heat Flux With Secondary Reactions	150
u	Inlet Velocity, Station 1	160
β	Relative Flow Angle	160
V_{iR}	Relative Velocity at Station i	160
U	Rotor Velocity	160
α	Absolute Flow Angle	160
V	Absolute Velocity	160
w	Radial Component of Velocity	160
v	Tangential Component of Velocity	160
ε	Slip Factor	162
n	Number of Rotor Vanes	162
τ_c	Compressor Temperature Ratio	162
e_c	Polytropic Efficiency	162
η_c	Adiabatic Efficiency	162

Symbol		Page
γ	Ratio of Specific Heats	162
N	Rotor Rotation Rate	163
ω	Angular Rotation Rate	164
ψ	Stage Loading Coefficient	165
Φ	Flow Coefficient	166
$^{\circ}R_t$	Degree of Reaction	166
Kn	Knudsen Number	169
$\vec{v}$	Three-Dimensional Velocity Vector	171
$\bar{\bar{\tau}}$	Stress Tensor	171
$\rho\vec{g}$	Gravitational Force	171
$\vec{F}$	Externally Applied Force	171
μ	Molecular (Dynamic) Viscosity (Pa·s)	171
Re	Reynolds Number	172
U	Characteristic Velocity	172
L	Characteristic Length Scale	172
ν	Kinematic Viscosity (m^2/s)	172
y^+	Non-dimensional Distance From a Wall	174
u^+	Non-dimensional Velocity	174
δ_v	Viscous Length Scale	174
u_τ	Friction Velocity	174
τ_w	Wall Shear Stress	174
y	Dimensional Distance from the Wall	174
$\bar{U}$	Average Velocity (m/s)	174
κ	von Kármán Constant (0.41)	174

Symbol		Page
B	Log-law Constant (5.2)	174
μ_T	Eddy or Turbulent Viscosity	176
E	Energy	185
i	Integer	185
h	Planck's Constant, $6.626 \cdot 10^{-34}$ J·s	185
ν	Frequency of Light	185
c_0	Speed of Light in a Vacuum, $2.998 \cdot 10^{8}$ m/s	185
$\epsilon_p, true$	Potential Energy	185
Stk	Stokes Number	188
t_0	Relaxation Time of a Particle	189
l_0	Characteristic Dimension	189
σ	Standard Deviation	191
I_R	Intensity Ratio	196
$I_{\lambda,b}(\lambda, T)$	Spectral Intensity	196
λ	Wavelength	197
k	Blotzmann's Constant, $1.381 \cdot 10^{-23}$ J/K	197
E_λ	Spectral Gray Body Emissive Power	198
n	Refractive Index	199
ϵ	Angular Light Ray Deflection	200
U_0	Centerline Velocity (m/s)	328
y	Half Height of the Channel (m)	328
ΔP	Total/Static Differential Pressure	329
dB	Decibels	397
VR	Velocity Ratio (Tunnel/Jet)	464

Symbol		Page
$\forall$	Oscillator Volume	473
A_{PJ}	Area of an Oscillator Power Jet Throat	473
A_{FB}	Cross-sectional Area of the Oscillator Feedback Loop	473
n	Number of Oscillator Jets	474
Re_D	Reynolds Number Scaled by Hydraulic Diameter	475
Ψ	Pressure Head	505
K	Discharge Coefficient	511

COMBUSTION DYNAMICS AND HEAT TRANSFER IN AN ULTRA COMPACT COMBUSTOR

I. Introduction

1.1 Ultra-Compact Combustor

Engineers have always strived to improve their inventions; to make them do more with less. The turbine engine is no exception. A reduction in size and an increase in efficiency of an engine means the weight is reduced so the thrust-to-weight ratio is increased while providing lower fuel consumption. The operating cost of an aircraft is largely driven by fuel consumption and the size and weight of the aircraft. It is obvious then how a smaller, more efficient engine has a direct impact on operational budgets. One way to achieve these engine improvement goals is to modify the combustion section of the engine. A typical combustor in operation today requires swirling airflow from the compressor to be straightened by a compressor exit guide vane before entering the combustion region. The combustion region itself has an axial length on the order of 25 - 50 cm. The hot combustion products must then pass through a turbine Inlet Guide Vane, IGV, before entering the high-pressure turbine.

Not only is this combustion section, including the two sets of vanes on either end, rather long, but it is also very heavy. Due to the extreme temperatures in the combustor, there is a requirement for robust metallic structures and extensive cooling. The cooling requires ducting to route the coolant from the compressor bleed to the combustor structures. If the combustor could be made smaller, it would shorten the length of the engine and have a significant impact on the overall weight of the engine

by removing metallic mass and ducting. Historically, the overall fuel-to-air ratio used in the combustors of turbine engines has been well below stoichiometric [1]. Over the past many years the turbine inlet temperature, T_4, has been steadily increased to improve efficiency and specific thrust. Higher combustion temperatures can be achieved by operating at a fuel-to-air ratio closer to stoichiometric.

Early combustors featured very long axial lengths to provide adequate mixing of the fuel and air and ensure complete combustion prior to entering the turbine section. With improvements in fuel and air distribution the axial lengths were shortened to the lengths typically seen in operation today. These modern combustors allowed for shorter engines and reduced liner cooling air demand [2]. There is still a lot of room for improvement in combustor design beyond the current state of the art. An Ultra-Compact Combustor, UCC, could be the solution to further reduce the combustor axial length by up to 66% [3], while producing a rise in T_4 to achieve efficiency and specific thrust improvement goals. UCC research was begun at the Air Force Research Laboratory, AFRL, around 2003 [3] with a design based on swirling flow combustion researched by Lewis [4] in the early 1970's, and a cycle analysis utilizing combustion through the turbine researched by Sirignano et al. [5] in the mid-1990's. The UCC reduces the axial combustor length by combining the compressor exit guide vane, turbine inlet guide vane, and a circumferential combustion cavity into a single package. Figure 1 shows a comparison of the UCC to a traditional combustor. AFRL proposed two versions of the UCC; one with a trapped vortex which rotates fuel and air in the short direction of the circumferential cavity; the other swirling the bulk flow in the circumferential direction of the cavity at high centrifugal loads. The difference in flow patterns between the variants is shown in Figure 2. Early AFRL UCC research studied both types, but later they focused on the trapped vortex version and handed off research on the high-g variant to the Air Force Institute of Technology, AFIT.

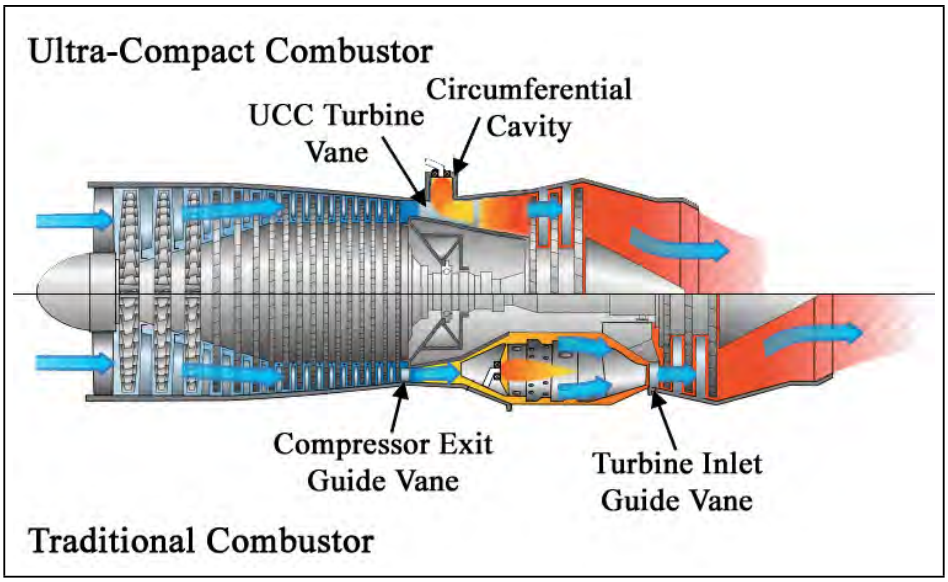


Figure 1. Traditional combustor (below), Ultra-Compact Combustor (above) [6]

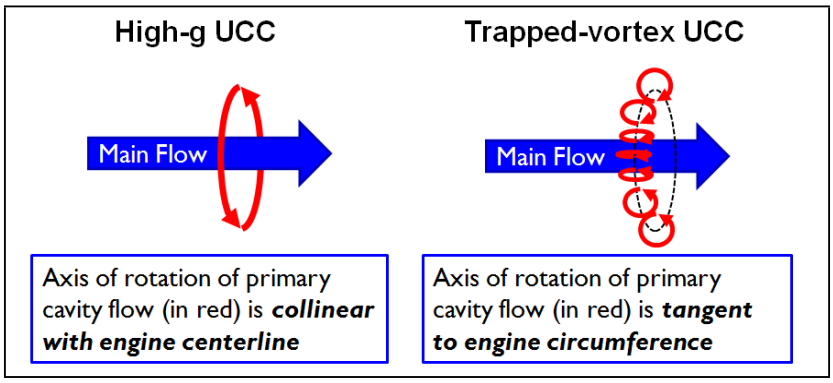


Figure 2. Swirl differences between the high-g and trapped-vortex UCC variants

The high-g UCC shortens the axial length compared to a typical combustor by burning a swirling mixture of fuel and air in the circumferential direction in a cavity situated around the outside diameter, OD, of the engine. The UCC turbine vanes are positioned radially inward of the circumferential cavity and guide the hot gases exiting the cavity to the correct flow angle required by the turbine. In a traditional axial combustor the residence time of the fuel is a function of the flow velocity and combustor length. The combustor must be sufficiently long to allow for complete combustion

prior to the exit of the combustion section. In the UCC, however, the residence time is no longer a function of axial length. Air is injected into the circumferential cavity at an angle to force the fuel-air mixture inside to swirl circumferentially around the cavity at a high rate of speed. The circumferential swirl increases the centrifugal loading on the fuel-air mixture to levels on the order of $3{,}000g_e$, where g_e is the gravitational acceleration on Earth which has a value of 9.82 m/s^2. The centrifugal loading provides two potential benefits. First, according to Lewis [4], the increased centrifugal load causes an increase in the turbulent flame speed. Due to the increase in reaction rate, the combustor volume can be decreased. Second, the heavier unburned fuel particles are forced to the OD of the cavity by centrifugal force where they can evaporate and breakdown into smaller particles to burn. As combustion takes place, the lighter exhaust products are displaced by the heavier particles and forced to the inside diameter, ID, of the cavity where they exit and flow through the turbine vanes. This process ensures the heavier particles are allowed to remain in the cavity until they are fully broken down and consumed. Since the residence time is now based on the weight of the particles and not the flow conditions or combustor axial length, the circumferential cavity is equivalent to having an infinite combustion length, yet occupies only a fraction of the axial length of a traditional combustor.

In addition to the benefits offered by the UCC as the main combustor, the compact geometry of the UCC is well suited as an Inter-Turbine Burner, ITB. An ITB is a smaller combustor positioned between the high-pressure and low-pressure turbine to provide a temperature rise to maximize power extraction from the low-pressure turbine. The additional power could be used to drive a large fan for ultra-high bypass ratio engines or to run an alternator to provide large amounts or electricity [7]. Zelina et al. [7] found that optimal power extraction occurred for a ITB temperature rise of only 150 C. Operating in vitiated air conditions, this modest temperature rise

means that the ITB would be operating at near-lean-blowout limits of conventional systems. The UCC, however, has a lean blowout fuel-to-air ratio 25-50% lower than current systems meaning it is well suited for this application. These findings are supported by Spytek who conducted experimental testing of a UCC ITB with a 200 - 315 C temperature rise in 100% vitiated air conditions and saw a 16 - 22% increase in engine power through the use of the ITB [8].

While the UCC offers many advantages, there are some significant challenges resulting from the design that must be overcome. One of the largest challenges is in cooling the walls of the circumferential cavity and UCC turbine vanes below the cavity. Due to the integrated nature of the design and the operational fuel-to-air ratio near or above stoichiometric, introducing oxygen rich cooling films in the cavity or on the turbine vanes increases the potential for secondary combustion reactions to occur in the cooling film. These secondary reactions between the cooling film and any unburned fuel in the bulk flow take place directly on the surface of the engine components and can significantly reduce component life. A second challenge presented by the UCC geometry is to present a uniform temperature distribution in the radial direction to the first rotating turbine stage. The hot gases exiting the circumferential cavity must be mixed with the core flow and evenly distributed across the UCC turbine vane radial span. Undesirable temperature distributions include excessive heating on either the ID or OD portions of the vane or a distribution that fluctuates with time. All of these conditions result in increased cooling requirements on the turbine blades.

1.2 Turbine Film-Cooling

The steady increase in T_4 mentioned in the previous section resulting from a desire to improve efficiency has caused the fluid temperature in the turbine section to exceed

turbine material limits. Beginning around 1960, turbine cooling methods were introduced that allowed the maximum temperature of the combustion products, T_{4max}, surrounding the turbine to exceed the normal turbine material operating limits. The early cooling methods were focused on convective cooling of the inside of the turbine airfoils using high-pressure bleed air from the compressor. Beginning in the 1970's more advanced cooling methods were used that incorporated holes drilled into the turbine airfoil to allow the internal cooling air to escape. The exiting coolant formed a protective cooling film over the airfoil surface ushering in the era of film-cooling [9]. Other more advanced film-cooling techniques have been introduced through the 1990's and 2000's including film impingement convection and transpiration cooling to name a few [10].

A diagram showing the magnitude of key advances in turbine airfoil cooling methods and the dramatic affect on T_{4max} is shown in Figure 3. From this figure it is easy to see the importance of film-cooling when comparing the "Allowable Metal Temperature" on the plot to T_{4max} in use today. Improvements in more heat tolerant metal alloys and ceramic materials have raised the "Allowable Metal Temperature," but not significantly enough to remove the need for film-cooling.

The UCC turbine vane row is uniquely positioned to allow for the possibility of a new film-cooling technique to be used for this row of vanes. In a traditional combustor all rows of turbine components are positioned fully downstream of the combustor and are thus fully exposed to the combustion products across the entire airfoil. These airfoils rely on coolant ducted to the turbine section from compressor bleed. However, in the UCC the leading edge of the turbine vanes positioned radially inward of the circumferential cavity are upstream of the combustion products and are thus only exposed to the core air exiting the compressor. This arrangement means that cool core air may be able to enter the turbine vane through holes in the vane stagnation

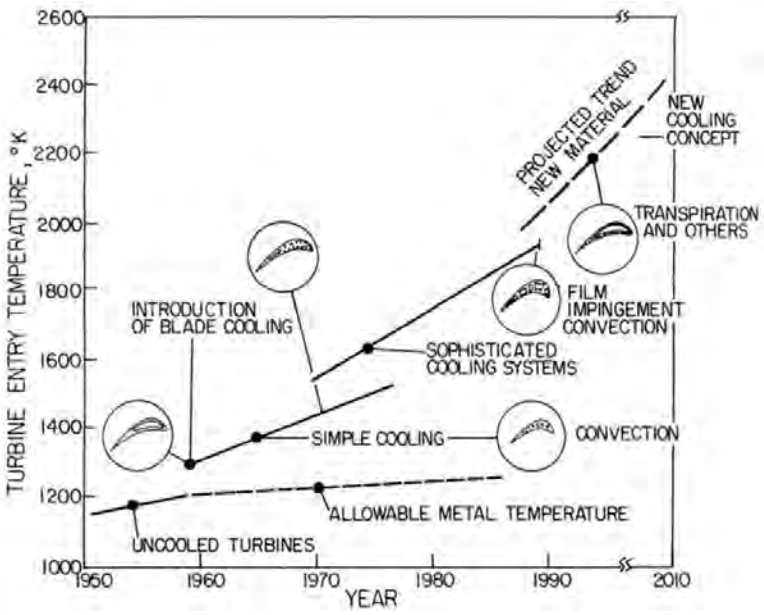


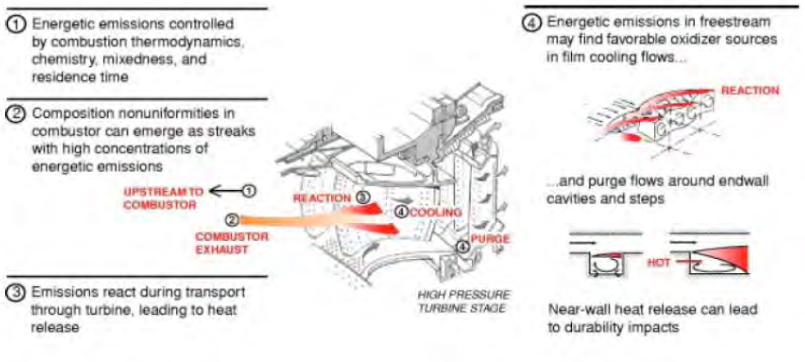
Figure 3. Comparison of turbine inlet temperature to material limits [10]

region and then exit the vane through film-cooling holes drilled into the vane surface in regions that are exposed to the hot combustion products. If this technique works, it could provide an improvement in efficiency by reducing the quantity of compressor bleed air needed and save weight by reducing ducting.

Film-cooling will be a necessity well into the foreseeable future. The rate of development of durable high temperature turbine materials is currently well outpaced by the increasing T_{4max} desired in engine operation. Until a time when a turbine material can withstand the extreme temperatures exiting the combustor on its own, film-cooling will serve to bridge the gap between material operating limits and T_4. There is an issue with putting so much of a dependence on film-cooling. If the cooling method were to fail for any reason, the turbine would be damaged in a very short time thereafter.

1.3 Potential for Heat Release in Film-Cooling

There is an additional concern that with shorter combustors and higher operational fuel-to-air ratios that unburned fuel products will enter the turbine section. While the intent of the circumferential cavity is to provide an infinite combustor length by spinning heavier fuel particles to the cavity outer diameter, past performance has shown that some unburned fuel does exit the cavity. When the unburned fuel comes in contact with the oxygen-rich cooling film a secondary combustion reaction can take place directly on the surface of the airfoil that is supposed to be getting cooled. In this case the film-cooling method may be functioning properly, but the airfoil surface would not be getting cooled and thus would quickly lead to component failure. The mechanism for secondary combustion is shown pictorially in Figure 4a. Figure 4b shows a test result from a secondary reaction experiment in which fuel-rich combustion products were exhausted over a row of offset normal cooling holes upstream of fan-shaped cooling holes. The white streak near the ruler is a visible flame resulting from a secondary combustion reaction of the exhaust products with the cooling film from both sets of holes.



(a) Secondary combustion reaction process in a traditional combustor [11]



(b) Visual secondary combustion reaction [6]

Figure 4. Secondary combustion reactions

In addition to reacting fuel streaks, there is yet another challenge that needs to be overcome in film-cooling turbine components. As the fuel-to-air ratio of combustion increases towards stoichiometric, resulting in increased T_4, some of the energy from combustion will be stored in the flow as highly energetic dissociated species [12]. An example of such a species is carbon monoxide. As these dissociated species are convected downstream, there is the possibility that they could release energy in the relatively cool turbine section where the reduced temperatures promote molecular recombination. This is especially true in the cooling films used to cool the turbine components where the coolant is significantly cooler than the core flow. The release of energy from the dissociated molecules in the turbine cooling films would have the same effect as a secondary combustion reaction as described above. Whether the energy release in the turbine cooling films comes from secondary reactions or molecular recombination, the negative impact on cooling effectiveness is virtually the same. Without effective cooling there will be a substantial reduction in turbine component life, or potential failure of the turbine components will occur.

1.4 Small Turbojet Integration

All prior research on the high-g UCC was focused on an isolated combustor. Air was fed from a large external compressor at moderate flow rates and nearly atmospheric pressure. The exit of the combustor opened to an ambient environment. Limitations of this compressor means that higher mass flow rates and pressure ratios cannot be tested with the current equipment. However, higher mass flow rates and pressure ratios can be achieved by installing a variant of the UCC into a small turbine engine like the one shown in Figure 5. The relatively simple construction of these small turbines makes it possible to remove the current combustor and replace it with an appropriately sized UCC that can be tested in a laboratory. While these turbines

are small, they can achieve air mass flow rates nearly five times, and 2.3 times the pressure ratio, of the AFIT COAL Lab air supply at the time of this publication.

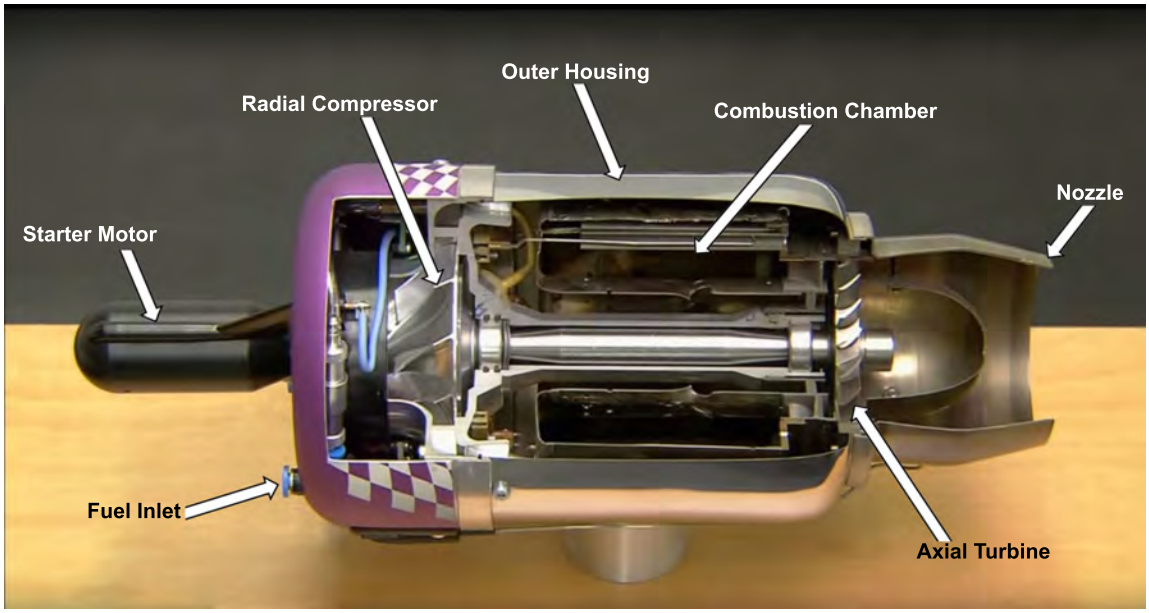


Figure 5. Small turbine engine cutaway [13]

The lack of film-cooling in these small turbines means that there is no coolant ducting. Rather, a single outer wall made of sheet metal encases the engine. The simplicity of the design makes it useful as a research tool. The single outer wall allows easy access for thermocouple or pressure taps to be installed for additional diagnostics. In future versions a window could be incorporated into the wall to allow optical access and diagnostics to be conducted on the UCC while installed.

In addition to being able to study the impact of higher mass flow rates and pressure ratios, a UCC integrated into a small-scale turbine enables the effects of rotating machinery, both upstream and downstream of the combustor, to be researched on the combustion properties and combustion stability. This configuration enables better refinement of the UCC cavity and flow dynamics to optimize combustion performance under more realistic operating conditions.

1.5 Research Objectives

There was one primary goal for this research that required several supporting objectives to be achieved and incorporated together in order to achieve the primary goal. The primary goal of this research was to produce a small-scale, self-sustaining, UCC powered turbine engine. In this context self-sustaining means that there was no external air feed or external motors driving a compressor. The supporting objectives cover topics in UCC cavity airflow management, fuel injection variations, alternate circumferential cavity configurations, component cooling, advanced numerical modeling, and compressor/turbine integration. More specifically the supporting objectives were as follows:

1. Determine the viability of UCC vane cooling using coolant extracted from the core flow through the vane stagnation region.

2. Numerically investigate the effect of conjugate heat transfer on reacting flow analysis in the baseline UCC model.

3. Investigate the impact of airflow split ratio between the core and circumferential cavity and alternate fuel injection schemes on tangential velocity, combustor performance, flow path pressure balance, and Rayleigh losses.

4. Determine how cavity configuration influences combustion product migration and the ability to achieve a desirable turbine inlet temperature distribution.

5. Investigate the impact of higher flow rates and pressure ratios on combustion performance, exit temperature distributions, and system pressure losses.

1.6 Uniqueness of Research

The objectives listed in Section 1.5 build on past research findings, but are all the first of their kind. First, prior research has been conducted on a common flow source full-annular UCC, however, that rig did not have the ability to dynamically control the mass flow split between the core and cavity to study the implications on UCC operation. Second, the proposed redesign of the fuel injection methods and UCC cavity orientation in Objectives 3 and 4 will completely alter the employment of the circumferential cavity compared to what has been studied since the inception of the UCC starting around 2000. Finally, the work outlined in Objectives 1, 4, and 5 is pioneering. Research has been conducted with a high-g UCC rig at elevated pressures, but not with the unsteadiness upstream of a spinning compressor. Additionally, no research has integrated the UCC with a rotating turbine, or integrated a compressor, UCC, and turbine together in a self-sustaining package. Finally, no UCC turbine vane cooling has been implemented prior to this study. More specifically, no cooling scheme has ever been investigated that utilizes an opening in the leading edge of the vane to take in core flow as coolant. This opportunity is only afforded due to the unique UCC geometry of the hybrid vanes. Additionally the trade study analysis on the cooling scheme, as well as portions of Objectives 2, 3 and 4, will employ computational fluid dynamics, CFD, to model the complex UCC flow with combustion reactions and conjugate heat transfer in a three-dimensional domain. Utilizing conjugate heat transfer in a three-dimensional domain is a first for AFIT. To this end Objective 2 served to quantify the benefit of conjugate heat transfer analysis in a UCC.

II. Background

The background information presented in this section is intended to outline the fundamental aspects and past research related to gas turbine combustion, Ultra Compact Combustors, film-cooling, secondary combustion in cooling films, conjugate heat transfer and reacting flow computational fluid dynamics (CFD), secondary flows, combustion analysis techniques, and turbines. While this represents a number of varied topics to review, all of these topics are needed to address the many areas the previously outlined research objectives will touch. Most of the following sections begin with an overall textbook treatments of a topic and quickly moves into a more research oriented discussion on the evolution of the ideas.

2.1 Gas Turbine Engine Overview

A propulsion system is defined by Mattingly [14] as, "A unit submerged in a fluid medium about and through which fluid flows." This definition can go one step further to define an engine as a type of propulsion system that operates with a defined thermodynamic cycle and is used to increase the kinetic energy of the fluid inside it. A gas turbine engine generates thrust by pressurizing and accelerating the incoming fluid. As work is done on the fluid to accelerate it, there is an equal and opposite force applied to the engine in the form of thrust. The amount of thrust produced is dependent on the mass of fluid accelerated and the magnitude of the velocity difference between the incoming and exiting fluid as described by the general thrust equation, Equation 1 [15]. If the fluid is perfectly expanded through the engine nozzle such that the fluid pressure at the exit exactly matches the atmospheric pressure, the last term in Equation 1 becomes zero. If the fluid exit pressure is higher than atmospheric pressure, there is an additional pressure force applied and the thrust is increased. In

Equation 1, F is the general thrust force, $\dot{m}$ is the mass flow rate of fluid, V is the fluid velocity, P is the fluid pressure, and A_{exit} is the exit area of the engine nozzle.

$$F = \dot{m}_{out}V_{out} - \dot{m}_{in}V_{in} + (P_{exit} - P_{atmospheric})A_{exit} \tag{1}$$

The operational cycle for a gas turbine engine is the air-standard Brayton cycle as described in Boyce [16] and it is shown in its idealized form in Figure 6. Plots are provided of pressure (P) versus volume (V), temperature (T) versus entropy (S), and a generalized gas turbine engine diagram to define the stations used in the plots. The plots show an ideal cycle where compression (1 - 2) and turbine expansion (3 - 4) are isentropic and adiabatic. The combustion stage (2 - 3) is shown as isobaric.

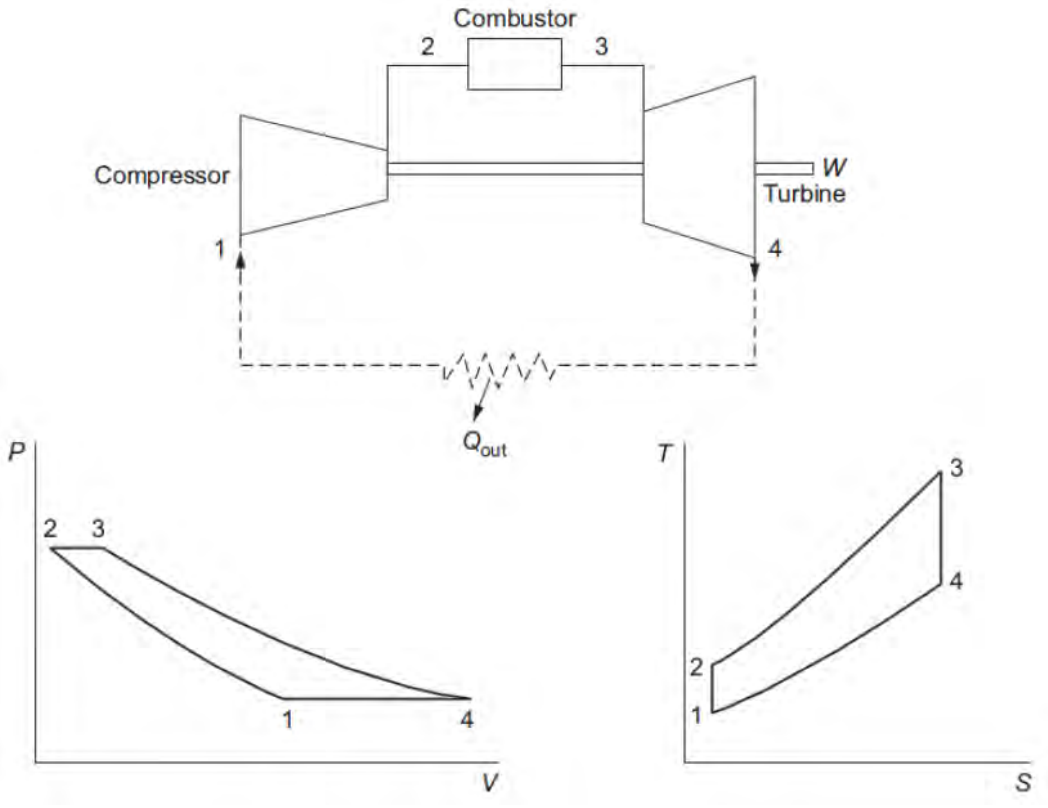


Figure 6. Ideal Air-standard Brayton cycle [16]

Applying the general thrust equation to a fuel burning turbine engine requires the mass flow rate of the fuel be factored into the exhaust calculation. The addition of the mass flow rate of the fuel, $\dot{m}_f$, to Equation 1 results in what Mattingly [14] defined as the uninstalled thrust, F, for a single stream engine. This relationship is shown in Equation 2.

$$F_{uninstalled} = (\dot{m}_{air} + \dot{m}_f)V_{out} - \dot{m}_{air}V_{in} + (P_{exit} - P_{atmospheric})A_{exit} \tag{2}$$

Installed thrust, T, accounts for penalties associated with inlet and nozzle external losses. Mattingly [1] accounts for these losses as fractions of the uninstalled thrust, F, and the inlet or nozzle drag force, D. The installed thrust is given in Equation 3 with the loss components given in Equations 4 and 5.

$$T = F(1 - \phi_{inlet} - \phi_{nozzle}) \tag{3}$$

$$\phi_{inlet} = \frac{D_{inlet}}{F} \tag{4}$$

$$\phi_{nozzle} = \frac{D_{nozzle}}{F} \tag{5}$$

The installed fuel consumption, also referred to as Thrust Specific Fuel Consumption (TSFC), can be defined in terms of the uninstalled thrust specific fuel consumption, S, (fuel mass flow rate divided by uninstalled thrust) and the same inlet and nozzle losses defined above. The $TSFC$ definition is given in Equation 6 [14].

$$TSFC = \frac{S}{1 - \phi_{inlet} - \phi_{nozzle}} = \frac{\left(\frac{\dot{m}_f}{F}\right)}{1 - \phi_{inlet} - \phi_{nozzle}} \tag{6}$$

A thermodynamic analysis of engine performance can be performed using several basic measurable values. Hill and Peterson [17] defines the propulsion efficiency (η_p), thermal efficiency (η_{th}), and overall efficiency (η_o) in Equations 7, 8, and 9, respectively.

$$\eta_p = \frac{TV_{in}}{0.5[(\dot{m}_{air} + \dot{m}_f)V_{out}^2 - \dot{m}_{air}V_{in}^2]} \tag{7}$$

$$\eta_{th} = \frac{0.5[(\dot{m}_{air} + \dot{m}_f)V_{out}^2 - \dot{m}_{air}V_{in}^2]}{\dot{m}_f LHV_f} = \frac{\dot{W}_{out}}{\dot{Q}_{in}} \tag{8}$$

$$\eta_o = \eta_p \eta_{th} = \frac{TV_{in}}{\dot{m}_f LHV_f} \tag{9}$$

In Equations 8 and 9, LHV_f refers to the lower heating value of the fuel. The LHV_f multiplied by the mass flow rate of fuel, $\dot{m}_f$, gives the rate of heat addition to the system, $\dot{Q}_{in}$. The collection of terms in the denominator of Equation 7 or the numerator of Equation 8 is also called the work output of the system, $\dot{W}_{out}$.

A gas turbine engine is made up of a highly coupled set of discrete operational stages. Each engine stage has its own purpose, but the design considerations and operational performance of each is dependent on the others. As an example. the size of the compressor and its operating limits dictate the mass flow rate provided to the combustor, less any bleed air that is removed for cooling or other purposes. To maintain stable combustion and achieve a significant enough heat release to drive the turbine, the mass flow rate of air in the combustor and the desired equivalence ratio drives the fuel flow rate. The mass flow rate of air and the heat release in the combustor control the amount of power extraction that can take place in the turbine. The maximum compression limit of the compressor is set by the power provided by the turbine. The internal passage sizing is driven by the velocity requirement at each stage as well as the mass flow rate and pressure ratio produced by the compressor. Overall engine sizing and operational limits are typically dictated by component material properties of melting point or mechanical stresses due to rotation.

2.1.1 Combustor Design.

The combustor in a gas turbine engine provides the means to achieve the heat input in the Brayton cycle discussed earlier. This component increases the temperature and entropy of the system in a near constant pressure process. The heat release increases the thermal energy of the fluid to a level necessary to drive the turbine. There are other combustion zones possible in a turbine engine, most commonly the afterburner or an inter-turbine burner, which would be present in a modified Brayton cycle or a reheat cycle. This section will focus on the traditional main combustor.

An aircraft mounted gas turbine and a ground based gas turbine operate on the same general principles, but for the aircraft engine the desire is to make the system as compact and light-weight as possible. The difference in size is easily seen by comparing combustion intensity, which is the energy release rate in a combustor per unit volume. For a typical aircraft based system the main burner combustion intensity is on the order of 11,000 MW/m^3, where a ground based steam power plant packs in only 3 MW/m^3 [14]. The significantly higher level of combustion intensity in the aircraft system drives concerns of component durability and reliability.

Mattingly [14] summarized a list of desired properties that an aircraft gas turbine combustor should achieve in order to meet the demands of current operational requirements and reliability. This list includes: complete combustion, low total pressure loss, combustion stability, proper exit temperature distribution, short length and small cross section, freedom from flameout, relightability, and operation over a wide range of mass flow rates, pressures, and temperatures. Several of these objectives are contradictory, such as complete combustion and short length. The ability to achieve all eight desired properties while reducing emissions and improving fuel efficiency presents a very difficult challenge for any combustor designer.

A traditional engine cross section usually takes the form of one of three typical

combustor configurations as shown in Figure 7. The can-type was used in the earliest gas turbines, but they tend to be longer and heavier than the other types making them less efficient for use in an aircraft engine. The tuboannular, or can-annular, saves on space by installing all of the cans inside a single outer annular liner. This design has issues with maintaining a consistent flow pattern inside the combustor. The annular type is used in most modern gas turbines due to its clean flow path, low pressure losses, and compact size.

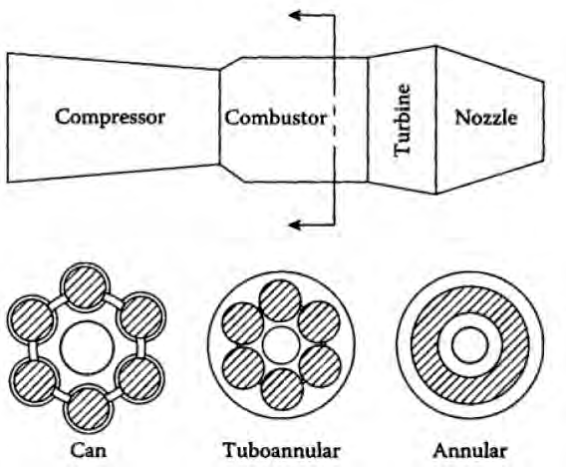
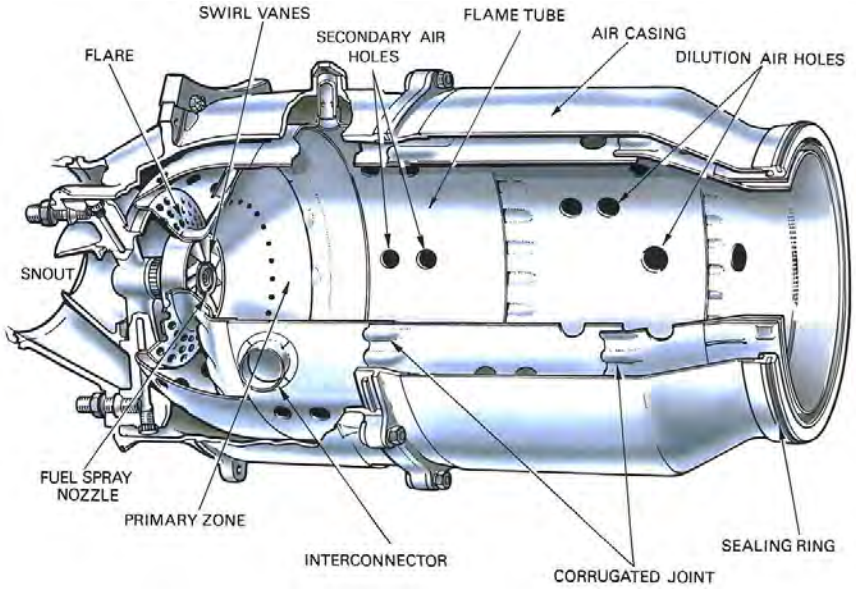


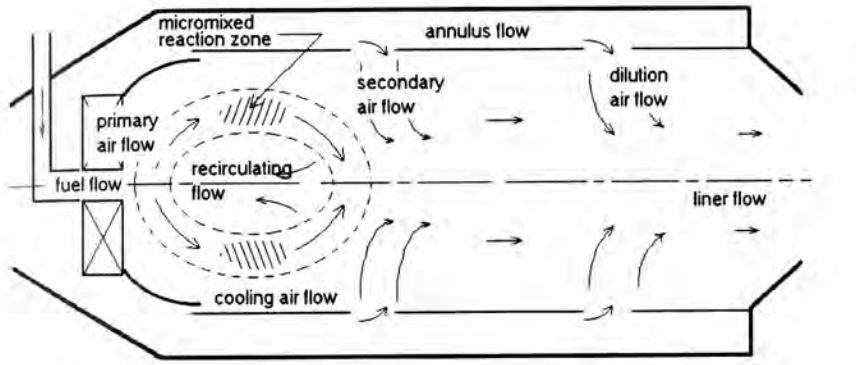
Figure 7. Traditional combustor types [18]

Mattingly [1] presents an annular cross section of a traditional modern main combustor as shown in Figure 8. Figure 8a shows the principle components in the combustor while Figure 8b shows the flow pattern inside the combustor. High pressure air exits the compressor and enters the combustor at Station 3.1. The fluid decelerates in the diffuser section as the passage expands. Air enters the primary zone through air swirlers that are co-flowed around an atomized liquid fuel spray. The high degree of swirl results in fast mixing with the fuel particles. The primary zone is where ignition occurs and where the flame is anchored. The recirculation in the primary zone provides sufficient time, temperature, and mixing to achieve nearly complete

combustion [18]. This type of flow pattern has been shown to lead to wide stability limits, good ignition characteristics, and avoids pulsation and noisy combustion instabilities.



(a) Principle features [19]



(b) Flow pattern [1]

Figure 8. Principle features and flow pattern of a modern traditional main combustor

The combustion products exiting the primary zone are cooled slowly through the introduction of smaller quantities of dilution air in the secondary combustion zone. The slow cooling process allows for the completion of CO reactions and supports the combustion of soot and unburned hydrocarbons that were not consumed in the primary zone. If the products from the primary zone are cooled too quickly, the

CO, soot, and unburned hydrocarbons would remain unburned and discharged to the turbine. The remaining 20-40% of the air that entered the combustion station passes through the dilution holes into the dilution zone. This air drops the temperature of the combustion products exiting the secondary zone and establishes the temperature profile in the transition duct that enters the turbine (see Section 2.1.3). The transition duct contracts the fluid passage to accelerate the flow prior to entering the turbine.

2.1.1.1 Combustion Basics.

Turns [20], relying on a definition from Webster's Dictionary, defines the type of combustion used in all practical combustion devices as, "rapid oxidation generating heat, or both light and heat." A slow oxidation process can still be considered combustion, but this combustion type has little practical use. Chemical reactions are important in all combustion events as the process converts energy stored in chemical bonds into heat. The heat can then be used in a number of different applications. The combustion process can occur in both flame and non-flame modes, with the flame mode dividing into sub-categories of premixed and non-premixed (diffusion) flames [5].

Combustion requires fuel and oxidizer combined with an ignition source to proceed. In a gas turbine engine the fuel is typically hydrocarbon based and can be either gaseous or liquid. For an airborne gas turbine a liquid hydrocarbon fuel is used almost exclusively due to the higher volumetric energy density. When the ratio of oxidizer and fuel are exactly balanced such that all of the fuel and oxygen are consumed for the given amount of oxidizer the mixture is said to be stoichiometric. Turns [20] describes a stoichiometric equation for a generic hydrocarbon, C_xH_y, as shown in Equation 10. The real combustion process is not this straightforward and is comprised of many individual elemental reactions.

$$C_xH_y + a(O_2 + 3.76N_2) \rightarrow xCO_2 + \left(\frac{y}{2}\right)H_2O + 3.76aN_2 \tag{10}$$

$$a = x + \frac{y}{4} \tag{11}$$

The equations above assume that combustion is taking place in air, and that air is comprised of 21% oxygen (O_2) and 79% nitrogen (N_2) by volume. By this ratio, for every mole of O_2 in air, there are 3.76 moles of N_2. Using Equation 11 and the molecular weights, MW, of air and the fuel, the stoichiometric air-to-fuel ratio, $(A/F)_{stoich}$, can be calculated using Equation 12.

$$\frac{A}{F}\Big|_{stoich} = \left(\frac{m_{air}}{m_{fuel}}\right)_{stoich} = \frac{4.76a}{1}\frac{MW_{air}}{MW_{fuel}} \tag{12}$$

The equivalence ratio, Φ, is used to define a combustion mixtures composition relative to the stoichiometric condition. Mixtures with $\Phi > 1$ are classified as fuel-rich, $\Phi < 1$ is fuel-lean, and $\Phi = 1$ is stoichiometric. All fuels have a range of Φ where combustion can take place known as the flammability limit, but they all typically fall between approximately $0.3 < \Phi < 3.0$. Mathematically, Φ is defined in Equation 13.

$$\Phi = \frac{\left(\frac{A}{F}\right)_{stoich}}{\left(\frac{A}{F}\right)} \tag{13}$$

In Equation 12 the mass of fuel and air can be replaced by the mass flow rate of fuel and the mass flow rate of air. Rearranging Equation 13, and using the definition of air-to-fuel ratio, allows the required mass flow rate of fuel to be found for a known mass flow rate of air at a desired equivalence ratio as shown below.

$$\left(\frac{A}{F}\right) = \frac{\left(\frac{A}{F}\right)_{stoich}}{\Phi} \tag{14}$$

$$\dot{m}_{fuel} = \frac{\dot{m}_{air}}{\left(\frac{A}{F}\right)} = \frac{\dot{m}_{air}\Phi}{\left(\frac{A}{F}\right)_{stoich}} \tag{15}$$

2.1.1.2 Flame Characteristics.

The word "flame" can be taken to mean different things to different people. Some people may think of a candle, a camp fire, a gas stove, or gas turbine combustor. While the flames in each example may look different, at their core they all function in the same way. Turns [20] defines a flame as "A self-sustaining propagation of a localized combustion zone at subsonic velocities." A laminar flame propagates through a flammable mixture as a sheet or wave and travels at a defined velocity that is fuel specific. For stationary flames the combustion products must approach the flame front at the flame speed to keep the flame from moving. If the combustion wave travels at a subsonic speed the combustion process is designated as a deflagration and is characterized by a pressure drop across the combustor. If the wave travels supersonically the combustion process is a detonation. While detonating combustors offer several benefits to gas turbines, most notably a pressure rise across the combustor, there are still many challenges that need to be worked out. [21]

The most common physical characteristics that are used to describe flames are the flame speed and flame thickness. The definitions of laminar flame speed, S_L, and flame thickness, δ, shown in Equations 16 and 17 are taken from Turns [20].

$$S_L = \Big[-2\alpha(\nu+1)\frac{\bar{\dot{m}}_F'''}{\rho_u}\Big]^{1/2} \tag{16}$$

$$\delta = \frac{2\alpha}{S_L} \tag{17}$$

In the above equations α is the thermal diffusivity, ν is the mass oxidizer to fuel ratio, $\bar{\dot{m}}_F'''$ is the mean volumetric mass production rate of fuel (this will be a negative

number since the fuel is being consumed), and ρ_u is the density of unburned gas.

At its core, the characteristics of a turbulent flame are identical to a laminar flame, but the smooth laminar flame sheet is wrinkled and distorted due to turbulent eddies in the mixture. The turbulent flame speed, S_T, is a direct function of the laminar flame speed and the level of turbulence in the mixture. Two definition of the turbulent flame speed are provided below which yield similar results. Equation 18 is from Law [22], and Equation 19 from Turns [20]. In both of these equations u' is the turbulent velocity fluctuation in the flow.

$$S_T = S_L \sqrt{1 + \left(\frac{u'}{S_L}\right)^2} \tag{18}$$

$$S_T = 3.5 S_L \left(\frac{u'}{S_L}\right)^{0.7} \tag{19}$$

While there is a difference in flame speed between laminar and turbulent combustion, there is seldom a distinction made between laminar flame thickness and turbulent flame thickness. Since a turbulent flame is essentially a wrinkled, corrugated, or otherwise distorted laminar flame, the flame thickness is still taken to be the thickness of the actual combustion event. Turbulent flames appear thicker because the human eye integrates the otherwise laminar flame front as it moves and distorts due to eddy motion. Thus, Equation 17 is also applicable to turbulent flames.

There are three regimes that turbulent flames can fall into depending on the flame thickness and turbulent length scales of the flow. There are two turbulent length scales of interest that define the size extremes of turbulent eddies. The integral length scale, ℓ_0, is the largest turbulent scale and represents the size of the largest eddies in a given flow. This scale is usually limited by bounding geometry such as a channel height or pipe diameter. The Kolmogorov length scale, ℓ_K, is the smallest turbulent scale and represents the size of the smallest eddies in a flow. At this smallest

scale the rotational eddy motion is broken down by viscous dissipation and generates thermal energy. The three regimes of turbulent flames are shown below with their corresponding relationship of flame thickness to the turbulent scales [20].

Wrinkled laminar-flame	$\delta \leq \ell_k$
Flamelets-in-eddies	$\ell_0 > \delta > \ell_k$
Distributed reactions	$\delta > \ell_0$

In the Wrinkled Laminar-Flame regime the flame is thinner than the smallest turbulent scales. This means that the turbulent motion can only wrinkle or distort the flame zone. At the other extreme is the Distributed Reactions regime, also called the Damköhler criterion. In this regime the flame thickness is larger than all the turbulent scales. At these proportions the mass transport in the reaction zone is aided or controlled by the turbulence and does not rely on molecular transport alone [20].

The Damköhler number, Da, is another important parameter in combustion. This non-dimensional number is defined as the ratio of the convective rate to the reaction rate in a reacting flow. Stated another way, it is the ratio of a characteristic flow time, τ_{flow}, to a characteristic chemical time, τ_{chem}. The Damköhler number is defined in Equation 20 with example definitions of τ_{flow} and τ_{chem} provided in Equations 21 and 22. In these equations A_{exit} is the exit area of the combustor, V_f is the flame propagation velocity, and V_{flow} is the local flow velocity.

$$Da = \frac{\tau_{flow}}{\tau_{chem}} \tag{20}$$

$$\tau_{flow} = \frac{\sqrt{A_{exit}}}{V_{flow}} \tag{21}$$

$$\tau_{chem} = \frac{1cm}{V_f} \tag{22}$$

A combustion condition with $Da >> 1$ represents fast chemistry, which means the chemical reaction rate is much faster than the fluid mixing rate. The opposite is true for a combustion condition with $Da << 1$.

For a turbulent premixed flame, the Damköhler number can be expressed in terms of the integral length scale, root-mean-square velocity fluctuation u'_{rms}, flame speed, and flame thickness as shown in Equation 23.

$$Da = \frac{\tau_{flow}}{\tau_{chem}} = \frac{\ell_0/u'_{rms}}{\delta/S_L} \tag{23}$$

In Figure 9 the three flame regimes are plotted for turbulent premixed combustion with respect to the Damköhler number and turbulence Reynolds number. The turbulence Reynolds number is given in Equation 24.

$$Re_{\ell_0} = \frac{\ell_0 u'_{rms}}{\nu} \tag{24}$$

In Figure 9, each of the three flame regimes, labeled A through C, are bounded by the heavier weight solid black lines. These boundaries represent $\ell_K = \delta$ and $\ell_0 = \delta$. The boxed region shows experimental estimates of the domain associated with spark-ignition. Additionally, the two dashed lines are lines of constant ℓ_K/δ; the dot-dash line is a line of constant ℓ_0/δ; and the thin solid lines are lines of constant u'_{rms}/S_L.

In 2006 Anthenien and Zelina [23] experimentally analyzed the combustion regime of an ultra compact combustor test rig. They found that the primary combustion regime was classified as "Perturbed Flamelets" as they called them, which falls under the "Flamelets in Eddies" regime in Figure 9. This result highlights the importance of turbulent transport and mixing to the UCCs operation.

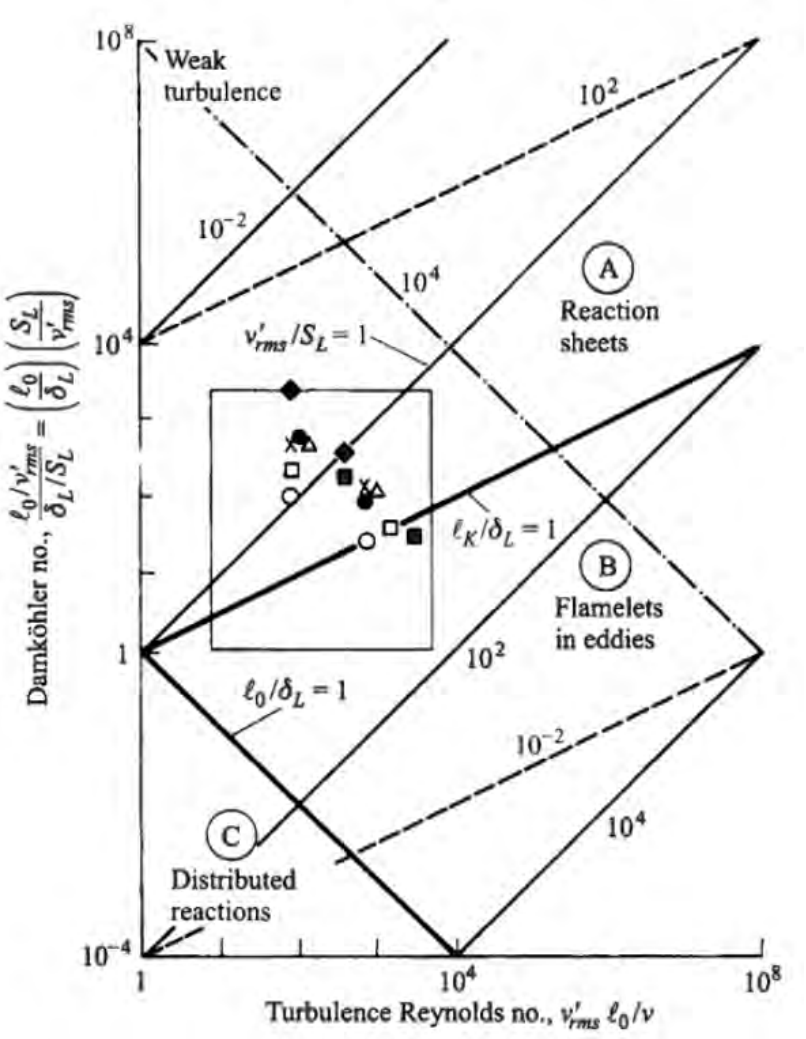


Figure 9. Turbulent premixed combustion flame regimes [20]

2.1.1.3 Combustor Performance Parameters.

Combustion stability is important for smooth operation of a gas turbine engine. Mattingly [14] defines combustion stability as, "the ability of the combustion process to sustain itself in a continuous manner." Stable performance can be disrupted due to the fuel-air ratio becoming too lean or too rich. At these fuel quantity extremes the temperature and reaction rates drop below the necessary level to vaporize incoming fuel and often results in blowout. In Equation 25 Mattingly [14] defines the com-

bustion loading parameter, CLP, which takes into account the mass flow rate ($\dot{m}$), combustion volume (V_{comb}), and pressure (P) on the stability of the combustion process. The value of n has been experimentally determined to be 1.8 for hydrocarbon combustion in air.

$$CLP = \frac{\dot{m}}{P^n V_{comb}} \tag{25}$$

Spalding [24] found that the CLP stability limits of a well stirred reactor using n=1.8 to be 90 lbm/(s·atm$^{1.8}$·ft^3) at Φ=1 and 10 lbm/(s·atm$^{1.8}$·ft^3) at Φ=0.5 and 1.7. This result really highlights how much the flow rate must be pulled back at the fuel quantity extremes to maintain stability.

Anthenien et al. [25] describe a loading parameter for a high-g ultra compact combustor that was derived from well-stirred reactor studies called the Longwell Parameter, Θ. This relationship is given in Equation 26 where P is pressure in units of Pascals, V_{comb} is combustion volume in units of m^3, T is the burned air temperature in units of Kelvin, and $\dot{m}_{cav}$ is the mass flow rate of fuel and air into the circumferential cavity in units of kg/s.

$$\Theta = \frac{P^{1.75} V_{comb} e^{T/300}}{\dot{m}_{cav}} \tag{26}$$

Equation 26 is essentially the inverse of Equation 25 with a temperature correction. As a result, higher cavity loading comes from a lower Θ, which corresponds to a higher CLP. Anthenien et al. [25] demonstrated a Longwell value of about 10^7 in their high-g test rig. At comparable efficiency levels, a conventional annular combustor would operate at a Longwell value of about 10^8. Anthenien et al. also found that combustion efficiency increased with increased loading in a high-g combustor, where traditional combustor efficiency is reduced with an increase in loading.

The required length of a combustor is determined by the speed of the fluid in the combustor and the time it takes for fuel to mix and fully burn prior to exiting

the combustor. The amount of time a particle spends in the the combustor is called the residence time. The residence time is simply found by dividing the combustor length by the average velocity in the combustor. To ensure that the residence time is sufficient to allow the combustion reaction to take place, an understanding of chemical reaction rates is necessary. Steinfeld et al. [26] define many ways to calculate the chemical rate depending on the order and complexity of the reaction. However, in many cases the Arrhenius rate equation, shown in Equation 27, can be used to approximate the temperature dependent chemical reaction rate, $k(T)$.

$$k(T) = Ae^{\frac{-E_{act}}{RT}} \tag{27}$$

In Equation 27, E_{act} is the activation energy, R is the universal gas constant (8.314 J mol^{-1} K^{-1}), and T is temperature in units of Kelvin. The activation energy is the amount of energy that must be supplied to the reactants to get them to react. The pre-exponential factor, A, has a weak temperature dependence, and is proportional to pressure, P^n, for hydrocarbons. The units of A are the same as for the rate constant, k. For first order reactions k has units of seconds^{-1} and the reaction time is inversely proportional to the reaction rate. Thus the reaction time is proportional to P_{t3}^{-n}. [26] Using the above principles Mattingly [14] derived the combustor length scaling parameter, L, shown in Equation 28. In this equation $r = 1.51$ for cases where $n = 1.8$. From Equation 28 it can be seen that the length of the combustor is a function of the total pressure entering the combustor and the total temperature exiting the combustor. There is no direct dependence of the combustor length on the size of the engine.

$$L \propto \frac{P_{t3}^{-r}}{\sqrt{T_{t4}}} \tag{28}$$

The total pressure loss across the combustor is important to understand as it has a direct impact on the inlet pressure the turbine sees. Higher pressures at the turbine inlet results in more work that can be extracted by the turbine. The remainder of this paragraph focuses on combustor pressure losses due to geometry, while Section 2.1.2 addresses pressure losses due to heat addition, also known as Rayleigh losses. Lefebvre [18] defines two pressure loss parameters. The first is the overall pressure loss, $\Delta P_{3-4}/P_3$, which is dependent on the operating condition of the engine. The second parameter is the pressure loss factor, PLF. This parameter is the ratio of the total pressure drop across the combustor to a reference dynamic pressure, q_{ref}, as shown in Equation 29.

$$PLF = \frac{P_{t3} - P_{t4}}{q_{ref}} \tag{29}$$

Unlike the overall pressure loss, the pressure loss factor is not dependent on operating condition and is only a function of the geometry of the combustion chamber. The PLF combines the pressure drop across the diffuser and the drop across the liner. Lefebvre [18] gives some representative PLF values for traditional combustors as being between 20 and 40. There is a balance that must take place within the combustor as higher pressure losses across the liner aid in secondary jet penetration into the chamber and also allows for cooling air to be taken from a lower compressor stage.

Combustion efficiency is an obvious combustor performance parameter that is of great significance. Aside from low efficiency not making good use of fuel, low combustion efficiency has a direct link with the level of emissions of pollutants. Mattingly [14] states that modern combustors achieve greater than 99.5% efficiency at takeoff and cruise conditions. Off-design conditions in the past have been marked by efficiency levels in the low 90%'s. However, the increase in emission regulations in recent years have caused the combustion efficiency at off-design conditions to need to exceed 98.5%

to meet the stringent levels of carbon monoxide and unburned hydrocarbons in gas turbine exhaust.

Mattingly [14] presents an empirical model of combustion efficiency, η_b, based on the reaction rate parameter, θ. Using the plot in Figure 10 and the definitions provided in Equations 30 and 31 the combustion efficiency can be found.

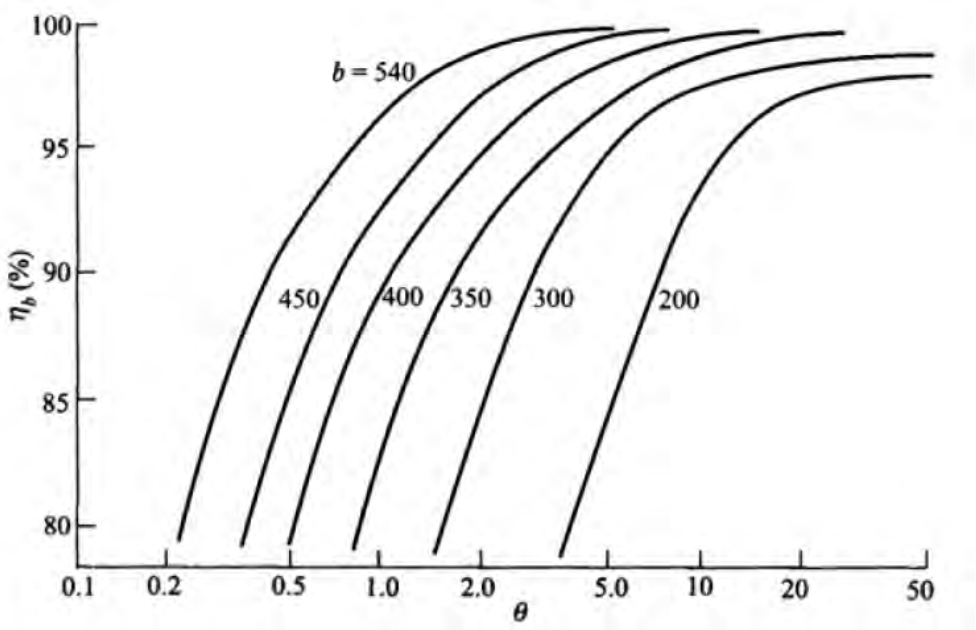


Figure 10. Combustion efficiency (η_b) versus reaction rate parameter (θ) [14]

$$\theta = \frac{P_{t3}^{1.75} A_{ref} H e^{(T_{t3}/b)}}{\dot{m}_3} \times 10^{-5} \tag{30}$$

In Equation 30, P_{T3} is the main burner inlet total pressure in psi, A_{ref} is the main burner reference area in square inches, H is the height of the main burner in inches, T_{T3} is the main burner inlet total temperature in Rankine, $\dot{m}_3$ is the main burner inlet airflow in pounds per second, and b is defined in Equation 31.

$$b = 382\left(\sqrt{2} \pm ln\frac{\Phi}{1.03}\right) \tag{31}$$

In Equation 31, Φ is the equivalence ratio and the plus is used when $\Phi < 1.03$ and a minus is used when $\Phi > 1.03$.

2.1.2 Rayleigh Losses.

Rayleigh losses are defined as a drop in total pressure due to heat addition in a fluid flow. The pressure losses become increasingly large for an equivalent increase in Mach number or the ratio of exit to inlet stagnation temperatures. The cause of this disproportionate increase in pressure drop due to heat addition or flow acceleration is shown in Equation 32 as defined by Hill and Peterson [17]. In this equation P_o is the stagnation pressure, M is the Mach number, and T_o is the stagnation temperature.

$$\frac{dP_o}{P_o} = -\frac{\gamma M^2}{2}\frac{dT_o}{T_o} \tag{32}$$

Erdmann et al. [27] highlight the dependence of Mach number on changes in cross-sectional area and total temperature as shown in Equation 33. Due to changes in flow path geometry or heat addition the fluid could accelerate causing an even greater Rayleigh loss than the pressure drop due to heat addition alone. The variables in the equation are the same as defined above with the addition of A, which is the cross-sectional area.

$$\frac{dM^2}{M^2} = \frac{1+\frac{\gamma-1}{2}M^2}{1-M^2}\left[-\frac{2dA}{A} + (1+\gamma M^2)\left(\frac{dT_o}{T_o}\right)\right] \tag{33}$$

Erdmann et al. [27] plotted the above relationships to show the dependence of Rayleigh losses on inlet Mach number and the exit to inlet stagnation temperature ratio. This plot is shown in Figure 11. The plot does not include area variations.

As Erdmann et al. point out, flows with a Mach number of 0.3 have Rayleigh pressure losses around 5% and 15% for stagnation temperature ratios of 1.8 and 2.6,

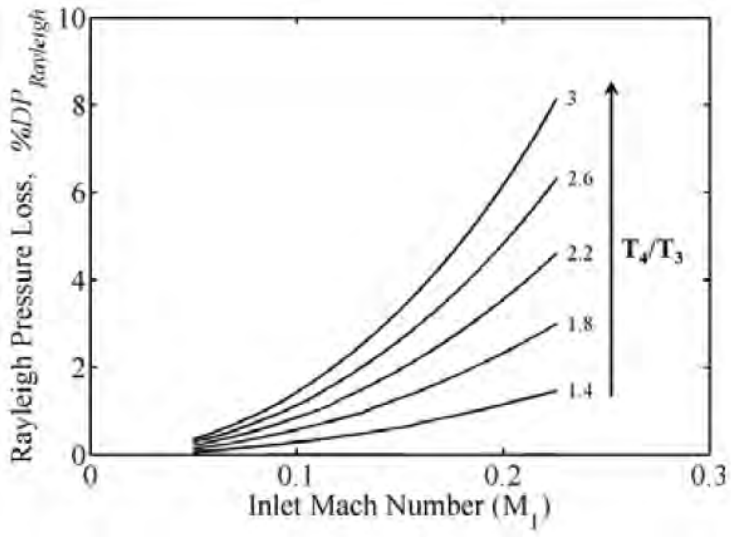


Figure 11. Rayleigh pressure loss as a function of inlet Mach number and exit to inlet stagnation temperature ratio [27]

respectively. For the same stagnation temperature ratios, flows with a Mach number of 0.1 have a Rayleigh pressure loss of about 1% for both. A current state-of-the-art turbine engine features a pressure drop of approximately 5% across the combustor. This low percentage loss is achieved despite a very large stagnation temperature increase because these combustors maintain Mach numbers around 0.1 through the use of a dump diffuser. In order for a UCC to be a viable combustor solution in a turbine engine it is important to understand the mechanisms of Rayleigh losses and be able to control these losses across the UCC. The ultimate goal would be to have a UCC that meets the same loss levels as the current state-of-the-art traditional combustor.

2.1.3 Combustor Exit Temperature Profiles.

The temperature profile presented to the turbine is extremely important given the magnitude of the temperatures exiting the combustor. Achieving a desirable and consistent temperature profile on the exit plane ensures the placement and magnitude

of cooling on the first stator row in the high-pressure turbine will be effective across all operating conditions. Other than turbine component longevity, the other reason to control the temperature profile of the exiting combustion gases is to maximize power extraction from the turbine. It is common practice to specify that the temperature at the mid-span be hottest with the temperature decreasing at the hub and tip of the turbine blade. However, Samuelsen [28] and Barringer [29] both state that a slight OD skew in the thermal profile is needed to maximize power extraction from the turbine and protect critical components on the ID of the engine. Figure 12 shows combustor exit temperature profiles for four commercial engine combustors. The temperature is presented in nondimensional fashion where Θ is defined by Equation 34.

$$\Theta = \frac{T - T_{avg}}{T_{avg}} \tag{34}$$

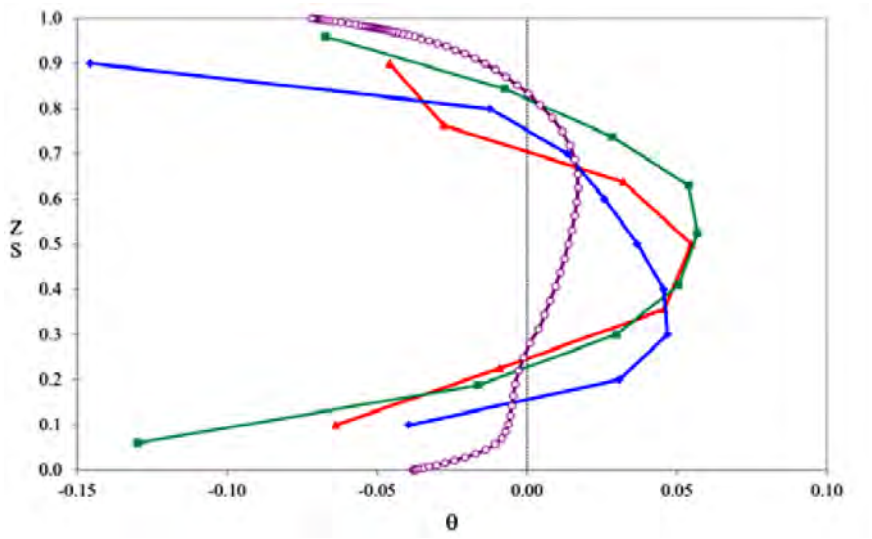


Figure 12. Commercial engine combustor exit temperature profiles [30]

One metric for defining the turbine inlet temperature is the pattern factor, PF, as defined by Mattingly et al. [14] and shown in Equation 35. The pattern factor

is a measure of the uniformity of the temperature distribution on the combustor exit plane. It describes the deviation of the average maximum temperature to the average exit temperature and compares that to the difference between the average exit temperature and the combustor inlet temperature. For a traditional combustor the PF is typically between 0.25 and 0.45. For newer high temperature rise combustors the PF requirement becomes more restrictive at a value between 0.15 and 0.25. In Equation 35, T_{t4max} is the maximum measured exit total temperature, T_{t4avg} is the average of all temperatures on the exit plane, and T_{t3} is the average of all temperatures on the combustor inlet plane.

$$PF = \frac{T_{t4max} - T_{t4avg}}{T_{t4avg} - T_{t3}} \tag{35}$$

The second metric defining the turbine inlet temperature is the profile factor, Pf, shown in Equation 36 [14]. The Pf describes the maximum circumferentially averaged temperature ($T_{t4max-avg}$), relative to the combustor inlet temperature (T_{t3}) and combustor exit plane temperature (T_{t4avg}). The profile factor offers an alternate method to the pattern factor to quantify the combustor exit temperature distribution as a single number. Profile factors for a traditional combustor range from 1.04 to 1.08 with 1.06 being the common design goal.

$$Pf = \frac{T_{t4max-avg} - T_{t3}}{T_{t4avg} - T_{t3}} \tag{36}$$

2.1.4 Emissions.

The process of converting fuel to the stoichiometric products of water, carbon dioxide, and nitrogen is seldom accomplished without also producing additional unintended products. These unintended species, plus carbon dioxide, are considered pollutants and the quantities in which they are produced is a global concern. Turns [20]

lists the pollutants from a gas turbine engine which are summarized in Table 1. The particular product species that are produced is dependent on the conditions in the combustor.

Table 1. Pollutant types and examples [20]

Pollutant Type	**Examples**
Particulate Matter	Soot, Fly Ash, Metal Fumes, Aerosols
Unburned/Partially Burned Hydrocarbons	Aldehydes, CH_4
Sulfur Oxides	SO_2, SO_3
Nitrogen Oxides	NO_x, NO, NO_2
Carbon Oxides	CO, CO_2
Greenhouse Gases	CO_2, N_2O, CH_4

Pollutants can have an effect on the atmosphere, the environment, and humans. Pollution particulate can cause reduced visibility, smog, and acidic fog or precipitation. The addition of greenhouse gases to the atmosphere can trap thermal radiation near the earth and raise the global temperature. Phytotoxicants such as SO_2 destroy chlorophyll in plants which can disrupt photosynthesis and kill the plant. Sulfur based particulates have acidic or alkaline properties which can corrode exposed items. Humans can be sickened or killed due to exposure to pollutants in larger quantities or small quantities over extended periods of time. [20]

The emission index, EI, presented by Turns [20] is one method to quantify the production of a specific species, i, of pollutant. The emission index is the ratio of the mass of the species of interest over the mass of fuel burned as shown in Equation 37. The EI can also be written in terms of the mole fractions, χ, and molecular weights, MW, of the species and the fuel, F. Equation 37 assumes that all carbon atoms from the hydrocarbon fuel is converted to CO or CO_2, and x is the number of moles of carbon in a given fuel (C_xH_y). The EI is designed to be a dimensionless quantity, however, sometimes units of g/kg or g/lb are used to avoid very small numbers.

$$EI_i = \frac{m_{i,emitted}}{m_{F,burned}} = \left(\frac{\chi_i}{\chi_{CO} + \chi_{CO_2}}\right)\left(\frac{xMW_i}{MW_F}\right) \tag{37}$$

Table 2 shows data from Bahr[31] outlining the distribution of mass of specific emission constituents from a twin-engine transport in a typical 500 nautical mile flight profile. The table provides the mass of constituents during a landing-takeoff cycle which includes all aircraft movement below 3000 feet, including final descent, landing, taxi, and takeoff; and the mass components during climbout, cruise, and descent. The majority of the emission are in the form of nitrogen oxide compounds specifically during cruise.

Table 2. Distribution of total emission mass quantities generated during a typical flight profile of a twin-engine transport over a 500 nautical mile range [31]

Category	**Landing-Takeoff**	**Climbout, Cruise, Descent**	**Total**
Smoke	-	0.1	0.1
Unburned HC	0.6	1.0	1.6
CO	5.4	7.0	12.4
NO_x	7.8	78.1	85.9
Total	13.8 (56.5% NO_x)	86.2 (90.6% NO_x)	100.0

Carbon monoxide formation occurs in two temperature bands as shown in Figure 13. At the lower temperature band (1500 K) the equilibrium concentration of CO is significantly lower than the concentration at the higher band. At higher temperatures (such as flame temperatures, 2000-2260 K) the equilibrium concentration of CO is much higher due to the dissociation of CO_2 into CO. In both cases the lowest concentrations were achieved around Φ=0.8. Higher CO production is linked to low-power engine operation or fuel-rich combustion. Experimental quantities of CO have been found between 8 and 80 g/kg of fuel, with this value decreasing at higher combustion pressures. The formation of unburned hydrocarbons follows a similar trend [18].

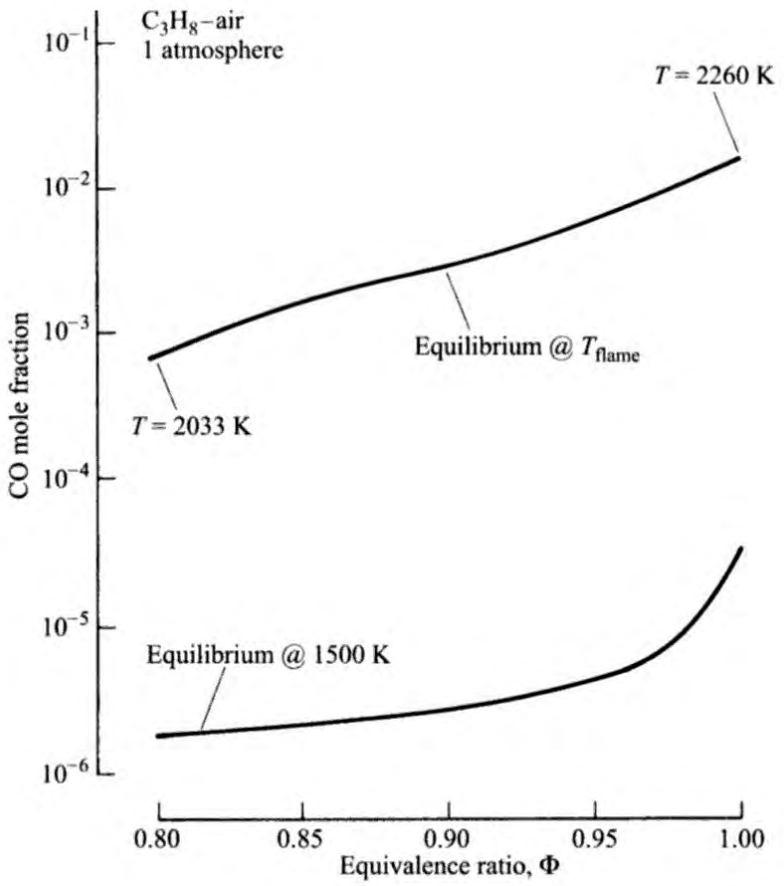


Figure 13. Equilibrium CO mole fractions in propane-air combustion at adiabatic flame temperatures and 1500K [20]

Particulate emissions such as soot and smoke generally only occur during fuel rich combustion or due to fuel additives such as aromatic compounds. [20] [18] Soot formation generally occurs in the primary combustion zone and is burned in the secondary and dilution zones. Higher combustion pressures generally result in higher soot production.

Nitrogen oxides can largely be controlled by limiting the temperature and residence time in the combustor. Thermal NO production is controlled by limiting the combustion temperature to values below 1850 K. Thermal NO production peaks around stoichiometric conditions where peak temperatures are achieved and drops off

on each side as shown in Figure 14. Better mixing can also help to ensure there are no pockets of near stoichiometric combustion which can locally increase NO_x production. Decreasing the residence time inside the combustor has been shown to reduce NO_x production.

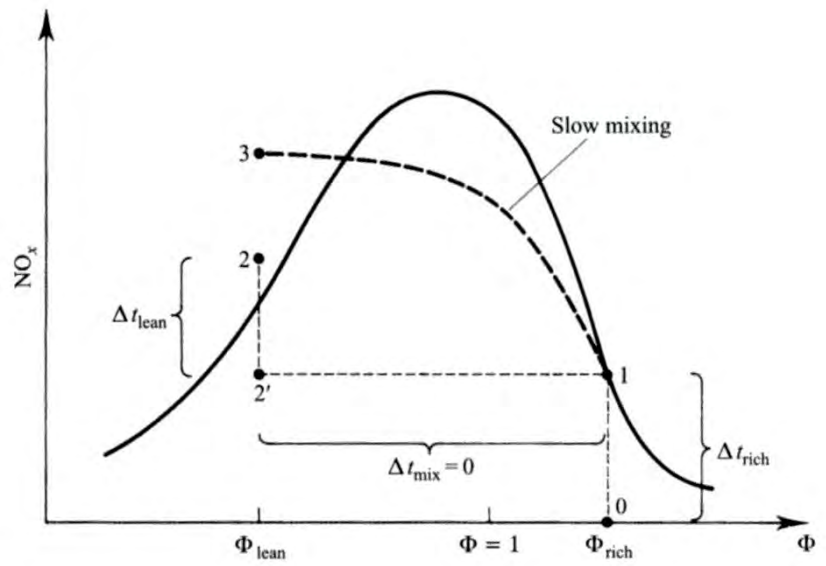


Figure 14. NO_x production in staged combustion. The path 0-1-2'-2 is ideal with instantaneous secondary air mixing, 0-1-3 indicates a path for slow mixing [20]

Looking at the information in the previous few paragraphs, the conditions needed to reduce production of a specific pollutant will generally result in the increased production of another. As an example, all of the mitigation techniques mentioned for reducing NO_x production would result in an increase in CO and unburned hydrocarbon production. Trade-offs must be made to strike an acceptable balance for each of the emission species produced by a specific combustor design.

Anthenien at al. [25] conducted experimental measurements on a high-g UCC and found CO production levels between 20 and 180 g/kg of fuel running a liquid JP-8. Additionally, Zelina et al. [32] confirmed the CO levels and found that NO_x production was in the range 1.5 to 3.0 g/kg using the same high-g UCC and fuel.

2.2 Compact Combustion Theory and History

The idea of compact combustion has only been around since about 2000 and is based on centrifugally loaded combustion findings and turbine burning cycle analysis. Since its inception there have been two primary types of compact combustors that differ fundamentally in the direction of their swirl. In both cases, fuel and air are swirled inside a cavity that is recessed around the outside diameter of the engine and away from the primary core flow. Both combustor types are shown in Figure 15. The trapped vortex combustor, TVC, rotates fuel and air inside the cavity such that the axis of rotation is tangent to the engine circumference. The high-g combustor, HGC, rotates fuel and air inside the cavity such that the axis of rotation is collinear with the engine centerline.

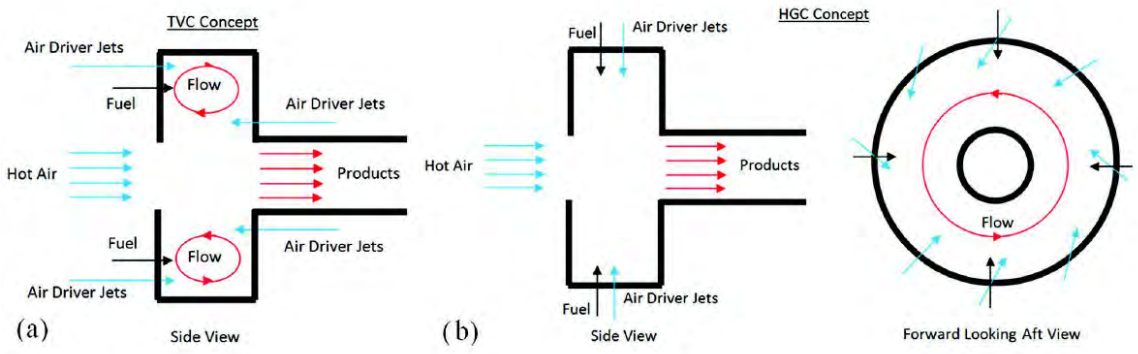


Figure 15. a) TVC cross section b) High-g UCC cross section and front view [33]

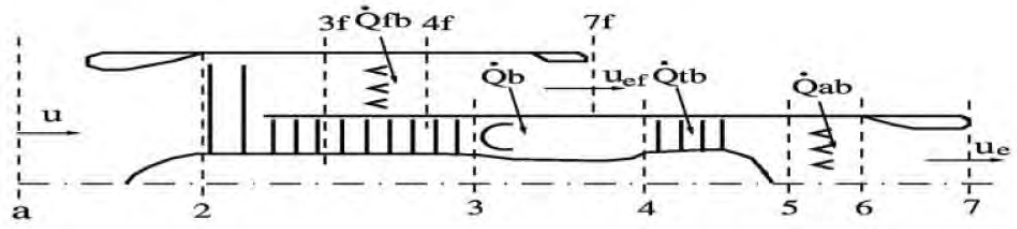
There are still many areas of research that need to be conducted on both combustor types. The primary areas that need further examination include 1) air and fuel injection techniques and their influence on cavity flow dynamics and combustion characteristics, and 2) fluid migration mechanisms to transport the fluid in the recessed cavities into the main core flow. Beyond just fluid migration, it is important that the temperature distribution downstream of the combustor meet the desired profile for turbine operation.

Experimentally there is one benefit of the TVC over the HGC. A representative section of a TVC can be used to study combustion and migration dynamics without the need for a full annulus. To experimentally test the HGC a full annulus is needed to establish the high-g circumferential flow inside the recessed cavity. The remainder of this section focuses on the fundamental science of the TVC and HGC as it is currently understood by researchers, and the advancement of the high-g combustion rig at AFIT and understanding of high-g combustion dynamics.

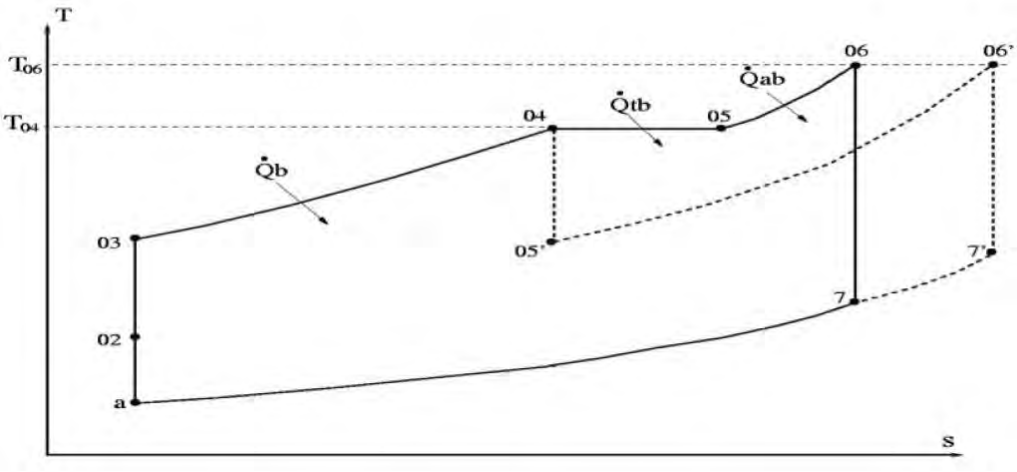
2.2.1 Compact Combustion Cycle.

In 1997 Sirignano et al. [5] published their findings of a preliminary study on a turbine burner. This publication was followed up two years later in Sirignano et al. [34] which provided additional detail on the subject. The concept of turbine burning involves a continuous heat release while extracting energy through the turbine. The ultimate goal of this cycle was to reduce thrust-to-weight and specific fuel consumption of the engine. Sirignano et al. modified a standard Brayton cycle by adding in heat at non-traditional points in the engine. Figure 16 shows a turbofan engine schematic and corresponding temperature-entropy diagram for the modified cycle. The dotted line in Figure 16b shows the T-s path taken for a traditional afterburner engine with no turbine burning and the all solid line includes turbine burning and a traditional afterburner.

Figure 16a shows all the locations Sirignano et al. [5] felt could be used to augment the standard Brayton cycle. These locations include heat addition in the main burner ($\dot{Q}_b$), fan augmenter ($\dot{Q}_{fb}$), standard augmenter ($\dot{Q}_{ab}$), and a turbine burner ($\dot{Q}_{tb}$). In Figure 16b it can be seen that the heat release in the turbine enabled a near constant stagnation temperature across the turbine similar to an ideal Carnot cycle. This arrangement allows for the same temperature to be achieved at Station 6 with



(a) Engine stations showing possible heat addition locations



(b) Sirignano modified Brayton cycle

Figure 16. Modified Brayton cycle from Sirignano et al. [5]

a reduced entropy. A traditional afterburner add power to the engine by increasing the temperature of the core stream, but it does this at a lower pressure and thus has a reduced overall cycle efficiency. Using the turbine burner allows heat addition while simultaneously extracting work. Since the temperature of the core stream at Station 5 was not reduced, less fuel is needed by the after burner to achieve the same temperature at Station 6, thus maintaining more efficiency.

The analysis by Sirignano et al. [5] shows that their turbine burning scheme could achieve the same amount of thrust by a shorter engine or greater thrust by the same size engine compared to a traditional afterburning engine. Sirignano et al. [34] looked to find a way to approximate the theoretical continuous turbine burner (CTB) with something that could be produced. In this study they introduced discrete combustion

stages that only allowed combustion to occur in the turbine stators, ie an inter-turbine burner (ITB). By increasing the number of ITB stages, the result begins to approximate the theoretical CTB as shown in Figure 17.

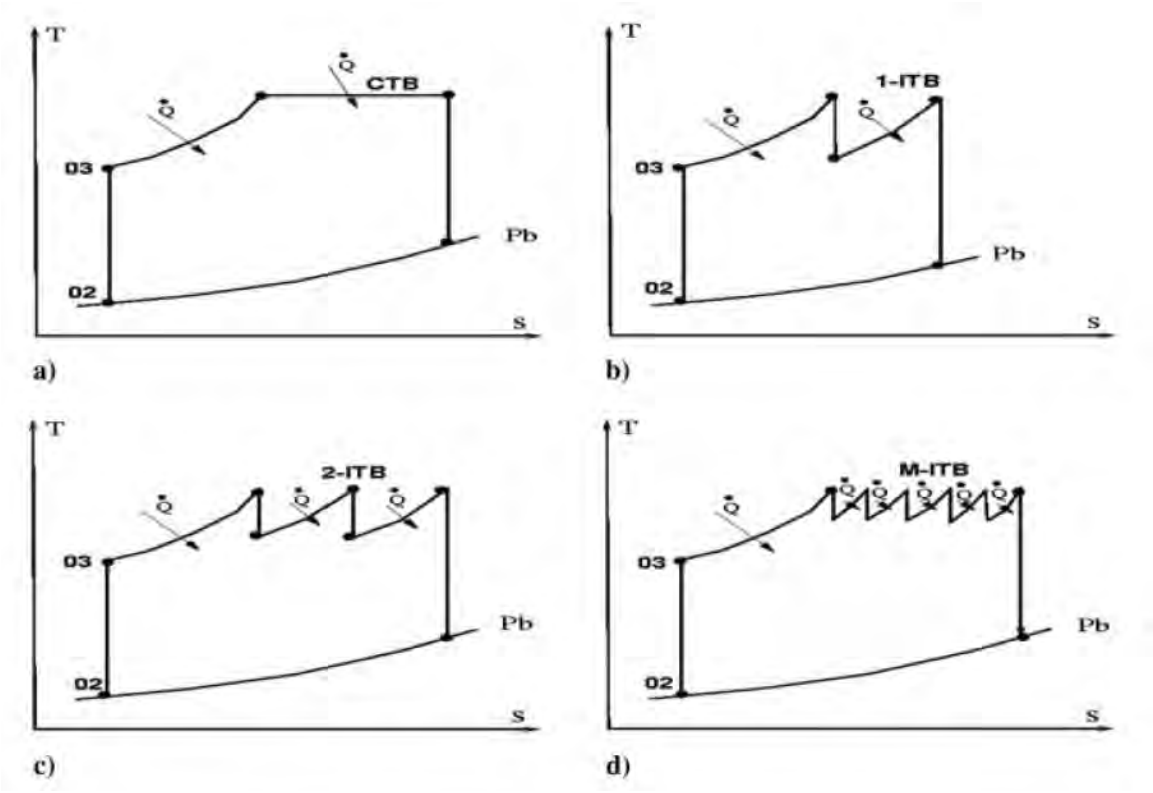


Figure 17. Cycle comparisons of CTB to various numbers of ITB stages (no afterburner) [34]

2.2.2 Turbine Passage Burning.

In order to implement the turbine burner concept and isolate combustion to the area within a single stator, a greater understanding of combustion behavior in the presence of strong pressure gradients was required. A row of turbine stators acts like a nozzle accelerating fluid as it moves through. To this end, Sirignano and Kim [35] and Fang et al. [36] numerically studied a laminar, two-dimensional reacting mixing layer in the presence of favorable pressure gradients due to acceleration. Sirignano and Kim

studied this arrangement with infinite-rate chemical kinetics while Fang et al. looked at finite-rate chemical kinetics. Mehring et al. [37] expanded on these studies by introducing turbulent effects into the same model. Accounting for turbulence allowed the velocity and temperature profiles to spread up to 23 times more than the laminar case.

More recently Cheng et al. [38] conducted an even more detailed numerical study that specifically looked at reacting flow through a curved accelerating passage representative of a turbine airfoil passage. In this study they had a split stream enter the passage with a faster and hotter air stream on the top and a cooler and slower fuel stream on the bottom of the passage. Methane was the fuel in this case. The test geometry and results are shown in Figure 18. Due to the difference in temperature and velocity between these two streams, a shear layer was established and instability began even before entering the passage. This result is evident in the wavy flame observed between x-axis position 0 and 200. Positions in the channel are marked by a function of the mixing layer thickness as measured at the inlet (δ_θ). The mixing layer thickness was taken to be a constant with a value of δ_θ=1.25x10^{-4}m. It is important to note that a similar result was obtained when the fluid streams were reversed with the faster air on the bottom and the slower fuel on the top.

The results shown in Figure 18 present a concern for implementation of the turbine burner concept. Starting at approximately s=500δ_θ, there appear to be flames burning directly on the airfoil surface. As the instability in the passage grows, the location of the flames appear to effect both sides of the passage. The resulting heat load to the airfoil surfaces will impose a sizable cooling requirement to the vanes. The additional coolant needed in the turbine burning case could remove the benefits gained when the entire engine system is considered.

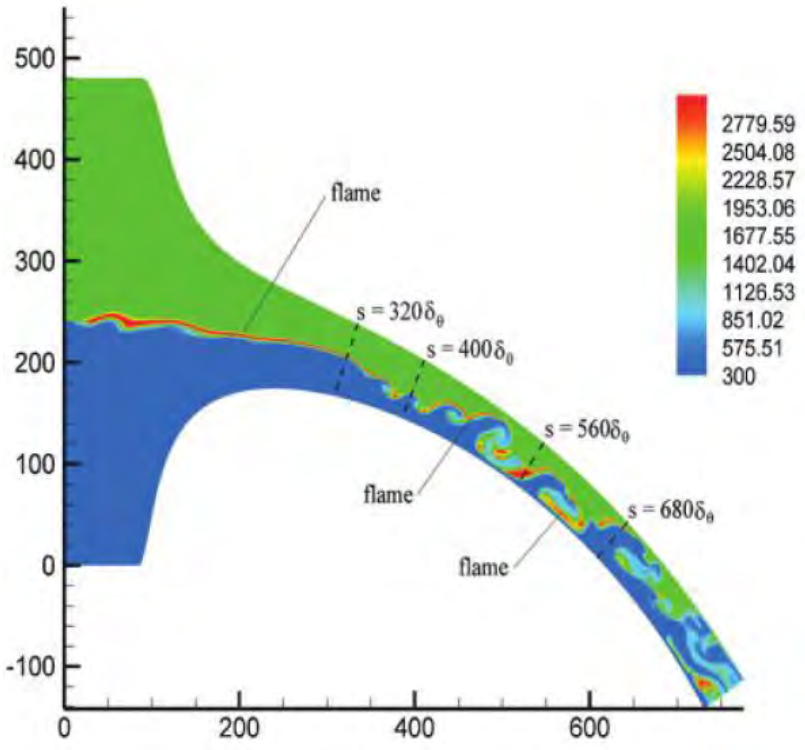


Figure 18. Temperature contours of a reacting mixing layer in a curved, converging channel [38][39]

2.2.3 Trapped Vortex Combustion.

The first of the two ultra compact combustor configurations to be discussed in detail is the trapped vortex combustor (TVC). All variants of the ultra compact combustor are designed to achieve the same performance goals and share a similar cross-sectional geometry, however the flow pattern and combustion dynamics are different. The TVC consists of two zones; a recessed combustion cavity to provide stability, and a main combustor for power. The recessed cavity provides a location for recirculation to hold a pilot flame. Air and fuel are injected into the cavity in a similar manner to that shown in Figure 15 to maintain the recirculation pattern. The cavity is positioned as a recess to the engine outer diameter casing with the hot combustion products exiting radially inward into the main combustor. Based on the

work of Sirignano et al. [5][34][35][36][37][38] the main burner generally takes the form of turbine passages with the recessed cavity located outboard and exhausting radially inward into the vane passages. The combustion process used for the ultra compact combustor is a rich-burn, quick-quench, lean-burn (RQL) process. This means that combustion is initiated in the cavity under fuel-rich conditions. When the products exit the cavity into the main combustor which has a higher volume of air flow, they are quickly quenched and a fuel-lean condition remains for the remainder of the burn. This process skips over the stoichiometric combustion regime which limits the heat load to the combustor hardware. [40]

Prior to 1980, Mair [41], and Little and Whipkey [42] studied cavity sizing behind a bluff body that reduced drag in a non-reacting flow. These cavities were formed by two parallel, axisymmetric discs on a central spindle similar to the arrangement used in Figure 19. Mair, and Little and Whipkey found that if the downstream disc was smaller than the upstream disc there was an ideal spacing between the discs that resulted in minimum drag. Katta and Roquemore [43] performed a time-dependent CFD analysis on the geometry used by Mair, and Little and Whipkey to try and replicate the results numerically. All three groups of researchers found that a stable vortex is trapped inside a cavity sized for minimum drag. At the minimum drag configuration very little fluid is entrained into the cavity. Taking an average of the correlations obtained by the three groups of researchers, the length of the cavity can be found using Equation 38, which is normalized by the diameter of the upstream disc, D_0.

$$L/D_0 = -(1.62)D_1/D_0 + 1.79 \tag{38}$$

The TVC was conceived in 1993 by the Air Force Research Laboratory operating under a program funded by the Air Force Office of Scientific Research (AFOSR). In their first generation TVC they used trial and error to find the cavity dimensions that

resulted in stable combustion. The cavity was formed between two parallel discs as shown in Figure 19. After several iterations of incremental sizing of the downstream cavity disc and linear disc spacing they found that stable combustion was achieved for a cavity length of $0.59D_0$ and downstream disc diameter of $0.73D_0$, where D_0 is the diameter of the upstream disc. [40]

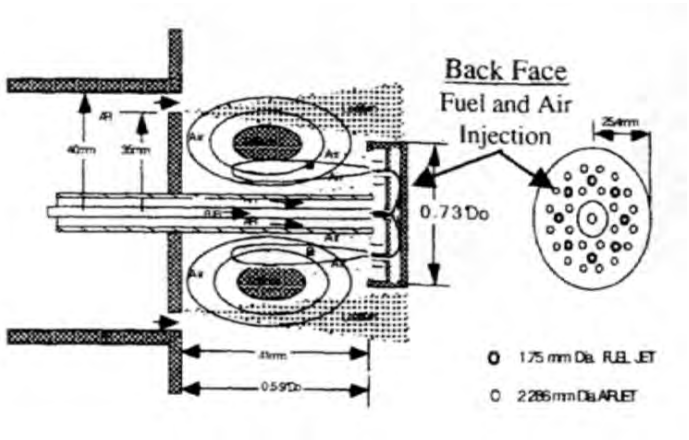


Figure 19. AFRL Generation 1 TVC [40]

Applying the geometry of the first generation TVC developed in [40] to Equation 38, an $L/D_0 = 0.60$ is obtained from the equation and $L/D_0 = 0.59$ from experimental trial and error. This result indicates that a cavity sized for minimum drag in a non-reacting environment, is also optimized for stable combustion.

The paper by Roquemore et al. [40] covered AFRL's TVC development from 1993 to 2001 and highlighted the benefits of the TVC. The TVC achieved greater than 99% efficiency and had a significantly better (up to 50%) improvement in ignition, and altitude relight compared to a traditional swirl-stabilized combustor. The TVC also achieved a 40 - 60% NO_x emissions reduction. All of these benefits were gained while achieving a 40% wider operating range over a traditional combustor.

The most recent publications on TVC research was from Erdmann et al. [44] and Blunck et al. [45] in 2014. The two studies used a common test geometry shown in

Figure 20. In the figure, arrows provide the locations of air and fuel injection points and flow paths, and boxes indicate the locations of viewing windows and emission probes. The test rig was capable of operating at pressures between 520 and 1030 kPa and with inlet temperatures between 480 and 620 K. The equivalence ratio in the recessed cavity was varied between 0.7 and 1.8.

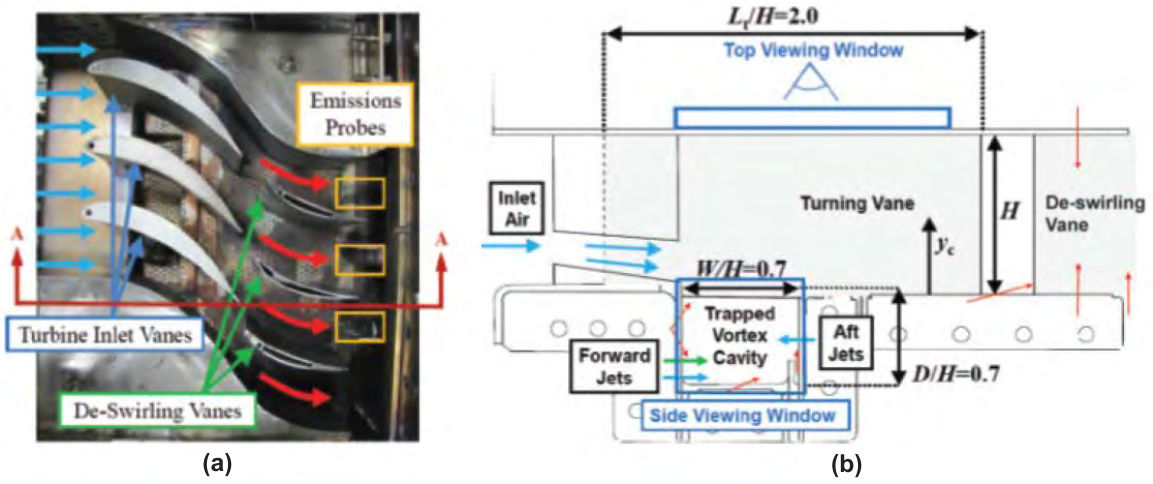


Figure 20. AFRL Current TVC a) photograph of a top view of the experimental setup; b) side view drawing, air flow path arrows are blue, fuel path is green, effusion cooling is red [45]

Erdmann et al. [44] investigated the effect of the turning vanes above the recessed cavity. They obtained results without the vanes, with smooth vanes, and with vanes that included a radial vane cavity (RVC). The RVC acts like a backward facing step to the cross flow and reduces the pressure in that section of the vane. The hot gases exiting the recessed cavity can then travel more freely in this path aiding flow migration across the entire passage height. Figure 21 shows a visual image of the three vane conditions and normalized downstream intensity profiles. The addition of the smooth vanes caused a decrease in intensity, however, the intensity is higher in the case with the radial vane cavity. The vanes also had an impact on the location of the peak temperature in the vane span. The addition of the smooth vane caused

the location of peak temperature to migrate from 30% to 70% of the span. When the RVC vanes were used, the peak temperature was located at almost exactly 50%. The RVC was a hot gas migration technique that was also carried into the high-g UCC with similar success.

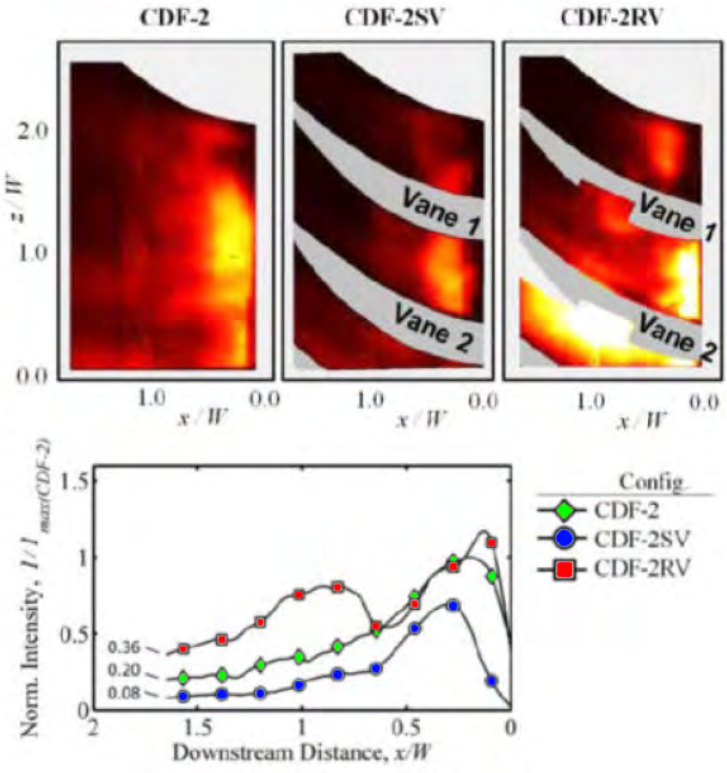


Figure 21. Top-view chemiluminescence images of the three vane cases (top) with normalized downstream intensity profiles (bottom) [44]

Blunck et al. [45] specifically focused on the impact of varying the direction of the inlet air either upward, horizontal, or downward toward the cavity. The final condition is what is shown in Figure 20. Emissions were measured using non-dispersive infrared analyzers, chemiluminescent detectors, and flame-ionization detectors with the sensors focused at the trailing edge of the de-swirling vanes. The flow in the cavity was analyzed with high-speed imagery and coherent-structure velocimetry to find fluid velocities. Blunck et al. found that the downward directed inlet air resulted in the

most coherent vortex inside the cavity, leading to the highest combustion efficiencies of greater than 99.5% across the range of equivalence ratios tested.

A TVC is commonly characterized by the air loading parameter (AL), which is defined in Equation 39. In this equation $\dot{m}_{air}$ is the air mass flow rate in kg/s, V_{cavity} is the cavity volume in m^3, P_{inlet} is the cavity inlet total pressure in kPa, and T_{inlet} is the cavity inlet total temperature in units of Kelvin. Cavity air loading can be applied to the high-g UCC as well.

$$AL = \frac{\dot{m}_{air}}{V_{cavity}\left(\frac{P_{inlet}}{101.325}\right)^{1.75} e^{T_{inlet}/300}} \tag{39}$$

Blunck et al. [45] expressed TVC efficiency results as a function of AL and cavity equivalence ratio. In the three plots of Figure 22 the areas of the cavity air inlet drivers were varied which led to different AL values. In the figure it can be seen that higher air loading resulted in regions of highest combustion efficiency occurring in more narrow ranges of equivalence ratio. When the AL got too high, flame stability decreased, emissions increased, and lower efficiencies were observed. Blunck et al. state that this decrease in performance is due to higher flame strain rates [45].

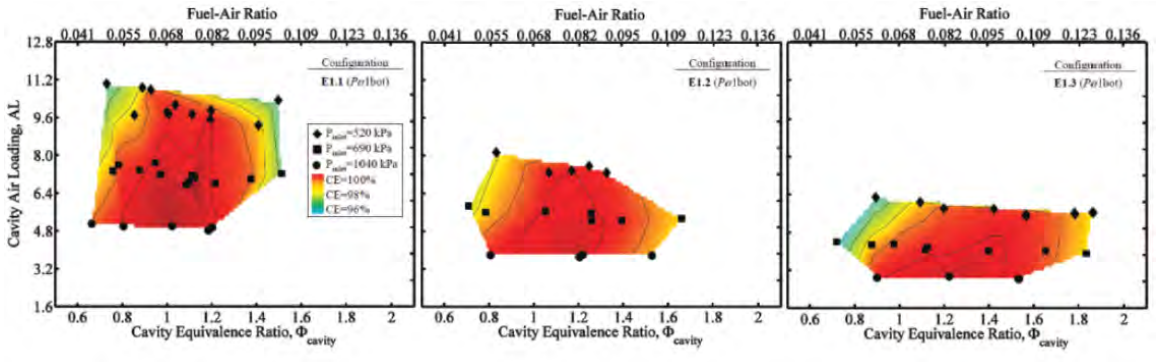


Figure 22. Combustion efficiency contours for varying cavity air loading and equivalence ratio; each panel represents a different cavity air driver area [45]

While the following research was originally intended to support turbine burning objectives, the findings are related to recessed cavity sizing and flame holding capabil-

ities in curved passages making them applicable to TVC and potentially high-g UCC applications. In 2007 Colcord and Sirignano [46] began a 2D numerical study looking at the impact of adding cavities in the side of turbine vanes to act as flame holders in their inter-turbine burner research. They injected air and fuel into these cavities in four configurations as shown in Figure 23. Of the four configurations tested, the parallel injection method resulted in the highest burning efficiency, while the reinforcing method had the lowest burning efficiency. Additionally, their study found that a long, shallow cavity achieved better mixing than a square cavity. Square cavities could not maintain a flame beyond Re = 5,000, where cavities with an aspect ratio of two maintained a flame for Re up to 10,000.

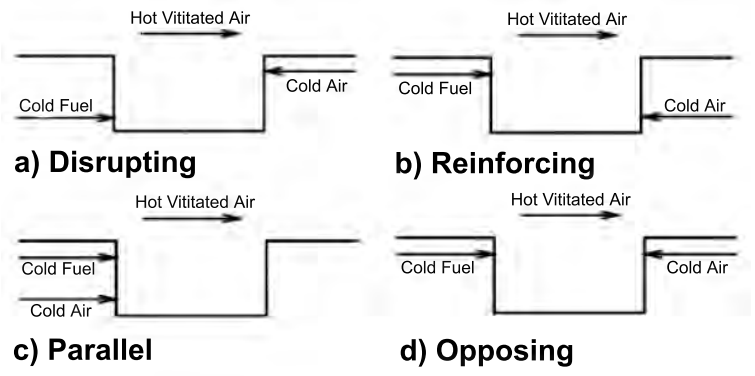
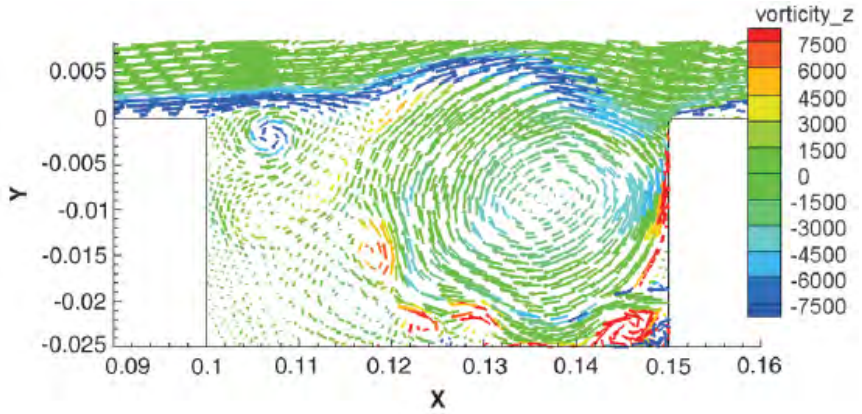


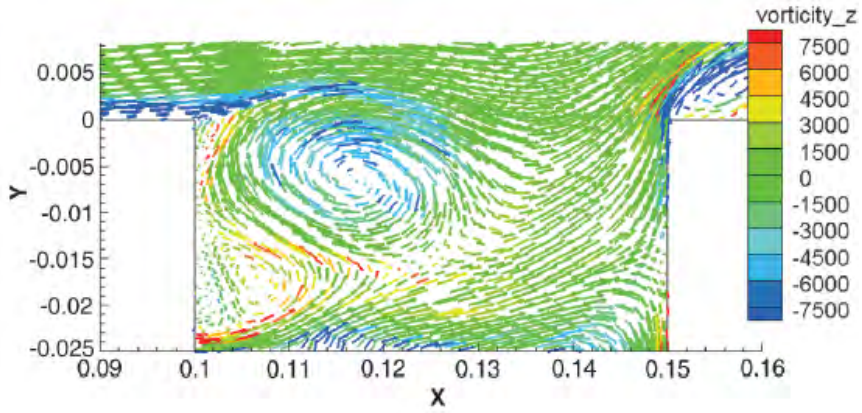
Figure 23. Cavity injection configurations tested by Colcord and Sirignano [46]

Figure 24 shows the flow fields in the highest (parallel) and lowest (reinforcing) burning efficiency cavity injection methods. The vectors in the figure are colored by vorticity. Sirignano et al. [46] [47] report that the large vortices in the reinforcing, disrupting, and opposing methods were largely stationary. The parallel injection method experienced much greater unsteady fluctuations in the cavity which resulted in interaction of the vortical structures. The increased mixing was the cause of the significantly higher burning efficiency for this method.

Colcord and Sirignano [46] extended their numerical research to cavities with an aspect ratio of 4:1 recessed into the side of curved channels. They also investigated



(a) Reinforcing Injection



(b) Parallel Injection

Figure 24. Flow field inside the recessed cavities using the reinforcing and parallel injection methods [46] [47]

the differences between cases with the cavity on the inside and outside of the curve. Representative results of an inside and outside cavity are shown in Figure 25 with flow at a Reynolds number of 2,000. For the inside cavity, parallel injection resulted in a stable condition where the disrupting method resulted in unstable flow. For the outside cavity, the disrupting method was stable and the parallel method was unstable. The outside cavity had a centrifugal instability and produced a Kelvin-Helmholtz instability which is simply due to the presence of the cavity itself.

Sirignano et al. [39][47] studied the effects on convergent channels with recessed cavities. An increase in efficiency was noted when the channels were allowed to

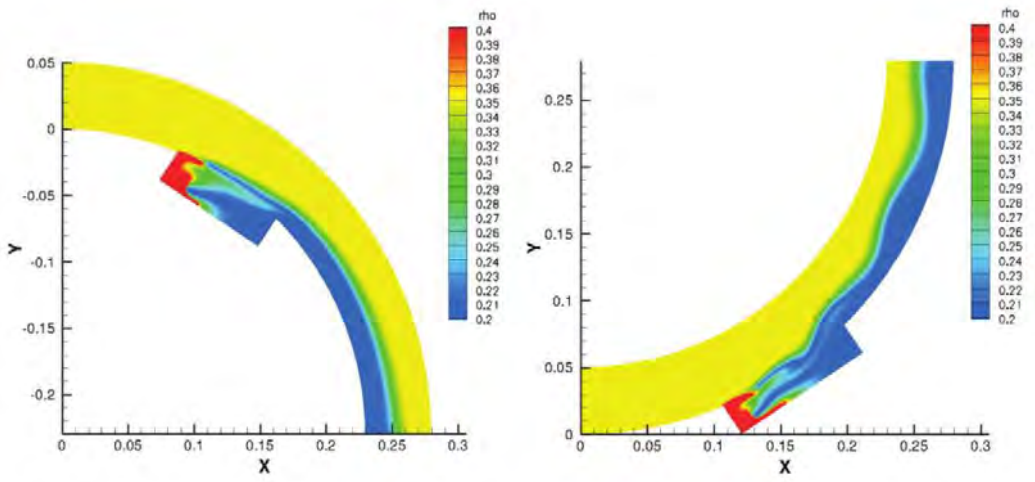
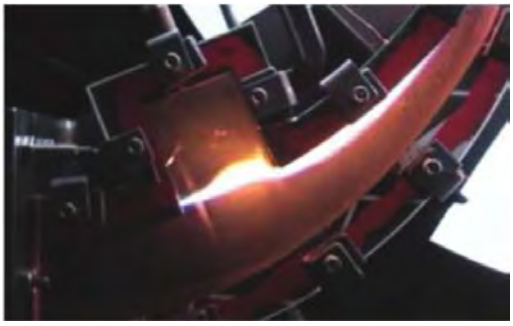


Figure 25. Density contours with parallel injection for an inside cavity (left) and outside cavity (right) from Colcord and Sirignano [46]

converge, however, the residence time was decreased due to accelerated flow. The decrease in residence time did not appear to impact the efficiency. It was also noted that in the case of the converging, curved channel with an outside cavity, the stagnation pressure losses were small. The impact of the cavity, fuel and air injection, cavity mixing, and combustion reactions accounted for approximately 1% of the entering pressure.

Puranam et al. [48] performed an experimental study to investigate the curved channel with an inside recessed cavity with a 1 and 2.5 aspect ratio. In all the cases they were burning propane with the jet originating from the upstream wall like the parallel injection method. Their results concluded that for this type of geometry, the three distinct combustion regimes were formed based on flow Reynolds number. The regimes were low ($Re < 5{,}000$), high ($Re > 40{,}000$), and moderate between these values. Photos of the combustion process for each of these flow regimes are shown in Figure 26.

In the low flow regime there was an insufficient amount of air in the cavity to produce any recirculation and the flame behaved similar to a diffusion flame stabilized



(a) Low regime ($Re < 5{,}000$)



(b) Moderate regime ($5{,}000 < Re < 40{,}000$)

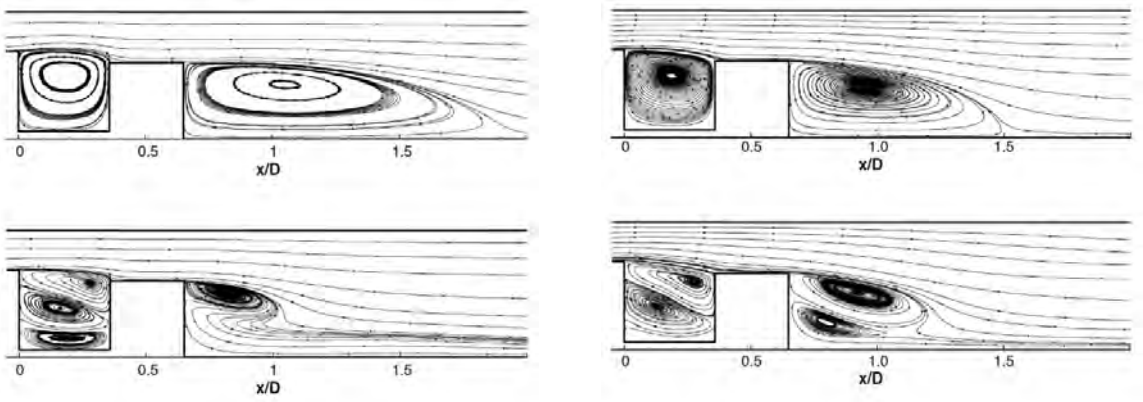


(c) High regime ($Re > 40{,}000$)

Figure 26. Combustion in three Reynolds number regimes for a recessed cavity in a curved channel [48]

in the shear layer along the inside wall. In the high flow regime the flame behaved like a well stirred reactor with most of the combustion taking place in the cavity. The flame in the moderate flow regime was not stable. Based on the position of the flames in Figure 26b, some recirculation must have been taking place inside the cavity, it was just insufficient to maintain stable combustion.

In 2016, Chen et al. [49] investigated the affect of a spinning recessed cavity in a TVC. The cavity geometry is similar to the parallel disc combustor shown in Figure 19 with a forebody disc and afterbody disc connected with a central spindle. In keeping with the findings discussed earlier, the afterbody diameter was less than the forebody. They conducted a steady-state numerical analysis for cold flow and with a methane combustion reaction in the cavity. Two-dimensional streamlines in the cross-section of the combustor for both cases are shown in Figures 27.



(a) 2D streamlines in cold flow top) 0 RPM bottom) 30,000 RPM

(b) 2D streamlines in combusting flow top) 0 RPM bottom) 30,000 RPM

Figure 27. 2D streamline comparison in cold flow and reacting flow with and without TVC cavity wall rotation [49]

There are several differences between the rotating and non-rotating results. First, in both the cold and reacting flow cases the non-spinning results showed a single vortex inside the cavity. Aft of the TVC there was an additional single vortex that extended out to 1.8 and 1.5 for the cold flow and reacting flow cases respectively. When rotation of the cavity was introduced, additional vortices were established in the cavity. This vortex breakdown caused strong 3D flow patterns and enhanced mixing in the cavity. Aft of the cavity, the trailing vortex was considerably shortened, with a tighter rotation. In the case of the reacting and spinning case an additional vortex was formed aft of the cavity. The addition of cavity rotation enhanced mixing which the authors report resulted in slightly higher combustion efficiency in the region from x=0 to x=1.5. The combustion efficiency was decreased beyond x=1.5 due to the smaller recirculation zone which ultimately resulted in a longer flame. [49]

2.2.4 High-g Combustion.

In 1990 Yonezawa et al. [50] published the results of a numerical and experimental study that aimed at increasing the combustor loading compared to a traditional

combustor. They cite the benefits of increased loading as a shorter combustor section, higher efficiency, and thus a better thrust-to-weight ratio resulting from the shorter overall engine length. They achieved these benefits by injecting air into a circular combustor annulus at an angle to impart a swirl to the burning gases inside the combustor. The swirl pattern was established in the primary reaction zone, with dilution occurring in the intermediate and dilution zones. Their combustor geometry is shown in Figure 28.

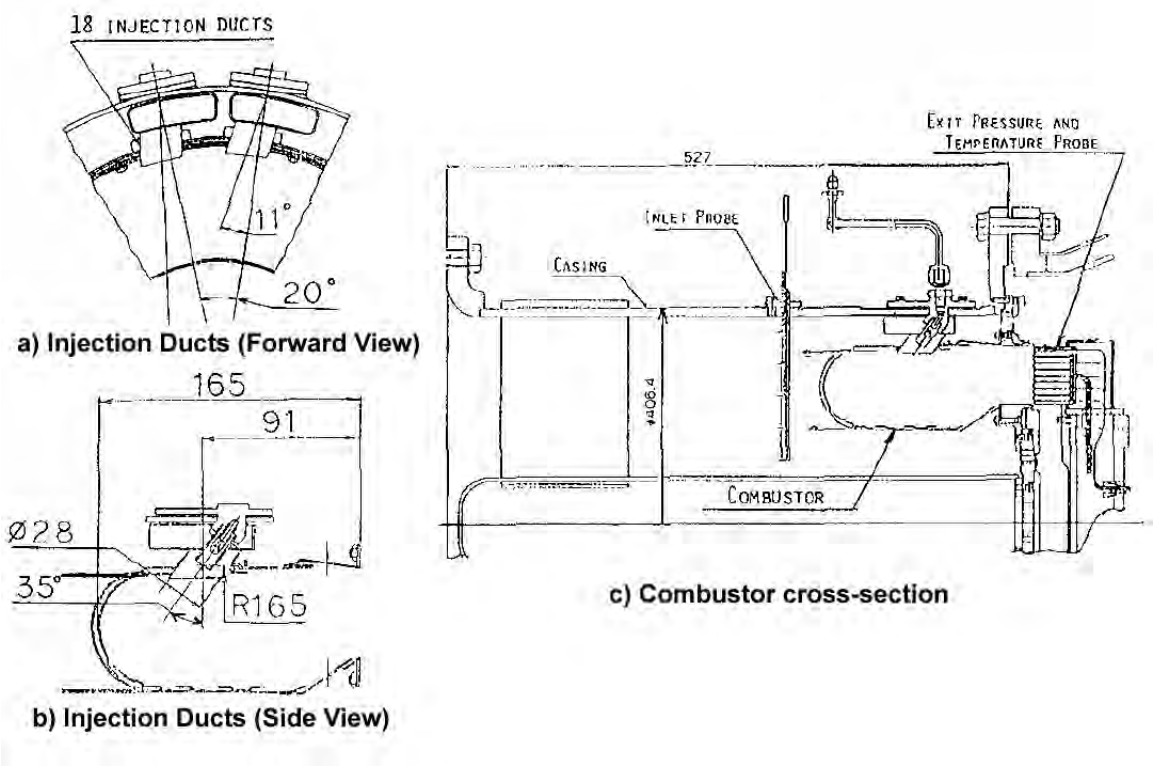


Figure 28. Geometry of Jet-Swirl Combustor used by Yonezawa et al. [50]

Yonezawa et al. [50] discussed the combustion efficiency in the primary zone being influenced by the fuel-air mixing time, chemical reaction time, and residence time. They combined these parameters into a single parameter defined by the relationship in Equation 40. In this equation τ_m is the fuel-air mixing time, τ_c is the time for chemical reactions to occur, and τ_r is the residence time.

$$\frac{(\tau_m + \tau_c)}{\tau_r} \tag{40}$$

The combustion efficiency in the primary zone is maximized when the parameter defined in Equation 40 is minimized. This translates to a need to decrease the mixing time, decrease the combustion time (i.e. speed up the chemical reaction), or increase the residence time. In the Jet-Swirl combustor developed by Yonezawa et al., mixing was enhanced and accelerated by the use of high-speed jets feeding the primary zone. These jets not only created a circumferential swirl in the combustor, they also created a helical swirl to aid in mixing. The increase in residence time was achieved by flowing the fuel-air mixture in a circumferential pattern rather than axially, which slowed the rate of travel in the axial direction. The decrease in the characteristic time for chemical reactions was achieved based on the work of Lewis [4], which is discussed later in this section.

Yonezawa et al. proved computationally that there was a direct correlation between injector angle and the centrifugal loading in the combustor. They were able to then conduct a parametric study varying the angles to optimize the design. An experimental study was conducted on their optimized hardware. They tested a design point of 500 kPa, an inlet temperature of 500 K, and an air mass flow rate of 5.9 kg/s. They also tested an off design location at 200 kPa, an inlet temperature of 370 K, and an air mass flow rate of 2.5 kg/s. Using an air loading parameter defined in Equation 41 they showed that the jet-swirl combustor achieved greater combustion efficiency for the same air loading value compared to a traditional combustor as shown in Figure 29. This result also shows that the jet-swirl combustor can achieve the same efficiency as a traditional combustor, but it will do it at a higher loading. In Equation 41, W_a is the inlet mass flow rate, V_l is the combustor loaded volume, P_3 is the combustor inlet pressure, and T_3 is the combustor inlet temperature. [50]

$$\Omega = \frac{W_a \times 10^9}{P_3^{1.8} V_l e^{(T_3/300)}} \tag{41}$$

In Figure 29 pay careful attention to the scale of the y-axis which starts at 100% efficiency at the origin and decreases moving up the axis.

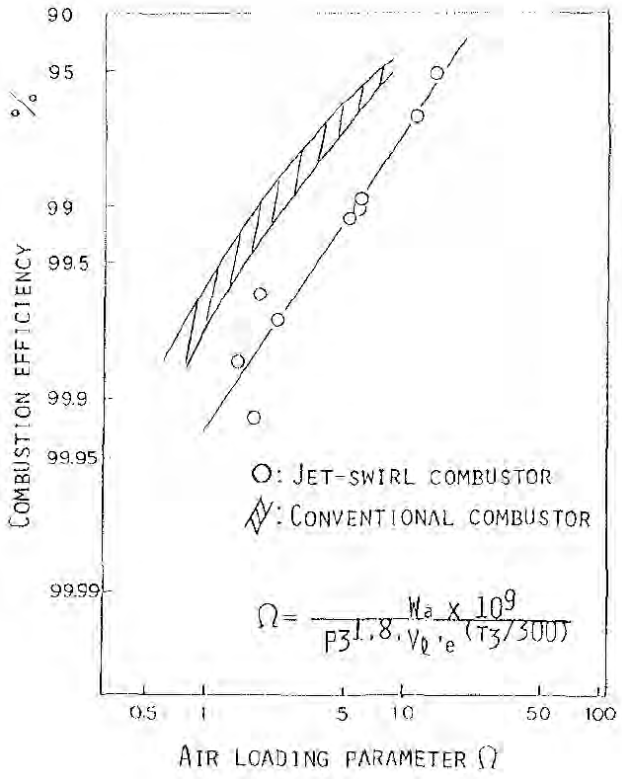


Figure 29. Combustion efficiency vs. air loading as found by Yonezawa et al. [50]

Lewis [4] discovered in the early 1970's that there was a flame speed increase in combustion that took place under elevated centrifugal force (g-load) beginning around $200g_e$. Between approximately $500g_e$ and $3{,}500g_e$ there was a steady, almost linear, increase in flame speed for increased centrifugal acceleration. Within this region Lewis calculated the burning rate of the combustion products under centrifugal loading to be proportional to the square root of the acceleration. He speculated that the increase in flame speed was the result of bubbles or eddies that were pushed ahead of the flame

front due to centripetal acceleration. Beginning around $200g_e$ the bubble velocity, S_B, was traveling faster than the turbulent flame speed and thus the flame propagated at the bubble velocity, as defined in Equation 42 [4]. Below $200g_e$ the bubble velocity was lower than the turbulent flame speed and thus the turbulent flame speed controlled the rate of combustion. These two conditions are shown graphically in Figure 30 where the dark circles represent the bubbles at $t = 0$ and at a time $t + \Delta t$ after traveling at a speed S_B. The dashed lines represent the turbulent flame front at the time $t + \Delta t$. The condition on the left side of Figure 30 shows the g-load effect where the flame front is being pushed upward by the centripetally accelerated bubble. In the example on the right side of Figure 30 the bubble velocity is slower than the turbulent flame speed (lower g-load) and the flame propagates at the turbulent flame speed.

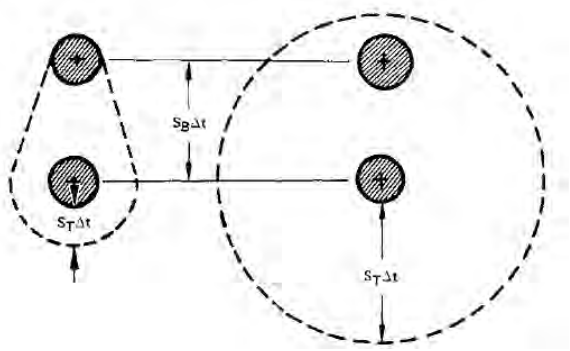
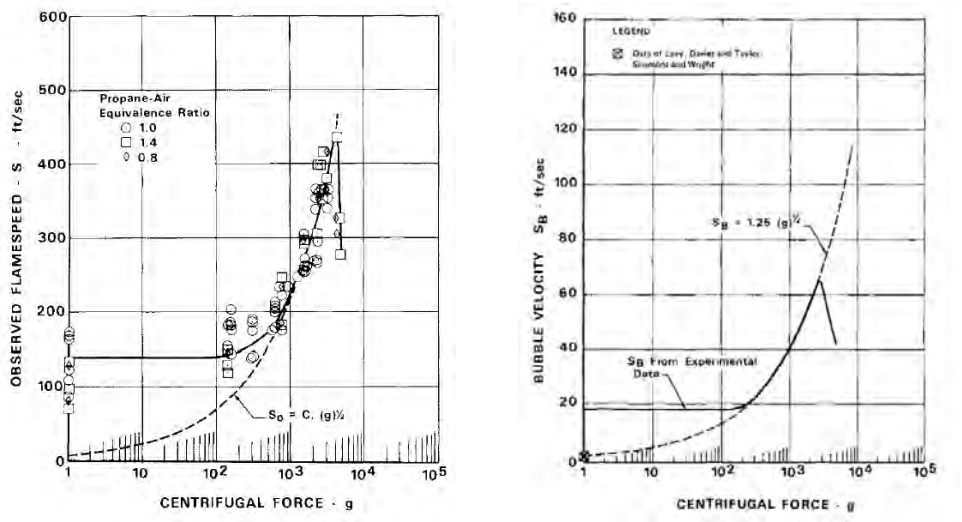


Figure 30. Bubble velocity controlled flame propagation (Left) and turbulent flame speed controlled reaction (Right) [4],[3].

$$S_B = 1.25\sqrt{g} \tag{42}$$

The term g in Equation 42 is the non-dimensional g-loading. The value 1.25 has units of ft/s. As noted by Lewis, at g=1 the resulting bubble velocity is 1.25 ft/s. This value is in agreement with the velocity of air bubbles in water. Even though the equation can be extrapolated down to g=1, experimental results showed that under

the test conditions the equation was only relevant to define the speed of the flame front when greater than $200g_e$. In addition to a minimum acceleration needed for flame speed enhancement, Lewis observed that there was a maximum acceleration as well. Above $3{,}500g_e$ he found that the flame speed and bubble velocity quickly dropped off and ultimately resulted in blowout between $7{,}000g_e$ and $8{,}000g_e$. Plots of this relationship are shown in Figure 31. The units in both of these plots are ft/s. In order for Lewis' findings to be employed in a UCC, a control method would need to be used to keep the centrifugal loading high enough to get a flame speed enhancement, but still below $3{,}500g_e$ so the benefit is not lost.



(a) Propane flame propagation rate (b) Bubble velocity

Figure 31. Flame propagation rate and bubble velocity as a function of g-loading [4]

The high-g UCC concept as originally proposed was developed by AFRL around 2003 [3] based on a thermodynamic cycle proposed by Sirignano [5], and high centrifugal loading in the combustion cavity incorporating the work of Lewis [4]. Sirignano's thermodynamic cycle, previously discussed in Section 2.2.1, was based on his analysis of systems that included burning in the turbine. Early UCC analysis involved fuel-rich combustion in the high-g environment of the circumferential cavity. Since

there was not enough oxygen to fully combust the fuel in the cavity, the combustion process was forced to finish in the UCC turbine vanes located radially below the circumferential cavity, thus making use of both Lewis' and Sirignano's findings.

Sirignano found that while most people view burning in the turbine as a problem, there are benefits. Ignoring the cooling issues associated with turbine burning, he found that augmented combustion in the turbine can reduce afterburner length and weight, reduce specific fuel consumption compared to using the full afterburner, and increase the specific thrust. The specific thrust increase means that more thrust can be achieved for the same engine cross-section or the engine diameter could be reduced to achieve the same thrust. There are additional challenges beyond cooling the turbine vanes such as reacting in high speed flow, changes in pressure distribution across the turbine vane due to combustion, and an impact on aerodynamic performance due to flow instabilities [5]. For the UCC to take advantage of these benefits it would require the use of turning vanes below the cavity not only when the UCC is used as an inter-turbine burner, but when used as a primary combustor as well.

In 2004 Zelina et al. conducted a computational fluid dynamics analysis on centrifugally loaded combustion using the UNICORN solver [3]. The study looked at the time-dependent laminar flame propagation of a hydrogen-air mixture in a 50-mm by 1000-mm two-dimensional tube. Numerous cases were run with variations on the g-load between 0 and $500g_e$. Figure 32 shows three time step results for a $10g_e$ and $500g_e$ applied load case. From these results it is clear that the flame under a loading of $500g_e$ has propagated significantly further, and thus has a much faster flame speed.

In addition to their CFD analysis, Zelina et al. [3] conducted an experimental study on a small scale UCC system operating at atmospheric and elevated pressures. A schematic of this initial baseline UCC rig is shown in Figure 33. In this design the fuel and air were injected into the cavity from the top wall. There were 24

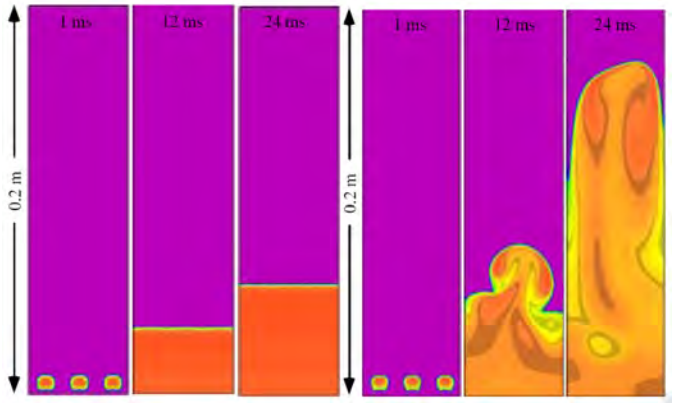
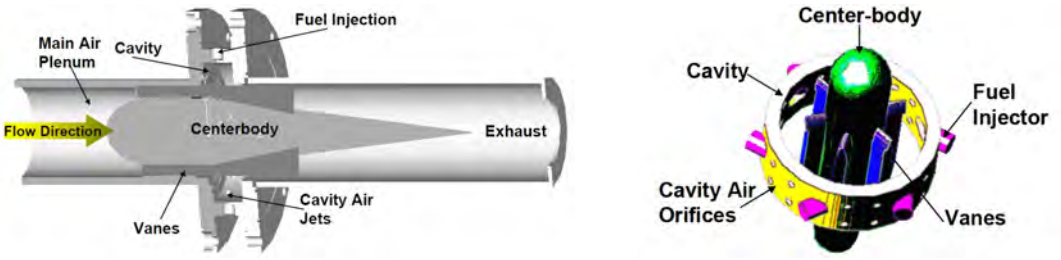


Figure 32. Flame propagation at $10g_e$ (Left), Flame propagation at $500g_e$ (Right) [3].

air injection holes fed from a plenum and six discrete fuel injectors. The air was injected into the cavity at a 45° degree angle to cause a high-g swirl of the fluid in the circumferential direction. There were six axially straight UCC vanes located below the circumferential cavity. The cavity and core flow were fed from separate laboratory supply lines. Even with this design being the baseline, tests showed a combustion efficiency between 95% and 99% burning JP-8 +100 fuel and operating over a wide range of conditions. Zelina et al. also found that the axial flame length resulting from centrifugally loaded combustion in the UCC was approximately 50% shorter than the flame from a conventional combustor. These findings support the theory that faster flame speeds result in shorter flame lengths and are in agreement with their CFD results and the findings of Lewis [4].



(a) Baseline UCC flowpath

(b) Baseline UCC cavity, vanes, fuel/air injector placement

Figure 33. 2003 Baseline UCC design used by Zelina et al. [32]

In an effort to confirm Lewis' maximum acceleration limit as applied to the UCC, Zelina et al. [3] conducted a series of lean blowout, LBO, tests which recorded the centrifugal acceleration limit to achieve blowout across a range of equivalence ratios. These results define the area in which stable combustion could be maintained for various combinations of equivalence ratio and g-loading as shown in Figure 34. The study found that the maximum sustainable g-load occurred for a slightly lean mixture and flamed out between 7,000g_e and 8,000g_e, supporting Lewis' finding.

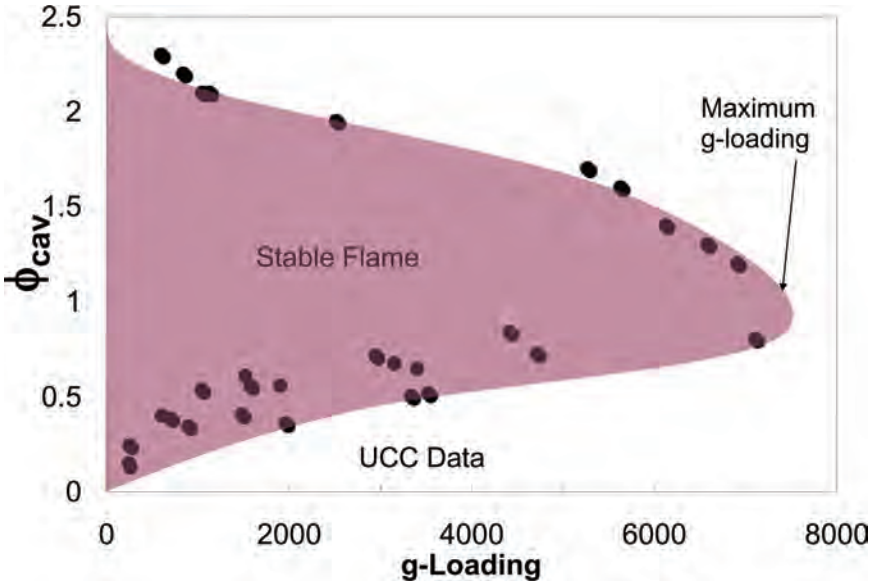


Figure 34. UCC cavity equivalence ratio at blowout as a function of cavity g-loading [3]

In January 2015 Briones et al. [33] published the results of a CFD numerical study focused on analyzing the results of Lewis [4] and their applicability to the UCC. Using a 2D computational domain they simulated a rotating combustion tube replicating the test setup of Lewis. They performed the simulation using propane-air, kerosene-air, and n-octane-air fuels across a range of g-loads. The fuel was ignited with a constant energy of 300 J applied to a region on the left end of the tube. Measurements of pressure, temperature, and reaction progress were taken at the same locations along the tube that Lewis used.

Briones et al. observed by monitoring the pressure contours in the tube during the combustion event that there was a pressure wave that traversed back and forth inside the closed tube and interacted with the flame. The interactions of the pressure wave and the flame caused the flame front to wrinkle and corrugate which enhanced its velocity and volume. Figure 35 shows flames at t = 8 ms for five g-loads. From this figure it is evident that g-load does have an impact on flame propagation velocity with a maximum occurring at 2,000g_e.

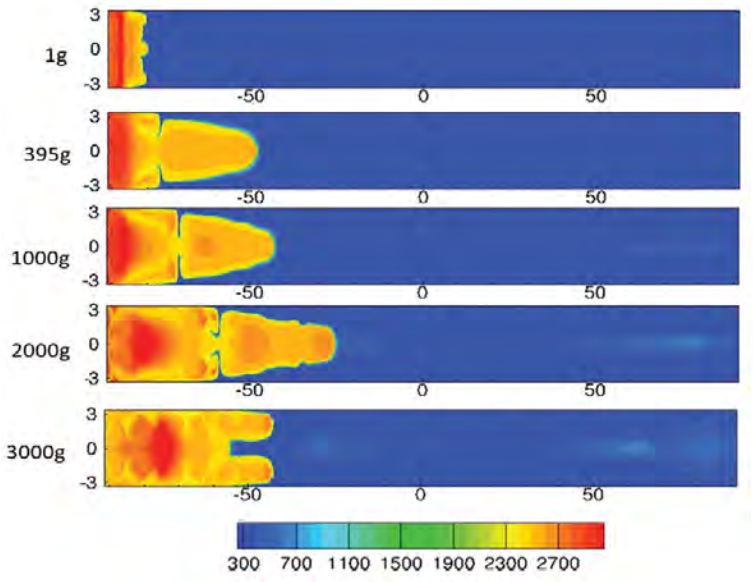


Figure 35. Instantaneous temperature contours for 1g_e, 395g_e, 1000g_e, 2000g_e, and 3000v stoichiometric propane-air premixed ame at t = 8 ms. The contour units are in Kelvin. Dimensions are in centimeters [33]

The 2,000g_e peak flame propagation found by Briones et al. occurred at a lower g-load than the 3,500g_e claimed by Lewis [4]. Briones et al. found that at 3,000g_e the flame exhibits excessive corrugation which breaks the flame and allows it to mix with large amounts of unburned fuel. This process locally quenches the flame and slows down the propagation process [33]. Additionally, Lewis claimed that there was no flame speed enhancement below 500g_e, but Briones et al. observed that there is a gradual increase in flame propagation velocity until 395g_e where the increase becomes

more pronounced. Figure 36 shows a comparison of the Briones CFD simulation data to Lewis' experimental data.

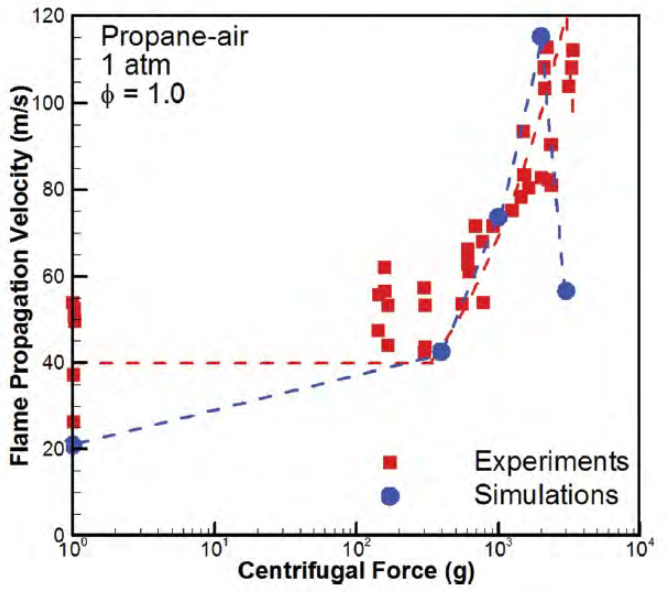


Figure 36. Comparison of simulation data to Lewis' measured data [33]

Based on their results, Briones et al. concluded that the flame propagation velocity, V_f, is a function of the turbulent flame speed, S_T, and local flow velocity, V_{flow}, as shown in Equation 43. The flow velocity is mainly controlled by Rayleigh-Taylor instability and thermal expansion. Additionally, they found that with each interaction of the flame with the pressure wave inside the tube, S_T was increased, but only to a maximum value of 4 m/s for all g-loads. Since S_T was not significantly affected by g-load, they concluded that the increase in flame propagation velocity, V_f, is primarily due to Rayleigh-Taylor instability and thermal expansion [33].

$$V_f = S_T + V_{flow} \tag{43}$$

To summarize the results of Briones et al., there was a very minor increase in turbulent flame speed resulting from g-load, but the cause of the increase was an artifact of pressure wave reflections off the end cap of the test geometry and would

not be present in a UCC circumferential cavity with no end cap. The main benefit from g-loaded combustion is the increase in flame wrinkling and corrugation which both enhance mixing and result in a higher flame propagation velocity. Additionally, based on these findings the g-load in the UCC cavity would need to remain at or below $2{,}000 g_e$ to not cause local quenching of the flame and slow the flame propagation. [33]

2.2.4.1 Rayleigh-Taylor Instabilities.

Rayleigh-Taylor instabilities occur at an interface between two fluids with different densities when the lighter fluid accelerates the heavier fluid, or alternatively, the lighter fluid supports the heavier fluid against gravity or in another accelerated field [51]. According to Cook and Zhou [52], this condition causes the density and pressure gradients to be opposed, inducing vorticity at the interface through baroclinic torque, and allowing the fluids to interpenetrate and mix as shown in Figure 37. In this figure the red fluid is higher density and the blue fluid, which starts as a layer below the red fluid in the upper left quadrant, is lower density. The fluid layer sheets were subject to an acceleration, such as gravity, and the remaining three images show the resulting interpenetration and mixing.

As shown in Figure 37, Rayleigh-Taylor instabilities follow four main stages of development. Stage one is characterized by small wavelength perturbations with a sinusoidal shape. The second stage begins development of larger perturbations with non-linear effects. The misalignment of the density and pressure gradients along the waves increase the baroclinic torque further driving instabilities. The third stage is characterized by the formation of bubbles (lighter fluid pushing up), and spikes (heavier fluid pushing down). In the fourth stage these bubbles and spikes merge to form larger structures which leads to a fully turbulent mixing region with characteristic mushroom shaped spikes.

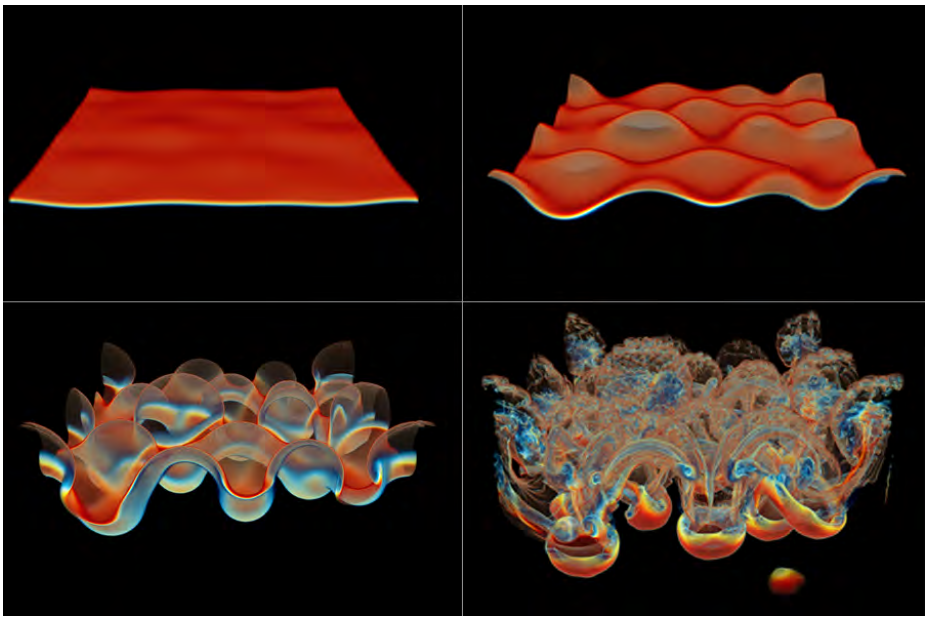


Figure 37. Sequenced development of Rayleigh-Taylor instabilities due to gravity [53]

Rayleigh-Taylor instabilities occur at all length scales from microscopic, to a mushroom cloud from a nuclear detonation, to a supernova explosion. While the Rayleigh-Taylor instabilities enhance mixing of different density fluids on their own, secondary mixing can also occur along the shear surfaces between the fluids of a spike formation. This secondary mixing is usually in the form of characteristic crested wave structures known as Kelvin-Helmholtz instabilities [54] (shear driven instability), as shown along the shear layer in the third and fourth images of Figure 38.

2.2.4.2 Step-Stabilized Combustion.

In 2009, Lapsa and Dahm [56] published the results of their study on propane-air flames stabilized by backward-facing steps in three configurations as shown in Figure 39. The straight channel is used to study a non-accelerating baseline case, while the two curved channel cases produce a positive acceleration (b), and a negative acceleration (c) in the stepped region. The fluid flow pattern and the flame locations were found for each case using shadowgraph images and chemiluminescence. Visual

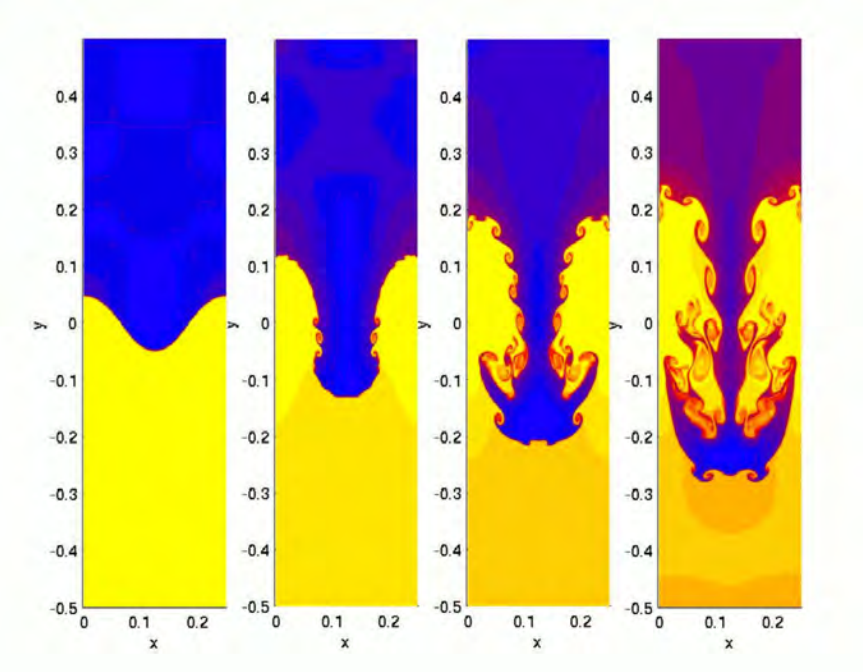


Figure 38. Development of a Rayleigh-Taylor instability induced spike with Kelvin-Helmholtz instabilities along the shear surface [55]

results were produced for channel flow velocities of 4 and 40 m/s which respectively translates to $\pm 28.5 g_e$ and $\pm 2{,}850 g_e$ in the curved channels.

The propagation of the flame was quantified by measuring the downstream location at which the flame contacted the wall opposite the step. For the linear channel (case a), it was found that the propagation length was linearly dependent on the flow inlet velocity. The propagation length for the positively accelerated step (case b) was less than the straight case and became independent of flow velocity beyond approximately 25 m/s. The negatively accelerated step had the longest propagation length of the three cases at each flow speed. These results are shown in Figure 40.

Lapsa and Dahm also found that the blowout limit was greatly increased for the positively accelerated case. The linear test case achieved blowout at about 40 m/s, where the positively accelerated case reached its blowout limit just above 70 m/s. Below 25 m/s (or $1{,}100 g_e$), the positively accelerated case and the linear case behaved

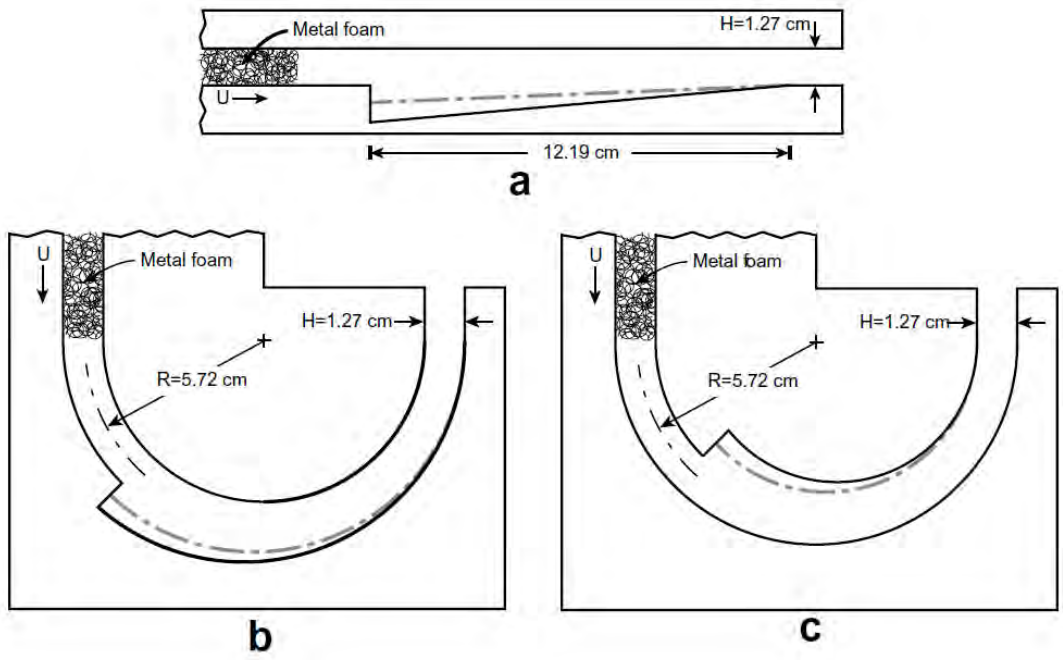


Figure 39. Experimental configurations of step-stabilized flames [56]

nearly identically. The positive acceleration helps to enhance mixing of reactants and products but results in large scale inertial distortions that reduce the blowout limit. The negatively accelerated case resulted in the highest blowout limits, well in excess of 80 m/s over the widest range of equivalence ratios. The body forces acting on the fluid in this case help to suppress the large scale distortions in the flame that result in blowout. These same body forces separate the products and reactants and produce a nearly flat flame that hugs the inside wall. The blowout test results can be seen in Figure 41 with images of the shadowgraph and chemiluminescence shown in Figures 42 through 44.

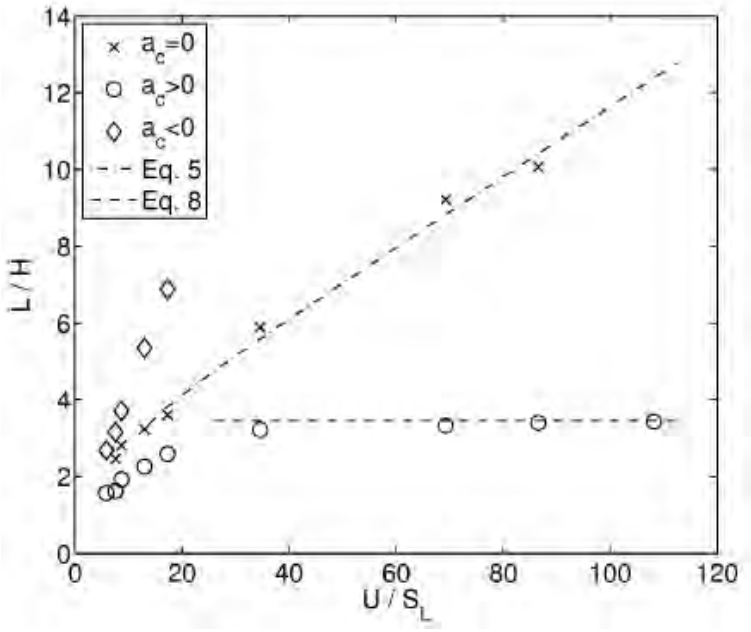


Figure 40. Flame propagation length (L) normalized by channel height and flow velocity normalized by flame speed for the three Lapsa and Dahm test cases [56]

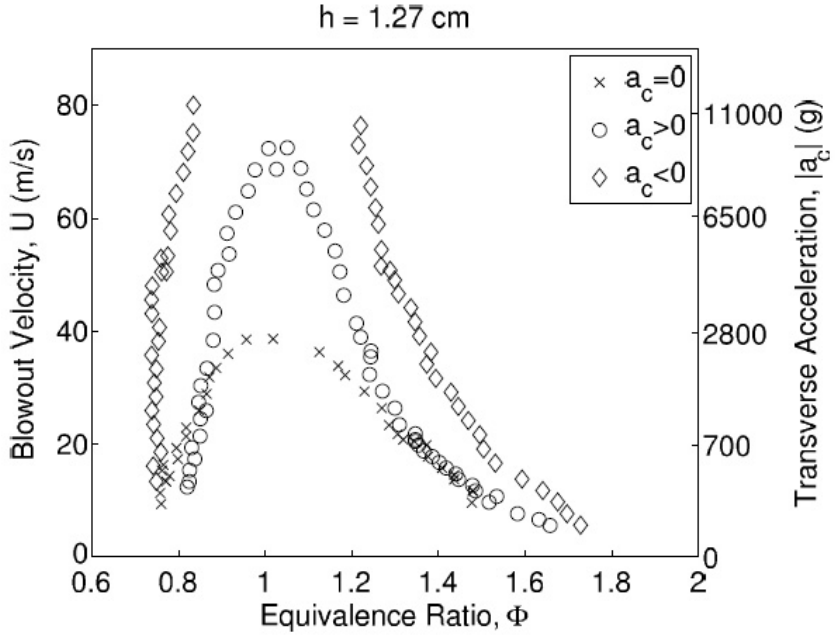


Figure 41. Effect of acceleration on blowout velocity for the three Lapsa and Dahm test cases [56]

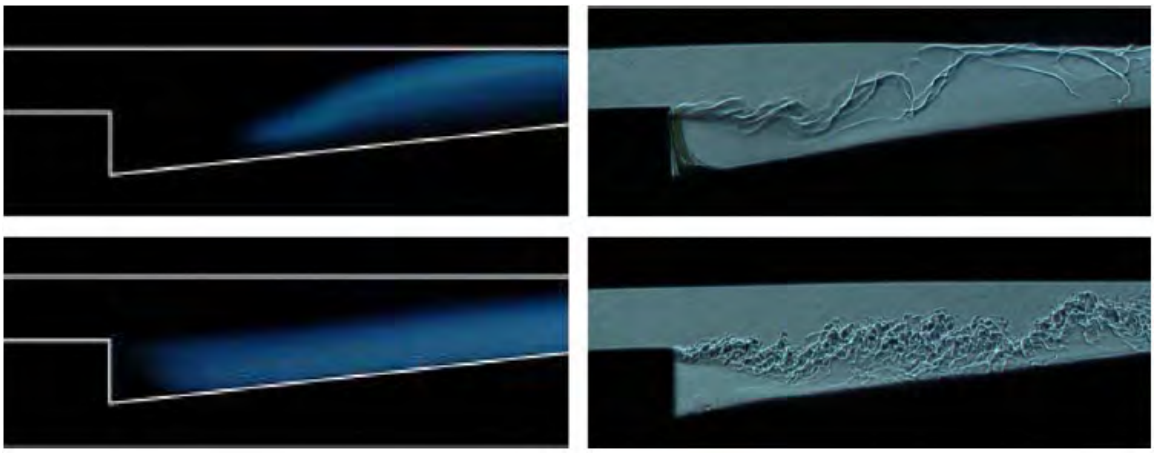


Figure 42. Chemiluminescence (left) and shadowgraph (right) for the straight channel. Top images are for U = 4 m/s, bottom images are for U = 40m/s [56]

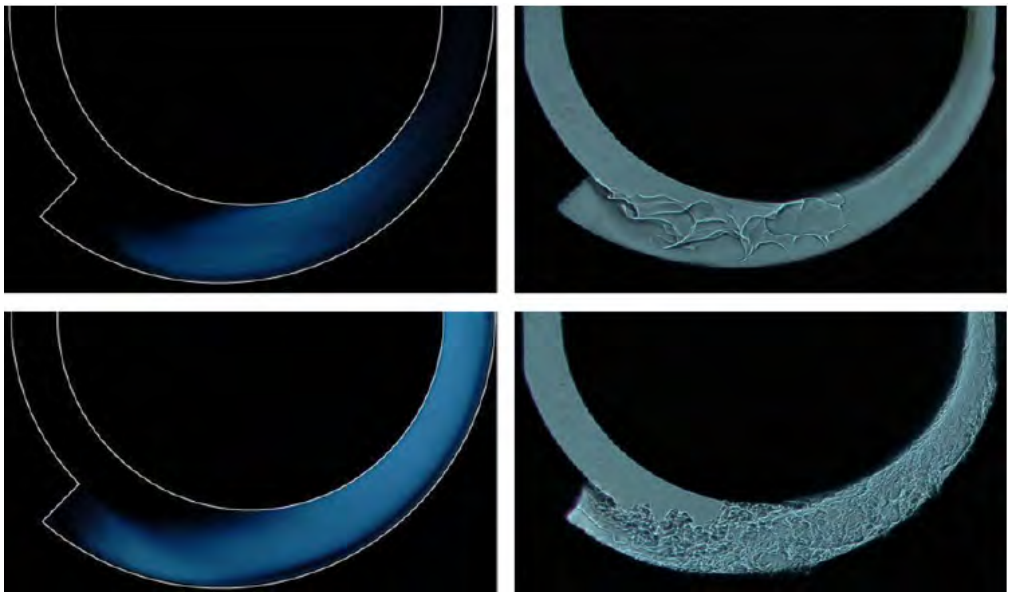


Figure 43. Chemiluminescence (left) and shadowgraph (right) for the positively accelerated channel. Top images are for U = 4 m/s (+28.5 g), bottom images are U = 40m/s (+2,850 g) [56]

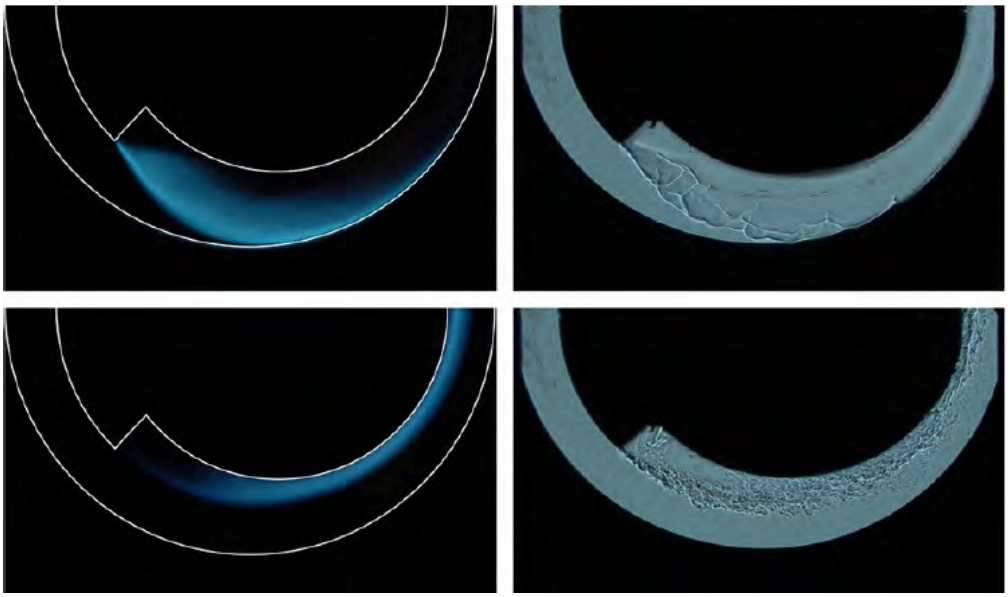


Figure 44. Chemiluminescence (left) and shadowgraph (right) for the negatively accelerated channel. Top images are for U = 4 m/s (-28.5 g), bottom images are U = 40m/s (-2,850 g) [56]

While the Lapsa and Dahm study was not specific to the UCC, the findings are directly applicable. Future iterations of the UCC cavity design may benefit from incorporation of steps on the cavity walls.

2.2.4.3 Effects of Component Geometry in High-g UCC.

In 2008 a study was conducted by Anderson et al. [57] to determine if swirl direction inside the circumferential cavity had an effect on high-g combustion. The test was conducted with both experimental and numerical analysis using an updated UCC design that improved on the baseline design used by Zelina et al. [3]. There were two differences in the design used by Anderson et al. First, the turning vanes in their rig were curved like a typical turbine vane, and featured a radial vane cavity. The purpose of the cavity was to create a region of low pressure in the backward facing step that would pull the fluid down out of the cavity and across the radial span. Second,

the fuel was injected into a recess in the top wall of the circumferential cavity to allow the fuel to stabilize and spread across the width of the cavity before being pulled into the main flow to combust. They referred to this region as a "cavity-in-cavity." This rig still operated with independent air feeds for the cavity and core flow. The rig used by Anderson is shown in Figure 45.

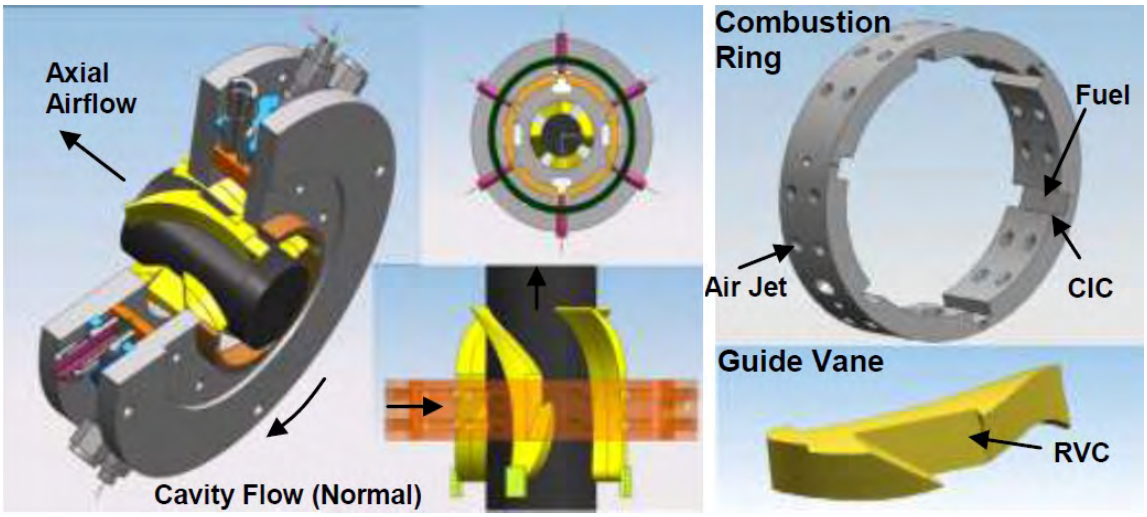


Figure 45. Test rig used by Anderson et al. [57]

The Anderson study determined that there was in fact a difference in the stability of the flame within the circumferential cavity depending on flow direction. The difference, however, seemed to be more of a function of the positioning of the fuel injection and air drivers relative to the UCC turbine vanes located below the cavity. The fuel injector and vane positioning was not symmetric and the distances between these components measured in the flow direction were different depending on direction of rotation. When fluid flowed in one direction, the fuel exited the cavity almost immediately after impacting the top of a UCC turbine vane. When the flow was moving in the reverse direction the fuel remained in the cavity longer and exited after passing over the UCC turbine vane. This study was important in that it highlighted the effect fuel injector placement can have on the combustion stability, residence time, and overall usefulness of the system.

In 2010 Bohan [58] looked at the impact of UCC turbine vane angle on circumferential cavity flow properties and migration of hot gases out of the circumferential cavity. This study was a CFD based analysis using both fighter-sized engine flow conditions and a smaller laboratory engine test rig flow condition. Using the same airfoil shape for each test section, the UCC turbine vane angle was varied from 30° into the cavity flow, perpendicular, and 30° away from the cavity flow as shown in Figure 46. In each case the axial placement of the turbine vane below the circumferential cavity was identical. This airfoil shape shown in Figure 46 was only used for this analysis and was replaced by the "hybrid vane" design that is discussed in Section 2.3.3.

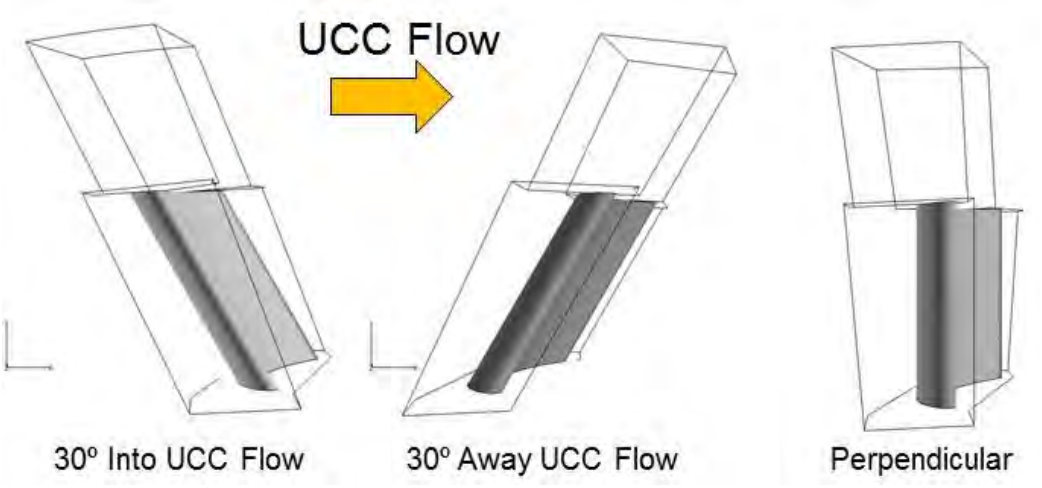


Figure 46. Angled UCC turbine vanes [58]

From the angled vane analysis, Bohan found that when the vane was angled into the flow, the lowest circumferential cavity velocities and mass flow rates were observed. Additionally, this condition resulted in the most non-uniform temperature distribution at the exit of the test section. When the vane was angled away from the direction of flow, the highest circumferential cavity velocities and mass flow rates were achieved, along with the most uniform temperature distribution at the exit of the test section. The flow properties in the cavity and the temperature distribution at the test section exit plane for the perpendicular vane fell between the two angled

vanes. The conclusion from this analysis was that vane geometries that made it easier for fluid to exit the circumferential cavity, i.e. the vane leaned into the direction of flow, resulted in lower cavity velocities and mass flow rates because the fluid exited without building up in the cavity. When the vane was angled away from the direction of flow, fluid was directed back up into the cavity and the highest mass flow rates and cavity velocities were achieved. [58]

From a cooling perspective, however, the vane angled into the flow is a better choice than the vane angled away. While the vane angled into the flow caused the hot gases to easily exit the cavity, the hot fluid stayed localized to a much smaller region of the suction side of the vane. This result means that only a small section of the turbine vane would need to be cooled. Contrary to that, the vane angled away from the flow diffused the exiting hot gases across the entire suction side of the vane surface. Due to the high velocity of the exiting fluid, some hot gases were able to wrap around the leading edge of the vane and heat part of the pressure side as well. This vane would require much more extensive cooling. The suction surface and exit temperature profiles for the three vanes are shown in Figure 47. The size of the heated vane sections on the perpendicular and angled away vane could be reduced by changing the airfoil geometry and using an airfoil with less camber in the region below the cavity. Accounting for all the trade-offs between flow properties in the cavity and cooling requirements on the vane, Bohan's research went forward with a perpendicular vane. [58]

2.2.4.4 High-g UCC Flow Calculations.

The test rig employed by Lewis [4] was a combusting centrifuge. It featured a long capped tube that was spun at a high rate to produce centrifugal force on the combustion products inside. The contents were then lit under a centrifugal acceleration. In the UCC, only the fluid is rotating which requires a different calculation method

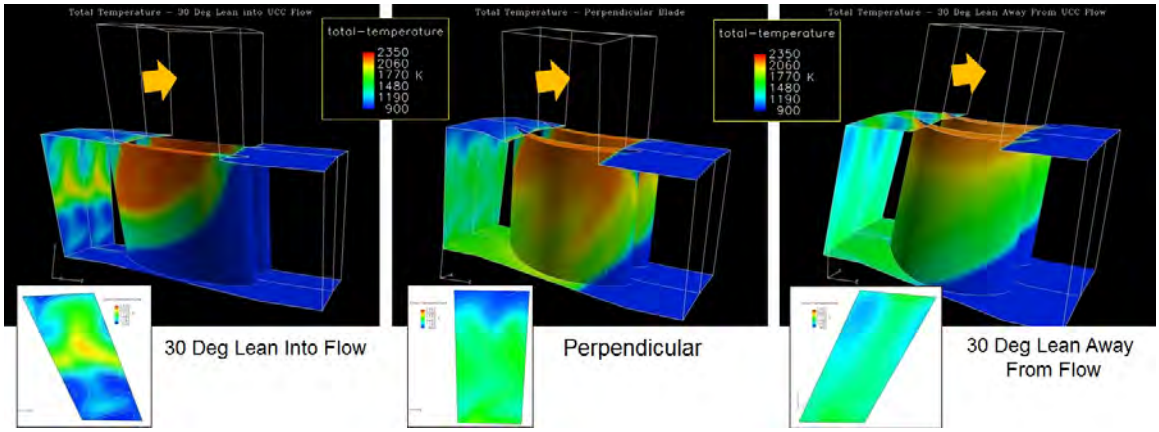


Figure 47. Angled UCC turbine vane suction surface temperature distributions [58]

of the g-load on the fluid. Zelina et al. [32] defined the g-loading for the UCC which is given in non-dimensional form in Equation 44.

$$g = \frac{V_{tan}^2}{g_e r_{cavity}} \tag{44}$$

In the above equation, g_e is the gravitational acceleration on Earth which has a value of 9.82 m/s^2, r_{cavity} is the radius of the UCC cavity, and V_{tan} is the tangential velocity as defined by Equation 45 [57]. Since the g-load is based on the radius, the g-load will decrease inside the cavity as the measurement moves radially outward.

$$V_{tan} = \frac{\dot{m}_{cavity}}{\rho_{cavity}\ A_{exit}\ tan\beta} \tag{45}$$

In defining the tangential velocity, β is the angle from the tangent line to the surface of the circumferential cavity, $\dot{m}_{cavity}$ is the mass flow rate through the circumferential cavity, ρ_{cavity} is the density of the fluid in the circumferential cavity, and A_{exit} is the area of the circumferential cavity exit.

The tangential velocity can also be calculated using pressure measurements from the circumferential cavity following the relationships shown in Equations 46 and 47.

In these equations M is the Mach number, P_T is the total pressure, P is the static pressure, γ is the ratio of specific heats (1.37 for reacting flows and 1.4 for non-reacting flows), R is the universal gas constant (287 J/kg/K), and T_T is the total temperature.

$$V_{tan} = M\sqrt{\gamma RT} \tag{46}$$

$$M = \sqrt{\left(\left(\frac{P_T}{P}\right)^{\frac{\gamma-1}{\gamma}} - 1\right)\frac{2}{\gamma-1}} \tag{47}$$

Additionally, the local velocity, V, can be determined using pressure measurements and incompressible flow relationships as shown in Equation 48. In this equation, P_T and P are still total pressure and static pressure, respectively, and ρ is the density.

$$V = \left(\frac{P_T - P}{\rho}\right)^{1/2} \tag{48}$$

Cavity air loading defined for the trapped vortex combustor in Equation 39 can be used to characterize the air loading in the high-g UCC as well. Alternatively, Equation 41 can also be used to define the air loading in the combustor.

2.3 High-g UCC Advancement

Much of the high-g UCC development has been accomplished by students at AFIT over the past several years. The following sections work through a semi-chronological progression of high-g UCC areas of study, most of which come from AFIT, along with the major findings and difficulties that were reported. This is not a complete history of the high-g UCC program, but rather is intended to provide sufficient background into the key points of understanding and difficulty that led to the selection of current research objectives and development of new test hardware.

2.3.1 Sector Rigs.

After initial proof of concept studies were completed by AFRL in 2005 [3][32] and AFIT in 2007 [59] using small-scale, high-g UCC test rigs, there was a desire to study individual aspects of the UCC and characterize the g-loading enhancement on combustion properties. Using a curved sector rig (Figure 48 left), and an infinite radius (straight) sector rig (Figure 48 right), the shear layer and interaction zone between the combustion products in the UCC cavity and the core flow were studied. Additionally, the role the UCC turbine vane plays in cavity flow migration and the effect of cavity curvature on combustion was examined [60][61][62]. Comparing the difference between the two rigs, LeBay et al. [60] hoped to quantify the impact of g-load on the combustion properties, flow migration, and combustion location within the cavity. A side benefit of the sector rigs was that the geometry allowed for the use of non-intrusive laser diagnostics to study flow properties without affecting the flow in any way. These two rigs operated at atmospheric pressure and had separate feeds for the core air flow and the cavity air flow.

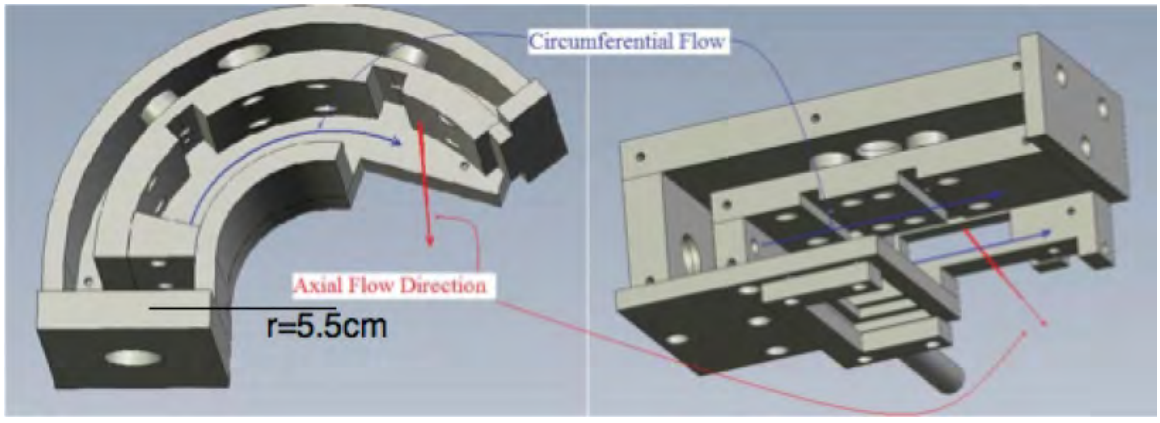


Figure 48. Curved sector rig (left) and Infinite radius sector rig (right) [60]

LeBay et al. [60] used Particle Image Velocimetry, PIV, to calculate the turbulence intensity in the straight and curved cavity. These measurements were used to char-

acterize the extent that turbulence intensity caused enhanced mixing that resulted in increased flame speed. They calculated the turbulent flame speed using Equation 18 and Equation 19. LeBay et al. applied their PIV data to Equation 18 and calculated a turbulent flame speed of 700 cm/s in the straight rig and 1,400 cm/s in the curved rig yielding a 1:2 ratio. Using the same data applied to Equation 19 produced flame speeds of 1,700 cm/s in the straight rig and 3,000 cm/s in the curved rig yielding a 1:1.7 ratio. These results showed a two-fold increase in turbulent flame speed in the curved rig where the fluid was experiencing g-loads on the order of $10{,}000g_e$.

LeBay et al. cited Lewis [4] to explain the turbulent flame speed enhancement beyond what could be achieved by the increased turbulent mixing alone. In light of the recent paper by Briones et al. [33] which points to turbulent mixing as the primary driver for increased combustion speed, LeBay et al. were probably on the right track by basing their flame speed measurements on turbulent intensities.

LeBay et al. [60] also calculated the enhancement due to g-loading through the Damköhler number, Da. Using Equations 20, 21, and 22 they found a Damköhler ratio of 1:3; implying the reaction timescale was reduced by a factor of three under g-load. This meant that complete combustion was reached faster under g-load. They used PLIF tuned to excite OH molecules in the flow to find the reaction locations. OH molecules are an intermediate species in the reaction of hydrocarbons.

LeBay et al. [61] also studied the impact of changing the mass flow ratio, MFR, and velocity ratio, VR, between the UCC cavity and core flow on the migration of hot gases from the cavity. They tested a 14, 28, and 56 mm radial vane height while maintaining identical flow conditions by using MFR = 0.1, 0.2, 0.3. The g-load in the cavity was controlled by varying the mass flow rate in the cavity to achieve $500g_e$, $1{,}000g_e$, and $2{,}000g_e$. A combination of high-speed video and PLIF was used to capture the results.

Maintaining a constant g-load in the cavity and varying the MFR, LeBay et al. were able to show a variation in the injection angle using high-speed video. A sample of these results are shown in Figure 49 for the 28 mm vane. From the images in Figure 49 it can easily be seen how the injection angle increases for increasing MFR.

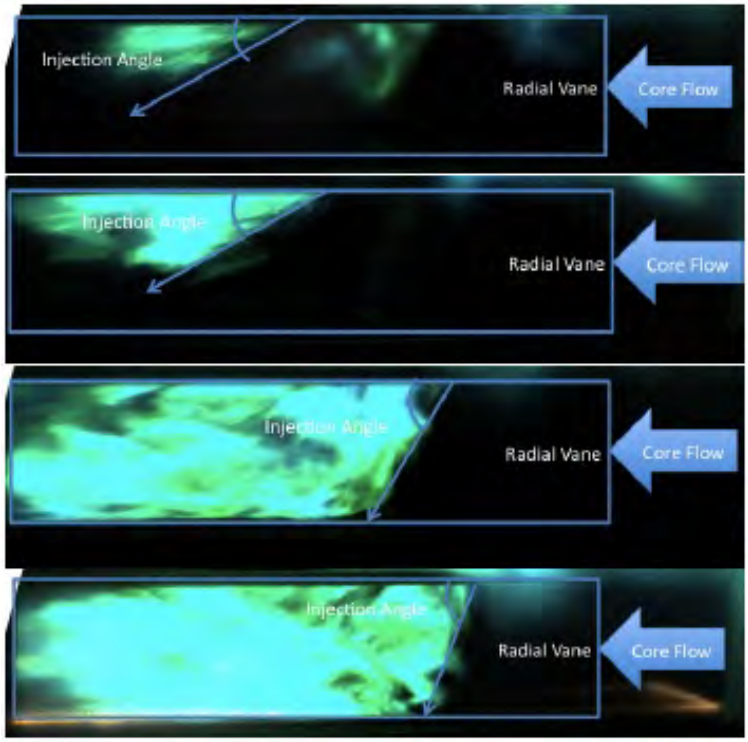


Figure 49. High-Speed Video Image Above Radial Vane of 28 mm vane, 1000g_e, ϕ = 2.0 at MFR=0.05 (top), 0.1 (middle top), 0.2 (middle bottom), and 0.3 (bottom) [61]

After completing their full test matrix, they determined that MFR = 0.2 was the optimal value to achieve a desirable injection angle that caused the hot gases to span the radial vane and produce a desirable exit temperature profile downstream. They were also able to determine that the injection angle varies very little for changes in g-load. Injection angle appeared to be a function of the core flow velocity almost exclusively. A nearly identical injection angle was achieved for constant core flow velocity for each of the three vane heights when the VR was also held constant [61]. Using this information, for a given vane height, the injection angle could be calculated

that would result in hot gases migrating the full radial span. The VR and MFR could then be adjusted by modifying the engine geometry to achieve the desired injection angle. The authors did acknowledge that achieving desired ratio through modification of engine hardware may be difficult.

2.3.2 Fighter Engine Scale Analysis.

In 2011, Bohan and Polanka [63] completed a CFD numerical analysis on a fighter jet scale engine utilizing a UCC as a main combustor. They also analyzed a flow condition on the same geometry that was achievable in a laboratory. This was the first analysis designed to show if the g-loads needed to achieve a flame propagation velocity enhancement could be achieved in a large-scale engine. Also as part of this study they examined the impact of the number of UCC turbine vanes below the circumferential cavity, the relationship of cavity inlet area to tangential velocity (which translates to g-load for fixed geometry), and computational domain exit temperature profiles. The geometry of the UCC section is shown in Figure 50. The inner radius of the passage at the exit of the UCC section was 31.75 cm with an outer radius of 38.1 cm.

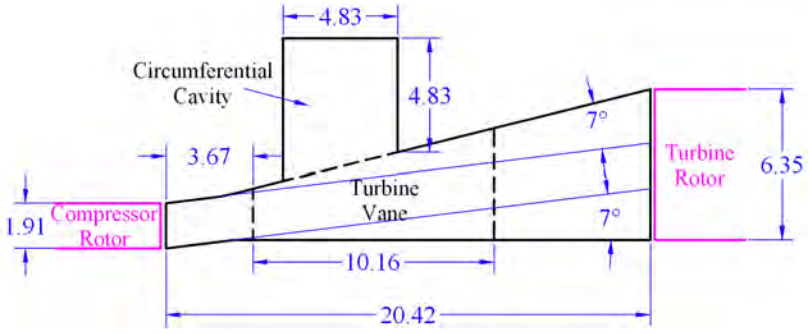
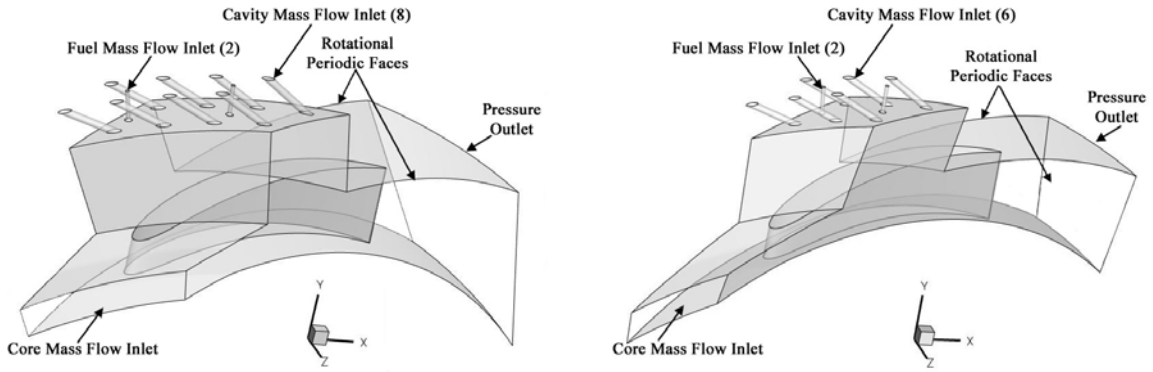


Figure 50. Cross-section of the UCC section analyzed by Bohan and Polanka [63]

The computational domain was tested with 20 and 30 vanes evenly spaced below the circumferential cavity. All vanes were perpendicular to the tangential cavity flow, and had a "hybrid" airfoil shape that is discussed in Section 2.3.3. Using periodic

boundary conditions, only the volume surrounding a single vane was analyzed. This variation caused the width of the computational domain to change for the two vane configurations as shown in Figure 51. Details of the geometry are provided in Table 3. The total engine model included 160 air driver inlets and 40 fuel injectors for the 20 vane geometry, and 180 air drivers with 60 fuel injectors for the 30 vane geometry. In each domain four air inlet port size variations were tested, each with an increasing diameter. The specific dimensions of the air inlet ports are given in Table 4. All air drivers, regardless of diameter, injected air into the cavity at 35° relative to the tangent of the cavity.



(a) 20 vane computation domain

(b) 30 vane computation domain

Figure 51. 2011 computational domains used by Bohan and Polanka for fighter-scale analysis [63]

The value of solidity, σ, referenced in Table 3 is defined as the vane airfoil chord, c, divided by the vane spacing, s. This relationship is shown in Equation 49.

$$\sigma = \frac{c}{s} \tag{49}$$

The operating parameters for the engine representative condition and the test rig representative conditions are shown in Table 5. The analysis was performed in the FLUENT solver with both reacting and non-reacting flow in the circumferential

Table 3. UCC turbine vane spacing and circumferential cavity inlet port specifications per test section [63][6]

Parameter	20-Vane	30-Vane
Vane spacing (cm)	10.0	6.65
Throat width (cm)	2.82	1.34
Axial solidity	2.09	3.11
Number of air inlet ports	8	6
Air Inlet Port Spacing*(cm)	3.16	2.81
Air Inlet Port Spacing (deg)	4.5	4
Number of Fuel Injectors	2	2
Fuel Injector Spacing*(cm)	6.34	4.23
Fuel Injector Spacing*(deg)	9	6

* Linear distance between hole centers

Table 4. Domain air inlet port variations [63][6]

	20-vane		30-vane	
Inlet Name	**Port Diameter**	**Total Inlet Area**	**Port Diameter**	**Total Inlet Area**
Baseline	0.54 cm	3.19 cm^2	0.54 cm	2.40 cm^2
2x	1.08 cm	12.87 cm^2	0.99 cm	8.05 cm^2
3x	1.62 cm	28.75 cm^2	N/A	N/A
Upper Wall	N/A	57.29 cm^2	N/A	37.89 cm^2

cavity. For the simplified non-reacting cases, 17.5 kg/s of air was injected into the circumferential cavity at 2,200 K for the engine case, and 1,000 K for the rig case. The higher mass flow rate was used to account for the mass flow rate of the fuel that was not being injected separately in those cases. When reacting flow was used, liquid kerosene was injected into the circumferential cavity at the fuel mass flow inlet points for the engine representative condition, or gaseous propane was flowed into the cavity for the rig condition analysis. These conditions were run with a 5-species and 12-species combustion model.

Bohan and Polanka [63][6] found that is was possible to exceed $3{,}500g_e$ in the

Table 5. Operating parameters used in preliminary analysis for engine condition and rig condition for complete annulus [63][6]

Parameter	Engine Condition	Rig Condition
Operating Pressure (Static)	4,626,377 Pa	101,325 Pa
Core Mass Flow Rate	50.5 kg/s	1.47 kg/s
Core Flow Inlet Angle	54°	54°
Core Flow Temperature	960 K	530 K
Core Flow Turbulence Intensity	5 %	5 %
Core Flow Inlet Mach Number	0.18	0.2
Cavity Inlet Mass Flow	15.5 kg/s	0.45 kg/s
Cavity Inlet Flow Temperature	960 K	366 K
Cavity Inlet Turbulence Intensity	2 %	2 %
Fuel Mass Flow Rate	2 kg/s	0.064 kg/s
Fuel Inlet Temperature	300K	300K

larger diameter circumferential cavity. Following the results of Lewis [4] they conducted a parametric analysis to determine the factors that contributed to tangential velocity. It was found that only the cavity inlet velocity had any appreciable effect on tangential velocity. For a fixed mass flow rate into the cavity there was a direct correlation between cavity inlet velocity, controlled by cavity inlet hole diameter, and cavity tangential velocity, and thus to g-load. The solid lines in Figure 52 show the relationship between inlet velocity and tangential velocity for the various geometries and conditions tested. For a target g-load, Equation 44 can be used to determine the needed tangential velocity. Working from the left side vertical axis in Figure 52, align the tangential velocity and the corresponding geometry line, and read the needed inlet velocity off the horizontal axis. Then starting from the inlet velocity on the horizontal axis work up to the dotted line matched to the color in the legend of the geometry used, and read the inlet hole diameter needed to achieve the inlet velocity on the right side vertical axis. The hole diameter, ϕ, was calculated using Equation 50.

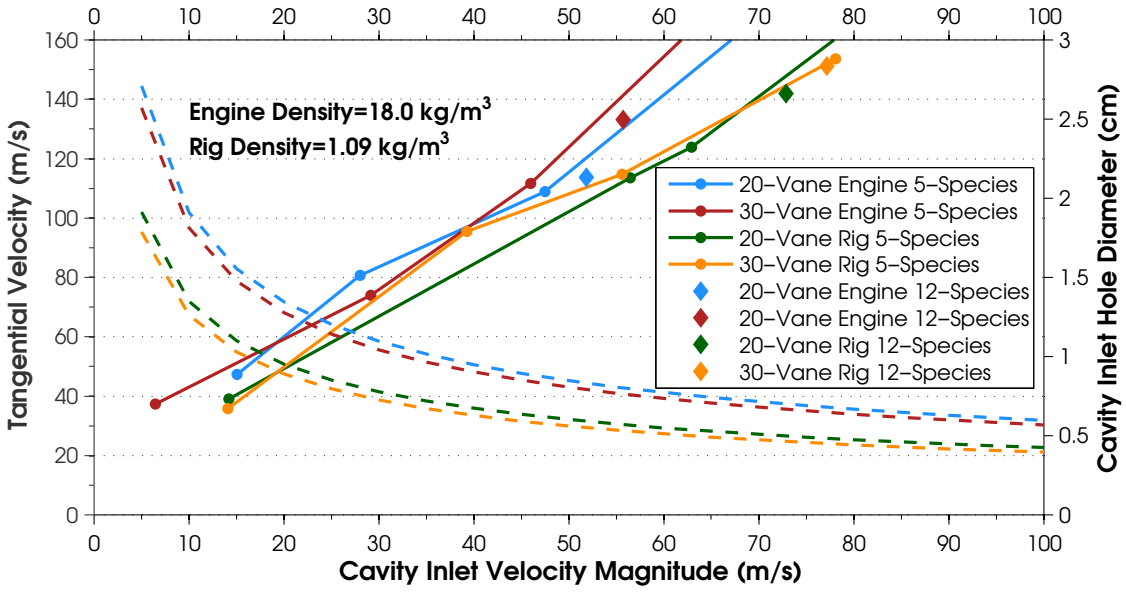


Figure 52. Relationship of cavity inlet velocity to cavity tangential velocity and hole diameter [63][6]

$$\phi = \left(\frac{4\dot{m}_{section} sin(\theta)}{I \rho_{inlet} V_{inlet} \pi}\right)^{0.503} \times 100 \tag{50}$$

In Equation 50, $\dot{m}$ is the mass flow rate into the test section, θ is the inlet injection angle, I is the number of air inlet ports, and V_{inlet} is the cavity inlet velocity.

2.3.3 UCC Turbine Vanes.

The UCC turbine vanes have gone through several design changes since the first UCC tested c.2003. The baseline test rig used by Zelina et al. [32], shown in Figure 33, featured straight vanes that did not turn the flow below the circumferential cavity. Anderson et al. [57], used a vane that had an axially aligned leading edge and turned the flow below the circumferential cavity as shown in Figure 45. Since this vane started axially aligned, it still required a compressor exit guide vane to straighten the flow before reaching the UCC. Depending on the amount of turning done at the

trailing edge, an additional vane may be needed to achieve the turbine in flow angle. The sectional models used by LeBay et al. [60] also featured straight vanes.

In 2009 Bohan [6] created a "hybrid" vane design to replace the UCC turbine vanes that were in use at the time. This vane combined the compressor exit guide vane and the turbine inlet guide vane into a single vane located below the circumferential cavity as shown in Figure 53. This design allowed the swirl coming off the compressor to continue, then turned the air more circumferentially to achieve the turbine inlet flow angle, eliminating two unnecessary vanes. Some variation of the hybrid vane concept was continued by all follow-on AFIT researchers that studied the UCC as a primary combustor.

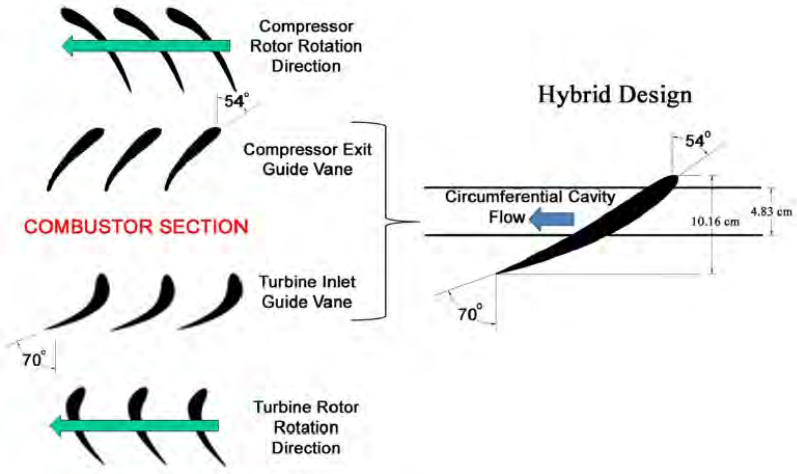


Figure 53. Hybrid vane origin and orientation [6]

Many of the UCC turbine vanes studied also included a radial vane cavity located directly below the circumferential cavity. The purpose of the vane cavity was to act as a backward facing step and locally reduce the pressure in the vane cavity region and help draw fluid out of the circumferential cavity and across the entire radial span. Cottle et al. [64] used a hybrid vane design, with and without a radial vane cavity, in a small scale UCC to study flow migration. The two designs are shown in Figure 54.

Due to the angles of the vane and the small diameter of the engine hub, the vanes have a corkscrew appearance. Cottle et al. found that the radial vane cavity was successful in changing the shape of the exit temperature profile by moving the peak temperature from the normalized radial height of 0.6 to 0.4 at the channel exit.

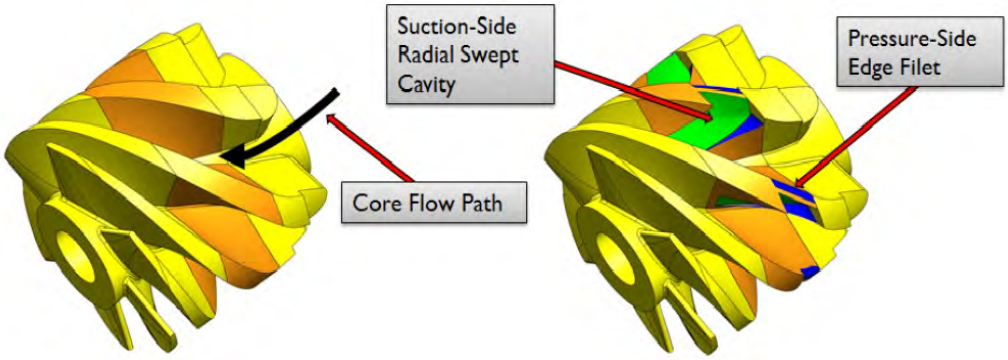


Figure 54. Hybrid vane with and without radial vane cavity [64]

2.3.4 AFIT Full Annular Test Rig.

Wilson et al. [65] developed a full annular small scale test rig in 2012 based on the findings of Bohan and Polanka [63]. The proportions of the core flow passage and circumferential cavity highlighted by dotted lines in Figure 55 shows the Wilson et al. rig similarity to Figure 50. The main difference between the designs is that the ID of the Bohan et al. profile remained constant while the OD of the Wilson et al. profile remained constant. Both rigs used air inlet drivers on the top wall of the circumferential cavity and both the core flow and cavity flow were fed from different sources. Additionally, the Wilson et al. rig incorporated the hybrid vane developed by Bohan [6]. Wilson et al. used this rig to conduct two focused studies. The first looked at varying the air inlet hole diameter at 0.35, 0.45, and 0.65 cm and observing the corresponding tangential velocity in the circumferential cavity. The second test focused on combustion stability based on swirl direction in the circumferential cavity.

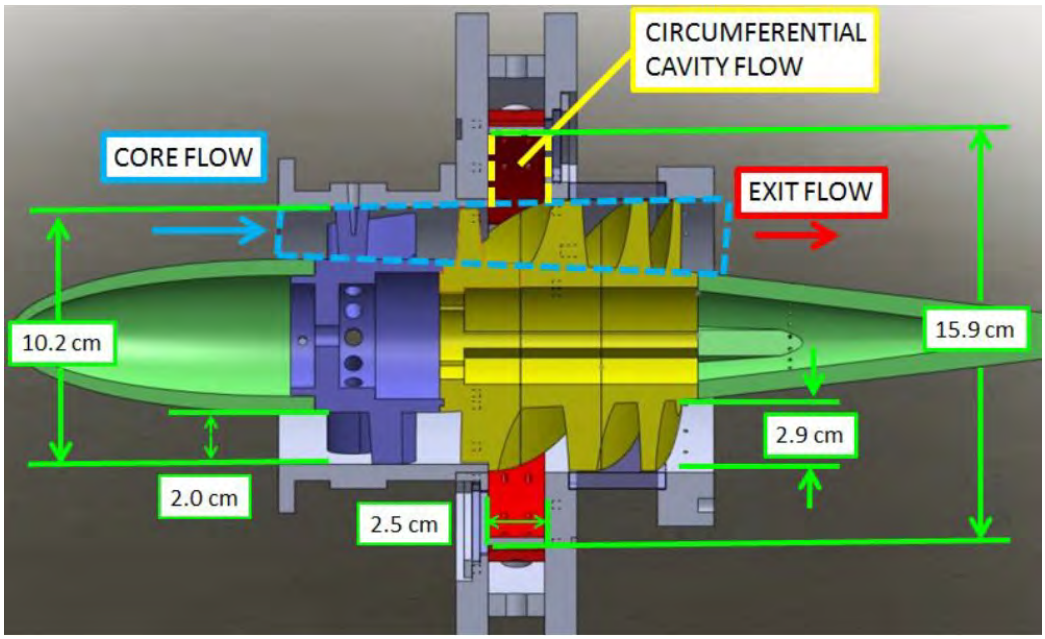


Figure 55. Full annular test rig with tapered centerbody used by Wilson et al. [65]

The first study that varied the air inlet hole diameter confirmed the results of Bohan and Polanka [63] that claimed the tangential velocity, and thus g-load, was a direct result of the inlet velocity that is controlled by the hole diameter. The results also showed that for a fixed air inlet hole diameter, increasing the mass flow rate into the cavity increased the g-load.

Unlike the earlier study by Anderson et al. [57] which used a UCC turbine vane that was relatively straight in the region below the circumferential cavity, the geometry of the vanes below the circumferential cavity in the Wilson et al. study on flow direction was quite different. Anderson et al. showed that the placement of the vanes and injector components in the cavity had an effect on residence time. Wilson et al. on the other hand showed that there was a substantial reduction in combustion stability when the cavity flow was swirled counter clockwise. Looking at Figure 56 shows why. In the clockwise direction the gases in the circumferential cavity can easily exit and follow the suction surface of the hybrid vane. In the counter clockwise direction

the gases have to turn nearly 135° to enter the hybrid vane passage. This turning caused disruptions in the flow field that propagated back into the circumferential cavity and destabilized the flame. [65]

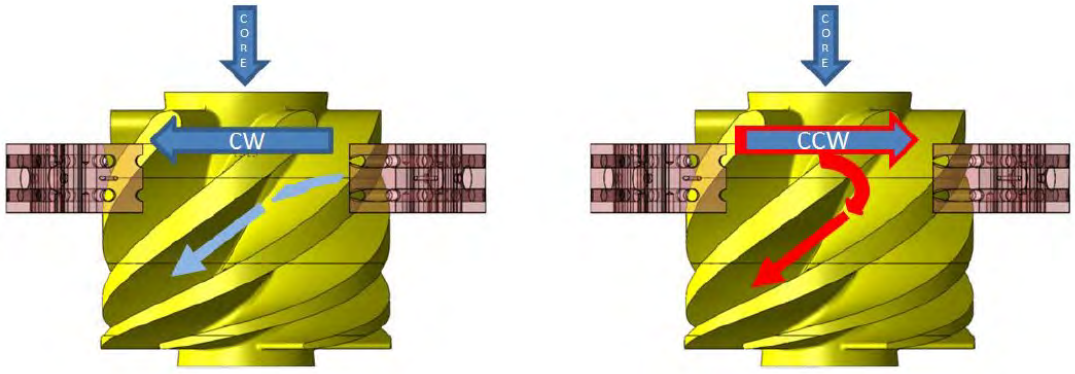


Figure 56. Wilson et al. swirl direction study [65]

Damele [66] upgraded the fuel control system of the Wilson rig and modified the propane injection system to remove a leak path of high pressure propane. He then instrumented the rig with total and static pressure sensors as well as thermocouples to characterize the exit temperature profiles, flow properties, and losses throughout the UCC. His results are discussed in Section 2.3.7 which addresses cavity flow migration.

2.3.5 Common Flow Source Diffuser.

At the conclusion of his 2011 numerical analysis on a fighter-scale UCC, Bohan [6] conducted an engine condition domain modification study to determine if it was possible to operate the UCC from a single air source such as a compressor in an engine. This domain routed air from the core flow up to a cavity inlet plenum when it flowed through cavity inlet ports in the top wall. Figure 57 shows the domain geometry.

While Bohan's ducted domain was far from optimized, he did show that it was possible to run a UCC from a common flow source and establish high-g flow in the

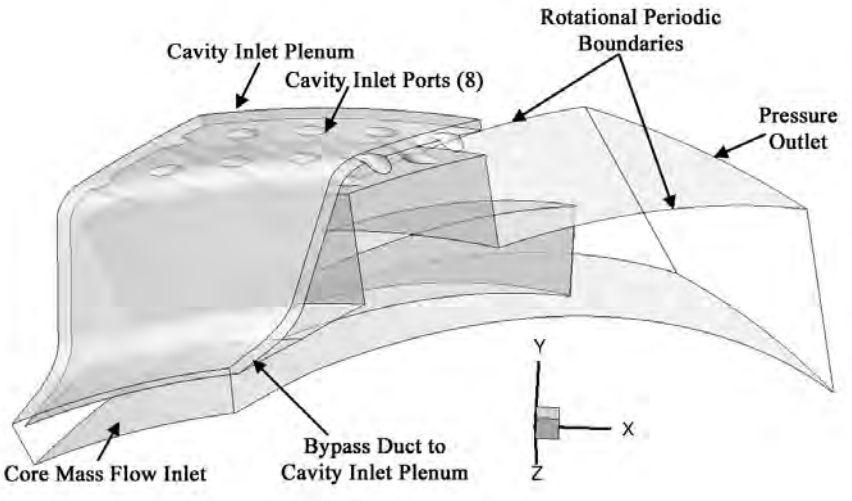


Figure 57. 20 hybrid vane domain with cavity inlet splitter duct [6]

circumferential cavity. This study also highlighted a limitation of this design. Fixed splitter geometry eliminates the ability to control the mass flow rate entering the circumferential cavity. The mass flow rate that was achieved was the result of a balance of pressures between the core flow path and the cavity flow path in the system.

In 2013 Conrad [67] published his efforts on the development and testing of a UCC that featured a common flow source. He designed a diffuser section with circumferential cavity air drivers that were mounted on the front wall of the cavity and fit with the remaining components of the Wilson rig [65]. The positioning of the air drivers allowed the diverted flow to directly enter the circumferential cavity without excessive turning to inject the air through the top wall as it had been done previously with discrete air sources. The air injection holes were drilled at an angle to impart the necessary circumferential flow to develop g-load. Figure 58 shows the cross section of the Conrad diffuser and UCC. Figure 59 shows the components of the diffuser in an exploded view. Finally, Figure 60 shows the air injection panels on the front wall of the UCC cavity.

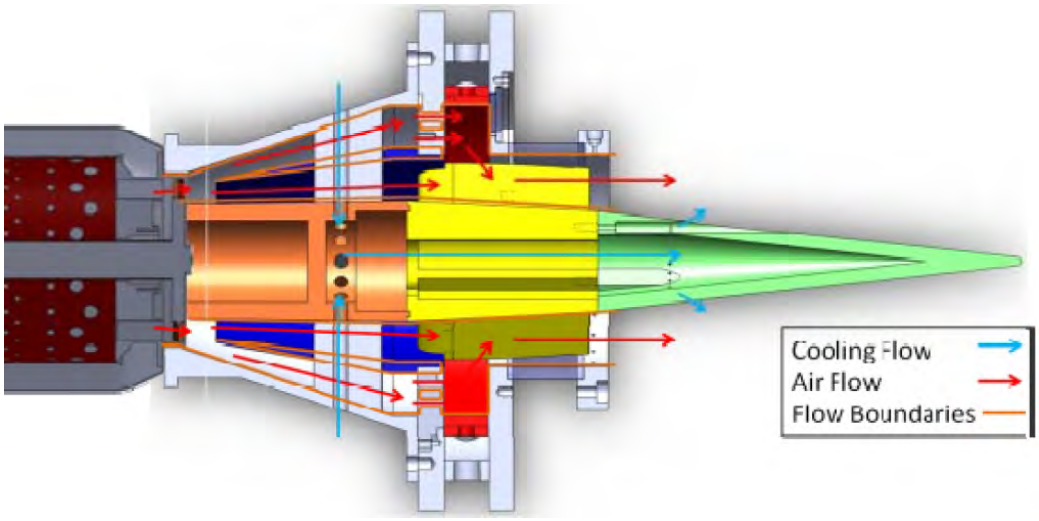


Figure 58. Cross sectional view of the Conrad UCC with common flow source [67]

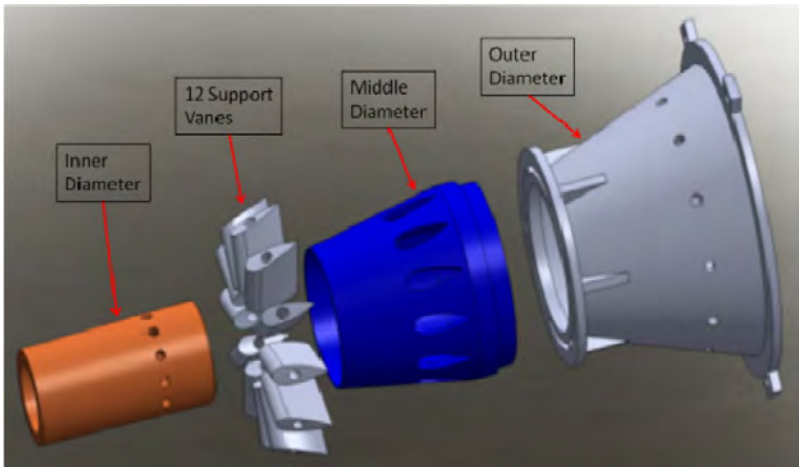


Figure 59. Exploded view of the Conrad diffuser [67]

Miranda [68] modified the Conrad design the following year to study the impact of differing middle diameter sizes. The three middle diameters were made corresponding to an 80/20, 70/30, and 60/40 core flow to cavity flow split. Miranda also increased the size of the air injection holes to 0.45 cm injecting at a 30° angle from the axial direction to match the configuration used by Wilson [65]. Both Miranda and Conrad used the hybrid UCC turbine vane used by Wilson. Their analysis was for a UCC acting as an inter-turbine burner (ITB).

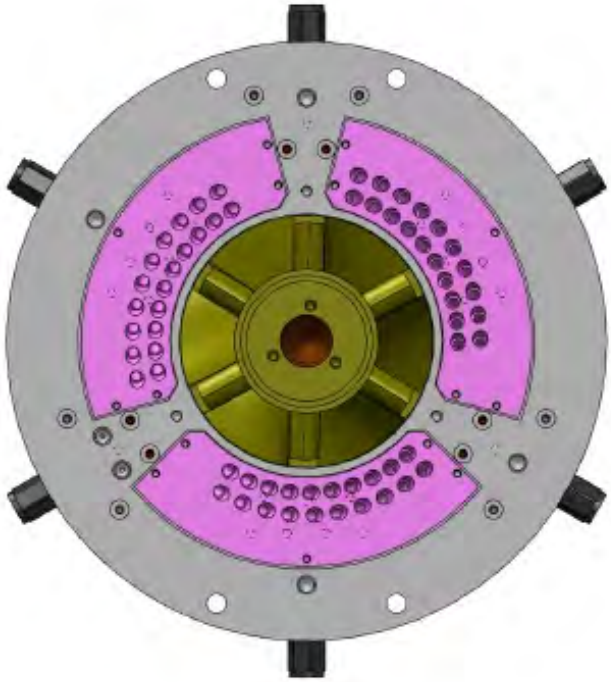


Figure 60. Air injection panels mounted to the UCC front plate [68]

Both Conrad [67] and Miranda [68] found it difficult to drive the desired mass flow rates of air into the circumferential cavity even with variations in the middle diameter. It was presumed that the cause of this issue was due to relative pressures between the core and cavity flow paths in the system. The core flow was mostly unrestricted, while the cavity flow path involved pushing the flow through the small holes of the injector plate. The injector plate caused a pressure loss that was not experienced by the core flow and thus resulted in less mass flow rate through the cavity section. Cottle et al. [69] fixed this problem by adding a restrictor plate downstream of the 12 support vanes in the diffuser core flow. The restrictor plate provided the necessary pressure loss in the core flow to balance the pressures between the core and cavity paths. An example of the restrictor plate is shown in Figure 61. They also introduced a non-dimensional factor, λ, that represents the ratio of allowable flow area to the total annular area. This relationship is defined in Equation 51 [69]. Based on parametric

analysis, Cottle et al. [64] determined that $\lambda = 5.0$ was a value that yielded desirable total flow parameters.

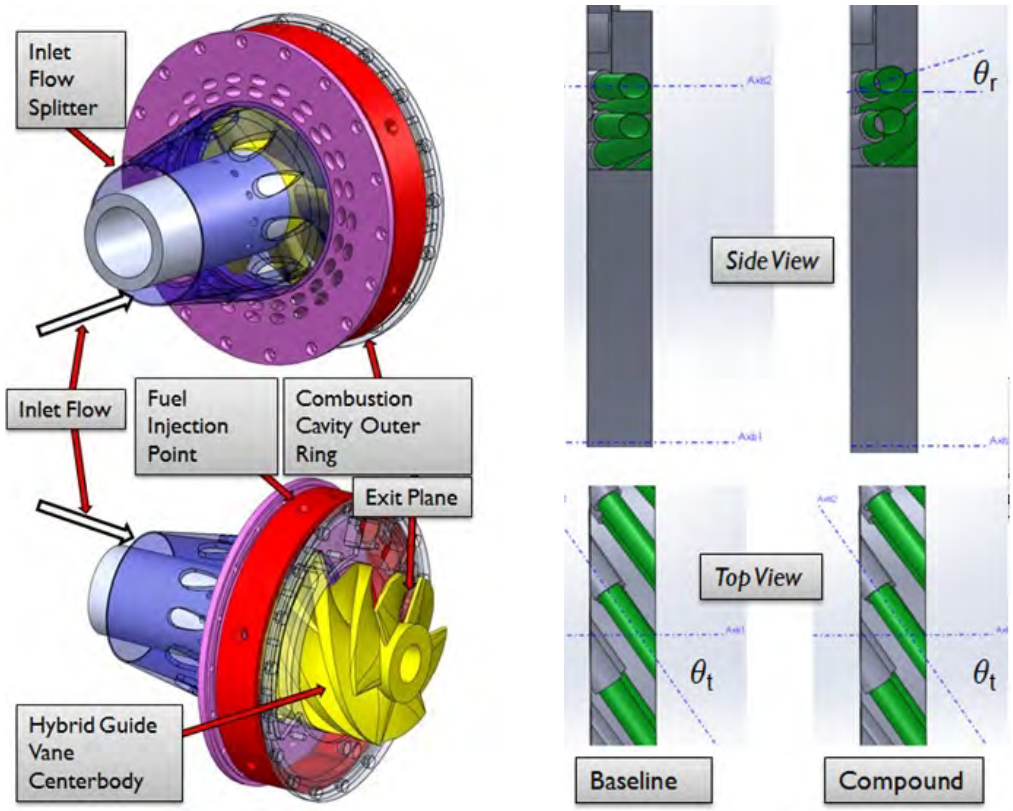
$$\lambda = \left(\frac{A_{ChannelPlate}}{A_{Core}}\right) / \left(\frac{A_{InjectionHoles}}{A_{Cavity}}\right) \tag{51}$$



Figure 61. Cottle et al. restrictor plate with $\lambda = 4.6$ [69]

In addition to the work on the restrictor plate, Cottle et al. [69] also modified the cavity air inlet drivers from three individual plates as shown in Figure 60 to a single plate as shown in Figure 62a. Using a single plate produced a more uniform flow by eliminating portions of the cavity that were not being driven. They also introduced the idea of compound air drivers which used a tangential angle, θ_t, of 55° and give the injector holes a 10° radial angle, θ_r, toward to OD of the circumferential cavity. They demonstrated that this small change in radial angle had a positive affect on increasing the residence time in the cavity and smoothing the temperature distribution downstream. A diagram of the compound drivers is shown in Figure 62b. They kept the hybrid vane in the UCC but made a modification to the leading edge to accept axial flow. This arrangement was convenient based on the configuration of the UCC air supply.

Using CFD, Cottle and Polanka [70] found that the velocity profile of the fluid in the outer diffuser passage was not as expected for typical channel flow as shown in



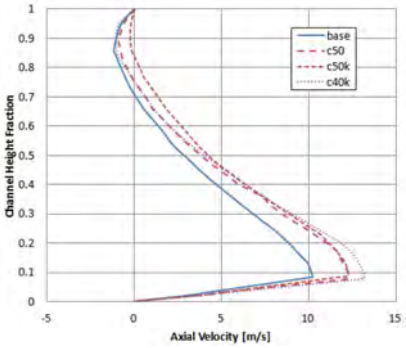
(a) AFIT UCC rig used by Cottle et al. (b) Compound air driver detail

Figure 62. AFIT UCC rig used by Cottle et al. [69]

Figure 63. From Figure 63b it can be seen that the highest velocity is just above the middle diameter plate at a height fraction of 0.1 and in the upper third of the channel there was reversed flow. This irregular pattern is likely the result of the placement of the leading edge of the middle diameter splitter. In Figure 63a it can be seen that the leading edge of the middle diameter splitter is nearly in-line with the OD of the air supply line. In this arrangement it relies on the air diffusing immediately with no separation to provide air that fully fills the outer diffuser passage. If the leading edge of the middle diameter was extended to be in-line with the start of the diffuser outer diameter housing this profile would likely be more uniform. The irregular velocity profile in the channel also made it difficult to accurately calculate mass flow rates entering the circumferential cavity.



(a) Diffuser cross section



(b) Velocity profile in outer diffuser passage

Figure 63. Diffuser outer passage velocity profile [70]

2.3.6 Controlling Rayleigh Losses.

Rayleigh pressure losses occur in fluid flows when the core flow temperature is raised which results in a velocity increase. According to Wilson and Polanka [71] and Radtke [72], the UCC experiences these losses for two reasons. First, the hot gases exiting the circumferential cavity are mixed with the core flow which causes the temperature to increase in the core flow. Second, there are unfinished combustion reactions taking place in the UCC turbine vanes below the circumferential cavity in the region where the core and cavity air mix. Both of these methods result in a change in flow Mach number due to heat addition in the form of Rayleigh losses. The Rayleigh losses are calculated using Equation 52, where the subscripts hot and cold refer to reacting and non-reacting flows. $P_{T,3}$ refers to the combustor inlet total pressure and $P_{T,4}$ refers to the combustor exit total pressure. Techniques that have been used to reduce Rayleigh losses in the UCC will be discussed in a later section.

$$\left(\frac{P_{T,3}-P_{T,4}}{P_{T,3}}\right)_{Rayleigh}=\left(\frac{P_{T,3}-P_{T,4}}{P_{T,3}}\right)_{Reacting}-\left(\frac{P_{T,3}-P_{T,4}}{P_{T,3}}\right)_{Non-Reacting} \quad (52)$$

The analysis conducted by Bohan and Polanka [63] using the geometry shown earlier in Figure 50 had very high Rayleigh losses. For a compressor exit Mach number of 0.3 that was maintained through the combustion section, the pressure losses due to Rayleigh effects was on the order of 12% for static and 9% for total pressure [73]. Parks and Polanka [74] documented the pressure losses across components of a traditional combustor and found the total to be 8.7%. They also set a pressure drop goal for the UCC of 5%. Obviously, the geometry used by Bohan and Polanka [63] more than doubled that amount. Johnson [73] conducted a study to reshape the engine ID wall to reduce the Rayleigh losses. The results he presented showed the UCC achieved a 0.05% drop in static pressure and a 4.21% drop in total pressure with the redesigned ID. These losses are low, however, as shown in Figure 64 the ID wall was extremely distorted just aft of the circumferential cavity to achieve these results. The abrupt change in area caused flow separation, leading to high aerodynamic losses. Additionally, this design resulted in a uniform temperature distribution at the turbine inlet, an undesired thermal profile from a durability standpoint.

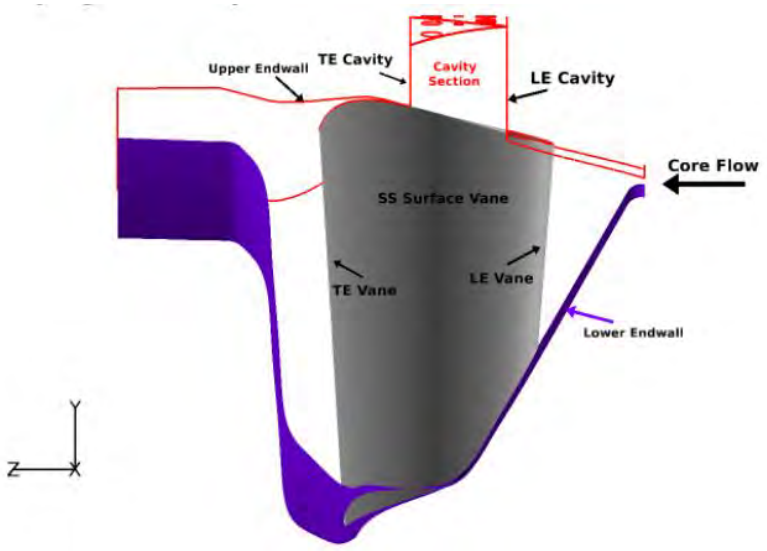


Figure 64. Layout of Johnson's low Rayleigh loss geometry [73]

Wilson and Polanka [71] developed a new UCC core model based on mathematical analysis that successfully integrated the compressor exit area, turbine inlet area, and a realistic ID wall profile. To achieve these results, the combusting Mach number was reduced from 0.3 to 0.2 resulting in a Rayleigh loss of 5.2%. The new geometry dubbed the "Low-Loss Center Body", or LLCB, is shown in Figure 65. The differences in the LLCB geometry can be seen when compared to the tapered center body geometry of the initial Wilson full annular rig [65] shown in Figure 55, or the Bohan and Polanka geometry shown in Figure 50.

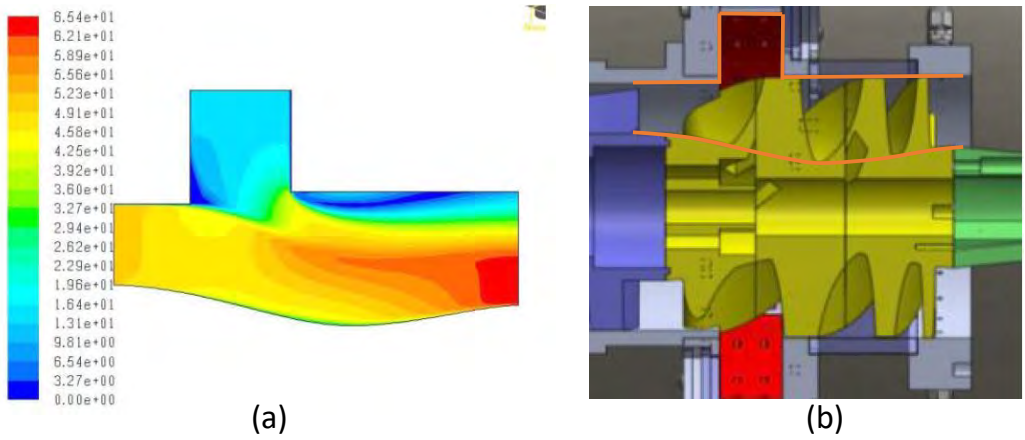


Figure 65. a) Velocity contours in the LLCB b) LLCB cross-section with hybrid vane integration [71]

Erdmann et al. [27] conducted a Rayleigh loss study on a trapped vortex UCC with turning vanes as shown earlier in Figure 20. They took experimental measurements and conducted a 1D and 3D numerical study for optimization and non-tested values. The analysis was conducted at pressures above 5 atm and temperatures above 500 K which is representative of exit conditions from a small compressor.

Erdmann et al. [27] found that for an inlet Mach number of 0.2 and a T_4/T_3 ratio of 1.2, the Mach number was significantly increased to 0.37 and the resulting experimentally derived Rayleigh pressure loss was 1% total. Numerically, the same conditions yielded a 1.4% and 1.7% pressure loss for the 3D and 1D cases, respectively.

These loss results are lower than the high-g pressure loss in the optimized LLCB. It is unclear if the difference in pressure loss is due to the higher starting temperature and pressure, the difference in combustion swirl pattern, or the overall scale and geometry of the test rigs.

2.3.7 Flow Migration Studies.

Controlling the flow migration of hot gases exiting the circumferential cavity is very important, specifically as the UCC transitions from a smaller scale to a larger scale engine. Without controlling the location of peak temperatures entering the turbine section there could be a mismatch between the positioning of cooling holes on the turbine vane and the peak temperatures. This mismatch could lead to material failure in the turbine.

Bohan and Polanka [63] studied the exit temperature profiles as part of their large scale engine analysis. Figure 66 shows the temperature profiles at the combustion section exit plane for both the engine and rig conditions using 20 and 30-vanes below the circumferential cavity. The peak temperatures occurred between 0.3 and 0.6 non-dimensional radial height using an adiabatic 12-species reaction model.

The pattern factor, as defined in Equation 35, is around 0.2 for a traditional combustor. For the 20 and 30-vane engine conditions the values were 0.47 and 0.37, respectively, meaning there was more variation in the exit temperatures in the UCC than a traditional combustor. Additionally, the inner diameter endwall temperatures were very high. The ideal temperature profile would be cooler at both endwalls, since they are difficult to cool, and a peak temperature near the middle of the passage. Bohan and Polanka's results indicate too much migration. These results also indicate that the cavity tangential velocity to core flow velocity ratio is the key metric in determining migration.

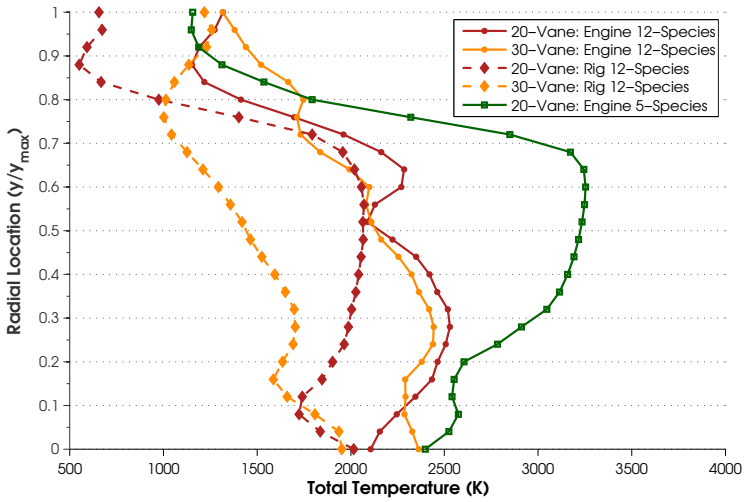


Figure 66. Circumferentially averaged total temperatures at the combustor section exit plane using the 12-species model and ideal air inlet diameters to achieve 3,500g_e in the cavity [63]

Damele et al. [75] conducted a thermal exit profile study using the Wilson small-scale full annular test rig with the LLCB described previously. He instrumented the rig exit area just aft of the trailing edge of the hybrid vane with two sets of seven K-type thermocouples. The first set varied the height of the probe as each probe was installed with equal spacing within a 120° arc of exit area. The seven probes were positioned at radial heights to equally divide the 2.5 cm passage into seven equal increments. The second set of thermocouples were all positioned at the same radial height with equal spacing around a different 120° arc section to capture circumferential variations of temperature, including vane wake effects.

Damele et al. [75] conducted tests at a range of equivalence ratios and g-loads. This rig had independent air supplies for the cavity and core flow so they could easily test the effect of core/cavity percentage air flow splits. A 70/30, 75/25, and 80/20 core to cavity split ratio was tested. The results from the varied probe heights indicated a consistently skewed hotter temperature at the OD of the exit. Within a single core/cavity flow split, this trend was exhibited regardless of cavity equivalence ratio

as seen in Figure 67. Further analysis indicated that the temperature profiles were most sensitive to changes in the core/cavity flow split and not changes in equivalence ratio. These results support the findings of Lebay et al. [61] that showed the mass flux ratio of the cavity to core air was the primary driver of flame injection angles out of the circumferential cavity, and was independent of equivalence ratio. Damele et al. found that the 70/30 core to cavity flow split was the preferential ratio.

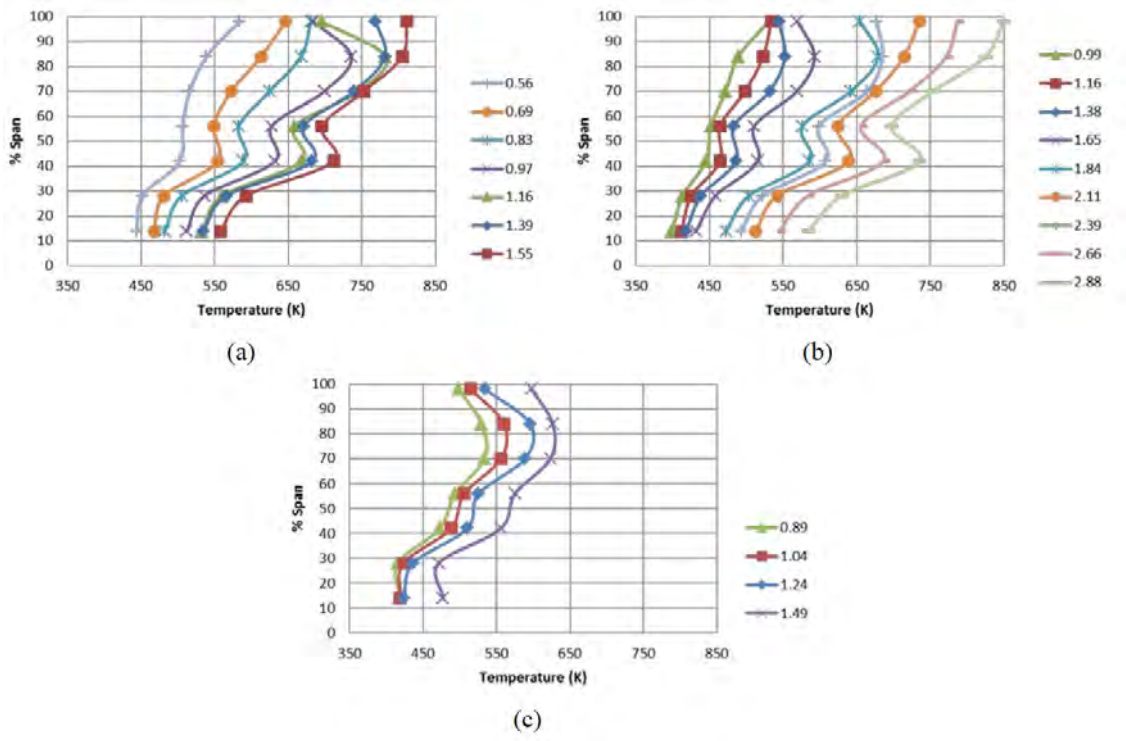


Figure 67. Measured temperature profiles for height varied probes with a) 70/30 b) 75/25 and c) 80/20 core to cavity flow splits [75]

In 2016 Gilbert et al. [76] published the results of their work on migration and emissions studies in the AFIT UCC rig. The rig geometry used was designated "Version 3" and featured a common flow source, the continuous air driver ring shown in Figure 62, and had a circumferential cavity with updated dimensions from previous versions. The modified cavity dimensions changed the aspect ratio of the cavity (height-to-width) from 2.04 to 2.51 with the cavity height growing from 5.2 cm to 6.4

cm. The geometry used was a blend of the best of the previous components tested in the AFIT rig and marked a major advancement in the rig. Gilbert et al. combined the findings of the migration work of Damele et al. [75], and research published in 2006 by Mawid et al. [77] on numerical analysis of radial vane cavities to provide additional migration of the hot gas across the full radial span of the UCC turbine vane. Of the three designs they tested, Mawid et al. found that only designs with a forward and backward facing step (rectangular vane cavity) had success in focusing the temperature in the mid-span region of the UCC turbine vane while maintaining adequate residence time for the fuel in the circumferential cavity. Based on these findings, Gilbert et al. tested the rectangular radial vane cavity shown in Figure 68.

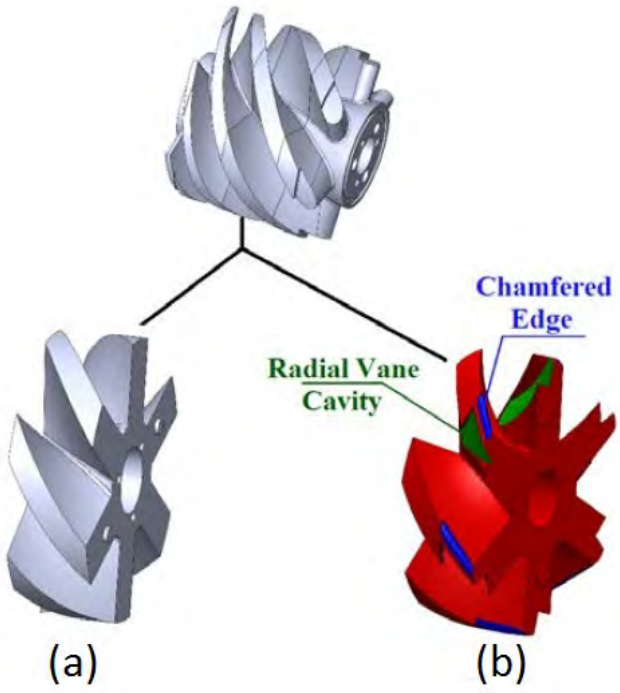


Figure 68. LLCB hybrid vane with a) original middle section and b) Gilbert et al. RVC modification [76]

Gilbert et al. [76] conducted experiments under similar conditions to Damele et al. [75] who used the "Version 2" rig, so comparisons could be made between "Version 2" and "Version 3". Figure 69 shows the exit temperature profiles from Damele et

al. and the "Version 3" rig with and without the RVC. From the figure it can be seen that the temperature profile is much closer to an ideal shape with the ID and OD experiencing cooler temperatures than the mid-span. It is also evident from this figure that the increased combustor volume allowed for more complete combustion inside the cavity and achieved a greater exit temperature magnitude compared to the same conditions of the "Version 2" rig. The re-sizing of the combustor alone had a profound impact on the exit temperature profile, but the RVC further localized the peak temperature to the 40% - 60% span.

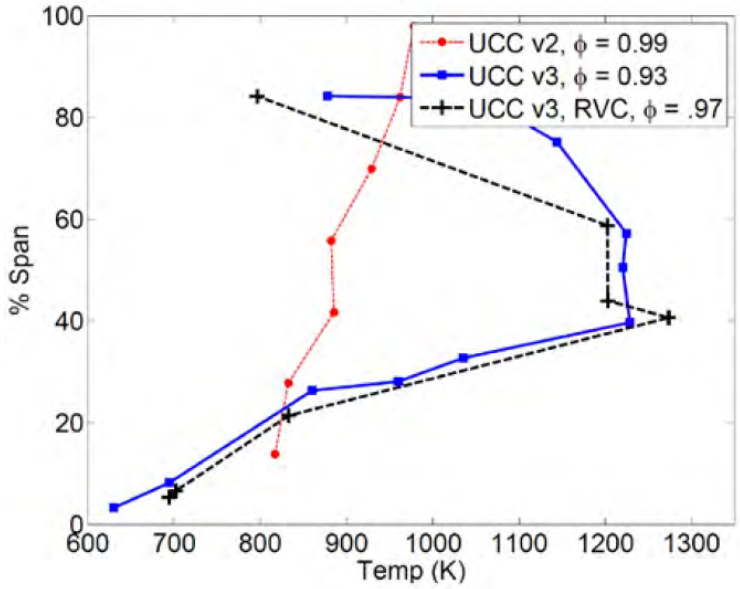


Figure 69. Comparison of exit temperature profiles between "Version 2" and "Version 3" of the AFIT UCC [76]

Cottle et al. [64] also studied the RVC vane shown in Figure 68 in UCC Version 2 and 3 but operated at different cavity equivalence ratios than Gilbert et al. Cottle et al. was also successful in moving the radial height of the peak temperature at the exit profile while maintaining cooler endwalls. Without the use of a radial vane cavity the experimental peak temperature was positioned at 0.4 in the non-dimensional radial height. Using the radial vane cavity the experimental peak temperature was moved

up to 0.5 of the non-dimensional radial height. Their adiabatic numerical results indicated a reversed trend along with a less uniform exit temperature profile with the radial vane cavity. The cause of the discrepancy between the numerical and experimental results is unknown. The results of their analysis is shown in Figure 70.

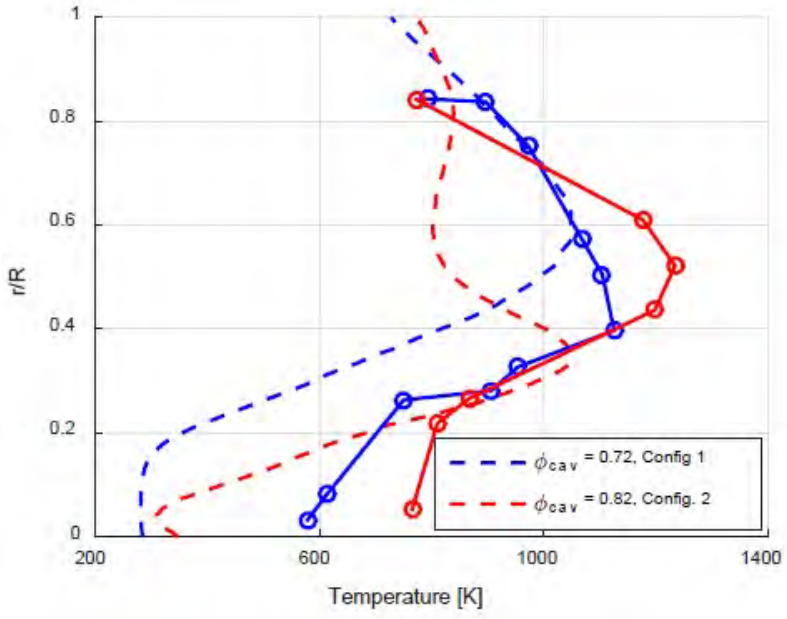


Figure 70. Exit temperature profiles of simulated (dotted lines) and experimental (open circles) for hybrid vanes without a radial vane cavity (blue) and with a radial vane cavity (red) [64]

Cottle et al. [64] also looked at the axial variation of temperature from just upstream of the cavity to the engine exit plane for UCC Version 2 and 3. The data were reported as area-weighted averages at each axial position and measured through adiabatic CFD solutions for configurations with and without a radial vane cavity. They also looked at the effect of cavity equivalence ratio by looking at a lean (Φ=0.76) and a rich (Φ=1.37) case. The temperature plots for these cases for the Version 2 UCC are shown in Figure 71. Between all four of the cases shown, the general temperature trends in the cavity were similar, with the fuel rich cases resulting in reduced temperatures as expected. The temperature distribution in the cavity was

skewed to the aft (right) wall due to cavity air injection entering from the forward (left) wall. The drop in temperatures following the aft wall of the cavity was due to quenching as the hot combustion products entered the cool core flow path. This drop was more pronounced for the configuration featuring the RVC. In both configurations the temperature rose steadily after the quench for the fuel rich cases and ended at a nearly identical area-weighted averaged temperature. The lean cases between both configurations also began to converge to the same lower temperature.

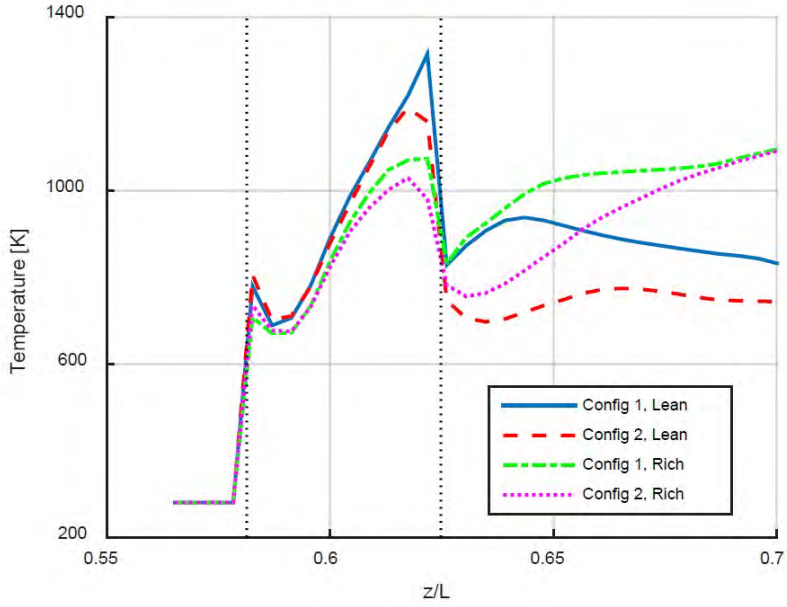


Figure 71. Area-weighted average of temperature with axial position Version 2 UCC (Config 1 = without a radial vane cavity; Config 2 = with a radial vane cavity)(Rich = 1.37, Lean = 0.76) - Vertical dotted lines indicated the forward and aft walls of the circumferential cavity [64]

Cottle et al. [64] went on to compare the Version 2 UCC solutions with the Version 3 UCC data as shown in Figure 72 for the axial temperature variation, and Figure 73 for the adiabatic combustion cavity temperature profiles at three axial positions. Version 3 featured the variation in circumferential cavity aspect ratio and compound air drivers. From Figure 72 it can be seen that the cases featuring the RVC resulted in less temperature rise in the vane passage after exiting the circumferential cavity.

The addition of the compound air drivers also helped stabilize the temperature aft of the circumferential cavity beyond what the Version 2 UCC with an RVC could achieve. In Figure 73 it can be seen that the configurations with the RVC had reduced temperatures at the exit plane of the cavity. This trend supports the theory that the RVC has a strong quenching effect on cavity combustion.

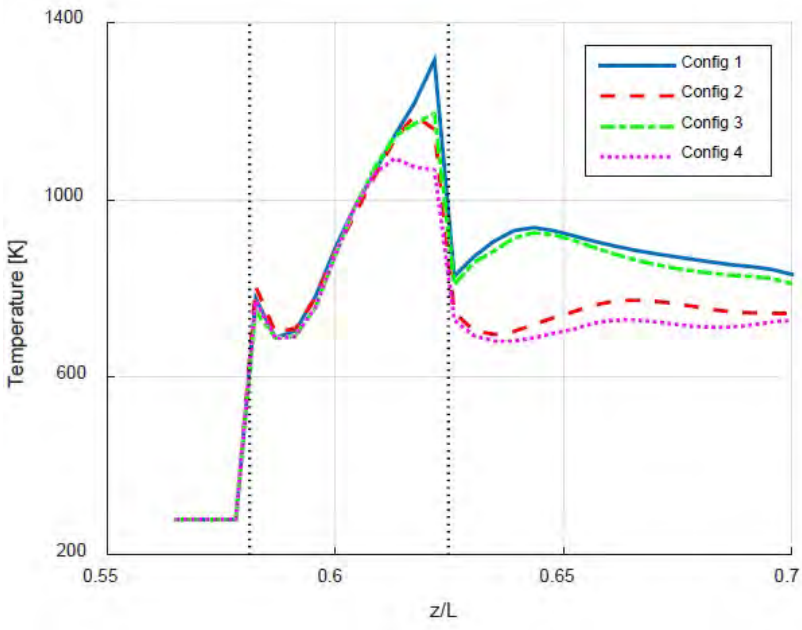


Figure 72. Area-weighted average of temperature with axial position (Config 1 = Version 2 UCC without RVC; Config 2 = Version 2 UCC with RVC; Config 3 = Version 3 UCC without RVC; Config 4 = Version 3 UCC with RVC) - Vertical dotted lines indicated the forward and aft walls of the circumferential cavity [64]

With the success of the UCC Version 3 modifications coupled with the baseline RVC, Cottle [78] numerically investigated six additional RVC designs shown in Figure 74 with an adiabatic analysis. Vane 1 was considered the original low loss centerbody design with no modification, and Vane 2 was the RVC discussed earlier as shown in Figure 68. He found that all of the new RVC designs produced a similar result of inducing more swirl into the vane passages. Vane 3 caused a substantial inward migration and produced a cooler OD and hotter ID. Vane 4 impeded inward-radial migration and entrained hot gases. Vanes 5 and 6 both exhibited good radial migra-

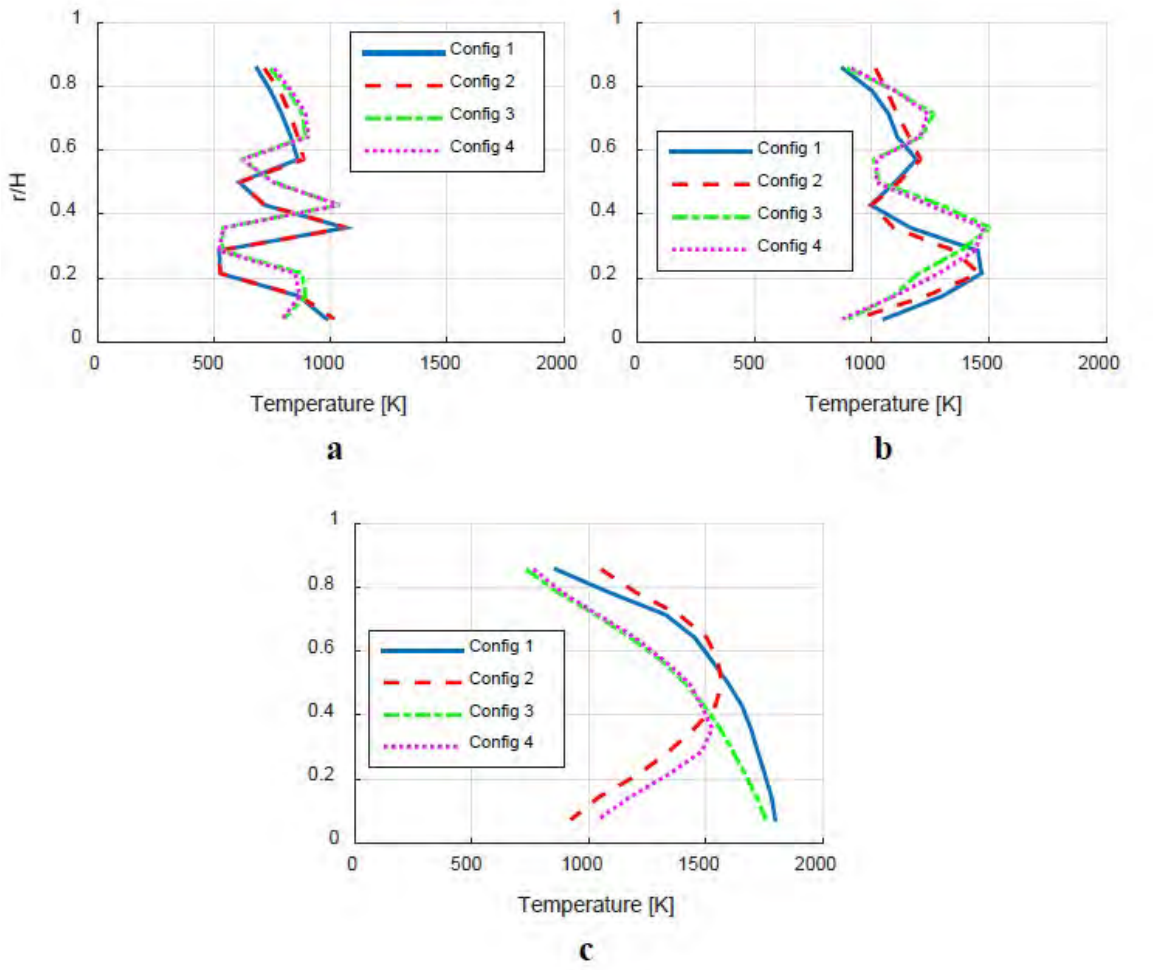


Figure 73. Combustion cavity temperature profiles (Config 1 = Version 2 UCC without RVC; Config 2 = Version 2 UCC with RVC; Config 3 = Version 3 UCC without RVC; Config 4 = Version 3 UCC with RVC) [64]

tion, while Vane 6 additionally achieved good lateral dispersion of hot gases. Vane 7 was highly effective at laterally distributing hot gases, and Vane 8 produced nearly identical results to the baseline. Cottle ultimately concluded that Vane 6, the double back step, produced the most desirable distribution of hot combustion products at the exit plane and achieved a nearly complete radial migration.

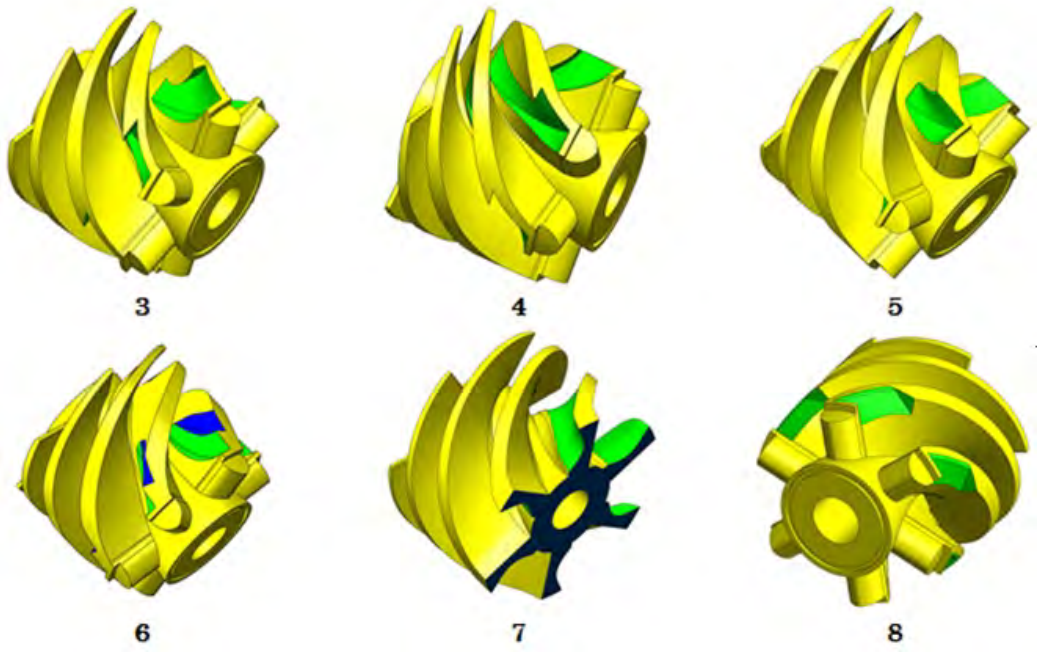


Figure 74. Other RVC designs tested by Cottle [78]

2.3.8 High-g Flame Structures and Circumferential Cavity Analysis.

One of the earliest papers on the AFRL high-g UCC concept was published in 2002 by Zelina et al. [79]. This paper covered the results of a numerical simulation of the combustion process in the UCC as well as an atmospheric pressure experimental test. They showed that for a 22% cavity air split, the temperature distribution in cross section of the UCC cavity was bimodal and appeared as an inverted "V" originating from the fuel inlet as shown in Figure 75. This pattern is likely formed due to a dual vortex in the cavity resulting from the shear layer interaction. Additionally, the fuel concentration in the center of the cavity was likely too high to combust.

In 2009, Drenth [80] observed this v-shaped flame experimentally at the exit plane of the AFIT sector rig with a straight cavity. The curved cavity sector rig produced a single localized flame as shown in Figure 76. Drenth postulated that the v-shaped flame in the straight sector rig was due to a dual vortex pattern induced by the

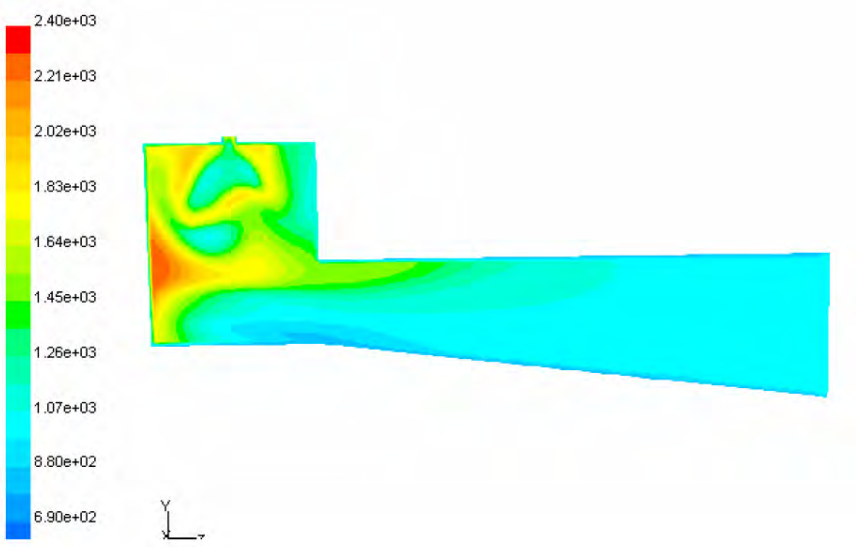


Figure 75. Temperature calculations (°K) along the combustor cross section for 22% cavity air at high-g load [79]

shear layer. He went on to say that the dual vortex was possibly present in the curved cavity sector, but that it just wasn't present at the exit plane where he was taking measurements due to hardware geometry. It is also possible that the geometry differences in fuel and air inlet locations between the two sector rigs he tested was enough to eliminate the combustion pattern for the curved rig. Drenth used planar laser induced fluorescence (PLIF) to find the reaction location. PLIF highlights the location of OH radicals in the flow. Since OH radicals are an intermediate species in hydrocarbon combustion, the presence of OH indicates the presence of a reaction.

In 2011, Bohan [6] completed his numerical analysis on a fighter-scale UCC and also found a bimodal reaction in a curved cavity under g-load. The bimodal presence was found by creating iso-surfaces of OH as shown in Figure 77. These iso-surfaces are for a level that is 1/3 of the maximum OH value seen in the test domain. Even at this reduced quantity there were two distinct regions of reactions that ultimately exited the cavity to be completed in the core flow after passing over the vane.

The experimental work of Wilson et al. [65] using a full annulus test rig supported

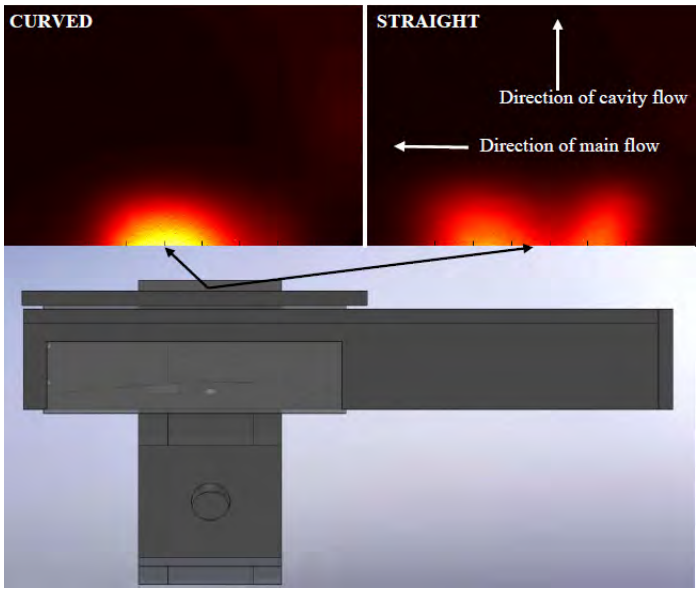


Figure 76. PLIF images from the exit plane of the curved and straight sector rig [80]

the trend and location of the OH iso-surface produced by Bohan [6]. Wilson's work was conducted and published several years after Bohan concluded his analysis. Only the circumferential position could be verified as Wilson et al. did not produce plots of combustion intensity at different axial locations in the cavity. In Figure 78 the instantaneous and averaged flame intensities are shown for the AFIT full annular UCC rig as viewed through a monitoring window in the aft cavity wall. The fuel injectors are located over the turbine vanes, so the location of the averaged flame is in the same position as the OH iso-surface in Figure 77 that was produced by steady-state analysis. In both cases there is a downward slope to the flame and it exits the cavity into the core flow after passing over the vane.

With multiple CFD solutions showing a bimodal reaction in the cavity, but the curved AFIT sector rig not showing the same result, LeBay [62] expanded on Drenth's research [80] with the sector rigs to discover the cause of the differences. He discovered a variation in the exit area between the two sector rigs that resulted in the curved rig not displaying the v-shaped flame. When the area of the curved rig was increased

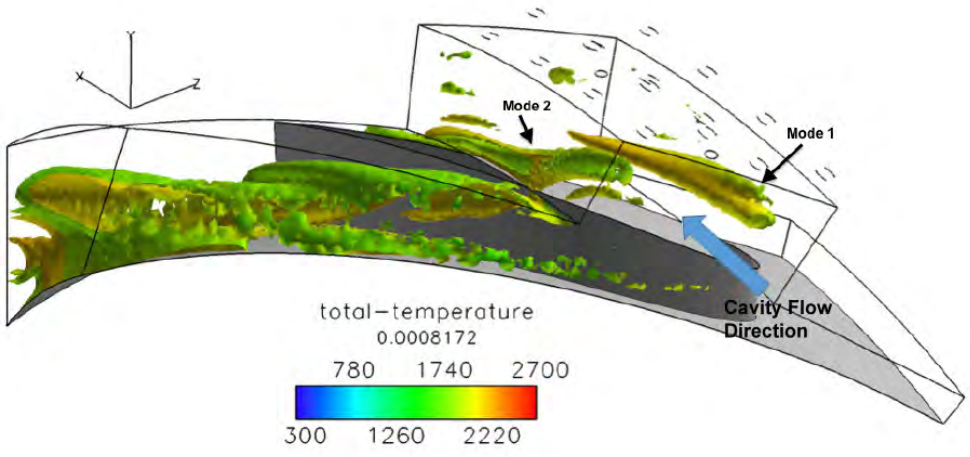


Figure 77. 3D iso-surface of OH in a large-scale UCC operated at test rig conditions showing 2 modes. Surface is colored by total temperature [6]

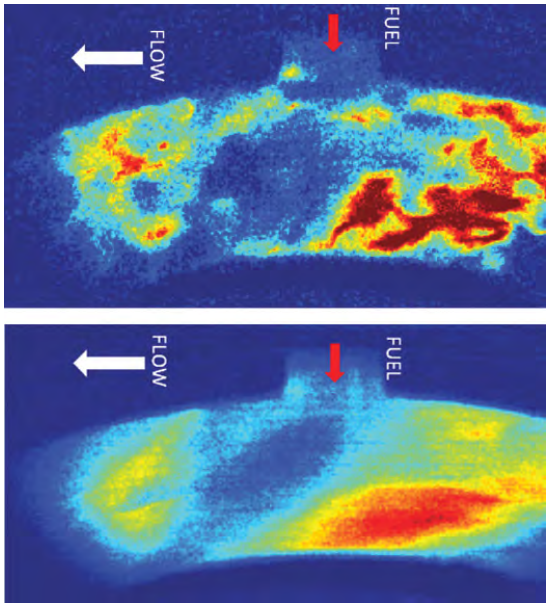


Figure 78. Flame intensities in the UCC cavity at an instantaneous measurement (top) and a 50 frame average (bottom) [65]

to the size of the straight section, both rigs produced the v-shaped flame at identical conditions. Based on this result he concluded that the shape was independent of the presence of a g-load in the cavity. Under g-load, however, the orientation of the shape was changed. Further investigation showed that the v-shape was the result of

the shear interaction of the cavity flow with the core flow. When the core flow was removed, the v-shape was not present.

Katta et al. [81] conducted a numerical study with the intent of determining the impact of g-load on flame speed in a high-g UCC. They observed numerically that in a centrifuge tube with laminar analysis, the flame speed was increased under g-load due to the bubble hypothesis presented by Lewis [4]. They did not, however, observe a similar bubble transport mechanism in the full UCC simulations. They speculated that the high speed circumferential flow that was perpendicular to the centrifugal force did not allow the bubble to accelerate in the buoyant direction. They observed that the circumferential acceleration made the flame thinner and longer. This result is in support of Briones et al. [33] who claimed the g-load served to enhance mixing in the UCC cavity.

The majority of the UCC experimental testing has been conducted with gaseous propane fuel, however, in 2014 Brinker et al. [82] published the results of a liquid fuel spray analysis in a high-g UCC. They concluded that heavy liquid fuel particles injected into a circumferential flow resulted in the particles being convected downstream with the air flow. The particle speed increased with increasing distance from the injector, and was more pronounced at higher g-loads. Also at higher g-loads the particles were accelerated to the OD of the cavity. Figure 79 shows water droplet velocities and trajectories under three levels of g-loading and two levels of injection pressure drop across the nozzle. When they investigated the flow properties of varying sized particles they confirmed that smaller particles followed the air flow, while heavy particles were forced to the OD of the cavity. This result confirms one of the key concepts that the high-g UCC is based on. Forcing heavy fuel particles to stay inside the cavity until burned or broken down creates the appearance of an infinite combustion length.

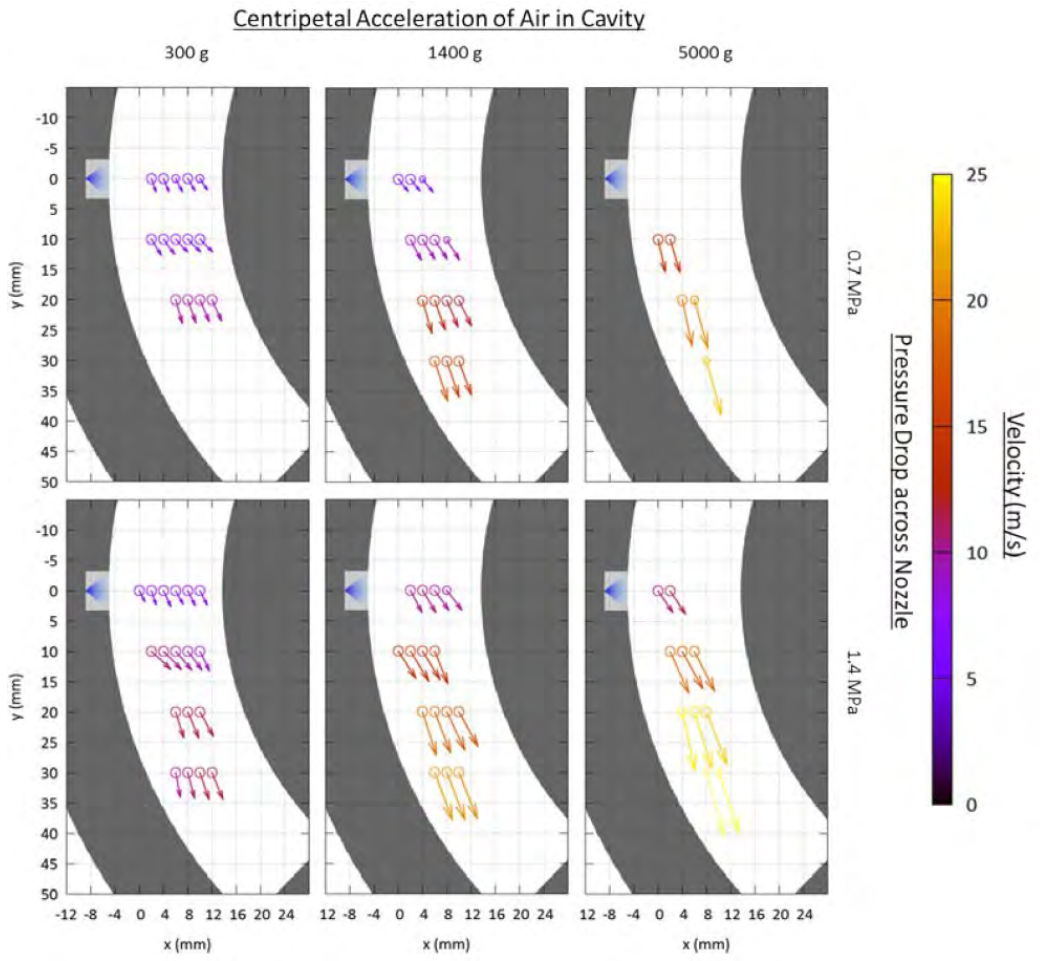


Figure 79. Water velocity and trajectory for g-loads of 300g_e, 1400g_e, and 5000g_e at 0.7 and 1.4 MPa pressure drop [82]

While Brinker et al. [82] showed that heavier liquid fuel particles in g-load would in fact stay in the cavity longer, this result was not seen with gaseous fuels. Cottle [83] performed several fuel particle stream traces and showed that the vast majority of particles exiting a gaseous fuel inlet exited the cavity after 60 to 120 degrees of circumferential travel. As shown in Figure 80 for four combustion conditions in the Version 3 UCC, there were some particles that remained in the cavity longer, specifically in the fuel-rich cases, which is likely just due to the excess quantity of fuel present.

In Figure 80 the "med" and "high" refer to the flow rate (0.11 kg/s and 0.15 kg/s) and "rich" and "lean" refer to the fuel level (equivalence ratios of 1.37 and 0.8). In

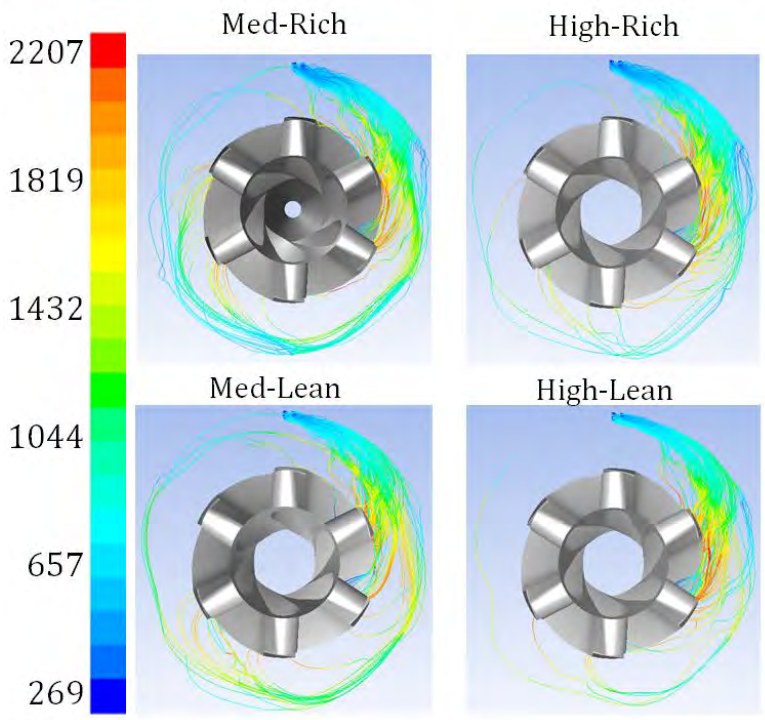


Figure 80. UCC Version 3, Single-point fuel injection stream traces colored by temperature (K); med-rich (top left), high-rich (top right), med-lean (bottom left), high-lean (bottom right) [83]

the high-lean condition (bottom right), all of the fuel particles had exited prior to making a complete revolution. The results presented above for the Version 3 UCC, which featured the compound air drivers, was greatly improved over the results in the Version 2 UCC where all fuel particles exited within one vane passage downstream of injection. Both of these results are based on gaseous fuel (propane).

Using two additional combustion conditions, Cottle [83] also studied the tangential velocity variation with radial position at three axial locations inside the circumferential cavity. He observed higher peak velocities for the Version 3 UCC compared to the Version 2 UCC, however, the Version 3 UCC had a much larger variation in tangential velocity with radial position. The tangential velocities for both UCC versions are shown in Figures 81 and 82. In these plots the "fore", "mid", and "aft" refer to the axial measurement location in the cavity. The "low" flow rate is 0.06 kg/s.

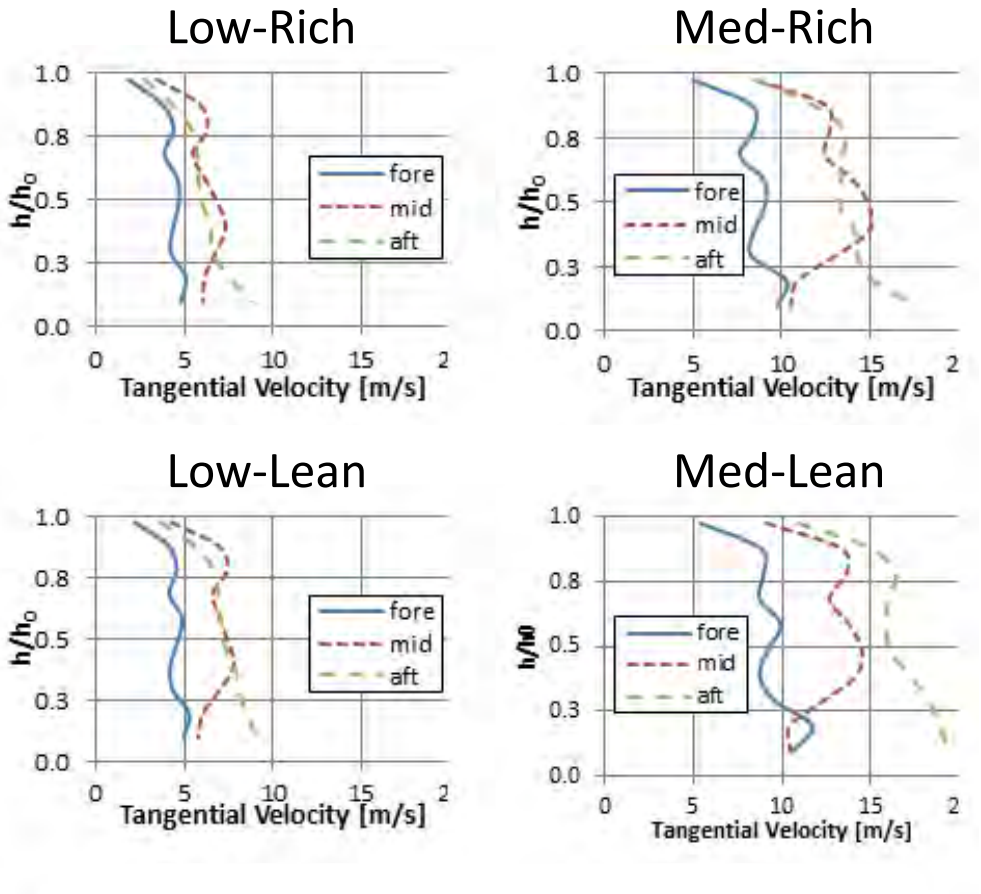


Figure 81. Radial profiles of circumferentially-averaged tangential velocity (Version 2 UCC) [78]

Due to a variation in both tangential velocity and cavity radial position, the g-load became a variable based on Equation 44. Cottle [78][83] calculated the circumferentially-averaged g-load based on radial position and presented it for variations in flow rate, equivalence ratio, and axial position for the Version 3 UCC. These plots are shown in Figure 83. As Lewis [4] discussed, g-loads below $350g_e$ would have minimal or no effect on the flame front. At the lower mass flow rates shown in Figure 83 there are many regions where the flow is below this threshold. Lapsa and Dahm [56] proposed a more stringent threshold of $1{,}000g_e$ to observe a flame front effect. As Cottle shows in Figure 84, the primary combustion region within the AFIT Version 3 UCC is be-

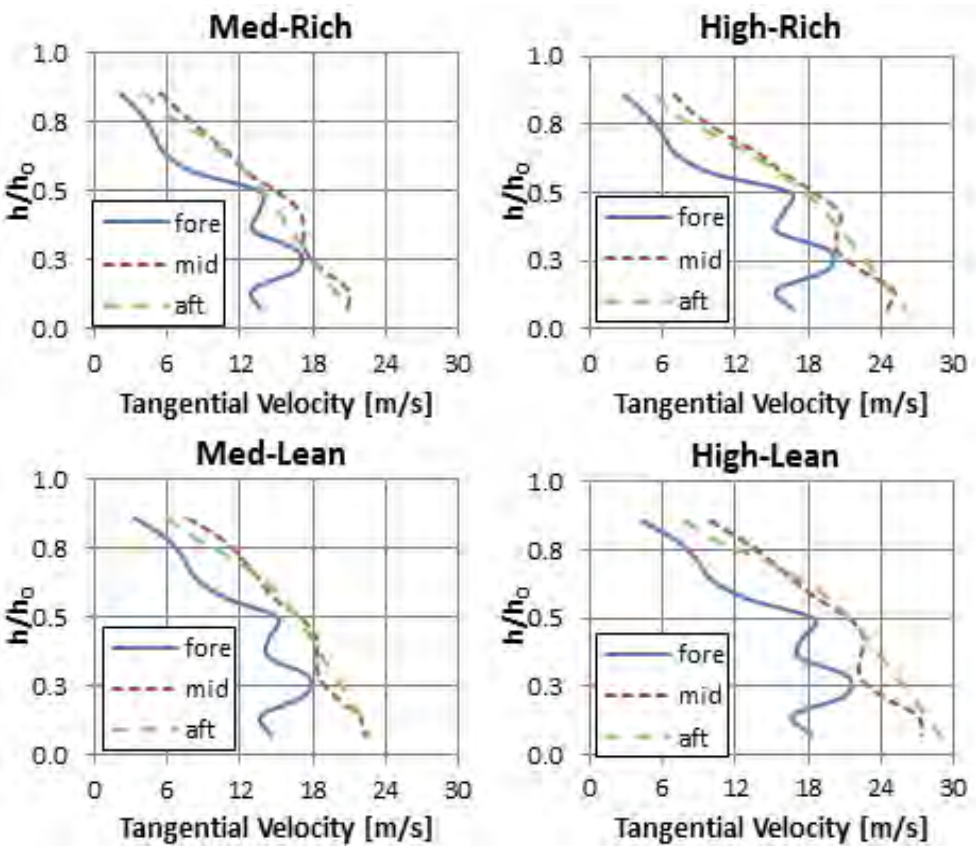


Figure 82. Radial profiles of circumferentially-averaged tangential velocity (Version 3 UCC) [78]

tween the mid position and aft wall below 50% radial height. Looking at the three plots in Figure 84 it can be seen that this is the region of highest heat release. At the more restrictive 1,000g_e threshold, there were only two flow rates that achieved this g-load in the primary combustion zone. All but the lowest flow rate achieved the Lewis threshold in the primary combustion zone.

The numerically obtained velocity measurements were compared to particle emission streak velocimetry (PSEV) experimental results with reasonable agreement. Cottle's results did not display the same bimodal or v-shaped combustion region. All the results that experienced the bimodal reaction were based on geometry that featured air and fuel injection from the top wall of the cavity. The hardware used by Cottle

had fuel injection on the top wall with air injection on the upstream wall. Even with the presence of a comparable core flow and shear layer, the change in the air injection location was enough to change the combustion characteristics in the cavity.

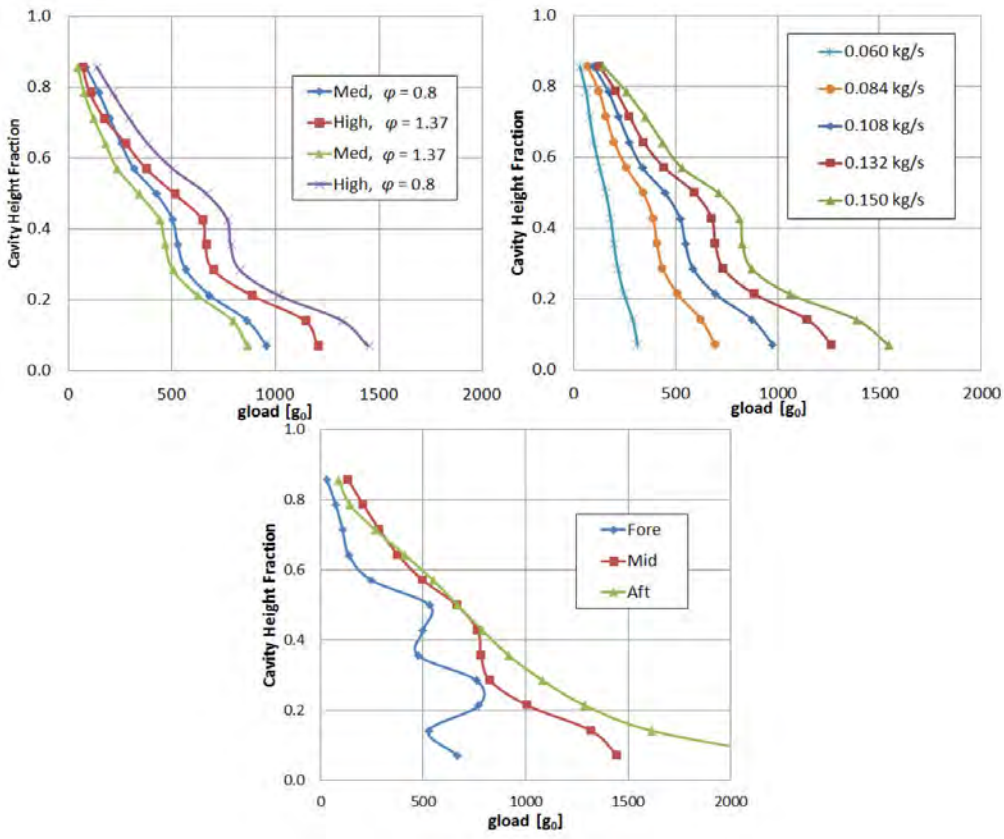


Figure 83. Radial profiles of circumferentially-averaged g-loads in the circumferential cavity (Version 3 UCC) [78][83]

The findings by Cottle showed that higher mass flow rates lead to higher tangential velocities, and thus g-loads, for a fixed diffuser mass flow rate split and fixed cavity inlet air driver hole diameter. This result supports the earlier work of Bohan and Polanka [63] that showed the tangential velocity, and thus g-load, was a function of cavity inlet velocity almost exclusively. Higher mass flow rates would produce higher injection velocities for a fixed inlet hole diameter and resulted in higher tangential velocities.

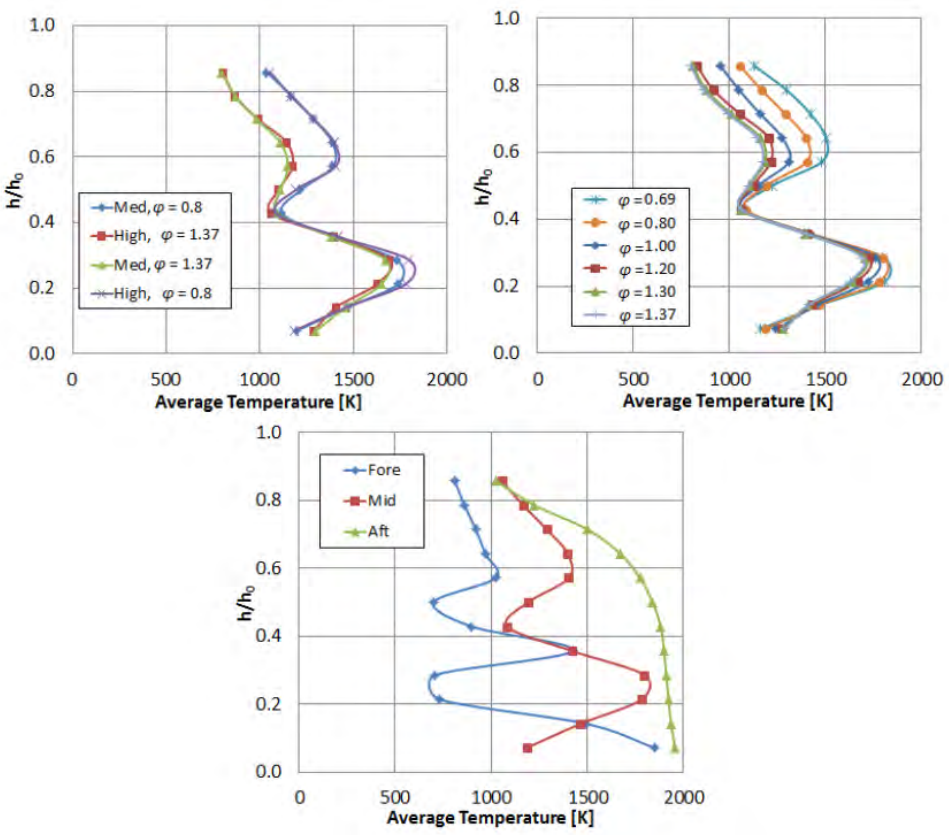


Figure 84. Radial profiles of circumferentially-averaged temperatures in the circumferential cavity (Version 3 UCC) [83]

2.3.9 Emissions Analysis.

If a high-g UCC is ever to be used as a replacement for a traditional combustor in a jet engine, it must be at least as efficient and not produce any more emissions than its predecessor. To that end, emissions and efficiency have been a topic of interest in the high-g UCC research community since the beginning. The primary pollutants of interest are NO_x, CO, and unburned hydrocarbons (UHC).

A 2002 paper by Zelina et al. [79] reported the results of an atmospheric pressure high-g UCC test rig. They tested cavity air flow splits of 16, 22, and 27%. They found that at the 22% cavity air flow split the UHCs were an order of magnitude lower than at the 16% air flow case. The 22% cavity air split also produced the

lowest CO emissions of the three conditions tested. The lowest NO_x levels, however, were achieved by the 27% air split case. Figure 85 shows the emissions index (EI) for NO_x and CO plotted against each other for each of the three flow conditions and at a number of equivalence ratios. It was found that at atmospheric conditions, increasing air flow to the cavity had a positive affect on reducing both NO_x and CO. This is counter to a traditional combustor which requires the designer to make tradeoffs to reduce NO_x or CO. Zelina et al. also found that their preliminary test rig achieved 99+% efficiency in the flame holding zone.

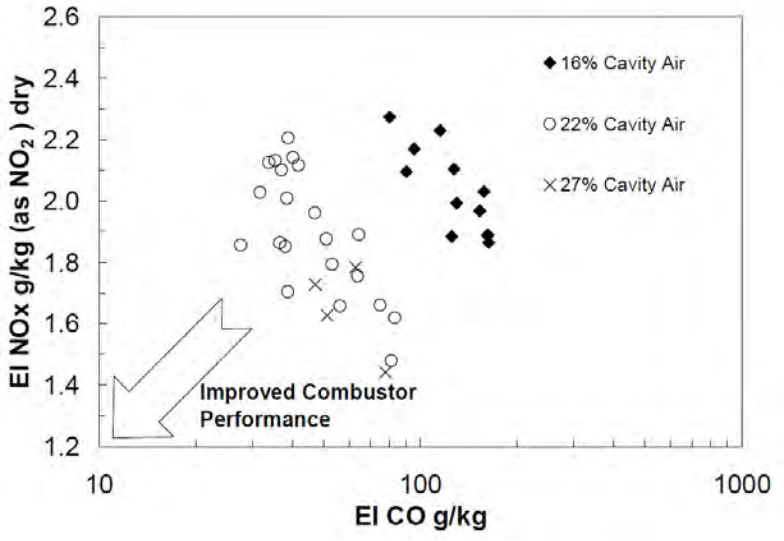
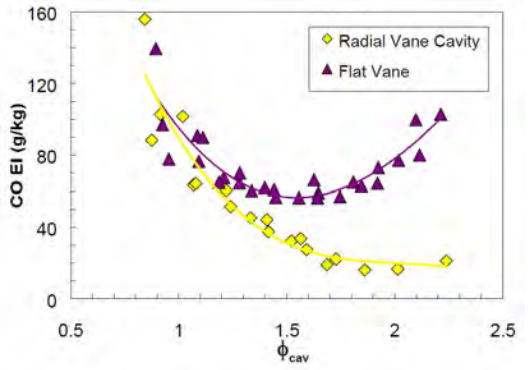


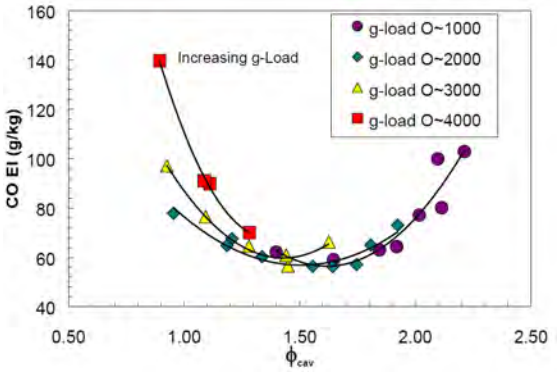
Figure 85. Emission maps of high-g UCC performance at three cavity air flow splits [79]

A follow-up study by Zelina et al. [3] in 2004 specifically highlighted the difference in emissions output in a high-g UCC test rig with and without a radial vane cavity (RVC) in the UCC turbine vane. As shown in Figure 86a, the RVC had a significant impact on reducing CO emissions, specifically when the engine was run at cavity equivalence ratios of greater than 1.2. The production of CO is highest at low-power engine operations or fuel-rich combustion. Zelina et al. concluded that the RVC caused greater air entrainment into the cavity to reduce the effective equivalence ratio, or that the CO was burned out in the RVC.

Zelina et al. [3] also showed the relationship of CO emission index to cavity equivalence ratio and g-load as shown in Figure 86b. This plot shows that CO production is independent of g-load for cavity equivalence ratios above 1.5. Below 1.5, g-load was a factor, with the CO emissions index increasing for higher g-loads.



(a) CO emission index as a function of cavity equivalence ratio for a flat vane and a vane with an RVC



(b) CO emission index as a function of cavity equivalence ratio and g-load

Figure 86. CO emissions index in the UCC under varying conditions [3]

Gilbert et al. [76] also investigated emissions from a high-g UCC with and without an RVC. The test rig they used was the AFIT Version 3 UCC with a 30% cavity air flow split. The low loss centerbody (LLCB) hybrid vane was used with a variant of it manufactured with an RVC as shown previously in Figure 68. An emissions map showing the relationship between NO_x and CO production at various conditions for both vane configurations are shown in Figure 87. The vane with the RVC produced more NO_x than the LLCB. The cavity temperatures with the RVC were higher than with the LLCB which could have initiated the NO_x production. The LLCB produced a relatively linear relationship between NO_x and CO. Gilbert et al. found an emissions minima at equivalence ratios between 0.75 and 0.90.

As part of their migration study discussed in Section 2.3.7, Cottle et al. [64] looked at numerically produced levels of UHC at each axial position in the Version 3 UCC rig. Figure 88 shown the calculated UHC mass fractions. In this figure the dotted

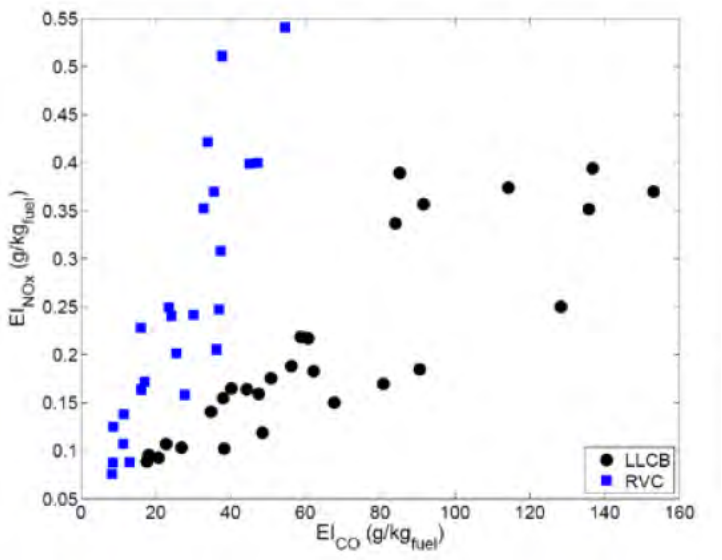


Figure 87. Emission maps of high-g performance in the Version 3 UCC with the LLCB and LLCB with an RVC [76]

vertical lines indicate the inside walls of the circumferential cavity. As expected the highest UHC levels were located in the cavity where fuel was injected. The UHC levels dropped off sharply in the aft end of the cavity ($0.62 < z/L < 0.63$) where primary combustion occurred. Figure 72 shows the temperature distributions in the cavity for the same test conditions. By $z/L = 0.7$, product production had dropped considerably to approximately 5 1/s for all configurations which is well below peak production levels of approximately 50 1/s. Additionally by that location, the mass fraction of UHC was more than three orders of magnitude below cavity levels.

2.4 Combustion Instability & Acoustics

Combustion stability is of critical importance when evaluating the suitability of new combustion systems. According to Montfort et al. [84], many new combustors rely on a combination of large and small scale turbulent eddies and vortical structures to control mixing, fuel distribution, flame holding, and heat release. These turbulent

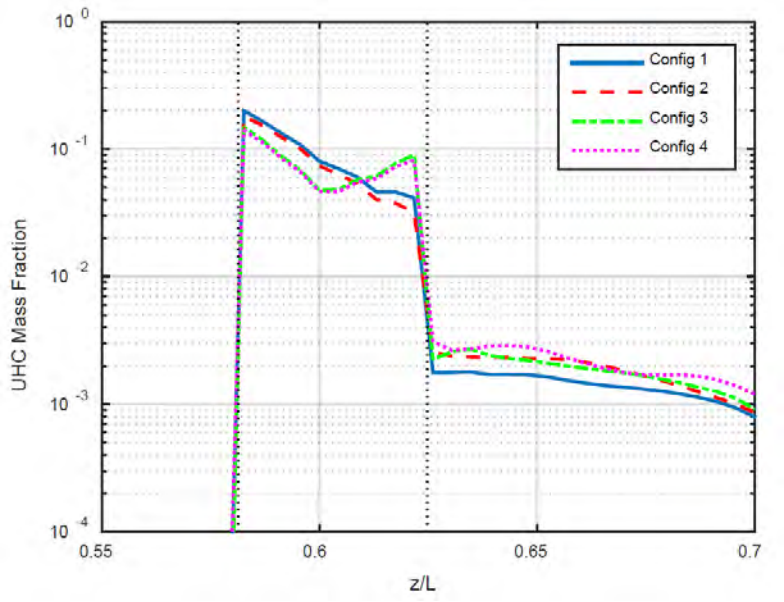


Figure 88. Area-weighted average of UHC with axial position (Config 1 = Version 2 UCC without RVC; Config 2 = Version 2 UCC with RVC; Config 3 = Version 3 UCC without RVC; Config 4 = Version 3 UCC with RVC) - Vertical dotted lines indicated the forward and aft walls of the circumferential cavity [64]

eddies can lead to combustion instabilities. As a definition, combustion instability is a feedback process between pressure and heat release oscillations coupled with acoustic resonant modes of the combustion chamber. These thermoacoustic pulsations can negatively impact performance, emissions, and even structural integrity of the engine itself [85]. The noise associated with the unsteady process of heat release resulting in volumetric expansion are said to be direct sources of noise. Indirect noise sources are the result of accelerating a fluid with a non-uniform entropy or vorticity distribution within the engine [86]. Figure 89 shows a diagram of the noise sources in a traditional combustor.

Allison et al. [87] state that within a combustor, "The magnitude of the response of a flame to a given acoustic perturbation is determined by the degree of coupling between the pressure field and the heat release, as described by the Rayleigh criterion." The Rayleigh criterion shown in Equation 53 states that if the product of the

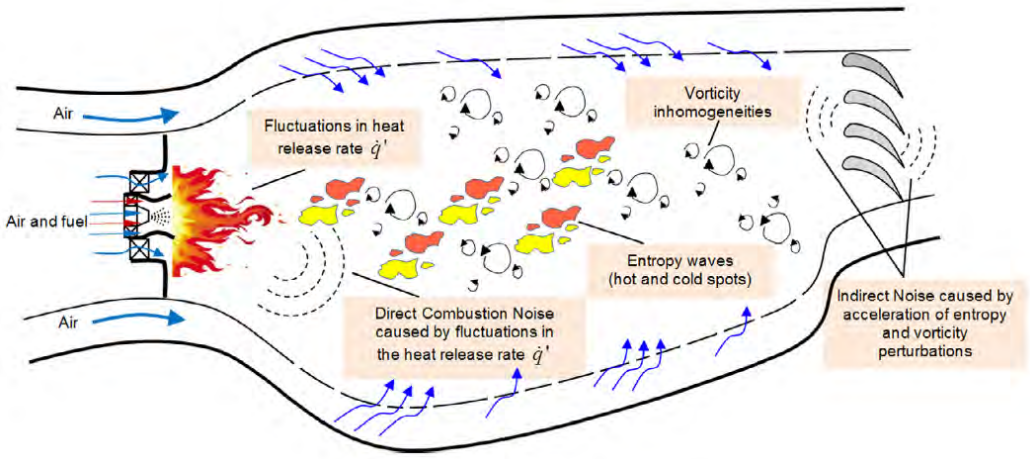


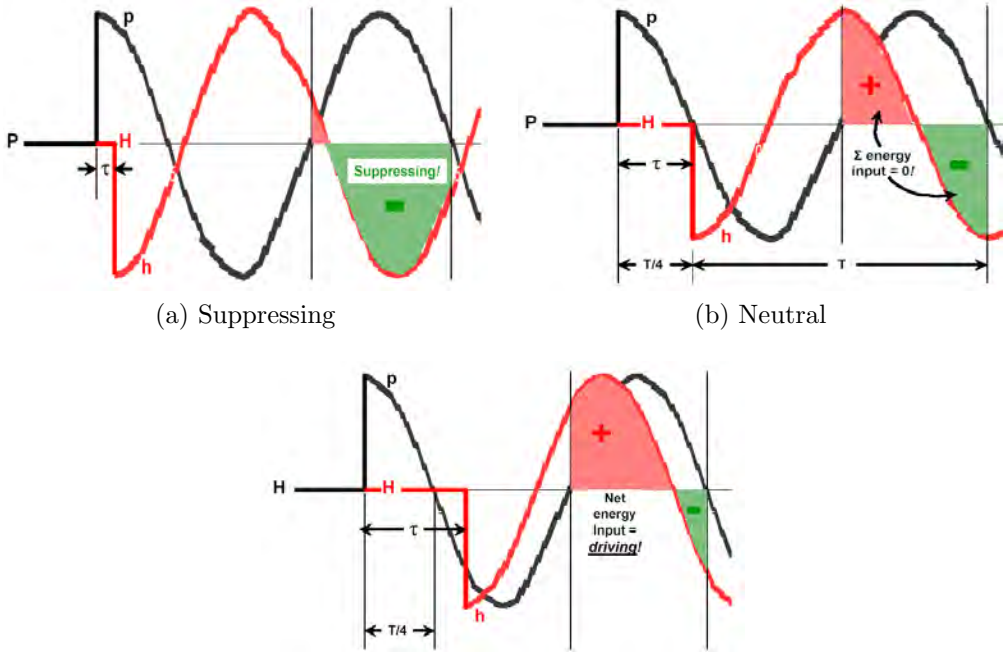
Figure 89. Direct and indirect combustion noise sources in a traditional gas turbine combustor [86]

fluctuating component of pressure (p) and heat release (h), integrated over a vibration cycle, is positive, the vibration will be maintained assuming there are no sources of damping. This means that if the fluctuations in heat release are more in-phase than out-of-phase with the pressure oscillations in the chamber, the conditions feed the oscillations and the instability grows. [88]

$$\oint phdt > 0 \tag{53}$$

The relative phase between acoustic pressure oscillations (p) and the temporal response (τ) of heat release (h) are controlled by a time delay that is dependent on fuel chemistry, constituent temperatures, and fluid dynamics in the combustion chamber [87]. This is better illustrated in Figure 90 which shows the phase relationship for a suppressing, neutral, and driving acoustic instability response. In the suppressing case the volumetric expansion from the fluctuating heat release is out-of-phase with the pressure fluctuation, thus acoustic oscillations would not be produced and present instabilities could be damped out. In the neutral case which shows a delay in the heat release of up to 1/4 period of the pressure oscillation, there is no damping or driving

of the instability. For heat release oscillations beyond 1/4 period of the pressure oscillation, the volumetric expansion due to heat release is closer to in-phase with the pressure oscillation and the combined energies enhance the acoustic instability.



(a) Suppressing

(b) Neutral

(c) Driving

Figure 90. Acoustic responses to relative phase shifts between pressure oscillations and heat release [88]

Results shown in Figure 91, published by Cai et al. [89], support the conclusion that the burners acoustic response is a function of fuel properties and fluid flow dynamics. This figure shows a variation in combustion noise spectrum based on equivalence ratio as recorded by an AKG microphone external to the combustion chamber. In these findings the quantity of fuel had an impact on timing of the heat release in the combustion chamber which changed the acoustic frequency response of the system. Across the range of equivalence ratios there were three dominant frequency bands at 280, 420, and 600 Hz. At low equivalence ratios, below 0.38, the combustion was considered loud. Above Φ=0.38, however, the combustion abruptly changed to quiet operation. The cause of the noise intensity change is not clear.

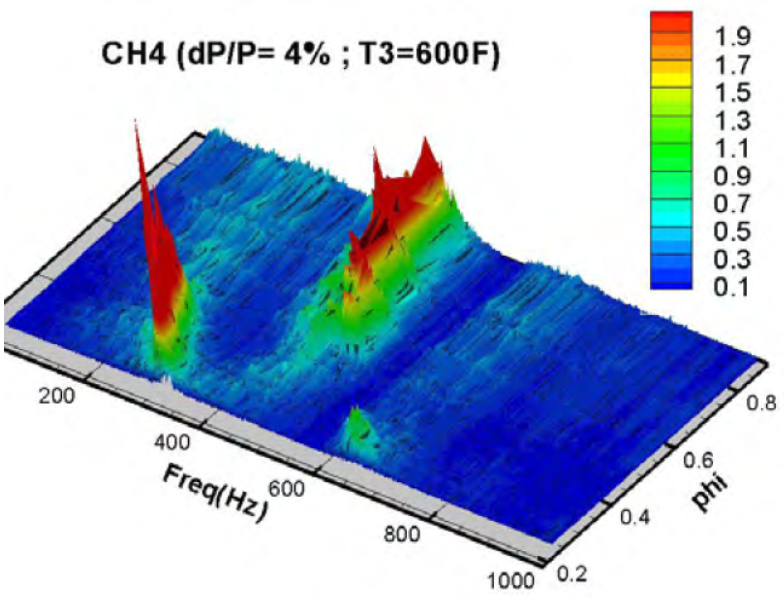


Figure 91. Dynamic energy iso-contours as a function of acoustic frequency response and equivalence ratio recorded by an AKG microphone [89]

The location of measurement of the pressure oscillations also has an affect on the frequency spectrum observed. In Figure 92 the frequency spectrum recorded by four pressure transducers located at four axial positions downstream of the combustor inlet is shown for an equivalence ratio of 0.62. While there is still a spike around 400 Hz, as observed by an external AKG microphone, there are additional peaks near 500 Hz with higher frequency responses recorded closest to the combustor inlet. These high frequency responses are assumed to be due to local turbulent processes at the inlet and dissipate quickly as they are not seen by the other pressure transducers.

Instantaneous images of flame structures can be used to determine the combustion conditions that cause specific acoustic responses. In the study by Cai et al. [89] they found that at very lean combustion conditions the first acoustic mode (280 Hz) dominated. In this mode, combustion was anchored to the combustor dome and had no interaction with dilution air. The instability in this mode was strongly tied to the swirling flow at the inlet and primary recirculation zone in the dome only. When the

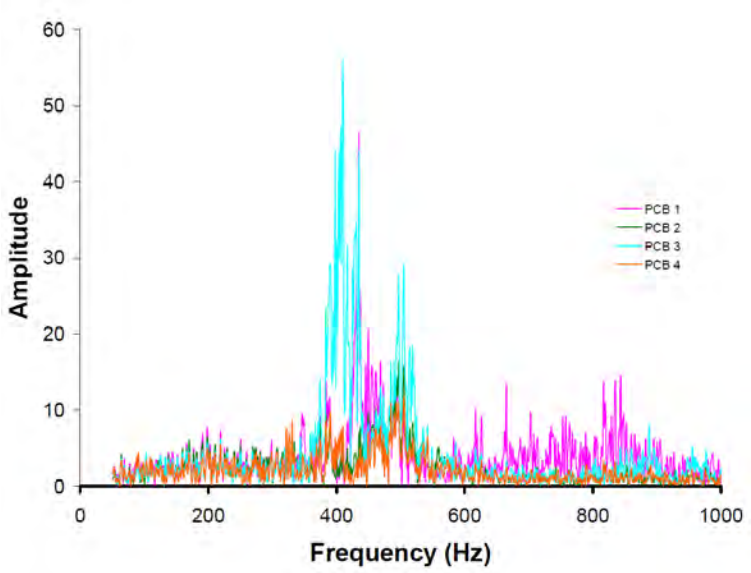


Figure 92. Frequency spectra at an equivalence ratio of 0.62 recorded at four axial locations [89]

equivalence ratio was increased, the second mode dominated as the reaction zone was moved to downstream of the dilution holes and virtually no combustion took place in the dome. This response is seen in Figure 91 by the loss of the 280 Hz frequency. The primary response of this second acoustic mode around 400 Hz was due to the interaction between the flame front and aerodynamics in the dilution region.

In addition to the behavior shown above where the combustor responds with one acoustic mode for a given operating condition, there is the possibility of a self-excited transition from a stable state to a thermoacoustically unstable condition. As discussed by Boxx et al. [85], despite the focused effort of research on this topic over many years, there are still extreme challenges associated with understanding and predicting the onset of a self-excited response. Boxx et al. did find an acoustic mode that existed for fractions of a second between stable and unstable operation of a test combustor, but the mechanisms associated with the transition are still unknown.

An external microphone can be used to measure the combustion acoustic response, but if more detail is needed measurements can be taken in the combustion chamber.

He and Chang [90] describe a method of collecting and processing acoustic combustor data using pressure transducers. They inserted metal tubes with a diameter of 0.46 cm into a combustion chamber at three axial locations to collect dynamic data. A piezoelectric dynamic pressure sensor was attached at a "T" junction 0.9 m away from the tube inlet. The other leg of the "T" connector was connected to a 30 m length of tubing to damp out the dynamic signals. Dynamic pressure readings were recorded for 30 seconds at 20 or 30 kHz. The dynamic pressure signals were transformed to the frequency domain using the Fast Fourier Transform (FFT). During the signal processing the recording was divided into segments of 2^{15} points. This resulted in an FFT analysis on 1.1 to 1.5 seconds of data. The frequency spectrum was then adjusted to compensate for sampling line loss following the guidance of Samuelson [91]. When each FFT was adjusted, the values could then be averaged to reduce noise.

2.5 Secondary Flows

When an object protruding from an endwall exists in cross flow, such as a turbine vane, secondary flows must be considered. An example of a secondary flow is a three-dimensional vortical structure that develops around the object. Much of the early work on secondary flows was produced by Langston [92]. His research led to the identification of what is commonly referred to as a horseshoe and passage vortex. Langston produced an illustration of these vortical structures shown in Figure 93. These structures develop as the result of the boundary layer. As fluid passes over the endwall a boundary layer forms resulting in low speed fluid near the wall and higher speed fluid away from the wall. As the fluid impacts the leading edge of the solid obstruction, the higher momentum fluid flows down the face of the obstruction towards the endwall and into the lower momentum fluid. The higher momentum fluid then hits the endwall where it turns again flowing opposite the direction of the

bulk flow. When the higher momentum fluid has lost enough energy from opposing the bulk flow, it is rolled up to again flow in the original direction. This flow path is shown in Figure 94 which displays the time averaged streamlines in a streamwise plane positioned at the obstructions leading edge. From this figure it can also be seen that the formation of the horseshoe vortex also results in the development of a secondary, tertiary, and corner vortex. These structures are much smaller and weaker than the primary horseshoe vortex. As long as there is a continuous flow of bulk fluid, these structures roll up into a vortex that is swept around both sides of the obstruction and grows as it is convected downstream.

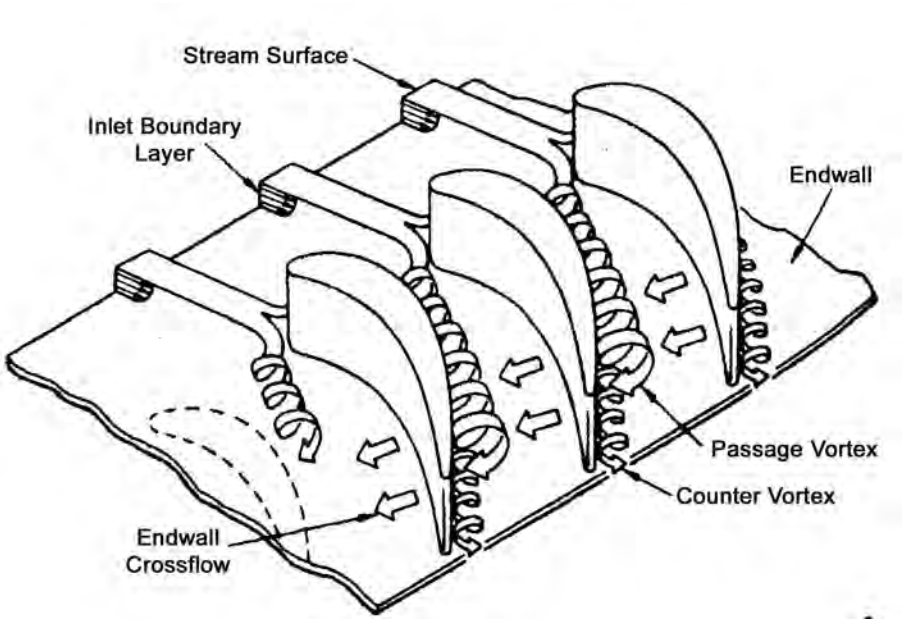


Figure 93. Illustration of secondary flows [92]

Secondary flows must be considered when investigating flow migration of hot gases from the UCC. Depending on the positioning of these structures around the UCC turbine vane (hybrid guide vane) they could either aid or hinder the migration and mixing efforts to present a desirable temperature distribution to the turbine. Additionally, these secondary structures could interfere with film-cooling of the UCC turbine vane. These vortical structures entrain fluid near the wall which could sweep away cooling

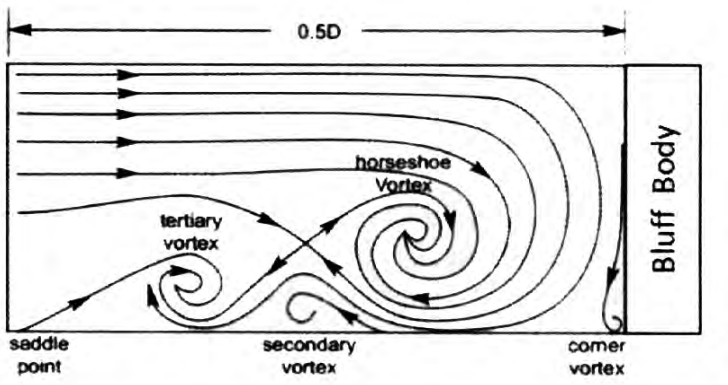


Figure 94. Symmetry plane streamlines of a horseshoe vortex system by Sabatino et al. [93]

flows and negate the cooling effort [10]. While secondary flows could prove useful for blending the hot gases from the UCC cavity with the core flow, there are techniques to eliminate these structures if the negative impact to cooling is too great. Lethander [10] assessed variations of fillets in the endwall/turbine vane interface that effectively removed the secondary structures.

In a gas turbine engine the primary area of interest regarding secondary flows is in the turbine section of an engine using a traditional combustion system. The smooth extended surfaces of a can-type, or annular-type, combustor provide a sufficient endwall for a boundary layer to form. The turbine vanes then serve as the obstruction protruding from the endwall. Hermanson and Thole [94][95] researched the impact of Mach number and turbine inlet condition on the formation of secondary flows around turbine vanes. Using combustor exit conditions as the inlet to their study, they found that larger boundary layers produced a horseshoe vortex that spread further around the turbine vane leading edge. They also found that in cases where no stagnation pressure gradient was present, there was no production of a horseshoe or passage vortex. Applying these results to the UCC it can be seen that understanding the compressor exit conditions will directly impact the ability to predict the formation

and position of the secondary flow structures around the hybrid guide vane.

As part of their inlet condition study, Hermanson and Thole [95] also performed a comparison of numerical computation of secondary flows with experimental results obtained utilizing Laser Doppler Velocimetry, LDV. The goal of this project was to determine the ability of two turbulence models to accurately predict secondary flow performance. They computed results with both the $k-\epsilon$ and the Re-Normalization Group (RNG) $k-\epsilon$ models in a three-dimensional domain. The results taken along the streamwise stagnation plane from a turbine vane for their two CFD cases and the LDV experimental results are shown in Figure 95. Of the two turbulence models tested the RNG $k-\epsilon$ model most accurately represented the experimental result. This model predicted the magnitude of the y-vorticity equal to the experimental result and positioned the center of the vortex in nearly the same axial and vertical position. In addition to the stagnation plane, Hermanson and Thole also compared the CFD results to experimental data at six additional planes around the turbine. The RNG $k-\epsilon$ model continued to approximate the experimental result at all six locations with the largest notable difference being a calculated vortex placement that was 1-3% higher off the endwall. The standard $k-\epsilon$ model predicted the vortex too close to the wall and failed to capture the rotation. The standard model is typically better suited for external flows. The modifications made in the RNG $k-\epsilon$ model through the addition of terms to the standard transport equations of k and ϵ allow this version to handle stagnation flows and high streamline curvature.

Hermanson and Thole [95] conducted all of their numerical analysis on relatively simple geometry with a structured grid. Bohan [6] conducted a numerical test to determine the ability of the RNG $k-\epsilon$ model to produce secondary flow features in a more complex UCC flow environment with an unstructured grid. The boundary layer decay was set such that a y^+ value between 30 and 60 was achieved. The com-

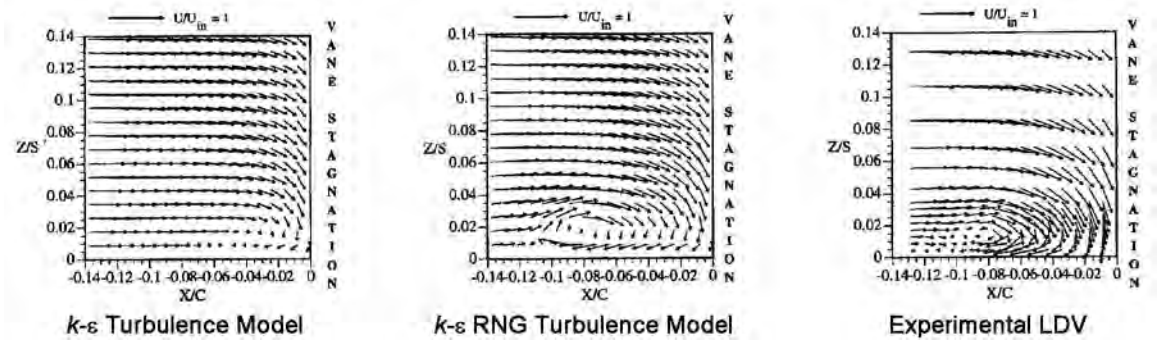


Figure 95. Comparison of turbulence models to experimental LDV measurements along the stagnation plane of a turbine vane [95]

putational domain entrance length was set at 3.67 cm. This dimension represented the design distance between the trailing edge of the last axial compressor rotor and the leading edge of the hybrid guide vane in a fighter scale engine.

As shown in Figure 96, the use of a fully unstructured grid did not detract from the ability of the RNG $k - \epsilon$ turbulence model to produce secondary flow structures. It was found, however, that due to the short entrance length in the UCC geometry the vortex structures were weak and dissipated quickly rather than grow as expected in the vane passage. This outcome indicated that secondary flows may not be as influential in the UCC as originally anticipated. If, however, geometry changes are made to the entrance length or component arrangement, these structures could once again become influential.

A 2006 study by Lei et al. [96] produced a criterion to determine if hub corner stall would be present on a compressor stator based solely on parameters available during the design process. They determined that the secondary flows were the principal three-dimensional effect that generated hub corner stall. The horseshoe vortex was convected from the pressure surface of one vane to the suction surface of the adjacent vane by the cross passage pressure gradient. This vortex brought low stagnation pressures and low momentum fluid to the aft vane hub corner region which could result

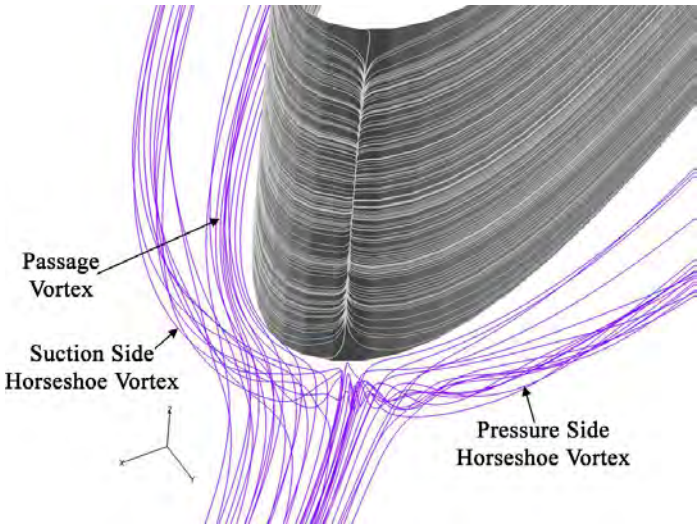


Figure 96. Resulting horseshoe and passage vortices with surface trace on the vane for a fully unstructured grid [6]

in separation. The compressor endwall flow field with separation is shown in Figure 97. Concern over compressor stator separation is relevant to the UCC as the hybrid guide vanes serve as a replacement for the last compressor stator row. Separation could be used as a mixing tool within the vane passage, but like the secondary flows themselves, the recirculation cased by separation could have a negative impact on vane cooling near the trailing edge.

A related 2008 study on compressor stators by Bailie et al. [97] numerically looked at the flow physics governing separation and the resulting recirculation off a stator vane. They performed this analysis using the $k-\omega$ Shear Stress Transport (SST) turbulence model. This model blends the free-stream performance of the $k-\epsilon$ model with the near wall performance of the $k-\omega$ model. Combined it offers excellent behavior for internal flows, and flows with adverse pressure gradients and separation. This study found that increases in vane incidence angle (up to 5°) and increased Mach numbers (tested up to Mach 0.72) resulted in much larger hub corner stall and recirculation, and greatly increased total pressure loss.

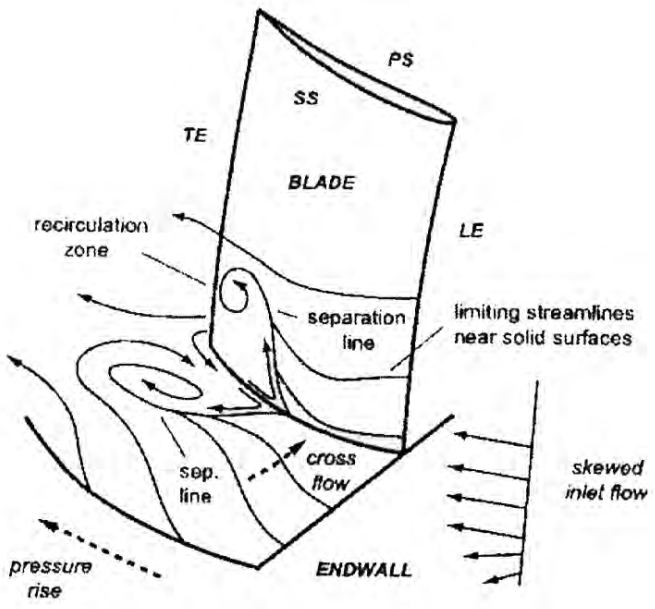


Figure 97. Compressor blade endwall flow field showing the flow separation process due to hub corner stall [96]

2.6 Fluidic Oscillators

A fluidic oscillator is a class of devices with no moving parts that results in an oscillating fluid jet moving at high frequency when provided with a pressurized fluid [98]. The oscillations are achieved solely by a fluid dynamic instability, but the physics behind the oscillations are not completely understood. The fluidic oscillator has its roots in fluid logic circuits. Spyropoulos [99] was the first to apply fluid logic concepts to create a self-oscillating jet. These devices are useful in flow control applications due to their relative simplicity, variable frequency, and the effectiveness of their dispersion. At the smaller scales, these devices have been shown to operate in very low flow rate microfluidic oscillators with jet diameters on the order of 325 μm [98]. These small devices oscillate at frequencies up to 22 kHz, and low flow rates as low as 1 L/min (or approximately 1 g/min for air) [98]. There is no known maximum scale, providing enough fluid could be supplied to drive the device.

The class of oscillators used in the present research were based on a wall-attachment type device originally patented by Stouffer [100] in 1979. In 2017, Hossain et al. [101] used a modified version of this design to test fluidic oscillators in place of film-cooling holes to achieve more surface coverage from a single jet. The wall-attachment type devices use the Coanda effect to enhance oscillation motion by pulling an internal jet of air to the wall as it is pushed back and forth by air flowing through recirculation loops.

Figure 98 shows the sequence of the switching mechanism inside a wall-attachment type oscillator. The internal oscillation is established when a fluid exits the power nozzle from a pressurized plenum. The jet expands to fill the throat and feedback channels inside the device. Opposing vortices form on each side of the power jet. One of the vortices eventually dominates the other causing the power jet to be pushed to the opposite wall and stay in place due to the Coanda effect. From this position a portion of the power jet fluid enters the feedback loop as shown in Figure 98a. This fluid enters the control port as shown in (b) where the power jet is pushed to the opposite wall. In (c) the power jet has fully transitioned to the opposite wall and a portion of the jet fluid has entered the feedback channel. In (d) the fluid in the feedback channel has made it to the control port to push the power jet back to the opposing wall, and the cycle continues. As the power jet is moved back and forth the fluid exiting the throat shares a similar oscillatory pattern but exits the throat opposite to the power jet.

Hossain et al. [101] described the relationship of geometrical features in the oscillator they tested as shown in Figure 99. The dimensions are given in terms of the throat hydraulic diameter (D), the width of the throat (W_t), and throat height (H_t). The relationship of frequency to flow rate, as well as the jet spread angle at a 0.39 g/s flow rate obtained by Hossain et al. [101] is shown in Figure 100. The

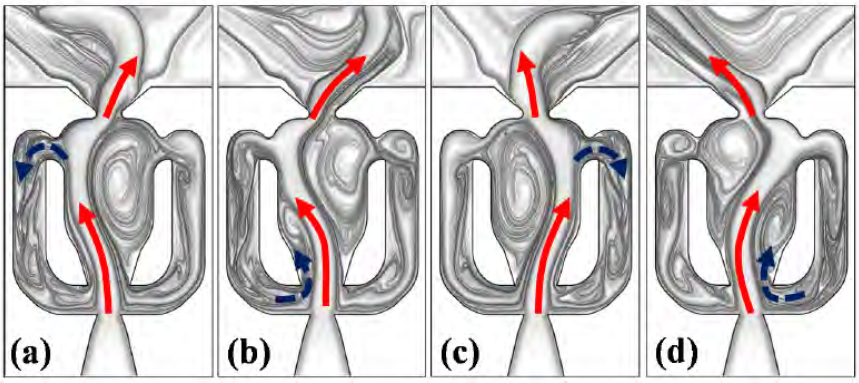


Figure 98. Fluidic oscillator sequence of switching [101]

frequency measurements were taken with an acoustic microphoneand displayed as a power spectrum for each flow rate. The dotted line in the frequency plot is overlaying the oscillator frequency with the other two bands above it representing harmonics.

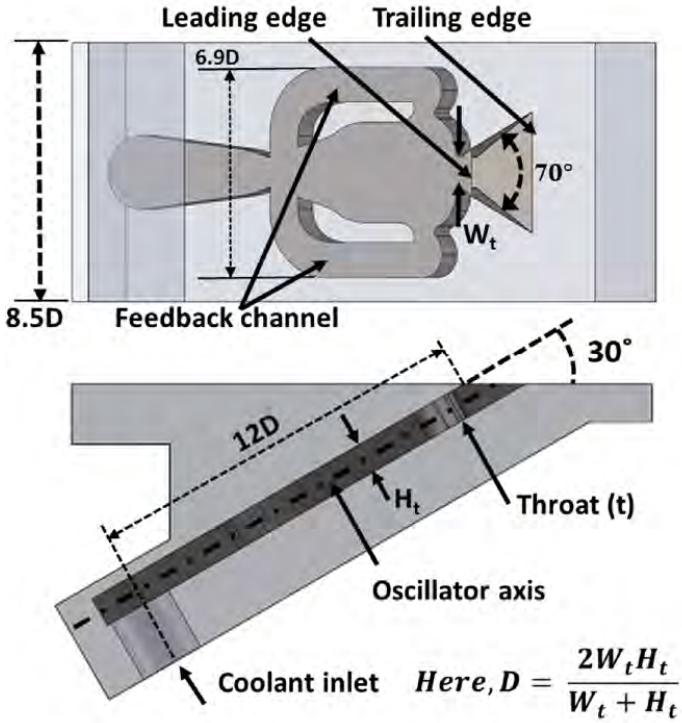


Figure 99. Fluidic oscillator schematic [101]

Researchers at NASA worked on linking fluidic oscillators in pairs to achieve in-phase and out-of-phase configurations as shown in Figure 101 [102]. The linkages

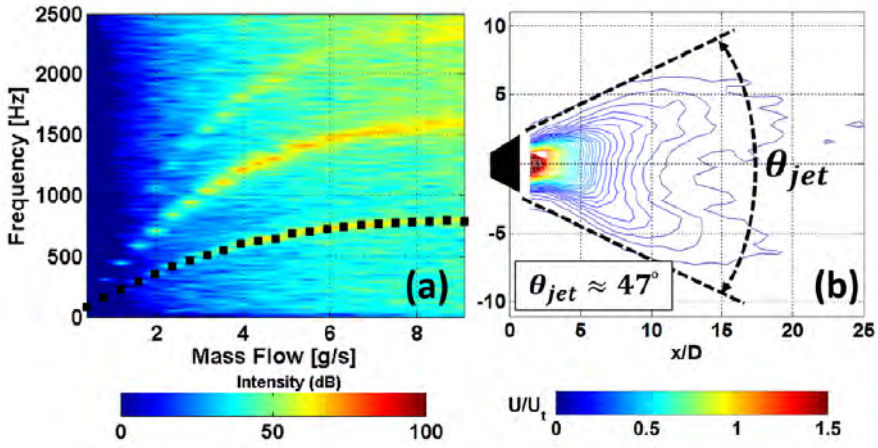


Figure 100. Fluidic oscillator frequency response to mass flow rate and a representative time-averaged spreading angle at 0.39 g/s [101]

between the oscillators were provided by connecting tubes that joined the feedback channels. Due to the orientation of the connecting tubes relative to the oscillation direction, this method of linkage could not used to connect a series of oscillators that sweep across a surface such as those in Figure 99. This study also showed that the oscillators (nozzle width = 19.05 mm) achieved a maximum oscillation frequency that asymptotically approached 200 Hz as the nozzle pressure ratio increased. Comparing this result to the microfluidic oscillators shows a relationship of oscillator scale to frequency.

While the size of the oscillator appears to be linked to the oscillation frequency, to the knowledge of the author there is no equation set that links the physical dimensions of the oscillator to the output oscillation frequency. AL-Asady and Razouqi [103] show calculations of the oscillation frequency by drawing similarity of the oscillator to an electrical circuit, however, these calculations still require knowledge of the pressure distribution inside the oscillator and are not based solely on geometry. At this time the determination of oscillation frequency is still found by experimental analysis.

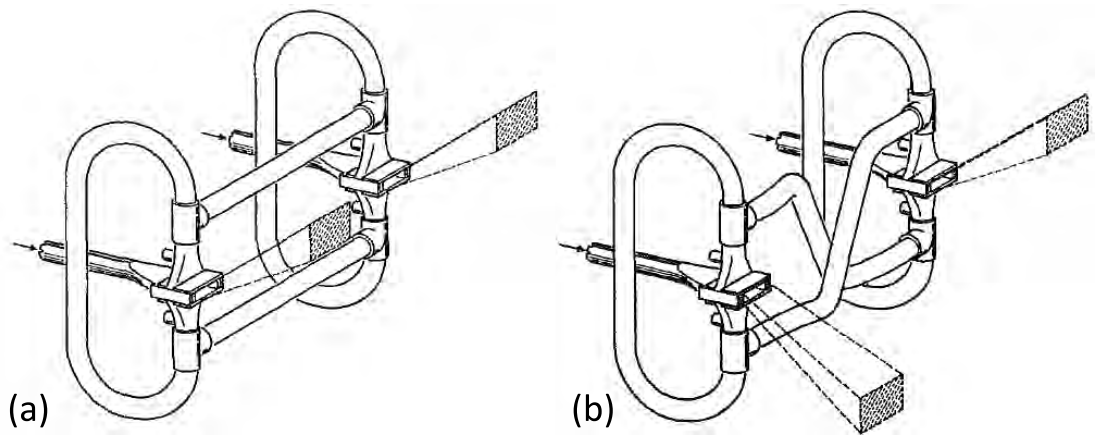


Figure 101. Linked fluidic oscillators for (a) in-phase jets, and (b) out-of-phase jets. Adapted from [102]

2.7 Heat Transfer

This section outlines the basic equations and concepts related to heat transfer within a turbine engine. All three heat transfer mechanisms; conduction, radiation, and convection, take place within the complicated thermal environment of an engine. The convection discussion also includes the equations of film-cooling as this process is of significant importance within the turbine stage.

2.7.1 Conduction.

Incropera et al. [104] describe conduction as "The transfer of energy from the more energetic to the less energetic particles of a substance due to interactions between the particles." Within a specific medium, higher temperatures are associated with higher molecular energy. Within a gas the energy transfer is the result of molecular collisions. In this exchange, higher energy molecules collide with lower energy molecules and transfer some of the energy to the lower energy molecule, raising their energy level. In a solid the higher levels of molecular vibration transfer some of that energy to an adjacent molecule which then begins to vibrate faster. The dissipation of energy

within the medium is the process of conduction. In both of these cases the energy is transferred without any bulk movement of the material.

Heat transfer processes are governed by rate equations that describe the amount of energy that is being transferred per unit time. For conduction this equation is given by Fourier's Law shown in Equation 54. This equation can be simplified for a one dimensional analysis by using Equation 55.

$$q'' = -k\nabla T = -k\Big(i\frac{\partial T}{\partial x} + j\frac{\partial T}{\partial y} + k\frac{\partial T}{\partial z}\Big) \tag{54}$$

$$q''_x = -k\frac{\partial T}{\partial x} \tag{55}$$

In the above equations, q'' is the heat flux, and has units of Watts per meter squared (W/m^2). Equation 55 has a subscript on q'' implying that it is the heat flux in the x direction only. The variable, k, is the thermal conductivity of the material and has units of (W/(m·K)). This value will vary by material and is generally also temperature dependent. The derivative, $\frac{\partial T}{\partial x}$ or $\frac{dT}{dx}$, is the temperature gradient in the specified direction, x in the case of the examples listed. For steady-state conditions with a linear temperature distribution the gradient can be reduced to:

$$\frac{dT}{dx} = \frac{T_2 - T_1}{L}, \tag{56}$$

where T_1 and T_2 are the temperatures at known locations in units of Kelvin, and L is the distance between the temperature measurement points in units of meters.

The transient heat diffusion equation, or heat equation, in a homogeneous material is defined by Equation 57. This equation describes the temperature distribution as a function of time. This equation also describes the relationship between the net rate of energy transfer into the material and the rate of change of the thermal energy stored in the material. [104]

$$\frac{\partial T}{\partial t} = \alpha \nabla^2 T \tag{57}$$

In the above equation, T is the temperature (K), t is the time (s), and α is the thermal diffusivity defined in Equation 58. In this equation, k is the thermal conductivity (W/(m·K)), ρ is the density (kg/m^3), and c_p is the specific heat (J/kg·K).

$$\alpha = \frac{k}{\rho c_p} \tag{58}$$

Experimental work conducted by Evans [12] used temperature measurements from two thermocouples embedded at different depths in a metal block to calculate the surface temperature and the heat flux at the surface. He assumed one-dimensional heat transfer, and applied the version of Fourier's Law shown in Equation 55 to find the heat flux between the thermocouples. For steady-state conditions, q''_x is constant which allows Equation 55 to be rearranged and integrated as shown in Equation 59.

$$\int q''_x dx = -\int k dT \tag{59}$$

Evans [12] used Equation 59, accounting for the variable nature of the thermal conductivity, k, with temperature, to arrive at the definition of heat flux given in Equation 69 which is useful when two temperature values, and the location of those measurements, are know. See Reference [12] for the derivation of this equation. The values of a_0 and a_1 are the y-intercept and slope, respectively, of the equation governing the linear variation of thermal conductivity with temperature for the test material. For Hastelloy-X®, the material used in the UCC, $a_0 = 3.7164$ and $a_1 = 0.0197$.

$$q''_x = \frac{\frac{a_1}{2}(T_1^2 - T_2^2) + a_0(T_1 - T_2)}{(x_2 - x_1)} \tag{60}$$

When the value of q''_x was known, Equation 61 could be used to find the value of C. Once q''_x and C were both known, the surface temperature could be found using Equation 62 and solving for T.

$$\frac{a_1 T_1^2}{2} + a_0 T_1 + q''_x x_1 - C = 0 \tag{61}$$

$$\frac{a_1 T^2}{2} + a_0 T - C = 0 \tag{62}$$

While the method described above allows for the calculation of the surface temperature and heat flux on a non-interference basis with the surface, there are difficulties associated with internal experimental measurements of metal components. The primary difficulty in this case is that the presence of the embedded thermocouple alters the heat transfer field. By drilling into the metal and inserting a thermocouple, a potential heat transfer path was cut. While the presence of the hole may not greatly impact the temperature measurement at that specific location, the presence of upstream holes may greatly influence the heat flux and temperature at downstream measurement locations.

Hilbert and Morris [105] showed though experimental 1-D and 2-D analysis that using a thermally conductive epoxy to fill around the thermocouple in the drill holes improved results for an inverse heat conduction problem like the one outlined above. They located conductive epoxies with thermal conductivities as high as 25 W/(m·K). While this value limits the type of metal it can be used in, there are materials such as stainless steel and Hastelloy-X® that have thermal conductivity values below that limit. The epoxy cure process has a significant impact on the thermal conductivity, and care must be taken to cure the epoxy correctly so the thermal conductivity matches the metal. In their experimental work, Hilbert and Morris used The Epoxy

Technology EK1000™ compound and 17-4 PH H1150 Steel. Following manufacturers recommendations they were able to match the thermal conductivity of 16.4 W/(m·K) for the metal with the epoxy. While the metal and epoxy had equal thermal conductivity, comparable specific heats, they differed greatly in density. From Equation 58 it can be seen that the metal and epoxy would thus have very different values of thermal diffusivity. They were unable to find any epoxy that matched the density of metal, and thus no epoxy that matched the metal thermal diffusivity. Their work showed that the inhomogeneity of α resulting from the use of the epoxy had a small effect on the measurement technique, but allowed for correct conduction through the material without the interference due to drill holes. They also found that this technique could be used with an embedded thermocouple grid around a turbine rotor casing that could be realistically installed in hardware.

2.7.2 Radiation.

Radiation is the emission of energy from matter. Energy emission from solids is the most common, but radiation can occur with liquids and gases. The energy transfer process in radiation requires changes in the electron configuration of the materials atoms. The resulting energy emission is transported in the form of electromagnetic waves. Unlike conduction and convection which require a material medium for energy transfer, radiation does not. In fact radiation is more efficient through a vacuum. [104]

Radiation emitted by a surface is measured in energy per unit area (W/m^2), and given the name "emissive power", E. The maximum amount of radiation that can be given off from a surface is determined by the Stefan-Boltzmann Law shown in Equation 63. In this equation, T_s is the surface temperature (K), and σ is the Stefan-Boltzmann constant (σ =5.67 $\times 10^{-8}$ W/(m^2·K^4)). E has a subscript of b indicating it is the upper bound of emissive power from an ideal radiator. [104]

$$E_b = \sigma T_s^4 \tag{63}$$

For real surfaces, an additional term, ϵ, is added to Equation 63 as shown in Equation 64. The term ϵ is referred to as the emissivity and has a value between 0 and 1. This value indicates how efficiently a material surface emits energy. An ideal emitter would have a value of 1, while an ideal insulator has a value of 0. [104]

$$E = \epsilon \sigma T_s^4 \tag{64}$$

A surface may also be incident to radiation coming from another source. The rate at which radiation is incident on a unit area of a surface is called the irradiation, G. A surface may absorb a portion or all of the incoming radiation thereby raising its thermal energy. The absorptivity, α, which also ranges from 0 to 1 determines the percentage of irradiation received by the surface. The material properties such as opacity and surface finish have a large effect on the amount of irradiation reflected, transmitted, or absorbed by the material. The absorptivity can also vary depending on the type of radiation received. Equation 65 provides the relationship for the amount of irradiation absorbed. [104]

$$G_{abs} = \alpha G \tag{65}$$

The net rate of heat transfer due to radiation from a surface is defined in Equation 66 in terms of energy per unit area of the surface (W/m^2). [104]

$$q''_{rad} = \epsilon E_b T_s - \alpha G \tag{66}$$

If the radiation of interest takes place between an object and an isothermal surface

that completely surrounds it, the equations can be reduced. For this case, Incropera et al. [104] show that $G = E_b T_{sur}$, where T_{sur} is the temperature of the isothermal surrounding surface. This substitution into the heat transfer equation is shown in Equation 67. For materials that have $\alpha = \epsilon$, or any surface inside an enclosure, the equation reduces to that shown in Equation 68. In this equation, $T_s > T_{sur}$ and q''_{rad} is still the radiation energy from the surface of the internal object.

$$q''_{rad} = \epsilon E_b T_s - \alpha E_b T_{sur} \tag{67}$$

$$q''_{rad} = \epsilon\sigma(T_s^4 - T_{sur}^4) \tag{68}$$

2.7.3 Convection and Film-Cooling.

The convective heat transfer mode includes two mechanisms; diffusion and bulk motion. The diffusion mechanism encompasses energy transfer due to molecular motion, while the bulk motion mechanism features a larger mass of molecules moving collectively. The collective superposition of the diffusion and bulk motion mechanisms is termed convection. The term advection is used to refer to the bulk motion alone. [104] Convection exists throughout the turbine engine, but specifically in the hot gas path. One of the primary areas where convection is prevalent is in application of film-cooling of engine components. Film-cooling of turbine components allows T_{t4} to exceed the turbine material operating limit by buffering hot free stream gases off the metal components with a thin film of coolant air ejected from discrete holes or slots in the surface. The relative position of components in a film cooled turbine vane are shown in Figure 102. In the figure, T_g is the free stream gas temperature, T_c is the coolant air temperature, and T_w is the turbine vane wall temperature. While this dependence on film-cooling has allowed for better engine performance through

increased thermal efficiency, any deviation from the optimal cooling effectiveness can result in failure of the turbine blade.

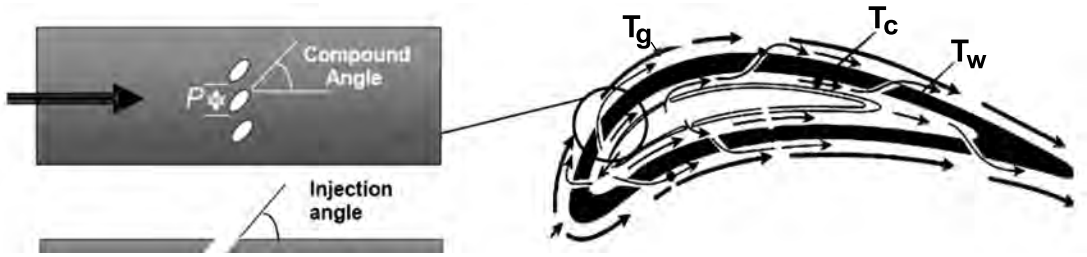
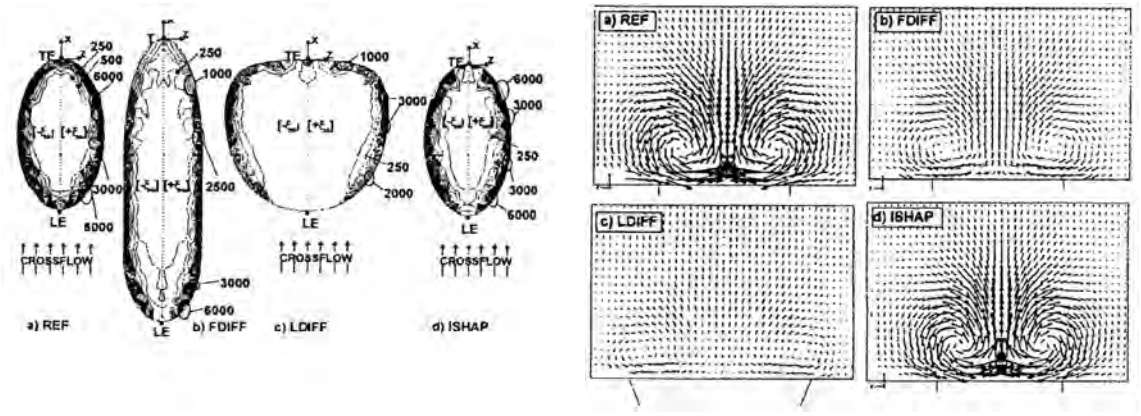


Figure 102. Diagram of a typical film-cooling configuration with hole detail [9]

The implementation of film-cooling is a delicate balancing act with the ultimate goal of reducing turbine airfoil surface temperatures to levels below their operating limit. In a traditional engine arrangement, cooling air for film-cooling is taken as bleed air from the high-pressure compressor. If too much coolant is removed the overall engine performance is degraded, however, if not enough is used then there is a limit on T_{T4max} or engine durability is reduced [9]. Additionally, adding discrete cooling holes that inject fluid into the boundary layer causes increased turbulence and enhanced mixing of the coolant with the fluid above the wall as shown in Figure 103. Depending on the cooling hole geometry, the vortical structures at the exit of the cooling holes can be strong and advect hot gases directly to the surface. The addition of turbulent structures and the increase in mixing at the surface results in an increase in the local convective heat transfer coefficient downstream of the cooling hole [9]. Smith et al. [106] found that the heat transfer coefficient with film-cooling, h_f, was 21% larger than h_0 without film-cooling. A determination must be made if adding a cooling hole in a particular location on the blade offers enough of a net reduction in the heat flux to the surface to offset the cost of adding a hole, the blade durability requirement, and the increase in heat transfer coefficient. For the same cooling hole inlet flow conditions, the magnitude of the secondary flow formation can be controlled through hole shaping.



(a) Vorticity at coolant hole exit plane

(b) Velocity vectors at $x/D = 2$

Figure 103. Coolant hole exit plane vorticity and corresponding velocity vectors highlighting secondary flows. REF=cylindrical, FDIFF=Forward Diffused, LDIFF=Laterally Diffused, ISHAP=Inlet Shaped. [107]

The equation defining convective heat flux without film-cooling on a per area basis, $q_0^{''}$, is given in Equation 69 [108]. Applying this equation to film-cooling becomes more complicated because there are three temperatures involved; the wall temperature, the coolant temperature, and the free stream gas temperature as shown in Figure 102. Bogard and Thole [9] suggest that the temperatures of interest are the wall temperature, T_w, and the adiabatic wall temperature, T_{aw}, which is the temperature of the fluid directly above the wall of an adiabatic surface. Plugging in the appropriate temperatures and accounting for the different heat transfer coefficient due to the presence of film-cooling, the heat flux with film-cooling, $q_f^{''}$, can be defined as shown in Equation 70. From this equation it can be seen that T_{aw} must be reduced sufficiently enough to overcome the increase in h_f compared to h_0 and achieve a net reduction in $q_f^{''}$ to keep T_w below its operating limit.

$$q_0^{''} = h_0(T_1 - T_2) \tag{69}$$

$$q_f^{''} = h_f(T_{aw} - T_w) \tag{70}$$

Since T_{aw} is one of the most important parameters in determining wall temperatures in film-cooling, many studies report the adiabatic wall temperature in nondimensional form, η, also called the adiabatic effectiveness, as shown in Equation 71. In this equation, T_∞ is the free stream temperature and $T_{c,exit}$ is the temperature of the coolant at the exit of the film hole. Greiner [109] defined a slightly different definition of η, shown in Equation 72, which replaced the free stream temperature with the recovery temperature, T_r, to account for viscous heating in the boundary layer resulting from high speed free stream flow.

$$\eta = \frac{T_\infty - T_{aw}}{T_\infty - T_{c,exit}} \tag{71}$$

$$\eta = \frac{T_r - T_{aw}}{T_r - T_{c,exit}} \tag{72}$$

where,

$$T_r = T_\infty + r\frac{U_\infty^2}{2c_p} \tag{73}$$

$$r = \frac{T_r - T_\infty}{T_t - T_\infty} \tag{74}$$

In Equation 73, U_∞ is the free stream fluid velocity, and in Equation 74, T_t is the total temperature of the flow that can be found using Equation 73 and setting $r = 1$. For laminar flows the recovery factor, r, can be simplified to $r = \sqrt{Pr}$.

It can be very difficult to physically measure T_{aw} and $T_{c,exit}$ due to the temperatures or sizes involved. If a measurement can be taken it can be difficult to get an accurate measurement where the measuring device does not impact the result. As an alternative to η, the nondimensional parameter, ϕ, called the overall effectiveness, is used as defined in Equation 75 [9]. This parameter uses the wall temperature and coolant temperature in the internal blade passages, $T_{c,i}$ rather than at the coolant hole exit. As with η, Greiner defined the variable in terms of the recovery temperature as

shown in Equation 76.

$$\phi = \frac{T_\infty - T_w}{T_\infty - T_{c,i}} \tag{75}$$

$$\phi = \frac{T_r - T_w}{T_r - T_{c,i}} \tag{76}$$

The ultimate goal of film-cooling is to keep T_w within the material operating limits by reducing the heat flux to the surface. The net heat flux reduction due to film-cooling, NHFR, is given in Equation 77 [9]. This value indicates if the film-cooling method is effective enough to warrant the costs of adding cooling.

$$NHFR = 1 - \frac{q_f^{''}}{q_0^{''}} = 1 - \frac{h_f(T_{aw} - T_w)}{h_0(T_\infty - T_w)} = 1 - \frac{h_f}{h_0}\left(1 - \frac{\eta}{\phi}\right) \tag{77}$$

A recent publication by Rutledge et al. [110] described a method of evaluating film-cooling performance with a difference in ϕ, called the $\Delta\phi$ method. There is a limitation of the NHFR equation shown above in that it does not account for the actual reduction in metal temperature. The $\Delta\phi$ method agrees with the NHFR in terms of whether a particular film-cooling scheme is beneficial or detrimental, but it additionally provides the temperature reduction that the film-cooling scheme provides. As discussed by Han et al. [111], a reduction in turbine blade temperature of only 30 K could result in as much as a doubling of the component life expectancy. For this reason, understanding the reduction in surface temperature by using a particular cooling scheme is vitally important. Equations 78 and 79 give the $\Delta\phi$ relationship.

$$\Delta\phi = \phi - \phi_0 \tag{78}$$

$$\Delta\phi = \frac{T_{s0} - T_s}{T_\infty - T_c} \tag{79}$$

In the above equations, ϕ_0 is the overall effectiveness without film-cooling, T_{s0} is the surface temperature without film-cooling, T_s is the surface temperature with film-cooling, T_∞ is the free stream temperature, and T_c is the coolant temperature. As an example if $\Delta\phi = 0.061$, using a notional value of $T_\infty - T_c = 1000$ K, then there was a decrease in surface temperature of 61 K with the addition of film-cooling.

The $\Delta\phi$ method can also be used to compare film-cooling schemes to each other. This comparison is made by subtracting the $\Delta\phi$ from one scheme from the other to produce a nondimensional difference in surface temperature between the schemes. Assuming the same free stream and coolant temperatures yields the relationship in Equation 80, where a and b denote the two cooling schemes.

$$\Delta\phi_a - \Delta\phi_b = \frac{T_{s,b} - T_{s,a}}{T_\infty - T_c} \tag{80}$$

2.7.3.1 Film-Cooling Flow Physics.

The film-cooling effectiveness of a given cooling scheme is highly dependent on the flow properties of the coolant film and the geometry of the hole exit. The blowing ratio, M, also referred to as the mass flux ratio, is an important parameter in determining the amount of coolant at the surface and is useful in comparing different cooling schemes. The definition of M is given in Equation 81;

$$M = \frac{\rho_c U_c}{\rho_\infty U_\infty}, \tag{81}$$

where ρ_c is the coolant density, ρ_∞ is the free stream density, U_c is the coolant velocity and U_∞ is the free stream velocity. This equation does have the limitation that it requires knowledge of the exact density and velocity at the hole exit for both the coolant and free stream fluid. Obtaining values for these parameters can be extremely difficult in a fluctuating flow field. Using the definition of mass flow rate

given in Equation 82, and substituting into Equation 81, the definition of M can be modified to make it easier to calculate experimentally.

$$\frac{\dot{m}}{A} = \rho U \tag{82}$$

$$M = \frac{\dot{m}_{c,total} A_{\infty}}{\dot{m}_{\infty} A_{c,total}} \tag{83}$$

In the above equations, $\dot{m}$ is the mass flow rate, A is the cross-sectional area of the coolant hole or channel, $\dot{m}_{c,total}$ is the total mass flow rate through all coolant holes or the mass flow rate into the coolant plenum assuming no pressure rise in the plenum, $A_{c,total}$ is the total area of all coolant holes, A_{∞} is the cross-sectional area of the free stream fluid inlet and $\dot{m}_{\infty}$ is the mass flow rate of the free stream fluid. The blowing ratio definition given in Equation 83 allows for the prior calculation of areas, and a measurement of flow rates during an experiment to determine the blowing ratio more easily.

The effect of blowing ratio on adiabatic effectiveness downstream of a film-cooling hole has been documented in many sources, with many of those sources referencing Baldauf et al. [112]. Figure 104 shows results obtained by Baldauf et al. for a cooling hole with a 30° incidence angle to the surface at eight blowing ratios. The small triangles downstream of each cooling hole show the location of the peak adiabatic effectiveness. From the figure it can be seen that as the blowing ratio was increased, the location of the peak effectiveness was moved further downstream. Additionally, the magnitude of the effectiveness, or the area of peak effectiveness, was reduced for higher blowing ratios. This trend was likely due to the tendency for coolant jets with higher blowing ratios to separate from the surface. In the cases with M=1.2 - 2.0, the separated jets reattached to some level further downstream in the region of higher effectiveness, but at the penalty of a reduced effectiveness level.

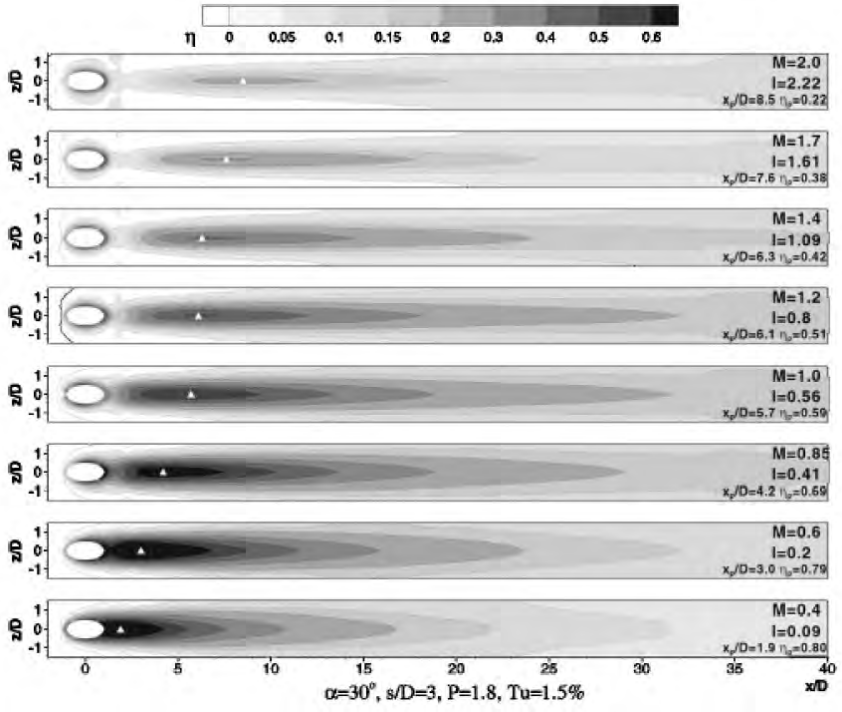


Figure 104. Spatial distribution of film-cooling effectiveness at various blowing ratios [112]

The angle of coolant injection can also have a large impact on the downstream effectiveness. An additional study performed by Baldauf et al. [112] compared the effectiveness results for coolant injected at a 30° incidence angle with that of coolant injected normal to the surface at four blowing ratios. The results of this study are shown in Figure 105. The angled holes achieved a higher downstream adiabatic effectiveness at all blowing ratios. This results is due to coolant from the normal holes separating from the wall and resulting in minimal coverage over the downstream wall.

The momentum flux, I, is an important parameter in determining whether a coolant jet will separate from the wall. This value is a ratio of the coolant momentum to the free stream momentum as defined in Equation 84.

$$I = \frac{\rho_c U_c^2}{\rho_\infty U_\infty^2} \tag{84}$$

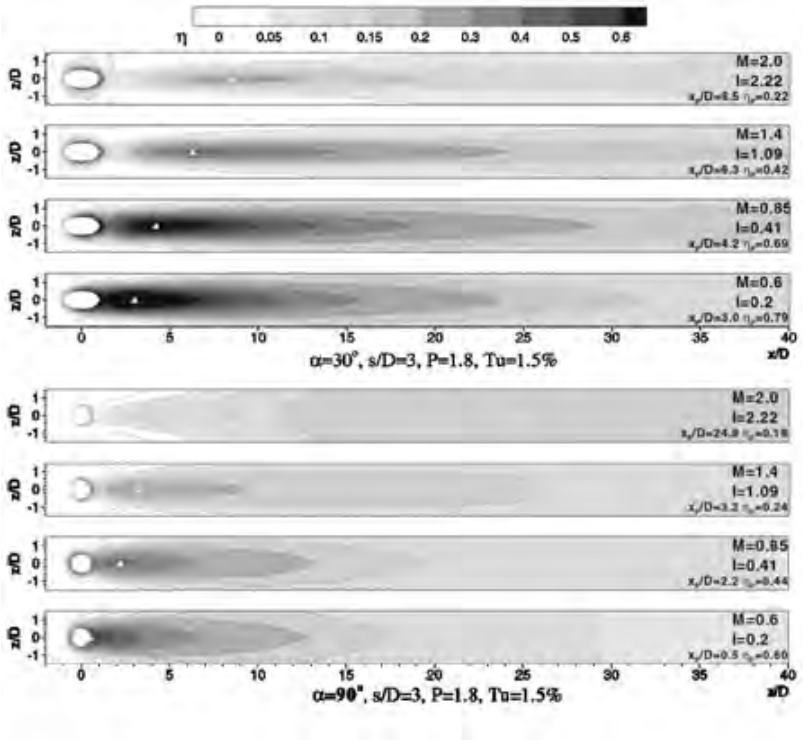


Figure 105. Effect of injection angle on film-cooling effectiveness [112]

The determination of whether separation will occur is based on how forcefully the coolant ejects from the coolant hole relative to how forcefully the free stream flow can push the coolant jet downstream and turn it back into the wall. While this result is also dependent on geometry, in general a coolant jet will separate for $I > 0.8$, remain attached for $I < 0.4$ and initially separate then reattach downstream for $0.4 < I < 0.8$ [113]. Figure 106 from Thole et al. [114] shows thermal profiles along the centerline of a coolant hole for each of the above mentioned situations. In the three parts of the figure, the coolant remained attached in (a), the coolant detached then reattached in (b), and fully separated from the wall in (c). The contours are colored by values of θ, the normalized temperature, as defined by Equation 85.

$$\theta = \frac{(T_\infty - T)}{(T_\infty - T_c)} \tag{85}$$

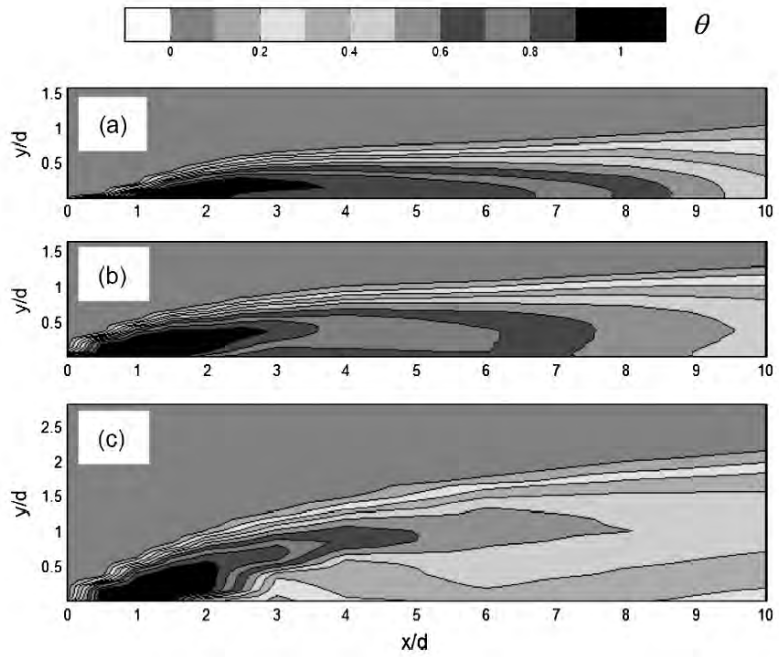


Figure 106. Thermal profiles along coolant hole centerline for (a) attached, (b) detached then reattached and (c) fully separated coolant flow [114]

2.8 Secondary Combustion in Cooling Films

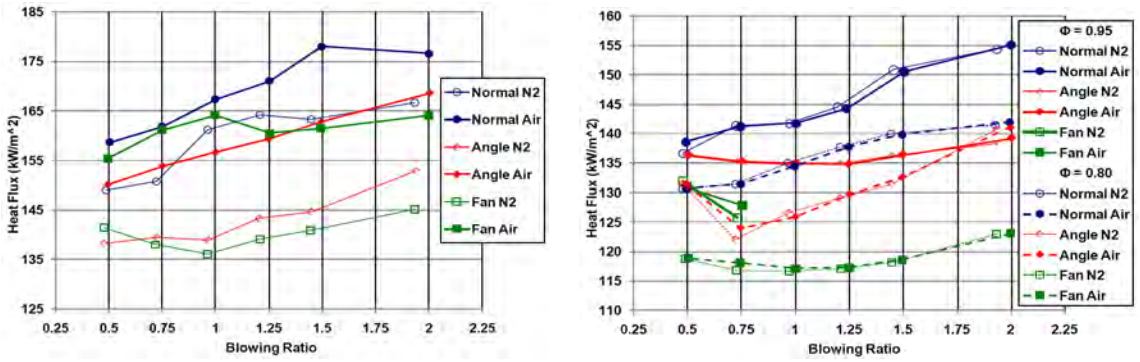
Applying film-cooling in regions downstream of fuel rich combustion further complicates the film-cooling process. During fuel rich combustion there is insufficient oxidizer to fully combust all of the fuel in the flow. When the unreacted fuel reaches the oxygen-rich cooling films a secondary reaction can occur. This secondary reaction is a combustion process occurring directly on the surface of an engine component that was intended to be cooled. In this situation the coolant is no longer available to cool the metallic surface, and instead has allowed heat release directly on the surface. The magnitude of the impact of the secondary reaction is measured as the heat flux augmentation, σ, and is defined in Equation 86. This relationship represents a ratio of the heat flux without secondary reaction, $q_f^{''}$, and the heat flux with secondary reactions, $q_r^{''}$.

$$\sigma = 1 - \frac{q''_f}{q''_r} \tag{86}$$

2.8.1 Identification of Secondary Combustion.

The heat flux with and without secondary reactions can be found experimentally using air and nitrogen as the coolant gases for identical test conditions. Nitrogen being an inert gas will provide cooling, but lacks an oxidizer to produce secondary reactions. Several studies, such as those by Anderson et al. [115], Evans [12], Polanka et al. [116], Lin et al. [117], Katta et al. [118], and Pohl et al. [119], have been conducted to study and quantify the magnitude of the heat flux augmentation due to these reactions. The general consensus across all of these studies was that the heat flux due to secondary reactions increased with increasing blowing ratio and that angled holes produced a higher heat flux augmentation than normal holes. Evans [12], Polanka [116], and Anderson[115] went on to show that fan-shaped angled holes had an even higher augmentation than cylindrical angled holes, or normal holes. These results are shown in Figure 107a. The outcome of these studies are not surprising. For an equivalent blowing ratio the fluid from a normal hole will separate farther off the wall than for an angled hole, and much farther than a fan-shaped hole. If a secondary reaction occurred farther off the surface, less heat was conducted to the surface due to a secondary reaction. Shaped holes are generally very effective at cooling a surface under non-reactive conditions because they slow the coolant at the exit of the hole to reduce coolant penetration and help ensure the coolant remains attached to the surface across a range of blowing ratios. It is this same characteristic that makes it the worst offender for secondary reactions as combustion now occurs directly on the blade surface. The data in Figure 107b confirmed that secondary

reactions only occur in fuel rich combustion; below a free stream equivalence ratio of 1.0 no secondary reactions occurred. This result is shown by the air and nitrogen coolant producing nearly identical heat flux measurements across all tested blowing ratios.



(a) $\Phi = 1.5$ (b) $\Phi = 0.8$ and $\Phi = 0.95$

Figure 107. Graphical relationship of blowing ratio to heat flux for three equivalence ratios at $x/D = 20$ [116]

2.8.2 Secondary Combustion Mitigation.

The previous investigations all focused on examining the conditions where secondary reactions could take place and characterizing the heat flux associated with varying film-cooling hole geometries. Once the conditions surrounding the formation of secondary reactions were understood and quantified, the research in this area was focused on mitigating these reactions. Bohan et al. [120], and DeLallo et al. [121] focused on two row cooling schemes that used a slot or offset normal hole row upstream of a row of fan-shaped hole, a trench, or a ramp. These hole geometries are detailed in Figure 108.

Using cooling schemes in series, it was thought that the upstream row would initiate and complete a secondary reaction and thus allow the downstream row to provide cooling as intended. Both of these studies found that the augmentation was lower when the slot was used in the upstream position. These findings are consistent

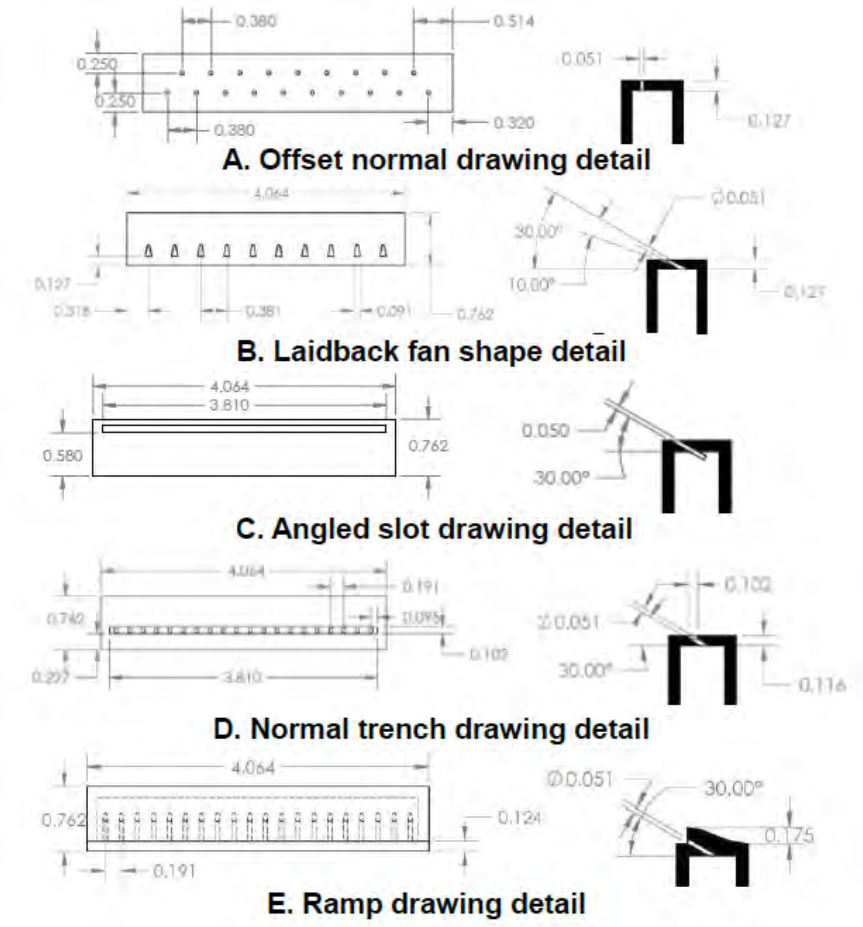


Figure 108. Detailed cooling hole geometry used by Bohan et al. [120] and DeLallo et al. [121]

with Lin et al. [117] who showed that separated jets, such as the offset normal holes, caused an increase in fuel near the wall by sweeping the fuel towards the wall and under the jet as a result of secondary flows and turbulent motion. A slot does not have the same secondary flow pattern and does not move more fuel to the wall to perpetuate a reaction. The slot also provides a higher volume of fluid for the same blowing ratio and thus provided more oxygen to complete the secondary reactions. Of the hole configurations tested in the downstream position, the trench offered the lowest augmentation, with a near zero value when behind the slot. Fluid exiting a trench has a similar flow pattern to a slot and thus does not produce the vortical

structures that can sweep hot gases or fuel to the surface.

Shewhart et al. [122] [123] tested mitigation schemes using 5 rows of cooling holes spaced closely together. Shewhart et al. tested the three hole pattern in the top row of Figure 109, where Lynch et al. tested the same three cooling schemes as Shewhart et al. plus the additional five shown in Figure 109. The eight schemes tested by Lynch were divided into two categories; enhanced mixing schemes, and well attached schemes. The goal of the mixing schemes were to initiate a reaction quickly, with a shorter flame length, and in a predictable manner. The goal of the well attached schemes were to produce a buffering film layer to keep the hot gases and fuel away from the wall.

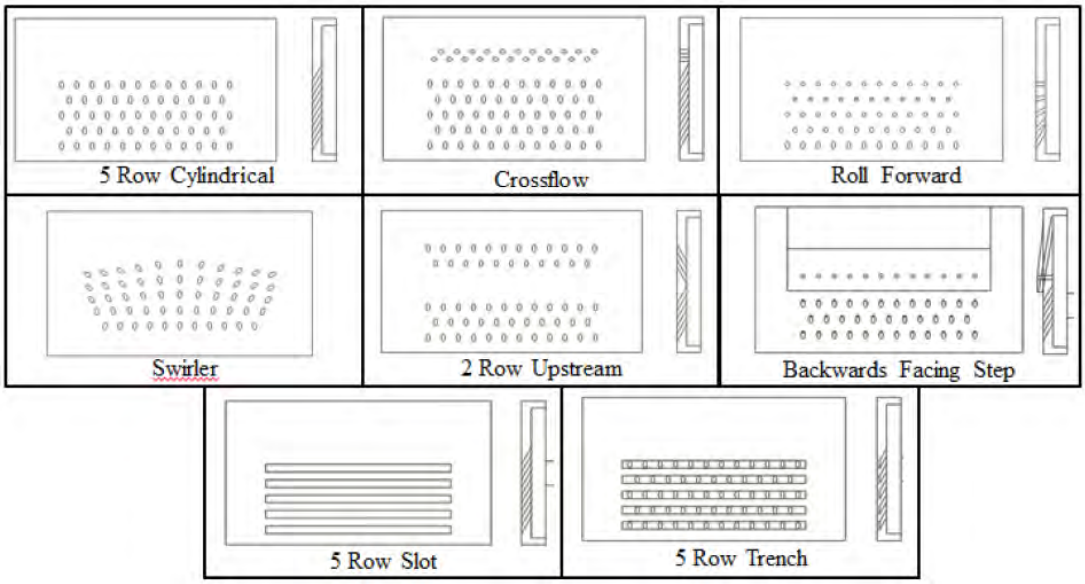


Figure 109. Hole patterns used by Shewhart et al. [122] [123]. Free stream flow was from top to bottom.

In the enhanced mixing schemes category, Shewhart et al. [123] found that there were schemes that offered a net heat flux reduction for a blowing ratio of one or greater. These beneficial schemes were those that minimized the disturbance to the upstream air and then had several rows of angled holes downstream. Two of their

conditions tested did not offer an improvement, the "swirler" and the "2 row upstream", both of which had counter-flow holes that produced significant turbulent structures as it convected downstream. All of the protective schemes produced a positive net heat flux reduction for blowing ratios of 1.5 and greater, with two of the three schemes providing a reduction at a blowing ratio of one. The magnitude of the heat flux reduction with the protective schemes was significantly greater than the reduction offered by any of the mixing schemes.

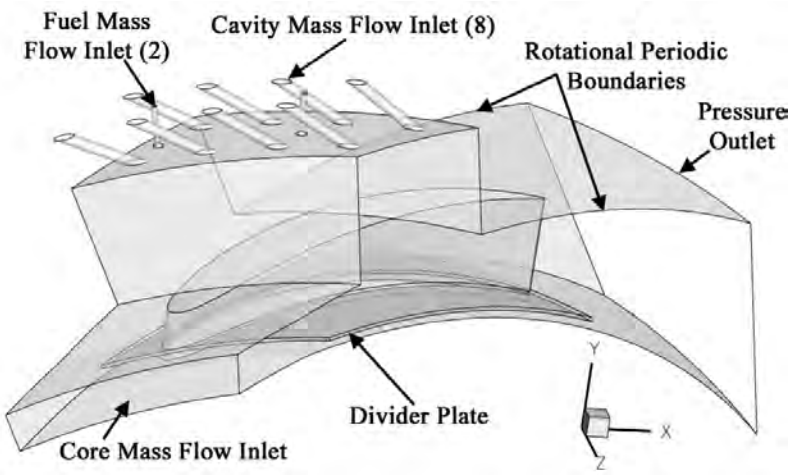
Across the four studies that investigated secondary mitigation techniques, the results all showed that protective schemes in series work better than schemes designed to force combustion of the fuel near the wall. The turbulent vortical structures resulting from the forced combustion schemes had negative impacts on the ability of the downstream rows to cool effectively. Upstream schemes that formed thick protective fluid layers, and minimized the production of vortices, allowed downstream schemes to function as intended with little or no interference. These conclusions show promise that film-cooling will be possible in the complex fuel-rich environment of the UCC cavity and hybrid vane surface.

2.8.3 Cooling a Hybrid Vane.

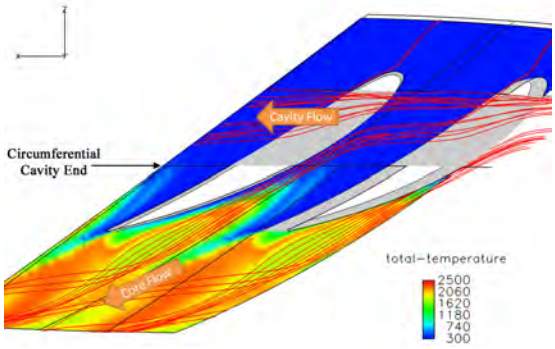
The hybrid guide vanes located below the UCC circumferential cavity are exposed to high temperatures and unreacted fuel species primarily on the suction surface of the vane. Several previous studies by Bohan [6], Parks [124], and Johnson [73] aimed at cooling the ID endwall in the region of the hybrid vane and the vane itself.

Bohan [6] found that the hot fluid exiting the circumferential cavity had sufficient momentum to span the entire vane passage and impinge on the ID endwall causes very high surface temperatures. In an attempt to mitigate this effect he investigated a divider plate that was slightly elevated off the ID wall. The plate allowed cool core

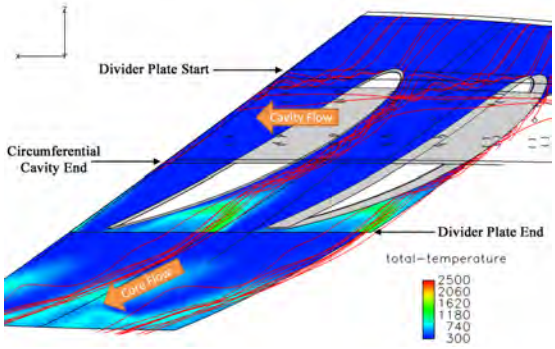
flow to pass under the plate and cool it, while the top of the plate was exposed to the extreme temperatures from the impinging hot gases. A diagram of the geometry and resulting temperature distribution is shown in Figure 110. It was found that this plate was effective at reducing the endwall temperature and trapping the horseshoe vortex below the plate. There were vortices generated by the leading edge of the plate, however, that interacted with the vortex exiting the circumferential cavity and served to pull hot gases from the suction surface of the vane.



(a) Domain with divider plate



(b) Without divider plate



(c) With divider plate

Figure 110. Plan view of UCC hybrid vane section with and without a core flow divider plate. Contours are colored by temperature (K) [6]

In addition to the large temperature reduction, Bohan [6] also found that the plate reduced the static pressure loss by 2% and the total pressure loss by 1%, resulting in a

UCC system pressure loss of 9.6% and 8.3% for static and total pressure, respectively. This reduction in pressure loss could be attributed to better management of secondary flows with the addition of the plate. The main drawback of this design is that the divider plate caused an increase in the pattern factor at the turbine entrance from 0.34 to 0.44 due to a larger gradient between the peak temperature and the now much cooler ID endwall.

Parks [124] developed a "tiger claw" variant of the hybrid vane that featured three backward facing steps cut into the suction surface of the vane as ahown in Figure 111. Computational modeling by Johnson [73] on this design showed that the tiger claw routed the hot gases from the UCC cavity streamwise rather than allowing them to traverse the vane span and impact the ID endwall prior to turning in the streamwise direction. While this design protected the endwall, the resulting pattern factor at the turbine inlet plane was found to be 0.85, well above the desired value, and the value achieved by Bohan's [6] divider plate. This design did show an ability to control the flow migration from the UCC cavity and with further optimization it could potentially achieve a desirable temperature profile downstream.



Figure 111. The tiger claw hybrid vane variant [124]

In addition to his work with the tiger claw vane, Johnson [73] also numerically investigated film-cooling the hybrid vane using a normal hole and contoured trench scheme with an adiabatic model. The addition of the cooling films reduced the total pressure loss of his system from 10.5% to an average of 9.2% for blowing ratios of 1.0,

1.5, and 2.0. The cooling scheme had a negative impact on the downstream patter factor, however, achieving an average value of 0.78.

The flow environment surrounding the hybrid vane makes it difficult to cool. As reported by Wurm et al. [125], swirling flow can hinder film coolant penetration and it can take up to two rows of cooling holes to return to normal coolant flow. A similar finding by Marosky et al. [126] showed that swirl present in the core flow can create a suction effect that can pull coolant from the vane surface. In both cases, swirling flow can lead to strong fluctuations in the amount of coolant provided to the surface and thus lead to significantly degraded cooling performance. As shown in Figure 112, coolant was entrained by the passage vortices and the vortex exiting the UCC cavity caused by the shear layer at the core/cavity interaction layer. This entrainment caused a significant reduction in the surface area that was cooled.

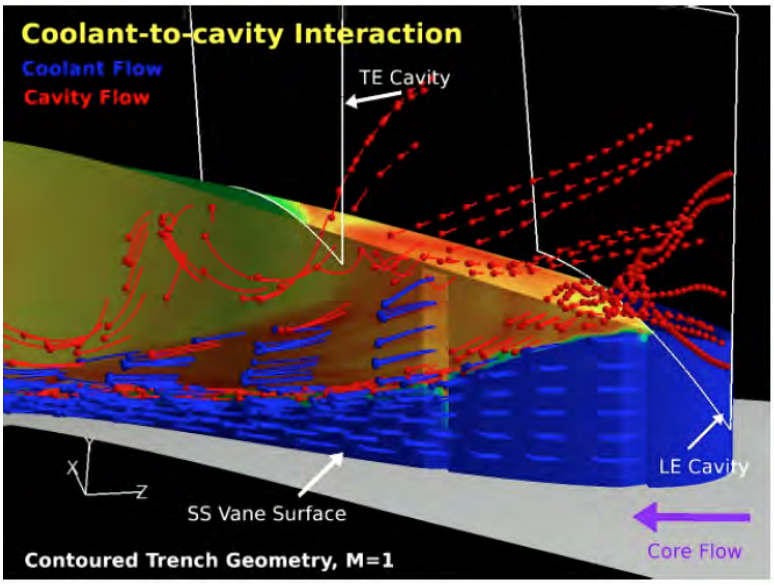


Figure 112. Interaction of hybrid guide vane film-cooling flow with UCC cavity flow [73]

2.9 Turbomachinery

Turbomachinery is a mechanical device used to exchange energy between a working fluid and rotating components. Both a compressor and a turbine are examples of turbomachinery. A turbine converts flow energy into shaft work, while a compressor converts shaft work back into flow energy. Both of these devices include axial and radial varieties with examples shown in Figure 113a and 113b. While the fluid flow paths are different between the axial and radial variants, both varieties share a common purpose. A compressor and turbine used in small scale engines look very similar with the primary differences existing in the blade angles.



(a) Axial variant (b) Radial variant

Figure 113. Comparison of typical engine compressor/turbine types [127]

In the axial device the working fluid flows parallel to the axis of rotation and interacts with the blades similar to the way an airfoil interacts with freestream flow. In the case of a turbine, however, the "lift" comes in the form of a rotational torque. For a compressor, an applied torque generates "lift" and pulls air through the device. The axial compressor and turbine usually requires multiple stages with alternating rows of rotating blades and stationary vanes.

The radial inflow turbine is driven by the working fluid entering from the outside diameter with some tangential velocity component and flowing radially inward. As the

working fluid flows through the vanes, the direction is changed from radially inward to an exhaust direction roughly parallel with the axis of rotation. The flow path is reversed for a radial compressor, with torque being an input rather than output. The radial varieties are generally less complex and more efficient than the axial turbine at lower flow rates and power scales, however, they are limited on the maximum usable size. Taking the two devices shown in Figure 113 to be turbines, they are classified as impulse turbines since they change the direction of flow of the working fluid. While there is also a change in direction if the working fluid in axial and radial compressors, they are not referred to as impulse compressors.

The following sections provide the basic equations needed to define the performance and inlet/exit flow conditions in a radial compressor and an axial turbine like those used in small scale turbojets.

2.9.1 Radial Compressors.

Figure 114 shows the arrangement of components within a radial compressor. In the cross sectional view, the flow enters from left to right between r_{1t} and r_{1h} at Station 1 and enters the rotor vane passages. Flow exits the rotor at Station 2 through a cylindrical passage at a radius of r_2 and a width of b. The flow then passes through diffuser vanes and into a collector scroll or annulus at Station 3.

The velocity triangles describing the fluid flow at the rotor entrance (Station1) and rotor exit (Station 2) are shown in Figure 115. The inlet velocity (u_1) is assumed to be uniform and constant across the inlet face. The relative flow angle (β) varies between hub and tip. The relative velocity (V_{iR}) at each station is related to the relative flow angle and the rotor velocity (U) at that radial position. The absolute flow angle (α) is related to the absolute velocity (V) and the components of velocity (w and v) by trigonometric relationships. The radial component of velocity (w_2)

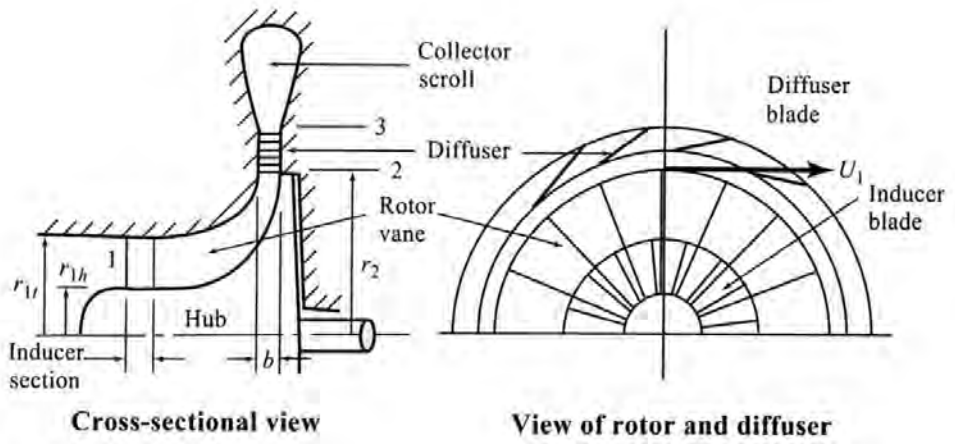


Figure 114. Radial compressor component diagram [14]

is approximately equal to u_1 and the tangential component of velocity is typically around 90% of the rotor velocity (U_t). Unless otherwise specified, the subscripts in this section reference compressor station numbers and not engine station numbers.

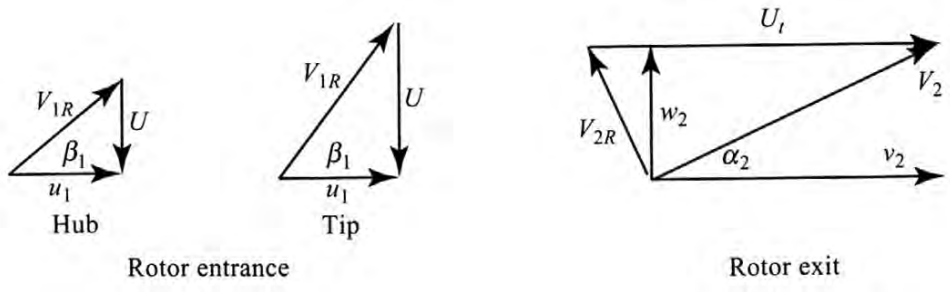


Figure 115. Radial compressor velocity triangles [14]

The following set of equations are taken from Mattingly [14] and use the velocity relationships from Figure 115 and basic freestream conditions at the rotor inlet to calculate a number of compressor performance properties. If specific velocity component values are needed, the reader is referred to p.600-607 in [14]. Within any turbomachine there are inefficiencies that arise in the transfer of energy between the mechanical components and the fluid. The follow equations take these losses in efficiency into account.

Ideally the fluid exiting the rotor at Station 2 would have a tangential component of velocity (v_2) equal to the rotor speed at the tip (U_t). These two velocities do not match in an actual compressor due to a slip between the fluid and the rotor. The ratio between these velocities is called the slip factor (ε) and is given in Equation 87. The value of the slip factor is related to the number of vanes on the rotor. When more vanes are present the slip factor approaches 1, however, frictional losses are increased. Thus a balance must be made between the number of vanes to achieve a high slip factor, while keeping friction losses low, typically around $\varepsilon = 0.9$. The relationship between slip factor and the number of vanes (n) is also shown in second relationship of Equation 87.

$$\varepsilon = \frac{v_2}{U_t} = 1 - \frac{2}{n} \tag{87}$$

The temperature rise across the compressor is given by Equation 88 in terms of the slip factor, rotor tip speed, and specific heat of air (c_p = 1,004 J/(kg·K)). This relationship can be applied to define the compressor temperature ratio (τ_c) as shown in Equation 89.

$$T_{t3} - T_{t1} = \frac{\varepsilon U_t^2}{c_p} \tag{88}$$

$$\tau_c = \frac{T_{t3}}{T_{t1}} = 1 + \frac{\varepsilon U_t^2}{T_{t1} c_p} \tag{89}$$

The pressure ratio across the compressor is given by Equation 90 in terms of the polytropic efficiency (e_c), and Equation 91 in terms of the more common adiabatic efficiency (η_c). The ratio of specific heats (γ) has a value of 1.4 for air below combustion temperatures. Polytropic efficiency is the "ratio of the ideal work per unit mass to the actual work per unit mass for a differential pressure change" [14]. The adiabatic efficiency is the "ratio of the actual energy output to the theoretical isentropic output for the same input total state and same exit total pressure" [14].

$$\pi_c = \frac{P_{t3}}{P_{t1}} = \left(1 + \frac{\varepsilon U_t^2}{c_p T_{t1}}\right)^{\gamma e_c/(\gamma-1)} \tag{90}$$

$$\pi_c = \frac{P_{t3}}{P_{t1}} = \left(1 + \frac{\eta_c \varepsilon U_t^2}{c_p T_{t1}}\right)^{\gamma/(\gamma-1)} \tag{91}$$

The rate of rotation of the rotor (N) in revolutions per minute (RPMs) is a function of the rotor tip speed and geometrical relations as shown in Equation 92.

$$N = \frac{60 U_t}{\pi d_2} \tag{92}$$

If there is no build up of air or bleed from the compressor, the mass flow rate in the compressor can be found at any of the compressor stations. Equation 93 gives the generic relationship for the mass flow rate at Station i. In this equation A is the area, R is the gas constant defined in Equation 94, and M is the Mach number.

$$\dot{m}_i = \frac{P_{ti} A_i}{\sqrt{T_{ti}}} \sqrt{\frac{\gamma_i}{R_i}} M_i \left(1 + \frac{\gamma_i - 1}{2} M_i^2\right)^{-\frac{(\gamma_i+1)}{2(\gamma_i-1)}} \tag{93}$$

$$R_i = \frac{\gamma_i - 1}{\gamma_i} c_p \tag{94}$$

The mass flow rate can be found more simply using the relationship in Equation 95, where $R = 287$ J/(kg·K) and $\gamma = 1.4$.

$$\dot{m}_{air} = \frac{P_{t3}}{R T_{t3}} A_3 \sqrt{\gamma R T_{T3}} \tag{95}$$

Finally, the efficiency of the compressor can be found using Equation 96. The efficiency could also be solved using Equation 91 if P_{t3} and P_{t1} are experimentally measured values.

$$\eta_c = \frac{(\pi_c)^{\frac{\gamma}{(\gamma-1)}} - 1}{\tau_c - 1} \tag{96}$$

2.9.2 Axial Turbines.

A cross section, blade diagram, and velocity triangles for an axial turbine is shown in Figure 116. Air flow is traveling from left to right in all sections of the figure. For reference, a stage consists of a stator and a rotor, where the stator vanes are stationary and the rotor blades are rotating at a rate of ω. The station numbers for the turbine stage are also shown in the figure below. Multiple stages can be analyzed by conducting the analysis described below in series where the output of one stage is the inlet of the next. Like the compressor, the subscript R stands for "relative" as observed by the rotor.

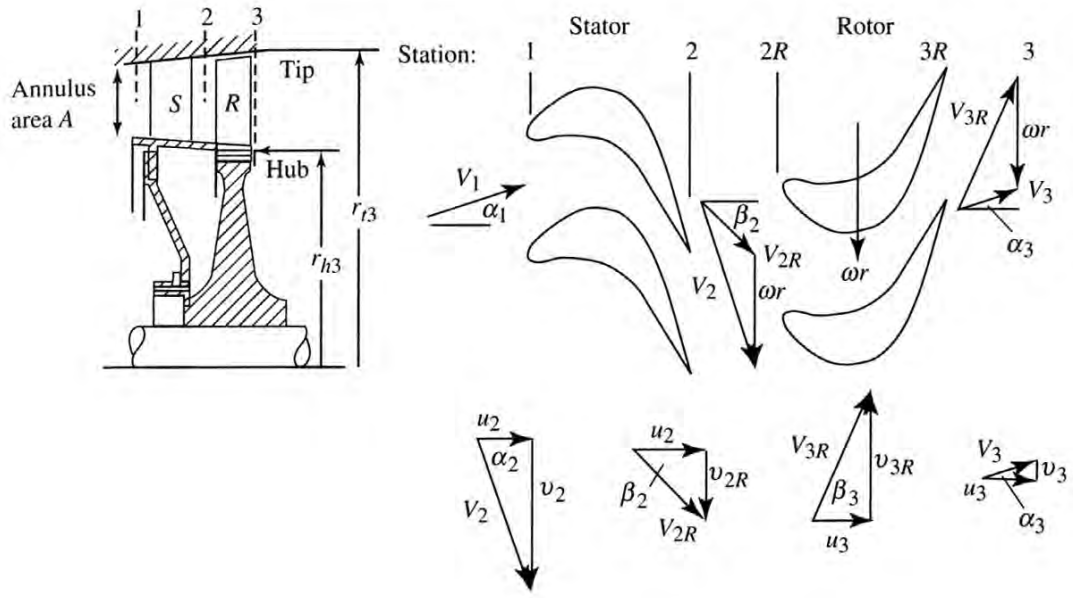


Figure 116. Axial flow turbine stage diagram and velocity triangles [14]

The following set of equations are taken from Mattingly [14] for consistency in nomenclature, and use the velocity relationships from Figure 116 and basic freestream conditions at the turbine stage inlet to calculate a number of turbine performance properties. If specific velocity component values are needed, the reader is referred to p.607-634 in Mattingly [14] or Chapters 5, 6, and 7 in Aungier [128]. Within

any turbomachine there are inefficiencies that arise in the transfer of energy between the mechanical components and the fluid. The follow equations take these losses in efficiency into account. Unless otherwise specified, the subscripts in this section reference turbine stage station numbers and not engine station numbers.

The temperature ratio across the turbine stage is defined in Equation 97. The ratio can be calculated directly from measured values of temperature, or by using the rotor velocity ($U = \omega r_{mean}$) and the stage loading coefficient (ψ) defined in Equation 102.

$$\tau_s = \frac{T_{t3}}{T_{t1}} = 1 - \psi \frac{(\omega r)^2}{T_{t1} c_p} \tag{97}$$

The stage pressure ratio can be found directly from experimental measurements or by using the temperature ratio and the polytropic efficiency of the turbine to calculate the value. These relationships are shown in Equations 98.

$$\pi_s = \frac{P_{t3}}{P_{t1}} = \left(\frac{T_{t3}}{T_{t1}}\right)^{\gamma/[(\gamma-1)e_t]} = \tau_s^{\gamma/[(\gamma-1)e_t]} \tag{98}$$

The mass flow rate through the turbine can be found by adding the mass flow rate of air through the compressor (Equation 95) to the mass flow rate of fuel into the combustor. The mass flow rate of fuel can be calculated using Equation 99 with the total mass flow rate through the turbine expressed in Equation 100. In Equation 99, T_B is the temperature at the combustor exit, T_C is the compressor exit temperature, and Q is the heat value of the fuel.

$$\dot{m}_{fuel} = \frac{\dot{m}_{air} c_p (T_B - T_C)}{Q} \tag{99}$$

$$\dot{m}_{total} = \dot{m}_{air} + \dot{m}_{fuel} \tag{100}$$

The adiabatic efficiency for the stage can be calculated using Equation 101. Due

to the elevated temperature in the turbine section, γ typically has a value around 1.28.

$$\eta_s = \frac{1 - \tau_s}{1 - (\pi_s)^{\frac{(\gamma-1)}{\gamma}}} \tag{101}$$

The stage loading coefficient is a ratio of the work performed by the stage per unit mass to the rotor speed squared. Using the assumption that the fluid in the turbine is calorically perfect the flow coefficient can be defined by Equation 102. A typical value for the stage loading coefficient in a modern high-pressure turbine ranges from 1.3-2.2 [14].

$$\psi = \frac{c_p \Delta T_t}{(\omega r_{mean})^2} = \frac{c_p \Delta T_t}{U^2} \tag{102}$$

The flow coefficient (Φ) is the ratio of the axial velocity entering the turbine rotor and the rotor speed as shown in Equation 103. For a typical modern high-pressure turbine this value ranges from 0.5-1.1 [14].

$$\Phi = \frac{u_2}{\omega r_{mean}} = \frac{u_2}{U} \tag{103}$$

Finally, the degree of reaction of the turbine ($^\circ R_t$) given in Equation 104 is the ratio of the static enthalpy drop in the rotor to the drop in total enthalpy across the rotor and stator. For a calorically perfect gas the degree of reaction can be defined as shown in Equation 105.

$$^\circ R_t = \frac{h_2 - h_3}{h_{t1} - h_{t3}} \tag{104}$$

$$^\circ R_t = \frac{T_2 - T_3}{T_{t1} - T_{t3}} \tag{105}$$

In the special case where there is zero exit swirl leaving the turbine, the degree of

reaction can be defined as shown in Equation 106. The case of zero exit swirl (α_3=0 and v_3=0) is desirable to reduce engine leaving losses and ensure the flow through the nozzle is purely axial to achieve the greatest thrust.

$$^{\circ}R_t = 1 - \frac{v_2}{2\omega r_{mean}} = 1 - \frac{\psi}{2} \tag{106}$$

Turbine vanes are typically highly cambered airfoils that can be loaded forward or aft on the vane. [128] The pressure distribution on a turbine vane is generically represented by the plot shown in Figure 117. When air is moving over the airfoil the highest pressure is located at the leading edge stagnation zone, with a slightly reduced pressure located on the lower surface (pressure side) of the airfoil. The upper surface of the airfoil experiences a much greater pressure reduction due to the fluid accelerating over that region, but as the passage between the vanes contracts due to the nature of the geometry, the fluid from approximately mid-chord to the trailing edge acts like a converging-diverging nozzle. The imbalance of pressure between the top and bottom surfaces causes a lifting force. In the case of a turbine vane that lifting force is transfered to the engine case while the vane stays stationary. [129]

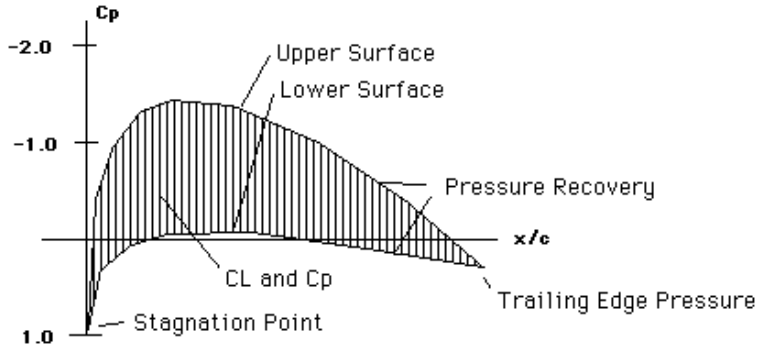


Figure 117. Airfoil pressure distribution [93]

While Figure 117 shows a typical pressure distribution around an airfoil, a turbine vane cascade also behaves as an array of nozzles as fluid passes through the vane

passage throat. Figure 118 shows streamlines through a converging-diverging nozzle as well as a plot of the pressure distribution along the axial length of the nozzle.

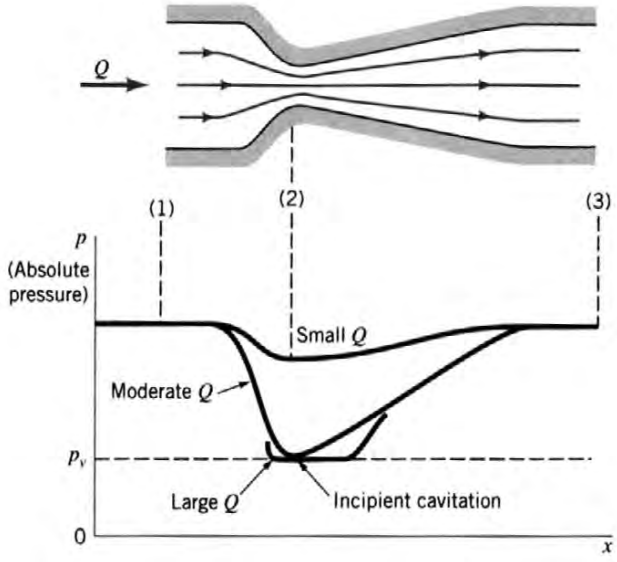


Figure 118. Streamlines in a nozzle with pressure distribution plot. $Q = AV$ **[130]**

2.10 Numerical Analysis

The equations governing the motion of fluids is generally well understood, yet applying these equations to any detailed flow geometry can be difficult. To fully define the flow field of a given geometry, the geometry must be divided into small pieces and the equations of motion solved within each of those sections. This process greatly increases the number of calculations involved, even to solve a relatively simple geometry. Computers are exceptionally good at performing large numbers of repetitive calculations, making them suitable to solve the equations fluid flows for a defined geometry. This process of computer numerical calculations is the basis of the computational fluid dynamics (CFD) model. As the saying goes, "all models are wrong, some are useful." With this understanding there will be discrepancies between the results of the CFD calculations and real life, however, when performed correctly

with properly defined boundary conditions, the CFD solution can provide very detailed insights into the dynamics of the fluid flow. In order to make the models useful to engineers and designers, the geometry needs to be as detailed as possible, yet is generally simplified as much as possible to reduce computation time and stability of the solution.

The current study will utilize CFD for insight into the flow physics inside the test hardware, as well as a tool to parametrically investigate design options prior to building new hardware. The remainder of this section provides details of the foundational governing equations, followed by applications of these governing equations in the CFD model. These discussions will be focused on the details needed for UCC and film-cooling studies. The commercial code FLUENT will be used for all flow simulations. As such, this section will also serve as a summary of the implementation of models within the FLUENT code.

2.10.1 Conservation Equations of Fluid Motion.

The simple definition of a fluid is any substance that flows. The distinction between a fluid and a solid is in the molecular interactions and motion. Generally speaking, the spacing of atoms and molecules in a fluid is greater than that of a solid, and the arrangement of molecules in a solid is generally arranged in some form of matrix. Under normal temperature and pressure conditions, the spatial and temporal scales of bulk fluid motion are much greater than the motion in the molecular scales. This relationship is defined by the Knudsen number (Kn), given in Equation 107, which describes the ratio of these two scales. In this equation l is the smallest geometric length scale experienced by the bulk fluid, and λ is the mean free path which represents the length between molecular collisions.

$$Kn \equiv \frac{\lambda}{l} \tag{107}$$

Since, under normal operating conditions, l is much greater than λ, therefore $Kn \ll 1$. For these conditions the fluid can be viewed as a continuum rather than discrete molecules. Using this continuum hypothesis allows fluid properties to be defined at any arbitrary location within the fluid. This means that vectors defining the fluid flow field are differentiable everywhere [131].

There are three governing mathematical relationships for fluid properties known as the conservation of mass, momentum, and energy. The collection of these three conservation equations is commonly referred to as the Navier-Stokes equations. Momentum conservation can be further defined for a specific class of fluids by incorporating Newton's viscosity law. This law states that the stress on a fluid element is proportional to the rate of strain in that fluid. When this proportionality is linear, in addition to a few other criterion, the fluid is said to be "Newtonian". The Navier-Stokes equations can be found in many fluid dynamics references, however, the form of the equations shown in Equations 108, 109, and 110 which show the mass, momentum, and energy equations, respectively, are as defined and used by FLUENT [132], which references Batchelor [133].

$$\frac{\partial \rho}{\partial t} + \nabla \cdot (\rho \vec{v}) = S_m \tag{108}$$

$$\frac{\partial}{\partial t}(\rho \vec{v}) + \nabla \cdot (\rho \vec{v} \vec{v}) = -\nabla p + \nabla \cdot (\bar{\bar{\tau}}) + \rho \vec{g} + \vec{F} \tag{109}$$

$$\frac{\partial}{\partial t}(\rho E) + \nabla \cdot (\vec{v}(\rho E + p)) = \nabla \left(k_{eff} \nabla T - \sum_j h_j \vec{J}_j + (\bar{\bar{\tau}}_{eff} \cdot \vec{v}) \right) + S_h \tag{110}$$

The conservation of mass usually states that no mass can be created or destroyed and therefore the right-hand side of Equation 108 is typically zero. FLUENT adds

the term S_m to account for multi-phase interactions and user-defined source terms. The remainder of the variables in Equation 108 are the density (ρ), time (t), and the three-dimensional components of the velocity field ($\vec{v}$). This equation is valid for both compressible and incompressible flows.

The conservation of momentum as defined for an inertial reference frame in Equation 109 uses the same definition of variables as described for Equation 108, plus the static pressure (p), stress tensor ($\bar{\bar{\tau}}$), gravitational body force ($\rho\vec{g}$), and externally applied forces ($\vec{F}$). The definition of the stress tensor is given in Equation 111. In this definition μ is the molecular viscosity, $\vec{v}$ represents the components of the velocity field in three dimensions, and I is the unit tensor.

$$\bar{\bar{\tau}} = \mu\left[(\nabla\vec{v} + \nabla\vec{v}^T) - \frac{2}{3}\nabla\cdot\vec{v}I\right] \tag{111}$$

In the energy equation shown in Equation 110, k_{eff} is the effective conductivity of the fluid which is the sum of the thermal and turbulent conductivity. There remaining terms are the temperature (T), internal energy (E), enthalpy (h), and diffusion flux of species j ($\vec{J}_j$). The first three terms on the right-hand side, moving from left to right, correspond to the energy transfer due to conduction, species diffusion, and viscous dissipation, respectively. The additional term specific to FLUENT, S_h, accounts for the heat of chemical reactions and other volumetric heat sources as defined by the user. The governing equations of energy and heat transfer were given in Section 2.7.

2.10.2 Turbulence.

Equations 108, 109, and 110 may be used to directly solve the flow solution for a very specific class of flow conditions. These classes are limited to smooth laminar flows that are largely academic exercises rather than a typical realistic flow. In many cases, the flow conditions of interest, specifically in combustors, are turbulent. The

Reynolds number (Re), given in Equation 112 can be used to make a determination of whether a flow is turbulent. The Reynolds number is the ratio of inertial to viscous forces and defined by the product of a characteristic velocity (U) and a characteristic length scale (L) over the kinematic viscosity (ν).

$$Re = \frac{UL}{\nu} \tag{112}$$

In consideration of flow through a straight pipe, U is the axial velocity of the fluid and L is the pipe diameter. Experimental correlations have shown that the flow is laminar for $Re <$ 2,300 and is turbulent for $Re >$ 4,000 [131]. Between these values the flow is said to be in transition. The mechanism for causing a transition between laminar and turbulent flow is somewhat experiment specific as several factors can cause the transition. Air for the AFIT UCC is fed through a straight pipe with a diameter of 7.62 cm. At a mass flow rate of 0.1 kg/s, the incoming air is turbulent with a Reynolds number of approximately 1 x 10^5.

2.10.2.1 Reynolds Averaging.

Due to the random and chaotic nature of turbulent flows they are often dealt with in statistical terms. Since the properties of turbulent fluid motion vary, generally around some mean value, it is desirable to present the variables as a sum of their mean and fluctuating components. The turbulent definition of a fluid property variable is shown in Equation 113 for the velocity variable. In this equation, $\bar{u}_i$ is the mean velocity, u_i' is the fluctuating component of velocity, and the subscript i refers to the x, y, or z component of velocity. This decomposition into a mean and fluctuating component can be applied to all the state variables in the Navier-Stokes equations, however, assumptions such as incompressible flow generally simplify the problem by assuming many of them to be constant.

$$u_i = \bar{u}_i + u_i' \tag{113}$$

If Equation 113 is substituted into Equations 108 and 109, and then that equation is time (ensemble) averaged, the Reynolds-averaged Navier-Stokes (RANS) equations are produced as shown in Equations 114 and 115. In these equations the overbar was dropped from the mean components, but it is still assumed that all variables without a prime symbol represent the mean values in the flow. [132]

$$\frac{\partial \rho}{\partial t} + \frac{\partial}{\partial x_i}(\rho u_i) = 0 \tag{114}$$

$$\frac{\partial}{\partial t}(\rho u_i) + \frac{\partial}{\partial x_j}(\rho u_i u_j) = -\frac{\partial p}{\partial x_i} + \frac{\partial}{\partial x_j}\left[\mu\left(\frac{\partial u_i}{\partial x_j} + \frac{\partial u_j}{\partial x_i} - \frac{2}{3}\delta_{ij}\frac{\partial u_l}{\partial x_l}\right)\right] + \frac{\partial}{\partial x_j}(-\rho\overline{u_i' u_j'}) \tag{115}$$

$$\delta_{ij} = \begin{cases} 1 & \text{if } i = j \\ 0 & \text{if } i \neq j \end{cases} \tag{116}$$

The term $\overline{u_i' u_j'}$, is a second-order tensor referred to a the Reynolds stress. This value is not a true stress, it is merely a result of the averaging process, however, it introduces a difficulty in solving the RANS equations. In the instantaneous form of the Navier-Stokes equations there were an equal number of variables as there were equations to simultaneously solve for the value of those variables. With the addition of the Reynolds stress term, there is now an insufficient number of equations to solve for all the unknowns. The most common approach to resolve this closure problem is to model the Reynolds stresses, and then solve for the remaining variables in the equations. Solving the closure problem has been the subject of many decades of research.

2.10.2.2 Wall Coordinates.

Wall bounded turbulent flow regimes are defined by their non-dimensional position relative to a wall (y^+). Within each of these regimes there is a uniform behavior and relationship between non-dimensional distance from the wall and non-dimensional velocity (u^+). The definition of y^+ is shown in Equation 117 with the definitions of the viscous length scale (δ_v), friction velocity (u_τ), and wall shear stress (τ_w) provided in Equations 118, 119, and 120, respectively. The value of y^+ also shows the relative importance of viscous and turbulent processes independent of the Reynolds number of the flow. Due to the no-slip condition at the wall, the contribution of turbulent motion to the total Reynolds stress is zero, thus the viscous stresses account for 100% of the Reynolds stress at the wall. As the measurements are taken further from the wall the proportion of contribution changes. By $y^+ \approx 12$ the viscous contribution to the Reynolds stresses is 50%, and by $y^+ \approx 50$ is less than 10%.

$$y^+ \equiv \frac{y}{\delta_v} = \frac{u_\tau y}{\nu} \tag{117}$$

$$\delta_v \equiv \nu\sqrt{\frac{\rho}{\tau_w}} = \frac{\nu}{u_\tau} \tag{118}$$

$$u_\tau \equiv \sqrt{\frac{\tau_w}{\rho}} \tag{119}$$

$$\tau_w = \rho\nu\Big(\frac{d\bar{U}}{dy}\Big)_{y=0} \tag{120}$$

In the above equations, y is the dimensional length of the measurement position off the wall, ρ is the fluid density, ν is the kinematic viscosity, and $\bar{U}$ is the average fluid velocity at the measurement position. The non-dimensional velocity near the wall is defined in Equations 121 and 122. The values of κ and$B$ in Equation 122 are generally accepted as $\kappa = 0.41$ and $B = 5.2$.

$$u^+ \equiv \frac{\bar{U}}{u_\tau} \tag{121}$$

$$u^+ = \frac{1}{\kappa}\ln y^+ + B \tag{122}$$

As mentioned earlier, turbulent flow regimes are classified by their relative position to the wall where the relationship of u^+ and y^+ follows a known behavior. The region $y^+ < 5$ is referred to as the viscous sublayer. In this region there is a linear relationship between y^+ and u^+ such that $y^+ = u^+$. The range $5 < y^+ < 30$ is a transition region followed by $30 < y^+ <$ 5,000 known as the log-law region. In this region the relationship of y^+ and u^+ is defined by Equation 122. The boundary layer usually occurs inside of $y^+ <$ 10,000. Outside of this region the wall has a negligible influence and freestream conditions dominate. [131] The relationships present in the viscous sublayer and the log-law region are often used in turbulence model "wall functions" to reduce the resolution needed in numerical models. More detail on wall functions is provided in Section 2.10.3.1.

2.10.3 Turbulence Models.

There are several ways to address turbulent flow within CFD, each with its own set of challenges. As described by Pope [131], the turbulent velocity field is three-dimensional, time-dependent, and random. Fluctuations must be resolved at multiple length scales with different time scales that can be vastly different in magnitude. The largest length scales are dependent on the boundary geometry. The smallest scales are Reynolds number dependent with the length scale decreasing as $Re^{-3/4}$ and the time scale decreasing as $Re^{-1/2}$. Even seemingly small changes in Re can result in large increases in computational complexity.

The first method to address turbulent flow within CFD is the flow simulation ap-

proach. This approach involves solving for the time-dependent velocity field for one realization of the flow. Two common techniques within the flow simulation category include direct numerical simulation (DNS), and large-eddy simulation (LES). In DNS all length and time scales are resolved through direct application of the Navier-Stokes equations for one realization of the flow. This approach offers the highest fidelity of any computational method, ofter serving as a validating authority for less accurate models. The penalty for accuracy in this approach comes with the highest computation cost, increasing with Re^3. Within this method the large flow structures are easily resolved, with 99% of the effort focused on resolving the smallest length and time scales within the dissipation range [131]. The LES approach saves on computational expense, compared to DNS, by resolving the large flow structures and modeling the small scale motion. The behavior of fluids in the dissipation range is typically universal, thus making it suitable for modeling with minimal loss of solution fidelity.

The second approach to address turbulent flows in CFD is with a turbulence model. This approach involves using solutions for mean quantities within the flow utilizing the RANS equations shown in Equations 108 and 109. As described in Section 2.10.2.1, the RANS equations require a closure method to address the additional Reynolds stress term. These closure methods are generally grouped by the number of additional equations that are used to find a solution. The most common methods use zero-, one-, and two-equations, but higher order models do exist. The Reynolds stress tensor is modeled using the Boussinesq approximation and a parameter known as the eddy or turbulent viscosity (μ_T) as shown in Equation 123 [132]. The additional transport equations that make up the various turbulence models are used to define a value for μ_T.

$$-\rho\overline{u_i'u_j'} = \mu_T\Big(\frac{\partial u_i}{\partial x_j} + \frac{\partial u_j}{\partial x_i}\Big) - \frac{2}{3}\Big(\rho k + \mu_T\frac{\partial u_k}{\partial x_k}\Big)\delta_{ij} \tag{123}$$

The most used approach to solve for the eddy viscosity is with a two-equation model. There are two common two-equation models, the $k-\epsilon$ and $k-\omega$ models. The $k-\epsilon$ model uses equations for the turbulent kinetic energy (k) and the turbulent dissipation rate (ϵ). The standard $k-\epsilon$ model assumes fully turbulent flow and thus is technically only valid under those conditions. Additionally, the $k-\epsilon$ model requires a damping function in near wall regions to maintain accuracy in the viscous sublayer. The $k-\omega$ model uses equations for the turbulent kinetic energy (k) and the specific dissipation rate (ω). The $k-\omega$ model does not require a damping function at the wall, but can have issues in the freestream due to sensitivity of the value of ω in this region. While no damping functions are used, this model does require grid resolution at the wall in the viscous sublayer with a first point at approximately $y^+ = 1$. The $k-\omega$ shear stress transport (SST) model blends the best aspects of the $k-\epsilon$ and $k-\omega$ models together. [134]

There is a third approach to address turbulent flows in CFD by using a hybrid variation of the flow simulation and flow modeling techniques described above. These hybrid RANS-LES approaches are found in methods such as detached eddy simulation (DES) and scale-adaptive simulation (SAS). These techniques can reduce the computational effort related to full resolution of the flow, without an excessive loss of accuracy. The SAS method allows the solver to dynamically adjust between regions of low instability solved by RANS methods to regions with high instability solved with LES-like scale-resolved solutions. This method has been shown to have superior results to a purely RANS approach in predicting turbulent flow structures specifically in complex flows such as swirl burners. Additionally, the RANS portion of SAS is not affected by grid spacings, alleviating the grid sensitivity common in LES solutions. [135][136][137]

2.10.3.1 Wall Functions.

There are two primary approaches to dealing with near wall flows. The first approach is direct simulation of the near wall behavior. This method requires a sufficiently refined grid in the near wall region to fully resolve the behavior at the wall. To meet these grid resolution requirements there must be at least one point in the viscous sublayer ($y^+ < 5$) and multiple points in the range $y^+ < 50$. Just like the flow simulation approaches to the bulk flow, near wall simulation offers that same fidelity in the near wall region. The penalty for increased fidelity is a significantly increased cell count which increases the computational coat. The second option for near wall treatment are "wall functions". These functions bridge the gap between the no-slip condition on the wall and the fully-turbulent regime away from the wall. These functions require the first cell near the wall to be position at approximately $y^+ = 30$, and will not work if the grid is too refined. In FLUENT there are several wall function options including standard wall functions, and enhanced wall functions. Using the standard wall functions, Mongia [138] found that the first grid point should be positioned in the range $30 < y^+ < 500$ to achieve the most accurate result. When enhanced wall treatments were used the range of positioning of the first cell opened up to $1 < y^+ < 500$, making enhanced wall treatments the preferred option for any CFD case that is not directly simulating the near wall behavior.

2.10.3.2 Turbulence Model Application.

Early numerical work on the UCC was performed using the standard $k - \epsilon$ model with some success [139][140][141]. The unmodified version of the $k - \epsilon$ model has difficulties with wall-bounded flows and flows with high streamline curvature. The UCC experiences both of these conditions meaning these early results only allowed qualitative comparisons with experimental data. When the RNG $k - \epsilon$ model variant

was shown to produce better accuracy in resolving turbulent flows, this model was used by AFIT and AFRL to model UCC flows [142][143][144][145].

Improvements in the availability of computational resources have allowed the use of more accurate simulation techniques to be used in recent years in UCC analysis as well as other advanced combustion analyses. Briones et al. [146] and Cottle [78] used the Realizable $k-\epsilon$ with enhanced wall functions in their UCC analysis. The Realizable $k-\epsilon$ model is an improvement over the standard and RNG $k-\epsilon$ models in that it satisfies physical mathematical constraints that are present on the Reynolds stresses, and thus is more representative of the flow physics of turbulent motion. Bills et al. [147] investigated multi-phase fuel film-cooling with conjugate heat transfer in a two-dimensional domain with the $k-\omega$ SST turbulence model. This model was selected since the conjugate heat transfer analysis requires a $y^+ \leq 1$ to achieve an accurate model of the boundary layer heat transfer properties. The $k-\omega$ model will resolve to the wall without a damping function and thus was a good pairing with the conjugate heat transfer grid requirements.

Andreini et al. [136] studied combustor-turbine interaction and ran steady simulations using the Realizable $k-\epsilon$ and $k-\omega$ SST models as well as an unsteady analysis using SAS. By comparing these three results they were able to assess the importance of the large-scale fluctuations to the overall accuracy of the solutions. Law and Gimbun [137] conducted a comparative analysis of predicted temperatures in a combustor using the unsteady standard $k-\epsilon$, Reynolds stress, and SAS models. They concluded that for each of the turbulence models paired with a non-premixed combustion model, the SAS model most accurately predicted the combustion temperature with an error of 0.85% compared to an experimental result. The standard $k-\epsilon$ model had a error of 5.7%, and the Reynolds Stress Model had a prediction error of 5.6%. The reduced temperature prediction error came with an increased computational expense to run

the SAS model. Briones et al. [33] moved away from prior steady-state analysis and performed a recent high-g combustion analysis using the SAS turbulence model.

2.10.4 Combustion Modeling.

Modeling reactions in FLUENT can be performed using a number of methods with increasing complexity. The simplest method is the species transport model. This method uses conservation equations to track the mixing and transport of specific chemical species. Reactions in this model are volumetric and thus occur in the bulk phase. The determination of the mass fraction for a given species is found using specific convection diffusion equations. Moving up the complexity level is the premixed and non-premixed combustion models. These combustion models incorporate laminar flamelet models and utilize pre-processed probability density functions (PDFs) for combustion values. During the computations, species properties are found from the pre-processed lookup tables to avoid making repetitive calculations during each iteration. The next level of combustion model complexity blends the non-premixed and premixed models into the partially premixed model. Many combustion systems require a combined model to accurately represent the combustion environment. Specific species concentrations can still be found with the non-premixed, premixed, and partially premixed models, however, some species such as emissions are determined during a post-processing step. [132]

2.10.4.1 Combustion Model Application.

The early UCC numerical simulations [139][140][141][143] all used the non-premixed combustion model with a PDF lookup table and single-step global kinetics in the FLUENT flow solver. Mawid et al. [142] and Thornburg et al. [145] used a different flow solver, but still modeled combustion using a similar single-step approach and an eddy-dissipation scheme. Mawid et al. [144] also used a similar approach but used a two-step reaction scheme instead.

More recent UCC analyses switched to premixed and partially premixed combustion models. Briones et al. [33] used a two-step global reaction with premixed combustion for a propane-air flame. To determine the make up of the flame properties, Briones et al. [146] performed a detailed analysis on a trapped vortex combustor with an externally calculated PDF that was then uploaded into FLUENT for use in a non-premixed combustion model. The results of this analysis indicated that both non-premixed and premixed combustion was present in the combustor. They recommended using the partially premixed combustion model for all future work. The most advanced UCC simulation to date was conducted by Briones et al. [148] which used a flamelet model coupled with a custom user-defined function (UDF) that accounted for variability in the molecular viscosity and thermal conductivity of the mixture. Mongia [138] supported the method used by Briones et al. [148], and stated that the flamelet model is the best approach to take when dealing with complex combustors. These models, however, still lack in accuracy when premixed and non-premixed combustion are both present. Cottle [78] used the recommendation of Briones et al. [146] and Mongia [138], and conducted his analysis with the FLUENT partially premixed combustion model utilizing the flamelet generated manifold.

Mongia [138] highlighted the benefits to be gained by using LES simulations with combustion modeling if the computational expense can be managed. Short of using LES, hybrid techniques such as SAS can offer better accuracy in combustion than RANS based models without the huge increase in computational expense. Law and Gimbun [137] investigated the use of three different combustion models and compared the results to experimental data for a combustor with distinct fuel and air injectors. During this analysis they tested an eddy-dissipation model, non-premixed flame model, and a partially premixed flame model. Their analysis showed that the non-premixed flame model achieved the best combustion temperature prediction com-

pared to experimental data with an error of 6.6%. The eddy-dissipation model had a prediction error of 6.8% and the partially premixed flame model had a prediction error of 7.3%. All three of these models under predicted the experimental temperature. The partially premixed flame model had the largest error and also had the highest computational expense. In the case of the UCC, which has discrete fuel and air injectors, perhaps the best model to use is the non-premixed flame model.

2.10.5 Conjugate Heat Transfer in FLUENT.

A conjugate heat transfer problem arises when heat transfer occurs across a solid/fluid interface [149]. At the junction between these two mediums the heat flux conducted by the fluid must balance with the heat flux conducted by the solid plus any radiation as shown in Equation 124. In many cases radiation is neglected in the analysis meaning the heat flux between the fluid and solid must exactly match.

$$\left(k\frac{\partial T}{\partial y}\right)_{fluid} + q''_{rad} = \left(k\frac{\partial T}{\partial y}\right)_{solid} \tag{124}$$

Applying conjugate heat transfer to a CFD model allows for greater analysis into the heat transfer problem. This process provides a much more accurate depiction of solid surface temperatures, over adiabatic analysis, and provides gradients within the solid components. In order to conduct this type of analysis both the fluid and the solid must be gridded. The interface between the two grids is treated as a thermally coupled wall. Bills et al. [147] conducted a multi-phase film-cooling study utilizing conjugate heat transfer. They were able to produce detailed results of film-cooling performance and made the determination that previous simplifications to the geometry had a significant impact on the surface temperature of the test plate. Without modeling the heat conduction to, and through, the solid surface these results would not have been possible.

Lee et al. [150] presented a significant reason to include conjugate heat transfer into a reacting flow model. The incorporation of heat transfer to the walls allows for flame quenching at the wall and a lower combustion cavity temperature. These changes can lead to significant differences in flame structure and heat release compared to an adiabatic model. Figure 119 shows the differences in the mean temperature field in a reacting flow model with (top) and without (bottom) conjugate heat transfer. Figure 120 shows comparisons of the radial profiles of mean temperature with and without conjugate heat transfer.

The results shown in Figures 119 and 120 provides the magnitude of wall-heat loss on temperature within the combustor. The effects of the non-adiabatic wall are not localized only to the near-wall region, but impact the temperature distribution through the entire combustor volume. In regions near the fuel injectors, Lee et al. [150] found as much as a 500 K temperature reduction in bulk temperature, with quenching and additional gas temperature reductions along the wall.

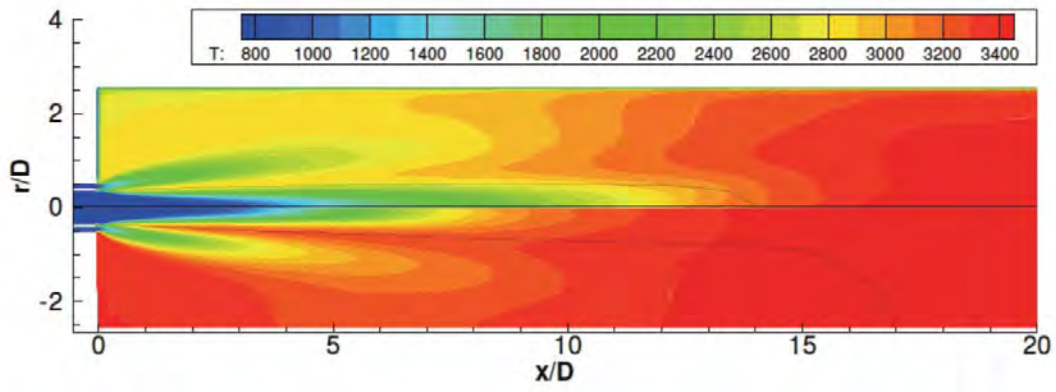


Figure 119. Comparison of mean temperature fields with (top) and without (bottom) conjugate heat transfer [150]

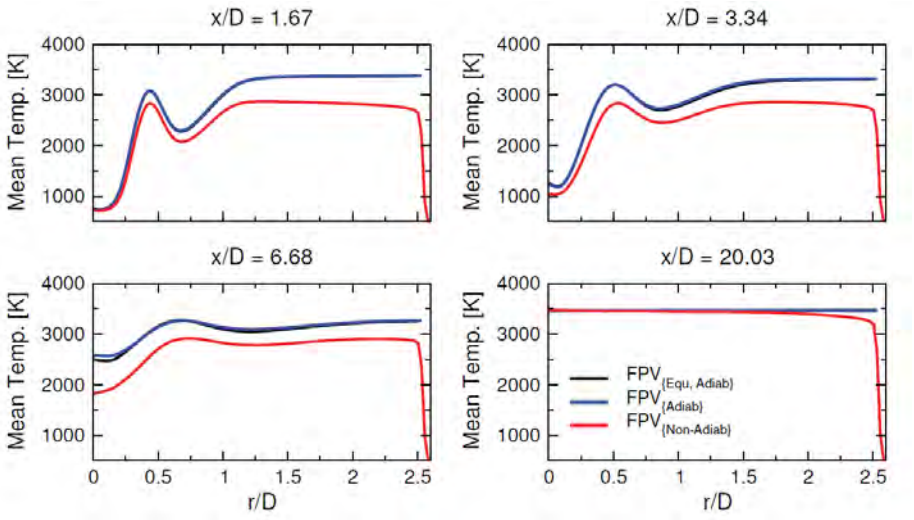


Figure 120. Comparison of radial profiles of the mean temperature computed at four different downstream positions (Blue=adiabatic, red=non-adiabatic) [150]

2.11 Optical Combustor Measurement Methods

The use of probe type measurement devices has been common place in the laboratory for many years. The issue with probes used to take aerodynamic measurements is that the presence of the probe often interferes with the fluid flow and thus causes changes in the flow properties. The impact of the probe is typically minimal for larger experiments where the ratio of the size of the probe to the size of the region of interest is small. For these larger rigs the spatial and temporal resolution is usually sufficient with a probe to acquire the data of interest. With decreasing rig size and increasing complexity, the data requirements often force the use of alternative, non-probe, measurement methods. The alternative method of choice is typically an optical technique where data are acquired with a camera and lens with little to no intrusion into the test rig. The remainder of this section provides the details of optical techniques used in the acquisition of UCC combustion and flow data.

2.11.1 Chemiluminescence.

Chemiluminescence is the emission of energy in the electromagnetic spectrum during the course of a chemical reaction such as burning hydrocarbon fuels. The chemical reactions provide an excitation energy to the molecular species in the burning flow. Max Planck theorized that the energy transfer between atoms must be in "chunks" or quantum [151]. Thus the minimum amount of energy transferred in a quantum is given by Equation 125. By this definition all energy transfer is quantized into integer multiples of $h\nu$.

$$E = ih\nu = \frac{ihc}{\lambda} \tag{125}$$

In Equation 125, E is the energy transfer in the quantum packet, i is an integer defining the number of quantum states transferred, h is Planck's constant ($h = 6.626 \cdot 10^{-34}$ J·s), ν is the frequency of light, c_0 is the speed of light in a vacuum ($c_0 = 2.998 \cdot 10^8$ m/s), and λ is the wavelength of light.

Figure 121 shows the potential energy curve $(\epsilon_p, true)$ of a diatomic molecule with respect to the distance between the molecules, r. When the molecules are pulled far enough apart they approach the dissociation energy (D). At the ground state (r_o), ϵ_p is at a minimum and the molecule will stay at rest indefinitely. If an activation energy is applied, the energy can be stored in the vibrational modes of the molecule represented by the horizontal lines in the energy well, or by pushing the electrons in the atoms to a higher energy orbit which causes the entire potential curve can be shifted upward. In the visible spectrum the activation energy required to move the molecule to a higher energy state is between 1.8 electron volts for red light and 3.1 electron volts for violet light per mole [152]. When the molecule is at an excited state and spontaneously returns to the ground state, an emission of energy in the form of a photon is given off at the proper wavelength dependent on the energy difference between the states (change in quantum level, i) as described in Equation 125 [151].

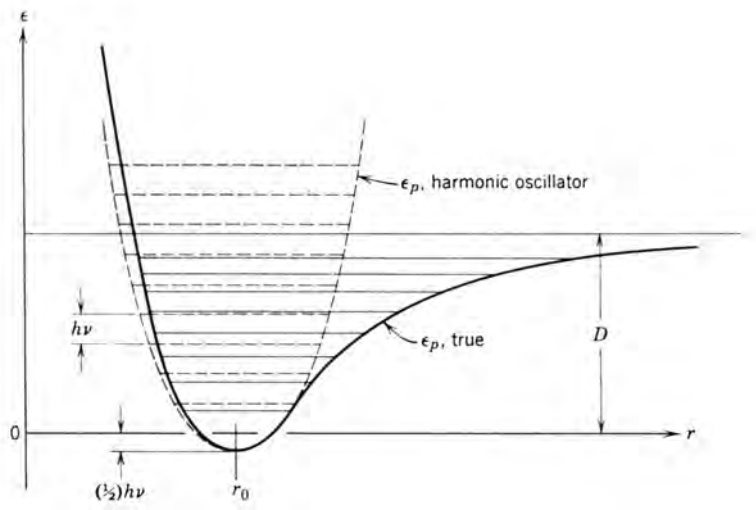


Figure 121. Potential energy and vibrational levels for diatomic molecules [153]

When molecules spontaneously return to their ground states, each molecule acts individually and the emission of light, or invisible energy, is incoherent. Each type of molecule will absorb and emit energy at different wavelengths. By using band pass filters to only accept emissions from specific molecules, an electronic sensor can count the specific photon emissions. These emissions are proportional to the amount of the specific species in the flow which allows the system to determine the location and quantity of the tracked species based on photon count or image intensity. In combustion reactions chemiluminescence of the OH radical is common. The OH radical is an intermediate combustion species usually found at the flame front. By tracking the emissions from OH molecules the location of the flame front and the intensity of the combustion reaction at that location can be determined.

The OH emissions are in the 300 - 330 nm wavelength range below the 390 - 700 nm wavelength visible spectrum. An image intensifier is often used to amplify the strength of these photon emissions and project them on a fast decay phosphor screen. The addition of the photons to the phosphor screen causes the phosphor to illuminate in the visible spectrum allowing the image the intensifier saw to be

recored with a traditional camera. The use of fast decay phosphor means that the illumination will not be present for a long period of time allowing high-speed imagery of the chemiluminescence.

Dr. Larry Goss of ISSI has developed a post-processing technique used on high-speed chemiluminescence video files to determine the velocity field in the flow. This processing technique was based on a Schlieren image velocimetry technique [154][155] which utilized high-speed videos of refractive turbulent flows. Like the Schlieren technique that used naturally occurring refractive eddies in the flow as virtual seed particles, the chemiluminescence velocimetry technique used naturally occurring chemiluminescence markers in the same way. The analysis program called *DPIVB*, written by Dr. Goss, performed chemiluminescence velocity measurements using an auto-correlation method between two sequential video frames acquired at 10,000 frames per second, with a delay of 100 μs. The accuracy of this velocimetry method is comparable to PSEV and PIV. This processing is the same as for PIV described in more detail in Section 2.11.3. When used for chemiluminescence velocimetry the *DPIVB* program used a minimum pixel intensity threshold of 200 counts to identify and use only strong OH markers and ensure the program was not correlating image noise.

2.11.2 Particle Streak Emission Velocimetry (PSEV).

Particle Streak Emission Velocimetry (PSEV) is a new diagnostic technique developed by Innovative Scientific Solutions, Inc. (ISSI) that can be used to determine fluid velocity and flow path on a non-intrustion basis. The accuracy of this measurement method is within 0.10 m/s. PSEV only appears in literature in direct terms in the works of Cottle [78] and Cottle et al. [83]. This technique is a blend of particle tracking and the optical capture of natural blackbody radiation.

Seed particles are introduced into the flow upstream of the area of interest. PSEV

can only be used in flow conditions where the particle temperature can exceeds 920 K. Since there is no laser to illuminate the particles, the particles must reach their minimum temperature where they will emit blackbody radiation in the visible spectrum (i.e. glow). A monochrome high-speed camera records the spectral emissions from the seed particles as viewed through an optical access window in the test rig wall. Raw images from the high-speed camera must then be processed to isolate the emission streaks from any background noise such as illumination from flames. When clear particle streaks are isolated, the length of the streaks can be measured and the local velocity (u and v components) calculated by using the streak length and the camera shutter speed. The average velocity over all frames can then be determined by creating a square grid (10x10 pixels) over the image area, aligning the random particle streaks with this grid, and averaging streaks from all frames relative to this grid. Using composite images of several image frames allows the flow path of the fluid within the cameras' field of view to be found. The PSEV technique can be applied for a two-dimensional or three-dimensional analysis. The three-dimensional analysis requires two cameras, or a single camera with mirrors, to provide an additional view angle to resolve the third dimension.

The seed particles are made of silicon carbide (SiC) with a diameter of approximately 1 μm. To determine how closely a suspended particle will follow fluid streamlines, the non-dimensional parameter called the Stokes number (Stk) is used. This parameter, shown in Equation 126, is the ratio of the characteristic time of the particle to the characteristic time of the fluid.

$$Stk = \frac{t_0 u}{l_0} \tag{126}$$

$$t_0 = \frac{\rho_p d_p^2}{18 \mu_g} \tag{127}$$

In Equation 126, t_0 is the relaxation time of the particle as defined in Equation 127, u is the fluid velocity, and l_0 is the characteristic dimension of the test hardware. In Equation 127, ρ_p is the particle density, d_p is the particle diameter, and μ_g is the dynamic viscosity of the gas the particle is suspended in. For $Stk \gg 1$, the particle will detach from the flow and not follow the fluid streamlines. For $Stk \ll 1$, the particle follows the fluid streamlines. If $Stk \ll 0.1$, the error between the particle trace and the fluid streamline is below 1%. [156]

The post-processing of the high-speed images is an essential component of the PSEV technique to isolate the blackbody emissions of the particle streaks from the light emissions produced by the combustion flames. The raw images are processed using a Laplacian convolution filter which is an application of the discrete Laplace operator. This processing technique can be found in literature in references such as Reuter [157], but the online reference by Fisher et al. [158] provides the requisite background to discuss how this filter works.

The Laplacian of an image highlights regions with high intensity gradients and is often used in edge detection. In more technical terms, the Laplacian is a two-dimensional isotropic measure of the second spatial derivative of an image. In the case of PSEV, the Laplacian is used to identify high-intensity particle streaks. The operator works best with a grayscale image input, and will produce a grayscale image output. The general form of the Laplacian, $L(x, y)$, of an image with pixel intensity $I(x, y)$ is described in Equation 128. [158]

$$L(x, y) = \frac{\partial^2 I}{\partial x^2} + \frac{\partial^2 I}{\partial y^2} \tag{128}$$

The above equation can be calculated by means of a convolution filter. Convolution provides a method of combining two number arrays of different sizes, but the same dimensionality, to produce a third array with the same dimensionality. In im-

age processing this can produce output pixel values that are linear combinations of specific input pixel values. One input array is normally the baseline grayscale image. The second array is typically a much smaller two-dimensional kernel. An example of these two input arrays are shown in Figure 122. The convolution is performed by sliding the kernel over the image starting at the upper left corner and moving it to all positions on the image where the kernel can fit in its entirety within the bounds of the image. Each kernel position corresponds to an output pixel. The output pixel value is computed by multiplying the kernel value and the underlying image pixel value together for each of the cells in the kernel, then adding those values together. In the example image and kernel shown in Figure 122, the value of the bottom right output pixel is defined by Equation 129. [158]

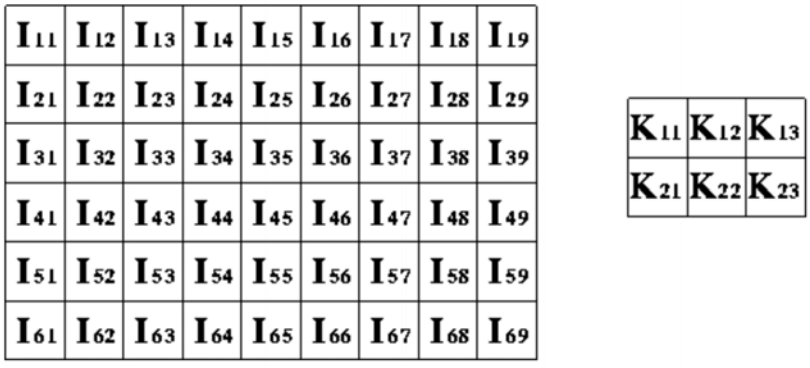


Figure 122. Example convolution input arrays. Left is a small image, Right is a kernel [158]

$$O_{57} = I_{57}K_{11} + I_{58}K_{12} + I_{59}K_{13} + I_{67}K_{21} + I_{68}K_{22} + I_{69}K_{23} \tag{129}$$

For an image with M rows and N columns, with a kernel of m rows and n columns, the output image will have $M-m+1$ rows and $N-n+1$ columns. The general form of the convolution process is given in Equation 130, with i covering 1 to $M-m+1$ and j extending from 1 to $N-n+1$. [158]

$$O(i,j) = \sum_{k=1}^{m} \sum_{l=1}^{n} I(i+k-1, j+l-1) K(k,l) \tag{130}$$

Figure 123 shows two commonly used kernels that approximate the second derivatives of the image in the definition of the Laplacian. The Laplacian of the image can then be found using either of these kernels and the standard convolution method described above.

0	−1	0
−1	4	−1
0	−1	0

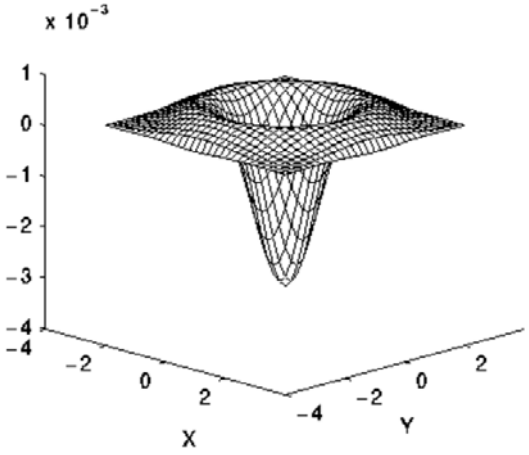
−1	−1	−1
−1	8	−1
−1	−1	−1

Figure 123. Two common kernel arrays used in Laplacian filters [158]

The kernels above are approximating the second derivative on an image, they are very sensitive to noise. The image is often Gaussian smoothed before applying the Laplacian filter to reduce high-frequency noise. Because the convolution operation is associative, the Gaussian smoothing filter and the Laplacian filter can be combined, then the hybrid filter can be convolved with the image to achieve the same result. The hybrid filter is called the "Laplacian of Gaussian" or "LoG". Using the hybrid filter reduces the number of mathematical operations, and the LoG filter can be pre-calculated so only one convolution needs to be calculated per image. The two-dimensional LoG function centered on zero with the Gaussian standard deviation (σ) is given by Equation 131 and shown graphically in Figure 124a. Figure 124b shows a discrete LoG kernel. [158]

$$LoG(x,y) = -\frac{1}{\pi\sigma^4}\left[1 - \frac{x^2+y^2}{2\sigma^2}\right] e^{-\frac{x^2+y^2}{2\sigma^2}} \tag{131}$$

Putting the LoG operator into practice, it can be shown that in image regions with constant intensity the LoG response will be zero. In regions with changes in intensity, the LoG response will be positive on the dark side of the gradient and negative on the lighter side. Thus, at a reasonably sharp edge between two regions of uniform contrast but differing intensity the LoG response will be: zero at a long distance from the edge, positive just to one side of the edge, negative just to the other side of the edge, and zero at some point between, on the edge itself. These responses are shown in Figure 125b for a one-dimensional step edge shown in Figure 125a. [158]



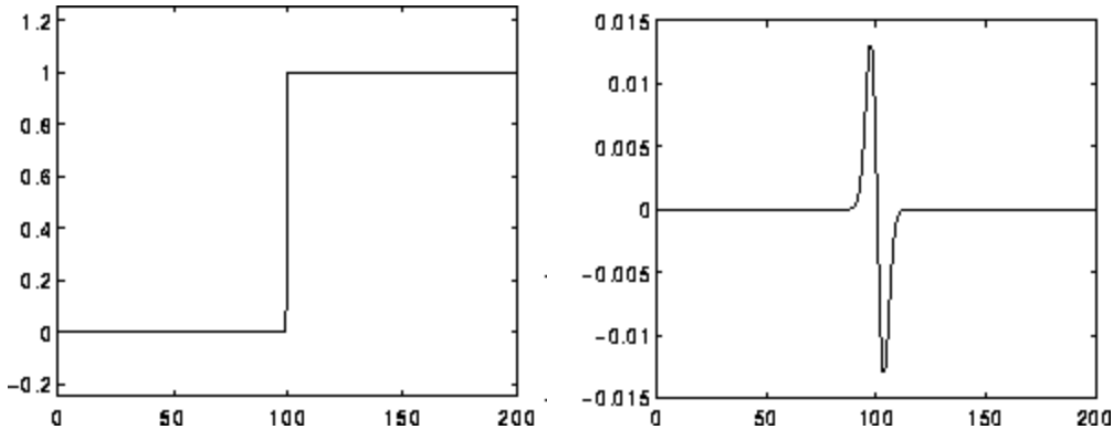
(a) 2-D LoG function (x & y axes units of σ)

0	1	1	2	2	2	1	1	0
1	2	4	5	5	5	4	2	1
1	4	5	3	0	3	5	4	1
2	5	3	-12	-24	-12	3	5	2
2	5	0	-24	-40	-24	0	5	2
2	5	3	-12	-24	-12	3	5	2
1	4	5	3	0	3	5	4	1
1	2	4	5	5	5	4	2	1
0	1	1	2	2	2	1	1	0

(b) Discrete LoG kernel (σ=1.4)

Figure 124. LoG function and kernel [158]

Figure 126 shows the processing sequence for PSEV analysis. Figure 126a shows a raw single frame image from the high-speed camera. Several bright streaks can be seen in this image, however, many of the particle streak emissions are obscured by the flame illumination. Figure 126b shows the resulting image after the application of the Laplacian convolution filter. In this image it can be seen that the particle streaks have been isolated and the flame illumination has been removed. Finally, in Figure 126c the length of each streak has been measured and the local velocity (u and v components) were calculated. These values were then averaged over all frames



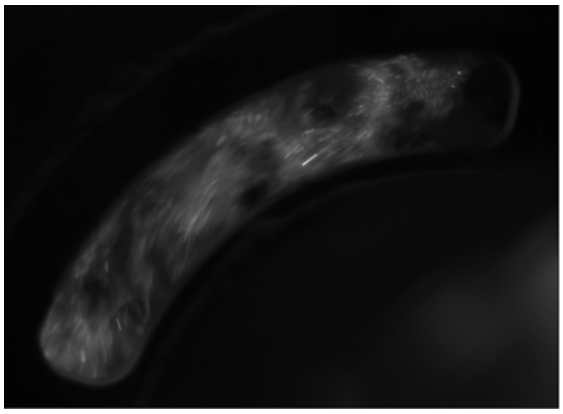
(a) 1-D image, 200 pixels long, with a step edge (b) 1-D LoG filter response with σ=3 pixels

Figure 125. LoG function response at an edge [158]

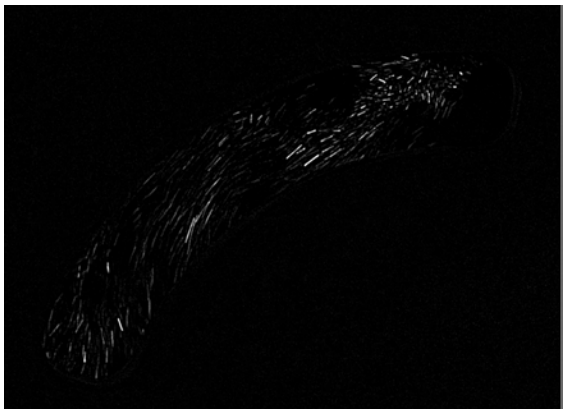
by aligning them to a 10x10 pixel grid. From these averages the tangential velocity was calculated and the flooded contour map was produced. Velocity vectors were also shown to indicate the direction of flow within each grid cell.

2.11.3 Particle Image Velocimetry (PIV).

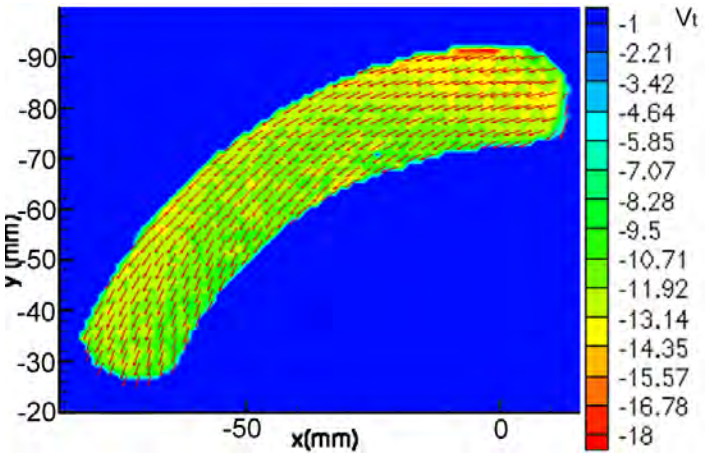
Particle Image Velocimetry (PIV) is a non-intrusive flow visualization and velocity measurement technique that requires seed particles and a laser sheet. A single laser sheet can be used for 2D measurements, however, adding additional sheets can allow for 3D flow field measurements. As described by Adrian [159], the typical modern setup of a PIV diagnostic system is comprised of a double pulsed Nd:Yag laser, beam shaping optics, seed particles, and a CCD camera as shown in Figure 127. The beam forming optics are used to direct the beam to the test location and then form a laser sheet for the analysis plane. Seed particles are introduced into the flow upstream of the laser sheet. The size of the particles must be sufficiently small to follow the fluid flow path, yet large enough to be seen with a high-speed camera when illuminated by the laser sheet. Like in PSEV analysis, a Stokes number of $Stk \ll 1$ (See Equation



(a) Raw image



(b) Filtered image to isolate streaks



(c) Fully processed V_{tan} (m/s)

Figure 126. Sample PSEV processing sequence

126) is required to ensure the seed particles follow the fluid streamlines. If $Stk \ll 0.1$, the error between the particle trace and the fluid streamline is below 1% [156]. The requirements for the scattering cross-section of the particle to ensure sufficient visibility by the camera are given by Melling [160].

The imaging camera must be synchronized to the laser pulses such that the shutter is open when the laser is illuminating the particles. Two separate images are taken during each pulse, each with different exposures. The images are then post-processed as outlined earlier in Figure 128. Each image is divided into a grid, usually an overlapping grid to increase solution resolution. Each cell of the grid is referred to

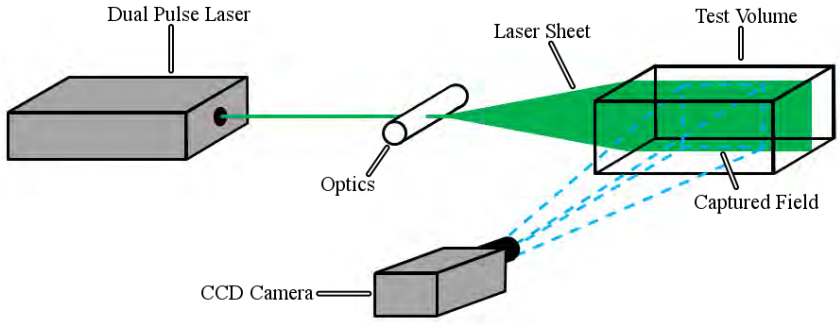


Figure 127. Basic PIV setup [161]

as an "interrogation spot". Using a Fourier transform based auto-correlation of the two image exposures in small interrogation spots enabled flow vectors and velocity fields to be established. The vectors within each interrogation spot are averaged with the resulting vector field determined to be that of the flow field. The analysis program called *DPIVB*, written by Dr. Larry Goss of ISSI, performed PIV flow field and velocity measurements using this method in the present analysis. When this program was used for PIV analysis, the pixel intensity threshold that was used in chemiluminescence velocity analysis was not used.

2.11.4 Thin-Filament Pyrometry (TFP).

Thin-filament pyrometry (TFP) is a higher fidelity temperature measurement alternative to using thermocouples. This technique uses thin filaments of β-Silicon Carbide (SiC) with a diameter of 125 μm installed in cross flow to the local flow field. This is the wire form of the same material used in PSEV, which has a high emissivity and easily emits blackbody radiation in the visible spectrum when heated above 920 K. Below that temperature the blackbody radiation is not in the visible spectrum to be recorded by a camera. SiC has a melting point of 2673 K making it suitable for very harsh combustion environments. The temperature of the filament is

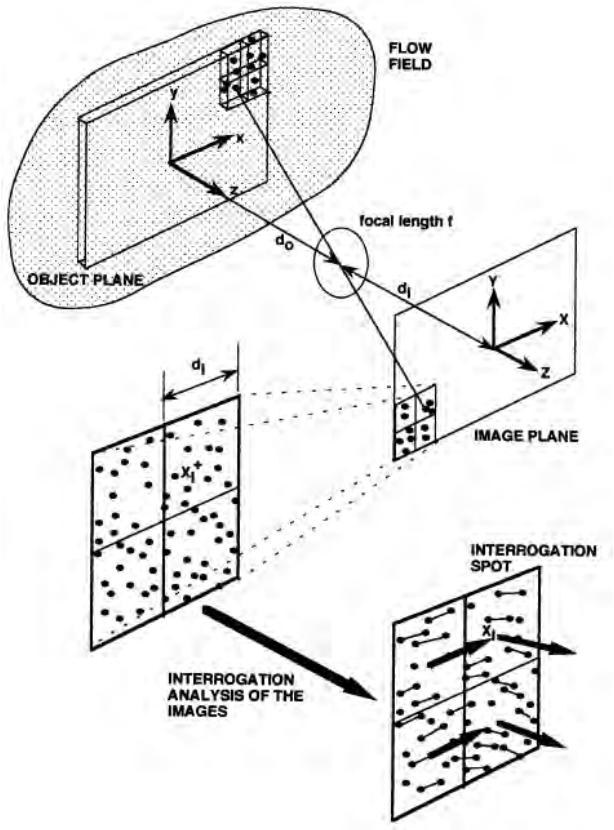


Figure 128. PIV image post-process [159]

measured from the incandescence of the heated wire, with the gas temperature calculated from the filament temperature after applying a radiation loss correction. The temporal response of the filament is around 500 Hz with a measurement accuracy of approximately 50 K [162].

TFP uses the intensity-ratio (I_R) method to determine the filament temperature [162]. This method uses a measured I_R and then compares the filament intensity at a measured temperature to the intensity at a reference temperature, as shown in Equation 132. In this equation $I_{\lambda,b}(\lambda, T)$ is the spectral intensity given by Planck's Law shown in Equation 133 at the central wavelength. The value of T_0 is the reference temperature, and C_2 is Planck's second constant; $C_2 = hc_0/k = 1.439$ x 10^4 μm· K. In Equation 133, h is Planck's constant ($h = 6.626 \cdot 10^{-34}$ J·s), c_0 is the speed of light

in a vacuum ($c_0 = 2.998 \cdot 10^8$ m/s), λ is the wavelength of emission, k is Boltzmann's constant ($k = 1.381 \cdot 10^{-23}$ J/K), and T is the filament temperature.

$$I_R = \frac{\epsilon I_{\lambda,b}(\lambda, T)}{\epsilon I_{\lambda,b}(\lambda, T_0)} = e^{\left(\frac{C_2}{\lambda}\left(\frac{1}{T_0} - \frac{1}{T}\right)\right)} \tag{132}$$

$$I_{\lambda,b}(\lambda, T) = \frac{2hc_0^2}{\lambda^5\left[exp\left(\frac{hc_0}{\lambda kT}\right) - 1\right]} \tag{133}$$

The reference spectral intensity at a known temperature can be obtained by using a calibrated pyrometer. Compared to other methods, the pyrometer allows the reference values to be obtained under the same environmental conditions as the experimental temperature which helps to reduce measurement uncertainty. A disappearing filament pyrometer is used to measure the color temperature of the filament at a fixed flame condition. The color temperature is then corrected for losses and emissivity of the SiC filament ($\epsilon = 0.9$) which leads to the reference temperature and reference spectral intensity at the specific operating condition [162].

When the temperature of the filament is known, Equation 134 can be used to calculate the gas temperature surrounding the filament [162]. The filament temperature is lower than the gas temperature due to large radiation losses compared to convective heat transfer between the gas and the filament. Conduction through the filament can be ignored due to the low thermal conductivity of the SiC. In Equation 134, T_g is the gas temperature, T_f is the filament temperature, T_∞ is the ambient temperature, σ is the Stefan-Boltzmann constant, ϵ is the filament emissivity, and h is the convective heat transfer coefficient.

$$T_g = \frac{\epsilon\sigma(T_f^4 - T_\infty^4)}{h} + T_f \tag{134}$$

2.11.5 Infrared Thermography.

Infrared (IR) thermography is a surface temperature measurement technique commonly used to evaluate film-cooling schemes or heated metallic components. An IR camera is used to capture surface temperatures based on IR emissions. This technique is often used when knowledge of the temperature on an entire surface if needed rather than discrete point measurements. The spectral emissive power (E_λ) from the surface of a gray body is given by Equation 135 in simplified form. The gray body emissive power is simply Planck's Law given in Equation 133 multiplied by π and the surface emissivity, ϵ. In this equation, $C_1 = 2\pi hc_0^2 = 3.742 \cdot 10^8$ W$\cdot\mu$m/m^2 and $C_2 = hc_0/k = 1.439$ x 10^4 μm$\cdot$.

$$E_\lambda = \epsilon E_{\lambda,b} = \frac{C_1}{\lambda^5\left[exp\left(\frac{C_2}{\lambda T}\right) - 1\right]} \tag{135}$$

Since the temperature is the desired value, yet the camera measures gray body emissive power in the IR wavelength band, Equation 135 can be rearranged as shown in Equation 136 to solve for T.

$$T = \frac{C_2}{\lambda ln\left(\frac{\epsilon C_1}{\lambda^5 E_\lambda} + 1\right)} \tag{136}$$

The surface emissivity in Equation 136 is typically unknown and varies with respect to wavelength. Additionally, the IR camera will typically pick up emissions from surrounding surfaces and heated gases. In instances where the camera is viewing the test surface though a window, additional losses in transmissivity must be accounted for. *In situ* calibration discussed by Martiny et al. [163] accounts for all additional environmental factors by embedding thermocouples in the test surface.

The thermocouple measured surface temperature(s) can then be used to calibrate the IR image by converting the measured spectral intensity to a known surface temperature. When using *in situ* calibration the measured surface temperature must cover the entire range of interest.

As discussed by Schulz [164], the placement of the thermocouple(s) on the surface is critical to an accurate calibration. The accuracy is based on the position relative to surface and flow temperature gradients. Poor thermocouple placement will result in an incorrect calibration curve and potentially large errors is measured temperature. When multiple thermocouples are used for calibration the user has the ability to remove thermocouples located in regions with large gradients, which reduces the measurement uncertainty due to poor thermocouple placement.

2.11.6 Schlieren Imaging.

Schlieren imaging is a flow visualization technique used for transparent media and relies on density variations in the flow to create shadows. The resulting image is a 2D projection of the shadows in real-time. The refractive index (n), shown in Equation 137, is used to describe the change in phase speed of a light ray when passing between two materials. Here, c_0 is the speed of light in a vacuum and c is the speed of light in the medium. For gases, the refractive index is a linear function of the gas density as shown by the Gladstone-Dale relationship in Equation 138. In this equation K is the Gladstone-Dale constant which is dependent on the gas composition and wave length of light passing through it, but typically ranges between 0.1 x 10^{-3} and 1.5 x 10^{-3} (kg/m^3) [165].

$$n = \frac{c_o}{c} \tag{137}$$

$$n = K\rho + 1 \tag{138}$$

When light rays pass between materials of different densities (refractive indices), assuming the light rays are incident to the interface at an angle (Θ), the light rays will refract according to Snell's Law shown in Equation 139, and shown graphically in Figure 129.

$$n_1 \sin \Theta_1 = n_2 \sin \Theta_2 \tag{139}$$

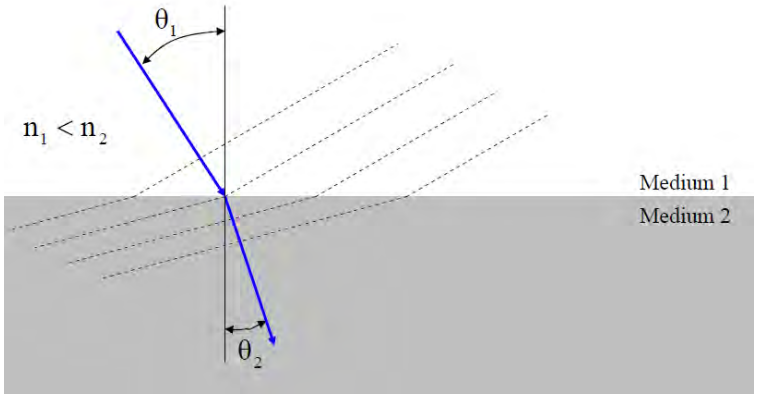


Figure 129. Arrangement for deriving the refraction angles. Adapted from [166]

A light ray traveling in the z-direction that encounters a region with a different refractive index will achieve a curvature according to Equation 140. In this equation the x-direction is orthogonal to the ray propagation. If Equation 140 is integrated once, the angular ray deflection (ϵ) is given by Equation 141. This equation shows the ray deflection is dependent on the index of refraction, but also the gradients of n orthogonal to the ray propagation direction. The deflection is also sensitive to the amount of varying density in the z-direction. These deflections are the cause of the shadows that become visible in schlieren imaging. The contrast in a schlieren system responds to changes in the first derivative of density, $\partial n/\partial x$. This is a distinction from the shadowgraph technique which has a contrast that responds to the second derivative of density.

$$\frac{\partial^2 x}{\partial z^2} = \frac{1}{n}\frac{\partial n}{\partial x} \tag{140}$$

$$\epsilon = \frac{1}{n} \int \frac{\partial n}{\partial x} \partial z \tag{141}$$

There are two commonly used schlieren arrangements; a dual-field-lens shown in Figure 130, and a z-type mirror system shown in Figure 131. Both setups require a point light source, high precision optics polished to $\lambda/8$ or better [167], parallel light rays through the test section, and a knife edge. In the z-type system the mirrors are typically symmetric, on-axis parabolas that are oppositely tilted. The knife edge is positioned at the focal point of lens 2 or the second mirror. The knife edge uniformly effects the undeflected light rays where the image intensity is reduced as more rays are cutoff. Deflected rays that are turned in the direction of the knife edge will be cutoff and the region of the image where those rays originated will appear darker than the surrounding field. Deflected rays that are turned away from the knife edge will appear lighter than the surrounding field. The orientation of the knife edge is important as schlieren setups are only sensitive to density gradients normal to the knife edge [165]. Figure 132 shows the path of two light rays that were deflected in opposite directions, how the knife edge interacts with these rays, and the resulting light and dark regions on the image.

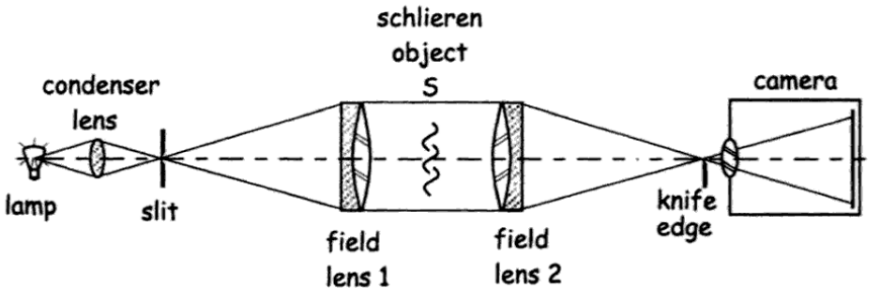


Figure 130. Dual-field-lens schlieren arrangement [167]

Since a point light source is required, a light source is typically coupled to a condensing lens followed by a slit or hole at the lens focal point to ensure a point source is developed. A high powered lamp is required to ensure sufficient light exists the slit

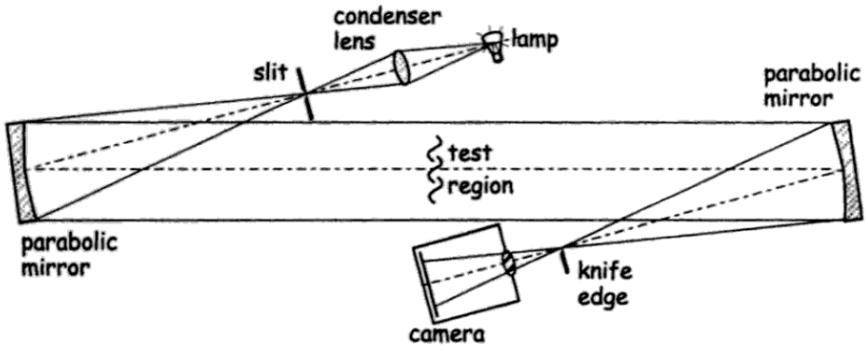


Figure 131. Z-type schlieren arrangement [167]

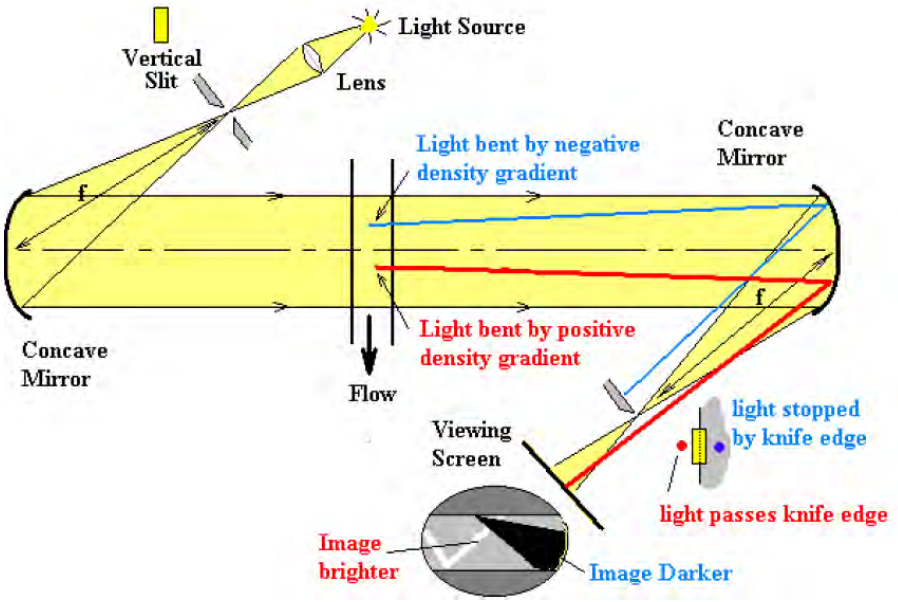


Figure 132. Z-type schlieren arrangement with light ray paths [166]

or hole. A continuous light source is required when taking high-speed schlieren imagery. A continuous light source can be found in specialized schlieren lamps and light emitting diodes (LED) that operate on direct current. Light sources that operate on alternating current flicker at approximately 60 Hz corresponding to rate of electrical voltage oscillation which would be visible on the high-speed imagery.

2.12 Limitations of Previous Research

While research has been conducted at some level on each of the areas related to the research objectives outlined in Chapter 1, there is still much room for additional research and improvements. Prior to the present analysis, no other research has been conducted on variable flow splits within a UCC operating from a common flow source. Additionally, the impact these splits have on combustion stability and dynamics are yet to be seen.

While film-cooling has been around for nearly six decades, no one has yet to look into the possibility of using cooling air entering a turbine vane through the stagnation region to feed either internal or film-cooling methods. The desire to draw in cool air at the stagnation region of a turbine vane is unique to the UCC configuration, however, this study in fluid flows has applicability to other research areas such as providing air to recessed cavity inter-turbine burners.

A number of numerical studies have been conducted on the high-g UCC, yet all of them were conducted at adiabatic conditions. These studies suffered from overestimates of combustion temperatures, unrealistic metal component surface temperatures, and larger flame volumes due to a lack of a quenching mechanism. Additionally, UCC analysis has maintained the same type of fuel injection mechanism for all of the previous studies leaving the door open to investigate the impact of alternate fuel injection schemes.

The high-g UCC has also suffered from difficulty in achieving hot gas migration from the circumferential cavity with a desirable temperature profile at the turbine inlet. This problem leaves an area of research open to investigate alternate cavity orientations to achieve the benefits of high-g combustion, without the migration issues of the current configuration. Additionally, the current UCC design would not fit inside of an engine casing as the circumferential cavity is designed to be positioned outside

of the core flow path. This geometry changes the outer mold line of an engine and would force changes to engine mounts and engine bays as well.

Finally, no research on the UCC has been conducted with air supplied from a dynamic spinning compressor and the UCC feeding a spinning turbine stage. In the case of the high-g UCC, no research has been conducted at operating pressures above atmospheric. An integration of a high-g UCC variant with a small-scale turbine engine would provide the ability to test the impact of turbomachinery up and downstream of the UCC and achieve higher operational pressures.

III. Facilities & Baseline Hardware

The combustion experiments outlined in the objectives of Chapter 1 will all be performed in the Combustion Optical Analysis Laser (COAL) laboratory at the Air Force Institute of Technology. The capabilities of this lab have evolved over the past decade as the research on the UCC has changed. Section 3.1 outlines the capabilities and equipment in the lab at the time of this publication focused on the systems needed to achieve the proposed objectives. Section 3.2 outlines the computational equipment and software available. Finally, Section 3.3 outlines the details of the UCC test rig as configured at the start of the present research.

3.1 Experimental Facilities

This section outlines the physical resources in the COAL lab that supported UCC combustion research including the air and fuel supply systems, ventilation system, laboratory control station, hardware and software instrumentation, and optical diagnostics at the time of publication.

3.1.1 Air Supply.

Air was supplied to the COAL lab by two sources and split into three separate primary feed lines as shown in Figure 133. In the figure, supply air came from the right and was distributed to the left through lines numbered 1, 2, and 3 which had diameters of 7.62 cm, 3.81 cm, and 1.91 cm, respectively. The "COAL supply" came from a dedicated Ingersroll Rand H50A-SD compressor. This compressor was rated to supply 1 kg/s at 862 kPa, but in practice it was limited to 0.1 kg/s at atmospheric conditions to maintain steady operation. It could supply a peak flow rate of 0.24 kg/s for a total of 20-25 seconds. The "AFIT Supply" came from a pair of Kaeser BSD-50

compressors that supplied air to all AFIT labs. This supply line had been found to be capable of providing air at flow rates identical to the COAL supply.

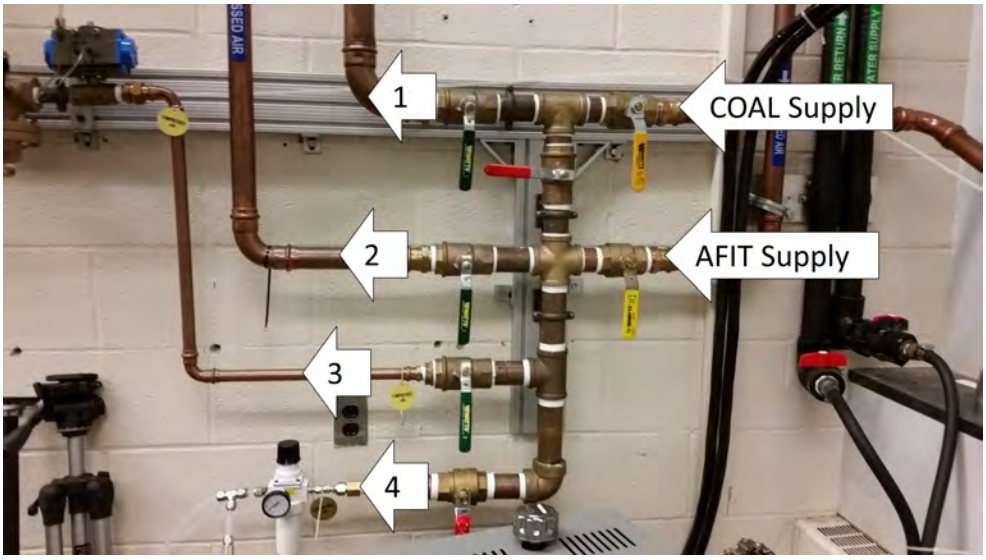


Figure 133. COAL Lab air supply lines

Each of the three primary air feed lines (labeled 1, 2, and 3) had the same type of flow control setup but used appropriately sized hardware. Each line featured a pneumatic solenoid valve (computer controlled), a pressure regulator (manually controlled), a flow meter, and a flow control valve (manually or computer controlled). Lines 1 and 2 used MaxFlo 3 flow controllers which were rated to 0.6 kg/s and 0.3 kg/s, respectively. Line 3 used a Badger valve flow controller rated to 0.03 kg/s. The flow meters were wired to three individual Eurotherm 2404 PID controllers which were responsible for the interface with the control stations LabView software.

Line 4 was added by Cottle [78] to provide air to the UCC ignition system and SiC seeder for PSEV and PIV testing. This line had a dedicated manual pressure regulator (white component with dial gauge in Figure 133) and manual valves. The portion of air from this line directed to the UCC ignition system had a computer controlled solenoid valve and used an MKS flow meter to regulate the ignition air supply to achieve proper fuel/air ratios.

At the request of personnel from neighboring labs, the muffler shown in Figure 134 was added to the Ingersroll Rand H50A-SD pressure relief. The muffler (McMaster-Carr Part Number 1213T15) threaded into the compressor pressure relief port with a 1" NPT connection and reduced the noise output by 30-35 dB. The muffler was porous enough to still allow moisture from the air dryer and compressor to exit the pressure relief lines.



Figure 134. Ingersroll Rand H50A-SD compressor pressure relief muffler

3.1.2 Fuel Supply.

The UCC could be configured to run off a number of different fuels, but the primary combustion fuel was gaseous propane. Ethylene was also used, but only during ignition. All fuels were stored in a fuel farm located outside the lab. Figure 135 shows the ethylene and propane tanks used by the UCC. The ethylene was plumbed directly from the tank to the COAL lab, however, to ensure the liquid propane stored in the tanks was provided to the lab in gaseous form, there were two in-line electric Zimmerman LPG liquid-to-gas vaporizers as shown in Figure 136. The fuel from tanks 1 and 2 was provided to vaporizer 1, and the fuel from tanks 3 and 4 went to vaporizer 2. After exiting the vaporizers the gaseous propane left the fuel farm in two 1.27 cm copper lines in the direction of the blue arrow.

As shown in Figure 137, the two propane supply lines (orange arrows on the left side) were combined and then split to two high flow rate mass flow controllers. The



Figure 135. Ethylene and propane tanks in the AFIT fuel farm

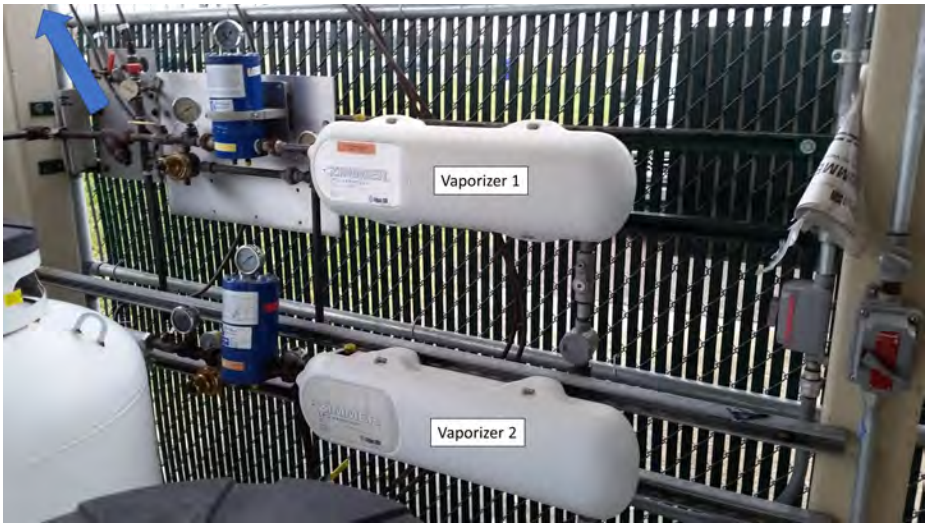


Figure 136. Propane vaporizers

first mass flow controller was a Brooks SLA 5853 with a flow rate of up to 200 standard liters per minute (SLPM). The flow rate was commanded from a four-channel Brooks 0154 interface at the control station. A selector valve (indicated by the green arrow) downstream of the Brooks controller allowed the propane to be directed to the UCC or a well-stirred reactor also housed in the COAL lab. The second controller was an Alicat MCR-250SLPM-D-40X55 also capable of flowing up to 200 SLPM which was

controlled by LabView at the control station. This controller only provided fuel to the UCC rig.

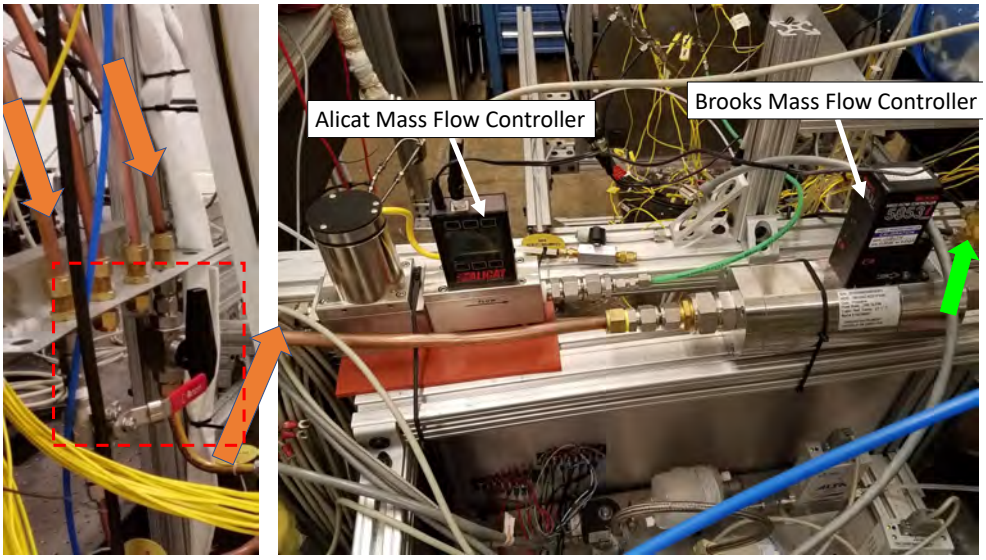


Figure 137. Propane distribution and control

The ethylene was used to fuel the torch igniter shown in Figure 138. The igniter was coupled to the UCC rig by a threaded port located in the back wall of the circumferential cavity. In this configuration the flames and hot exhaust products from the igniter directly impinged on the propane/air mixture in the UCC cavity to achieve propane ignition. Ethylene and air were provided to the igniter through MKS mass flow controllers that were controlled through the MKS interface at rates of 3.5 and 25 SLPM, respectively. These flow rates were used consistently since they achieve a self-sustaining burn in the igniter after a brief spark.

The ignition spark for the torch igniter was provided by a standard automotive spark plug. The plug was powered by a Dongan ignition transformer, model A10-LA2, which converted a 120V input into a 10,000V, 22 mA output. Power to the transformer and spark plug were controlled through a LabView interface at the control station.

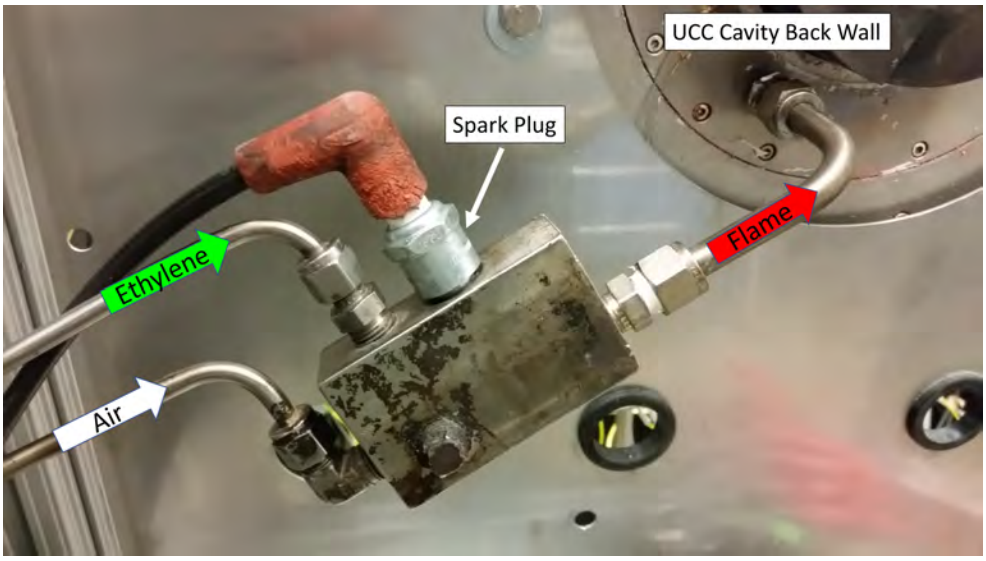


Figure 138. Ethylene fueled torch igniter

3.1.3 Ventilation.

As combustion was a primary operation in the COAL lab, there was an extensive exhaust ventilation and gas sensing safety system installed to protect researchers. The exhaust system consisted of a high mass flow rate ventilation fan and ducting to draw air from each of the three resident projects in the COAL lab; the UCC, the Film-Cooling Rig (FCR) which used the well-stirred reactor, and a materials test rig called the HVOF. The ducting from each of the three projects combined into a single duct to exit the lab. When the UCC or Film-Cooling Rig were in operation the "UCC" damper selector switch shown in Figure 139 needed to be in the ON position. This operation closed the damper to the HVOF duct to maximize the suction from the other duct branches. Figure 139 also shows that the Film-Cooling Rig duct and the UCC duct combine. The damper in the duct from the UCC or Film-Cooling Rig needed to be manually closed to only draw air from around the project in use. Additionally, when the UCC was in operation an additional booster exhaust fan (the control switch is indicated by the red arrow in Figure 139) needed to be turned on.

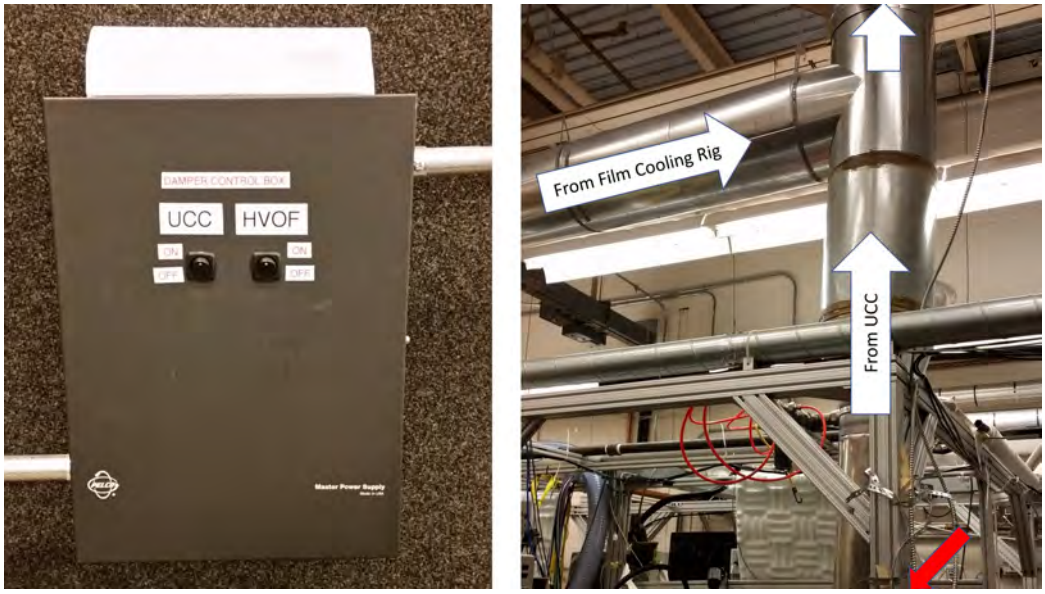


Figure 139. Damper selector (left) and UCC and well-stirred ventilation ducts (right)

The UCC was mounted to a test stand such that its exhaust could be contained in an emissions control box as shown in Figure 140. The exhaust vent duct was fitted into a hole in the aft wall of the box to extract the contained exhaust. The box was designed by Mr. Christian Schmiedel, a visiting researcher from Germany, and was highly configurable. All box walls could be removed or repositioned to enable a variety of test configurations and instrumentation. Optical access windows and grommeted instrumentation ports were also built in for visual and cabling access. This box was built in response to exhaust emissions leakage issues that were experienced at high equivalence ratios while performing specific types of testing.

The Drager gas sensing safety system was used to ensure that quantities of specific gases including carbon monoxide (CO), hydrogen (H), oxygen (O), and propane stayed within acceptable levels. The propane was measured as a percentage of its lower explosive limit (LEL), while the other monitors measured raw concentrations of the specific gases in parts per million (ppm). Figure 141 shows an example gas sensor and the control panel located in the hallway just outside the entrance to the

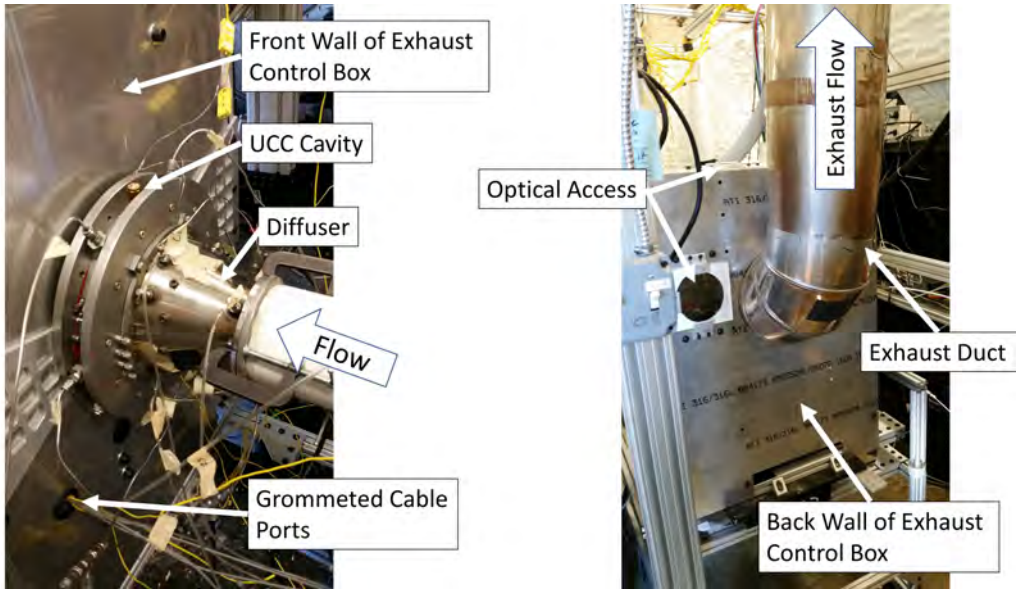


Figure 140. UCC emissions control box front side (left) back side (right)

lab. The red arrow in the figure is pointing to a colored indicator ring. The color indicated which gas that sensor monitored. A sensor with a white marker monitored CO, a red marker monitored H, and a blue marker monitored O.

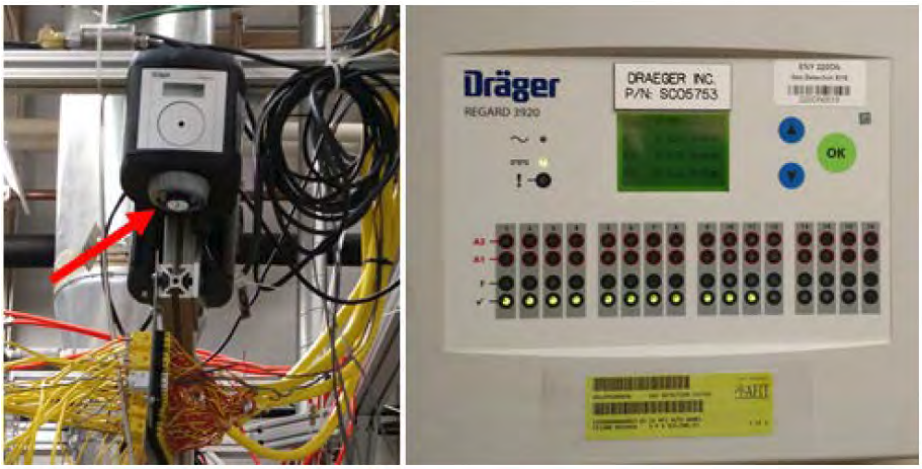


Figure 141. CO sensor above the UCC test stand (left) and the hallway control panel (right) [78]

A total of eleven sensors were installed in the COAL lab with their relative positions to the three resident projects shown in Figure 142. The black arrow and "E"

indicate the east wall. The three propane LEL sensors were located near the floor since propane is heavier than air. The remaining sensors were installed at higher positions. The yellow and red circles represent wall-mounted alarm lights. The system was programmed to provide a warning which consists of activation of the yellow warning light, illumination of the "A1" light on the control panel, and an audible low-volume high-pitch alarm noise from the hallway control panel for emissions above 20 ppm of CO. Above 35 ppm of CO, the red alarm light was activated, the "A2" indicator on the control panel was illuminated, and an extremely loud audible alarm was activated in the lab. The alarms could be acknowledged and silenced by pressing the green "OK" button on the hallway control panel. The thresholds for these alarms were well below the National Institute for Occupational Safety and Health exposure limits for short term exposure, but these values have remained because it would be costly to have the alarm company reprogram the alarm to the actual instantaneous exposure limit of 200 ppm of CO.

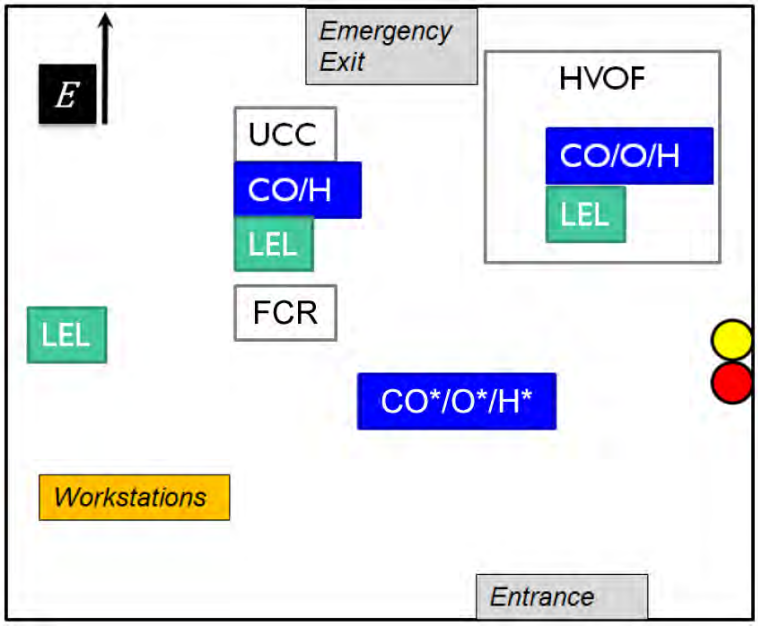


Figure 142. COAL Lab gas sensor layout. * indicates ceiling mounted [78]

3.1.4 Control Station.

The control station had interface panels for all mass flow controllers, the data acquisition system, closed circuit television (CCTV) display to monitor the test hardware, and a Raspberry Pi interface for computer numerical control of hardware with details provided in Appendix A. The Brooks and MKS interface panels were used to control the mass flow rates in their respective mass flow controllers, while the LabView interface was used to control the primary air supply, operate solenoid valves, control ignition spark, and provide feedback from thermocouples, position sensors, and pressure transducers. Additional information on components in the control station are given in Section 3.1.5.

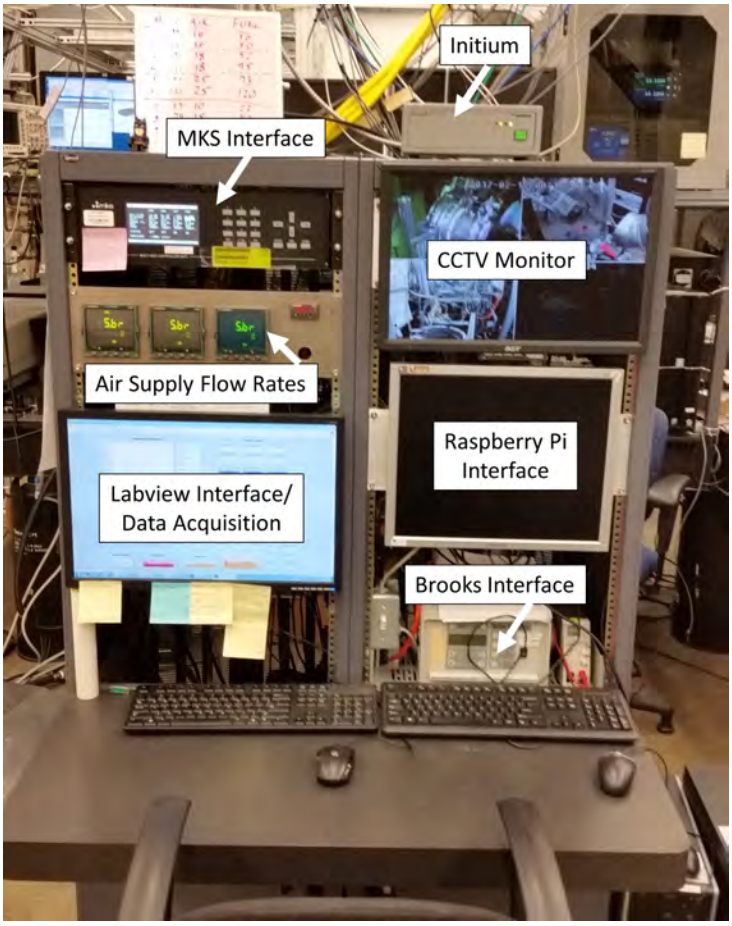


Figure 143. COAL Lab control station

3.1.5 Instrumentation.

This section outlines the hardware and software instrumentation equipment available in the COAL lab.

3.1.5.1 Hardware.

The COAL lab was wired for temperature and pressure measurement instrumentation with relay panels located near the UCC test rig. Pressure measurements were taken by a 32-channel Esterline Initium pressure scanner. The transducer panel for this device is shown in Figure 144 with the communication interface labeled "Initium" in Figure 143. Power to the Initium transducer panel was provided through the communication interface. The measurements from this system could be acquired through a standalone computer running the Initium acquisition software, or by using an Initium LabView visual interface (VI) named *Initium_MainDataAcquisition_andy.vi* on the control station computer. K-type and B-type thermocouples could be plugged into the appropriate relay panel also shown in Figure 144. These panels were directly wired to data acquisition modules at the control station and could be recorded using the LabView VI named *BrianBohan UCC RIG CONTROL11.vi*.

3.1.5.2 Software.

Labview 11.0.1 was used for control of the primary air flow rates, spark ignition, solenoid actuation, temperature feedback, Kulite pressure transducer feedback, variable geometry diffuser position feedback, thermocouple rake position feedback, and data logging. Figure 145 shows the primary UCC LabView VI that incorporated the feedback signals from the newly designed and implemented variable geometry diffuser discussed in Chapter VI, and the two-axis dynamic thermocouple rake described in Appendix B. A separate VI was required to record data through the Initium pressure

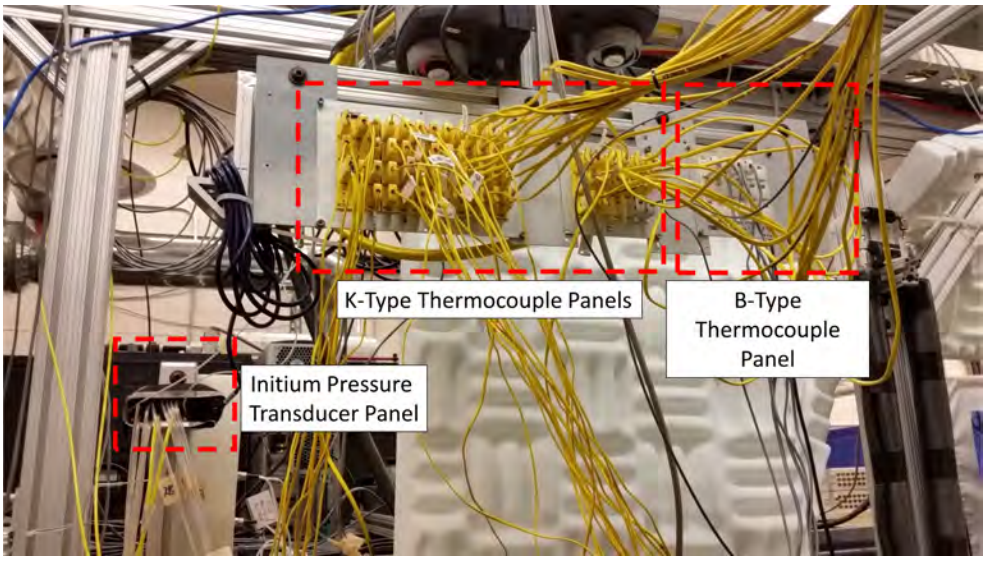


Figure 144. Initium pressure transducer panel and thermocouple panels (right)

scanner. Both VI's could be run together and both of them had data logging capability. All collected values were output to a time stamped text file for post-processing. Temperature measurements in the primary VI were taken at 10 Hz and updated to the screen at 1 Hz. The primary VI had continuous data logging capability with the temperature measurements printed to the file at the 10 Hz rate. A separate VI was developed for JetCat control and monitoring needed as part of Objective 5 and is discussed in Appendix D.

3.1.6 Optical Diagnostics.

A variety of optical equipment was available in the COAL lab for measurement in the visible and invisible spectrum to include techniques that required lasers. The following sections provide additional information on high-speed imagery, chemiluminescence, particle streak emission velocimetry (PSEV), particle image velocimetry (PIV), thin-filament pyrometry (TFP), and infrared thermography. High-speed imagery, PSEV, PIV, and chemiluminescence were used in support of Objective 3, with



Figure 145. Custom Labview VI for UCC control

infrared thermography providing vane surface temperature data in support of Objective 1. Planar laser induced fluorescence (PLIF) and laser-induced breakdown spectroscopy (LIBS) techniques were available in the lab, but were not used in the present study.

3.1.6.1 High-Speed Imagery.

To capture qualitative observations of combustion events, the COAL lab was equipped with a number of high-speed and specialty cameras. The first was a Visions Research Phantom V12.1 color high-speed camera with a Nikon 85 mm lens. Second was a monochrome Phantom V12 high-speed camera with a Nikon 85 mm lens. Third was a monochrome Phantom V16 high-speed camera. All three of these high-speed cameras were capable of recording up to one million frames per second. These cameras needed to be coupled to a computer running Vision Research PCC software to control camera settings and download the high-speed imagery.

3.1.6.2 Chemiluminescence.

For chemiluminescence the COAL lab was equipped with a LaVision HS-IRO S20, 25 mm, 10 ns, two-stage image intensifier that was coupled to the Phantom V16 high-speed camera as shown in Figure 147. IRO stands for intensified relay optics. An optical band pass filter could be applied to the lens of the image intensifier to allow spectral emissions from specific combustion product species to enter the lens. In the case of OH* analysis, a band pass filter that allowed spectral emissions in the 300 - 330 nm wavelengths to pass through was used. As described in Section 2.11.1 the intensifier amplified these emissions and produced a visible image on a phosphor screen. That image was then recorded by the high-speed camera. This capability allowed for chemiluminescence of OH radicals in the combustion chamber to be observed providing a better indication of the UCC reaction zones than a visible image alone. A software program called *DPIVB*, written by Dr. Larry Goss of ISSI, used correlation techniques of OH illuminated markers between successive frames from the high-speed chemiluminescence videos to calculate the velocity field within the combustion chamber as discussed in Section 2.11.1. The benefit of this velocity measurement technique is that it did not require a laser or seed particles. As shown in Figure 146, chemiluminescence images are produced from all available spectral emissions within the IRO field of view and have no means to distinguish the axial depth of the emissions origin. As such, one draw back to chemiluminescence velocimetry is that since it used all available illuminated markers in the flow, the axial location of the velocity measurement in the cavity was unknown.

The IRO and Phantom v16 high-speed camera shown in Figure 147 were mounted to a common rail to aid in component alignment. The hardware to attach the v16 camera to the mounting post were two 1/4-20 machine screws, while the IRO mount required two M6 x 1.0 screws. Additionally, the lens and lens mount were removed

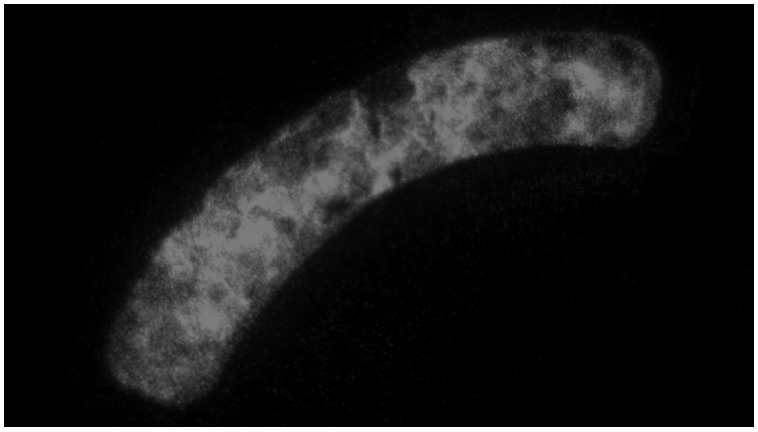


Figure 146. Example chemiluminescence imagery

from the v16 and a coupler was installed in their place using the existing camera hardware. Due to the removal of the lens from the v16, the camera was focused by adjusting the distance between the v16 and the IRO. When proper focus was achieved a pair of setscrews on the coupler locked the two components in place. The band pass filter was connected to the IRO lens using a threaded adapter to match the differing lens and filter thread diameters.

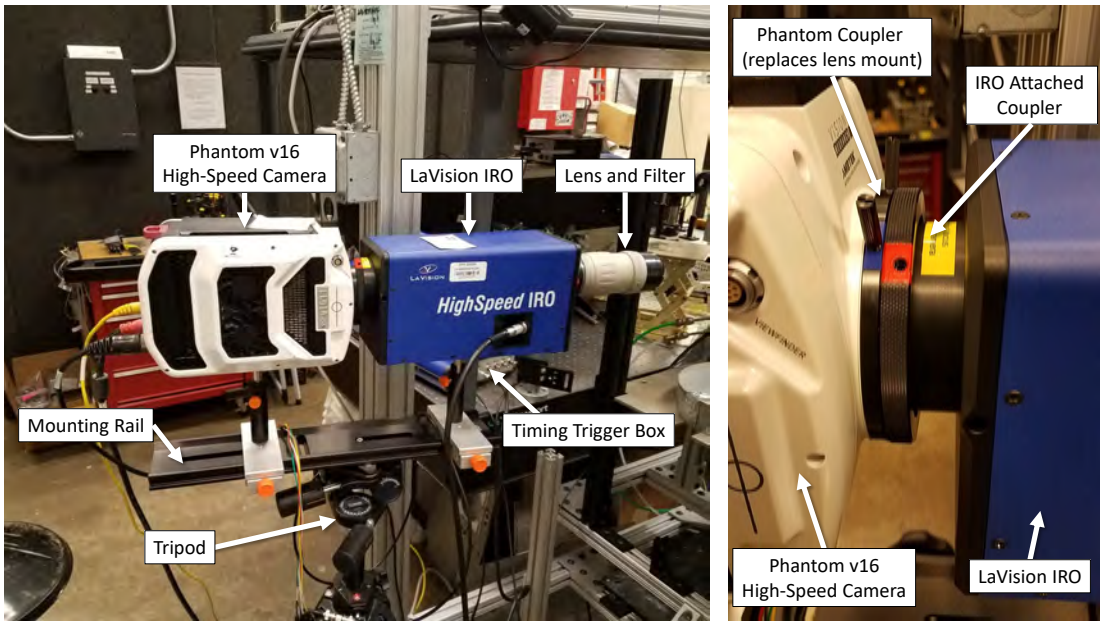


Figure 147. High-speed IRO mated to the Phantom v16 high-speed camera

Chemiluminescence measurements were taken on the UCC with two different back plates. One back plate featured an 80° arc quartz window and the other a much smaller 20° arc quartz window to work around fuel injectors in the plate. When the smaller window was used a lens doubler ring was added between the IRO lens and IRO body to magnify the incoming image. In both cases the complete assembly was positioned such that the filter was 48 cm from the optical access window on the back plate of the UCC test rig. The IRO assembly had a clear view of the window, but was positioned at a slight angle relative to the engine centerline due to the presence of the test rig exhaust duct that was aligned with the engine centerline.

The IRO and camera were connected to a timing trigger box to ensure the camera and IRO shutters operated at the same time. The wire connections between the controlling laptop, trigger box, IRO, and v16 camera are shown in Figure 148. The additional unlabeled red connector on the v16 camera provided was used for power. The "Trig In" wire on the trigger box received a signal from the green "strobe" wire connected to the large circular connector on the camera. The "I/IHead" connection was the linkage between the IRO and the Trigger box. The trigger box also functioned as an IRO setup device where the gate, delay, gain, and mode were specified. For all testing conducted in this report the delay was set to 5 ns, the delay was set to 5,000 ns, the gain was 68%, and the mode was set to "internal". The v16 high-speed camera was operated at 10,000 frames per second (fps) with a 99 μs exposure and a 1280 x 800 pixel resolution.

3.1.6.3 PSEV.

The PSEV technique discussed in Section 2.11.2 is a new capability for measuring fluid velocity and trajectory in two or three axes. This technique used a compressed air pressurized dual shaker-type seeder, shown in Figure 149, to inject silicon carbide

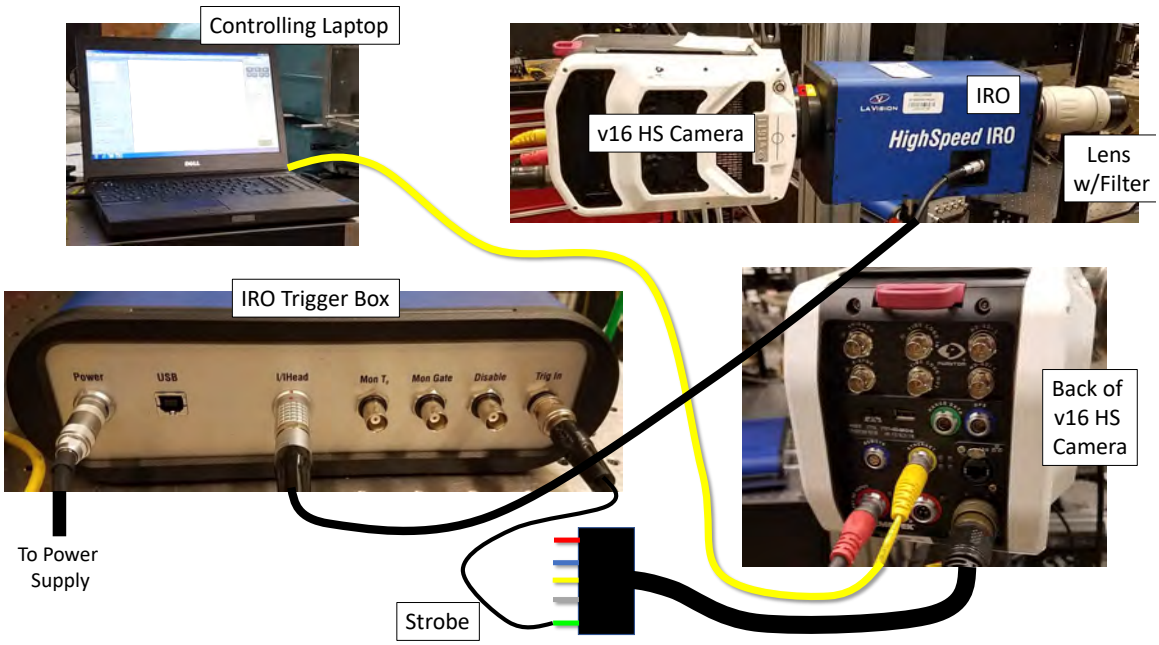


Figure 148. High-speed IRO chemiluminescence setup

particles from a drum into the UCC air inlet stream. The hot combustion gases inside the UCC caused the particles to emit blackbody radiation in the visible spectrum. The blackbody emissions were captured by a single monochrome Phantom v12 camera with an 85 mm f/1.2 micron lens and an exposure rate of 126 μs (7900 fps) positioned to look through the optical access window of the test rig as shown in Figure 150. Post-processing required the use of a free software program called "ImageJ" and software applications developed by ISSI called "Streaks" and "AverageStreaks" to calculate the fluid velocity and trajectory values. This technique provided high resolution data with a simple setup that only required a single camera. The spatial resolution of this technique is on the order of 130 μm per pixel, which combined with the exposure time, produced a conversion factor of 1.032 m/s/pixel which correlates to a velocity accuracy within 0.10 m/s.

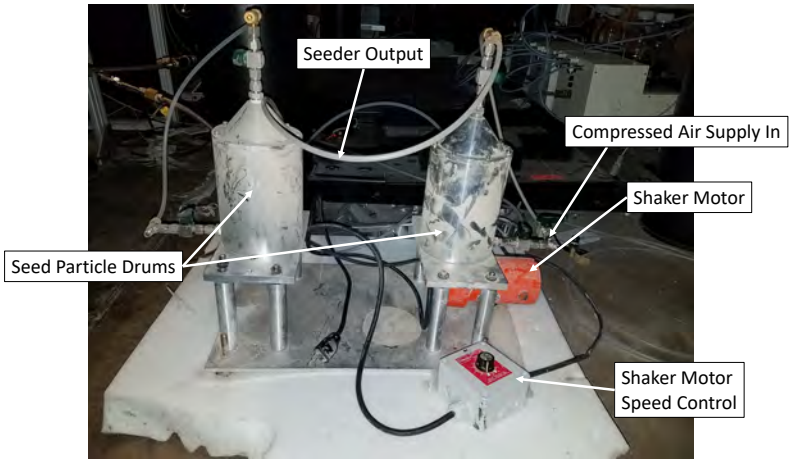


Figure 149. Compressed air pressurized dual shaker-type SiC particle seeder

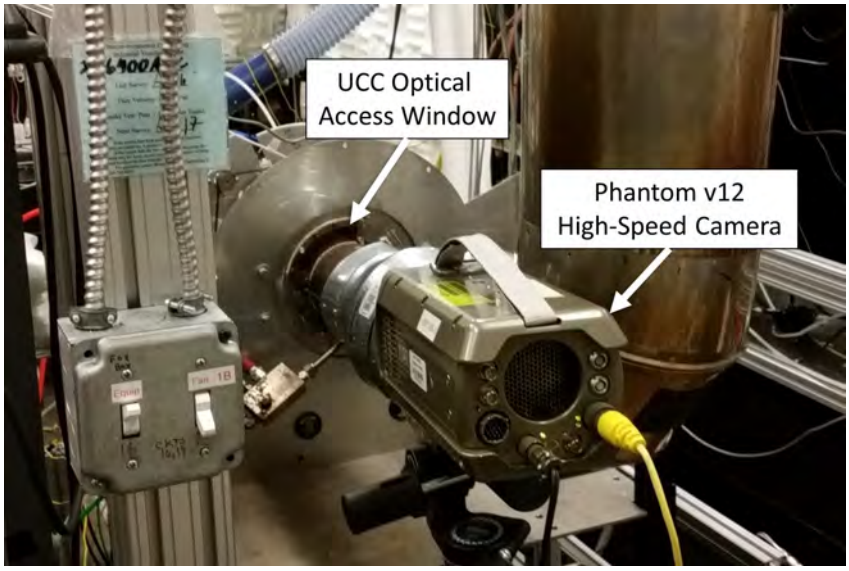


Figure 150. Orientation of v12 high-speed camera and UCC optical access window for PSEV measurements

3.1.6.4 PIV.

The COAL Lab PIV setup uses a Spectra Physics Quanta-Ray PIV400 5 Hz dual-pulsed Nd:YAG laser with frequency conversion units to produce dual 532 nm pulses. This laser system featured two laser heads that output at different polarizations inside the laser housing. The output beams from each internal laser were combined to form

a single beam prior to exiting the housing. Each internal laser put out 30mJ per pulse with the pulses between the two lasers offset by 20 μs. Visible imagery was recorded at a resolution of 1600x1200 pixels by a PCO camera with a 50 mm lens and an f/11 aperture. The camera was controlled with CamWare V3.03 software. The exposure rate on the camera was set to 33 ms with the camera taking two images in that time; a short gate and a long gate. The short gate total duration was 195 μs and consisted of a 180 μs delay and a 15 μs exposure. The long gate featured an approximate 30 ms exposure making up the remainder of the 33 ms total exposure. PIV image processing was accomplished using *DPIVB*, a correlation program written by Dr. Larry Goss of ISSI. The time resolution of this system was limited by the camera frame rate and the laser pulse frequency of 5 Hz. This system also used the compressed air pressurized dual shaker-type seeder shown in Figure 149.

The laser beam was routed from the Nd:YAG laser to the test rig in open air with the setup shown in Figure 151. The beam was routed from the source over two laser tables and turned 90° by a planar mirror. The beam was then turned vertically up a telescope and then back horizontal once at an elevation above the UCC test rig. The beam then passed over the test rig and was reflected approximately 135° back on itself to enter the UCC. Before entering the UCC, however, it passed through a single lens and was then formed into a sheet by a glass rod. The laser sheet then entered the UCC combustion cavity through two quartz windows in the outer and inner cavity rings. These two windows were obviously in line with each other, but they were also in line with the cavity back plate optical access window that the PCO camera was looking through. During testing the laser sheet illuminated the seed particles which were then visible to the PCO camera. The analysis software tracked the path of discrete particles at see how far they moved between exposures and converted that to a velocity.

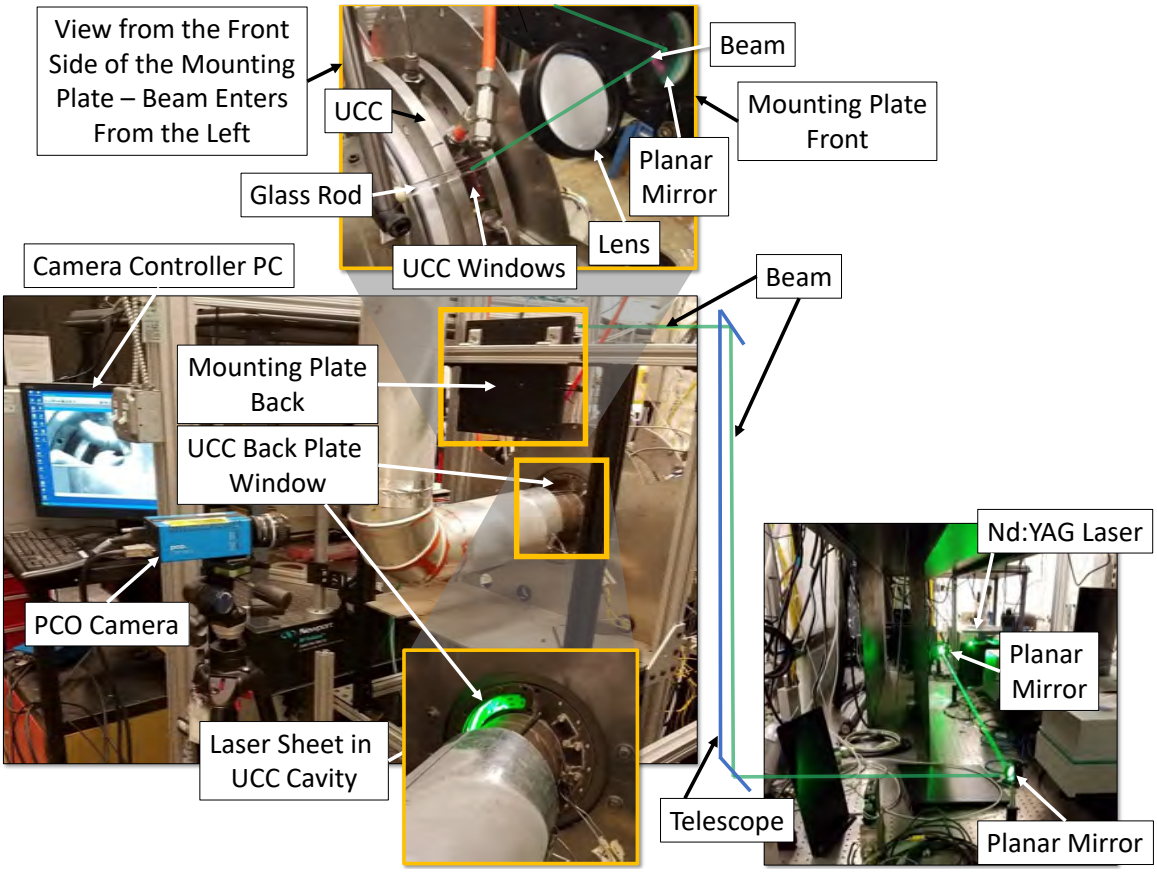


Figure 151. PIV setup, camera orientation, and beam path

3.1.6.5 TFP.

The Thin Filament Pyrometry (TFP) measurement technique discussed in Section 2.11.4 was used to collect linear temperature measurements within a HGV passage at the throat. Thin filaments of β-Silicon Carbide with a diameter of 125μm were installed in cross flow to the local flow field as shown in Figure 152. When heated to temperatures above 920 K, the filaments emit blackbody radiation which varies in intensity with the temperature of the filament. Imagery of the wires was recorded by a Bobcat Imprex monochrome camera with a 75 mm lens and 990 nm filter with 10 nm bandwidth. The cameras were positioned as shown in Figure 152 to capture imagery from the vane passage or cavity.

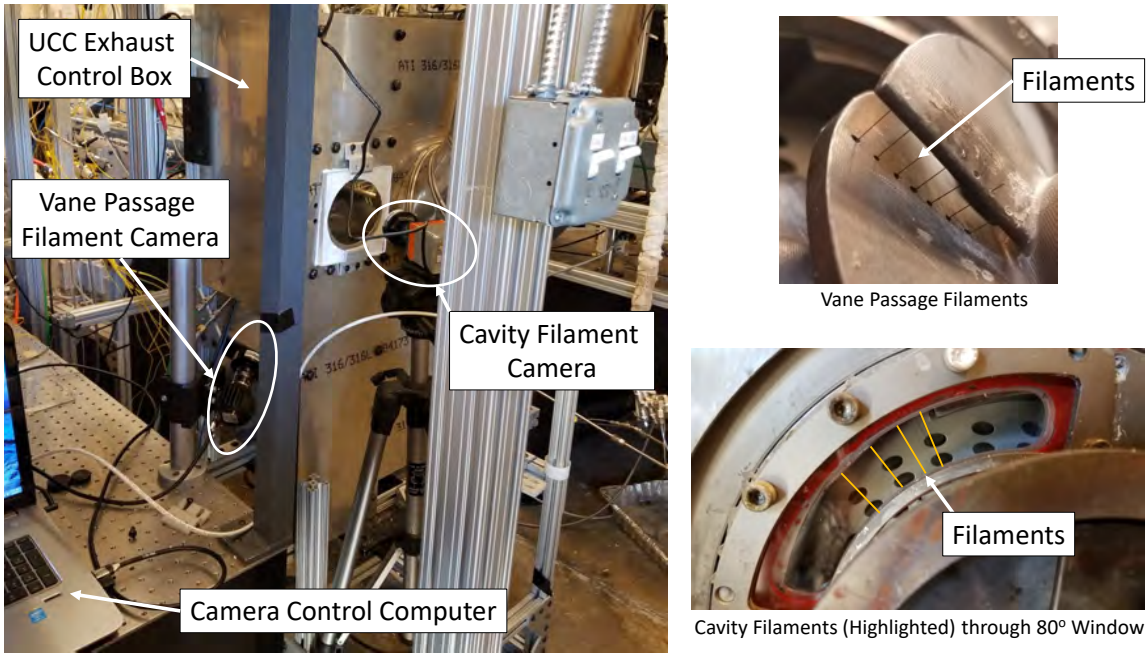


Figure 152. TFP setup, camera orientations, and filament locations

In-situ calibrations must be performed throughout testing using a disappearing filament optical pyrometer. The Spectrodyne Inc. model DFP2000 disappearing filament optical pyrometer, owned by ISSI, has been used for this calibration in the past. The optical pyrometer measures the SiC filament emission and compares it to the disappearing filament. When the intensity of the disappearing filament is the same as the SiC filament the color temperatures are the same. This balance provides the filament emission intensity at a given filament temperature. Using the pyrometer calibration data, the intensity of the blackbody emissions recorded at each point along the SiC wire can be converted into a wire temperature at each location. Heat transfer calculations need to be performed to convert the wire temperature into a gas temperature. Due to the extremely small diameter of the wires, the dynamic thermal response is on the order of 500 Hz. Also, since the heat transfer properties of a cylinder in cross flow and the emissivity of SiC are well known, the uncertainty of the temperature measurement is only 50 K.

3.1.6.6 Infrared Thermography.

The lab was also equipped with a FLIR SC 6700 IR camera system and sapphire viewing windows to capture infrared imagery. Due to high transmissivity in the IR spectrum uncoated sapphire windows that were 2 mm thick and 63.5 mm in diameter were installed in the UCC exhaust box to allow optical access and protect the camera from high temperature gases. As discussed in Section 2.11.5 the IR camera measures the radiant energy emission off of a surface of interest and requires line of sight access to that surface. In the UCC there are limited visual surfaces, however, the trailing edges of the HGV's are visible. Figure 153 shows the IR camera positioning and the sapphire window placement in the UCC exhaust box. The box can be configured with two sapphire windows on opposite sides of the exhaust duct to allow two IR cameras to each view half of the six HGV's simultaneously. In the setup shown in Figure 153 only one camera was used, with a quartz window installed in the other optical port.

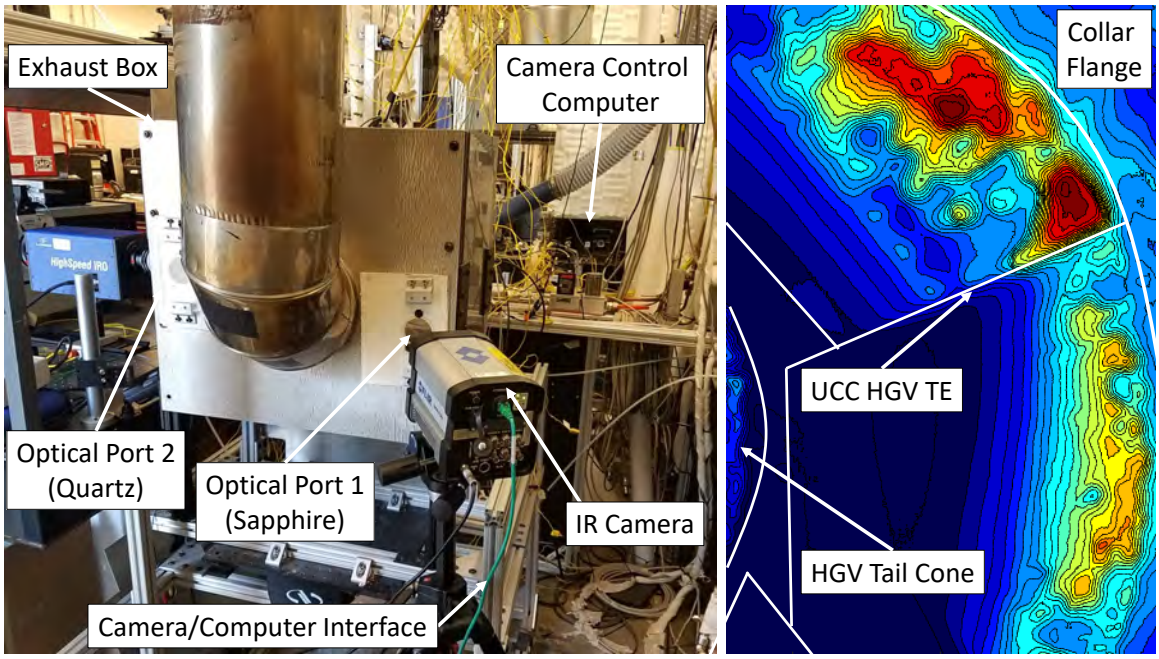


Figure 153. IR thermography setup, camera orientations, and window placements on the left, with a sample intensity count image of the HGV on the right

The IR camera was controlled by a software program called ExamineIR and was the provided software from FLIR for use with their camera. The program allowed filters to be applied to the images, record video of the IR scenes, and export the imagery data for post-processing. Since the IR camera measures radiative intensity, not a temperature, a calibration must be performed to associate an intensity with a temperature. Embedded thermocouples at several specific locations on the surface of interest provide the requisite calibration temperature measurements. MATLAB was used to average several frames of IR imagery exported from ExamineIR as comma separated values and convert the intensity to a temperature based on the thermocouple temperature readings at known locations. The MATLAB script named *IR_Combined.m* was produced by Kevin DeMarco and is discussed in detail in Appendix A of his thesis [161].

3.2 Computational Resources

This section describes the computer resources available for computer aided drawing (CAD) and computational fluid dynamics used to achieve the five objectives outlined in Chapter 1.

3.2.1 Software Tools.

Software was required for solid model development, grid generation, and CFD analysis. Solidworks 2013-2014 is a Windows based computer aided drawing program available for solid model generation. This program is capable of producing complex three-dimensional solid models with high precision. The output files from Solidworks could be used for 3D printing, or could be used in native format for grid generation. Pointwise® V18 R2 is a Linux based program available for grid generation. This program could generate structured, unstructured, and hybrid meshes using native

Solidworks part files as the model database. To reduce model size, the program is capable of generating periodic boundaries in symmetric or rotationally periodic domains. Pointwise also offers a function known as "T-Rex", which can create three dimensional anisotropic tetrahedrals extruded off selected surfaces to create prisms in the boundary layer upon export. These tetrahedrals could be made from structured or unstructured surface meshes and can be generated off perpendicular walls where the cells would overlap. This feature offers an automated method to generate grid refinement in the boundary layer. ANSYS FLUENT® version R16.2 is a Linux based program that provides computational fluid dynamics flow solving and post-processing capabilities. FLUENT could be used for steady-state or transient analysis and has models for turbulence, heat transfer, reacting flows, multi-phase flows, radiation, and acoustics. This program also has parallel processing capability to greatly reduce computation time by performing calculations on many processors simultaneously.

Appendix A lists several freeware software tools that were needed to enable computer numerical control of hardware in the variable diffuser and thermocouple rake.

3.2.2 High-Performance Computing Hardware.

The COAL lab was equipped with an HP Z820 Linux workstation with Pointwise® and FLUENT® installed. The workstation was configured with two Intel Xeon E5-2690 v2 processors which contained ten cores each. Each core had two threads resulting in 40 total processing threads for parallel computing. There was 256 GB of 8-channel DDR3-1866 MHz ECC Registered SDRAM installed. This quantity of memory was sufficient to process complex detailed chemistry reacting flow models with nearly 70 million cells. Graphics were handled by an NVIDIA Quadro K6000 video card. Three similarly configured workstations with 48 available processing threads each were available in the AFIT Linux laboratory.

3.3 Baseline UCC Test Rig

This section describes the UCC hardware as inherited at the start of research. This configuration is consistent with what Cottle [78] and Gilbert [168] describes as UCC "Version 3", or "v3". A cross-section of the v3 UCC is shown in Figure 154, which also includes dimension labels of primary dimensions related to the circumferential cavity. The dimensions for the labels in Figure 154 are given in Table 6 along with specifications of the air driver holes. The orientation of the figure is such that air enters the diffuser from the left-hand side and exits to the right. An overall assembly drawing of the v3 UCC is shown in Figure 155. In this view core air also flows from left to right with fuel and air swirled around the circumferential cavity in the clockwise direction. UCC Version 3 featured a fixed position common flow source diffuser, upgraded air inlet driver with compound angle holes, an enlarged circumferential cavity, and a channel plate.

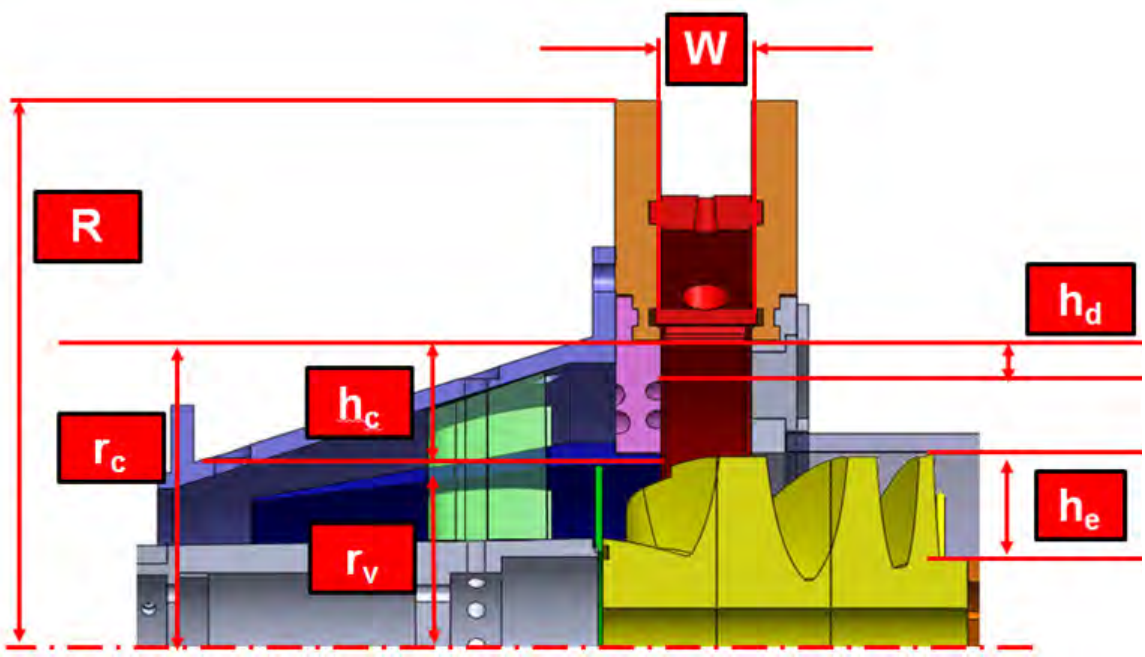


Figure 154. UCC Version 3 cross-section with dimension labels [78]

Table 6. UCC Version 3 Dimensions

Measurement		Dimension (cm)
Ring Dimensions	R	15.2
	W	2.54
	r_c	8.50
	h_c	3.17
	r_v	5.33
	h_e	3.0
Air Drivers	Hole Count	48
	Hole Angle	55 deg
	Hole Diameter	0.45
	h_d	1.05

The UCC Version 3 diffuser featured a fix position middle diameter splitter ring shown in blue in Figure 154 and green in Figure 156. Three versions of the middle diameter were made with different leading edge diameters relating to an 80/20, 70/30, and 60/40 core to cavity area split ratio. The middle diameter was supported by 12 support vanes that were connected between the inner diameter centerbody and the outer diameter. A channel plate [78] was incorporated into the design to create a pressure drop and force more air to the diffuser outer passage and into the circumferential cavity. The channel plate caused the air mass flow split between the core and cavity to approximately match the area ratio split for the 70/30 middle diameter. The drawback to the channel plate is that it created a pressure loss in a combustion system intended to minimize losses.

The diffuser was coupled to the air supply line using an adapter made from off-the-shelf PVC components and glued together. Due to the connection method of the PVC fittings the walls of the adapter included a forward and backward facing step just upstream of the inlet to the diffuser as shown in Figure 157. The adapter was coupled to the diffuser outer diameter forward flange using three c-clamps as seen in Figure 140. The seam between the adapter and diffuser was sealed with Ultra Blue

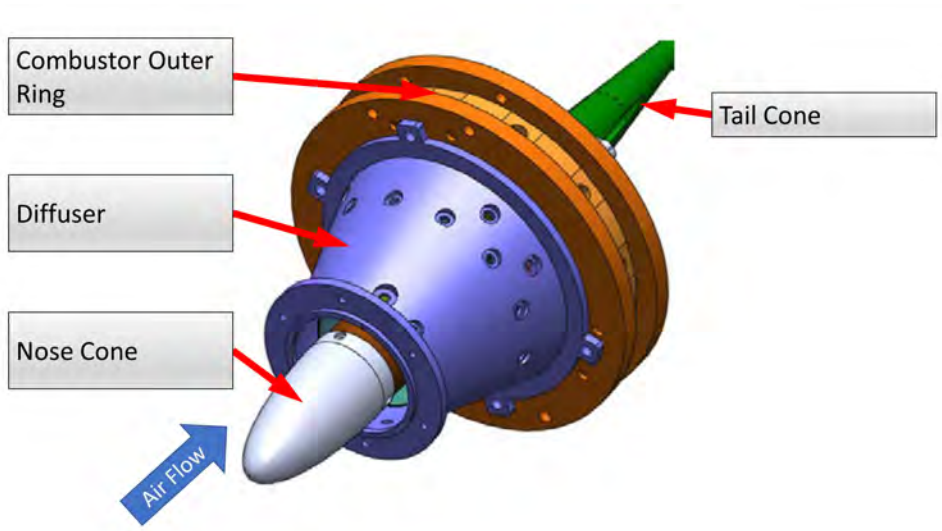


Figure 155. UCC Version 3 [78]

RTV sealant discussed in Section 3.3.1.

Figure 158 shows a front view of the v3 UCC with the diffuser removed. From this view the air driver plate is clearly visible. This plate contained 48 evenly spaced 0.45 cm diameter holes. The holes were drilled at compound angles giving them a tangential angle, θ_t, of 55° relative to the UCC centerline, and a 10° radial angle, θ_r, toward to OD of the circumferential cavity. This hole orientation was shown to increase residence time of fuel in the circumferential cavity.

The back wall of the v3 UCC is shown in Figure 159. This wall featured an 80° arc optical access window. The window was made of 1.27 cm thick quartz and was retained by a metal plate that was screwed onto the back wall. The plate had the same shape as the window but was larger to accommodate screw holes outside the dimensions of the quartz. Additionally, the center portion of the plate was cut out to allow visual access through the window. This attachment method allowed the quartz window to expand freely within a slot to prevent cracking. Ultra Copper RTV sealant and exhaust sealant discussed in Section 3.3.1 were used to seal the window to the rig to prevent leaks from the circumferential cavity.

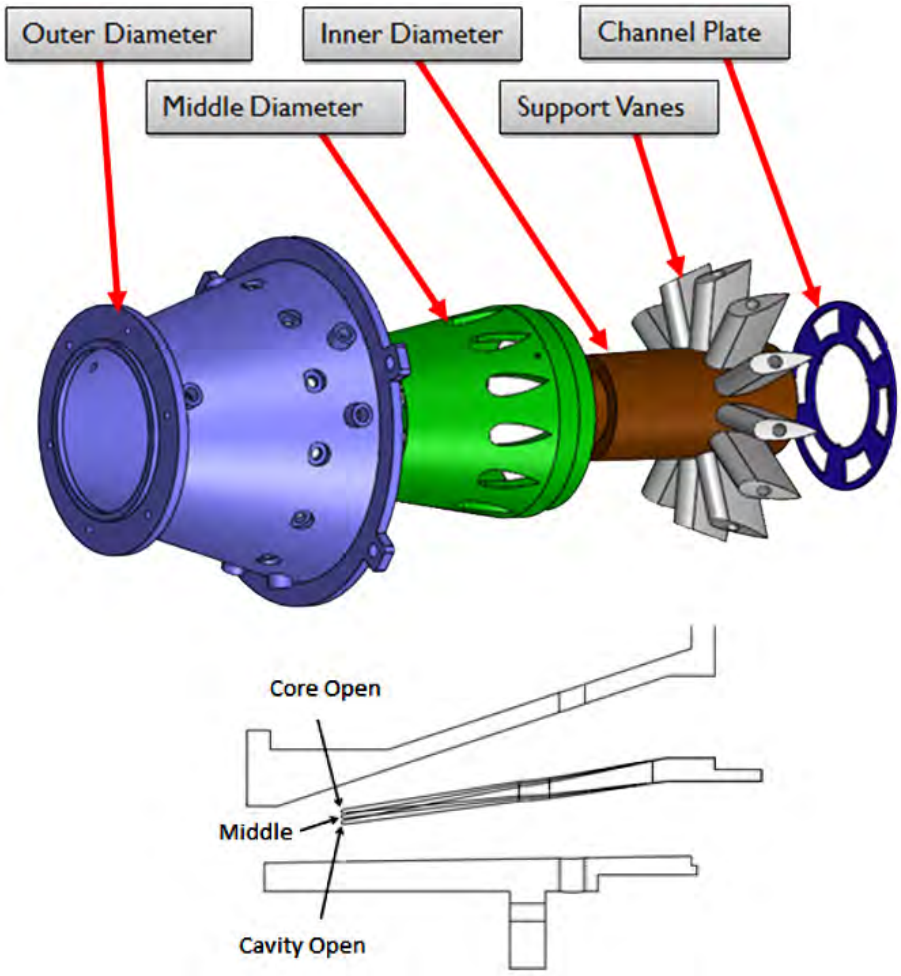


Figure 156. UCC Version 3 diffuser exploded view (top) and middle diameter variations (bottom) [78]

The back wall also contained three interchangeable instrumentation blocks. These blocks allowed entry of thermocouples and pressure ports into the cavity without having a number of discrete holes through the wall. A total of four thermocouples or pressure ports could be installed in each block. If no instrumentation was required at a particular block location, solid blank blocks could be used to fill the hole. Each block was secured to the UCC back wall with two screws positioned diagonally across the block face. Exhaust sealant discussed in Section 3.3.1 was used to seal the seams between the blocks and the wall, and the instrumentation ports and the block.



Figure 157. UCC Version 3 air supply to diffuser adapter photo (left) cross-section (right) [78]

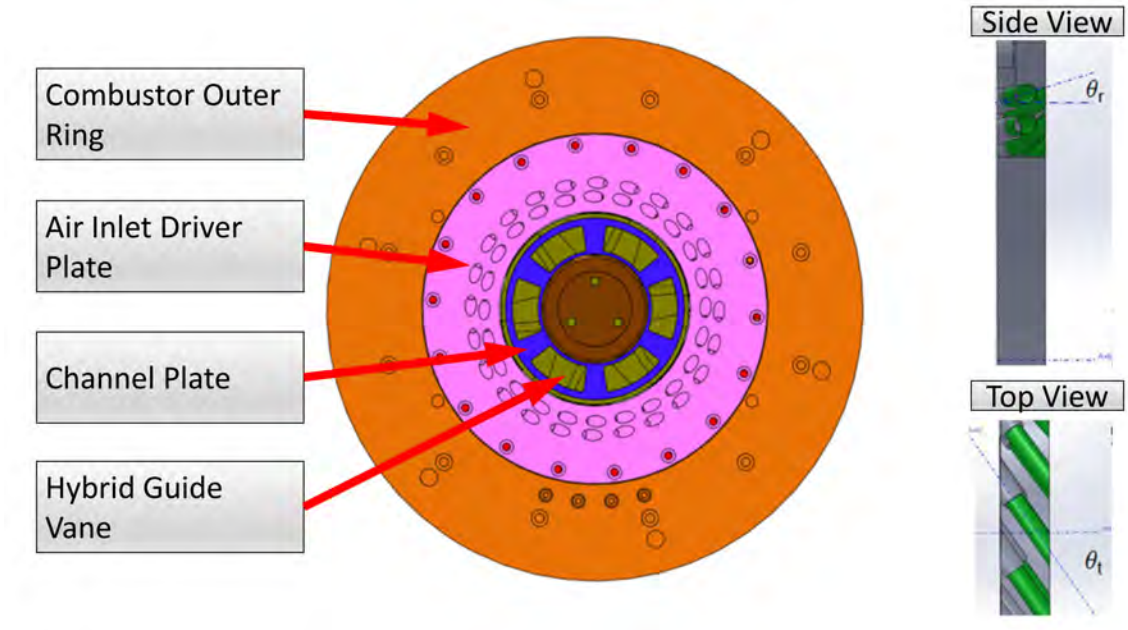


Figure 158. UCC Version 3 front view (with diffuser removed) showing the air driver ring plate (left) and compound hole details (right) [78]

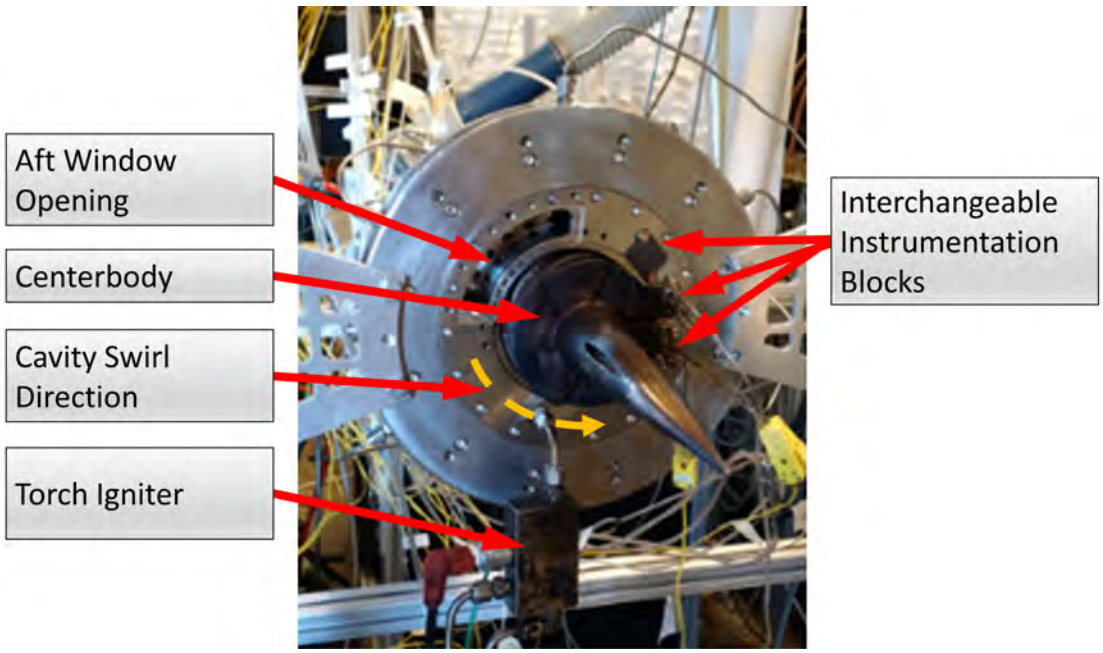


Figure 159. UCC Version 3 back wall showing optical access window and cavity instrumentation blocks [78]

The hybrid guide vane was used to help migrate hot gases from the circumferential cavity and to turn the flow to a representative turbine inlet angle. The design shown in Figure 160 uses the Wilson and Polanka [71] low-loss centerbody (LLCB) scoop discussed in Section 2.3.6 with rectangular vanes extruded along a helix. The original intent of the hybrid guide vanes, as conceived by Bohan [6], was to accept swirling flow from the compressor and turn the flow to the desired turbine inlet angle. The hybrid guide vane variant used in UCC v3 had a modified leading edge to accept axial or nearly axial flow from the diffuser.

Fuel was injected into the circumferential cavity at six distinct locations spaced 60° apart. Each fuel injection location was positioned radially in-line with the leading edge of the hybrid guide vane. At each of the six injection locations, the fuel was distributed axially across the cavity by a fuel baffle shown in Figure 161. The left image of Figure 161 shows the assembled baffle in the combustion ring, with the other



Figure 160. UCC Version 3 low-loss centerbody hybrid guide vane [78]

three images showing the baffle components and installation process. Fuel entered the baffle through a single hole axially centered on the combustor ring. An "I" bar was positioned below the inlet holes to try and disrupt the incoming fuel jet and disburse the fuel across its length. An eight-hole plate was installed below the "I" bar to allow the fuel to exit.

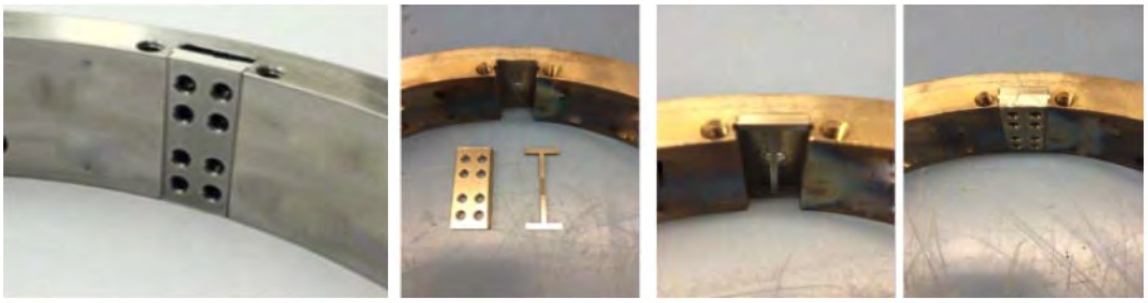


Figure 161. UCC Version 3 fuel baffle assembled (left) and installation of fuel baffle components (right three images) [78]

The Version 3 UCC incorporated mechanical seals in an effort to reduce flame and emission leakage from between component seams. Figure 162 shows a cross-section

through the combustor which highlights the interlocking seals. It can also be seen that the tabs on the air inlet driver plate, inner combustion ring, and back wall plate are in-line. This orientation allowed for screws from the front to join the air inlet driver plate, combustor forward mounting plate, and inner combustion ring together. Screws installed from the rear joined the back wall plate, combustor aft mounting plate, and inner combustion ring together. The holes in the inner combustion ring were threaded while all other holes were clearanced. To supplement the mechanical seals, Ultra Copper RTV, discussed in Section 3.3.1, was used in the seams as well.

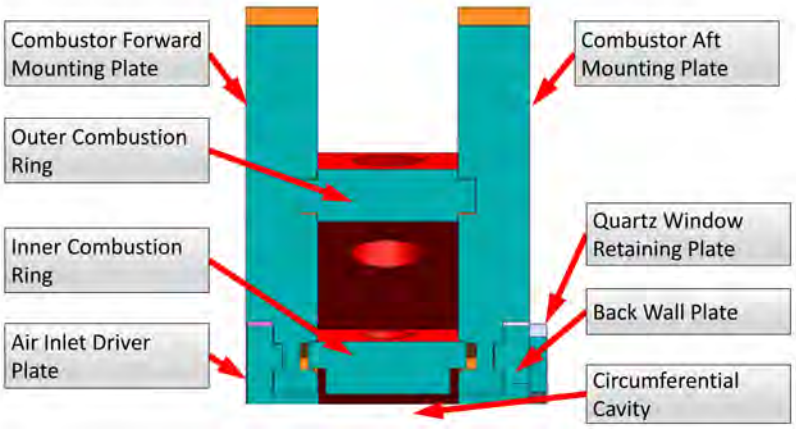


Figure 162. UCC Version 3 mechanical seals [78]

3.3.1 Sealants.

Ensuring a good seal between components in the UCC is difficult due to the combination of materials, the geometry of the hardware, and high temperatures. If not sealed properly, flames and exhaust emissions can leak from seams around optical access windows, instrumental blocks, and fuel injectors under certain operating conditions. Cottle [78] and Gilbert [168] tried several dry gasket options, a preferred sealing technique of AFRL, with no success. They were successful at sealing these joints using the liquid gasket makers and exhaust sealant shown in Figure 163.



Figure 163. "Wet-seal" sealants used in the COAL lab

Working through the materials in Figure 163 from left to right is a lower temperature "Ultra Blue", higher temperature "Ultra Copper", and a high temperature muffler and exhaust sealant. The Ultra Blue is an RTV silicone sealant with a temperature range from -54 C to 260 C. The Ultra Copper is also a silicone based RTV but has a temperature range of -54 C to 343 C. The exhaust sealant is rated for continuous exposure to temperatures up to 538 C, and intermittent exposure to temperatures up to 815 C. Unlike the silicone based RTV sealants which remain pliable after cure, the exhaust sealant dries rigid making it more likely to crack as hardware seams expand.

IV. Objective 1: Stagnation Cooling Study

Determine the viability of UCC vane cooling using coolant extracted from the core flow through the vane stagnation region

The purpose of this objective was to determine the ability to provide UCC vane cooling using coolant extracted from the core flow through the vane stagnation region. The cooling methods included several variations of internal cooling and two film-cooled variants to determine if there was sufficient pressure head inside the vane to cause coolant to exit through film-cooling holes. The majority of the work performed for this objective was computational and intended as a proof of concept to show that the unique orientation of components in the UCC could enable a unique cooling scheme for the hybrid guide vane. A three-dimensional conjugate heat transfer method in the FLUENT® flow solver was used. When a viable solution was computationally found that allowed for surface temperature reductions and sufficient internal pressure to enable film-cooling, the vane was manufactured and experimental testing was conducted.

4.1 Objective 1 Background

To the knowledge of the author this type of cooling method has not been researched or previously published. As a result, the background research focuses on the basic environment that this type of cooling system operates in, i.e. an environment more typical of a combustor liner than a turbine vane. However, this cooling scheme is also subject to the pressure distribution around an airfoil, specifically in an airfoil cascade.

The UCC hybrid guide vanes are in many ways analogous to the traditional combustor liner shown in Figure 8. The passages between the vanes serve as secondary

combustion chambers if there is still reactive species remaining in the flow exiting the circumferential cavity. Also, since the vanes are semi-airfoil shaped, and the passage constricts from leading edge to trailing edge, there is a pressure reduction as the fluid convects downstream and accelerates. Additionally, the HGVs are exposed to different temperatures in different zones on the vane.

The combustor liner is also exposed to a variety of temperatures and experiences a similar pressure drop. [1] The outer portion of a combustor liner is exposed to cool air exiting the compressor while the inside is exposed to hot combustion products. Compressor air is distributed into the different zones of the combustor through the liner walls by balancing pressure drops through the system and controlling hole sizes in the casing to ensure the correct amount of air is delivered in each combustion zone. The corrugations in the joints of the liner serve to bring in cool air along the wall for cooling purposes. Within the combustor there is an inherent pressure drop due to the physical geometry and forcing high-pressure air through a series of holes. Additionally, there is a pressure drop due to heat addition from combustion. Wilson [71] quantified the pressure drop across a traditional combustor at 3.5% of the inlet pressure. Including the compressor exit guide vanes, compressor exit diffuser, traditional combustor, and turbine inlet guide vanes which are all components integral to the UCC, the pressure drop across comparable hardware would be approximately 8.7%.

Section 2.9.2 discussed the pressure distribution around a generic airfoil as well as the pressure distribution resulting from air flow through a constriction like that seen in a turbine cascade. The basic equations of heat transfer for conduction and convection, including the relationships relating to film-cooling, were discussed in Section 2.7. Since the likelihood of finding unburned reactive species in the fluid around the UCC vane film-cooling holes is very high, secondary reactions in the cooling film must

be considered as discussed in Section 2.8. Finally, since the UCC turbine vane is a protrusion in cross flow relative to the UCC core flow, secondary flow structures must be considered as discussed in Section 2.5.

As shown in Figure 164, the majority of the heat load to the HGVs was focused on the suction side of the vane. Due to the direction of flow in the circumferential cavity, the hot gases exiting the cavity impinge on the suction surface of the vane and only make contact with the pressure surface much further downstream. This pattern simplifies the cooling requirements on the vane.

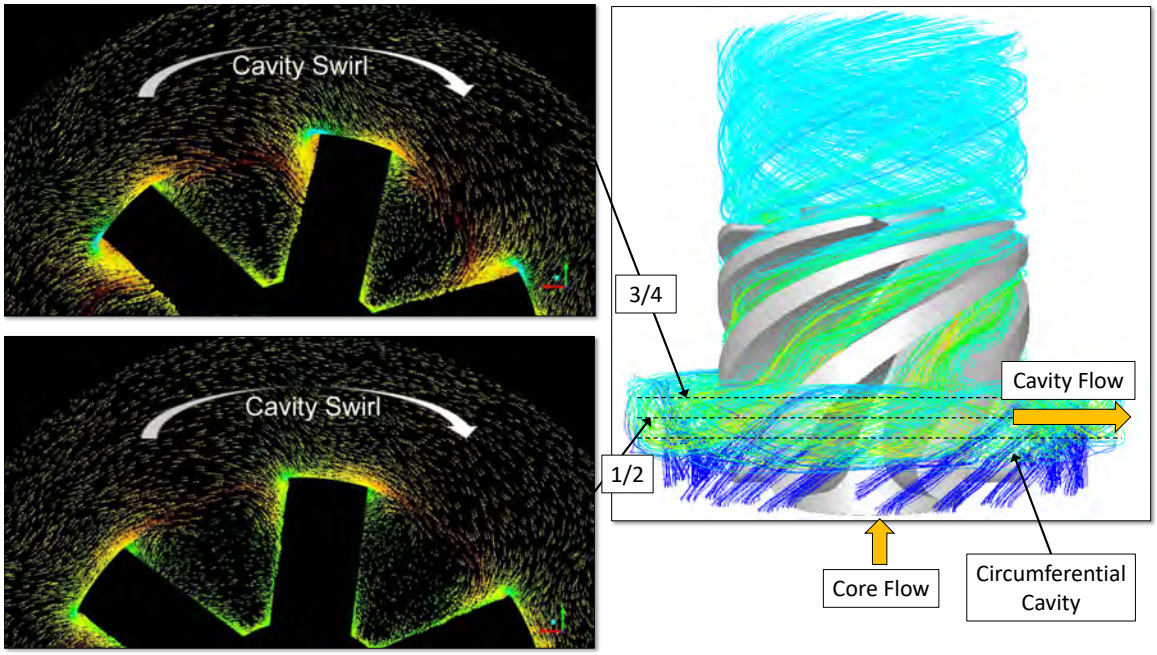


Figure 164. Flow patterns of hot gases from the circumferential cavity interacting with the HGV

4.2 CFD Case Setup

The computational analysis was performed numerically on a three-dimensional domain and included a complex fluid flow, reacting chemistry, and conjugate heat transfer to the UCC HGV. This process allowed for heat exchange between the fluid

and the solid and vice versa. Away from the interface, the conduction in the solid and the advection in the fluid were solved independently. For this problem, both the solid components and the fluid region were gridded with a volume mesh. The two volume mesh blocks were assigned as a fluid and a solid prior to exporting the mesh from the pre-processing software. Conjugate heat transfer was only considered between the surfaces of the turbine vane and fluid. All other walls were treated as adiabatic.

The UCC test rig used a common flow source to supply air to the core and cavity flow paths as shown in Section 3.3. The computational domain for this investigation was simplified to have independent core and cavity inlets. The core inlet had an inner radius of 3.05 cm with a channel height of 1.98 cm. The cavity inlets were circular with a diameter of 0.45 cm and entered the circumferential cavity at a 55° relative to the engine centerline. The HGVs were modeled along with the circumferential cavity and an entrance and exit passage to establish the correct flow field around the vanes. The HGV had a leading edge span of 2.06 cm and an axial chord of 8.8 cm. The circumferential cavity had an axial length of 2.54 cm and a height of 3.17 cm above the vane. The dimensions specified above matched the physical hardware at the time of the analysis. Additionally, due to the periodic nature of the UCC geometry, the domain was further reduced using rotationally periodic boundaries. This simplification allowed for a single vane to be isolated, yet retain the ability to reassemble the full geometry as needed. Two sets of periodic boundaries were created; one for the solid that was joined at the HGV hub and one for the fluid. Figure 165 shows an example of a CFD case domain. In the figure, only one of each of the periodic boundaries are labeled. The other corresponding boundary is positioned 60° rotated around the z-axis. The orange arrows in the domain indicate the direction of flow through the core and the green arrow indicates the flow direction in the circumferential cavity.

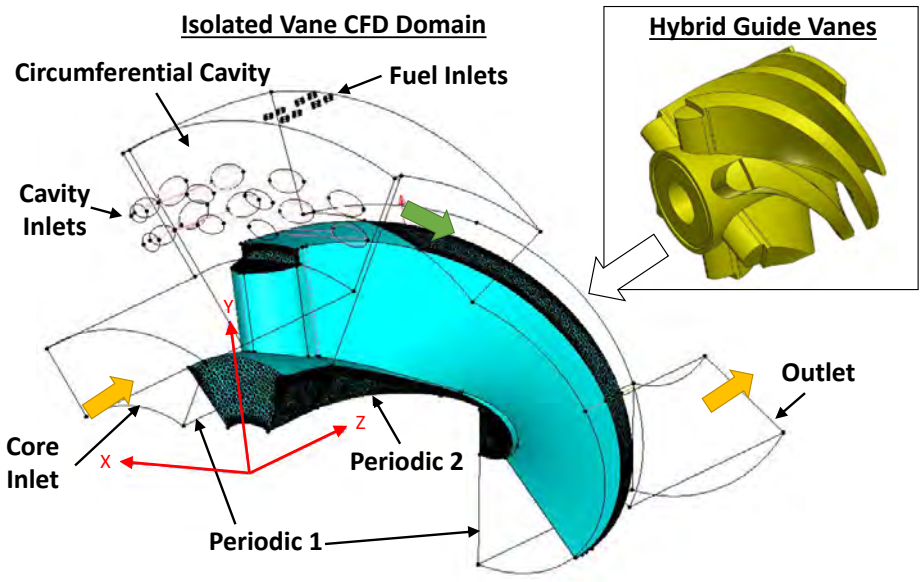


Figure 165. Representative test domain. Solid vane is shown shaded and gridded. The boundaries of the fluid domain are outlined in black wireframe

Several vane variations were examined as part of this study. A top view of the different internal variations are shown in Figure 166. The first variation was a baseline solid metal vane as shown in Figure 166a. The second variation was a hollow vane with an inlet in the stagnation region (166b) and a trailing edge slot shown in Figure 166e. Third was a hollow vane with an inlet in the stagnation region and a trailing edge slot with a central plug that extended through the entire vane span (166c). Figure 167 shows an isometric view of Vane C with transparent walls allowing the internal features to be displayed more clearly. The plug was positioned 5.84 mm from the leading edge inlet and 20% closer to the pressure side of the vane to allow greater airflow to the hotter suction side. Additionally, the tip material of the vane was made approximately three times thicker than the material thickness of the hollow vane tip. The last variation, 166d, was the same as the previous, but the internal vane plug was positioned closer to the stagnation inlet at a distance of 2.29 mm. In all cases the vane inlet was rectangular with an area of 0.839 cm^2. Two variations of trailing

edge slot exit areas were tested; a baseline area of 0.587 cm^2 (70% of the inlet area), and a smaller area of 0.477 cm^2 (56% of the inlet area). The smaller exit area was tested with domains c and d only. The vane exterior wall thickness for all hollow and plugged vane variants was 1.27 mm.

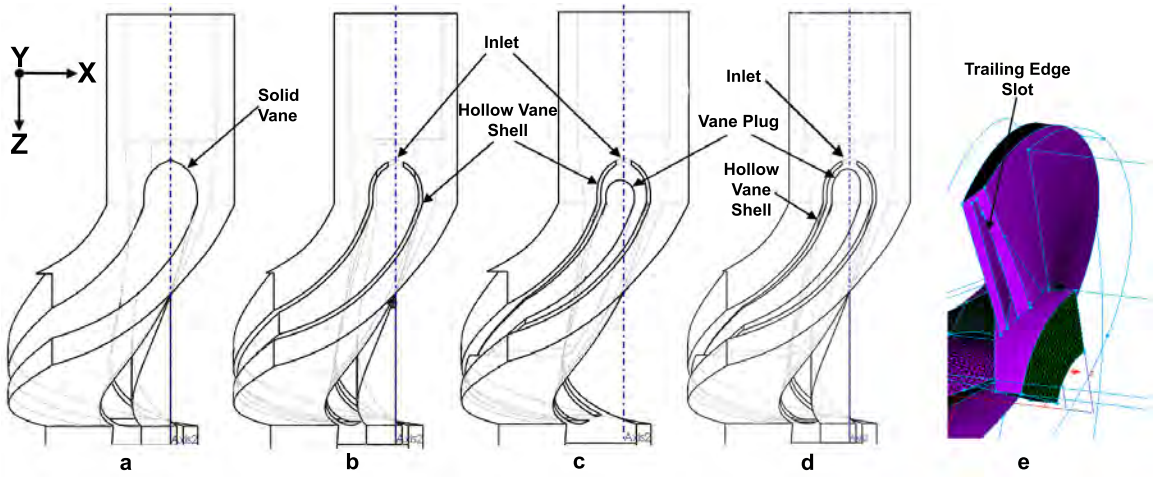


Figure 166. Test domain top view showing internal vane variations: a) solid vane, b) hollow vane, c) hollow with offset plug, d) hollow with offset plug closer to inlet, e) trailing edge slot

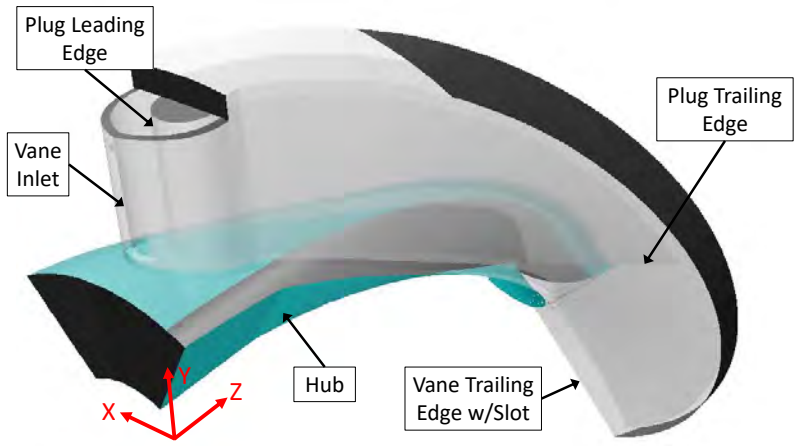


Figure 167. Isometric view of vane c with transparent walls to view the details of the internal plug

Two additional domains was created by adding eight 0.762 mm diameter cooling holes drilled at a nominal 30° angle into the suction surface of vane variations c and

d with the smaller exit area as shown in Figure 168. Two sets of cooling holes were positioned on the suction surface. The first set, labeled Holes 1 - 3, were positioned at 4.5 cm radially from the engine centerline between 25 and 45% axial chord. The second, labeled Holes 4 - 8, were positioned along a curve that extended between points at 4 centimeters radially from the engine centerline and 28.8% axial chord, and 2.8 cm radially from the engine centerline and 57% axial chord. While this hole pattern would not be used in an actual cooling application, it provides the placement of cooling holes across a large section of the suction surface for analysis. The film-cooling variation was tested to show, beyond looking at the pressure contours from the internal and external vane surface, that it was possible for coolant to exit the vane, and to quantify the blowing ratio for each of the holes. Figure 168 also shows the extent of the solid volume mesh which had the same external geometry in all cases. The central hub that connects each of the vanes was modeled since it was expected that conduction was taking place and was important to distributing heat throughout the vane.

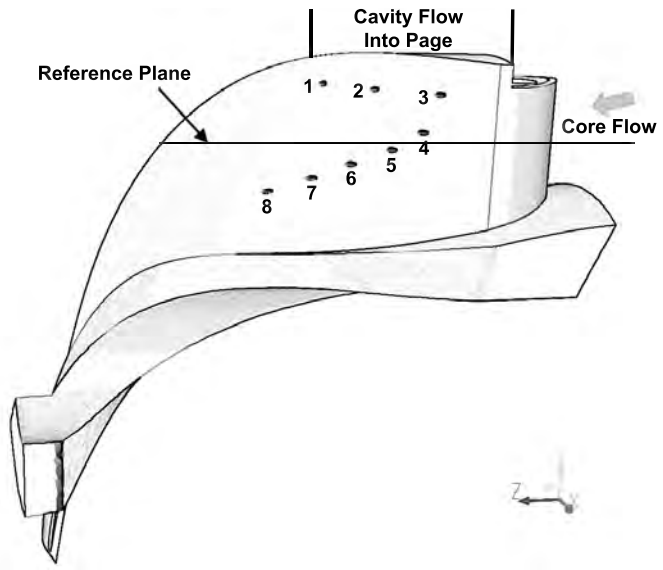


Figure 168. Suction surface view of the HGV with film-cooling hole placement

4.3 Grid Independence Check

Each domain was gridded in Pointwise V17.3 R5 utilizing unstructured surface meshes and the T-Rex hybrid mesh generator for the fluid volume mesh. The T-Rex function enabled three dimensional anisotropic tetrahedrals to be extruded off selected surfaces to create prisms in the boundary layer upon export. When structured prisms could no longer be created due to geometry or adjacent cell interference, the generator filled in the remaining volume with unstructured cells. The solid regions were gridded with an unstructured volume mesh only. Table 7 shows the resolutions of each of the cases used.

Table 7. Grid resolutions of CFD case domains

Domain	Total Cell Count
Solid	15M
Hollow	30.5M
Baseline Plug w/ Baseline Exit	63.2M
Baseline Plug w/Small Exit	62M
Close Plug w/ Baseline Exit	65.25M
Close Plug w/ Small Exit	52.4M
Film Cooled Vane w/Baseline Plug	53.7M
Film Cooled Vane w/Close Plug	58.5M

A grid independence test was performed on the solid vane geometry. Since the solid vane geometry domain had the lowest cell count, if the fluid motion and temperature were fully resolved at those levels, then the high resolution vane variation cases would be fully resolved as well. Three solid vane domains were created with resolutions of 6M, 15M, and 18.5M cells. Three sets of griding parameters including first cell wall spacing, solid volume mesh boundary decay, and fluid volume mesh boundary decay were used to generate these three grid resolutions. The first two domains had a first prism height of 1 x 10^{-3} mm while the last case had a first step height of 1 x 10^{-4} mm.

All three cases were run with the same boundary condition inputs and the velocity and temperature along a line parallel to the x-axis that went through the vane roughly at the location of Hole 4 in Figure 168 was plotted. Positive position values were on the suction side of the vane and negative position values were on the pressure side. The zero position was located inside the vane. As shown in Figures 169 and 170, the profiles in the two higher resolution domains were nearly identical with only a slight variation in the 6M cell domain in the temperature plot. The temperature spike in Figure 170 at roughly 0.007 m was caused by hot gases from the circumferential cavity impinging on the vane suction surface and convecting downstream. This was the region not fully resolved by the low resolution domain. These results indicate that the fluid flow and conjugate heat transfer were both fully refined in the higher resolution domains. The linear portions in the plots were locations along the line that were inside the vane. The griding technique used to generate the baseline (15M cell) domain was selected for use in the other cases of this stagnation cooling analysis.

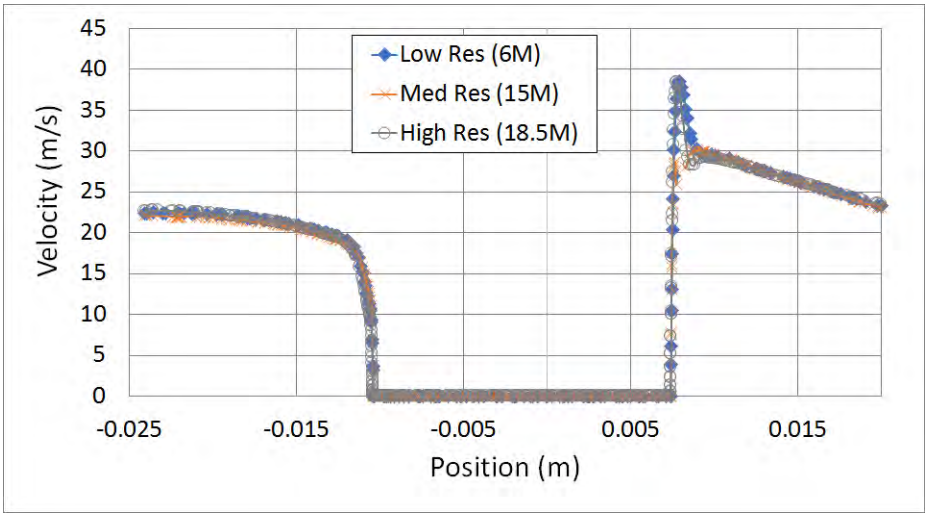


Figure 169. Grid independence check results of velocity for three grid resolutions of the solid vane test case

The resolution of the solid volume grid and the fluid volume grid were linked. As more detail was added to the vane geometry with thinner walls, a finer mesh was

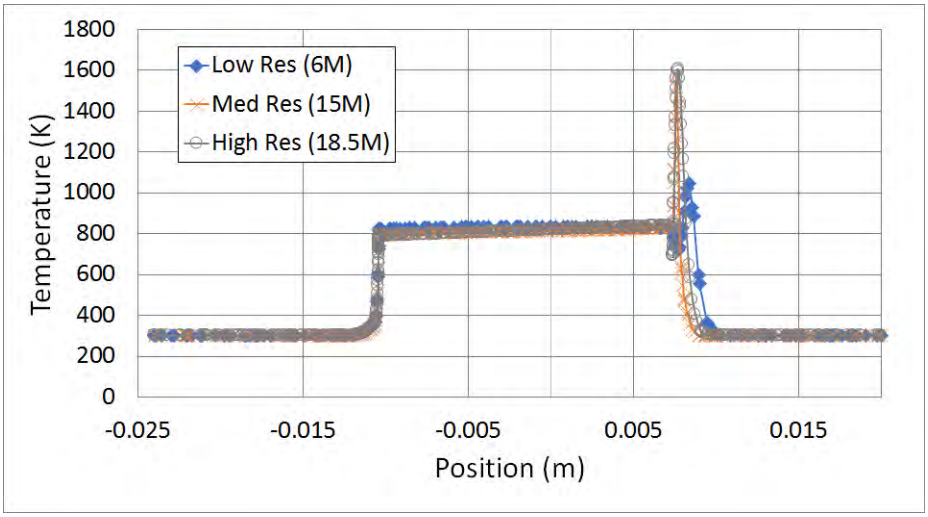


Figure 170. Grid independence check results of temperature for three grid resolutions of the solid vane test case

needed to ensure the walls were more than one cell thick. This requirement led to a very fine surface mesh on the vane. The surface cells of the fluid and solid were coupled meaning that the same fine mesh used to resolve the details in the vane were also used to build the fluid volume mesh. This necessity explains why there was a drastic difference in cell count between the solid vane and the other vane variants.

4.4 Computational Settings

The steady-state CFD solution was run in FLUENT R16.2 with a pressure-based solver with an absolute velocity formulation. The following settings were selected based on a review of the works of Briones et al. [148], Cottle [78], prior experience, and a review of the FLUENT manual [132]. Briones et al. and Cottle were both successful in comparing their solutions using the following settings to UCC experimental data.

The coupled fluid-solid energy equation was turned on to account for the non-adiabatic conditions. The fluid was treated as turbulent using the k-ω shear stress transport (SST) model with viscous heating. There are a number of turbulence models that could be used, however, the k-ω SST model was selected for its performance in

wall bounded flows. The grid was resolved to obtain a value of $y^+ = 1$ or better over most of the vane surface to accurately model heat transfer and wall properties.

Gaseous propane fuel and air were added to the UCC circumferential cavity in the positions shown in Figure 165. Reacting chemistry was handled with the Partially Premixed Model using the Flamelet Generated Manifold (FGM) with diffusion flamelets. The FGM model assumes the scalar evolution in a turbulent flame to be approximated by the same in a laminar flame. This model parameterizes the species and temperature values in the flow based on a few variables such as mixture fraction, scalar-dissipation, and reaction progress. The GRI 3.0 chemical equilibrium tables were also added to more accurately calculate combustion values inside of FLUENT. The FGM model is based on reaction progress and can be quenched by heat extraction due to wall contact or the addition of dilution air. This behavior makes it a desirable model for the UCC wall bounded domain.

The fluid entering the domain was modeled as air, but the distribution of fuel and air inside the domain was defined by a FLUENT calculated mixture probability distribution function (PDF). The solid metal components were modeled as the default steel from the FLUENT material database to approximate the properties of typical engine hardware. Table 8 shows the boundary conditions at each of the domain inlets. These boundaries were defined as mass flow inlets. As such, the gauge pressures listed in the table were used to define an initial value at the inlet but the value was free to fluctuate to meet the requirements of the mass flow boundary condition. The ambient static pressure was set at 101,325 Pa. All gases entered the model at 300K, with a turbulence intensity of 5% to approximate the behavior behind a compressor. The mean mixture fraction was set to zero at all inlets but the fuel inlet which was set to one. This setting indicates that only air entered the cavity and core inlets and only fuel entered the propane inlets. Based on the fuel and air flow rates, the equivalence

ratio in the cavity was approximately 0.72. The boundary at the fluid/solid interface which was made a wall boundary condition which FLUENT automatically converted to a coupled boundary and created a second shadow boundary at the same location to assign one surface to the fluid domain and one surface to the solid domain. This coupled boundary at the fluid/solid interface behaved like a wall, but allowed for heat transfer across the surface.

Table 8. Inlet boundary condition settings

Boundary	$\dot{m}$ (kg/s)	**Gauge Total Pressure** (Pa)
Cavity Air Inlet	0.0054	4800
Core Inlet	0.0126	4800
Fuel Inlet	0.00025	5200

The coupled pressure-velocity coupling scheme was selected to solve for pressure and velocity together. Spatial discretization was selected as second order upwind for all parameters. The solution was run steady-state, however, the pseudo transient option was checked to accelerate convergence. Convergence was evaluated by residual and surface temperature monitors to ensure a steady state solution had been achieved.

4.5 Computational Results

There were three categories of results of interest in this study; pressure distributions, mass flow rates into the vane, and temperature distributions on the vane. While this is a film-cooling study, the purpose was primarily to determine if air could be moved through the vane in sufficient quantities to have a cooling effect.

To show the importance of including conjugate heat transfer and conduction through the vane, the static surface temperatures for the suction side of the solid vane is shown for an adiabatic wall solution in Figure 171. In this figure the location

and path of the hot gases exiting the circumferential cavity is clearly visible. Without conduction and heat transfer, the vane remained cold in areas not directly impacted by hot gases. Note that this figure is shown with a different temperature scale than the remaining figures because the maximum temperature in the adiabatic solution was nearly twice that of the solid vane with heat transfer.

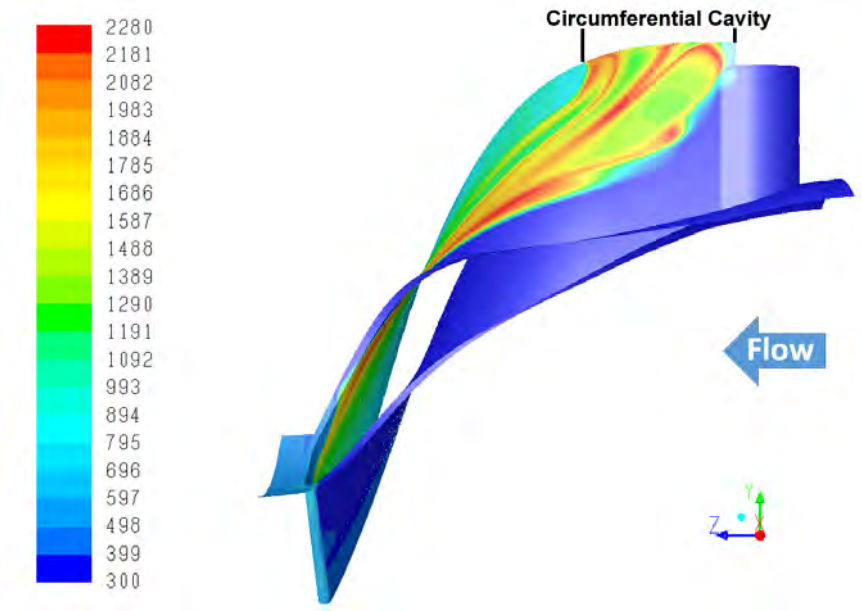


Figure 171. Static temperature (K) contours on an adiabatic baseline solid vane suction surface. Core flow direction is labeled

Unless otherwise specified the pressure and velocity contours are shown for a ZX plane that began at the half span of the vane leading edge. This location is shown in Figure 168 labeled "Reference Plane". As a result of the location, the image shows a cross section of the vane and the associated fluid properties at that level. Because the vane twists but the plane does not, the plane shows the properties at the mid-span of the vane at the leading edge and at full span at the top of the image.

4.5.1 Solid Vane.

Figure 172 shows the static gauge pressure contours around the solid vane variant and Figure 173 shows the static temperatures on the vane suction surface. Figure 173 is in the same orientation as Figure 168 with flow moving from right to left. The peak temperature on the surface was calculated to be 1035 K below the circumferential cavity with a 735 K leading edge temperature. These values are in stark contrast to the 2205 K peak temperature and 300 K leading edge temperature from the adiabatic vane case. The low pressure region in Figure 172 labeled "cavity vortex" is a vortex that exits the circumferential cavity resulting from the shear layer interaction between the core and cavity flows. In Figure 172 the bounds of the selected pressure scale did not go low enough to define this region. The pressure drop in the center of the vortex for this image reached approximately -4,000 Pa (1,000 Pa below the scale).

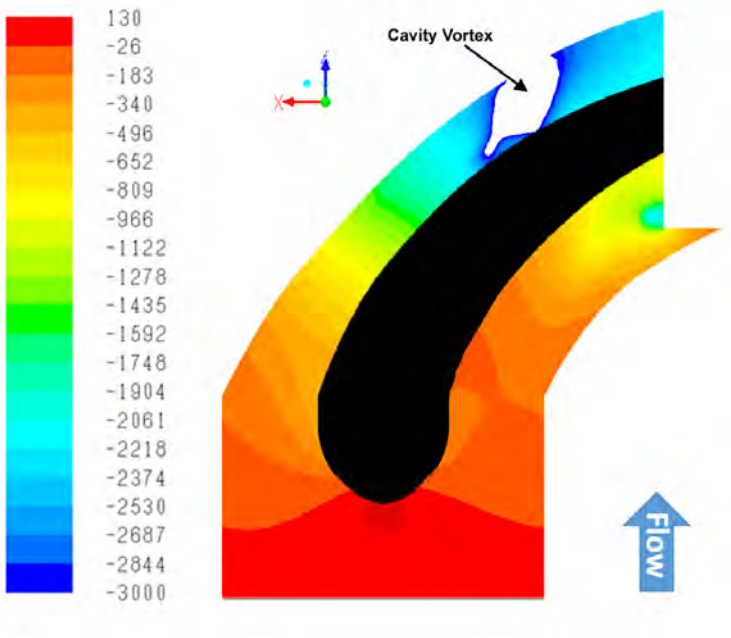


Figure 172. Static gauge pressure (Pa) contours around the baseline solid vane.

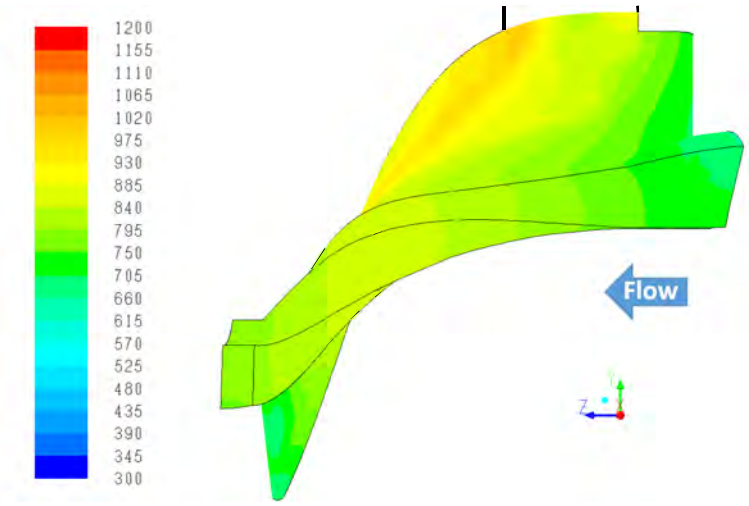


Figure 173. Static temperature (K) contours on the baseline solid vane suction surface.

4.5.2 Hollow Vane.

Compared to the solid vane, the hollow vane offered an overall reduction in surface temperatures with the exception of the area directly below the circumferential cavity, as shown in Figure 174. The peak temperature reached 1210 K. It was speculated that the increased temperature below the cavity was due to the reduction in conduction paths resulting from hollowing the vane, coupled with poor circulation of air inside near the vane tip. However, the flow of coolant through the interior of the vane did serve to reduce to temperature in most regions on the vane. Due to the internal flow, the higher temperature zones were localized and the leading edge temperature on this vane was reduced to 365 K. With the solid vane the hottest temperatures were observed in the region below the aft end of the circumferential cavity. In the hollow vane the hottest temperatures on the surface were distributed below the entire axial length of the circumferential cavity. This pattern was seen in all of the cooled cases. It is possible that this change in temperature distribution at the exit of the circumferential cavity is the result of a change in the shear layer properties caused by allowing some of the core flow to go through the vane.

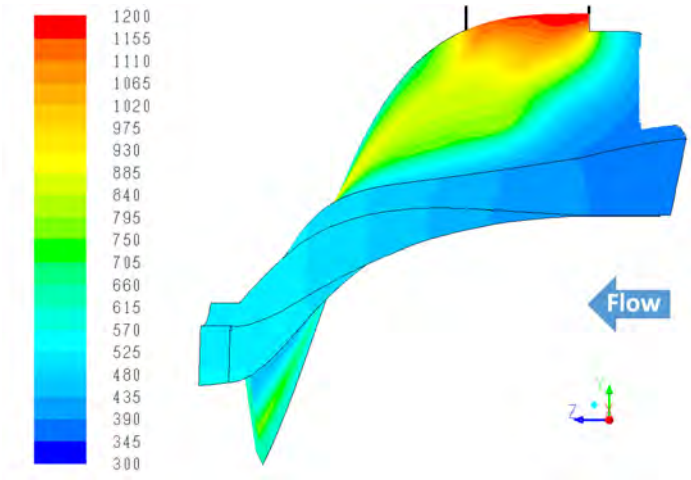


Figure 174. Static temperature (K) contours on the hollow vane suction surface.

The pressure contours for the hollow vane shown in Figure 175 outlined the challenge in achieving a result where fluid could exit a film-cooling hole near the leading edge of the vane. The contours outside the vane are very similar to the baseline solid vane (Figure 172), however, due to some of the core flow entering the vane, it took a slightly greater distance downstream from the leading edge to achieve the same pressure drop with the hollow vane. Additionally, with less air moving around the vane due to ingestion through the vane, the shear interaction between the core and cavity flows was lessened and resulted in a weaker vortex with a lower pressure drop.

There was a considerable pressure drop across the vane inlet which resulted in the vane internal pressure being considerably lower than the external pressure in the region shown in Figure 175. By the trailing edge slot the external pressure had dropped sufficiently such that air was able to flow through the vane. The mass flow rate of air through the vane inlet was calculated at 0.0040 kg/s which equates to 32% of the core flow entering the domain. While these results show that internal cooling was possible, modifications to the internal geometry were needed to boost the internal pressure to levels where the internal pressure was higher than the external if film-cooling was to be applied.

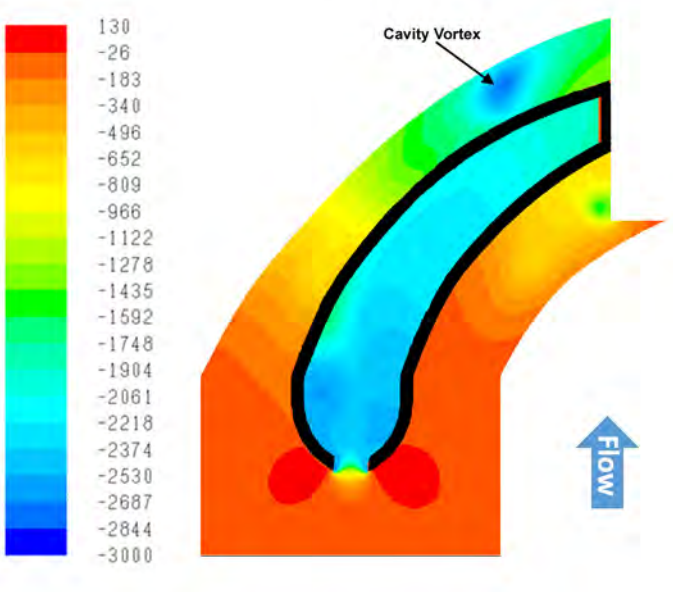


Figure 175. Static gauge pressure (Pa) contours around the hollow vane.

4.5.3 Plugged Vanes.

The plugged vanes featured variations of a small airfoil like shape inside of the HGV shell that was intended to push the internal air to the inner pressure and suction surfaces while helping slow the internal flow and build pressure. Table 9 shows the mass flow rates and percent of the total core flow that was entrained into each of the plugged vane variations. The mass flow rate through the baseline plugged vane and the closer plugged vane, both with the baseline trailing edge slot, were less than 1% different. However, the smaller exit had a much larger impact on the mass flow rate at nearly a 7% reduction compared to the baseline trailing edge slot cases. Figure 176 shows the effect these variations had on the internal pressure distribution. In the two baseline exit cases, with higher internal mass flow rates, the internal pressures were consistently below the external pressures at all points along the vane surface shown. The smaller exit area variations had a point approximately halfway down the displayed suction surface labeled "Internal/External Pressure Even" in Figures 176c

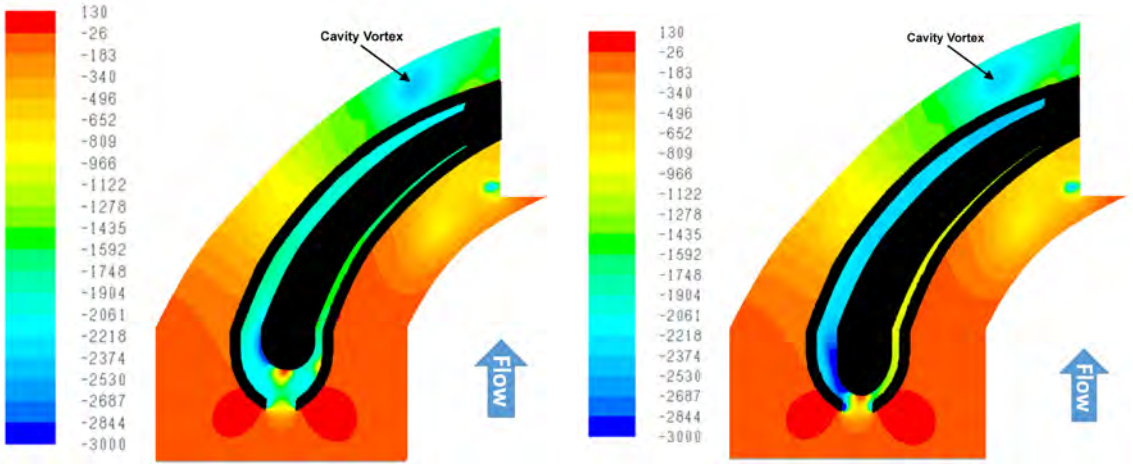
and d where the internal pressure matched the external pressure. This increase in pressure was caused by the reduction in internal mass flow rate through these vanes.

Table 9. Mass flow rates through the plugged vane variations

Vane Variant	**Exit Area** cm^2	$\dot{m}$ (kg/s)	**% of Core Flow**
Baseline Plug, Baseline Exit	0.587	0.00362	28.7
Closer Plug, Baseline Exit	0.587	0.00371	29.4
Baseline Plug, Smaller Exit	0.477	0.00277	22.0
Close Plug, Smaller Exit	0.477	0.00291	23.1

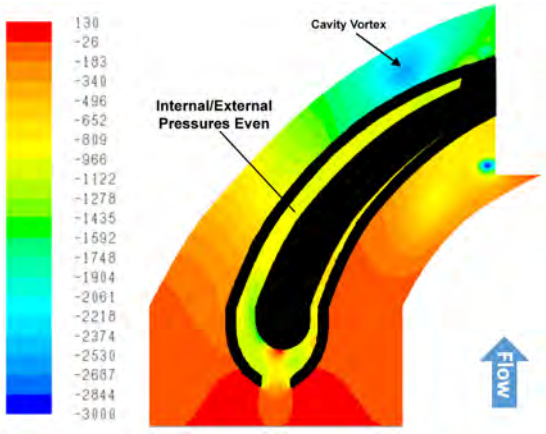
The mass capture area at the inlet of the vanes is shown in Figure 177 for the closer plug variant with a smaller exit area. The black arrows adjacent to the vane inlet show the stagnation points. All fluid between the black arrows is entrained into the vane. This mass capture area was nearly identical for all of the plugged cases, yet the mass flow rates varied as previously shown in Table 9. This result indicates that the size of the exit area was the driver in controlling mass flow rate through the vane, which was independent of mass capture area.

The temperature distribution on the suction surface of the baseline plugged vane shows that the thicker tip material and the addition of the central plug were successful in reducing the high temperatures directly below the circumferential cavity that were observed in the Hollow Vane analysis. These results are shown in Figure 178. The variation with the closer central plug had a suction surface temperature distribution that was nearly identical with a peak temperature of 915 K as with the baseline plugged vane. The smaller exit area cases with the baseline and closer plug positions had a similar temperature distribution to that shown in Figure 178, but the peak temperature was higher at 990 K. The increase in temperature was likely due to a lower internal mass flow rate cased by constricting the area of the trailing edge slot.

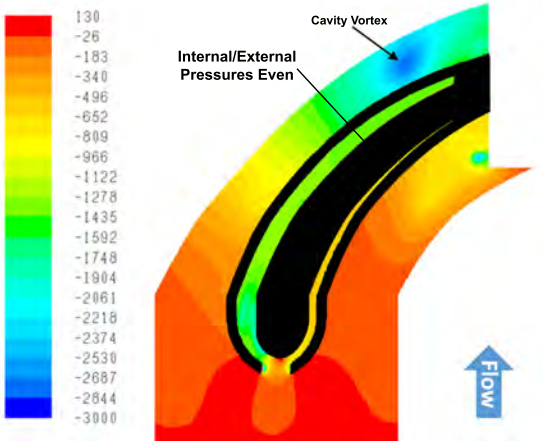


(a) Baseline Plug & Baseline Exit

(b) Closer Plug & Baseline Exit



(c) Baseline Plug & Small Exit



(d) Closer Plug & Small Exit

Figure 176. Static gauge pressure (Pa) comparison of variation on the plugged vanes

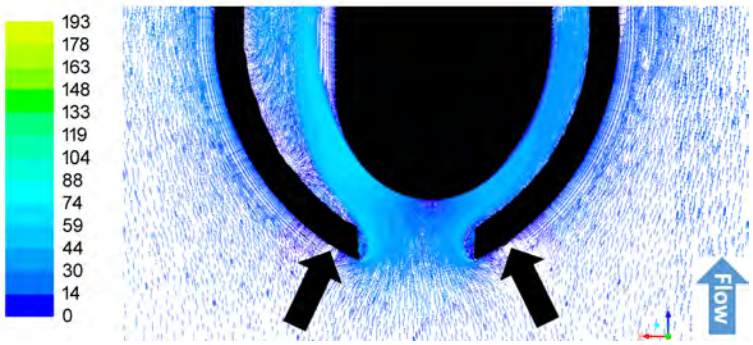


Figure 177. Velocity vectors colored by velocity magnitude (m/s) at the vane inlet for the closer plug variant.

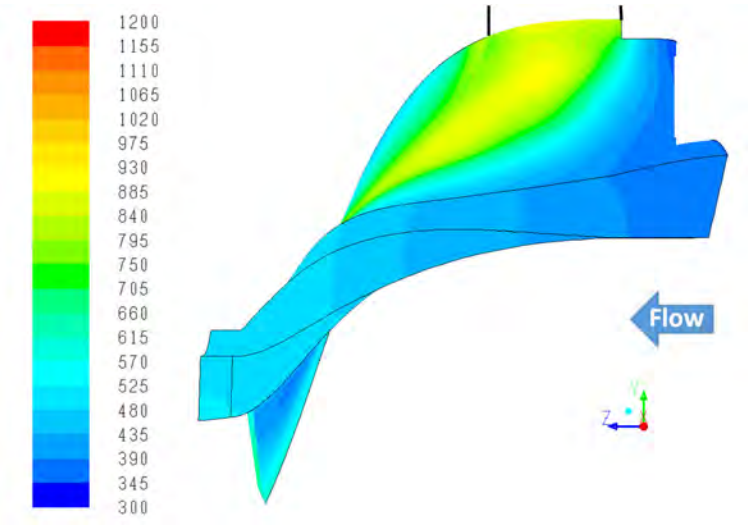


Figure 178. Static temperature (K) contours on the baseline plugged vane suction surface.

4.5.4 Plugged, Film-Cooled Vanes.

The final vane variations were the film-cooled vanes which combined the baseline plug and the closer plug each with the smaller exit area (0.477 cm^2), as described in the previous section, with eight film-cooling holes. The static temperature profile on the vane suction surface was nearly identical between both film-cooled vanes and closely resembled the temperature distribution of the corresponding non-film-cooled smaller exit area cases including the same peak surface temperature of 990 K. The mass flow rates through the film-cooled vanes were 0.00292 kg/s (23.1% of total core flow) with the baseline plug, and 0.00284 kg/s (22.5% of the total core flow) with the closer plug. The similarity of these flow rates to the bottom two variants listed in Table 9 indicate that the mass flow rate of the internal coolant dictates the metal temperatures.

Figure 180 shows the static pressure contours through Holes 1, 2, and 3 on the ZX plane of the vane with the baseline plug and small exit area. The pressure mismatch in Holes 2 and 3 is evident as the higher pressure is on the exterior with a lower

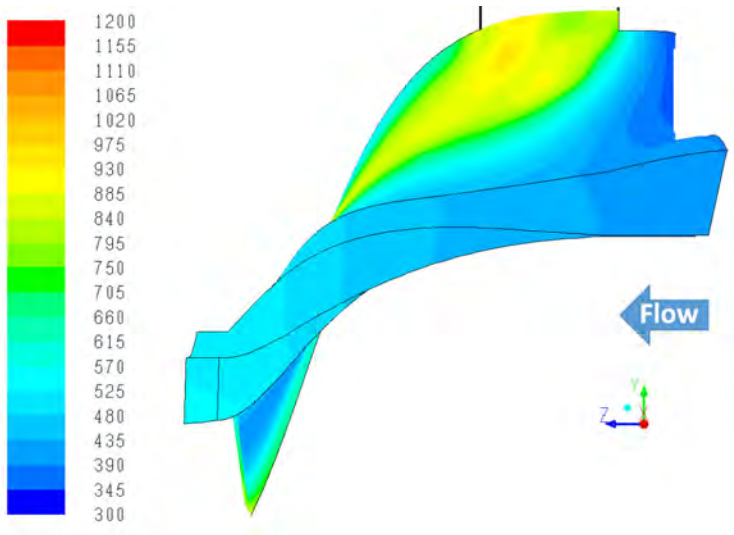


Figure 179. Static temperature (K) contours on the film cooled vane suction surface. Both film-cooled cases produced identical results

pressure inside. By Hole 1, the external pressure had dropped enough that coolant flowed out.

Since the cooling holes were not located only on the ZX plane half way through the leading edge span, the pressure contours on the vane external suction surface were plotted in Figure 181 to see the pressure around each hole. Based on the peak internal pressures seen in Figures 176 and 180, and comparing to the external pressures in Figure 181, there was a low expectation that Holes 2-6 had coolant flowing out due to the external pressure around those holes exceeding the peak internal pressure. However, Holes 1, 7, and 8 exited into a lower pressure green region and did have coolant exiting these holes.

The pressure differential between the inner and outer regions of the suction surface is better illustrated in Figure 182 which shows a Cartesian plot of non-dimensional axial chord versus static gauge pressure on the inside and outside suction surface. These measurements were taken along a line directly below Holes 1, 2, and 3. From this figure it can be seen that the internal and external pressures are equal at approx-

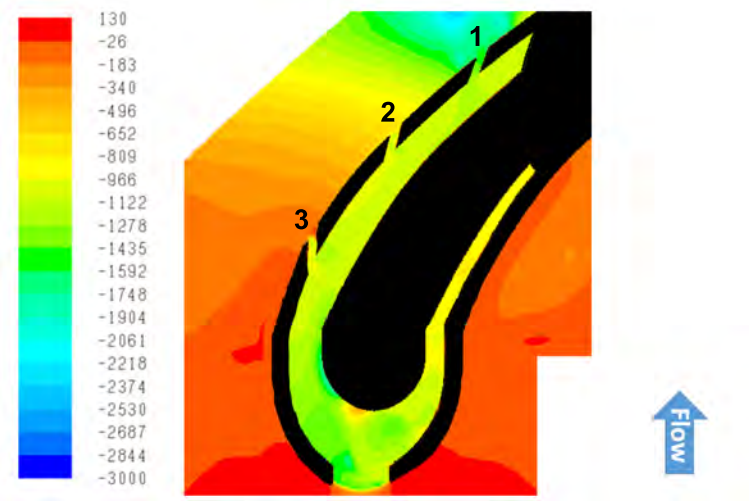


Figure 180. Static gauge pressure (Pa) contours through Holes 1, 2, and 3 on the ZX plane with the baseline plug, small exit area vane

imately 41% chord which is axially located between Holes 1 and 2. Coolant was free to exit from Hole 1 because at that position the internal pressure was greater than the external pressure.

Figure 183 shows a Cartesian plot of non-dimensional axial chord versus static gauge pressure on the inside and outside suction surface of the film-cooled vane with the baseline plug and small exit area along a line of constant radius that passes between Holes 5 and 6. As shown in Figure 181 the pressure contours on the external surface form nearly uniform radial bands that vary with axial position. This pressure distribution means that Figure 183 can be used to approximate the distribution along Holes 4 - 8. From Figure 183 it can be seen that the internal and external pressure are equal between Holes 6 and 7 located at approximately 46% axial chord. Based on this plot, Holes 7 and 8 would achieve coolant exiting from the vane as well as any additional holes placed aft of 46% axial chord.

Table 10 shows a summary of the results for each of the three cooling holes in the baseline plug, small exit area vane that had coolant exiting. The properties of interest include the mass flow rate out of the hole, average velocity of the coolant,

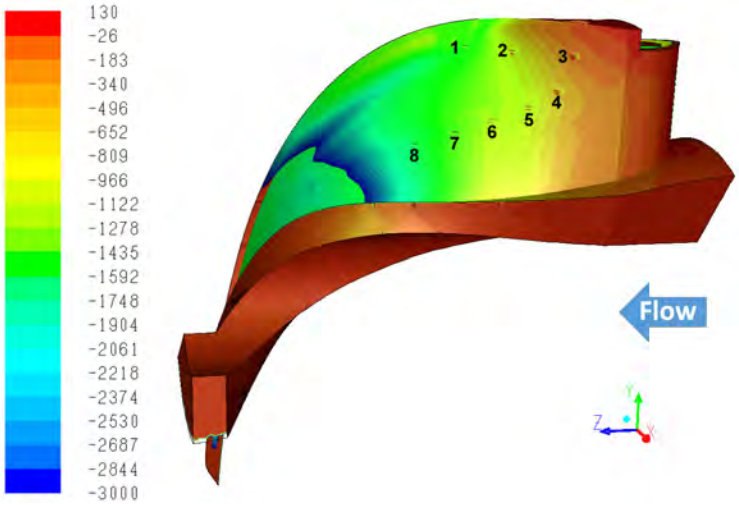


Figure 181. Static gauge pressure (Pa) contours on the film cooled vane suction surface

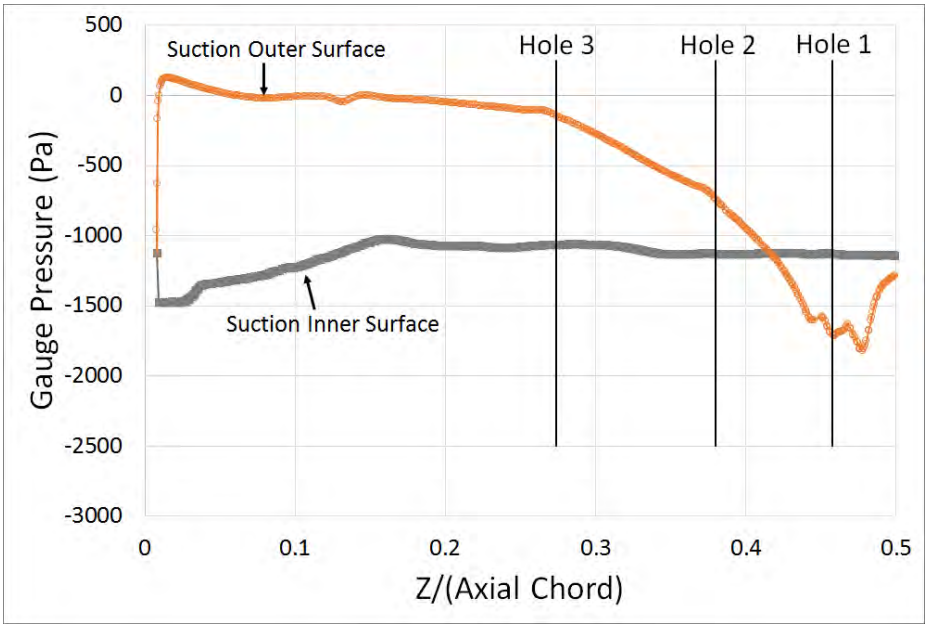


Figure 182. Static gauge pressure (Pa) along a line on the vane surface just below Holes 1, 2, and 3 with the baseline plug, small exit area vane

and the corresponding blowing ratio. Keep in mind that the blowing ratio is also dependent on the local freestream velocity near the hole.

Figure 184 shows the static pressure contours through Holes 1, 2, and 3 in the film-cooled vane with the closer plug and small exit area. A similar pressure mismatch

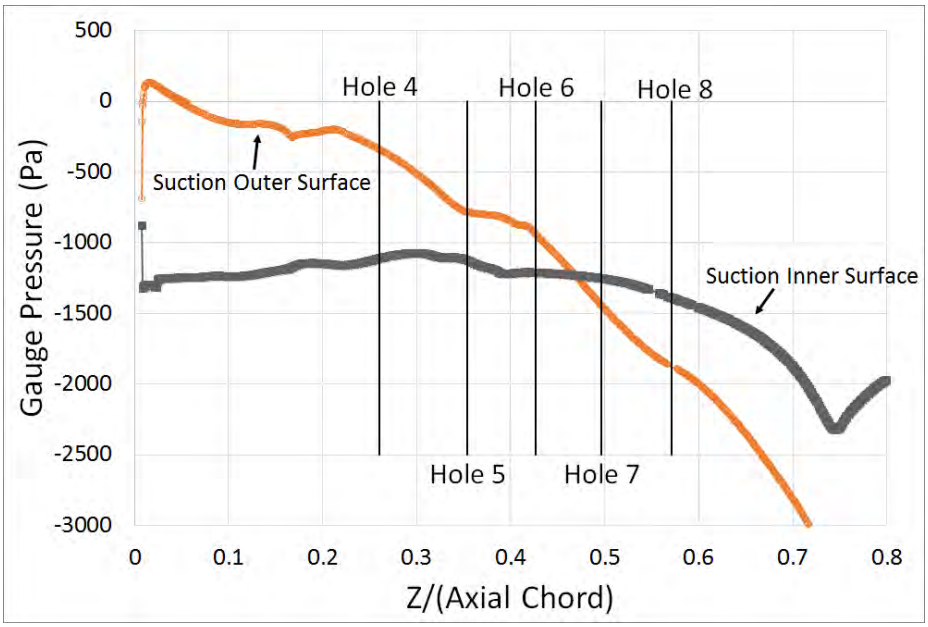


Figure 183. Static gauge pressure (Pa) along a line of constant radius on the baseline plug, small exit area vane surface between Holes 5 and 6

Table 10. Fluid properties for cooling holes with exiting flow using the baseline plug, small exit area vane

Hole	$\dot{m}_{out}$ (kg/s)	Velocity (m/s)	M
1	8.13x10$^-$6	21.26	0.56
7	2.06x10$^-$7	20.35	0.29
8	7.45x10$^-$6	28.29	0.38

across Holes 2 and 3 is evident for this case as it was with the baseline plug and small exit area. Again, by Hole 1, the external pressure had dropped enough that coolant flowed out. The pressure differential is better illustrated in Figure 185 which shows a Cartesian plot of non-dimensional axial chord versus static gauge pressure on the inside and outside suction surface of the closer plug, small exit area vane along a line directly below Holes 1, 2, and 3. From this figure it can be seen that the internal and external pressures are equal at approximately 42% axial chord which is located between Holes 1 and 2. Coolant was free to exit from Hole 1 because at that position

the internal pressure was greater than the external pressure. Figure 186 shows the velocity vectors through Hole 1 showing the coolant exiting the vane.

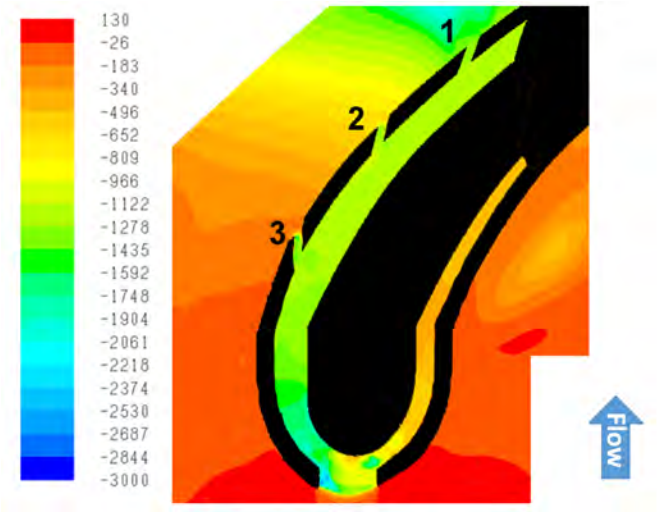


Figure 184. Static gauge pressure (Pa) contours through Holes 1, 2, and 3 on the ZX plane with the closer plug, small exit area vane

Figure 187 shows a Cartesian plot of non-dimensional axial chord versus static gauge pressure on the inside and outside suction surface of the film-cooled vane with the closer plug and small exit area along a line of constant radius that passes between Holes 5 and 6. As described above, the pressure contours on the exterior vane surface form nearly uniform radial bands that varying with axial position. This pressure distribution means that Figure 187 can be used to approximate the distribution along Holes 4 - 8. From Figure 187 the internal and external pressure are equal just upstream of Hole 7 which is located at 50% axial chord. Since the pressure differential across Hole 7 was close to zero, there was a negligible amount of coolant that exited. However, from the figure it can be seen that any holes placed aft of 50% axial chord would allow a much greater amount of coolant to exit.

In both film-cooled vanes tested, there was a larger pressure differential across Hole 8 than across Hole 1, which resulted in a larger mass flow rate of coolant out of Hole 8. In the closer plug, small exit area vane, the pressure differential across Hole 7

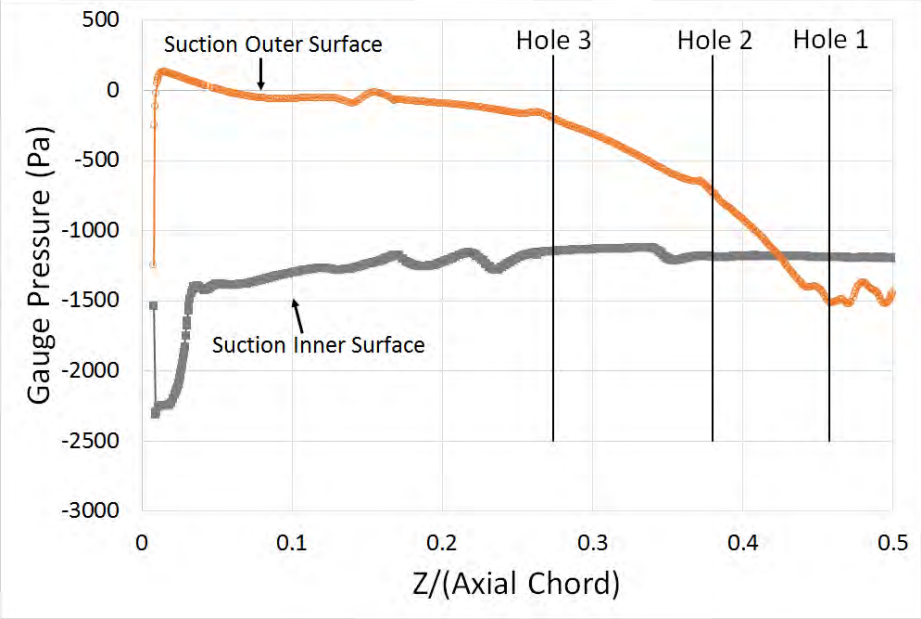


Figure 185. Static gauge pressure (Pa) along a line on the vane surface just below Holes 1, 2, and 3 with the closer plug, small exit area vane

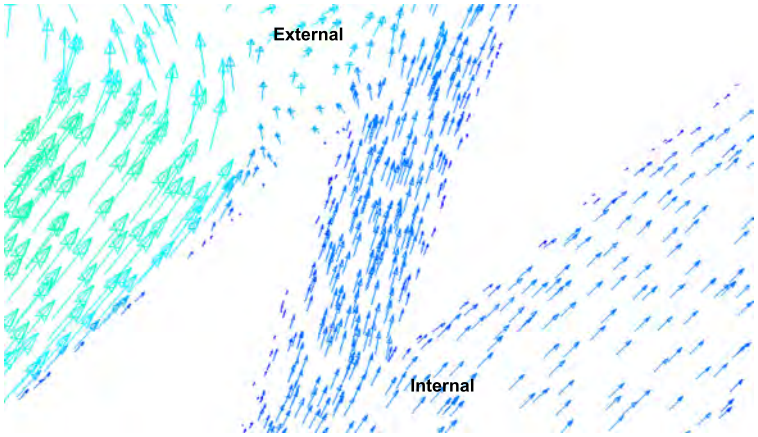


Figure 186. Velocity vectors through Hole 1 with the closer plug, small exit area vane

was close to zero. With a very small pressure differential across the hole, the velocity vectors confirmed nearly stagnant flow inside the hole.

Table 11 shows a summary of the results for each of the three cooling holes that had coolant exiting from the closer plug, small exit area vane. The blowing ratios and mass flow rates for these three holes are slightly reduced from those shown in

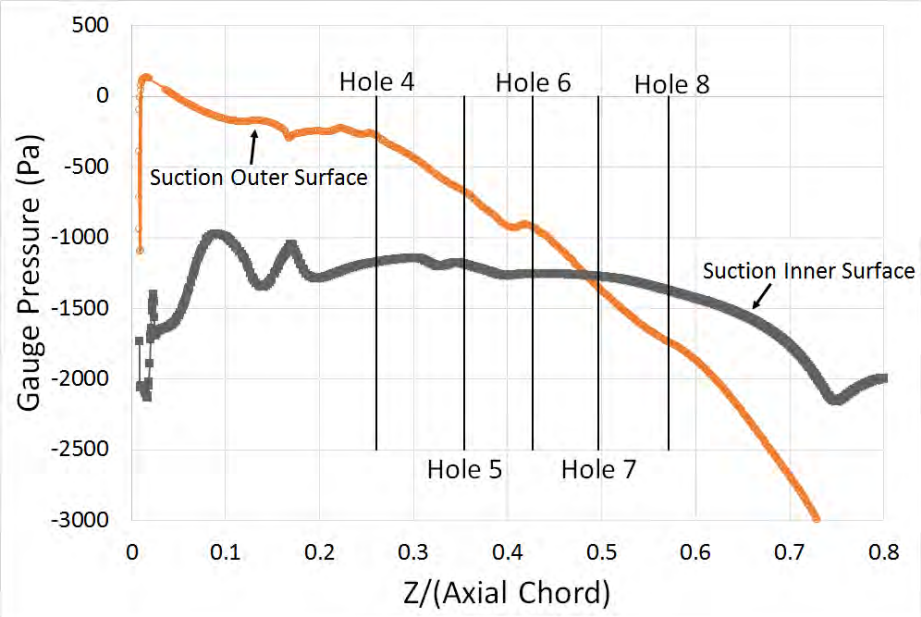


Figure 187. Static gauge pressure (Pa) along a line of constant radius on the closer plug, small exit area vane surface between Holes 5 and 6

Table 10 for the baseline plug, small exit area vane due a lower internal pressure in the closer plug vane.

Table 11. Fluid properties for cooling holes with exiting flow using the closer plug, small exit area vane

Hole	$\dot{m}_{out}$ (kg/s)	Velocity (m/s)	M
1	4.87x10⁻6	17.96	0.50
7	1.39x10⁻7	<1	0.00
8	7.74x10⁻6	27.18	0.46

4.6 Stagnation Cooled HGV Manufacturing Study

Following the success of the initial computational study detailed above, the decision was made to pursue manufacturing a stagnation cooled hybrid guide vane for experimental testing in the UCC test rig. Experimental hardware would enable validation of the proof-of-concept CFD results. A six-vane solid model of the HGV was

drawn by Nathan Clark, a summer intern assigned to the COAL lab, with direction from Lt Kevin DeMarco, a master's student studying the UCC. The vane was designed with one solid vane to act as the reference condition, and the other five vanes were designed with cooled variations of the plugged vanes described above. Figure 188 shows the 3D solid model of the stagnation cooled HGV. Table 12 gives the specifications for each vane's cooling scheme, with the sixth vane being the solid, uncooled vane. The size of the vane span, chord, wall thicknesses, inlet area, plug distances, and trailing edge slot areas were the same as specified in Section 4.2.

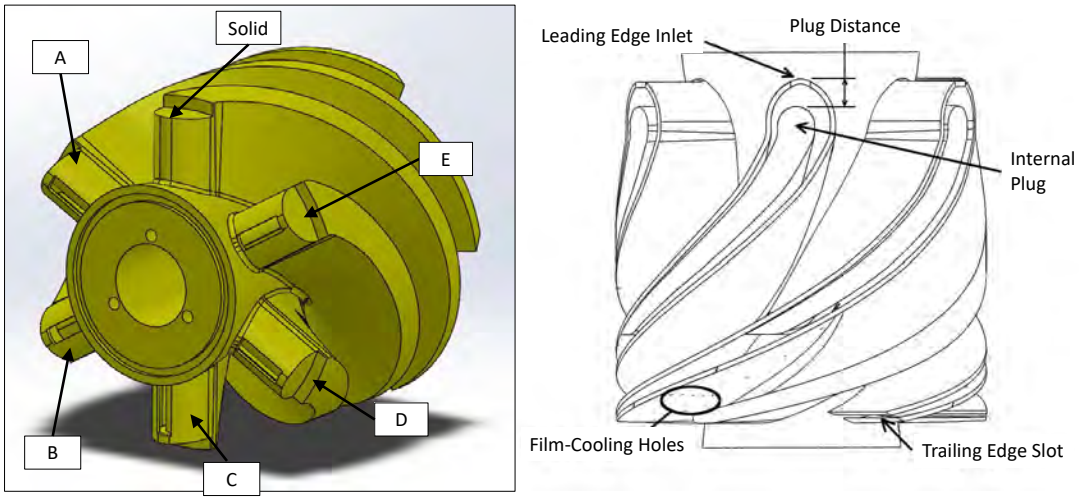


Figure 188. Stagnation cooled HGV 3D solid model

Table 12. Manufactured HGV cooling schemes by vane

Vane	**Plug Distance** (mm)	**Cooling Holes**	**Exit Area** (cm^2)
A	5.84	Yes	0.477
B	2.29	No	0.587
C	5.84	Yes	None
D	5.84	No	0.587
E	5.84	Yes	0.587

Based on the findings from the initial computational stagnation cooling study discussed above that showed film-cooling was only possible past approximately 50% axial chord, combined with the difficulty in visually seeing regions of the vane near the leading edge resulting from the helical twist of the vane, the film-cooling scheme on the production vane was changed from what was specified in Section 4.2 for the initial study. The new cooling scheme shown in Figure 189 positioned holes at six different axial locations, all downstream of 50% axial chord. The first location only had one hole located at 87% radial span. The second, third, fourth, and sixth locations had two holes located at 87% and 60% radial span. The fifth hole location had six holes located at 87%, 82%, 76%, 70%, 64%, and 60% radial span. All cooling holes were circular, unshaped, with a diameter of 0.508 mm drilled at a 30° angle from surface normal. Like the film-cooling hole pattern in the initial study, this hole pattern was not designed for optimal cooling, but rather to evaluate the effects of coolant distribution over a wide variety of axial and spanwise locations.

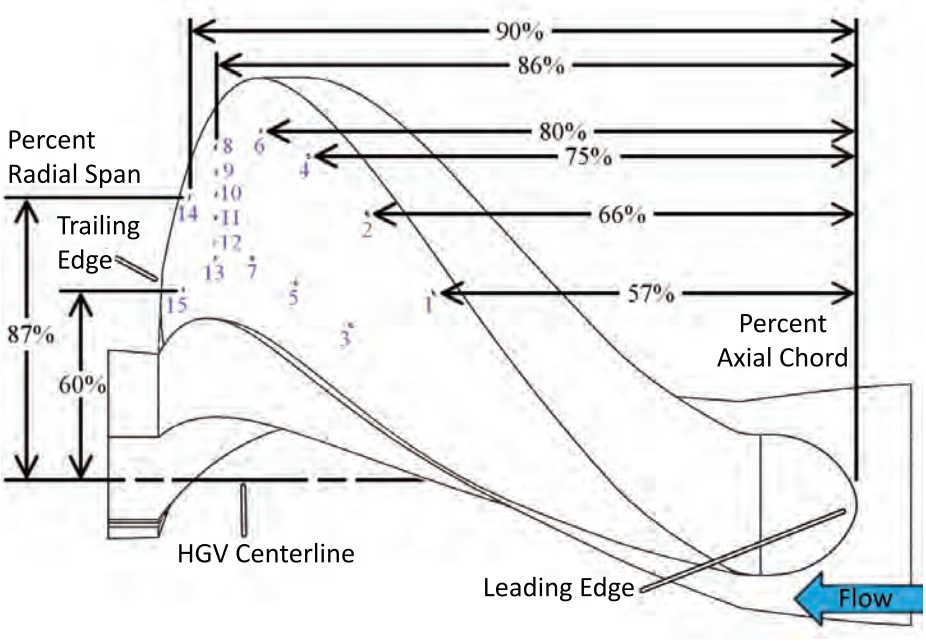


Figure 189. Manufactured cooling hole locations

Once the 3D solid model was complete, Lt DeMarco coordinated with Linear AMS to have the part 3D printed in 17-4 stainless steel. Due to the thin walls and high twist rate of the vanes that resulted in large unsupported overhangs during the printing process, additional internal supports were required to be able to produce the part. Lt DeMarco's thesis [161] provides a detailed summary of the manufacturing problems and solution process that ultimately led to being able to produce the cooled HGV. The final printable part featured 2 mm diameter internal support pins spaced 3 mm apart arranged in a matrix. This spacing was selected because 3 mm was the maximum unsupported overhang that the Linear AMS printer could tolerate. Figure 190 shows a transparent view of the stagnation cooled HGV with an internal plug and the internal support pins.

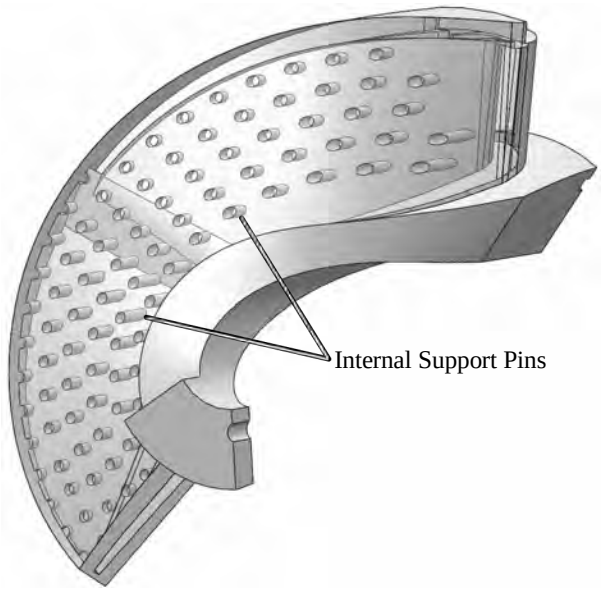


Figure 190. Manufactured HGV internal support structure

4.6.1 Numerical Analysis of the Manufactured HGV.

When it was realized that internal pins were required to be able to manufacture the stagnation cooled HGV, a computational analysis was completed on the Vane

A variation, from Table 12, which included the baseline plug position, small exit area, and the new cooling scheme arrangement shown in Figure 189. This vane configuration was selected because it was the best performer from the original proof-of-concept study. While the internal vane passage was kept as open as possible, it was anticipated that the addition of the internal support pins would result in lower internal pressures. The comparison of the Vane A design with and without pins was used to determine the extent of the impact of the pins on the internal pressure and surface cooling. Table 13 shows the four computational cases that were analyzed, with Cases 1 and 2 coming directly from the results presented in Sections 4.5.1 and 4.5.3, respectively.

Table 13. Manufacturing study CFD cases

Case	**Plug Distance** (mm)	**Cooling Holes**	**Exit Area** (cm^2)	**Internal Pins**
1		Solid Vane		
2	5.84	No	0.477	No
3	5.84	Yes	0.477	No
4	5.84	Yes	0.477	Yes

The CFD case setup (with the exception of the cooling scheme and the addition of the internal support pins), as well as the computational settings, were identical to those for the initial study as presented in Sections 4.2 and 4.4, respectively. The grids for Cases 3 and 4 were generated using the settings for the mid-resolution case shown to be grid independent in Section 4.3. These settings resulted in cell counts of 68M and 80M cells for Case 3 and Case 4, respectively. These cases had more cells than any of the cases in the initial study, but the addition of more cooling holes and the support pins caused more cells to be required to fully resolve the geometry detail.

4.6.1.1 Manufactured HGV Pressure Results.

Like the initial computational study, the pressure distribution around the vane and the surface temperature effects were primarily of interest. The pressure distribution around the vane controls the locations where coolant could be ejected, as well as the quantity of coolant issuing from a cooling hole. Figure 191 shows the pressure distribution on the internal and external suction surface of Cases 2, 3, and 4. For all three cases, the internal surface pressure distribution was plotted as a dotted line, while the external surface pressure was plotted as a solid line. The Case 2 data was the same as that shown in Figure 183, replotted here for comparison.

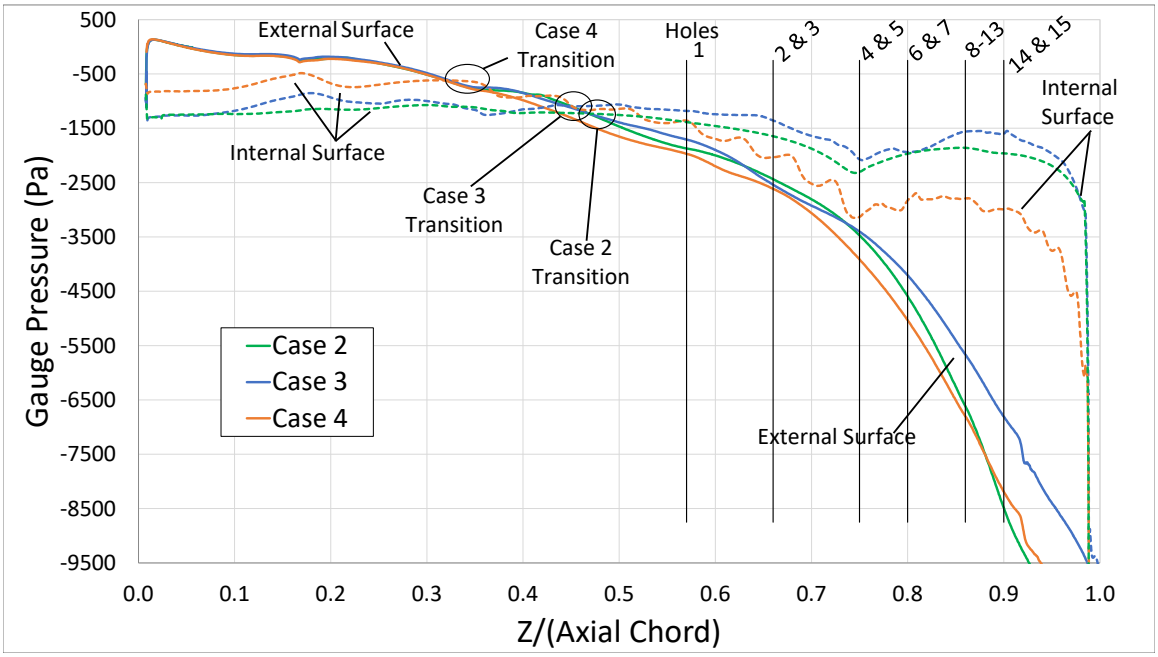


Figure 191. Static gauge pressure (Pa) along a line of constant radius on the vane suction surface for Cases 2, 3, and 4

As shown in Figure 191 there is very little difference between the magnitude and trend of the pressure traces of Cases 2 and 3 despite the addition of the cooling holes in Case 3. The transition point where the internal and external pressures matched between these two cases were only 4% different at approximately 43 and 46% axial chord, respectively, resulting from nearly identical mass flow rates through the vanes

of approximately 0.0029 kg/s. The addition of the pins in Case 4 resulted in a lower pressure drop across the vane inlet resulting from a lower mass flow rate through the vane of 0.0025 kg/s. Thus a higher internal pressure was reached compared to the other two cases for the first 45% axial chord. This increase in internal pressure caused the transition point for Case 4 to move forward to approximately 33% axial chord, a significant improvement compared to the other two cases. After the transition point for Case 4 the internal pressure stayed above the external pressure for the remainder of the vane, however, the pressure differential between the internal and external surface compared to Cases 2 and 3 was considerably lower. Additionally, the internal surface pressure line was considerably more unsteady than the other two cases due the presence of the support pins.

While all of the cooling holes were positioned in regions of favorable pressure gradients for coolant extraction, the mass flow rate of coolant issuing from the holes generally increased with increasing axial position due to the rise in pressure differential. For Case 3, Hole 1 experienced the minimum mass flow rate of 0.0032 g/s while Hole 15 was calculated to have the maximum coolant mass flow rate of 0.0157 g/s. Case 4 experienced a reduction in mass flow rates through the holes resulting from a 15% reduction in mass flow rate of air through the vane inlet and the decreased pressure differential caused by the pins. In Case 4, Hole 2 had the lowest mass flow rate at 0.0017 g/s and Hole 15 experienced the largest mass flow rate at 0.0138 g/s; a reduction of 55% and 12%, respectively, compared to Case 3.

Using the FLUENT calculated velocity and density of the fluid through the holes, and the freestream velocity and density around the exit of each hole, the blowing ratio for each hole was calculated with the results shown in Table 14. The blowing ratios ranged from 0.44 to 1.10, with the lowest value occurring in Case 4 and the highest value occurring in Case 3. Bogard [169] suggests that cylindrical holes are

most effective at a blowing ratio of 0.6, with the effectiveness decreasing considerably at 0.85. The elevated values shown in Table 14 could be reduced in future cooling schemes by increasing the number of holes to change the pressure distribution across the vane surface, or by using a shaped hole. It is also important to note that no effort was made to position the pins advantageously relative to the hole positions. The holes at 87% radial span experienced a nominal 16% reduction in blowing ratio from Case 3 to Case 4 because these holes were in the wake region of the pins. This reduction is compared to the nominal 10% decrease in blowing ratio from the holes in Case 4 at 60% radial span which were not directly impacted by pin placement.

Table 14. Film-cooling hole locations and computational blowing ratio results

Hole	Percent Axial Span	Percent Radial Span	Case 3 Blowing Ratio	Case 4 Blowing Ratio
1	57%	87%	0.66	0.62
2	66%	87%	0.64	0.44
3	66%	60%	0.85	0.68
4	75%	87%	0.65	0.45
5	75%	60%	0.75	0.54
6	80%	87%	0.69	0.67
7	80%	60%	0.80	0.94
8	86%	87%	0.74	0.60
9	86%	82%	0.96	0.73
10	86%	76%	1.03	0.80
11	86%	70%	1.07	0.86
12	86%	64%	0.93	0.97
13	86%	60%	1.10	0.84
14	90%	87%	0.81	0.73
15	90%	60%	0.85	0.89

4.6.1.2 Manufactured HGV Temperature Results.

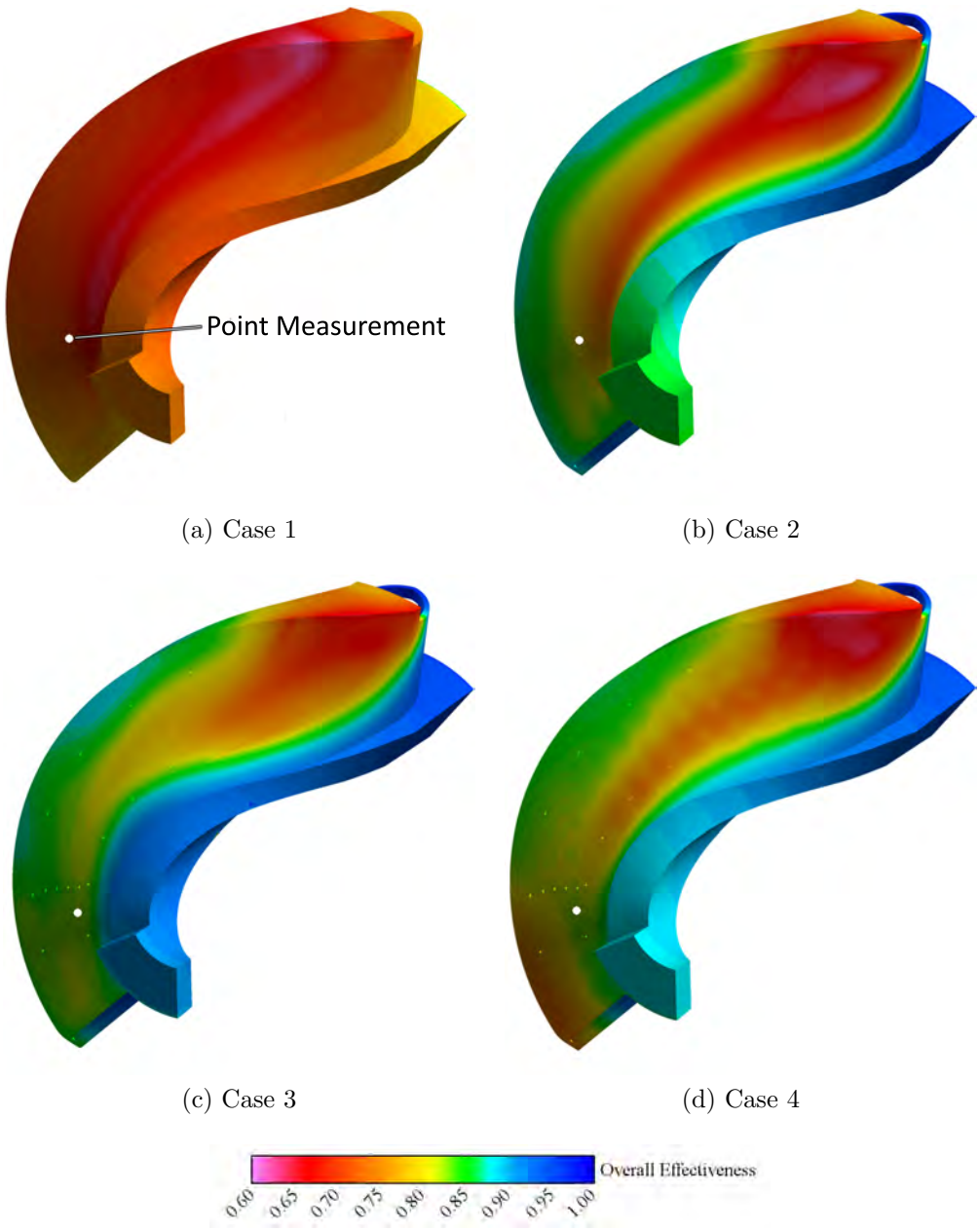
The surface temperatures for each case are presented in non-dimensional form as the overall effectiveness in Figure 192. The vane surface temperature was calculated

by FLUENT, with the coolant temperature specified as 300 K from the fluid temperature at the inlet to the vane, and the freestream temperature specified as 2220 K from the peak temperature calculated in the circumferential cavity. The resulting contours from Case 3 and Case 4 were compared with the Case 1 and Case 2 results which were adapted from the analysis in Sections 4.5.1 and 4.5.3, respectively. As a means of comparison between the vane configurations the maximum temperature on the vane surface and the corresponding minimum effectiveness were found as well as the temperature and overall effectiveness at 88% axial chord and 64% radial span, indicated in Figure 192 by the white dot. This point was located near the vane trailing edge, 3.5 diameters downstream of Hole 12. The calculated values at the point measurement location and minimum effectiveness locations are displayed in Table 15.

Table 15. Minimum effectiveness and corresponding surface temperature, with point measurement values at 88% axial chord and 64% radial span

	Case 1	Case 2	Case 3	Case 4
Min ϕ	0.61	0.64	0.65	0.63
Max Temp.	1035 K	990 K	956 K	1007 K
Point ϕ	0.70	0.79	0.83	0.83
Point Temp.	878 K	697 K	631 K	630 K

Case 1 was evaluated to have a minimum overall effectiveness of 0.61 corresponding to a peak surface temperature of 1035 K located below the CC. This case also had the highest temperature and lowest overall effectiveness at the point measurement location at 878 K and 0.70, respectively. The incorporation of an internal passage, plug, and trailing edge slot for Case 2 resulted in the minimum overall effectiveness increasing to 0.64, which corresponds to a peak surface temperature of 990 K also located below the CC. The internal cooling in this case reduced the point measurement temperature by 21% to 697 K, or a 0.79 overall effectiveness. While Case 2 had a lower peak temperature and an overall cooler surface, both Cases 1 and 2 had a hot



(a) Case 1

(b) Case 2

(c) Case 3

(d) Case 4

Figure 192. Overall effectiveness contours for each case

streak which extended downstream starting at the CC. As the hot streak progressed it tapered toward the hub while approximately maintaining a 60% radial span.

Case 3 experienced a minimum overall effectiveness of 0.65, corresponding to a peak surface temperature of 956 K located below the CC, which is a reduction from both Cases 1 and 2. Incorporating the cooling holes into Case 3 further reduced

the point measurement temperature to 631 K, a 28% reduction from Case 1. When compared to Case 2 the surface under the CC looks almost identical. However, the presence of cooling holes broke up the hot streak from the CC where it did not extend past 80% axial chord. After 86% axial chord the vane surface was close to a uniform temperature of approximately 630 K from the hub to the tip, which is different from Case 2 where the tip is cooler than the hub.

Case 4 displayed a minimum overall effectiveness of 0.63, corresponding to a maximum surface temperature of 1007 K at the vane tip within the bounds of the combustion cavity. This maximum surface temperature was a 3% decrease from Case 1, but a 5% increase from Case 3. At the point location Case 4 had a surface temperature of 630 K, or 0.83 overall effectiveness. Case 4 was comparable to Case 3, and achieved a 28% and 10% reduction compared to Cases 1 and 2, respectively. The hot streak present in Cases 2 and 3 can still be seen in Case 4, as shown in Figure fig:overall effectiveness cases 1-4. Although this streak extended further axially than Case 3, the temperature of the streak was reduced when compared to Case 2. The reduced temperature was a result of the additional conduction paths introduced by the pins. These paths allowed heat transfer through the interior plug to the pressure side of the vane, but had a negligible impact on the overall effectiveness at the point measurement location.

In addition to adding a conduction path, the pins also acted as pin fins and increased heat transfer to the internal coolant and raised the average coolant temperature at the trailing edge slot. The coolant in all three cases entered the vane at 300 K. Cases 2 and 3 had an average coolant exit temperature of 412 K and 411 K, respectively. However, Case 4 had an average coolant exit temperature of 490 K, a 19% increase from Case 3. This phenomenon is also noticeable in the overall effectiveness profile for Case 4, shown in Figure 193. The contours have a scalloped shape around

the pins where the overall effectiveness at the location of the pin was higher than the surrounding area. The contour and the increased coolant exit temperature shows the pins were pulling heat away from the surface and heating the coolant more effectively. The temperature profile could be smoothed further by relocating the cooling holes between pins within the hot streak. This movement would increase the coolant released in that region and thus protect the surface from the hot combustion gases and reduce the heat transfer into the vane.

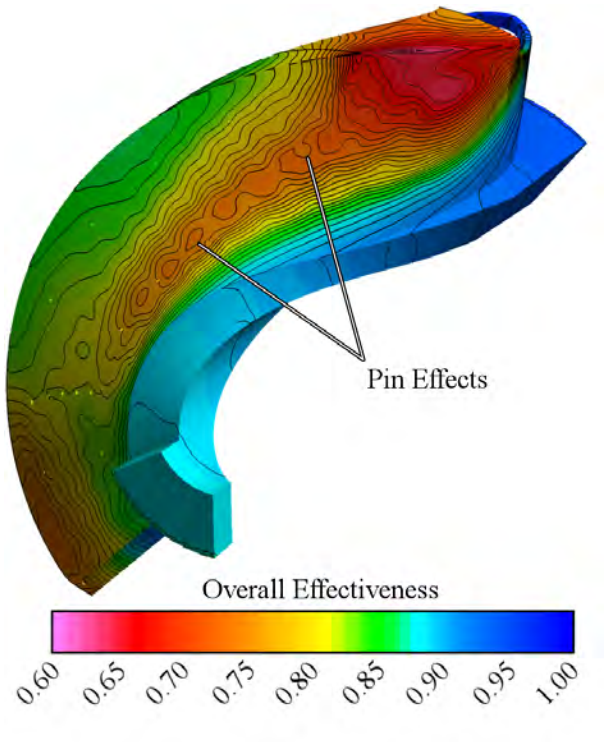


Figure 193. Case 4 overall effectiveness with contour edges shown

The pins provided a more distributed heat load, as shown by the heat flux profile of Cases 3 and 4 shown in Figure 194. The vane surface can be split into two regions, as labeled in the figure. Region 1 contained the outer holes and showed a similar heat flux of around 4 x 10^4 W/m^2 in both cases. The differences between the two cases were seen within Region 2. Here, Case 3 showed significant gradients while Case 4 shows these gradients had smooth by a factor of two. The Region 2 high heat flux

values found on the profiles correspond to the low overall effectiveness region shown in Figure 192. This was most likely a result of both the highly turbulent nature and completing reactions of the flow exiting the circumferential cavity.

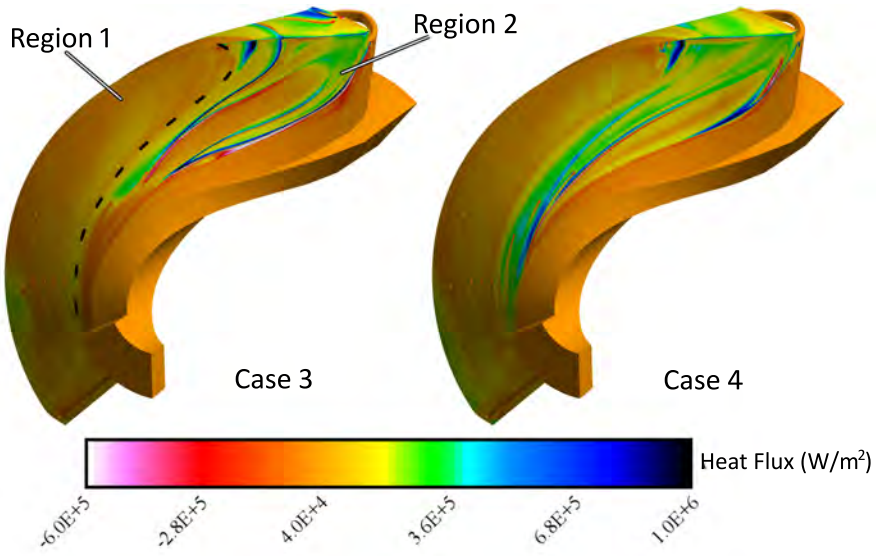


Figure 194. Case 3 and 4 heat flux contours

4.7 Experimental Test Methodology

An experimental test was conducted to determine the validity of the computational results and ensure that the cooled vane referred to as "Vane A" achieved a cooler surface than the baseline solid vane. Two temperature measurements near the trailing edge of each vane were made using thermocouples installed into the 0.51 mm diameter thermocouple ports shown in Figure 195 such that the measurement bead was in contact with the surface with half inside the channel and half exposed to the flow. These thermocouple ports positioned the beads 4.19 mm and 11.90 mm from the vane trailing edge at 60% and 90% radial vane span, respectively. Static pressure measurements were made for Vane A only, even through all internally cooled vanes included pressure taps. The internal vane pressure measurement was made through

a 1.59 mm pressure tap hole, 15.875 mm upstream from the vane trailing edge, as shown in Figure 195. Additionally, static pressure measurements were made in the vane passages on the pressure and suction sides of Vane A. These passage pressure taps were inserted through 1.59 mm diameter holes in the UCC collar and were in line axially with the internal vane pressure measurement. Unlike the computational results shown in Figure 191 which looked at internal and suction surface pressures at the vane half span, the experimental pressure taps were positioned at the vane tips and vane passage OD to minimize blockage by the pressure tubing. A pressure tap was also installed through the diffuser and bent backward toward the HGV through the core flow passage to take a static pressure measurement at the vane leading edge. All pressures were measured using the Initium pressure scanner discussed in Section 3.1.5.

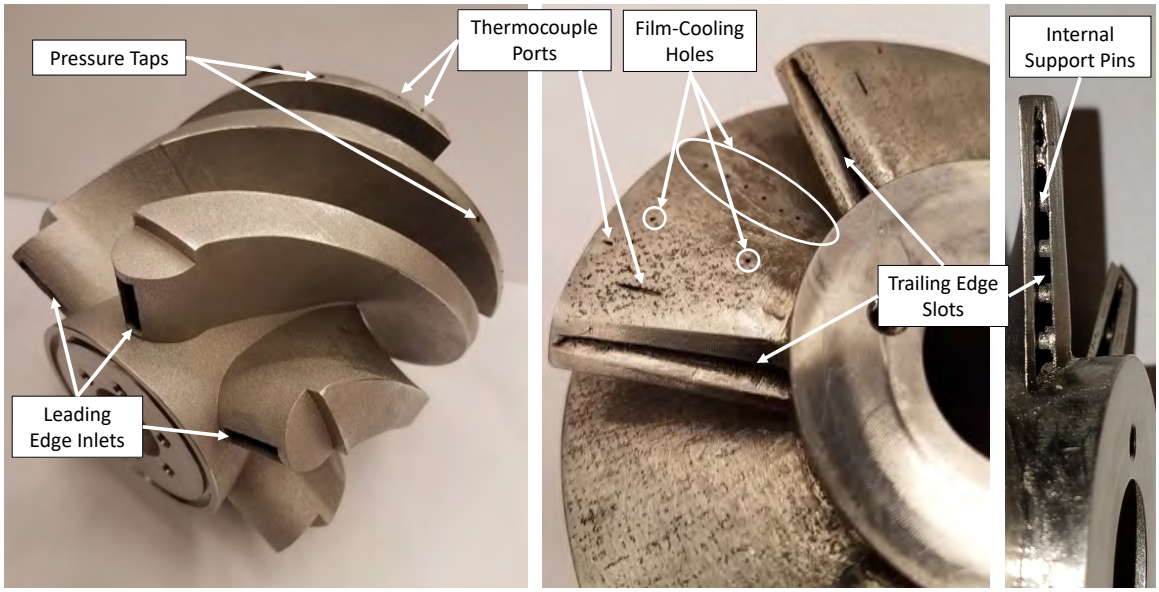


Figure 195. 3D printed HGV from Linear AMS with finish machining completed by the AFIT Model Shop

Figure 196 shows the 3D printed HGV painted, instrumented, and installed in the UCC. The vane was primed and painted with VHT Flame Proof silica-ceramic paint rated to 1093 C. The black paint helps create a uniform high emissivity surface to

more accurately compare emitted intensity values recored by the IR camera. Infrared thermography was used to map the surface temperatures on the solid vane and Vane A visible trailing edges. The single camera IR thermography setup outlined in Section 3.1.6.6 was used for this experiment. Internal bypass filter #12 in the SC6700 IR camera allowed emissions at 3,900 nm ±150 nm range to be visible while blocking all emissions outside of that range. This filter eliminated any emissions from flames that may have been visible over the vane surface. The thermocouples embedded in the vane surface shown in Figure 196 were used in the calibration of IR intensities into temperature values through the use of the *IR_Combined.m* MATLAB script discussed in Section 3.1.6.6. Table 16 gives the coordinates of the thermocouple bead locations with respect to the ExamineIR image coordinate system (origin is in the upper left corner). These coordinates were the same for all IR images taken during the test. The beads were identified by heating the tip of a small flathead screwdriver and aligning the blade and corner of the head with the bead. The hot screwdriver was visible in ExamineIR allowing the user to move the cursor to the corner of the screwdriver blade and read the corresponding coordinate displayed on the computer screen.

Table 16. Thermocouple bead locations in IR image coordinate system (required for calibration)

Thermocouple	X Coordinate	Y Coordinate
Solid Vane, 60% Span	219	129
Solid Vane, 90% Span	273	68
Vane A, 60% Span	389	308
Vane A, 90% Span	457	326

Only one flow condition was run to match the computational flow condition above, but this single condition was repeated three times (Runs 1 - 3). The condition was a 0.108 kg/s total air mass flow rate, with a 70/30 core-to-cavity flow split, at an equivalence ratio of 0.72 (0.0015 kg/s flow rate of propane). The experimental testing

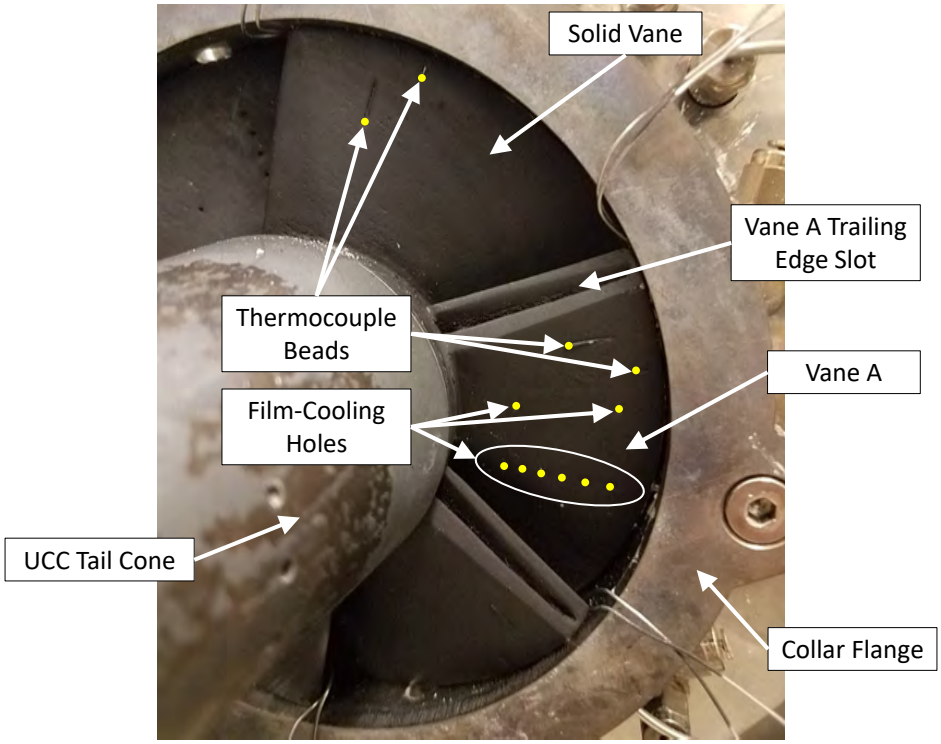


Figure 196. 3D printed HGV, painted, instrumented, and installed in the UCC (Bead locations and cooling holes are highlighted with yellow dots to be visible against the black background)

used the baseline fuel injection scheme outlined in Section 3.3, but incorporated the variable geometry diffuser discussed in detail in Sections 6.1.1 - 6.1.3 to control the flow splits. At these conditions a 70/30 split required a diffuser total-to-static pressure differential of 330.9 Pa (0.048 psi) which was obtained by a diffuser opening of 5.8 mm. For each of the three runs the rig started cool and was brought to the specified flow condition. The temperatures were allowed to stabilize for approximately five minutes before taking measurements.

4.8 Experimental Test Results

The results of interest included the experimental pressure drop internally from the leading edge to the internal measurement location, and the pressure drop across the vane shell that enabled coolant to flow out of the cooling holes. The surface

temperature of the solid vane and Vane A was also important to show there was a benefit to using this cooling scheme. How well the computational results matched the experimental results in each of these properties was also of interest.

Figure 191 showed the computational pressure distribution inside and outside the vane shell for Vane A (displayed as Case 4 in the figure) at the mid-span at each axial position. At the leading edge of the vane just past the inlet the fluid had a computational gauge pressure of 124 Pa externally. This position lines up with the upstream experimental pressure measurement location. At the internal pressure tap location, approximately 85% axial chord, the computational internal pressure at the mid-span on the inside suction surface was calculated to be -2,797 Pa. These values result in a calculated static pressure drop of 2,921 Pa from leading edge to the internal pressure tap location as reflected in Table 17.

Table 17. Vane A pressure drop measurement data from the vane leading edge to the internal pressure tap at approximately 85% axial chord

Data Source	LE Pressure	Internal Pressure	Pressure Drop
CFD	124 Pa	-2,797 Pa	2,921 Pa
Run 2	3,285.1 Pa	114.6 Pa	3,170.5 Pa
Run 3	3,570.6 Pa	660.7 Pa	2,910.0 Pa

Experimentally the Run 2 leading edge gauge pressure was measured at 3,285.1 Pa, with a Vane A internal pressure measurement at the 85% axial chord internal gauge pressure tap reading 114.6 Pa. While the absolute values differed from the computational result due to the way the operating pressure (101,325 Pa) was specified and where that value was applied in the computational domain, the static pressure drop was measured at 3,170.5 Pa which is within 7.9% of the computational result. In Run 3 the leading edge gauge pressure was measured at 3,570.6 Pa, with a Vane A internal pressure measured at 660.7 Pa, for a static pressure drop of 2,910.0 Pa. The pressure drop in Run 3 was even closer to the computational result at at 0.3%

difference. The pressure results for Run 1 were unusable due to an Initium calibration issue, however, the Run 1 temperature data was usable and is shown later in this section.

The 200 Pa variation in pressure drop between Runs 2 and 3 was likely due to unsteadiness in the air mass flow controller as discussed by Lt. DeMarco in Section 3.4 of his thesis [161]. The 200 Pa variation in pressure drop between Runs 2 and 3 and the computational result was consistent with the pressure swings behind the pins seen in Figure 191 which were greater than 200 Pa and the overall pressure variation seen in the vane.

The pressure difference across the suction surface vane shell from inside the vane to outside the vane at 85% axial chord was more difficult to compare between computational and experimental results due to the measurement locations. This pressure differential was important because it was the driving force to move coolant through the film-cooling holes. Experimentally, the pressure measurements were taken near the OD of the vane passage or near the vane tip so the pressure tubing wouldn't block the narrow passages. Computationally the pressure distribution shown in Figure 191 was taken at the mid-span along the vane surfaces. To make an accurate comparison, the computational pressure was also found at the location of the experimental pressure measurements. Figure 197 shows an axial slice through the vane at the pressure measurement location with the red cross hairs highlighting the location of the end of the pressure tubing slightly protruding into the passages. Internally there was little pressure change from the mid-span to the vane tip along the suction surface inner wall. However, externally there was a large radial gradient along the suction surface.

Table 18 shows the internal pressure, external pressure, and difference across the vane shell for the experimental runs and at both computational positions. While there were differences in the pressure drop between the computational and experimental

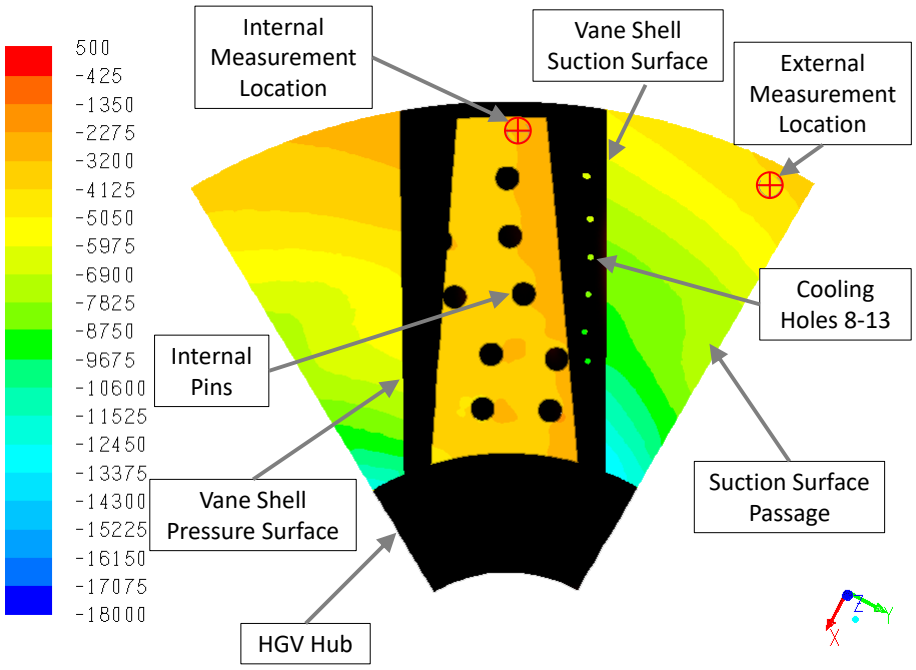


Figure 197. Vane A computational pressure distribution at 85% axial chord

result, it is important to point out that a physical pressure drop was observed across the vane shell which could drive coolant through film-cooling holes. This outcome validates the cooling concept. As shown in Table 18 the experimental drop across the vane shell was repeatable, with a value that fell between the two computational results. There were slight differences between the computational and experimental hardware that could account for the variation in results. Computationally the vane tip was modeled in contact with the OD collar wall. The physical hardware had a small gap (approximately 1 mm) between the vane tip and the OD collar to allow for independent thermal expansion. This gap could explain a different pressure distribution near the passage OD that resulted in the discrepancy in pressure.

The embedded thermocouples in the vane surface provided useful temperature information at two discrete points that could be used for comparison between the solid vane and Vane A, as well as a comparison to computational results. Table

Table 18. Vane A pressure drop measurement data from internal vane to the external suction surface across the vane shell at approximately 85% axial chord

Data Source	Internal Pressure	External Pressure	Pressure Drop
CFD mid-span	-2,797 Pa	-6,431 Pa	3,634 Pa
CFD OD	-3,177 Pa	-4,342 Pa	1,165 Pa
Run 2	114.6 Pa	-2,070.3 Pa	2,184.9 Pa
Run 3	660.7 Pa	-1,441 Pa	2,102.1 Pa

19 shows the average computational and experimental temperature readings for the thermocouples on the solid vane and Vane A at 60% and 90% radial span for each of the three runs.

As shown in Table 19 the surface temperatures for Vane A at 60% radial span were consistently below the solid vane surface temperatures at the same location. The fact that the surface temperatures on Vane A were consistently less than those of the solid vane further supports the validity of this cooling scheme. Since there were a minimal number of film-cooling holes, the temperature reduction was almost exclusively due to internal cooling. At 90% radial span the surface temperatures on Vane A remained less than those of the solid vane, but by less of a difference. There was a temperature increase at the vane tips of both vanes due to the hot gases being centrifugally slung toward the OD of the passage as the vanes turned the fluid more in the circumferential direction near the trailing edge. In the case of Vane A there

Table 19. Average computational and experimentally measured temperatures at the 60% and 90% radial span for the solid vane and Vane A

Vane	CFD		Run 1		Run 2		Run 3	
	60%	90%	60%	90%	60%	90%	60%	90%
Solid Vane	898 K	955 K	835 K	912 K	802 K	873 K	749 K	818 K
Vane A	627 K	668 K	790 K	889 K	754 K	849 K	716 K	816 K
Difference	271 K	267 K	45 K	23 K	48 K	24K	33 K	2 K

was reduced internal cooling in this region due to the presence of the wall at the vane tip. Also, due to the small gap between the vane tips and the OD collar, hot gases were able to migrate up and over the vane tips. This flow path allowed the tips to be heated from an additional surface further elevating the temperature.

While the computational models were run steady state, the inherently unsteady nature of the UCC flow field caused variations in the calculated surface temperatures at the thermocouple locations over a cycle of approximately 1,000 iterations. The converged solutions for the solid vane and Vane A computational models were allowed to continue for 2,000 more iterations with the surface temperatures at both thermocouple locations recorded for each additional iteration. These temperatures are shown in Figure 198 for both vanes. This figure shows the magnitude of the predicted cooling at these two locations by comparing the solid vane results to those of Vane A. Taking an average of the temperatures across all 2,000 data points for each location yielded the results shown in Table 19.

Comparing the predicted temperatures to the experimental values in Table 19 shows the CFD results over predicted for the solid vane and under predicted for Vane A. The solid vane was over predicted by 103 K at 60% span and 87 K at 90% span compared to the average of the three experimental temperatures. Vane A was under predicted by 126 K at 60% span and 184 K at 90% span compared to the average of the three experimental temperatures. When comparing computational surface temperature results to experimental values on a 3D printed part, Zhang et al. [170][171] found that due to the surface roughness of the 3D printed experimental hardware the computations over predicted the temperatures on uncooled surfaces, and under predicted temperatures on cooled surfaces by approximately 7%. There are several possible additional causes to account for the remaining variation. The first is that the material properties that were modeled did not exactly match the characteristics

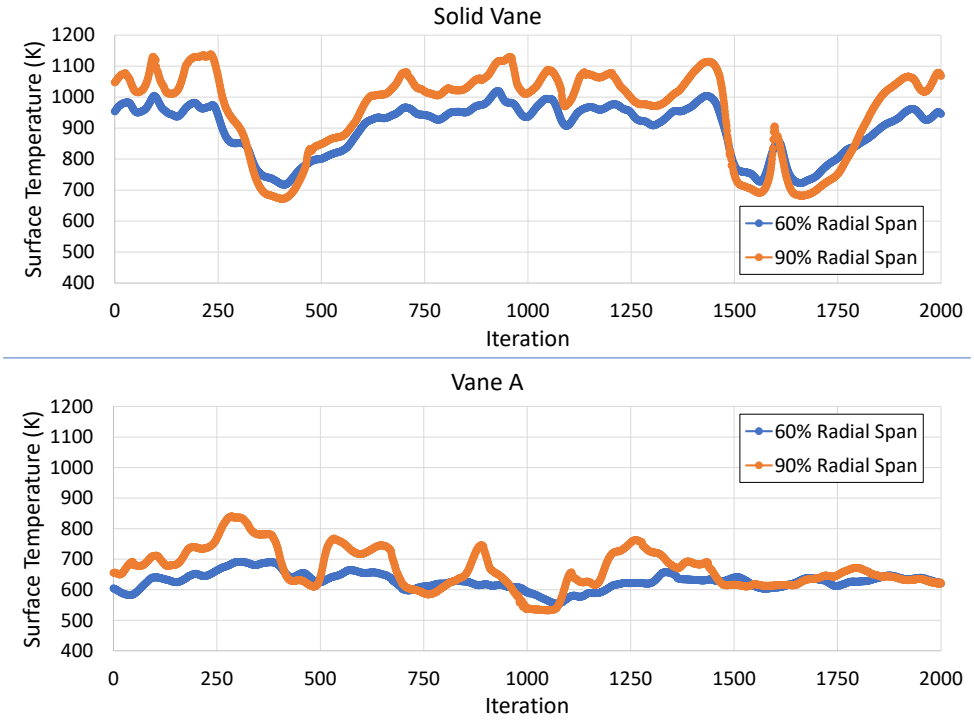


Figure 198. Computational variation of surface temperatures with iteration at the thermocouple measurement locations for both vanes

of the material of the experimental hardware. The vane was manufactured from 17-4 stainless steel which has a variable thermal conductivity of 17.9 W/m-K at 422 K and 22.6 W/m-K at 755 K. The specific heat of 17-4 is 460 J/kg-K from 273-373 K, a value at higher temperatures could not be found. The thermal properties were defined in the computational analysis by selecting "steel" from the FLUENT material database. This database specified these values as constants with the thermal conductivity set at 16.27 W/m-K and a specific heat of 502.48 J/kg-K. With a higher thermal conductivity in the experimental hardware there would be greater conduction through the material and a greater heat flux assuming the same temperature differentials. The higher energy transfer could result in hotter or cooler surface temperatures depending where on the vane the measurement was taken and whether energy was free to conduct into or out of that region.

The second potential cause of the temperature deviation, as mentioned earlier, is the variation in geometry resulting from a gap between the vane tip and the collar wall in the experimental hardware but not in the computational model. In addition to allowing hot gases to pass over the vane tip and experimentally heat a surface that was not exposed to hot gases computationally, this gap could alter the flow field near the thermocouple measurement locations and result in a modified heating pattern. With greater heating of the vane tip and a higher thermal conductivity to distribute the thermal energy through the thin vane shell, it is not surprising that the 90% span thermocouple on Vane A read 184 K higher than computationally predicted.

Finally, the CFD solution was modeled with periodic boundaries which created an equivalent flow situation to having six identical vanes arrayed around the HGV hub. The experimental hardware featured a different vane cooling configuration in each of the six positions around the HGV hub. This configuration may have resulted in a non-uniform distribution of air through the vane passages if some cooling schemes were more free-flowing than others. Additionally, the cooled vanes that allowed air to flow though them resulted in less air moving through the vane passages surrounding them and thus potentially altering the flow field of the adjacent vane. This was particularly true for the solid vane which was modeled computationally as having identical vanes in the adjacent positions, and thus all of the air went through the vane passages. In the experimental hardware the adjacent vanes were cooled and allowed air to flow through them reducing the mass flow rate of air in the vane passages surrounding the solid vane.

Using the computational and experimental pressure drop from the vane leading edge to 85% axial chord, and converting the drop to velocity, yielded a 9% difference between CFD and the larger experimental value. This change could be the result of a change in airflow around the vanes. While the reduced quantity of air experimen-

tally still resulted in lower measured surface temperatures than the computationally predicted value, the change in flow rate could have altered the flow pattern of the hot gases through the vane passage and produced a locally cooler surface at the measurement locations, but created a hotter than expected region at a different location.

IR thermography was planned to map the solid vane and Vane A surface temperature distributions on the suction surface at the visible regions near the trailing edge. Figure 199 shows the IR temperature image on the vanes after converting the IR camera intensity counts at each pixel to temperature data. Figure 200 shows the calibration curve of temperature versus camera intensity counts using the embedded thermocouple measurements from the solid vane and Vane A from all three runs. The correlation of the data was poor with an R^2 value of only 0.756. The cause of the low correlation is explained using Figure 201 which shows flaking paint on the vanes following Run 1. As shown in the figure there were large sections of paint that were burned away to bare metal, however, it was not always in continuous zones leaving patches of paint. Since the dark paint and light colored metal have very different emissivities, the temperatures from the dark surface appeared hotter to the IR camera than the temperatures from the light surfaces even for equal temperatures. These paint issues affected the thermocouple locations resulting in variations of intensity counts for equal temperatures. Since the displayed temperature in the image was then a function of the actual surface temperature and the color of the region on the vane it was emitting from the results were not overly useful. The paint continued to burn off and degrade through Run 2 and 3 so those temperature profiles are not shown.

While the IR images were not useful for comparison of the temperature distribution to computational results, they do provide some qualitative information comparing the solid vane to Vane A. Using comparable locations that also had the same surface

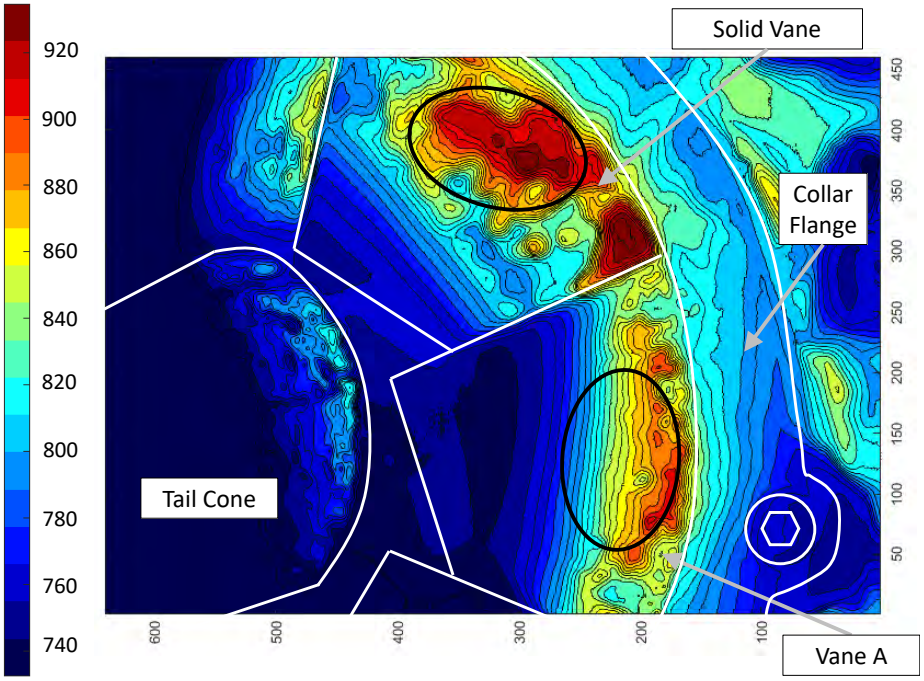


Figure 199. IR measured surface temperatures (K) on the solid vane and Vane A from Run 1. Hardware outlines were added for clarity

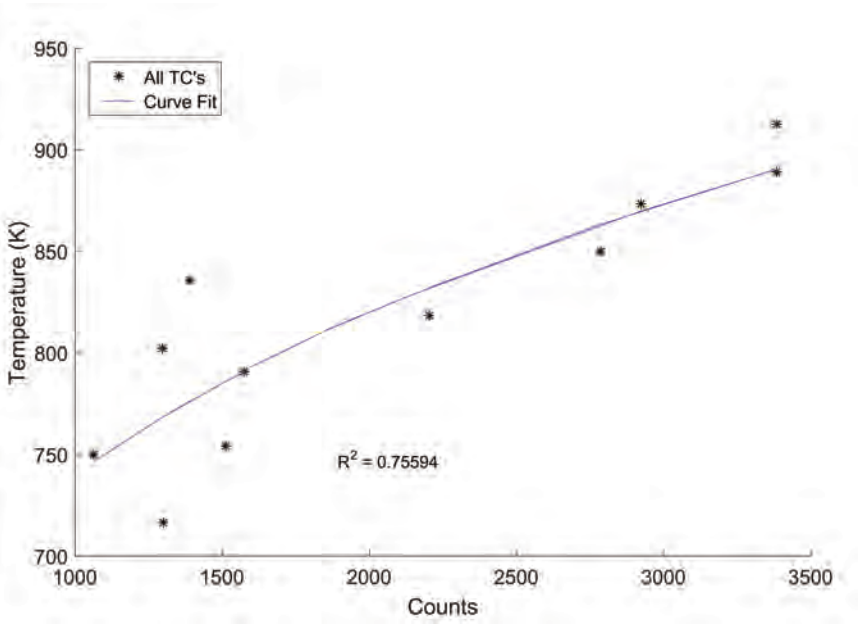


Figure 200. IR image calibration plot using embedded thermocouple measures from the solid vane and Vane A for all three runs

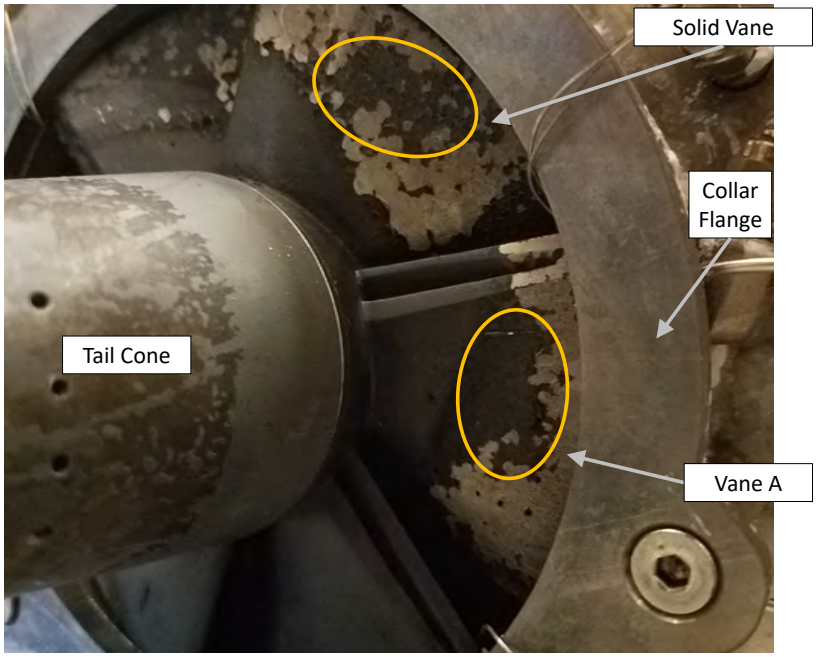


Figure 201. Vane paint following Run 1

color between the two vanes in the IR temperature image (black ellipses in Figure 199 and orange ellipses in the corresponding locations in Figure 201) showed the solid vane had higher temperature magnitudes than Vane A. While there are other factors that influence how much paint burned off of each vane, such as poor adhesion due to a number of factors, the solid vane lost more paint, possibly indicating that it experienced higher surface temperatures.

4.9 Objective 1 Conclusions

Through the use of numerical tools an analysis was conducted that included complex fluid flow, chemical reactions, and heat transfer. An initial proof-of-concept study analyzed several internal geometry variations of the HGV where several conditions were found that reduced vane surface temperatures compared to the baseline solid vane results using only internal cooling. Additionally, through pressure analysis on the internal and external regions of the HGV across all vane variations, the smaller

exit area slot was found to result in elevated internal pressures compared to the external pressures at the same locations along the suction surface of the vane showing film-cooling could be possible. Adding film-cooling holes to the plugged vanes with the smaller exit area showed that it was possible to move coolant from the stagnation region of a vane and have it exit through three of the eight cooling hole locations with a blowing ratio ranging between 0.29 and 0.56.

An additive manufacturing approach was used to produce a single piece, six-vane, stagnation cooled HGV to enable experimental testing in the AFIT UCC test rig. Due to the requirements of the printing process a matrix of internal pins was needed to support the thin vane walls. A modified film-cooling hole pattern was also added to three of the six vanes based on the results of the proof-of-concept study that showed the holes needed to be placed downstream of 50% axial chord. Prior to receiving the final printed part, a computational analysis was performed on the baseline plug, small exit area vane with the modified film-cooling scheme with and without pins to quantify the impact of the pins on surface temperatures and pressure distributions. The pins caused a 15% drop in mass flow rate through the vane which also resulted in a nominal 14% reduction in blowing ratio in each hole. Even with this reduction, the blowing ratios still ranged from 0.44 to 0.97. As a benefit, the pins caused the transition point of the pressure differential to shift from approximately 45% axial chord to 33% axial chord. This movement would enable cooling holes to be added to the suction surface closer to the leading edge. The computational results also showed that the pins caused local increases in overall effectiveness on the vane surface.

When the additively manufactured HGV was experimentally tested the results validated the outcome of the computational analysis. The trends in pressure and surface temperature were also validated, but with some deviation. The experimental pressure drop from the vane leading edge to the 85% axial chord internal pressure

measurement was less than 1% of the computational value for Run 3 and 7.9% for Run 2. The pressure drop at 85% axial chord from the vane interior to exterior was not as close, but the experimental results still demonstrated a larger internal pressure to drive coolant flow to the vane surface. The pressure deviation was likely due to a gap between the vane tip and collar that was present in the experimental hardware but not in the computational model. The experimental temperature measurements demonstrated that Vane A achieved an average surface temperature reduction of 5.3% at 60% radial span and 1.9% at 90% radial span compared to the solid vane. Since the film-cooling scheme was designed for flow analysis and not specially for cooling, the surface temperature reduction on Vane A was almost exclusively from internal cooling. By applying a film-cooling scheme designed for surface temperature reduction to the Vane A internal configuration further temperature reductions could likely be achieved. While the computational surface temperatures at the two specific thermocouple measurement locations were on average 11% over predicted for the solid vane, and 19% under predicted for Vane A, the cause of these deviations is explainable and was attributed to flow through the vane tip gap and differences in the core velocity between the computational model and the experiment.

The present research was conducted on the LLCB UCC HGV that was not optimized for pressure drop or coolant extraction. Despite this limitation the results showed the viability of this cooling concept to reduce the vane surface temperature. With additional modification to the exit area of the trailing edge slot, and reshaping of the suction surface to add additional curvature, it is expected that the forward-most point where coolant could exit the vane could be moved forward to cover more of the region of elevated temperatures below the circumferential cavity.

In addition to cooling the HGV, this technology could also be applied to small turbine-burners such as those being tested by Colcord et al. [39]. They desire the

addition of small rectangular cavities in the suction surfaces of turbine vanes to serve as pilot burners. Small amounts of heat addition between turbine stages can have a large impact on the available power to the turbine. The method of moving higher pressure air from the stagnation region to the lower pressure vane cavity could be used to provide an air injection source directly into the recessed cavity rather than relying on compressor bleed air or cavity entrainment.

V. Objective 2: Effect of Conjugate Heat Transfer

Numerically investigate the effect of conjugate heat transfer on reacting flow analysis in the baseline UCC model

In Objective 1 conjugate heat transfer was used to allow for the calculation of HGV surface temperatures and the effectiveness of different cooling schemes on the ability to reduce those temperatures. In this Objective, conjugate heat transfer analysis was used to determine the effect on gas temperatures in the UCC circumferential cavity and at two positions at the exit of the combustor. One position was between the vane passages just upstream of the HGV tailing edge, while the other was just downstream of the HGV trailing edge. The computational results were compared to experimental data taken at comparable test conditions.

5.1 Objective 2 Background

All prior UCC numerical analysis was run adiabatic. There seemed to be reasonable agreement with experimental data taken within the circumferential cavity, however, through the vane passage and at the exit plane of the combustor the agreement with experimental data broke down. At the exit region the magnitude of the computational temperatures were well above experimental results and the thermal distribution in the exiting gases presented a skewed or distorted distribution. As discussed in Section 2.10.5, conjugate heat transfer in a combustor accounts for heat loss from the fluid to the solid to help produce more representative gas temperatures. Additionally, when reacting chemistry is modeled, the addition of conjugate heat transfer can allow quenching of the flame at the wall to produce a more realistic flame volume. One added benefit of including conjugate heat transfer is the reduction of error in selecting incorrect boundary conditions. While a boundary condition must

be specified at the edge of the computational domain, with conjugate heat transfer the flow solver will calculate the conditions at the fluid/solid interface which is typically more difficult to measure or define.

5.2 CFD Case Setup

The basic case setup for this objective was nearly the same as for Objective 1 outlined in Section 4.2, including the use of 60° periodic boundaries and independent core and cavity inlets. Calculations were performed using a three-dimensional domain and included a complex fluid flow, reacting chemistry, and conjugate heat transfer. The present study expanded the surfaces included in the conjugate heat transfer analysis from just the solid HGV to also include the diffuser middle diameter, circumferential cavity walls, exhaust collar, and tail cone as shown in Figure 202. All other walls were treated as adiabatic. The thickness of the diffuser middle diameter was specified at 6.35 mm and the circumferential cavity walls were 1.27 cm to match experimental hardware. All remaining domain dimensions also matched the experimental hardware as specified in Section 3.3.

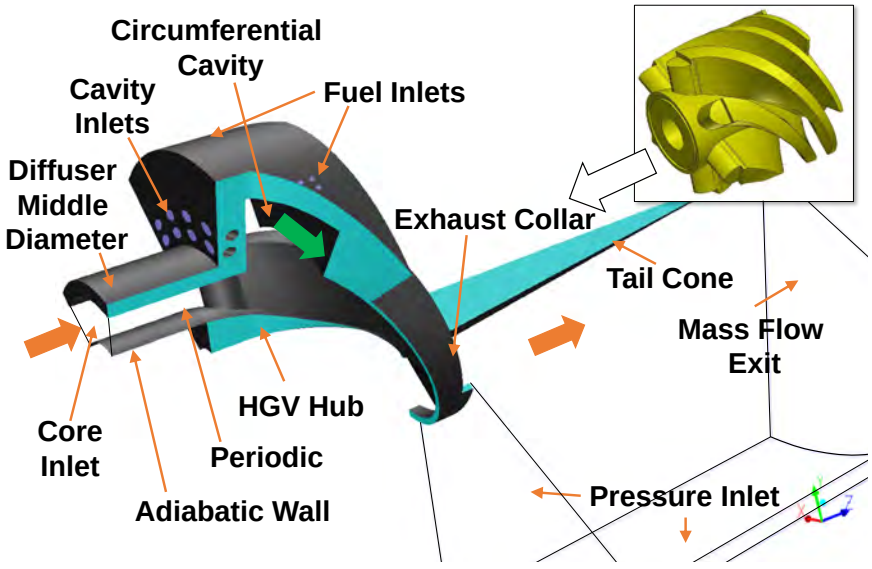


Figure 202. Computational test domain with solid walls shaded

The computational domain included a core mass flow inlet, cavity mass flow inlet, pressure inlet over the tail cone, and a mass flow exit at the end of the domain. The mass flow exit was added to account for suction caused by the exhaust ventilation system in the lab. The pressure inlet was specified at atmospheric pressure and allowed air to be pulled into the domain around the combustor exit to achieve the specified mass flow rate at the domain exit.

The domain shown in Figure 202 had fuel injectors positioned over the vane passages, rather than over the vane tips as studied in Objective 1. The reason for this change was due to the available experimental data being taken from cases that used the variable geometry diffuser that will be discussed in Chapter VI. When the rig was reassembled after the addition of the variable diffuser, the position of the vane tips had shifted from under the fuel injectors, to the space between injectors as shown in Figure 203. This change was due to a difference in the way the vane position was clocked relative to the diffuser mounts with the variable diffuser. The configuration of the fuel injectors themselves was still as described in Section 3.3, and shown in Figure 161, but clocked 20° from the baseline position as shown in Figure 203.

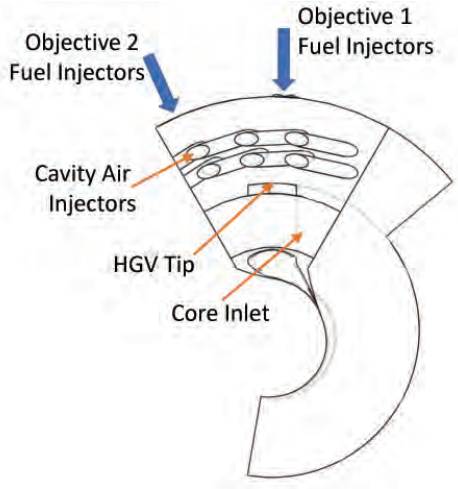


Figure 203. Front view of the computational domain showing the shift in fuel injector position for the present study

5.3 Grid Development

The grid was generated in Pointwise V17.3 R5 utilizing unstructured surface meshes and the T-Rex hybrid mesh generator for the fluid volume mesh. The solid regions were gridded with an unstructured volume mesh only. The same grid was used for the conjugate and adiabatic domains, however, only the fluid volume mesh was exported from Pointwise for the adiabatic cases. The same griding parameters including the first cell wall spacing, solid volume mesh boundary decay, and fluid volume mesh boundary decay were used for the present study that generated the medium resolution domain discussed in Section 4.3 that was previously shown to be grid independent. These parameters included a first prism height of 0.001 mm, solid volume mesh boundary decay of 0.95, and fluid volume mesh boundary decay of 0.92. The resulting conjugate domain grid had 25.2M cells, while the adiabatic domain grid had 10.3M cells.

5.4 Computational Settings

The computational settings for the present study were identical to those outlined in Section 4.4. There were, however, several additional fluid boundary specifications caused by modeling the exhaust ventilation, and additional temperature boundary conditions resulting from replacing adiabatic domain exterior walls with conjugate walls. Keep in mind the temperature boundary specifications were only for the exterior walls of the domain, the fluid/solid interface temperatures were calculated by FLUENT. The fluid boundary specifications are given in Table 20 for the periodic domain sector. To convert to a total engine flow rate the given values need to be multiplied by 6. The flow rates correspond to a total inlet mass flow rate of 0.108 kg/s with a of 70/30 core-to-cavity mass flow rate split. The specified fluid temperature on the "Domain Exit" is the backflow temperature. There are two fuel inlet

flow rates specified which correspond to computationally and experimentally tested equivalence ratios of 0.72 and 1.1.

Table 20. Inlet/Exit boundary condition settings

Boundary	$\dot{m}$ (kg/s)	**Gauge Total Pressure** (Pa)	**Temperature** (K)
Cavity Air Inlet	0.0054	4800	300
Core Inlet	0.0126	4800	300
Fuel Inlet Φ=0.72	0.00025	5200	300
Fuel Inlet Φ=1.1	0.000379	5200	300
Domain Exit (Vent)	0.0365	0	300
Pressure Inlet	0	0	300

The temperature boundary conditions are given in Table 21. These temperatures were experimentally derived from thermocouple measurements on the circumferential cavity walls, however, the diffuser middle diameter and exhaust collar temperatures were estimated because an experimental measurement was not available. A best effort was made to obtain experimental temperature measurements that were at steady-state to most closely match the steady-state computations.

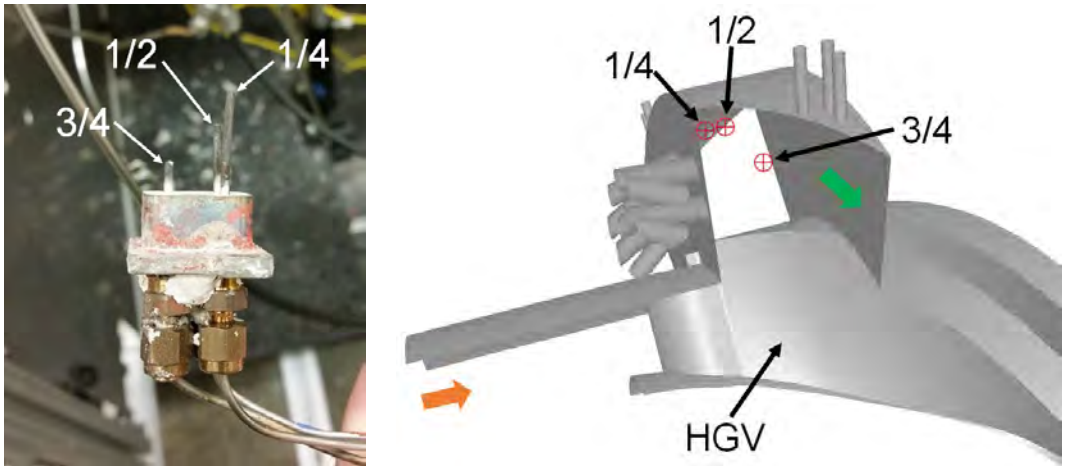
Table 21. Wall temperature boundary conditions

Boundary	**Temperature** (K)
Cavity Forward Wall	383
Cavity Top Wall	580
Cavity Back Wall	870
Diffuser Middle Diameter	355
Exhaust Collar	850

5.5 Experimental Instrumentation

There were three locations of comparison between the computational and experimental results including the circumferential cavity, vane passages just upstream of the trailing edge, and the combustor exit plane 6.5 mm downstream of the vane trail-

ing edge. Three K-type thermocouples were used to take temperature measurements in the circumferential cavity at three axial positions. Figure 204a shows these three thermocouples mounted into a removable instrumentation block that was installed in the back cavity wall of the UCC test rig (see Figure 159). The corresponding location of the thermocouple beads in the computational domain is shown in Figure 204b indicated by the red cross-hairs. It is difficult to get a circumferential perspective of the thermocouple placement from this image, but they are clustered radially outboard over the vane.

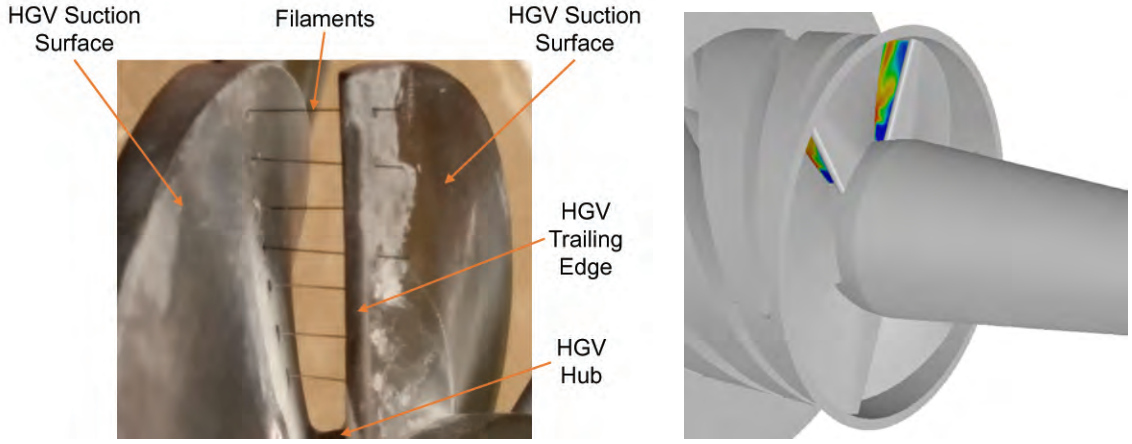


(a) Cavity Thermocouple Block (b) Thermocouple Locations in Domain

Figure 204. UCC cavity thermocouple block and corresponding placement in computational domain

In the vane passages just upstream of the trailing edge, thin filament pyrometry (TFP) was used to acquire temperature measurements along seven evenly spaced discrete wires to resolve the span as shown in Figure 205a. Figure 205b shows the corresponding computational plane at the approximate filament locations. The filaments were made of β-Silicon Carbide with a diameter of 125 μm and installed through holes burned into both vanes. The filament was bonded in place with high temperature epoxy. The experimental results using TFP were able to report filament temperatures above 920 K. Below that temperature the black body radiation from the wire was not

in the visible spectrum to be recorded by the camera. Using monochrome cameras calibrated with a separate pyrometer, as discussed by Gilbert[11], these radiation frequencies were recorded and traced back to the gas temperature that generated the intensity. TFP data were recorded at 50 Hz.



(a) Experimental Hardware (b) TFP Computational Plane

Figure 205. TFP filaments installed between vanes just upstream of the vane trailing edge with computational plane comparison

At the combustor exit plane, the thermocouple rake described in Appendix B was used to map the exit temperatures over an 80° arc as shown in Figure 476a. The four-headed thermocouple rake probe was connected to a computer controlled traverse that moved the probe head both radially and circumferentially with high spatial precision. A pre-programmed script commanded the probe position to ensure correct positioning and dwell time. A two second dwell stabilized the temperature measurement before moving to the next location. Measurements were taken at 4.8 mm increments radially and every 10° circumferentially to cover the 80° arc. The thermocouples were aligned into the flow, but were 6.5 mm axially downstream from the vane trailing edge. Post-processing of the temperature measurements using the MATLAB script printed in Appendix B allowed for the production of temperature contour maps of the exit plane. Figure 206 shows the computational exit plane.

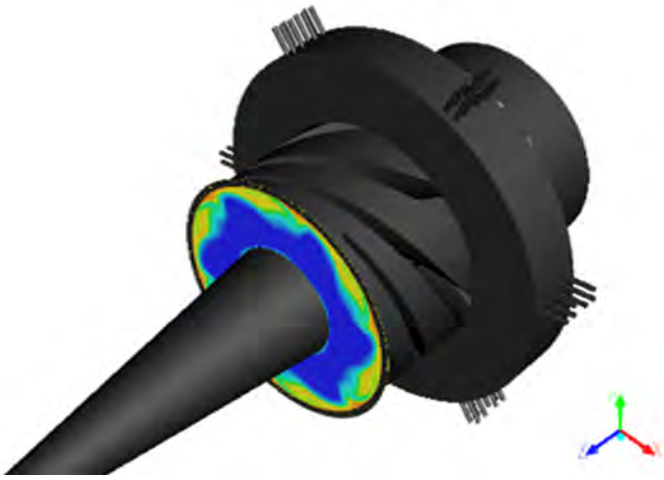


Figure 206. Computational plane at the combustor exit to compare to thermocouple rake data

5.6 Results

The comparative results between the computational and experimental data are presented by comparison location and equivalence ratio. A short summary of results displaying flame quenching and comparing metallic surface temperatures between the computational models is provided followed by computational/experimental comparisons in the circumferential cavity, vane passage TFP plane, and the combustor exit plane 6.5 mm downstream of the vane trailing edge for a cavity equivalence ratio of 0.72. The location based comparisons are then repeated for a cavity equivalence ratio of 1.1.

5.6.1 Computational Flame Quenching and Metal Temperatures.

One of the benefits of using the partially premixed combustion model with the flamelet generated manifold is the ability of the model to handle quenching due to wall contact or large quantities of fuel or dilution air. The quenching model helps produce more realistic surface temperatures because reacting flows are not in direct contact with the walls. It also helps to produce a more realistic combustion volume

within the combustion cavity. Figure 207 shows an example of temperature contours around the HGV in the adiabatic and conjugate models. The conjugate model shows a temperature reduction at the vane surface indicative of quenching, while the adiabatic model reacts all the way to the wall.

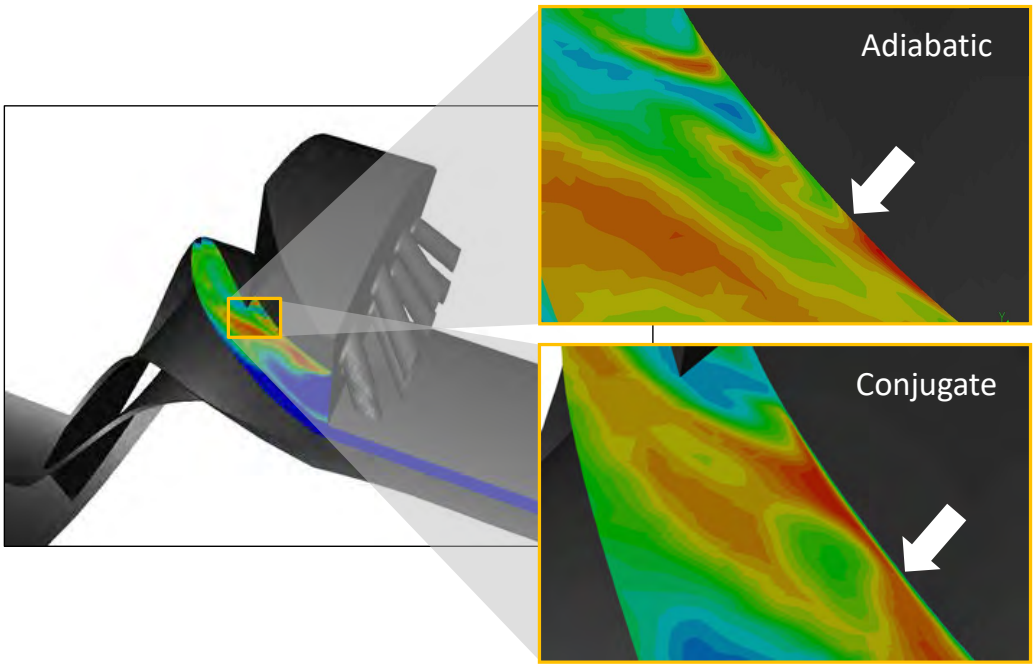
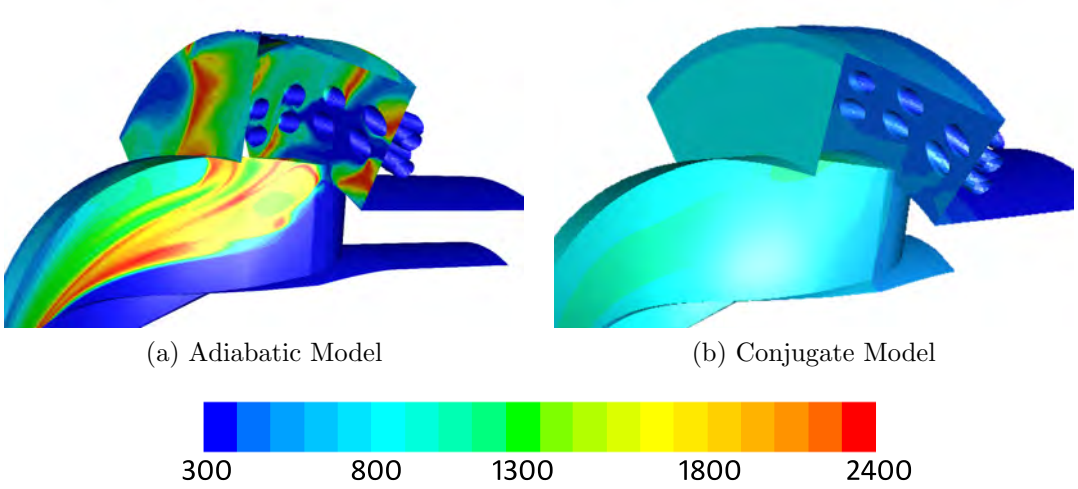


Figure 207. Comparison of temperature contours between the adiabatic and conjugate models showing quenching at the vane surface in the conjugate domain

Modeling the transfer of heat between the solid structure and the fluid could prove to have an effect on fluid injection velocities and dissipation of heat throughout the engine. Figure 208 shows an example of the metal surface temperatures inside the combustor at the 0.72 equivalence ratio computational setting outlined in Section 5.4 using both model types. It is obvious that the conjugate model allows for dissipation of heat through the metal components as shown by the lower metal temperatures and more diffuse thermal gradients. The adiabatic model is a display of the fluid temperature directly above the surface with no means to dissipate surface heat.



(a) Adiabatic Model (b) Conjugate Model

Figure 208. Comparison of computational metal surface temperatures (K) at the 0.72 equivalence ratio condition using the adiabatic and conjugate models

5.6.2 Circumferential Cavity Comparison, Φ_{Cav}=0.72.

A comparison was made between the experimental thermocouple measurements in the circumferential cavity and the temperatures predicted by the computational models at the thermocouple bead locations. The comparison results are shown in Tables 22 and 23 for the adiabatic and conjugate models, respectively. The tables show the experimentally measured temperature, the computationally predicted temperature at the exact thermocouple (TC) bead locations, an average temperature taken in close proximity around the thermocouple location, and the average temperature in the plane within the circumferential cavity at the 1/4, 1/2, and 3/4 axial planes. The numbers in parenthesis are the difference to the experimental result.

From the results shown in Tables 22 and 23 it can be seen that there was not an overwhelming difference between the two models. The adiabatic model tended to under-predict the experimental temperature at the thermocouple location while the conjugate model tended to over-predict the temperature, yet the average planar temperatures between the models differed by 8% or less. This result is not surprising as the addition of conjugate heat transfer to the model primarily impacts the walls

Table 22. Adiabatic model circumferential cavity temperature results compared to experimental data, Φ_{Cav}=0.72

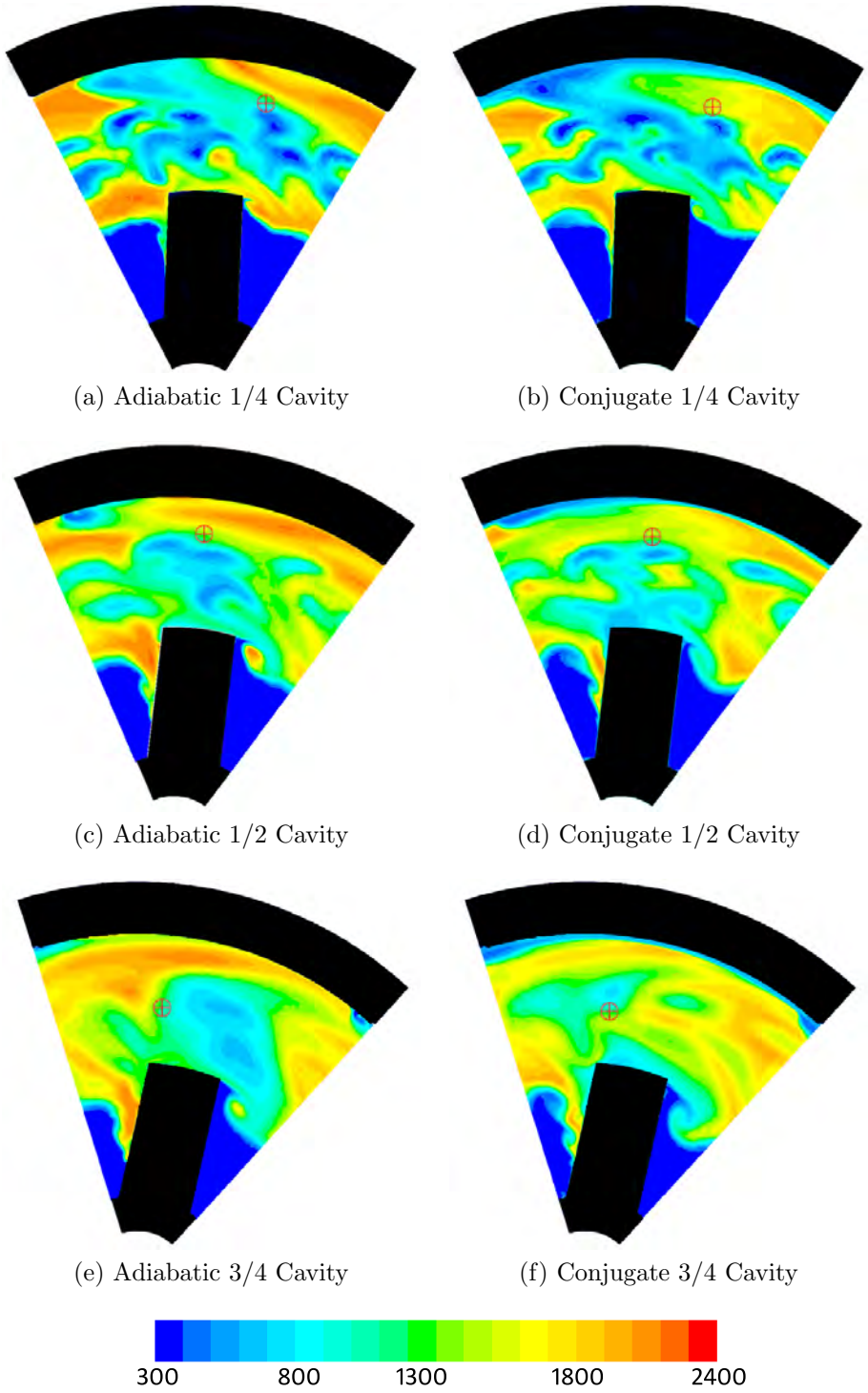
	1/4 Cavity (K)	**1/2 Cavity** (K)	**3/4 Cavity** (K)
Experimental	1273	1403	1319
CFD TC Point	1136 (-137)	1393 (-10)	1233 (-86)
CFD TC Region	1079 (-194)	1398 (-5)	1259 (-60)
CFD Plane Average	1172 (-101)	1286 (-117)	1332 (-13)

Table 23. Conjugate model circumferential cavity temperature results compared to experimental data, Φ_{Cav}=0.72

	1/4 Cavity (K)	**1/2 Cavity** (K)	**3/4 Cavity** (K)
Experimental	1273	1403	1319
CFD TC Point	1523 (+250)	1526 (+123)	1185 (-134)
CFD TC Region	1478 (+205)	1361 (-69)	1218 (-101)
CFD Plane Average	1167 (-106)	1268 (-135)	1441 (-122)

and local temperatures near the walls. Away from the walls these two models behave similarly. Some of the temperature variation that can be seen between the models is due to reactions setting up in different locations resulting from wall quenching and dissipation of combustion energy to the metal. Figure 209 shows the temperature contours at each axial plane for both models. The location of the thermocouple bead is indicated by the center of the cross-hair marker. In almost all cases the location of the thermocouple was on the edge of a steep temperature gradient. This location would cause slight variations in spatial positioning to result in several hundred degree differences in predicted temperature. These gradients could also explain some of the difference between experimental and computational results.

The gradients are caused by inefficient mixing between the fuel that enters from the combustor OD and the air that enters from the cavity front wall. The poor mixing resulted in pockets of cooler fuel that were too rich to burn. At the 1/4 plane, and to a lesser degree the 1/2 plane, the cool incoming air from the front wall air driver jets



(a) Adiabatic 1/4 Cavity

(b) Conjugate 1/4 Cavity

(c) Adiabatic 1/2 Cavity

(d) Conjugate 1/2 Cavity

(e) Adiabatic 3/4 Cavity

(f) Conjugate 3/4 Cavity

Figure 209. Temperature contours at the 1/4, 1/2, and 3/4 axial planes within the circumferential cavity, Φ_{Cav}=0.72

can be seen in Figure 209 as regularly spaced cool pockets. The flame holders in this cavity configuration setup between these air driver jets meaning that high temperature reactions occurred between cold non-reacting air jets. By the 3/4 plane the air driver jets were mostly dispersed leaving the remaining gradients to be a product of mixing. As shown in the variations between point, region, and planar measurements in Tables 22 and 23, pinpointing a value at an exact location is difficult. These variations were also observed experimentally where it was unclear if the measurements were taken in a pocket, on the edge of a gradient, or if the measurements were representative of the average cavity properties. In a repeatability study, DeMarco [161] showed UCC experimental measurement variations of up to 200 K in the cavity from one day to the next. The variation was due to the cavity reactions setting up in different spatial locations, and thus impinging differently on fixed position thermocouples, as a result of changes in atmospheric conditions.

5.6.3 Vane Passage Comparison, Φ_{Cav}=0.72.

Experimental and computational measurements at the TFP plane, described in Figure 205, using both computational models are shown in Figures 210, 211, and 212. Comparing the adiabatic model results to the experimental results, it can be seen that the magnitude of the predicted temperatures are over estimated by more than 300 K. Additionally, the distribution of the temperatures in the model show peak temperatures at the 15.7, 28.8, 39.6, 49.7, and 60.2% radial span with a skew towards the 30% filament span. The experimental data shows the peak temperatures at 39.6 and 49.7% and relatively centered along the filaments. This discrepancy shows larger hot gas volume and incorrect temperature profiles compared to the experimental results. The dual peaks in several of the line plots is the result of a rotation of the fluid in the passage that was caused by the hot gases exiting the circumferential cavity with a radial velocity component.

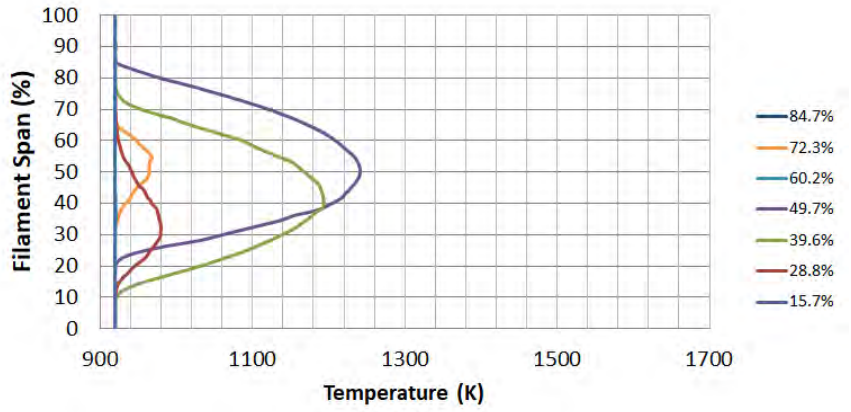


Figure 210. Experimental results at the TFP plane, Φ_{Cav}=0.72

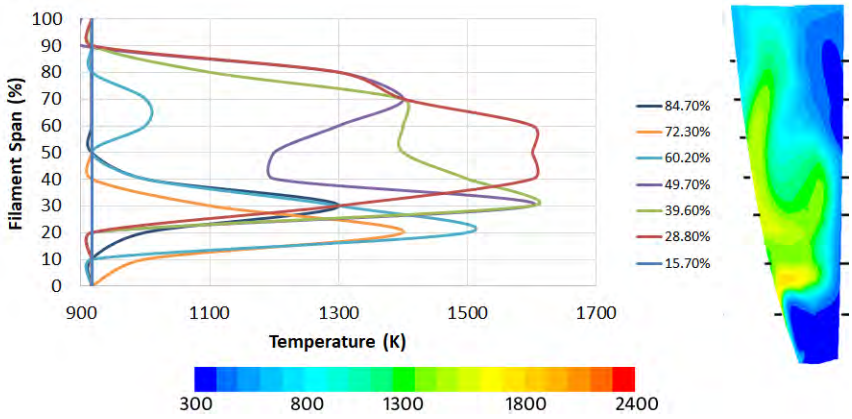


Figure 211. Adiabatic computational results at the TFP plane, Φ_{Cav}=0.72

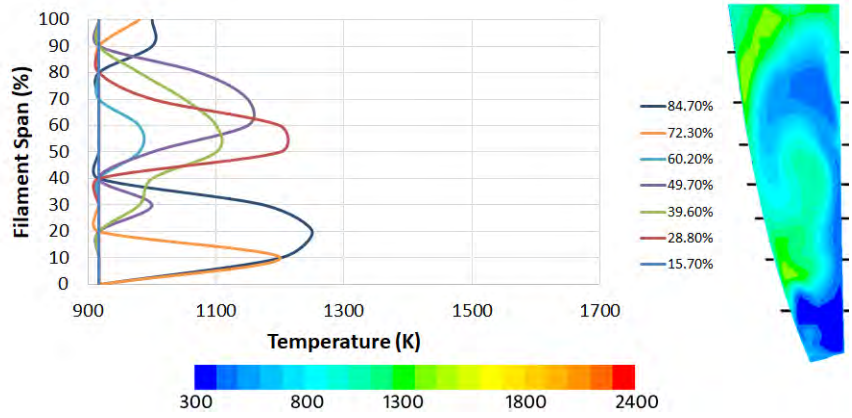


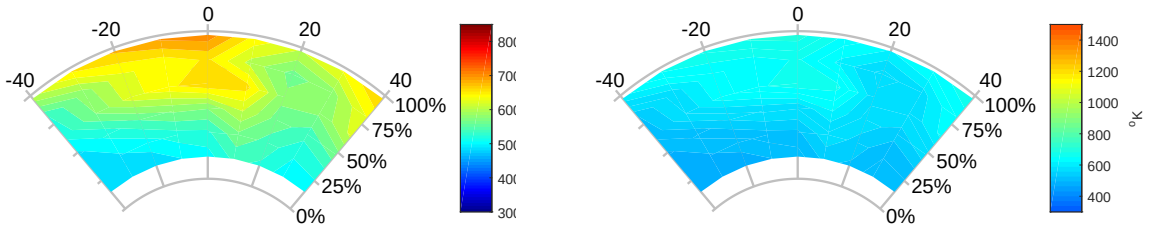
Figure 212. Conjugate computational results at the TFP plane, Φ_{Cav}=0.72

The magnitude of the conjugate model temperatures was on par with the experimental results due to the ability to dissipate heat to the vane, but came in about 50-100 K low at mid-vane span. The conjugate model and experimental results showed reasonable agreement in magnitude and placement at the 39.6 and 49.7% radial spans. The model also showed elevated temperatures at the mid-filament span at 28.8% radial span, and at the 20% filament span at 72.3 and 84.7% radial span. The elevated temperatures near the vane tip could be the result of an incorrect exhaust collar thermal boundary condition. Since there was no experimental measurement at that location, an over estimate of the boundary condition temperature would result in an artificially elevated gas temperature near the OD. The elevated temperature at the 28.8% radial span matches well to experimental data at 39.6% which could be an indication of a spatial positioning error of the lower bound of the hot gas streak in the passage.

There was a slight geometry difference between the computational model and the physical hardware that could potentially impact the results at the TFP plane and the exit plane discussed in the next section. The computational model connected the vane tip to the OD wall and would not allow gases to pass over the tip. In the physical hardware there was a gap at the vane tip to allow for independent thermal expansion of the vane and OD collar. This gap could allow gases to pass over the vane tip and thus alter the flow path and resulting distribution in the passage. While neither computational model matched the experimental data completely, the conjugate model showed much more accurate predictions of temperature due to the ability to dissipate energy from the fluid to the solid and showed a distribution that more closely represented the experimental result.

5.6.4 Exit Plane Comparison, Φ_{Cav}=0.72.

The thermocouple measurements at the combustor exit plane are shown as a contour map in Figure 213. The same results are shown at two temperature scales to highlight the details of the temperature distribution and then to match the computational result scale. The temperature profile shown in Figure 213 is significantly different than the temperature distribution at the TFP plane less than 1 cm axially upstream. In the experimental TFP plane the hottest temperatures were located at the lower to mid-span region of the passage. Due to the centrifugal load imparted on the fluid as a result of being turned through the vanes, the hot gases were slung outward to the passage OD while the ID remained cool. This highly skewed exit



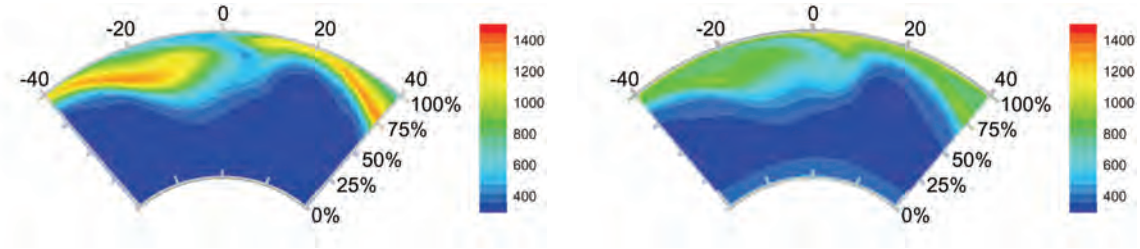
(a) 300-850K Scale

(b) 300-1500K Scale

Figure 213. Experimental results at the combustor exit plane (thermocouple rake plane) at two temperature scale, Φ_{Cav}=0.72

The computational model results are shown in Figure 214 for the adiabatic (a) and conjugate model (b). Like the measurements at the TFP plane, the adiabatic model drastically over predicted temperatures with a peak temperature on the exit plane of 1350 K; an increase of 637 K compared to the peak experimental result of 713 K. The conjugate model produced a peak exit plane temperature of 925 K; an increase of 212 K over the experimental result. As previously discussed, thermocouples read measurements that are below the gas temperatures around them. When the thermocouple measurement error is accounted for, the conjugate model result is likely very

close to the experimental gas temperatures. The temperature distribution pattern in both models is representative of the experimental distribution. All distributions show a region of reduced temperature at +20 and -40 degrees circumferentially with the largest region of elevated temperatures occurring near 0 degrees. While both models accurately replicated the temperature distribution pattern at the exit plane, only the conjugate model predicted realistic temperature values that were comparable to corrected experimental thermocouple measurements.



(a) Adiabatic Model (b) Conjugate Model

Figure 214. Computational results at the combustor exit plane (thermocouple rake plane), Φ_{Cav}=0.72

5.6.5 Circumferential Cavity Comparison, Φ_{Cav}=1.1.

The results in the circumferential cavity at an equivalence ratio of 1.1 produced similar patterns to the lean test case results, including the large gradients. The adiabatic model tended to under-predict the temperature while the conjugate model tended to over-predict the temperature. The magnitudes of the difference between the calculated temperature and the experimental result was larger for both models at this condition, but the differences were greater for the conjugate model. The average temperature on each plane between the two models yielded similar results with a maximum difference of 9.9%. For unknown reasons the temperature differences at the 3/4 plane were an order of magnitude larger than any other result. Both models predicted substantially higher temperatures around the thermocouple bead location than was measured experimentally.

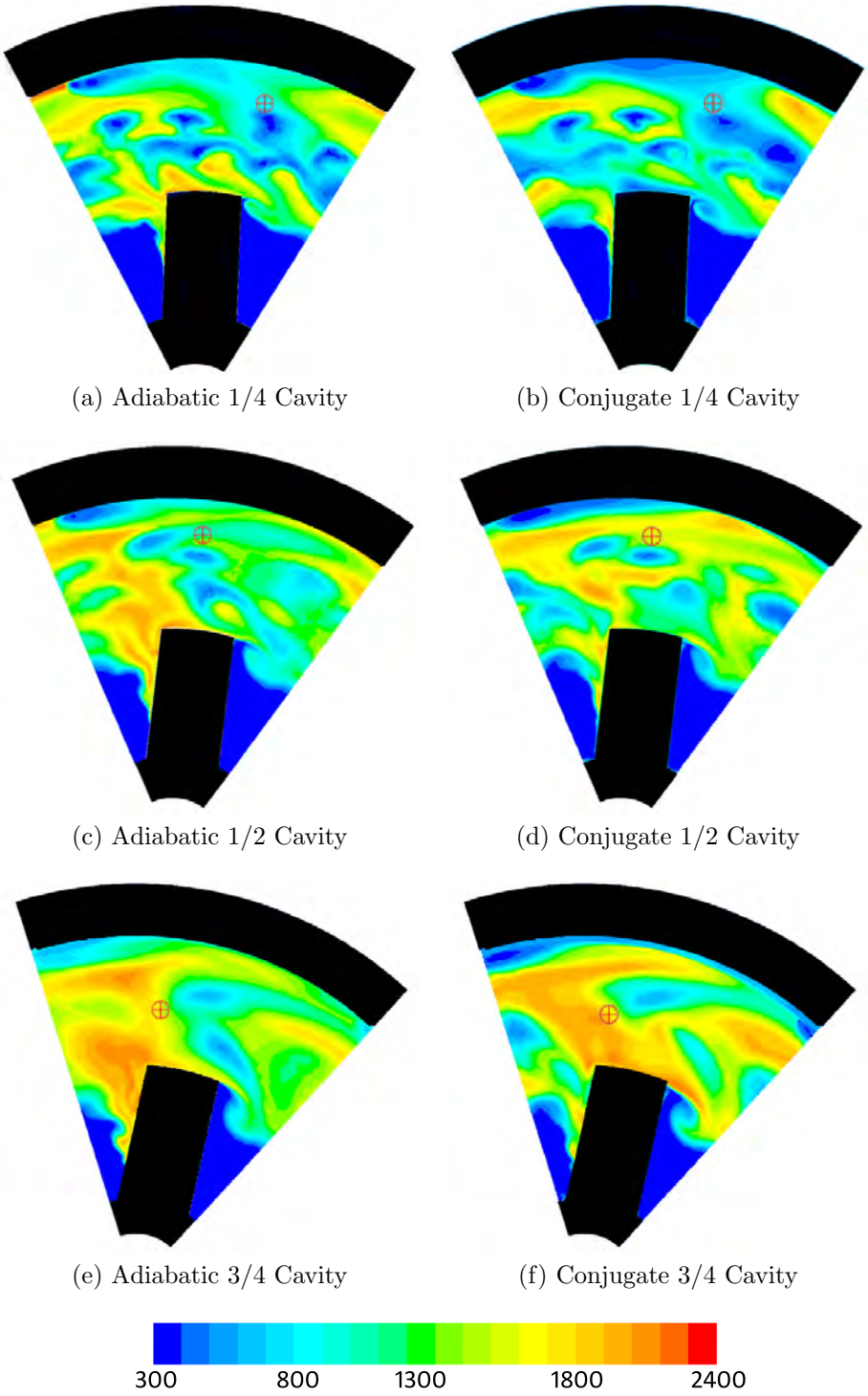
Table 24. Adiabatic model circumferential cavity temperature results compared to experimental data, Φ_{Cav}=1.1

	1/4 Cavity (K)	**1/2 Cavity** (K)	**3/4 Cavity** (K)
Experimental	1203	1207	1145
CFD TC Point	899 (-304)	1121 (-86)	1705 (+560)
CFD TC Region	891 (-312)	1191 (-16)	1636 (+491)
CFD Plane Average	1167 (-36)	1345 (+138)	1501 (+356)

Table 25. Conjugate model circumferential cavity temperature results compared to experimental data, Φ_{Cav}=1.1

	1/4 Cavity (K)	**1/2 Cavity** (K)	**3/4 Cavity** (K)
Experimental	1203	1207	1145
CFD TC Point	783 (-420)	1585 (+378)	1950 (+805)
CFD TC Region	785 (-418)	1592 (+385)	1931 (+786)
CFD Plane Average	1051 (-152)	1337 (+130)	1534 (+389)

Once again there were large gradients in the temperature contours at all three axial planes with both computational models. The location of the thermocouple beads were again near the edge of a gradient where small spatial differences could mean a temperature change of several hundred degrees. The contours at each axial plane for both models are given in Figure 215. For temperature measurements within the circumferential cavity there is not a clearly defined benefit to use one of these models over the other as the heat transfer at the wall has little effect on temperatures inside the cavity sufficiently away from the walls. However, with the conjugate model quenching the reactions at the wall, the locations of the reactions shifted. In the adiabatic model the large high temperature zones are shown anchored to the OD wall, the vane suction surface (left side of the vane in the figures), and the vane tip. In the conjugate model the reactions are quenched at the walls which greatly reduced the high temperature regions around the vane in the 1/4 and 1/2 cavity planes. At the 3/4 cavity plane the reactions on the suction surface were significantly reduced



(a) Adiabatic 1/4 Cavity

(b) Conjugate 1/4 Cavity

(c) Adiabatic 1/2 Cavity

(d) Conjugate 1/2 Cavity

(e) Adiabatic 3/4 Cavity

(f) Conjugate 3/4 Cavity

Figure 215. Temperature contours at the 1/4, 1/2, and 3/4 axial planes within the circumferential cavity, Φ_{Cav}=1.1

with the conjugate model instead anchoring the flames over the vane tip. While these reaction locations moved between models, the average temperature in each cavity plane differed by less than 10% at the 1/4 cavity, and less than 3% in the other two planes.

5.6.6 Vane Passage Comparison, Φ_{Cav}=1.1.

Experimental and computational measurements at the TFP plane using both computational models are shown in Figures 216, 217, and 218. The experimental results showed a peak temperature of 1670 K at the 39.6% radial span and 45% filament span. At 49.7% the results showed a pocket of elevated temperature closer to both vane walls and a region of reduced temperature in the mid-filament span. While the experimental results did show temperatures approaching 1300 K at 15.7 and 28.8% radial span, the computed temperatures were significantly higher at these locations for both models. Like the experimental data, both models showed the same dual-peak temperature distribution at 49.7% radial span. With the conjugate model the 30% filament span local maximum matched the experimental value, the second maximum, however, was over predicted with a peak approaching 1800 K. The conjugate model also very closely matched the profile and magnitude on the 39.6% filament. In the conjugate model, as the hot gases traversed along the suction surface of the vane energy was removed from the fluid and disbursed into the metal vane. This removal of energy from the fluid took place along the entire vane passage and thus produced lower fluid temperature magnitudes by the TFP plane. Almost all of the magnitudes of the adiabatic model over predicted the temperatures compared to the experimental results by at least 200 K, and as high as 500 K, because this model had no mechanism to transfer energy out of the fluid to reduce its temperature.

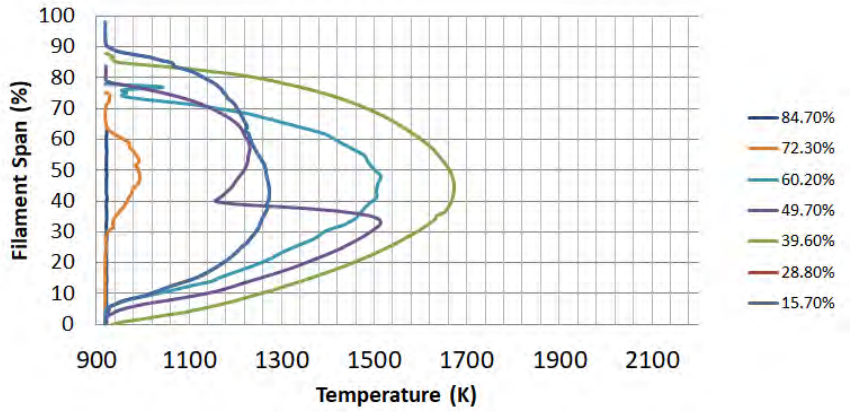


Figure 216. Experimental results at the TFP plane, Φ_{Cav}=1.1

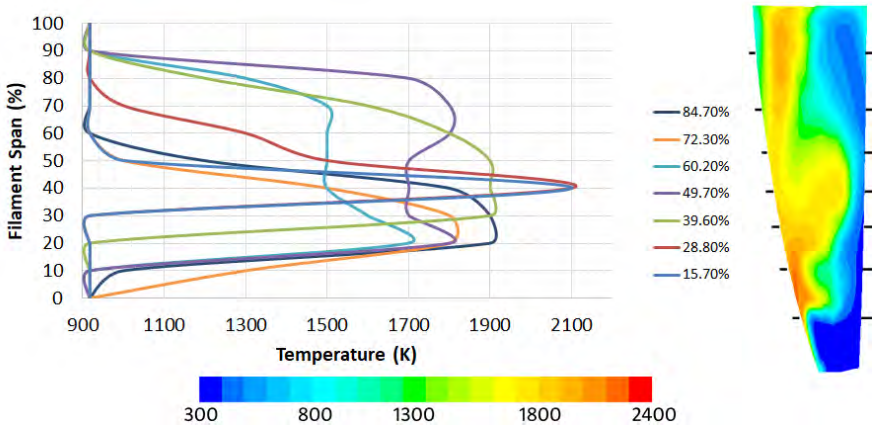


Figure 217. Adiabatic computational results at the TFP plane, Φ_{Cav}=1.1

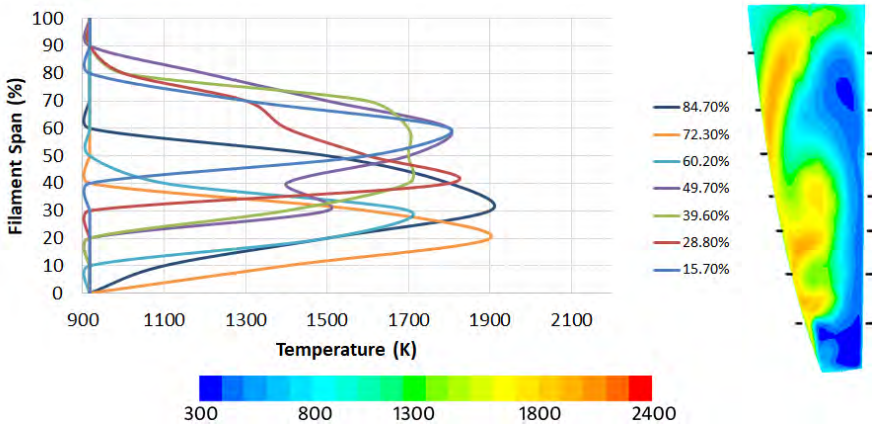
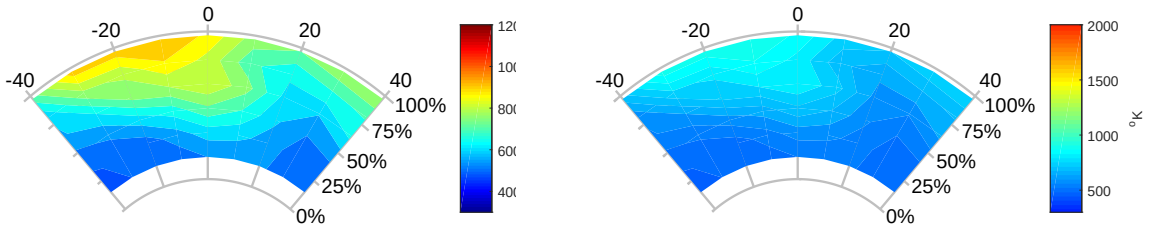


Figure 218. Conjugate computational results at the TFP plane, Φ_{Cav}=1.1

Like the lean test case, neither model accurately predicted the temperature magnitudes and profiles for all filaments, however, the conjugate model matched the experimental result at several locations in both position and magnitude. Aside from the matching points, the remaining values in the conjugate model more closely represented the experimental temperatures.

5.6.7 Exit Plane Comparison, Φ_{Cav}=1.1.

The thermocouple measurements at the combustor exit plane are shown assembled as a contour map in Figure 219. The same results are shown at two temperature scales. The lower scale is shown to highlight the details of the temperature distribution. The



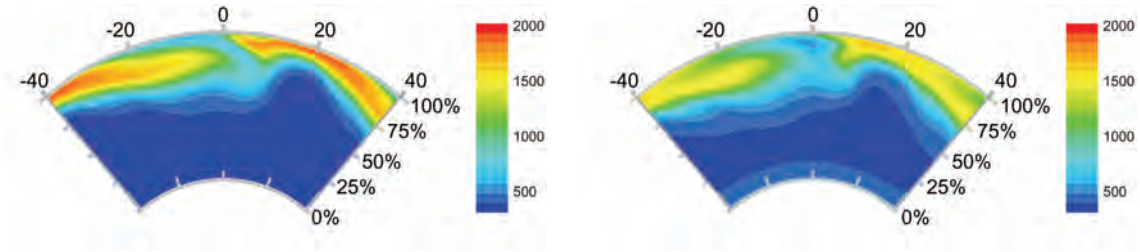
(a) 300-1200K Scale

(b) 300-2000K Scale

Figure 219. Experimental results at the combustor exit plane (thermocouple rake plane) at two temperature scale, Φ_{Cav}=1.1

The computational model results are shown in Figure 220 for the adiabatic (a) and conjugate model (b). Like the measurements at the TFP plane, the adiabatic model drastically over predicted temperatures with a peak temperature on the exit plane of 1900 K; an increase of 952 K compared to the peak experimental result of 948 K. The conjugate model produced a peak exit plane temperature of 1400 K; an increase of 452 K over the experimental result. When the thermocouple measurement error is accounted for, the peak conjugate model result is likely still 250 K above the experimental gas temperatures, but still much closer than the adiabatic results. The temperature distribution pattern in both models is representative of the experimental

distribution. All distributions show a region of reduced temperature at +20 and -40 degrees circumferentially with the largest region of elevated temperatures occurring between 0 and -20 degrees. This test case also demonstrated the significant variation in temperature distribution between the TFP and combustor exit planes that would make integration with a turbine difficult.



(a) Adiabatic Model (b) Conjugate Model

Figure 220. Computational results at the combustor exit plane (thermocouple rake plane), Φ_{Cav}=1.1

5.7 Objective 2 Conclusions

The purpose of this objective was to determine the effect of the conjugate heat transfer model on the gas temperature and thermal distribution predictions in a reacting flow UCC domain. Since the computational modeling in Objectives 3 and 4 were performed on geometries that had never been tested, this objective served to demonstrate the level of fidelity of the predictions for a test configuration where experimental data were available for comparison.

The UCC circumferential cavity region is dominated by high temperature gradients both computationally and experimentally making exact comparisons difficult. Temperature variations of up to 200 K have also been recorded experimentally for the same operating conditions from day to day depending on a number of external environmental factors which impacted how the reaction distribution set up that day. With all the variation that is possible, cavity temperatures were approximated rea-

sonably well with either method. It will be shown in Chapter VI, however, that the boundary conditions and temperature of the air drivers play an important role in establishing bulk cavity velocities, a property that wasn't looked at in the present study. For this reason the conjugate model is recommend for cavity analysis.

The conjugate model provides realistic metal temperatures and accounts for flame quenching at the walls. Additionally, the temperature distribution at the TFP plane was more closely approximated in both pattern and magnitude by the conjugate model. The adiabatic model significantly over-predicted the temperatures because it did not disburse heat to the metal surfaces, thereby reducing the fluid temperature as it traversed downstream. As such the temperature contours at the TFP and exit plane show combustion level magnitudes for the adiabatic model, on the order of 2000 K, at both downstream measurement locations. At the combustor exit plane the conjugate model more accurately approximated the experimental temperatures, however, both models produced the same temperature distribution patterns which were representative of experimental results.

Given the performance of both models at all locations of interest, the conjugate model was determined to be beneficial to the UCC analysis. While there is more computational expense and increased time in griding and analysis with the conjugate model, the benefit was more realistic temperatures. Additionally, the conjugate model provided the ability to predict the metal component temperatures and the ability to limit error associated with incorrect boundary condition specifications by having the conjugate model calculate the fluid/metal boundary values.

VI. Objective 3: Impact of Airflow Splits and Alternate UCC Fuel Injection Schemes

Investigate the impact of airflow split ratio between the core and circumferential cavity and alternate fuel injection schemes on tangential velocity, combustor performance, flow path pressure balance, and Rayleigh losses

This objective focused on the impact of air split ratio between the core and circumferential cavity on tangential velocity, combustor temperature performance, flow path pressure balance, and Rayleigh losses. A variable geometry diffuser was designed, built, and integrated into the remaining V3 UCC hardware to dynamically control the flow split between the core and cavity during testing. Additionally, two variations of stepped cavity outer rings were manufactured and tested to quantify the impact in variations in fuel and air injection location and orientations as well as flameholder positions in the combustor.

6.1 Variable Geometry Diffuser with Baseline Fuel Injection

With the understanding of the limitations in tangential velocity and exit temperature distribution of the Version 3 Baseline UCC test rig outlined in Section 3.3, the goal of this investigation was to utilize a variable geometry diffuser to overcome the pressure differential between the core and cavity flow paths to produce the desired mass flow rate splits without the use of a flow restrictor plate. Additionally, there was a desire to correlate the diffuser physical configuration to the mass flow rate split and tangential velocity within the cavity. A parametric approach was used to systematically vary the size of the diffuser middle diameter and measure the resulting mass flow splits and cavity tangential velocity. While this initial study aimed to characterize the performance of the diffuser, the impact of the flow split was quantified on the

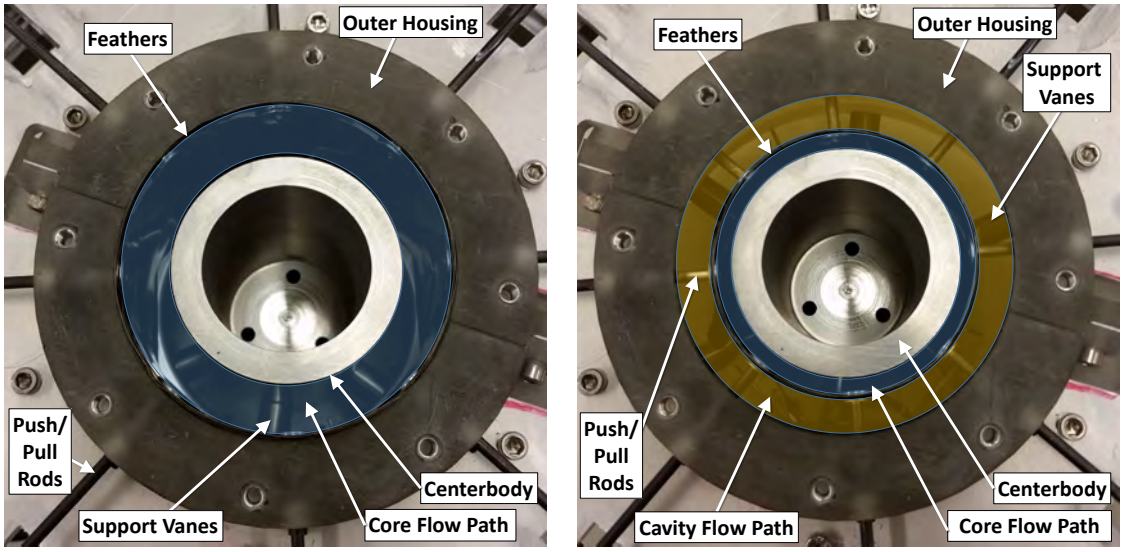
Baseline combustor in the form of cavity tangential velocity, centrifugal acceleration, cavity temperature, exit temperature, and Rayleigh loss measurements.

A follow-on diffuser study with the Baseline combustor aimed to demonstrate control of the air flow split across a range of operating conditions from 0.06 kg/s to 0.12 kg/s total air flow rate at equivalence ratios of 0.72 and 1.1. The diffuser was used to maintain a constant cavity air mass flow rate independent of the total combustor section inlet flow rate to determine if combustion and cavity flow properties remained the same for identical inlet conditions. The diffuser was then used to maintain a constant core-to-cavity flow rate split independent of total inlet flow rate to observe the resulting performance trends. Cavity temperatures, exit temperature profiles, Rayleigh losses, and cavity flow velocities were documented for each condition. Using high-speed chemiluminescence of OH radicals the combustion dynamics and combustion frequency were also determined.

With the exception of the diffuser, the remainder of the experimental rig hardware was the same as UCC Version 3 shown in Section 3.3, featuring the hybrid vane and compound air drivers. As explained in Section 5.2, the attachment of the hybrid guide vane to the variable diffuser resulted in a rotation of the vane which made the fuel inlet baffles and the vane leading edge no longer aligned. Looking from the upstream position, the fuel baffles were rotated 20° counter-clockwise as shown in Figure 203. The test rig was instrumented for pressure and temperature and positioned for optical diagnostics in the circumferential cavity. Pitot static pressure ports were placed in the core flow passage to calculate the mass flow rate through that annulus. Subtracting the core mass flow rate from the total inlet mass flow rate yielded the cavity inlet mass flow rate. Additional static pressure measurements were taken in the core and outer diffuser passages for comparison purposes.

6.1.1 Diffuser Design.

The variable geometry diffuser was based on a "turkey feather" design using eight overlying sheets of 0.178 mm (0.007 in) thick stainless steel flashing. Figure 221 shows an end on view of the diffuser inlet in the full closed (100/0 core-to-cavity area split) and open (30/70 core-to-cavity area split). In this figure the passage between the centerbody and the feather continued to the core flow path, while the passage from the feather to the outer housing supplied air to the cavity. The base of each feather was connected to a fixed diameter ring coupled to the cavity air inlet driver plate and held in place by six support vanes. There were no hinges for the feathers; instead, movement was allowed due to the flexibility of the thin sheet metal. Eliminating hinges reduced the number of potential leak points between the two flow paths. The feathers were contoured to allow each one to overlap with the next two feathers in only one direction. Figure 222 shows the shape of a single feather. Each feather was actuated using a linear push/pull rod entering the outer housing from the exterior. Each rod was o-ring sealed to the housing to minimize system leakage.



(a) Closed - (100/0 core-to-cavity area split) (b) Open - (30/70 core-to-cavity area split)

Figure 221. Turkey feather variable diffuser



Figure 222. Single feather shape

The actuation system, shown in Figure 223, was based on a scroll gear and block design that allowed the blocks to only translate in the radial direction as the scroll gear turned. The blocks were positioned in radial channels in a restrictor plate (not shown in Figure 223, but is shown in Figures 225 and 226) that was bolted to the diffuser outer housing. One end of the push/pull rods were connected to the feathers while the other end was connected to the blocks with a setscrew to allow fine tuning of the positioning. As the scroll gear turned, the blocks translated radially and the diffuser feathers expanded or contracted depending on the direction of rotation. The scroll gear was turned by a stepper motor with a 51:1 gear box that was coupled to the scroll gear using a timing belt. The stepper motor allowed for precise movement. The electronic motion controller discussed in Appendix A sent a specified number of pulses to the motor, which was converted into a specified number of steps. Each step was on the order of 0.225° of motor rotation, which equated to 0.0044° of rotation out of the gear box. The combination of incremental movement of the motor and the gear reduction through the actuation drive train resulted in control over the positioning of the diffuser feathers resolved to better than 0.01 mm.

The diffuser outer housing was 3D printed in VeroClear-RDG810 plastic. A ceramic insulator disc was installed between the plastic outer housing and the metal UCC front wall to protect the plastic from high metal surface temperatures. As shown

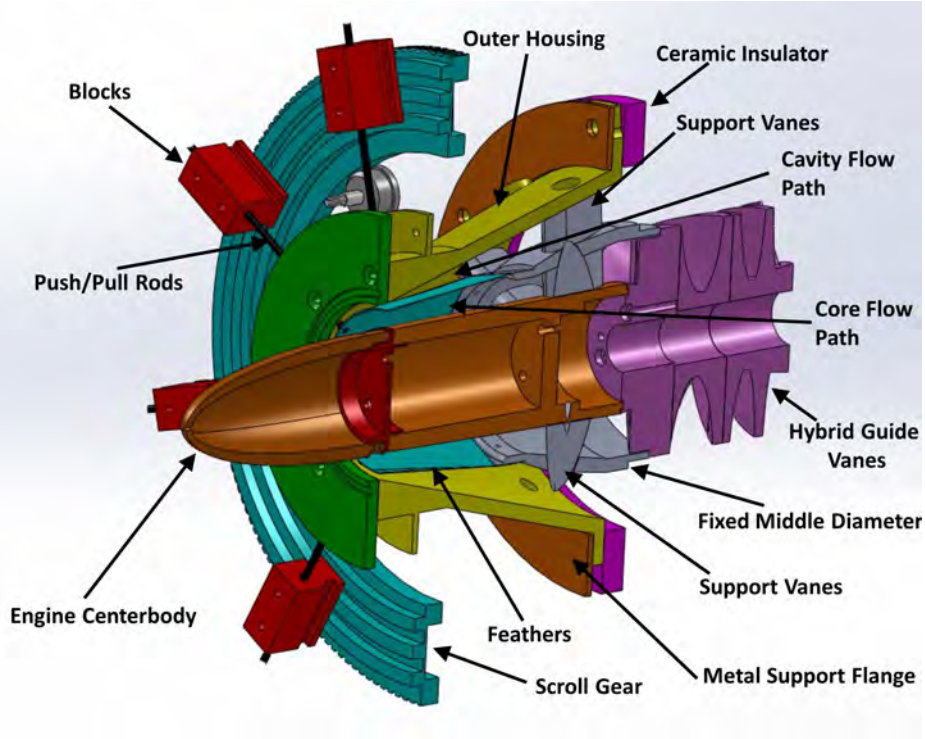


Figure 223. Cross-section of variable diffuser and actuation system (block restrictor plate and stepper motor removed for visibility)

in Figure 224 this ceramic component went through three design iterations. The first design was a solid ceramic disc. The second iteration added air cooling along the ceramic/plastic interface to increase the allowable metal interface temperature while maintaining an acceptable plastic interface temperature. Versions 1 and 2 relied on RTV seals to join the ceramic to the diffuser and metal combustor walls. With the RTV seals there was no way to disassemble the combustor rig without damaging the ceramic disc. The third iteration added an o-ring grove on the ceramic/metal interface side of the disc to allow the diffuser to be o-ring sealed to the combustor. The ceramic disc was still sealed to the diffuser with RTV. During disassembly the o-ring allowed the diffuser to be easily separated from the combustor without damage to the ceramic disc. The temperature between the ceramic and the plastic housing was monitored by a thermocouple embedded in the RTV seal between the materials. This

interface temperature was limited to 60 C as temperatures above this value resulted in softening of the plastic.

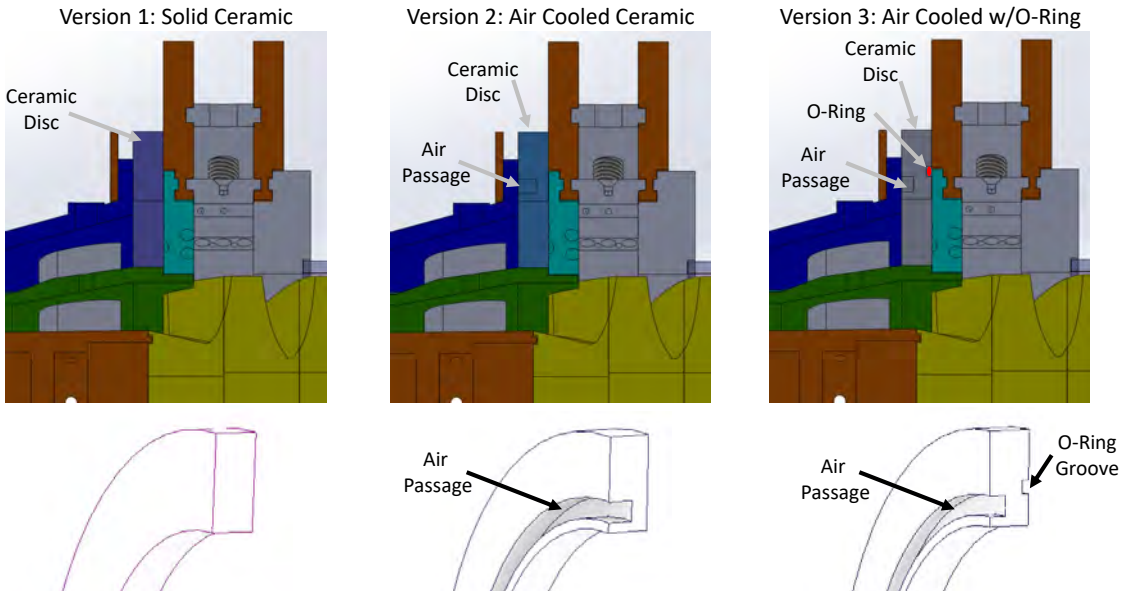


Figure 224. Cross-sections of iterations of the ceramic insulator disc

Figure 225 shows the variable diffuser installed on the UCC including the positioning of the stepper motor, a linear position sensor, and the restrictor plate. In this figure a new diffuser to air supply line adapter can be seen (light blue component). This adapter was also 3D printed and designed for a smooth transition between the diffuser inlet and the slightly larger diameter supply pipe. The adapter was sealed to the supply pipe flange with a fiber gasket and bolts. The adapter was connected to the diffuser with four 1/4-20 socket head cap screws and sealed by an o-ring. Figure 226 shows the o-ring seal on the front of the variable diffuser and the cross-section of the adapter.

The diffuser motion was electronically controlled using an Arduino, grblShield, and a Raspberry Pi. The Raspberry Pi was the host platform running the Raspbian operating system. An open-source Java program called "Universal G-Code Sender" was installed on the Raspberry Pi and sent the positioning signals. When a g-code

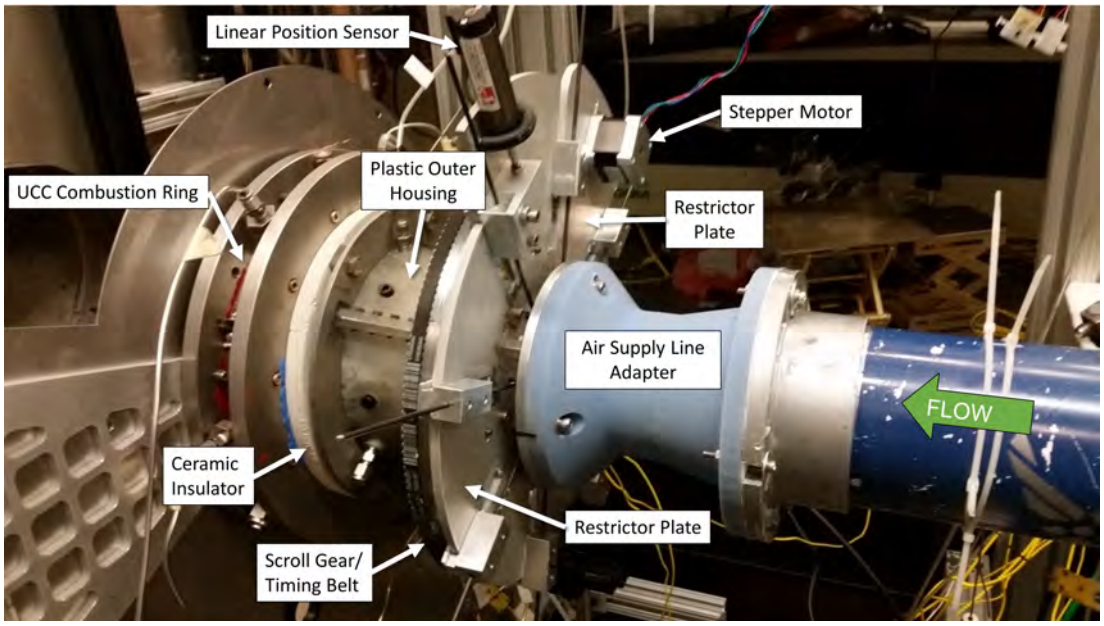


Figure 225. Variable diffuser installed on the UCC

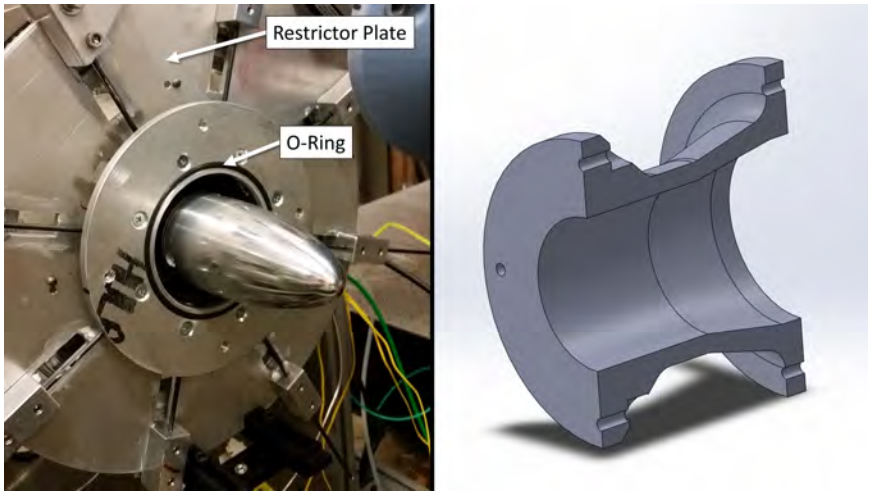


Figure 226. Variable diffuser adapter o-ring seal (left), adapter cross-section (right)

positioning command was sent from the Raspberry Pi, it was converted to the grbl language on the Arduino. The Arduino then interfaced with the grblShield which sent the appropriate number of pulses to the stepper motor to move the commanded distance. The motion control electronics are discussed in greater detail in Appendix A. A linear position sensor connected to one of the push rods on the actuation system

verified the commanded position was achieved and sent the position to the LabView data acquisition system to be recorded.

Table 26 provides specifications of off-the-shelf replacement wear items that were used on the diffuser.

Table 26. Off-the-shelf wear items on the diffuser

Item Description	Supplier	Part Number
Ceramic Insulation Sheet, 1/2"x12"x12"	McMaster-Carr	9353K31
1/16" Buna-N O-Ring, ID=1/8", OD=1/4"	McMaster-Carr	9452K14
1/8" Buna-N O-Ring, ID=3.5", OD=3.75"	McMaster-Carr	9452K226
1/8" Silicone O-Ring, ID=7.5", OD=7.75"	McMaster-Carr	1283N227
Timing Belt, 39", XL Series, 3/8" Wide	McMaster-Carr	6484K444
Timing Pulley, 3/8"W, 0.2"P, OD=0.993"	McMaster-Carr	6495K713
NEMA17 Bi Stepper Motor, 51:1 Gearbox	Stepper Online	17HS19-1684S-PG51
Molex 4-Pin Connector Kit, 0.093"	Amazon.com	4330132643

6.1.2 Diffuser Computational Analysis.

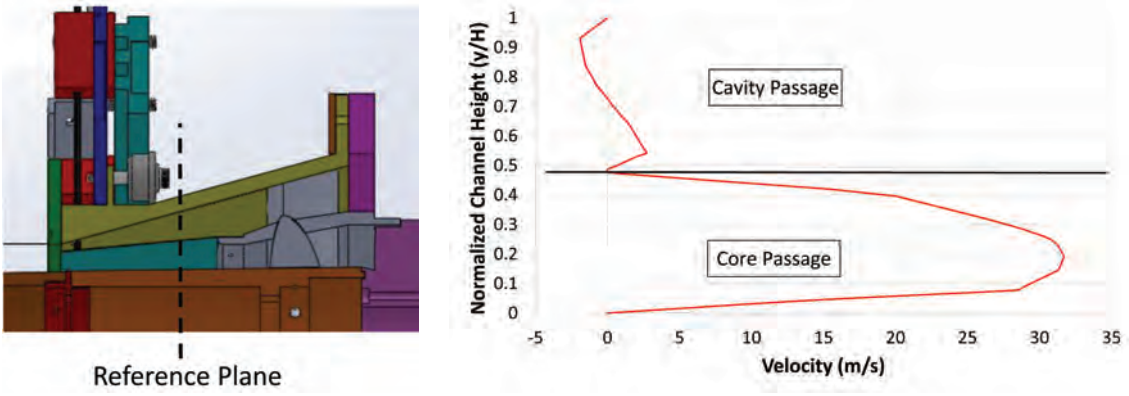
An aerodynamic CFD analysis was conducted on the variable diffuser with the feathers positioned at a 70/30 core-to-cavity area ratio to check the velocity profile in the outer diffuser passage and find the corresponding mass flow rate split. The variable diffuser geometry was added to a pre-existing mesh analyzed by Cottle et al. [172] and previously shown to be grid independent. The variable diffuser was gridded at the same resolution as the original diffuser tested by Cottle et al. The domain was modeled as a full annulus from upstream of the diffuser inlet to the hybrid guide vane exit plane. The modified domain had 60 million cells and was run in the FLUENT flow solver. The solver settings used matched those of Cottle et al. which included the realizable k - ϵ turbulence model with enhanced wall functions and the partially premixed combustion model. Spatial discretization was set at second order for all quantities. The pseudo-transient option was employed to accelerate

convergence with a user-defined length scale of 12.7 mm. The inlet mass flow rate of air was set at 0.108 kg/s with a desired equivalence ratio of 0.8. The quantity of fuel burned in the circumferential cavity changed the pressure distribution inside the combustor and was found to have an impact on the core-to-cavity air mass flow rate split for a fixed feater position. As such it took several iterations to determine that a fuel flow rate of 0.059 kg/min resulted in the correct core-to-cavity air mass flow rate split to achieve an equivalence ratio of 0.83. This process highlights the utility of a variable diffuser which can independently control the air mass flow rate split to ensure the correct equivalence ratio is achieved for a specified fuel flow.

A 70/30 core-to-cavity area split was tested numerically with and without combustion reactions. The mass flow rate into the cavity was calculated at 0.019 kg/s for both the cold flow and reactive case, which equates to an 82/18 core-to-cavity air mass flow split. This is far from the 70/30 geometric area split, but a vast improvement over the non-restricted diffuser design of Conrad [67]. It was not expected that the area ratio would produce an exact match to the mass flow rate ratio due to the presence of a boundary layer at the supply conduit walls and a possible pressure differential between the flow paths. For a 70/30 area split, the leading edge of the feathers was only 0.34 cm away from the outer housing. At this distance the majority of the fluid diverted into the outer diffuser passage was lower velocity, and thus had a lower mass flow rate. Even though the mass flow rates in the cold flow and reacting cases were identical, the reacting flow solution calculated a higher average tangential velocity in the cavity due to a reduced density caused by the elevated temperature. The cold flow solution resulted in a average tangential velocity of 12.2 m/s while the reacting solution calculated the average tangential velocity at 16.1 m/s. These velocities represent an average cavity centrifugal acceleration of $205g_e$ and $360g_e$, respectively.

A review of the velocity profiles in the outer diffuser passage showed the same

non-parabolic profile and reversed flow that was observed by Cottle et al. [70] with the fixed geometry diffuser. The calculated velocity profile in the variable diffuser with a 70/30 core-to-cavity area split, at an axial station with an approximately equal channel height in both passages, is shown in Figure 227. As shown in the figure the change in the feather leading edge position in the current diffuser design was not sufficient to overcome the reversed flow behavior of the air in the cavity passage resulting from the low mass flow rate and adverse pressure gradient due to diffusion. Regardless of the regions of reversed flow, the static pressure through the UCC cross-section for this case shows that the pressure in the diffuser outer passage built faster due to a greater diffusion volume as shown in Figure 228. The pressure at the entrance to the UCC cavity was slightly higher than in the core flow at the leading edge of the hybrid vanes. This higher pressure was maintained inside the circumferential cavity while the pressure was reduced below the cavity in the vane passages. The pressure differential at the vane/cavity interface is what allowed fluid to travel through both paths.



(a) Diffuser Station (b) Velocity Profile

Figure 227. Velocity profile at a diffuser reference station with approximately equal channel heights

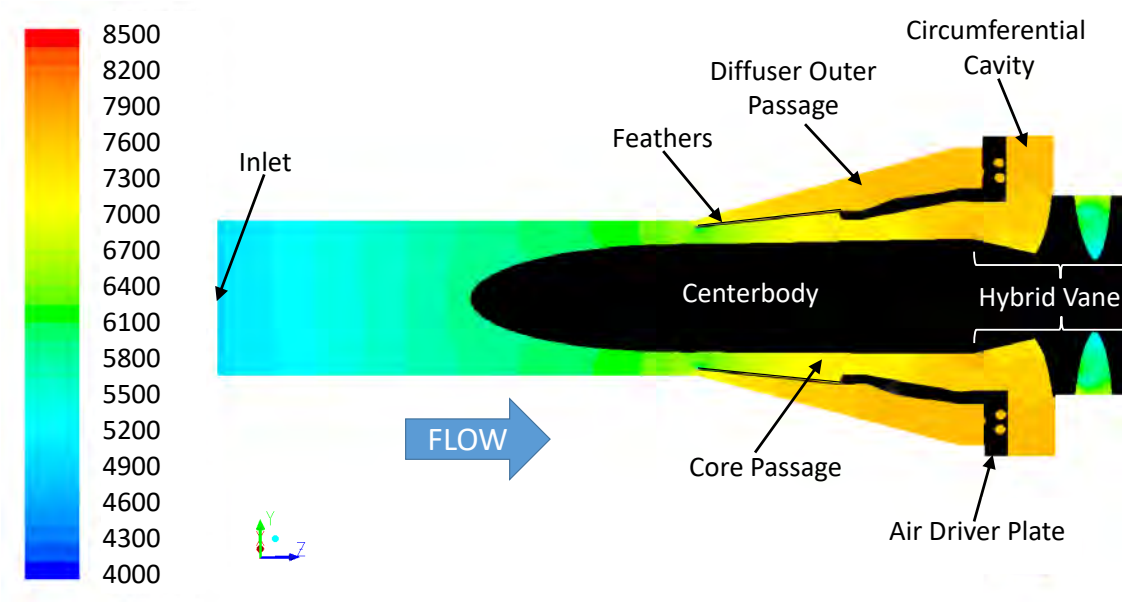


Figure 228. Gauge static pressure (Pa) distribution in a cross sectional plane of the UCC with variable diffuser at a 70/30 core-to-cavity area split

6.1.3 Mass Flow Rate Measurements.

Since the computational results in the diffuser outer passage showed a non-parabolic velocity profile, that passage was not suitable for mass flow rate measures. As a result the mass flow rate measurements were made in the core passage and subtracted from the inlet mass flow rate to determine the cavity mass flow rate. The inlet mass flow rate measurements were taken from the air mass flow controller output. The mass flow rate of air in the core passage was determined by using a pitot static probe located at the center of the channel. The pressure measurements were converted to velocity at the location of the probe using Bernoulli's Equation, given as Equation 142. Figure 229 shows an axial cross-section of the diffuser at the location of the probe tip.

In the diffuser core passage annulus, modeled as channel flow, the axial velocity is a function of the position off the wall. For turbulent flows, such as those seen in the UCC, Equation 143 is used to solve for the friction velocity, u_τ. The friction velocity

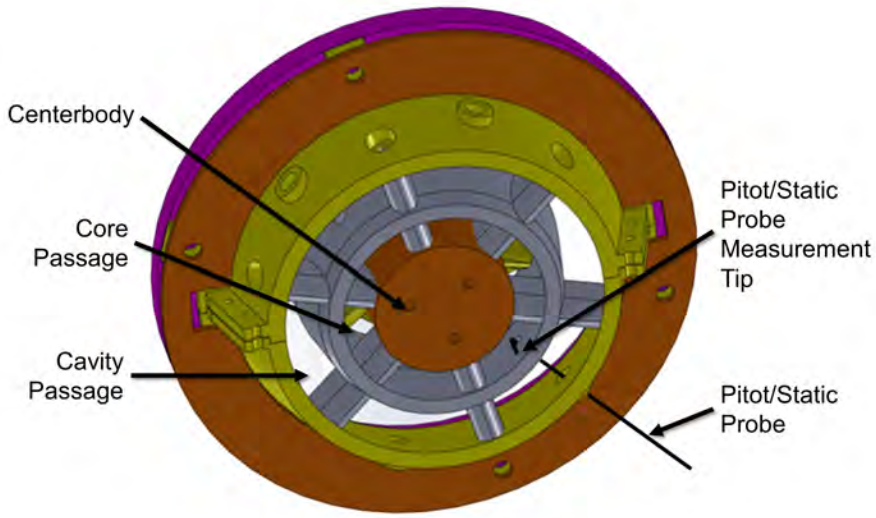


Figure 229. Diffuser core passage pitot/static measurement plane

can then be used in Equation 144 to find the average velocity in the channel assuming a typical turbulent velocity profile. In these equations, U_0 is the centerline velocity found experimentally using Bernoulli's Equation (Equation 142), $\bar{U}$ is the average velocity in the channel, ν is the kinematic viscosity of air (m^2/s), y is half the height of the channel, B (= 5.2) is the log-law constant, and κ (= 0.41) is the von Kármán constant. These relationships and the validity of using log-law approximations at the channel centerline is outlined by Pope [131] in Chapter 7 of his book.

$$U_0 = \sqrt{\frac{2(P_t - P_s)}{\rho}} \tag{142}$$

$$\frac{U_0}{u_\tau} = u^+ = \frac{1}{\kappa} ln\Big(\frac{y u_\tau}{\nu}\Big) + B \tag{143}$$

$$\frac{U_0 - \bar{U}_{channel}}{u_\tau} = \frac{1}{\kappa} \tag{144}$$

To find the mass flow rate in a circular pipe flow, such as the air feed duct to the UCC rig, Equation 143 can be used to find the friction velocity where $y = R - r$. In

this relationship, R is the radius of the pipe, and r is the radial position where the equation is being evaluated. For measurements on the centerline, this relationship reduces to $y = R$, as $r = 0$. When the friction velocity is known, it can be applied to Equation 145 to solve for the average velocity in the pipe. [131]

$$\frac{U_0 - \bar{U}_{pipe}}{u_\tau} = \frac{3}{2\kappa} \tag{145}$$

Multiplying the average velocity found using one of the methods above to the air density and annulus or pipe cross-sectional area yields the mass flow rate.

LabView was not capable of solving the system of equations above to find the mass flow rate into the cavity in real-time. As a work around a series of look-up tables were produced using a MATLAB script that gave the differential pressure (ΔP) in psi with the corresponding core velocity, cavity flow rate percentage, cavity mass flow rate (kg/s), and a fuel setpoint in SLPM to achieve a specific cavity equivalence ratio. The MATLAB script, shown below, requires the total inlet mass flow rate to be specified. For a specific test point the desired cavity mass flow rate or percentage would be known. Using the look-up table output for the specific total inlet flow rate, the mass flow rate or percentage could be converted to ΔP. The ΔP value was provided experimentally in real-time from the display unit shown in Figure 231 which gave the difference in pressure (psi) between the total and static measurements from the pitot static probe shown in Figure 229. The diffuser position could then be adjusted until the desired ΔP and the experimental ΔP matched. An example look-up table is shown in Figure 230.

Look-up table MATLAB Script:

```
clear
clc
fileID=fopen('Lookup_0945_phi72.txt','w');   %Save file name
Mdot=.0945;  %total inlet flow rate kg/s
phi=.72; %select an equivalence ratio to output fuel setpoint
```

```
syms x
k=.41;      %von karman constant
y=.0067;    %meters
a=.0031;    %m^2
v=16.04*10^(-6); %assumes 300K air
rho=1.165; %kg/m^3
B=5.2;      %log-law constant
fprintf(fileID,'DeltaP \t Core Velocity \t Cavity Percent \t Cavity Mass
           Flow \t Fuel Setpoint\r\n');
for DeltaP=0:.001:.190;
        velocity=sqrt((2*6894.76*DeltaP)/rho);
        fric_vel=vpasolve(velocity/x==(1/k)*log(y*x/v)+B,x,[0 5]);
        fric_vel=double(fric_vel);   %convert symbolic to numerical value
        u_bar=velocity-(fric_vel/k);  %find average channel velocity
        mdot_channel=rho*u_bar*a;    %find mass flow rate in core channel
        split=(Mdot-mdot_channel)/Mdot*100;   % percent in cavity
        mdot_fuel=(Mdot-mdot_channel)*phi/15.64; %fuel flow for phi
        fuel_setpoint=mdot_fuel*60/(.001*1.882);  %fuel setpoint for phi
        fprintf(fileID,'%4.3f\t\t %4.1f\t\t %4.1f\t\t\t %4.3f\t\t\t %4.1f
        \r\n', DeltaP, velocity, split, Mdot-mdot_channel, fuel_setpoint);
end
fclose(fileID);
```

Total Inlet: 0.108 kg/s Phi: 0.72

DeltaP	Core Velocity	Cavity Percent	Cavity Mass Flow	Fuel Setpoint
0.000	0.0	100.0	0.108	158.5
0.001	3.4	90.2	0.097	143.0
0.002	4.9	86.1	0.093	136.4
0.003	6.0	82.9	0.090	131.4
0.004	6.9	80.2	0.087	127.1
0.005	7.7	77.8	0.084	123.3
0.006	8.4	75.6	0.082	119.9
0.007	9.1	73.6	0.080	116.7
0.008	9.7	71.8	0.078	113.8
0.009	10.3	70.0	0.076	111.0
0.010	10.9	68.4	0.074	108.4
0.011	11.4	66.8	0.072	105.9
0.012	11.9	65.3	0.071	103.5
0.013	12.4	63.9	0.069	101.2
0.014	12.9	62.5	0.067	99.0
0.015	13.3	61.1	0.066	96.9
0.016	13.8	59.9	0.065	94.9

Figure 230. Example section of a look-up table



Figure 231. Diffuser total/static differential pressure measurement display

6.1.4 Diffuser Characterization Test Methodology.

The LabView interface described in Section 3.1.5.2 was used to control and record all air flow and temperature measurements during testing. The Brooks fuel mass flow controller was used to meter the fuel into the combustor cavity. Three K-Type thermocouples were inserted into the circumferential cavity through the back wall with the measurement bead positioned at the $\frac{1}{4}$ (front of the cavity), $\frac{1}{2}$ (middle of the cavity), and $\frac{3}{4}$ (back of the cavity) axial locations as previously shown in Figure 204.

The thermocouple rake discussed in Appendix B was used to collect temperature data at the UCC turbine vane exit plane with four B-type thermocouples. Figure 472 shows the thermocouple rake and combustion section exit. The probe traverse was computer controlled to move both radially and circumferentially to precisely position the thermocouples across the exit plane. The control script commanded the positioning of the rake to ensure correct positioning with a repeatable 2 second dwell time at each stop location. Measurements were taken every 4.8 mm radially and every 10° circumferentially across an 80° arc at the combustor exit. The probe

head was aligned into the flow, with the thermocouple beads located 6.5 mm axially downstream from the vane trailing edge. The B-type thermocouples had a range of 273 - 1973 K with an accuracy of ±0.5%. The thermocouple rake positioning accuracy was ±0.5 degree circumferentially and ±0.025 mm radially.

Velocity measurements of the fluid in the circumferential cavity were made using PSEV. The PSEV setup, camera settings, and post-processing were identical to those discussed in Section 3.1.6.3. Seed particles were introduced to the test rig through the large diameter blue feed pipe upstream of the diffuser inlet and light blue adapter.

Diffuser flow split positions were tested that resulted in a core-to-cavity area ratio split from 100/0 to 30/70 in increments of 10 with total inlet air mass flow rates of 0.06, 0.108, and 0.12 kg/s. This combination of conditions resulted in a total of 24 data points. The fuel flow was modified for each test condition to try and maintain an equivalence ratio of 0.8 in the cavity. Experimental tests were conducted at both reacting and cold flow conditions to obtain the mass flow split between the core and the cavity at the three total inlet mass flow rates.

After the diffuser performance was characterized at a constant equivalence ratio, the total inlet mass flow rate was fixed at 0.108 kg/s and the fuel flow was varied to observe the diffuser performance and combustion characteristics at five different equivalence ratios. The equivalence ratios selected were 0.62, 0.74, 0.86, 0.99, and 1.1. The combustion characteristics were evaluated by measuring the temperature at the three axial positions within the circumferential cavity. The target mass flow rate split for these points was a 74/26 core-to-cavity ratio to allow the outcomes from these tests to be compared to test results using the Baseline fixed position diffuser with a core flow restrictor plate at the same equivalence ratios.

6.1.5 Diffuser Characterization Experimental Test Results.

It was found that the changes in fuel flow rate had only a minor impact on the mass flow rate split. However, in some cases several iterations were required to get a balance between the correct fuel setpoint and the air mass flow rate. The final cavity mass flow rate splits are shown in Figure 232 for all 24 characterization test cases. For a diffuser opening of 4.5 mm and greater, the cavity mass flow rate percentage behaved in a predictable, nearly linear fashion. Below this position, very little flow entered the outer cavity flow passage. Additionally, in all but one of the test conditions, it was found that reacting flow caused a larger cavity flow split percentage than the cold flow at an equal diffuser opening. On average, the reacting flow achieved 4.2% greater cavity mass flow. The results presented in Figure 232 highlight the problems of Conrad [67] and Miranda [68]. The area splits they tested were all in the region of non-linearity with the largest ratio set at 60/40 core-to-cavity. Even at that position the difference between the area ratio and the mass flow ratio is largely different.

Figure 233 shows the relationship between diffuser opening and average tangential and radial velocities from the PSEV analysis for each of the reacting flow cases. At the small diffuser openings with small cavity mass flow rates the tangential velocity was low with a velocity increase as the diffuser opening increased. The tangential velocity results for larger diffuser openings produced an outcome that was not entirely expected. The unexpected result comes from the two lower total inlet mass flow rate cases achieving a peak tangential velocity at a 60/40 and 50/50 area ratio and then decreasing with increased diffuser opening. As shown in Figure 232, the mass flow rate in the cavity for both of these cases continued to increase, yet the tangential velocity decreased. In the highest total inlet mass flow rate cases there was a local maximum at a 60/40 area split, followed by a slight tangential velocity decrease. In this test series, however, after the slight drop in velocity, the tangential velocity again

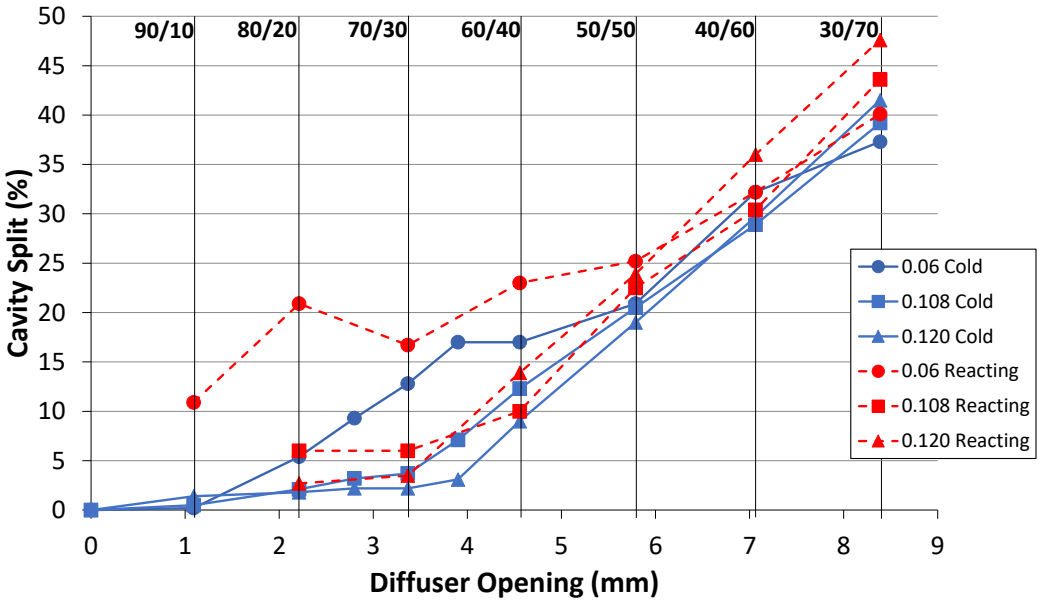


Figure 232. Experimental results of the relationship between diffuser feather position and cavity mass flow split percentage for a cavity equivalence ratio of 0.8. Numbers along the top of the figure show the core/cavity geometric area split related to the diffuser position.

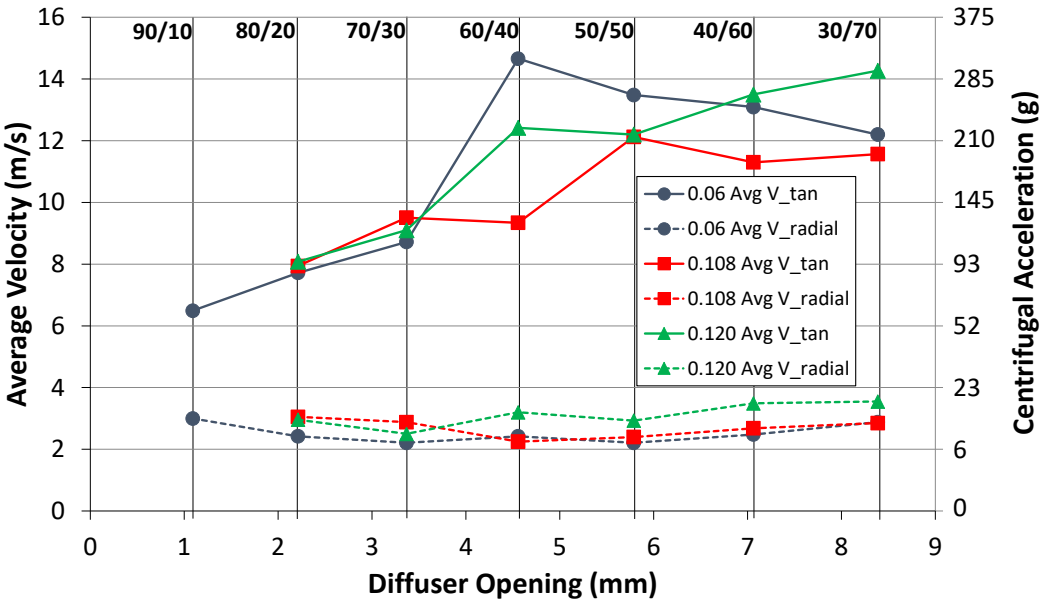
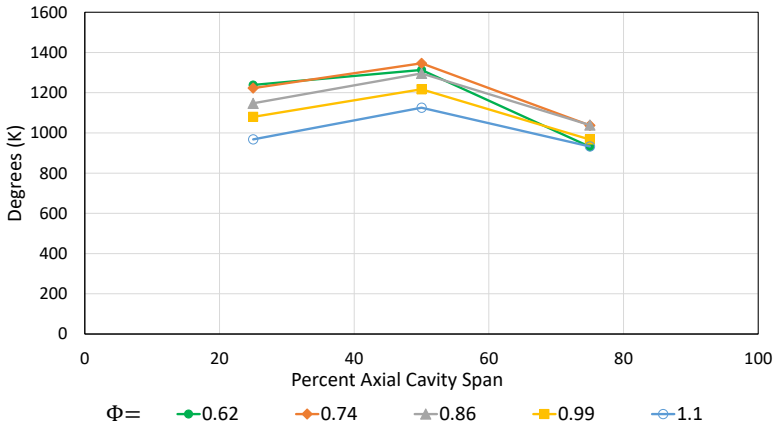


Figure 233. Experimental results of the relationship between diffuser feather position and average cavity tangential and radial velocities for a cavity equivalence ratio of 0.8. Numbers along the top of the figure show the core/cavity geometric area split related to the diffuser position.

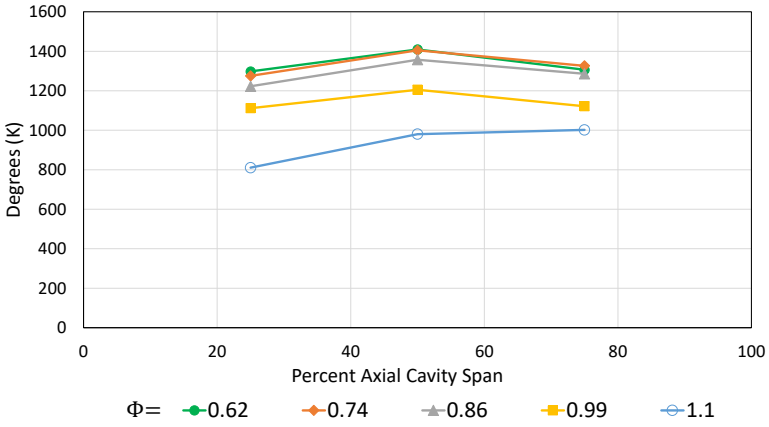
increased for the next two points. The cause of the decrease in tangential velocity with increasing cavity mass flow rate is hypothesized to be the result of increased fuel flow required to maintain a fixed cavity equivalence ratio at higher air mass flow rates. The fuel enters the cavity normal to the OD wall. The radial fuel flow shears the tangentially flowing gases and slows them down. Cottle [78] saw a similar behavior in his numerical cavity analysis with the fixed position diffuser. Across all of the diffuser opening positions the radial velocity remained relatively unchanged with a variation of less than ± 0.5 m/s from the average for each point in the test series. It was determined that repeatability of the tangential and radial velocities were within 2%.

The results of measuring the temperature at three axial positions in the circumferential cavity showed an additional benefit of the variable diffuser. Without the use of a flow restrictor plate in the core flow path, the combustion patterns within the circumferential cavity were altered. As shown in Figure 234 the fixed position diffuser showed peak temperatures in the center of the cavity with reduced temperatures at 1/4 and 3/4 axial span. The temperature variation between the center and the other two stations was as high as 29.1% with an average variation of 16.1%. With the variable diffuser the peak temperature was still located at the axial center of the cavity, but the temperature at the other two stations remained higher, resulting in a more axially uniform temperature. For the variable diffuser the peak temperature difference between center and the outer stations was 17.3% with an average temperature variation of only 7.5%.

The variable diffuser was also used to conduct testing on an alternate hybrid guide vane configuration featuring dual backward-facing steps below the circumferential cavity. This research is discussed in Reference [173], but an important finding from this study is relevant to the present analysis. Using the baseline LLCB hybrid vane



(a) Baseline fixed position diffuser



(b) Variable diffuser

Figure 234. Comparison of cavity temperatures with the baseline fixed position and variable diffuser at a total inlet mass flow rate of 0.108 kg/s at a 74/26 core-to-cavity mass flow split.

it was found that a variable diffuser feather opening of 6.15 mm produced the desired 74/26 core-to-cavity mass flow split for all of the cavity equivalence ratios tested. This opening amount is in line with the plot shown in Figure 232 for the 0.108 kg/s case. Using the dual backstep vane, the feathers were required to be opened to 5.5 mm for the highest three equivalence ratios, and then opened an additional 0.3 mm to 5.8 mm for the lower two equivalence ratios to maintain the desired 74/26 mass flow split. The fact that different feather openings were needed for the different vanes

using the variable diffuser indicates that a 74/26 mass flow rate split was most likely not achieved or maintained with the fixed position diffuser as operating conditions were changed. Having the ability to monitor the mass flow rate split and adapt the diffuser in real time to correct any deviations is a desirable capability.

The CFD results in the circumferential cavity did not match particularly well to the experimental data above. CFD predicted an 18% cavity mass flow rate percentage for a 70/30 core-to-cavity area ratio for the 0.108 kg/s total inlet mass flow rate case. Experimental results didn't achieve this mass flow split until approximately a 50/50 area ratio. The CFD solution also calculated the same cavity mass flow rate with and without combustion in the cavity. It was shown experimentally that a higher cavity mass flow rate was obtained with all but one of the reacting cases. Additionally, the CFD solution predicted an average tangential velocity of 15 m/s in the reacting case. The experimental data for the 0.108 kg/s total inlet mass flow rate at a 50/50 area split, to approximately match the mass flow rate in the cavity, showed an average tangential velocity of 12.1 m/s. The CFD solution was run adiabatic which resulted in a higher cavity temperature than was seen experimentally and did not account for heating the air through the inlet air driver plate which could cause an injection velocity increase due to a lower air density. The higher cavity temperature would result in a lower fluid density and thus higher velocity in the CFD solution. Additionally, some simplifications in geometry could have unknowingly altered the results. As an example, in CFD the feathers were defined as a single entity that made a smooth transition from a circular leading edge to an octagonal trailing edge. There were no gaps or holes. While the real feathers fit tightly together, they were not completely air tight.

6.1.6 Diffuser Follow-on Test Methodology.

The cavity and exit plane temperature measurements in the follow-on study were taken in the same way as described above in Section 6.1.4. To analyze the combustion performance and identify the locations of the flame fronts in the circumferential cavity, OH chemiluminescence was used following the setup and settings described in Section 3.1.6.2. For this test series PSEV was not used for velocity measurements, instead the velocity was determined using the high-speed chemiluminescence videos using the method discussed in Section 2.11.1.

Combustion frequency data was calculated from the high-speed chemiluminescence videos. ImageJ software was used to extract the OH intensity from a single point centered in the combustor window for all video frames as a function of time. The time series data was then converted to frequency space using a Fourier transform to produce a power spectrum which displayed frequency versus amplitude. A sample location test was performed where the results from three points within the field of view of a representative chemiluminescence video were compared to ensure that the sample location did not have an impact on the determination of the dominant frequency results. The comparison showed a 19% variation in amplitude between the different sample locations, but the dominant peaks all occurred at the same frequency.

In this series four total inlet air mass flow rates of 0.06, 0.09, 0.108, and 0.12 kg/s were tested with equivalence ratios of 0.72 and 1.1. Two types of testing were conducted at each of the conditions above. In the first test type the diffuser was adjusted to maintain 0.037 kg/s cavity air mass flow rate for the 0.09, 0.108, and 0.12 kg/s total inlet flow rates for a total of six test points. Ideally, all four of the total inlet flow rates would have been run at the same cavity air mass flow rate, but the system was only capable of diverting a maximum of 0.024 kg/s to the cavity at the 0.06 kg/s total inlet air flow rate. The second test type used the diffuser to maintain

a constant 74/26 core-to-cavity air mass flow ratio at each equivalence ratio and total inlet flow rate for a total of eight additional test points. These combined 14 test points were repeated three times due to differing data capture techniques. During the first data capture configuration pressure and chemiluminescence data were captured with reacting flow for all 14 test points in both test types. During the second data capture configuration the rig was allowed to completely cool and all 14 points in both test types were run at cold flow conditions to collect pressure data for Rayleigh loss calculations. It was found that the cold flow aerodynamic losses ranged from 0.8% at 0.6 kg/s to 2.4% at 0.12 kg/s. In the third data capture configuration thermocouple rake measurements were taken with reacting flows to map the temperatures at the combustor exit plane for all 14 points in both test types.

6.1.7 Diffuser Follow-on Experiment Test Results.

The following results show the temperature, pressure (Rayleigh losses), frequency, and velocity measurements grouped by the test series. The first two sections show results from the tests with a constant cavity inlet mass flow rate of 0.037 kg/s at equivalence ratios of 0.72 and 1.1, respectively. The last two sections report on results from tests with a constant core-to-cavity mass flow rate split of 74/26 at equivalence ratios of 0.72 and 1.1, respectively.

6.1.7.1 Cavity Mass Flow Rate = 0.037 kg/s, Cavity Φ = 0.72.

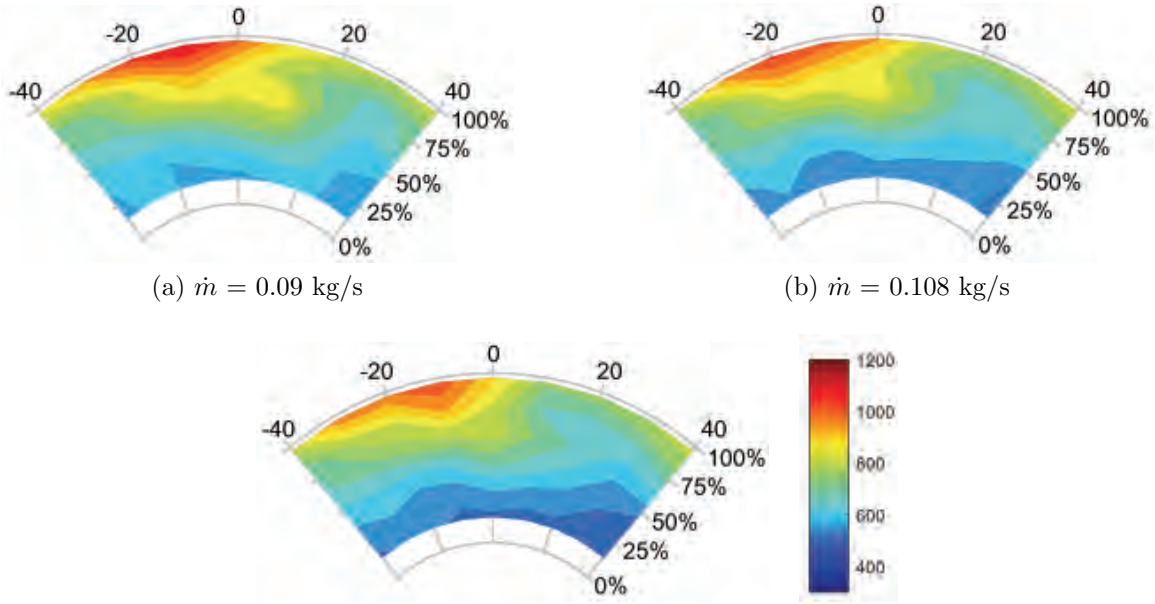
In this test sequence the diffuser successfully maintained the cavity inlet mass flow rate at a constant 0.037 kg/s which resulted in a core-to-cavity split ranging from 30.5 - 40.8 %. Across all three total inlet mass flow rates the combustor cavity properties of average temperature and average velocity remained consistent with a standard deviation of 9.4 K in temperature and 0.26 m/s in velocity as shown in Table 27. Taking the average velocity across all three cases yielded a centrifugal acceleration of $600g_e$.

Furthermore, no correlation was experienced in the frequency data due presumably to the similarity in the cavity temperature and velocity. Additionally, as the total inlet mass flow rate was increased, the Rayleigh loss was also slightly increased and ranged from 2.25% to 3.11%. From this data it can be seen that the diffuser was capable of maintaining constant cavity properties independent of the total inlet mass flow rate of air. This means that centrifugal load and combustion temperatures in the primary zone could be optimized independent of the engine operating condition to maximize performance and efficiency, or minimize losses, across the operating envelope.

Table 27. Temperature, velocity, dominant frequency and amplitude, and Rayleigh losses for 0.037 kg/s constant cavity mass flow rate and cavity $\Phi = 0.72$

Total Inlet $\dot{m}$ (kg/s)	**Cavity Split** (%)	**Avg. Cavity Temp.** (K)	**Cavity Velocity** (m/s)	**Frequency/ Amplitude** (Hz)	**Rayleigh Loss** (%)
0.09	40.8	1258	20.6	400/1,500	2.25
0.108	34.5	1270	20.7	317/2,175	2.58
0.12	30.5	1281	21.2	359/6,610	3.11

As shown in Figure 235 the temperature profile at the combustor system exit plane showed similar temperature magnitudes, but the size of the peak temperature islands in the contour map were slightly decreased with increasing total inlet mass flow rate. The cause of this reduction was likely due to greater dilution of the hot gases exiting the cavity at higher total inlet mass flow rates. As shown in Table 27, the percentage of air that was directed to the circumferential cavity was reduced with each increase in total inlet flow rate to maintain the constant 0.037 kg/s cavity flow rate. Thus there was a larger total inlet mass flow rate of air, with less air directed to the circumferential cavity, resulting in more core air available to dilute the hot gases at the higher total inlet flow rate cases. This change is evident in the global equivalence ratio which changed from 0.29 at 0.09 kg/s total inlet flow rate to 0.22 at 0.12 kg/s total inlet flow rate.



(a) $\dot{m} = 0.09$ kg/s

(b) $\dot{m} = 0.108$ kg/s

(c) $\dot{m} = 0.12$ kg/s

Figure 235. Experimental exit temperature profiles (K) for 0.037 kg/s constant cavity mass flow rate and cavity $\Phi = 0.72$

The behavior of the flame as observed by the high-speed OH chemiluminescence videos showed a pulsation that was experienced by the entire visible region of the combustion chamber. The pulse rate corresponds to the reported frequencies in Table 27 and the OH intensity was uniformly changed across the entire visible region of the flame. Figure 236 shows a collection of equally spaced frames from a representative high-speed OH chemiluminescence video showing the uniform variation in OH intensity across the frame. The cause of this uniformly pulsating combustion intensity could be due to a back-pressuring of the unchoked propane inlets resulting from an expansion wave caused by combustion. An expansion wave interacting with a fuel inlet momentarily reduced the flow rate of propane causing the decrease in OH intensity as there was less fuel available to burn. As the combustion reduced, the expansion waves in the combustion chamber were also reduced, and propane was allowed to flow normally. The increased fuel caused additional expansion which again reduced the flow of propane from the inlets and the cycle continued.

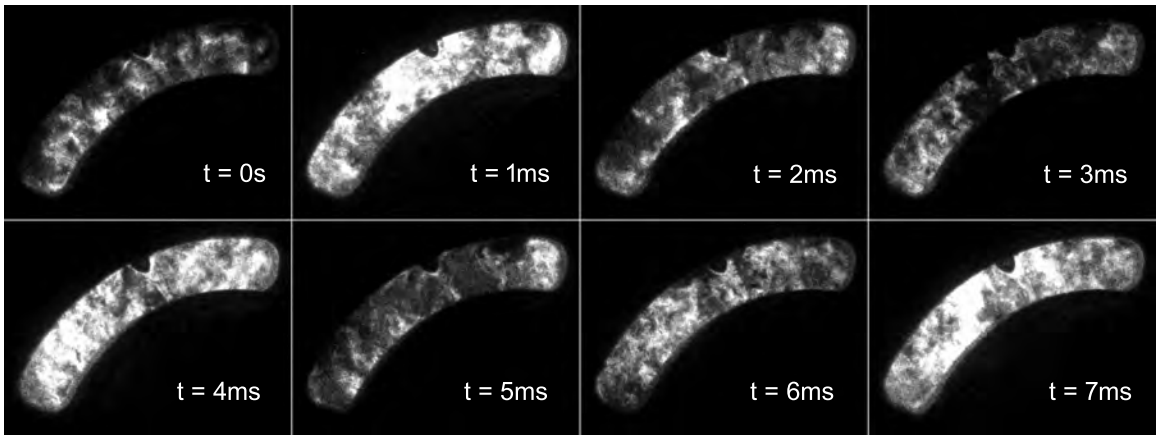


Figure 236. Frame montage from the high-speed OH chemiluminescence video from $\dot{m}$ = 0.108 kg/s, cavity Φ = 0.72, showing uniform OH intensity pulsation across the entire field of view

6.1.7.2 Cavity Mass Flow Rate = 0.037 kg/s, Cavity Φ = 1.1.

With the cavity inlet mass flow rate again held constant at 0.037 kg/s, but at an equivalence ratio of 1.1, the combustor cavity average temperature remained constant for the first two cases with a standard deviation of only 4.5 degrees, and the average velocity deviated by only 1 m/s across all three cases as shown in Table 28. The variation in cavity velocity produced g-loads ranging from $440g_e$ - $576g_e$. The reduction in temperature for the 0.12 kg/s case was unexpected and the exact cause is unknown. There was a reduction in pressures observed throughout the combustor for this condition which could indicate that the desired 0.12 kg/s mass flow rate of air was not maintained during data collection for this point. If this was the case, the combustion in the cavity would have been richer than intended which would explain the temperature reduction. However, a similar drop in temperature and pressure was observed for the equivalent test point during the constant core-to-cavity flow split cases discussed in the next section. As with the previous test series, this data showed the diffuser could maintain constant cavity properties independent of the total inlet flow rate with the ability to maximize performance across the operating envelope.

Table 28. Temperature, velocity, dominant frequency and amplitude, and Rayleigh losses for 0.037 kg/s constant cavity mass flow rate and cavity $\Phi = 1.1$

Total Inlet $\dot{m}$ (kg/s)	**Cavity Split** (%)	**Avg. Cavity Temp.** (K)	**Cavity Velocity** (m/s)	**Frequency/ Amplitude** (Hz)	**Rayleigh Loss** (%)
0.09	40.8	1144	17.9	42.5/18,540	1.86
0.108	34.5	1135	18.6	42.5/2,330	2.24
0.12	30.5	866	20.5	44.9/5,625	1.99

The frequencies obtained from OH chemiluminescence as shown in Table 28 were all within 5.6%. Unlike the 0.72 equivalence ratio case which showed a larger variation in frequency between cases with a peak frequency of 400 Hz, this series achieved a nearly consistent frequency across all three cases at 42.5 Hz. Using the velocity data reported in Table 28 and the geometry of the combustor, a theoretical frequency can be found for the number of rotations a fluid particle could make around the combustion chamber in one second. These theoretical frequencies are 38.3, 39.7, and 43.9 Hz for the 0.09, 0.108, and 0.12 kg/s flow rate cases, respectively. These theoretical frequencies nearly match the frequencies obtained from the OH chemiluminescence videos.

Unlike the 0.72 equivalence ratio case which showed a uniform pulsation of the flame across the visible region of the cavity, the 1.1 equivalence ratio OH chemiluminescence videos showed discrete flame events that always originated from the upstream side of the video frame and traveled downstream as shown in Figure 237. It is possible that at these conditions there was a flame front that was traveling around the combustor annulus at the cavity bulk velocity. This behavior would explain why the OH chemiluminescence intensity frequency and theoretical frequency based on cavity velocity and geometry matched. In these fuel-rich cases the momentum of the fuel injected into the cavity was higher than the $\Phi = 0.72$ cases due to passing a high

mass flow rate of fuel through identical fuel injectors. The higher momentum allowed fuel from the radially injecting ports to pass through the cavity with less mixing and reactions with the cavity air. The reduced reactions was evident in the chemiluminescence videos which showed discrete flames traveling around the cavity, and in the lower cavity temperatures. The lower heat release also presented as lower Rayleigh losses and lower exit temperature magnitudes compared to the lean test cases.

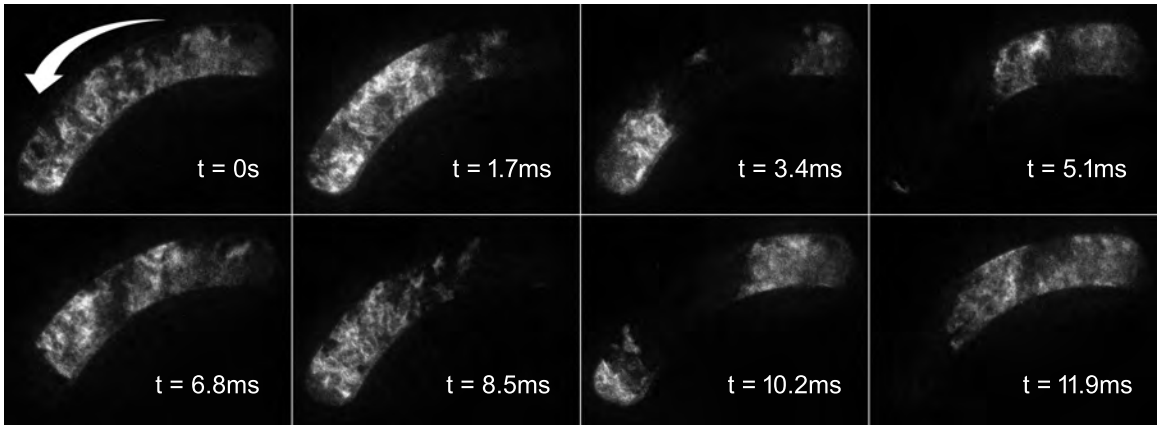
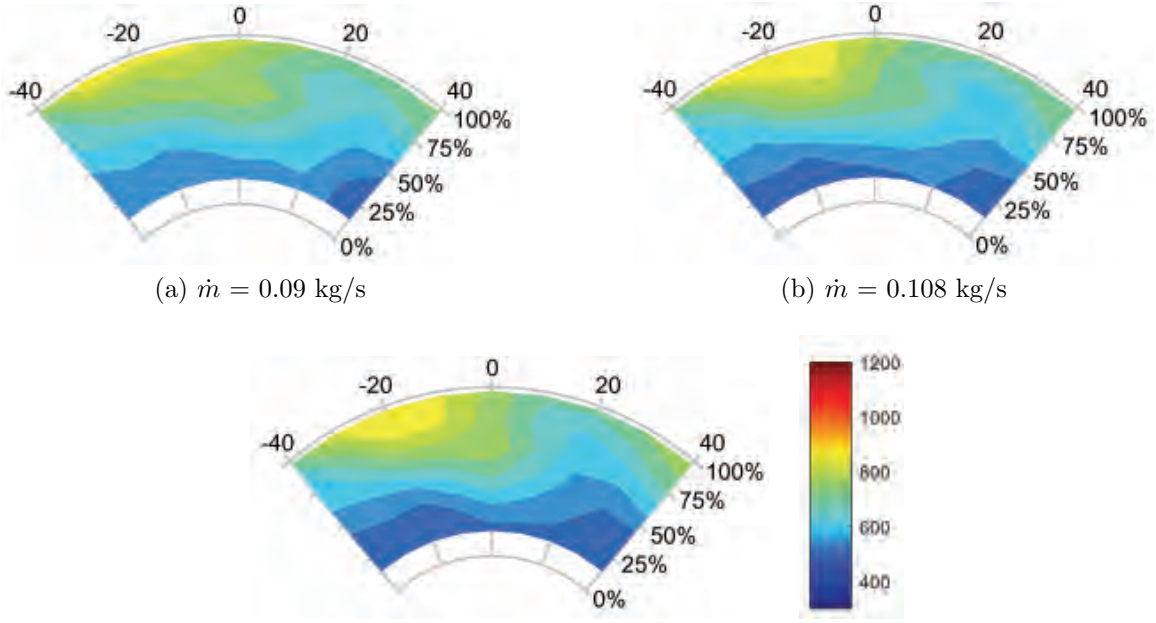


Figure 237. Frame montage from the high-speed OH chemiluminescence video from $\dot{m}$ = 0.108 kg/s, cavity Φ = 1.1, showing flames propagating from the upper right of the field of view and traveling to the lower left. White arrow indicates the direction of air injection and bulk fluid swirl

The exit temperature profiles for these cases, shown in Figure 238, indicate a reverse trend from the 0.72 equivalence ratio cases. In the results below the size of the region of elevated temperature increases with increasing total inlet mass flow rate. As the unburned fuel exited the circumferential cavity it was allowed to mix with air from the core flow to enable the reaction to finish. All three test cases had the same fuel and air mass flow rates in the cavity, however, the additional air present in the core flow of the higher total inlet mass flow rate cases enabled more reactions to complete, but in a localized area. For these three cases the global equivalence ratio decreased from 0.41 at 0.09 kg/s total inlet flow rate to 0.31 at 0.12 kg/s total inlet flow rate. At the higher total mass flow rates the momentum in the core and cavity

were more balanced which reduced the cavity fluid penetration into the core flow. The reduction in fluid penetration resulted in a more localized zone of hot gases on the exit plane as the reactants had completed the combustion process by that point.



(a) $\dot{m} = 0.09$ kg/s

(b) $\dot{m} = 0.108$ kg/s

(c) $\dot{m} = 0.12$ kg/s

Figure 238. Experimental exit temperature profiles (K) for 0.037 kg/s constant cavity mass flow rate and cavity $\Phi = 1.1$

6.1.7.3 74/26 Core-to-Cavity Flow Split, Cavity $\Phi = 0.72$.

In this test sequence the mass flow rate of air into the circumferential cavity was allowed to change between 0.017 kg/s and 0.032 kg/s while maintaining a constant 74/26 core-to-cavity air mass flow rate split at an equivalence ratio of 0.72. This split ratio was tested because it traces back to historical common flow source UCC testing. Table 29 shows the results of the average cavity temperature, velocity, g-load, frequency, and Rayleigh losses for the four total inlet mass flow rates tested. The velocity at 0.12 kg/s is comparable to the velocity achieved in Section 6.1.7.1, which is expected given that the cavity mass flow rates differed by only 0.005 kg/s. A review of the data in Table 29 shows a steady increase in temperature and Rayleigh

losses with increasing total inlet flow rate. There is a trend of increasing velocity and centrifugal acceleration with increasing total inlet mass flow rate, however, it appears that the data may be reaching a plateau as the rate of increase in velocity and centrifugal acceleration diminished with each mass flow rate increase.

Table 29. Temperature, velocity, g-load, dominant frequency and amplitude, and Rayleigh losses for 74/26 core-to-cavity flow splits and cavity $\Phi = 0.72$

Total Inlet $\dot{m}$ (kg/s)	**Avg. Cavity Temp.** (K)	**Cavity Velocity** (m/s)	**Cavity g-load** (g)	**Frequency/ Amplitude** (Hz)	**Rayleigh Loss** (%)
0.06	1224	13.4	246	262/3,550	0.40
0.09	1240	17.0	396	312/3,300	1.16
0.108	1322	19.4	516	355/3,400	1.51
0.12	1332	20.1	554	372/2,855	2.10

Table 29 also indicates that the dominant frequency increased for rising mass flow rates with only minor changes in amplitude. These results are also shown in Figure 239 which is a plot of the frequency spectrum for all four test cases in this sequence. The increase in frequency may be due to an elevated vortex shedding rate in the cavity caused by pushing a larger quantity of air through the same air inlet holes, or possibly as a result of the higher cavity velocity. Within the combustor annulus the increase in velocity directly relates to an increase in centrifugal acceleration. Briones et al. [33] showed computationally that higher centrifugal acceleration results in enhanced mixing of combustion reactants due to added Rayleigh-Taylor instabilities. Thus the increased frequency observed experimentally could be the manifestation of the additional mixing caused by the elevated acceleration. The frequency of the 0.12 kg/s test point is comparable to those achieved in Section 6.1.7.1 which further demonstrates repeatability. An additional trend was observed in the lower frequency range between 0 - 100 Hz shown in Figure 239. In this range the local maximum amplitude showed an increase in frequency with increasing mass flow rate, but at a

decreasing amplitude with each flow rate increase. The high-speed OH chemiluminescence videos for these four test points showed a uniform pulsation of the reaction evenly across the entire camera field of view which is also consistent with the flame behavior from Section 6.1.7.1.

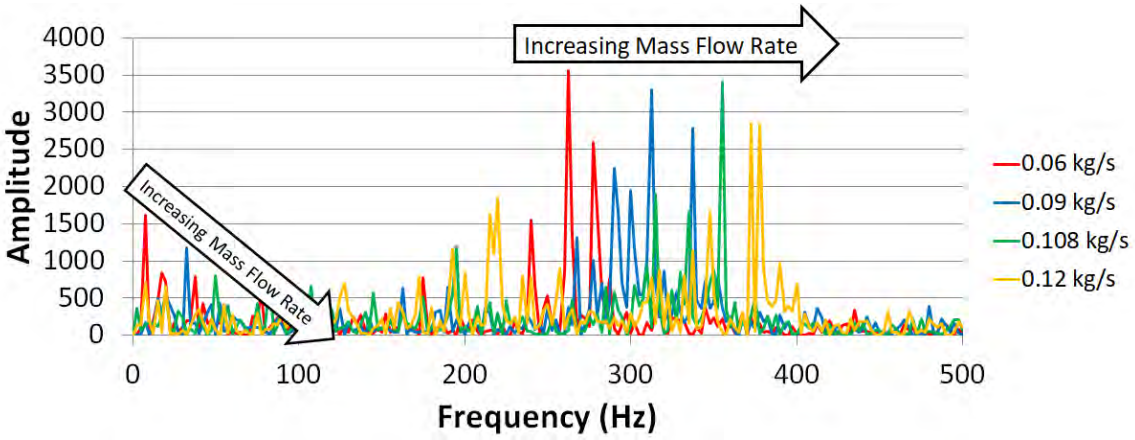
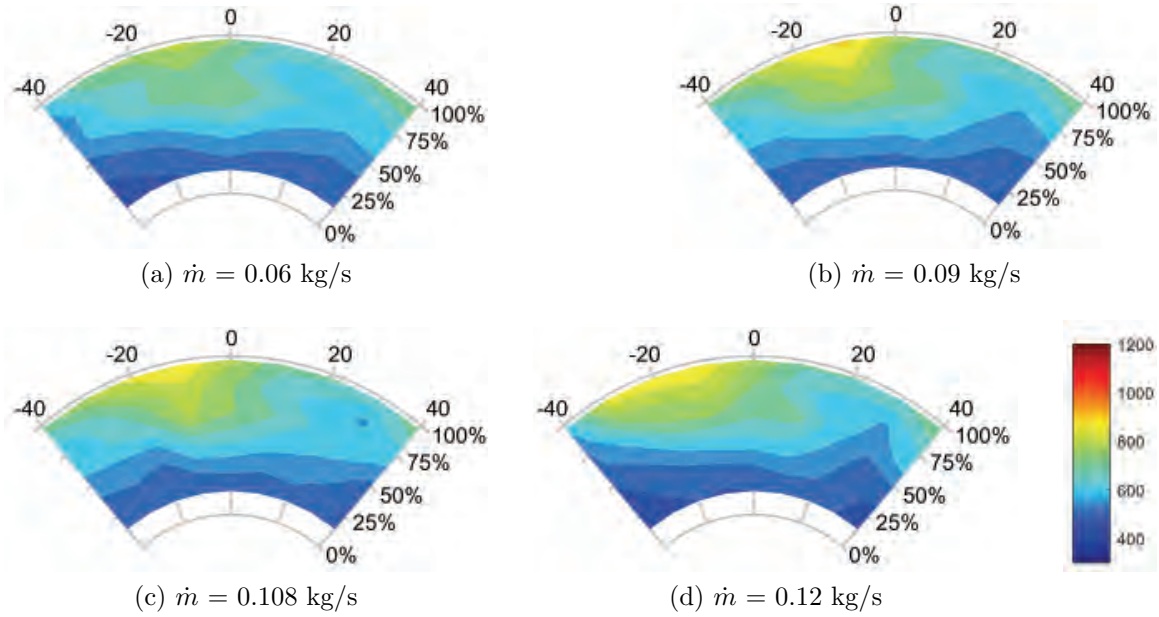


Figure 239. Chemiluminescence frequency measurements for the 74/26 core-to-cavity flow split cases at cavity $\Phi = 0.72$

As shown in Figure 240 there were minimal differences between the exit temperature profiles for these four cases as the constant flow split percentage resulted in a constant global equivalence ratio of 0.19. There was a slight increase in the area of the high temperature contours at the higher mass flow rates which is expected given that these test points also experienced higher average cavity temperatures. The placement and orientation of the contours on the exit plane were similar due to the constant mass flow rate split resulting in similar momentum ratios between the core flow path and the bulk fluid in the cavity for all four test points.

6.1.7.4 74/26 Core-to-Cavity Flow Split, Cavity $\Phi = 1.1$.

The final test series also maintained the 74/26 core-to-cavity air mass flow rate split but at an equivalence ratio of 1.1. As with the previous section the mass flow rate of air into the circumferential cavity varied between 0.017 kg/s and 0.032 kg/s. Table 30 shows the results of the average cavity temperature, velocity, g-load, frequency, and



(a) $\dot{m}$ = 0.06 kg/s

(b) $\dot{m}$ = 0.09 kg/s

(c) $\dot{m}$ = 0.108 kg/s

(d) $\dot{m}$ = 0.12 kg/s

Figure 240. Experimental exit temperature profiles (K) for the 74/26 core-to-cavity flow split cases at cavity Φ = 0.72

Table 30. Temperature, velocity, g-load, dominant frequency and amplitude, and Rayleigh losses for 74/26 core-to-cavity flow splits and cavity Φ = 1.1

Total Inlet $\dot{m}$ (kg/s)	**Avg. Cavity Temp.** (K)	**Cavity Velocity** (m/s)	**Cavity g-load** (g)	**Frequency/ Amplitude** (Hz)	**Rayleigh Loss** (%)
0.06	1251	14.5	288	307/40,830	0.76
0.09	1273	19.0	495	232/19,030	1.58
0.108	1206	19.2	506	150/4,545	2.33
0.12	1037	16.0	351	87/3,430	2.18

Rayleigh losses for the four total inlet mass flow rates tested. The cavity temperature, velocity, and total system Rayleigh losses initially increased, then decreased with increasing mass flow rate. This behavior was previously studied computationally by Cottle [78] for this same cavity geometry, and observed during experimental diffuser characterization testing discussed in Section 6.1.7.2. Since the mass flow rate of air in the cavity increased for each total inlet flow rate increase to maintain a constant core-to-cavity flow split, there was also a corresponding fuel flow rate increase for each

successive case to maintain a constant equivalence ratio. It was suspected that since the fuel was injected into the circumferential cavity normal to the outer diameter wall, that a shear force between the fuel and the tangentially flowing gases caused a reduction in cavity velocity at higher fuel flow rates. For the 0.12 kg/s test case the shear force was significant enough to cause a reduction in the cavity bulk velocity compared to the previous two cases. As the fuel momentum increased for each case it penetrated across the radial span of the cavity with less mixing resulting in reduced cavity reactions and lower cavity temperatures.

The frequencies shown in Table 30 exhibit a trend of a reduction in frequency with increasing mass flow rate. These results are better shown in Figure 241 which also displays a reduction in amplitude as the frequency is reduced for each mass flow rate increase. This trend is counter to the frequency trend in the 0.72 equivalence ratio case where the amplitude remained relatively constant as it increased in frequency. Also of note is the difference in the amplitudes between the 0.72 and 1.1 cases which peaked at 3,552 and 40,828, respectively. The higher amplitude of the fuel-rich cases are due to a stronger correlation to specific frequencies present in the flow. The high-speed OH chemiluminescence videos for the two lower mass flow rate cases indicated a uniform pulsation of the flame in the same manner as the lean test cases. The two higher flow rate test cases, which produced the lower frequency responses, showed discrete flame events that transitioned from the upstream side of the video frame and convected downstream, but with less of a gap between flames than the cases in Section 6.1.7.2.

Despite the constant global equivalence ratio of 0.29 for all four of these cases, there was a more pronounced change in the exit temperature profile with increasing mass flow rate as shown in Figure 242, compared to the lean results previously presented. As the mass flow rate was increased, the intensity and size of the heated contours were

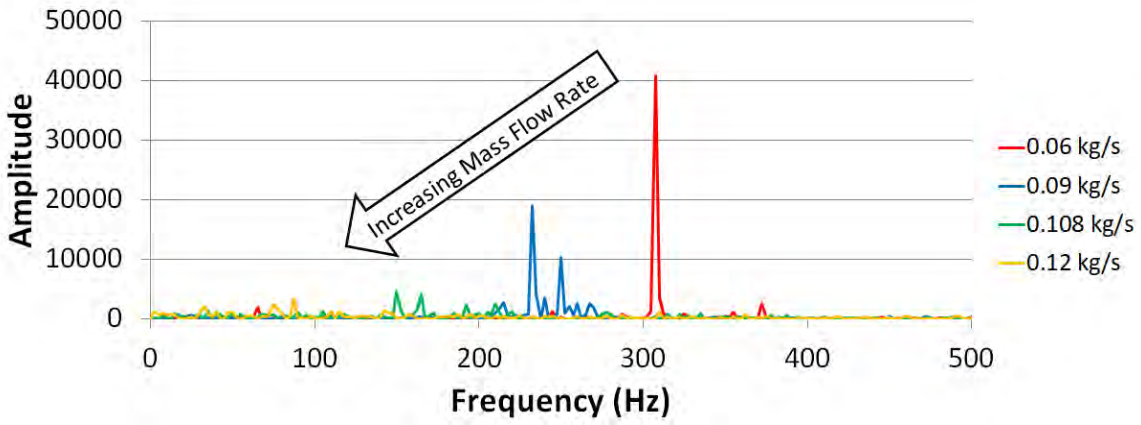
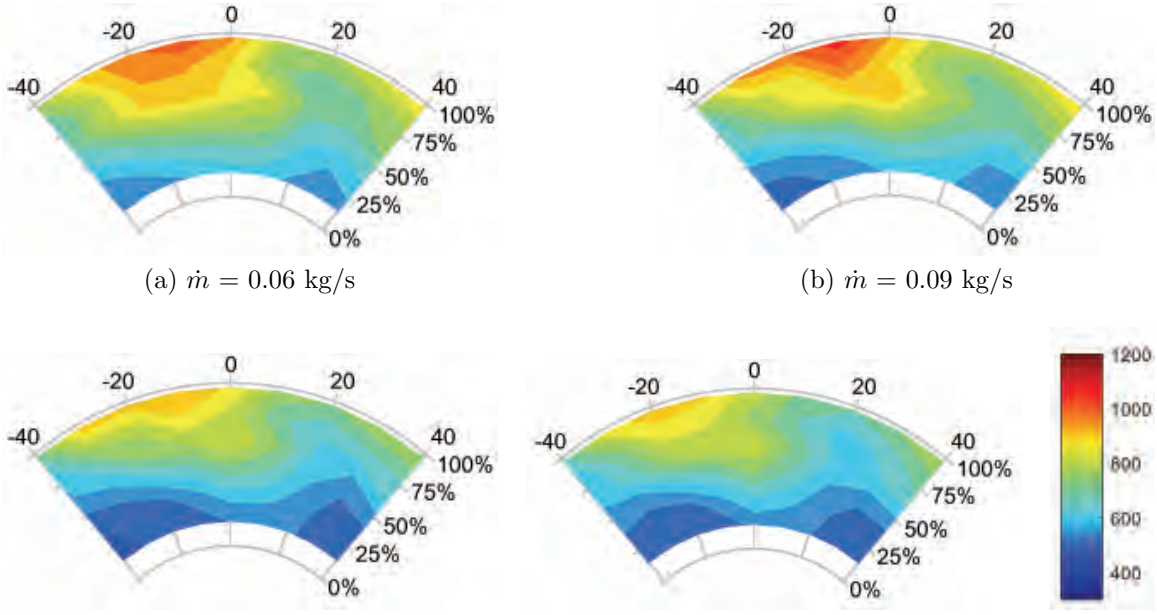


Figure 241. Chemiluminescence frequency measurements for the 74/26 core-to-cavity flow split cases at cavity $\Phi = 1.1$

reduced. This decrease is the result of the fuel injection geometry and the additional fuel present in these fuel-rich cases. Higher air flow rates drove an increase in fuel flow rates to maintain a constant equivalence ratio. The additional fuel increased the shear between the fuel stream and the swirling flow which reduced the bulk velocity, and thus the centrifugal acceleration. This behavior is evident at the higher total mass flow rate cases where the cavity velocities were not proportional to the increase in total inlet flow rate given a constant flow rate split. Despite the cavity behavior the core flow velocity did increase proportionally with increases in total inlet mass flow rate. This means that the penetration of the hot gases exiting the cavity would be lower at the higher mass flow rate cases. Additionally, the higher fuel flow rates resulted in faster fuel jet velocities which may have allowed fuel to span the cavity height and exit without reacting since the fuel jets inject radially inward. If fuel exited the cavity without reacting, this would also explain the reduced average cavity temperatures at the higher total inlet flow rates. Applying the reduced core flow penetration, the lower magnitude of the temperatures in the cavity, and the potential for fuel to exit the cavity without reacting accounts for the difference in the exit temperature profiles with increasing total inlet mass flow rate.



(a) $\dot{m} = 0.06$ kg/s

(b) $\dot{m} = 0.09$ kg/s

(c) $\dot{m} = 0.108$ kg/s

(d) $\dot{m} = 0.12$ kg/s

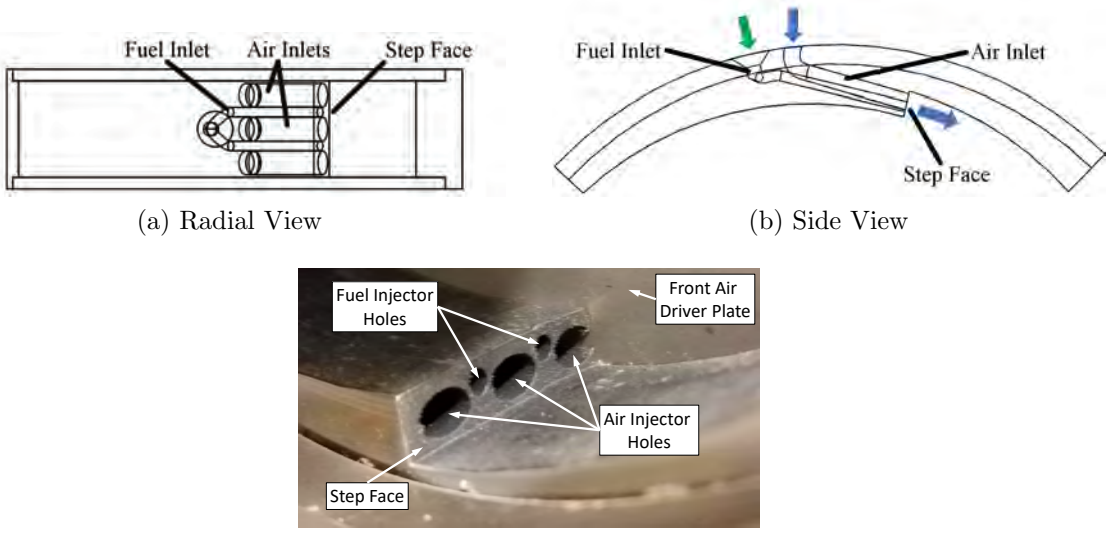
Figure 242. Experimental exit temperature profiles (K) for the 74/26 core-to-cavity flow split cases at cavity $\Phi = 1.1$

6.2 6-Step Ring

The baseline circumferential cavity configuration used by Cottle [78] and described in Section 3.3, as well as used experimentally in the variable diffuser testing above, was successful in maintaining cavity combustion and developing a centrifugal load on the reactants. However, this design suffered from a lack of air at the cavity OD which resulted in a high local equivalence ratio due to fuel buildup. These high-concentration fuel streaks were generally too rich to burn which resulted in lower combustion temperatures along the streaks as shown in Figure 80. Additionally, as discussed in Section 6.1, the radial fuel injection caused a reduction in tangential velocity at higher equivalence ratios due to the shear between the fuel jets and the swirling bulk cavity fluid. To improve these characteristics, changes were made to the fuel and air injection schemes to aid in the development of centrifugal loading while providing air to all radial positions of the cavity. These new changes to the

injection schemes were based on all the past UCC studies discussed in Chapter II and the backward-facing step stabilized combustion work of Lapsa and Dahm [56]. These schemes were enhanced by a redesign of the cavity back plate which allowed for some fuel to be introduced lower in the cavity to reduce the local equivalence ratio at the cavity OD.

The first modified injection scheme tested was a new cavity outer ring that featured six backward-facing steps. This configuration was referred to as the 6-Step Ring. The steps were 6.35 mm tall and evenly spaced at 60° increments around the ring. These steps were planned to be flame stabilizing through the recirculation that occurs behind a backward-facing step, as well as injecting fuel and air as shown in Figure 243. Each step included five injecting holes; three 5 mm diameter ellipses at the outboard position of the step for air injection, and two 2.5 mm diameter circular holes on the inboard position of the step for fuel injection. These holes were sized to deliver a total of 0.014 kg/s of air at 34 m/s (approximately 1,600g_e) which represents half of the cavity air at a 74/26 core-to-cavity flow split at 0.108 kg/s total inlet mass flow



(a) Radial View

(b) Side View

(c) Injector Holes

Figure 243. 6-Step Ring air and fuel injector ducting and hole pattern

rate. The fuel holes were sized to deliver a total of 0.0015 kg/s of propane with an injection velocity of 12 m/s. This fuel flow rate equates to a cavity equivalence ratio of 0.72. Only half of the cavity air was planned to be delivered from the outer ring, the remaining air would still be delivered through the baseline compound air driver plate on the cavity front wall with half the holes blocked. This concept required the variable geometry diffuser to direct the correct mass flow rate to the cavity front air driver plate. Figure 244 shows a cross-section of the UCC with the 6-Step Ring and variable geometry diffuser.

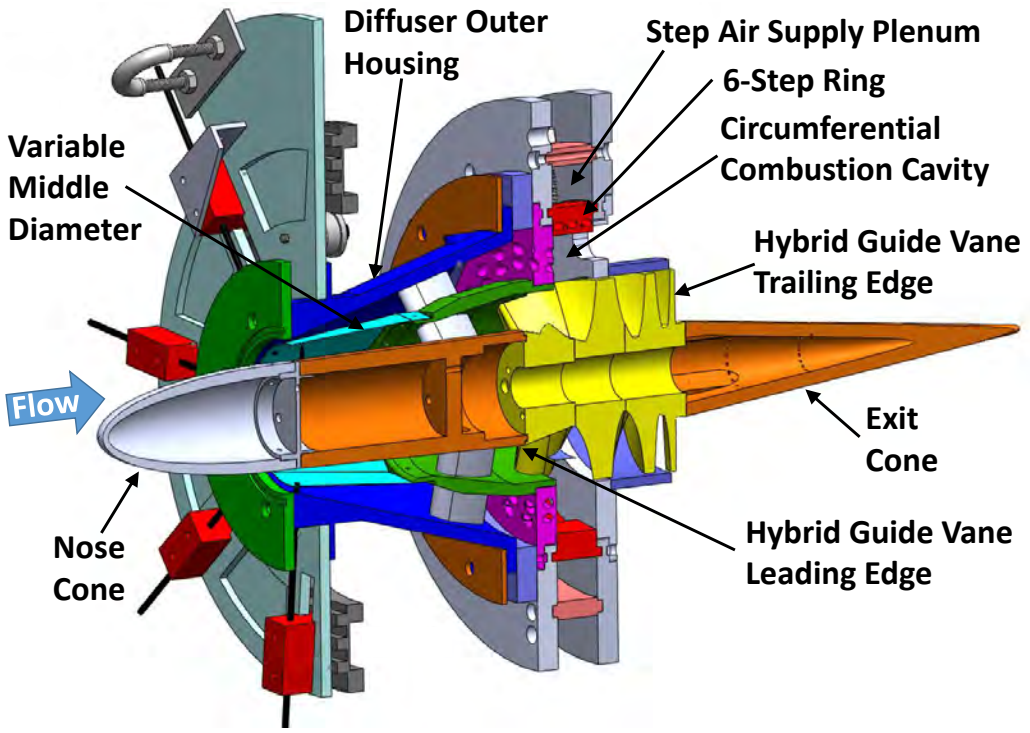
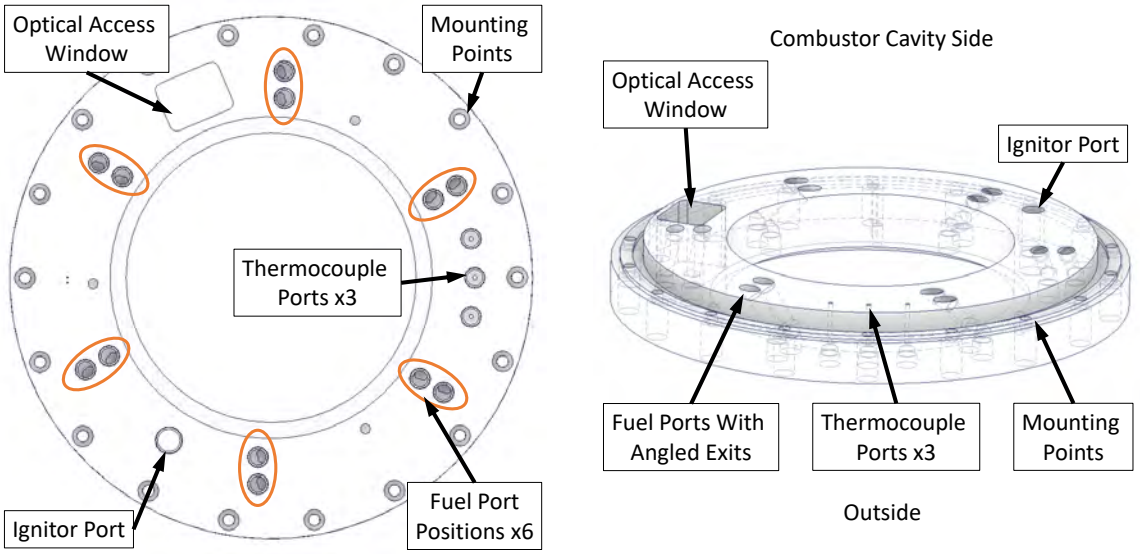


Figure 244. Version 3 UCC with variable geometry diffuser and 6-Step Ring

A second fuel injection location was made possible through a modified cavity back plate that incorporated six sets of evenly spaced injectors as shown in Figure 245. Fuel would only be injected through the holes at one of the radial positions at a time with the remaining holes plugged. Only the inboard set of holes was tested in the present study. The mass flow rate of fuel through these injectors could be independently

controlled to send some portion of the total fuel flow through these holes with the remainder entering the cavity through the injectors in the steps. Allowing fuel to be injected from multiple locations in the cavity was thought to enhance mixing and reduce the local equivalence ratio around the injectors to aid in combustion.



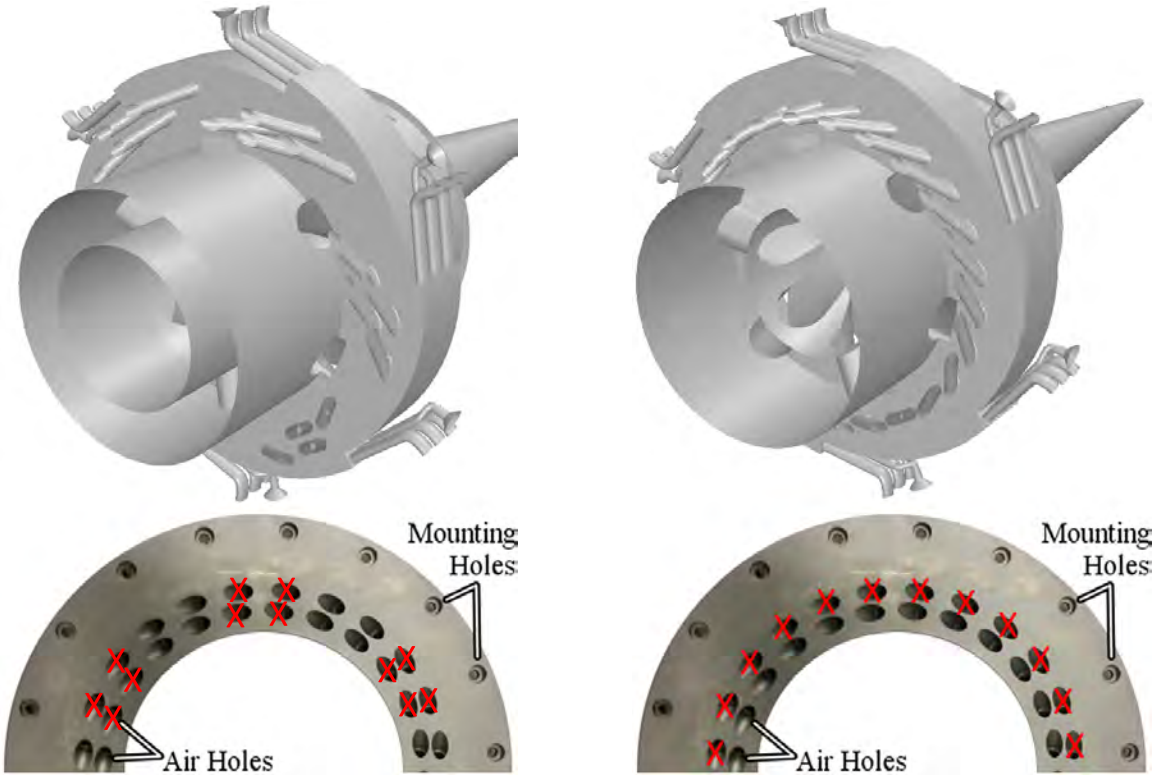
(a) Outside View (b) Internal View

Figure 245. Modified back plate with angled fuel injectors concept

6.2.1 6-Step Ring Computational Analysis.

Since only half of the cavity air was planned to flow the front air driver plate, half of the holes needed to be removed to keep the injection velocity through these holes high. A computational study was performed that looked at the two front wall hole pattern options shown in Figure 246 with the 6-Step Ring. The red "X"s over the holes in the front air drive plate show which holes were removed in the corresponding computational study. In Pattern 1 the holes located over the vane tips were removed leaving the holes located over the vane passages. In Pattern 2 the outer ring of holes was removed leaving all of the holes in the inner ring. These patterns were iterative with Hole Pattern 2 selected in response to the results from Hole Pattern 1. The

upper half of these figures show the fluid/metal interface surface of the computational domain, which was periodic about 60° sectors, arrayed to show the full test rig.



(a) Hole Pattern 1 (b) Hole Pattern 2

Figure 246. 6-Step Ring front air driver plate hole patterns

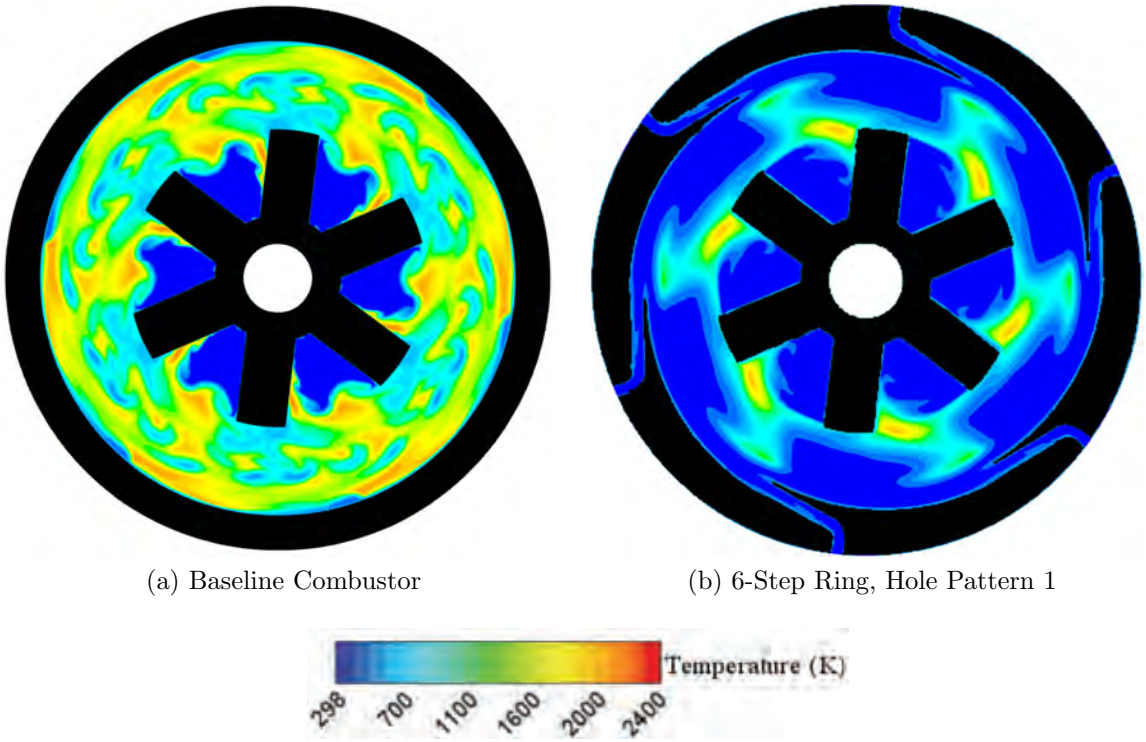
The computational settings and grid resolutions were identical to those discussed in Sections 5.2, 4.3, and 4.4. The only changes to the domain in the present study were the modification to the OD cavity wall to incorporate the steps and the fuel and air ducting through that wall, and a reduction in the number of air driver holes on the cavity forward wall. There was also an additional boundary condition caused from the air drivers on the outer ring. Table 31 gives the fluid boundary conditions for the 6-Step analysis. These values correspond to a 74/26 core-to-cavity flow split at a 0.108 kg/s total air inlet flow rate. The exterior surface temperature boundary conditions are the same as those given in Table 21.

Table 31. 6-Step Ring Inlet/Exit boundary condition settings

Boundary	$\dot{m}$ (kg/s)	**Gauge Total Pressure** (Pa)	**Temperature** (K)
Front Wall Air Inlets	0.0027	4800	300
Outer Ring Air Inlets	0.0027	4800	300
Core Inlet	0.0126	4800	300
Fuel Inlet (Φ=0.72)	0.00025	5200	300
Domain Exit (Vent)	0.0365	0	300
Pressure Inlet	0	0	300

The resulting temperature distribution at the half cavity plane for front wall Hole Pattern 1 is shown in Figure 247b, with the corresponding contours in the Baseline combustor shown in Figure 247a. While the tangential velocity in the 6-Step combustor cavity was significantly improved to approximately 35 m/s (approximately 1,700g_e), the position of the reactions and magnitude of the heat release was poor. The faster cavity flow rate prevented core flow entrainment which had previously caused a circulation in the cavity that traveled up the back wall, across the top wall collecting propane and down the front wall to help distribute fuel. In the 6-Step cavity with Hole Pattern 1, the forward air drivers pushed the fuel to the back wall. Without the entrainment induced circulation there were no mechanisms to pull fuel to the front wall to distribute the reactions.

Hole Pattern 2 was developed to position the front air drivers in a position that would minimize the fuel being pushed to the back wall. The temperature distribution at the half cavity plane for front wall Hole Pattern 2 is shown in Figure 248b, again with the corresponding contours in the Baseline combustor in Figure 247a for comparison. The position of the reactions in the cavity were greatly improved over Hole Pattern 1, and the magnitude of the reaction was greater than the Baseline combustor. The 6-Step analysis showed more areas of continuous burning compared the the Baseline combustor which had many localized pockets of reactions. The locations



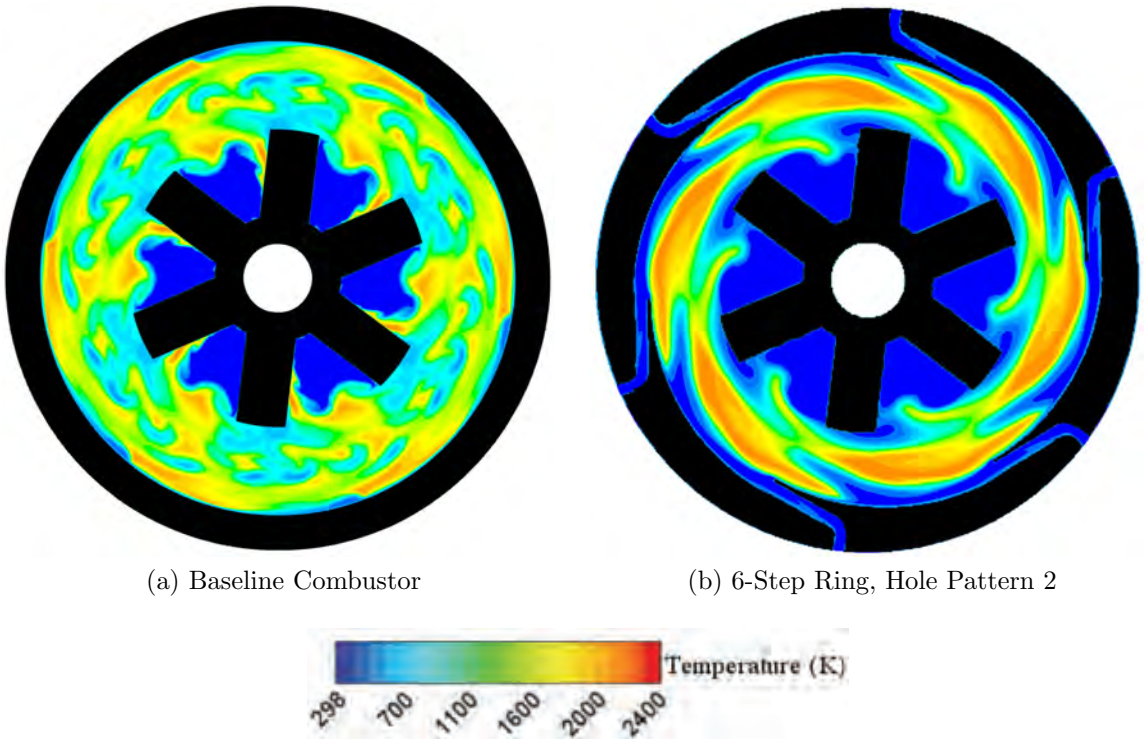
(a) Baseline Combustor (b) 6-Step Ring, Hole Pattern 1

Figure 247. Temperature contours (K) on the half cavity plane of the Baseline combustor and the 6-Step Ring combustor with Hole Pattern 1 at cavity Φ=0.72

of the front air drivers can also be seen in the Baseline combustor as cold pockets equally spaced around the cavity.

The tangential velocity was also increased in Hole Pattern 2 to an average value of 38.2 m/s (approximately 2,000g_e). The injection velocity from the air drivers in the steps was greater than that from the front wall injectors. In Hole Pattern 1 the tangential velocity in the cavity was a blend of both air drivers locations. In Hole Pattern 2 the front air drivers did not contribute to the bulk tangential velocity until almost the cavity exit. The tangential velocity contours at the half cavity plane for Hole Pattern 2 is shown in Figure 249b, with the corresponding contours in the Baseline combustor in Figure 249a for comparison. The average tangential velocity in the Baseline cavity was predicted to be 28.5 m/s.

Based on the computational performance of the 6-Step Ring with front wall Hole

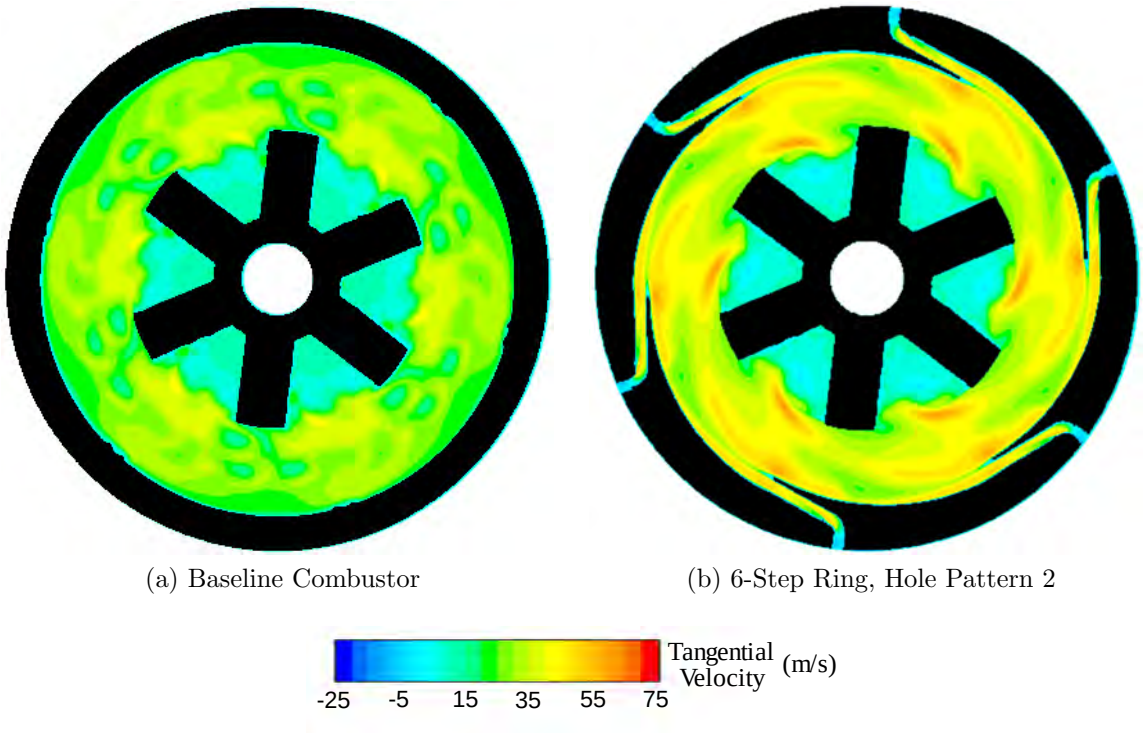


(a) Baseline Combustor (b) 6-Step Ring, Hole Pattern 2

Figure 248. Temperature contours (K) on the half cavity plane of the Baseline combustor and the 6-Step Ring combustor with Hole Pattern 2 at cavity Φ=0.72

Pattern 2, the decision was made to manufacture the 6-Step Ring to enable experimental testing. While the ring was being produced additional computational cases were run on the 6-Step Ring with front wall Hole Pattern 2, but at elevated cavity equivalence ratios of 1.0 ($\dot{m}_f$=0.00345 kg/s), 1.1 ($\dot{m}_f$=0.00380 kg/s), 1.2 ($\dot{m}_f$=0.00414 kg/s), and 1.3 ($\dot{m}_f$=0.00449 kg/s). Computations started directly at an equivalence ratio of 1.3 resulted in flameout. A flame was maintained, however, when started at an equivalence ratio of 1.0 and incremented by 0.1 up to 1.3. The temperature contours at these four equivalence ratios are shown in Figure 250.

These cavity equivalence ratios are based on the total amount of fuel and the total amount of air entering the cavity. Since only half the air entered the outer ring, but all of the fuel was injected through the steps, the outer regions of the cavity were locally very rich with limited or no reactions. When the reactants migrated radially

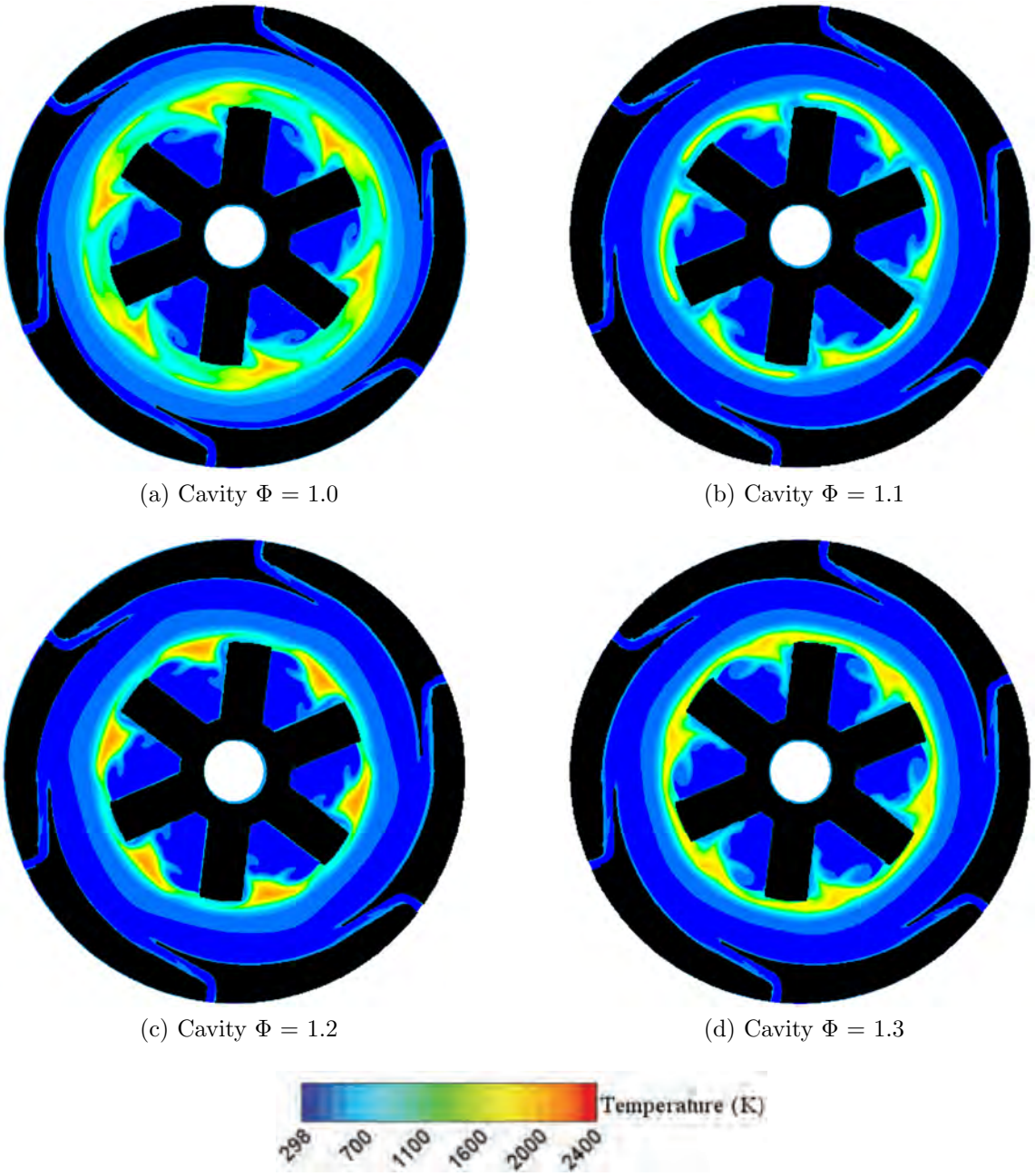


(a) Baseline Combustor (b) 6-Step Ring, Hole Pattern 2

Figure 249. Tangential velocity contours (m/s) on the half cavity plane of the Baseline combustor and the 6-Step Ring combustor with Hole Pattern 2 at cavity Φ=0.72

inward where the front air drivers introduced the second half of the cavity air, the reactions increased. In all four cases in Figure 250 the reactions did not burn until the air from the front air drivers was introduced. As more fuel was added to the cavity the reactions were continually pushed inward toward the cavity exit.

Six evenly spaced fuel injectors were added to the cavity back wall. They were positioned over the vane tips and approximately centered radially from the cavity ID to the most outboard point on the stepped outer ring as shown in Figure 251. This figure also shows an iso-surface of OH species colored by static temperature. All of the computational settings and domain characteristics for this analysis were the same as the previous studies but with the addition of a back wall fuel injector inlet boundary condition. Two back wall injector hole diameters were tested at 0.3175 cm and 0.635 cm, both injecting tangentially into the direction of cavity swirl at a 45°



(a) Cavity $\Phi = 1.0$

(b) Cavity $\Phi = 1.1$

(c) Cavity $\Phi = 1.2$

(d) Cavity $\Phi = 1.3$

Figure 250. Temperature contours (K) on the half cavity plane of the 6-Step Ring combustor with Hole Pattern 2 at stoichiometric and rich cavity equivalence ratios

angle off normal from the back wall. The penetration of the fuel exiting both of these injector sizes into the core flow was found computationally to be minimal. In both cases the fuel exited the back wall injectors at a negligible speed and was pushed

along the back wall by the bulk cavity fluid until it reacted or was pushed out of the cavity. The experimental hardware used the larger diameter holes.

The computational results of the 6-Step Ring, with front wall Hole Pattern 2, and 0.635 cm diameter back wall fuel injectors was analyzed at an equivalence ratio of 1.3 and 0.72. The cavity air was split 50/50 between the front wall and the step air inlets. The fuel was split 50/50 between the step fuel inlets and the back wall fuel injectors. Figure 252 shows the temperature contours at the half cavity plane with and without back wall fuel injection for the 1.3 equivalence ratio case. By splitting the fuel and air and distributing them around cavity the magnitude of the reactions was greatly increased and the position of the reactions were pulled up into the cavity. The temperature contours look similar to the distribution in the 0.72 equivalence ratio case without back wall injection. This configuration represents a major improvement for the rich cases.

The performance of the combustor with back wall fuel injection at a cavity equivalence ratio of 0.72 had a negative impact. The combustor without back wall injection

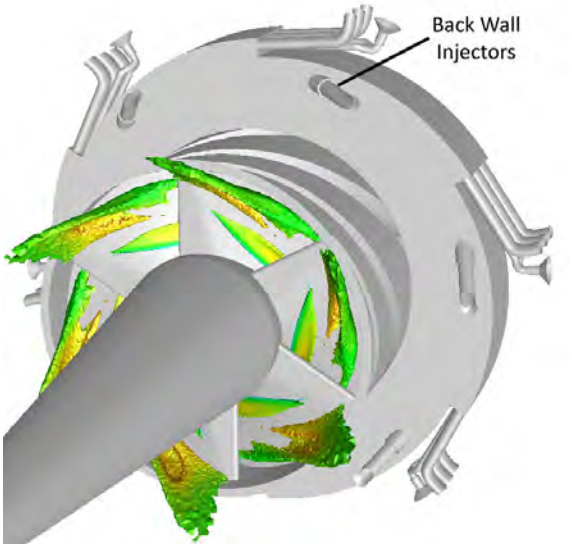
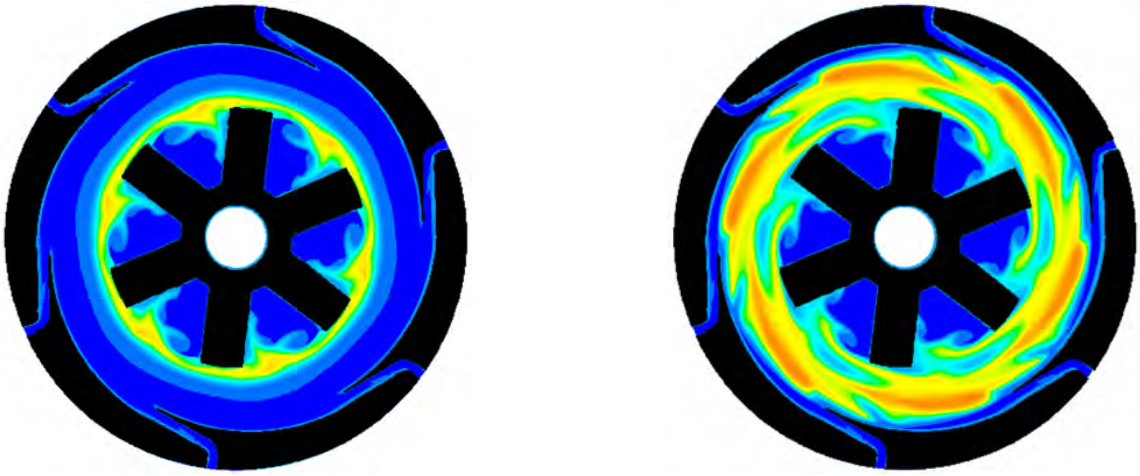
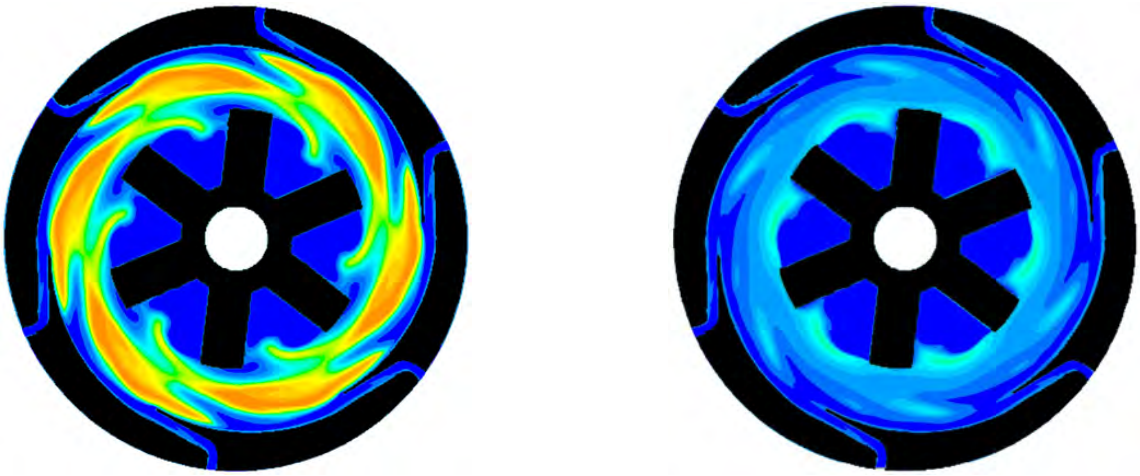


Figure 251. Fully arrayed computational domain showing back wall injectors



(a) Without Back Wall Fuel Injection (b) With Back Wall Fuel Injection

Figure 252. Temperature contours (K) on the half cavity plane of the 6-Step Ring combustor with Hole Pattern 2 with and without back wall fuel injection at a cavity equivalence ratio of 1.3



(a) Without Back Wall Fuel Injection (b) With Back Wall Fuel Injection

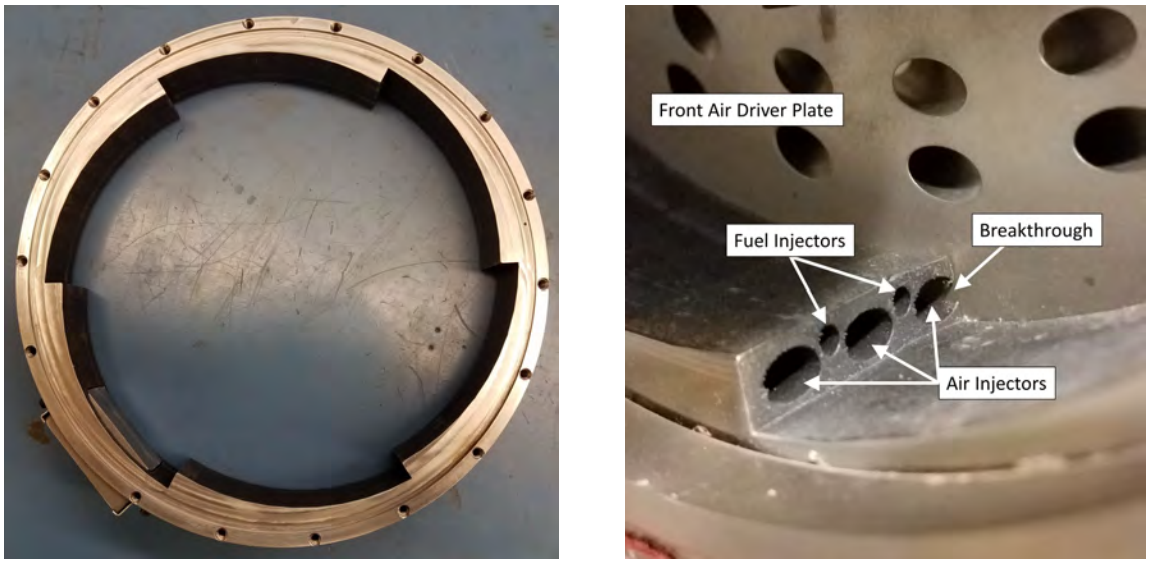
Figure 253. Temperature contours (K) on the half cavity plane of the 6-Step Ring combustor with Hole Pattern 2 with and without back wall fuel injection at a cavity equivalence ratio of 0.72

was able to burn the fuel in the cavity without difficulty. By splitting and distributing the fuel to two positions in the cavity the resulting reactions were too lean. The temperature contours in Figure 253 show drastically reduced cavity temperatures resulting from the extremely lean combustion. This result demonstrates that to make this technique useful in an experimental rig, the step fuel injectors and back wall fuel injectors would need independent mass flow controllers to be able to turn off the back wall injection or balance the flow rates as needed to optimize performance.

6.2.2 6-Step Ring Experimental Testing.

To accommodate the curved internal ducting of the fuel and air ports, the 6-Step Ring was additively manufactured as a single piece in inconel on a Concept Laser M2 3D printer in the AniMaL Lab at AFIT. The injector holes were sized the same as those used in the computational study. The manufactured hardware is shown in Figure 254. This was the first part made on this machine and the technicians in the AniMaL Lab were still learning. The part was printed on a steel build plate which caused the ring to separate from the plate due to internal stresses resulting in a slightly warped part. Due to the way fuel was introduced through the outer cavity plenum the fuel ports in the 6-Step Ring needed to be centered axially to maintain alignment with the port locations in the outer plenum ring. Since the part was warped, the side of the upstream air inlet hole broke through during the finish machining process conducted by the AFIT model shop as shown in Figure 254b. When the 6-Step Ring was installed in the rig, however, this break through was covered by the front air driver plate allowing the part to still be used.

The baseline front air driver plate was used in the 6-Step experimental testing, but the outer ring of holes were covered with a high-temperature foil tape to replicate Hole Pattern 2. The resulting part is shown in Figure 255. The 3.81 cm air supply line described in Section 3.1.1 was used to provide air to the step air supply plenum labeled



(a) 6-Step Ring (b) Ring installed & detail view of inlets

Figure 254. 3D printed 6-Step Ring hardware

in Figure 244. The plenum was fed from four lines split from the 3.81 cm supply line. The step air injectors connected the air supply plenum to the circumferential cavity. Controlling the air flow rate to the cavity required a combination of diffuser split settings to establish the air flow rate to the front wall, as well as commanding a flow rate through the 3.81 cm supply line mass flow controller. The 7.62 cm supply line that fed the diffuser inlet was reduced by the amount of air that was supplied to the cavity by the 3.81 cm supply line to maintain the desired total air mass flow rate to the test rig.

A redesigned back plate was machined for the UCC test rig that incorporated 6 sets of two back wall injectors as shown in Figure 256. As with the computational study, only one of the two radial injector positions would be used at a time. All 12 injectors had a diameter of 0.615 cm and were angled to inject into the direction of cavity swirl at a 45° angle off normal from the back wall. One set of injectors exited at 7.73 cm radially with the other set at 6.72 cm radially outward from the engine centerline. The internal passages of the injectors were drilled in two stages to

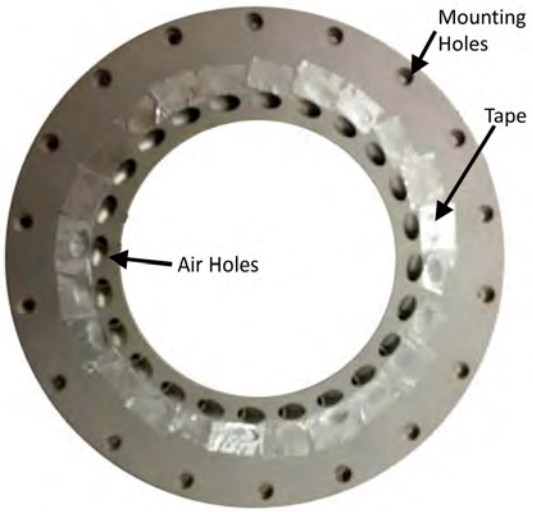
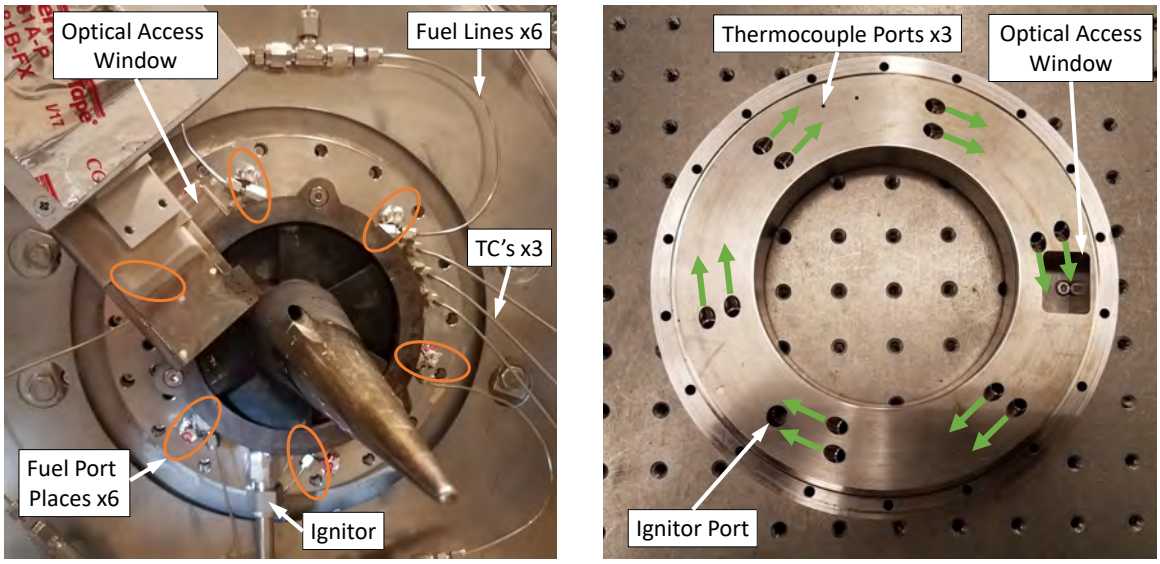


Figure 255. Modified baseline front air driver plate to replicate Hole Pattern 2, diffuser side view

allow for a perpendicular hole from the exterior and a 45° angled hole from the cavity interior. This arrangement allowed the external fuel fittings to be screwed into the back plate normally. Metal fuel lines were used to make the connections around the combustor exit to eliminate a threat of melting. A Swagelok 90° elbow was used to connect the fuel tubing to the back plate to eliminate interference of the fuel lines with the exhaust collar. Figure 256b shows the back plate configured with fuel lines. The fittings in the back plate could also be capped if no fuel injection was needed, or when the alternate injectors were being used. When configured for injection, the back plate was connected to the AliCat fuel mass flow controller and the cavity injectors were connected to the Brooks mass flow controller.

When the 6-Step Ring was tested experimentally, without back wall fuel injection, the combustor was unable to sustain a flame in the cavity at the computationally tested operating conditions with a 50/50 front wall-to-step air injection split. When the air flow through the step was reduced to 1%, with 99% air flow through the front air drivers, the combustor operated well and maintained combustion. There were



(a) Outside View (b) Cavity Side View

Figure 256. Redesigned cavity back plate with back wall fuel injectors

two proposed causes of the flameout. The first was that this cavity configuration experienced a reduction in flameholders. In the baseline design the spaces between the air jets from the front wall air drivers served as the cavity flameholders. In the 6-Step cavity the outboard set of these injectors were removed eliminating the first flameholder location. The backward-facing steps were intended to serve as flameholders, however, air injection from the steps removed most of the recirculation regions behind the step, eliminating this as a useful flameholder location.

The second proposed cause for the flameouts was that the injection velocity, and corresponding bulk tangential velocity, predicted in CFD was incorrect. If these values were predicted lower than the experimental velocities, the resulting experimental centrifugal loading could have exceed the blowout limits documented by Zelina [3] and shown in Figure 34. A cold flow PIV analysis, discussed in the next section, was conducted on the 6-Step Ring combustor to determine the tangential velocity and centrifugal loading in the cavity.

6.2.2.1 6-Step Ring PIV Analysis.

This PIV test series was intended to determine the cold flow cavity velocities in the 6-Step cavity, and thus determine the cause of the combustor flameout. If the velocities were found to be consistent with the CFD analysis the cause of the flameouts could be contributed to a lack of cavity flameholders. Prior velocity measurements were made using PSEV or chemiluminescence, however, both of these techniques require the combustor to be lit. Since combustion could not be sustained, PIV became became the only option for velocity measurements.

The PIV setup and processing were consistent with those described in Section 3.1.6.4. Silicon carbide seed particles were introduced to the air supply upstream of the diffuser as shown in Figure 257, using the dual shaker system shown in Figure 149. The shaker was supplied with air at 241,316 Pa (35 psi) to pick up and transport the seed to the UCC supply line. The seed particles followed the flow path through

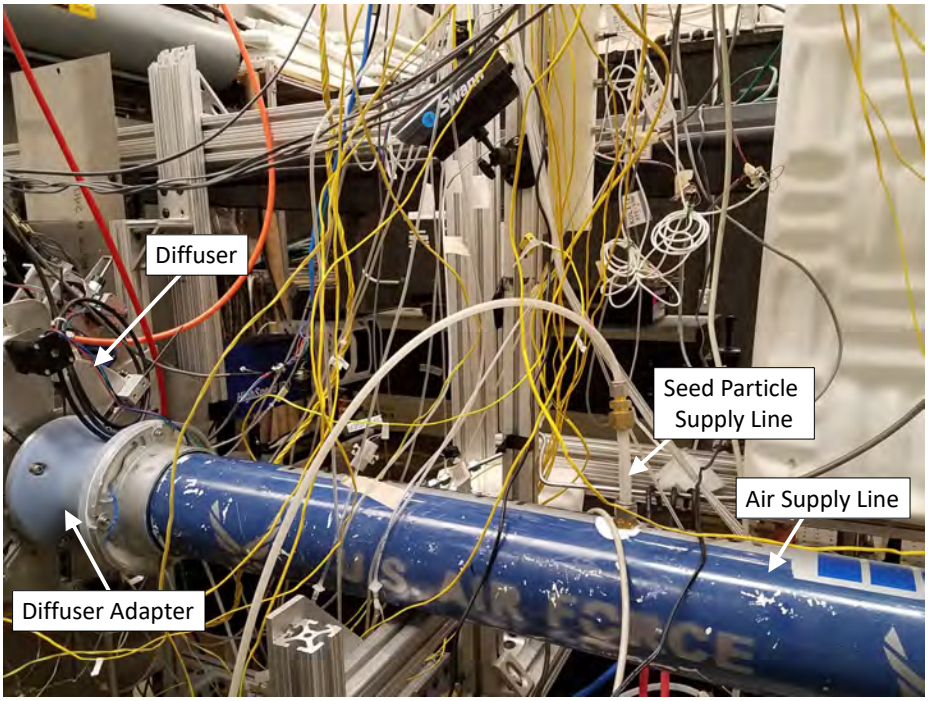


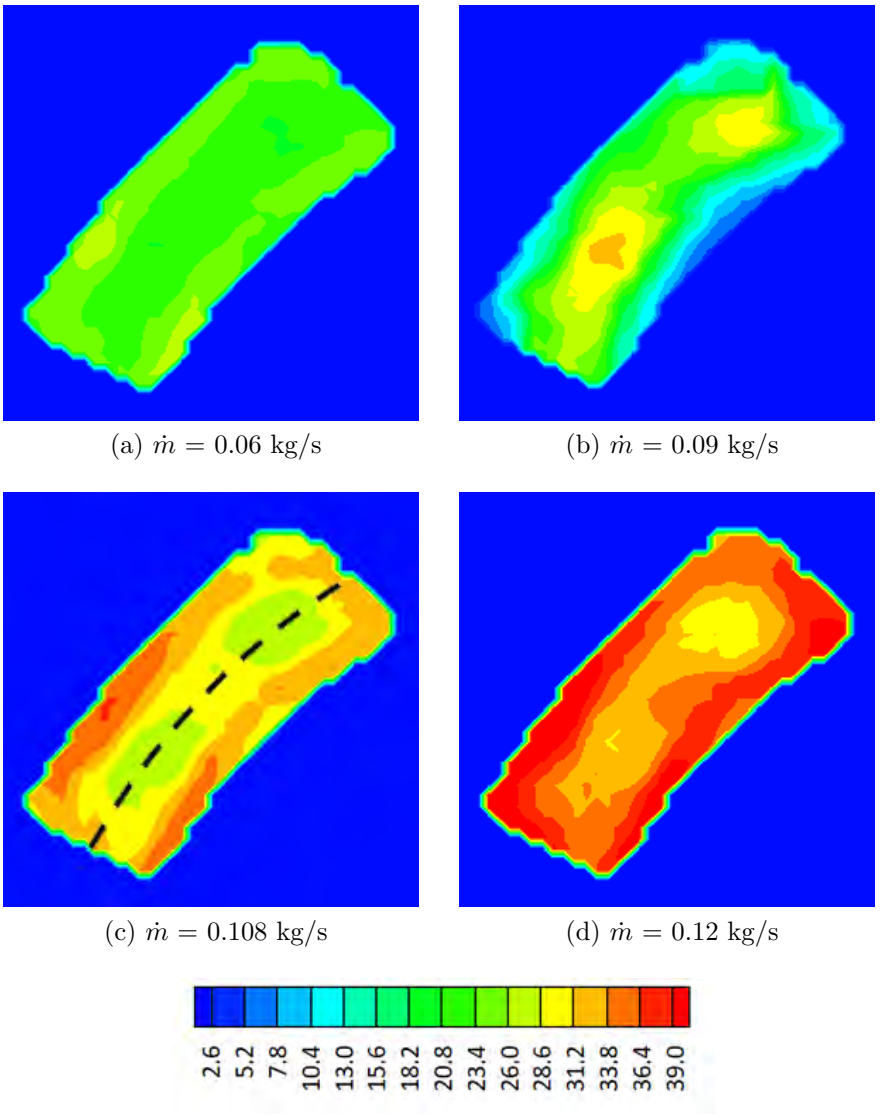
Figure 257. PIV seed supply location upstream of the diffuser inlet

the diffuser and into the circumferential cavity where they were illuminated by the laser sheet and were thus visible to the PCO camera.

PIV measurements were taken at 0.06, 0.09, 0.108, and 0.12 kg/s total inlet flow rates with a 74/26 core-to-cavity airflow split, and a 50/50 front wall-to-step cavity air split. Since the combustor was not burning, air was supplied through the fuel injectors at a rate consistent with a 0.72 cavity equivalence ratio. Figure 258 shows the resulting tangential velocity contour maps as viewed through the cavity optical access window.

Taking the average of the values along the middle of the window (dotted line in Figure 258c) yielded tangential velocities of 23.5, 25.3, 28.5, and 32.2 m/s for the 0.06, 0.09, 0.108, and 0.12 kg/s total inlet flow rate cases, respectively. The 0.108 kg/s flow rate case was run again in CFD with cold boundary conditions to approximate the PIV wall temperatures and also obtained an average tangential velocity through the middle of the window of 28.5 m/s. This velocity corresponds to $1{,}113 g_e$, well below the defined blowout limits. From this analysis it was determined that the cause of the cavity flameouts were the result of a lack of flameholders, and not due to a centrifugally induced blowout. Reevaluating the computational temperature and tangential velocity contours for the 6-Step Ring combustor with Hole Pattern 2 at a cavity equivalence ratio of 0.72 supports this finding as shown in Figure 259. The flames were unanchored to a physical cavity feature and there was a lack of reversed flow behind the backward-facing steps.

While the computational results predicted combustion that was not achieved experimentally, the cavity bulk velocities were accurate, and trends in the CFD analysis were believed to be realistic if flameholders could be added to the cavity. The combustion model was based on species concentrations and predicted combustion if these concentrations were sufficient to support a reaction. It apparently did not take into

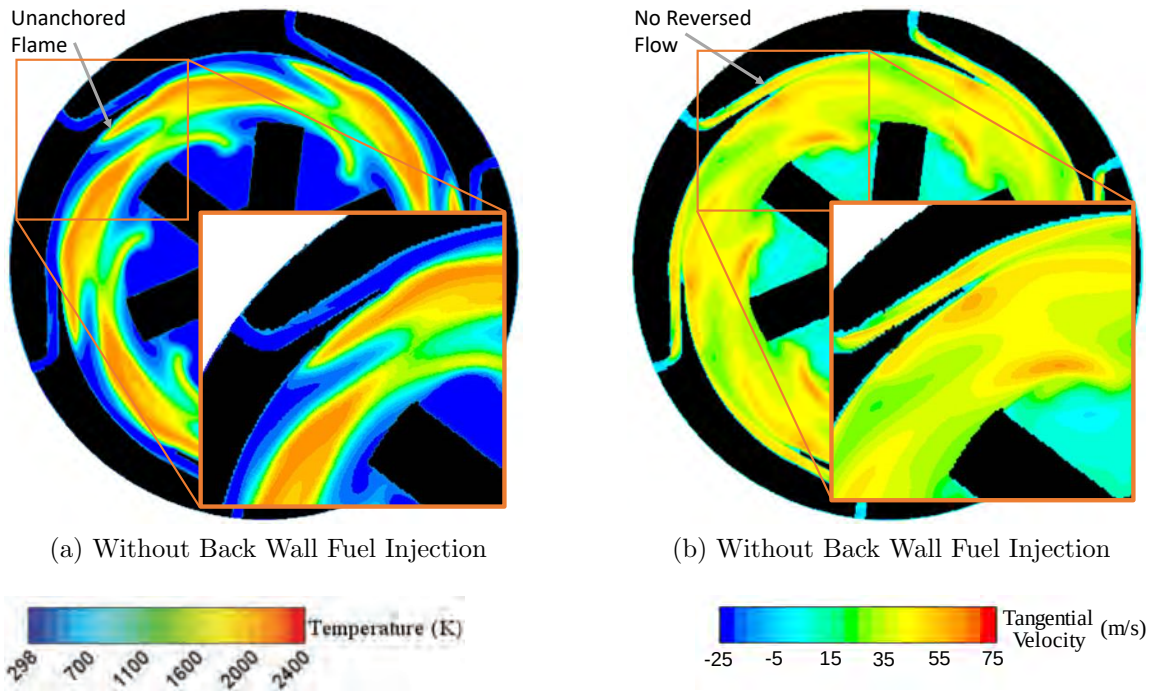


(a) $\dot{m} = 0.06$ kg/s (b) $\dot{m} = 0.09$ kg/s

(c) $\dot{m} = 0.108$ kg/s (d) $\dot{m} = 0.12$ kg/s

Figure 258. Cold flow PIV tangential velocity contours (m/s) in the circumferential cavity

account the requirement to anchor the reaction to a flameholder as needed in real life. This study enabled an understanding what flow structures to look for in future computational analysis to ensure the cavity could maintain combustion. As shown in the next section, the back wall fuel injection trends were shown to be accurate, even though the flow conditions were not identical to the computational settings and the resulting absolute values changed.



(a) Without Back Wall Fuel Injection

(b) Without Back Wall Fuel Injection

Figure 259. Review of CFD contours for the 6-Step Ring combustor with Hole Pattern 2 at a cavity equivalence ratio of 0.72

6.2.2.2 6-Step Ring with Back Wall Fuel Injection.

Back wall fuel injection was tested with the 6-Step cavity combustor at modified airflow splits to enable combustion. The step injectors flowed 1% of the cavity air with the remaining 99% entering the cavity through the front wall. The design point 74/26 core-to-cavity flow split was maintained. These conditions were run for a 0.06 kg/s and 0.09 kg/s total air flow rate at cavity equivalence ratios of 0.72 through 1.4. Each condition was run three times. The first run was with no back wall fuel injection to establish a baseline cavity temperature at each equivalence ratio. The second run injected fuel through the step injectors up to the fuel needed to reach a cavity equivalence ratio of 0.9. The additional fuel added to reach cavity equivalence ratios beyond 0.9 was added through the back wall injectors. This back wall injection pattern was repeated a third time but the transition point to include back wall injection was moved to an equivalence ratio of 0.8. Figures 260 and 261 show the

results of the three injection variations at total air flow rates of 0.06 kg/s and 0.09 kg/s, respectively.

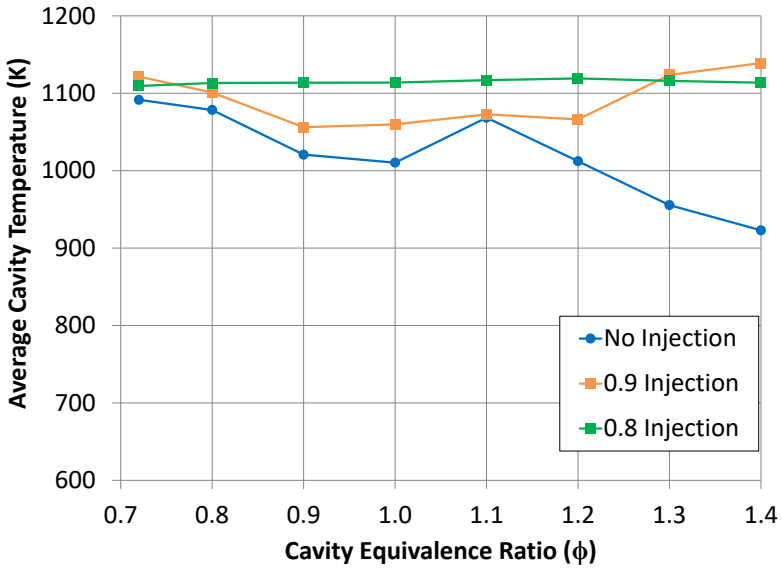


Figure 260. Average cavity temperatures (K) at increasing cavity equivalence ratios with and without back wall fuel injection at a total air flow rate of 0.06 kg/s

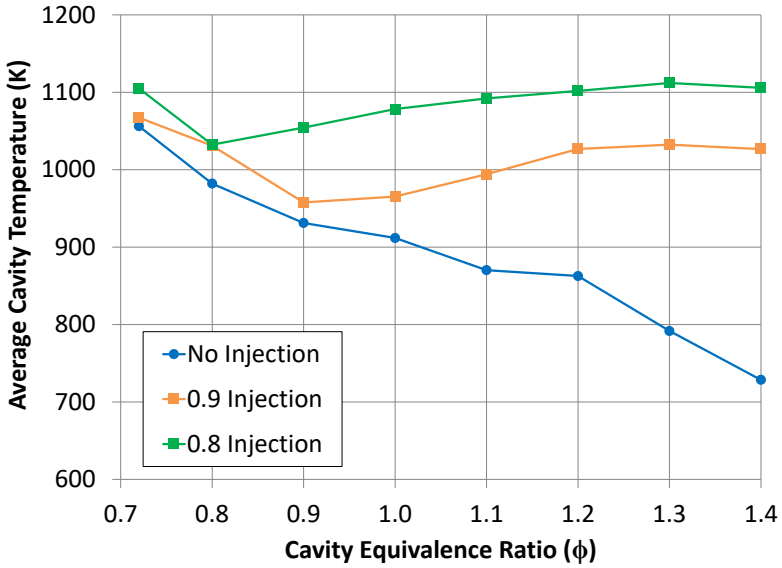
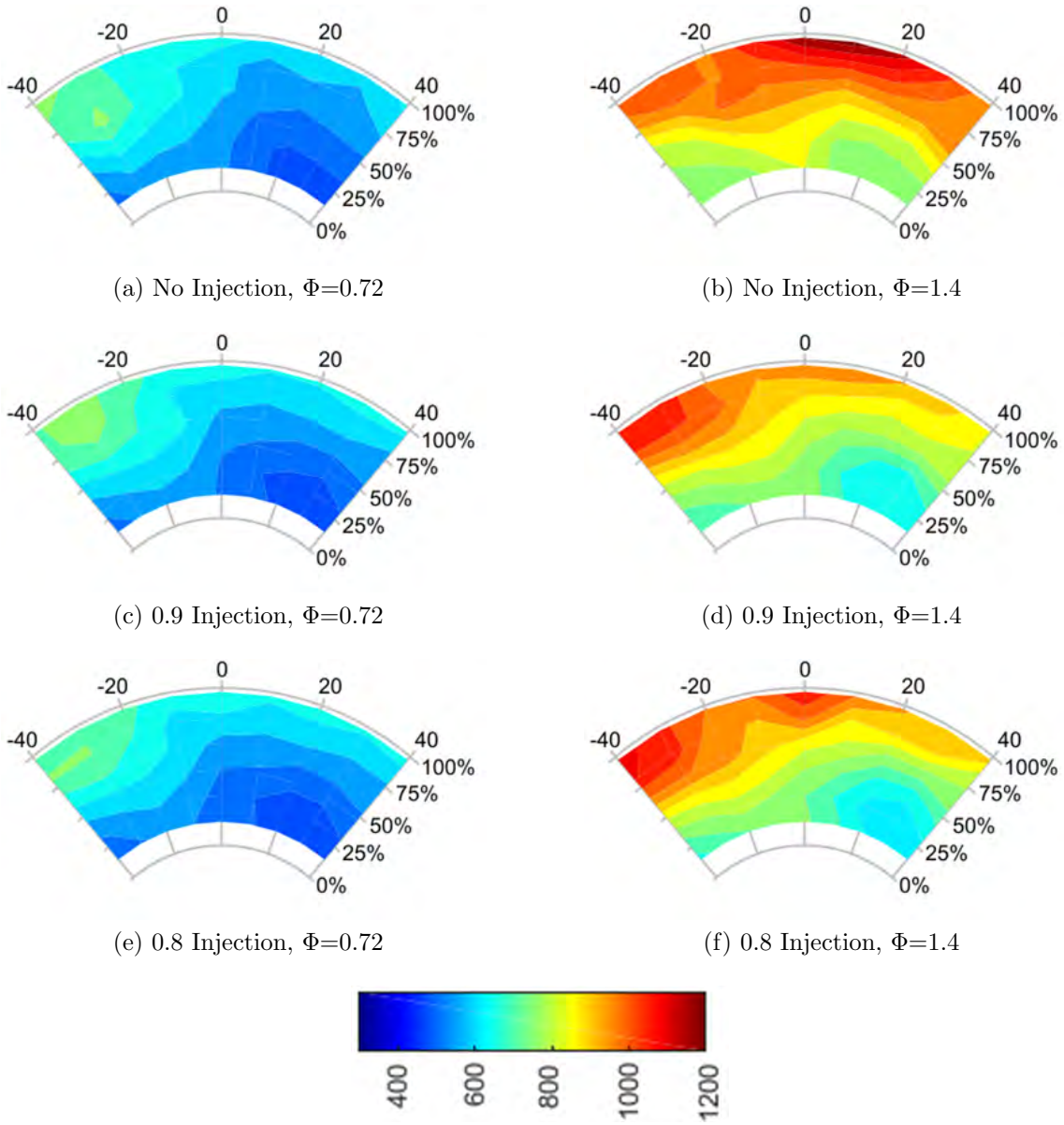


Figure 261. Average cavity temperatures (K) at increasing cavity equivalence ratios with and without back wall fuel injection at a total air flow rate of 0.09 kg/s

Both back wall injection result plots show a reduction in average cavity temperature with increasing cavity equivalence ratio with no back wall injection. While there was no difference between each of the conditions plotted at equivalence ratios of 0.72 and 0.8, the variation in temperature shown in the plots is within the repeatability of the UCC rig as explained by DeMarco [161]. Both back wall injection schemes show a much more consistent average cavity temperature with increasing equivalence ratio and overcame the typical temperature drop associated with fuel rich combustion at both flow rates. This result was accomplished by maintaining combustion in the majority of the cavity at lean or near stoichiometric conditions. The additional fuel added by the back wall injection enabled combustion radially inboard in the cavity with the reactions finishing in the HGV passages. Figures 262 and 263 show the differences in exit plane temperature distributions as measured with the thermocouple rake for the 0.06 kg/s and 0.09 kg/s total air flow rates, respectively.

The exit temperature contours at 0.06 kg/s total air flow rate show minimal differences between the injection schemes at a 0.72 cavity equivalence ratio as expected because there was no back wall injection for that fuel flow rate. These plots are included to show the magnitude of the variation between repeated runs. While the contours shifted slightly, the average temperature on the exit plane for each of these three cases varied by less than 0.65% with an average temperature of 602 K and an average pattern factor of 0.55. The contours at a 1.4 cavity equivalence ratio show a reduced temperature magnitude of the hottest values at the exit plane for the cases that included back wall injection. The average temperature on the exit plane was identical for the two back wall injecting cases at 842 K, with the baseline average temperature measuring 8.5% hotter at 921 K. The pattern factors of Figures 262 b, d, and f were 0.49, 0.47, and 0.52, respectively.

The exit temperature contours at 0.09 kg/s total air flow rate show a slightly



(a) No Injection, Φ=0.72

(b) No Injection, Φ=1.4

(c) 0.9 Injection, Φ=0.72

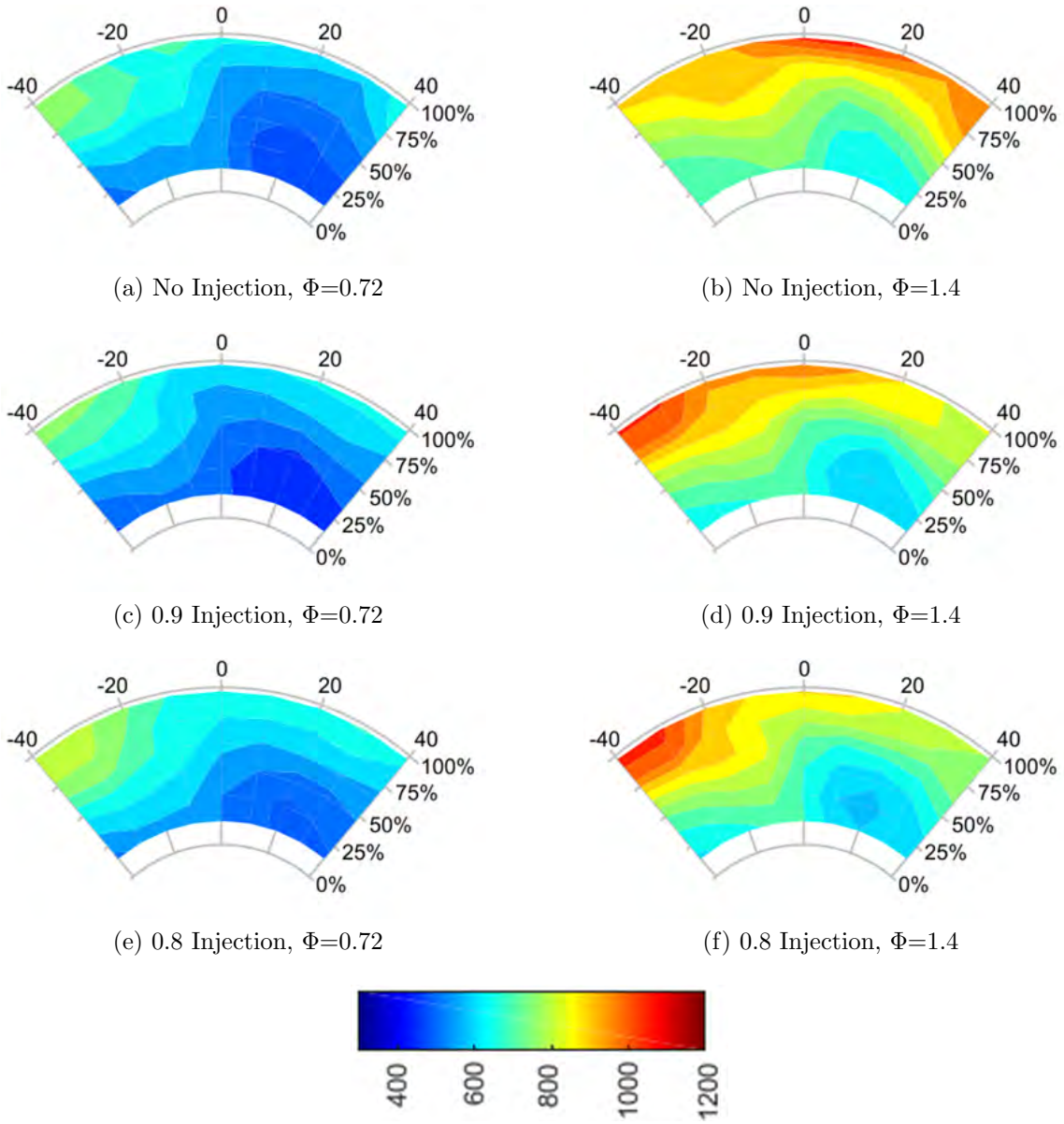
(d) 0.9 Injection, Φ=1.4

(e) 0.8 Injection, Φ=0.72

(f) 0.8 Injection, Φ=1.4

Figure 262. Experimental exit plane temperature contours (K) at 0.72 and 1.4 cavity equivalence ratios with and without back wall fuel injection at a total air flow rate of 0.06 kg/s

larger variation in the exit plane temperature contours in the 0.72 cavity equivalence ratio cases than was seen at 0.06 kg/s. At 0.09 kg/s there was a 4% variation in average exit plane temperature with the largest average temperature occurring in Figure 263e at 627 K. The average pattern factor of Figures 263 was 0.64. At a 1.4



(a) No Injection, Φ=0.72

(b) No Injection, Φ=1.4

(c) 0.9 Injection, Φ=0.72

(d) 0.9 Injection, Φ=1.4

(e) 0.8 Injection, Φ=0.72

(f) 0.8 Injection, Φ=1.4

Figure 263. Experimental exit plane temperature contours (K) at 0.72 and 1.4 cavity equivalence ratios with and without back wall fuel injection at a total air flow rate of 0.09 kg/s

cavity equivalence ratio there was a 3% variation in average temperature between all three injection schemes. The highest average temperature occurred with no back wall injection at an average value of 819 K. The pattern factors of Figures 263 b, d, and f were 0.51, 0.54, and 0.64, respectively.

While the 6-Step cavity was not operated with air flow splits as designed, the cavity configuration was successful in demonstrating the ability to achieve higher cavity temperatures at high cavity equivalence ratios. At fuel rich conditions the addition of back wall injection resulted in reduced average exit temperatures. It is unclear if the reduced temperature in the back wall injection cases was the result of incomplete combustion by the measurement plane, or another factor. The pattern factors between the no injection and 0.9 injection cases were comparable, however, the pattern factor at the 0.8 injection cases were always larger than the no injection cases.

6.2.3 Computational Boundary Condition Study.

As part of the response to the 6-Step cavity flameouts, the boundary conditions used in the computational analysis were reexamined to determine the impact of these specified values on the velocity of air injected from the step, as well as the impact on the cavity bulk velocity. The temperature boundary conditions used in all prior computational analysis was based on thermally soaked steady-state metal temperatures that were experimentally measured. However, during velocity measurement tests the rig was lit, the desired operating condition was reached, cavity gas temperatures were allowed to stabilize, velocity measurements were taken, and the rig was shut down while data were transfered from the high-speed camera to the controlling computer. During these tests the metal temperatures never reached the steady-state conditions used in the computational analysis.

Three boundary conditions were compared for a 0.72 cavity equivalence ratio, 74/26 core-to-cavity flow split, 50/50 front wall-to-step air injection split, front wall Hole Pattern 2, at a total air flow rate of 0.108 kg/s. The three boundary conditions were referred to the hot steady-state, heat flux, and cool boundary conditions. The hot steady-state values are given in Table 21 in Chapter V. The heat flux boundary

values and the cool boundary values are defined in Table 32 and 33, respectively. The heat flux values were experimentally measured on the three cavity walls using the dual embedded thermocouple technique described in Section 2.7.1, and assuming one-dimensional heat transfer. A temperature boundary condition was used on the exhaust collar and diffuser middle diameter, with the other three heat flux boundary values, because no heat flux measurements were taken at those two locations. The cool boundary conditions were also experimentally derived as the temperature measured by the embedded thermocouples that were furthest from the reactions in the air driver plate, 6-Step Ring, and back plate after a duration representative of the time needed to take a velocity measurement. These temperatures approximated the exterior metal surface temperatures of the test rig which corresponds to the exterior surfaces of the computational domain.

Table 32. Heat flux boundary conditions

Boundary	**Heat Flux or Temperature**
Cavity Forward Wall	82,420 W/m^2
Cavity Top Wall	31,390 W/m^2
Cavity Back Wall	18,320 W/m^2
Diffuser Middle Diameter	355 K
Exhaust Collar	850 K

Table 33. Cool temperature boundary conditions

Boundary	**Temperature** (K)
Cavity Forward Wall	398
Cavity Top Wall	423
Cavity Back Wall	473
Diffuser Middle Diameter	355
Exhaust Collar	700

The computational results using each of these boundary conditions showed a large reduction in injection velocity and corresponding bulk velocity with the cool boundary conditions. The hot steady-state and heat flux boundary conditions produced

very similar results. The temperatures on the cavity exterior surfaces calculated with the heat flux boundary conditions were comparable to the hot steady-state temperature boundaries. This result makes sense as the computations were performed at steady-state using experimentally derived heat flux values. The resulting surface temperatures from the specified heat flux values should be comparable to experimentally derived steady-state temperatures.

The calculated peak injection velocity, average injection velocity, and the corresponding bulk cavity tangential velocity averaged along a line of constant radius at 7.44 cm (halfway through the cavity window) from the engine centerline are given in Table 34. Figure 264 shows the velocity magnitude profiles along a radially oriented line that stretched across the middle injector in the 6-Step Ring just after the injector exit. Figure 265 shows temperature and velocity magnitude contours of the 6-Step Ring metal hardware and air in the injector duct. In all computations the air entered the domain at 300 K. The contours show the magnitude the air was heated as it flowed through the injection duct. As more heat was transferred to the air, the fluid density was reduced and the velocity was increased. The gas temperature contours in the cavity are not shown to allow a smaller colorbar scale to be used. These contours show a similar region of the 6-Step Ring shown in Figure 243.

Table 34. Step injection and bulk velocities calculated for each boundary condition

Boundary Condition	Peak Step Injection Velocity	Average Step Injection Velocity	Cavity Tangential Velocity
Hot Steady-State	45.8 m/s	39.4 m/s	38.2 m/s
Heat Flux	47.1 m/s	40.9 m/s	38.1 m/s
Cool	37.1 m/s	31.8 m/s	28.5 m/s

Based on these results the calculated velocities are sensitive to the boundary conditions. The appropriate boundary condition should be used depending on the

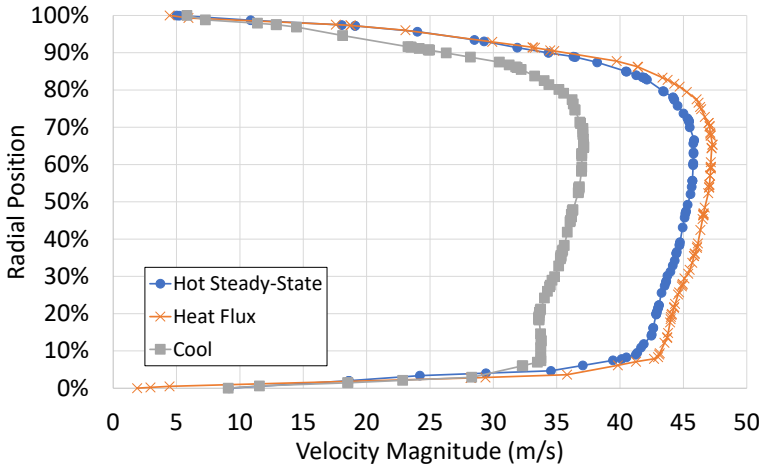
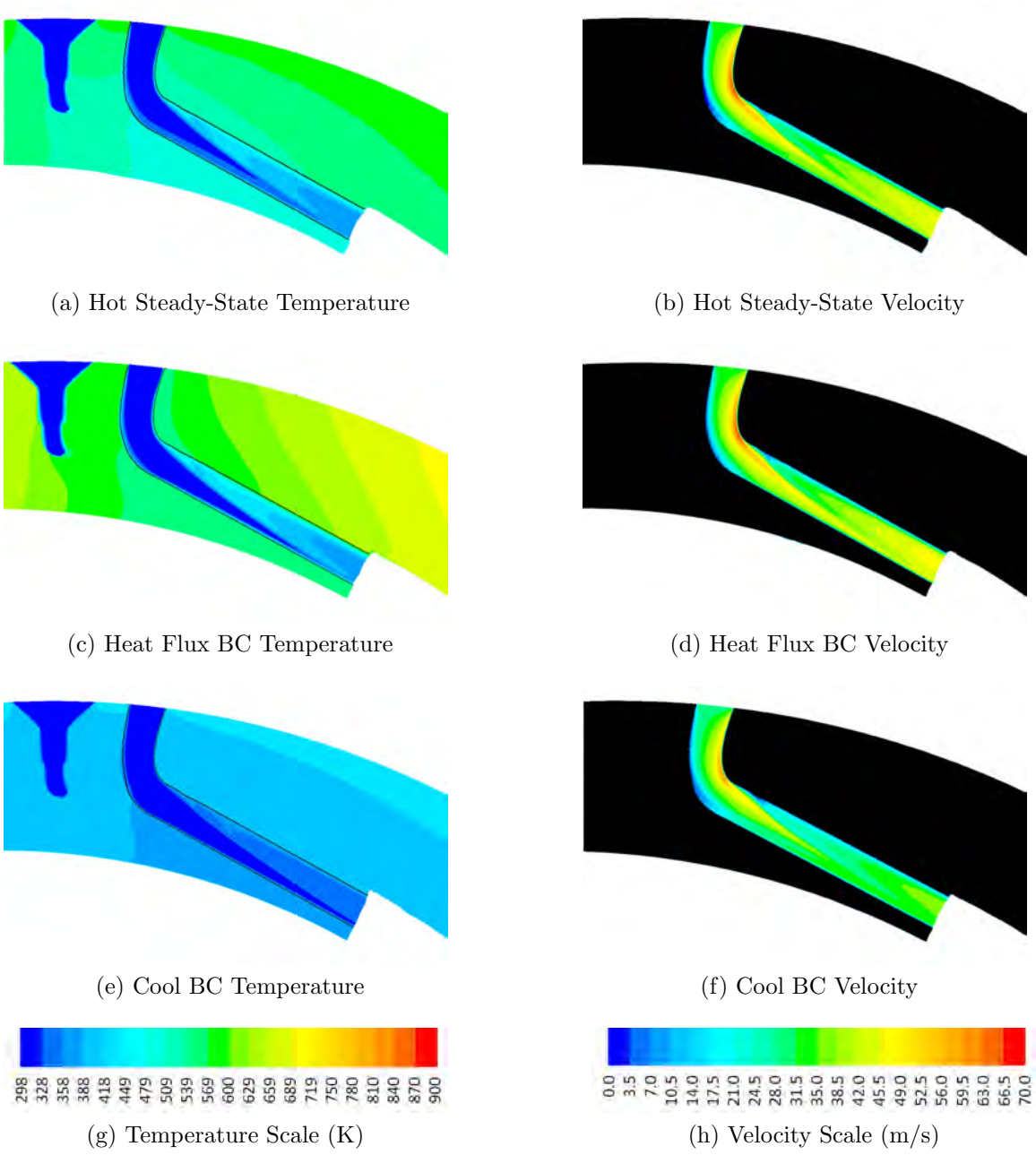


Figure 264. 6-Step Ring air injector velocity profiles using different boundary conditions

desired outcome. For comparison to experimental data the cool boundary should be used, unless sufficient time can be given to reach a steady-state metal temperature.

6.3 12-Step Ring

While the 6-Step Ring demonstrated an ability to develop higher cavity tangential velocity and centrifugal loading than the Baseline design in cold flow PIV tests, the lack of cavity flameholders made the design unusable with step air injection. The 12-Step Ring, shown in Figure 266, was designed to combine the positive aspects of the 6-Step Ring, while incorporating additional flameholders. As the name implies, the 12-Step Ring featured 12 steps spaced 30° apart. The steps were alternated with six steps featuring fuel and air injection with an identical Hole Pattern to the 6-Step Ring. The other six steps injected fuel only from two 2.5 mm diameter holes and were planned to act as stabilizing steps. The fuel injectors in the stabilizing steps were offset with a skew towards the cavity front wall such that one hole was 3.1 mm and the other was 12.7 mm away from the front wall. Since axial fuel migration was observed with the 6-Step Ring that caused the fuel to be pushed towards the back



(a) Hot Steady-State Temperature

(b) Hot Steady-State Velocity

(c) Heat Flux BC Temperature

(d) Heat Flux BC Velocity

(e) Cool BC Temperature

(f) Cool BC Velocity

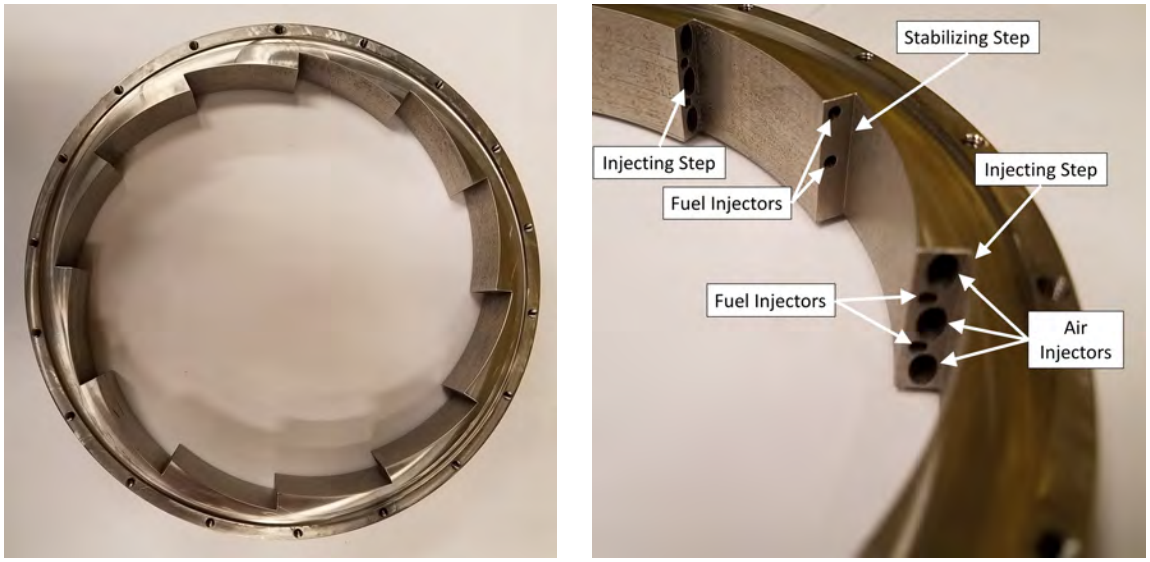
(g) Temperature Scale (K)

(h) Velocity Scale (m/s)

Figure 265. Computational temperature contours (K) and velocity magnitude contours (m/s) around a 6-Step Ring air injector with three different boundary conditions

wall, the offset was introduced to allow the fuel to start nearer to the cavity front wall to compensate for this migration. The step height remained at 6.35 mm.

The 12-Step Ring internal ducting for fuel and air are shown in Figure 267. The green arrows in Figure 267b represent the fuel inlets and injection locations while the



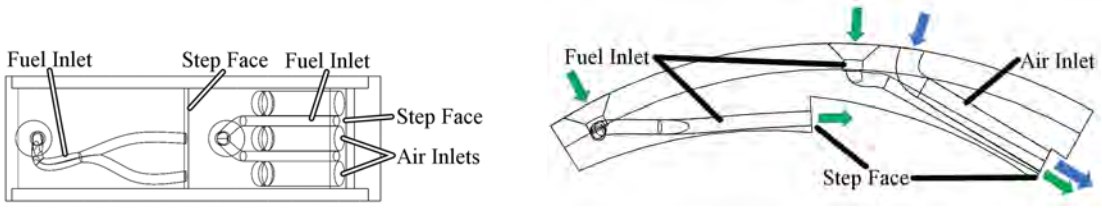
(a) 12-Step Ring (b) Detail view of inlets

Figure 266. 3D printed 12-Step Ring hardware

blue arrows represent the air inlets and injection locations. Like the 6-Step Ring, the complexity and geometry of these internal ducts required the part to be made with additive manufacturing. This part was made from inconel in the AniMaL Lab at AFIT on a Concept Laser M2 3D printer. Applying lessons learned during the print of the 6-Step Ring, the 12-Step Ring was printed on an inconel build plate and fillets were added to the OD of the ring in contact with the build plate to increase the plate attachment surface area. Both of these changes prevented the part from lifting off the build plate and warping during the print process. The AFIT Model Shop performed the finish machining of the part to produce a smooth surface where the component interfaced with the rest of the test rig.

6.3.1 12-Step Ring Computational Analysis.

The 12-Step Ring was analyzed computationally using the same settings as the 6-Step Ring computational analysis described in Section 6.2.1, but applying the cool boundary conditions described in Table 33 which was more representative of the



(a) Radial View (b) Side View

Figure 267. 12-Step Ring air and fuel injector ducting

experimental results. The design point at 0.108 kg/s total air flow rate, at a 0.72 cavity equivalence ratio, with a 74/26 core-to-cavity flow split, 50/50 front wall-to-step cavity air split, and front air drivers arranged in Hole Pattern 2 (see Figure 246b) was run to enable direct comparison of the results to the 6-Step Ring and Baseline combustor. As shown in Figure 268 the tangential velocity was increased from the previous two designs with an average tangential velocity along a line of constant radius at 7.44 cm (halfway through the cavity window) was 36.9 m/s, or equivalently 1,867g_e. This result represents an improvement of 258% over the experimental Baseline design loading, and a 68% increase in loading over the experimental and cold boundary CFD results of the 6-Step design. The velocity increase over the 6-Step design for identical mass flow rate injection was due to a smaller cavity volume resulting from the six additional steps in the 12-Step design. Recirculation zones were found behind the stabilizing steps (light blue regions at the cavity OD) indicating these steps should function as flameholders as designed.

The temperature contours from the computational analysis at 0.108 kg/s total air flow rate, at a 0.72 cavity equivalence ratio, with a 74/26 core-to-cavity flow split, 50/50 front wall-to-step cavity air split, and front air drivers arranged in Hole Pattern 2 is shown in Figure 269a. In this configuration reactions were present along the injecting shear layer following around the OD of the cavity, and at the shear layer with the core flow at the cavity exit. The center volume of the cavity lacked

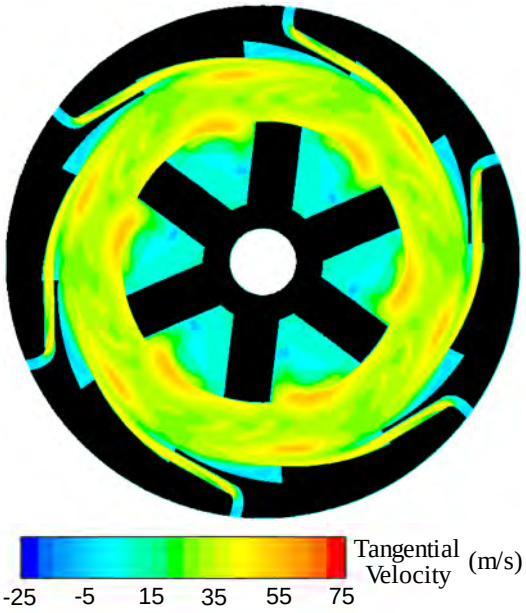
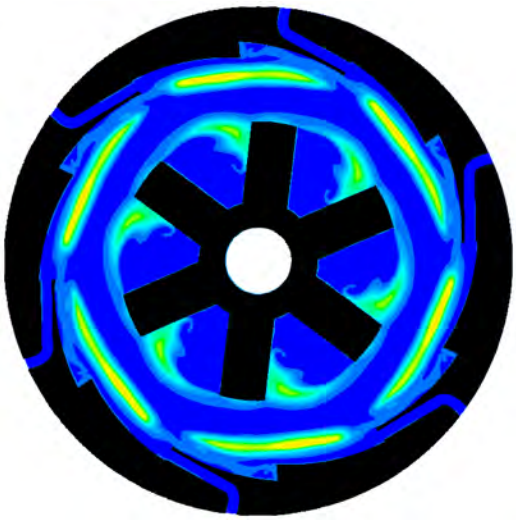
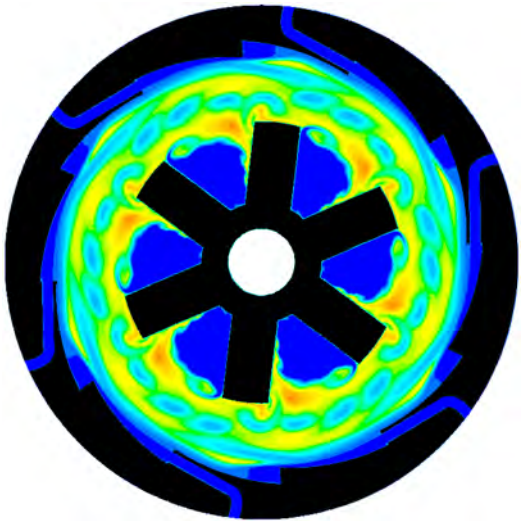


Figure 268. Tangential velocity contours (m/s) on the half cavity plane of the 12-Step Ring combustor. 74/26 core-to-cavity flow split, 50/50 front wall-to-step cavity air split



(a) 74/26 core-to-cavity flow split, 50/50 front wall-to-step cavity air split



(b) 80/20 core-to-cavity flow split, 66/33 front wall-to-step cavity air split

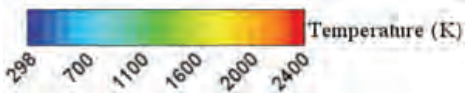


Figure 269. Temperature contours (K) on the half cavity plane of the 12-Step Ring combustor at an equivalence ratio of 0.72 at two different air split configurations

reactions. This combustion pattern was undesirable as it did not use the cavity volume effectively. The temperature contours of a modified air split configuration consisting of an 80/20 core-to-cavity flow split and 66/33 front wall-to-step cavity air split, while maintaining a 0.108 kg/s total air flow rate, at a 0.72 cavity equivalence ratio, with the front air drivers arranged in Hole Pattern 2, showed a greatly improved combustion pattern as shown in Figure 269b. The combustion pattern in this figure shows a better indication of functional flameholders with the flame anchored to the recirculation zone shear layer which is consistent with the flame positioning from Lapsa and Dahm's research [56] shown in Figure 43. At this air split configuration the full cavity volume was used for reactions. While this alternate air split had a positive impact on the cavity temperatures, the reduced cavity airflow had a negative impact on the tangential velocity achieving an average value of just 17.0 m/s along a line at 7.44 cm radially from engine centerline (half window). This velocity equates to $398g_e$, a reduction of 369% from the 12-Step 74/26 core-to-cavity flow split, 50/50 front wall-to-step cavity air split loading, and a 31% reduction from the experimental Baseline loading.

6.3.2 12-Step Ring Experimental Testing.

The 12-Step Ring was installed in the UCC test rig described in Figure 244 in place of the 6-Step Ring. The modified front wall air driver plate shown in Figure 255 in Section 6.2.2 was reused. The redesigned back plate capable of back wall fuel injection, shown in Figure 256, was also used, however, back wall injection was not performed in all five of the 12-Step Ring test series'. The first test series was an initial analysis of the 12-Step combustor at specific operating conditions to allow comparison to the Baseline combustor. The second series created operating maps of the 12-Step combustor at a constant global equivalence ratio, across a range of air splits, four levels of back wall fuel injection, and three total air flow rates. The third

test series duplicated the development of operating maps at 0.108 kg/s total air flow only, with 0% back wall injection, but at two alternate global equivalence ratios. The fourth series looked at the effect of exhaust duct configuration on 12-Step combustor performance at several select points. The final test series examined the impact on combustion stability of fuel distribution between the steps in the 12-Step Ring on operating points along the flameout line of the 0.108 kg/s, 0% back wall injection, operating map.

6.3.2.1 12-Step Ring Comparison to Baseline Combustor.

The 12-Step Ring was initially tested at the design point with a 74% core flow and 50% front plate split to match the previous operating conditions used with the Baseline combustor. At that air split, however, the experimental results showed low cavity temperatures or unstable combustion leading to flameouts. These results confirmed the computational results at this condition. When the rig was operated at the alternate split of 80% through the core, and 66% through the front plate, combustion stability and positive performance were achieved; again confirming the computational results at that condition. The 80% core, 66% front wall split was used to characterize the performance of the 12-Step combustor at cavity equivalence ratios of 0.96, 1.47, and 1.73, and total air flow rates of 0.056, 0.084, 0.101, and 0.112 kg/s. These parameters were combined into 12 test points as shown in Table 35 to yield global equivalence ratios of 0.20, 0.31, and 0.36.

The 12-Step Ring combustor was compared to the Baseline combustor based on average cavity temperatures and temperature distributions at the exit plane of the combustor. The Baseline cavity temperatures were taken from test points used in Objective 2, and the diffuser characterization testing described in Section 6.1. In the Baseline combustor the average cavity temperature was determined from averaging the temperatures measured using the thermocouple configuration shown in Figure

Table 35. 12-Step Ring Comparison Test Cases

Case	Φ_{Global}	Φ_{Cav}	$\dot{m}_{in}$ (kg/s)	$\dot{m}_{core}$ (kg/s)	$\dot{m}_{cav}$ (kg/s)
1	0.20	0.96	0.056	0.045	0.011
2	0.20	0.96	0.084	0.067	0.017
3	0.20	0.96	0.101	0.081	0.020
4	0.20	0.96	0.112	0.090	0.022
5	0.31	1.47	0.056	0.045	0.011
6	0.31	1.47	0.084	0.067	0.017
7	0.31	1.47	0.101	0.081	0.020
8	0.31	1.47	0.112	0.090	0.022
9	0.36	1.73	0.056	0.045	0.011
10	0.36	1.73	0.084	0.067	0.017
11	0.36	1.73	0.101	0.081	0.020
12	0.36	1.73	0.112	0.090	0.022

204a. The average cavity temperatures in the 12-Step cavity were determined by averaging the readings from the thermocouples identified in Figure 256. These thermocouples were inserted into the cavity to place the bead at the quarter, half, and three-quarter cavity axial positions. One important distinction between these two measurement locations is that the baseline thermocouple configuration included measurements at two radial positions, while the thermocouples through the redesigned back plate used with the 12-Step Ring were all positioned at the same radial location.

Figure 270 shows the average cavity temperatures for a single total mass flow rate of air for the Baseline combustor, compared to the average cavity temperatures at four total air flow rates with the 12-Step combustor. With the Baseline design, the average cavity temperature decreased considerably with each successive increase in equivalence ratio. The Baseline combustor could not maintain combustion at equivalence ratios of 1.3 or above at any other air flow rate. While the 12-Step combustor also experienced a reduction in average cavity temperature with increased equivalence ratio, the operating range of this combustor greatly exceed the Baseline as combustion was maintained at cavity equivalence ratios of 1.73. The average cavity

temperature in the 12-Step combustor decreased for each increase in total air mass flow rate. This trend may be due to the higher flow rate air removing more fuel from the cavity prior to reacting. Less cavity reactions would result in lower cavity temperatures.

In Figure 270, the Baseline combustor appeared to have higher average temperatures, however, a review of Figures 248a and 269b, with the radial positions of the thermocouples in mind, can explain this variation. The temperature contours of both combustors show reduced temperatures at the half cavity radial position due to the cool air injection from the front air driver plate. In the Baseline combustor, however, two of the thermocouples were measuring at a radial height above the region influenced by these air injectors. In the 12-Step combustor all three of the thermocouples were at approximately mid-cavity radially, and thus were all influenced by the air injectors, resulting in lower temperature readings.

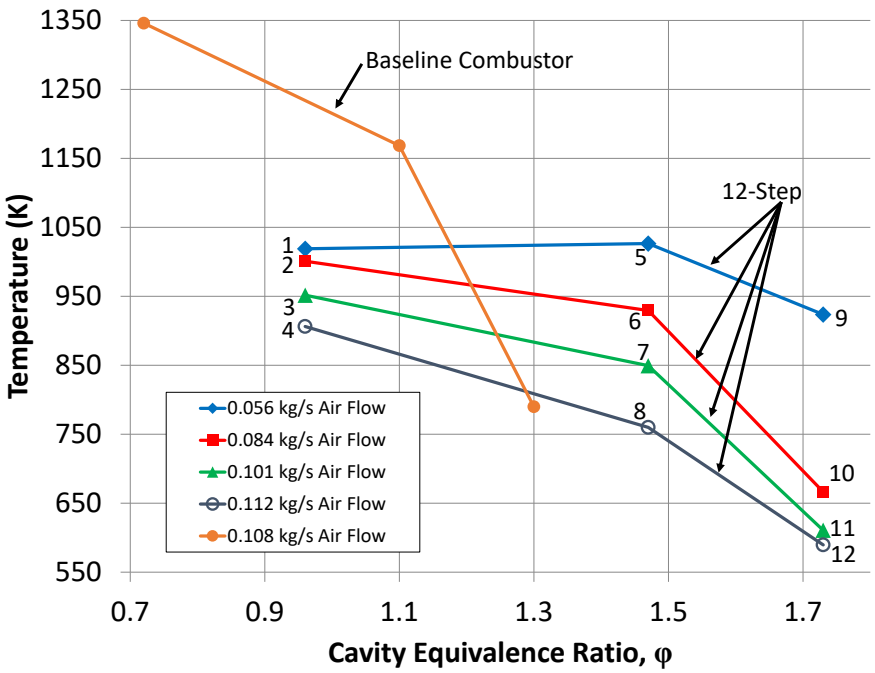


Figure 270. Average cavity temperatures for the Baseline and 12-Step combustor as a function of cavity equivalence ratio

The 12-Step combustor achieved better performance than the Baseline combustor in all aspects at the exit plane. Table 36 gives the maximum temperature, T_{max}, average temperature, T_{avg}, and pattern factor at the exit plane for the 12-Step and Baseline combustor. These temperatures were measured by the thermocouple rake described in Appendix B. The comparisons between the Baseline and the 12-Step combustor were made for the comparable global equivalence ratios and total air flow rates that were less than 7% different in both parameters.

Table 36. 12-Step and Baseline combustor exit plane performance

Case	Φ_{Global}	**12-Step Ring**				**Baseline Design**			
		$\dot{m}_{in}$ (kg/s)	T_{max} (K)	T_{avg} (K)	Pattern Factor	$\dot{m}_{in}$ (kg/s)	T_{max} (K)	T_{avg} (K)	Pattern Factor
1	0.20	0.056	769	667	0.27	0.060	822	613	0.67
2	0.20	0.084	810	692	0.30	0.090	911	636	0.82
3	0.20	0.101	799	677	0.32	0.108	894	631	0.79
4	0.20	0.112	792	664	0.34	0.120	892	618	0.86
5	0.31	0.056	1015	800	0.42	0.060	1035	745	0.65
6	0.31	0.084	1036	826	0.40	0.090	1076	731	0.80
7	0.31	0.101	1083	822	0.49	0.101	949	663	0.79
8	0.31	0.112	1032	790	0.48	0.120	931	658	0.76
9	0.36	0.056	1119	866	0.44	0.060	—	—	—
10	0.36	0.084	1134	888	0.41	0.090	—	—	—
11	0.36	0.101	1073	839	0.42	0.108	792	598	0.64
12	0.36	0.112	996	770	0.47	0.120	—	—	—

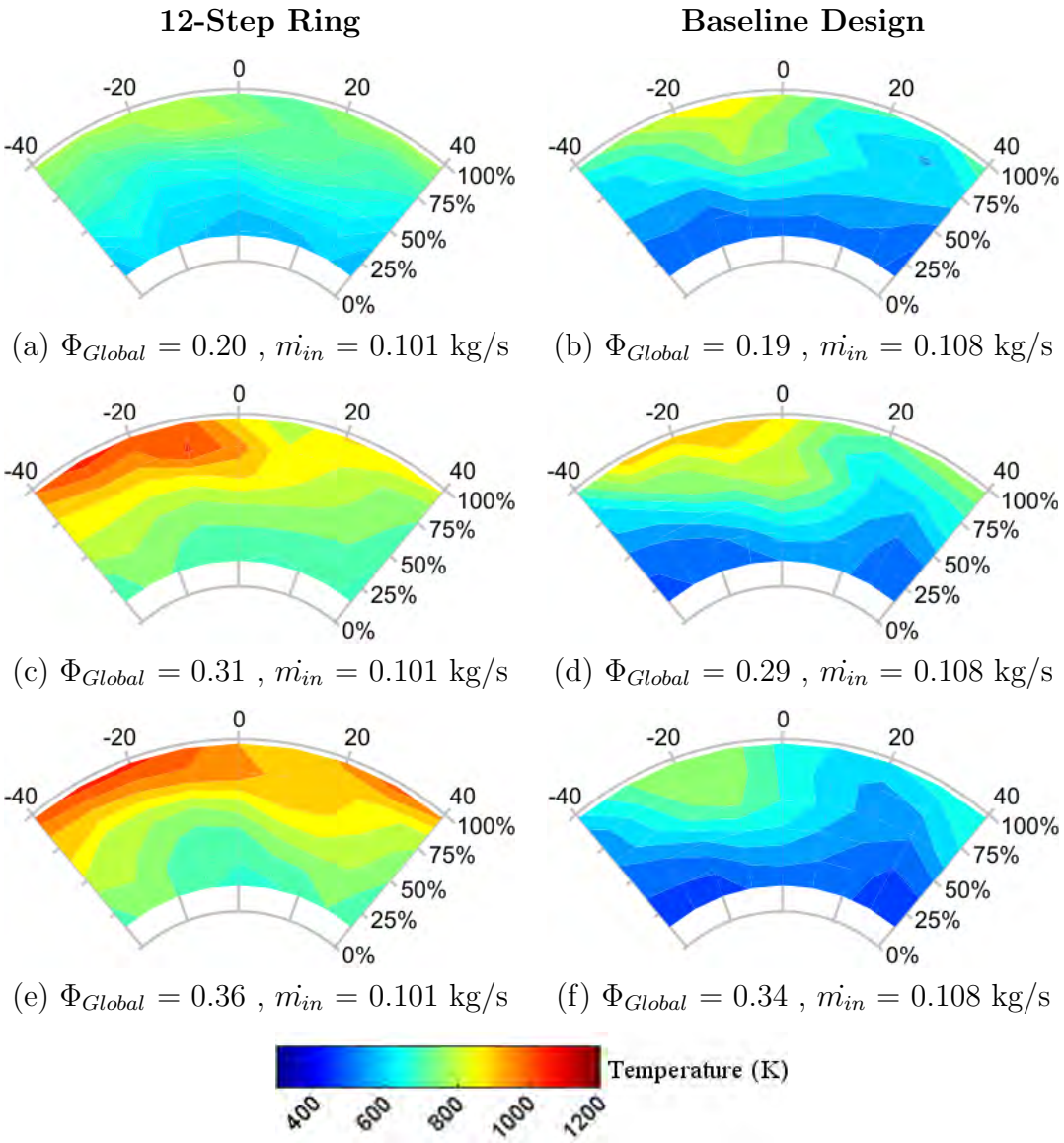
Reviewing the data presented in Table 36 showed the 12-Step design increased the average temperature at the exit plane while simultaneously reducing the pattern factor compared to the Baseline combustor in all test cases. The largest average temperature difference between the two configurations occurred in Case 11 which demonstrated a 241 K (40%) increase. This temperature difference is due to the Baseline combustor having difficulty maintaining combustion at the high cavity equivalence ratio. The Baseline design could not maintain combustion in Cases 9, 10, and 12. The 12-Step

design had no difficulty with Cases 9 - 12 which shows the benefit of this geometry to maintain combustion at engine representative global equivalence ratios. The pattern factor was reduced in all cases, with the largest decrease achieving a 63% reduction. The pattern factors for the 0.20 global equivalence ratio cases achieved the lowest values, with all of them falling in the desirable range of 0.25 to 0.43 defined by Mattingly et al.[14]. The cause of the increase in pattern factor at higher total air mass flow rates was likely due to a reduction in the penetration of the gases exiting the circumferential cavity into the core flow. The reduced penetration, combined with the likelihood of unburned fuel in the gases exiting the cavity, meant a lower uniformity of reactions through the HGV passages and thus a higher pattern factor.

Figure 271 shows the experimental exit plane temperature contours for the 12-Step and Baseline combustors at comparable conditions that approximate 0.108 kg/s total air flow rate and global equivalence ratios of 0.20, 0.31, and 0.36. In all of the profiles shown, the 12-Step exit plane temperatures are more uniform with higher temperatures extending all the way to the passage ID. At the 0.20 global equivalence ratio the minimum temperature on the passage ID was increased from 484 K with the Baseline combustor, to 577 K with the 12-Step. At 0.31 global equivalence ratio the minimum temperature on the ID was increased from 479 K to 682 K with the 12-Step. Finally, at the 0.36 global equivalence ratio the minimum ID temperature at the exit plane was increased from 465 K to 683 K with the 12-Step. In these three examples the minimum ID temperature experienced a 20% increase, with the other two increasing by 42% and 47%. The magnitude of the peak temperature at the OD was also increased for the 12-Step combustor with the maximum temperature of 1083 K exceeding the Baseline peak temperature of 949 K by 14%.

Without using sensors to quantify the amount of unburned hydrocarbons exiting the combustors, a comparison of the adiabatic flame temperature to the average

exit plane temperature provided an indication of the completeness of the reactions by the exit plane. At a global equivalence ratio of 0.36, the 12-Step average exit temperature reached 69% of the adiabatic flame temperature, while the Baseline design only reached 49%. These values are likely lower than the actual percentages as thermocouples measure lower temperatures than the physical gas temperature.



(a) $\Phi_{Global} = 0.20$, $\dot{m}_{in} = 0.101$ kg/s (b) $\Phi_{Global} = 0.19$, $\dot{m}_{in} = 0.108$ kg/s

(c) $\Phi_{Global} = 0.31$, $\dot{m}_{in} = 0.101$ kg/s (d) $\Phi_{Global} = 0.29$, $\dot{m}_{in} = 0.108$ kg/s

(e) $\Phi_{Global} = 0.36$, $\dot{m}_{in} = 0.101$ kg/s (f) $\Phi_{Global} = 0.34$, $\dot{m}_{in} = 0.108$ kg/s

Figure 271. Experimental exit plane temperature contours (K) from the 12-Step and Baseline combustors at approximately 0.108 kg/s total air flow rate at global equivalence ratios approximating 0.20, 0.31, and 0.36

6.3.2.2 Airflow Split Characterization at $\Phi_{global} = 0.36$.

As displayed in Figure 269, even seemingly small changes in air flow splits had a large difference in the combustion performance of the 12-Step combustor. To quantify the extent of the combustion variation across the entire operating envelope, a series of tests were conducted at three total air flow rates, for a fixed 0.36 global equivalence ratio, that varied the percentage of air through the core and how the remaining air was divided to be introduced to the circumferential cavity. The three total air mass flow rates tested included 0.060, 0.108, and 0.12 kg/s. The variable geometry diffuser was used to control the amount of air sent through the core. This value was varied between 50 and 90%. The cavity air was split to introduce 10 - 90% through the front air driver plate with the remaining cavity air injected through the outer ring. Like the controls described for the 6-Step Ring experimental testing, the cavity air introduced through the front air driver plate was controlled by the diffuser split. The air that entered through the outer ring steps was controlled by the mass flow rate controller on the 3.81 cm air line which was commanded through LabView. The total air introduced to the diffuser inlet by the 7.62 cm air line was reduced by the amount of air fed through the 3.81 cm line to keep the total air flow rate through the rig at the desired level. As part of this study fuel was also introduced into the cavity through the back wall fuel injectors. The amount of fuel injected from these ports included 0, 10, 20, and 30% of the total fuel flow rate. Additional thermocouples were inserted through the back plate utilizing the unused back wall fuel injection ports that were positioned radially outward from the injecting ports. When all thermocouples were working, there were 2 measurements at the 1/4 axial cavity plane, 4 measurements at the 1/2 axial cavity plane, and 1 measurement at the 3/4 axial cavity plane.

Up to this point the fuel in the 12-Step injectors was controlled by separate fuel controllers with the AliCat delivering propane to the fuel only (stabilizing) steps,

and the Brooks delivering propane to the air and fuel injecting steps. Even though there was independent control, all prior testing had been conducted at a 50/50 split between the controllers. A study was conducted to determine the impact on cavity and exit temperatures with variations in the amount of fuel delivered between both types of steps in the outer ring with no back wall injection. The purpose of this test was to determine if there was an optimum fuel split that resulted in peak combustion performance. Since only two high flow rate fuel controllers were available, one of those controllers was needed to enable fuel injection from the back wall injectors in the next test series. This test determined how the fuel from a single mass flow controller would be split between the two step types in the outer ring to optimize combustion, while also freeing one fuel mass flow controller to meter propane to the back wall injectors.

This test was conducted at a total air mass flow rate of 0.108 kg/s, with the total fuel flow rate fixed at 0.0025 kg/s which corresponds to a global equivalence ratio of 0.36. The air split was 80% to the core, with 66% of the cavity air through the front plate. The percentage of fuel delivered through the AliCat and Brooks controllers were varied as listed in Table 37, with the average cavity temperature and exit temperatures evaluated at each split. The exit temperatures were determined by averaging the measurements from the four thermocouples in the thermocouple rake that remained stationary at -20° circumferentially and 9.65 mm radially. This position was routinely the location of peak temperatures in prior exit plane measurements.

Figure 272 shows the results of the fuel split study where the blue lines represent the average cavity temperature, and the red lines represent the average exit temperature. There was a greater variation in average cavity temperature than the temperature at the exit plane. The average cavity temperature increased by 100 K from Case 12, which directed all the fuel to the air/fuel injecting steps, to Case 6, which pushed all the fuel through the fuel only steps. The average exit temperature

Table 37. 12-Step Ring fuel split evaluation test points

Case	Fuel Only Step (Alicat)	Air & Fuel Step (Brooks)
1	50%	50%
2	60%	40%
3	70%	30%
4	80%	20%
5	90%	10%
6	100%	0%
7	50%	50%
8	40%	60%
9	30%	70%
10	20%	80%
11	10%	90%
12	0%	100%

remained much more consistent, with an average value of 760 K and a standard deviation of only 11 K. The average and standard deviations are represented in Figure 272 by the dashed horizontal lines centered on 760 K. The temperature rise across the combustor is a more significant metric than the cavity temperature as the total temperature rise dictates the amount of available power that can be extracted by the turbine. For this reason the 12-Step combustor performance was determined to be insensitive to changes in the step fuel distribution. The remaining 12-Step airflow split characterization studies were conducted with a 50/50 step type fuel distribution controlled by the Brooks mass flow controller. The AliCat was configured to control fuel to the back wall injectors.

With the fuel distribution specified, operating maps were created for the 12-Step combustor at 0.060, 0.108, and 0.120 kg/s total air flow rates at a global equivalence ratio of 0.36. Table 38 provides the air flow splits within the rig, and Table 39 provides the fuel distribution and flow rates for each total air mass flow rate, at each of the four back wall fuel injection percentages.

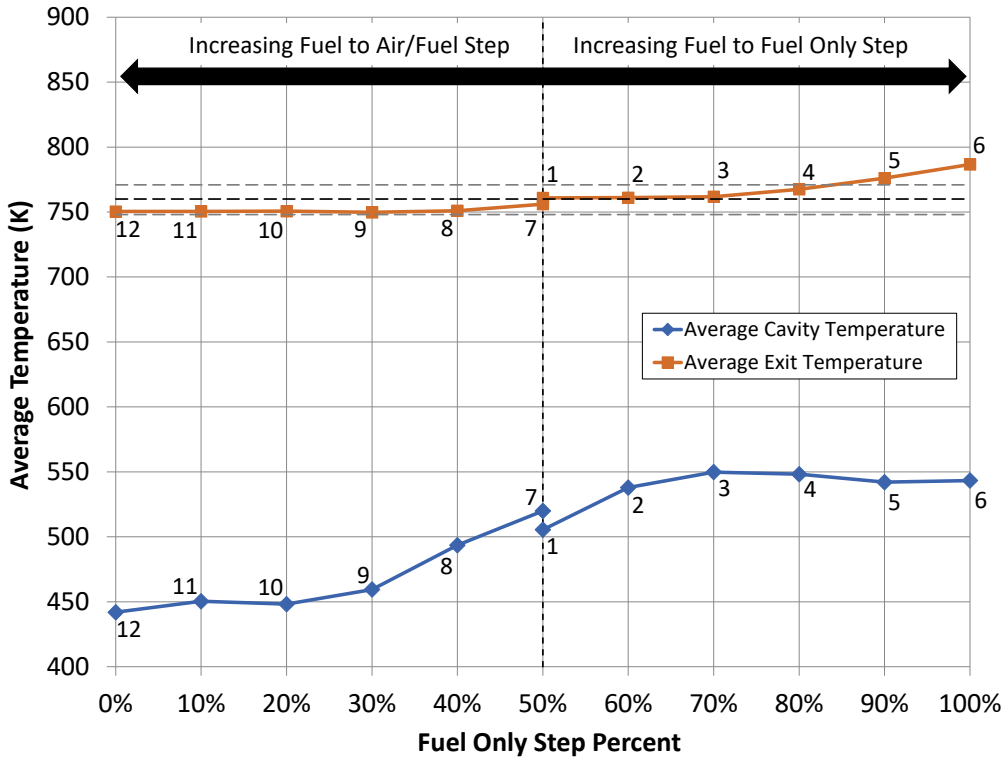


Figure 272. Average cavity and exit temperatures in the 12-Step combustor as a function of step fuel balance

To clarify how these splits work, the core-to-cavity flow split dictates how much air is sent to the circumferential cavity. A 0.108 kg/s total air flow case at an 80% core flow split results in 0.022 kg/s sent to the cavity, with the remaining 0.086 kg/s passing through the core. Of the 0.022 kg/s that is to be delivered to the cavity, the front wall split percentage dictates how much of it goes through the front air drivers, and how much goes through the outer ring steps. For a 60% front wall split, 0.009 kg/s of the 0.022 kg/s is passed through the front air drivers, with 0.013 kg/s pushed through the outer ring step injectors. To achieve these splits the variable diffuser was used to control the air flow split between the core flow and the cavity front air driver plate. The air that entered through the outer ring steps was controlled by the mass flow rate controller on the 3.81 cm air line which was commanded through LabView. The air mass flow rate delivered to the diffuser inlet was reduced by the amount of

Table 38. 12-Step combustor airflow split characterization test points

Test Point	Core-to-Cavity Split	Front Plate-to-Outer Ring Split	Φ_{Cavity}
1	50%	10%	0.72
2	50%	70%	0.72
3	50%	90%	0.72
4	55%	80%	0.80
5	60%	70%	0.90
6	60%	80%	0.90
7	65%	90%	1.03
8	70%	50%	1.20
9	70%	70%	1.20
10	70%	80%	1.20
11	75%	60%	1.44
12	75%	70%	1.44
13	75%	80%	1.44
14	80%	40%	1.80
15	80%	60%	1.80
16	80%	90%	1.80
17	85%	20%	2.40
18	85%	30%	2.40
19	85%	50%	2.40
20	85%	80%	2.40
21	90%	10%	3.60
22	90%	20%	3.60
23	90%	30%	3.60
24	90%	40%	3.60
25	90%	70%	3.60
26	90%	90%	3.60

air that was fed through the 3.81 cm air line to ensure the total air delivered to the test rig matched the desired 0.06, 0.108, or 0.120 kg/s flow rates.

Operating maps were created that showed the average cavity temperature, average exit temperature, diffuser ΔP (see Section 6.1.3), audible dominant frequency, and sound pressure level for each test point, at each flow rate, at each back wall fuel injection level. The average exit temperatures were measured using the thermocouple rake again fixed at -20° circumferentially, and 9.65 mm radially to capture the peak

Table 39. 12-Step combustor characterization fuel distributions for Φ_{global}=0.36

Case	**Total Air Flow Rate** (kg/s)	**Back Plate Percent**	**Back Plate Fuel Flow** (kg/s)	**Outer Ring Fuel Flow** (kg/s)
1	0.060	0%	0	0.00138
2	0.060	10%	0.00014	0.00124
3	0.060	20%	0.00028	0.00110
4	0.060	30%	0.00041	0.00097
5	0.108	0%	0	0.00249
6	0.108	10%	0.00025	0.00224
7	0.108	20%	0.00050	0.00199
8	0.108	30%	0.00075	0.00174
9	0.120	0%	0	0.00276
10	0.120	10%	0.00028	0.00248
11	0.120	20%	0.00055	0.00221
12	0.120	30%	0.00083	0.00193

exit temperatures. Figure 273 shows the average exit temperature operating map for the 0.108 kg/s air mass flow rate test case with 0% back wall fuel injection. These maps were arranged to highlight three different areas; the combusting region, the diffuser limited region, and the flameout region. The combusting region is shown in white with test points that maintained stable combustion indicated as green circle markers. The flameout region was shaded red with the test points that flamed out indicated by red triangle markers. The diffuser limited section was shaded in blue. Each test point required a specific ΔP through the diffuser core to achieve the target air flow split. The diffuser had a fair amount of movement and control, but ultimately still relied on pressure balances throughout the rig. There were some test points that required a diffuser ΔP that could not be achieved. These points were labeled with a blue square to identify they were diffuser limited. The thick dashed line at the edge of the flameout region corresponds to a 0.0098 kg/s air flow rate, or roughly 9% of the total air flow rate through the outer ring steps. This same 9% boundary also exited for the 0.120 kg/s flow rate case at 0% back wall fuel injection. The exact cause of

the boundary positioned at 9% total air flow rate is not known, but several possible causes are presented in Section 6.3.2.5.

The average exit temperature operating maps for the 0.06 and 0.120 kg/s total air mass flow rate cases are shown in Figures 274 and 275, respectively. The 0.060 kg/s flow rate case did not have any flameout points due the much larger diffuser limited region compared to the other two flow rates. All of the points that likely would have resulted in flameout because they were below the 9% step airflow line were diffuser limited and could not be tested. It was found that the ΔP that could be achieved by the diffuser was a function of total air flow rate, outer ring air flow rate, and combustion stability and acoustics. In some instances, specifically noted in the alternate global equivalence ratio testing discussed in the next section as well as the

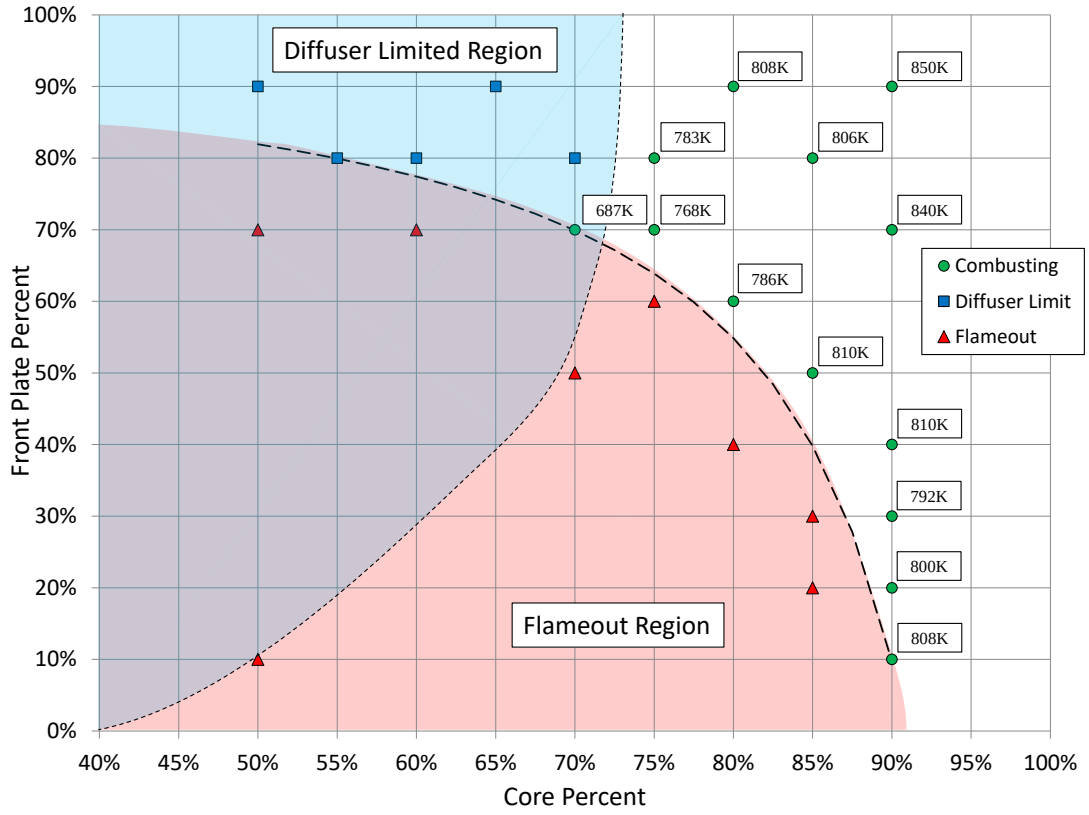


Figure 273. Average exit temperature (K) operating map at $\dot{m}_{in} = 0.108kg/s$, 0% back wall fuel injection

back wall fuel injecting cases of the present study, there were points well outside of the diffuser limited region that could not be reached because of acoustic shifts in the rig. The complete collection of operating maps including average cavity temperatures, average exit temperatures, and ΔP for each total air flow rate at all four back wall fuel injection percentages are shown in Appendix C.

The audible combustion acoustics are shown in Figure 276 for the 0.108 kg/s total air flow case with 0% back wall fuel injection. In this figure the flooded contours show the dominant frequency response (Hz) across the operating envelop, while the overlaid line contours show the sound pressure levels in decibels (dB) for the corresponding points on the map. For obvious reasons combustion acoustics could only be measured

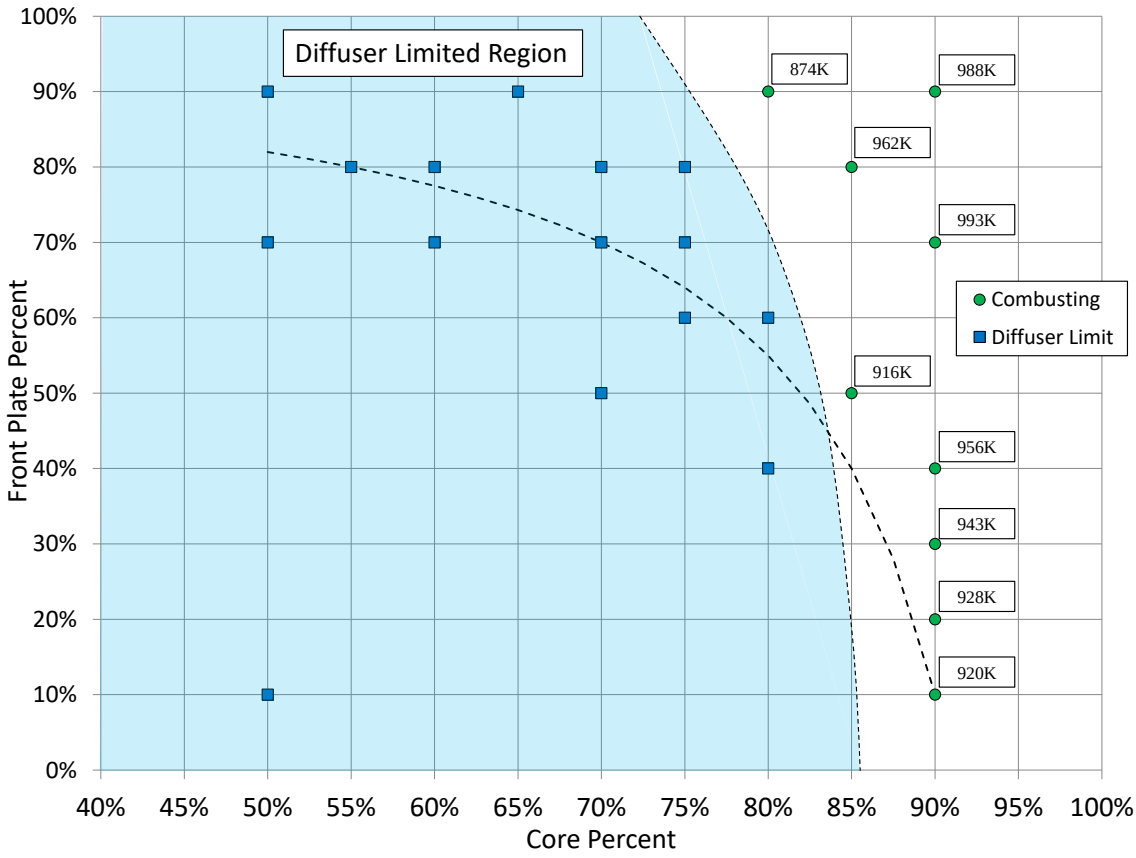


Figure 274. Average exit temperature (K) operating map at $\dot{m}_{in} = 0.060 kg/s$, 0% back wall fuel injection

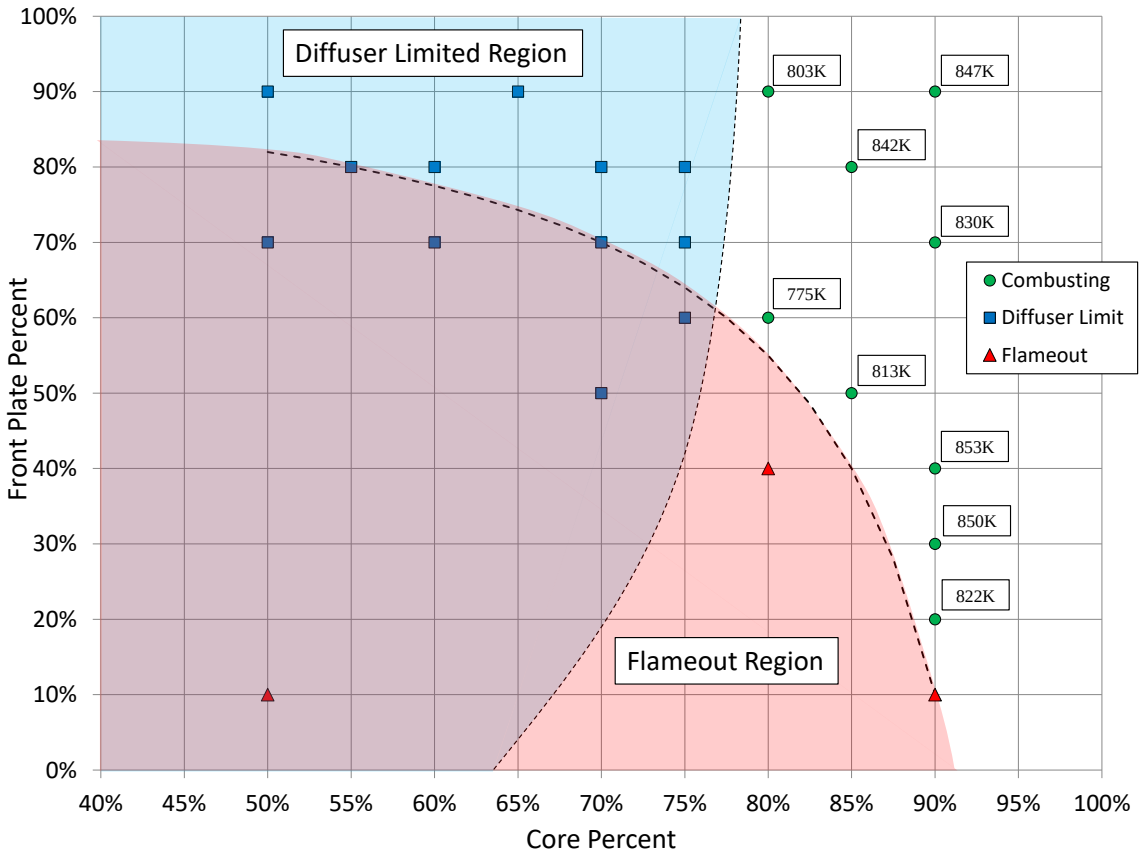


Figure 275. Average exit temperature (K) operating map at $\dot{m}_{in} = 0.120 kg/s$, 0% back wall fuel injection

in combusting regions of the operating maps. The 0% back wall acoustic maps for the 0.060 kg/s and 0.120 kg/s total air flow rate cases are shown in Figures 277 and 278, respectively. The acoustic maps for cases with back wall fuel injection are shown in Appendix C. Frequencies of 215 Hz were physically uncomfortable at sound pressure levels at or above 82 dB; the other frequencies didn't become physically uncomfortable until upwards of 87 dB, or upwards of 91 dB at 194 Hz. Unfortunately, 215 Hz was a commonly generated frequency.

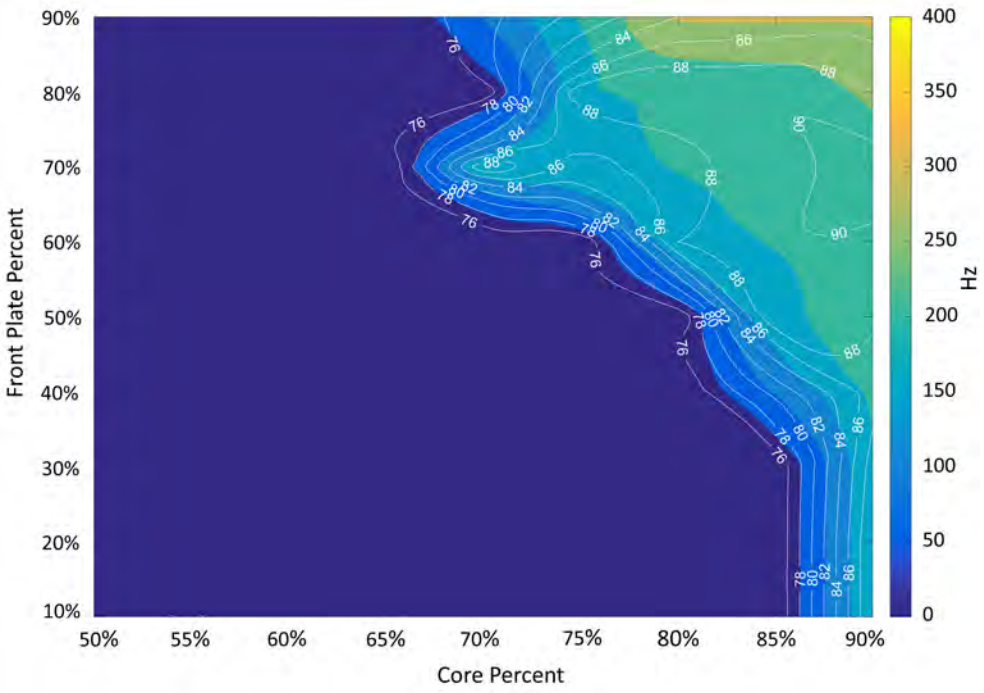


Figure 276. Flooded contours of dominant audible frequency (Hz) with overlaid line contours of sound pressure level (dB) at $\dot{m}_{in} = 0.108kg/s$, 0% back wall fuel injection

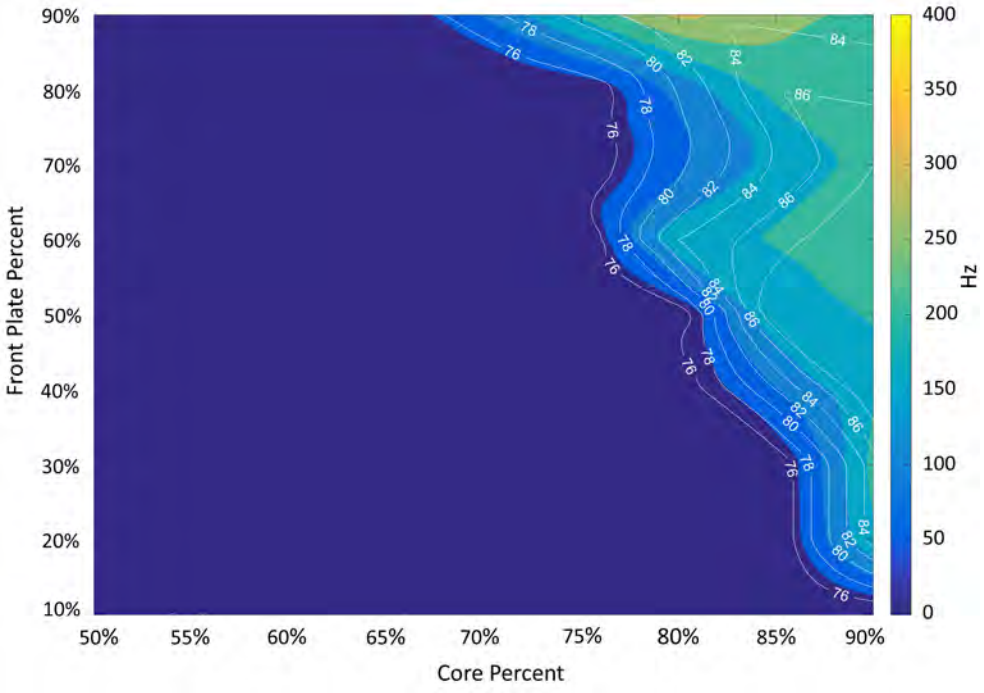


Figure 278. Flooded contours of dominant audible frequency (Hz) with overlaid line contours of sound pressure level (dB) at $\dot{m}_{in} = 0.120kg/s$, 0% back wall fuel injection

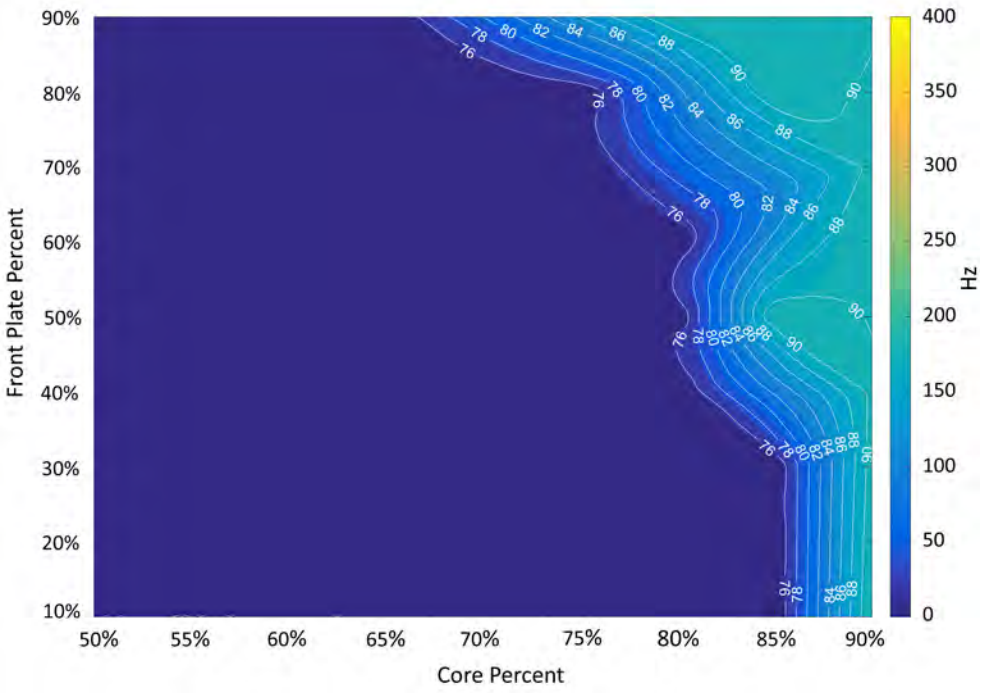


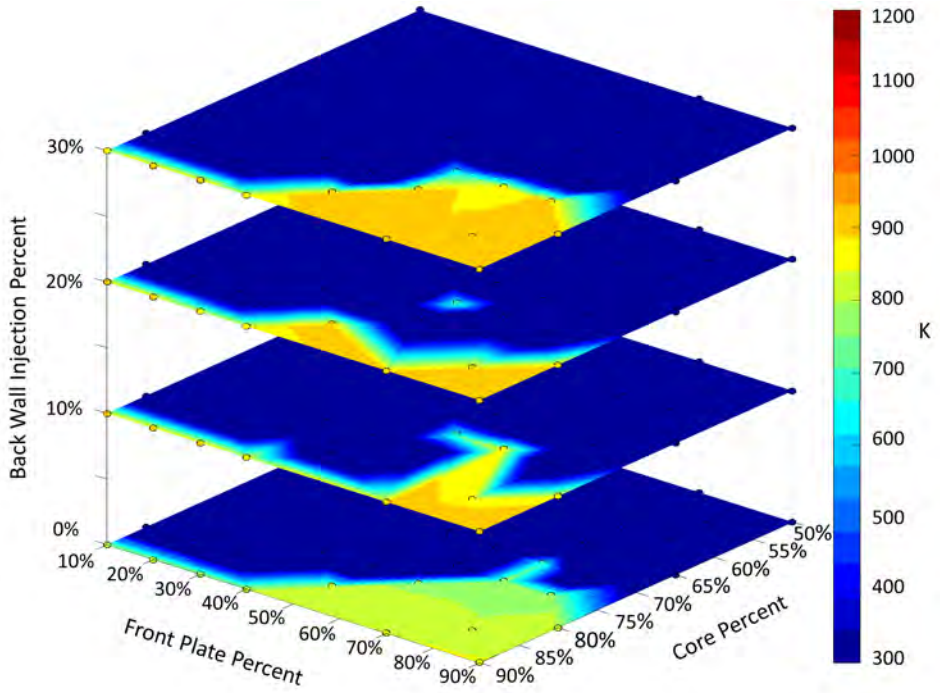
Figure 277. Flooded contours of dominant audible frequency (Hz) with overlaid line contours of sound pressure level (dB) at $\dot{m}_{in} = 0.060 kg/s$, 0% back wall fuel injection

While the operating maps shown above, and in Appendix C to include all of the back wall fuel injection operating maps, provide detailed information at each back wall fuel injection percentage, they do not allow for quick comparison to see how the reported values trend with variations in input parameters. For this reason the data from each operating map was loaded into MATLAB to produce 4D plots of the average exit temperature, average cavity temperature, dominant audible frequency, and sound pressure levels. For the temperature plots the diffuser limited and flameout points were assigned values of 300 K. For the acoustic plots the diffuser limited and flameout values were given ambient lab values under under non-reacting conditions. The MATLAB output was a series of stacked contour maps at each of the back wall injection percentages as shown in Figures 279 and 280 for the 0.108 kg total air mass flow rate. The point markers were also plotted to show the location of the actual

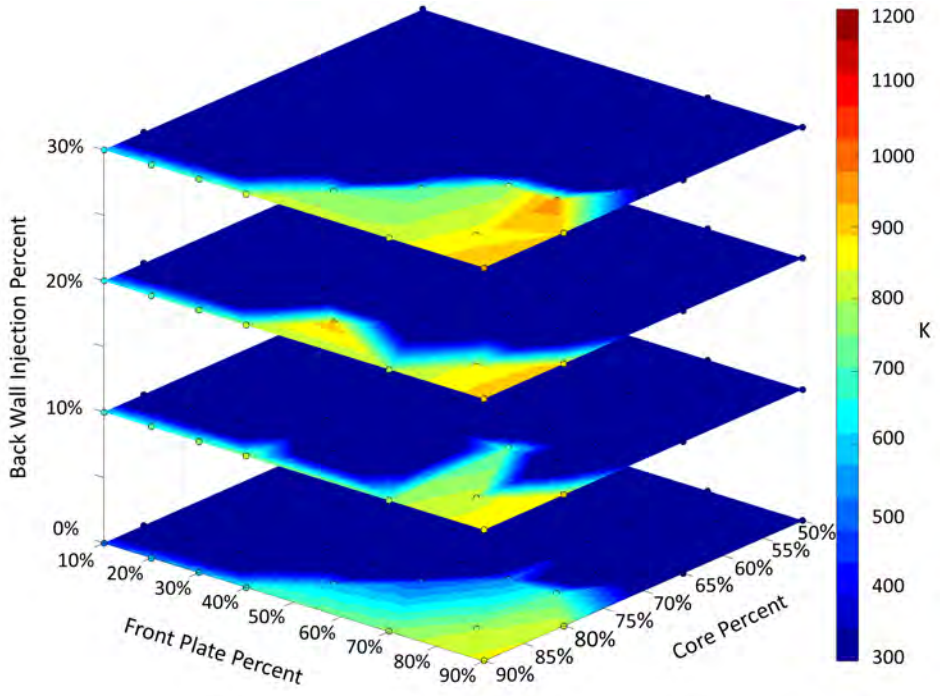
data that went into the contour maps. Note that the 4D plots were rotated from the single layer operating maps shown above to get a better view of the values in the combusting region. The 4D plots for the 0.060 total air flow rate cases are provided in Figures 281 and 282, and Figures 283 and 284 for the 0.120 kg/s total air flow rate cases.

Reviewing all the data collectively through the 4D operating maps, or through the single layer maps shown in Appendix C, it can be seen that peak temperature out of the combustor occurred at the 90% core flow, 90% front plate injection at all three flow rates at 0% back wall injection. This trend was also seen for the average cavity temperatures. After identifying this result, computational analysis was performed on the 90% core flow, 90% front plate injection at 0.108 kg/s total air mass flow rate using the same CFD settings as described earlier in Section 6.3.1. The CFD average cavity temperature results matched well to the experimental data at the 1/2 cavity plane with a difference of 88 K (7%) with the experimental result measuring below the computational value. Thermocouples measure lower than the gas temperature, so the CFD result of the predicted gas temperature is likely accurate. The peak experimental exit temperature with 0% back wall injection was 988 K for the 0.060 kg/s total air mass flow rate at the 90% core, 90% front plate test point. Also noted in the higher two mass flow rate cases was that as fuel was injected through the back wall, the exit temperatures and cavity temperatures generally increased for increasing back wall injection. The cavity temperature increase was due to introducing fuel radially inward in the cavity, inside of the thermocouple measurement locations. With less fuel at the cavity OD, the high cavity equivalence ratios were reduced which leads to comparatively higher combustion temperatures.

At 0.108 kg/s total air flow rate there was a considerable reduction in the operating region at 10% and 20% back wall injection due to additional diffuser limitations caused

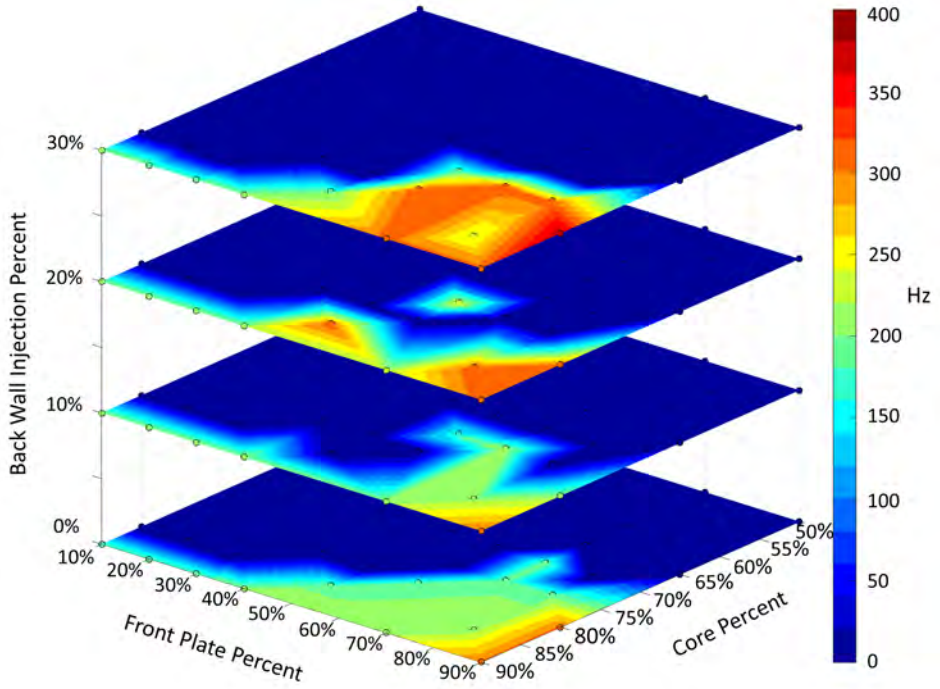


(a) Average Exit Temperatures

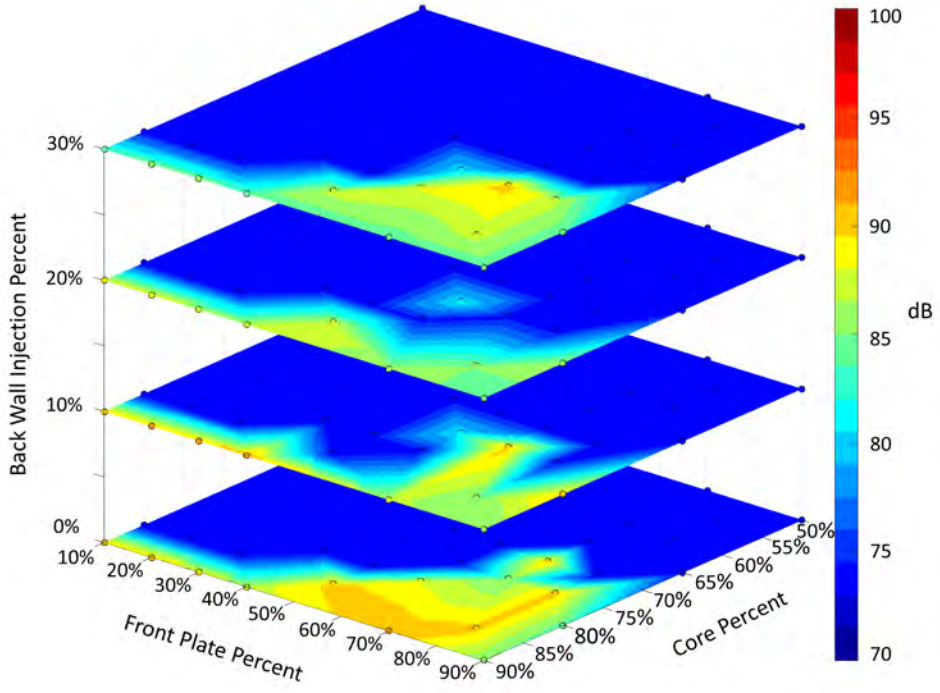


(b) Average Cavity Temperatures

Figure 279. 4D temperature operating maps of the 12-Step combustor at $\dot{m}_{in} = 0.108kg/s$

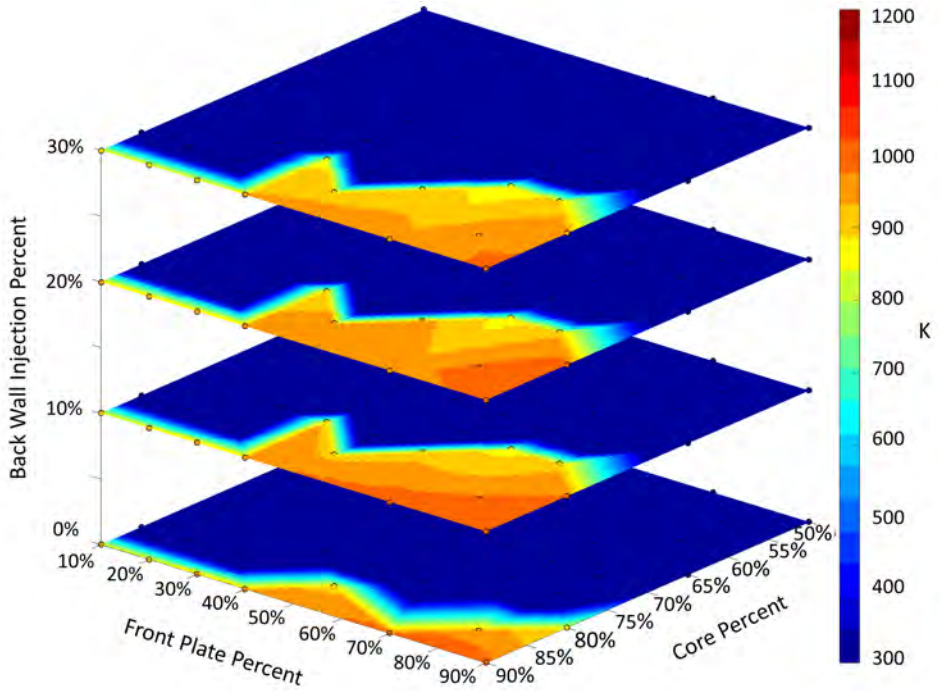


(a) Dominant Audible Frequency

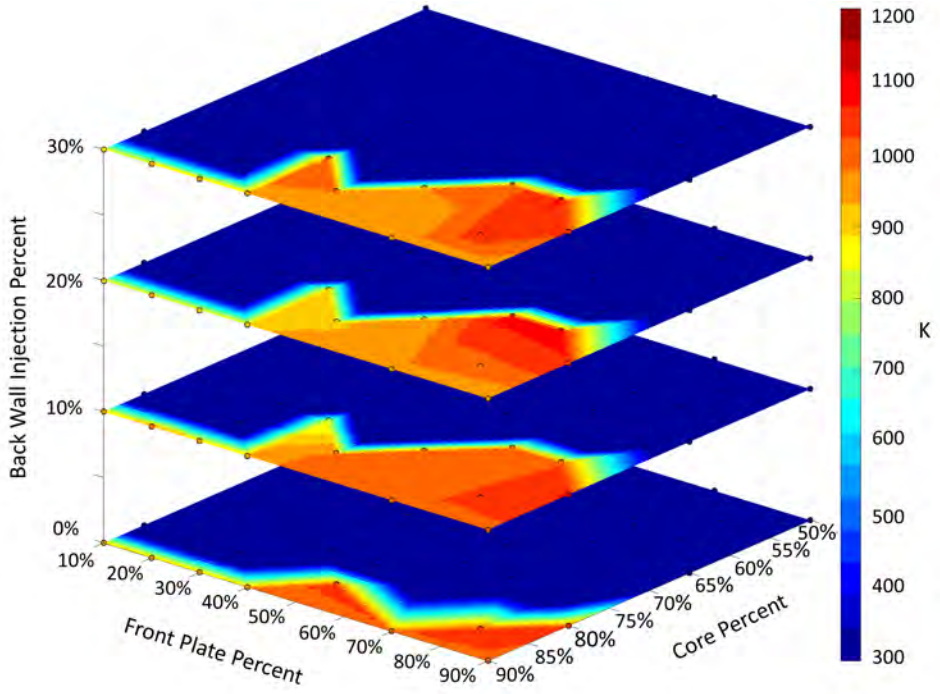


(b) Sound Pressure Level

Figure 280. 4D acoustic operating maps of the 12-Step combustor at $\dot{m}_{in} = 0.108kg/s$

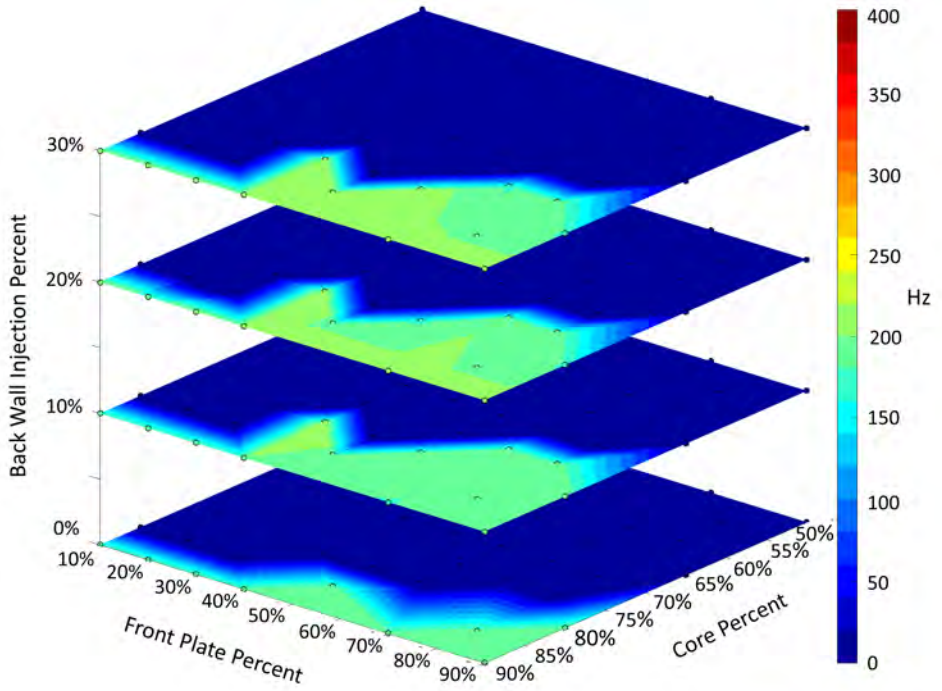


(a) Average Exit Temperatures

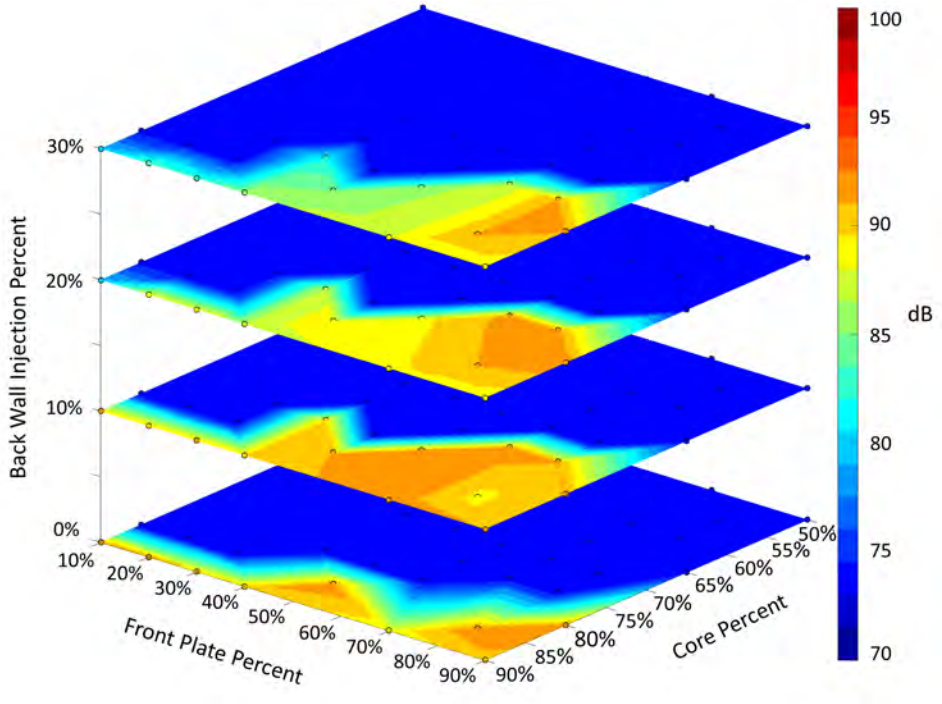


(b) Average Cavity Temperatures

Figure 281. 4D temperature operating maps of the 12-Step combustor at $\dot{m}_{in} = 0.060kg/s$

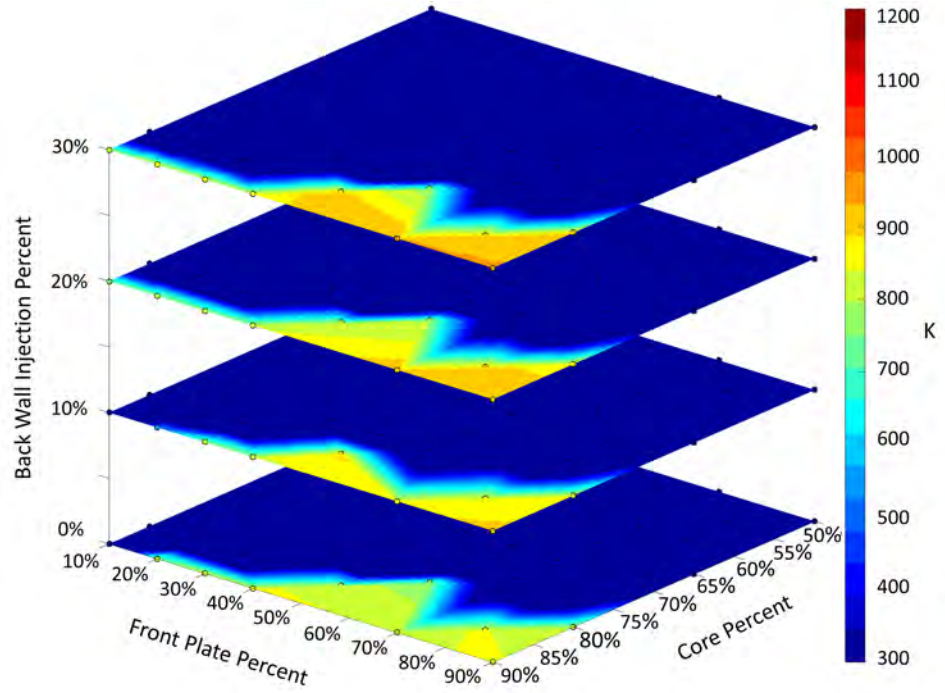


(a) Dominant Audible Frequency

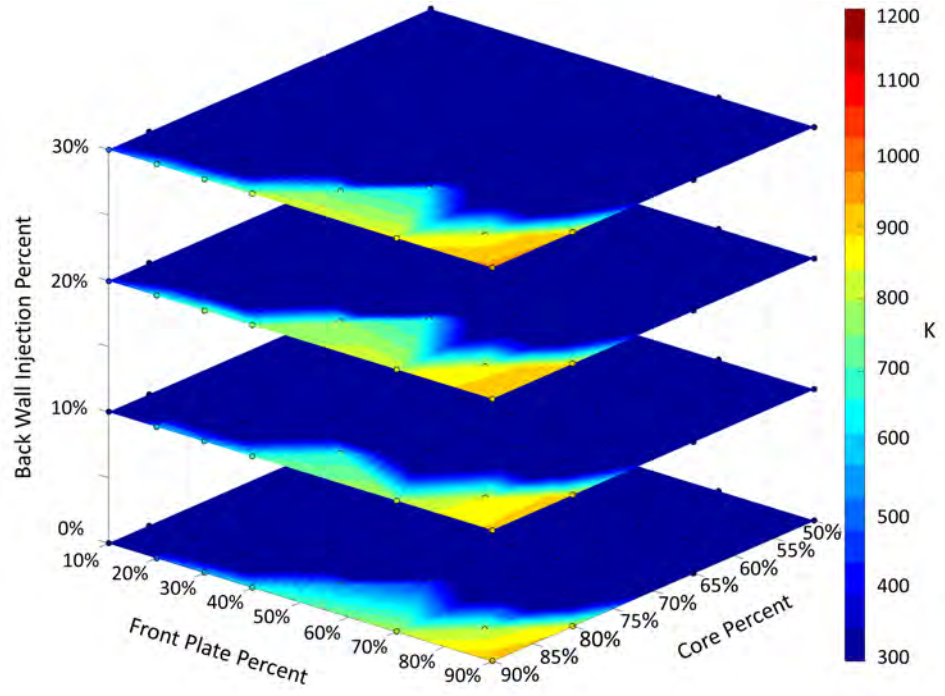


(b) Sound Pressure Level

Figure 282. 4D acoustic operating maps of the 12-Step combustor at $\dot{m}_{in} = 0.060kg/s$

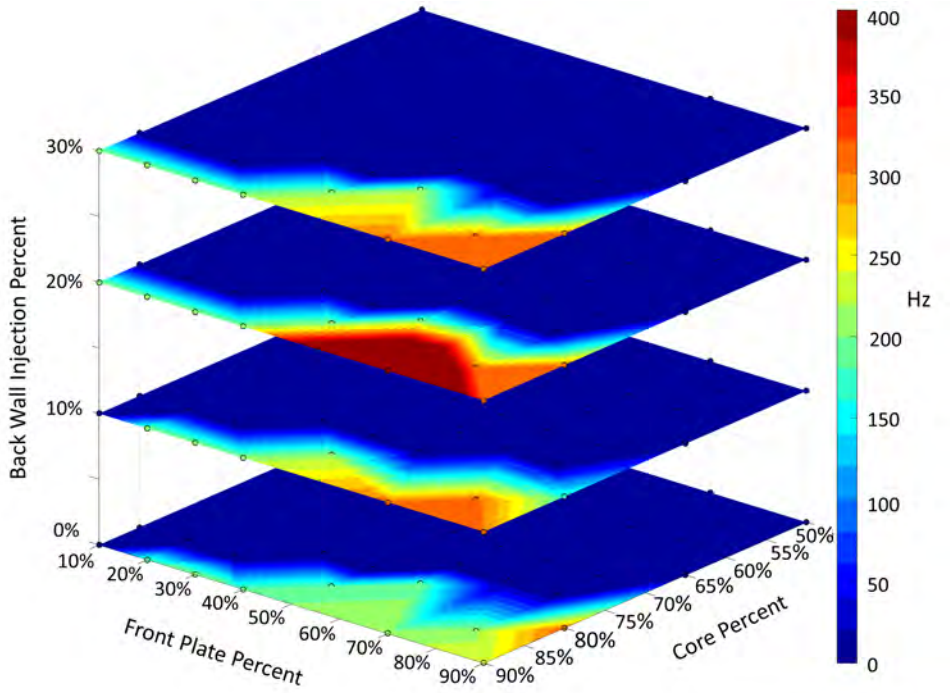


(a) Average Exit Temperatures

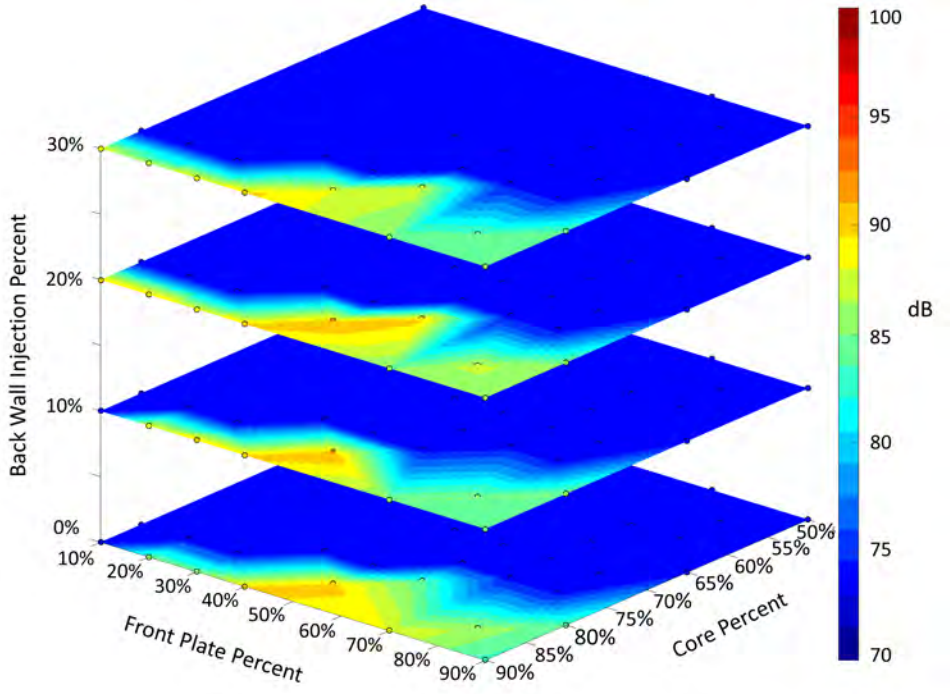


(b) Average Cavity Temperatures

Figure 283. 4D temperature operating maps of the 12-Step combustor at $\dot{m}_{in} = 0.120kg/s$



(a) Dominant Audible Frequency



(b) Sound Pressure Level

Figure 284. 4D acoustic operating maps of the 12-Step combustor at $\dot{m}_{in} = 0.12kg/s$

by changes in acoustics and pressure balance through the combustor. By 30% back wall injection the operating range had returned to the 0% back wall injection levels, minus the 70% core, 70% front plate point. At 20% back wall injection the 75% core, 60% front plate point was combusting where that point could not be reached at the other injection levels. The points 10% higher in both core and front plate percentage from the 75% core, 60% front plate point were also no longer obtainable at that injection level. The acoustic response at 0.108 kg/s yielded higher frequencies with additional back wall injection increasing from an average of 216 Hz at 0% back wall injection, to 261 Hz at 30% back wall injection. As the frequency increased the sound pressure level was reduced from an average of 88 dB at 0% back wall injection, to 85 dB at 30% back wall injection.

Unlike the 0.108 kg/s total air flow rate cases, at 0.060 kg/s total air flow rate the operating area was increased with the addition of back wall fuel injection and remained at a consisted size at all back wall injection levels. This total air mass flow rate was the exception to the increase in cavity and exit temperature with increasing back wall injection. From 0% to 30% back wall injection the average temperatures dropped approximately 20 K. This variation is close enough to say that back wall injection did not significantly effect this flow rate condition in temperature, but the improved operating range afforded by the back wall injection is a significant benefit. The addition of back wall injection also benefited the sound pressure levels which were reduced from an average of 91 dB at 0% back wall injection, to 86 dB at 30% back wall injection. The frequency response remained virtually unchanged at 194 Hz.

At 0.12 kg/s total air flow rate there was a minor reduction in the size of the operating map due to the loss of one point between 0% and 10% back wall injection. At 20% and 30% back wall injection the operating map returned to match the 0% map. Like the 0.108 kg/s total air flow rate, these test cases experienced an increase in cavity

and exit temperatures with increasing back wall injection. The exit temperatures increased an average of 50 K and the cavity temperatures increased an average of 75 K from 0% to 30% back wall injection. The average sound pressure levels decreased by 1 dB (86 - 87 dB) from 0% to 30% back wall injection, however, 20% back wall injection saw the highest average sound pressure levels of the set at 88 dB. The highest average frequencies across all of the operating maps was achieved at 20% back wall injection at an average frequency of 296 Hz.

Back wall injection could be a useful tool, but the benefits varied with total air mass flow rate. As the mass flow rate was increased, the size of the combusting region on the operating maps decreased. The addition of back wall injection did help reduce combustion noise in some cases and allowed some additional test points to be reached. Across all 12 of the maps, the best combustion performance was achieved for a total air flow rate of 0.060 kg/s at a 10% back wall injection. This condition had the widest operating range with 13 points, and the highest exit temperatures, peaking at 1,006 K. This condition did, however, have the highest sound pressure levels, with an average value of 91 dB.

Velocity measurements were taken at select points shown in Table 40 at all three total air mass flow rates with 0% back wall fuel injection using post-processing of chemiluminescence high-spreed videos. Rayleigh losses and frequencies of OH intensity at a single location from the chemiluminescence videos were also found for these points. This data was collected using the chemiluminescence setup discussed in Section 3.1.6.2, which included static and total pressure measurements at the exit of the long exhaust collar off the UCC for Rayleigh loss calculations.

To quantify the impact of back wall injection on cavity velocities and Rayleigh losses, two additional measurement sets were taken at 90% core, 40% front wall injection, and 90% core, 90% front wall injection, at all four back wall fuel injection

Table 40. 12-Step combustor velocity measurement test points

Case	Core-to-Cavity Split	Front Plate-to-Outer Ring Split	Φ_{Cavity}
1	80%	90%	1.08
2	85%	90%	2.40
3	90%	20%	3.60
4	90%	40%	3.60
5	90%	70%	3.60
6	90%	90%	3.60

percentages, and a total air mass flow rate of 0.108 kg/s. One final test point was added to the matrix at 80% core, 66% front wall injection, with no back wall injection, also at a total air mass flow rate of 0.108 kg/s. This point was added to compare experimental velocity results to the computational results discussed in Section 6.3.1.

The velocity results for the 0.060, 0.108, and 0.120 kg/s total air mass flow rates, with 0% back wall fuel injection, are plotted on the operating maps shown in Figures 285, 286, and 287, respectively. In all three of these maps the velocity trends showed increasing velocity for a decreased core flow, or decreased front plate percentage. These results are logical since decreased core flow results in more air through the cavity injectors to drive up the injection velocities. The step air injectors had less holes (18) at a smaller diameter than the front air driver plate (24), so diverting more air to the step injectors would result in higher cavity injection velocities for the same mass flow rate. One trend that was unexpected was the 0.060 kg/s total air mass flow rate case producing the highest velocities, with the velocity magnitudes decreasing for increasing total air mass flow rate. Due to the small amount of cavity air at the tested locations the velocities were very low, resulting in centrifugal loadings between $18g_e$ and $77g_e$. These values are well below the centrifugal acceleration enhancement regime identified by Lewis [4], yet the corresponding points achieved the best combustion performance across the operating maps. This result may indicate

that a slower velocity, which achieves a longer residence time, is more beneficial than a centrifugally loaded enhancement.

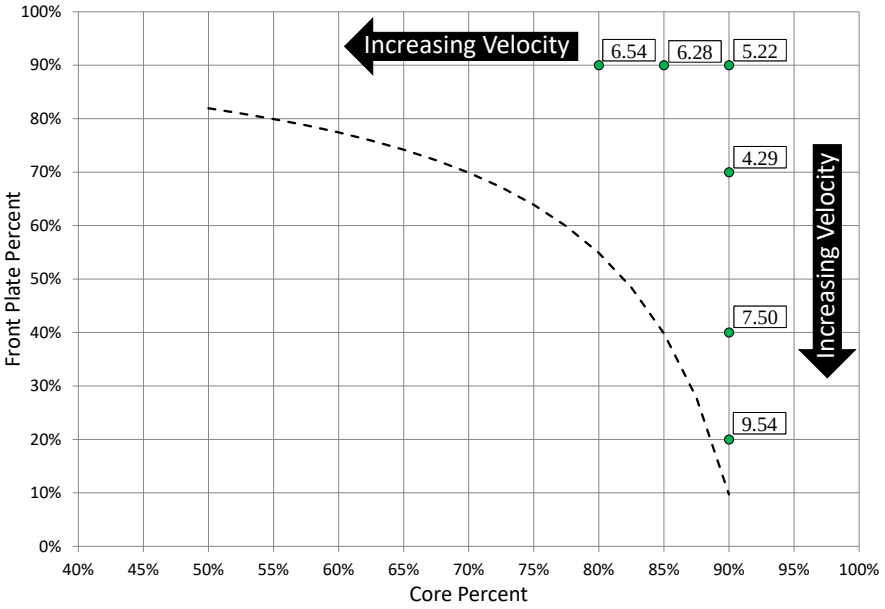


Figure 285. Average velocity (m/s) operating map at $\dot{m}_{in} = 0.060kg/s$, 0% back wall fuel injection

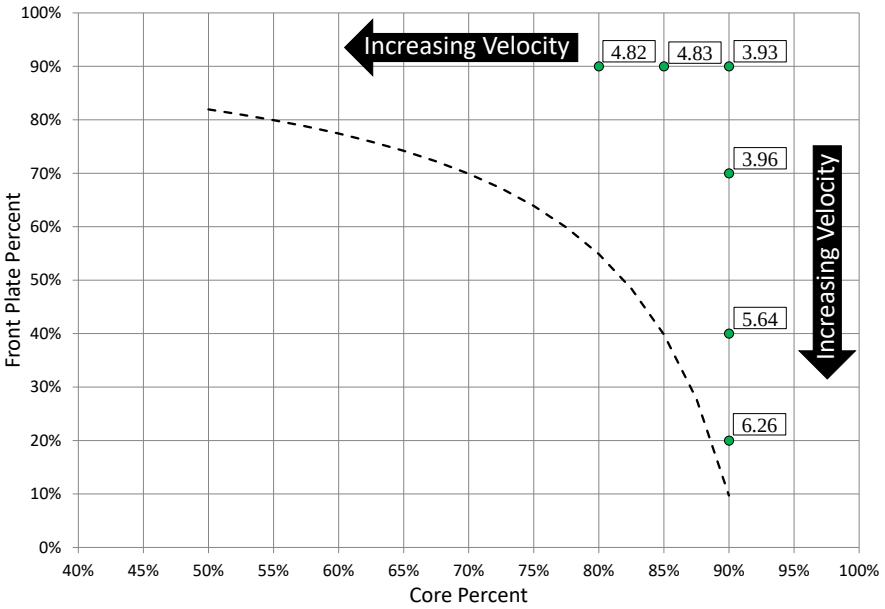


Figure 286. Average velocity (m/s) operating map at $\dot{m}_{in} = 0.108kg/s$, 0% back wall fuel injection

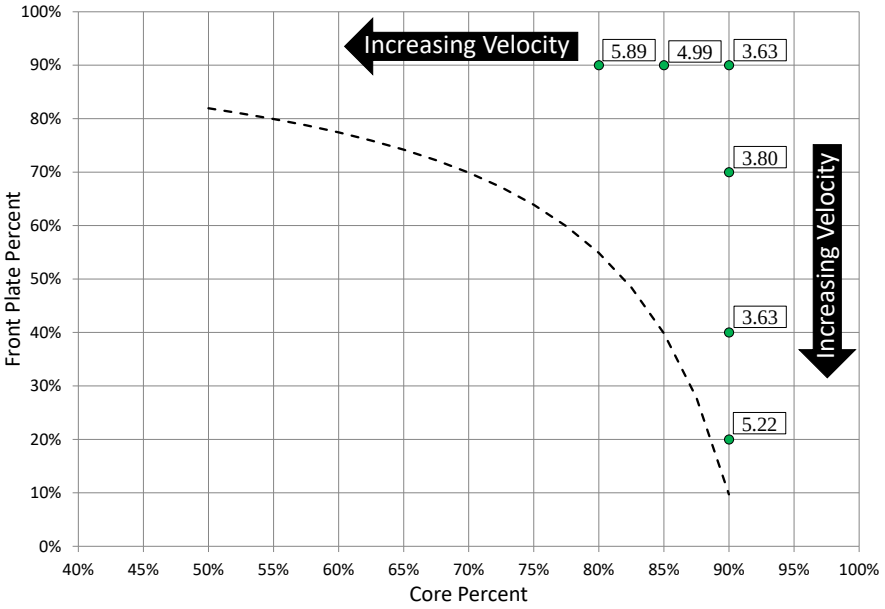


Figure 287. Average velocity (m/s) operating map at $\dot{m}_{in} = 0.120 kg/s$, 0% back wall fuel injection

The Rayleigh losses at these conditions were relatively unchanged within each total air mass flow rate. At 0.060 kg/s the average Rayleigh losses averaged 1.21%, with a standard deviation of 0.09%. At 0.108 kg/s the average Rayleigh loss was 3.01%, with a standard deviation of 0.12%. Finally, at 0.120 kg/s the average Rayleigh loss was 3.14%, with a standard deviation of 0.34%. From these results it can be seen that as the total air mass flow rate increased, so did the Rayleigh losses and deviation of loss values across the operating map.

Table 41 shows the dominant audible frequency and sound pressure level compared with the OH chemiluminescence intensity frequency and correlation amplitude for all 18 test points with 0% back wall fuel injection. A review of these results does not show a correlation between chemiluminescence frequency and acoustic results or relative positioning on the operating map. There were several instances, such as Cases 4, 5, and 6 at 0.060 kg/s and Case 4 at 0.108 kg/s, where the audible frequency and chemiluminescence frequency were consistent. Case 3 at 0.060 kg/s had the same 194 Hz audible frequency yet the chemiluminescence frequency was

doubled to 268 Hz. Since this value is a perfect double, perhaps harmonics produce the same values. While those values were consistent, there results at frequencies above and below approximately 194 Hz were not consistent with the relationship between audible and chemiluminescence frequency. In some cases increases in audible frequency resulted in increases in chemiluminescence frequency, while other other time the chemiluminescence frequency decreased for an audible frequency increase. One trend that was consistent was the amplitude of the chemiluminescence frequency correlation decreasing considerably as the total air mass flow rate increased.

Table 41. 12-Step combustor acoustic comparison to chemiluminescence frequency

Case	**Total Air Flow Rate** (kg/s)	**Audible Frequency** (Hz)	**Sound Pressure Level** (dB)	**Chemil. Frequency** (Hz)	**Amplitude**
1	0.060	215	80	197	12,956
2	0.060	178	76	117	3,537
3	0.060	194	85	268	2,579
4	0.060	194	88	134	2,683
5	0.060	194	79	131	2,109
6	0.060	194	80	133	3,881
1	0.108	242	83	55	937
2	0.108	307	83	183	340
3	0.108	242	80	33	321
4	0.108	199	82	134	368
5	0.108	215	83	147	905
6	0.108	307	80	82	234
1	0.120	307	82	65	189
2	0.120	307	83	213	368
3	0.120	242	80	16	354
4	0.120	242	82	92	188
5	0.120	242	82	147	623
6	0.120	242	82	224	148

Figure 288 shows the trends in Rayleigh loss and velocity with back wall fuel injection at two points locations on the operating map. At 90% core, 40% front wall

injection the average Rayleigh loss across all levels of back wall fuel injection was 2.77%, with a standard deviation of 0.47%. At 90% core, 90% front wall injection the average Rayleigh loss across all levels of back wall fuel injection was 3.11%, with a standard deviation of 0.09%. This result indicates that the test condition with the higher cavity velocity also yielded the higher losses. In both cases the velocity peaked at 20% back wall fuel injection, with a considerable drop off in velocity with the increase to 30% back wall injection.

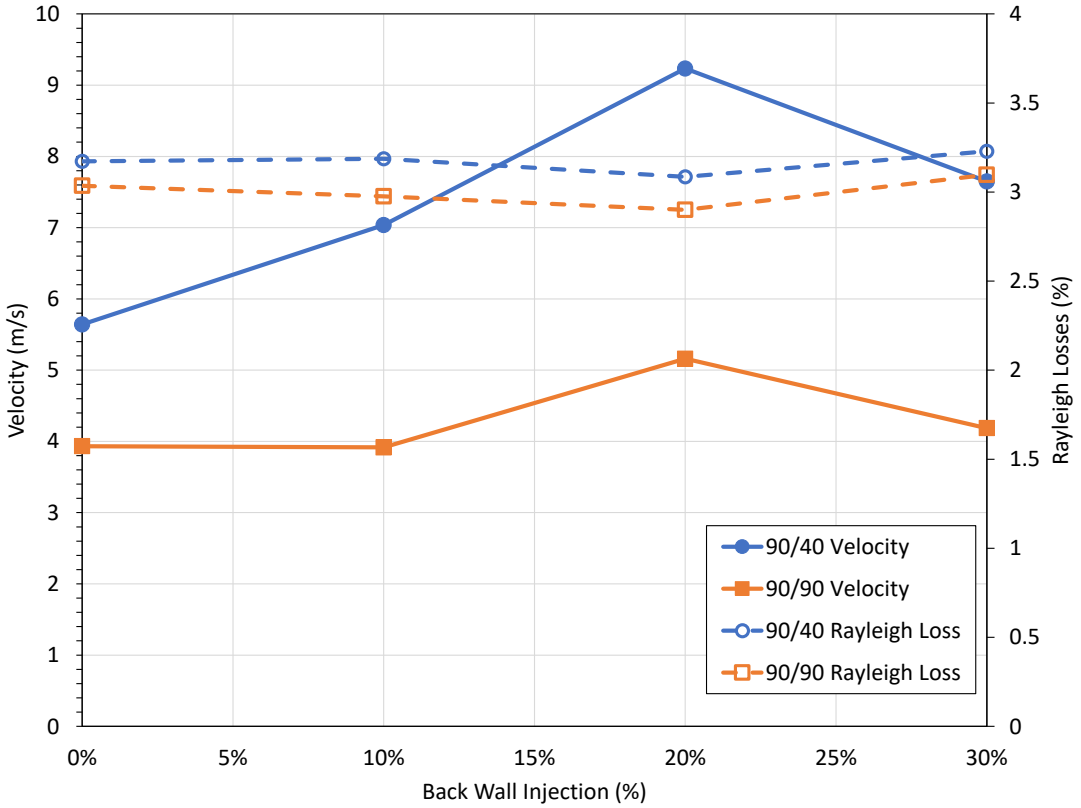


Figure 288. Average velocity (m/s) and Rayleigh loss operating map at $\dot{m}_{in} = 0.108 kg/s$, 0% - 30% back wall fuel injection

Table 42 shows the audible acoustic response and the chemiluminescence frequency and correlation amplitude. The audible frequency within each set remained consistent after the slight initial increase from 0% to 10% back wall injection. The 90% core, 40% front wall injection case displayed a significant 6 dB increased from 0% to 10%

back wall injection with all of the back wall injecting levels yielding the same 88 dB sound pressure level. The 90% core, 90% front wall injection case showed a much lower initial increase in sound pressure level, but continued to increase by 2 dB for each increment from 0% to 30% back wall injection. There was no correlation between audible frequency and chemiluminescence frequency observed in these data sets.

Table 42. 12-Step combustor acoustic comparison to chemiluminescence frequency

Back Wall Percent	**Core %/ Front Wall %**	**Audible Frequency** (Hz)	**Sound Pressure Level** (dB)	**Chemil. Frequency** (Hz)	**Amplitude**
0	90/40	199	82	134	369
10	90/40	215	88	293	296
20	90/40	215	88	147	1,647
30	90/40	221	88	180	831
0	90/90	307	80	82	234
10	90/90	312	82	210	154
20	90/90	312	84	148	997
30	90/90	312	86	82	234

The velocity measurement for the CFD comparison case with an 80% core split, and 66% front wall split at 0.108 kg/s total air mass flow rate yielded an average velocity along a line of constant radius at 7.5 cm that was centered in the redesigned back plate window that was 10.7 m/s. The computational temperature contours for this case are shown in Figure 269b, with a discussion of the velocity in the text surrounding the figure. The computationally predicted velocity was 17.0 m/s along a line at 7.44 cm radially from engine centerline. This radial position was the half window location in the baseline back plate that was used for comparison to Baseline combustor data. Taking the computational measurement at the half window radial position for the redesigned back plate (7.5 cm), yielded a tangential velocity of 16.0 m/s at the half cavity plane. The experimental velocity was determined from OH chemiluminescence, meaning that measurement location may not have been centered

at the half cavity, but rather was dictated by where the concentration of OH was positioned in the cavity. The CFD needed to be reexamined to look for the positioning of OH in front of the cavity window, and find the velocity of the OH concentration and see how that compared to the experimental result.

Figure 289 shows an iso-surface of OH mass fraction at 1/3 maximum value inside the 12-Step combustor. The iso-surface is colored by tangential velocity and the approximate location of the redesigned back plate window is indicated. In the circumferential region of the window the largest concentration of OH was located along the back wall of the cavity, in contact with the window. Averaging the displayed tangential velocity in the region visible through the window would yield a result at approximately 10.7 m/s, matching the experimental data. While the computational result indicated that there was higher velocity fluid at the axial half cavity plane, that fluid was not visible to the IRO through the high concentration of slower moving OH on the back wall. This result shows indicates that comparing chemiluminescence velocity measurements through small windows to CFD results requires the velocity of the OH visible through the window to be considered. The only way to take velocity measurements at specific cavity axial planes is to use PIV with a laser sheet positioned at the desired measurement plane. Unfortunately, the ducting through the 12-Step Ring does not allow room for a window to be installed to provide optical access for a laser sheet.

6.3.2.3 Airflow Split Characterization at Φ_{global} = 0.32 and 0.28.

Based on the results presented in Section 6.3.2.2, it was anticipated that operating at a lower global equivalence ratio would open the operating envelop by shifting the flameout line down and to the left. To test this theory two additional sets of 50 test points each were run at 0.108 kg/s total air mass flow rate at global equivalence ratios of 0.32 and 0.28, with 0% back wall fuel injection. The 50 test points included all

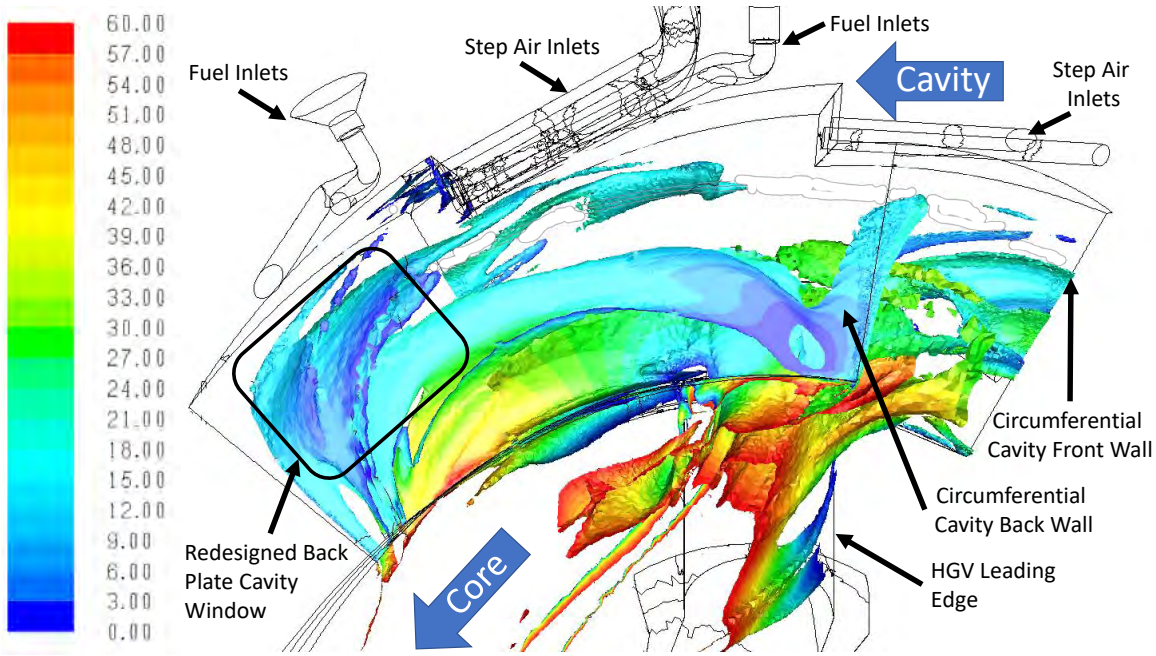


Figure 289. Iso-surface of OH mass fraction at 1/3 maximum value, colored by tangential velocity (m/s), in the UCC configured with an 80% core split, and 66% front wall split at $\dot{m}_{in} = 0.108kg/s$, 0% back wall fuel injection

the splits in Table 38 (Φ_{Cavity} changed), except for Test Point 1, and the additional test points shown in Table 43. The additional points were needed to ensure adequate coverage on the map if the flameout line did in fact shift down. For a global equivalence ratio of 0.32 the fuel flow rate was set to 0.0022 kg/s, and 0.0019 kg/s at a global equivalence ratio of 0.28.

Table 43. Additional 12-Step combustor airflow split characterization test points

Test Point	Core-to-Cavity Split	Front Plate-to-Outer Ring Split	Φ_{Cavity} @ Φ_{global}=0.32	Φ_{Cavity} @ Φ_{global}=0.28
27	50%	50%	0.64	0.56
28	50%	60%	0.64	0.56
29	50%	80%	0.64	0.56
30	55%	50%	0.71	0.62
31	55%	60%	0.71	0.62
32	55%	70%	0.71	0.62
33	60%	40%	0.80	0.70
34	60%	50%	0.80	0.70
35	60%	60%	0.80	0.70
36	65%	50%	0.91	0.80
37	65%	60%	0.91	0.80
38	65%	70%	0.91	0.80
39	70%	30%	1.07	0.93
40	70%	40%	1.07	0.93
41	70%	60%	1.07	0.93
42	75%	10%	1.28	1.12
43	75%	20%	1.28	1.12
44	75%	30%	1.28	1.12
45	75%	40%	1.28	1.12
46	75%	50%	1.28	1.12
47	80%	10%	1.60	1.40
48	80%	30%	1.60	1.40
49	80%	50%	1.60	1.40
50	85%	10%	2.13	1.87
51	85%	40%	2.13	1.87

The shift in the flameout line on the cavity and exit temperature operating maps shown in Figures 290 and 291 for a global equivalence ratio of 0.32, and Figures 292 and 293 for a global equivalence ratio of 0.28, were not as large as expected. In both cases the flameout line did shift slightly (red dashed line) from the previous 9% step air flow rate flameout line (black dashed line) to include two additional combusting test points. The gain of these two points, however, came at the expense of a larger diffuser limited region (blue dashed line) and sporadic diffuser limited points within the combusting region near the previous flameout lines.

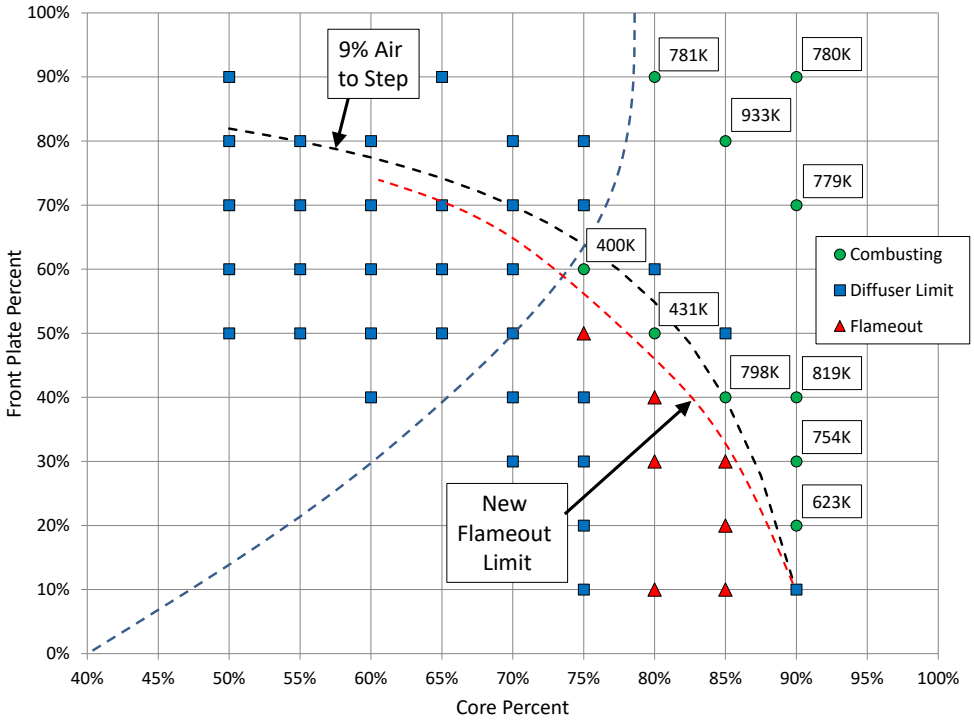


Figure 290. Average cavity temperature (K) operating map at $\dot{m}_{in} = 0.108kg/s$, 0% back wall fuel injection, $\Phi_{global} = 0.32$

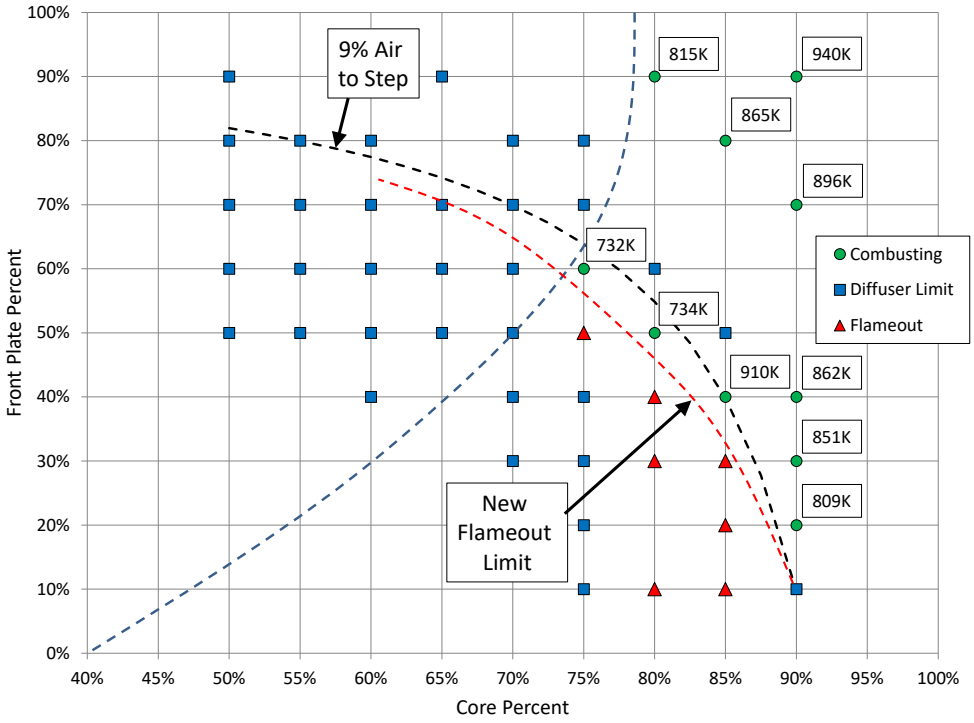


Figure 291. Average exit temperature (K) operating map at $\dot{m}_{in} = 0.108kg/s$, 0% back wall fuel injection, $\Phi_{global} = 0.32$

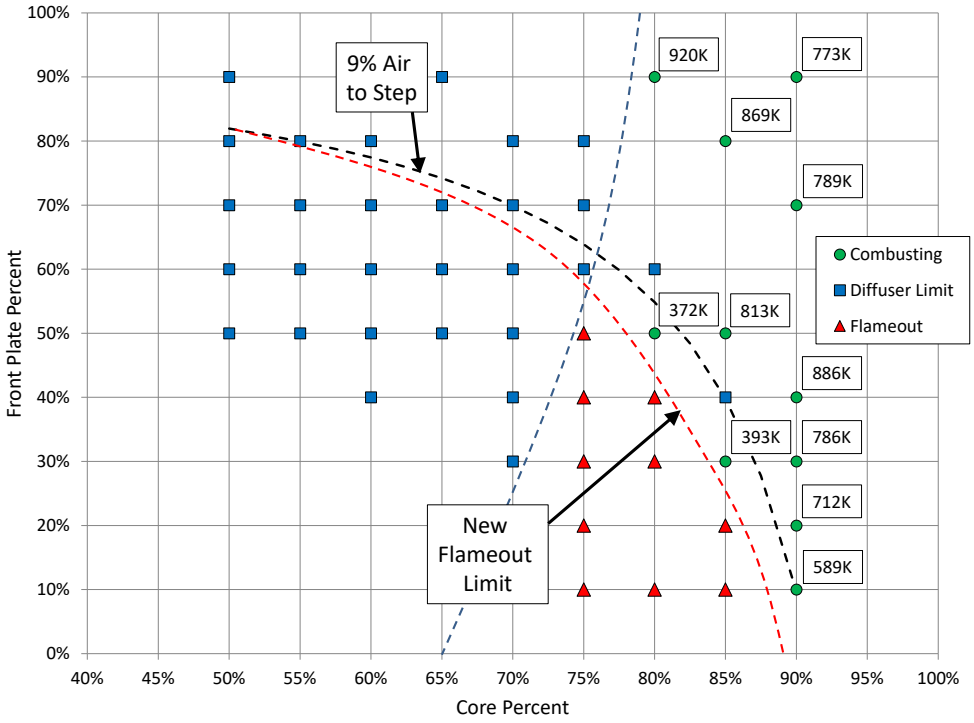


Figure 292. Average cavity temperature (K) operating map at $\dot{m}_{in} = 0.108kg/s$, 0% back wall fuel injection, $\Phi_{global} = 0.28$

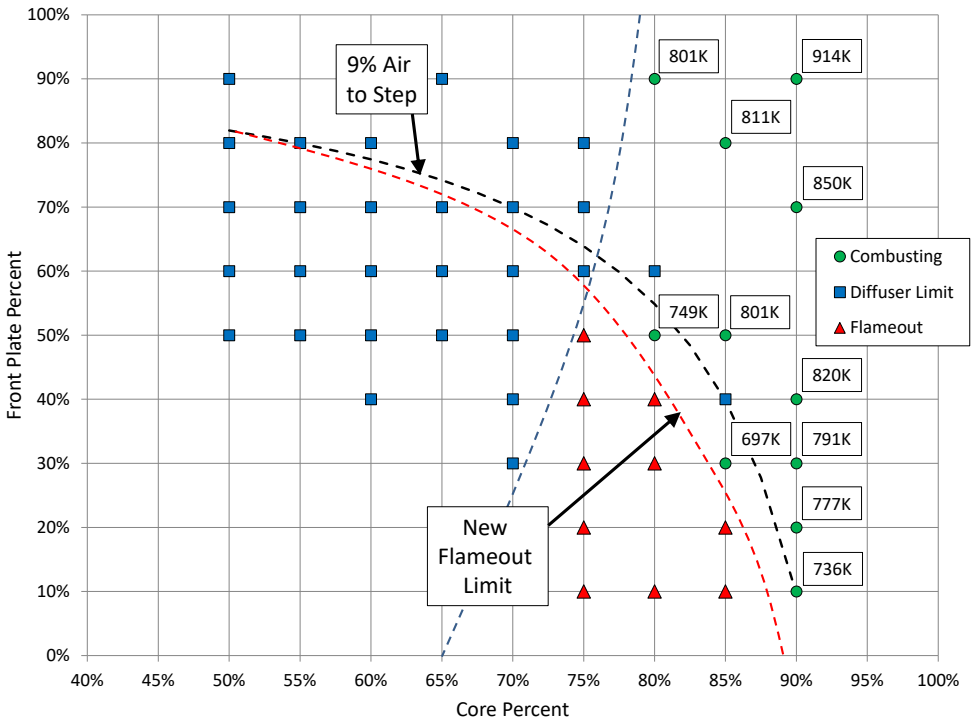


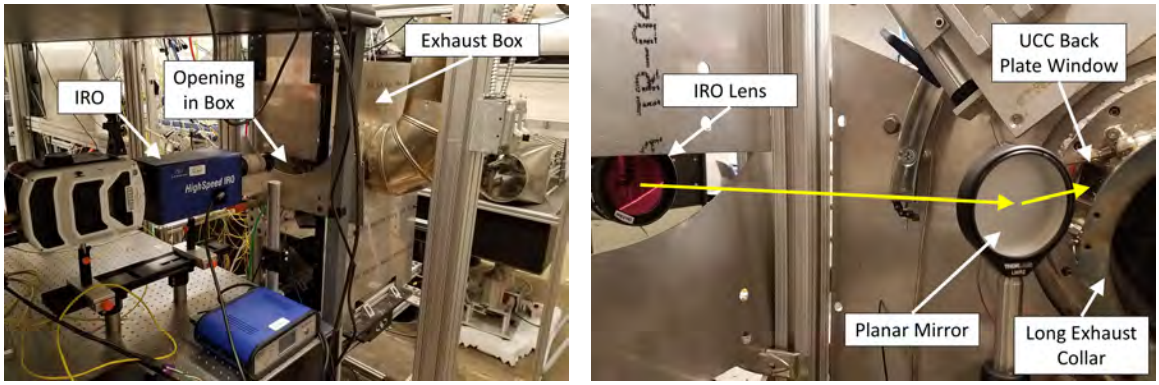
Figure 293. Average exit temperature (K) operating map at $\dot{m}_{in} = 0.108kg/s$, 10% back wall fuel injection

Cavity temperatures aside, a reduction in the global equivalence ratio should result in lower exit temperatures. This behavior was seen moving from a global equivalence ratio of 0.32 to 0.28 which showed on average a reduction of 46 K. As a note, both of these data sets were taken on the same day. The average exit temperatures at a global equivalence ratio of 0.36 (see Figure 273) were all lower than the exit temperatures at a global equivalence ratio of 0.32 with the exception of a single point. The average difference between the exit temperatures at a global equivalence ratio of 0.32 and 0.36 was also 46 K; meaning the average exit temperature across the entire operating map was the same for global equivalence ratios of 0.36 and 0.28. A comparison of the peak temperatures showed a 90 K reduction at a global equivalence ratio of 0.36, compared to 0.32. Since the global equivalence ratios of 0.32 and 0.28 followed the trend of lower exit temperatures at lower global equivalence ratios, it is difficult to determine if there were other factors causing the data at a global equivalence ratio of 0.36 to not follow the pattern, or if it was a result of seemingly large day-to-day variations in performance.

6.3.2.4 Effect of Exhaust Configuration on Combustor Performance.

The majority of the 12-Step combustor cavity and exit plane characterization was performed with the exhaust box shown in Figure 140 and a short exhaust collar to allow the thermocouple rake access to the region directly behind the HGV trailing edges. However, all chemiluminescence, velocity, and Rayleigh loss measurements were conducted with a direct coupled exhaust as shown in Figures 147, 150, and 151, with a long exhaust collar extending from the UCC. The direct exhaust was used for any testing that required visual access to the back plate window for optical measurements. A five point test series was performed to quantify the impact of the difference in the exhaust on cavity properties and system losses. To enable optical cavity measurements with the exhaust box, the modified chemiluminescence setup

shown in Figure 294 was used. The long collar was used on the exit of the UCC to protect the mirror from direct flame impingement by exhausting the hot combustion products further into the box.



(a) IRO setup outside the box (b) Mirror inside the box

Figure 294. Modified chemiluminescence setup for use with exhaust box

All five test points were run at a total air mass flow rate of 0.108 kg/s with a global equivalence ratio of 0.36 and no back wall fuel injection. Table 44 shows the specific air split configuration for each point.

Table 44. Exhaust configuration test matrix

Case	Core %	Front Plate %	Φ_{Cavity}
1	80	90	1.80
2	85	90	2.40
3	90	20	3.60
4	90	40	3.60
5	90	90	3.60

Average cavity temperatures, Rayleigh losses, and cavity velocity measurements calculated from high-speed chemiluminescence videos from the five test points shown in Table 44 were compared with identical test points that were taken using the direct coupled exhaust. The average cavity temperatures and velocities were found to be 7% lower in the cases that used the exhaust box than the direct coupled exhaust.

The average Rayleigh loss deviated by 0.4 percent, which equates to a 13% variation between exhaust configurations, with the cases that used the exhaust box producing larger losses. The reacting total pressure losses were larger in the cases that used the exhaust box while cold flow losses were found to be comparable between the two exhaust configurations.

While not the basis for performance comparisons, the audible frequencies and sound pressure levels were different between the two exhaust configurations as well. The cases that exhausted directly into the ventilation duct produced dominant frequencies that were on average 38 Hz higher, and on average at a sound pressure level that was 4 dB lower than the cases that used the exhaust box. The exhaust duct acted as a muffler for the direct coupled configuration, while the panels on the sides of exhaust box were free to reverberate and amplify the sound pressure levels at lower frequencies. The sound pressure levels and dominant frequencies between matching cases using the exhaust box with the short and long collar were identical, or nearly identical, for all five cases.

While there was some minimal variation in the results between the two different exhaust setups, there is also routinely variation between identical configurations when tested on different days. The results compared above were taken on different days, making it difficult to quantify the differences due to day to day variation from the differences caused by the exhaust arrangement. In either case, it was determined that both exhaust configurations could be used with comparable results.

6.3.2.5 Effect of Fuel Injection on Combustion Stability.

In another attempt to enlarge the combusting region of the operating maps, fuel was removed from the fuel only (stabilizing) steps and pushed through the fuel/air steps with no back wall fuel injection. It was thought that at higher global equivalence ratios, injecting fuel into the recirculation zone behind the stabilizing steps would

create a condition that was too rich to burn. If flame could not be maintained behind the stabilizer steps, there was another loss of a flameholder location. Operating at 0.108 kg/s total air flow rate and a global equivalence ratio of 0.36, several test points were run that were just inside the flameout region. These points included 75% core, 60% front wall injection, 80% core, 40% front wall injection, and 85% core, 30% front wall injection. It was found, however, that even removing the fuel from the stabilizer steps did not shift the flameout line at these splits.

The lack of improvement with the removal of fuel injection from the stabilizing steps can be explained with the help of Figure 295. With no fuel through the stabilizing steps, the velocity of the fuel jets and air jets were comparable at points near the flameout line. The velocity ratio between the air and fuel jets was 1.05 along the flameout line at all total air flow rates for a global equivalence ratio of 0.36. Since the velocities were nearly equal and injected parallel to each other there was an insufficient shear layer developed between the air and fuel to aid in mixing. Since the air was above the fuel and there was a much greater volume of air flowing from the injecting steps, the fuel was unable to penetrate the air jets in sufficient quantity to make it to the stabilizing step recirculation zone to burn as a pilot flame. With the air jets buffering the fuel off the wall, only air is recirculated behind the step which has no stabilizing quality and thus made no improvements to the operating region.

There are several factors that help explain the cause of the 9% flameout line using the fuel distribution with fuel delivered evenly to every step. In Figure 269, which showed computational temperature contours at the half cavity axial plane, there is no reaction in the recirculation zone behind the stabilizing steps. Instead, at these conditions the reaction is formed off the shear layer along the recirculation zone and the bulk flow near the wall. This behavior, along with a review of the propane mass fraction contours, confirms the theory that the recirculation zone is in fact too fuel

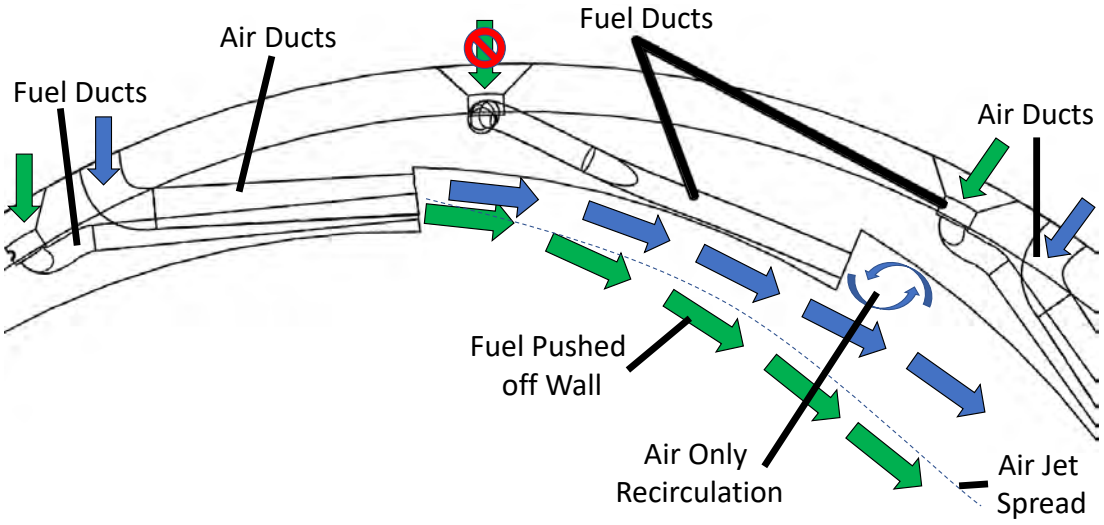


Figure 295. Flow behavior in the 12-Step combustor with no fuel injection from the stabilizing steps

rich to burn. The quantity of propane issuing from the fuel injectors in the stabilizing step was enough to disrupt the recirculation pattern behind the step and thus reduce mixing with air. Figure 296, which shows the temperature contours at the 3/4 axial cavity plane of the 80/20 core-to-cavity flow split and 66/33 front wall-to-step cavity air split, indicates a slightly elevated temperature behind the step. While it is still too rich to burn, the increase in temperature is due to a secondary recirculation pattern that forms with the axis of circulation perpendicular to the cavity outer ring wall. The pattern is explained in greater detail in Chapter VII, but the circulation caused the gases behind the recirculating steps to be pulled to the forward cavity wall and slightly entrain gases from the freestream to fill in gases at the back wall side of the step. The quantity of fuel behind the step was too significant to allow this secondary circulation pattern to push enough fuel away from the back wall to allow it to burn, but it was significant enough to cause a slight pre-heat of the fuel.

While the above mentioned fuel concentrations and secondary circulation patterns behind the stabilizing steps are contributing factors, the real cause of the 9% step air

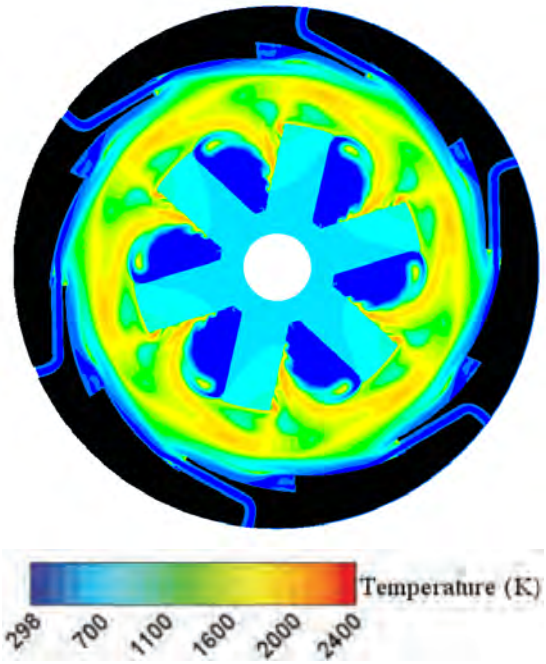


Figure 296. Temperature contours (K) on the three-quarter cavity plane of the 12-Step Ring combustor. 80/20 core-to-cavity flow split, 66/33 front wall-to-step cavity air split

flameout line is likely due to the ratio of the fuel jet velocity to the velocity of the air passing directly below the stabilizing step. As discussed above, the air jet from the fuel/air steps is the driving fluid that would interact with the stabilizing steps. Figures 297, 298, and 299 show the velocity of the air jets across the operating maps for 0.06, 0.108, and 0.120 kg/s total air flow rates, respectively, with the 9% step air line indicated by the dashed white line. For a global equivalence ratio of 0.36, the fuel jet velocities are 6.34, 11.45, and 12.7 m/s at 0.060, 0.108, and 0.120 kg/s total air flow rate conditions. Along the 9% flameout line the air jet to fuel jet velocity ratio is 2.13 for all three air mass flow rate conditions. As shown and explained in greater detail in Chapter VII, there is a distinct difference in the fuel locations and flow patterns behind the stabilizing steps at a velocity ratio of 2 than at the lower ratios. At the lower ratios the recirculation behind the step is not strong enough to fully impact the fuel jets and the fuel is beneficially fanned out along the OD wall and mixed with air to enable reactions in the shear layer. This is the behavior within the

combusting region. At a velocity ratio of 2 or greater, the recirculation behind the step is stronger than the fuel jets and thus the fuel is pulled in towards the step face rather than fanned out. This behavior is thought to reduce fuel/air mixing and thus impact the ability to burn at the shear layer. This is the condition at the flameout line and in the flameout region. The exact cause of the flameouts from this behavior is not currently known, but it is evident that the distinct change in behavior and fuel distribution at this ratio is connected.

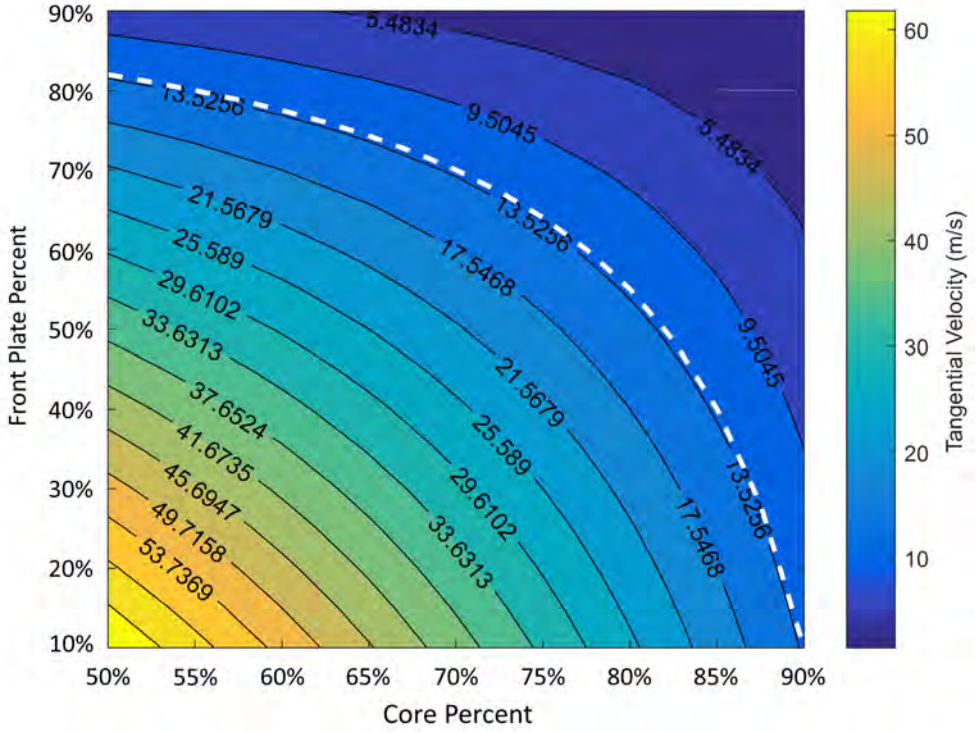


Figure 297. Air jet velocity from the fuel/air steps at $\dot{m}_{in} = 0.060 kg/s$

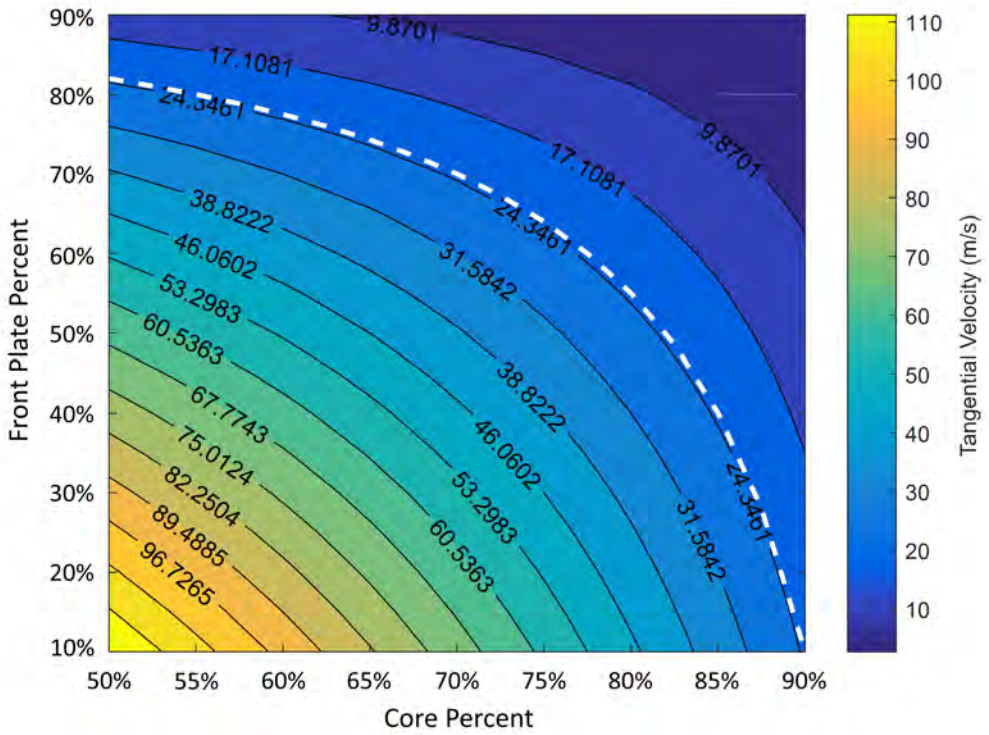


Figure 298. Air jet velocity from the fuel/air steps at $\dot{m}_{in} = 0.108kg/s$

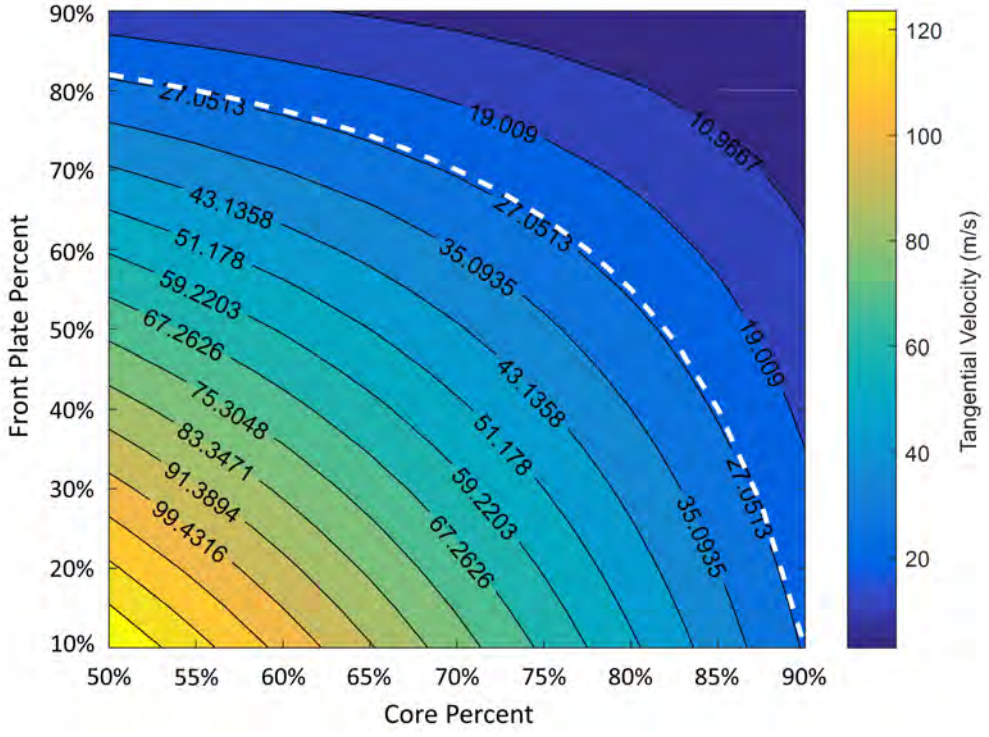


Figure 299. Air jet velocity from the fuel/air steps at $\dot{m}_{in} = 0.120kg/s$

If the understanding of the flameout behavior based on the air and fuel jet velocity ratios is correct, increasing the fuel jet velocity through all steps by decreasing the injector diameter should result in an increased combusting region and larger operating map. Conversely, decreasing the air jet velocity by enlarging the air injection hole diameters should have the same effect. This velocity ratio phenomenon could also be the cause of the increased cavity temperatures seen in Figure 272 when more fuel was pushed to the fuel only step. In that condition the increased fuel flow resulted in higher fuel jet velocities, and thus had a lower velocity ratio and improved fuel distribution.

6.4 Objective 3 Conclusions

The tests performed in support of the diffuser characterization in this objective were successful in demonstrating the ability of the variable geometry diffuser to maintain a constant cavity mass flow rate at both fuel-lean and fuel-rich conditions for a range of total air inlet mass flow rates. Additionally, the diffuser was able to be adjusted to maintain constant core-to-cavity flow rate splits across the same total air inlet mass flow rates. Comparing the Rayleigh losses for all of these test cases to previous UCC studies [174] that used independent core and cavity air supplies produced comparable aerodynamic and Rayleigh losses. This result indicates the diffuser is controlling the flow split without introducing additional system losses. Comparing the peak total pressure loss in the UCC of 5.51% to a traditional combustor which features a typical loss of 8.7% [71], including the compressor exit guide vanes and turbine inlet guide vanes since they are also integral to the UCC, shows a pressure loss reduction of 36% for the UCC system.

In the test sequence that maintained a constant cavity mass flow rate with the Baseline combustor, the average cavity temperature, velocity, and combustion frequency response remained reasonably constant at the fuel-lean conditions. However,

these same cavity properties were not as consistent at the fuel-rich condition. The frequency response at the fuel-rich condition was also found to match the frequency obtained by calculating the number of times a fluid particle could travel around the combustor annulus at the cavity fluid bulk velocity. This result indicates that there may be a rotating flame front that travels around the annulus at fuel rich conditions with a cavity mass flow rate split greater than 30%. The 0.12 kg/s total inlet flow rate case at $\Phi = 1.1$ and a core-to-cavity split of 74/26 achieved a 0.005 kg/s lower cavity mass flow rate compared to the constant mass flow rate cases, but exhibited behavior that it was trending toward this same result.

When a constant core-to-cavity mass flow rate split of 74/26 was tested at fuel-lean and fuel-rich conditions in the Baseline combustor different trends were observed. For the fuel-lean cases the average cavity velocity, frequency, and Rayleigh losses increased with increasing total inlet mass flow rate. The exit temperature profiles for these cases were similar to each other but the size of the higher temperature contour islands were larger in the higher total inlet mass flow rate cases due to the higher cavity temperatures. At fuel-rich conditions the cavity temperature and velocity, and system Rayleigh losses, initially increased to a peak at the 0.108 kg/s total inlet flow rate case, then decreased with increasing total inlet mass flow rate. The reduction of these values was due to the geometry of the fuel injectors and the additional fuel present in these rich cases. The added fuel created a stronger jet which increased the shear force between the fuel jets and the bulk cavity flow and allowed fuel to exit the cavity without reacting. Due to the reduction in average cavity temperatures and velocities, the size and intensity of the elevated temperature contours on the exit plane decreased for increasing total inlet mass flow rate. The frequency response of these fuel-rich cases showed a decrease in both frequency and amplitude with increasing total inlet mass flow rate.

Computational and experimental testing of the 6-Step Ring showed that when air and fuel were injected from every step, there was a lack of recirculation behind the step, and thus a lack of flameholders in the cavity. PIV testing was performed to confirm the computational bulk tangential velocities were accurate and that the cause of the flameouts was in fact due to a loss of cavity flameholders and not an increase in centrifugal loading beyond the stable combustion region. Testing with the 6-Step Ring at an off-design condition that only flowed 1% of the cavity air through the step air injectors demonstrated stable performance. The benefit of back wall fuel injection to cavity and exit plane temperatures was demonstrated with this configuration.

The 12-Step Ring, developed in response to the performance of the 6-Step Ring, introduced additional stabilizing steps to the OD wall to add flameholders back to the cavity. The previous design point of a 74/26 core-to-cavity split with a 50/50 front wall-to-outer ring cavity air split was tested computationally and demonstrated a significant improvement in centrifugal loading compared to the Baseline combustor. However, this operating condition did not burn during experimental testing. The combustor performance was improved at conditions with a slower tangential velocity, and burned the best at centrifugal loadings of $18g_e$ - $77g_e$. Even with the reduction of centrifugal loading compared to the Baseline combustor, the 12-Step combustor demonstrated a significantly wider operating range, up to and including cavity equivalence ratios of 3.60.

Operating maps were created at three total air mass flow rates with four levels of back wall fuel injection percentage from 0 - 30%. These maps demonstrated control over the UCC performance through the use of the variable diffuser to produce varying flow splits. In future versions of the UCC an engine controller could be used to manipulate the flow splits to optimize combustor performance in accordance with these operating maps at all throttle settings.

Changes in global equivalence ratio and fuel distribution within the 12-Step combustor were shown to have little to no impact on the size of the operating map. In many cases these changes caused increases in the instability of previously combusting points in the operating regions of the maps. The flameout boundary line was found to consistently occur across all three total air flow rates at a step air jet velocity to fuel jet velocity ratio of 2.13. The behavior and flow pattern at this transition point is described in detail in Chapter VII. If the understanding of this flameout behavior is correct, the combusting region of the operating maps could be enlarged by a reduction of the fuel injector diameters. The smaller injectors would result in higher fuel jet velocities and lower velocity ratios, where combusting behavior was previously demonstrated.

Across all of the fuel injection schemes tested, the air mass flow rate split between the core and circumferential cavity had a distinct impact on the cavity flow and combustion properties. It was found that cavity temperature and velocity behaviors could be replicated by different total air mass flow rate cases by changing the core-to-cavity flow split to direct the same flow rate of air and fuel to the cavity in both cases. Additionally, the operating maps generated in the 12-Step Ring analysis highlighted how variations in the air and fuel balance throughout the combustor changed the temperature, velocity, and acoustics in the cavity. Having fine control over these distributions means the combustor is tunable to optimize performance for the given total flow condition and adapt to environmental changes day to day. The operating maps also showed that the 12-Step Ring maximum cavity temperatures were achieved at the lowest tangential velocities. This result may indicate that there is more of a benefit from the residence time increase due to the UCC circumferential flow path then from a centrifugally loaded combustion enhancement.

VII. Fluidic Oscillator Fuel Injectors

The fluidic oscillator research discussed in this chapter stemmed from the fuel injector research in Objective 3. This research is not its own objective, but was investigated as a possible alternative for fuel injection to the circumferential cavity

In 2017 Hossain et al. [101] published the results of a study that used fluidic oscillators for film-cooling. The oscillating jet of coolant from the surface mounted hole enabled better coverage than just using a typical shaped coolant hole. The low-profile shape of the oscillator device, as shown in Figure 99 in Section 2.6, and the ability to direct a jet of gas in a variable direction was appealing for fuel distribution. Investigation into fluidic oscillators occurred in conjunction with the fuel injection research presented in Objective 3 as that study was transitioning to the 12-Step Ring analysis. The low-profile geometry of the oscillators would allow them to fit under the air injectors in each step with only a slight increase in step height. If fluidic oscillators were used in place of the straight parallel jets shown in Figures 254 and 266 for the 6- and 12-Step Rings, respectively, there would be less reliance on the recirculation in the step to distribute the fuel as the jets could direct fuel from the forward cavity wall to the aft cavity wall while sweeping in between.

7.1 Oscillator Designs and Computational Analysis

The single oscillator design used in the present research is a slight variation of the wall-attachment type device used by Hossain et al. [101] in 2017 and originally patented by Stouffer [100] in 1979. Within the present study the oscillators went through several iterations with each modification based on the findings of the previous result. Computational analysis was used for this initial qualitative comparison, with the intent of manufacturing the final designs for use in a quantitative experimental analysis. The Version 1 oscillator was modeled to match the shape from published

results from Hossain et al. [101] and is shown in Figure 300. Applying the same geometry relationship to the oscillator as shown in Figure 99 yielded a throat width (W_t) of 1.99 mm and a throat height (H_t) of 2.08 mm assuming a jet velocity of 15 m/s for an oscillating gas flow rate of 1.25 x 10^{-4} kg/s per step. The oscillating gas was propane since this study was used to determine the effectiveness of the oscillators to distribute fuel in the UCC. The specified propane flow rate equates to an equivalence ratio of 0.72 at a 0.108 kg/s total air flow rate in the AFIT UCC rig.

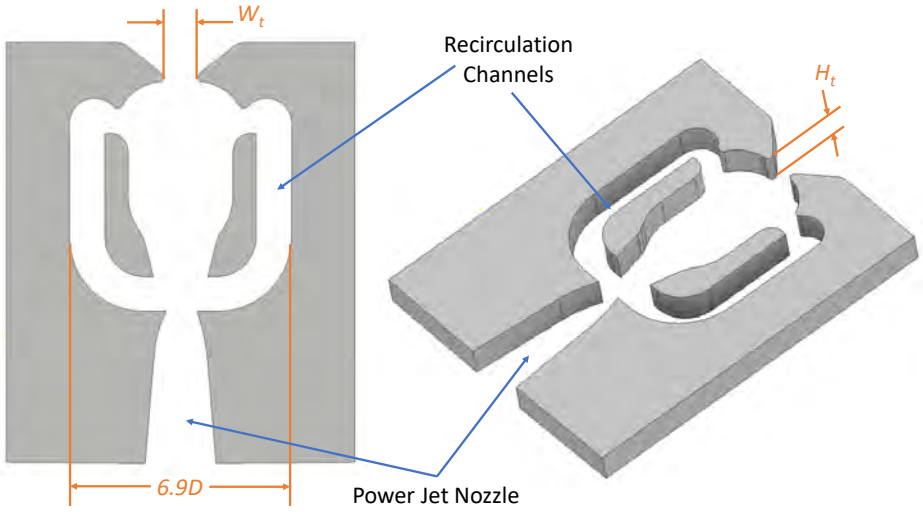


Figure 300. Fluidic oscillator Version 1

A non-reacting two-dimensional pressure-based transient computational analysis was performed in FLUENT on the V1 oscillator using propane as the oscillating gas injecting into air. To enable multi-species analysis the species transport model was enabled using only propane and air. The solution settings specified a coupled pressure-velocity solution scheme with pressure set to "standard", energy and turbulent properties set to first order, with all other properties set to second order. Based on the throat height, mass flow rate, and power jet inlet width shown in Figure 300, the inlet velocity was found to be 6.5 m/s and was used in a velocity inlet boundary

condition at the power jet entrance. The k-ω SST turbulence model was used with a grid that enabled a y^+ of one or better at the wall. The transient time step was set at 0.0001 seconds. A grid independence check was not performed as the computational results were only used for qualitative comparisons. As shown in Figure 301 the oscillation angle reached 52° from the jet edge based on instantaneous results. This value was within 5° of the time-averaged sweep angle of 47° to the edges of the jet reported by Hossain et al. [101]. Since these were wall attached flows there is some dependence on the fluid properties. The use of propane in the present study compared to air used by Hossain et al. [101] could be a cause for the slight deviation. Variations in oscillations with time could also contribution to the deviation. Either way the predicted properties matched well to experimental data and validated the grid and the process.

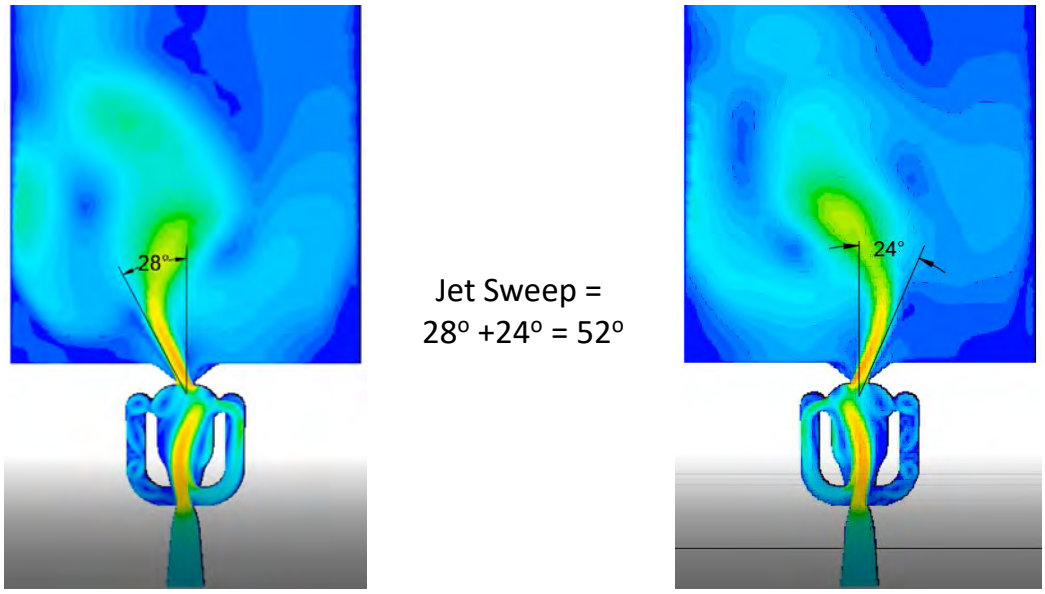


Figure 301. Fluidic oscillator Version 1 2D transient results showing the jet at maximum travel

After observing the transient flow behavior in the oscillator it was determined that slight modifications to the curvature of the dome inside of the throat, spacing of the central islands, curvature of the exit outside of the throat, and width to length

variations could improve the ability of the fluid to remain attached to the walls and thus improve the overall oscillation coverage. The modifications, referred to as Version 2, are shown as the red outline in Figure 302 compared to the Version 1 outline in black. When scaled to the same throat dimensions as V1 and run in a 2D transient CFD study the results indicated an increase in jet sweep angle to 68° at the outer jet edges as shown in Figure 303, with the sweep angle as measured at the jet centerline reaching 56 degrees of oscillation.

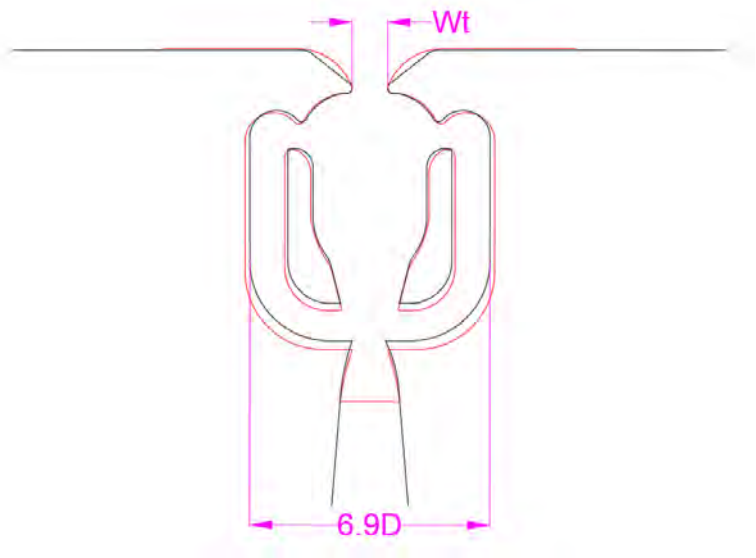
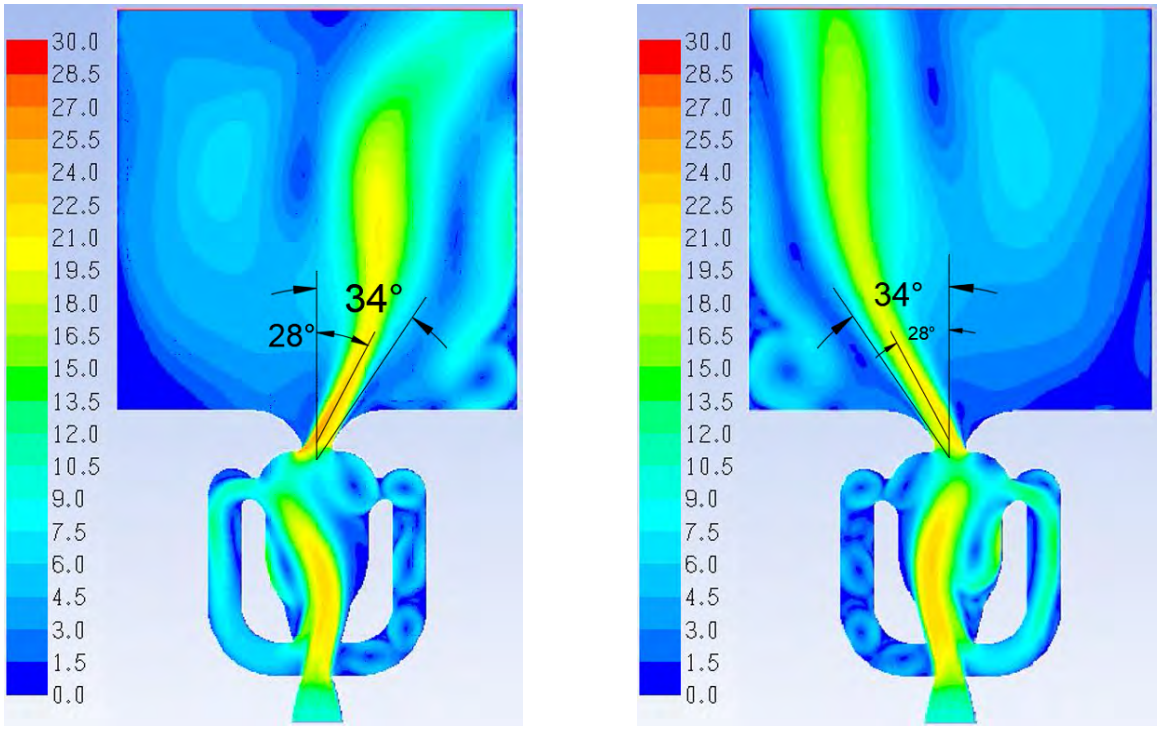


Figure 302. Fluidic oscillator Version 2 shown in red compared to the Version 1 oscillator in black

Seeing how the oscillators behaved and how the feedback loops controlled the oscillation, two double linked oscillator variations were created that shared the feedback loops in different ways to try and create exiting jets that were in-phase in one, and out-of phase in the other. Figure 304 shows these two variations named V2 Double and V3 Double. The V2 Double was created by taking two V2 oscillators and overlapping the feedback loop and then smoothing the lines that joined the two oscillators. V3 received a new variant designation as the central islands along the join line were modified to attempt to have the fluid in the feedback loop criss-cross between

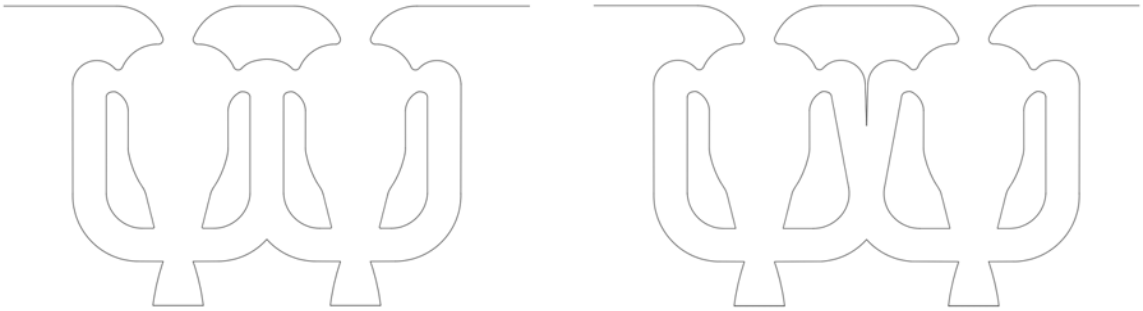


(a) Left Extreme (b) Right Extreme

Figure 303. Contours of velocity showing V2 Single oscillators at sweep extremes

oscillators. The size of the oscillators was reduced to fit the double oscillators in the same width as the single oscillators. The fuel flow rate that was provided to the single oscillator was split between the inlets of the linked oscillators. To maintain the same jet velocity through each of the two linked oscillators compared to the single oscillator required the throat width (W_t) to be reduced to 1.41 mm and the throat height (H_t) to be reduced to 1.47 mm. For a 2D analysis the linked oscillator inlet velocities were specified at 9.26 m/s. This inlet velocity increase from Version 1 was due to a reduction in the inlet area resulting from shortening the power nozzle, but the change resulted in the same mass flow rates. These measurements applied to the V2 and V3 Double oscillators.

The 2D computational results of the linked oscillators showed that the V2 Double produced in-phase motion with the jets sweeping back and forth like windshield

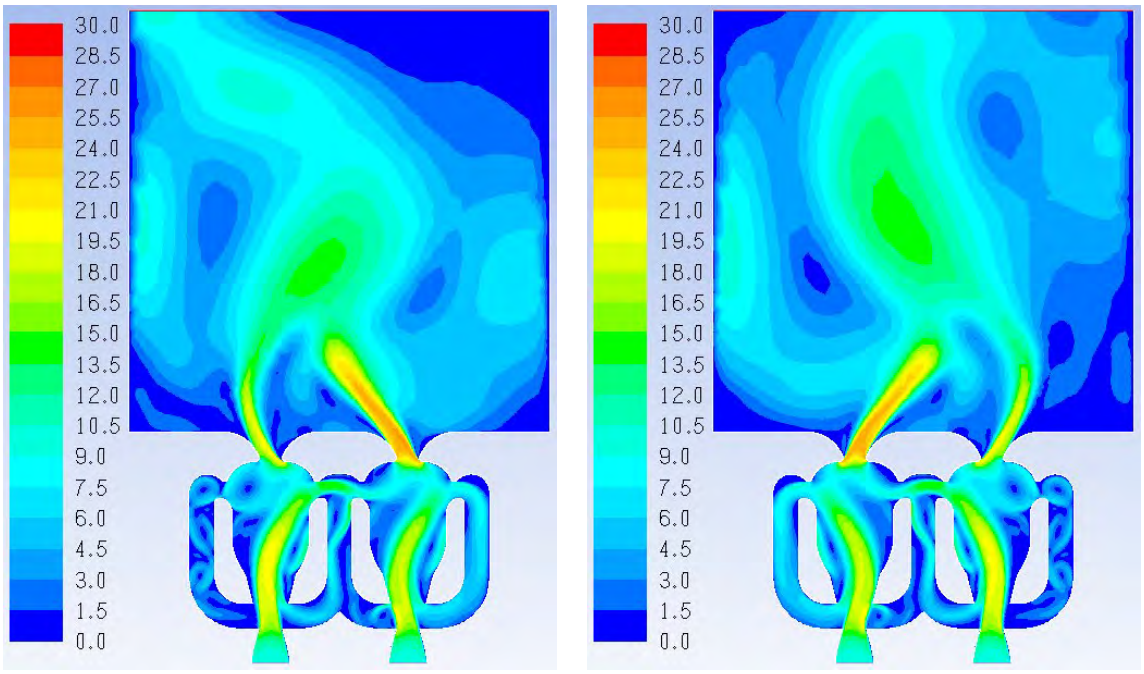


(a) V2 Double (b) V3 Double

Figure 304. Linked pairs of oscillators

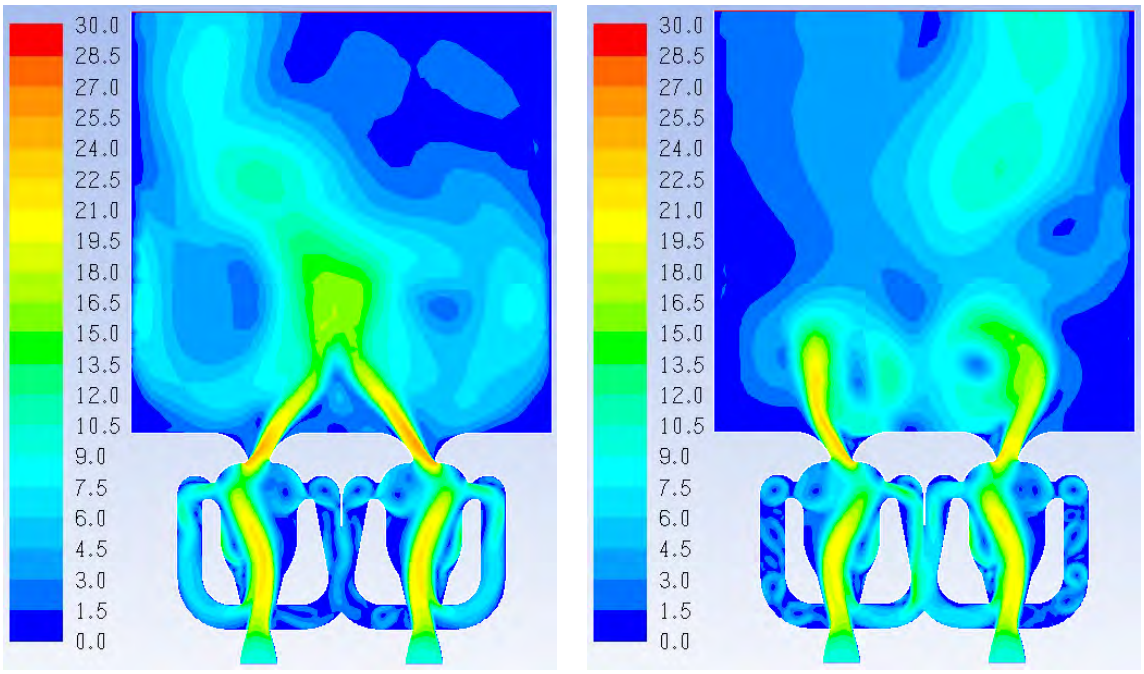
wipers, and V3 Double produced out-of-phase motion with the jets touching at the center and then moving apart. These results are shown in Figures 305 and 306 for the V2 Double and V3 Double results, respectively. The V2 Double oscillator didn't direct much fluid down the center feedback loop. Instead the jets moved with a slight delay with one trailing the other due to fluid passing directly across the top of the central feedback channel and pushing the tops of the interior jets back and forth. Due to this behavior one jet was always stronger than the other and demonstrated a higher velocity. The V3 Double did use the central feedback channel but did not pass fluid back and forth between the oscillators across this channel. Instead the fluid that entered the channel was split evenly to act on both oscillators together which caused the out-of-phase motion. This uniform behavior resulted in exiting jets that were evenly matched in strength and jet velocity.

Due to the very short height of these oscillators, a three-dimensional analysis was conducted on the V2 Single, V2 Double, and V3 Double to ensure that the addition of top and bottom wall effects would not impact the oscillation angles and overall oscillation behavior. A representative domain is shown in Figure 307 for the V2 Single oscillator. This domain was designed to install an oscillator in the fuel injector position in the 12-Step Ring. Domain inlets for a bulk flow velocity below the step



(a) Left Extreme (b) Right Extreme

Figure 305. Contours of velocity showing V2 Double oscillators at sweep extremes



(a) Together (b) Apart

Figure 306. Contours of velocity showing V3 Double oscillators at sweep extremes

and step air injectors were included. To observe the behavior of the oscillator without an effect from the recirculation behind the step the bulk flow velocity below the step was only set to 5 m/s with 0 kg/s air flow rate through the step air inlets. The mass flow rate of propane through the oscillator was set to 1.25 x 10^{-4} kg/s as specified earlier. All other computational conditions remained the same as the 2D analysis.

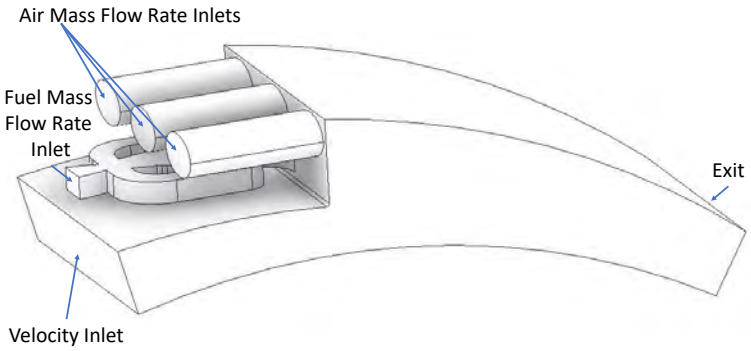
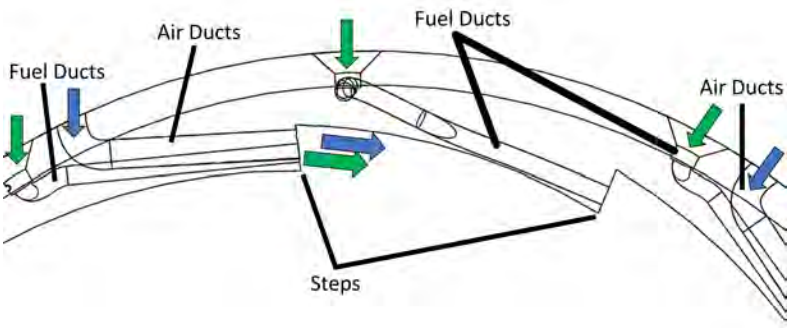


Figure 307. Representative domain for 3D computational analysis

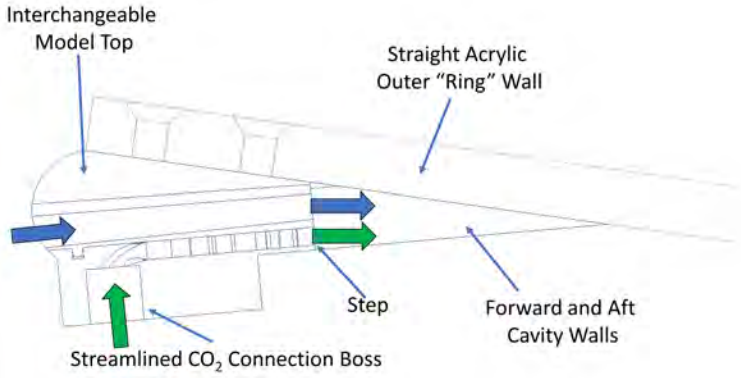
Using the 3D domains the computations were run for the V2 Single, V2 Double, and V3 Double and resulted in oscillations angles within 1° of the 2D results for all cases. In addition to the angles, the general flow behavior in each of the oscillators remained the same. Clearly the addition of the top and bottom oscillator walls did not have an impact in the exiting jet oscillation behavior.

7.2 Experimental Methodology

The experimental models for this analysis were sized and designed to act like the steps in the 12-Step Ring. There were several simplifications made to the models including removing curvature of the ring and approximating it with a flat piece of acrylic. These oscillators were viewed using schlieren imaging and the flat acrylic allowed for an undistorted image. Figure 308 shows a comparison of the 12-Step Ring to the squared off cross-section of the oscillator model used to approximate a single step.



(a) 12-Step Ring



(b) Oscillator Model

Figure 308. Comparison of the oscillator model to the 12-Step Ring

As labeled in Figure 308b, the models were made as two pieces, plus the acrylic sheet, with two interchangeable upper model options as shown in more detail in Figure 309. As shown in Figure 308a there were two types of steps that included fuel and air injection in one, and fuel only in the other. These conditions are each represented in one of the two model upper sections. In order to replicate the flow patterns below and behind the backward-facing steps this test series was conducted in a wind tunnel. Carbon dioxide (CO_2) gas was substituted for propane during testing because they have a similar density and CO_2 is inert. CO_2 was provided to the model from a mass flow controller and exhausted through the injection scheme under test. The CO_2 was introduced to the model base through a streamlined boss. A 1/16-27 NPT Swagelok fitting was installed into the boss to allow standard pneumatic supply lines

to connect the model to the mass flow controller. Air was not provided to the model from a mass flow controller to replicate the flow from a fuel and air step, but rather the interchangeable model upper component for this variation included three holes that allowed air from the flowing wind tunnel freestream to pass through the model and inject from the air injection holes as shown in Figure 309.

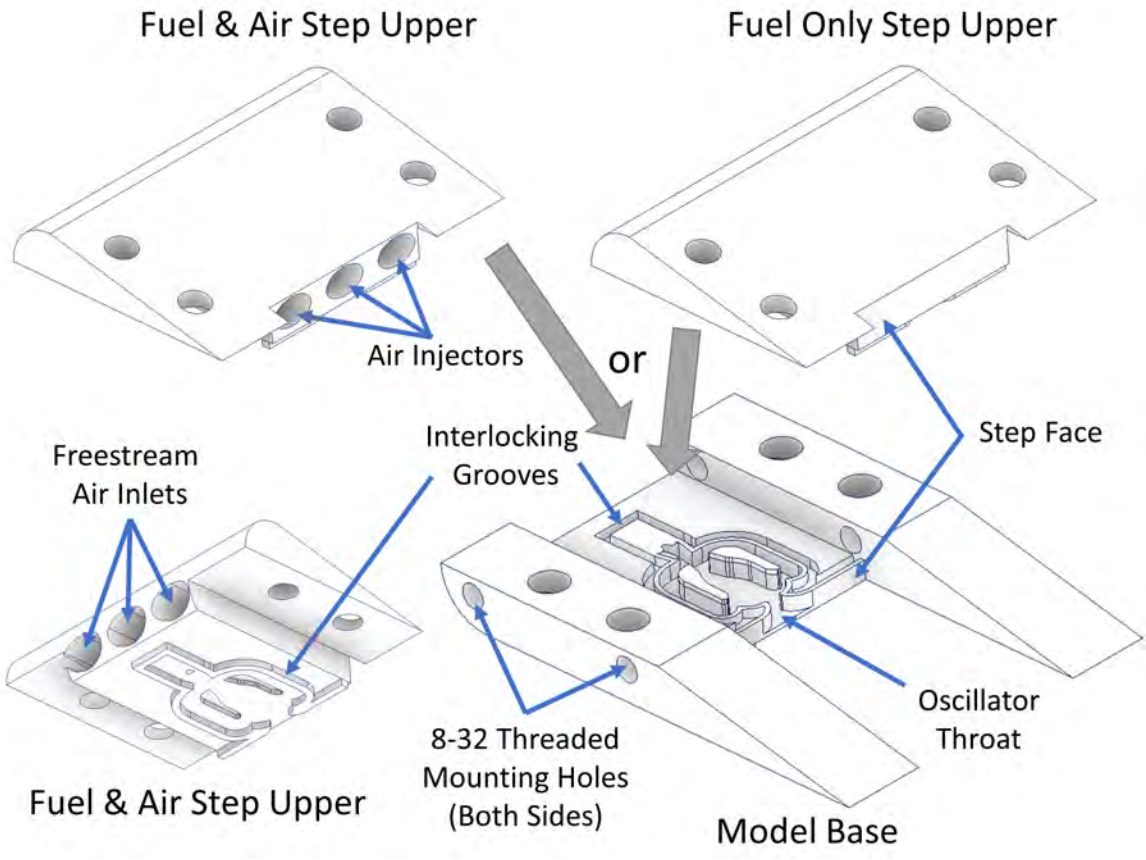


Figure 309. Interchangeable model upper halves shown for the V2 Single oscillator

Figure 310 shows the bases of the five types of models tested. All bases were identically sized with a 2.54 cm width step face to match the 12-Step Ring and the oscillator throat dimensions matched those described above as analyzed in CFD. The model bases that were tested included the V2 Single, V2 Double linked, and V3 Double which all performed well in CFD. Also manufactured for experimental testing were the baseline non-oscillating parallel jets that were used in the 12-Step Ring in

Chapter VI, and a V2 Double oscillator that was the same scale as the double linked oscillator, but without the link so each oscillator was free to move on its own.

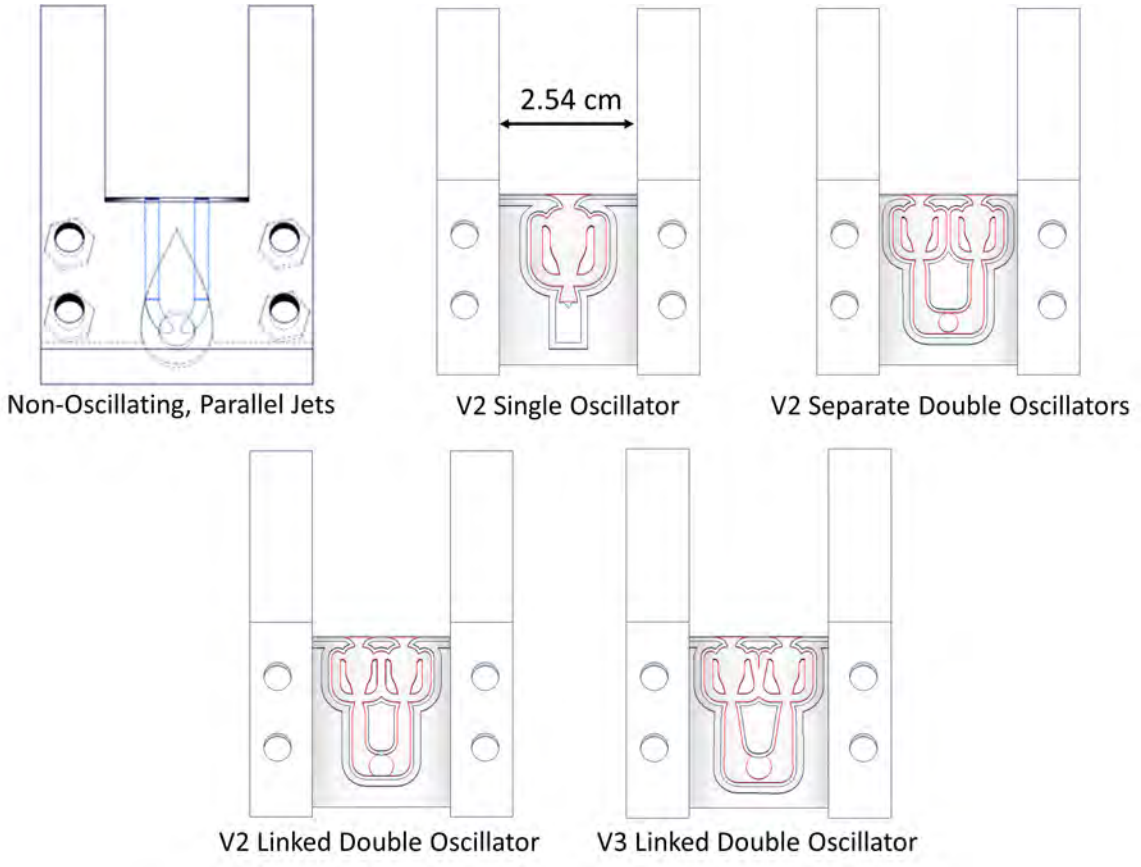


Figure 310. Oscillators printed into the model base

The models were 3D printed in VeroClear-RDG810 plastic. The first set of models used for proof of concept testing did not include the interlocking grooves and were found to leak CO_2 along the seam between the upper and lower model halves at higher flow rates. The updated models represented in Figure 309 incorporated interlocking grooves to prevent leaks. Since the interlocking grooves were matched to a specific oscillator type, custom uppers were made to mate to each type of base. Additionally, two sets of each base were printed to allow each type of model upper component to be epoxied to the base to permanently seal the model and further eliminate leaks. It would seem easier to just print the model as a single piece, however, they were

printed in two halves to ensure all the printer support gel was removed from the internal oscillator passages and then assembled. The only models that were printed as a single piece were the baseline non-oscillating parallel jets representing the fuel injectors from the 12-Step Ring as those passages were simple and easy to clean out. The CAD models of these components were shown in Figure 310 because the translucent property of the VeroClear-RDG810 makes it difficult to see details in photos of the physical hardware.

An initial set of models were manufactured that looked like those shown in Figures 309 and 310 but without the interlocking grooves. These models were installed in the dual-field-lens schlieren setup shown in Figure 311 for proof of concept testing. This schlieren setup used a Guard Dog Solaire LED flashlight as the continuous light source, a light condition lens setup, lenses on both sides of the test section, a knife edge, and the Phantom v16 high-speed camera with an f/1.8, 50 mm lens. The light conditioning setup included a 300 mm focal lens plano convex lens with a 5.08 cm diameter in light lens Position 1, and a 75 mm focal length plano convex lens with a 5.08 cm diameter in light lens Position 2. These lenses were used to try and produce a true point light source at the aperture. Imaging Lens 1 was biconvex with a 100 mm diameter and a 150 mm focal length. Imaging Lens 2 was also biconvex with a 100 mm diameter, but with a 250 mm focal length. Several flow rates of CO_2 were pushed through the V2 Single and V2 Double linked oscillators. Oscillations were observed, but the high-speed video image was of poor quality due to the low-tech light source, and aberrations in the lenses. The images were good enough to show the oscillators were working and that the oscillation angles matched very closely to CFD results. Based on the success of these proof of concept tests, arrangements were made to test in the small Discovery wind tunnel at the Air Force Research Laboratory.

The AFRL wind tunnel facility allowed for schlieren imaging of the models while

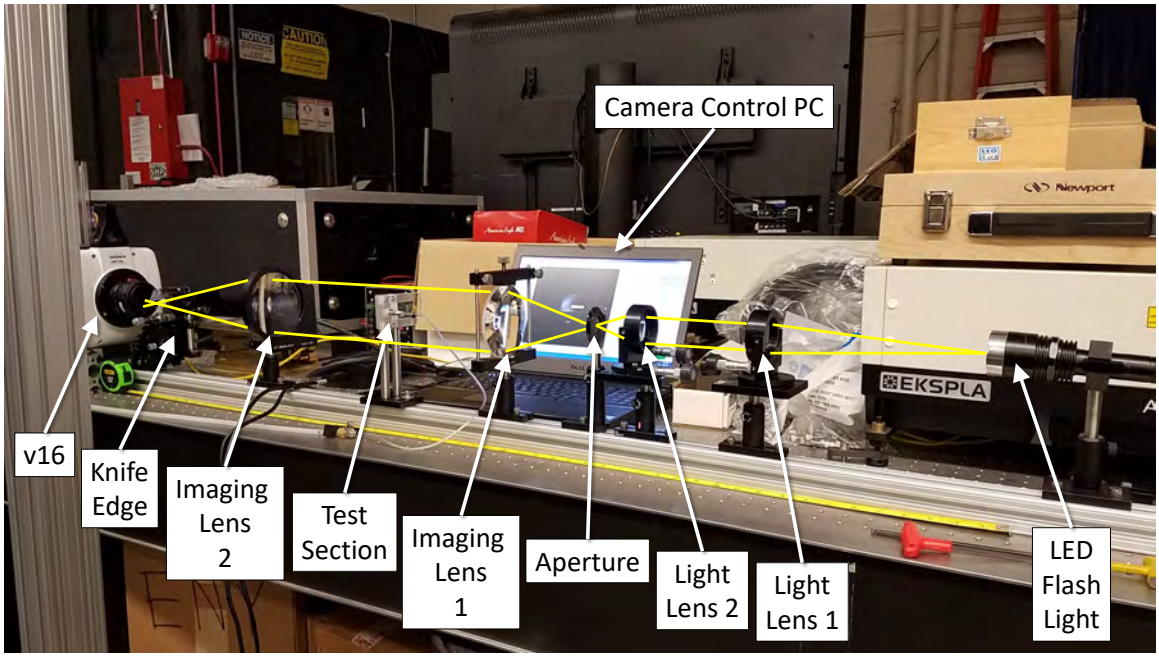


Figure 311. Proof of concept schlieren setup in the AFIT COAL laboratory with light ray paths shown

inside the wind tunnel due to acrylic walls through the test section. A Z-type schlieren setup was used with the wind tunnel as shown in Figure 312. This setup provided much higher image contrast and clarity compared to the initial proof of concept setup. A safety review process was required to allow a tank of CO_2 to be brought to the AFRL facility and discharged during testing. Channel 2 of a portable MKS Type 247 mass flow controller input box (S/N 016085617) and 10,000 SCCM range controller (S/N 016076244) was used to manage the flow rate of CO_2 during testing. A CO_2 gas correction factor of 78.0 was dialed into Channel 2 on the back of the MKS Type 247 mass flow controller to ensure the correct flow rate with a fluid that was different than the calibration gas. Computerized control and real-time feedback of the wind tunnel allowed the airflow speed through the test section to be maintained within 0.2 m/s of the specified speed. Testing started with a 24V, 250W bulb in the ORIEL continuous light source. This bulb burned out during the first day of testing and

was replaced with a 12V, 50W bulb that was on hand. The images after the bulb change were darker than the initial images, but clarity was unaffected. Out of the light source the light rays were passed through a focusing lens and then an aperture to create a point light source. The Phantom v16 was configured with a Nikon 180 mm lens with an f/2.8 aperture. High-speed image exposure duration was specified at 2 μs with a frame rate of 10,000 frames per second.

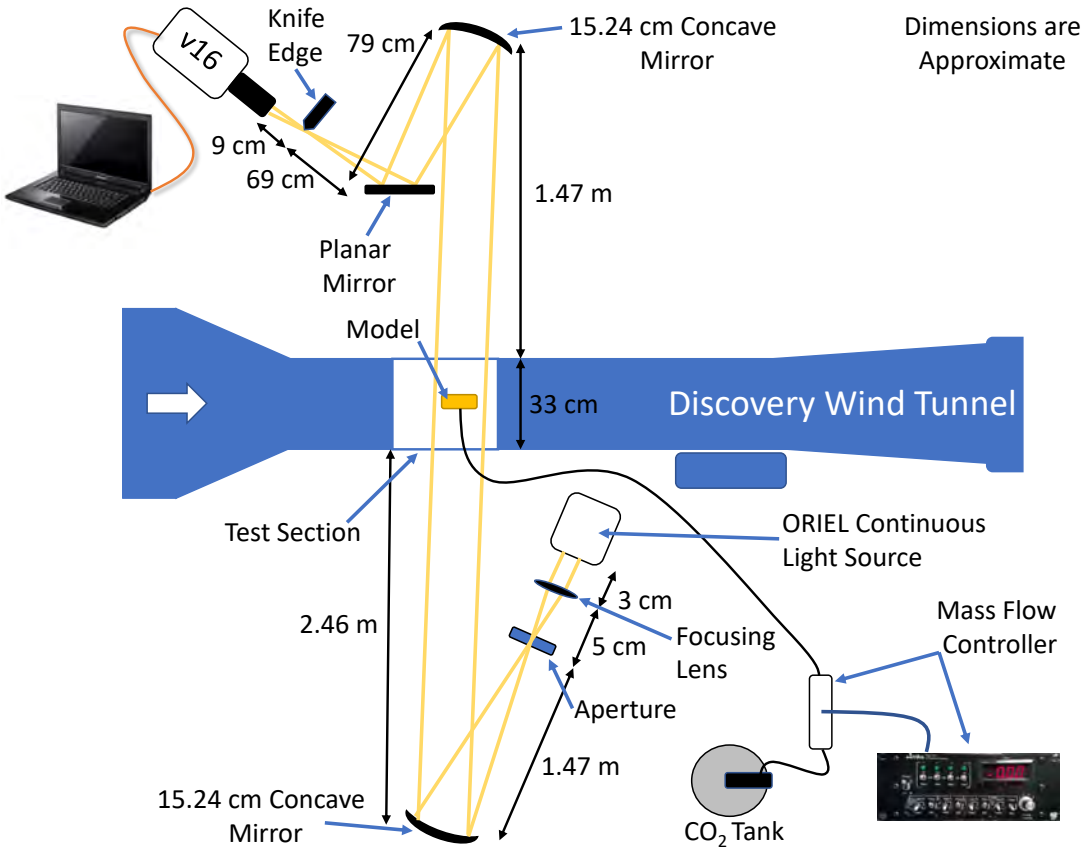


Figure 312. Z-type schlieren setup in the AFRL Discovery wind tunnel facility with light ray paths shown

Figure 313 shows the non-oscillating parallel jet model installed in the Discovery wind tunnel. The model was mounted to two four inch optics standoffs through the 8-32 threaded holes on the side of the model. The standoffs were mounted to an optics base spaced at 2.54 cm centers using 1/4-20 socket-head cap screws. The model was aligned with the flow and the base was then secured to the floor of the wind tunnel.

The CO_2 supply line was run into the wind tunnel test section through a small hole in the tunnel floor and fitted to the 1/16-27 NPT fitting in the supply boss.

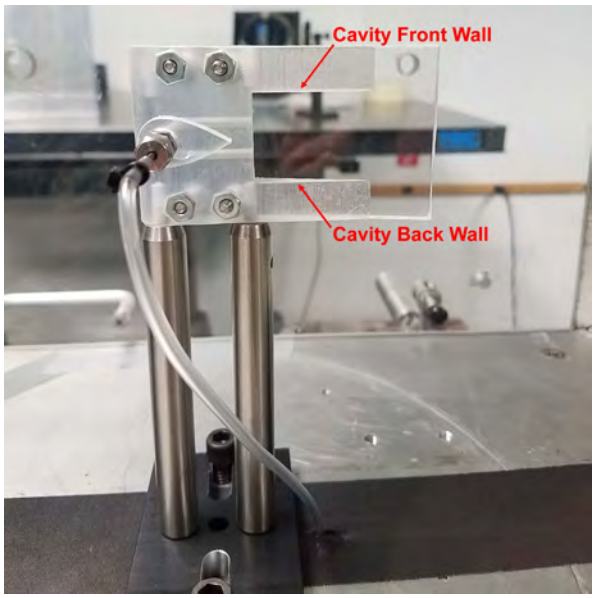


Figure 313. Model installed in wind tunnel

Oscillator frequency measurements were made by manually counting the oscilla-

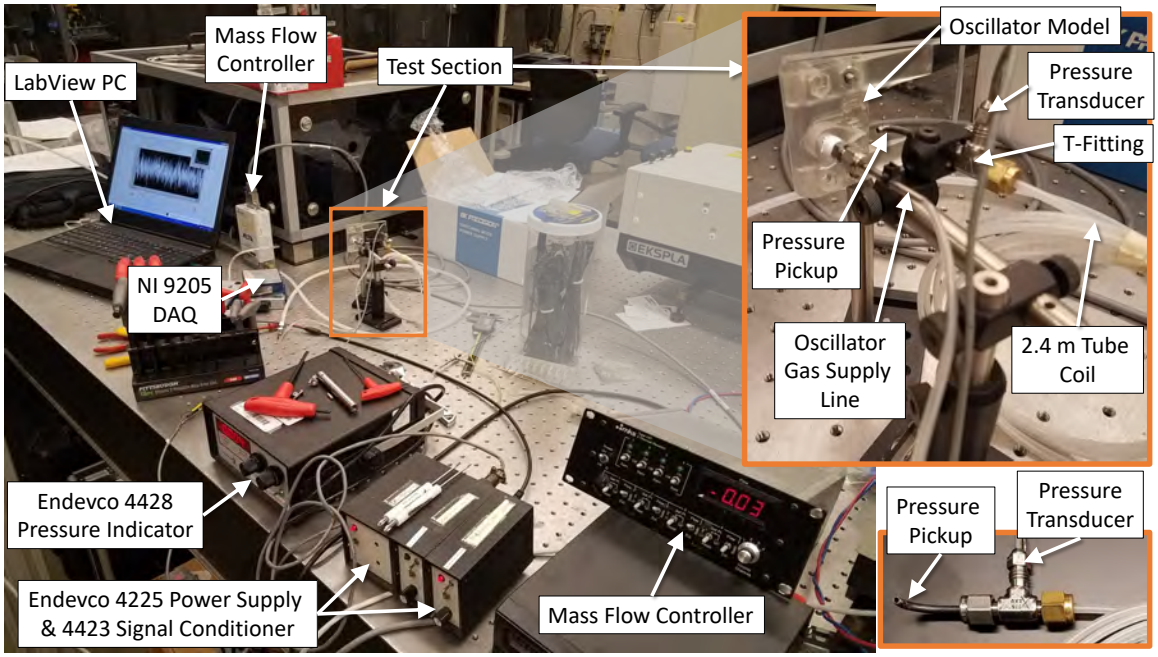


Figure 314. Pressure transducer based frequency calculation setup

tions from high-speed videos, however, the videos saved out 1,500 frames for a total of 0.15 seconds in real-time requiring an extrapolation to up sample the number to samples per second. This method also required an assumption that the frequency didn't vary with time. After the wind tunnel test series were complete, dynamic pressure measurements using a fast response pressure transducer in an infinite tube pressure (ITP) configuration were used to sample and measure the oscillation frequency over a 10 second period for a more accurate measurement. The test setup is shown in Figure 314 with the pressure transducer probe head assembly detailed in the bottom right of the figure. In this setup the oscillator models were mounted on the same optics stands as used in the wind tunnel and positioned on a laser table. The pressure transducer probe head pickup was positioned behind the model's backward-facing step and offset below the oscillator centerline. This positioning ensured the ITP would not be double counting passes of the oscillating jet as it moved past in its cycle. The pressure pickup was made from 3.175 mm diameter stainless steel tubing with an ID of 1.97 mm. It was connected to a standard Swagelok T-fitting that also had the vertical leg of the tee drilled and tapped with a 10-32 thread to allow the pressure transducer to screw in. The pressure transducer was an Endevco 8510B 5 psig differential (S/N PP81). The last leg of the T-fitting was connected to a 2.4 m coil of 3.175 mm OD plastic tubing. The long length of tubing was used to allow air to flow past the pressure transducer, but would damp out oscillations to give a more accurate pressure fluctuation measurement.

The remaining components in Figure 314 were used for amplifying, conditioning, and processing the signal from the pressure transducer. The transducer was connected to an Endevco Model 4428 pressure indicator which provided clean power to the transducer, received the signal back, and had a signal output. The output from the Model 4428 was connected to an Endevco Model 4423 signal conditioner that was

powered by an Endevco Model 4225 power supply. The signal conditioner allowed for enhanced signal gain to be added without distorting the signal. The output from the Model 4423 signal conditioner was connected to a National Instruments 9205 DAQ module to bring the signal into LabView. In LabView the signal was filtered and counted in Hz with the output averaged and recorded at 1 Hz. The LabView data was taken at 1000 Hz. The same MKS Type 247 mass flow controller input box (S/N 016085617) and 10,000 SCCM range controller (S/N 016076244) were used to provide CO_2 to the model at the same conditions used in the wind tunnel testing.

Two test series were accomplished in the wind tunnel with differing goals. The first series tested each of the five oscillators at four CO_2 flow rates and wind tunnel flow speed pairs with three different flow conditions; no wind tunnel flow, the fuel only model upper configuration, and the fuel and air model upper configuration. This sequence was repeated three times for different CO_2 flow rates representing UCC cavity equivalence ratio fuel flows of 0.72, 1.0, and 1.3. Table 45 shows the twelve test points taken with each model at each CO_2 flow rate. This matrix resulted in 180 test points. After observing the results and performance for the models, several test points were omitted during testing resulting in a total of 118 series one high-speed video recordings. This series was designed to observe the oscillator behavior at UCC representative conditions.

The second series only used the baseline non-oscillating parallel jets, the V2 Single oscillator, and the V2 Double linked oscillator. In this series the CO_2 flow rate was fixed and the wind tunnel speed was ramped to observe how the flow patterns change with varying CO_2 and wind tunnel flow rate and velocity ratios. This series was split into two test events. In the first event the CO_2 flow rate was specified at 4.75 SLPM (1.5×10^{-4} kg/s) through all three models which resulted in jet velocities of 8.1 m/s in the baseline non-oscillating parallel jets, and 19.1 m/s in the V2 Single and V2

Table 45. Fluidic oscillator series one test matrix for each model type

Model Config.	**Wind Tunnel Speed** (m/s)	**Φ=0.72 CO_2 Flow Rate** (SLPM)	**Φ=1.0 CO_2 Flow Rate** (SLPM)	**Φ=1.3 CO_2 Flow Rate** (SLPM)
Fuel Only	0	1.92	2.67	3.42
	0	2.83	4.00	5.17
	0	3.42	4.75	6.17
	0	3.83	5.25	6.83
Fuel Only	23	1.92	2.67	3.42
	25	2.83	4.00	5.17
	28	3.42	4.75	6.17
	32	3.83	5.25	6.83
Fuel & Air	23	1.92	2.67	3.42
	25	2.83	4.00	5.17
	28	3.42	4.75	6.17
	32	3.83	5.25	6.83

Double linked oscillators. At this flow rate, wind tunnel speeds of 0, 4, 6, 8, 10, 14, 16, 18, 19, 20, and 24 m/s were tested. In the second test event of series two, an attempt was made to change the flow rates to invert the jet velocities but the mass flow controller limited the maximum flow rate to 7.96 SLPM (2.44 x 10^{-4} kg/s). The flow rate through the V2 Single and V3 Double linked oscillators were 2.08 SLPM (6.40 x 10^{-5} kg/s) and 2.11 SLPM (6.47 x 10^{-5} kg/s), respectively, resulting in jet velocities of 8.4 and 8.5 m/s. The flow rate was set as high as it would go for the baseline non-oscillating parallel jets, which resulted in a flow rate of 7.96 SLPM and a jet velocity of 13.5 m/s, several meters per second below the desired 19.1 m/s velocity. At these flow rates, wind tunnel speeds of 0, 4, 8, 12, 16, 20, and 24 m/s were tested. Between both series two test events a total of 67 high-speed video recordings were captured.

7.3 Experimental Results

The results presented below are broken out by each of the two test series with the final results subsection showing the fluidic oscillator frequencies. The first test series observed the behavior from all five models at UCC representative flow conditions with both upper model components. The second test series used a reduced set of models and varied the wind tunnel speeds with fixed fuel flow rates to observe the differences induced by a fuel jet to freestream velocity ratio. Oscillator results were compared to the non-oscillating parallel jets used as a performance baseline.

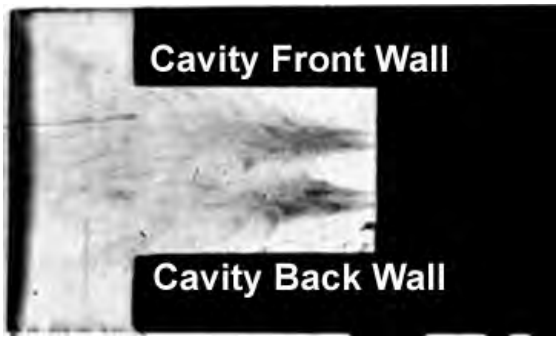
7.3.1 Test Series One.

The results of test series one showed good performance from the V2 Single and V2 Double linked oscillators. The results from the V2 Double separate and V3 Double oscillators indicated minimal oscillations. The results from the baseline, non-oscillating jets are shown first to provide the basis for comparison.

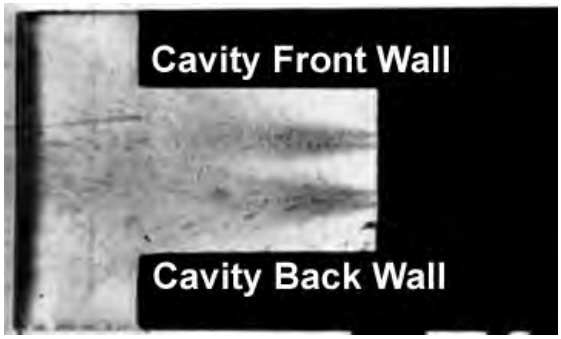
7.3.1.1 Baseline, Non-Oscillating Jets.

Figure 315 shows the time-averaged schlieren results using all 1,500 frames from the high-speed video files with the baseline, non-oscillating model. The top row of images (a, b) show the jet spread pattern at the lowest and highest CO_2 flow rates with the wind tunnel off. The second row of images (c, d) shows the concentrations of CO_2 at these same two flow rates with the wind tunnel flowing at the lowest and highest tested speeds for the fuel only model. The bottom row of images (e, f) show the concentrations of CO_2 at these same two flow rates with the wind tunnel flowing at the lowest and highest tested speeds for the fuel and air injecting model. The effect of the recirculation behind the backward-facing step when the wind tunnel was on (c - f) is very pronounced. While the location of CO_2 injection is visible as the two dark regions pushed up against the step, there is no distinguishable jet and the

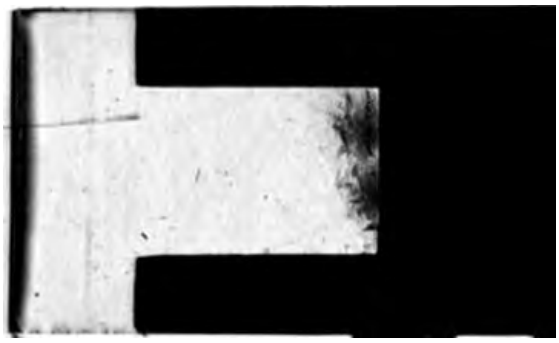
CO_2 appears to cover the majority of the step despite only injecting from two small holes. This distribution is a desirable behavior in a fuel system to ensure coverage across the entire cavity width. The difference between the fuel only step and the air injection step was fairly minor. The concentration of CO_2 appears to be less in the



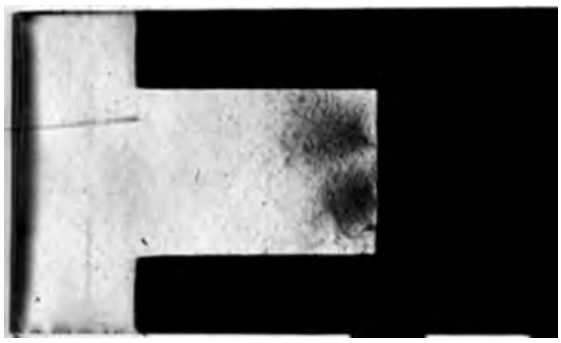
(a) CO_2 = 1.92 SLPM, Tunnel = 0 m/s



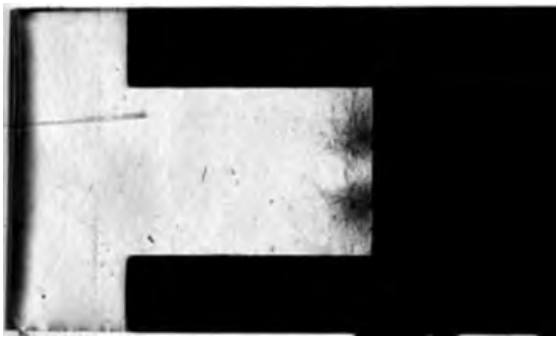
(b) CO_2 = 6.83 SLPM, Tunnel = 0 m/s



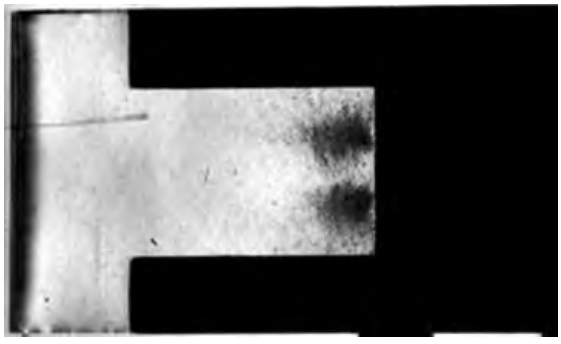
(c) CO_2 = 1.92 SLPM, Tunnel = 23 m/s, fuel only model upper configuration



(d) CO_2 = 6.83 SLPM, Tunnel = 32 m/s, fuel only model upper configuration



(e) CO_2 = 1.92 SLPM, Tunnel = 23 m/s, fuel & air model upper configuration

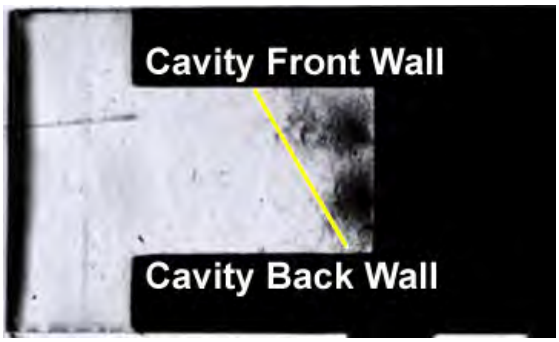


(f) CO_2 = 6.83 SLPM, Tunnel = 32 m/s, fuel & air model upper configuration

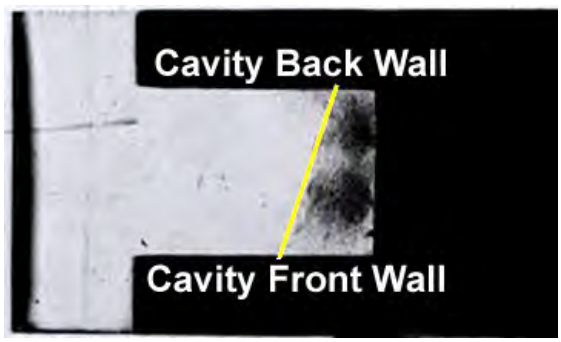
Figure 315. Baseline non-oscillating parallel jets, time-averaged composite images at the lowest and highest CO_2 flow rates and three model and wind tunnel configurations

fuel and air step (e, f) as the CO_2 shadows are slightly less dark. Additionally, there is more symmetry between both injectors in the fuel and air step. In the fuel only step the concentration of CO_2 closer to the cavity front wall is larger and extends out further off the step face.

The skew of CO_2 towards the forward cavity wall is highlighted in Figure 316a by the sloping yellow line at the downstream boundary of the CO_2 concentrations. Based on Figure 315 the amount of skew appears to be related to the flow rate of CO_2, or possibly the strength of the recirculation behind the step with varying wind tunnel flow speeds. To confirm that this skew was a function of flow pattern behind the step and not simply a response to gravity (which was unlikely since CO_2 is heavier than air) the test was repeated with the model installed upside down. As shown in Figure 316b the skew direction shifted when the model was inverted indicating that the offset of the CO_2 concentration was a result of the fluid flow behind the step.



(a) $CO_2 = 4.75$ SLPM, Tunnel = 28 m/s, Model Right Side Up



(b) $CO_2 = 4.75$ SLPM, Tunnel = 28 m/s, Model Up Side Down

Figure 316. Secondary circulation behavior observed with the baseline non-oscillating parallel jets using a time-averaged composite image with the model in its original orientation and flipped over

A normal recirculation behind a backward-facing step exists with an axis of rotation parallel to the step face as shown in the cross-section view at the bottom of Figure 317. However, when fluid was injected into the recirculation pocket behind the step there appeared to be a secondary circulation pattern that developed as shown

in the upper view of Figure 317. This secondary flow pattern would account for the asymmetric CO_2 concentrations around each injector and follows the right-hand rule in terms of the direction of motion of the secondary circulation resulting from the typical recirculation behind a backward-facing step.

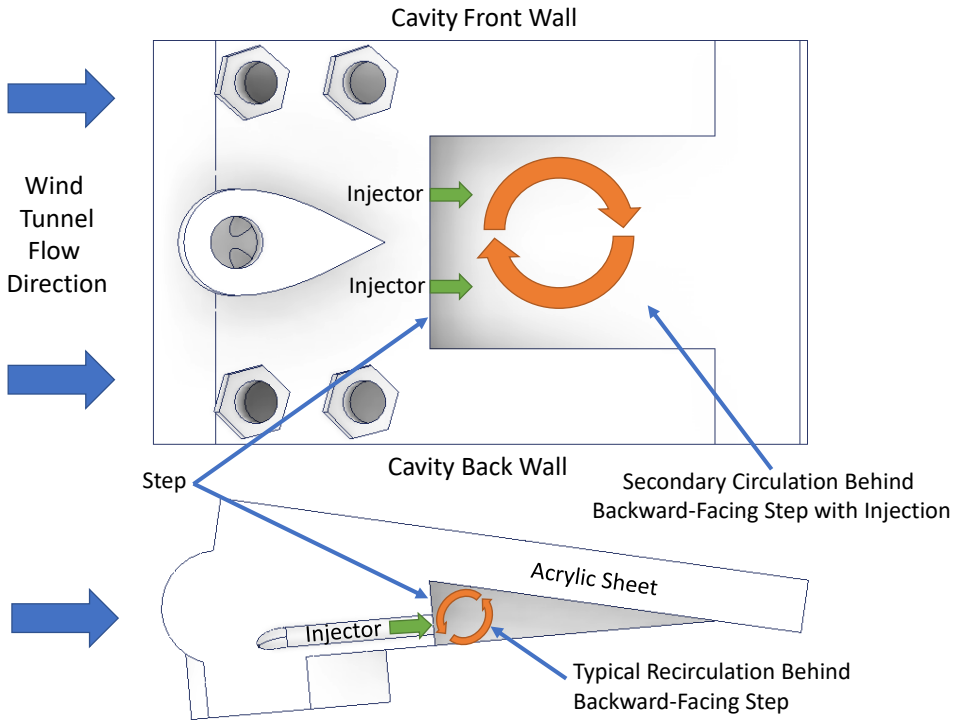
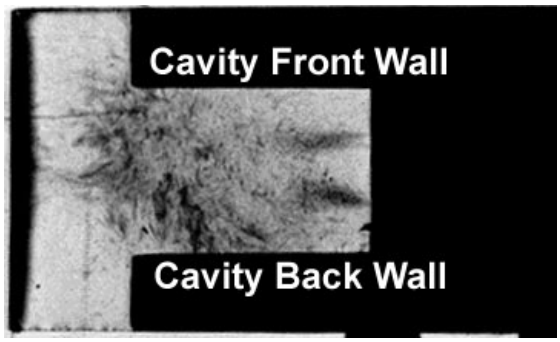


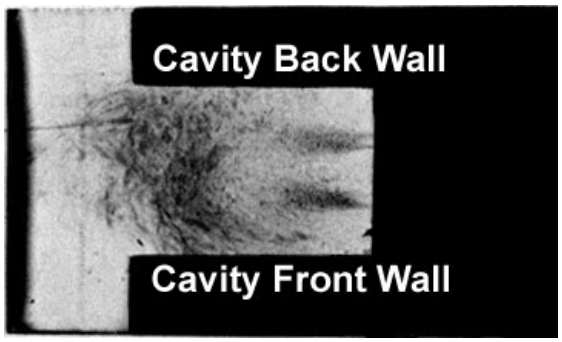
Figure 317. Secondary circulation pattern observed behind backward-facing steps with injection

Figure 318 shows the CO_2 distribution behind the step with a wind tunnel flow speed of 8 m/s. At this lower flow speed the CO_2 distribution looks nearly identical between cases with the model upright and inverted. This result lends further support to the conclusion that the secondary circulation is a result of the typical recirculation behind a backward-facing step. This result also shows that the effect of the primary recirculation on the jet is a function of the CO_2 jet velocity to wind tunnel flow speed. This relationship is better explained in the results of test series two.

Figure 319 shows measurements of the jet spread angle at the lowest and highest



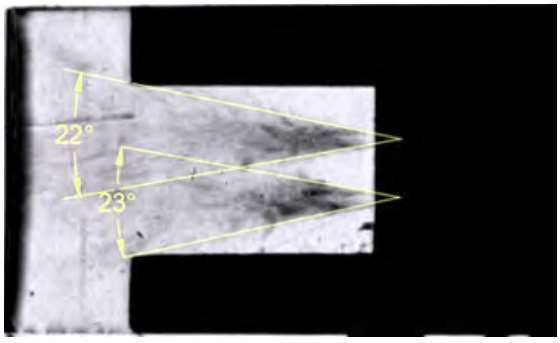
(a) CO_2 = 4.75 SLPM, Tunnel = 8 m/s, Model Right Side Up



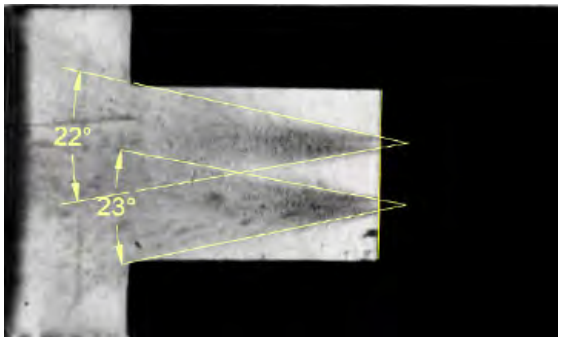
(b) CO_2 = 4.75 SLPM, Tunnel = 8 m/s, Model Up Side Down

Figure 318. No secondary circulation behavior observed at slower wind tunnel speeds

CO_2 flow rates with the wind tunnel off. Fluids theory states that the jet should spread symmetrically at 11.8° from the jet centerline to the edge of the jet, or 23.6° from jet edge to edge starting at a virtual origin [131]. The jets in Figure 319 measured between 20 and 23° from the subjective jet edge to edge. At the true edge of the jet the concentration of CO_2 would be low and thus difficult to identify visually in a schlieren image. Assuming the true jet boundaries are just wider than the measured edges, the experimental results are consistent with theory.



(a) CO_2 = 1.92 SLPM, Tunnel = 0 m/s

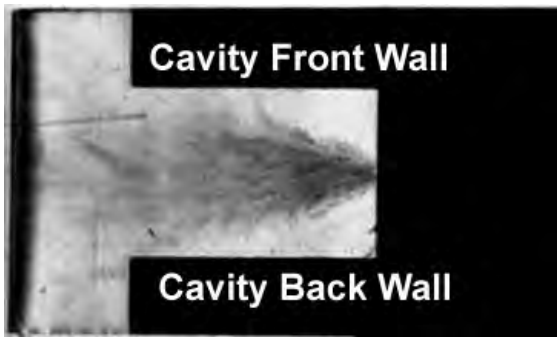


(b) CO_2 = 6.83 SLPM, Tunnel = 0 m/s

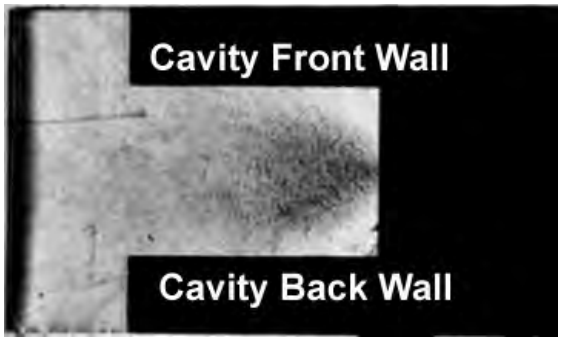
Figure 319. Jet spread angle measurements for the baseline non-oscillating parallel jets using a time-averaged composite image at the lowest and highest CO_2 flow rates with 0 m/s wind tunnel speed

7.3.1.2 V2 Single Oscillator.

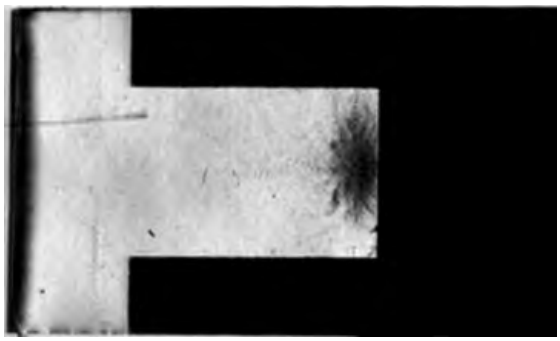
The time-averaged schlieren results using all 1,500 frames from the high-speed video files with the V2 Single oscillator models are shown in Figure 320. The images are arranged in the same order as for the baseline, non-oscillating results and at the



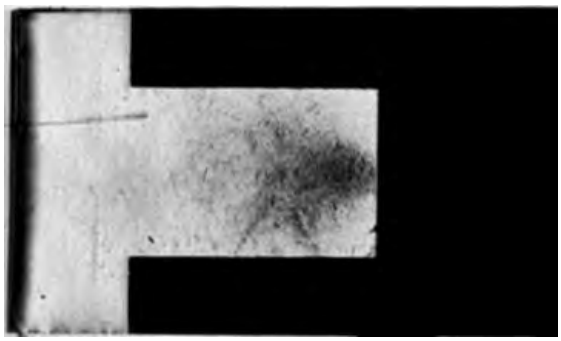
(a) CO_2 = 1.92 SLPM, Tunnel = 0 m/s



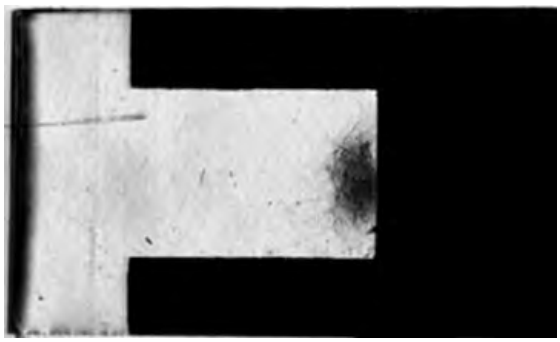
(b) CO_2 = 6.83 SLPM, Tunnel = 0 m/s



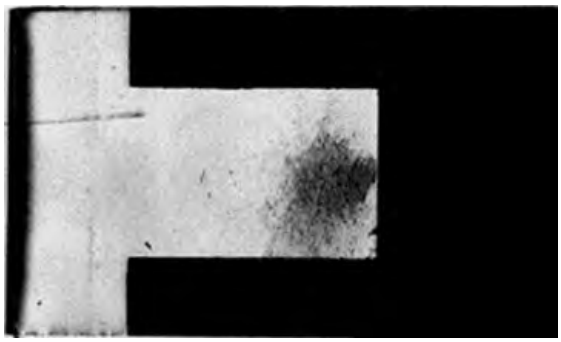
(c) CO_2 = 1.92 SLPM, Tunnel = 23 m/s, fuel only model upper configuration



(d) CO_2 = 6.83 SLPM, Tunnel = 32 m/s, fuel only model upper configuration



(e) CO_2 = 1.92 SLPM, Tunnel = 23 m/s, fuel & air model upper configuration

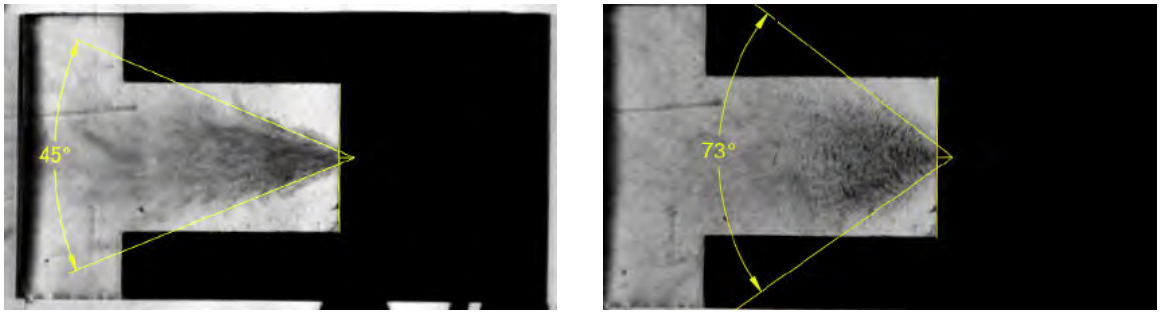


(f) CO_2 = 6.83 SLPM, Tunnel = 32 m/s, fuel & air model upper configuration

Figure 320. V2 Single oscillator, time-averaged composite images at the lowest and highest CO_2 flow rates and three model and wind tunnel configurations

same flow rates. As with the baseline, non-oscillating jets the effect of the recirculation behind the backward-facing step was detrimental to the CO_2 jet flow field. Comparing Figures 320c through f to Figure 315c through f shows many similarities. Aside from the fact that there is a single concentration of CO_2 in Figures 320c through f where there are two parallel concentrations in Figures 315c through f, not much is different. In Figure 320c there is a slight skew of the concentration upward indicating there may be an impact on the flow field from the secondary circulation pattern, however, at the higher flow rate case shown in Figure 320d the results are symmetric. It is possible that since the jet oscillated back and forth, when the jet was pointed toward the cavity back wall it was opposing the secondary circulation and stopped the rotation. Some rotation may have been present in the low flow rate case of Figure 320c because the CO_2 jet was not strong enough to fully oppose the secondary circulation forces.

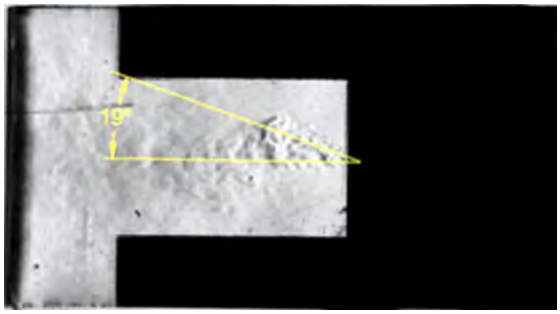
Figure 321 shows the time-averaged oscillation spread angle to the edges of the jets at the lowest and highest CO_2 flow rates with the wind tunnel off. These results show that the coverage angle of the oscillating jets is dependent on the mass flow rate through the oscillator. For an increase of 4.91 SLPM the oscillation angle was increased by 28°. Figure 322 shows the instantaneous jet angles measured to the jet centerline at the lowest and highest CO_2 flow rates. Between these two flow



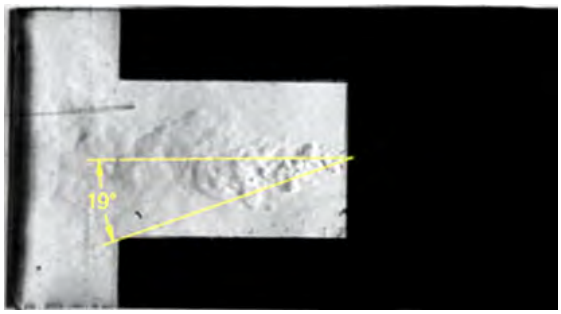
(a) CO_2 = 1.92 SLPM, Tunnel = 0 m/s (b) CO_2 = 6.83 SLPM, Tunnel = 0 m/s

Figure 321. V2 Single oscillator time-averaged composite image at the lowest and highest CO_2 flow rates with 0 m/s wind tunnel speed

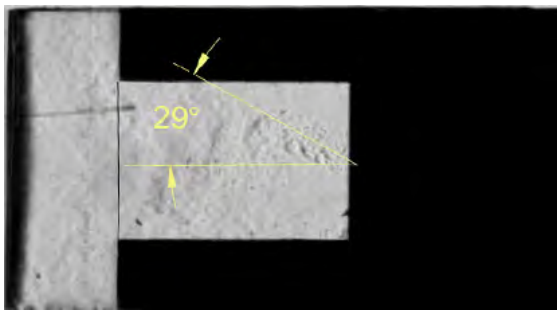
rates the instantaneous angle increased by 10° in each direction. The computational results of the high flow rate case shown in Figures 321c and d predicted a maximum instantaneous spread angle from the oscillator centerline to the jet centerlines to be 28°, or 56° from the extremes of the jet motion; a difference of 1° between the computations and the experimental result.



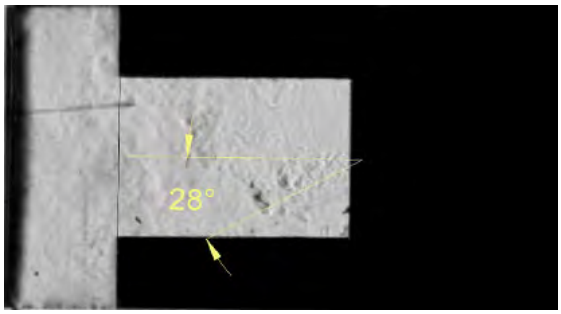
(a) CO_2 = 1.92 SLPM, Tunnel = 0 m/s



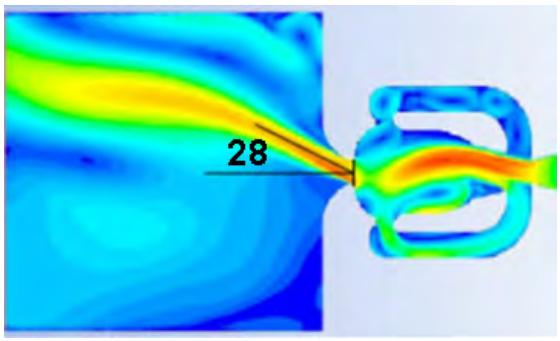
(b) CO_2 = 1.92 SLPM, Tunnel = 0 m/s



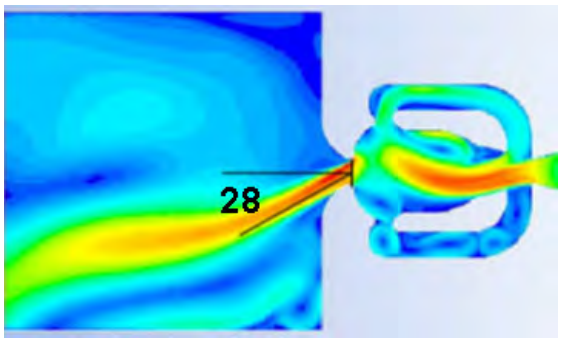
(c) CO_2 = 6.83 SLPM, Tunnel = 0 m/s



(d) CO_2 = 6.83 SLPM, Tunnel = 0 m/s



(e) CO_2 = 6.83 SLPM, Tunnel = 0 m/s, CFD

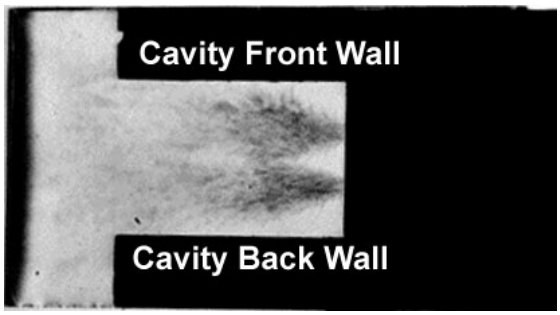


(f) CO_2 = 6.83 SLPM, Tunnel = 0 m/s, CFD

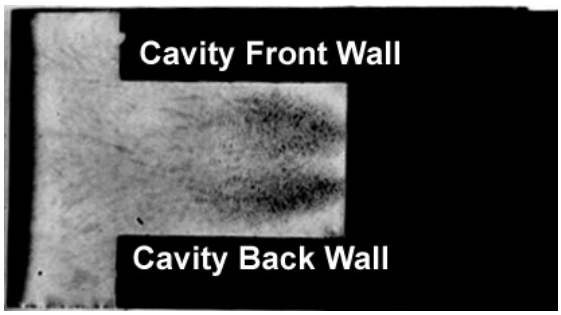
Figure 322. V2 Single oscillator instantaneous maximum oscillation angles measured at the jet centerlines at the lowest and highest CO_2 flow rates with 0 m/s wind tunnel speed

7.3.1.3 V2 Double Linked Oscillator.

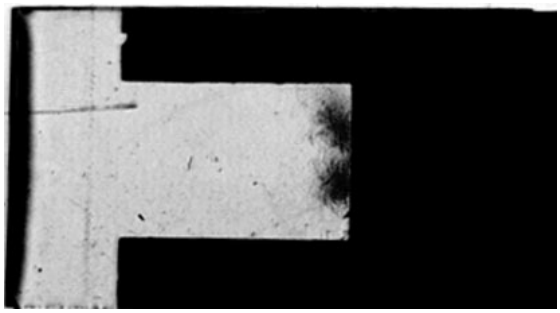
The time-averaged schlieren results using all 1,500 frames from the high-speed video files with the V2 Double linked oscillator models are shown in Figure 323. The images are arranged in the same order as the previous two sets of results and at the same CO_2 flow rates. As with the baseline, non-oscillating jets the effect of



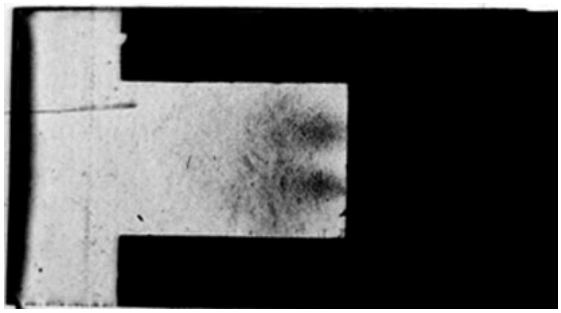
(a) CO_2 = 1.92 SLPM, Tunnel = 0 m/s



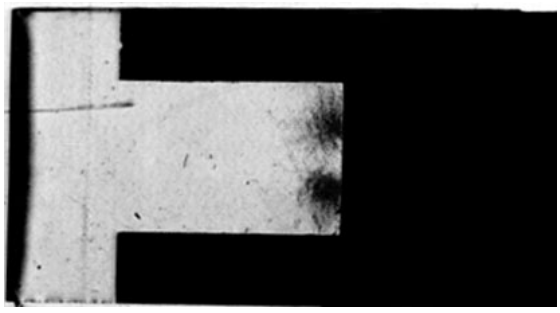
(b) CO_2 = 6.83 SLPM, Tunnel = 0 m/s



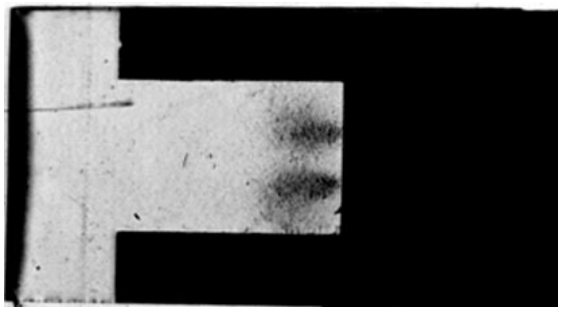
(c) CO_2 = 1.92 SLPM, Tunnel = 23 m/s, fuel only model upper configuration



(d) CO_2 = 6.83 SLPM, Tunnel = 32 m/s, fuel only model upper configuration



(e) CO_2 = 1.92 SLPM, Tunnel = 23 m/s, fuel & air model upper configuration



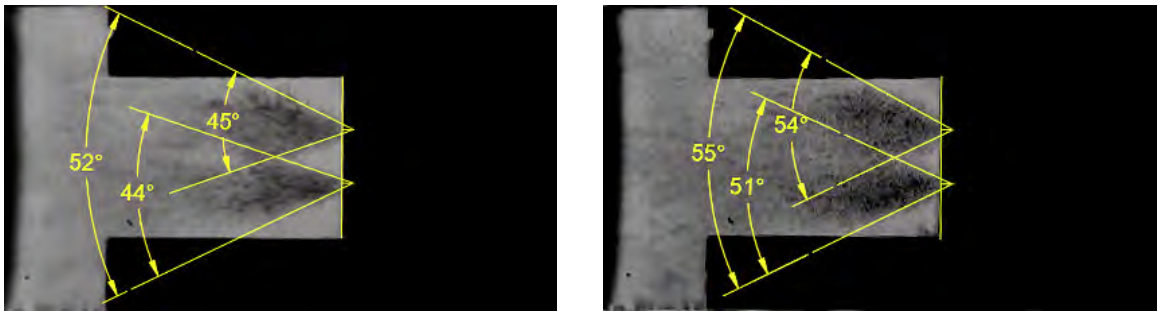
(f) CO_2 = 6.83 SLPM, Tunnel = 32 m/s, fuel & air model upper configuration

Figure 323. V2 Double linked oscillator, time-averaged composite images at the lowest and highest CO_2 flow rates and three model and wind tunnel configurations

the recirculation behind the backward-facing step was detrimental to the jet flow field. The results without the wind tunnel flowing looked similar to the baseline, non-oscillating case shown in Figures 320a and b, however, the spreading angle of the V2 Double oscillator jets was significantly higher than the baseline jets. The V2 Double linked oscillator jets impinged on the forward and aft cavity walls in less than half the distance downstream compared to the baseline jets. With the wind tunnel flowing, and the recirculation formed behind the backward-facing step, the baseline and V2 Double linked results are nearly indistinguishable at the 1.92 SLPM flow rate, and very similar at the 6.83 SLPM flow rate. At 6.83 SLPM the CO_2 concentrations in the V2 Double linked results are more diffuse indicating a slightly better fuel distribution for that case. One important difference between the baseline and V2 Double linked oscillator is the symmetry of the CO_2 concentrations at the exit of both oscillators in the V2 Double linked results. The baseline jet CO_2 concentration was skewed due to the secondary circulation that does not appear to be present in the V2 Double linked results. As with the V2 Single, when the oscillating jets were pointed at a downward angle toward the aft cavity wall, the force of the jets flowing opposite to the secondary circulation direction could have been preventing it from forming.

As shown in Figure 324 the oscillation angle of the V2 Double linked oscillators was also dependent on flow rate, although to a lesser degree than the V2 Single. The output for each oscillator was not uniform with the lower oscillator consistently measuring a smaller sweep angle. The upper oscillator only increased the angle of oscillation by 9° with the increase in mass flow rate. It is also interesting to note that while the V2 Single and V2 Double linked oscillators were scaled to match the jet velocities between the two models for the same CO_2 flow rates, the oscillation angles do not match in all cases. The angles are comparable at 1.92 SLPM, however, the V2 Double linked oscillators swept 19+ degrees less than the V2 Single at 6.83 SLPM.

This result shows that there is likely a connection between oscillator scale and sweep angles, even under comparable conditions.



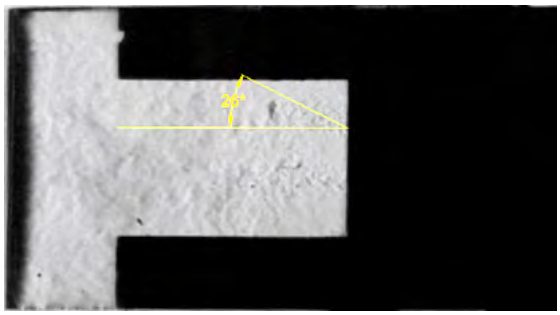
(a) CO_2 = 1.92 SLPM, Tunnel = 0 m/s (b) CO_2 = 6.83 SLPM, Tunnel = 0 m/s

Figure 324. V2 Double linked oscillator time-averaged composite image at the lowest and highest CO_2 flow rates with 0 m/s wind tunnel speed

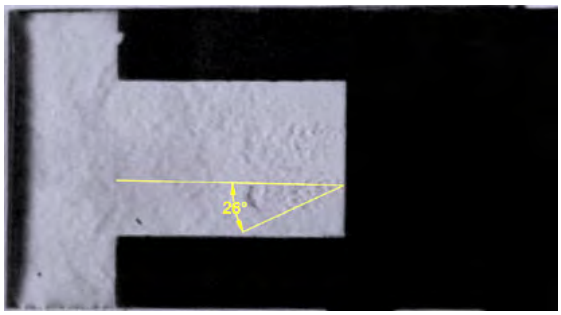
The oscillation angles were not symmetric about the centerline of each of the linked oscillators. As shown in Figures 325a and b the instantaneous angle from the centerline of each oscillator to the outward sweeping jets were consistent at 26°, however, both jets do not sweep out a total of 52°. This result means the sweep angle on the opposite side of the oscillator centerline was not as large as the outward angle, specifically in the lower oscillator. In both cases the oscillation angle towards the center of the step was the smaller angle. It is likely that the presence of the other jet and/or residual swirl or flow between the two jets kept the lower jet from making a symmetric sweep. The maximum instantaneous sweep angles from the oscillator centerline to the outward angled jet found experimentally matched exactly for the same measurement from an identical computational case as shown in Figures 325c and d.

7.3.1.4 V2 Double Separate and V3 Double Oscillator.

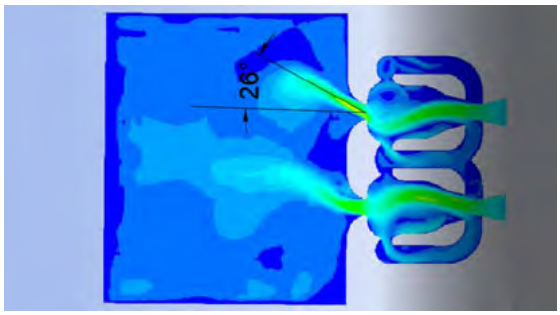
A review of the composite frames from the high-speed videos producing a time-averaged image showed the jet spread angles from edge to edge of the jets were 29° and 31° at the lowest flow rate for the V2 Double separate and V3 Double, respectively.



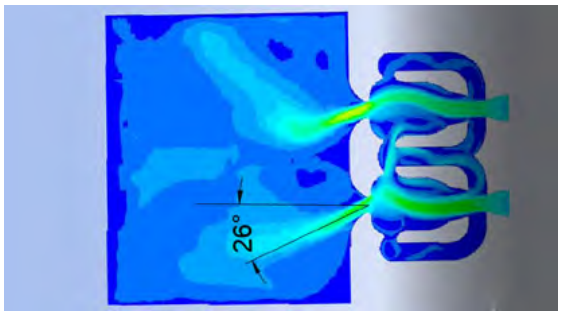
(a) CO_2 = 6.83 SLPM, Tunnel = 0 m/s



(b) CO_2 = 6.83 SLPM, Tunnel = 0 m/s



(c) CO_2 = 6.83 SLPM, Tunnel = 0 m/s, CFD



(d) CO_2 = 6.83 SLPM, Tunnel = 0 m/s, CFD

Figure 325. V2 Double linked oscillator instantaneous maximum oscillation angles measured at the jet centerlines at the lowest and highest CO_2 flow rates with 0 m/s wind tunnel speed

Based on fluid theory a non-oscillating jet has a spread angle of 23.6° measured from edge to edge [131]. These two oscillators achieved just above 5° more spread angle than a non-oscillating jet. Due to this minimal amount of travel it was difficult to discern the jets were oscillating. As such the results for these cases will not be shown.

The V3 Double jets did move out of phase where they touched at the center and moved outward to touch both side walls at the same time, but the magnitude of oscillation was generally minimal with larger sporadic movements. The very thin feature that separated the two oscillators and directed gas down the common feedback channel was partially missing. Either the printer that generated the model couldn't print the feature because it was too thin, or the feature was broken off during pressure washing of the model to remove the printer support material. In either case, the lack of a complete divider between the oscillators is believed to be the cause of the poor

oscillation magnitude. The V3 Double model was not remade or redesigned to enable testing further because the V2 Double Linked oscillator performed well and displayed a more desirable flow pattern that could achieve a more uniform fuel distribution than the V3 Double.

The V2 Double separate model had no known manufacturing issues. While the magnitude of the oscillation did scale with CO_2 flow rate, it is believed that the arbitrary oscillation behavior of the two fluidic oscillators next to each other caused the reduction in oscillation magnitude for this model. The interaction of the exiting jets external to the oscillator somehow affected the behavior inside the oscillators. Due to this external influence the jets only quivered back and forth rather than achieve the full movement experienced by the other oscillator models previously shown. If this is the true cause of the minimal movement in this case it becomes very important to synchronize the oscillators if they are positioned close enough that the external jets could interact.

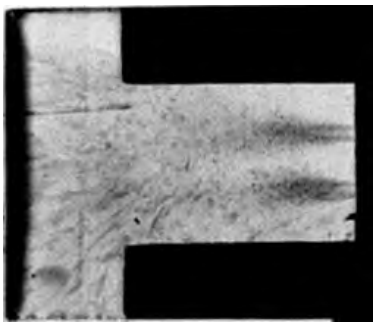
7.3.2 Test Series Two.

In this second test series the flow rate to the oscillators were fixed and the wind tunnel flow speed was increased to observe the impact of the recirculation behind the step on the CO_2 flow pattern at varying recirculation strengths. While data were collected with both the fuel only, and the air and fuel injecting steps, only the results from the fuel only step will be shown. Like the results shown in test series one, the injection of the air from the air and fuel injecting steps significantly lessened the effects of the recirculation. As a result of this flow pattern the CO_2 remained relatively uniform in each case with only the concentration of CO_2 becoming smaller with increased tunnel speed. As shown below in the fuel only step results, the recirculation caused the CO_2 flow pattern to form distinct features in separated flow regimes governed by the ratio of the jet velocity to the wind tunnel flow speed.

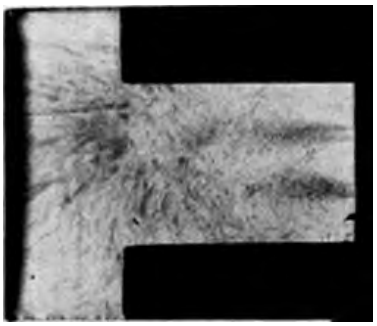
Starting with the baseline, non-oscillating jets, Figures 326 and 327 shows time-averaged composite images using 1,500 frames from high-speed videos arranged in order by velocity ratio. The velocity ratio, VR, is calculated as the wind tunnel flow speed divided by the CO_2 jet velocity. In each of these figure sets the CO_2 jet



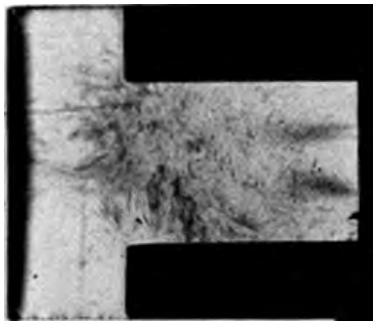
(a) Tunnel = 0 m/s, Velocity Ratio = 0



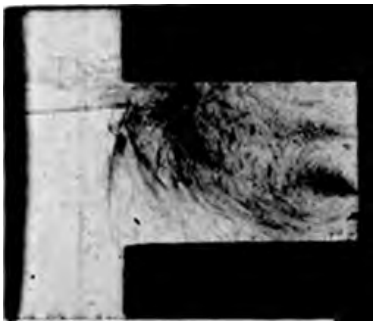
(b) Tunnel = 4 m/s, Velocity Ratio = 0.50



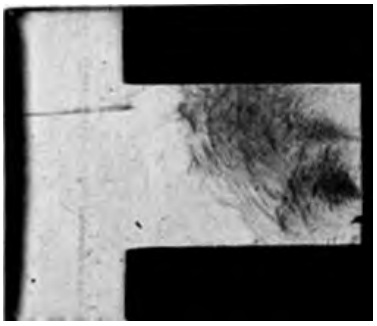
(c) Tunnel = 6 m/s, Velocity Ratio = 0.74



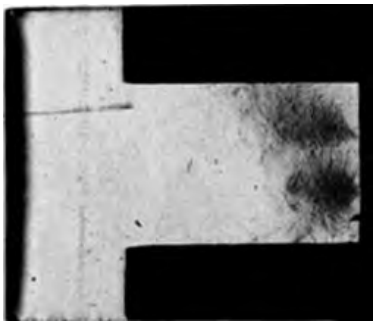
(d) Tunnel = 8 m/s, Velocity Ratio = 0.99



(e) Tunnel = 10 m/s, Velocity Ratio = 1.24



(f) Tunnel = 14 m/s, Velocity Ratio = 1.74

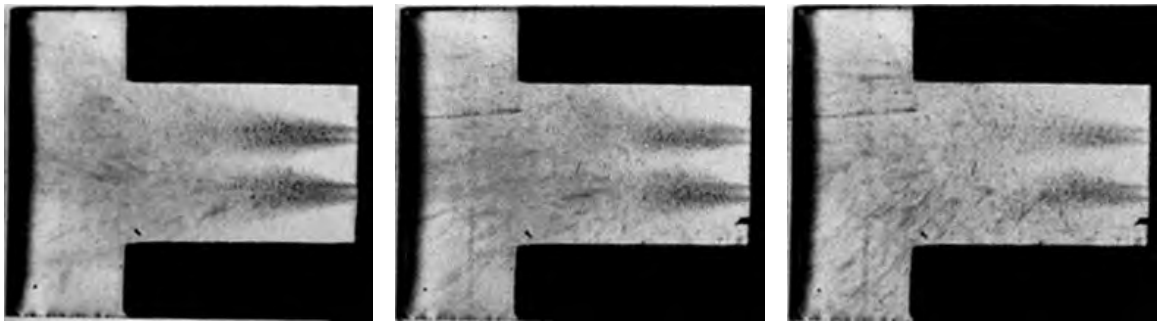


(g) Tunnel = 18 m/s, Velocity Ratio = 2.23



(h) Tunnel = 28 m/s, Velocity Ratio = 3.47

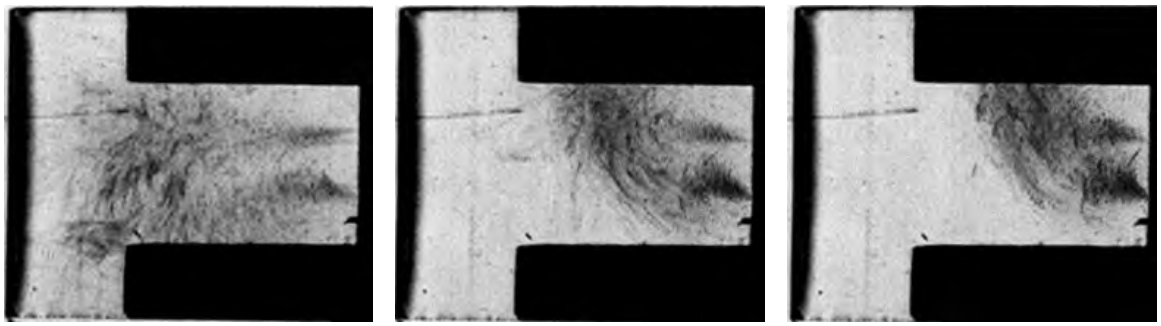
Figure 326. Baseline, non-oscillating jets, time-averaged composite images at a CO_2 flow rate of 4.75 SLPM (8.1 m/s jet velocity) with the fuel only step model



(a) Tunnel = 0 m/s, Velocity Ratio = 0

(b) Tunnel = 4 m/s, Velocity Ratio = 0.30

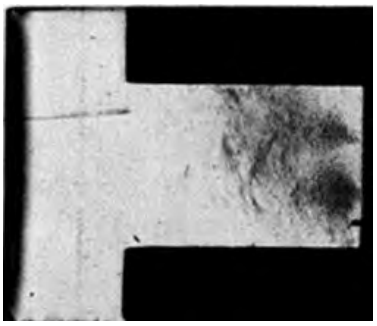
(c) Tunnel = 8 m/s, Velocity Ratio = 0.59



(d) Tunnel = 12 m/s, Velocity Ratio = 0.89

(e) Tunnel = 16 m/s, Velocity Ratio = 1.18

(f) Tunnel = 20 m/s, Velocity Ratio = 1.48



(g) Tunnel = 24 m/s, Velocity Ratio = 1.78

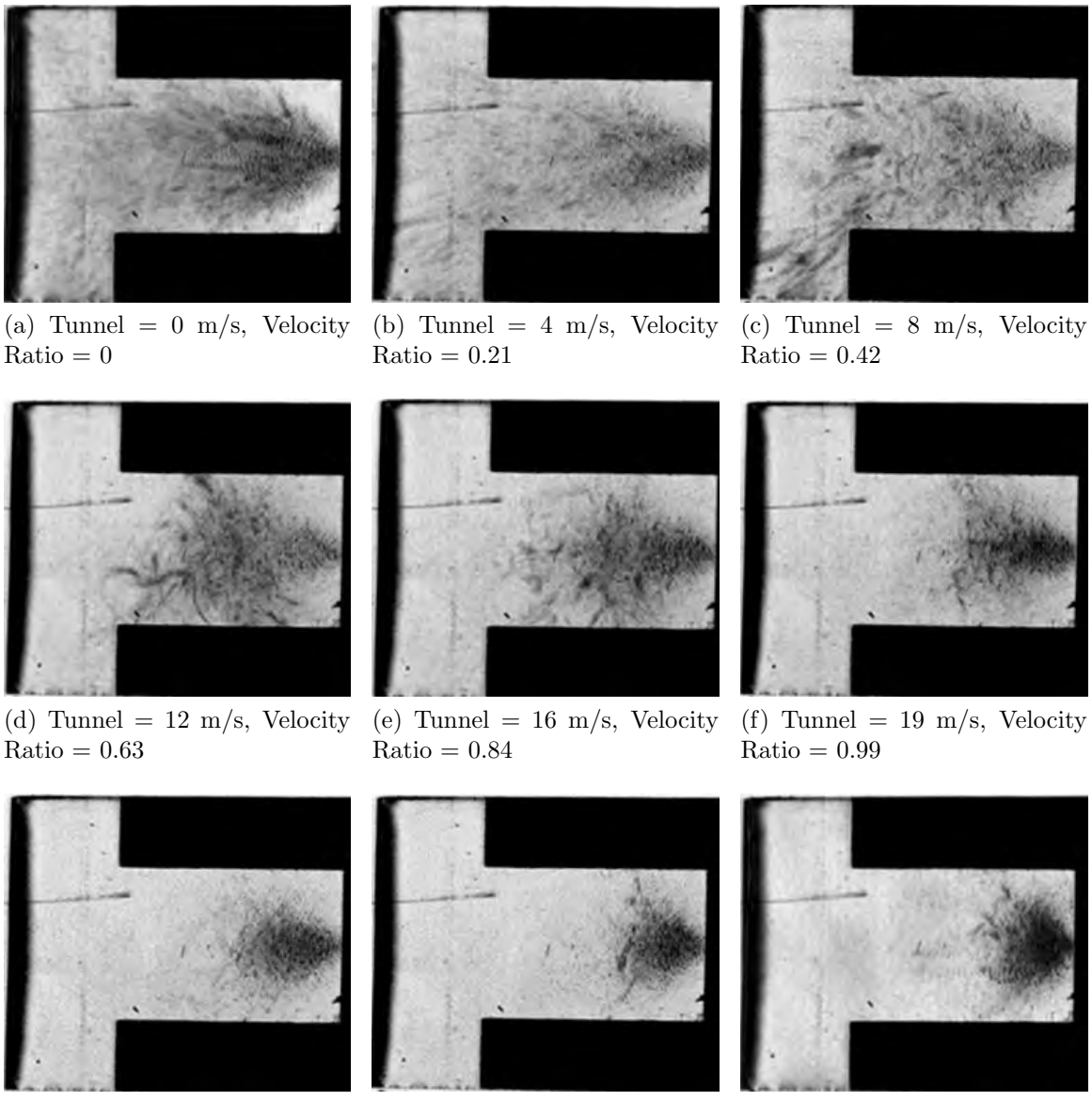
Figure 327. Baseline, non-oscillating jets, time-averaged composite images at a CO_2 flow rate of 7.96 SLPM (13.5 m/s jet velocity) with the fuel only step model

velocities were fixed. Comparing these two figures shows how the resulting CO_2 flow structures are based on the velocity ratio. Despite the difference in jet velocity and wind tunnel speeds, similar velocity ratios produced similar flow structures. The flow structures could be divided into three general classes. The first spans velocity ratios

from 0 to 1 and is defined by structures that still show discrete jets and the CO_2 structures extend downstream beyond the edge of the model. In the second regime from 1 to 1.75, the discrete jets are pushed together due to a greater impact from the recirculation behind the step, but the CO_2 concentration still filled to majority of the region between the step face and the end of the model. Beyond a velocity ratio of 1.75 the CO_2 concentrations were pulled much closer to the step face and formed a nearly continuous mass behind the step. The effect of the secondary circulation pattern can be seen as early as a velocity ratio of 0.75 where the flow pattern indicated a downstream flow near the cavity front wall (top of the images), and an upstream flow along the cavity back wall (bottom of the images), resulting in a skew in the CO_2 concentration.

Figures 328 and 329 show time-averaged results for the V2 Single oscillator at two jet velocities. Like the baseline results, there were three distinct flow regimes, but the velocity ratio cutoffs between regimes differed with this model. The first regime was between a velocity ratio of 0 to 0.5. In this range the oscillator was able to move with a maximum sweep angle and the CO_2 extended downstream in concentrations sufficient to still be visible beyond the end of the model. The next regime was between a velocity ratio of 0.5 and 1. In this band the oscillator was still moving freely to direct CO_2 from wall to wall, however, the CO_2 was not visible beyond the end of the model. In this regime the CO_2 did fill the majority of the region between the step face and the end of the model. The final regime was for velocity ratios greater than 1. In this band the CO_2 concentration was localized in front of the oscillator throat and was not visible near the walls. As the velocity ratio increased within this band the width of the CO_2 mass spread across the step face and extended less downstream due to the increased strength of the recirculation behind the step pulling the CO_2 to the wall. As shown in the series one results, there is no significant visible effect

of the secondary circulation pattern with this oscillator model. The force of the jet opposing the secondary swirling motion, when the jet was directed downward toward the cavity back wall, was likely the cause of the lack of this flow feature.



(a) Tunnel = 0 m/s, Velocity Ratio = 0

(b) Tunnel = 4 m/s, Velocity Ratio = 0.21

(c) Tunnel = 8 m/s, Velocity Ratio = 0.42

(d) Tunnel = 12 m/s, Velocity Ratio = 0.63

(e) Tunnel = 16 m/s, Velocity Ratio = 0.84

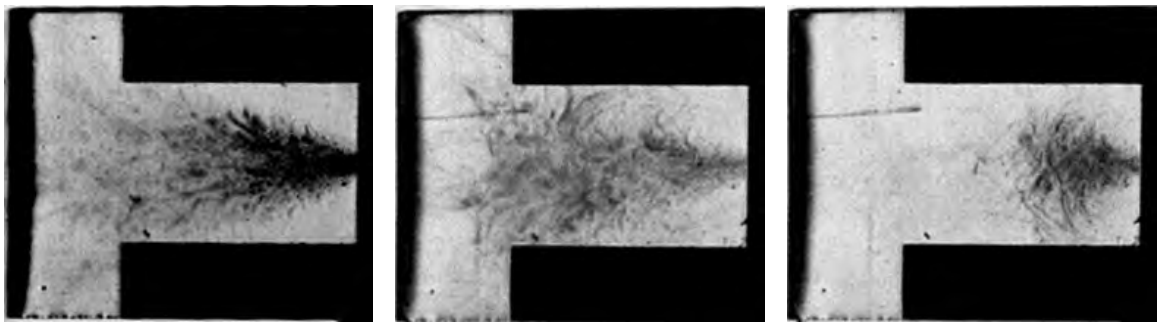
(f) Tunnel = 19 m/s, Velocity Ratio = 0.99

(g) Tunnel = 20 m/s, Velocity Ratio = 1.04

(h) Tunnel = 24 m/s, Velocity Ratio = 1.25

(i) Tunnel = 28 m/s, Velocity Ratio = 1.46

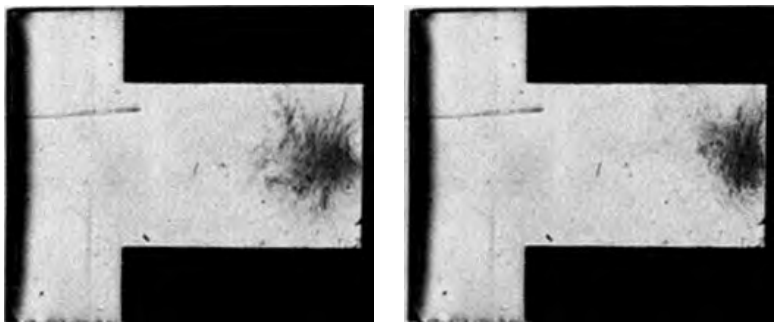
Figure 328. V2 Single oscillator, time-averaged composite images at a CO_2 flow rate of 4.75 SLPM (19.1 m/s jet velocity) with the fuel only step model



(a) Tunnel = 0 m/s, Velocity Ratio = 0

(b) Tunnel = 4 m/s, Velocity Ratio = 0.48

(c) Tunnel = 8 m/s, Velocity Ratio = 0.95



(d) Tunnel = 12 m/s, Velocity Ratio = 1.43

(e) Tunnel = 16 m/s, Velocity Ratio = 1.91

Figure 329. V2 Single oscillator, time-averaged composite images at a CO_2 flow rate of 2.08 SLPM (8.4 m/s jet velocity) with the fuel only step model

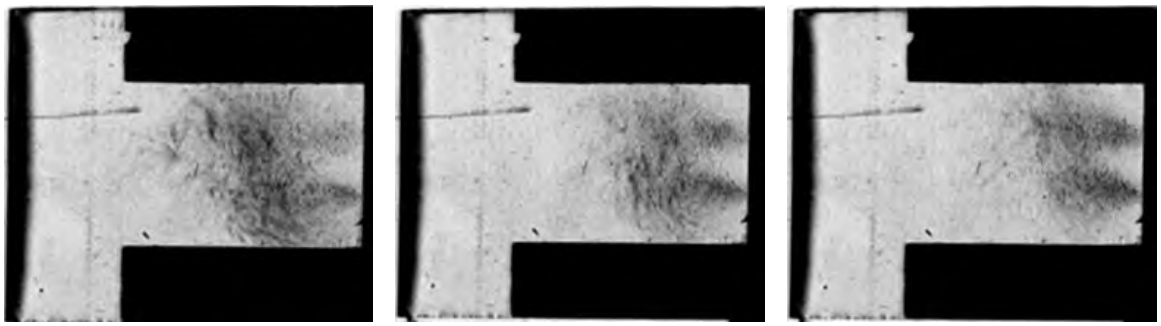
Figures 330 and 331 show the time-averaged composite images for the V2 Double linked oscillator at two jet velocities. The three flow regimes were closer to the velocity ratio cutoff of the V2 Single oscillator, but had a smaller middle regime. The first regime still ranged from a velocity ratio of 0 to 0.5. In this range the presence of both oscillating jets was visible with the CO_2 concentrations visible beyond the end of the model. The second regime extended from 0.5 to 0.85. This smaller band included flow structures that filled the majority of the region between the step face and the end of the model. Beyond a velocity ratio of 0.85 the CO_2 concentrations were pulled progressively closer to the step face to form a more continuous mass. The 0.5 velocity ratio boundary between the flow regimes, best shown in Figure 331b produced an interesting pattern. Because of the parallel jets sweeping in-phase with each other



(a) Tunnel = 0 m/s, Velocity Ratio = 0

(b) Tunnel = 4 m/s, Velocity Ratio = 0.21

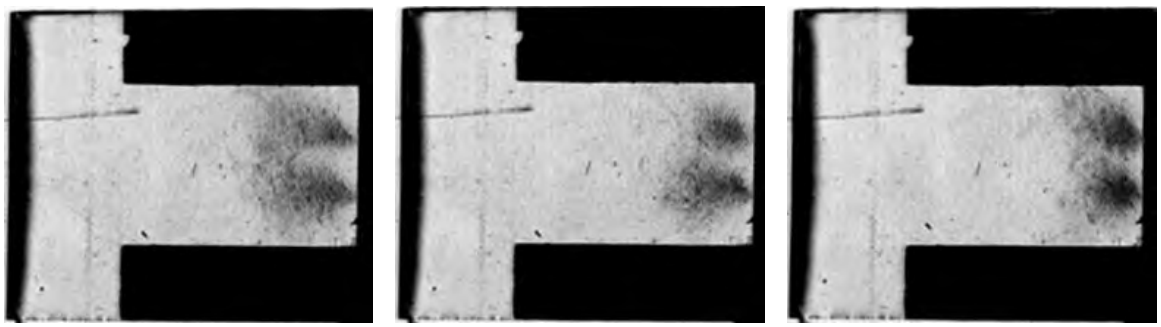
(c) Tunnel = 8 m/s, Velocity Ratio = 0.42



(d) Tunnel = 12 m/s, Velocity Ratio = 0.63

(e) Tunnel = 16 m/s, Velocity Ratio = 0.84

(f) Tunnel = 19 m/s, Velocity Ratio = 1.00



(g) Tunnel = 20 m/s, Velocity Ratio = 1.05

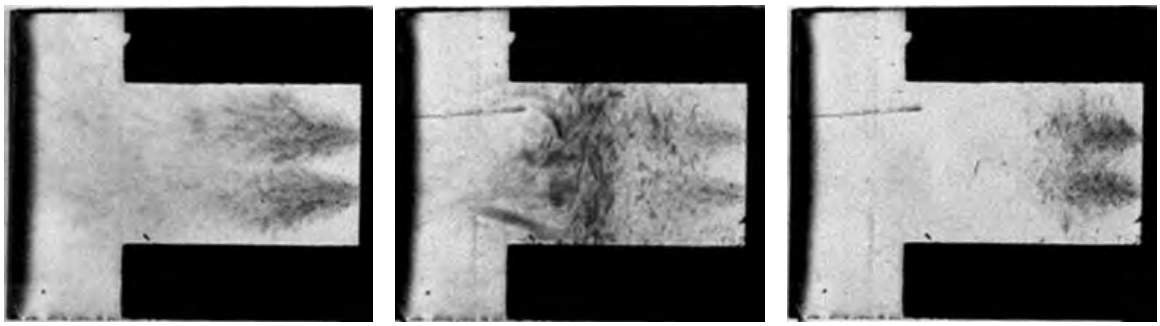
(h) Tunnel = 24 m/s, Velocity Ratio = 1.26

(i) Tunnel = 28 m/s, Velocity Ratio = 1.47

Figure 330. V2 Double linked oscillator, time-averaged composite images at a CO_2 flow rate of 4.75 SLPM (19.1 m/s jet velocity) with the fuel only step model

at a higher frequency than the V2 Single oscillator (see Section 7.3.3), the CO_2 jets were able to push off the weak recirculation and produced a standing wall of CO_2. In the high-speed video a slight rotation, with a rotational axis extending from the forward to aft cavity wall and parallel to the step face, was present as the flow feature

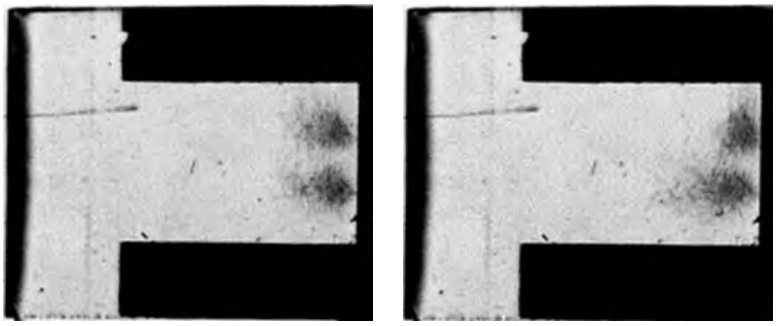
exchanged CO_2 coming in from the jets and exiting to the freestream. Despite the slow rotation, the concentration of CO_2 remained relatively stationary near the end of the model as the force between the sweeping jets and the recirculation were balanced.



(a) Tunnel = 0 m/s, Velocity Ratio = 0

(b) Tunnel = 4 m/s, Velocity Ratio = 0.47

(c) Tunnel = 8 m/s, Velocity Ratio = 0.94



(d) Tunnel = 12 m/s, Velocity Ratio = 1.42

(e) Tunnel = 16 m/s, Velocity Ratio = 1.89

Figure 331. V2 Double linked oscillator, time-averaged composite images at a CO_2 flow rate of 2.11 SLPM (8.5 m/s jet velocity) with the fuel only step model

Figure 332 shows a correlation plot between jet penetration depth into the free stream measured from the step face and the velocity ratio for all test cases. As shown in the figure the data arranged themselves into two groups; a non-oscillating set, and an oscillating set. In both groups the flow rate through the models was irrelevant since the flow rate was directly related to jet velocity which was then accounted for as a scaling parameter in the non-dimensional velocity ratio. In the oscillating group the type of oscillator (single or double) was not a variable as the data from both types collapsed together when plotted against the velocity ratio. The "Composite" data

points are simply a collection of the points from each group to enable the generation of trend lines through the entire group population. The equation of the trend line through the non-oscillating group was $Depth = 4.2696(VR)^{-1.076}$ which had an R^2 value of 0.98 indicating a strong correlation where 98% of the variation of jet penetration depth was explained by the variation in velocity ratio. The units of depth and the VR coefficient were cm. The equation of the trend line through the oscillating group was $Depth = 1.8011(VR)^{-1.023}$ which had an R^2 value of 0.97 also indicating a strong correlation where 97% of the variation of jet penetration depth was explained by the variation in velocity ratio. The units of depth and the VR coefficient were again cm. There were several test points at low velocity ratios that were left off of the plot because the jet penetration depth extended beyond the schlieren image field of view and thus could not be measured.

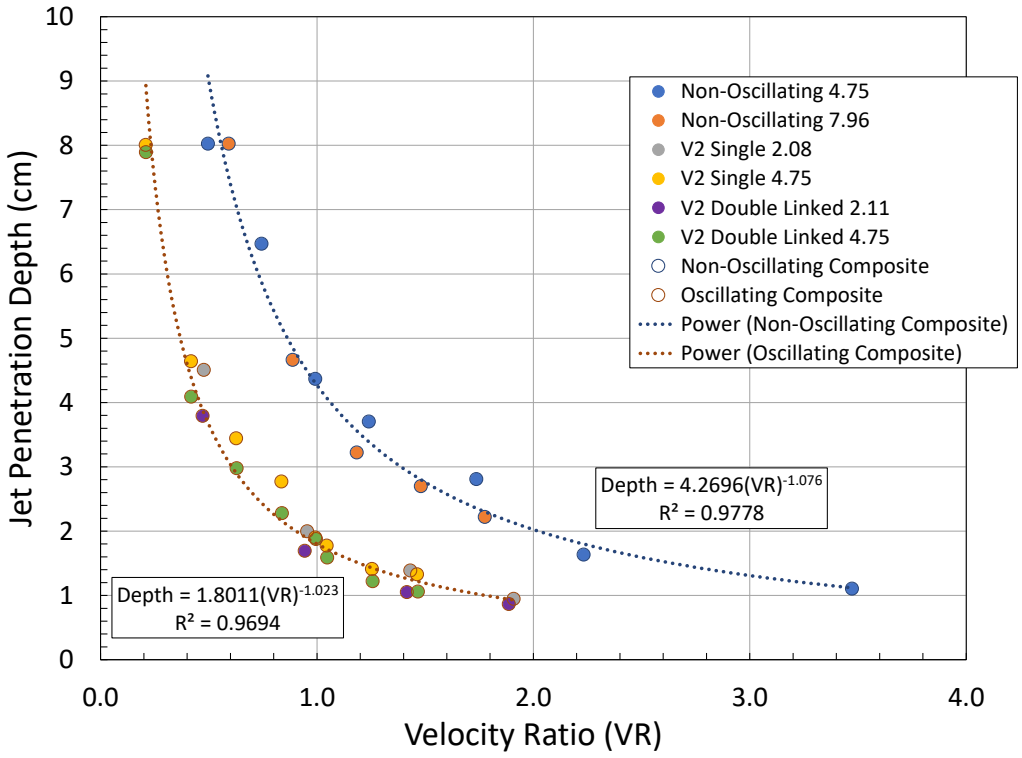


Figure 332. Correlation of jet penetration depth into the freestream relative to velocity ratio

7.3.3 Fluidic Oscillator Frequencies and Spread Angles.

The oscillation frequencies for the V2 Single and V2 Double linked oscillators are shown in Figure 333. There are two sets of lines showing the frequency results obtained by manually counting the oscillations in the high-speed video files and extrapolating to the number of cycles per second, and the frequency results obtained using a pressure transducer and averaging the LabView determined frequency over a 10 second period. There are error bars on the manually counted frequency measurements to account for partial cycles within the time frame of the high-speed video. The results for both oscillators show the manually counted frequency slightly under predicted compared to the pressure transducer based measurements, but the results typically fell within, or close to, the error bar band.

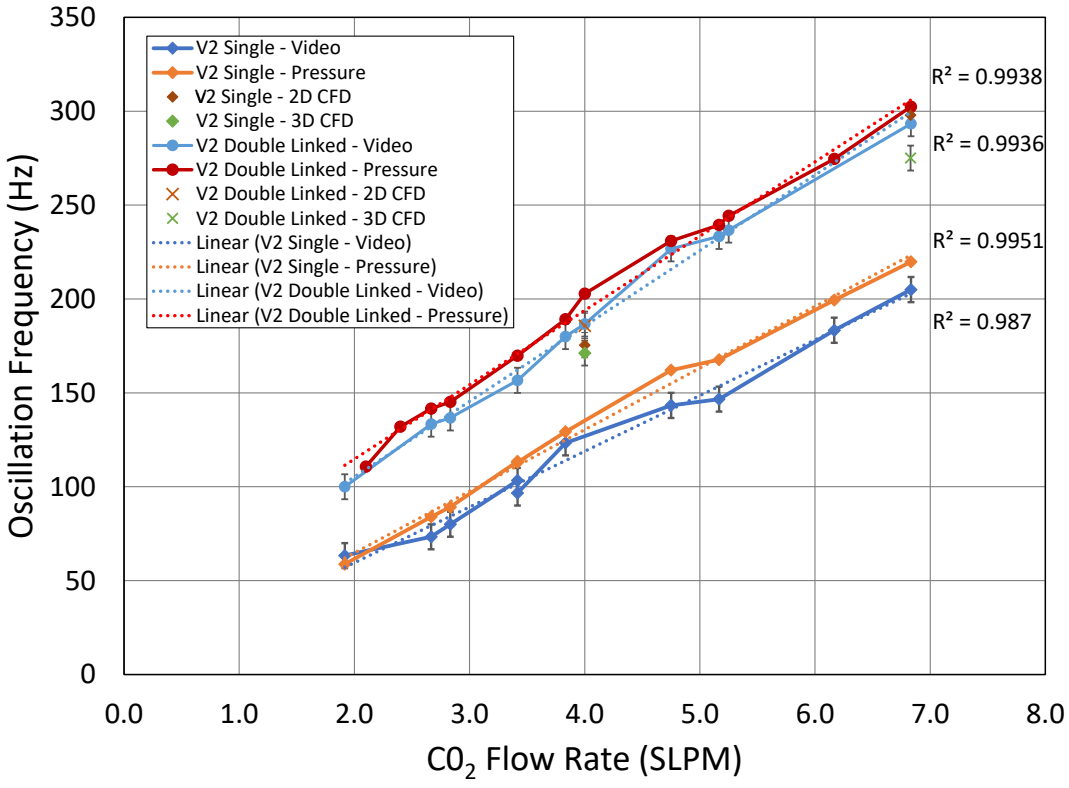


Figure 333. Experimental oscillator frequency measurements taken from high-speed video files and pressure transducers with plotted CFD calculated frequency points

There are linear trend lines plotted for each of the experimentally determined frequency measurements with the R^2 value shown for each line. With the exception of the manually counted frequencies for the V2 Single oscillator the remainder of the R^2 values were greater than 0.99, with the outlier still achieving an R^2 greater than 0.98. These values mean that approximately 99% of the variation in oscillation frequency is explained by the change in CO_2 mass flow rate. This is a strong correlation, but may only be linear within the range of flow rates tested.

Figure 333 also includes frequency measurements obtained from four CFD cases. These results were manually counted so they included error bars on the markers. There was a strong agreement between the CFD derived frequencies and the experimental frequencies for the V2 Double linked oscillator. However, the CFD calculated frequency for the V2 Single oscillator was approximately 26% higher than the experimental result at the same flow rate. The V2 Single oscillator CFD calculated frequency matched well with the CFD and experimental results from the V2 Double linked oscillator. While the frequency was over predicted, as shown earlier the oscillation angles were within 1° between CFD and the experimental result. The cause of the over prediction in frequency is unknown.

In Figure 334 the oscillation frequencies from the pressure transducer measurements were correlated to a non-dimensional correlation factor based on a Reynolds number. The correlation factor is defined in Equation 146 which specifies the Reynolds number length scale in terms of the oscillator volume ($\forall$) divided by the area of the power jet throat (A_{PJ}) multiplied by the cross-sectional area of a feedback loop (A_{FB}). This quantity has units of length, but was found to produce a significantly better correlation that accounts for more geometric variables in the oscillators than using a single length measurement. The remaining values in the equation include the mass flow rate through the oscillator ($\dot{m}$), the gas molecular viscosity (μ), and the number

of jets (n). The value of n is defined as 1 for a single oscillator and 2 for a double oscillator.

$$Correlation\ Factor = \frac{\dot{m}\forall}{A_{PJ}A_{FB}\mu n} \tag{146}$$

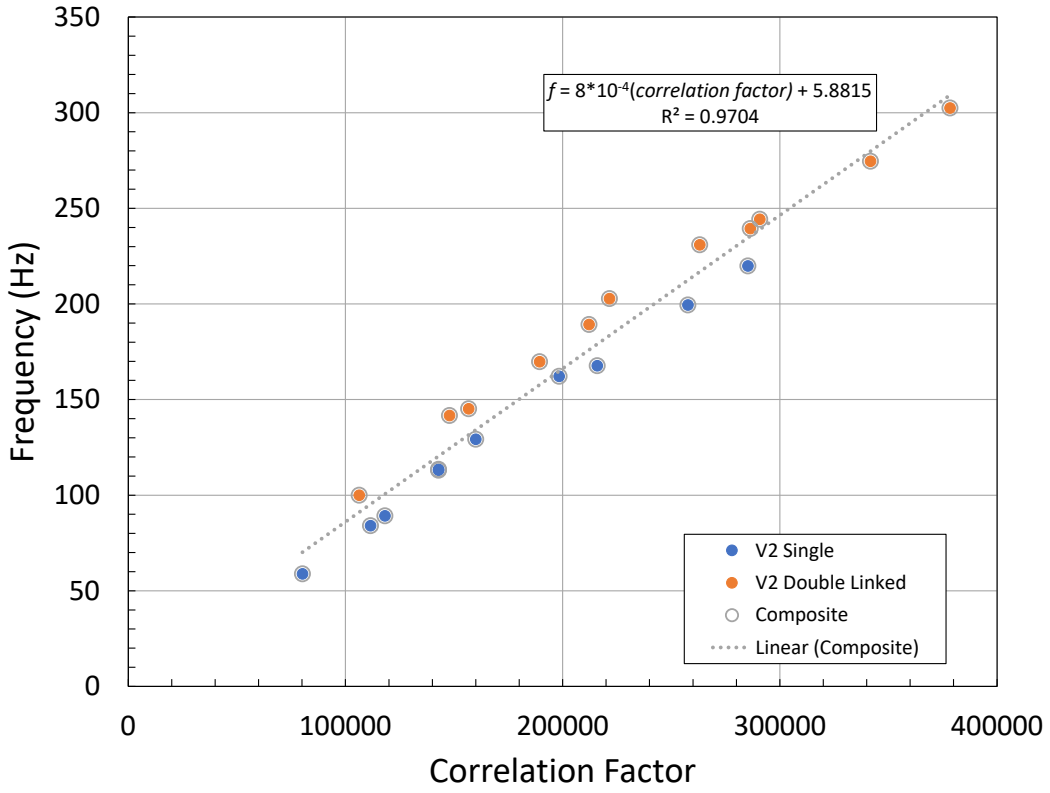


Figure 334. Correlation of oscillator frequency to a non-dimensional correlation factor

As shown in Figure 334 the correlation of oscillator frequency to the non-dimensional correlation factor in Equation 146 produced a linear relationship. The equation of the linear trendline through the collection of all data point shown as the composite points is $f = 8 \cdot 10^{-4}(CorrelationFactor) + 5.8815$. This trendline had an R^2 value of 0.97 indicating a strong correlation where 97% of the variation in oscillator frequency is determined by the geometrical features and gas properties defined in the non-dimensional correlation factor. The units of the dependent frequency were Hz, and since the Correlation Factor was non-dimensional the remaining constants also

had units of Hz. No other correlations have been found in literature that tie the oscillator geometry to frequency output. Additional testing would be required with other gases and different oscillator scales to determine if this correlation factor holds in those conditions as well.

A correlation of the oscillation angle was also plotted as shown in Figure 335 related to the Reynolds number scaled by hydraulic diameter of the exit jet throat (Re_D). The double oscillators were plotted twice to include the average of the angle from each oscillator in the first set, and the angle between the outer edge from one oscillator to the outer edge in the other oscillator in the second set. A non-dimensional parameter was not found that caused the results to collapse to a singe time. As such, there are three data sets and three logarithmic trendlines

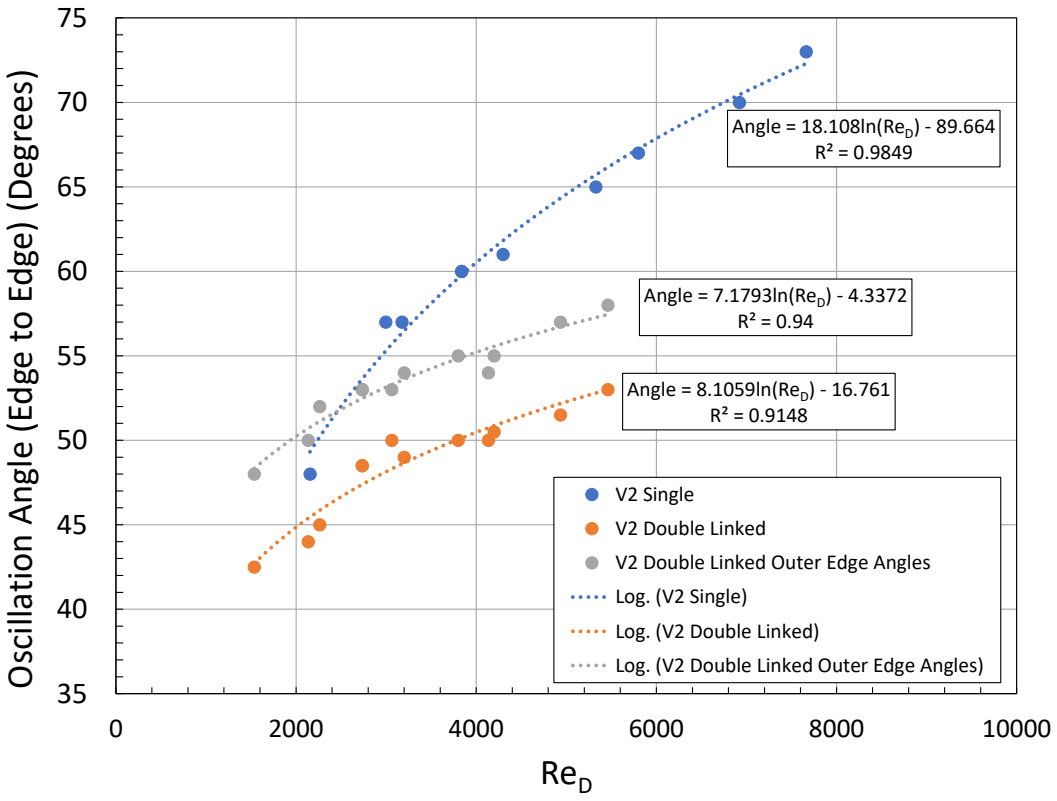


Figure 335. Correlation of oscillator angle to a hydraulic diameter scaled Reynold Number (RE_D)

through the data. The equation of the trendline through the V2 Single oscillators is $Angle = 18.108 \ln(Re_D) - 89.664$ which had an R^2 value of 0.98. The equation of the trendline through the V2 Double oscillators using the average angle between both output jets is $Angle = 8.1059 \ln(Re_D) - 16.761$ which had an R^2 value of 0.91. The equation of the trendline through the V2 Double oscillators using the outer edge of one oscillator to outer edge of the other oscillator measurement is $Angle = 7.1793 \ln(Re_D) - 4.3372$ which had an R^2 value of 0.94. The correlation in the V2 Single oscillators was strong, but the V2 Double correlations did not display this same strength. In all of these equations the dependent angle and the numeric constants had units of degrees.

7.4 Fluidic Oscillator Conclusions

Two of the four versions of fluidic oscillators performed well in experimental testing. The remaining two only achieved minimal oscillations with results comparable to the baseline, non-oscillating jets at all operating conditions. While the V2 Single and V2 Double linked oscillators distributed the fuel better behind the backward-facing step at slow wind tunnel flow speeds, the results were also comparable to the baseline, non-oscillating jets at high wind tunnel flow speeds. Computational results for frequency and oscillator sweep angle matched very well to experimental data in nearly all cases. A new correlation factor was proposed that was based on a Reynolds number and several geometric values from the oscillator. When the oscillation frequency was plotted against this new parameter the data from both oscillator types (single and double) collapsed to form a single line with a 0.97 R^2 value. This is the first known correlation between oscillator geometric properties and the oscillation frequency. Additional testing would be required with different oscillator scales and gases to determine if this correlation holds at other conditions. The oscillation angle was correlated to the Reynolds number with a hydraulic diameter reference

length. This correlation was strong for the V2 Single oscillator, but did not display the same correlation strength for the V2 Double oscillator using either oscillation angle measurement.

The flow patterns for the baseline, non-oscillating jets, the V2 Single oscillator, and the V2 Double linked oscillator were dependent on the velocity ratio between the CO_2 jet velocity and the bulk velocity below the model step. Each of these three models displayed three distinct flow regimes, but the cutoff velocity ratio between the regimes differed by model. At the conditions where the UCC operated, the velocity ratio was in the third regime for all models and thus achieved very similar flow patterns. At these conditions there was no benefit to using a fluidic oscillator for fuel distribution as the strong recirculation behind the step was distributing fuel effectively on its own. When the jet penetration depth measurements were plotted against the velocity ratio, the data collapsed into an oscillating and non-oscillating group. Trendlines through each group showed a power function produced a strong correlation in both cases. For the same velocity ratio the non-oscillating jets penetrated further off the step face than the oscillating jets.

A new flow pattern was discovered behind the step of the baseline, non-oscillating jet model that resulted in the typical recirculation along the step face, but also an additional circulation perpendicular to the step face that resulted from the added injection of fluid from the step face. This secondary circulation pattern was not observed in the oscillating models likely due to the oscillation pattern itself. At the downward sweep of the oscillator motion the CO_2 jets opposed the secondary flow direction and prevented that feature from forming.

VIII. Objective 4: Improving Turbine Inlet Temperature Distributions

Determine how cavity configuration influences combustion product migration and the ability to achieve a desirable turbine inlet temperature distribution

While there have been changes to fuel and air delivery methods in the UCC over the years [67][69][175], the relative position of components has not changed. The component positions are well defined in Figure 244 which shows a cross-section of the AFIT Version 3 UCC with the most recent fuel and air injection variations. In this figure, bulk airflow enters the diffuser with a variable diameter internal splitter from the left. A portion of the air is directed into the circumferential cavity through the purple front wall. The remainder of the air in the diffuser passes below the circumferential cavity through the hybrid guide vane passages as a central core flow. Fuel enters the circumferential cavity from the OD and is injected tangentially to the bulk cavity flow. The hot combustion products from the circumferential cavity exhaust radially inward into the hybrid guide vane passages to combine with the core flow. The hybrid vane passages also serve as secondary combustion zones in the event of fuel-rich cavity combustion to allow the reactions to complete prior to entering the turbine rotor.

While the UCC offers many favorable traits, one of the obstacles with the design is the migration of hot gases from the recessed circumferential cavity across the core flow to present a uniform temperature distribution to the first turbine rotor. To combat the issue of nonuniform exit temperatures, the study presented in this chapter computationally examined several alternative UCC configurations through an iterative design process. Based on the computational analysis, one of the designs was selected for manufacture for experimental testing. All of the new combustors featured

an exhaust exit in the axial direction rather than the radial direction and were sized as a combustor replacement for a JetCat P90RXi turbine engine.

Previous UCC configurations used the non-rotating hybrid guide vanes on the engine centerline to turn the hot exhaust products axially. The new combustors were designed to accept fluid from the JetCat compressor, turn the flow to establish a centrifugal load on the combustion products, burn in the circumferential direction, and deliver the hot gases to the turbine stage as if it came from the baseline JetCat combustor. By burning in the circumferential direction an axial length savings of at least 33% was achieved. The fundamental concept of combustion under high centripetal acceleration governing UCC operation remained the same. This new UCC configuration change eliminated the need for hot gas migration across the radial span of the hybrid guide vanes and thus eliminated the greatest challenge to the UCC concept. Furthermore, this cavity orientation change eliminates the need for the combustor to grow radially. Therefore, this UCC has an OD comparable to a traditional combustor. An additional enhancement was that secondary and dilution combustion zones were added to the circumferential cavity to allow all of the engine air (less any compressor bleed) to pass through the combustor prior to entering the turbine.

8.1 Objective 4 Background

The literature review in Chapter II provides an extensive background on gas turbine engine and combustion basics. Section 2.2 specifically addresses compact combustion and centrifugally loaded combustion that will not be repeated here. The new UCC configurations presented below are based on early work on swirling combustor benefits presented by Yonezawa et al. [50], and the high-g combustion effects presented by Lewis [4] and Briones et al. [33]. These designs also incorporate backward-facing steps for combustion stability based on the work of Lapsa and Dahm [56] covered in

detail in Section 2.2.4.2.

As discussed in Section 2.1.3 the temperature profile presented to the turbine is extremely important given the magnitude of the temperatures exiting the combustor. The temperatures near the mid-span should be hottest with the temperature decreasing at the hub and tip of the turbine blade. A slight OD skew in the thermal profile is needed to maximize power extraction from the turbine and protect critical components on the ID endwall of the engine. The pattern factor, PF, shown in Equation 35 in Section 2.1.3 is a measure of the uniformity of the temperature distribution on the combustor exit plane. For a traditional combustor the PF is typically between 0.2 and 0.45. For newer high temperature rise combustors the PF requirement becomes more restrictive at a value between 0.15 and 0.25 [14].

Several studies have been conducted on the UCC over the past seven years focused on the migration of hot gases from the circumferential cavity and the ability to present a desirable temperature distribution downstream. These studies are outlined in Section 2.3.7, and all tried a different method to address the difficulty of having all of the hot gases and combustion products originate at the OD of the engine. While some of these past migration studies were successful in moving the maximum temperature to the mid-span region, the location of the analysis where these results were obtained proved to be detrimental to the overall desired outcome.

In the most recent work by Cottle [78] and Gilbert [168], they reported the favorable temperature profiles shown in Figure 69, and 70. While these results look good, the computational and experimental data that went into these plots was taken at the TFP plane at the HGV trailing edge and projected perpendicular to the suction surface of the adjacent vane as shown in Figure 205. The results in Section 5.6 show temperature contours at the TFP plane and the resulting contours at the combustor exit plane, and the results are rather different despite their close axial proximity.

The reason for this difference is due to the ID profile of the low loss center body (LLCB) HGV as shown in Figure 65. This vane was designed to reduce Rayleigh losses by expanding the cross-sectional area of the vane passage to slow the flow. The downstream end of this profile has an upward slope which can act as a ramp to sling the high-speed gases flowing through the vane passage in the outward direction. Figure 336 shows the trailing edge of the LLCB with seeder dust providing a flow visualization on the vane surface. This flow pattern, highlighted by the green tangent lines on the ID, confirms the cause of the skewed exit temperature profiles that show high temperatures at the OD, and significantly cooler flow at the ID.

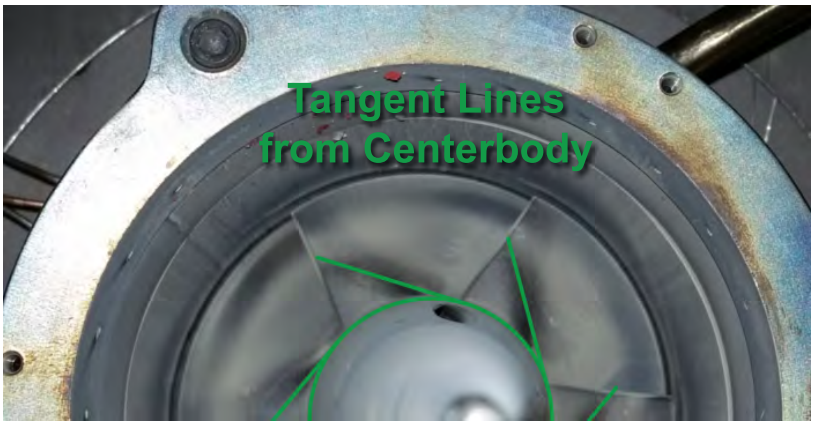


Figure 336. Flow pattern at HGV trailing edges as shown by seeder dust. Tangent lines from the centerbody are shown to highlight the flow path.

While some past UCC designs appeared to show favorable results and/or achieved a PF that was near typical values, these results were limited to specific operating conditions, or still maintained some undesirable characteristics due to the analysis location. This result is the primary reason the present study sought to develop a UCC orientation that eliminated the need for migration. Despite the best efforts of a number of researchers over the past 12 years, no UCC modification has resulted in a desirable exit temperature profile using the Version 3 UCC configuration at all operating conditions.

8.2 JetCat Integration Constraints

The current study investigated alternate UCC combustor configurations through an iterative approach in an effort to develop a new version of the UCC that achieved centrifugally loaded combustion with an axial exhaust and no migration. A total of seven combustor configurations were created and analyzed in this study, all of which were scaled to be a replacement burner for the JetCat P90RXi small-scale turbine engine. Figure 337 shows the cross-section of the P90RXi. This engine features a radial compressor and an axial turbine. There are stator vanes positioned at the exit of the compressor section to ensure axial flow into the combustor section. The green component in Figure 337 is a turbine stator assembly. The bounding axial dimensions of the combustor region from the compressor exit to the turbine inlet was 10 cm. The combustor minimum ID was 3.4 cm with a maximum diameter of 10.7 cm. The minimum combustor diameter was required to ensure the combustor could fit over the bearings located radially inward from the green stator assembly. All of

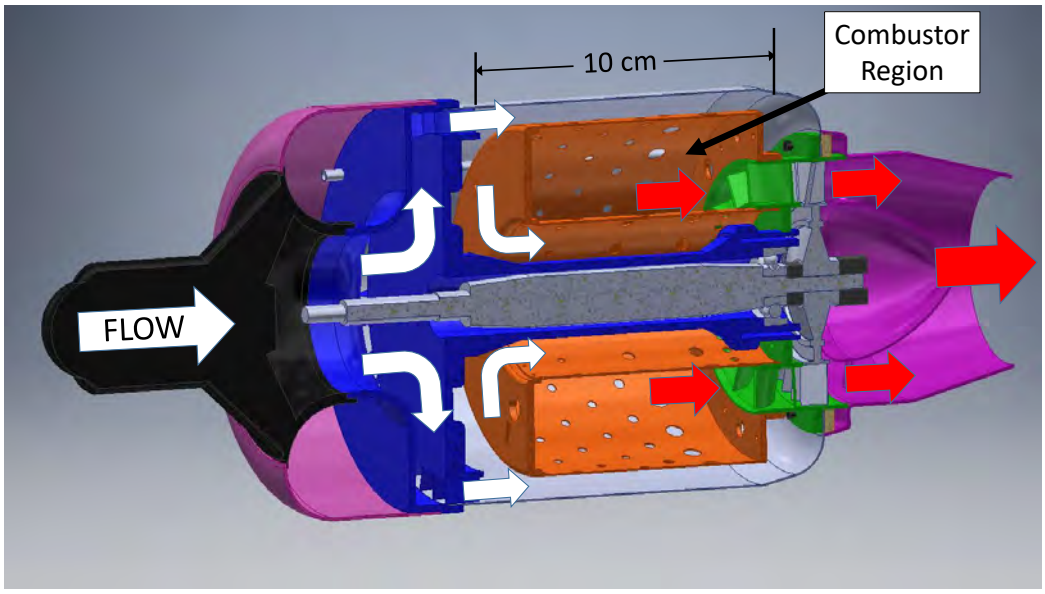


Figure 337. JetCat P90RXi cross-section with fluid flow path (stock combustor liner shown in orange)

the new combustor configurations maximized the radial dimension, while achieving an axial length reduction of at least 33%. Figure 338 shows a cross-section of the JetCat with the Configuration 6 combustor shown in position for comparison to the baseline burner.

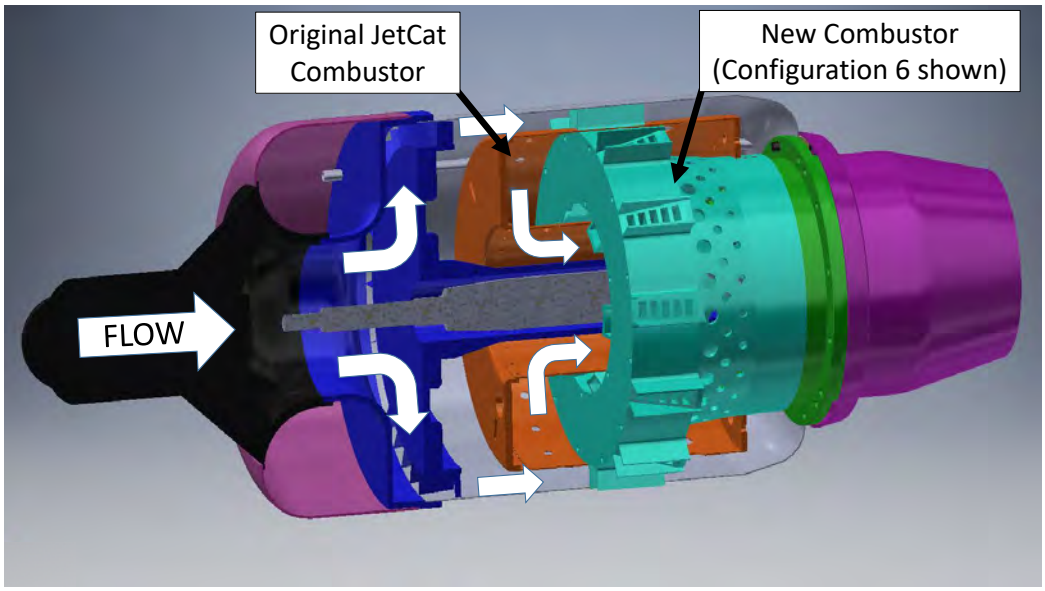


Figure 338. JetCat P90RXi cross-section with Configuration 6 combustor installed and compared to the stock combustor (shown in orange)

8.3 Computational Analysis

Computational analysis was used to quantify the fluid flow path, centrifugal loading, pressure losses, combustion performance, metal temperatures, and turbine inlet temperature profiles on each new UCC configuration. The computational settings and specifications are outlined in the remainder of this section.

8.3.1 CFD Case Setup.

This study was completed on three-dimensional domains with reacting chemistry and conjugate heat transfer to the combustor walls. Including conjugate heat transfer allowed for an energy exchange between the fluid and the solid. The solid regions,

gridded with a volume mesh, were then able to conduct and distribute the heat through the metallic components which could lead to an air or fuel preheat through the inlets.

The computational domain included the combustor as well as the air inlet, outer casing, centerbody, and exit geometry of the JetCat P90RXi. The domain, represented by Configuration 6, is shown in Figure 339. Each combustor configuration was "installed" into the JetCat hardware assembly using the SolidWorks drawing package. Since all of the new combustor configurations were shorter than the original JetCat combustor, there was a much larger gap between the compressor exit and the combustor forward face than is shown in Figure 337 for the stock combustor. If these new combustors were used in a production engine, that gap would be removed and demonstrates the axial length reduction, and thus weight savings, afforded by using these types of combustors.

Due to the rotationally periodic nature of the hardware around the engine center-

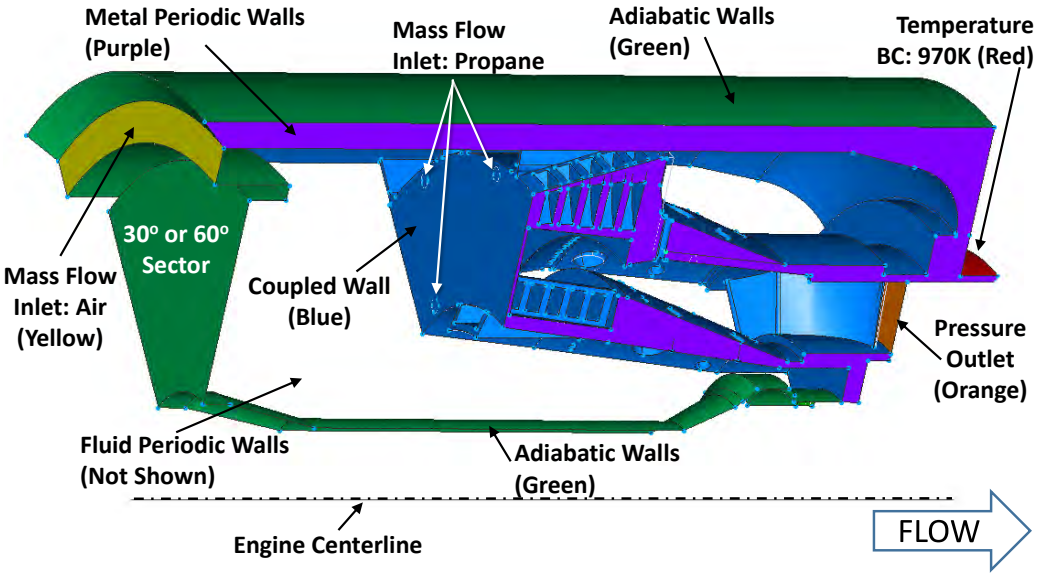


Figure 339. Representative computational domain, shown for Configuration 6, with boundary conditions labeled

line, the computational domain was simplified through the use of periodic boundaries. Depending on the combustor configuration being analyzed, the computational domain was reduced to a 30° or 60° sector. Each computational domain was gridded using Pointwise V18.0 R2 using unstructured surface meshes and the T-Rex hybrid mesh generator for the fluid volume mesh. The T-Rex function creates three-dimensional anisotropic tetrahedrals that are extruded off selected surfaces to create prism cells. The initial wall spacing and growth rate are specified to ensure adequate grid resolution at the wall to fully define the boundary layer and establish a y^+ value of 1 or less in the first cell for correct heat transfer analysis. When prism cells could no longer be generated due to geometry or adjoining cell interference, the mesh generator filled the remaining volume with unstructured cells. The solid volume mesh was gridded with an unstructured mesh only. The computational domains ranged from 16.6 - 35.9 million cells across the seven combustor configurations as shown in Table 46. Configuration 5 had very thick combustor walls around the dilution zone which drove the cell count up considerably. Configurations 6 and 7 required a domain that was periodic about a 60° sector which doubled the volume of the domain, and thus the cell count, compared to Configurations 1 - 4.

Table 46. Grid resolutions of UCC combustor CFD case domains

Domain	Periodicity	Total Cell Count
Configuration 1	30°	16.6M
Configuration 2	30°	19.9M
Configuration 3	30°	17.5M
Configuration 4	30°	17.1M
Configuration 5	30°	32.9M
Configuration 6	60°	35.2M
Configuration 7	60°	35.9M

8.3.2 Computational Settings.

The CFD analysis was run in FLUENT R16.2.0 using a pressure-based solver with an absolute velocity formulation. The remaining computational settings were based on the published works of Briones et al. [148], and Cottle [78][70], along with prior experience, a review of the FLUENT user manual [132], and the findings of Objective 2 discussed in Chapter V.

To allow for non-adiabatic conditions resulting in heat transfer between the fluid and solid, the coupled fluid-solid energy equation was turned on. FLUENT offers a number of turbulence model options, however, the k-ω shear stress transport (SST) model with viscous heating was selected due to its performance in wall bounded flows. This model does, however, require sufficient grid resolution to obtain a value of $y^+ = 1$ or better on the coupled walls to accurately model heat transfer and wall properties.

A multi-species analysis was conducted to allow gaseous propane to be injected into each combustor through discrete fuel inlet holes fed from an internal plenum. Combustion chemistry was dictated by the Partially Premixed Model using a Flamelet Generated Manifold (FGM) with diffusion flamelets. The FGM model assumes the scalar evolution in flames to be approximately the same between a turbulent and laminar flame. This model parameterizes the species and temperature values in the flow based on variables such as mixture fraction and scalar-dissipation, and is largely based on reaction progress. The GRI 3.0 chemical equilibrium reaction mechanism was added as an input to the model to more accurately calculate combustion values in FLUENT. The FGM model can be quenched by heat extraction due to wall contact or the addition of dilution air making it an ideal choice for wall bounded domains in these small combustors.

The fluid entering the domain from the compressor exit was modeled as air (nitrogen/oxygen blend only) with the distribution of fuel and air inside the domain

controlled by a FLUENT calculated mixture probability distribution function (PDF). The solid metal components in the domain were modeled as the default steel from the FLUENT material database which approximates the properties of physical hardware. Table 47 shows the boundary conditions at each of the domain inlets/outlets for a 30° sector domain. The given mass flow rates would be doubled for the 60° sector domain. The pressures specified in the table for the fuel and air inlets are the initial values used in the mass flow rate boundary condition. These values were free to fluctuate to maintain the specified mass flow rate and not over constrain the solution. The values in the table correspond to a total air inlet flow rate of 0.25 kg/s, and a fuel flow rate of 0.00505 kg/s. These values were taken from the JetCat experimentally derived cycle at 100,000 RPM, which approximates an 80% power cruise condition. The operating pressure inside the domain was set at 202,650 Pa which was also derived from experimental data at the specified condition. The above mentioned fuel and air flow rates result in a JetCat global equivalence ratio of 0.33. The boundary condition between the fluid and solid inside the domain was treated as a coupled wall, which the fluid sees as a wall, but allows for heat transfer across the interface. The exit boundary condition was run as a pressure outlet with zero gauge pressure. The exit temperature value specified in Table 47 is the reversed flow temperature which approximates the JetCat experimental exhaust gas temperature and the calculated average temperature on the exit plane.

Table 47. Inlet/Outlet boundary condition settings for a 30° sector domain

Boundary	$\dot{m}$ **(kg/s)**	**Gauge Total Pressure (Pa)**	**Temp (K)**
Air Inlet	0.02083	4800	375
Fuel Inlet	0.000421	5200	300
Exit	N/A	0	970

The "coupled" pressure-velocity coupling scheme was selected to solve for pressure and velocity as a linked pair. Spatial discretization was run first order upwind for all parameters during the comparison study discussed in Sections 8.3.4 and 8.3.5. Enhanced "accuracy" of a second order solution based on turbulent and combustion models of an unsteady flow modeled as a steady-state solution was seen as unnecessary. The three cases of detailed analysis on Configuration 7 discussed in Section 8.3.6 were run second order. All solutions were run steady-state, with the pseudo transient option enabled to accelerate convergence. Convergence was evaluated by residual and surface temperature monitors to ensure a steady state solution had been achieved with little or no output oscillation.

8.3.3 Grid Independence Check.

A grid independence check was performed on the initial combustor geometry, Configuration 1, described in detail in Section 8.3.4.1. This geometry was simplistic with the lowest cell count. If the fluid motion and temperature were resolved at these grid levels, then the higher resolution combustor variations would also be fully resolved given that they experience the same operating conditions. Three variations of the combustor Configuration 1 domain were created with resolutions of 14.7M, 16.6M, and 18.5M cells. Each resolution variant included different first cell wall spacing for prismatic cells, solid volume mesh boundary decay, and fluid volume mesh boundary decay. All three cases were run with the same boundary conditions and inputs. The velocity and temperature along six reference lines, shown in Figure 340, aligned with one of the three primary axes were obtained and compared. The average standard deviation across all three resolution variants was less than 1% in velocity and 1.8% in temperature. There were slight variations noted in the variants that were the result of modeling unsteady events in a steady-state solver. The solution variables oscillated within a narrow bound as the solver processed though all valid solutions of

the unsteady problem. Convergence was determined when plots of the residuals and force monitors oscillated within a narrow band (ringing) and did not experience any major variations. Since all of the grid resolutions yielded essentially the same result, the griding technique used for the medium resolution (16.6M cells) was selected for all remaining cases. This resolution helps ensure grid independence across all cases with minimal additional computational expense compared to the lower resolution case. The selected resolution used a first step wall spacing of 0.02 μm with a growth rate of 1.1, fluid volume boundary decay of 0.93, and solid volume boundary decay of 0.85.

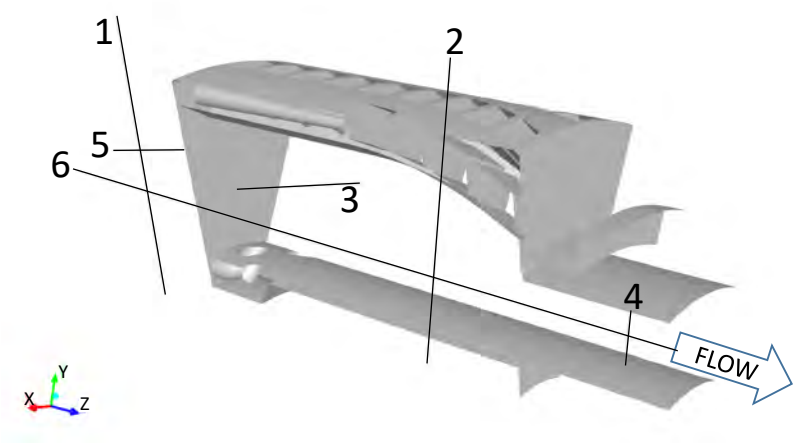


Figure 340. Initial combustor design, Configuration 1, grid independence check test locations on 30° sector domain

8.3.4 Design Evolution of New UCC Combustor Configurations.

This section provides the specific design motivation for each new UCC combustor configuration, diagrams of each configuration, and a short summary of the issues with each design found during computational analysis. These designs were developed using an iterative approach where the findings from each configuration were used to develop the successive design. The goals of this research were focused on the establishment of a centrifugal load on the combustion reactants, stabilizing combustion, distributing fuel effectively, presenting a uniform temperature distribution to the turbine rotor,

and achieving the correct turbine inlet angle. Following the subsections detailing each combustor, summarizing results are presented in Section 8.3.5 that look across all seven combustor configurations with these research goals in mind. These findings are not only useful to developing a small-scale UCC, but may be applicable to any small-scale combustor that could use swirl to increase combustor loading and shorten the axial length. Section 8.3.6 provides detailed analysis on Configuration 7, which was selected to be manufactured, including off-design results and pressure losses.

8.3.4.1 Configuration 1.

Design Motivation: The overall goal of these new combustor designs was to eliminate the need for migration of hot gases through the use of an axial combustor exit. This starting configuration had an overall diameter similar to the baseline JetCat combustor and incorporated backward-facing steps on the OD based on benefits observed in the concurrent testing outlined in Sections 6.2 and 6.3. Staying in line with the hardware that was tested in the concurrent study, the steps were alternated with one step injecting air and the next injecting fuel.

Prior experience from concurrent efforts on high-g combustion indicated that the injection velocity closely matched the bulk swirl velocity of the fluid in the combustor. A value of 2,500g_e was targeted because the Rayleigh-Taylor instabilities are optimized resulting in the fastest flame propagation rate [33]. Given the average radius of the new UCC combustors at JetCat scale, a g-load of 2,500g_e could be obtained by a 30 m/s inlet velocity to maintain a similar tangential velocity.

As part of this initial design an assumption was made that the compressor would evenly pressurize the plenum around the combustor and thus all inlet holes would see the same pressures. If all the injection holes were of uniform size and experienced uniform pressure then $\dot{m} = \rho AV$ was thought to apply equally through all holes. Since the total air inlet flow rate was known to be 0.25 kg/s, a total hole area of

approximately 3,600 mm^2 was used to try and achieve an injection velocity of 30 m/s through all holes. A total of 24 steps were needed to achieve the required hole area. The inlets on the OD were rectangular to maximize their area within the step. All of the fuel was injected within the first 50% of the combustor to establish a primary zone. The remainder of these fuel steps were used for air injection in the dilution half of the combustor. All prior UCC testing showed an exit temperature profile that was extremely hot on the OD, with a cold ID. For this reason nearly all of the air inlets were placed on the combustor OD, as shown in Figure 341, to push the hot gases off the OD wall.

This configuration also attempted to maintain the circumferential swirl from the combustor into the turbine rotor, thus no turbine stators were incorporated. Eliminating the stators would have further reduced axial length beyond the benefit from centrifugal swirl alone. All air was injected at a circumferential angle, or tangentially through backward facing steps, to drive the interior fluid in the circumferential direction. The intent here being that as the fluid migrated toward the turbine rotor it would maintain a sufficient uniform circumferential swirl to drive the turbine rotor from its intended inlet angle.

Configuration 1 Issues: There were two primary issues with this design. The first issue was that an acceleration of air over the first several inlet holes around the outside of the combustor caused a suction and pulled hot gases up into these holes rather than injecting air from them as shown in the temperature contours in Figure 342. The second issue was that there was very little mixing that took place in the dilution zone. The continuous angled air injection only from the combustor OD had limited shear with the bulk fluid in the combustor and only served to push the hot gases radially inward as they migrated axially. This result created a layered exit temperature profile that was cold at the OD and hot at the ID with a resulting

pattern factor of 1.84. This exit plane layering was also observed in the fluid velocity angle. The fluid near the OD traveled in a nearly circumferential direction, while fluid near the ID traveled nearly axially. The average velocity angle at the combustor exit was 23.8°. The air injecting from the dilution holes could not penetrate the bulk

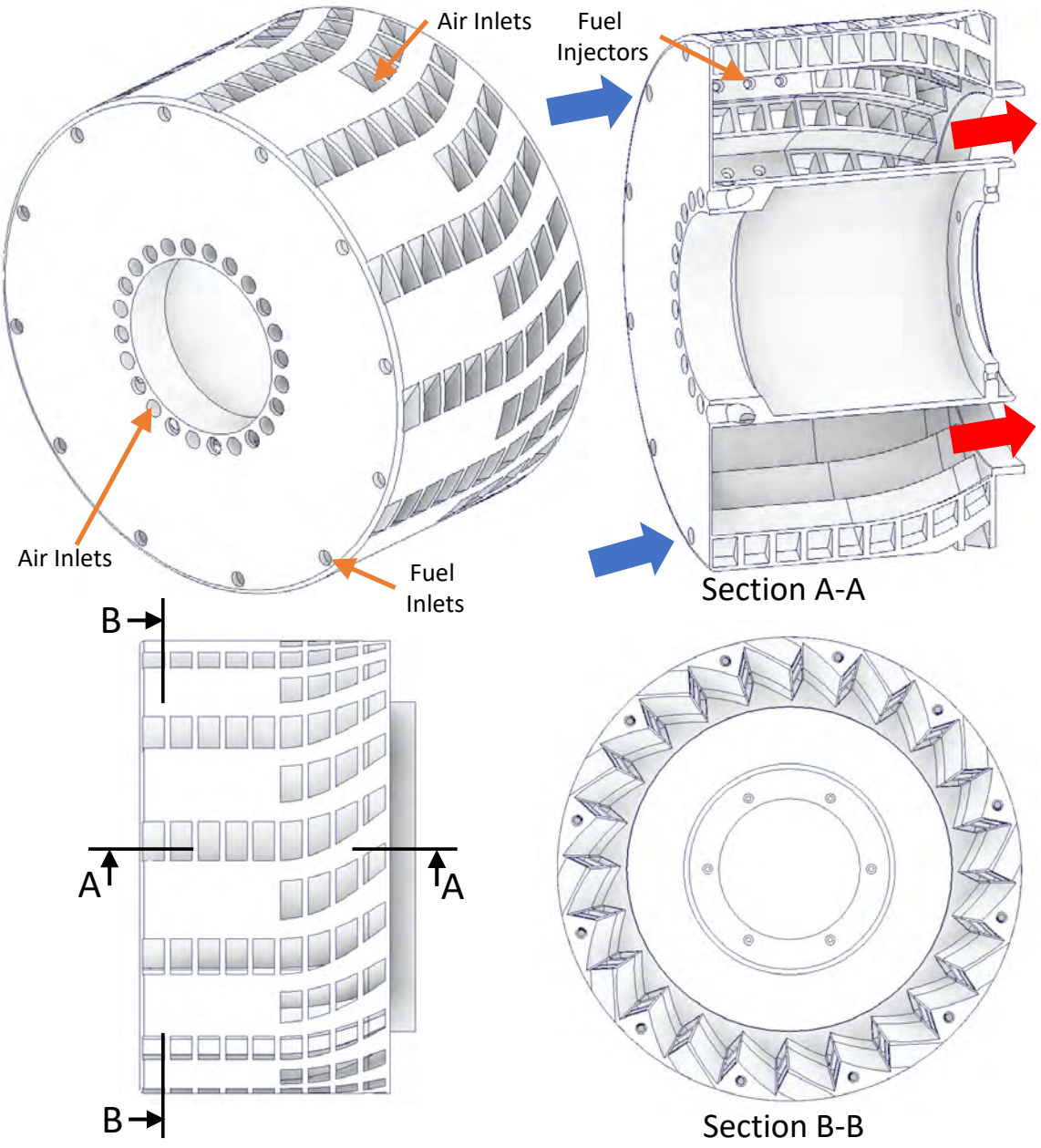


Figure 341. Combustor Configuration 1

fluid in the combustor and thus could not help maintain the circumferential swirl of the fluid near the ID.

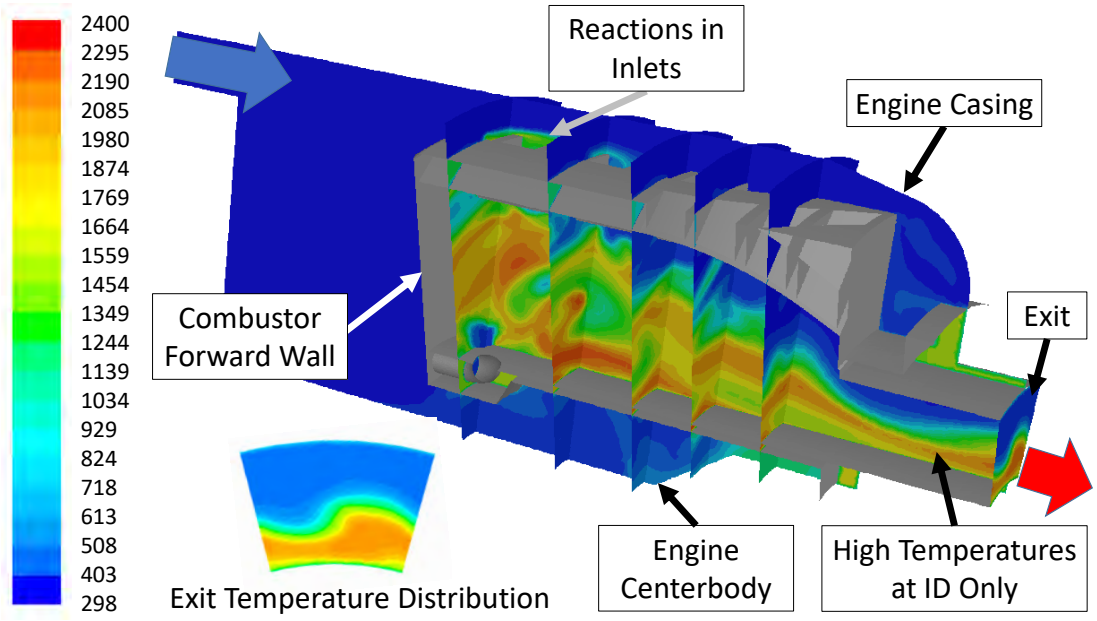


Figure 342. Temperature contours (K) at multiple reference planes in combustor Configuration 1

8.3.4.2 Configuration 2.

Design Motivation: This design attempted to address the suction on the inlet holes seen in Configuration 1 and add holes to the combustor ID to improve mixing and push the hottest temperatures on the exit plane to mid-span. To improve the airflow into the inlet holes a series of thin channels were made that stretched from the combustor OD to the JetCat casing. Each channel fed five air injectors, with the inlet holes positioned on a ramp. Internally the backward-facing steps were twisted to allow the channels around the combustor to begin turning the air in the circumferential direction even before entering the holes. The combination of the ramp, twisting channels, and fluid stagnating in each channel was thought to evenly pressurize the holes, prevent suction, and improve airflow into each hole.

Due to the change in the air inlet positioning, injectors were removed from the remainder of the fuel injection steps. The fuel steps were actually made to blend into the engine OD such that there were 24 steps at the forward end of the combustor and 12 steps at the downstream end. These step count differences are shown in Section B-B and C-C views of Figure 343. The reduction in step count was required to allow the hole ducting below the twisting channels to fit.

Holes were added to the ID of the combustor to push the hot gases off the ID wall. These holes were also drilled at an angle relative to the radial direction such that the exiting gases would have a circumferential swirl. The intent was that these holes would drive the bulk cavity fluid near the ID and up to the middle of the passage to maintain a circumferential swirl. The rectangular holes at the OD would then drive the bulk fluid near the OD down through the middle of the passage. This was the second attempt to try a statorless design. The total inlet hole area was 3,640 mm^2. Figure 343 shows several views of the Configuration 2 design.

Configuration 2 Issues: The addition of the holes on the ID wall served to push the hot gases toward the mid-passage, however, the injecting air from the ID and OD still had a limited amount of shear with the bulk cavity fluid which did not allow mixing. The pattern factor was slightly improved to 1.64, but still well above a desirable value. The angled injection air once again did not fully penetrate the bulk cavity fluid which allowed for gases at the mid-passage to flow nearly axially without being affected by the ID or OD air drivers. This flow path resulted in hot gases flowing nearly axially down the mid-passage, with the fluid near the ID and OD significantly cooler and moving with a greater circumferential angle. The resulting average velocity angle on the combustor exit plane was 19.6°.

It was also found that the fuel injection step created a low pressure region along the entire length of the step. This pressure distribution spread fuel throughout the

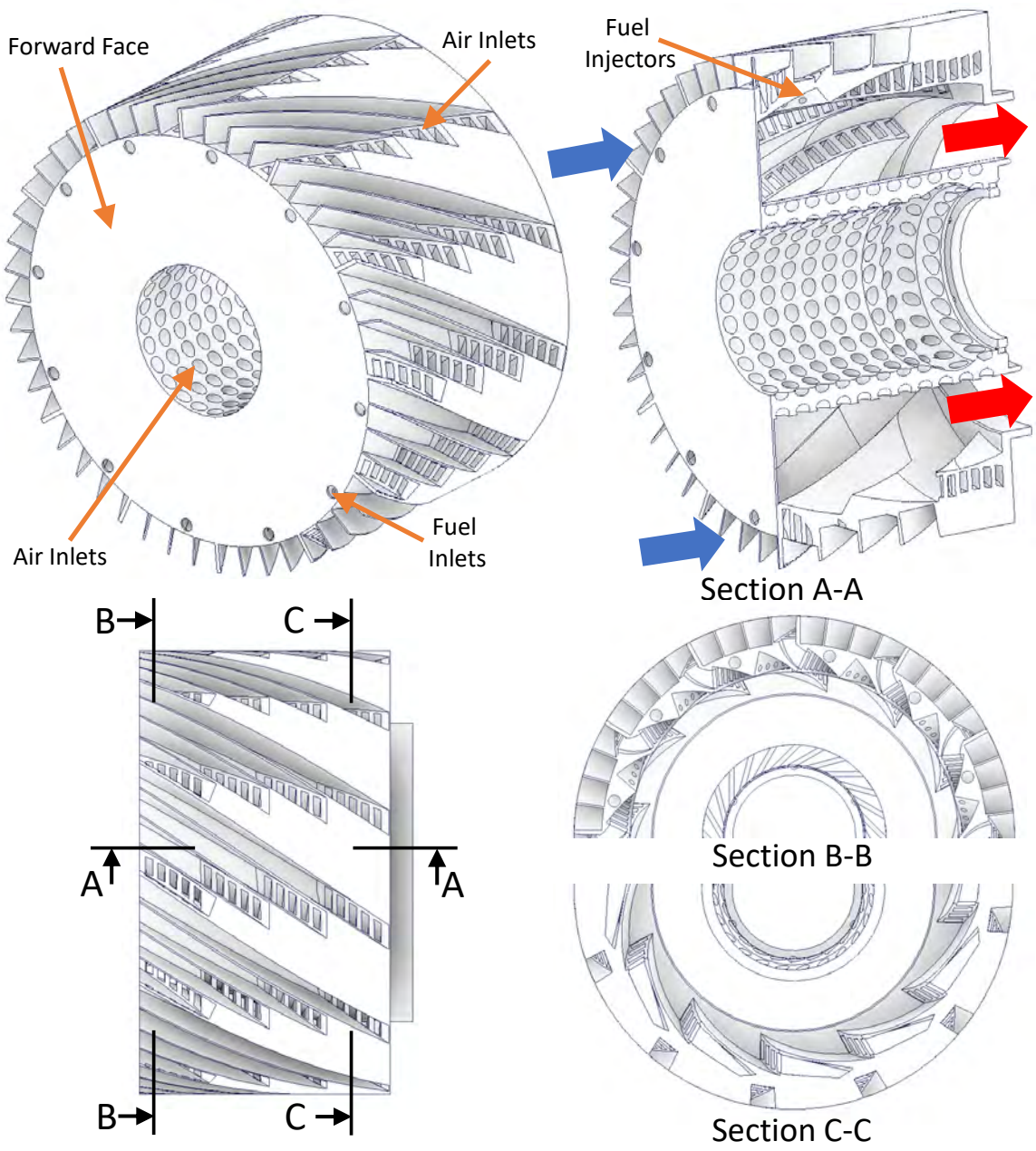


Figure 343. Combustor Configuration 2

entire combustor rather than maintaining it in a localized region at the upstream end (the primary zone) where the injection holes were located. Some of the fuel was able to travel axially and exit the combustor without reacting as shown in Figure 344.

As shown in Figure 343 the ID wall of the combustor was parallel to the engine

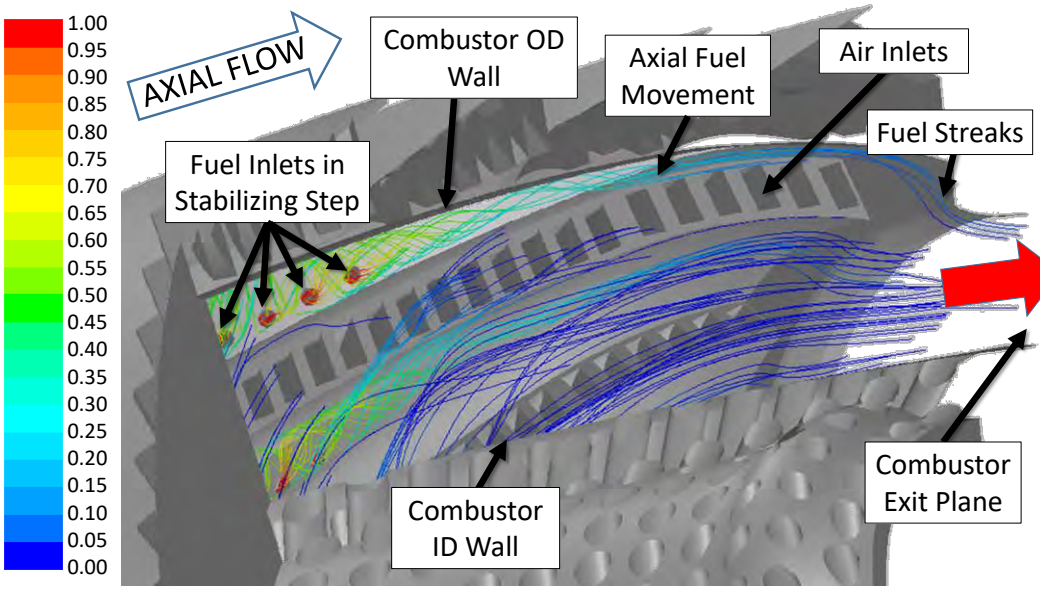


Figure 344. Fuel distribution in the stabilizing backward-facing steps (Results from C2). Colored by propane mass fraction

centerline. To reach the ID inlet holes, air from the compressor had to flow down the exterior forward face of the combustor and around the 90 degree turn into the cavity between the centerbody and combustor. The sharp turn resulted in a flow separation that caused the first several upstream rows of ID wall holes to have no flow or reversed flow through them. The updated OD air inlet hole design appeared to correct the outer injection issues.

8.3.4.3 Configuration 3.

Design Motivation: This design attempted to correct the axial movement of fuel behind the injecting steps. Fences were added to fuel injecting steps between the second and third, and after the fourth injectors to try and prevent the axial movement of fuel. The intent was to allow recirculation and mixing of fuel and air behind the step and between the fences, before being pushed radially inward to react. The OD injection pattern and transition from a 24-step to 12-step pattern was maintained from Configuration 2. Figure 345 shows several views of the Configuration 3 design.

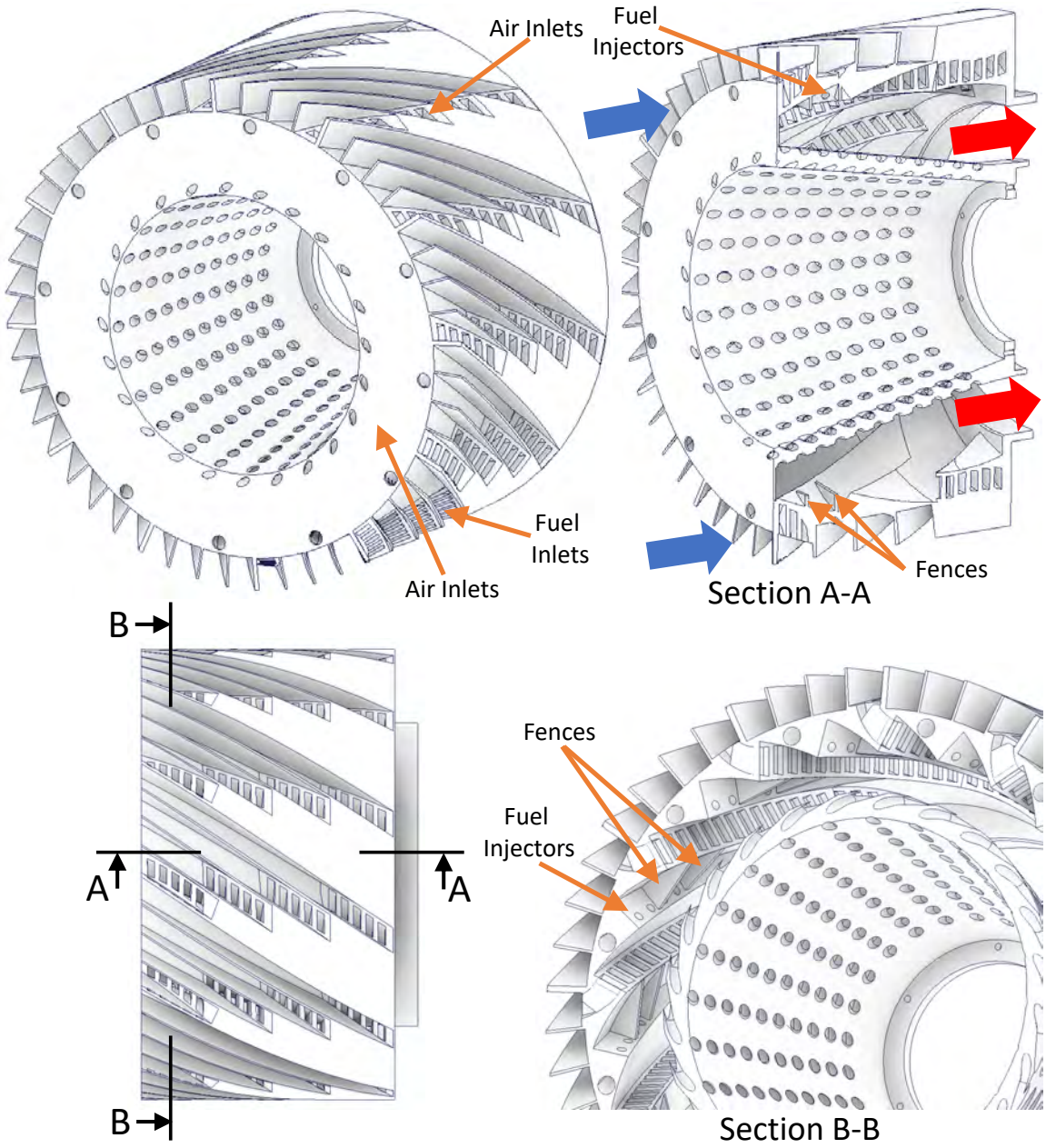


Figure 345. Combustor Configuration 3

In addition to the fuel fences, the ID wall was angled to produce a smaller passage at the upstream end of the combustor. This change also reduced the turning angle of air as it flowed between the forward wall of the combustor and the passage between the engine centerbody and the ID wall. The angled ID wall also served to increase the

passage height as more mass flow was added with downstream axial position. This design could potentially result in a more uniform circumferential velocity along the axial length of the combustor. The holes on the ID wall had to be resized to fit on the angled wall which resulted in a total inlet hole area of 3,217 mm^2.

Configuration 3 Issues: The fuel fences did prevent some fuel from exiting the primary zone, however, it didn't prevent all of it from moving as fuel was still able to flow around the fences and travel axially along the step length as shown in Figure 346. Additionally, there was still a flow separation around the exterior corner of the forward face to ID wall transition which resulted in the first several upstream rows of ID wall holes to have no flow or reversed flow through them.

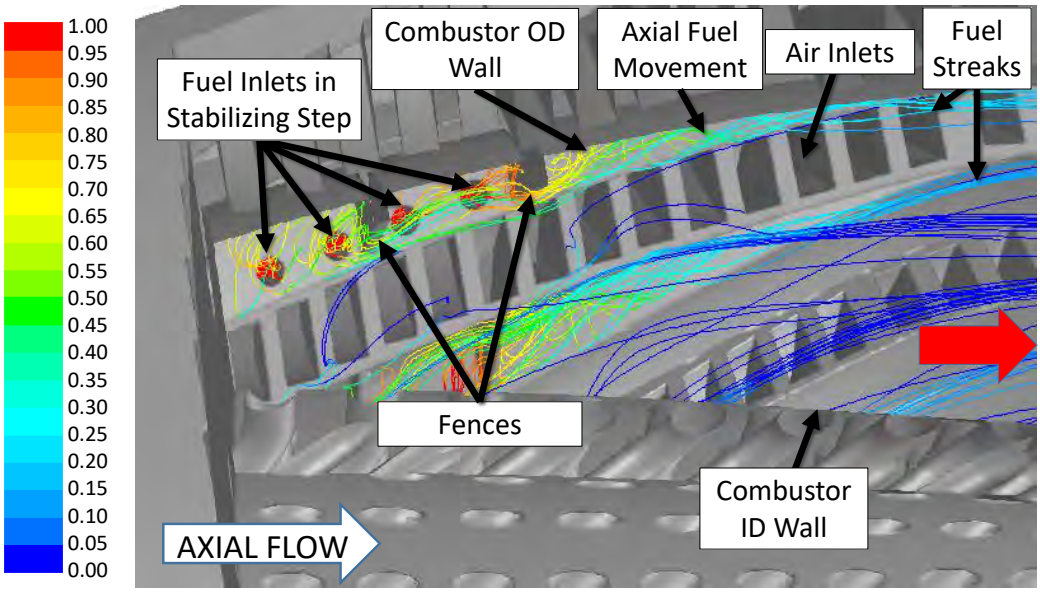


Figure 346. Fuel distribution in the stabilizing backward-facing steps with fences (Results from C3). Colored by propane mass fraction

As with the previous two configurations the angled injection air resulted in a lack of mixing with bulk cavity fluid and a layered combustor exit plane in temperature and velocity angle. The pattern factor was slightly improved from the previous configuration to 1.60. The average velocity angle on the combustor exit plane was 20.5°.

This was the first time the pressure distribution between the interior and exterior

of the combustor was examined as the primary driver of air distribution and injection velocity through the injection holes. By this point it was becoming apparent that the space outside the combustor was not behaving like a plenum and the pressure distribution was affected by the exterior flow paths and geometry.

8.3.4.4 Configuration 4.

Design Motivation: This configuration was identical to Configuration 3, but altered the position of the fuel injection to try and achieve a more complete distribution and prevent unburned fuel streaks from exiting the combustor. Given the success of the backward-facing step at distributing fuel, a radially oriented backward-facing step was added to the combustor forward wall for fuel injection as shown in Figure 347. The fuel steps, injectors, and fences from Configuration 3 were still present in Configuration 4, but no fuel exited the injectors positioned around the engine OD.

Configuration 4 Issues: The backward-facing steps along the forward wall did a better job of distributing the fuel across the radial span of the combustor, as shown in Figure 348, than the outboard mounted injectors from Configuration 1-3. However, since the ID and OD air injectors were not changed there was still a path down the mid-passage height that provided easy axial movement of fuel and air from the primary zone directly to the exit. The fuel and air that were well distributed along the forward wall of the combustor were quickly pushed to the mid-passage as the fluid moved axially. This consolidation of the fuel almost immediately after it was distributed negated the benefit of the radially mounted step and resulted in nearly the same exit profiles as the previous configurations. The pattern factor increased slightly to 1.69 and the average velocity angle at the combustor exit was 21.4°. Additional information on trying to maintain swirl through the dilution zone is given in Section 8.3.5.6.

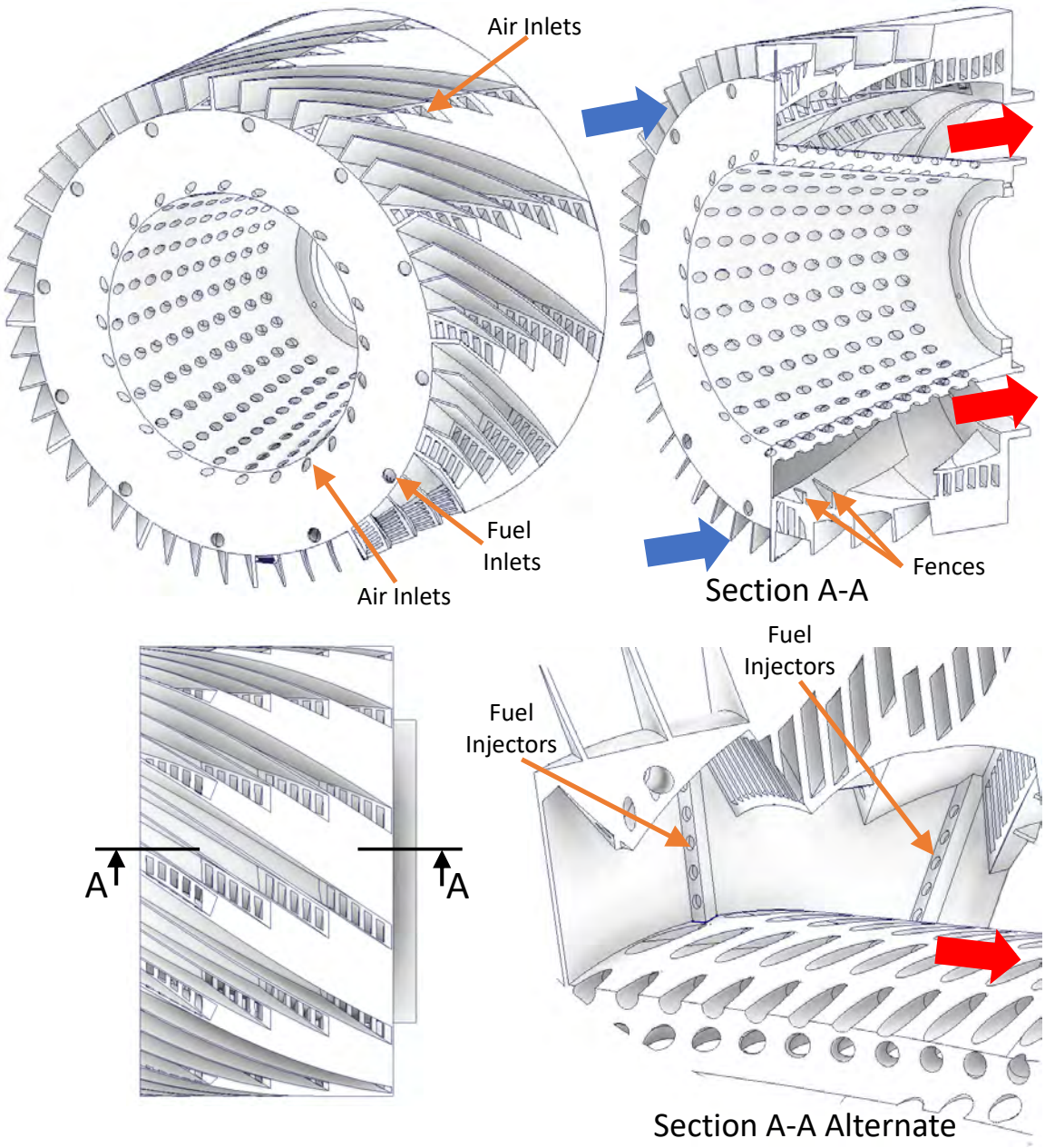


Figure 347. Combustor Configuration 4

8.3.4.5 Configuration 5.

Design Motivation: The purpose of this design change was to try and maintain circumferential flow through the entire primary zoneas well as attempt to correct the poor exit temperature distribution and exit velocity angles. Configuration 5 was the

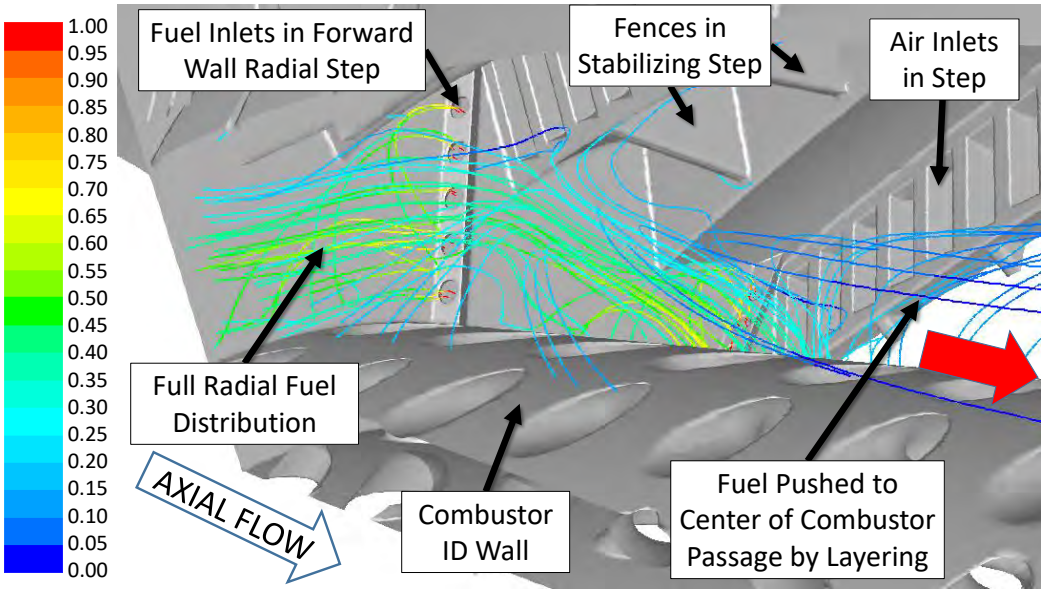


Figure 348. Fuel distribution in backward-facing steps on the combustor forward wall (Results from C4). Colored by propane mass fraction

first major departure from the initial designs. This configuration featured a primary zone that was isolated from the secondary/dilution zone by a hardware constriction as shown in Figure 349, and compared to the previous single chamber designs of Configurations 1 - 4 in Figure 357. Additionally, backward-facing steps were only found in the primary zone. Steps were added to the ID wall as well to try and improve airflow and add additional flame holder locations in the primary zone.

Fuel was no longer injected into the recirculation pocket of a step as was previously done. Instead, more injectors were added that directed fuel radially inward toward the center of the combustion annulus. This orientation caused a shear between the fuel, and air entering through the steps and allowed for fuel and air mixing prior to reaching the recirculation of the backward-facing step. This arrangement more closely approximates the conditions of Lapsa and Dahm [56] who experimentally demonstrated the benefits of backward-facing steps for centrifugally loaded pre-mixed combustion. Moving the fuel ports also created a step that was purely for flame

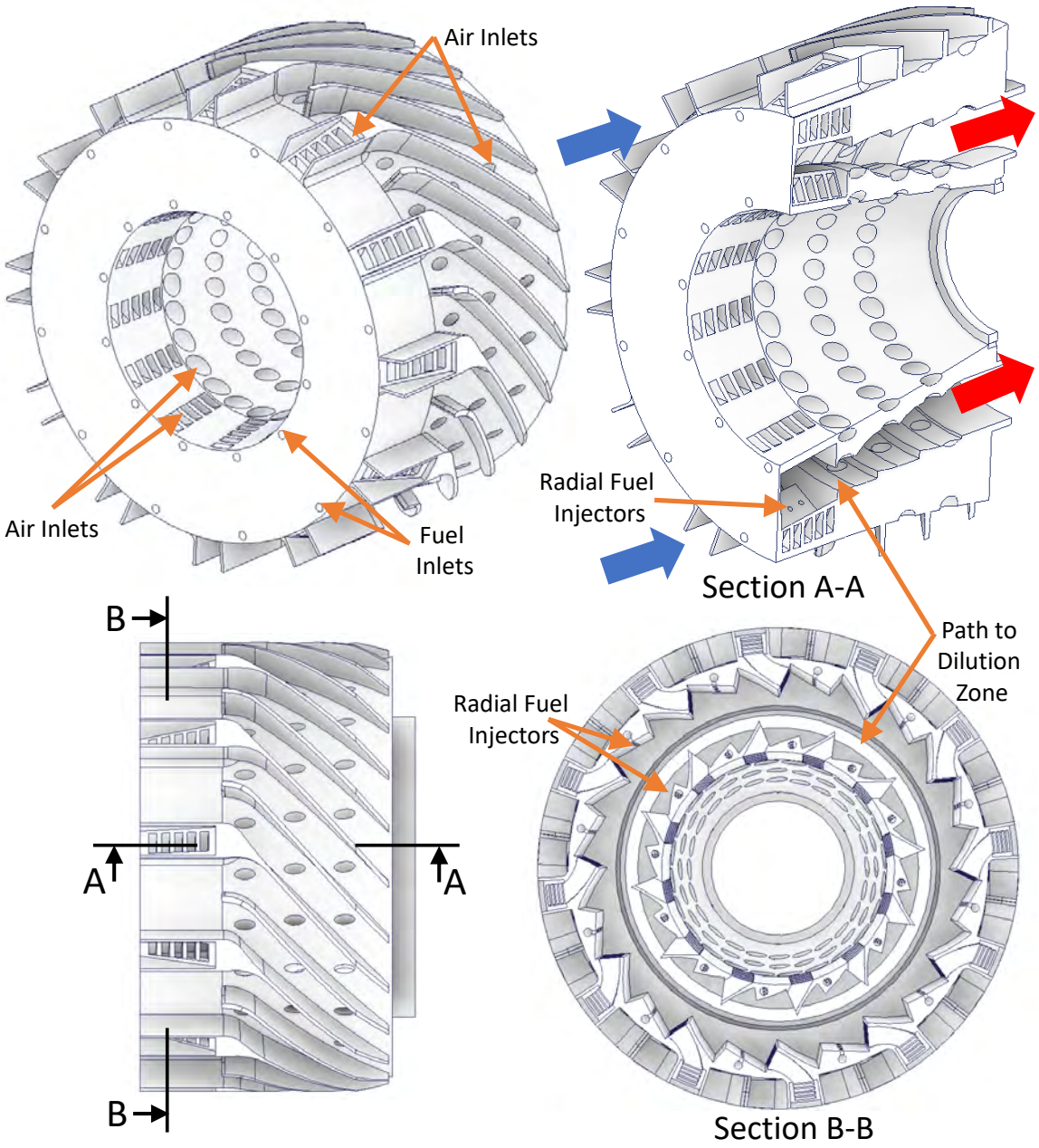


Figure 349. Combustor Configuration 5

stabilization as air was still only injected from every other step. The stabilizing step height was reduced to allow the air injection to happen more tangentially.

The dilution zone still tried to maintain a circumferential swirl to eliminate the need for stators. This configuration used fewer injecting holes with a larger diameter

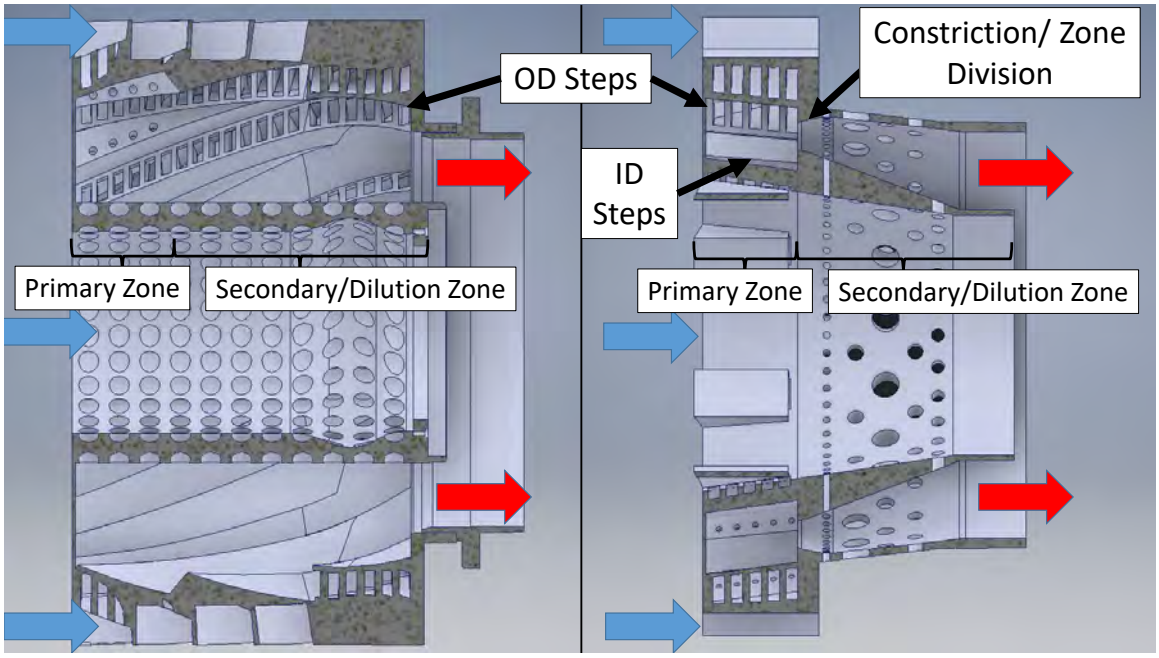


Figure 350. Comparison of single vs. dual chamber combustors

and staggered them such that injection occurred from the OD, then ID and repeated with axial location downstream, as shown in Figure 351. This offset would force the hot gases exiting the primary zone to travel in a more serpentine path to drive more mixing, yet keep the bulk fluid traveling in the circumferential direction. The total inlet hole area was 2,824 mm^2.

Exterior channels were again present to guide the flow into the primary zone inlets and the dilution zone OD inlets. The primary zone inlets were positioned linearly and used the same ramp technique discussed earlier to prevent suction across the first few holes. The channels in the dilution zone were curved around the combustor to start the air flowing in the circumferential direction and make it easier for the air to enter the holes. The channels were also ramped as the passage was shorter at the downstream end of the combustor than at the upstream end to help ensure air entered all three sets of OD dilution holes evenly. The ID wall was tapered as well but did not include channels or additional guides to direct the air into the holes.

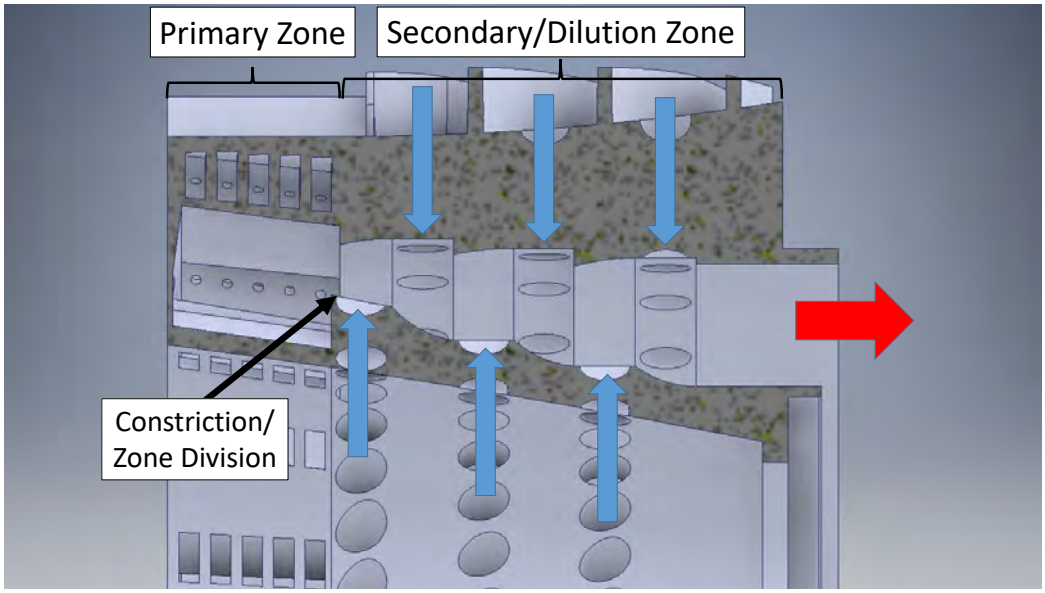


Figure 351. Configuration 5 cross-section with secondary/dilution air inlet holes labeled by blue arrows

Configuration 5 Issues: The combination of a separate primary combustion zone and alternating OD to ID dilution jets greatly improved mixing while still maintaining reasonable circumferential swirl at the exit plane. The pattern factor was reduced to 1.3, which is still well above the desired values, but the magnitude of the hot gases at the mid-passage were greatly reduced. The average velocity angle at the combustor exit plane was also increased significantly to 28.2°. While these values were improved, they were still not where they need to be.

There was still a flow separation around the exterior corner of the forward face to ID wall transition. This separation resulted in the first several upstream ID wall air injectors in the primary zone to have negligible airflow. The air that did move through the holes injected nearly radially due to the lack of curvature in the injector flow path through the step. Even without the ID holes contributing a significant amount of air, the primary zone equivalence ratio was 1.4. At that level this combustor was the first of the new configurations to follow the RQL cycle.

The tangential velocity in the primary zone was on the order of 40 m/s which equates to approximately $4{,}500 g_e$. This value is larger than desirable, but there are limited options to control velocities as discussed in Configuration 6.

8.3.4.6 Configuration 6.

Design Motivation: This configuration looked to re-balance the pressures around the combustor to better control the injection velocity and centrifugal loading. Poiseuille flow is pressure driven flow through pipes and ducts, yet is not applicable to the current geometry due to the very short duct lengths. It was unfortunate that Poiseuille flow could not be used as there is an exact solution for a number of pipe or duct shapes. Additionally, while the pressure differential between both ends of the pipe may be fixed by combustor geometry or flow conditions, the velocity through the pipe or duct could be controlled by varying the duct radius.

A hole length to diameter ratio greater than what can be achieved by sheet metal was required to turn the fluid from the axial direction outside the combustor to achieve tangential injection inside the combustor. In the present geometry, the wall thickness of the combustor was only on the order of 3-5 times the diameter of the holes, however, this ratio was small enough that the equations of orifice flow were valid. Using orifice flow properties, the velocity through the inlet holes is given by Equations 147 and 148, which define the velocity in terms of the head (Ψ), based on the pressure differential (P) across the inlet [176]. Using the pressure differential between the inside and outside of the combustor calculated by CFD, these equations could then be used to predict injection velocities at each axial position of the combustor. Having these values would allow the designer to re-distribute or re-angle the inlet holes to achieve desired values in a later design iteration.

$$\Psi = \frac{P}{\rho g} \tag{147}$$

$$V = \sqrt{2g\Psi} = \sqrt{\frac{2P}{\rho}} \tag{148}$$

To reduce the inlet velocity in the primary zone of Configuration 6, the ramp for the OD inlet holes was not fully closed off at the casing. Instead, a small opening was left at the top of the ramp to prevent stagnation of air over the holes as shown in the ramp detail inset in Figure 352. This small change was intended to help keep the pressure differential across the holes lower, and thus achieve lower injection velocities, and lower resulting tangential velocities. The number of steps on the ID wall was reduced from Configuration 5 to make room for a longer injecting step that enabled a more tangential exit angle. Scoops were added to overcome the separation along the exterior corner near the upstream ID inlets that had plagued the other configurations. These scoops were designed to stick out into the flow and pull air into the primary zone ID inlets as shown in Figure 352.

As explained further in Section 8.3.5.6, trying to achieve adequate mixing in a dilution zone that was driven to maintain circumferential swirl that eliminated the need for stators proved to be a difficult task due to contradictory requirements. As such, Configuration 6 was the first combustor of the series designed to use stator vanes to control the turbine rotor inlet angle. Since the stators eliminated the need to maintain a circumferential swirl in the dilution zone, radially injecting dilution holes were added. The shear between the radial dilution and the axial or slightly swirling hot gases through the dilution zone would greatly enhance mixing to present a more uniform temperature distribution to the turbine rotor. A centrifugally loaded swirl was still maintained in the primary zone. The total inlet hole area was 2,157 mm^2.

The fuel injection technique introduced in Configuration 5 was used again in this configuration. The number of injector locations circumferentially along the ID wall

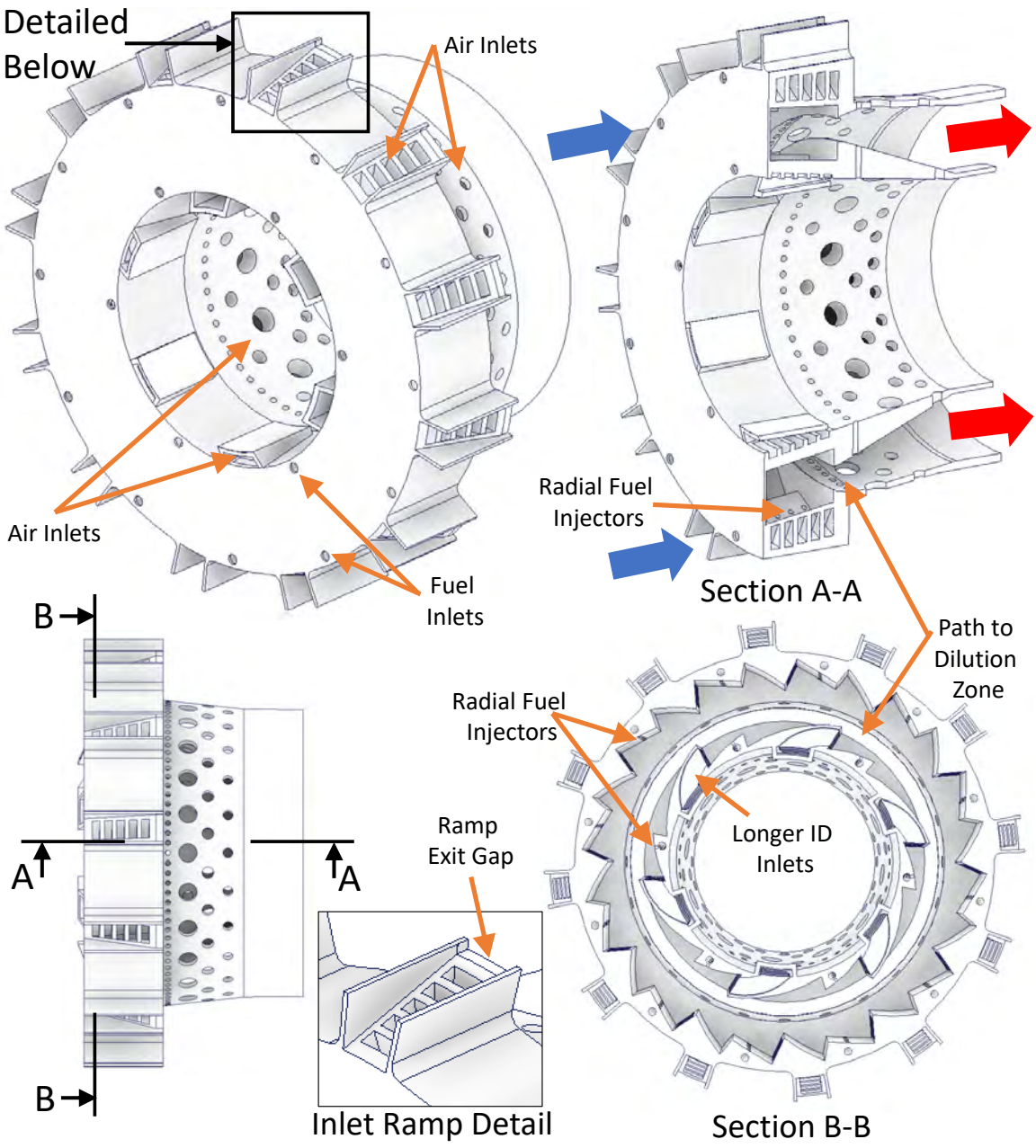


Figure 352. Combustor Configuration 6

was decreased from 12 in Configuration 5 to 6 in Configuration 6 due to the number of ID steps also being cut in half.

Configuration 6 Issues: The implementation of the radially injecting inlet holes caused a substantial reduction in the pattern factor down to 0.61. This value is still

high compared to modern large combustors, but it is not known how it compares to the baseline JetCat combustor. The equivalence ratio in the primary zone was increased to 1.7 due to the reduced number of inlet holes on the ID. The OD air injectors maintained the same mass flow rate as Configuration 5. The injection velocity in the primary zone was reduced slightly to 38.7 m/s, which was still approximately $4{,}200 g_e$, and larger than desired.

Due to the constriction between the primary zone and the dilution zone the hot gases and unburned species exit at high speed, which could potentially be hindering mixing. If the velocity could be reduced through the dilution zone the mixing might be enhanced resulting in an even better pattern factor.

8.3.4.7 Configuration 7.

Design Motivation: This design attempted to slow the axial flow rate of gases through the dilution zone to provide a greater residence time for reactions. This configuration was identical to Configuration 6 except for the passage shape downstream of the constriction between the primary and dilution zones. Configuration 6 used a diverging passage after the constriction. Configuration 7 opened the passage quickly to diffuse the exiting hot gases and slow the flow velocity. The same dilution hole pattern was used which maintained a total hole area was 2,157 mm^2. Configuration 7 is shown in Figure 353. This configuration was selected to be manufactured so additional design details are shown in Sections 8.3.6 and 8.4.1.

Configuration 7 Issues: The pattern factor increased from Configuration 6 to a value of 1.6 due to a single hot streak that originated in the primary zone and was not mixed out in the dilution zone. The circumferentially averaged temperature profile, however, still maintained a desirable distribution with the peak temperature just outboard of mid-passage. The ID and OD temperatures were approximately equal, but slightly cooler on the ID which is desired to protect the bearings. A future

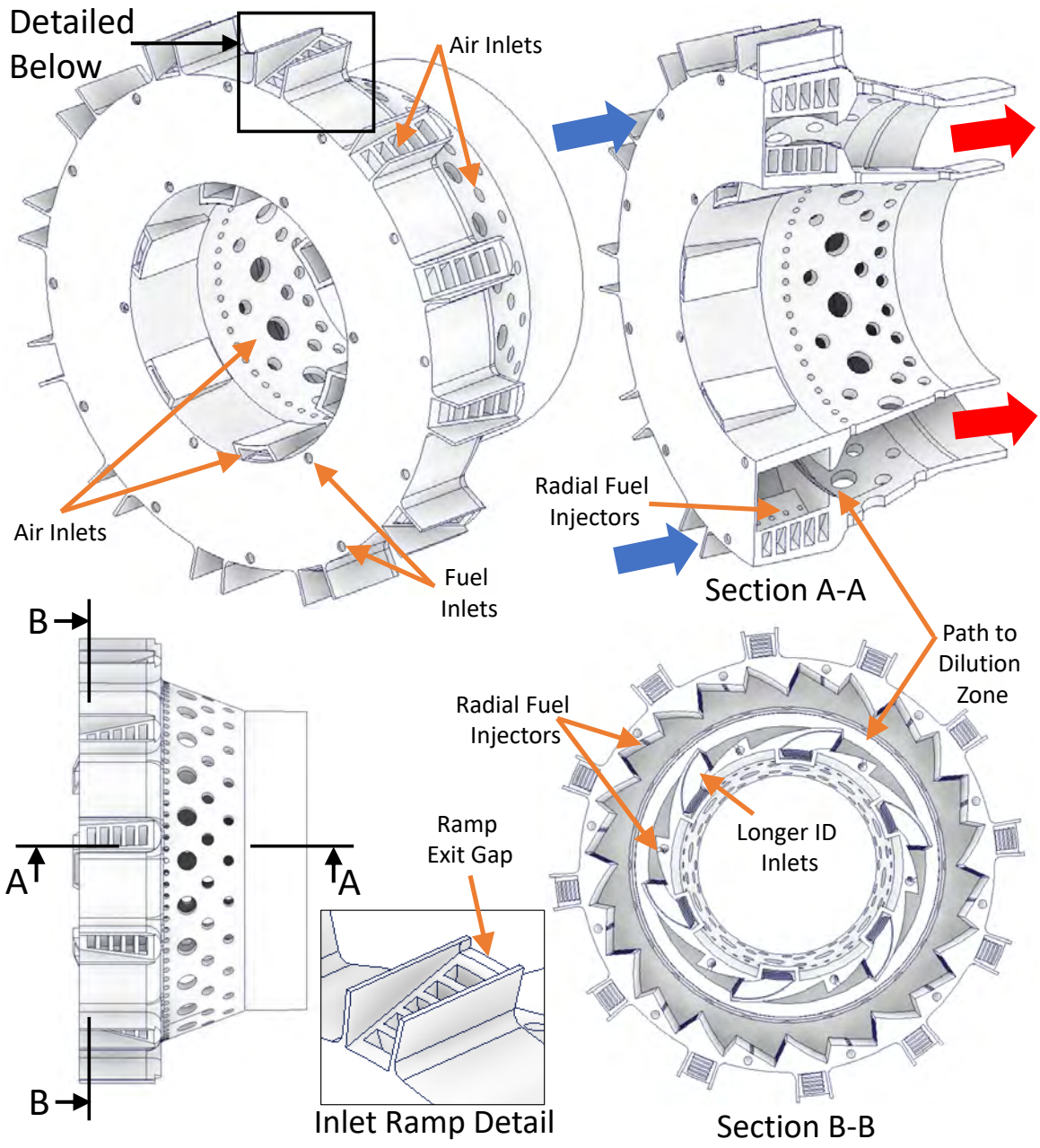


Figure 353. Combustor Configuration 7

effort could optimize the dilution hole pattern to achieve a better pattern factor, but maintain a similar temperature profile with a reduced peak temperature.

The velocity in the primary zone remained high, and actually increased slightly from Configuration 6 to 41.2 m/s. This velocity resulted in a centrifugal loading

of approximately 4,800g_e which was greater than the desired 2,500g_e to maximize Rayleigh-Taylor instabilities without localized quenching. This configuration still had several performance values that could be improved, however, based on the computational analysis it appeared that it would be operational in its current state to enable experimental testing.

8.3.5 Summarized Computational Results.

The following subsections provide summarizing results that looked across all seven combustor configurations. The results are focused on the research goals of establishment of a centrifugal load on the combustion reactants, stabilizing combustion, distributing fuel effectively, presenting a uniform temperature distribution to the turbine rotor, and achieving the correct turbine inlet angle.

8.3.5.1 Establishing Centrifugal Loading.

The primary goal in developing a UCC is to reduce weight. The high-g UCC does this by shortening the combustor and forcing the air to swirl in a recessed circumferential cavity to achieved the necessary residence time for complete combustion. This bulk swirl also establishes a centrifugal load on the combustion reactants which has been shown to aid in mixing an decreasing reaction times. Combustors that utilize swirling centrifugally loaded combustion must maintain bulk fluid tangential velocities below a value corresponding to a g-load of 7,500g_e or below at an equivalence ratio of one, or risk flameout [3]. For an increase or decrease in equivalence ratio from stoichiometric the g-load limit for stable combustion is reduced [3]. A value of 2,500g_e was targeted because the Rayleigh-Taylor instabilities are optimized [33] which required a 30 m/s inlet velocity to maintain a similar tangential velocity.

Due to the high flow rates and small-scale of the engine, the area outside the combustor did not behave like a plenum. As such the geometry of the outside of the

combustor was determined to be as important as the geometry inside the combustor. Inlets positioned near constrictions between the combustor and the engine casing resulted in increased flow velocity and thus a drop in pressure. Some of these pressure drops in early combustor configurations were significant enough to create a suction on the inlets and draw flames out of the combustion chamber. As a result of this behavior the outer contour of the combustor was shaped as a ramp, at least in the regions where inlets were present, to force fluid into the holes rather than allowing it to pass over them and create a suction like a venturi.

Since the wall thickness was approximately 3-5 times the diameter of the holes, the velocity through the holes was determined by orifice flow theory [176] with the injection velocity defined earlier in Equation 148. Equation 149 gives the volume flow rate (Q) through each hole; where A is the area of the hole, and K is a hole geometry correction factor (or discharge coefficient) which varies based on the hole style and material thickness. The value of K was 0.82 for holes through thick walls (2d to 4d). The volume flow rate is an important quantity when considering local equivalence ratios and dilution hole positioning. The equations of orifice flow theory were successfully used to confirm the relationship between inlet velocity and pressure differential when applied to converged CFD data. As a design tool these equations could then be applied to CFD pressure differentials between the inside and outside of the combustor to enable a designer to re-distribute or re-angle the inlet holes to achieve desired values in a later design iteration.

$$Q = AVK \tag{149}$$

Since the velocity is not a function of the hole area, this reduces the number of options available to control the inlet velocity in these small-scale combustors. The designer must reshape the hardware outside and inside the combustor to achieve a

different pressure distribution and thus a different pressure differential if a velocity change is needed. In the current study the pressure was controlled by adjusting the inlet hole ramp angle and in some configurations the ramps were extended to the outer engine casing and contained by side walls to force the fluid over the holes to stagnate and build pressure outside the hole.

8.3.5.2 Step-Stabilized Combustion.

The backward-facing steps were shown to aid in the development of centrifugal loading by enabling near tangential injection, but the non-injecting stabilizing steps played a major role in flame holding in the primary zone. Figure 354 shows temperature contours in the primary zone of Configuration 6 (which is the same as Configuration 7) where the pilot flame is visible behind the stabilizer steps. The larger reactions are anchored to the shear layer originating at the step air inlet. These steps would not function in their current configuration in an axial flow combustor, or in regions of the current combustors that experience axial flow. For this reason the dual chamber combustors only featured steps in the primary zone.

The steps in Configurations 1-4 (and the 6- and 12-stepped combustion rings in Chapter VI) included fuel injection into the recirculation zone of the stabilizing steps. This arrangement did not demonstrate the same flame holding characteristics behind the stabilizing steps that were shown in Figure 354. Due to a global equivalence ratio of 0.33 and a limited quantity of air in the primary zone, the recirculation region behind the stabilizing steps was likely too rich to burn. This difference in performance highlights the benefit of the radially injecting fuel ports upstream of the stabilizer steps demonstrating enhanced fuel/air mixing and enabling premixed combustion behind the step.

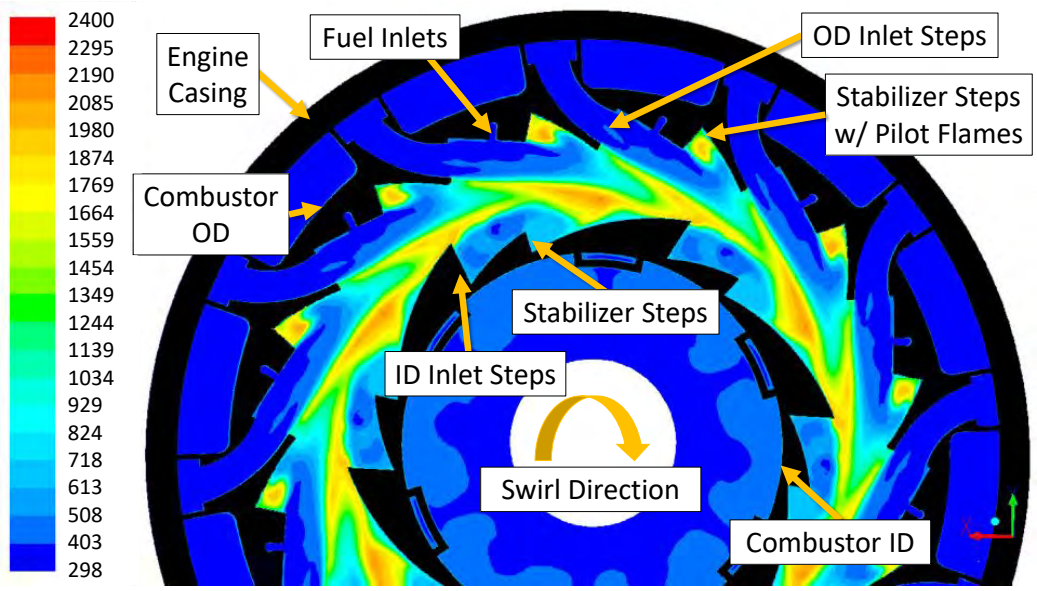


Figure 354. Temperature contours (K) showing flames anchored to steps (Results from C6)

8.3.5.3 Fuel Distribution in Backward-Facing Steps.

As demonstrated in Configurations 2-4, backward-facing steps were very effective at distributing fuel along the entire length of the step. In these configurations, however, the desire was to maintain the fuel behind the step toward the upstream end of the combustor (i.e. in the primary zone). By distributing the fuel to the entire combustor the idea of separate primary and dilution zones was eliminated. If reactions are initiating near the end of the dilution zone there is very little likelihood a uniform or desirable exit temperature distribution would be achieved. Additionally, as discussed in the previous section, the presence of high concentrations of fuel in the recirculation zone behind the steps limited pilot flames and flame holder performance.

For all the reasons just discussed Configurations 5-7 positioned the fuel injectors on the radially inward facing wall of the stabilizing step between the air inlets and the recirculating zone of the stabilizing backward-facing step. This arrangement allowed for fuel and air mixing prior to reaching the stabilizer step, and more closely approx-

imates the test conditions of Lapsa and Dahm [56] which demonstrated beneficial combustion behaviors. The results for this injection method were shown in Figure 354, which indicate sufficient mixing prior to reaching the stabilizing step to maintain a pilot flame in the recirculation zone of the step.

8.3.5.4 Controlling Exit Temperature Profiles.

After ensuring a g-load was established in the primary zone, the second major goal of this research was to establish a desirable turbine rotor inlet temperature distribution. In the first four configurations it was observed that due to the air inlets injecting at approximately 15° from tangent in the secondary/dilution zone, the incoming air had a negligible amount of shear with the bulk fluid in the combustor and formed a cold air layer on the OD and ID combustor walls. These fluid temperatures near the walls were roughly at the compressor exit temperature of 375 K as shown in Figure 355. Configuration 1 only had OD injection holes so there was a cold OD layer at approximately 375 K, and a hot ID layer at combustion temperatures. Circumferentially averaged temperatures on the combustor exit plane are shown in Figure 356 for all seven of the combustor configurations. The lack of mixing in the first four configurations is also demonstrated by the circumferentially averaged 1500-1850 K temperatures near 50% radial position.

In combustor Configuration 5, the combination of the more radial injection angle, the alternating injectors with axial position, and the more constricted passage due to the dual-chamber configuration, resulted in enhanced mixing through the secondary/dilution zone. The mixing was still limited and resulted in a temperature stratified exit plane, but it performed considerably better than Configurations 1-4. The mean temperature on the exit plane was 917 K with a peak circumferentially averaged temperature of 1231 K.

After the first five configurations failed to achieve a desirable exit temperature

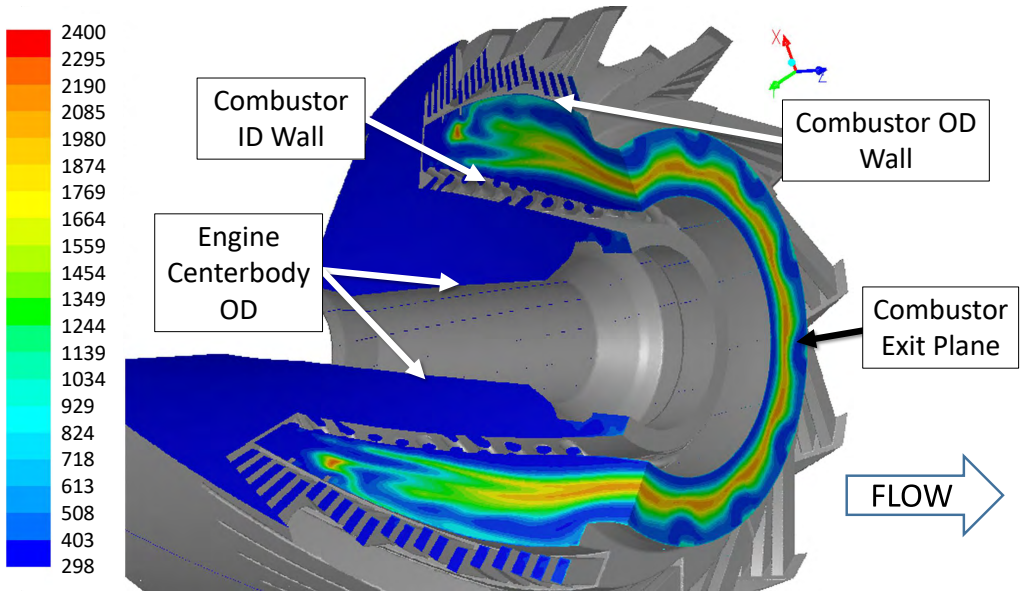


Figure 355. Secondary/dilution air layering. Temperature contours on periodic walls of combustor C4

distribution it was determined that the requirements of secondary/dilution swirl and adequate mixing are contradictory, and difficult to achieve together. For combustor Configurations 6 and 7, the secondary/dilution air inlets were positioned radially and the fluid in the combustor was allowed to flow axially after leaving the swirling primary zone. Configurations 6 and 7 eliminated the layering effect and achieved an average exit plane temperature of approximately 920 K. Configuration 7 also achieved the desirable slight OD skew of the peak temperature off the passage centerline as shown in Figure 356 which is needed for maximum turbine power extraction [28][29].

8.3.5.5 Additional Benefits of Dual Chamber Combustors.

The early single-chamber combustors of Configurations 1 - 4 experienced difficulty in maintaining swirl and g-load. In the open, single-chamber combustors, represented by Configuration 2 in the left side of Figure 357, the fluid began to transition from a circumferential swirl in favor of a more axial path within 7% of the overall length from the combustor forward wall. The dual-chamber designs added a mechanical

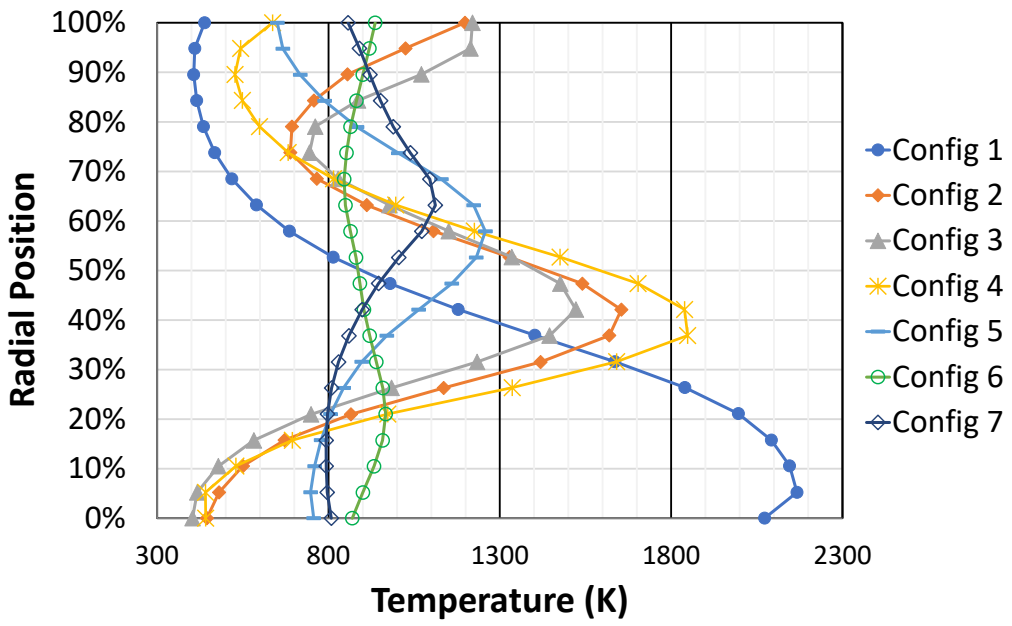


Figure 356. Circumferentially averaged temperatures on the combustor exit plane for all configurations

means (a wall) to help keep the fluid in the primary zone moving circumferentially as represented by Configuration 6 in the right side of Figure 357. In these dual-chamber combustors the primary zone maintained a circumferential swirl for the axial length of the primary zone. Both the single-chamber and dual-chamber combustors featured OD steps, but by constricting the exit area of the primary zone, steps were also added to the ID of the dual-chamber combustor without violating the combustor ID size restriction. This arrangement allowed for more uniform tangential air injection by injecting from both the OD and the ID, as well as adding flame stabilizing steps to the ID region.

One added benefit of the dual-chamber combustors was that they approximately followed the idealized rich-burn, quick-quench, lean-burn (RQL) cycle [20]. Since all of the fuel was added to the primary zone, the combustion in this zone took place at fuel-rich conditions. When the combustion products exited the primary zone chamber

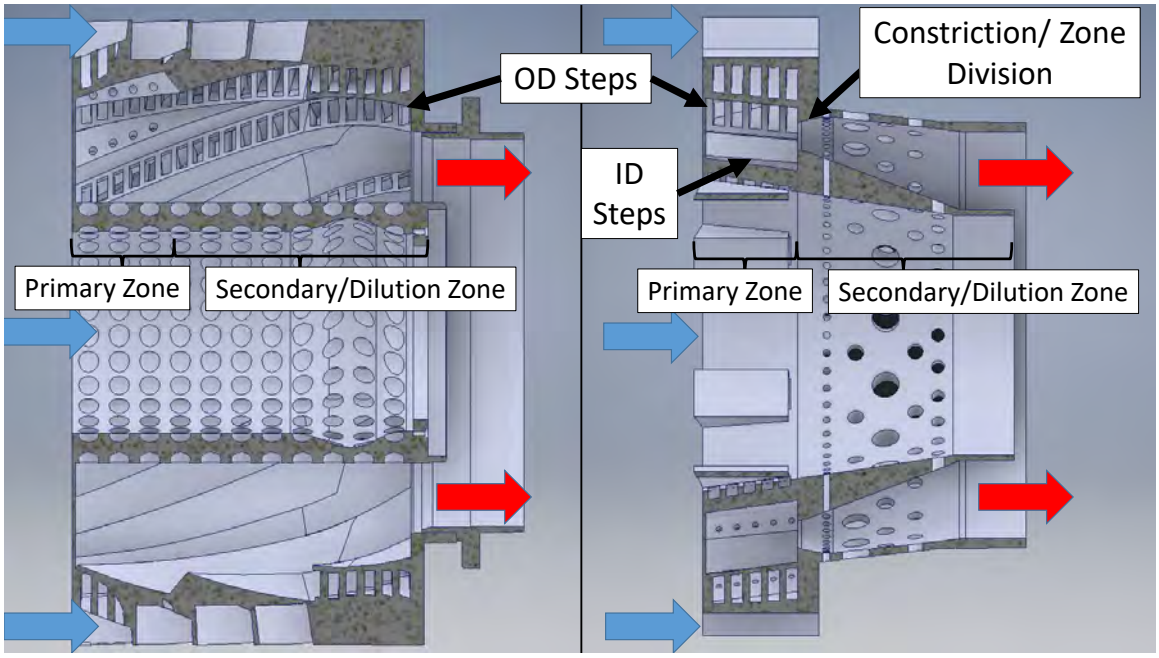


Figure 357. Comparison of single vs. dual chamber combustors

they were quickly introduced to secondary and dilution air which quenched the flame and a fuel-lean condition remained through the rest of the combustor. The benefit of this combustion cycle was that it skips the stoichiometric combustion regime which limits the heat load to the engine and reduces NO_x emissions [20].

There is a drawback to constricting the exit of the primary zone, which is that the reactions are kept in closer contact to walls which can quench the flame and increase the heat load to the metallic hardware. This affect is seen in the temperature distribution of Configuration 6 shown in Figure 358. Configurations 6 and 7 were nearly the same, differing only in the shape of the transition following the exit from the primary zone into the secondary/dilution zone. Combustor Configuration 7 featured a transition that quickly diffused the gases exiting the primary zone as shown in Figure 359 along with corresponding temperature contours. A comparison of Figure 359 to the Configuration 6 results in Figure 358 show a larger combustion volume in the secondary/dilution zone in Configuration 7 due to less wall quenching.

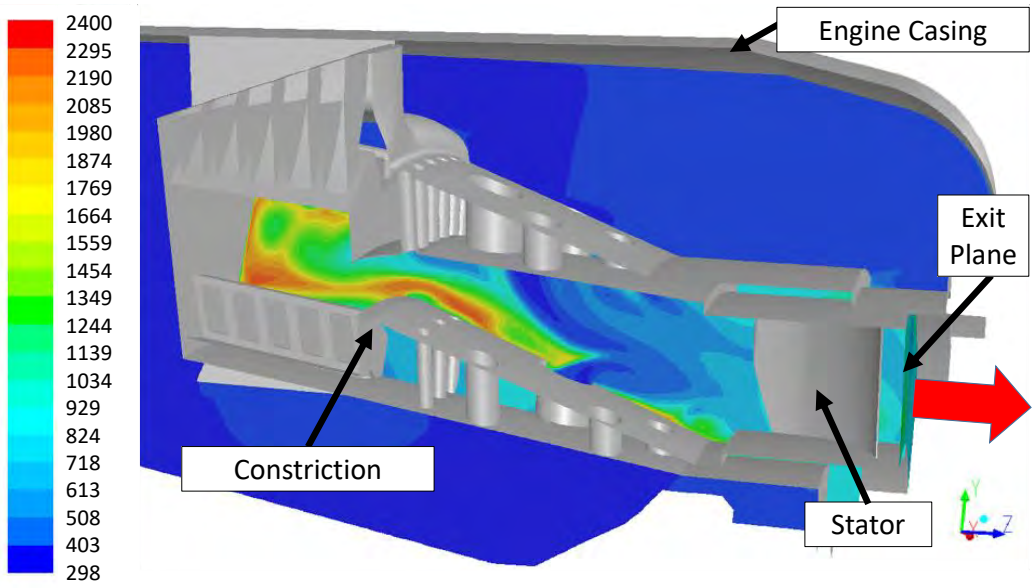


Figure 358. Temperature contours (K) in dual chamber Combustor Configuration 6

The diffuser just outside of the primary zone used in Configuration 7 caused an increase in the static pressure inside the combustor. This design feature provides the designer with one additional option to help control the pressures and velocities throughout the combustion chamber.

8.3.5.6 Maintaining Swirl Through The Combustor.

The final goal was to maintain sufficient swirl throughout the entire combustor to have the bulk fluid entering the turbine rotor angled at approximately 65°, thus eliminating the need for stators. The first five combustor configurations were developed without stators. Due to the axial acceleration of the bulk fluid in the combustor it was difficult to maintain a consistent swirl of any angle, nevermind a swirl with an angle of 65°. By the combustor exit plane the velocity angle was typically stratified where the ID and OD fluid achieved higher angles of swirl, up to 53°, but the middle portion of the exit plane produced nearly axial flow at just 11° as shown in Figure 360 for combustor Configuration 5.

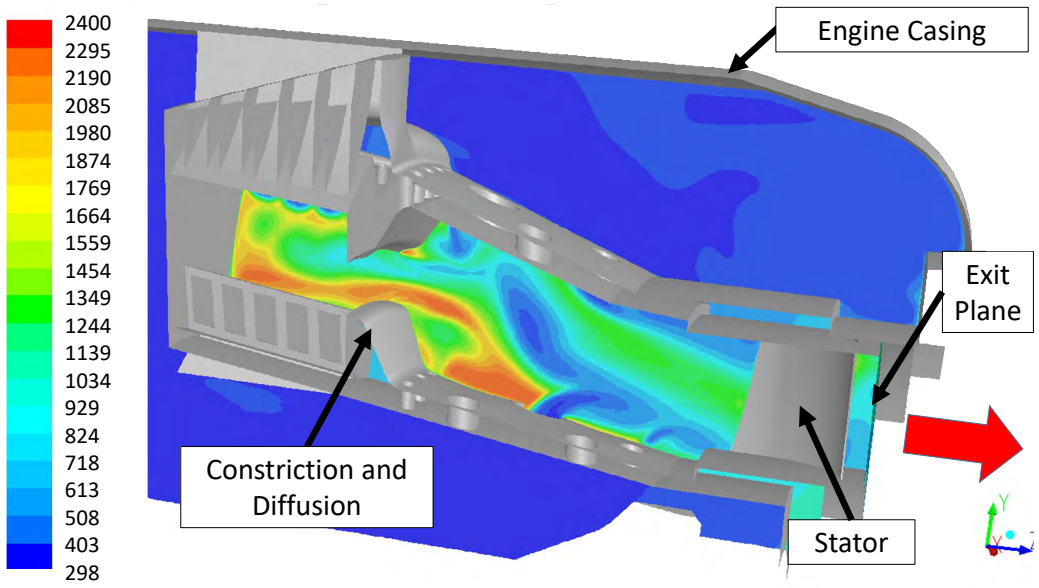


Figure 359. Temperature contours (K) in Combustor Configuration 7 with primary zone exit diffuser and larger secondary/dilution zone volume

Due to the air inlet holes through the secondary/ dilution section injecting at approximately 15° inward from tangent of the combustor OD, the fluid at the combustor ID and OD were driven to swirl, while the middle passage of the domain was largely unaffected by the injectors. Even with injection velocities approaching 200 m/s, the penetration of the inlet jet was only approximately 1/3 of the radial span due to the injection angle and the jet being turned by the fluid trying to exit axially. Since the fluid at the exit could not reach the required 65° velocity exit angle, and the angle across the exit plane was highly non-uniform, the use of stators was determined to be required.

The final two combustor configurations (see the line plot in Figure 360) implemented stators and radially injecting secondary/dilution air. The radial injecting jets not only improved the exit temperature profiles, but also improved the uniformity of the velocity angles entering the stators. The uniformity was maintained across the stators where a more consistent velocity angle was achieved at the turbine rotor inlet.

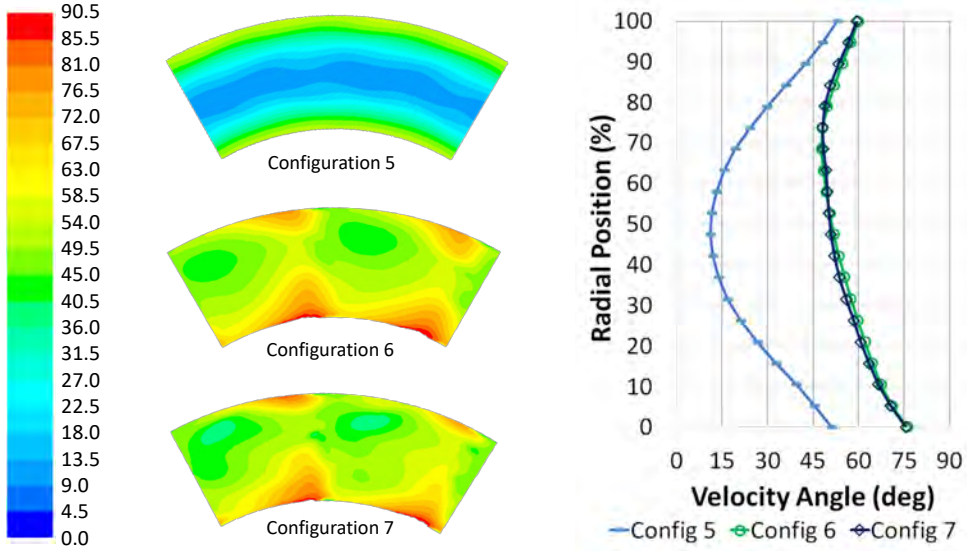


Figure 360. Contours of velocity angle (deg) on the combustor exit plane and circumferentially averaged velocity angles from Configurations 5, 6, and 7

The stators were modeled off the JetCat hardware, however, the turning angles were approximate and three stators were removed to make the computational domains periodic. The velocity angle uniformity was reduced due to the simplification of the computational model and would likely improve beyond the results presented if all of the stators that are present in the existing JetCat hardware were modeled.

8.3.6 Configuration 7 Detailed Computational Results.

Based on the results of the preliminary first order analysis, the Configuration 7 combustor was selected for more detailed computational analysis leading to the development of physical hardware. This analysis was accomplished using the same 35.9M cell grid from Section 8.3.4, and computational settings from Section 8.3.1, however, the solutions were calculated with spatial discretization set at first order for all parameters, and then re-run at second order for all parameters. The solutions were computed twice to show that there was a minimal variation in most properties between the first order and second order solutions and prove the comparison study

above was relevant. The second order solution also ensured the first order solution was not under predicting or missing important aspects of the flow.

A total of four operating conditions were run with the Configuration 7 combustor including half idle (a transitional point between ignition and idle), a 35,000 RPM idle condition, an 80,000 RPM flight condition, and the 100,000 RPM 80% power cruise condition which served as the design point in the comparison analysis in Sections 8.3.4 and 8.3.5. All of these conditions were experimentally derived from JetCat performance data using the baseline combustor. Table 48 shows the relevant input parameters for each of these conditions. The flow rate values specified in the table are for the entire engine, to determine the flow rate though the 60° sector domain the table values need to be divided by 6. The fuel inlet temperature was consistently 300 K. In each of these conditions the global equivalence ratio remained constant, with only a 2% variation between conditions.

Table 48. Combustor Configuration 7 detailed analysis operating conditions

Operating Condition	**Air Flow Rate** (kg/s)	**Air Inlet Temp.** (K)	**Fuel Flow Rate** (kg/s)	**Operating Pressure** (Pa)	**Global Equivalence Ratio**
1/2 Idle	0.0358	310	0.00071	110,316	0.310
Idle	0.0716	310	0.00142	110,316	0.310
80K RPM	0.157	345	0.003175	151,960	0.316
100K RPM	0.25	375	0.00505	202,650	0.316

Beginning with a discussion of the calculated conditions in the primary combustion zone, the airflow into the primary zone was found to scale with fuel flow to achieve an average cavity equivalence ratio of 1.59 with a standard deviation of 0.03 across all four operating conditions. Approximately 85% of the air entered the primary zone through the combustor OD inlets. This distribution was due to there being twice as many inlets on the OD than the ID, but also due to inefficient airflow through the ID

scoops and inlets. It was found that since the scoop was not closed at the downstream end it allowed air to pass below the inlets and not turn radially outward to enter the cavity. The last of the five ID inlets was found to move all of the ID inlet air with the four upstream inlets achieving negligible airflow or reversed flow. Comparing the first order to second order results showed that the mass flow rate of air into the cavity varied between 0.25% and 1.3% across the four operating conditions.

The largest difference between the first order and second order solutions were obtained for the tangential velocity and temperature in the primary zone. Both of these quantities had an average difference of approximately 15% as measured on a plane positioned at approximately 66% of the primary zone axially. In all cases, with the exception of the 1/2 Idle case, the second order solution calculated a faster tangential velocity. The average temperature in the cavity was consistently lower with the second order solution than with the first order solution. Table 49 shows the second order average cavity temperature, tangential velocity, and centrifugal loading in the primary zone as measured on this reference plane for each operating condition.

Table 49. Combustor Configuration 7 second order average temperatures, tangential velocities, and centrifugal loading in the primary zone

Operating Condition	**Avg. Cavity Temperature** (K)	**Avg. Tangential Velocity** (m/s)	**Avg. Centrifugal Loading** (g)
1/2 Idle	1115	10.33	302
Idle	1251	21.1	1262
80K RPM	1365	37.5	3986
100K RPM	1229	48.4	6640

Zelina et al. [3] quantified the stable combustion region within a UCC based on cavity equivalence ratio and centrifugal loading. This result was shown as Figure 34, and is adapted in Figure 361 with the centrifugal loading plotted for each operating condition. All of the points fall within the stable region with the exception of the

100K, second order solution. While the velocity only differed by approximately 15% between first order and second order, the calculation of the centrifugal loading uses the square of the tangential velocity which amplified the variation. These results indicate that the Configuration 7 UCC may flameout at the upper region of the JetCat operating range.

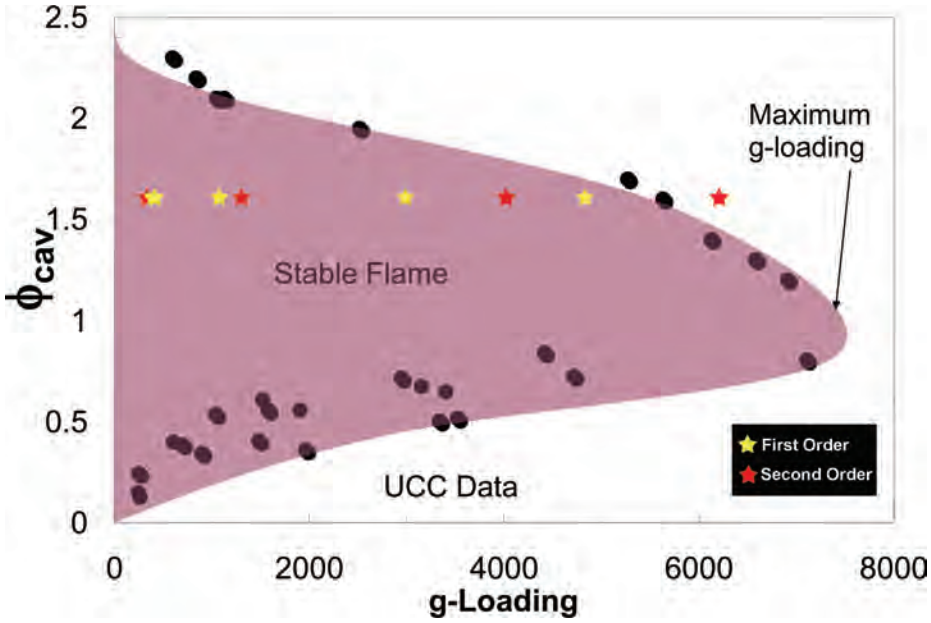
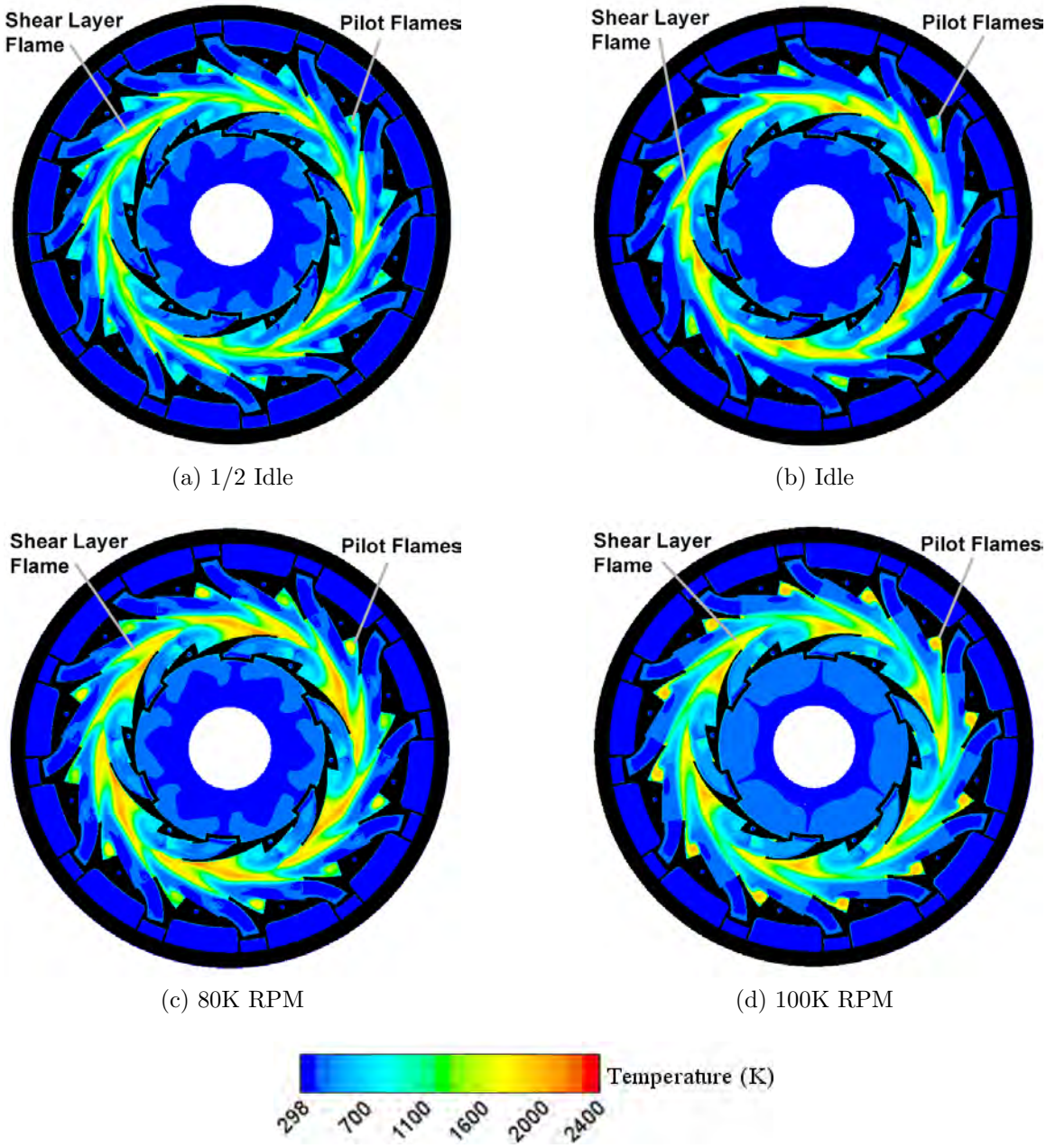


Figure 361. Cavity equivalence ratio at blowout as a function of centrifugal loading with operating conditions plotted, adapted from [3]

Figure 362 shows second order temperature contours at approximately 66% axial position in the Configuration 7 primary zone at all four operating conditions. All of these conditions show a pilot flame maintained in the recirculation zone behind the stabilizing step. The intensity of the heat release in the pilot flame increased with increasing RPM (flow rate). These figures also show flames anchored to the shear layer between the OD air injection jets and the bulk air extending to the recirculation zones on the combustor ID. Between the pilot flames and the anchored shear layer flames this combustor configuration shows a stable flame across all operating conditions. The UCC rig used by Zelina et al. [3] to produce the stability plot shown in Figures

34 and 361 did not included stabilizing backward facing steps or air injection from steps. The current UCC configuration could increase the stable region due to these geometry enhancements.



(a) 1/2 Idle

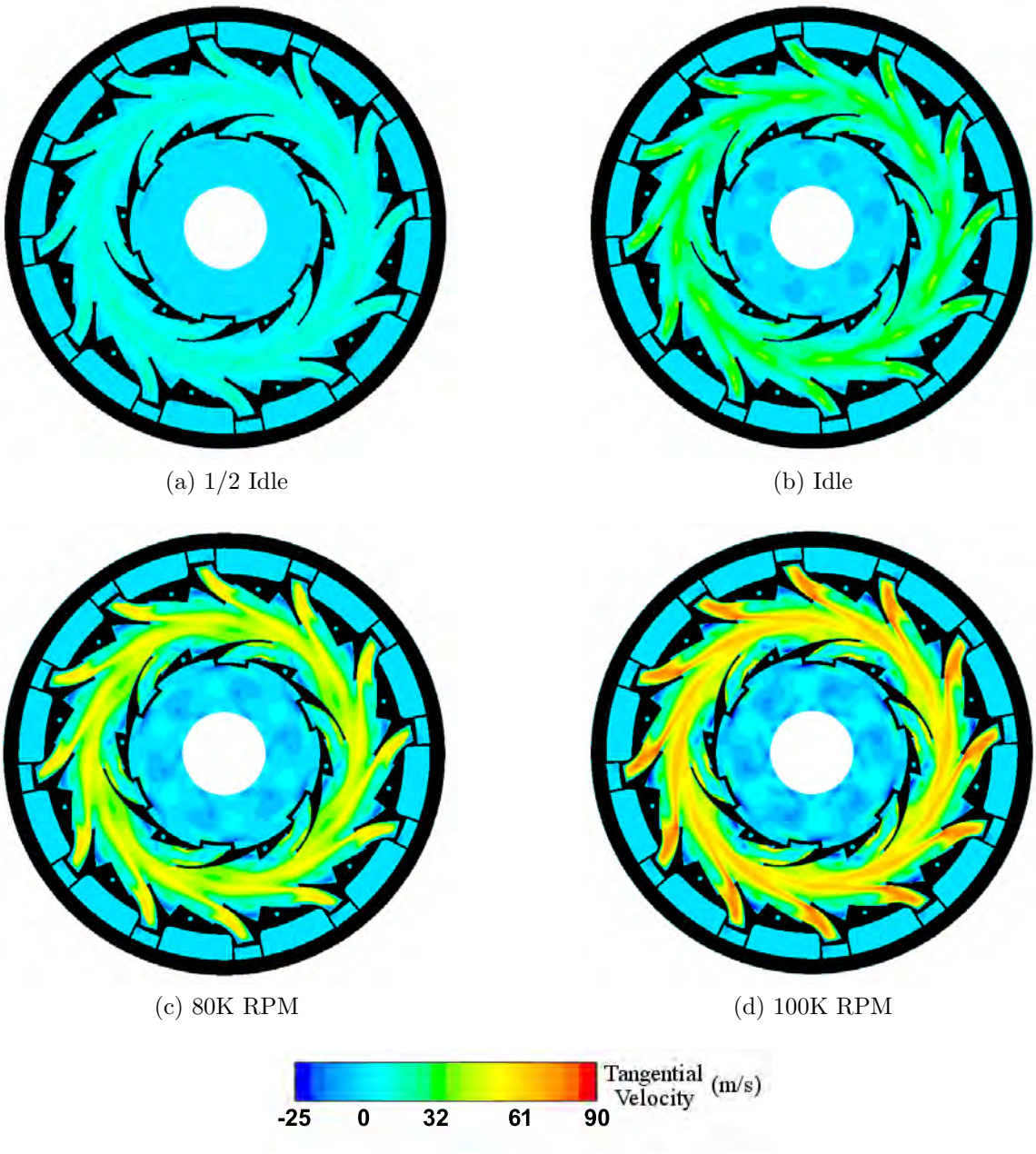
(b) Idle

(c) 80K RPM

(d) 100K RPM

Figure 362. Temperature contours (K) at approximately 66% axially in the Configuration 7 primary zone

Figure 363 shows the second order tangential velocity contours for the four operating conditions at the same reference plane as Figure 362. The tangential velocity figures show similar flow patterns in the primary zone across the operating conditions with only the magnitude of the velocities increasing with RPM (flow rate).



(a) 1/2 Idle

(b) Idle

(c) 80K RPM

(d) 100K RPM

Figure 363. Tangential velocity contours (m/s) at approximately 66% axially in the Configuration 7 primary zone

Moving to the combustor exit plane after the nozzle guide vanes, Figure 364 shows the variation in circumferentially averaged exit temperature profile in the second order 100K RPM operating condition with continued iterations in a converged solution. This plot is included to show that even though the solution was run steady state, there were cyclic fluctuations of up to 65 K in exit temperatures depending on when the data was extracted from the solution. At some level this value represents a CFD uncertainty.

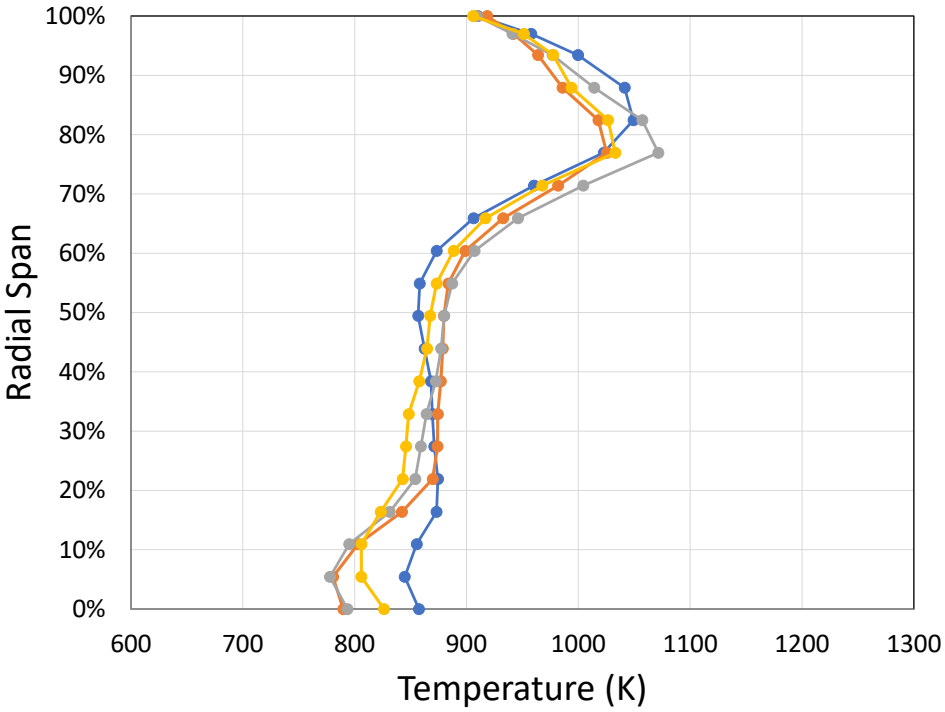


Figure 364. Configuration 7, 100K RPM operating condition circumferentially averaged combustor exit plane temperature profiles variation with iteration

Figure 365 shows the first and second order circumferentially averaged temperature profiles at the exit plane for all four operating conditions. Each line color and marker type represent an operating condition with the first order solution shown with a dashed line, and the second order solution shown as a solid line. There were some spatial changes in the positioning of peak temperatures, usually with the second order solution moving the peak temperature radially outboard, and some minor changes in

the temperature extremes within each condition. As shown in Figure 364 there was variation at a single operating condition with increased iteration. Since there was no way to stop the first order solution and second order solution in the same position in the variation cycles, some of the differences between these two results could be due to where in the converged solution each result was taken.

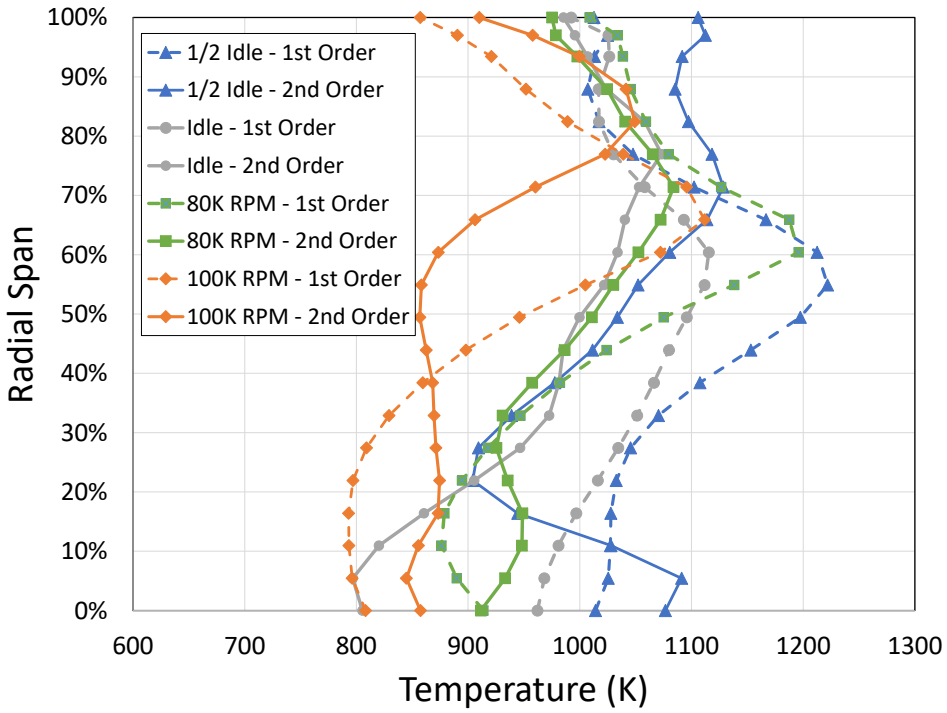


Figure 365. Configuration 7 circumferentially averaged combustor exit plane temperature profiles at all four operating conditions for first and second order solutions

Table 50 shows the average temperature, pattern factor, average velocity magnitude, and average velocity angle from the second order solution at the exit plane of each operating condition. The average difference in temperature between the first order and second order results was 3.2%. The second order results shown in the table had an average exit temperature of 981 K and a standard deviation of 53 K. The exhaust gas temperature reported by JetCat for the P90RXi model was 963 K. Since the computational results were predicting exit temperatures within a few degrees of the physical exhaust temperature there was confidence that the Config-

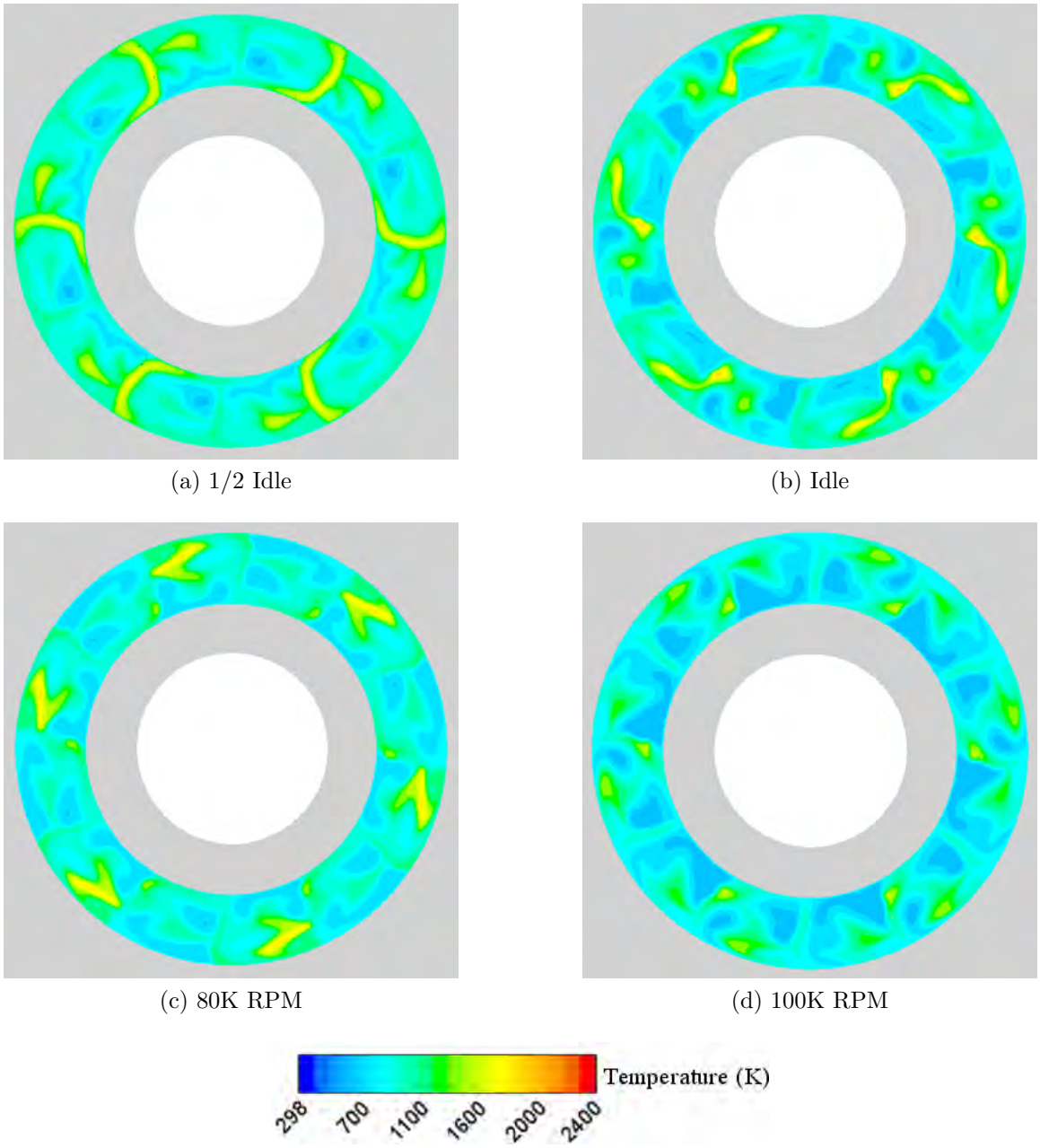
uration 7 combustor could be run safely without over heating the uncooled turbine vanes and blades. The pattern factor was larger than desirable, mainly due to a periodic localized hotspot on the exit plane caused by incomplete mixing of a fuel streak from the ID fuel injectors. This hot spot blended out in the circumferentially averaged temperature profiles due to cooler temperatures surrounding the hot streak. The exit velocities were proportional to the total air flow rate and were calculated without a nozzle on the exit. The peak velocity was 291.4 m/s (1,049 km/h) at the 100K RPM condition. JetCat reported that the maximum exhaust velocity was 1,454 km/h at maximum power. The 400 km/h difference was due to a maximum power condition not being run computationally, and the lack of a converging exit nozzle in the computational solution.

Table 50. Combustor Configuration 7 second order average temperature, pattern factors, average velocity magnitude, and average velocity angle at the combustor exit plane

Operating Condition	**Average Temperature** (K)	**Pattern Factor**	**Avg. Velocity Magnitude** (m/s)	**Avg. Velocity Angle** (Degrees)
1/2 Idle	1050	0.87	86.4	54.4
Idle	976.7	1.37	159.9	54.5
80K RPM	994	1.3	263.3	54.8
100K RPM	903	1.17	291.4	54.9

Figure 366 shows the exit plane temperature contours just downstream of the nozzle guide vanes. As expected the dominant color is the same in all four plots because the average temperature was comparable. Figures 366a, b, and c show localized yellow hot spots that peaked at 1,800 K in the Idle condition. While the 100K RPM case peaked at 1,520 K, considerably cooler than the other three conditions, this case also had larger regions of cooler temperatures along the ID that were not seen in the same quantities in the other conditions. The 100K RPM condition had the highest mass flow rate of these conditions as shown in Table 48 which could be resulting in

decreased residence time. These cooler temperatures contributed to the 100K RPM condition achieving the lowest average exit temperature of the four conditions tested as shown in Table 50.



(a) 1/2 Idle

(b) Idle

(c) 80K RPM

(d) 100K RPM

Figure 366. Temperature contours (K) on the Configuration 7 exit plane downstream of the nozzle guide vanes

Looking across the entire combustor, Table 51 gives the average gauge static and total pressures at three engine stations; the compressor exit, combustor exit upstream of the nozzle guide vanes, and the domain exit downstream of the nozzle guide vanes. The bottom two rows of the table show the pressure losses across the combustor (compressor exit to upstream of the NGV's), and across the combustor with the NGV's included. The average of the total pressure loss across the combustor in the 80K and 100K conditions was 6.5%. This value is larger than desired, but it is not so large that future iterations of the geometry couldn't reduce the losses to a more desirable level below 5%. The 1/2 Idle and Idle conditions experienced a considerably lower pressure loss due to a much lower air flow rate at these conditions. This combustor was also designed to work with the stock JetCat P90RXi flow path which achieve axial flow at the compressor exit. A modification to the compressor exit guide vanes that allowed a swirl to be maintained at the compressor exit would reduce the turning requirement of air entering the inlets in the primary zone and likely reduce the pressure losses.

Table 51. Combustor Configuration 7 second order gauge static and total pressures and absolute losses across the combustor, and across the combustor and nozzle guide vanes

Location or Loss	**1/2 Idle**		**Idle**		**80K RPM**		**100K RPM**	
	Static (Pa)	**Total** (Pa)	**Static** (Pa)	**Total** (Pa)	**Static** (Pa)	**Total** (Pa)	**Static** (Pa)	**Total** (Pa)
Inlet	2294	2442	8213	8802	30,304	32,266	55,399	59,005
Combustor Exit	1334	1812	4857	6534	17,453	23,405	31,142	41,712
NGV Exit	-0.518	1431	-3.71	5304	-11.16	19,163	-10.05	34,227
Combustor Loss	0.85%	0.56%	2.83%	1.9%	7.59%	6.44%	9.40%	6.61%
Combustor Loss w/ NGV's	2.04%	0.90%	6.93%	2.94%	16.6%	7.11%	21.47%	10.46%

Figures 367, 368, and 369 show contours of temperature, reaction location through OH mass fraction, and gauge total pressure contours, respectively, on the longitudinal YZ plane for the 100K RPM condition. Only the 100K RPM condition is shown since it was used as the design point, however, the remaining operating conditions produced comparable flow, temperature, and reaction distributions just with varying magnitudes. On this plane the majority of the reactions were located in the primary zone, in the recirculation pockets just downstream of the primary zone, and in the wake of the large OD dilution hole. It appears that all reactions had finished by the domain exit downstream of the NGV's.

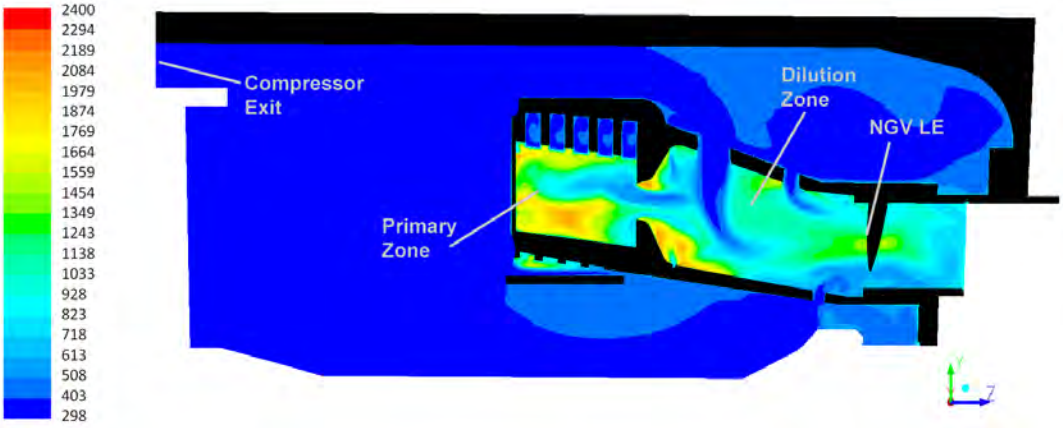


Figure 367. Second order temperature contours (K) on the YZ plane in the Configuration 7 combustor at the 100K RPM condition

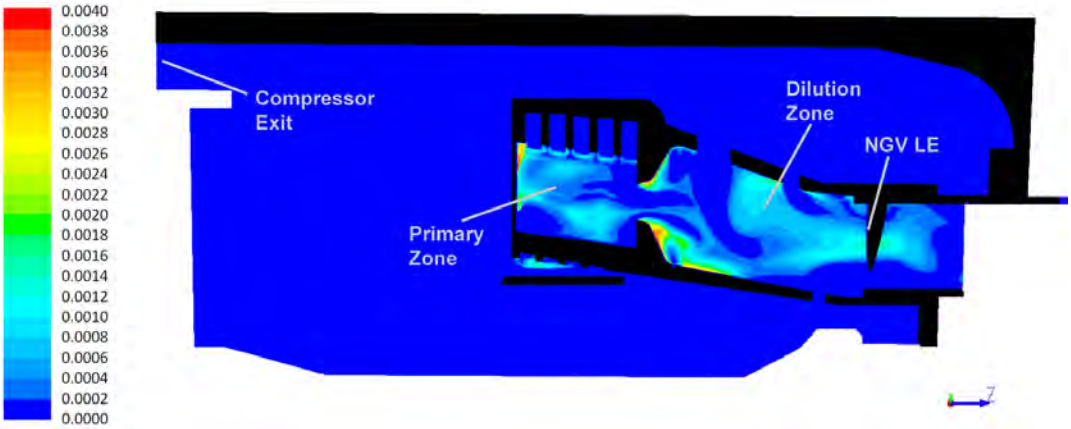


Figure 368. Second order contours of OH mass fraction on the YZ plane in the Configuration 7 combustor at the 100K RPM condition

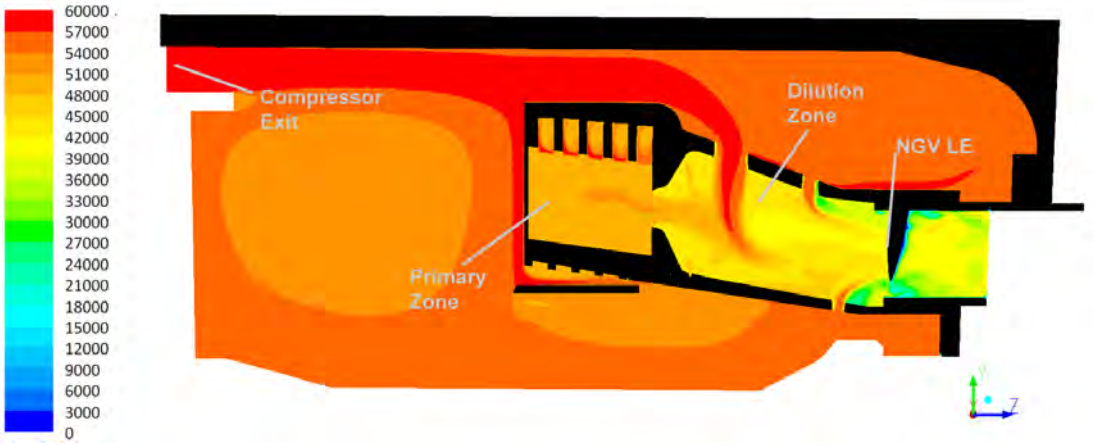


Figure 369. Second order gauge pressure contours (Pa) on the YZ plane in the Configuration 7 combustor at the 100K RPM condition

8.4 Experimental Analysis

This section covers the development of the Configuration 7 physical hardware and the experimental test methodology and results using this configuration in a near atmospheric combustion test at the idle condition described in Section 8.3.6. This test was used to verify ignition and sustained combustion without the use of a spinning compressor or turbine that were tested in Objective 5.

8.4.1 Combustor Configuration 7 Manufacturing.

Due to internal fuel passages that were tapered and angled, as well as the step geometry with curved air inlets, the combustor was manufactured using 3D printing technology. The combustor was printed in two pieces in inconel on a Concept Laser M2 3D printer in the AniMal lab at AFIT. The combustor could not be printed as a single piece due to the overhang of either the forward combustor wall or the aft primary zone wall along the primary/dilution constriction depending on print orientation. These surfaces would have required extensive support material to hold them in place while printing. Due to the scale of the combustor there would have been no way to remove the support material after printing, thus multiple parts were

required. Several changes from the part shown in Figure 353 were required to make it printable. These changes are discussed through the remainder of this subsection. Additionally the dilution hole sizes are given below.

The first change that was required to manufacture the combustor was that it was made as three major components. The combustor used in computational analysis was treated as a single entity. Two of these combustor components were manufactured on the 3D printer and comprised the combustor ID and OD walls and air inlets. The remaining component was cut from a piece of 0.55 mm inconel plate and was used as the forward combustor wall to join the ID and OD components and enclose the primary combustion zone. These three components are shown in Figure 370. The 3D printed parts did not come off the printer looking like this, they had been finished machined at the time the photo was taken. The combustor ID was welded to the inconel plate, while the plate was held to the combustor OD with 1/16" 4-40 panhead screws. The screws enabled the combustor to be disassembled for inspection or additional instrumentation at a later time if needed.

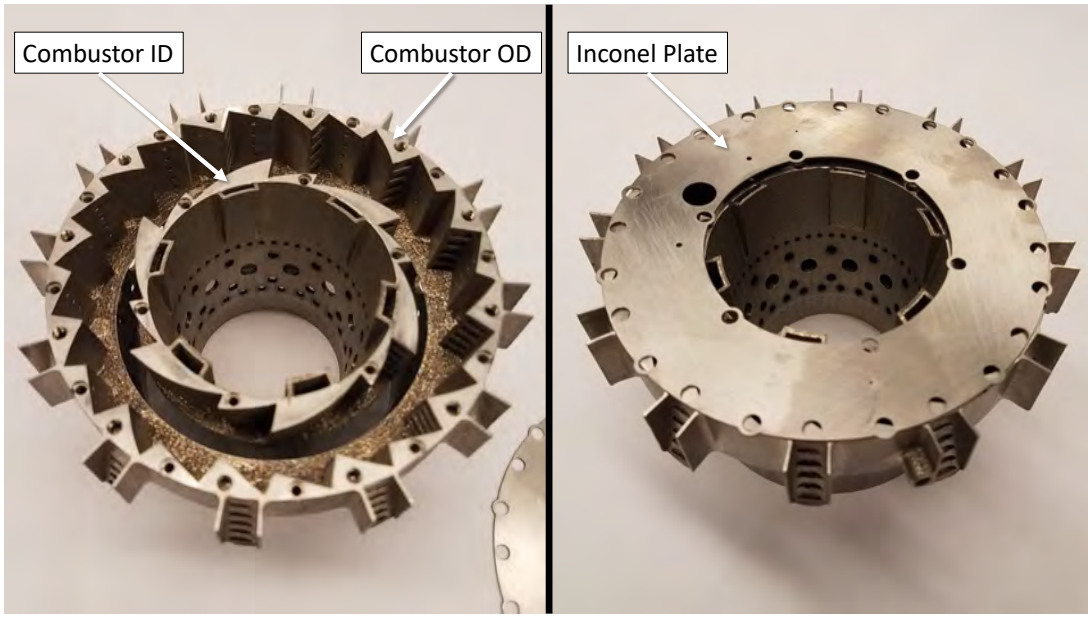


Figure 370. Three primary components of the Configuration 7 manufactured combustor

The second required change was to add fillets to the air inlet passages to create a dome shape rather than a rectangular profile. Even though the air inlets were small, the printer would still have had difficulty with an unsupported rectangular passage. By creating a dome there was considerably less area in the middle of the passage that was unsupported making it possible to print the curved inlets without supports. Due to the internal geometry of the inlets there would have been no way to remove supports, so the modification was required. While the addition of the dome slightly closed the hole area of the inlets, injection velocities should remain the same as they are a function of the pressure differentials across the holes and not a function of the hole area. The air volume was expected to remain approximately the same as the majority of the inlet air flowed down the rectangular half of the hole which remained relatively unchanged in size. Figure 371 shows the computational versus manufactured air inlet geometry. While not shown in the figure, the air inlets on the combustor ID were also domed in the manufactured part.

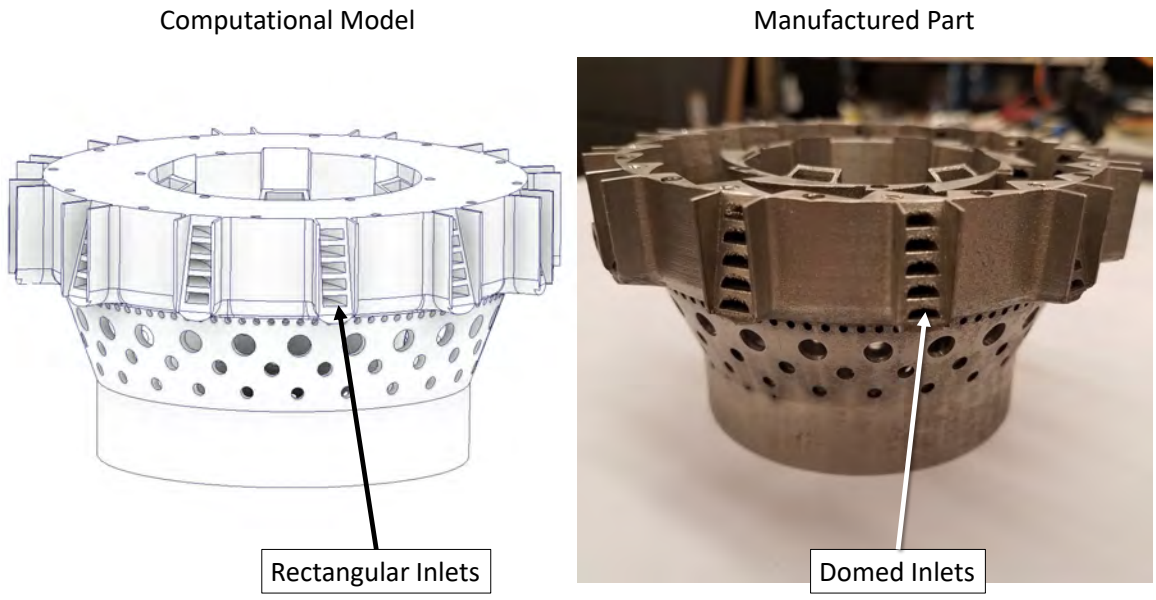


Figure 371. Configuration 7 manufactured hardware air inlet hole geometry modification

The third change was also required due to the 3D printing process. The scoops that were added to the combustor ID to pull air into the ID step inlets had an open exit in the computational model as shown in Figure 372. This opening was originally intended to prevent the air in the scoop from stagnating and building a higher pressure to drive a large injection velocity. The computational results showed that there was negligible or reversed flow in the first four upstream inlet holes with only the fifth air inlet hole showing flow exiting into the combustor. The 3D printer required that the scoop exit be molded into the ID wall to enable a smooth transition without an abrupt unsupported start. This requirement closed the exit to the scoop which should stagnate the air in the scoop and aid in the air injection from all five air inlet holes that the scoop feeds.

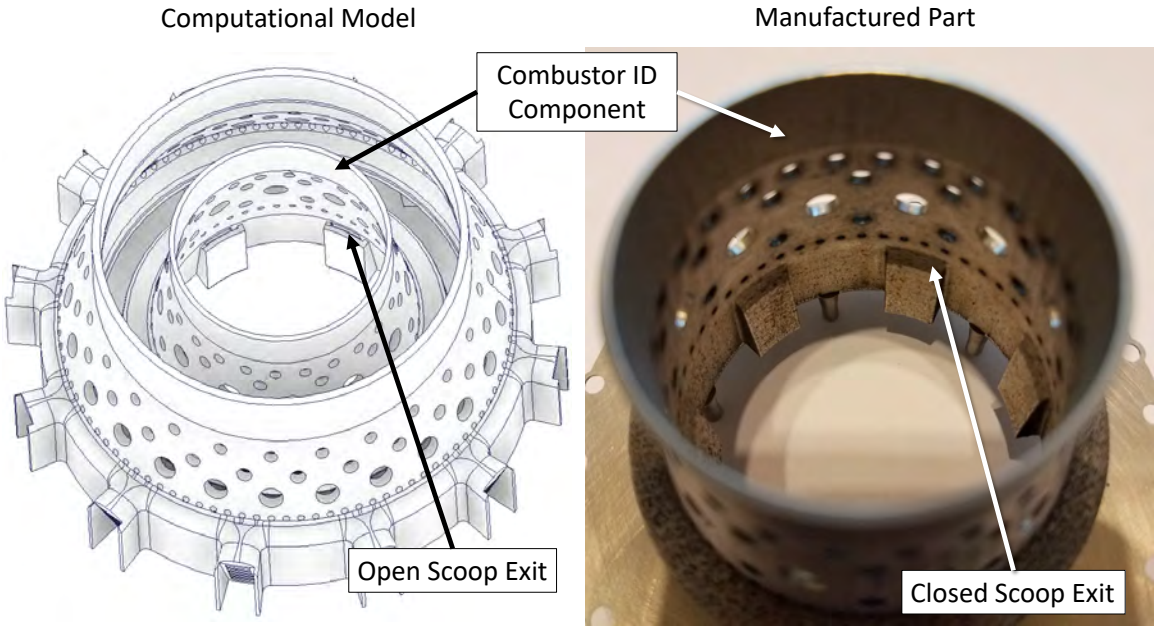


Figure 372. Configuration 7 manufactured hardware ID air scoop modification

A glow plug igniter was required for experimental testing and was not included in the computational analysis. As shown in Figure 373 the stock JetCat glow plug was planned to be used and was installed through the combustor forward wall. Due

to the larger gap between the compressor and the Configuration 7 combustor, the original glow plug mounting bosses could not used. New mounting bosses were created to mount the glow plug to the combustor forward wall. This system required an electrical connection back to the upstream compressor wall and also a small kerosene tube connection. During ignition a small amount of kerosene was pushed across the heated ceramic filament to flash and ignite the gases in the primary combustion zone. The flow of kerosene to the glow plug was controlled by a solenoid that was only open when the glow plug was energized. The glow plug provides an additional blockage to the flow external to the combustor and an additional hole into the primary zone that was not modeled computationally.

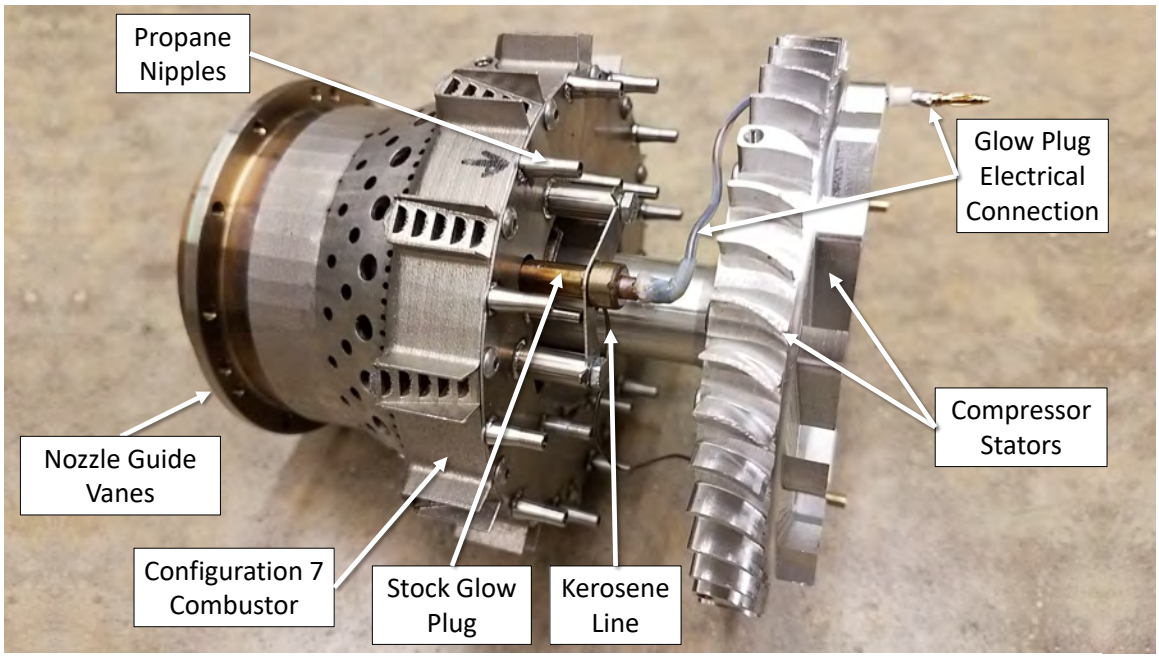


Figure 373. Configuration 7 with stock JetCat glow plug installed through the combustor forward wall

During ignition testing the stock glow plug failed to light the kerosene that was pushed directly over it. The plug was hot enough to rapidly vaporize the kerosene, but the vaporization process quenched the plug and left it too cold to ignite the vapors. An additional ignition source would then be required to ignite the vapors.

In the stock JetCat engine the computer had control over the igniter solenoid. The solenoid could then be controlled to allow only a small amount of kerosene to reach the ceramic heating element allowing the plug to remain hot enough after vaporizing the fuel to then light the vapors. Using the new electronics described in Appendix D, the igniter solenoid could not be independently and was opened when the glow plug was energized leaving the flow of kerosene to be controlled by the pump only. The pump was not capable of very precise control and required a tleast a 50% duty cycle to start turning. At this level more kerosene reached the ceramic element then desired. However, since the engine was operating on propane, there was no need to light the propane from kerosene when propane can be lit directly from a glow plug. As shown in Figure 374 the stock glow plug was replaced with a hotter glowing filament glow plug that could light the propane directly. A small mounting boss was manufactured that seated the filament plug inside the hole in the front wall of the combustor previously used for the stock glow plug. This filament system successfully demonstrated propane ignition using the new electronics. The ignition solenoid was not connected to the circuit board and the ignition kerosene line was removed and plugged.

The fuel system that was included in the computational analysis took advantage of the benefits of CFD to specify a boundary condition as an inlet without requiring the ducting to supply that inlet that is needed in real life. In the computational model the fuel inlets were specified as shown in Figure 353, which provided fuel to individual tapered fuel ducts that each fed five radially injecting fuel inlet holes. As shown in Figure 375 the real life fuel system required 18 fuel nipples to be press fit into the individual fuel ducts and laser welded to the inconel plate. The welding was performed by Wicked Welding of Dayton, Ohio. Nylon fuel tubing was bonded to the nipples, the 3D printed fuel manifold made from VeroClear-RDG810 plastic, and a

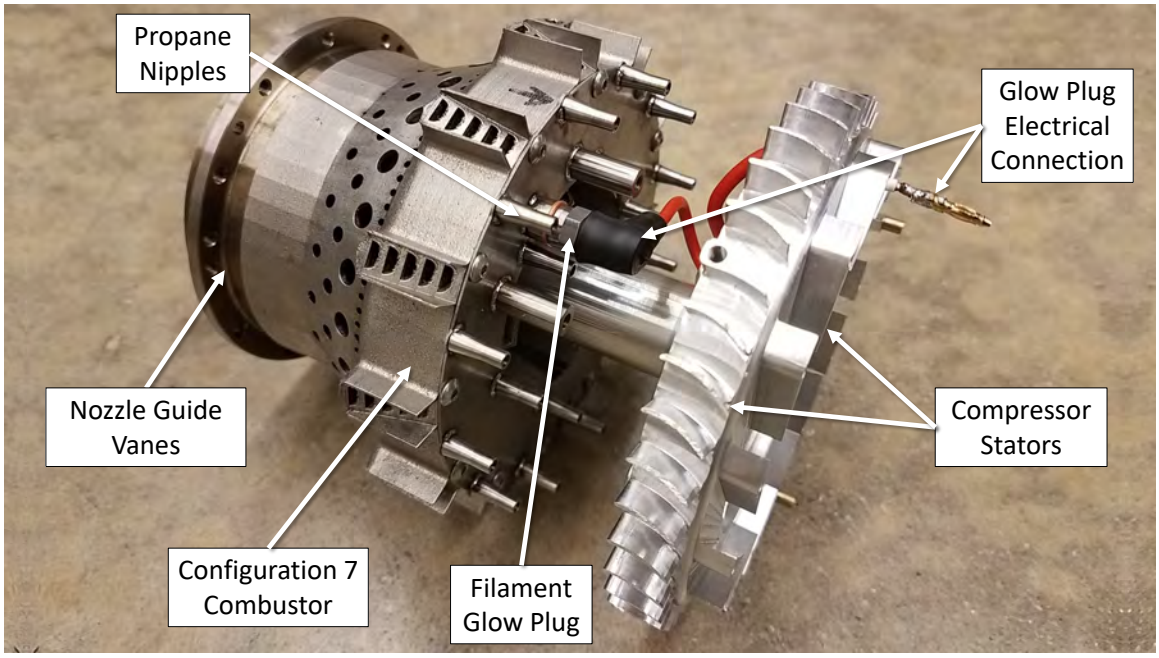


Figure 374. Configuration 7 with new filament glow plug installed through the combustor forward wall

modified 8-32 screw using JB Weld ClearWeld two-part epoxy. The tubing was used as a connector between the metal nipples and the 3D printed manifold because the nylon was more heat tolerant than the VeroClear plastic. The modified screw was bored through to enabled gaseous propane to be delivered through the JetCat casing from an internally threaded Swagelok fitting external to the engine. The additional fuel tubing, nipples, manifold, and screws were not modeled in the computational analysis and could alter the airflow pattern in the experimental testing. An effort was made to minimize the blockage around the engine OD and along the combustor external forward face to place the additional fuel tubing and manifold towards the center of the recirculation zone upstream of the combustor to reduce the impact of its presence.

There was one final difference between the computational model and the experimental hardware, but it was not an intended modification. The AFIT AniMal Lab

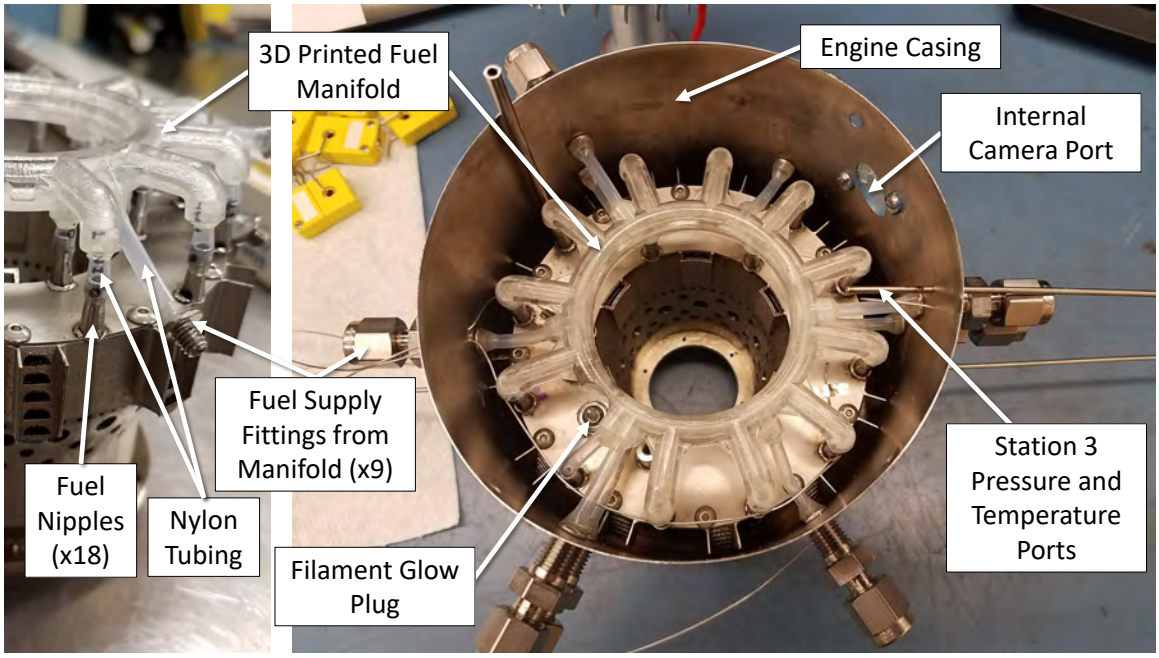


Figure 375. Configuration 7 experimental hardware fuel distribution system

did not compensate for part shrinkage which is a result of the printing process. As such the manufactured combustor major diameter at the OD inlet tips was 2.29 mm (2.13%) smaller, and the combustor ID component major diameter was 0.96 mm (1.8%) smaller than the desired dimensions used in the computational analysis. This smaller hardware created difficulty for the AFIT machine shop during finish machining because the manufactured parts did not match the dimensions in the drawing files. Due to the change in the shape of the primary zone inlet holes and the part shrinkage, the primary zone OD air inlet holes in the manufactured part were 10.9% smaller than the holes computationally analyzed. Additionally, the part was sized to fit tightly into the JetCat casing, however, due to the shrinkage there was an unplanned gap between the combustor and the casing. As discussed in Section 8.4.3 the additional gap had an impact on the operation of the combustor. That section outlines the problems and corrective measures that were taken to achieve predicted combustor performance.

The dilution holes in the combustor ID and OD components were added after printing by the AFIT machine shop to ensure they were smooth and round. All of the holes were burned through the parts using a wire end burner with the exception of the 4.6 mm diameter holes which were drilled. Figure 376 shows the hole schedule in the dilution zone of both components. The hole diameters, placement, and quantity matched the dilution hole schedule used in the computational model. There is one additional call out in the hole schedule for a 6-32 blind tap into a mounting boss. This boss was not modeled computationally, but the threaded hole was designed to received a machine screw through the JetCat casing to hold the combustor in place axially and circumferentially.

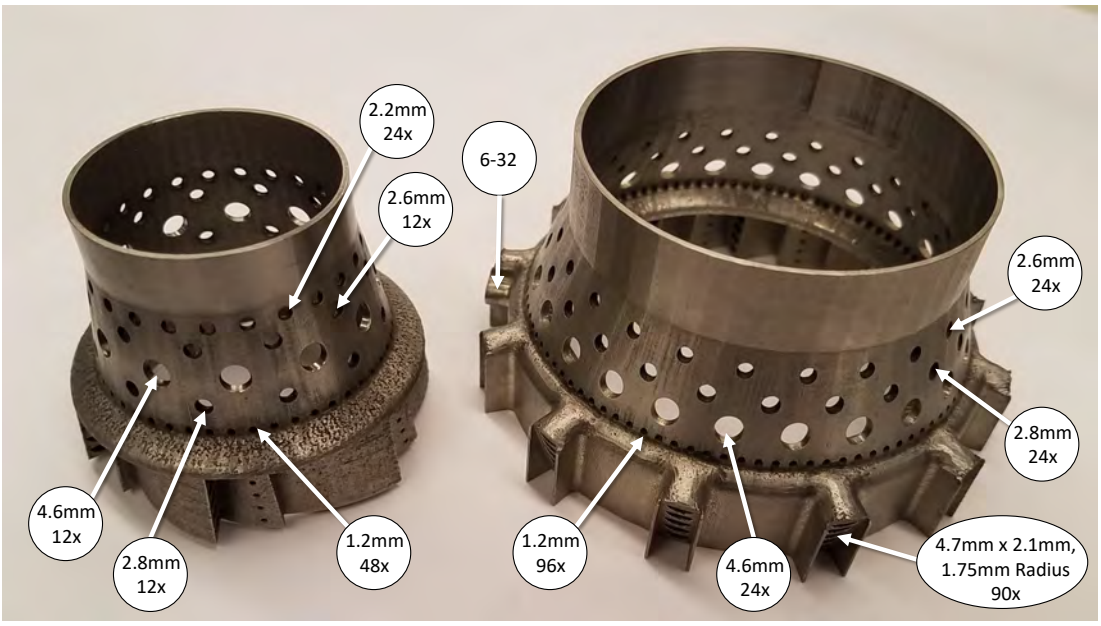


Figure 376. Configuration 7 ID and OD component hole schedule

The Configuration 7 combustor achieved a 32.9% installed axial length reduction compared to the baseline JetCat P90RXi combustor. The baseline combustor length was 72.03 mm with the Configuration 7 axial length measuring 55.84 mm. This difference accounts for 22.5% of the axial length reduction directly. Configuration 7 overlapped with the nozzle guide vane assembly significantly more than the baseline

combustor. This additional overlap put the nozzle guide vanes further into the Configuration 7 combustor and shortened the length between the stator vane leading edge and the combustor forward wall by an additional 10.4% to achieve a 32.9% installed axial length reduction. The weight, however, was doubled with the Configuration 7 combustor weighing 493.5 g and the baseline combustor weighing 244.8 g. It is important to note here that a considerable effort was put into shortening the combustor axial length, while no effort was made to minimize the weight. Additionally, the Configuration 7 combustor was printed in inconel which is an extremely hard and dense material that was not necessarily required for this application. Future iterations could take advantage of lighter-weight heat tolerant materials, or as more is learned about the capabilities of the Concept Laser M2 3D printer capabilities the inconel combustor walls could be thinned to save weight. Also, the excessive overlap material with the nozzle guide vane assembly could be removed to both shorten and lighten the combustor. Finally, material densities in more solid regions of the combustor could be reduced through the use of lattice structures to hold a volume while reducing the weight.

8.4.2 Experimental Methodology.

The Configuration 7 combustor described above was experimentally tested without the use of rotating hardware by using the custom components shown in Figure 377. These components allowed the combustor to be installed in the JetCat and tested at near atmospheric conditions using the COAL air supply system described in Section 3.1.1. The "custom bladeless compressor wheel" and "custom non-rotating shaft and tail cone" were installed in place of the stock compressor, center shaft, and turbine rotor to maintain the JetCat airflow path, but ensure that there were no rotating components as the engine was force fed air from the external compressor. The JetCat hardware was integrated with the air supply system through the use of the 3D printed

"air supply line adapter" as shown installed in Figure 378. The relative positions of the pressure and temperature instrumentation, fuel supply system, and new JetCat electronics are shown in the remainder of Figure 378 and in Figure 379. This setup used the air supply system outlined in Section 3.1.1 and the propane fuel system outlined in Section 3.1.2. The JetCat was mounted on the same engine mount used for the Version 3 UCC using the "Custom Engine Mount" to position the engine for thermocouple rake measurements and exhaust evacuation. Additional information on the custom JetCat LabView VI and dedicated JetCat pressure and temperature instrumentation are provided in Appendix D. Due to limitations in flow rate and pressure that could be supplied from the COAL lab compressor, the idle test condition described in Table 48 was the maximum flow condition that could be tested with this setup. A fully assembled engine with rotating hardware would be required for higher flow rate and pressure tests as discussed in Chapter IX.

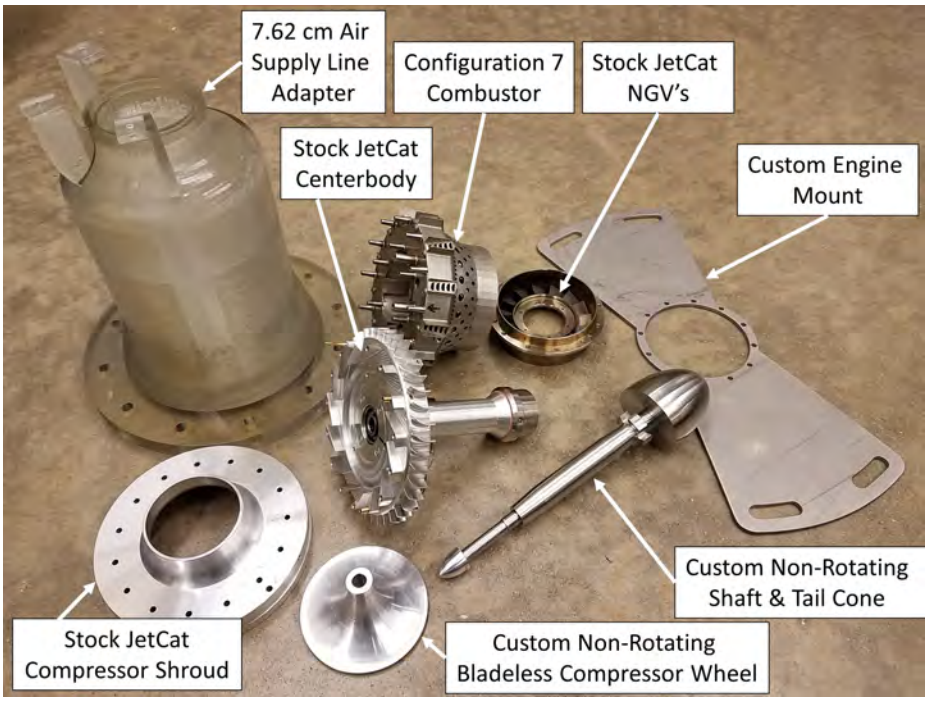


Figure 377. Custom and stock hardware needed for experimental validation testing

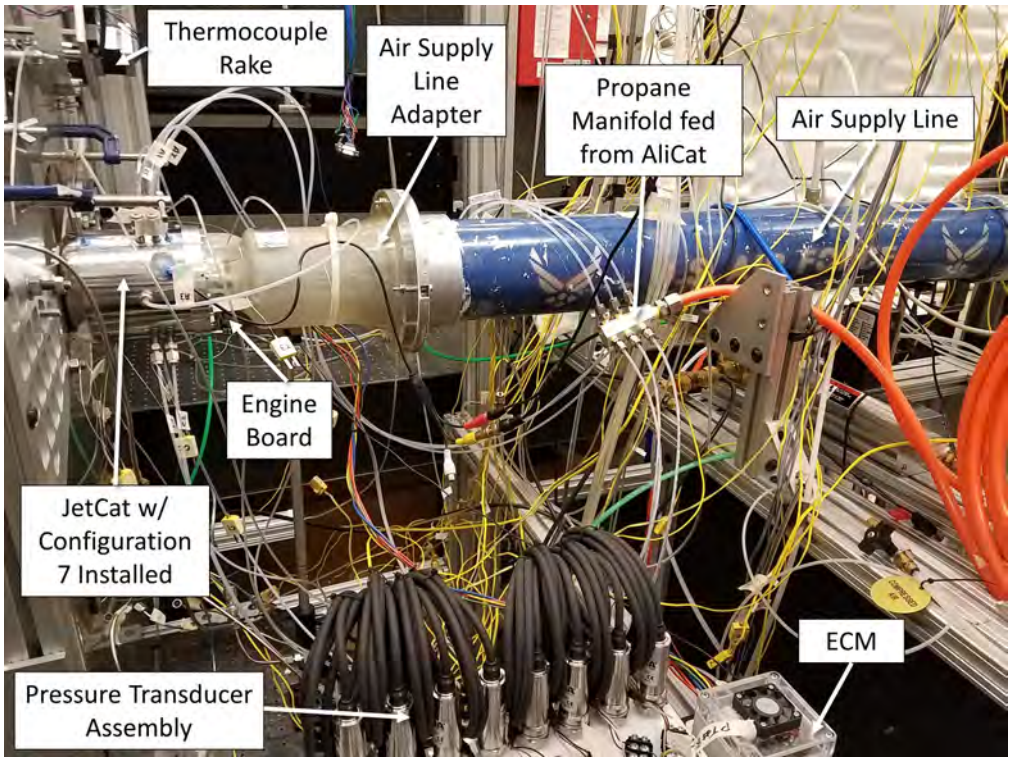


Figure 378. Configuration 7 installed in JetCat and configured for testing with no rotating hardware

Figure 380 shows a close up view of the propane distribution manifold shown in Figure 378. The manifold provided fuel from the AliCat mass flow rate controller which was commanded by LabView. The nine fuel outlets were directly connected to the nine fuel fittings on the engine casing using 3.175 mm OD, 2.63 mm ID, nylon tubing manufactured by FreelinWade that were each 1.22 m long. Maintaining a consistent tubing length ensured equal resistance in each tube and avoided a preferential path for the propane. The six axially downstream fuel fittings on the engine casing provided fuel to the 3D printed manifold and fed the 12 OD fuel injectors in the combustor. The three axially upstream fuel fittings on the engine casing fed a separate ring in the 3D printed manifold that fed the six ID fuel injectors in the combustor. The three upstream fuel fittings on the engine were fed from the middle fittings from each of the three sides of the manifold for consistency.

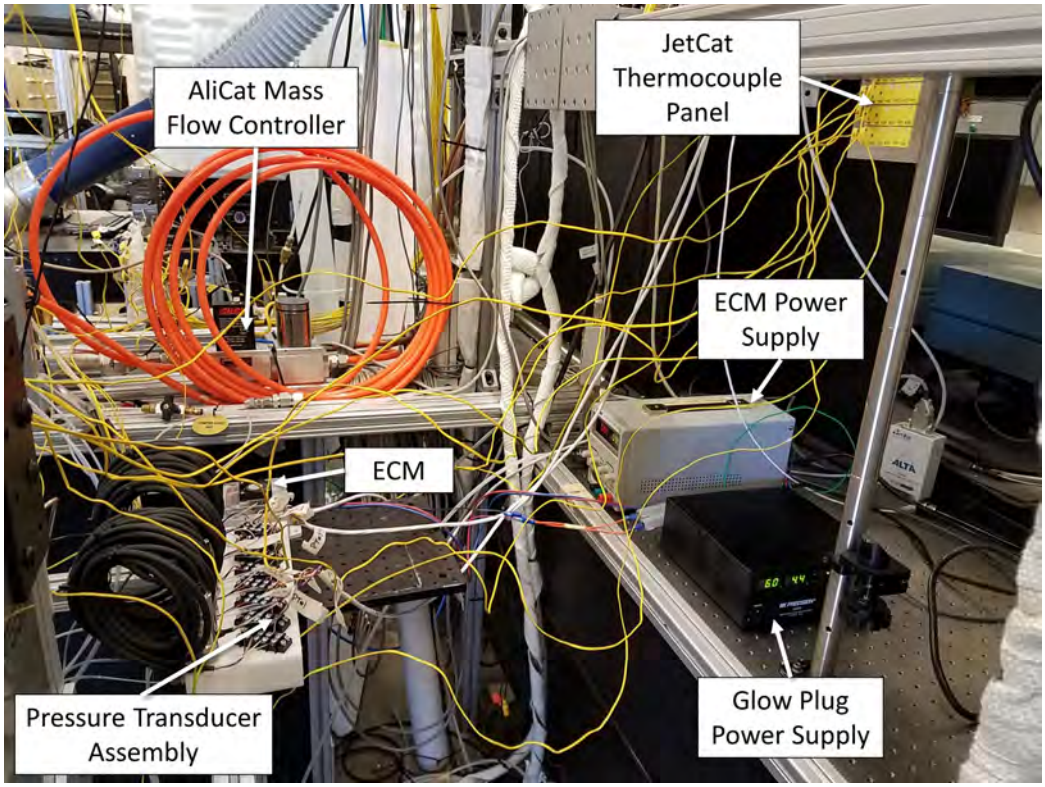


Figure 379. Remainder of the combustor test setup with no rotating hardware

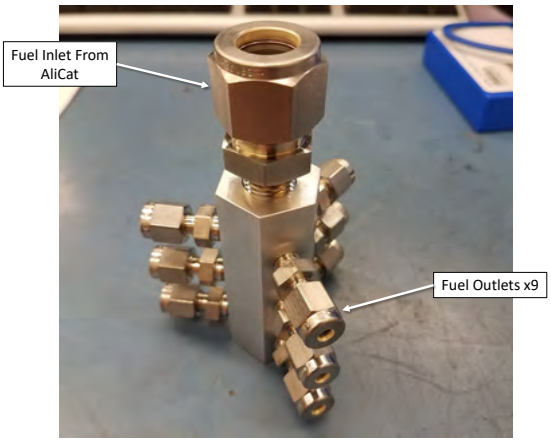


Figure 380. Propane distribution manifold external to the engine

The engine was instrumented for temperature and pressure at the specific engine stations as outlined in Figure 381. The pressure measurements were made by inserting 1.59 mm OD stainless steel tubing through the engine walls to the desired depth into

the engine. The stainless steel tubing was connected to the pressure transducers described in detail in Section D.6 with 1.59 mm ID pressure tubing that were all 0.6 m long. If pressure losses were experienced through the tubing, using equal lengths would help ensure scaled losses and relative measurements.

Temperature measurements were made with 0.5 mm diameter K-Type thermocouples installed through the engine walls. The thermocouples were held in place with nickel strips that were tack welded to the combustor, or with foil tape holding the thermocouple wire to the engine casing. The thermocouples were connected to the panel outlined in Section D.4. All measurement probes that penetrated the engine casing were sealed to the casing with the lower temperature "Ultra Blue" RTV sealant described in Section 3.3.1. Table 52 lists the ports and measurement location for each temperature and pressure measurement. The specified accuracy of each measurement is defined in terms of the full scale (FS) value. The EGT temperature measurement was made with the stock JetCat EGT probe so the accuracy is unknown.

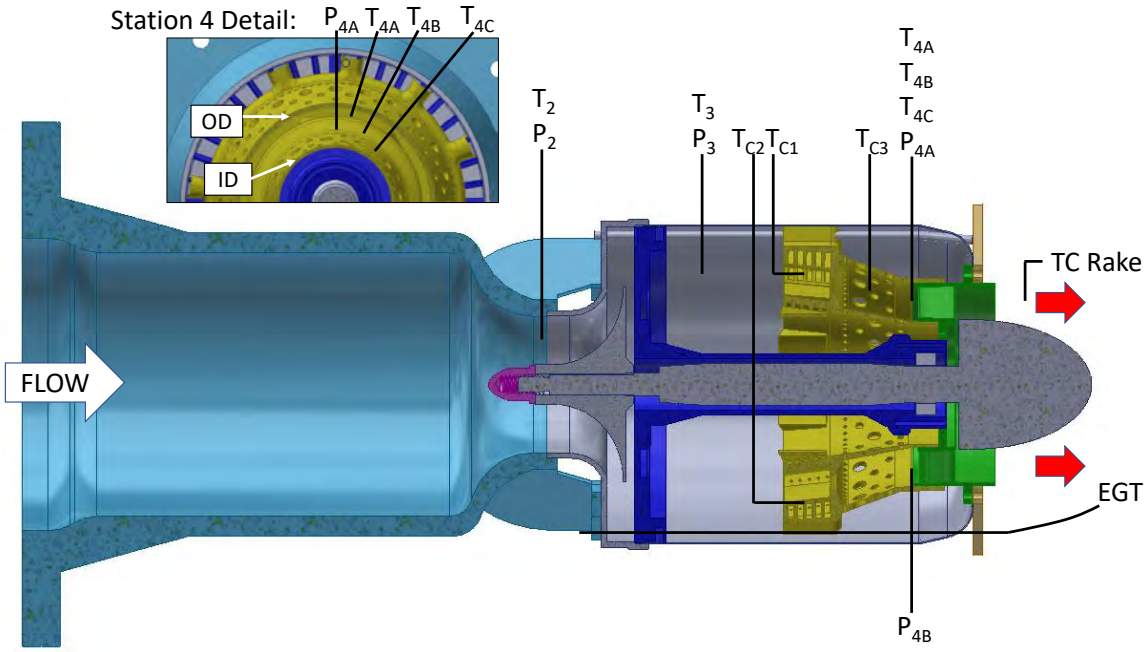


Figure 381. Experimental temperature and pressure measurement locations

Table 52. Combustor Configuration 7 experimental instrumentation details (Temperature (T) and pressure (P) measurements were static)

Engine Location	Designation	Depth	Port	Accuracy
Compressor Inlet	P_2	50% span	Transducer 1	±0.08% FS
	T_2	50% span	TC Panel, 2	±0.4% FS
Compressor Exit	P_3	1 cm from OD	Transducer 2	±0.08% FS
	T_3	1 cm from OD	TC Panel, 3	±0.4% FS
Combustor	T_{C1}	8.5 mm front wall	TC Panel, 4	±0.4% FS
	T_{C2}	8.5 mm front wall	TC Panel, 5	±0.4% FS
	T_{C3}	8 mm comb. OD	TC Panel, 6	±0.4% FS
Combustor Exit	P_{4A}	50% span	Transducer 3	±0.08% FS
	P_{4B}	50% span	Transducer 4	±0.08% FS
	T_{4A}	4 mm comb. OD	TC Panel, 7	±0.4% FS
	T_{4B}	8 mm comb. OD	TC Panel, 8	±0.4% FS
	T_{4C}	12 mm comb. OD	TC Panel, 9	±0.4% FS
Exhaust	EGT	OD	TC Panel, 1	N/A

As shown in Figure 382 a small camera was installed through the engine casing to provide visibility into the engine during operating. The camera (Vanxse TM10) featured a 3.6 mm lens, color Sony CCD image sensor (512x492), and six IR LEDs for imaging in dark areas. The camera was capable of connecting to the COAL lab closed circuit monitoring system with the feed from the camera displayed on a monitor at the control station. The camera was installed in a 3D printed mount with "Ultra Blue" RTV. The mount was attached to the engine casing with two 4-40 machine screws and "Ultra Blue" RTV. The main purpose of the camera was to ensure there were no flames exiting combustor inlets due to reversed flow.

The thermocouple rake discussed in detail in Appendix B was used to map the exhaust temperature distribution out of the JetCat. Spacers were added to the probe head mount as shown in Figure 383 to put the thermocouple beads in the kiel heads 7 mm downstream from the JetCat exit, and 23 mm downstream of the turbine vane trailing edges. The fourth (OD) thermocouple was radially outboard of the JetCat

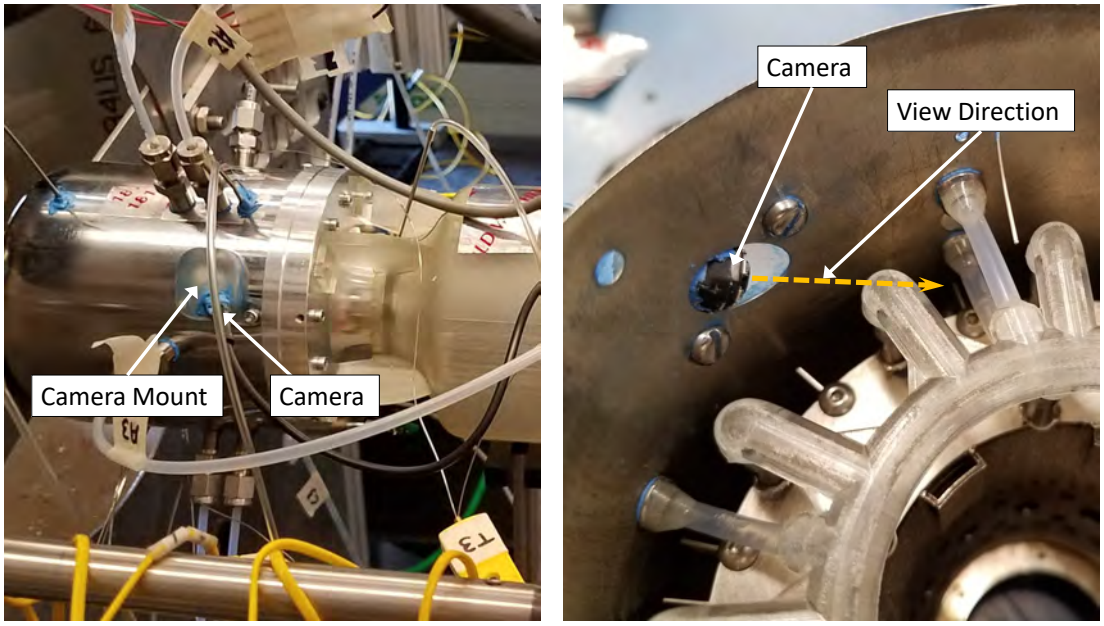


Figure 382. Internal inspection camera

exhaust ring, however, due to the circumferential swirl of the exhaust following the turbine vanes the exhaust was spun outward and all thermocouples were impacted by exhaust flow.

Evaluation of the combustor design was conducted with two different test series. The first series determined the maximum fuel flow rate at air set points of 5, 6, 7, 8, 9, 10, and 11 (0.030 kg/s to 0.07 kg/s) that maintained stable combustion. The second series fixed the air flow rate at 0.03 kg/s, 0.054 kg/s, and 0.07 kg/s and ramped the fuel flow rate while recording temperature and pressure data. This series enabled the approximate air flow splits to be calculated and the sensitivity of the combustor to changes in fuel flow rate to be determined. No data was obtained at 0.07 kg/s air flow rate because combustion could not be maintained.

8.4.3 Experimental Results.

The results presented below are divided into four sections. The first three sections are arranged by variations of the physical hardware from the as-printed combustor

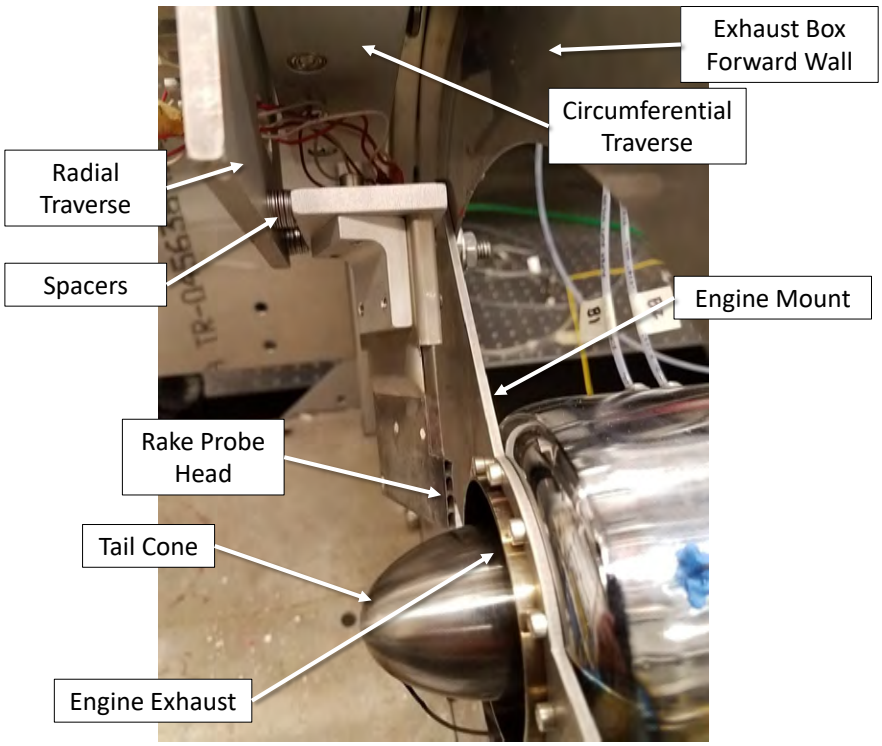


Figure 383. Thermocouple rake positioning at the JetCat exhaust

to inclusion of a Version 1 and Version 2 shim that were installed to compensate for part shrinkage. The final section is a discussion of the combustion performance at a flow condition on the JetCat operating line.

8.4.3.1 As-Printed Combustor.

Initial testing was conducted with the combustor installed in the JetCat casing with gaps between the OD inlets and the casing as shown in Figure 384. The goal of this first test was to verify ignition and then obtain the fuel flow operating bounds at airflow rates from 0.030 kg/s to 0.071 kg/s (idle flow rate). The initial testing of the combustor demonstrated propane ignition at an airflow rate of 0.030 kg/s and a fuel flow rate of 10 SLPM. At this airflow rate the fuel flow was able to ramp to a maximum of 15 SLPM to achieve a global equivalence ratio of 0.25, short of the 0.31 target. With this hardware configuration the maximum flow rates that could be achieved occurred

for an airflow rate of 0.060 kg/s at a fuel flow rate of 23 SLPM (Φ_{global}=0.19), but this condition suffered from a large reduction in temperature throughout the combustor.

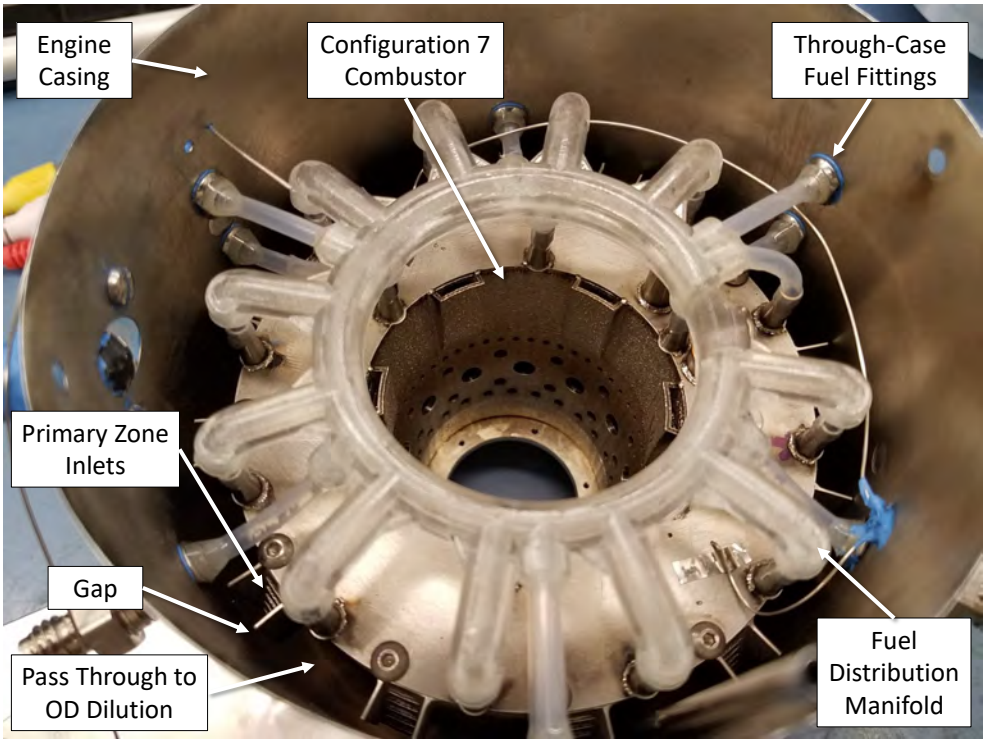


Figure 384. As printed combustor installed int he JetCat casing. A 1 mm gap is visible between the OD air inlets and the casing

To determine the completeness of the reactions at the exit of the combustor the adiabatic flame temperature was found for two flow rate conditions and compared to the experimental temperatures at Station 4. At an airflow rate of 0.030 kg/s and a fuel flow rate of 15 SLPM (Φ_{global}=0.25) the adiabatic flame temperature was calculated to be 973 K. Using only the value from T_{4C} the experimental temperature was found to be 918 K, a difference of 55 K from the adiabatic solution. Using the average of T_{4B} and T_{4C} the experimental temperature was found to be 873 K, a difference of 100 K from the adiabatic result. Applying the average of all three Station 4 temperatures yielded a temperature of 760 K, a difference of 213 K. At an airflow rate of 0.048 kg/s and a fuel flow rate of 20 SLPM (Φ_{global}=0.20) the adiabatic flame temperature was

calculated to be 842 K. Using only the value from T_{4C} the experimental temperature was found to be 878 K, a difference of 36 K above the adiabatic solution. Using the average of T_{4B} and T_{4C} the experimental temperature was found to be 782 K, a difference of 60 K from the adiabatic result. Applying the average of all three Station 4 temperatures yielded a temperature of 693 K, a difference of 149 K. The results from both flow rates showed that the experimental values were reasonably close to the adiabatic solution indicating fairly complete combustion. It also showed that there was a skew in the temperature at Station 4 where the ID was the hottest and the OD was the coldest.

The cause of the skew in temperature at the exit of the combustor was believed to be caused by the change in the size of the combustor in the as-printed part. The limitation of the maximum fuel flow rate, the inability to reach a global equivalence ratio of 0.31, and the inability to maintain combustion was also thought to be caused by the smaller combustor. Based on the available data at the time it was hypothesized that the maximum fuel flow rate was likely limited by to a shortage of air in the primary zone. Adding additional fuel made the primary zone richer than planned and resulted in flameout. Since there was a gap between the combustor OD and the casing, as shown in Figure 384, the air had an additional path available that bypassed the primary zone inlets. This design relied on stagnation of the air above the inlets to yield a greater pressure differential across the primary zone inlets to drive more fluid into the primary zone. The additional pressure differential was critical given that the primary zone inlets were 11% smaller than analyzed computationally. Thus with less air in the primary zone the combustor reached rich flameout at lower fuel flow rates and global equivalence ratios. The skew in the temperature at the combustor exit was related to the change in the airflow split. With less air entering the primary zone OD, and with a larger gap between the combustor and the engine

casing, air was more free to flow around the combustor and exit through the OD dilution holes. More air passing through the OD dilution holes created faster dilution jets that penetrated further through the combustor to push more air toward the ID. The flow pattern put more of the reactions along the combustor ID which led to significantly greater temperatures measured by T_{4C} than T_{4A}. The combustor had difficulty maintaining combustion as the air flow rate approached 0.071 kg/s. Due to the flameouts, modifications were made to the hardware as discussed in the next section to try and adjust the air distribution between the primary and dilution zones.

8.4.3.2 Configuration 7 with Version 1 Shim.

Based on the findings of the initial testing a 0.98 mm Version 1 Shim was cut from aluminum added around the OD of the combustor and completely spanned the primary zone in the axial direction. Figure 385 shows the shim in position prior to the shim and combustor being pushed completely into the engine casing. While the orientation of the compressor exit to the combustor OD inlets was still not an exact match for the hardware analyzed in CFD, the addition of the shim recreated the physical characteristics around the primary zone inlets and returned the combustor to the designed 2:1 area ratio between the pass through to the OD dilution holes and the primary zone inlets.

The results from Test Series One which tested for the maximum fuel flow rate that still maintained combustion at each air set point is shown later in Table 53 as a comparison to other results. Temperature plots of the Test Series Two measurements with air at 0.030 kg/s and 0.054 kg/s and the Version 1 Shim are shown in Figures 386 and 387, respectively. The limit on the x-axis reflects the upper bound of stable combustion at each condition. These plots were used to approximate the air mass flow rate in the primary zone, and the resulting air split percentage into the primary zone. For comparison, the split percentages from CFD calculated 19.76%, 19.69%, 19.29%,

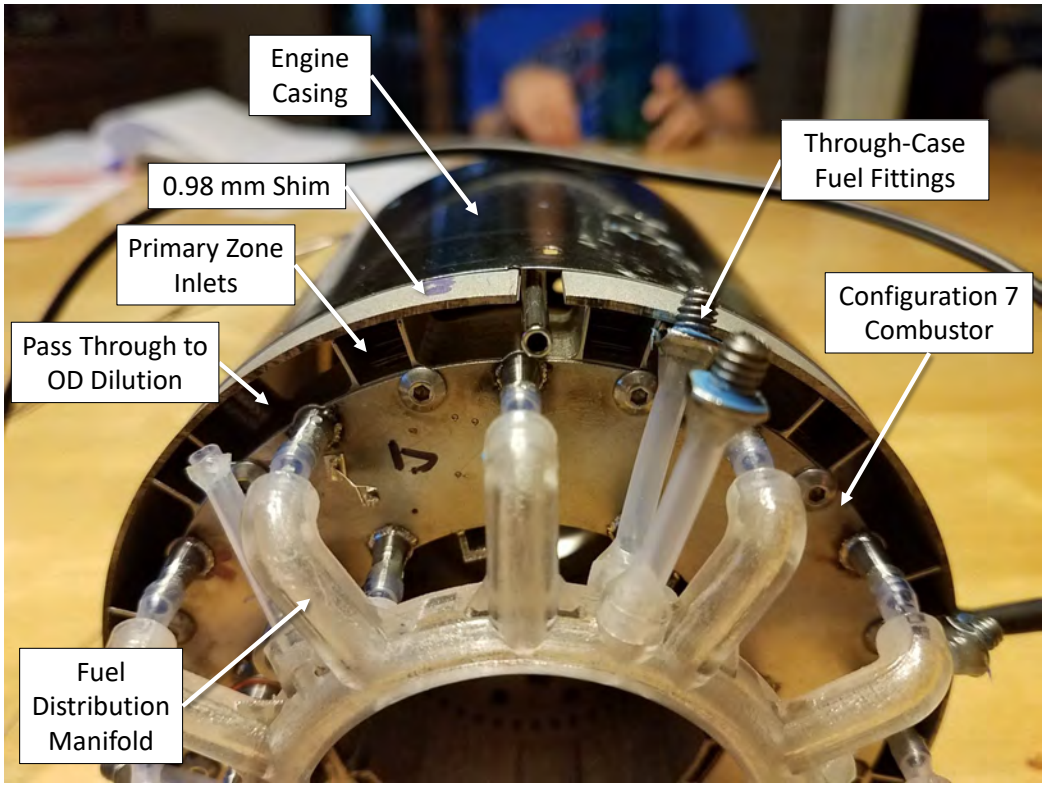


Figure 385. 0.98 mm Version 1 OD aluminum shim. The combustor was not pushed all the way into the engine casing get a better view of the shim and how it mated to the casing and combustor.

and 19.8% for the half idle, idle, 80K RPM, and 100K RPM conditions, respectively. Based on these results the air split percentage was expected to stay constant at approximately 19% to the primary zone across the operating range. Using the peak temperature in the primary zone (T_{C1} and/or T_{C2}) from the plots below combined with the assumption that that temperature occurred at stoichiometric conditions allowed for the air mass flow rate to be found using Equation 15, with $\Phi = 1$ and the stoichiometric air-to-fuel ratio of propane equal to 15.64. In Figure 386 the average of T_{C1} and T_{C2} peaked at a fuel flow rate of 12 SLPM (3.76 x 10^{-4} kg/s) resulting in an air mass flow rate of 5.87 x 10^{-3} kg/s and a primary zone air split of 19.6%.

Using a fuel flow rate of 21 SLPM (6.59 x 10^{-4} kg/s) in Figure 387 as the average peak temperature using a combined T_{C1} and T_{C2} value and assuming stoichiometric

combustion at that condition yielded an air mass flow rate of 1.03 x 10^{-2} kg/s and a preliminary air split of 19.1%. While the air splits to the primary zone in both air flow rates matched the computational results, the addition of fuel caused a steep reduction in temperatures and resulted in flameout before the correct global equivalence ratio was reached. In this combustor the propane was supplied from a pressurized source independent of the air and was injected into the primary zone only. The fuel lines contained enough pressure to always achieve the commanded flow rate. However, the air split was dependent on a pressure balance across all inlets in the combustor. It was hypothesized that the addition of fuel beyond the stoichiometric levels caused back pressure to the primary zone inlets and reduced the air flow into that zone. With more fuel introduced and less air able to enter the primary zone, the conditions quickly became fuel rich and reached a fuel rich flameout limit prematurely.

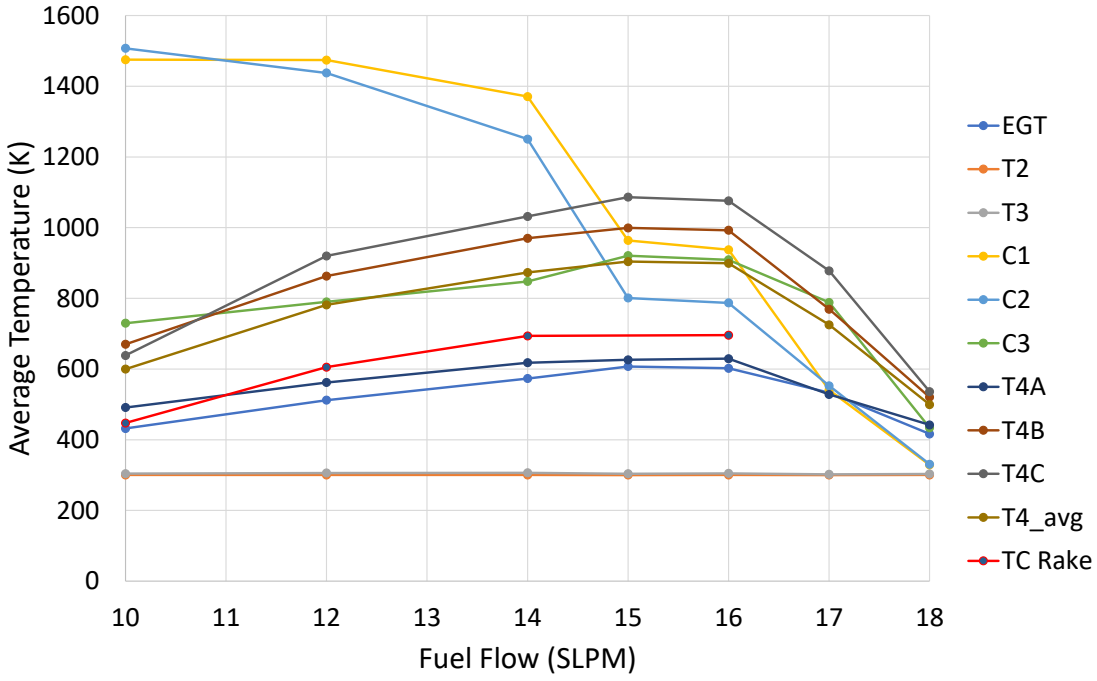


Figure 386. Test Series Two results of temperature (K) at an air flow rate of 0.030 kg/s and variable fuel flow rate with the Version 1 Shim

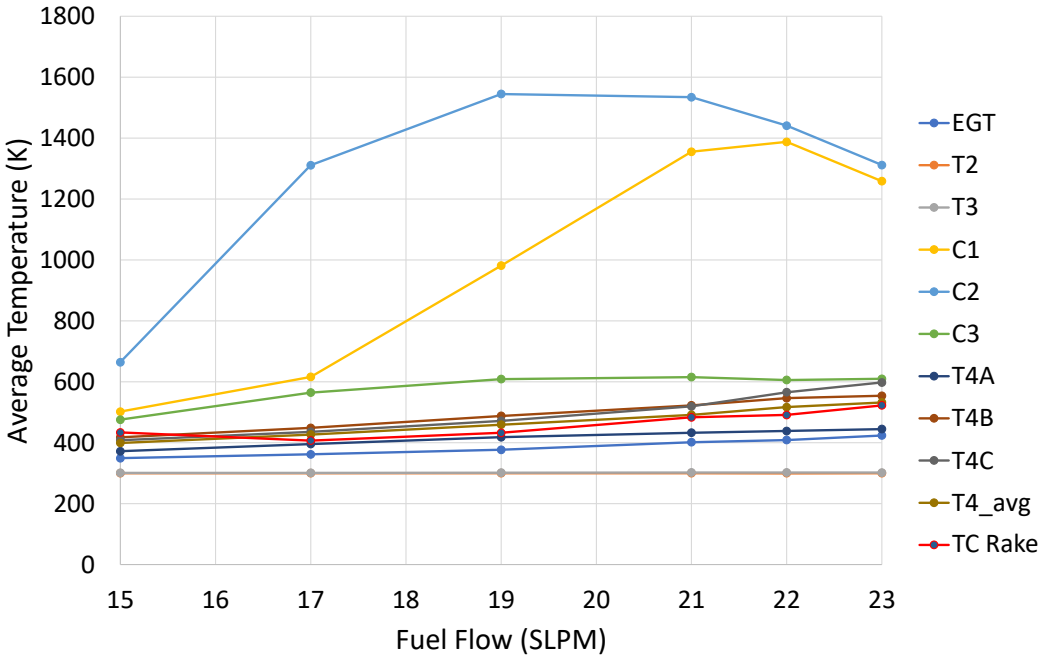


Figure 387. Test Series Two results of temperature (K) at an air flow rate of 0.054 kg/s and variable fuel flow rate with the Version 1 Shim

In Figures 386 and 387 it can be seen that the EGT measurement was routinely lower than the other exiting gas temperatures. In the fully assembled engine the bead of the EGT thermocouple is housed inside the nozzle where it could accurately measure the exiting gas temperature. Without the nozzle present the EGT probe was essentially free floating and only registered a temperature when hot gases happened to impinge at that location. Also shown in these figures is the average temperature measured by the four thermocouples in the thermocouple rake probe (TC Rake). The rake was held stationary at 0° circumferentially (top center) and 21.9 mm radially such that the tip of the probe was just outboard of the engine tail cone. In both of these plots it can be seen that the trends of the average rake temperatures follow the trends of the average T_4 temperatures but at a reduced magnitude. The reduction in temperature by the rake measurement plane was due to entrainment of ambient air.

One additional test series was conducted using the Configuration 7 combustor modified with the 0.98 mm shim. This test used the thermocouple rake to determine how much heated exhaust gas radial spin out took place at the engine exit. Temperature measurements were made at increasing rake radial positions at an air flow rate of 0.030 kg/s, a fuel flow rate of 15 SLPM (4.7 x 10^{-4} kg/s), and a circumferential position of -40, 0, and +40 degrees. The test was repeated at an air flow rate of 0.054 kg/s and a fuel flow rate of 22 SLPM (7.0 x 10^{-4} kg/s) but at 0° circumferentially only. The plots with the results from these four tests are shown in Figures 388 through 391, respectively. These plots are all formatted in the same way with the solid blue horizontal lines indicating the radial position of the JetCat ID and OD exit, and the green markers indicating the starting radial position of the thermocouple beads in the probe head. The remaining four sets of colored markers on each plot indicate the measurements obtained by each of the thermocouples in the probe at each radial position.

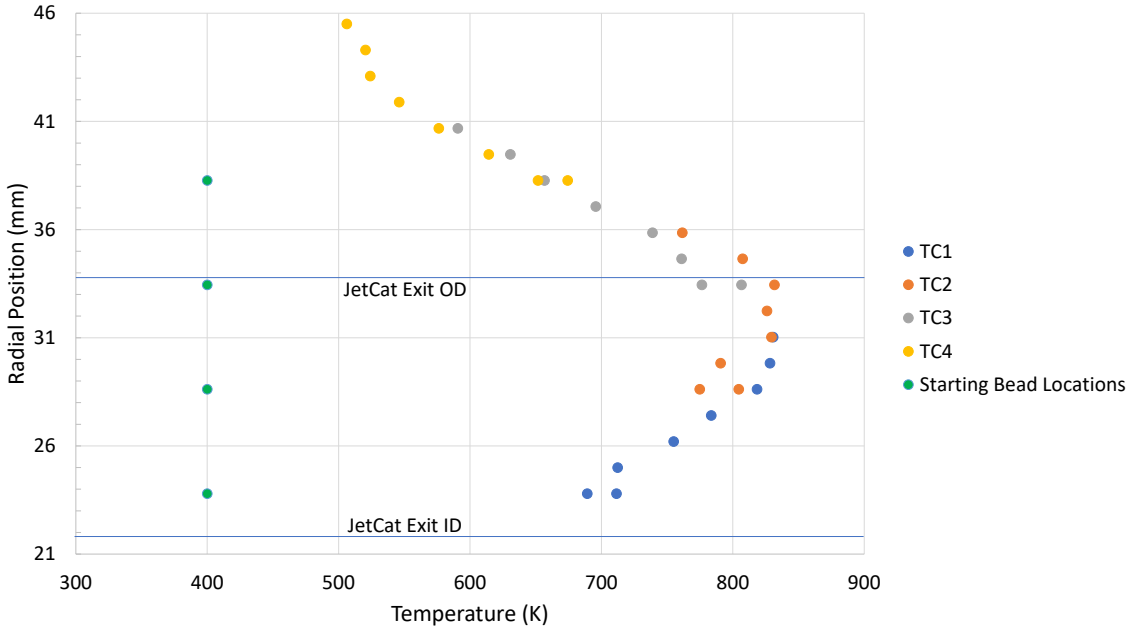


Figure 388. Thermocouple rake temperature (K) measurements with radial movement. Air flow rate 0.030 kg/s, fuel flow rate 15 SLPM, circumferential position fixed at -40°.

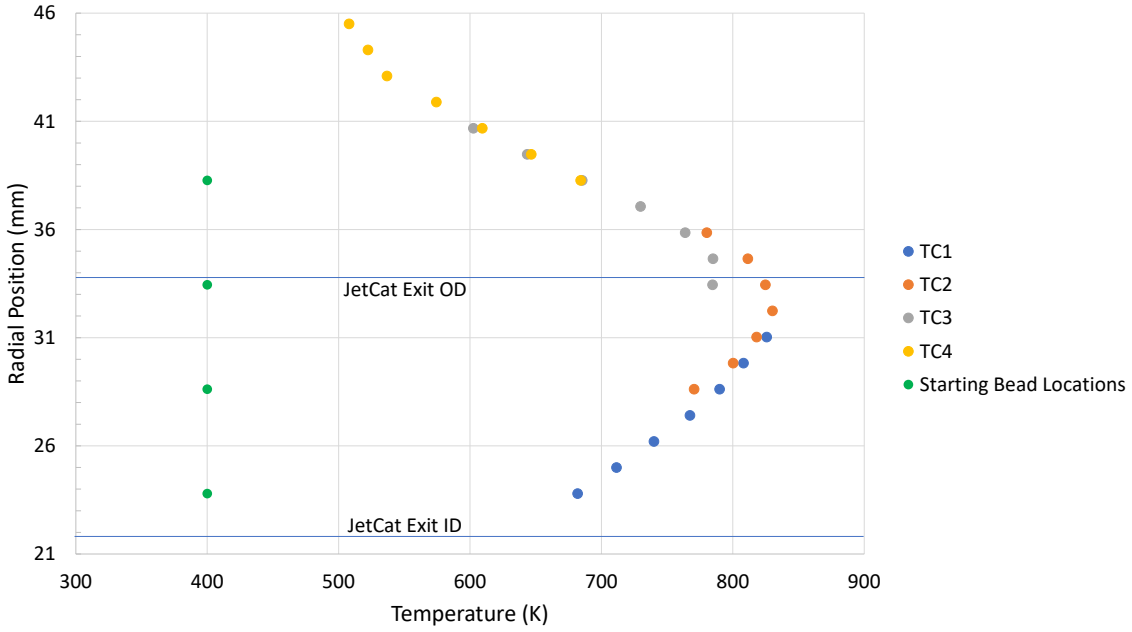


Figure 389. Thermocouple rake temperature (K) measurements with radial movement. Air flow rate 0.030 kg/s, fuel flow rate 15 SLPM, circumferential position fixed at 0°.

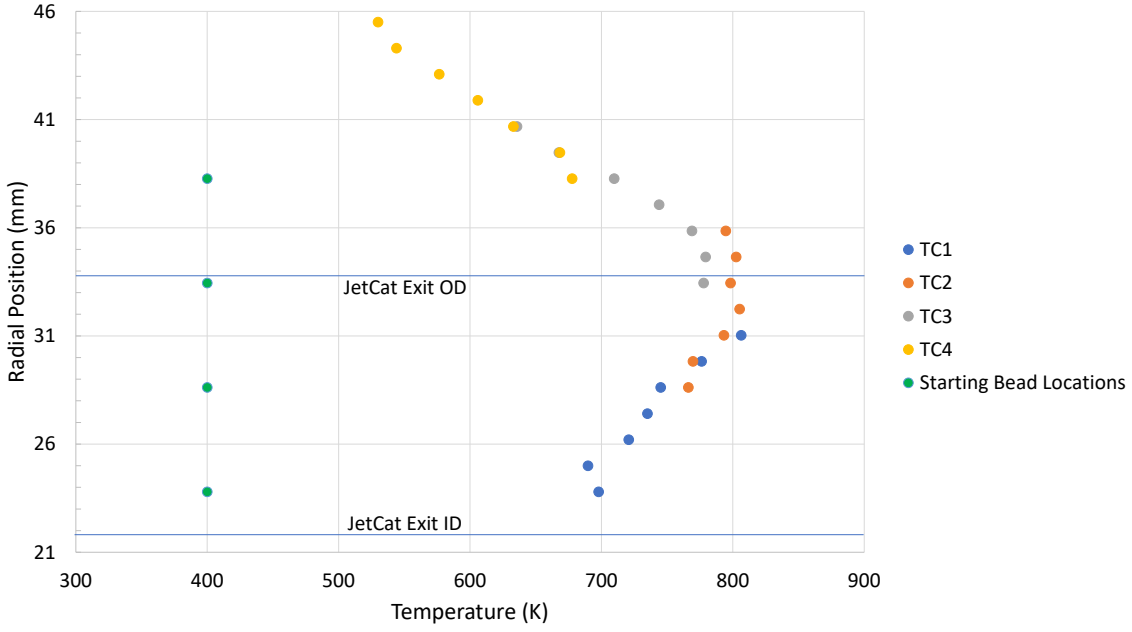


Figure 390. Thermocouple rake temperature (K) measurements with radial movement. Air flow rate 0.030 kg/s, fuel flow rate 15 SLPM, circumferential position fixed at +40°.

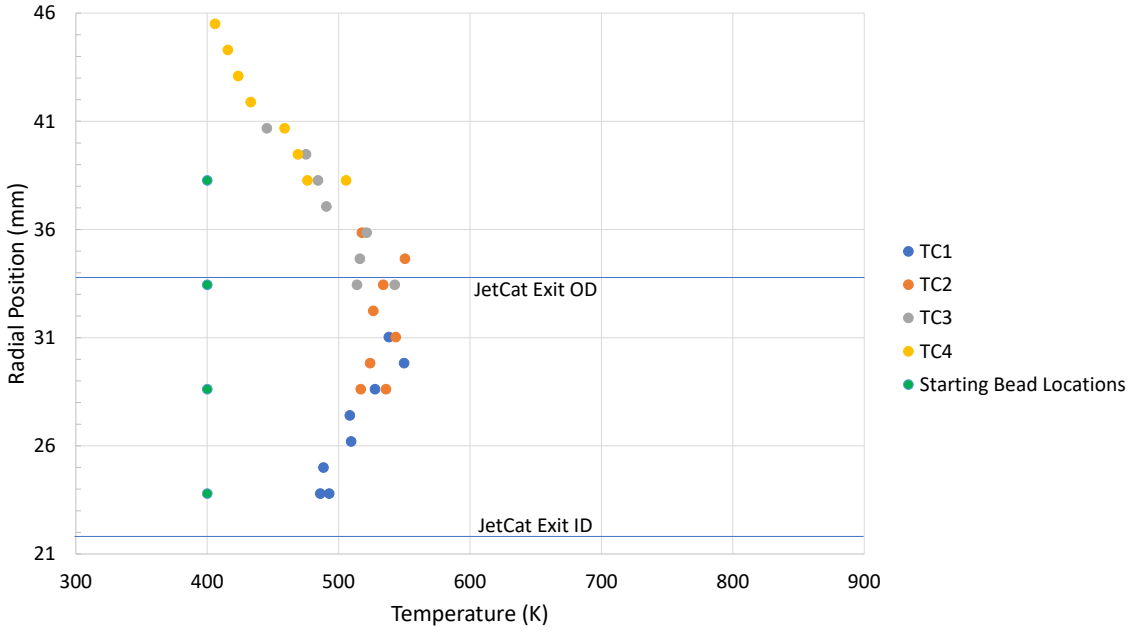


Figure 391. Thermocouple rake temperature (K) measurements with radial movement. Air flow rate 0.054 kg/s, fuel flow rate 22 SLPM, circumferential position fixed at 0°.

All four plots from this test series provide good agreement across all of the thermocouples with additional radial movement. This result is evident by the data overlaps of previous points as the rake was moved radially. Additionally, there was virtually no variation is temperature magnitude or distribution with changes in circumferential measurement position. The variations in temperature that were observed, resulting in a slight data spread rather than one continuous line, was the result of variations in air mass flow rate supplied to the engine. As discussed in Section 3.4 of Lt DeMarco's thesis [161], the 7.62 cm line mass flow controller maintained an average flow rate that matched the commanded value, however, there were flow variations on the order of ± 0.004 kg/s around the commanded value. These fluctuations resulted in slightly richer or leaner conditions leading to changes in downstream temperature with time.

While temperature measurements could not be made directly at the exit to the turbine vanes due to hardware interference, it was believed that the measurements

at the thermocouple rake plane were representative of the turbine vane exiting temperature distribution but magnified since the gases were allowed to expand and were centrifugally spun outward after exiting the engine. The temperature profile in each plot is approximately symmetric measuring from 22 mm to 38 mm radially. This range is believed to be the enlarged version of the turbine vane exit distribution. Beyond 38 mm radially there was a continued decrease in temperature indicating less exhaust gases made it radially that far out. The magnitude of the temperatures in Figure 391 was on average approximately 300 K cooler than the 0.030 kg/s flow rate cases in Figure 388 - 390 due to a reduction the global equivalence ratio for the 0.054 kg/s flow rate case.

8.4.3.3 Configuration 7 with Version 2 Shim.

The first two tests using the as-produced hardware and the Configuration 7 combustor with the 0.98 mm Version 1 Shim showed that there was a favorable temperature distribution at the engine exit, but there was an insufficient amount of air entering the inlets of the primary zone to allow the correct equivalence ratio to be reached. To combat this issue a new shim was manufactured as shown in Figure 392 that maintained the 0.98 mm band around the combustor primary zone inlets, but also added a 1 mm thick wall to the perimeter of the OD pass through to the dilution zone. This new shim added 30% blockage to the pass through passage to try and reduce the flow through that opening. The additional blockage was an attempt to redistribute the air across all combustor inlets, force more air into the primary zone, and create a pressure rise at Station 3 to more closely match the stock JetCat pressure distribution. When this level of blockage was found to be insufficient to produce the desired outcome, 3D printed inserts made from VeroClear-RDG810 plastic were produced to create 50%, 70%, and 75% pass through passage blockage with the inserts shown in Figure 393. The 50% insert featured at 0.8 mm wall thickness, the

70% insert featured a 1.2 mm wall thickness, and the 75% blockage insert featured three 1.698 mm diameter holes. Figure 394 shows the 70% blockage inserts installed in the engine. The results from tested conducted at each blockage level are reported together below and compared to the results using the 0.98 mm Version 1 shim (0% blockage).

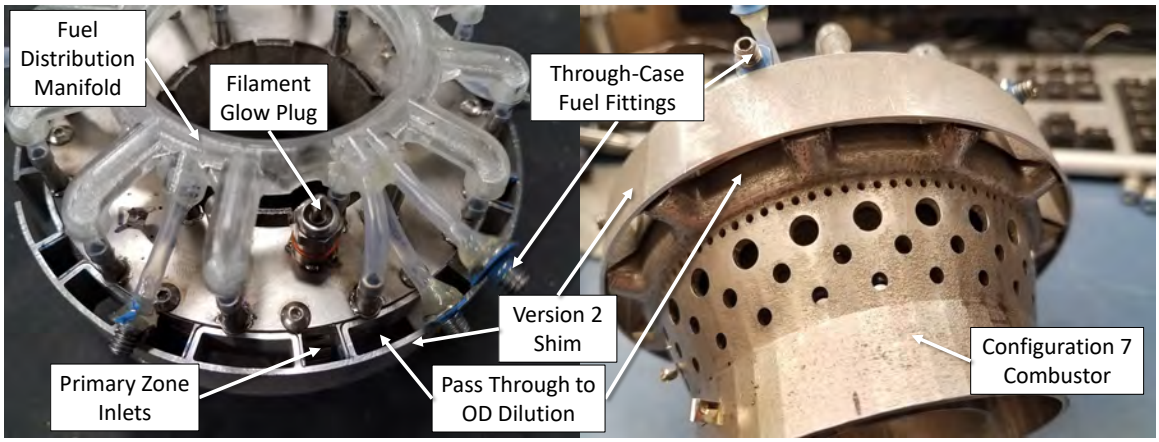


Figure 392. Version 2 shim installed on the Configuration 7 combustor (30% blockage)

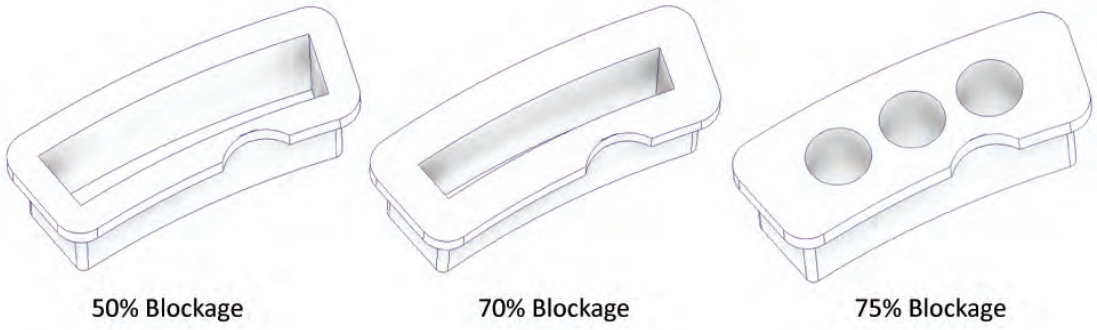


Figure 393. OD blockage inserts

Test Series One was conducted on the combustor at each blockage level with the resulting fuel limit that maintained combustion at each air flow rate given in Table 53. In each blockage level the global equivalence ratio started the highest at the lowest

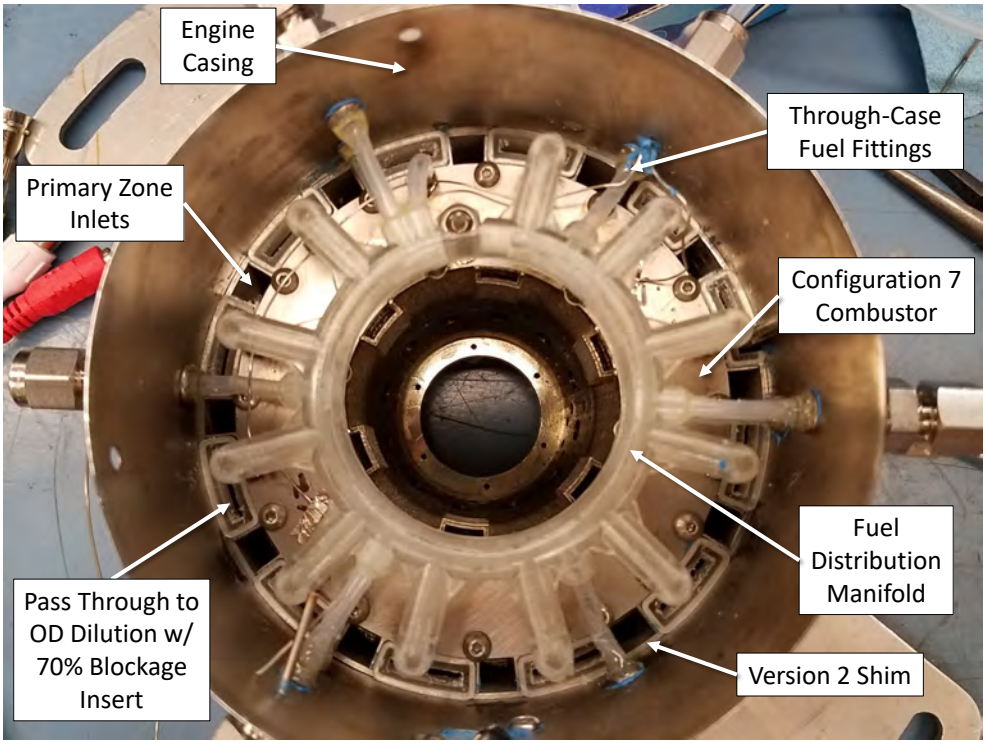


Figure 394. Version 2 shim installed with 70% blockage inserts

air flow rate and decreased with increasing air flow. The 50% blockage insert at an air flow rate of 0.030 kg/s with a fuel flow rate of 19 SLPM was the first condition to reach the targeted global equivalence ratio of 0.31. At 70 and 75% blockage this same air and fuel combination achieved combustion at a global equivalence ratio of 0.34. While an air flow rate of 0.030 kg/s with a fuel flow rate of 19 SLPM was a point on the engine operating line, the idle air flow rate of 0.07 kg/s could not be reached at any of the blockages tested at a global equivalence ratio of 0.31.

An additional pattern emerged from the data in Table 53 which showed that in addition to the fuel flow rate limit decreasing at higher air flow rates in all blockage levels, combustion could not be maintained at any fuel flow level at the higher flow rates with increasing blockage. A stair step pattern was produced in the table with each successive blockage level eliminating an additional air flow rate that previously

Table 53. Fuel flow rate limits (SLPM) to maintain combustion at each blockage level

Air Flow Rate (kg/s)	Fuel Limit 0% Block (SLPM)	Fuel Limit 30% Block (SLPM)	Fuel Limit 50% Block (SLPM)	Fuel Limit 70% Block (SLPM)	Fuel Limit 75% Block (SLPM)
0.030	18	18	19	20.5	20.5
0.036	19	19	20	22.5	23.5
0.042	21	21	22	24.5	26
0.048	23	23	24	26	27
0.054	24	25	25	-	-
0.060	22	23	-	-	-
0.066	22	-	-	-	-
0.070	-	-	-	-	-

maintained combustion. The only exception to this pattern was between 70 and 75% blockage which produced comparable values. It was thought that an incorrect pressure balance and distribution throughout the test setup may have been the cause of this performance pattern. An additional discussion on the pressure distribution is given below with the results of Test Series Two.

The Series Two testing that varied the fuel flow rate, at fixed air flow rates of 0.030 kg/s and 0.054 kg/s, showed a shift in the fuel flow rate that achieved the peak cavity temperature (T_{C1}) and exit temperature (T_{4avg}). This shifting trend was different for the two flow rates as shown in Figure 395 through 398. At the lower air flow rate the peak temperatures were achieved at higher fuel flow rates with increased blockage. While the location of the peak temperature was very similar between the 70 and 75% blockage cases, the 70% blockage case yielded higher cavity and exit temperatures than the 75% blockage case. At an air flow rate of 0.030 kg/s and a fuel flow rate of 19 SLPM the engine was maintaining a global equivalence ratio of 0.31 and was burning on the desired operating line. This location on the operating line was slightly lower than the 1/2 Idle condition. Additionally, at this condition the

cavity temperatures between the 70 and 75% blockage cases were nearly identical at approximately 1040 K, however, the average exit temperature was over 300 K hotter with 70% blockage.

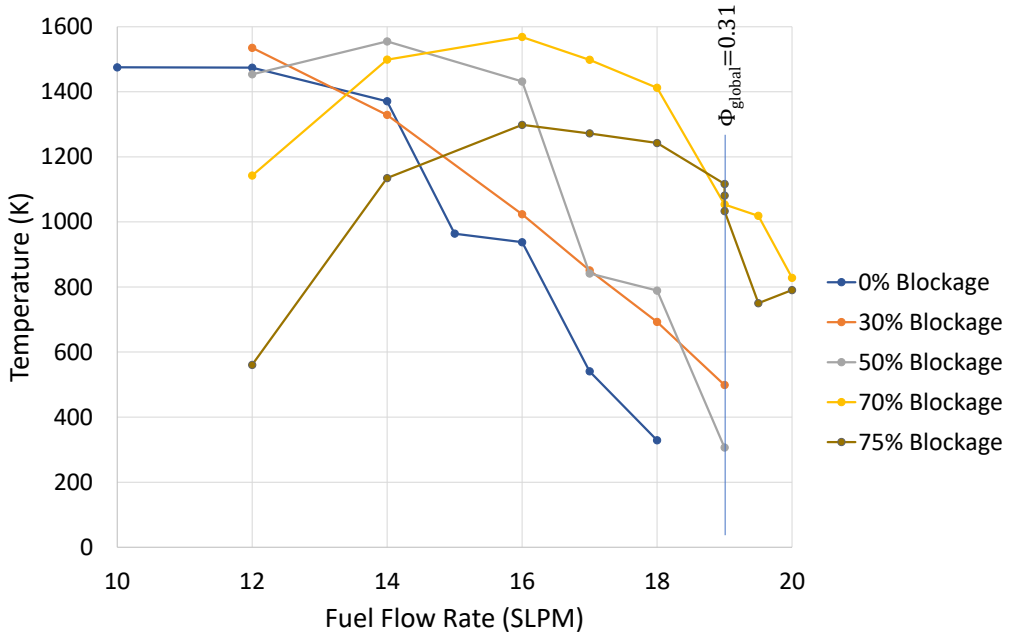


Figure 395. Variation in the T_{C1} combustor primary zone temperature measurement with increasing blockage at an air flow rate of 0.030 kg/s

At an air flow rate of 0.054 kg/s the two best performing cases from the lower flow rate analysis (70 and 75% blockage) did not maintain combustion. For the remaining three blockage configurations the cavity temperatures (T_{C1}) did not demonstrate a significant change in the location of the peak temperature or expand the operational range as shown in Figure 397. This result was expected as the most noticeable changes at the lower flow rate conditions occurred in the higher blockage cases. Additionally, as shown in Figure 398 the average exit temperature across the three blockage configurations remained relatively unchanged even across the fuel flow rate variations with a standard deviation of only 54 degrees. There were no points on the 0.054 kg/s air flow rate plots that were on the desired engine operating line. At this air flow rate

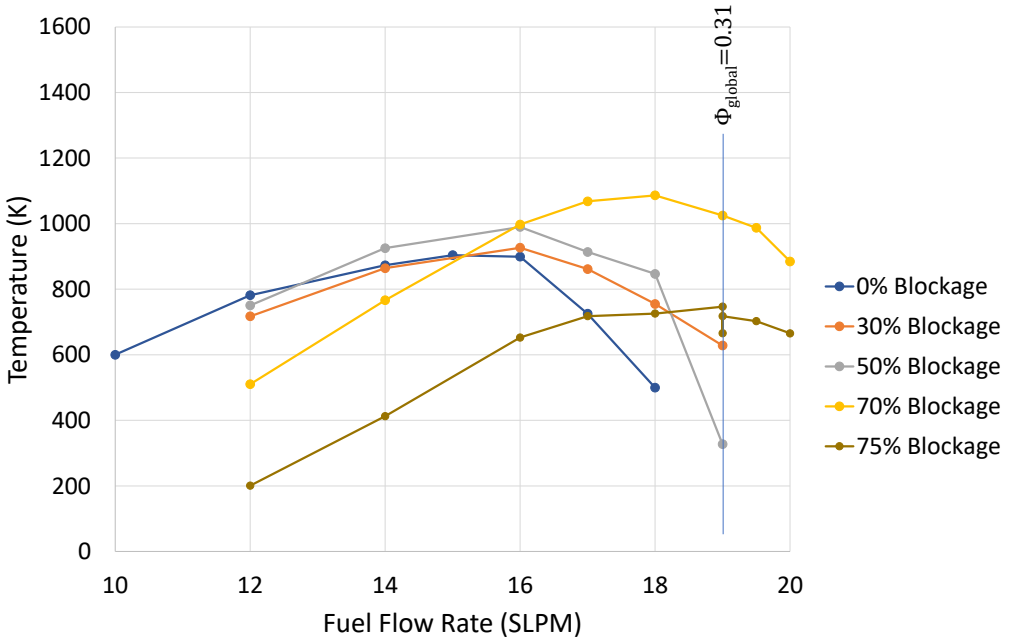


Figure 396. Variation in the average T_4 combustor exit temperature measurement with increasing blockage at an air flow rate of 0.030 kg/s

the fuel flow rate would have needed to be 34 SLPM to reach a global equivalence ratio of 0.31. The 25 SLPM fuel flow limit to maintain combustion fell well short of that target.

Figures 399 and 400 show the absolute pressure measured at Station 3 for a range of fuel flow rates, across all blockage conditions, at an air flow rate of 0.030 and 0.054 kg/s, respectively. In Figure 399 the peak pressure occurred with 70 and 75% blockage at a fuel flow rate of 19 SLPM, however, these peaks in pressure were only approximately 2,200 Pa above atmospheric values. In Figure 400 the peak pressure occurred with 0% blockage at a fuel flow rate of 23 SLPM. This peak pressure was only 2,500 Pa above atmospheric. The 0.054 kg/s air flow condition was approaching the idle flow rate of 0.070 kg/s. At the 0.030 kg/s air flow rate the combustor was able to maintain combustion at a global equivalence ratio of 0.31 because the lower air flow rate was expected to result in comparatively low pressures at Station 3. At

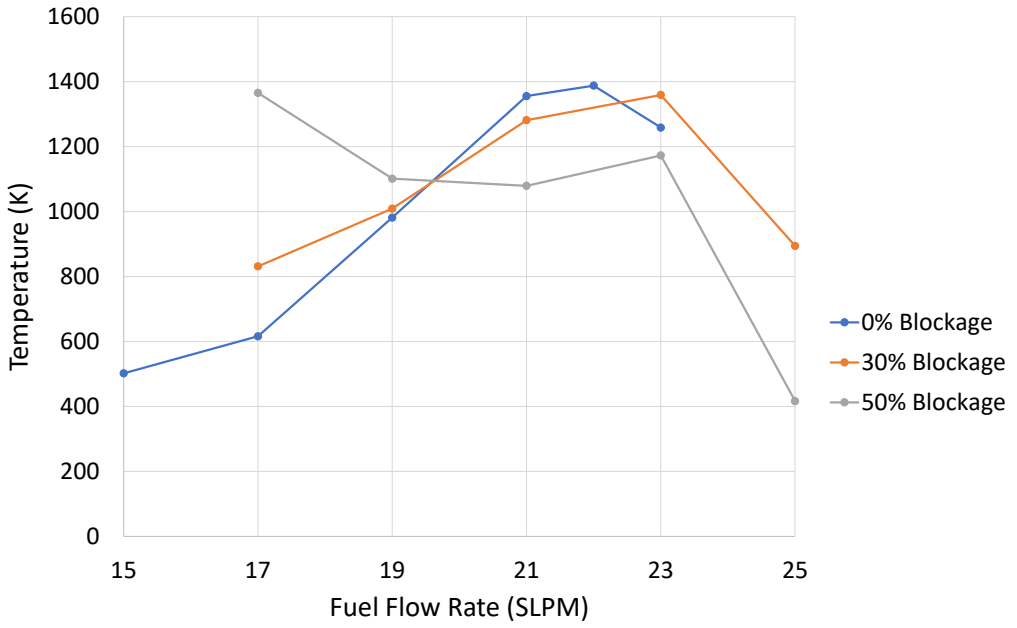


Figure 397. Variation in the T_{C1} combustor primary zone temperature measurement with increasing blockage at an air flow rate of 0.054 kg/s

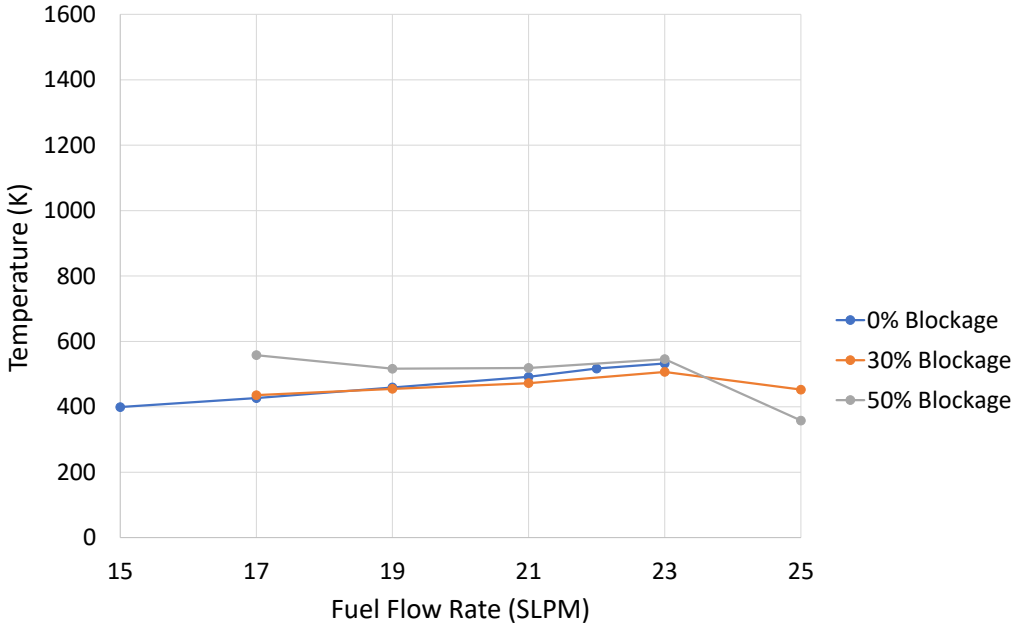


Figure 398. Variation in the average T_4 combustor exit temperature measurement with increasing blockage at an air flow rate of 0.054 kg/s

the 0.054 kg/s air flow rate the operating pressure at Station 3 was expected to be higher in order for the combustor to maintain a flame at a global equivalence ratio of 0.31. Because the pressure at Station 3 was lower than the expected value, it was presumed that there was an insufficient pressure to overcome a primary zone back-pressurization caused by propane injection and drive a higher mass flow rate into the primary zone to maintain combustion at higher fuel flow rates.

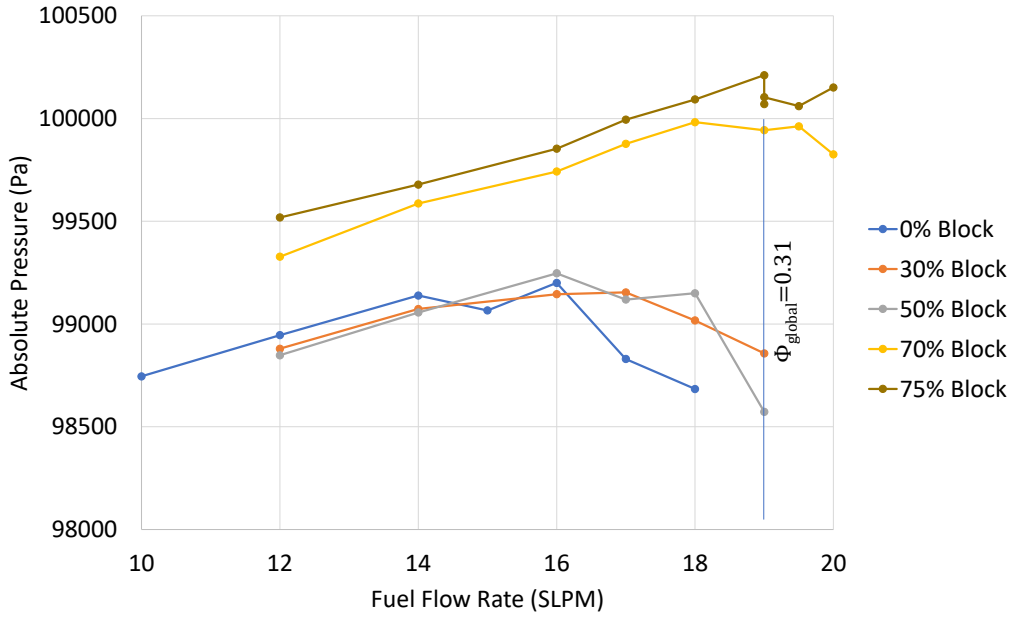


Figure 399. Variation in the P_3 pressure measurement with increasing blockage at an air flow rate of 0.030 kg/s

All of the air was force fed to the engine inlet from an outside source. Even though there were no blades on the compressor rotor in the current setup, there were still two sets of compressor stators and a narrow constriction at the exit of the compressor stage. This constriction resulted in large pressure drops across the compressor that would not have occurred if the device was spinning. In the current setup the largest pressures were achieved at Station 2 across all air flow rates as shown in Figure 401. The pressure drop that occurred across the compressor constriction was significant and resulted in greatly reduced pressures in Stations 3 and 4. Extrapolating the P_2

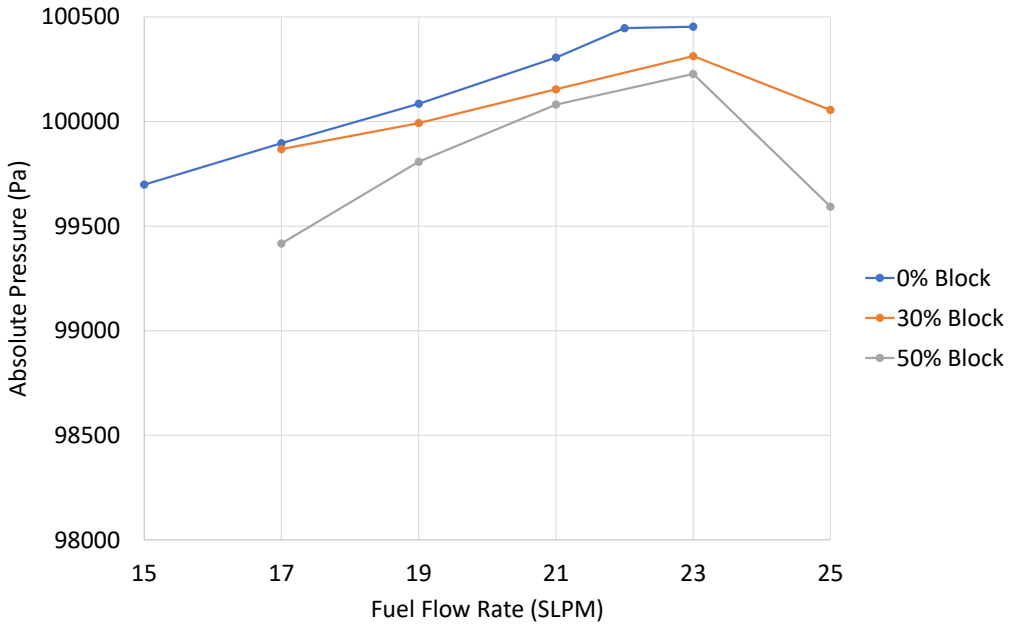


Figure 400. Variation in the P_3 pressure measurement with increasing blockage at an air flow rate of 0.054 kg/s

line to 0.070 kg/s air flow rate would yield an absolute pressure of approximately 107,600 Pa which is comparable to the stock JetCat performance at idle. Due to the significant drop in pressure at Station 3 it was presumed that there was a lack of pressurization compared to what would be achieved with rotating hardware. However, it is shown in Table 58 in Chapter IX that the measured Station 3 pressures were comparable to the pressures achieved with rotating hardware at an air flow rate of 0.03 kg/s.

8.4.3.4 Combustion on the JetCat Operating Line.

The remainder of this section provides additional details about the experimental test point with 70% blockage that achieved a global equivalence ratio of 0.31 and matched a point on the stock JetCat operating line (air flow rate 0.030 kg/s, fuel slow rate 19 SLPM (5.96 x 10^{-4} kg/s)). As shown in Figure 402 stable combustion was achieved at the test point. Experimental measurements produced a primary zone

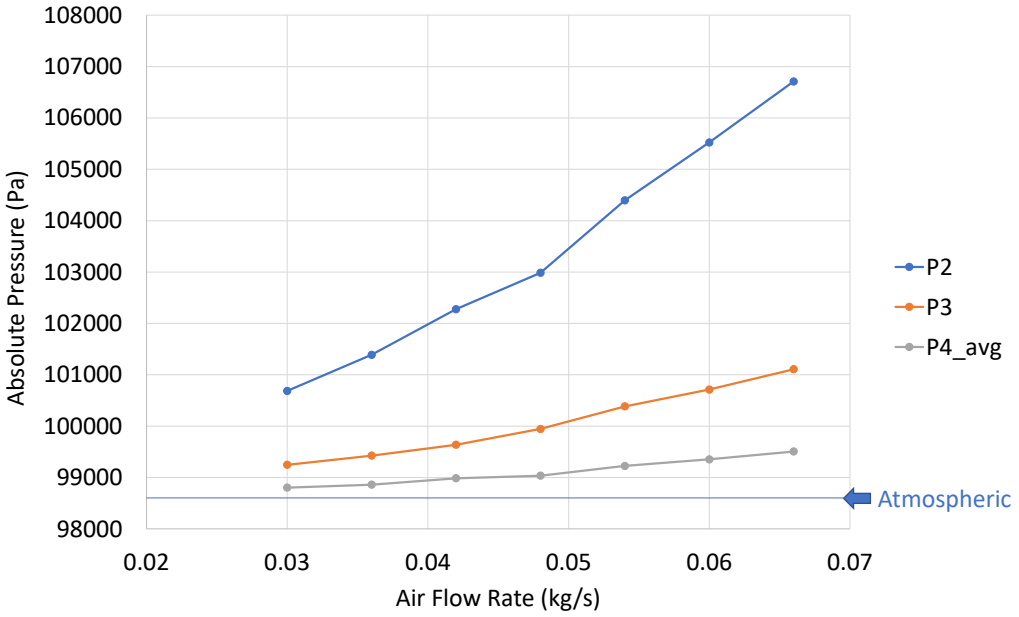


Figure 401. Cold flow pressure measurements at Stations 2, 3, and 4 with 75% blockage inserts at varied air flow rates

average temperature of 1052 K, with an average combustor exit temperature of 1016 K. The static pressure drop across the combustor was measured at 0.6%, and the static drop across the combustor and turbine stators measured at 2.8%. Comparing the experimental temperature value to the 1/2 Idle computational result from Table 50 shows a calculated average combustor exit temperature of 1050 K, a 3% deviation from the experimental results. For an additional comparison the stock JetCat produced a turbine inlet temperature of 1136 K at idle. The static pressure drop across the combustor was calculated at 0.85% as shown earlier in Table 51. The static pressure drop across the combustor and turbine stator was calculated at 2.04%, comparable to experimental values. The deviation from the experimental result was due to the computational model only including 12 vanes to allow for periodic boundaries, while there were 15 vanes in the experimental hardware. The additional vanes added blockage to the flow and created a larger pressure loss experimentally.

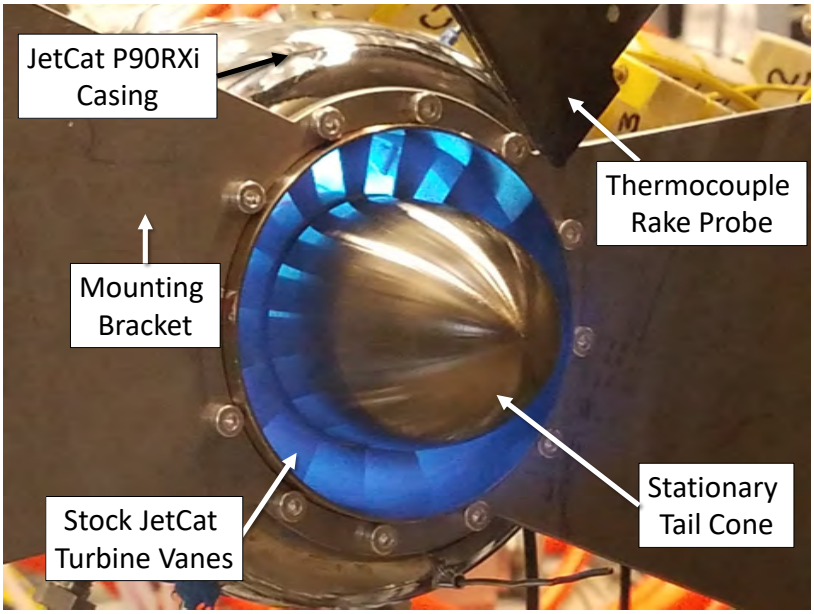


Figure 402. Configuration 7 experimentally combusting at a global equivalence ratio of 0.31 with 70% blockage

Using the thermocouple rake the temperature distribution at the exit of the engine was mapped. While the rake had the ability to move circumferentially and radially, due to the size of the probe head compared to the engine exit passage radial movement was not required. Figures 403 and 404 shows the temperature profiles at the rake measurement plane for repeated cases. Following the definition given in Equation 35, the experimentally measured pattern factors were 0.15 and 0.16, well within the desirable range between 0.15 and 0.25 [14], and an improvement over the 0.87 computational result shown in Table 50. The experimental and computational results produced comparable average temperatures at the combustor exit, however, the reduction in gas temperature at the thermocouple rake plane due to entrainment of ambient gases contributed to the change in pattern factor. Additionally, the thermocouple rake collected data from four radial positions at 10° circumferential increments. The pattern factor in the computational result was based on the average value across all cells on the reference plane and the peak temperature that could have

been present in as few as a single cell on the plane. The comparatively course spacing of the experimental measurements made it possible for hot streaks to be missed if they occurred between probe positions. Figure 405 shows the circumferentially averaged temperatures of the contours shown in Figures 403 and 404. The repeatability in the combustor performance is demonstrated in the similarity between Figures 403 and 404 and the fact that the data points from both tests are nearly an exact match in Figure 405.

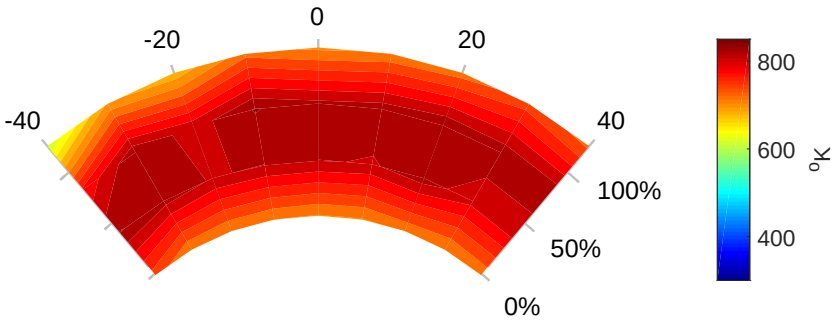


Figure 403. Configuration 7 experimentally derived exit temperature contours at a global equivalence ratio of 0.31 with 70% blockage

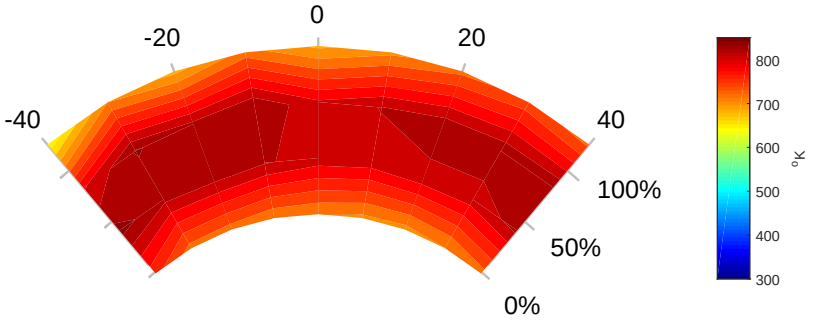


Figure 404. Configuration 7 experimentally derived exit temperature contours at a global equivalence ratio of 0.31 with 70% blockage repeated

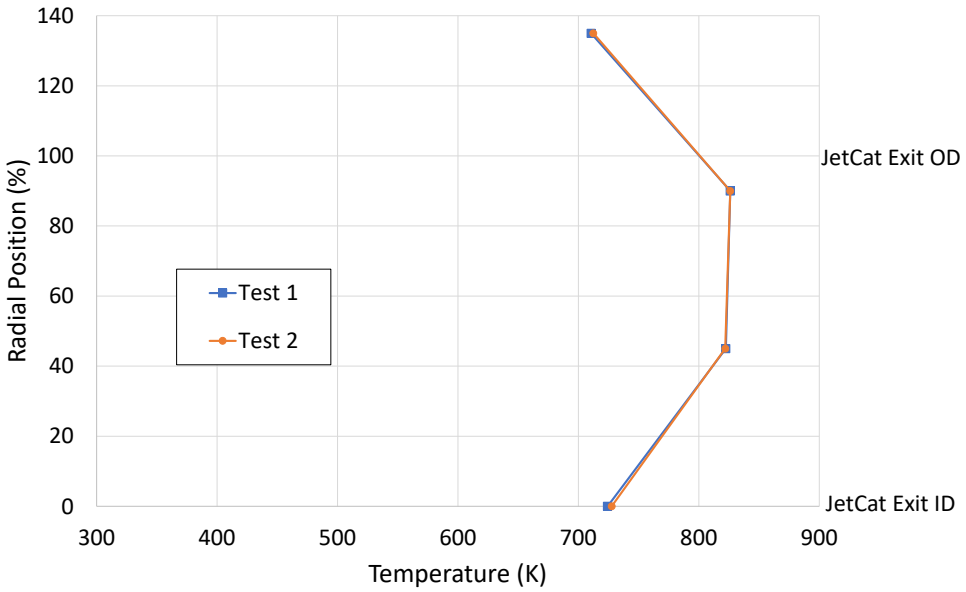


Figure 405. Configuration 7 experimentally derived circumferentially averaged exit temperature profiles for a repeated test point at a global equivalence ratio of 0.31 with 70% blockage

8.5 Objective 4 Conclusions

A new circumferential flow combustor was designed and tested to integrate into a JetCat P90RXi and achieve the same temperature profile at the inlet to the turbine while realizing a 33% reduction in the axial length. Several aspects to achieve this design were investigated including the ability to maintain a high-g swirl in the primary combustion zone, maintain combustion stability, control the fuel injection to achieve the required residence time, and achieve a uniform temperature distribution at the turbine rotor inlet.

To achieve the desired injection velocity it was found that the pressure distribution around the combustor was the only controlling parameter. Stable combustion was computationally shown to occur in the primary zone by using backward-facing steps to maintain a pilot flame in the recirculation zone behind the step. An alternating pattern of air injecting steps and non-injecting stabilizing steps provided sufficient

driving force to establish centrifugally loaded flow, while maintaining flame holders in the combustor. Fuel injection from the stabilizing steps did not allow for sufficient residence time for complete combustion. Fuel injected radially from the OD wall between the air injecting and stabilizing steps, as shown for Configurations 6 and 7, allowed for premixing of fuel and air before reaching the stabilizing steps ensuring a stable pilot flame.

A dual-chamber combustor could be used to maintain circumferential swirl in the primary zone followed by an axial flow secondary/dilution zone. In the combustor configurations that attempted to maintain swirl through the secondary/dilution zone, the incoming air formed a cool air layer on the ID and OD of the combustor and forced the hot reacting products to the center with minimal mixing. When an axial flow secondary/dilution zone was analyzed, mixing was greatly enhanced and a more uniform temperature distribution was achieved. In Configuration 7 a near ideal temperature profile was computationally produced with the peak temperature occurring with a slight OD skew from the passage centerline for maximum power extraction from the turbine.

Second order detailed off-design computational analysis of the Configuration 7 combustor showed repeatable and predictable behavior across the operating map. All test conditions produced a cavity equivalence ratio of approximately 1.55 with an air flow split of approximately 19.6% to the primary zone. Additionally this analysis showed manageable pressure losses across the combustor, but will require further optimization in future iterations of the design to reduce these losses.

Experimental validation testing confirmed positive combustion behavior and compared well to computational data in temperature with explainable deviations in pressure. This combustor design fixed the flow migration issues from past UCC configurations by achieving a radially symmetric exit temperature profile with an average

experimentally derived pattern factor of 0.155. Experimental combustion temperatures were comparable to the stock JetCat, however, the Configuration 7 combustor achieved these values with a 33% shorter combustor. Thus providing evidence that a UCC can produce the same thermal inlet conditions to a turbine at a substantially shorter axial length. Limitations in the operating range of the combustor were observed, but there were many positive attributes to the combustor performance that overall made this first attempt at a new UCC configuration a success.

IX. Objective 5: Effects of Increased Mass Flow Rates & Pressures

Investigate the impact of higher flow rates and pressure ratios on combustion performance, exit temperature distributions, and system pressure losses

The use of an engine as an operational test bed for combustor analysis is the logical next step from the stand alone testing conducted in Chapter VIII. With the limited flow rate and pressure ratio that could be supplied by the COAL lab air supply system, the use of an engine test bed expands the operational test range in both flow rate and pressure ratio to determine the impact on the combustor. Unlike the testing conducted in Chapter VIII, the use of an engine with rotating hardware removes the independent control over fuel and air flow rates. The only control input in this type of testing is the fuel flow rate with the response of the rotor dictating the air flow rate. While this testing has limited input controls, this setup is representative of an operational engine with the behavior of the combustor responding accordingly.

9.1 Objective 5 Background

The UCC results discussed in Chapter VIII showed success in correcting the combustor exit temperature distribution and demonstrating combustion with a 33% shorter combustor that fit inside the same JetCat engine casing. The AFIT COAL lab air supply system was limited to supplying 0.12 kg/s sustained at near atmospheric pressures. At these flow rates and pressures the maximum JetCat P90RXi operating condition that could be replicated was "Idle" at an air flow rate of 0.072 kg/s at 110,316 Pa. Additionally, due to the test setup which forced air through the engine inlet and across both sets of compressor stators, there was a significant reduction in pressure at Station 3 compared to Station 2 as shown in Figure 401. As discussed in Section 8.4 the operating range of combustor Configuration 7 was limited to 1/2

Idle due to what was thought to be a back-pressuring of the primary zone inlets by injecting gaseous propane into the primary zone only. With an insufficient air pressure at Station 3 to overcome the propane pressure inside the primary zone, there was an increased cavity equivalence ratio that quickly reached rich flameout due to the combined effect of increased fuel and decreased air.

By using rotating turbomachinery the engine would no longer be force fed air. The use of a rotating compressor would also correct the placement of the peak pressure observed in Chapter VIII, Figure 401 from Station 2 to Station 3. If the shift in the peak pressure to Station 3 corrected the primary zone air flow rate issues discussed above, the operating range of the engine could also be extended from that observed in stand alone combustor testing.

This test represents the first pairing of a UCC with rotating turbomachinery. This test demonstrated the ability of a UCC, with a 33% shorter combustor compared to the stock engine combustor, to drive a rotating turbine. Additionally the performance of the engine operating with a UCC was compared to the baseline engine performance.

9.2 Experimental Methodology

Combustor Configuration 7 outlined in Section 8.4.1 was combined with the 70% blockage inserts installed in Shim Version 2 described in Section 8.4.3. The majority of the engine components and instrumentation outlined in the Experimental Methodology in Section 8.4.2 was also used. The "7.62 cm Air Supply Line Adapter", "Custom Non-Rotating Bladeless Compressor Wheel", "Custom Non-Rotating Shaft & Tail Cone", and the "Custom Engine Mount" shown in Figure 377 were replaced by the stock compressor, turbine rotor, and center shaft. These components were pressed together and secured in place with their respective nuts as shown in Figure 406. The engine was brought to The Balancing Company in Vandalia, Ohio to have

the rotating components precision balanced to eliminate vibration at high rotation rates. The rotor was balanced to 7.2 x 10^{-4} g-cm (1.0 x 10^{-5} oz-in) or less.

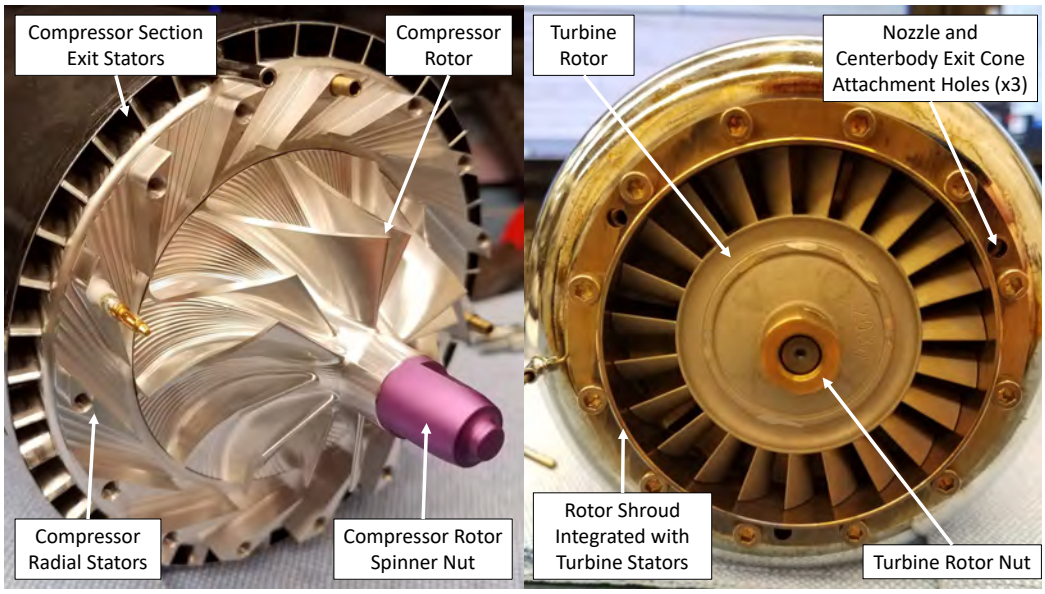


Figure 406. Rotating hardware components installed into the JetCat (Compressor left, Turbine right)

Appendix D details a redesigned JetCat electrical system to connect the hardware with LabView control and data acquisition. This appendix also provides additional details on temperature, pressure, and force measurement systems, glow plugs, fuel and lubrication delivery, calibration curves, and custom LabView visual interface. As discussed in the text surrounding Figure 375 there was a significant modification to the stock JetCat fuel system to run on propane as the primary fuel. The propane distribution plenum shown in Figure 380 that was connected to the AliCat fuel mass flow rate controller was reused for the current study. With the addition of rotating components in the present analysis a kerosene/oil blend was needed to lubricate the two main engine bearings as designed for the stock engine. The solenoid and lubricant fitting assembly shown on the left half of Figure 407 was installed with the redesigned JetCat electronics engine board to the stock compressor shroud as shown in Figure 408. The solenoid and lubricant fitting assembly was o-ring sealed to two tubes that

passed through the compressor shroud, compressor stators, and into a fitting and the lubricant plenum on the backside of the compressor as shown in the right side of Figure 407. The "Glow Plug Line" was closed off leaving the "Lubricant Line" as the only active fitting that flowed the kerosene/oil blend. The stock starter motor assembly was attached to the compressor shroud and the stock purple cowling was installed to hold the starter in place. The stock nozzle was attached to the downstream end of the engine. The completed engine assembly is shown in Figure 409.

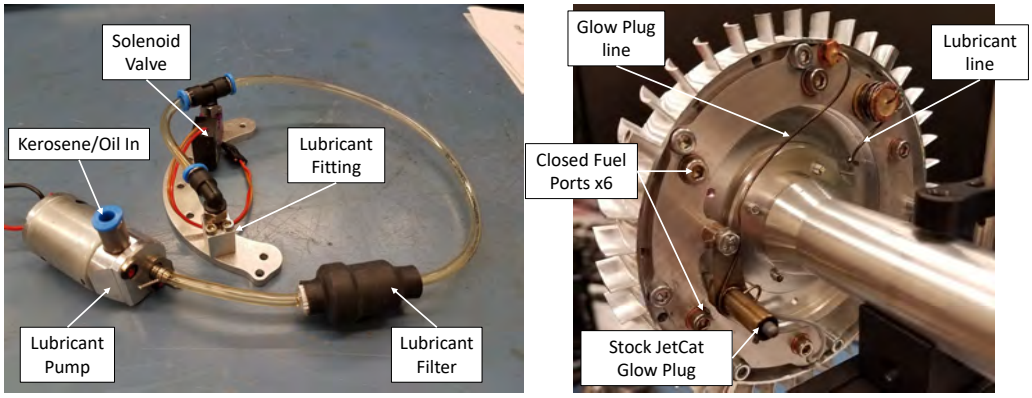


Figure 407. Pump, solenoid, and fittings in the modified JetCat

The stock JetCat had seven lines that split off the fuel plenum after the pump. Six of these lines fed kerosene into the combustion chamber, with the seventh providing lubricant to the upstream main engine bearing. Bleed air from the compressor pulled the lubricant through the forward main bearing to the aft bearing and then out a small space between the nozzle guide vanes and the turbine rotor where it could combust prior to exiting the engine. To determine the percent split of kerosene flowing to the combustion chamber versus the lubricant line, the pump was run at varying duty cycles between 0 and 100% with the stock JetCat fuel system configuration. As shown in Figure 410 the pump was connected to a kerosene/oil blend reservoir and the stock fuel connections on the JetCat centerbody and compressor shroud. The JetCat hardware was positioned over a beaker inside of a larger beaker. The engine centerbody was the lubricant flow conduit and was situated inside the smaller beaker.

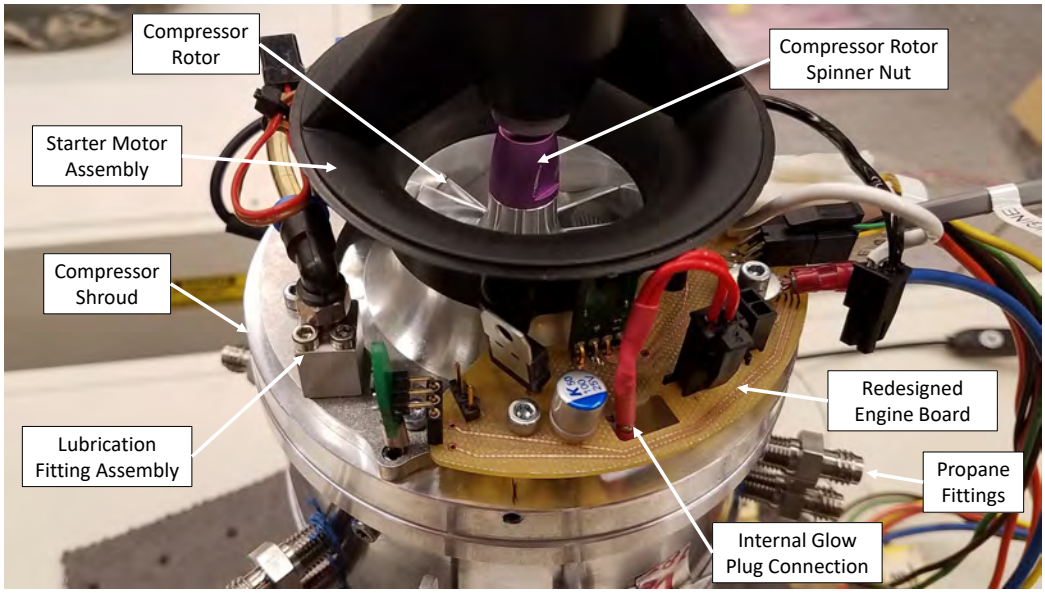


Figure 408. Lubrication fittings and the redesigned electronics engine board installed on the JetCat compressor shroud

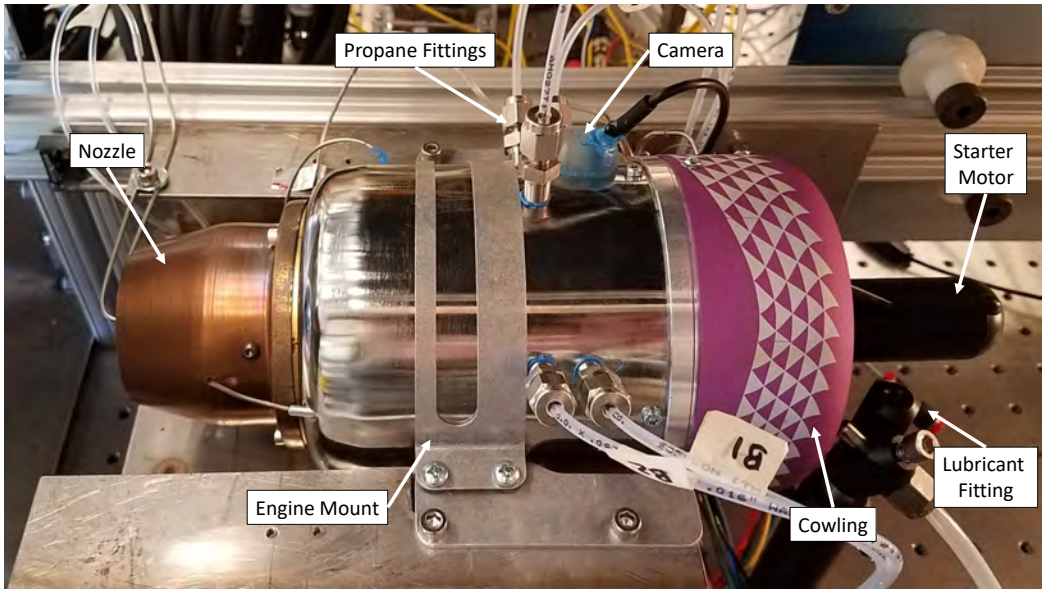


Figure 409. Completed engine assembly. Flow is from right to left

The six stock fuel lines were positioned between the two beakers. When the pump was run the fuel that would have gone to the combustion chamber filled the space between the beakers, while the lubricant flowed into the smaller beaker. The pump

was run for 30 seconds and then each beaker was weighed to determine the mass flowed through each path. The results from this study are shown in Figure 411 with the lubricant flow rate reaching approximately 5% of the fuel flow rate.

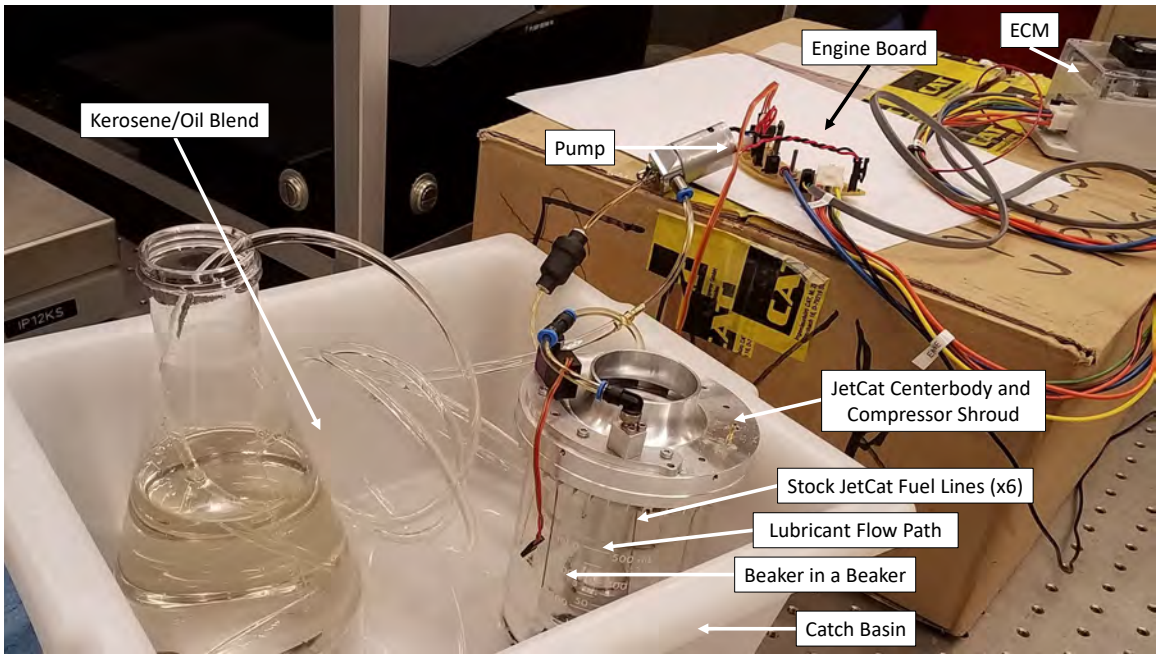


Figure 410. Lubricant pump calibration setup

During the test it was found that the pump could not operate below a duty cycle of 35%. In fact, in order to reach 35% a duty cycle of 50% was required to get the pump moving and then the commanded duty cycle could be backed down to 35%. It was also found that at 100% duty cycle the pump was not outputting the flow rates specified by JetCat as the maximum fuel flow rate. With the current setup a duty cycle of 125% would be required to reach that flow rate. Since values above 100% are not possible that value cannot be reached with the current setup. JetCat could possibly have been overdriving the pump motor to achieve better performance, or there was possibly an issue with the new electronics that prevented the pump from reaching peak performance. Fortunately, this engine runs on propane as the primary fuel and only uses the kerosene and pump for lubrication. The slope of the

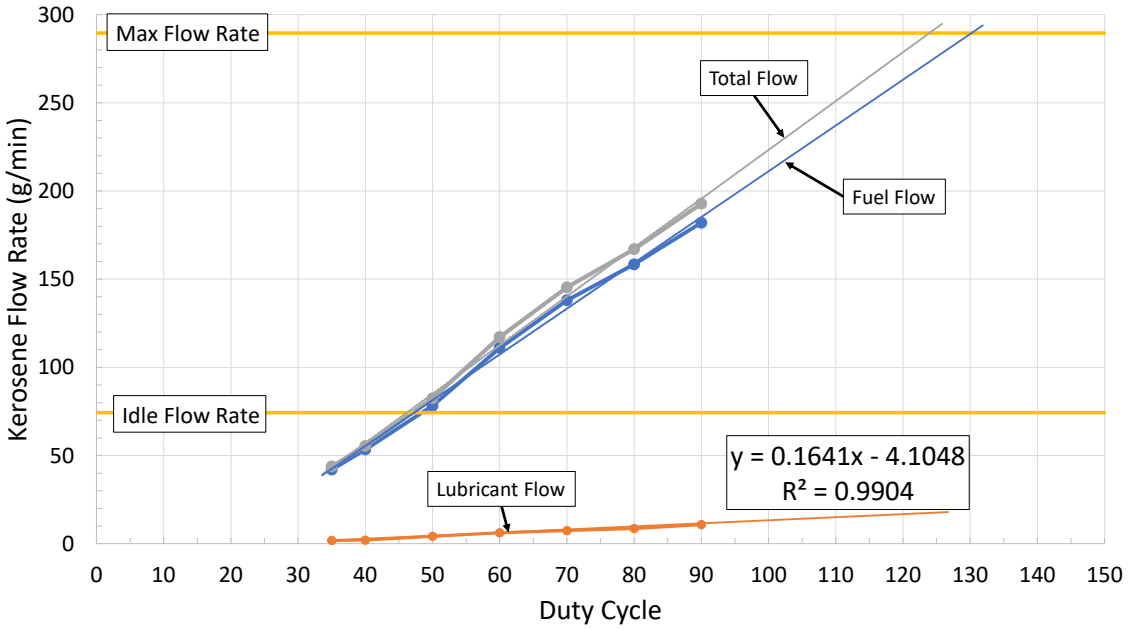


Figure 411. Pump calibration test results

linear trendline through the lubricant flow rate points in Figure 411 was relatively flat allowing the 90% duty cycle lubricant flow rate to be continued for higher fuel flow rates with only a minor reduction in lubricant flow rate compared to the requirement specified by the trendline.

As shown in Figure 412, the fuel flow rate, converted to propane, was related to the pump duty cycle required to achieve the needed lubrication flow rate through a second order relationship. In this figure it can be seen that above 100 SLPM of propane the curve is plateauing to peak at 90% pump duty cycle to account for the limitation of the pump flow capability. Using this second order relationship 98% of the variation in pump duty cycle could be explained by changes in propane flow rate. Based on it's accuracy to the experimental data this curve was used to command the pump duty cycle based on the commanded flow rate of propane, which was directly related to rotor RPM. For all propane flow rates below 55 SLPM the commanded duty cycle was specified at 60% to ensure the motor would start and lubricant would

be flowing. The propane flow rate threshold specifying when lubricant would begin flowing was user specified though an input on the LabView VI front panel. Below the specified propane flow rate value the lubricant pump would remain off. The linear equation for the trendline through the lubricant flow data in Figure 411 was used to convert the commanded pump duty cycle to a lubricant flow rate in g/min to display on the LabView VI gauge.

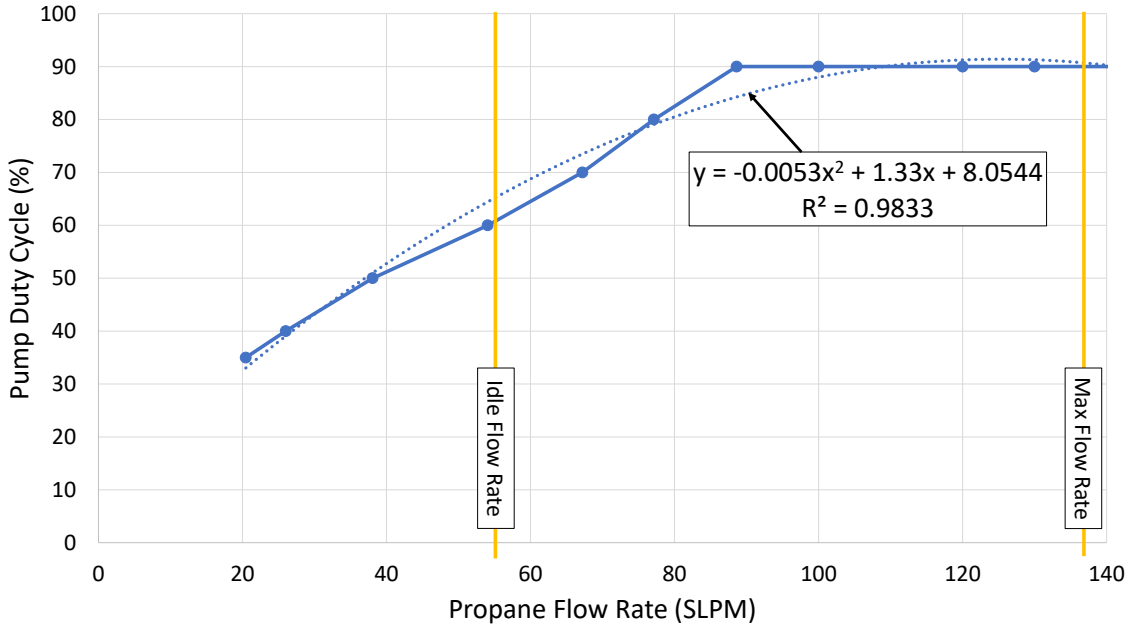


Figure 412. Relationship between propane flow rate and required pump duty cycle

Since the pump was calibrated with the stock fuel lines installed, the small plenum shown in Figure 413 was made to connect all six fuel lines to the pump, but delivered the fuel back to the kerosene reservoir. With this setup the pump could be run in the same configuration as it was calibrated, with only the lubrication line connected to the stock plenum in the engine, and the new plenum distributing the fuel through the stock fuel lines back to the kerosene reservoir.

A test stand with a sliding safety enclosure was designed to enable thrust, temperature, and pressure data to be taken on the JetCat engine from behind 11 gauge

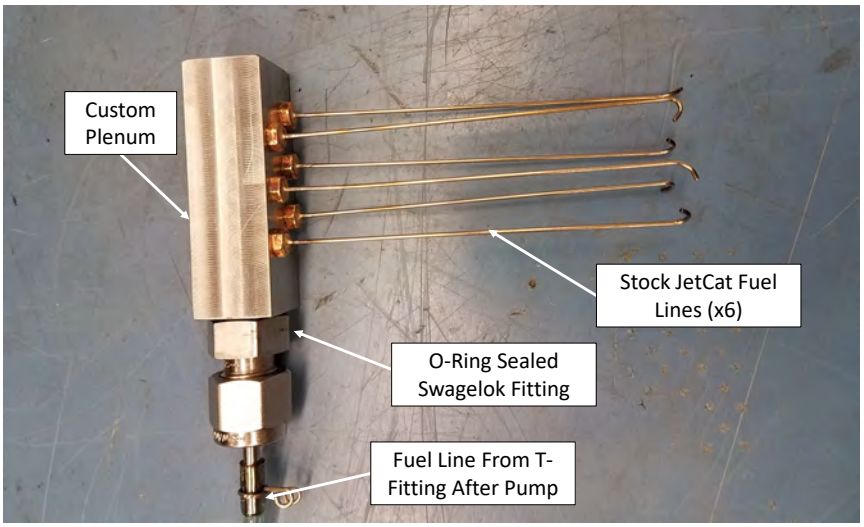


Figure 413. Custom plenum to use the stock fuel lines used in pump calibration and return the fuel to the kerosene reservoir

steel plates. The safety enclosure shown in Figure 414 was mounted to a laser table in the northeast corner of the COAL lab and was designed to contain any projectiles should the engine lose a component while rotating at high speed. The sliding enclosure traversed on 80-20 slide rails, as shown in Figure 415, to provide access to the engine for setup and instrumentation, and then quickly secure the engine for testing. The upstream end of the enclosure was made of two layers of steel mesh, offset from each other to create a tighter mesh pattern. The mesh sandwiched a fine gauge steel screen to prevent any small lose items near the test stand from being ingested by the engine or sucked up the exhaust ventilation system. At the downstream end of the test stand the sliding enclosure was connected to a fixed 11 gauge stainless steel transition by three steel clasps. The transition was manufactured by Air Cleaning Specialists, Inc. and went from a rectangle to mate with the sliding enclosure, to a circular duct to mate with the COAL lab exhaust system discussed in Section 3.1.3.

As shown in Figure 415 the JetCat was installed into a sliding engine mount that was connected to the fixed 80-20 slide rails by a set of precision ball bearing roller

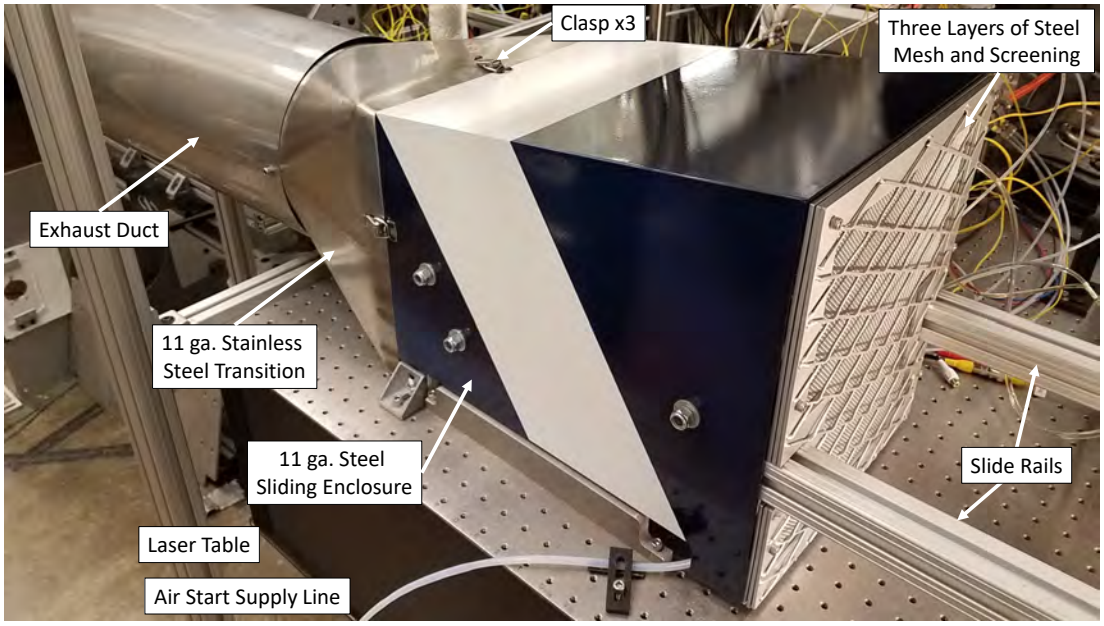


Figure 414. Safety enclosure and test stand closed position

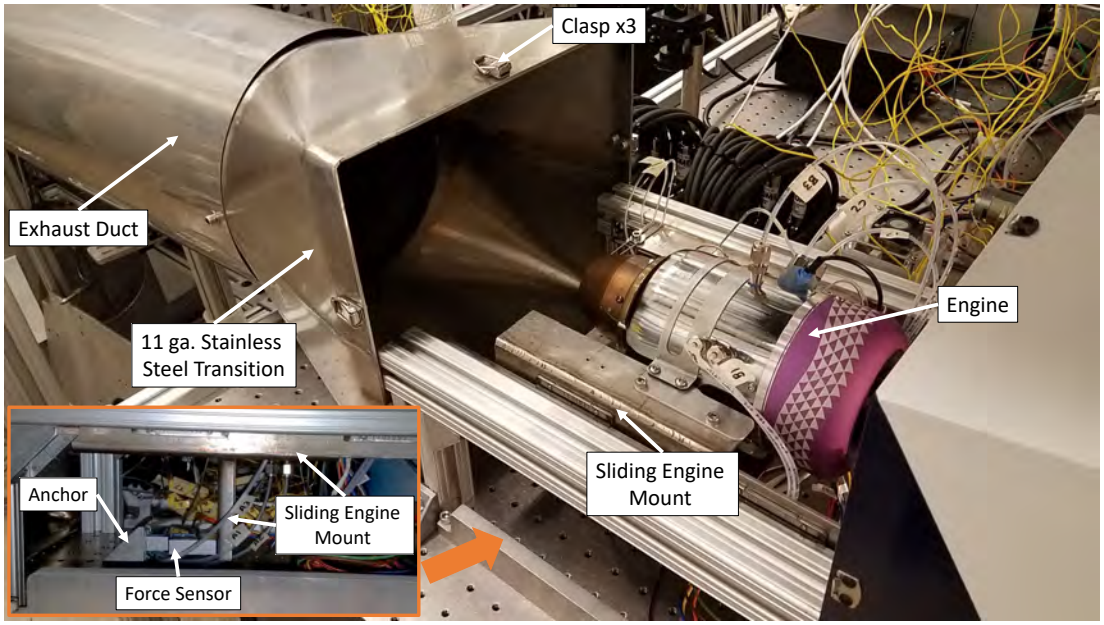


Figure 415. Safety enclosure and test stand opened position

slides. The sliding engine mount was then connected to one end of the Interface Force Sensor Model SM-50 whose electrical characteristics are discussed in Section D.5. The other end of the sensor was connected to an anchor that was coupled to the

laser table. This arrangement of components allowed the engine to pull on the sliding engine mount with the output thrust measured by the force sensor. The calibration of the force sensor is discussed in Section D.5 with the linear calibration curve specified as $T = 1.7507E + 1.3788$ with an R^2 value of 0.997. In this equation T is the thrust force in pounds, E is the voltage output from the sensor in mV, the units of the voltage coefficient is pounds/mV, and the units of the added constant is pounds. The force sensor had a load limit of 50 pounds-force (222 N) and a deflection of 0.08 mm at maximum load. The accuracy was defined by a non-linearity of $\pm 0.03\%$ of full scale value and a hysteresis of $\pm 0.02\%$ of full scale value.

During initial checkout it was discovered that the starter motor required more initial startup current than the motor driver chip (IC2 in Table 68) in the redesigned electronics would provide. The chip had a maximum output of 3.86A and was designed to limit the current output to this level regardless of the load torque on the motor. This current level was sufficient to drive the starter motor during independent component tests, however, when the motor was coupled to the engine spool at startup the current demand was higher than the chip would output. Due to a combination of the way the motor engaged with the engine spool and the way in which the motor driver chip limits the output current, the motor was barely able to rotate after the chip limited the current. The long term solution to this issue would be to replace the current motor driver chip with a driver that could handle the higher startup current demanded when under a load. The short term solution that was utilized to enable testing of this objective within a short time frame was to use an air start.

Figure 416 shows the air start setup that was used. This system used a jet of air that impinged on the compressor blades at an angle and caused the spool to rotate. The electric starter motor remained attached to the engine as the motor housing was integrally molded into the engine inlet nacelle. The air starter nozzle had an ID of

4.1 mm and was positioned 9 mm upstream of the engine cowling. The nozzle was held in place on an optics mount with the jet orientation set at the position where the maximum RPM occurred as determined by the audible response of the engine spin up, and confirmed by the engine RPM electronics. Startup air was supplied from Line 4 of the laboratory air source shown in Figure 133 with the in-line regulator set to 482,633 Pa (70 psi). An in-line solenoid enabled LabView on/off control of the starter air jet. The solenoid control was connected to the "Starter" button in the LabView visual interface shown in Figure 549 in Appendix D in addition to the electric starter motor control. The starter motor 3A fuse was pulled from the redesigned electronics ECM box to ensure the electric motor was not activated at startup. The air start system was capable of turning the engine spool at more than 6,000 RPM, well beyond the 3,300 RPM needed prior to ignition.

It was also discovered that the operation of the lubricant pump interfered with the RPM signal processing due to these systems sharing a common ground in the

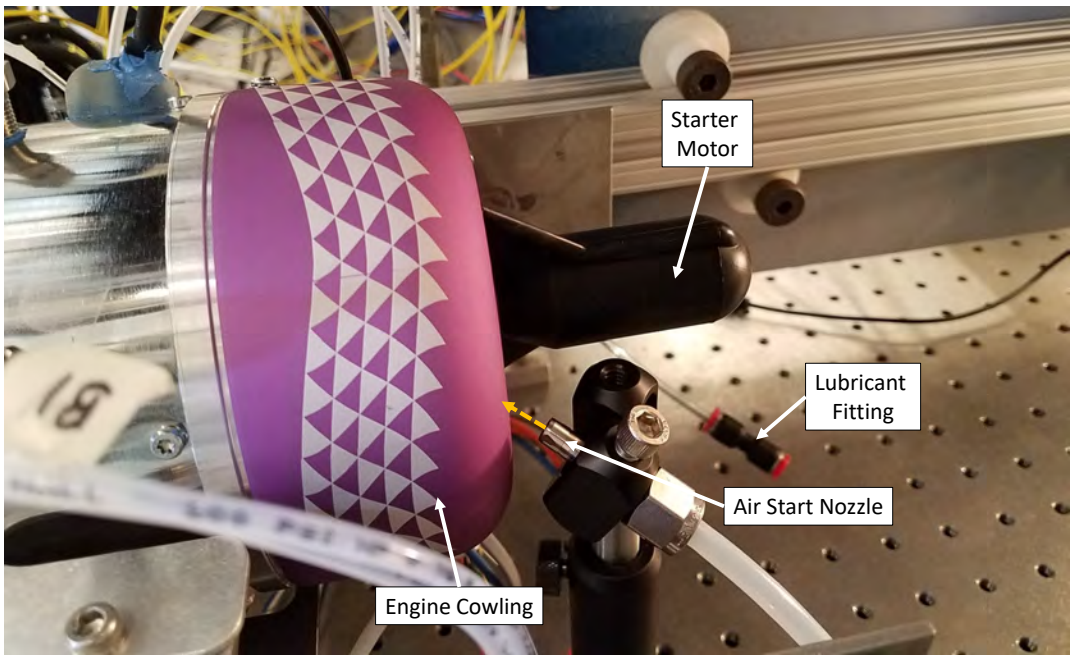


Figure 416. Orientation of the air start nozzle to the JetCat engine cowling

redesigned electronics. The RPM signals were very weak and were easily over powered by the pump pulse width modulation command signal. When the pump was activated the RPM gauge read approximately 4,500 RPM which is the first harmonic of the pump's pulse frequency. The ability to turn the lubrication pump on and off by specifying the propane flow rate that was required to be reached to begin automatic pump operation and flow control was added to the LabView visual interface. This option gave the operator the ability to stop the pump to verify engine RPM as needed.

Figure 417 shows the temperature and pressure instrumentation locations in the JetCat. This instrumentation plan builds on the Objective 4 instrumentation shown in Figure 381 to include sensors in the nozzle. All temperature measurements were made with K-Type thermocouples. The Station 2 through 4 thermocouples were 0.51 mm diameter probes with Stations 5 and 7 using 1.6 mm temperature probes to withstand higher velocity air through these stations. All pressure taps were made from 1.6 mm OD stainless steel tubing. The details of each of the temperature and pressure measurements are shown in Table 54. The Station 2 instrumentation was installed through the plastic inlet nacelle just upstream of the interface to the aluminum compressor shroud. Holes were drilled into the engine nozzle just downstream of the turbine rotor and just upstream of the nozzle exit to add Station 5 and 7 instrumentation. Two total pressure probes were mounted to the sliding engine mount and bent into the nozzle to take measurements at the 50% radius and engine centerline. The visible probes in Stations 2, 5, and 7 are shown in Figure 418.

The internal engine camera was maintained from Objective 4 testing as shown in the left side of Figure 419 to provide a view of the engine air inlets leading into the combustor. Visibility was limited due to the short distance between the camera lens and the hardware. However, this view would show any situation where flames were occurring in the inlets or outside of the combustion chamber. Due to the safety

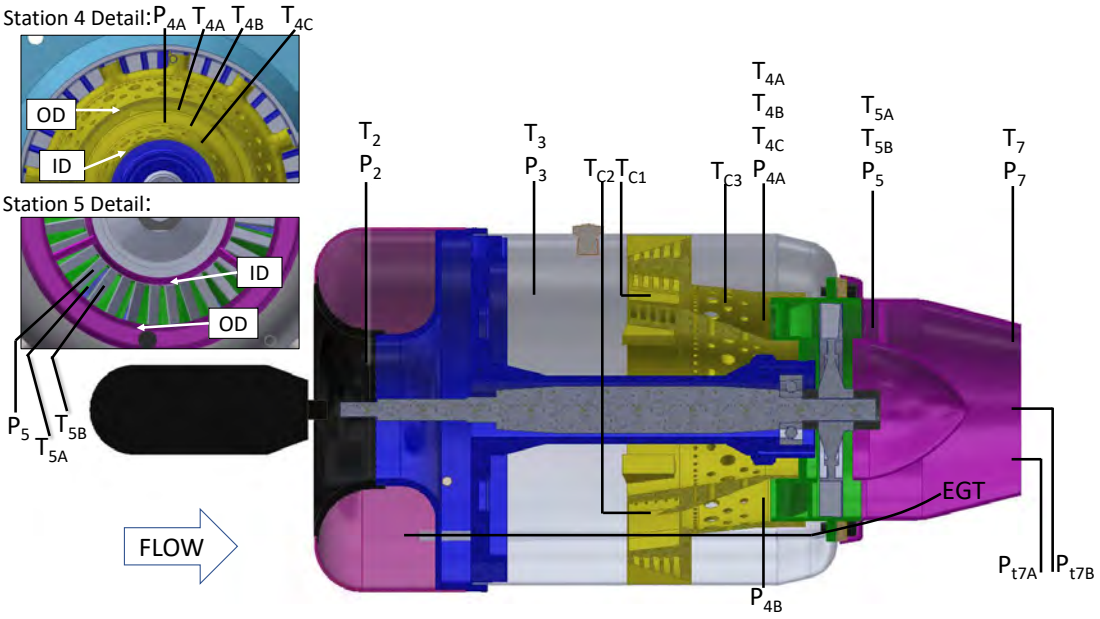


Figure 417. Objective 5 temperature and pressure instrumentation locations

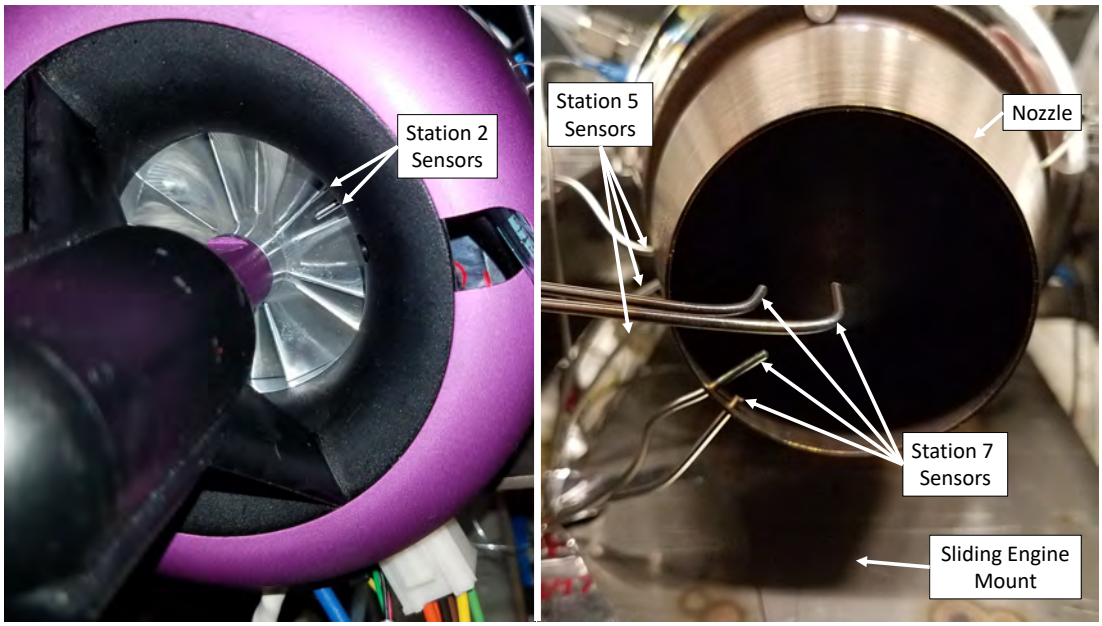


Figure 418. Stations 2, 5, and 7 visible temperature and pressure instrumentation

enclosure the normal COAL lab closed circuit television monitor cameras would not provide a useful view of the engine during testing. A small camera was added to the inside upstream wall of the sliding enclosure as shown in the right side of Figure 419

Table 54. JetCat with combustor Configuration 7 instrumentation details

Engine Location	Designation	Depth	Port	Accuracy
Compressor Inlet	P_2	25% span	Transducer 1	±0.08% FS
	T_2	25% span	TC Panel, 2	±0.4% FS
Compressor Exit	P_3	1 cm from OD	Transducer 2	±0.08% FS
	T_3	1 cm from OD	TC Panel, 3	±0.4% FS
Combustor	T_{C1}	8.5 mm front wall	TC Panel, 4	±0.4% FS
	T_{C2}	8.5 mm front wall	TC Panel, 5	±0.4% FS
	T_{C3}	8 mm comb. OD	TC Panel, 6	±0.4% FS
Combustor Exit	P_{4A}	50% span	Transducer 3	±0.08% FS
	P_{4B}	50% span	Transducer 4	±0.08% FS
	T_{4A}	4 mm comb. OD	TC Panel, 7	±0.4% FS
	T_{4B}	8 mm comb. OD	TC Panel, 8	±0.4% FS
	T_{4C}	12 mm comb. OD	TC Panel, 9	±0.4% FS
Turbine Exit	P_5	50% span	Transducer 5	±0.08% FS
	T_{5A}	33% nozzle OD	TC Panel, 10	±0.4% FS
	T_{5B}	66% nozzle OD	TC Panel, 11	±0.4% FS
Nozzle Exit	P_7	Nozzle OD	Transducer 6	±0.08% FS
	P_{t7A}	50% radius	Transducer 7	±0.08% FS
	P_{t7B}	Centerline	Transducer 8	±0.08% FS
	T_7	50% radius	TC Panel, 12	±0.4% FS
Exhaust	EGT	OD	TC Panel, 1	N/A

to provide a visual status of the engine during operation.

Since this was the first time a JetCat was operated in the COAL lab without its stock ECM, and an exact startup procedure could not be found because the stock JetCat ECM has automated starting, the engine was operated manually to provide greater flexibility and control. The automated startup sequence programmed into the custom JetCat LabView interface described in Section D.7.3 was created based on the findings of the manual operation. After the startup sequence was learned, the remaining starts used for testing followed the sequence outlined in Section D.7.3.

With propane flow rate being the only input variable, the test matrix was greatly simplified for this test series compared to other tests. After learning an efficient

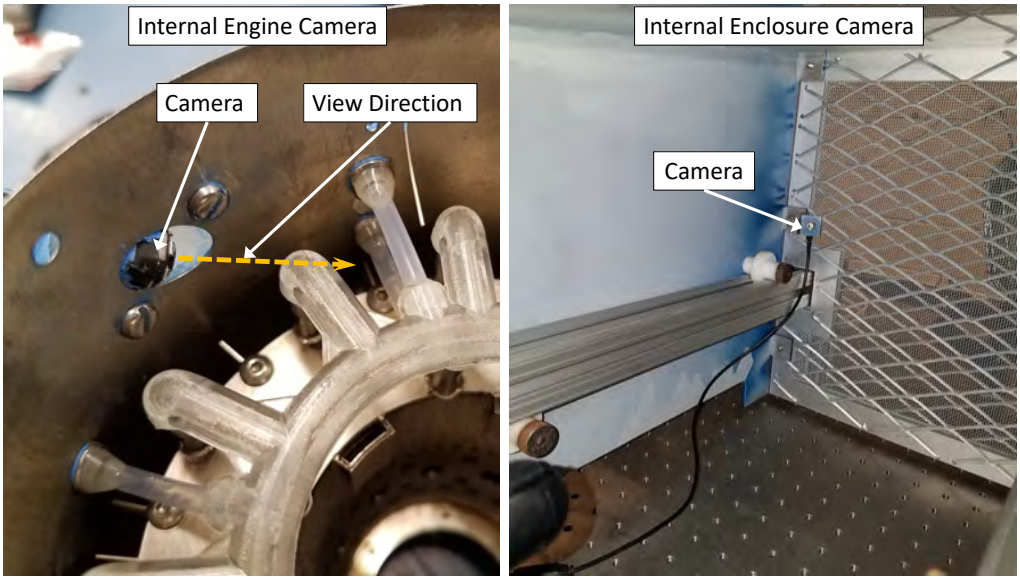


Figure 419. Internal engine camera left, internal safety enclosure camera right

startup sequence the engine was allowed to cool. Starting from a cold engine, data were collected through the entire startup sequence until the maximum fuel flow rate for stable combustion and engine operation was reached. After this ramping test it became evident that the flameout condition was not corrected by the use of rotating turbomachinery. However, to demonstrate the operational stability near the combustion limit, four longer duration operation tests were conducted at 18 SLPM and 19 SLPM of propane as these values still represented the stable limits of combustion. The data collected from all of these tests was processed and compared to the stock JetCat P90RXi performance data.

9.3 Results

The results of the engine operation with rotating turbomachinery presented below were divided into two sections. The first section shows detailed data on the Configuration 7 combustor with rotating hardware, and the second section shows the Configuration 7 combustor with rotating hardware results compared to the stock Jet-

Cat performance data. The hypothesis coming out of Objective 4 testing was that the cause of the combustor flameout at fuel flow rates above 19 SLPM was the result of an improperly placed peak pressure at Station 3. With a low Station 3 pressure there was an insufficient force to overcome the combustor pressure rise due to propane addition which resulted in reduced air flow into the primary zone and the engine flamed out. As shown in Section 9.3.1 the flameout limit and the Station 3 pressure remained relatively unchanged from the Objective 4 testing. After the rotating tests were complete additional testing of the combustor in a non-rotating configuration was conducted to try and definitively determine the cause of the flameout. The results of this follow-up study are shown in Section 9.3.4.

9.3.1 Combustor Analysis With Rotating Hardware.

Figure 420 shows the average temperatures at all engine stations at a quasi-steady state during a ramp test from 0 RPM. As the air starter drove the spool through 3,000 RPM the glow plug was energized. At approximately 6,000 RPM the propane flow rate was increased at a rate of approximately 1 SLPM every 0.5 seconds until ignition occurred between 6 and 7 SLPM. Following ignition the glow plug was turned off and the propane flow rate was ramped at approximately 1 SPLM every 3 seconds to ensure the temperatures and RPMs stabilized at each level before moving to the next value. During normal operation the propane flow rate could be increased at 1 SLPM every second until the desired fuel flow was reached. The delay in fuel addition was required to allow the spool to speed up and provide additional air without overheating the turbine.

As with the stand alone combustor testing with 70% blockage, the maximum propane flow rate was limited to 19 SLPM (5.96×10^{-4} kg/s) to maintain stable combustion. Beyond this value the combustion stability and temperatures were greatly reduced and led to flameout. A fuel flow rate of 19 SLPM resulted in 19,000 RPM

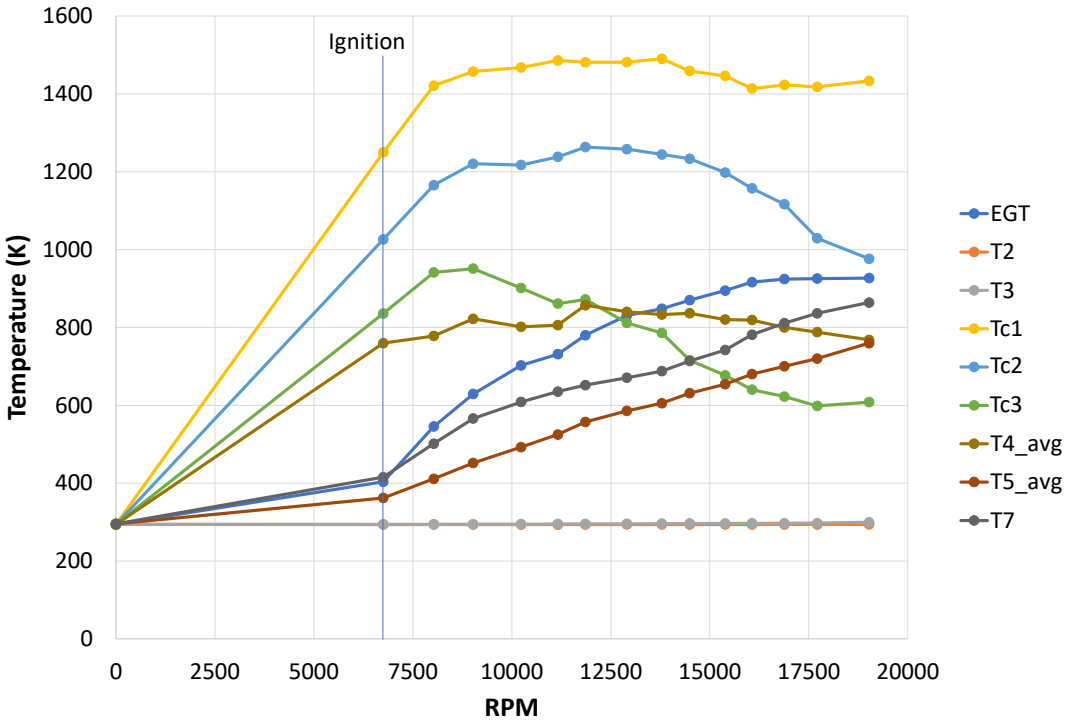


Figure 420. Temperatures at all JetCat stations during a ramping test from engine start to the 1/2 idle condition

which correlated to the 1/2 Idle test condition. Within the operating range the flow rate of propane was related to the engine RPM, where flow rate in SLPM x 1000 = RPM.

Looking at the temperature trends in Figure 420 showed that the primary zone T_{C1} temperature rose rapidly and remained relatively constant from 8,000 RPM - 19,000 RPM with an average value of 1438 K. The primary zone T_{C2} temperature, which measures at the same radial location in the cavity but 180° apart circumferentially, showed a reduced cavity temperature that peaked at 12,000 RPM and decreased for increasing fuel flow rate and RPM. A difference between the T_{C1} and T_{C2} temperature was also noted in the non-rotating stand alone combustor data, but the T_{C2} value was not always the lower temperature. The two thermocouples taking the T_{C1} and T_{C2} readings were 0.51 mm probes inserted through a 0.5 mm wall. It is thought that

the T_{C2} thermocouple did not install straight and was measuring the temperature at an offset location. The temperatures at engine Station 2 and Station 3 remained at 300 K for the duration of the test.

The T_{C3} temperature measurement was located directly behind the largest dilution hole. As RPM, and thus air flow rates, were increased, more air was forced through the dilution hole and the measured temperature decreased. Like the T_{C1} temperature, the average temperature at Station 4 remained relatively constant after ignition with an average value of 809 K. The peak T_{4avg} temperature occurred at 12,000 RPM, consistent with the peak T_{C2} temperature. The EGT, T_{5avg}, and T_7 temperatures increased steadily with increasing fuel flow rate and RPM, reaching maximum values of 926 K, 760 K and 864 K, respectively. The T_{4avg} and T_{5avg} temperatures at the 19,000 RPM 1/2 Idle condition were only 10 K different, however, it is concerning that the EGT and T_7 temperatures were greater than T_{4avg} as this could possibly indicate incomplete combustion in the combustion chamber. The T_{4avg} temperature was a composite of three temperature measurements. Neither the EGT nor the T_7 temperature exceeded the maximum T_4 temperature measurement. This result could mean that the measured EGT and T_7 temperatures were measuring this hotter T_4 value as it migrated from the engine ID to the engine OD from centrifugal acceleration on the exhaust due to the swirl induced by the turbine stators. An additional discussion on the radial temperature distribution is provided later in this section with the longer duration test results.

The pressure at all engine stations during the ramp test from 0 RPM to the operating limit of 19 SLPM of propane is shown in Figure 421. With the rotating turbomachinery the peak pressure occurred at Station 3. Unfortunately, as shown in Table 58, the pressure difference at Station 3 in the current study was not substantially greater than the Station 3 pressure in the non-rotating combustor testing for Objective

4. Based on the stock JetCat performance data shown in Section 9.3.3, the pressure at Station 3 with a rotating compressor follows a parabolic profile and does not show significant increases in pressure until at least 36,000 RPM, the Idle condition.

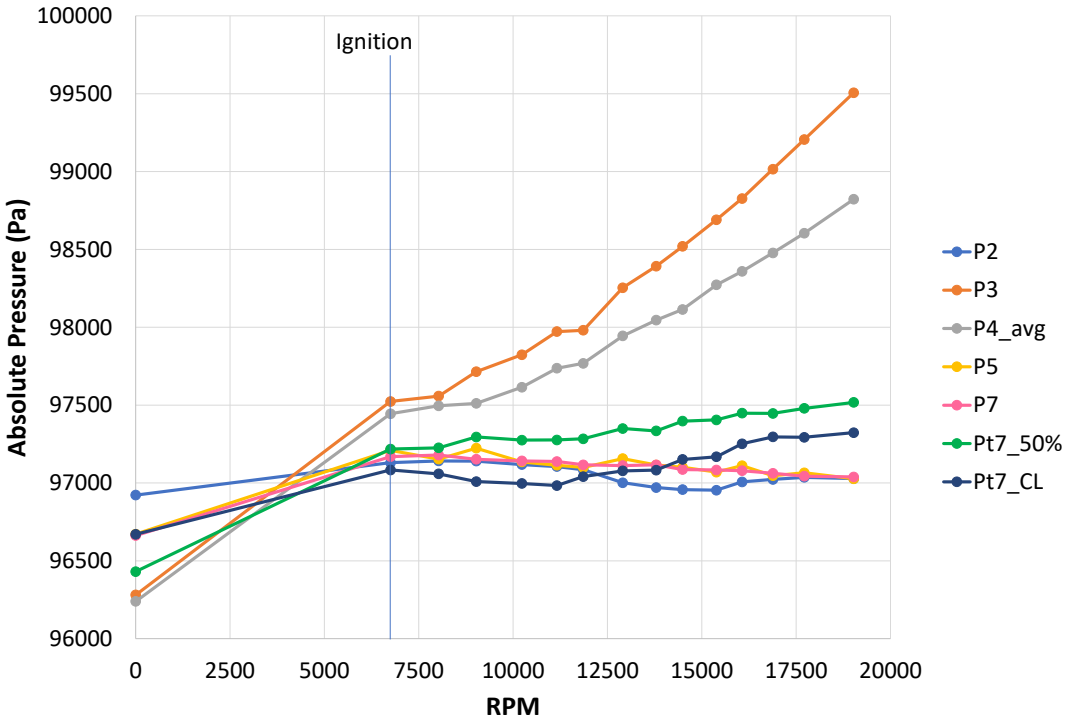


Figure 421. Pressures at all JetCat stations during a ramping test from engine start to the 1/2 idle condition

Table 55. Comparison of pressures from the non-rotating stand along combustor testing from Objective 4 to present rotating testing

Engine Station	Objective 4 Non-rotating	Objective 5 Rotating	Percent Difference
Station 2	100,663 Pa	97,031 Pa	3.6%
Station 3	99,250 Pa	99,441 Pa	0.19%
Station 4	98,801 Pa	98,710 Pa	0.09%

The longer duration tests were conducted at 18 SLPM of propane for three tests and 19 SLPM of propane for one test. An 11 minute test was conducted at 18 SLPM

one day, and three 8 minute runs were conducted the next day. The runs conducted on the same day were separated by a cool down period and the engine was restarted for the next run. These tests demonstrated the stability of the engine operation. Temperature data were taken at 10 Hz and pressure data was taken at 1 Hz providing a large data set to analyze. The average temperatures, pressures, and corresponding standard deviations of these values for the three 18 SLPM longer duration runs were averaged together with the results tabulated in Table 56. The average temperatures, pressures, and corresponding standard deviations of these values for the 19 SLPM run is shown in Table 57. These values are shown separate as there was several times greater variation for the 19 SLPM results than the 18 SLPM results for almost all measured values.

Table 56. Average temperatures and pressures at each engine station with corresponding standard deviations across all three 18 SLPM longer duration tests

Measurement Location	Average Temperature	Avg. Standard Deviation	Average Pressure	Avg. Standard Deviation
Station 2	295 K	0.035 K	97,035 Pa	10.9 Pa
Station 3	301 K	0.03 K	99,473 Pa	59.5 Pa
T_{C1}	1462 K	5.5 K	N/A	N/A
T_{C2}	1087 K	10.1 K	N/A	N/A
T_{C3}	630 K	5.5 K	N/A	N/A
Station 4	768 K	7.7 K	98,702 Pa	57.8 Pa
Station 5	748 K	2.0 K	97,018 Pa	46.2 Pa
Station 7	842 K	2.7 K	97,040 Pa	31.8 Pa
EGT	916.6 K	4.0 K	N/A	N/A

In the composite data for the three 18 SLPM longer duration tests the majority of the temperature standard deviations were less than 5 K. The largest variation in temperature was observed for the T_{C2} temperature in the primary zone with a standard deviation of 10.1 K, 0.9% of the temperature value. The second largest variation was the Station 4 temperature with a 1.0% variation. In both of these cases

Table 57. Average temperatures and pressures at each engine station with corresponding standard deviations for the 19 SLPM longer duration test

Measurement Location	Average Temperature	Standard Deviation	Average Pressure	Standard Deviation
Station 2	295.0 K	0.02 K	97,019 Pa	13.2 Pa
Station 3	299.8 K	0.1 K	99,514 Pa	133.7 Pa
T_{C1}	1382 K	100.5 K	N/A	N/A
T_{C2}	867 K	107.4 K	N/A	N/A
T_{C3}	622 K	19.3 K	N/A	N/A
Station 4	761 K	16.6 K	98,724 Pa	92.9 Pa
Station 5	761 K	4.8 K	97,025 Pa	49.9 Pa
Station 7	859 K	7.2 K	97,044 Pa	28.3 Pa
EGT	928 K	12.7 K	N/A	N/A

the variation with respect to the average temperature was almost negligible. For these test cases the peak pressure variation was 57.8 Pa at Station 4, a 0.06% variation. These results highlight the stability of the combustor operation at this condition.

At 19 SLPM the variations in temperature and pressure was larger. The peak temperature variations occurred in the T_{C1} and T_{C2} measurements with standard deviations of 100.5 K and 107.4 K, respectively. This condition is closer to the flame-out limit of the combustor which is evident by the 1000+% increase in the standard deviation in the primary zone temperature. The largest pressure standard deviation was measured at Station 3 with a variation of 133.7 Pa. This value is more than a 125% increase over the 18 SLPM standard deviation. System pressure and temperature are linked, so it is not surprising that the test case with the greater temperature oscillation also yielded a proportionately large pressure variation.

The combustor exit temperatures and turbine exit temperatures were measured by three thermocouples at Station 4 and two thermocouples at Station 5 as shown in the inset in Figure 417. At Station 4, position A was at 25% passage span nearest the OD, position B was at 50% span, and position C was at 75% span nearest the

ID. At Station 5, position A was at 33% span nearest the OD and position B was at 66% span nearest the ID. Since there was both a circumferential and radial position change for each of the thermocouples in the set at each station, they do not measure a pure circumferential or radial variation. Figure 366a from Section 8.3.6 shows the computational exit temperatures at the 1/2 Idle condition. In this figure it can be seen that while the majority of the temperature is uniform, there are several cooler pockets and one periodic hot streak. It would thus be possible for each of the thermocouples in the experimental hardware to be measuring in a hot, cold, and average temperature zone making the data difficult to interpret. More thermocouples would be desirable to build a more complete temperature map, however, given the small scale of the engine additional thermocouples would begin blocking the engine passages.

At Station 4 the average temperatures at positions A, B, and C were $T_{4A} = 694.2$ K, $T_{4B} = 680.9$ K, and $T_{4C} = 924.5$ K. This result indicates that the ID temperature was greatest entering the turbine stators. At Station 5 the average temperatures were measured as $T_{5A} = 698.1$ K and $T_{5B} = 804.3$ K. The average temperature across all three positions at Station 4 was 766 K with the average of the two positions at Station 5 measuring 751 K. This result indicates a slight temperature loss across the turbine stage which included the addition of a small amount of bypassed compressor air that was used to move the lubricant through the engine centerbody. The 100 degree variation between the two Station 5 measurements compared to the 244 K difference between the 50% and 75% span measurements at Station 4 could be due to an outward radial migration of the ID gases. Due to centrifugal loading on the gases as a result of the small engine radius and high turning provided by the stators, the highest temperatures could have migrated radially outward to create the smaller temperature variation at Station 5. Despite the 100 degree difference, this temperature distribution is still better than all previous UCC exit temperature profiles.

For comparison, the turbine inlet temperatures for the non-rotating combustor tests produced average values of T_{4A} =821.0 K, T_{4B} = 1082.7 K, and T_{4C} = 1142.9 K. These temperatures were greater than those from the rotating engine study, and contained a slightly different distribution for positions A and B but maintained position C as the hottest. As shown in Figures 403 - 405 a distribution with the Station 4 ID temperature measuring the hottest yielded a desirable distribution downstream of the turbine stators.

The cause of the decrease in turbine inlet temperatures in the rotating study is explained with the help of Figure 422. In the non-rotating study the fuel and air were controlled separately meaning that the desired global equivalence ratio could be achieved. With rotating components only the fuel flow rate could be controlled with the amount of air introduced to the engine dictated by the compressor output. Based on calculations of the air flow rate through the engine, the mass flow rate of air was larger than expected for the given fuel flow rate which resulted in a lower global equivalence ratio than in the non-rotating tests.

All of the data reported in this section was taken with the air starter turned on. The air starter was required to remain on to maintain operation. If the air starter was turned off the engine spool would rapidly decelerate and come to a stop. After stopping it would then windmill due to the exhaust air blowing past the compressor and turbine. At the time of the test it was thought that the air starter needed to remain on because the engine had not yet reached a condition where the turbine could extract enough energy from the flow to drive the compressor. Thus the air starter assisted in driving the compressor to overcome the shortfall from the power the turbine could provide. When the air starter was turned off it was hypothesized that the drag on the compressor due to forcing air into the engine caused the rapid deceleration of the spool. The use of the air starter assisted the combustor in driving

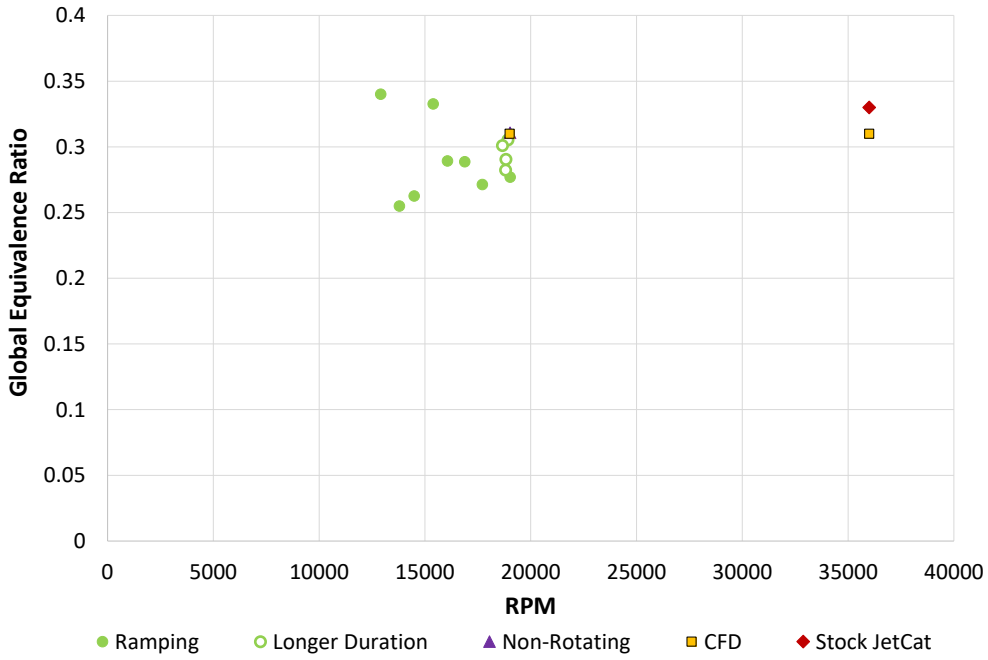


Figure 422. Calculated global equivalence ratio with the Configuration 7 combustor during all rotating tests. Non-rotating, CFD, and stock JetCat global equivalence ratios are also shown for comparison

the turbine and resulted in a higher RPM, and thus air flow rate, than what would otherwise be possible for the given fuel flow rate. This behavior explains the higher mass flow rate and lower global equivalence ratio.

It was discovered during the disassembly of the engine that there was 0.13 mm of play in the bearings holding the engine spool. The normal seated position of the spool was free spinning. However, when the engine was rotating and generating thrust, the spool was pushed forward which caused the compressor rotor to contact the compressor shroud in one location. The contact marks are visible on the rotor tips as shown in Figure 423. When the air starter was on, the force of the air jet pushed the spool backward enough to prevent rotor contact. When the air jet was turned off, the spool was free to move forward 0.13 mm to make contact with the compressor shroud and resulted in the rapid deceleration of the spool.

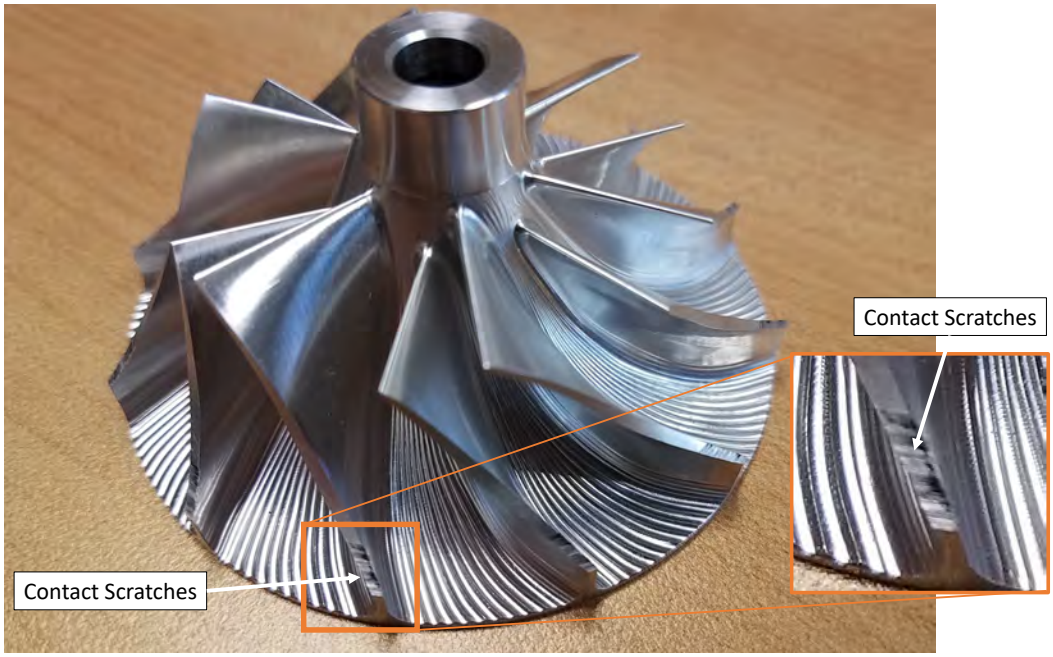


Figure 423. Contact marks visible on the compressor rotor tips

The average pressure losses across the combustor from the longer duration tests are shown in Table 58, with the losses computed by CFD and measured in the non-rotating tests included for comparison. In the second row of data the losses across the combustor and turbine included only the stator for the CFD and non-rotating analysis, and the stator and rotor combination in the rotating analysis. The pressure losses across the combustor alone in the rotating analysis were only 0.09% different than the computational result. The losses across the combustor and turbine were larger than computationally predicted because the computational model only had 12 stator vanes to make them evenly divisible for periodic analysis and did not model the rotor. The hardware in both experimental tests included 15 stator vanes, and in the case of the rotating analysis it included the rotor, which produced additional flow blockage and thus a greater loss across the components. While the results from all three measurement sources were comparable, the measurements in the rotating analysis were closer to the computational predictions than the non-rotating test data.

Table 58. Static pressure losses (%) across the combustor and combustor including present turbine components from CFD, non-rotating combustor testing, and rotating longer durations tests

Losses Across	1/2 Idle CFD	Objective 4 Non-rotating	Objective 5 Rotating
Combustor	0.85%	0.60%	0.76%
Combustor w/ Turbine	2.04%	2.82%	2.48%

Figure 424 shows the thrust output of the engine at incremental RPMs. While the output was small, the engine produced thrust proportionately to the RPM and air mass flow rate shown in Figure 425. The mass flow rate was a calculated value based on temperature and pressure measurements in the engine. As shown in Section 9.3.3 these values match well to the stock JetCat performance trends at the same RPM.

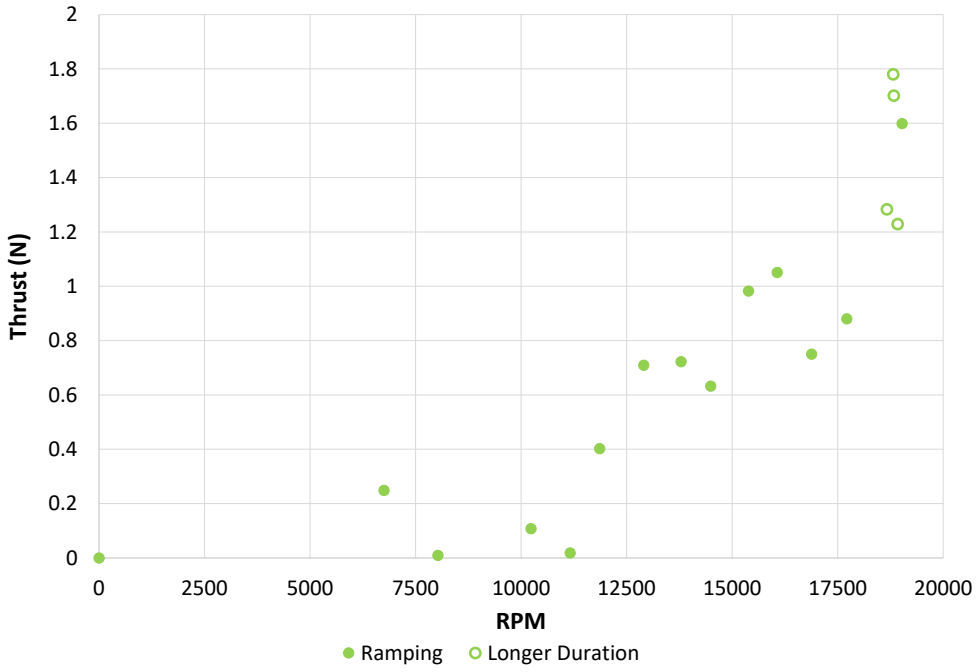


Figure 424. Engine thrust with the Configuration 7 combustor during all rotating tests

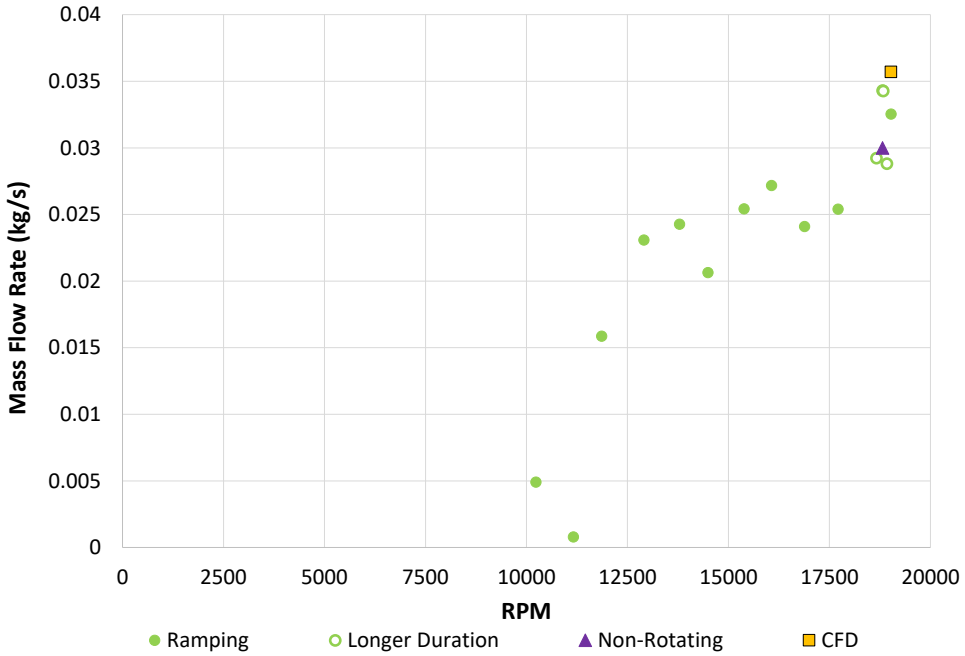


Figure 425. Calculated engine mass flow rate with the Configuration 7 combustor during all rotating tests. Non-rotating and CFD mass flow rates are also shown for comparison

Figure 426 is a qualitative picture of combustion at an engine operating speed of 19,000 RPM with 19 SLPM of propane. The view was taken up the engine nozzle and enabled by a small mirror positioned just outside of the exhaust jet inside the test stand transition and held in place on optics mounts. A cell phone was positioned with optics mounts above the engine inside the safety enclosure with a view of the mirror. The phone was configured to be triggered for video and photos with a bluetooth remote shutter. This setup enabled the safety enclosure to be in place during engine operation while supporting photo and video capture. The image shows uniform combustion around the engine centerbody. The dark spot labeled "Tail Cone Hardware" inside the engine nozzle is one of three screws that held the centerbody tail cone in place and is not a dead spot in combustion. Additionally, the temperatures exiting the turbine were high enough to cause the tail cone to glow red hot.

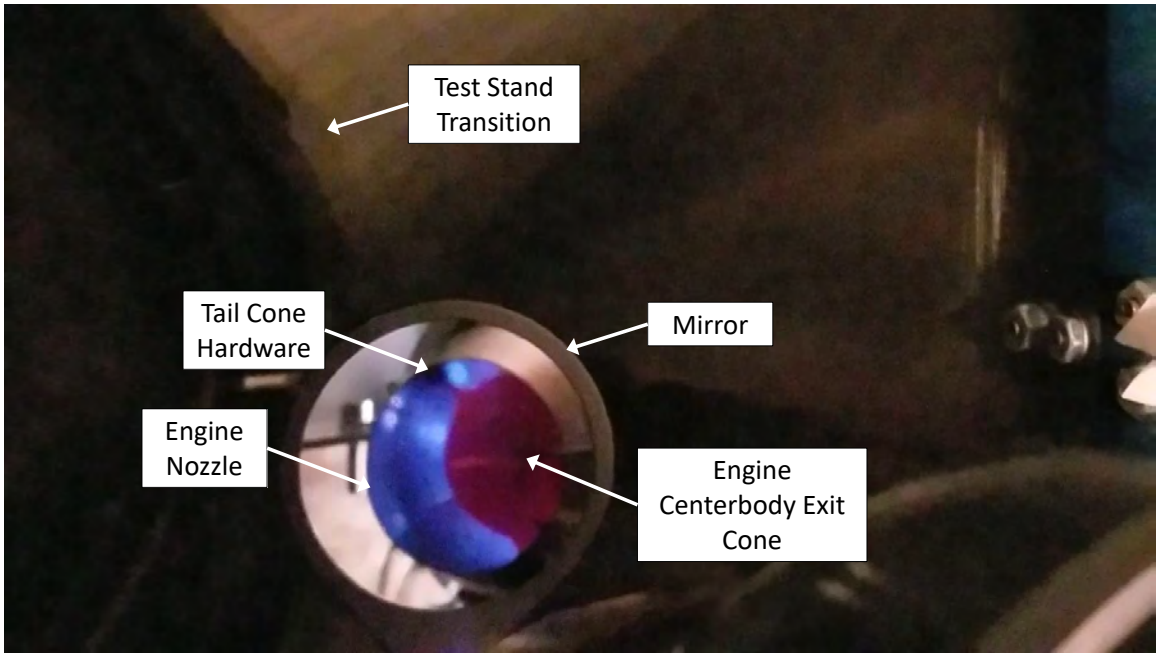


Figure 426. A reflected view up the engine nozzle during operation at 19 SLPM of propane, 19,000 RPM

9.3.2 Self-Sustaining Engine Operation.

To enable another attempt at self-sustaining operation the engine was reassembled and then rebalanced by The Balancing Company to the same 7.2 x 10^{-4} g-cm (1.0 x 10^{-5} oz-in) or less specification as the first balancing. The balanced engine was reinstalled in the test stand shown in Figures 414 and 415 and tested. The starter air pressure was reduced to approximately 124,100 Pa (18 psi) to reduce the assistance to the engine. This starter air flow rate produced approximately 2,000 RPM. Ignition was reduced to approximately 5 SLPM of propane due to the lower air flow rate through the engine resulting from the reduced spool speed. After ignition the fuel flow rate was incremented by 1 SLPM with the engine allowed to stabilize at the new condition before the fuel flow rate was increased again.

During this test series, with significantly less assistance from the starter, the stable operating limit was reduced to 14 SLPM of propane. A change in the air distribution

inside the engine must have occurred to drive this change. Even though the engine was provided minimal assistance by the starter, if the starter air solenoid was abruptly closed during operation the engine could not compensate properly and the spool decelerated, ultimately resulting in flameout. Therefore, when the engine reached operation at 14 SLPM of propane with the air starter on (approximately 14,600 RPM) the starter air pressure was slowly reduced to allow the engine to adjust to the decreased assistance. By slowly reducing the starter air down to 0 Pa before closing the solenoid, self-sustaining operation was achieved at 14 SLPM of propane and a slightly reduced spool speed of approximately 14,100 RPM. Figure 427 shows the temperatures and RPM of the engine during 19 seconds of self-sustaining operation. During this 19 second run the fuel flow rate was varied from 14 SLPM, up to 14.1 SLPM, and down to 13.9 SLPM to observe the sensitivity to small changes in fuel flow rate. The test ended abruptly at 19 seconds when the intended fuel flow rate of 14 SLPM was incorrectly entered as 143 SLPM of propane. This error resulted in a large flame out of the nozzle and flames were forced through the engine centerbody causing damage to the bearings. The damaged bearings prevented additional self-sustaining test runs from occurring.

As shown in Figure 427 there were only minor fluctuations in temperature at all positions upstream and downstream of the primary combustion zone. Temperature T_{c1} had more variability as it responded to changes in the fuel flow rate. Despite this variation, the turbine inlet temperature (T_{4avg}) remained relatively unchanged with an average value of 1,119 K. Additionally, the engine spool maintained smooth operation at an average value of 14,100 RPM with a standard deviation of 23 RPM. This test series demonstrated the first self-sustained operation of an engine utilizing a UCC.

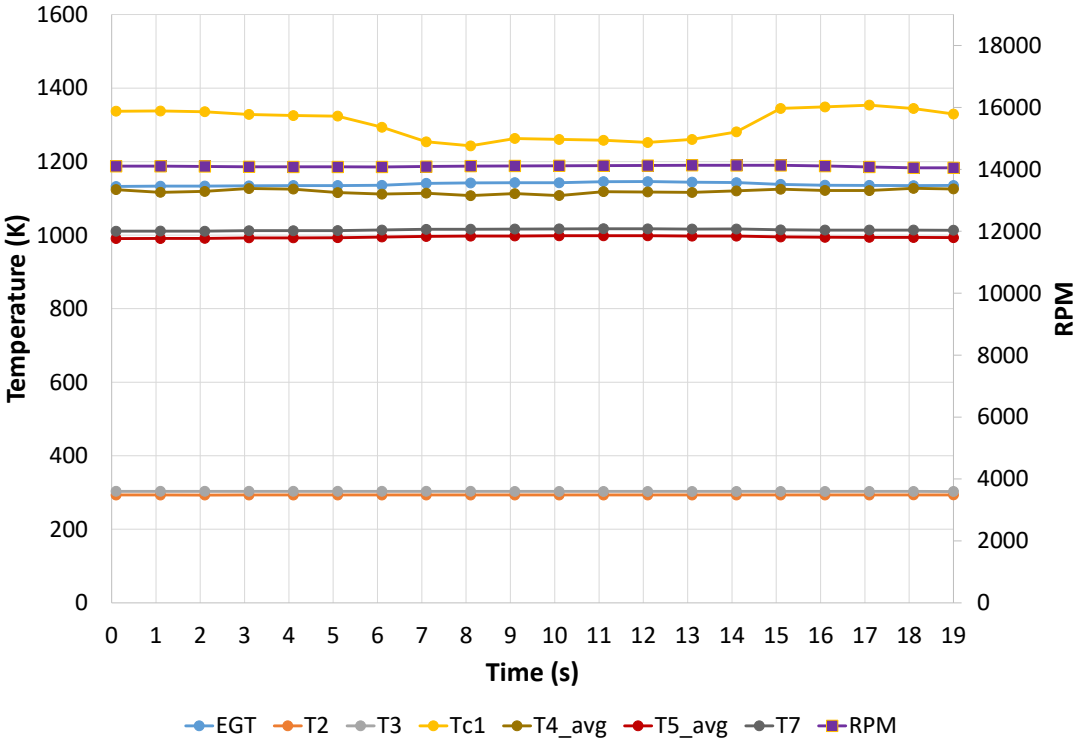


Figure 427. Time-dependent temperature and RPM data during self-sustaining operation at 14 SLPM of propane, 14,100 RPM

9.3.3 Comparison to Stock JetCat P90RXi Performance.

The performance of the JetCat outfitted with the Configuration 7 combustor was compared to the stock JetCat P90RXi performance. The stock data was obtained from Mr. Jacob Wilson who had previously collected the data for a different test series. Each of the performance plots covered the full JetCat operating range even though the Configuration 7 combustor was only able to perform up to a fraction of that range. By plotting the full data range trend lines of the stock engine performance were able to be plotted to observe where the Configuration 7 combustor fell relative to the stock operating lines. In each of the plots the stock JetCat data is plotted as a red diamond, the JetCat with the Configuration 7 combustor and rotating hardware with the air starter assist was plotted with green circles, the JetCat at self-sustaining

operation with the Configuration 7 combustor was plotted with green squares, and where applicable CFD data and the Configuration 7 combustor with non-rotating hardware from Objective 4 was plotted with dark yellow squares with a black outline and purple triangles, respectively.

In Figure 428 the compressor and turbine pressure ratios are plotted based on Equations 91 and 98. However, since total pressure measurements were not able to be obtained, the total measurements were replaced by static pressure measurements. Both the compressor and turbine pressure ratios follow a third order relationship with respect to engine speed. As such the pressure gains at lower speeds are negligible. At half idle, 18,000-19,000 RPM, the Configuration 7 combustor with starter assistance produced an average compressor pressure ratio of 1.02 with an average turbine pressure ratio of 0.98. The self-sustaining Configuration 7 test points at 14,100 RPM produced an average compressor pressure ratio of 1.015 and an average turbine pres-

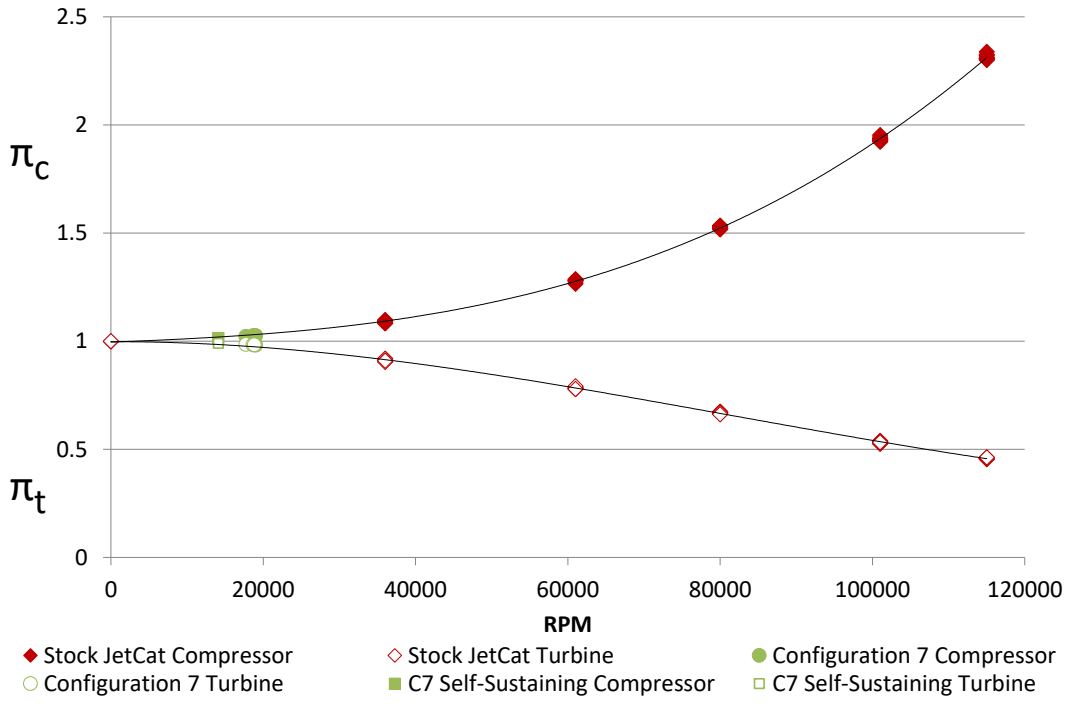


Figure 428. Compressor and turbine pressure ratios from a stock JetCat P90RXi and the Configuration 7 combustor with rotating hardware

sure ratio of 0.99. Both sets of these values fell on the stock engine operating line meaning the Configuration 7 combustor was capable of driving the turbine at a rate proportionate to the stock burner.

In Figure 429 the compressor and turbine temperature ratios are plotted based on Equations 89 and 97. Again, total measurements were not made as the flow was likely not stagnating on the exposed thermocouple beads. As such these relationships show the static temperature ratios. The compressor temperature ratio followed a second order relationship with respect to engine speed. For the stock JetCat turbine data the best fit was still a second order relationship with respect to speed, however, the stock turbine data at 36,000 RPM does not follow the trend of the other turbine data and skewed the trendline down. An additional trendline was added that showed the second order curve fit without the 36,000 RPM data point. This trendline fits the remaining data better and is more in line with the starter assisted Configuration 7 data. Second order relationships for both of these temperature ratios was consistent with the governing equations.

The average starter assisted Configuration 7 compressor temperature ratio was 1.02 and the average starter assisted Configuration 7 turbine temperature ratio was 0.96. The self-sustaining Configuration 7 test points at 14,100 RPM produced an average compressor temperature ratio of 1.03 and an average turbine temperature ratio of 0.82. The starter assisted Configuration 7 compressor temperature data fell on the trendline of the stock compressor data, but the self-sustaining Configuration 7 data point showed an elevated ratio. This ratio increase was due to a 5 K rise in the T_3 temperature during self-sustaining operation that was likely not the result of increased heating due to compression. The starter assisted Configuration 7 turbine temperature data sat above the trendline of the stock turbine data due to the skew caused by the 36,000 RPM data. With the 36,000 RPM stock data point omitted,

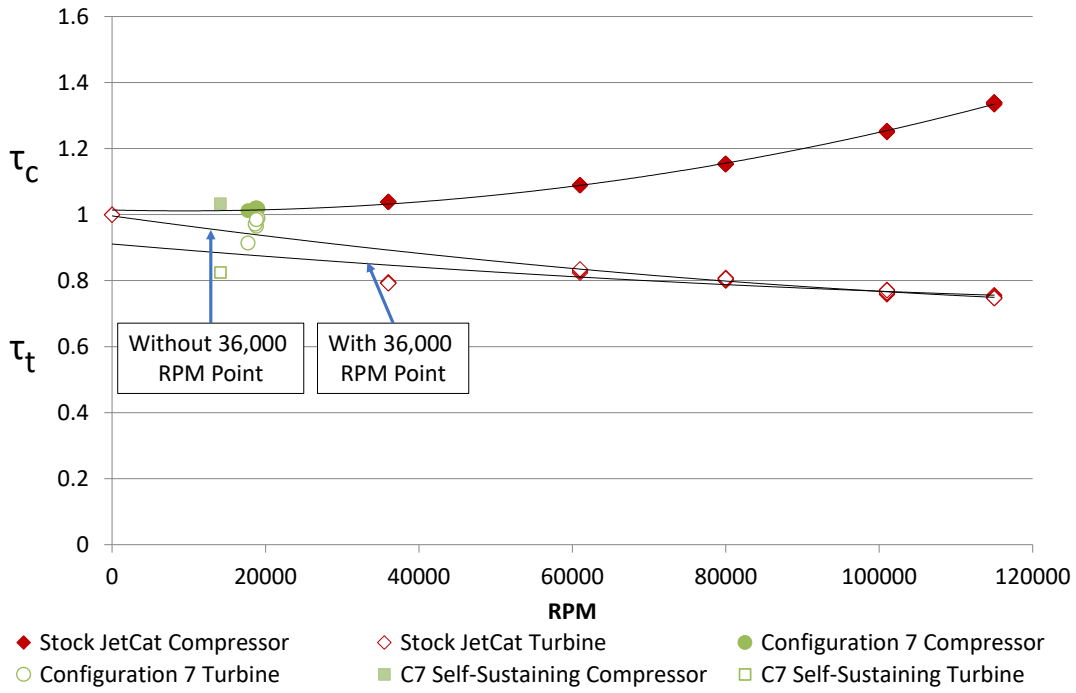


Figure 429. Compressor and turbine temperature ratios from a stock JetCat P90RXi and the Configuration 7 combustor with rotating hardware

the starter assisted Configuration 7 data fell in line with the remaining stock JetCat turbine data. The self-sustaining Configuration 7 turbine temperature ratio fell below both stock turbine trendlines.

Figure 430 shows the relationship of thrust to engine speed which is represented by a fourth order black curve through the data. There is not a straight forward correlation of speed to thrust since it is a function of the engine geometry, mass flow rate, velocities, pressure, and temperature. However, this trendline is consistent with the trends of the governing equations given in Section 2.1. Due to the spread, the data were bounded by blue upper and lower lines. The thrust data from both types of Configuration 7 engines fell below the trendline, however, the data still fell within the bounded range. Figure 431 shows thrust specific fuel consumption in units of $N/(kg/min)$. The data follow a third order relationship with respect to engine speed. In this plot the starter assisted Configuration 7 data span the stock

trendline showing equal fuel consumption for the generated thrust between the stock and starter assisted Configuration 7 combustors. The self-sustaining Configuration 7 combustor data point fell above the stock trendline indicating a higher thrust output for the same fuel consumption, indicating a potential performance improvement by the UCC.

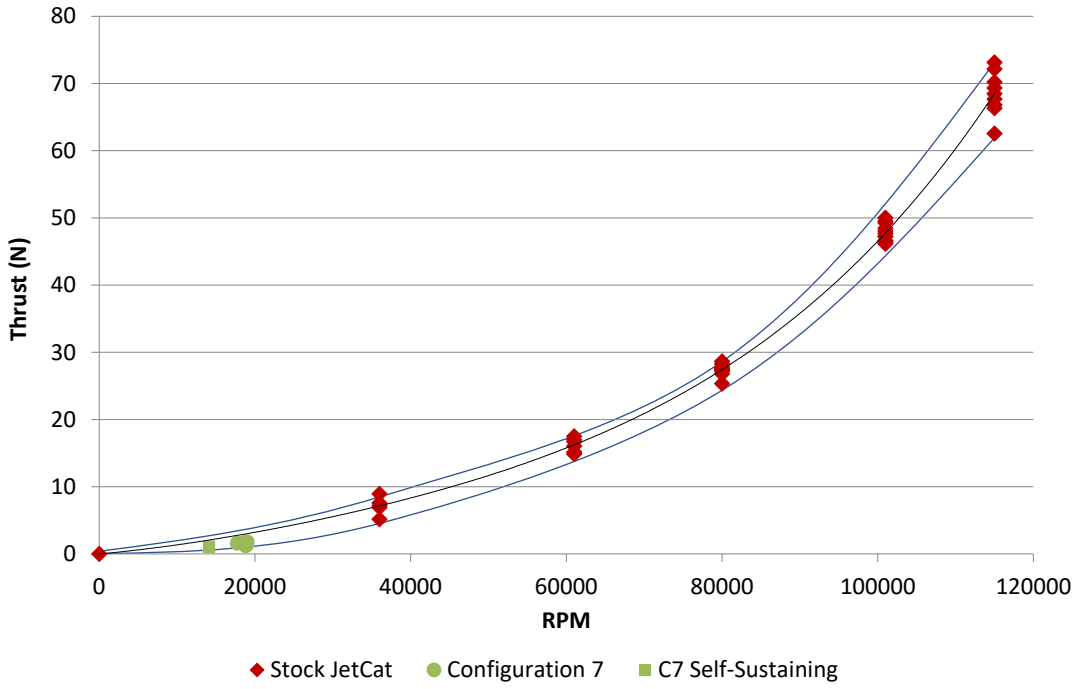


Figure 430. Thrust from a stock JetCat P90RXi and the Configuration 7 combustor with rotating hardware

The engine air mass flow rate was calculated using the relationships in Equations 93 and 95 with the values of the two methods compared and averaged. The result from both methods was within 10% of each other. The resulting air mass flow rates are shown in Figure 432 with a linear trendline displayed through the stock JetCat data. The mass flow rate from the CFD cases and non-rotating combustor Configuration 7 tests are plotted as well for comparison. At the 1/2 Idle condition all of the Configuration 7 related points fell below the stock data trendline. However, since the 1/2 Idle condition was a derived quantity and not available from stock data directly,

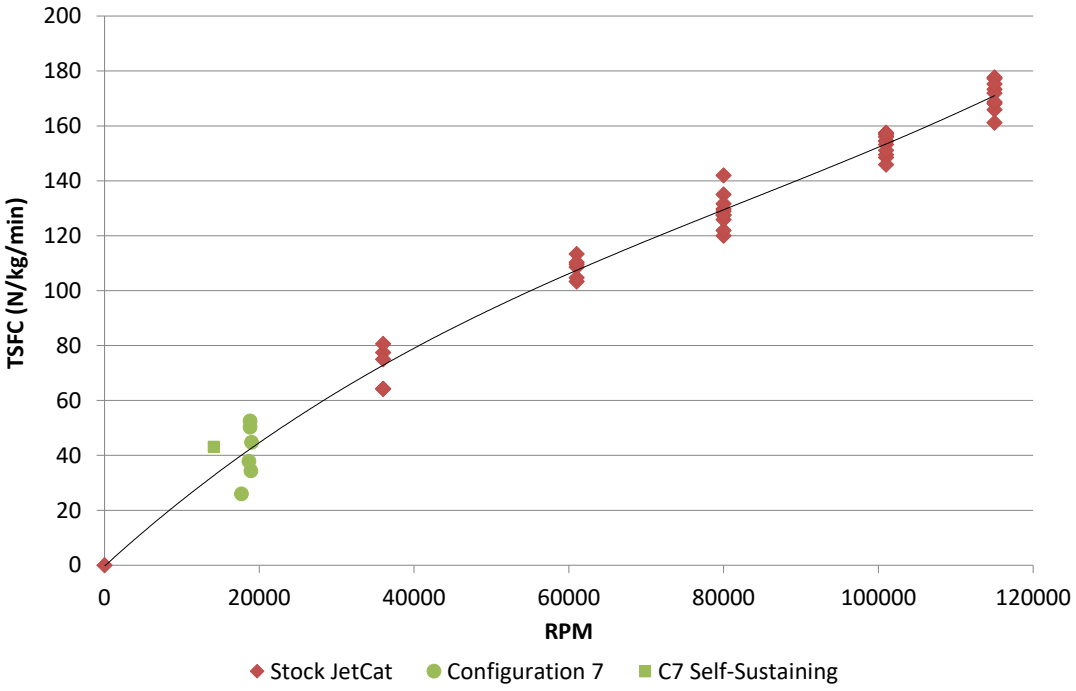


Figure 431. Thrust specific fuel consumption from a stock JetCat P90RXi and the Configuration 7 combustor with rotating hardware

the non-self-sustaining points are all consistent with a value at half of the average stock mass flow rate at idle. The self-sustaining Configuration 7 data point follows the trend of the other Configuration 7 results. The non-rotating test data are shown at approximate equivalent engine speeds.

The compressor efficiency is given in Figure 433 as defined by Equation 96 and plotted as a function of engine speed. As shown in Equation 96 the compressor efficiency is a function of the compressor pressure and temperature ratios and the ratio of specific heats for air. The burner properties do not come into play. The starter assisted Configuration 7 data straddled the third order stock data trendline as expected. However, the self-sustaining Configuration 7 data point fell well below the stock trendline due to the previously mentioned 5 K rise in T_3.

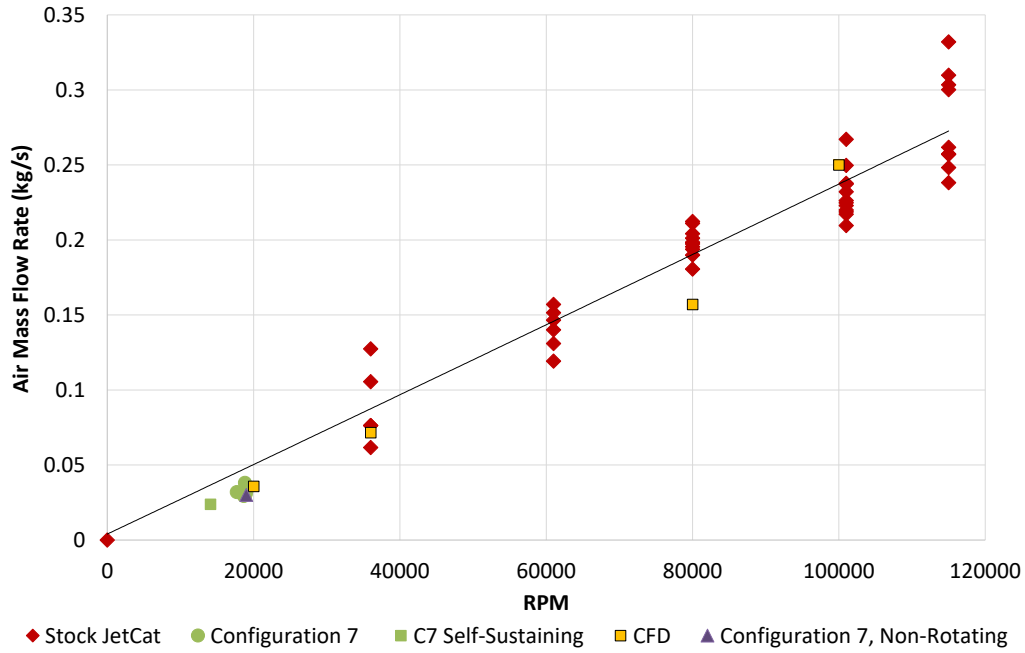


Figure 432. Air mass flow rate through a stock JetCat P90RXi and the Configuration 7 combustor with rotating hardware

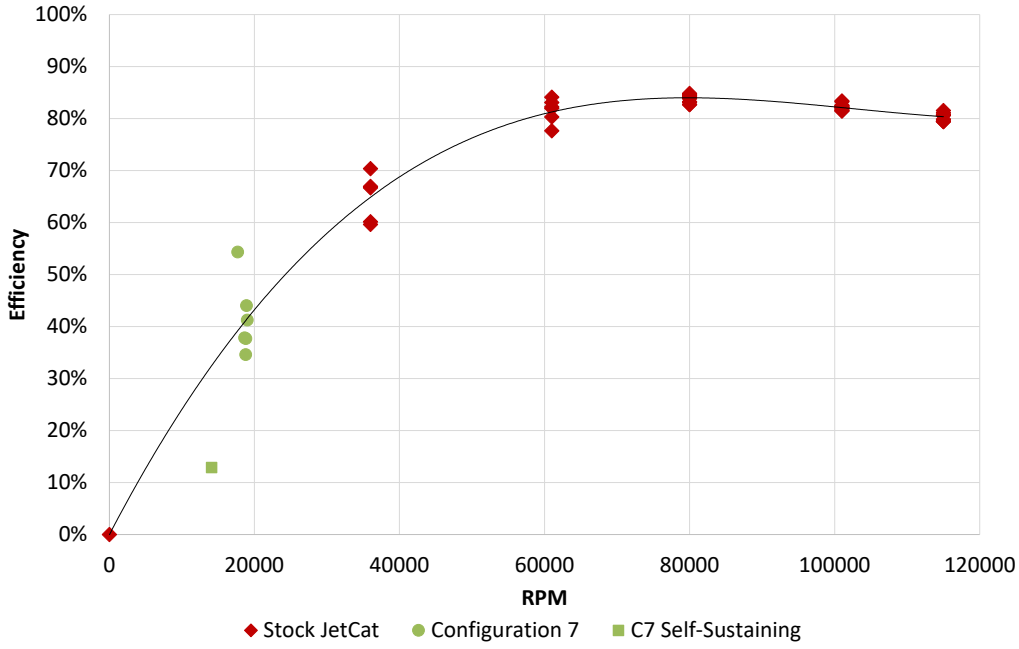


Figure 433. Compressor efficiency in a stock JetCat P90RXi and the Configuration 7 combustor with rotating hardware

Figure 434 shows the global equivalence ratio of the stock JetCat along with the Configuration 7 combustor with and without rotating hardware, and the computational results at corresponding conditions. The non-rotating test data are shown at approximate equivalent engine speeds. All Configuration 7 related tests used controlled fuel flow rates, with the non-rotating and computational tests also using controlled or specified air flow rates. Only the rotating tests relied on calculated air mass flow rate values. The stock JetCat global equivalence ratio values were based on calculated air mass flow rates as well as calculated fuel flow rates, following Equation 99, since it used kerosene and the uncalibrated stock fuel pump. As such there was more uncertainty in the stock JetCat values. The computational values were specified initially by JetCat fuel and air flow rates at full throttle and idle from manufacturer specifications before the experimental data from Wilson was provided.

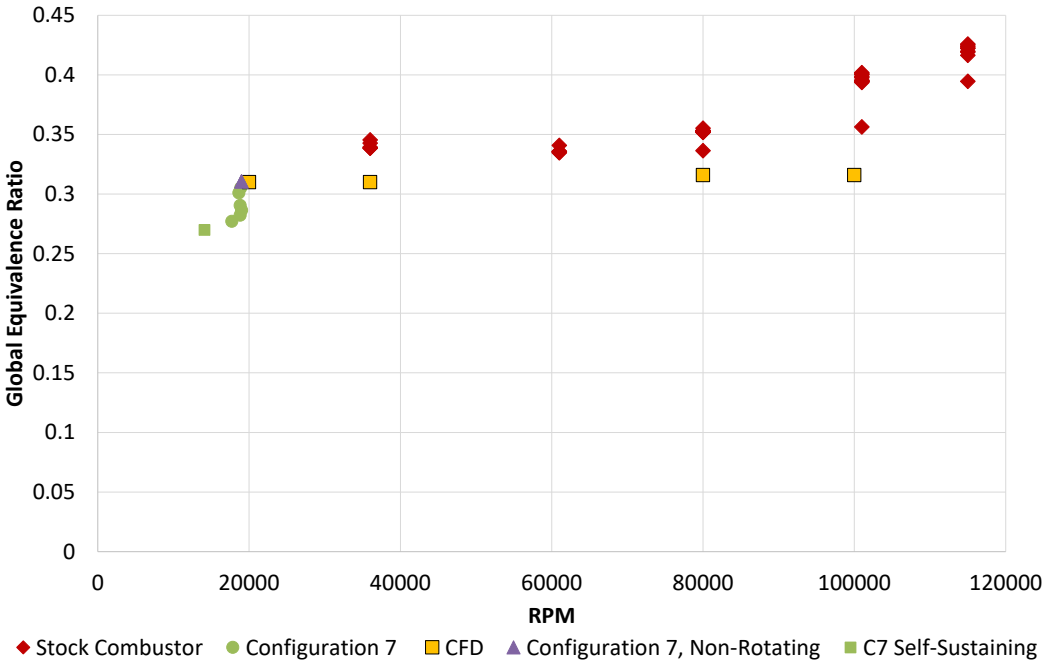


Figure 434. Global equivalence ratio in a stock JetCat P90RXi and the Configuration 7 combustor with rotating hardware

The trends in the computational global equivalence ratio data show a linear pattern that only varied from 0.310 to 0.316 over the operating range. The non-rotating

combustor Configuration 7 test matched the computational result at 1/2 Idle, however, both types of Configuration 7 rotating data produced a lower global equivalence ratio with an average value of 0.29 for the starter assisted cases and 0.27 for the averaged self-sustaining data point at 14,100 RPM. At idle the stock JetCat global equivalence ratio was higher than expected at an average of 0.34, with an increasing ratio that followed a parabolic relationship to peak at an average of 0.42. At Idle the stock JetCat burned 0.019 kg/min more fuel than the performance literature listed. At 100,000 RPM it burned 0.04 kg/min less than expected, but flowed 0.042 kg/s less air than expected resulting in a higher global equivalence ratio. The CFD test points represented the expected values based on the JetCat literature.

As stated previously the lower global equivalence ratio observed in the rotating starter assisted Configuration 7 tests was due to the requirement to keep the air starter on to prevent the compressor rotor from contacting the shroud. As such the spool rotated at a higher speed for a given fuel flow rate than it otherwise would if it was driven from the combustor alone. The higher speed resulted in a higher air mass flow rate for the given fuel flow rate which led to the lower global equivalence ratio. The 1/2 Idle CFD and non-rotating combustor Configuration 7 test points achieved a 0.31 global equivalence ratio, but the computations were run at a slightly higher fuel and air flow rate which is why the CFD 1/2 Idle test point in Figure 432 is higher than the majority of the other points around it. The rotating starter assisted tests and non-rotating Configuration 7 tests flowed identical fuel quantities at 19 SLPM, but the higher air mass flow rate in the rotating tests led to the comparatively lower global equivalence ratio. In the self-sustaining Configuration 7 combustor test the air mass flow rate through the engine was proportionate to the other test cases given the engine speed and fuel flow rate reduction.

The turbine inlet temperatures (T_{4avg}) plotted in Figure 435 reflect the variation

in global equivalence ratio in all cases but the self-sustaining Configuration 7 test. The higher temperatures measured in the stock JetCat directly correlate to the higher global equivalence ratios in that engine configuration. At the 1/2 Idle condition the reduction in turbine inlet temperature to an average of 770 K for the rotating starter assisted Configuration 7 engine was directly related to the reduced global equivalence ratio. The additional air mass flow rate in the rotating case dropped the turbine inlet temperature by 254 K from the 1024 K average in the computational and non-rotating Configuration 7 combustor. For the self-sustaining Configuration 7 test the turbine inlet temperature was increased to an average of 1119 K. It is possible that the reduction in turbine inlet temperature in the starter assisted cases was the result of incomplete combustion within the Configuration 7 combustor. The lower mass flow rate in the self-sustaining test would have resulted in a longer residence time potentially allowing the reactions the finish and thus resulting in a higher temperature. However, since the reduction in temperature was not seen in the non-rotating Configuration 7 data at roughly equivalent air mass flow rates to the starter assisted Configuration 7 tests the data are inconclusive.

At Station 7 the exit temperature of the rotating starter assisted Configuration 7 engine was comparable with the stock JetCat and within manufacturer specifications as shown in Figure 436. However, the self-sustaining Configuration 7 exit temperature exceed the upper manufacturer limit with a T_7 measurement of 1014 K. This value appears to fall in line with a parabolic curve through the stock data. It is not clear if the self-sustaining Configuration 7 combustor would result in decreased exit temperatures at higher engine speeds to remain consistent with the stock trend as higher speeds could not be tested. All exit temperature measurements were made by a single thermocouple making it difficult to state with certainty that the displayed temperatures are representative of the average exit temperature across the nozzle.

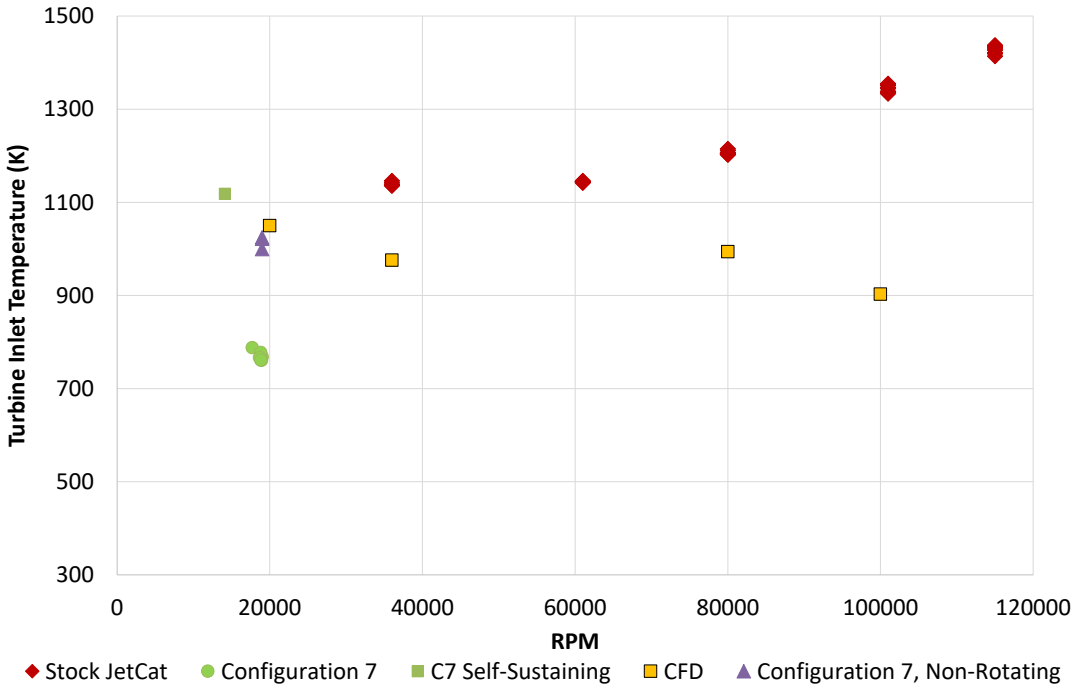


Figure 435. Turbine inlet temperature in a stock JetCat P90RXi and the Configuration 7 combustor with rotating hardware

The exit temperatures of the stock JetCat and self-sustaining Configuration 7 test were below the turbine inlet temperatures as expected, while the exit temperatures were higher than the average turbine inlet temperatures for the starter assisted Configuration 7 combustor. This behavior could again indicate incomplete combustion in the starter assisted Configuration 7 combustor, however, the exit temperature did not exceed the maximum measured T_4 value of 924.5 K. The measurement at the exit plane could be measuring a band of gases that were originally at the combustor ID and migrated outward due to centrifugal loading through the stators. In both the stock and Configuration 7 combustors all of the dilution air was introduced prior to Station 4 and there was no engine bypass. It is then possible that the stock temperature measurements were made in a hot streak which would also account for the 450+ K reduction in static temperature across the turbine and nozzle by the higher speeds.

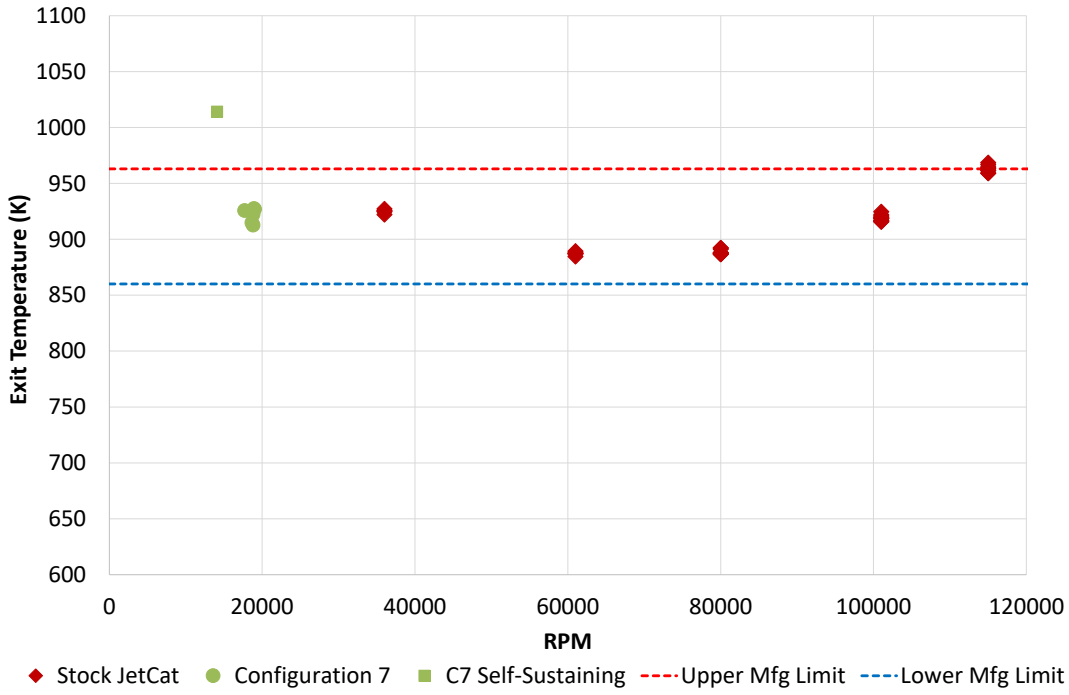


Figure 436. Exit temperature in a stock JetCat P90RXi and the Configuration 7 combustor with rotating hardware

Finally, Figure 437 shows the exhaust gas velocity at the nozzle exit as determined by Bernoulli's Equation using static and total pressure measurements. The total measurements were made at the engine centerline (CL) and 50% nozzle radius with the corresponding velocities computed at both locations. In all engine configurations the 50% radius velocity measurements were greater than the centerline velocity measurements due to presence of the centerbody tail cone. There was likely some flow separation off the tail cone meaning the centerline measurements were made in the wake, or velocity defect, region of the centerbody and thus measured a lower velocity. The velocity from the starter assisted Configuration 7 engine was proportional to the stock JetCat performance given the reduced RPM. The self-sustaining Configuration 7 combustor achieved velocities greater than expected given the reduction in engine speed due to a density reduction resulting from the elevated exit temperatures.

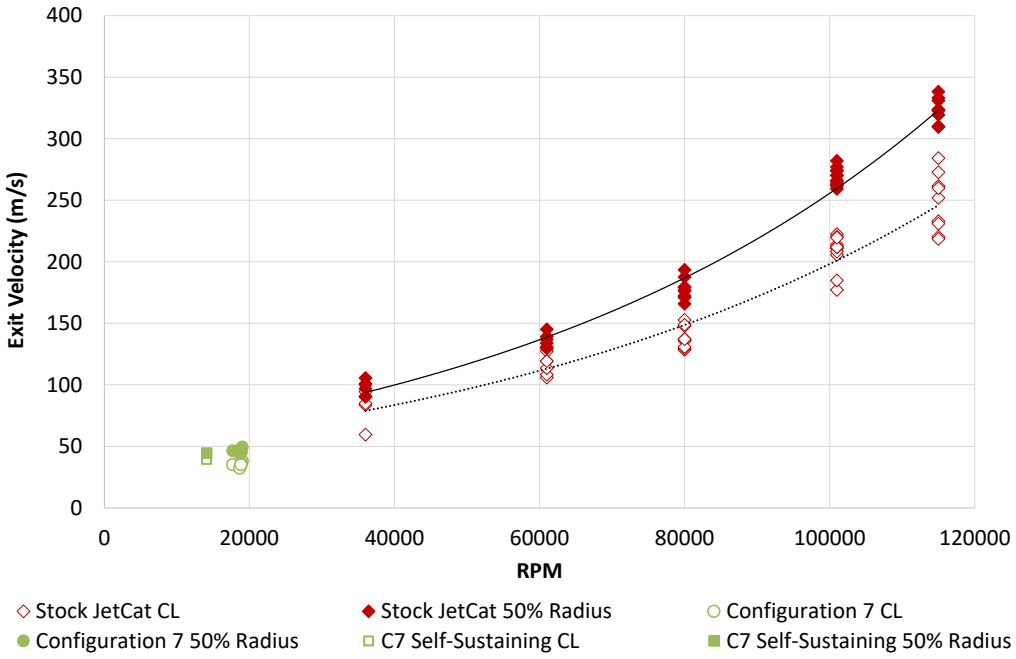


Figure 437. Exit velocity in a stock JetCat P90RXi and the Configuration 7 combustor with rotating hardware

9.3.4 Flameout Study Results.

The hypothesis coming out of Objective 4 testing was that the cause of the combustor flameout at fuel flow rates above 19 SLPM was the result of propane injection back-pressuring the primary zone and reducing air flow through the primary inlets. Since the propane was supplied from a high-pressure source the fuel pressure was always greater than the air pressure to guarantee the commanded fuel mass flow rate was achieved. With a low Station 3 air pressure there was an insufficient force to overcome the combustor pressure rise due to propane addition which resulted in reduced air flow into the primary zone leading to engine flameout. A secondary issue was that in testing without the compression occurring from engine operation there was a lower pressure at Station 3 compared to Station 2. The results from Sections 9.3.1 and 9.3.3 showed a correction of the position of the peak pressure from Station 2, as seen in Objective 4 testing, to Station 3, but did not result in a change in the

operating range. Table 58 showed that even with the correction of the peak pressure location, the magnitude of the pressure at Station 3 was comparable between the rotating and non-rotating testing. These results did not help to confirm or disprove the hypothesis. As such a detailed study was conducted to test the hypothesis that the fuel pressure was inhibiting air from entering the primary combustion chamber and determine the cause of the flameout.

The rotating components were removed from the engine with the non-rotating components reinstalled to achieve the configuration outlined in Section 8.4.2. Additional pressure taps were installed as shown in Figure 438 with the instrumentation details listed in Table 59. To accommodate the additional pressure taps all pressure measurements were made with the 32-port Initium pressure scanner described in Section 3.1.5.1. All channels in this scanner were limited to 34,474 Pa differential from atmospheric (5 psid) and could provide a greater accuracy for the small pressure readings compared to the JetCat pressure transducers.

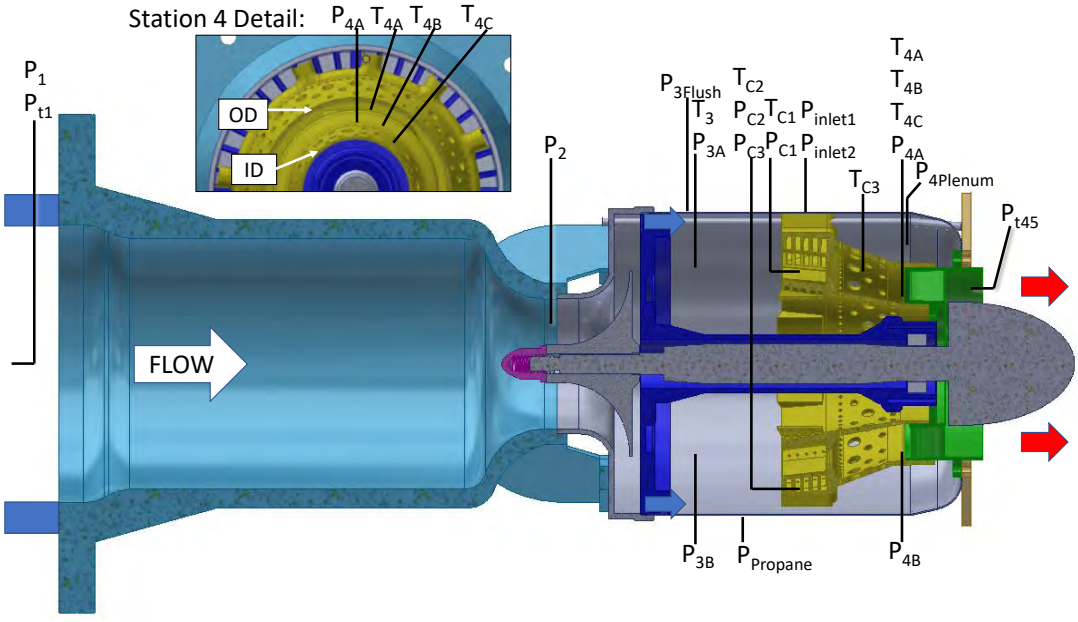


Figure 438. Flameout study temperature and pressure instrumentation locations

Table 59. Flameout study instrumentation details

Location	Designation	Depth	Port	Accuracy
Air Supply Line	P_1	Centerline	Initium Ch. 28	±0.05% FS
	P_{t1}	Centerline	Initium Ch. 20	±0.05% FS
Compressor Inlet	P_2	25% span	Initium Ch. 1	±0.05% FS
Compressor Exit	P_{3A}	1 cm from OD	Initium Ch. 3	±0.05% FS
	P_{3B}	1 cm from OD	Initium Ch. 4	±0.05% FS
	P_{3Flush}	OD Surface	Initium Ch. 2	±0.05% FS
	T_3	1 cm from OD	TC Panel, 3	±0.4% FS
Combustor	P_{C1}	Primary zone, Ctr	Initium Ch. 25	±0.05% FS
	P_{C2}	Primary zone, Ctr	Initium Ch. 26	±0.05% FS
	P_{C3}	Primary zone, Ctr	Initium Ch. 27	±0.05% FS
	P_{inlet1}	OD inlet	Initium Ch. 5	±0.05% FS
	P_{inlet2}	OD inlet	Initium Ch. 6	±0.05% FS
	T_{C1}	8.5 mm front wall	TC Panel, 4	±0.4% FS
	T_{C2}	8.5 mm front wall	TC Panel, 5	±0.4% FS
	T_{C3}	8 mm comb. OD	TC Panel, 6	±0.4% FS
Combustor Exit	P_{4A}	50% span	Initium Ch. 11	±0.05% FS
	P_{4B}	50% span	Initium Ch. 12	±0.05% FS
	$P_{4Plenum}$	0.5 cm case OD	Initium Ch. 18	±0.05% FS
	T_{4A}	4 mm comb. OD	TC Panel, 7	±0.4% FS
	T_{4B}	8 mm comb. OD	TC Panel, 8	±0.4% FS
	T_{4C}	12 mm comb. OD	TC Panel, 9	±0.4% FS
Stator Exit	P_{t45}	50% span	Initium Ch. 19	±0.05% FS
Fuel Line	$P_{Propane}$	OD fuel fitting	Initium Ch. 8	±0.05% FS

A total (P_{t1}) and static (P_1) measurement were added upstream of the engine along the centerline of the air supply duct. Two additional measurements were added at Station 3 for a total of three pressure taps. These three taps were arrayed 120° apart and in-line axially. Two of the taps (P_{3A}, P_{3B}) were inserted 1 cm from the engine outer casing which put the tap opening radially inward of the air coming from the compressor. This location was situated in a recirculation region which made the measurement value close to a total pressure. The third tap (P_{3Flush}) was surface mounted along the outer casing wall. Three pressure taps were added in the

combustor primary zone (P_{C1}, P_{C2}, P_{C3}). They were also arrayed 120° apart and centered axially between the combustor forward wall and the constriction between the primary zone and the dilution zone. To avoid having to open the engine casing these taps were inserted from the engine exit and passed through the nozzle guide vanes, dilution zone, and into the primary zone. Two pressure taps were added over adjacent primary zone inlets (P_{inlet1}, P_{inlet2}). Both taps were surface mounted to the inside lip of the shim that served as a spacer between the inlets and the casing. A pressure tap was added to the dilution zone supply plenum ($P_{4Plenum}$) between the casing and the combustor OD with the probe tip inserted approximately 0.5 cm from the casing OD. A total pressure measurement (P_{t45}) was added at the exit of the nozzle guide vanes and was aligned with the flow exiting the stators. Finally, a pressure tap was added to one of the OD propane supply lines ($P_{Propane}$).

Several tests were conducted with this setup that included: a cold flow 0.03 kg/s fixed air flow rate while ramping fuel from 0 to 22 SLPM, reacting operation at 0.03 kg/s fixed air flow rate while ramping fuel from 0 to flameout, a 17 SLPM and two 18 SLPM fixed fuel flow rates with ramped air flow rates, a high-speed pressure acquisition test that was time synced to temperature data with a fixed 0.03 kg/s air flow rate with ramping fuel from 18 SLPM to flameout, and a study of the fuel distribution effects by independently controlling the ID and OD fuel supply. These test cases were chosen because they enabled the behavior of the combustor to be studied with changes in fuel flow while holding airflow constant, and airflow while holding fuel constant. The cold flow test provided a baseline of aerodynamic performance without the coupling of combustion. The high-speed cases were attempting to identify any short duration transient events during flameout that may not have been evident with 1 Hz data collection. Finally, the fuel injection variation tests were conducted to determine the relative contributions of the ID and OD injectors to total

cavity combustion, and identify if a different fuel flow splits had a benefit to primary zone combustion stability. All of these tests spanned a flameout condition to try and determine performance trends leading up, and after, flameout.

9.3.4.1 Fuel and Air Variation Results.

The initial flameout hypothesis was quickly disproved as shown in Figures 439 and 440. The cold flow data in Figure 439 shows a constant primary zone pressure (PC_avg) across all fuel flow rates indicating there was no pressure build up in the primary zone to back-pressure the primary zone inlets and reduce air flow. When the combustor was lit the pressures throughout the engine varied with fuel flow rate, but they typically varied proportionately resulting in near parallel lines. If the primary zone was being back-pressured by the addition of propane, the propane pressure (Propane) and primary zone pressure (PC_avg) would show a disproportionate increase compared to the primary zone inlet (Primary Inlet_avg) pressure.

Figures 441 and 442 show the temperature and pressure at fixed fuel flow rates of 17 and 18 SLPM with ramping air flow rates from 0.024 kg/s to 0.048 kg/s. The results from the second 18 SLPM test are not shown as the results are nearly indistinguishable from the first test shown in Figure 442. Since the fuel flow was fixed and the air flow was increased the equivalence ratio in the primary zone became variable. Making the assumption that the peak primary zone temperature occurred at an equivalence ratio of one, along with the definition of equivalence ratio given in Equation 15, enables the air flow rate in the primary zone to be calculated since the fuel flow rate was known. Using this method the 17 SLPM data produced a primary zone total air mass flow rate of 0.00883 kg/s, or 25.6% of the total engine air flow rate. The 18 SLPM data produced a primary zone total air mass flow rate of 0.00884 kg/s, or 25.2% of the total engine air flow rate. These values are slightly higher than the 20% split predicted by CFD, but the additional blockage added to the experimental hardware to compensate

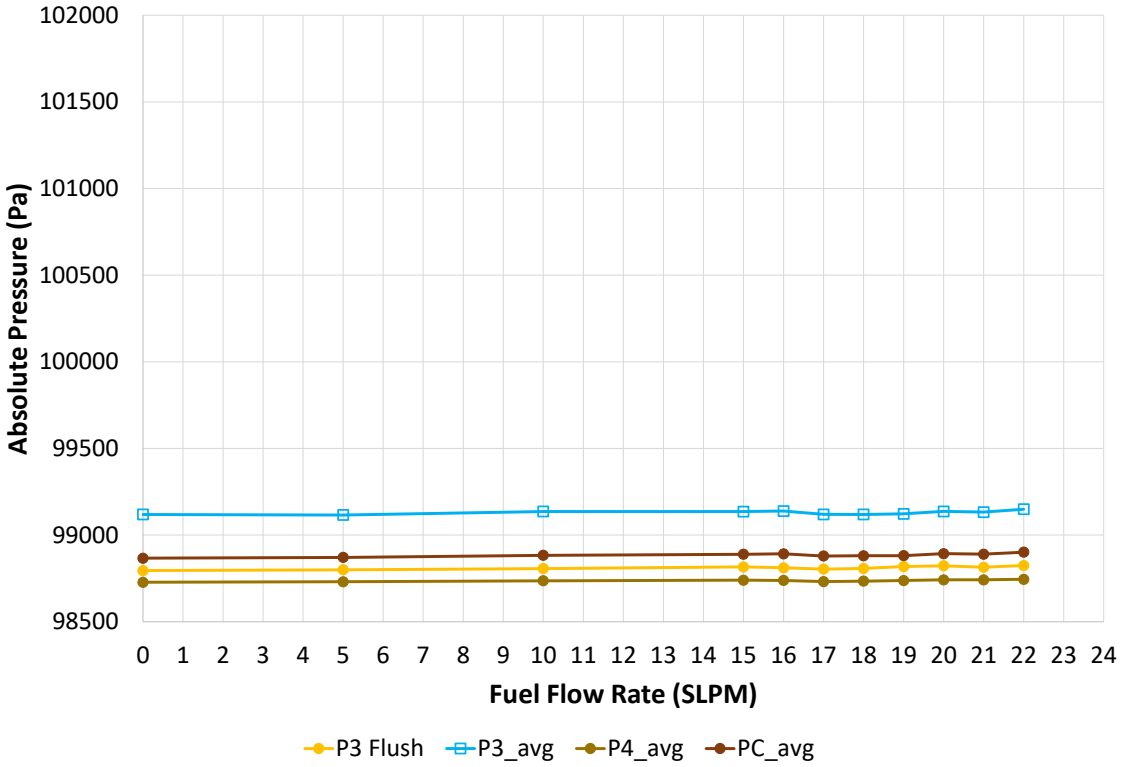


Figure 439. Cold flow pressures at fixed 0.03 kg/s air flow rate and ramping fuel flow rate

for the part shrinkage and primary zone inlet area change could have forced more air into the primary zone than intended.

Looking at the pressures in Figures 441 and 442 there was a steady rise in both static and total pressure at Station 1, and a steady rise in static pressure at Station 2, but at a slightly reduced rate. The pressure at Station 3 was also expected to rise linearly, as shown for cold flow in Figure 401. While the Station 3 pressures did increase, the rate decayed with increasing air flow rate. The primary zone pressure and both Station 4 positions measured values that increased up to the 0.036 kg/s air flow rate, and then decayed with increasing air flow rates as the temperatures in the combustor dropped. The difference in pressure between the surface mounted Station 3 pressure tap (P3 Flush) and the more deeply inserted Station 3 taps (P3_avg) provided

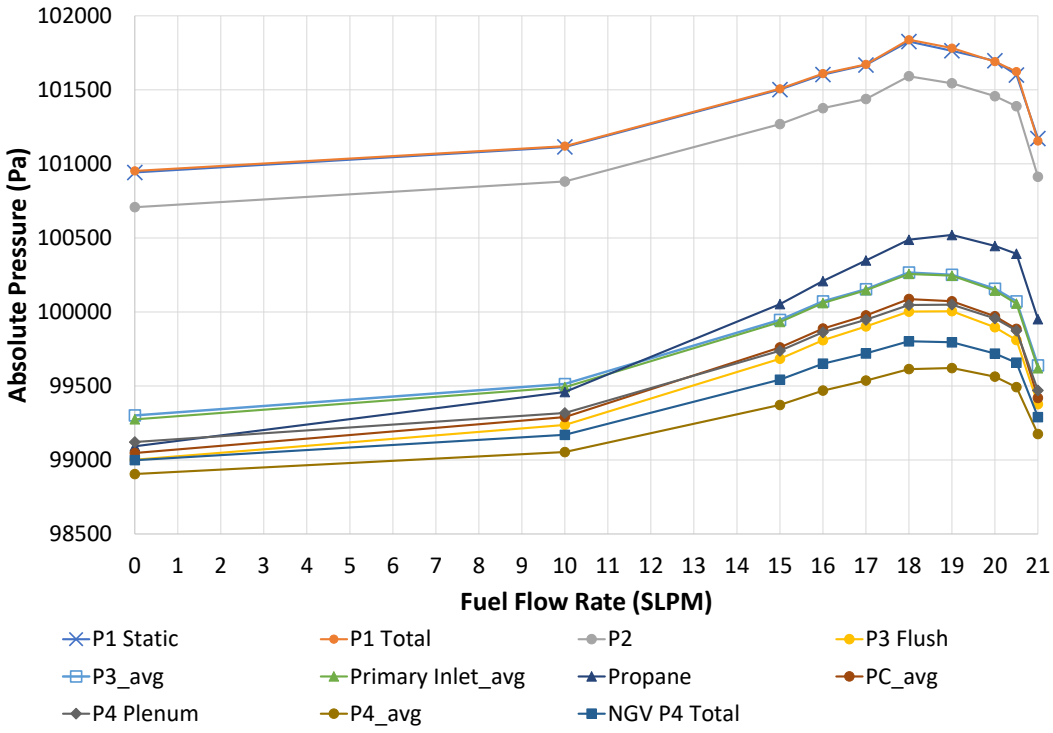


Figure 440. Reacting flow pressures at fixed 0.03 kg/s air flow rate and ramping fuel flow rate

an approximate static to total measurement difference. Based on this difference, which grew with increasing air mass flow rate, the flow velocity increased as the air mass flow rate increased as expected. The pressure measurements in the primary zone inlets (P_Primary Inlet_avg) were nearly identical to of the Station 3 measurement (P3_avg), that approximated a total pressure, indicating good pressure recovery by the inlet geometry. After an initial rise from 0.024 kg/s to 0.03 kg/s the propane pressure remained relatively unchanged for the remaining air flow rates.

The velocity of the air that entered through the primary zone inlets could also be calculated from the pressure differential across the primary zone inlet holes and the orifice flow theory relationship previously shown in Equation 148, given in Section 8.3.4.6. Due to the small size of the combustor, CFD predicted the air inlet velocity to be closely matched to the bulk swirl velocity in the primary zone. This relationship

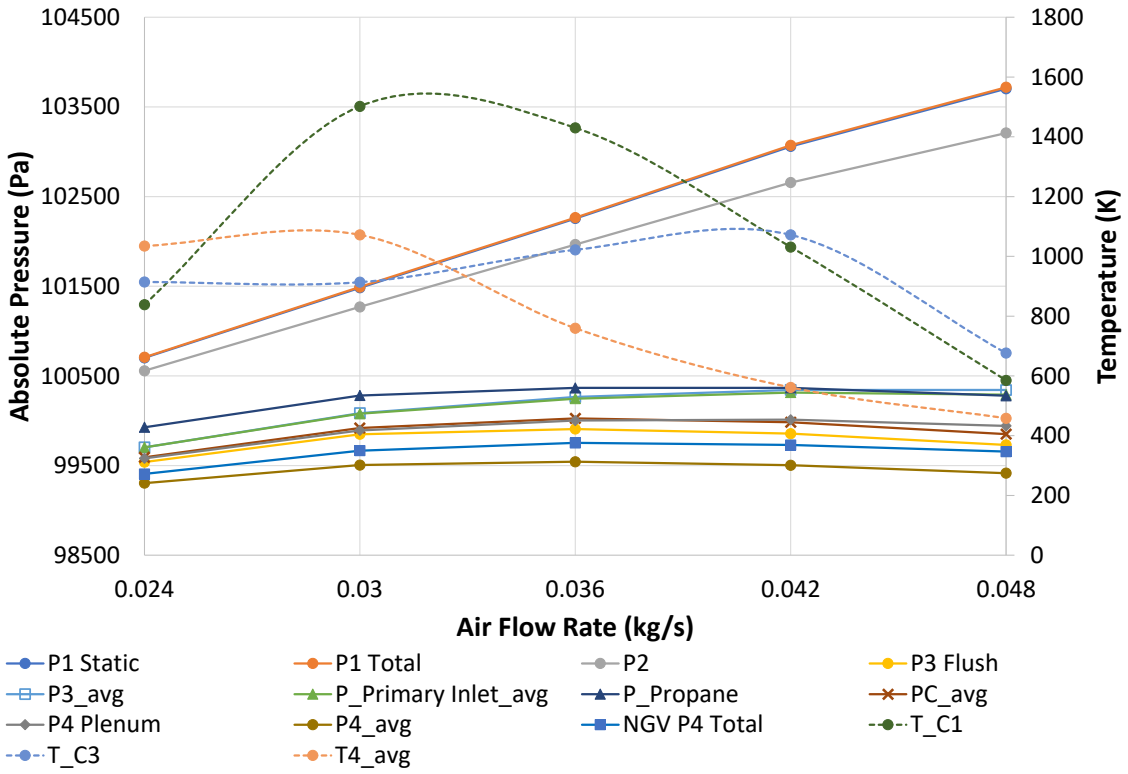


Figure 441. Reacting flow temperatures and pressures at a fixed 17 SLPM fuel flow rate with ramping air flow rate

means that the definition from Equation 148 also enabled the approximate centrifugal loading in the primary zone to be found. The volume flow rate through the primary zone inlets could then be found using Equation 149 given in Section 8.3.5.1, also derived from orifice flow theory. This definition includes a discharge coefficient, K, which varies from 0 to 1 and is a function of the hole geometry. Multiplying the gas density and the volumetric flow rate from Equation 149 yields the mass flow rate of air entering the primary zone. This process makes the assumption that all of the air entering the primary zone came from the OD inlets. This is not an unfounded assumption as CFD predicted only 17% of the primary zone air entered through the ID. With the part shrinkage and no blockage applied to the ID passage this value was expected to be lower in the physical hardware.

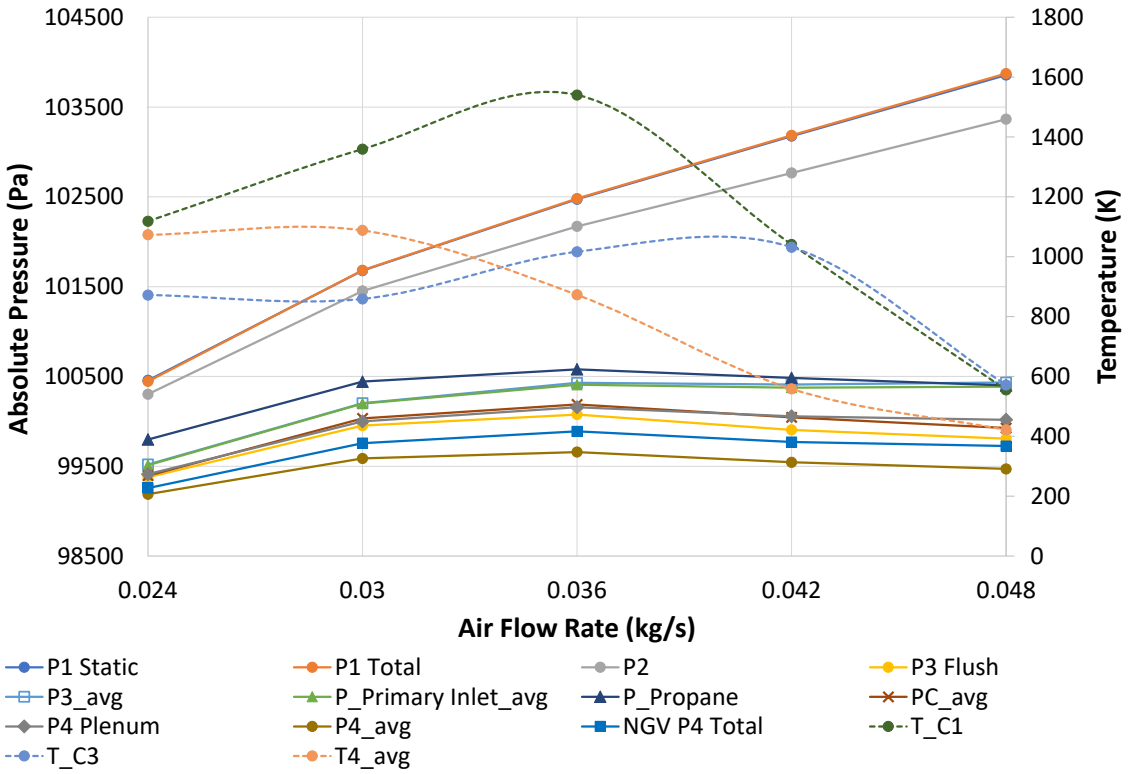


Figure 442. Reacting flow temperatures and pressures at a fixed 18 SLPM fuel flow rate with ramping air flow rate

The discharge coefficient was not known, so the mass flow rates calculated based on the equivalence ratios using Figures 441 and 442 were used to anchor the flow rate. The discharge coefficient was then varied until the mass flow rate calculated by orifice flow theory matched the mass flow rate calculated by equivalence ratio. This processed yielded a discharge coefficient of $K = 0.302$. While this value is low, it is not unexpected due to the irregular cross-sectional shape, the hole length, turning inside the holes, and the 3D printed hole surface roughness.

With a method to compute the air mass flow rate and velocity in the primary zone defined, these values were plotted for the ramping 18 SLPM fuel flow rate with a fixed air mass flow rate of 0.03 kg/s test case as shown in Figure 443. After a slight decrease in values from 0 - 15 SLPM, all of the properties remained relatively constant through

flameout at 21 SLPM with the exception of the pressure differential from the Station 4 plenum to Station 4 passage, and the pressure differential from the primary zone to the Station 4 passage. The variation in the pressure differential from the Station 4 plenum to Station 4 passage can be explained with the help of Figure 440 and Figure 444. In Figure 440 it can be seen that the Station 4 plenum pressure (P4 Plenum) was raised proportionately to the remaining pressures while the average Station 4 pressure (P4_avg) did not rise as fast. This smaller rise is due to the Station 4 measurements in the combustor passage being static pressure measurements that are affected by the exiting gas velocity. In Figure 444 the average Station 4 temperature (T4_avg) follows the same curvature as the pressure distribution with a peak at 18 SLPM. The increase in temperature would cause a decrease in the gas density and thus a faster gas velocity resulting in a lower passage static pressure. The pressure differential between the primary zone (PC_avg) and Station 4 passage (P4_avg) showed this same trend but with a much greater magnitude.

The pressure differential between the primary zone (PC_avg) and Station 4 passage (P4_avg) did not peak with the peak cavity temperature, but instead peaked at the highest Station 4 temperature at 18 SLPM of fuel. By this condition the cavity temperature had already dropped by 15% of its peak value as shown in Figure 444. However, also shown in this figure are the corresponding cavity equivalence ratios which were not large enough to cause this significant reduction in temperature alone. It was also noted that at the last fuel flow rate to sustain combustion (20.5 SLPM) the temperature at all three combustor zones were approximately equal. While this may just be a coincidence, the result is interesting to note.

Based on all the information presented in this flameout analysis section, the new conclusion of the cause of the poor combustion performance, and ultimately flameout, beyond 19 SLPM of propane was thought to be that the reaction was pushed out of

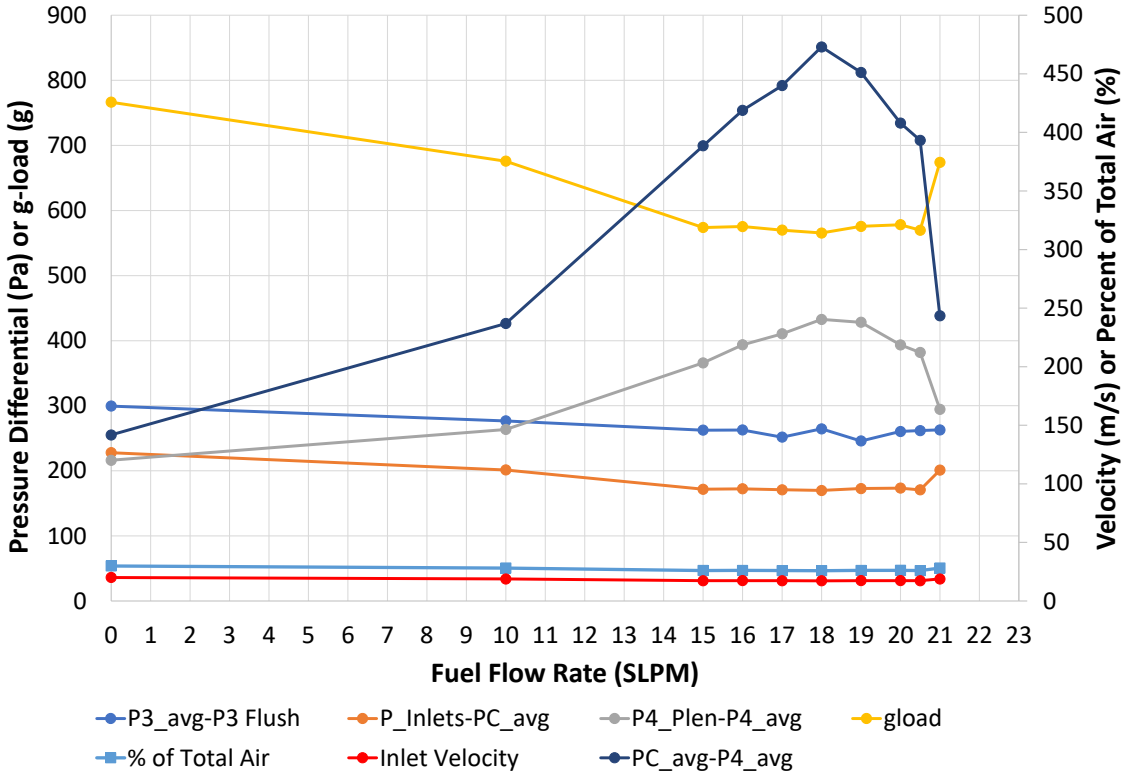


Figure 443. Reacting flow pressure differentials and calculated quantities at fixed 0.03 kg/s air flow rate and ramping fuel flow rate

the primary zone cavity. With a lack of flame holders in the dilution zone, combustion could not be sustained at the higher flow rates.

The biggest supporter of this theory was the pressure differential between the primary zone (PC_avg) and Station 4 passage (P4_avg). Stable combustion was achieved from 10 - 18 SLPM where this value was continuously increasing. Beyond 18 SLPM the differential was decreasing and instabilities were noted in the combustor as displayed previously in the standard deviations of temperatures and pressures in Table 57. The instabilities were marked by a reduction in temperature in the primary zone and a reduction in pressure throughout the combustor indicating reduced reactions in the primary zone. While the combustor recovered from all the transient instabilities at 19 SLPM of fuel, beyond this value the instabilities grew and the combustor

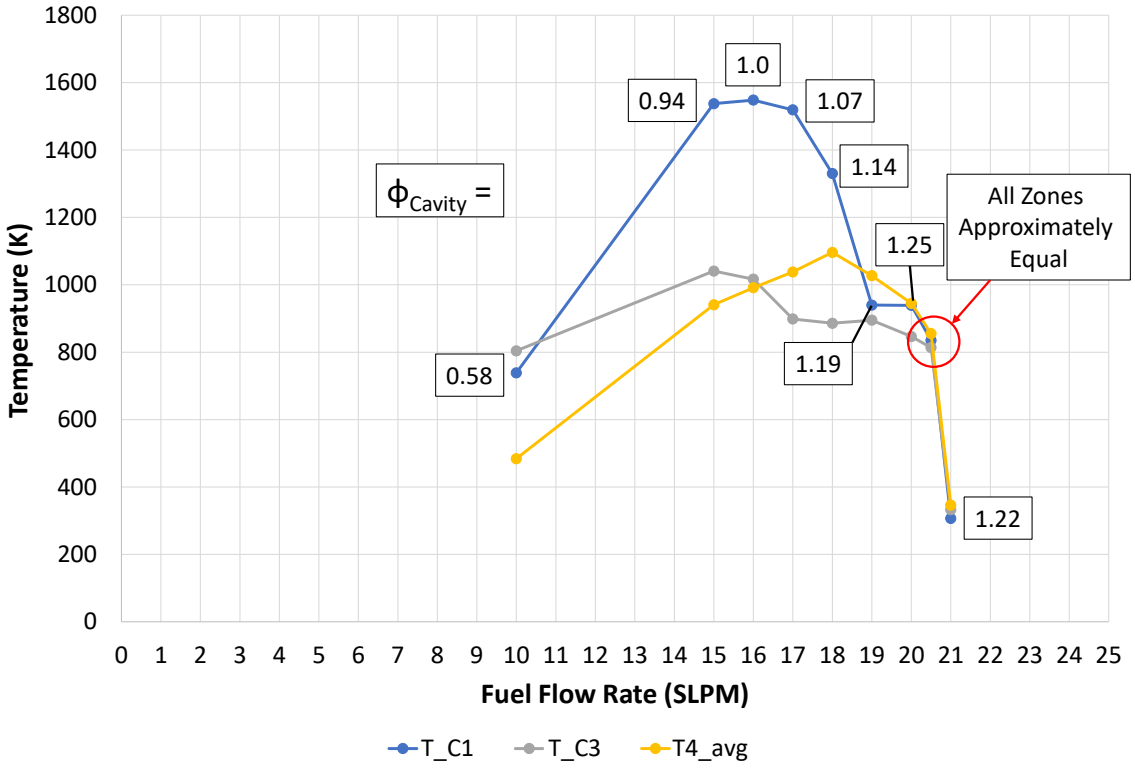


Figure 444. Reacting flow temperatures at fixed 0.03 kg/s air flow rate and ramping fuel flow rate

could not always recover. By 21 SLPM of fuel the instabilities were severe and the combustor always flamed out. While the audible response to the instabilities sounded like rich combustion, it was more likely premixed combustion reacting through the highly turbulent constriction between the primary zone and the dilution zone as the reactions were pushed out of the primary zone. Figure 445 shows the primary zone flame anchor points and the path of travel as the reactions were forced out into the dilution zone.

As shown in Figure 446, a similar trend in the pressure differentials was noted with a fixed fuel flow rate and a ramped air flow rate. The two upward sloping lines represent properties that were proportional to velocity. As the mass flow rate increased, so did the velocity, and thus the differential increased as well. The pressure

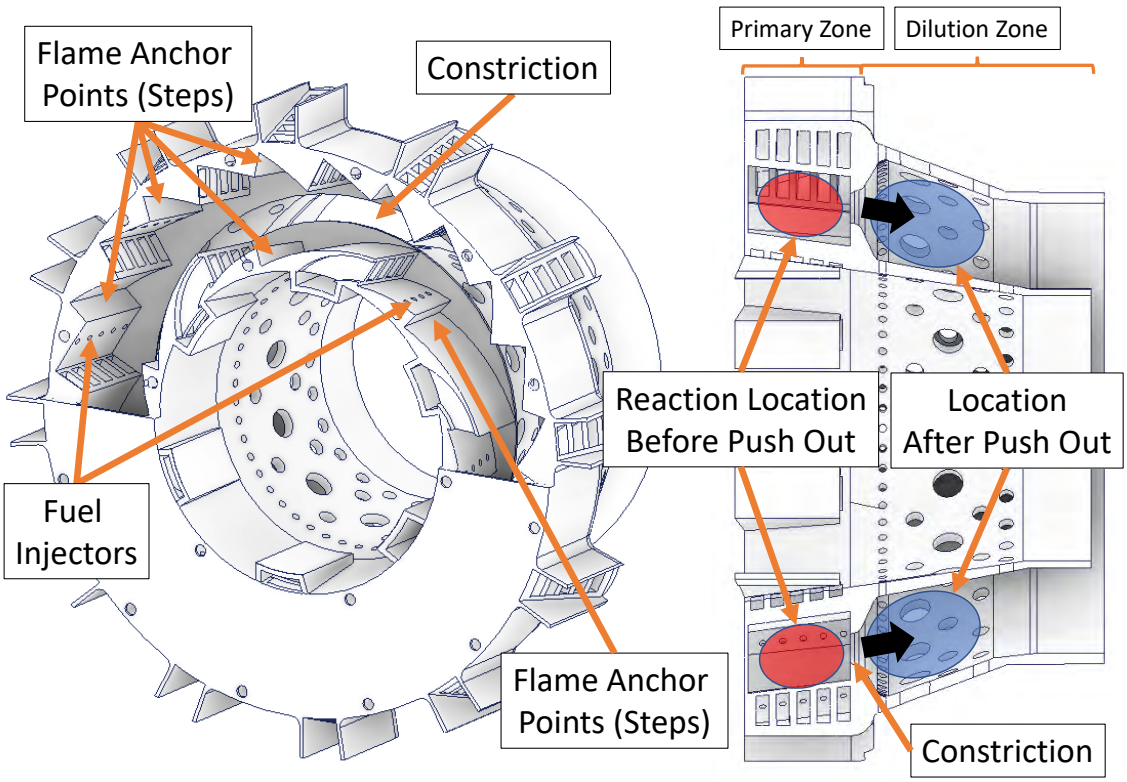


Figure 445. Configuration 7 primary zone cross-section with flame holders and fuel injectors identified. Combustor cross-section shows the path of travel when reactions were pushed from the primary zone

differential between the primary zone (PC_avg) and Station 4 passage (P4_avg) peaked at 0.036 kg/s air flow rate and decreased for larger air mass flow rates. Following the same trend as the ramped fuel case, the primary zone temperatures were reduced with increasing air mass flow rate as shown in Figure 442. Additionally, the behavior shown in Figure 443 which demonstrated increased instabilities with decreasing primary zone (PC_avg) to Station 4 passage (P4_avg) differential was noted for the ramped air and fixed fuel flow cases, with air flow rates greater than 0.048 kg/s unable to sustain combustion. This behavior demonstrates both a fuel flow rate and an air flow rate controlled initiation of instabilities that push the reactions out of the primary zone.

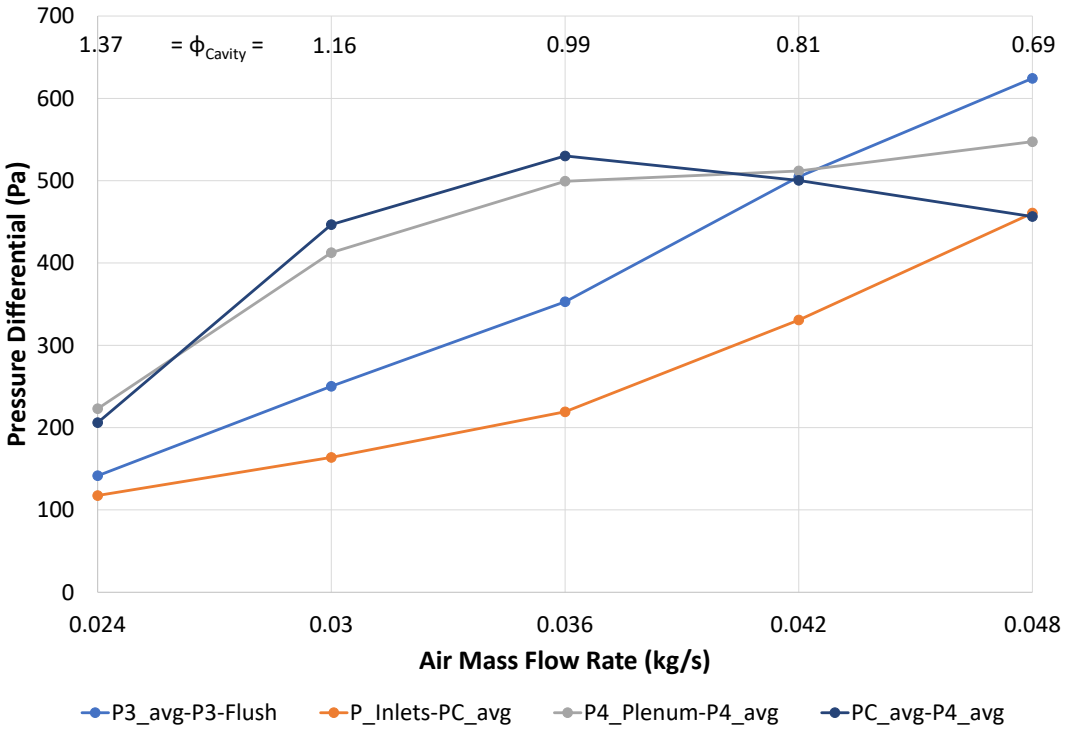


Figure 446. Reacting flow pressure differentials at a fixed 18 SLPM fuel flow rate with ramping air flow rate

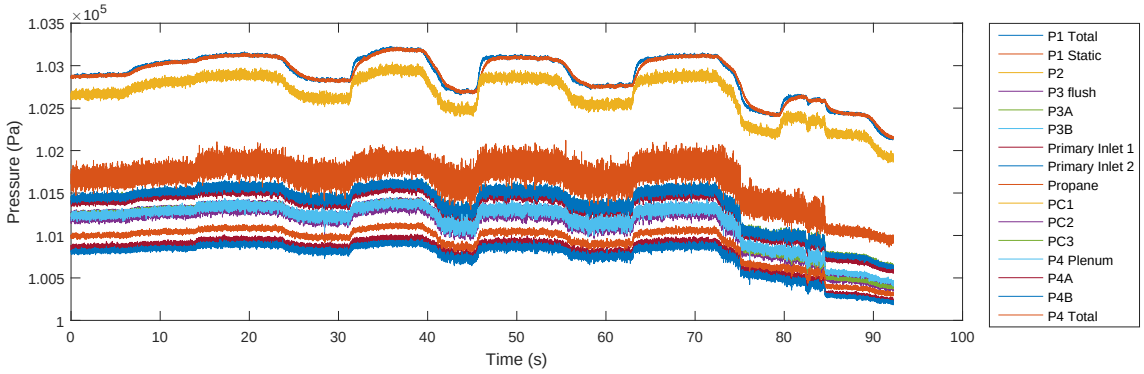
9.3.4.2 High-Speed Pressure Analysis Results.

High-speed pressure measurements were taken at 650 Hz from all installed taps using the high-speed function of the Initium system. This data was time synced to the temperature and fuel flow rate measurements collected by LabView. The pressures, temperatures, and fuel data are shown in Figure 447a, b, and c, respectively. The recording was started with the combustor operating at 0.03 kg/s air flow rate and 18 SLPM of propane. After 15 seconds the fuel was ramped to 19 SLPM, then 20 SLPM at 42 seconds, and 21 SLPM at 73 seconds.

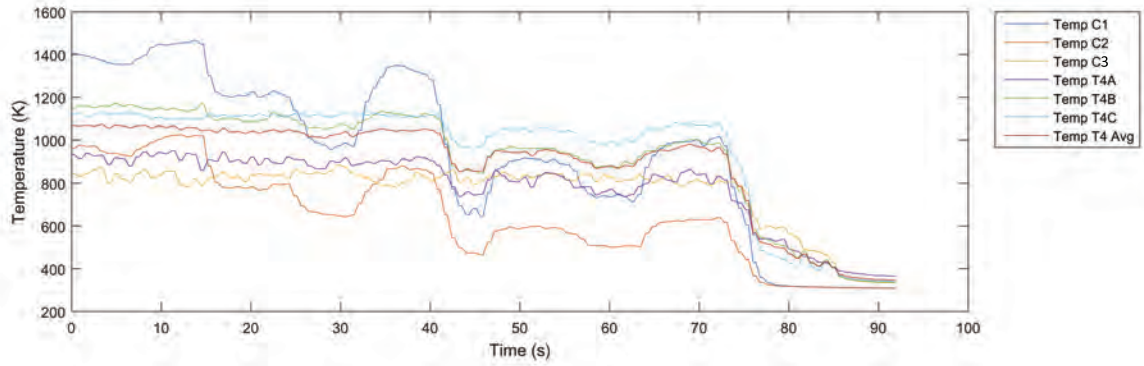
Figure 447a shows several instabilities that are not explained by changes in fuel flow rate. The first unstable pressure drop is between 23 and 30 seconds with the combustor recovering to full pressure by 33 seconds. The second instability induced pressure drop was between 55 and 62 seconds where again the combustor was able to

recover to full pressure. After the final fuel addition to 21 SLPM at 73 seconds there was a substantial pressure loss. The combustor attempted to recover as evident by the slight rise in pressure at 79 seconds, but as shown in Figure 447b the primary zone had already flamed out. Combustion could not be sustained in the dilution zone alone so the burner ultimately flamed out at the discontinuity at 84 seconds. When the pressure dropped due to these instabilities the total and static pressure measurements at Station 1 flipped with the static value reading larger. When the instability leveled off at the bottom of the pressure drop, the pressures returned to a larger total measurement. When the combustor recovered from the instability the total measurement increased significantly compared to the static value. Typically this behavior is indicative of reversed flow, however, the engine could not sustain combustion with reversed flow for several seconds and there were no visual indications of reversed flow from the engine's internal camera.

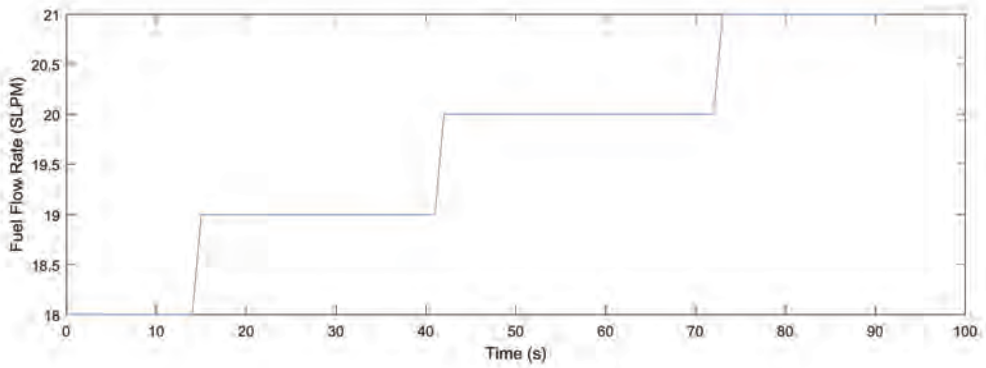
The temperature data in Figure 447b follows the pressure response with a temperature reduction in the primary zone for all instability induced pressure drops. It is interesting to note that temperature T_{C3} remained steady during all instabilities and the average turbine inlet temperature T_{4avg} was only disrupted by the fuel addition at 42 seconds into the test. These patterns indicated the instability was localized to the primary zone. With each fuel step addition the peak cavity temperature decreased as discussed earlier.



(a) High Speed Pressures (650 Hz)



(b) Time synced temperature (10 Hz)



(c) Time synced fuel flow rate data (1 Hz)

Figure 447. High-speed and time synced combustor data

9.3.4.3 Fuel Distribution Study Results.

With the understanding that the flameouts and instability were localized to the primary zone, a study was conducted to independently control the fuel to the ID and OD fuel injectors to determine if a different fuel split ratio could correct the problem. Figure 448 provides a baseline of the combustor primary zone (T_{C1}) and turbine inlet temperatures (T_{4avg}) at 0.03, 0.036, 0.042, and 0.048 kg/s air flow rates with variable fuel flow rates. At the lower three air flow rates the peak temperature was approximately the same magnitude but occurred at uniformly increasing fuel flow rates. This result is another indication that the primary zone experiences the same cavity air flow percentage of the total air flow rate at all conditions. In each of these cases the peak turbine inlet temperature occurred at approximately 1 SLPM greater flow rate than where the primary zone peaked.

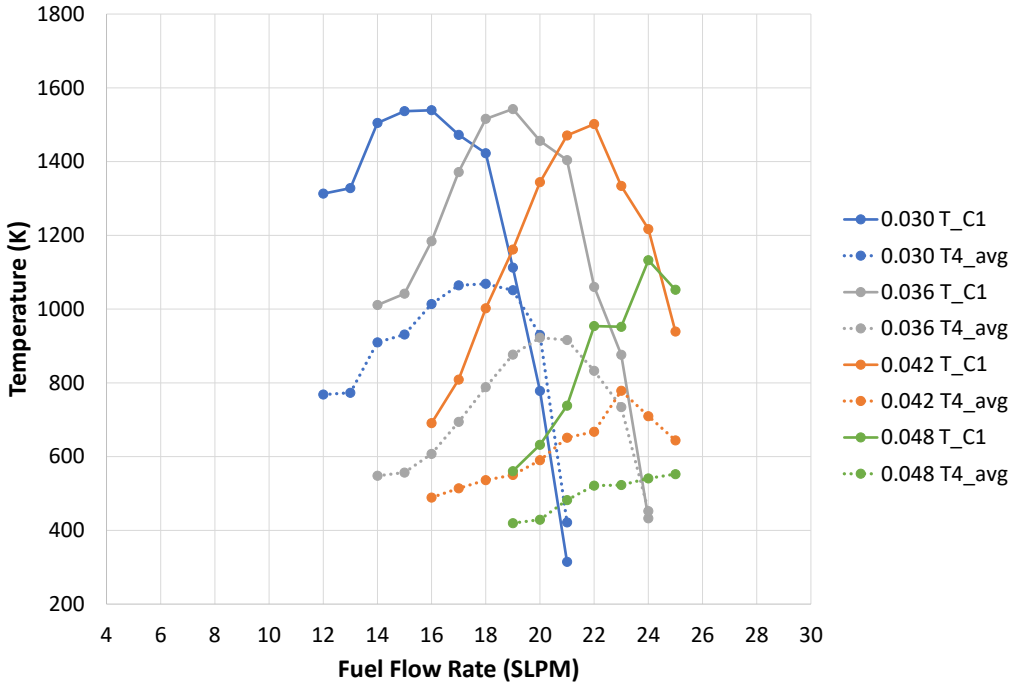


Figure 448. Primary zone (T_{C1}) and turbine inlet (T_{4avg}) temperatures at variable fuel and air flow rates with ID and OD fuel injection

The fuel flow split was designed to send 66% of the fuel to the OD and 33% to the ID, however, during operation on a single mass flow controller the ID and OD fuel plenums were fed from a common source and the fuel was free to rebalance as necessary. To test a theory that the majority of the primary zone combustion was the result of OD fuel injection, the ID fuel ports were turned off. With fuel from the OD only it was expected that the peak temperature would occur at 66% of the fuel flow rate where where the peak temperature was observed with the baseline fuel distribution. As shown in Figure 449 all of the peak primary zone temperatures shifted to the left, but not to 66%. Recalculating the fuel splits based on the OD only fuel results indicates the actual OD to ID ratio was 75% to 25%. It was also noted that while the primary zone peak temperatures reached the same peak temperatures from the baseline fuel distribution results, the temperatures at Station 4 were over 200

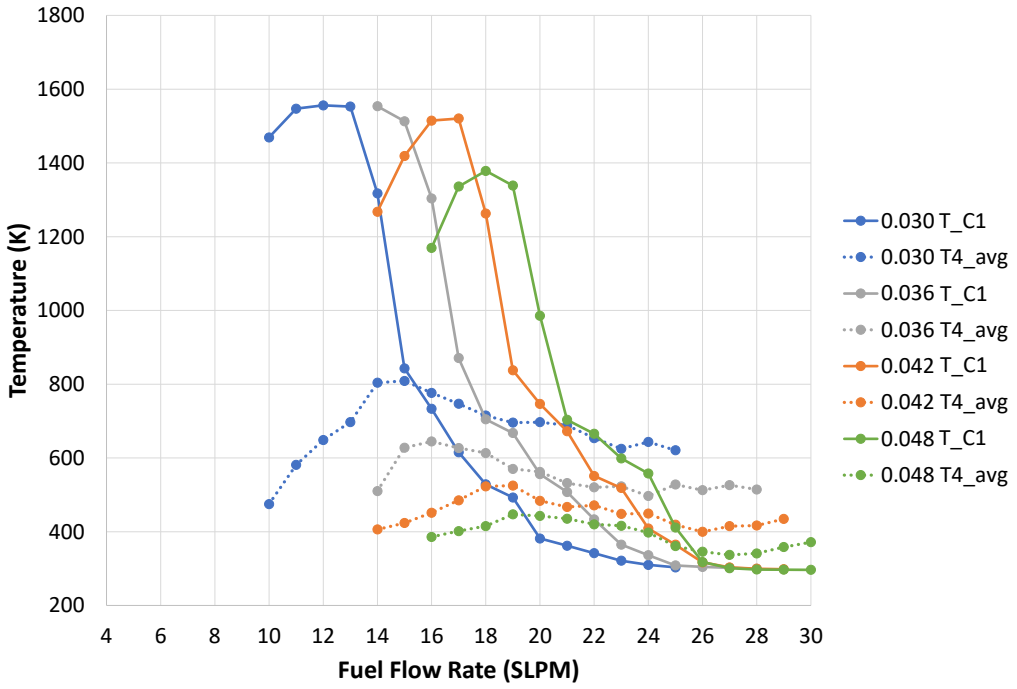


Figure 449. Primary zone (T_{C1}) and turbine inlet (T_{4avg}) temperatures at variable fuel and air flow rates with OD only fuel injection

K lower. This result indicates that the ID fuel was not a contributor to the primary zone cavity combustion, but rather exited and was burned in the dilution zone. By only using the OD fuel ports the peak fuel flow rate where flameout occurred was extended, but the combustion was poor and the Station 4 temperatures at the higher fuel flow rates were insufficient to drive a turbine.

To round out the fuel study the OD fuel ports were closed and the ID ports were opened. Flowing fuel from the ID ports only demonstrated that combustion could only be maintained with very low air flow rates and low fuel flow rates as shown in Figure 450. As determined from the first two fuel distribution plots, the ID fuel did not typically burn in the primary zone so this limited operational range with ID fuel only was not surprising.

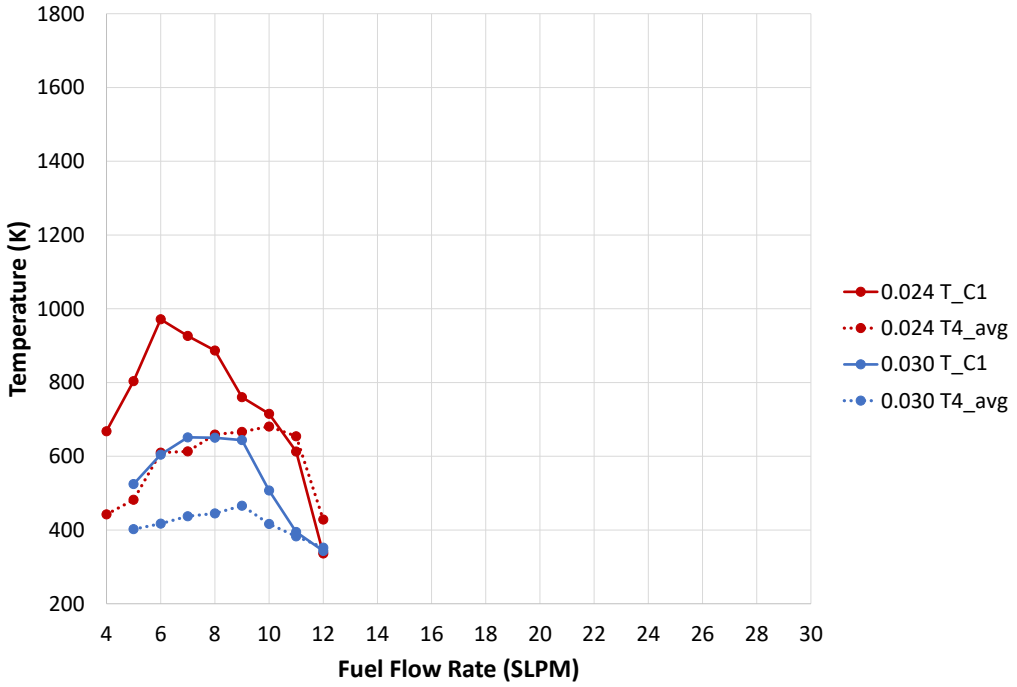


Figure 450. Primary zone (T_{C1}) and turbine inlet (T_{4avg}) temperatures at variable fuel and air flow rates with ID only fuel injection

Following the independent fuel distribution testing, a series of runs were conducted with the air flow rate fixed at 0.03 kg/s and a fixed OD fuel flow rate. The ID fuel flow

rate was then varied and the resulting primary zone and turbine inlet temperatures were recorded. This test sequence was repeated for seven fixed OD fuel flow rates. The resulting data was compiled into the contour plots shown in Figures 451 and 452 for the primary zone and turbine inlet temperatures, respectively. In both plots the OD fuel flow rate is on the X-axis and the ID fuel flow rate is on the Y-axis. The slanted lines indicate the total fuel entering the primary zone. The results confirmed that the best cavity and turbine inlet temperatures occurred below 20 SLPM of total propane flow, with flameout occurring above 21 SLPM total fuel flow. The peak turbine inlet temperatures occurred in a triangular region of the plot from 12 to 13 SLPM of OD flow and up to 7 SLPM of ID flow. This fuel distribution corresponds to an approximate 66/33 fuel split percentage.

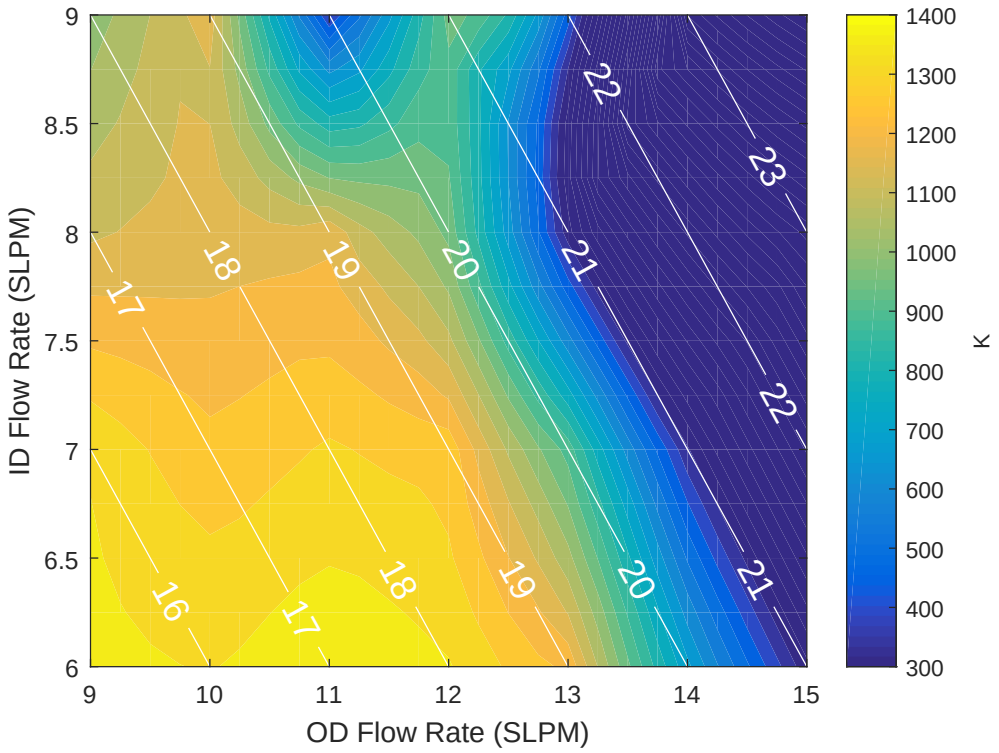


Figure 451. Temperature contours (K) of primary zone temperatures (T_{C1}) with ID and OD fuel distribution control

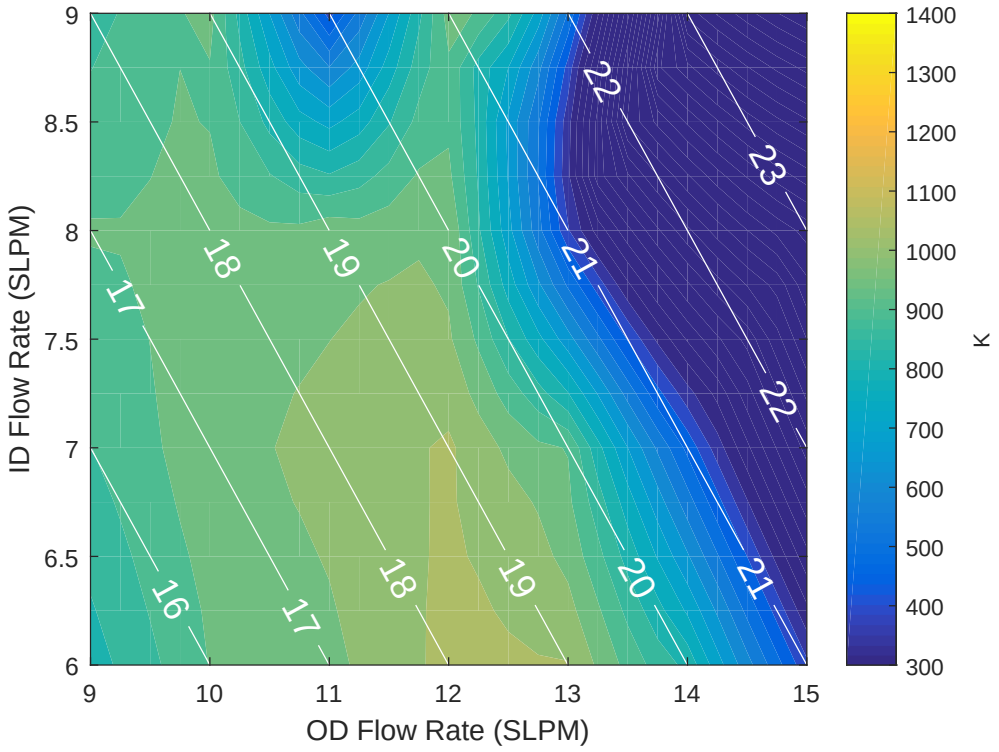


Figure 452. Temperature contours (K) of the average turbine inlet temperature (T_{4avg}) with ID and OD fuel distribution control

9.4 Objective 5 Conclusions

Building on the partial success from Objective 4, the current study took the Configuration 7 combustor with 70% blockage inserts in the Version 2 shim and tested it with a rotating turbine and compressor. To enable testing of a rotating engine in the COAL lab an extensive effort was put forth to design and manufacture a safety enclosure and integral JetCat test stand with dedicated pressure, temperature, and thrust measurement capability. Additionally, as discussed in Appendix D, the redesign of the JetCat electronics to enable communication of engine hardware components with the LabView control and data acquisition system required a significant amount of time and energy. While two issues were found with the new electronics during full

engine testing that were not seen in individual component checkouts, these issues were worked around to enable testing. Future modifications to the redesigned electronics could fix these two issues.

While this test configuration corrected the location of the peak pressure observed in Objective 4 from Station 2 to Station 3, there was not a significant increase in Station 3 pressure to overcome the suspected combustion issues first observed in Objective 4 experimental testing. At that time it was thought that the volume of propane that was injected into the combustor primary zone was sufficient enough to back-pressure the primary zone air inlets to reduce combustion stability and ultimately lead to flameout by 21 SLPM of propane.

While the rotating hardware did not fix the limited operating range issue observed in Objective 4, the rotating starter assisted Configuration 7 combustor functioned enough to reach 19,000 RPM and the 1/2 Idle condition which was a point on the stock engine operating line. Across the performance properties that were compared between the stock JetCat and the Configuration 7 combustor, the majority of them achieved comparable results and/or followed stock JetCat data trends. The reduced global equivalence ratio and turbine inlet temperature that was observed for the starter assisted Configuration 7 combustor were attributed to the requirement to maintain air starter operation after ignition was achieved to prevent the compressor rotor from contacting the compressor shroud. The air starter assisted the combustor in driving the spool and thus obtained a higher engine speed and air mass flow rate for the given fuel flow rate than would otherwise be achieved with a turbine driven by the combustor alone. When the combustor was lit and the fuel flow rate ramped to the combustor operating limit of 19 SLPM, an additional 13,000 RPM was achieved compared to the starter only. The engine exit temperature was comparable to the stock JetCat value and within the manufacturer published operating range.

Additionally the exit exhaust velocity with the Configuration 7 combustor at both the engine centerline and 50% radius were within the expected range when compared to the stock JetCat trends.

When the cause of the requirement to keep the air starter on was identified, the compressor shroud was honed and adjusted to enable testing without the compressor rotor contacting the compressor shroud with the air starter off. Without the air starter assistance the stable fuel flow limit was decreased to 14 SLPM presumably due to a change in the air distribution inside the combustor. Stable self-sustaining engine operation was achieved at 14 SLPM of propane and 14,100 RPM. This test represents the first self-sustaining operation of a UCC powered turbine engine. Many of the performance parametersat this engine configuration were comparable to the stock JetCat, but the self-sustaining Configuration 7 engine achieved a higher exit temperature and a TSFC that was better than the stock JetCat trend.

An additional non-rotating study was conducted using the configuration outlined in Objective 4 with additional pressure instrumentation to try and determine the cause of the combustor flameout beyond 19 SLPM of propane. It was quickly discovered that the suspected cause resulting from propane back-pressuring the primary zone air inlets was not the issue. Several tests were conducted with this setup that included: a cold flow 0.03 kg/s fixed air flow rate while ramping fuel from 0 to 22 SLPM, reacting operation at 0.03 kg/s fixed air flow rate while ramping fuel from 0 to flameout, a 17 SLPM and two 18 SLPM fixed fuel flow rates with ramped air flow rates, a high-speed pressure acquisition test that was time synced to temperature data with a fixed 0.03 kg/s air flow rate with ramping fuel from 18 SLPM to flameout, and a study of the fuel distribution effects by independently controlling the ID and OD fuel supply. Based on results from all of these tests it was hypothesized that the real cause of the flameout was due to the primary zone reactions being pushed

out of the cavity. The combustor experienced transient instabilities above 18 SLPM which partially pushed the reactions out of the cavity, but the combustor was able to recover. By 21 SLPM of fuel flow the instabilities were too strong and the reactions were completely pushed out of the primary zone leading to flameout.

While the Configuration 7 engine was not able to be tested across the entire JetCat operating range, the comparable performance between the stock and Configuration 7 combustor obtained from the available test points showed that a UCC that fits within an engine casing and still achieves a 33% shorter axial length compared to the stock combustor is not only feasible, but worth further future investigation.

X. Conclusions & Future Work

This section provides a summary of the major research activities and findings with a specific focus on activities that led to the completion of the five research objectives. The overall research plan was to advance the UCC program on four fronts; 1) cooling UCC turbine vanes to enable future high pressure operation, 2) advanced computational modeling of UCC systems, 3) system air split control and combustion characterization with alternate fuel injection designs, and 4) development of a new UCC orientation to correct exit temperature profiles and fit inside an engine case. The primary goal of of this research was to achieve self-sustaining operation with a small-scale UCC powered turbine engine. This goal was achieved through the completion of five supporting objectives.

10.1 Objective 1

Determine the viability of UCC vane cooling using coolant extracted from the core flow through the vane stagnation region

The unique component configuration of the UCC combustor relative to the UCC turning vanes enabled a novel cooling scheme to be studied that used free stream air ingested through the stagnation region of the vane as coolant. This design eliminated the need for compressor bleed air and could result in an engine efficiency boost by allowing all the air the engine takes in to be pressurized to the maximum capability of the compressor. The goal of the objective was to determine if this type of cooling scheme was possible and if sufficient pressure head could be built up inside the vane to enable film-cooling on the vane suction surface.

The initial feasibility study and geometry trade-off analysis was conducted numerically with a model that included complex fluid flows, chemical reactions, and conjugate heat transfer. This initial concept study focused on several internal ge-

ometry variations until a design was found that resulted in an internal pressure rise compared to the pressure on the suction surface, and reduced the surface temperatures compared to a baseline solid vane. It was found that film-cooling holes needed to be placed downstream of 50% axial chord to ensure coolant would flow out. The pressure differential across the vane skin from internal to external was sufficient enough to achieve a film-cooling blowing ratio that ranged from 0.29 to 0.56 in all 3 holes that were downstream of 50% axial chord.

An additive manufacturing approach was used to produce a single piece, six-vane, stagnation cooled HGV to enable experimental testing in the AFIT UCC test rig. Due to the requirements of the printing process a matrix of internal pins was needed to support the thin vane walls. This vane also featured a modified film-cooling hole pattern that positioned all of the holes downstream of 50% axial chord. Prior to receiving the printed part an additional computational study was conducted on the vane with internal support pins that was compared to the results found in the initial study. The pins caused a 15% drop in mass flow rate through the vane which also resulted in a nominal 14% reduction in blowing ratio in each hole. Even with this reduction, the blowing ratios still ranged from 0.44 to 0.97. As a benefit, the pins caused the transition point of the pressure differential to shift from approximately 45% to 33% axial chord. This movement would enable cooling holes to be added to the suction surface closer to the leading edge. The computational results also showed that the pins caused local increases in overall effectiveness on the vane surface.

The manufactured vane was experimentally tested and the results validated the computational findings. The trends in pressure and surface temperature were also validated, but with some deviation. A comparison of the experimental and computational results showed good agreement in the pressure drop from the vane leading edge to the 85% axial chord internal pressure measurement. Additionally, the experimen-

tal test confirmed a positive internal pressure relative to the suction surface pressure to enable film-cooling. The experimental temperatures at two measurement locations demonstrated that the cooled vane achieved an average surface temperature reduction of 5.3% at 60% radial span and 1.9% at 90% radial span compared to the solid vane. Since the film-cooling scheme was designed for flow analysis and not specifically for cooling, the surface temperature reduction on the cooled vane was almost exclusively from internal cooling.

This objective sought to determine if a cooling scheme that extracted coolant from the free stream through the vane stagnation area was possible. The initial computational study showed the cooling concept was possible, and thus answered the objective. However, the research activities extended far beyond showing feasibility to include a physical demonstration of the cooling ability and a validation of the computational model and results.

Future work in this area could be conducted to apply a film-cooling scheme designed for surface temperature reduction to achieve additional cooling. Furthermore, the shape of the UCC turning vanes was taken from the baseline geometry that was not designed for a maximum suction surface pressure drop. If the vane could be reshaped to achieve an external pressure reduction further upstream than 33% axial chord, film-cooling could be applied closer to the vane leading edge to help cool the hottest region below the circumferential cavity. Finally, this fluid ingestion and transport technique could be investigated as a means to provide non-vitiated air to small rectangular cavities in the suction surface of turbine vanes to serve as pilot burners in an intraturbine burner.

10.2 Objective 2

Numerically investigate the effect of conjugate heat transfer on reacting flow analysis in the baseline UCC model

It is easy to see the benefit and utility of conjugate heat transfer modeling in numerical surface temperature studies, such as the analysis conducted for Objective 1, but the effects of inclusion of conjugate heat transfer on a gas temperature study are not as clear. Objective 2's goal was to conduct a numerical study of the UCC with conjugate heat transfer to determine the effect on gas temperature distributions in the circumferential cavity and at the exit of the combustor. Previous analysis used an adiabatic domain, so this model was also run for comparison with the results from both models compared to experimental data.

The numerical study using an adiabatic model and conjugate heat transfer were run at a rich and lean combustion condition producing a total of four sets of computational results. Within the circumferential cavity temperatures were generally approximated within 10% by either model when using planar averages. The circumferential cavity region was dominated by high temperature gradients both computationally and experimentally making exact comparisons difficult. Temperature variations of up to 200 K have also been recorded experimentally for the same operating conditions from day to day depending on a number of external environmental factors which impacted how the reaction distribution set up that day. This initial study did not include the effects of the conjugate model on velocity determination within the circumferential cavity. However, it was shown in a smaller boundary condition study as part of Objective 3 that the temperature of the air drivers plays an important role in establishing bulk cavity velocities. For this reason the conjugate model was recommend for cavity analysis.

At the two positions near the exit plane the benefits of the use of the conjugate model were more pronounced. The conjugate model provided a realistic metal temperature and accounted for flame quenching at the walls. Additionally, the temperature distribution at the TFP plane was more closely approximated in both pattern

and magnitude by the conjugate model. The conjugate model achieved temperature magnitudes on par with the experimental result. The adiabatic model over-predicted the temperatures by more than 300 K because it was not able to use the metal vane surfaces to disburse heat and reduce the fluid temperature as it traversed downstream toward the combustor exit. The conjugate model more accurately approximated the experimental exit temperatures and also matched the experimental exit temperature distribution. If the exit temperature distribution pattern is the only item of interest, and the magnitude of the temperatures is not important, the adiabatic model offers a more simplistic solution with a similar pattern result.

In many UCC studies the temperature distribution and magnitude at the combustor exit plane are both important. For this reason the conjugate model was determined to be beneficial to the UCC analysis by providing a better approximation of the real result. In addition to the more realistic gas temperatures, the ability to predict the metal component temperatures, and the ability to limit error associated with incorrect boundary condition specifications by having the code calculate the fluid/metal boundary values was deemed worth the additional computational expense.

The goal of the objective was to investigate the effect of the addition of conjugate heat transfer to a reacting flow numerical simulation of the UCC. This objective concluded by showing the benefits of the conjugate solution. For all subsequent computational analysis, conjugate heat transfer was applied to the metal surfaces of interest with external boundaries specified as an adiabatic surface or by a constant temperature.

10.3 Objective 3

Investigate the impact of airflow split ratio between the core and circumferential cavity and alternate fuel injection schemes on tangential velocity, combustor performance, flow path pressure balance, and Rayleigh losses

Prior UCC common flow source experimental research demonstrated difficulty in achieving the desired core-to-cavity air flow split. If the desired split was achieved, it was then difficult to reconfigure to test a different flow split. For this reason a variable geometry diffuser was developed and characterized to enable testing of the UCC at a variety of core-to-cavity flow splits without hardware changes. The diffuser had the ability to precisely position radial splitter vanes to control the area split ratio. The objective of this research was to determine the impact the air flow split had on combustion, pressure, and loss properties in the baseline UCC fuel injection scheme as well as alternate injection schemes.

The initial characterization tests with the baseline fuel injection scheme was successful in demonstrating the ability of the variable geometry diffuser to maintain a constant cavity mass flow rate at both fuel-lean and fuel-rich conditions for a range of total air inlet mass flow rates. Additionally, the diffuser was able to be adjusted to maintain constant core-to-cavity flow rate splits across the same total air inlet mass flow rates. A comparison of Rayleigh losses in the current study to past UCC results that used independent core and cavity air supplies showed comparable results. This outcome shows the variable diffuser was able to control the air flow splits without introducing additional pressure losses. As demonstrated, the pressures losses in the UCC with the variable geometry diffuser were approximately 36% lower than a comparable set of components from a traditional combustion system.

A series of tests were conducted that maintained a constant cavity mass flow rate independent of the total inlet mass flow rate. In these tests the average cavity temperature, velocity, and combustion frequency response remained reasonably constant at the fuel-lean conditions. At a fuel rich condition it was found that the frequency response from a high-speed chemiluminescence video of the combustion event matched the frequency obtained by calculating the number of times a fluid particle could travel

around the combustor annulus at the cavity fluid bulk velocity. This result indicates that there may be a rotating flame front that travels around the annulus at fuel rich conditions with a cavity mass flow rate split greater than 30%.

At a constant core-to-cavity mass flow rate split of 74/26, the results at fuel-lean and fuel-rich conditions in the Baseline combustor produced different combustion behaviors. For the fuel-lean cases the average cavity velocity, frequency, and Rayleigh losses increased with increasing total inlet mass flow rate. At fuel-rich conditions the cavity temperature and velocity, and system Rayleigh losses, initially increased to a peak at the 0.108 kg/s total inlet flow rate case, then decreased with increasing total inlet mass flow rate. The reduction of these values was due to the geometry of the fuel injectors and the additional fuel present in these rich cases. The frequency response of these fuel-rich cases showed a decrease in both frequency and amplitude with increasing total inlet mass flow rate.

A computational and experimental study was conducted on a 6-Step outer combustor ring that enabled near tangential injection of fuel and air from the combustor OD. The results of this analysis showed that when fuel and air were injected from every step, there was a lack of recirculation behind the step, and thus a lack of flameholders in the cavity. With 1% air injection from the 6-Step Ring, the steps served to stabilize the flame in the circumferential cavity and stable operation was achieved. PIV tests confirmed the experimental results matched the computationally derived cavity velocities and the cause of the flameout was solidified as a lack of flameholders.

A 12-Step combustor ring was then computationally analyzed and experimentally tested that injected fuel and air from every other step, and fuel only from the alternate steps. This pattern enabled tangential injection from half of the steps to drive the bulk fluid at a high rate of speed while maintaining flameholders behind the fuel only steps. At a 74/26 core-to-cavity split with a 50/50 front wall-to-outer ring cavity air

split this design was shown computationally to achieved a significant improvement in centrifugal loading compared to the baseline combustor. However, this operating condition did not burn during experimental testing. The combustor performance was improved at conditions with a slower tangential velocity, and burned the best at centrifugal loadings of only $18g_e$ - $77g_e$. Even with the reduction of centrifugal loading compared to the Baseline combustor, the 12-Step combustor demonstrated a significantly wider operating range up to cavity equivalence ratios of 3.60.

Operating maps were created at three total air inlet flow rates with four levels of back-wall fuel injection ranging from 0 - 30%. The back-wall injection disbursed the fuel within the cavity and enabled a lower cavity equivalence ratio at the outer diameter of the annulus, typically resulting in increased cavity temperatures. The operating maps demonstrated control over the UCC performance through the use of the variable diffuser to produce a number of varying flow splits. Changes in global equivalence ratio and fuel distribution within the 12-Step combustor were shown to have little to no impact on the size of the operating map. A flameout line was identified on the maps that was consistently positioned at a step air jet velocity to fuel jet velocity ratio of 2.13.

Across all of the fuel injection schemes tested, the air mass flow rate split between the core and circumferential cavity had a distinct impact on the cavity flow and combustion properties. It was found that cavity temperature and velocity behaviors could be replicated by different total air mass flow rate cases by changing the core-to-cavity flow split to direct the same flow rate of air and fuel to the cavity in both cases. Additionally, the operating maps generated in the 12-Step Ring analysis highlighted how variations in the air and fuel balance throughout the combustor changed the temperature, velocity, and acoustics in the cavity. Having fine control over these distributions means the combustor is tunable to optimize performance for the given

total flow condition and adapt to environmental changes day to day. The operating maps also showed that the 12-Step Ring maximum cavity temperatures were achieved at the lowest tangential velocities. This result may indicate that there is more of a benefit from the residence time increase due to the UCC circumferential flow path then from a centrifugally loaded combustion enhancement.

A study of fluidic oscillators was included as part of the fuel injection analysis as an alternative enabling a larger coverage region for the fuel spray. The oscillator behavior was tested with no co-flow, one sided co-flow, and two-sided co-flow with the oscillating gases issuing from the face of a backward-facing step representative of the 12-Step Ring. A total of four oscillator configurations were numerically and experimentally tested with two of the four designs performing well in the experimental tests. A non-oscillating baseline model represented the fuel injectors from the 12-Step Ring served as a basis for comparison.

High-speed schlieren imaging was used to observe the flow pattern from the oscillator and the interaction of the oscillator with the recirculation behavior behind a backward-facing step. While the V2 Single and V2 Double linked oscillators improved the distribution of fuel behind the backward-facing step at slow wind tunnel flow speeds, the results were comparable to the baseline, non-oscillating jets at high wind tunnel flow speeds. Computational results for frequency and oscillator sweep angle matched well to experimental data in nearly all cases. A new correlation factor was proposed that was based on a Reynolds number and included several geometric values from the oscillator. When the oscillation frequency was plotted against this new parameter the data from both oscillator types (single and double) collapsed to form a single line with a 0.97 R^2 value. This is the first known correlation between oscillator geometric properties and the oscillation frequency. The oscillation angle was correlated to the Reynolds number with a hydraulic diameter reference length. This

correlation was strong for the V2 Single oscillator, but did not display the same correlation strength for the V2 Double oscillator using either of two different oscillation angle measurement methods.

The flow patterns for the Baseline, non-oscillating jets, the V2 Single oscillator, and the V2 Double linked oscillator were dependent on the velocity ratio between the CO_2 jet velocity and the bulk velocity below the model step. Each of these three models displayed three distinct flow regimes, but the cutoff velocity ratio between the regimes differed by model. At the conditions where the UCC operated, the velocity ratio was in the third regime for all models and thus achieved very similar flow patterns. At these conditions there was no benefit to using a fluidic oscillator for fuel distribution as the strong recirculation behind the step was distributing fuel effectively across the step face on its own. When the jet penetration depth measurements were plotted against the velocity ratio the data collapsed into an oscillating and non-oscillating group. Trendlines through each group showed a power function produced a strong correlation in both cases. For the same velocity ratio the non-oscillating jets penetrated further off the step face than the oscillating jets.

A new flow pattern was discovered behind the step of the Baseline, non-oscillating jet model that resulted in the typical recirculation along the step face, but also an additional circulation with a perpendicular axis of rotation induced by the additional injection of fluid from the step. This secondary circulation pattern was not observed in the oscillating models likely due to the oscillation pattern itself. At the downward sweep of the oscillator motion the CO_2 jets opposed the secondary flow direction and prevented that feature from forming.

The goal of this objective was to identify the impact of air flow split with the baseline and alternate fuel injection method. As discussed above the diffuser was used to vary the core-to-cavity splits in three fuel injection schemes to identify trends

in tangential velocity, combustor performance, and Rayleigh losses. Additionally, the behavior in the 12-Step Ring combustor was fully mapped. The diffuser was used to overcome changes in the flow path pressure balance due to combustion variations in real-time. The addition of the fluidic oscillator fuel injection study did not contribute to the understanding of how air splits impact combustion performance, but the findings led to several previously unpublished correlations, and a possible explanation of the flameout behavior in the 12-Step Ring combustor.

The bulk of the proposed future work is related to the 12-Step Ring and fluidic oscillators. A quartz backplate was developed and is planned to be tested at AFIT to enable high-speed chemiluminescence, visual imagery, cavity TFP, and velocity profile mapping of the entire circumferential cavity. In the current study air was supplied to the outer ring injectors from a separate mass flow rate controller. A modification could be made to the diffuser housing and UCC front walls to enable the diffuser to supply that air. Additional characterization of the combustion behavior would be required with this air split method. Additional testing is planned with fluidic oscillators of varying sizes paired with gases of varying density and viscosity to determine if the correlations derived in the present study still hold. Finally, a computational study could be conducted using the different combustion models available in FLUENT to determine if one of the other models could have predicted the poor performance and lack of burning at certain conditions in the 6- and 12-Step Ring combustors.

10.4 Objective 4

Determine how cavity configuration influences combustion product migration and the ability to achieve a desirable turbine inlet temperature distribution

Since the introduction of the UCC concept there have been difficulties with achieving a desirable turbine inlet temperature profile. This difficulty stemmed from the fact that the combustion process took place around the outside diameter of the en-

gine and required the hot combustion gases to migrate across a core flow and mix to produce a uniform temperature. Several variations of components in the UCC have been tested over the years to help with this migration, but the relative position of components has not changed since the design was introduced. Additionally, engine designers have been reluctant to use a UCC type combustor because it would require a modification to the engine casing to accommodate the circumferential cavity around the engine OD. This objective was specifically targeted as a modification to the UCC combustion cavity orientation to determine if improvements could be made to the turbine inlet temperature distribution. The response to this objective also addressed the issue of fitting the combustor inside the casing while maintaining the axial length savings desired from the UCC.

To have a target size to design to a new circumferential flow combustor was designed and tested to integrate into a JetCat P90RXi. The new combustor needed to achieve the same temperature profile at the inlet to the turbine while realizing a 33% reduction in the axial length. Several aspects to achieve this design were investigated including the ability to maintain a high-g swirl in the primary combustion zone, maintain combustion stability, control the fuel injection to achieve the required residence time, and achieve a uniform temperature distribution at the turbine rotor inlet. All of the proposed combustor variants included a circumferential cavity that exhausted downstream rather than radially inward like all previous UCC versions. This component arrangement eliminated the need for migration across the core flow and enabled a dilution zone to be established just downstream of the circumferential combustor to mix the hot gases with the free stream. This arrangement also shrunk the diameter of the cavity enabling it to fit inside the engine casing.

The initial trade space was investigated with a computational study of seven combustor design variations developed in an iterative manor. One of the major outcomes

found in the analysis of these designs was that the desired injection velocity was only controlled by the pressure distribution in and around the combustor. The combustor variations utilized a stepped outer ring, and in later iterations a stepped inner ring as well, to maintain stable combustion as demonstrated in the analysis for Objective 3. In later iterations fuel was injected radially from the OD wall between the air injectors and stabilizing steps, as shown for Configurations 6 and 7, to allow for premixing before reaching the stabilizing steps to ensure a stable pilot flame. Fuel injection from the face of stabilizing steps did not allow for sufficient residence time for complete combustion in this combustor orientation.

The final two iterations were dual-chamber combustors which maintained circumferential swirl in the primary zone followed by an axial flow dilution zone. In the earlier combustor configurations that attempted to maintain swirl through the dilution zone, the incoming air formed a cool air layer on the ID and OD of the combustor and forced the hot reacting products to the center with minimal mixing. When an axial flow secondary/dilution zone was analyzed, mixing was greatly enhanced and a more uniform temperature distribution was achieved. In Configuration 7 a near ideal temperature profile was computationally produced with the peak temperature occurring with a slight OD skew from the passage centerline for maximum power extraction from the turbine.

An additional off-design computational analysis was conducted on the Configuration 7 combustor which showed repeatable and predictable behavior across the operating map. All test conditions produced a cavity equivalence ratio of approximately 1.55 with an air flow split of approximately 19.6% to the primary zone. Additionally this analysis showed manageable pressure losses across the combustor that peaked at 6.61%, but will require optimization in future iterations to reduce this value.

Experimental validation testing confirmed positive combustion behavior and com-

pared well to computational data in temperature with explainable deviations in pressure. This combustor design fixed the flow migration issues from past UCC configurations by achieving a radially symmetric exit temperature profile with an average experimentally derived pattern factor of 0.15. Experimental combustion temperatures were comparable to the stock JetCat, however, the Configuration 7 combustor achieved these values with a 33% shorter combustor. Thus providing evidence that a UCC can produce the same thermal inlet conditions to a turbine at a substantially shorter axial length.

The combustor demonstrated a flameout behavior at fuel flow rates above 19 SLPM. At the conclusion of this objective the cause of the flameout was thought to be due to the high volume of propane that was injected into the combustor primary zone back-pressuring the primary zone air inlets to reduce air flow and combustion stability and ultimately lead to flameout by 21 SLPM of propane. The cause of the flameout was not determined until further analysis was conducted in Objective 5.

The outcome from the objective was to determine how cavity configuration influenced product migration and the ability to produce a desirable temperature distribution at the turbine inlet. The new combustor orientation was a major departure from the previous UCC designs and eliminated the migration of hot gases. Computational results showed favorable combustor exit temperature distributions, but the experimentally measured distribution was even better, achieving a pattern factor of 0.15. This temperature distribution improvement was accomplished with a combustor that was 33% shorter than the stock combustor and fit inside the same engine casing. All of these achievements address the goal of the objective, but are also major milestones in the UCC design evolution.

There is no planned future work for this objective as the next research step was accomplished in Objective 5.

10.5 Objective 5

Investigate the impact of higher flow rates and pressure ratios on combustion performance, exit temperature distributions, and system pressure losses

The COAL lab air supply system was limited in both flow rate and pressure. As such the maximum JetCat P90RXi operating condition that could be tested was "Idle". Thus the use of an engine as an operational test bed for combustor analysis was the logical next step from the stand alone testing conducted in Objective 4. Using the rotating components of the JetCat would enable flow rates up to 0.25 kg/s and pressure ratios of 2.6, both of these values are double what the COAL lab system could provide. This objective focused on analyzing the Configuration 7 combustor from Objective 4 at higher air flow rates and pressure ratios to determine the impact on performance.

To enable testing of a rotating engine in the COAL lab an extensive effort was put forth to design and manufacture a safety enclosure and integral JetCat test stand with dedicated pressure, temperature, and thrust measurement capability. Additionally, the JetCat electronics were redesigned to enable communication of engine hardware components with the LabView control and data acquisition system. While two issues were found with the new electronics during full engine testing that were not seen in individual component checkouts, these issues were worked around to enable testing.

This test configuration corrected the location of the peak pressure observed in Objective 4 from Station 2 to Station 3, but the magnitude of the Station 3 pressure remained nearly the same. While the rotating hardware did not overcome the flameout issue observed in Objective 4, the Configuration 7 combustor with rotating hardware was able to reach 19,000 RPM and the 1/2 Idle condition which was a point on the stock engine operating line. Across the performance properties that were compared between the stock JetCat and the Configuration 7 combustor, the majority of

them achieved comparable results and/or followed stock JetCat data trends.

During preliminary operational runs the air starter was required to remain on even after ignition was achieved to prevent the compressor rotor from contacting the compressor shroud due to 0.15 mm of play in the bearings. This contact and the cause of the requirement to leave the air starter on was not identified until after a first round of testing was complete. The air starter assisted the combustor in driving the spool and thus obtained a higher engine speed and air mass flow rate for the given fuel flow rate than would otherwise be achieved with a turbine driven by the combustor alone. This assistance also resulted in a higher air mass flow rate and lower global equivalence ratio for comparable fuel flow rates. When the combustor was lit and the fuel flow rate was ramped to the combustor operating limit of 19 SLPM, an additional 13,000 RPM was achieved compared to the starter only. The engine exit temperature was comparable to the stock JetCat value and within the manufacturer published operating range.

After the cause of the requirement to keep the air starter on was identified, the compressor shroud was honed and adjusted to ensure there was no contact from the compressor rotor during operation. During a second rotating test series the engine achieved self-sustaining operation at a fuel flow rate limit of 14 SLPM, 14,000 RPM. This new fuel limit resulted from a change in the air distribution through the combustor when operating without assistance.

Following the rotating study, an additional non-rotating study was conducted using the configuration outlined in Objective 4 with additional pressure instrumentation to try and determine the cause of the combustor flameout. It was quickly discovered that the suspected cause resulting from propane back-pressuring the primary zone air inlets was not the issue. Several tests were conducted with this setup that ranged from cold flow analysis, to reacting flow analysis that varied fuel and air indepen-

dently, to a primary zone fuel distribution study. Based on test results from all of these tests it was hypothesized that the real cause of the flameout was due to the primary zone reactions being pushed out of the primary zone cavity. The combustor experienced transient instabilities above 18 SLPM which partially pushed the reactions out of the cavity, but the combustor was able to recover. By 21 SLPM of fuel flow the instabilities were too strong and the reactions were completely pushed out of the primary zone leading to flameout.

Since the outcome for this objective was specifically focused on observing combustor behavior at higher mass flow rates and pressure ratios, this objective was not completed. The stability of the combustor at fuel flow rates greater than 19 SLPM led to a reduced operating range that did not exceed the capabilities of the COAL lab air system. While the Configuration 7 engine was not able to be tested across the entire JetCat operating range with higher pressures and temperatures, this research was still the first demonstration of a self-sustaining engine running with a UCC. Additionally, extensive analysis was performed on the combustor to identify operational behaviors and determine the cause of the flameout. The comparable performance between the stock burner and Configuration 7 combustor obtained from the available test points showed that a UCC that fits within an engine casing and still achieves a 33% shorter axial length compared to the stock combustor is not only feasible, but worth further future investigation.

There were two issues identified with the redesigned electronics. Both of these issues could be addressed in future work and a new circuit board manufactured for the ECM. Additional analysis should be conducted to determine if there is a way to keep the reactions from being pushed out of the Configuration 7 primary zone. Options may include increasing the axial length of the primary zone or adjusting the position or height of the constriction between the primary zone and dilution zone. A new com-

bustor iteration, referred to as Configuration 11, has been computationally analyzed and manufactured. This configuration is another major departure in the UCC design but has the ability to manually control tangential velocity and centrifugal-loading in the primary zone. This hardware will be tested following the same methodology outlined in Chapters VIII and IX.

10.6 Overall Research Conclusion

This research program was successful in achieving the desired outcomes from the four part UCC advancement plan, as well as achieving the primary goal to produce a self-sustaining UCC powered small-scale turbine engine. The four part advancement served to create UCC tools and greater understanding of the combustion and flow behavior mechanisms in the UCC. While the new UCC vane cooling scheme was not required to enable self-sustaining testing in the configuration tested in Objectives 4 and 5, it does provide a tool to enable future high-pressure testing with alternate configurations more representative of UCC Version 3. The enhanced computational modeling that included conjugate heat transfer was already shown to be beneficial in the Objective 3 and 4 research, but will also be useful in future analysis. The outcomes from Objective 3 demonstrated engine tuning by controlling the air and fuel distribution in the combustor, but also provided insights into mixing and stabilization that were fed into the Objective 4 analysis. Objectives 4 and 5 were linked as the outcome from Objective 4 fed directly into the analysis of Objective 5. These objectives identified a new UCC configuration that fit inside an engine casing, demonstrated a 33% axial length reduction with comparable performance to the stock combustor, and demonstrated self-sustaining engine operation in a small-scale turbine engine powered by a UCC.

Appendix A. Motion Control System Setup

The motion control system used to control the radial position of the turkey feathers in the variable diffuser discussed in Chapter IV and the two axes in the thermocouple rake discussed in detail in Appendix B was made from open-source hardware and software. The hardware consisted of a Raspberry Pi Model 2, Arduino Uno, grblShield v5, 24V power supply, 5V power supply, 9V power supply, and 3 stepper motors. Specific part numbers for the hardware components are provided in Table 60.

Table 60. Part numbers for motion control hardware components

Part Name	Manufacturer	Part Number
Raspberry Pi, Model 2	Raspberry Pi Foundation	100437
Raspberry Pi 5V Power Supply	CanaKit	DCAR-RSP-2A5
Raspberry Pi 7" Touchscreen	Raspberry Pi Foundation	B0153R2A9I
Arduino Uno	Arduino	A000066
Arduino 9V Power Supply	ZJchao	B003XZSZWO
grblShield v5	Synthetos	gShieldv5
24V, 15A Power Supply	Supernight	B007F7S4P4
Stepper Motor (1.3A)	ZJchao	B00C4P382G

The complete electronics setup is shown in Figure 453. The remainder of this appendix describes setup and connection of each component.

A.1 Arduino Uno Setup

The Arduino is designed as a multi-use interface platform. Specific software needed to be loaded into the Arduino firmware to enable it to operate as a 3-axis motion control interface. The Arduino was connected to a computer by a USB cable. An open-source program called "Xloader" was used to flash the grbl hex code to the Arduino. The hex code allows the Arduino to receive g-code and interface with the grblShield to control signal outputs to the motors. A screen shot of Xloader is shown in Figure 454. The "Hex file" input bar allows the user to select the location of the hex

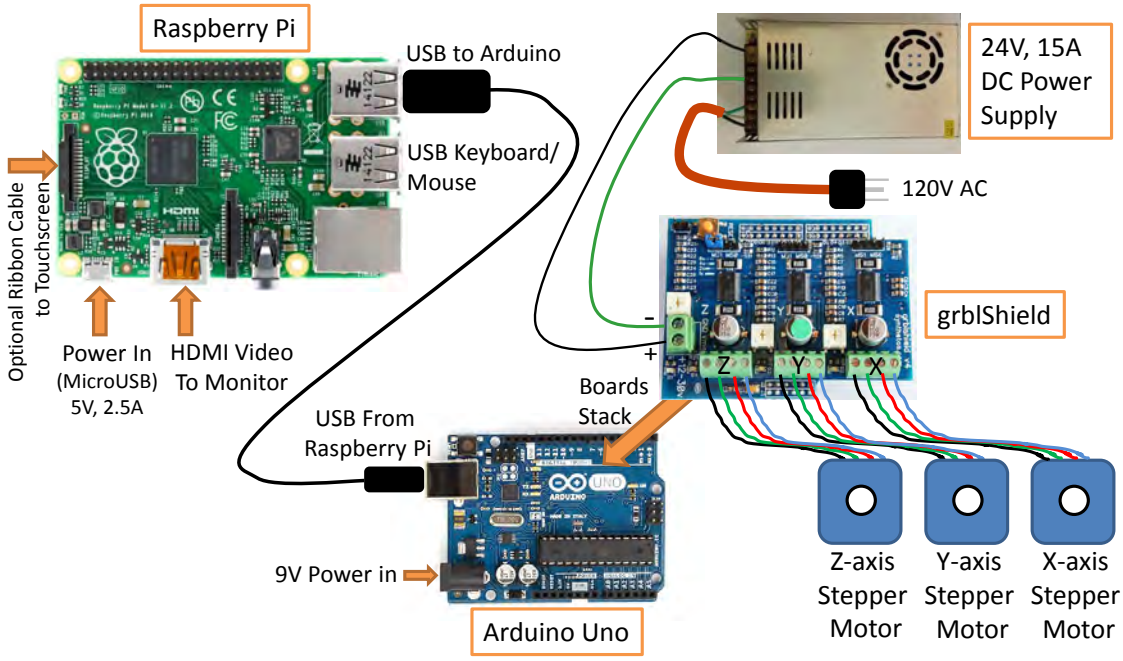


Figure 453. Electronics setup wiring diagram (Stepper motor pin-outs shown later)

file that will be flashed to the Arduino. The "Device" drop down must read "Uno", as in Arduino Uno. COM port and Baud rate were left at the default values. The available COM ports will be computer specific depending on what else is connected to the computer. In many cases the Arduino will be the only device that will show up in the drop down list, but if more devices are listed the Arduino port must be selected. When everything is entered correctly, click the upload button and the program takes care of the rest. The hex file used was *grbl_v0_8c_atmega328p_16mhz_9600.hex*' downloaded from *https://github.com/grbl/grbl*.

A.2 grblShield Setup and Installation

When the hex code was loaded on the Arduino, the next step was to test and install the grblShield on the Arduino. The grblShield is a purpose built board that is only designed to interface with an Arduino and output to an x, y, and z axis stepper motor. To test the grblShield, power was supplied to the board through the 24V



Figure 454. Xloader screen shot

green terminal block (taking care to verify the polarity). The pin-outs for the 24V power supply is shown in Figure 455. When power was supplied, a blue LED was illuminated on the grblShield board indicating it was functioning properly. Power was then removed from the board. The grblShield is designed to stack on the Arduino Uno using built-in header pins. The pins were aligned between the two boards and the connection was pressed together. The grblShield gets its logic power through the header pins from the Arduino. The Arduino can be powered through the USB alone, however, when the grblShield is connected, an external power supply connected to the Arduino is also required. The 24V power supply discussed above is needed to provide the necessary voltage and amperage to the stepper motors. Without that power supply the motors will not turn even if communication is established to the Arduino and grblShield. The power output to each axis can be controlled by adjusting the screw in the white blocks on the grblShield shown in Figure 453. The power to each motor is adjustable to be able to match the required torque on each motor to the drive train it is connected to.

The grblShield includes a built-in micro-stepping capability. It comes set to 8 micro steps per step. A typical step is 1.8° of rotation, but with micro-stepping that same 1.8° rotation takes 8 steps. This is a means of building in more precision without having to upgrade the hardware. If micro-stepping is not needed, a jumper on the

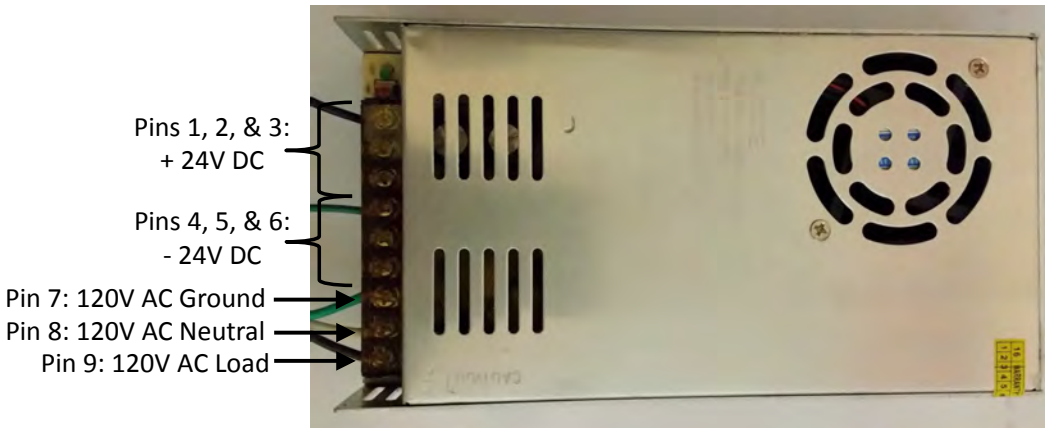


Figure 455. 24V power supply pin-outs

grblShield can be moved to a lower setting.

A.3 Stepper Motion Wire Pair Determination & Installation

With the Arduino and grblShield stacked together the stepper motor wires could then be connected to the x, y, and z-axis terminal blocks in the grblShield. The wires need to be installed with wire pairs next to each other. For a stepper motor, like the one shown in Figure 456, wire pairs can be determined by either checking a wiring diagram or by turning the output shaft. Without any of the wires touching anything, the motor output shaft should turn relatively freely. Next, take two of the four motor wires and touch the metal leads to each other. Keeping the leads in contact, turn the output shaft. If there is more resistance to turning, those two wires are a pair. If it still turns as freely as with no wires touching, try a different pair of wires. For the motors listed above the black and green wires were a pair, and the red and blue wires were the other pair.

To make assembly and disassembly of the test rig easier, Molex connectors were fitted to the ends of the stepper motor wires as a quick release of the motor from the extension wire. Two extension wires were used. The first was a 22/4 wire to

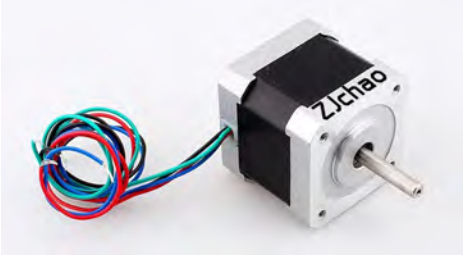


Figure 456. Stepper motor

connect the grblShield to the stepper motor in the diffuser (x-axis channel). The second was a 22/8 wire to connect the grblShield to the two stepper motors in the thermocouple rake (y and z-axis channels). Figure 457 shows the detailed stepper motor wire diagram.

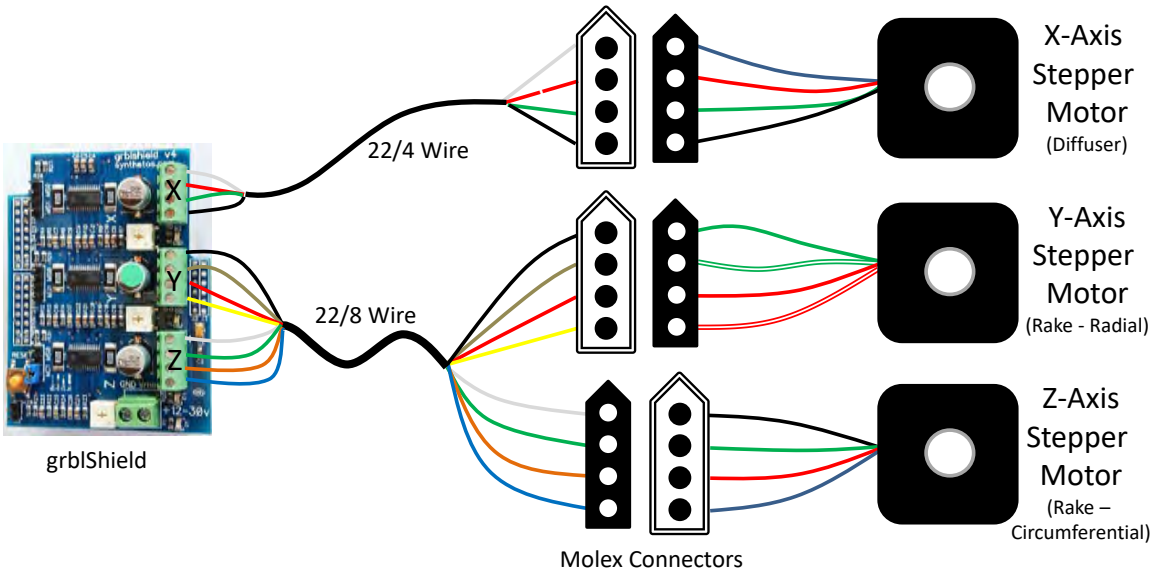


Figure 457. Stepper motor wire diagram detail

A.4 Raspberry Pi Setup

The Raspberry Pi was used as a cheaper alternative to using a larger standalone computer to run the motion control software. However, any computer that can run Java and has a USB port could be used in its place.

Setup of the Raspberry Pi began by formatting a 16 GB microSD card and copying a program called NOOBS to the root directory of the card. NOOBS is available from the Raspberry Pi Foundation website, *https://www.raspberrypi.org/downloads/noobs/*, and stands for "new out of the box." The program is designed to be an easy operating system installer for the Raspberry Pi. With the NOOBS program loaded on the microSD card, the card was inserted into the Raspberry Pi and the board was powered on. At that time the HDMI output was connected to a monitor, and there was a USB keyboard and mouse plugged into two of the USB ports. After power up, the NOOBS program took over and installed the Raspbian operating system on the microSD card.

Raspbian is a Linux based operating system and is easily navigated by using the terminal window. The Raspberry Pi was connected to the internet via its built in ethernet port and a media bridge to connect it to available Wi-Fi. A program called "UniveralGcodeSender" was downloaded from *https://github.com/grbl/Universal-G-Code-Sender*. The program was unzipped and moved to the home directory. The Raspberry Pi has a native capability to run Java based programs, however, the program can only be run from the command line. From the terminal window, with the directory set to the home directory, the program can be called by typing "java -jar -Xm256m UniversalGcodeSender.jar" and pressing enter. The program will open. The program interface and operation is shown in a later section of this appendix.

In addition to using an external monitor (connected to the Rasberry Pi HDMI port), keyboard, and mouse, the Rasberry Pi can also be connected to a 7-inch touchscreen monitor. The screen comes integrated with a display driver circuit board as shown in Figure 458. The white ribbon cable on the left was installed as were the power jumpers (red wire on pin 1, black wire on pin 5).

The Raspberry Pi was mounted on standoffs above the display driver board as

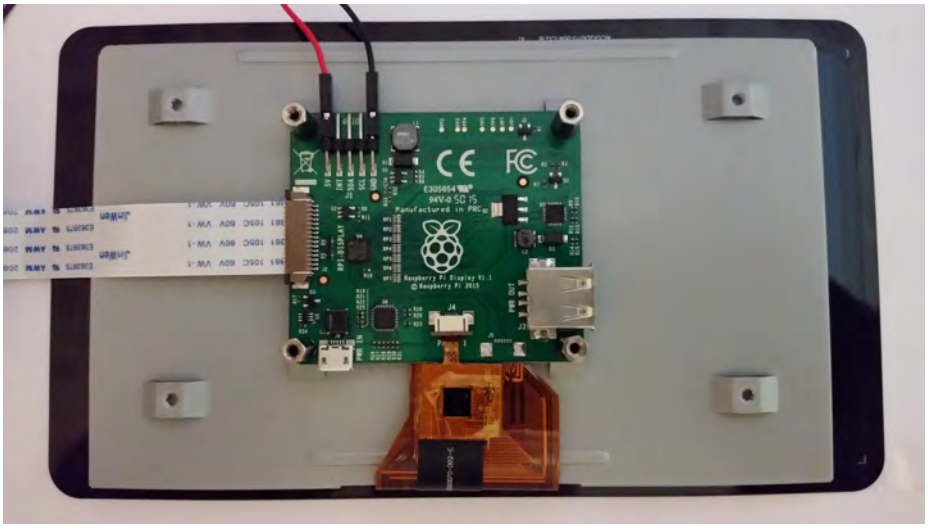


Figure 458. Reverse side of a Raspberry Pi touchscreen

shown in Figure 459. The other end of the ribbon cable was connected to the Raspberry Pi in the ribbon cable block, and the other end of the power jumpers were installed in Raspberry Pi pin 1 (red) and pin 3 (black). The 2.5A power power supply gets connected to the Raspberry Pi micro USB slot and the power is shared with the display driver board through the jumpers. The power supply must supply at least 2 Amps as the touch screen draws a considerable amount of power. Whether the touchscreen is used, or a separate monitor is connected via the HDMI output, the remainder of the wiring to the Raspberry Pi is done in accordance with Figure 453.

A.5 Universal G-Code Sender

G-code is a standardized language used in Computer Numerical Control (CNC) to instruct machines how to move, generally to make a part during manufacturing. The commands include the positioning, where to move, how fast to move, and the path to take. Universal G-code Sender is an open-source Java based program used to transmit the g-code to the controller. In this case the program sends commands to the Arduino where they are interpreted and sent to the grblShield for execution. A

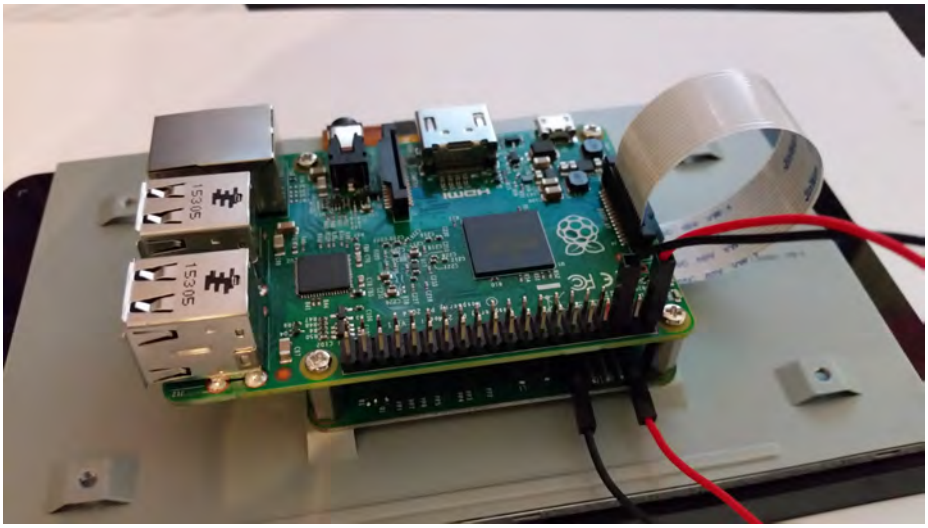


Figure 459. Raspberry Pi touchscreen setup

screen shot of the program is shown in Figure 460. When the program is opened it will open the COM ports that are available. Select the COM port connected to the Arduino, ensure the "Firmware" drop down is set to "GRBL" and press the "open" button to establish a connection.

Commands can be sent to the controller through several methods. The first is using the Universal G-code Sender command line. To command a position, the sequence begins *G01* and then the x, y, and z position to move to. A non-standard feed rate can be specified as well using an "F" command. As an example, if the desired position is x=10, y=15, z=2, at a feed rate of 300, the command string would be:

G01 X10 Y15 Z2 F300

All three axes do not have to be specified each time. *G01 X10* is a valid command if movement is only desired in the x-axis. Also, the feed rate does not need to be specified at all unless the user desires a rate different than the preset rate. The second way to command movement is through the "File Mode" tab in Universal G-

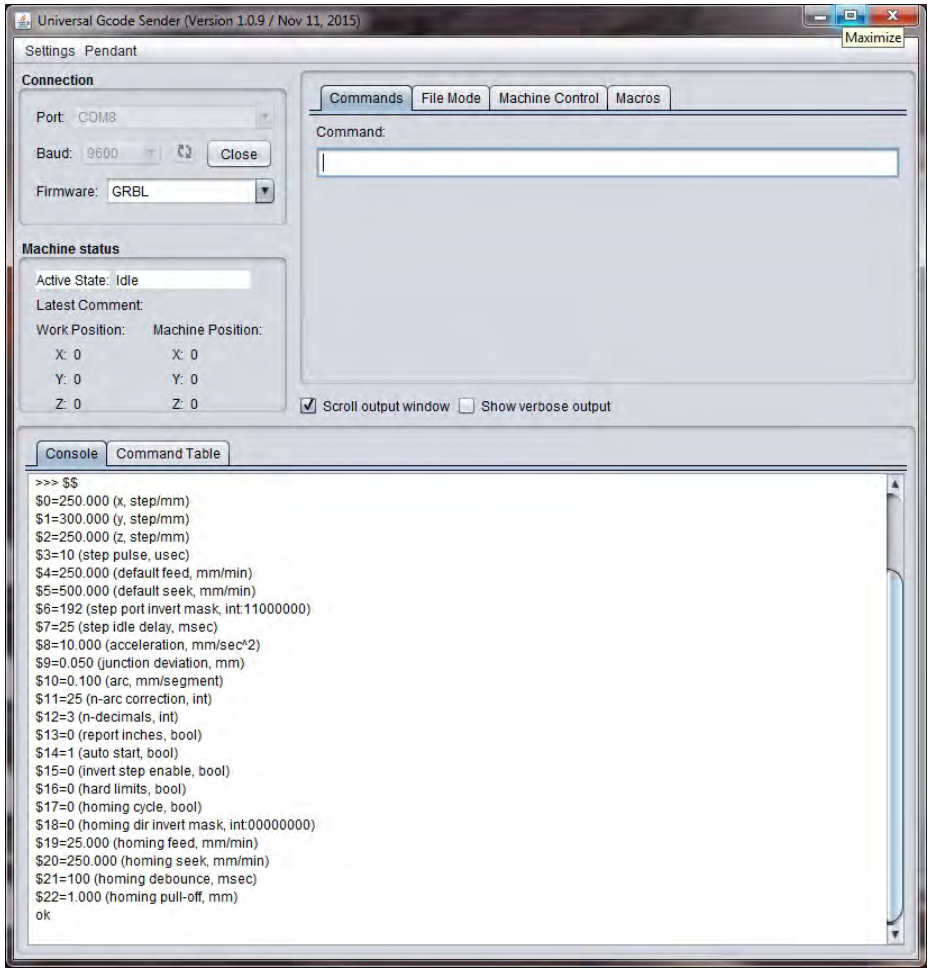


Figure 460. Universal G-code Sender screen shot

code Sender. Using an input file to provide G-code commands is a very efficient method if multiple commands need to be sent in a short period of time. For the application of the thermocouple rake used to measure the UCC exit temperature profile, a command file was generated to perform a serpentine sweep of the probe across the exit area. A dwell was also needed after each position change to allow the thermocouples to get a stable reading before moving to the next point. For a high-resolution sweep there would be hundreds of lines of commands in the input file, entering these by hand would not be practical.

The third option to command movement is with the "Machine Control" tab in

Universal G-code Sender. This tab gives buttons that allows the user to click +/- movement in each of the three axes, reset the position, or return to the zero position as shown in Figure 461.



Figure 461. Universal G-code Sender screen shot, Machine Control tab

Finally, there is the option to create macros in the "Macros" tab of Universal G-code Sender. This tab allows the user to enter five position inputs linked to buttons. Those commands could then be executed by clicking the corresponding button in the Macro tab. This option is useful if there are positions that are used regularly, but a command script in file mode is not needed. Macros were used during the variable diffuser characterization to command the largest five diffuser opening positions.

The command line can also be used to specify command parameters such as the number of steps per millimeter in each axis, the default feed rate, and acceleration, among a number of other options. These options can be accessed by typing *$$* in the command line. The console will display a list of options as shown in Figure 460. To change a parameter, type $ and the item number to change followed by the equal sign and the new parameter level. As an example, to change the number of steps per millimeter in the x-direction the command would be: *$0=300.000*. The default feed

rate was set at 5 mm/min due to the large number of steps per millimeter required for the X axis motion. That feed rate is too low for Y and Z axis motion so when positioning commands are given for those axes a feed rate of 300 mm/min should also be specified. Table 61 shows the required step per millimeter for each component direction to get the desired motion. Keep in mind that the y and z axes are really in the r and Θ direction of a cylindrical coordinate system.

Table 61. Programmed pulses (steps) per millimeter

Axis	Steps/mm	Corresponding Motion
X	101,901.396	Distance of Feathers from OD (mm)
Y	2624.672	Radial Height of Thermocouple Probe (mm)
Z	121.5	Circumferential position of Thermocouple Probe (deg)

To end the session and disconnect from the Arduino click the "close" button.

A.6 Position Sensors

Linear position sensors were used to provide positioning feedback of the X and Y (r) axis positions and an inclination sensor was used to confirm the angle of the thermocouple probe in the Z (Θ) axis. These feedback signals were sent to LabView for confirmation that the commanded position was achieved through a visual interface on the screen, but they were also recorded in the data log as a reference for post-processing. Figure 225 in Chapter IV shows the linear position sensor for the X axis measuring the diffuser opening. Figures 468 and 469 in Appendix B show the linear position sensor measuring the radial position of the probe head and the inclination sensor to measure the circumferential position, respectively. Table 62 shows the specifications for each sensor.

The linear position sensors act as potentiometers with a linear voltage output between 0% and 100% of the input voltage. The inclination sensor operates with a linear voltage output between 0.5V and 10V for an input voltage between 18V and

Table 62. Position sensor specifications

Axis	Type	Used On	Brand	Part Number	Range	V_{in} Max
X	Linear	Diffuser	HGSI	LPPS-025	28 mm	12V
Y	Linear	Rake	HGSI	LPPS-150	15.3 cm	36V
Z	Inclination	Rake	ASM	PTAM27-1-180-U2-CW	180 deg	36V

36V. The National Instruments Data Acquisition Module that these sensors were connected to had a maximum allowable input voltage of 10V. For this reason the two linear position sensors were run on 9V inputs to limit the maximum output voltage while the inclination sensor was run at an input voltage of 20V. A power supply operating with a 20V output was directly used to power the inclination sensor. An LM7809 voltage regulator chip was used to reduce the 20V supply to 9V to power the two linear position sensors. Capacitors were used in the circuit to smooth the +9V power signal. Figure 462 shows a wire diagram of the sensor power supply circuit.

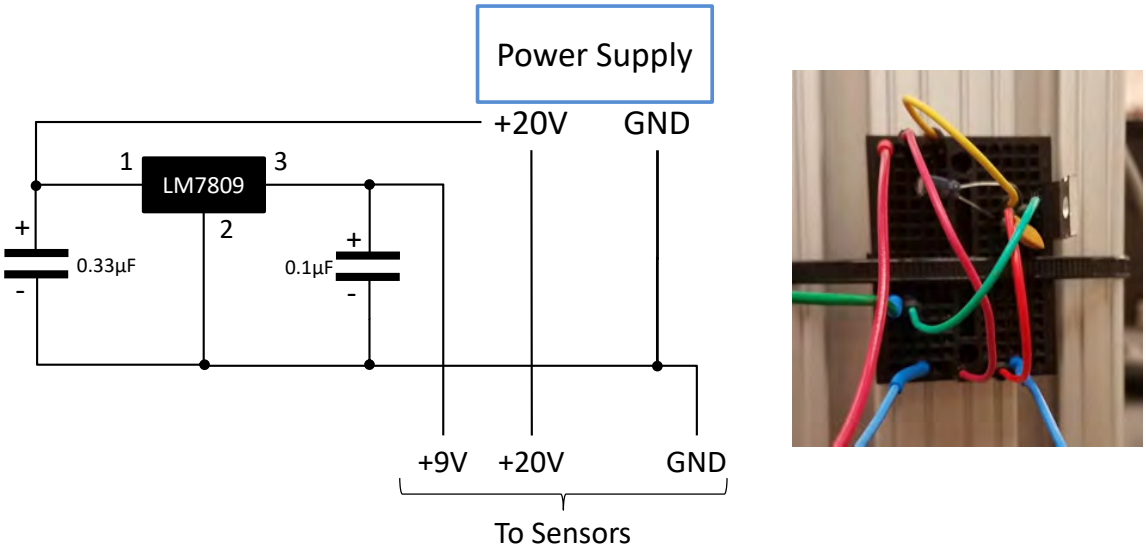


Figure 462. Position sensor power supply circuit wire diagram and hardware photo

The connection between the power supply, data acquisition module, and the sen-

sors were made using a 26/8 wire bundle. Figure 463 shows the wire assignments for the eight wires in the bundle. The sensor end of the eight wire bundle terminates at two 9-pin d-sub connectors. To ensure the correct sensor is connected to the right connector, the diffuser sensor connection is a male connector off the eight wire bundle while the thermocouple rake connector was female off the eight wire bundle.

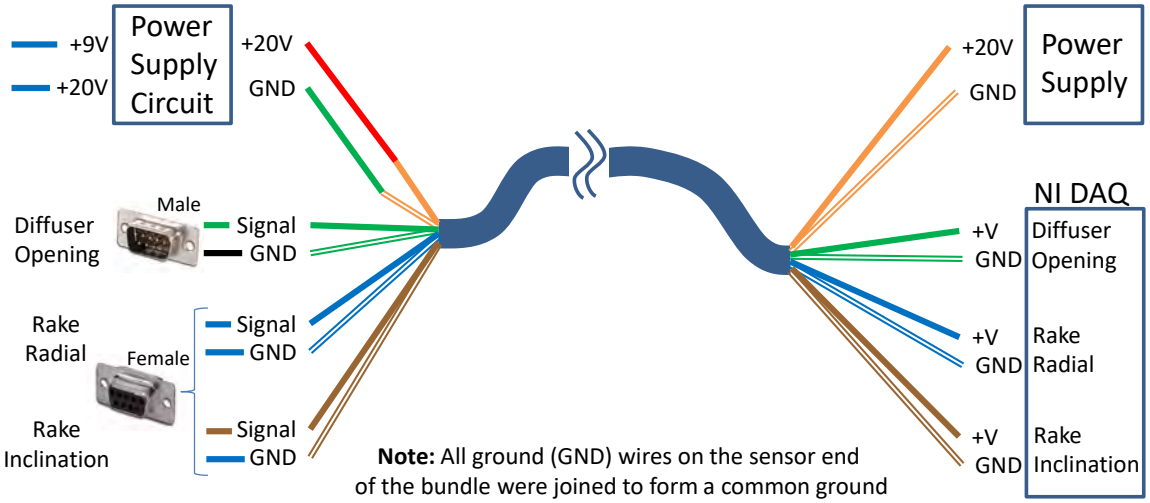


Figure 463. Position sensor wire breakout

Figure 464 shows the pin numbering for the male and female d-sub connectors. Tables 63 through 66 give the pin outs for the male and female d-sub connectors for the diffuser linear sensor and the thermocouple rake linear and inclination sensors. At the sensor end of the wire bundle several wires were joined to form a common ground and common +9V supply. As a result different color lead wires were used to connect the common connections to the d-sub connectors. These wire color changes are reflected in the diagrams and tables.



(a) Male (b) Female

Figure 464. D-sub connector pin numbering

Table 63. Diffuser male d-sub connector pin-outs (connected to the power supply/DAQ)

Pin	Function	Wire color
1	+9V	Blue to common +9V supply
2	Ground	Black to common GND to green/white stripe
3	Linear sensor signal (output)	Green
4	N/A	N/A
5	N/A	N/A
6	N/A	N/A
7	N/A	N/A
8	N/A	N/A
9	N/A	N/A

Table 64. Diffuser female d-sub connector pin-outs (connected to the sensor)

Pin	Function	Wire color
1	+9V input	Brown
2	Ground	Blue
3	Linear sensor signal (output)	Black
4	N/A	N/A
5	N/A	N/A
6	N/A	N/A
7	N/A	N/A
8	N/A	N/A
9	N/A	N/A

Table 65. Thermocouple rake male d-sub connector pin-outs (connected to the sensors)

Pin	Function	Wire color
1	N/A	N/A
2	Inclination sensor ground	Blue
3	Inclination sensor signal (output)	White
4	Linear sensor +9V input	Brown
5	Linear sensor ground	Blue
6	Linear sensor signal (output)	Black
7	N/A	N/A
8	N/A	N/A
9	Inclination sensor +20V input	Brown

Table 66. Thermocouple rake male d-sub connector pin-outs (connected to the power supply/DAQ)

Pin	Function	Wire color
1	+9V Input	Brown to common +9V supply
2	Inclination sensor ground	Blue to common GND to brown/white stripe
3	Inclination sensor signal (output)	Brown (smaller gauge)
4	Linear sensor +9V input	Brown to common +9V supply
5	Linear sensor ground	Blue to common GND to blue/white stripe
6	Linear sensor signal (output)	Blue (smaller gauge)
7	+9V input	Brown to common +9V supply
8	Ground	Blue to common GND
9	Inclination sensor +20V input	Blue to power supply circuit

Appendix B. Thermocouple Rake Actuator

A computer controlled thermocouple rake was created to produce temperature maps at the combustor exit plane. The temperature measurements were taken 6.5 mm axially downstream from the hybrid guide vane trailing edge, but this dimension could be changed by adjusting a set of spacers. The probe head was designed by Mr. Christian Schmiedel, a visiting researcher from Germany, and the traverse, actuation system, control scripts, and post-processing scripts were designed by the author. The full thermocouple rake assembly featured a probe head, circumferential rail, and a two-axis traverse as shown in Figure 465. Due to the presence of the tail cone and the circumferential direction of the exiting gases, the traverse was designed to operate in cylindrical coordinates. Movement around the circular rail provided the theta positioning, and a linear movement on the traverse produced a radial position. The axial position was fixed.

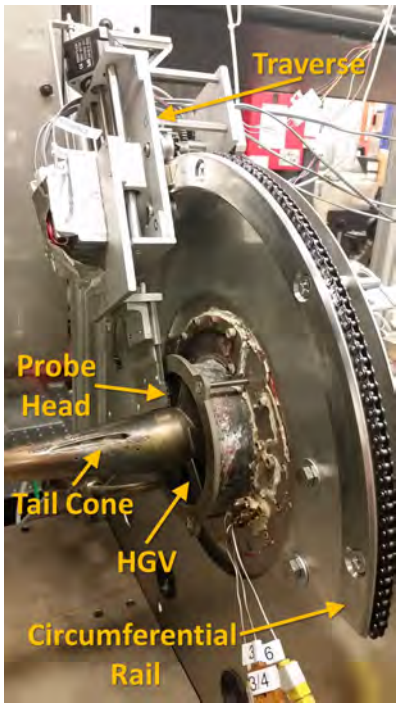
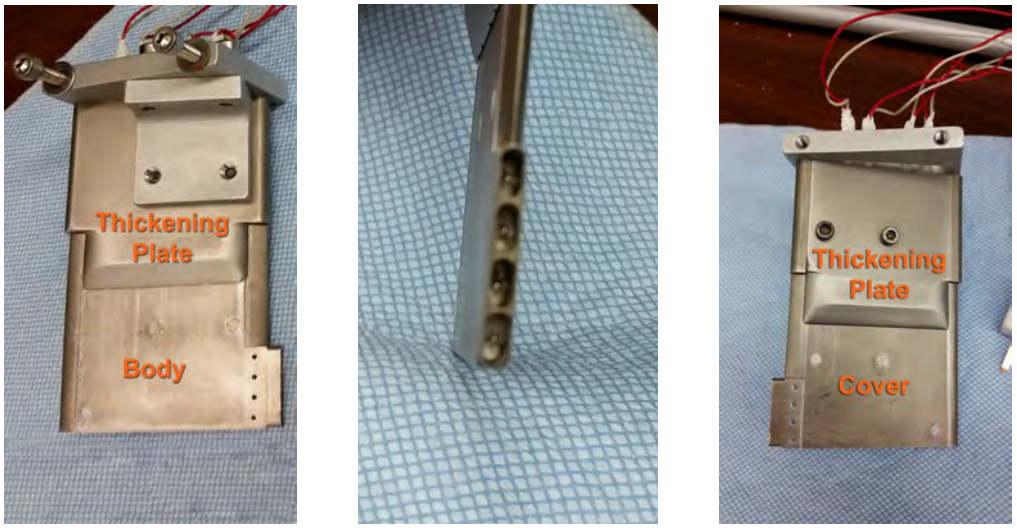


Figure 465. Thermocouple rake assembly

B.1 Probe Head

The probe head was centered around four B-type thermocouples. B-type thermocouples were selected due to their high temperature tolerance (up to 1,700 C). The probe head was made from four separate pieces not including the mounting bracket to the actuation system. The thin central section was made from two pieces; a body and a cover. The main body included the complete kiel heads and internal curved channels from the kiel heads to the upper exit that produced a conduit for the thermocouple wires. The wires were installed in thin ceramic tubes inside the conduit channels to insulate the wires from each other and the metal body. The second piece served as a cover for the curved channels. These two pieces were held together by being clamped between two beveled thickening plates. The same hardware that screwed the thickening plates together was used to attach the head the the actuator attachment bracket. The bracket was designed to attach to either side of the probe attachment plate to give greater control over the probe head positioning. The full probe head assembly is shown in Figure 466.



(a) Probe Left (b) Kiel Head Detail (c) Probe Right

Figure 466. Thermocouple rake probe

The thermocouple beads were located in the center of each kiel head. Figure 467 provides the dimensions of the probe and kiel heads.

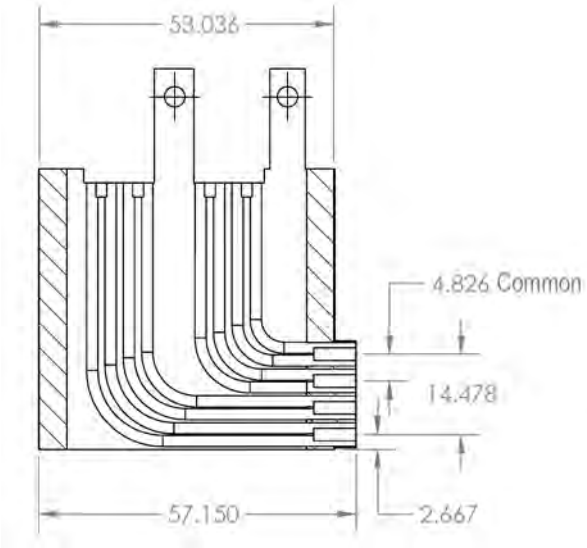


Figure 467. Probe head dimensions and internal channels

B.2 Actuator

The actuator was designed to operate in the cylindrical coordinate system to ensure the kiel heads and thermocouples were always directed into the circumferential exit flow. If a traditional x-y-z Cartesian coordinate system was used, only one position would allow the flow to directly enter the kiel heads, all others positions would cause the flow to enter the heads at an angle. The actuation system was also designed with cost and machining time in mind, so standard off-the-shelf parts were used where ever possible. Figure 468 and 469 show the full actuator assembly. The bottom pair of rail rollers shown in Figure 469 are attached in linear slots. These slots allow the rollers to be moved to adapt to curved rails with a minimum radius of 18 cm all the way up to a linear rail. The circumferential drive system is also adaptable to any radius of curvature including a infinite radius, or a linear rail.

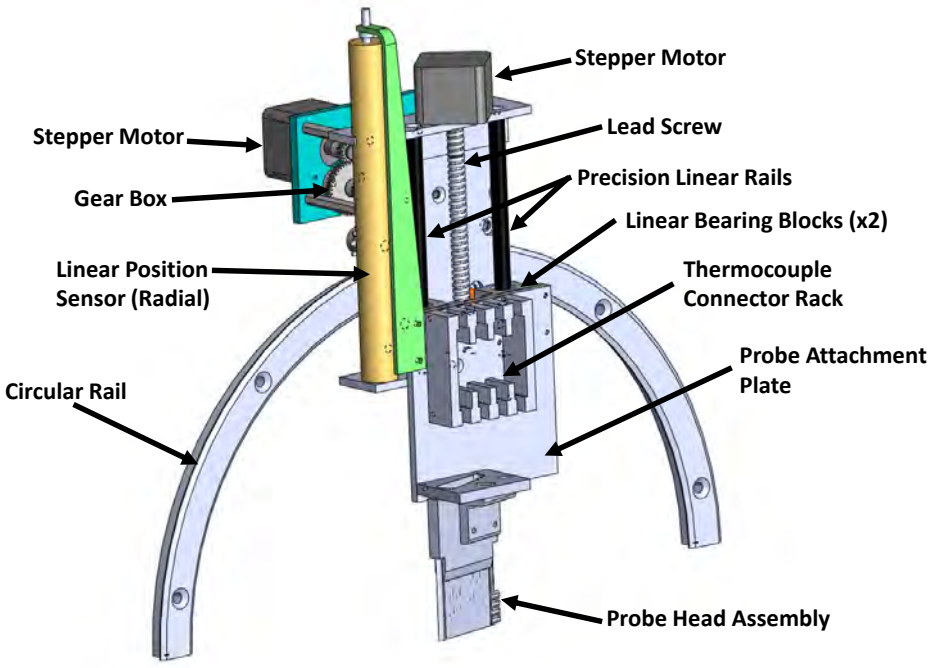


Figure 468. Actuator assembly downstream view

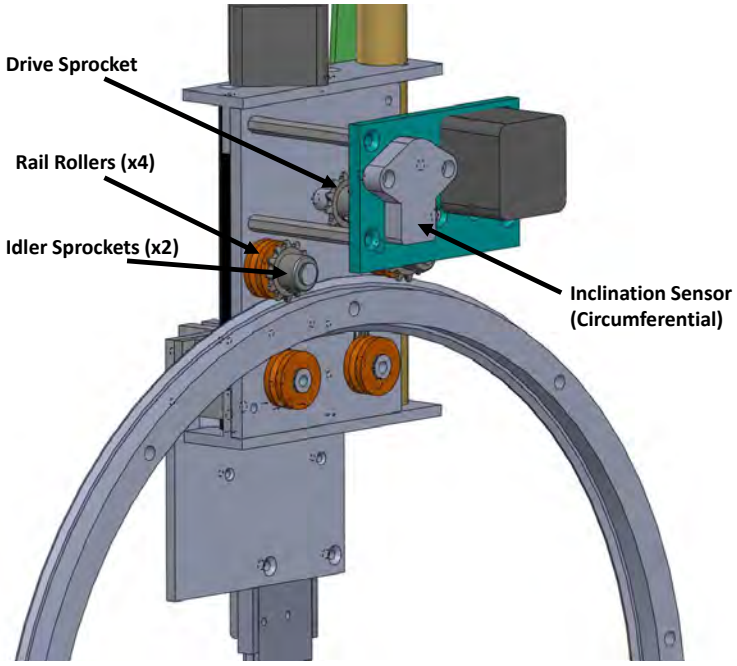


Figure 469. Actuator assembly upstream view

A linear position sensor was used as feedback that the commanded radial position was achieved, as well as to provide a radial position input to the data acquisition system. An inclinometer was used to provide the angle of the actuator which was converted into a circumferential position angle. This value was also recorded in the data acquisition system. The stepper motor connected to the lead screw was used to move the probe head assembly, probe attachment plate, thermocouple connector rack, linear bearing blocks, and lead screw nut in the radial direction. Figure 470 shows more detail of the linear actuation geometry.

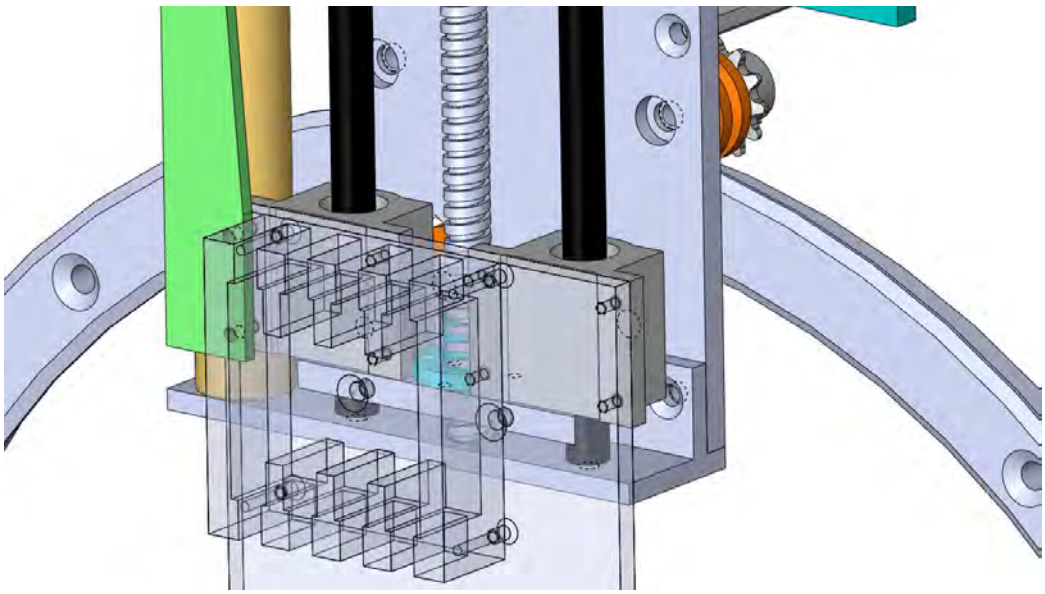
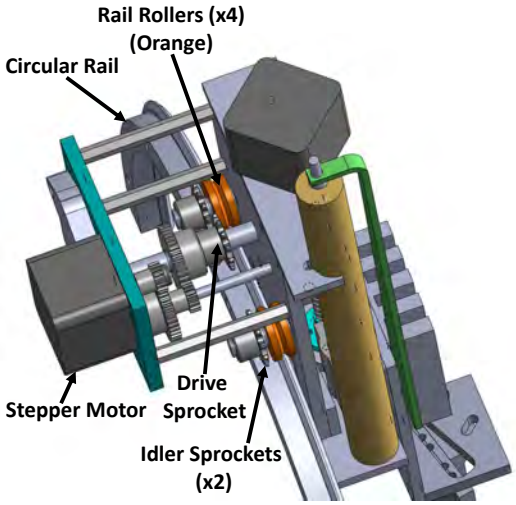


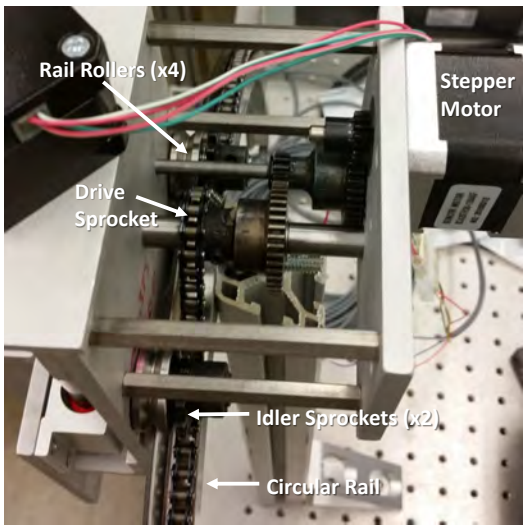
Figure 470. Linear actuator detail (radial movement)

The second stepper motor was used to drive the gearbox. The gearbox had a gear reduction of 6.25:1 to ensure adequate torque to move the entire actuator assembly around the circular rail. The gearbox also produced resistance to help prevent the actuator assembly from moving due to gravity when positioned on either side of top dead center. Figure 471a shows the computer model of the gearbox. Figure 471b shows a picture of the gearbox hardware. Note in this figure the positioning of the chain. The chain was connected to both ends of the circular rail and directed under

both idler sprockets and over the drive sprocket. The drive sprocket was 2.74 cm in diameter and coupled to the output gear from the gearbox. As the motor turned the drive sprocket, chain was pulled up from the leading idler sprocket and pushed down to the trailing idler sprocket. The idlers were positioned just above the rail surface to allow the chain to maintain contact with the rail until it passed under an idler and up to the drive sprocket. Alternate drive options such as worm drives and a direct sprocket drive were considered, but would have required substantially more machining on the rail, and added cost in gearing.



(a) Gearbox (CAD)



(b) Gearbox Picture. The circumferential drive chain can be seen

Figure 471. Thermocouple rake actuator gearbox

While the circular rail was a 180° arc, the actuator was not able to use all of the available rail. The motor and gearbox were strong enough to move the actuator from any starting positioning on the rail, including horizontal, but they did not provide enough resistance to prevent the actuator from traveling to the horizontal position when stopped beyond ±40° from top dead center on the rail. Without the addition of a higher ratio gearbox or a brake system, ±40° is the maximum usable travel. As it is, c-clamps were installed on the rail at the positions of maximum travel to hold

the actuator and prevent it from moving to greater angles on its own. Figure 472 shows the extent of the motion of the actuator with respect to the rail. The black heads of the c-clamps can also be seen in this figure.

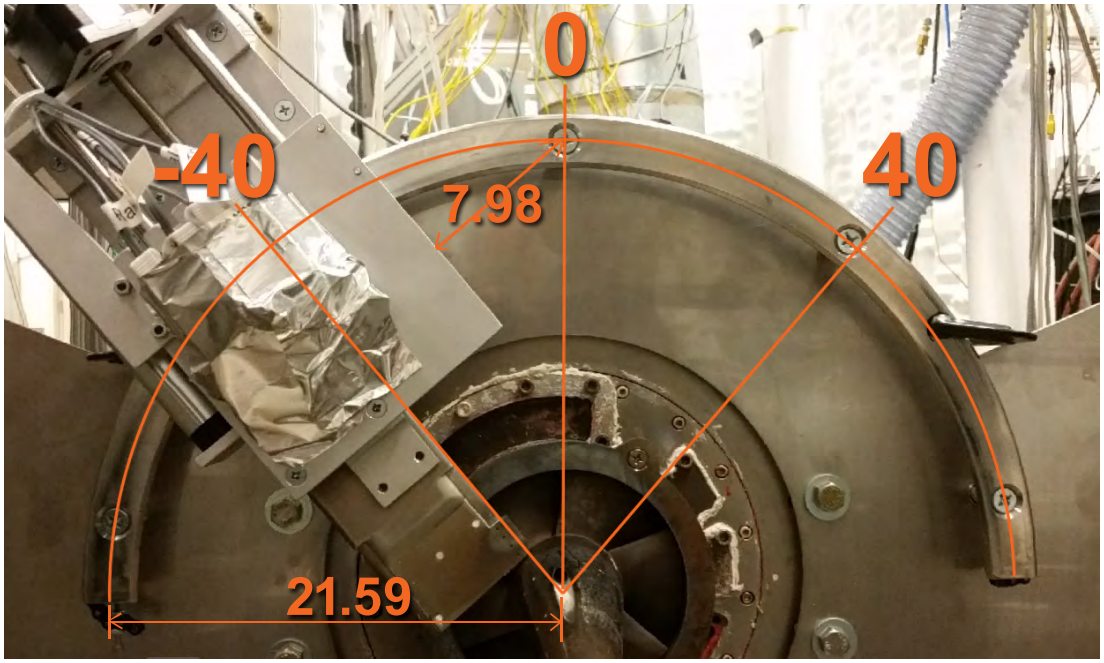
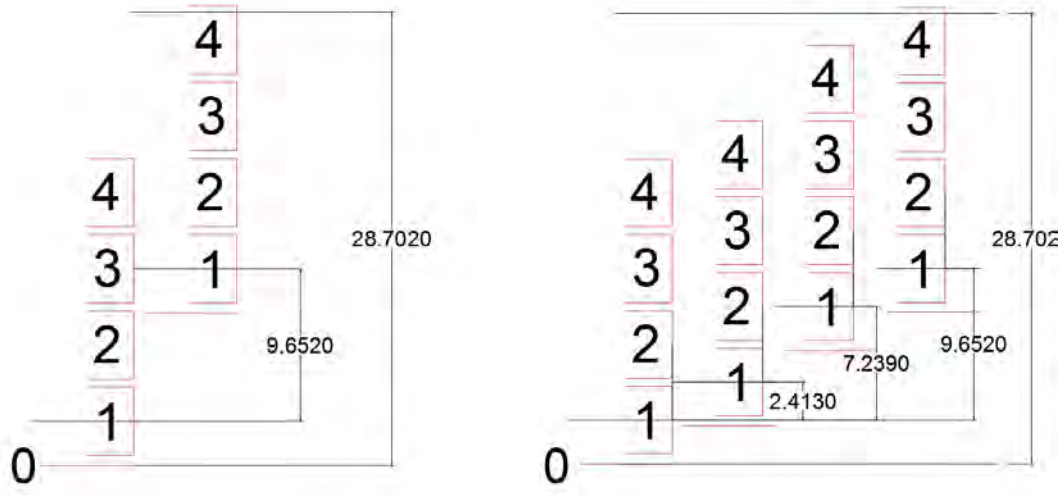


Figure 472. Actuator movement limits (Degrees, cm)

B.3 Probe Head Positioning

The thermocouple rake was designed to take temperature measurements across a sector of the UCC exit in order to map the temperature profile. As discussed in the previous section the circumferential sector was limited to ±40°. The radial span of the UCC exit was 28.7 mm. This dimension was the difference between the 25.4 mm radius of the tail cone, and the 54.1 mm radius of the inner diameter of the exit duct. To cover this span with the current probe, two positioning schemes were developed. The first was a course positioning method that only had one radial movement shown in Figure 473a. This method covered the radial span by dividing it into six zones each measured by a single kiel head. The second method had four radial positions

and covered the span in half kiel head height increments as shown in Figure 473b. These two methods are referred to as the course and half-space method, respectively.



(a) Course (b) Half-Space

Figure 473. Probe head positioning. Each number block represents one of the four thermocouples. Each new set of blocks represents the position after a radial movement. Upper and lower horizontal lines show the bounds of the exhaust channel.

G-code scripts were required to control the positioning of the probe head using the control hardware and software described in Appendix A. Rather than write out each line manually, which could introduce more human error, MATLAB was used to write the g-code input files. The g-code file was produced by running a 'for' loop sweeping through radial positions inside of a 'for' loop sweeping through circumferential positions. The loops allow the minimum and maximum position to be specified along with the resolution of the intermediate steps, or a discrete list of steps can be specified. The script is setup to output a course and half-space g-code file each time it is run. The MATLAB script below is for a 10 degree circumferential spacing. A 5 degree spacing was also tested. To change the circumferential step spacing, the "10" between the colons in the definition of theta would be changed to the desired step size. The g-code generating script is shown below:

```
fileID=fopen('thermocouple_sweep_half_space_10.txt','w');
delay=2; %time delay at each position, seconds
for theta=0:10:80; %deg
    for r=[0 2.413 7.239 9.652]; %mm
        %write radial & circumferential position to file (y=radial,z=circ)
        fprintf(fileID,'G01 Y%4.3f Z%4.3f F300 \r\n', r, theta);
        %write time delay to file to get thermocouple temp to stabilize
        fprintf(fileID,'G04 P%d \r\n', delay);
    end
end
fclose(fileID);
%%%%%%%%%%%%%%%%%%%%%%%%%%%%%%%%%%%%%%%%%%%%%%%%%%%%
fileID=fopen('thermocouple_sweep_course_10.txt','w');
delay=2; %time delay at each position, seconds
for theta=0:10:80; %deg
    for r=[0 9.6520]; %mm
        %write radial & circumferential position to file (y=radial,z=circ)
        fprintf(fileID,'G01 Y%4.3f Z%4.3f F300 \r\n', r, theta);
        %write time delay to file to get thermocouple temp to stabilize
        fprintf(fileID,'G04 P%d \r\n', delay);
    end
end
fclose(fileID);
```

An example of one string written to the text file looks like:

G01 Y9.652 Z10.000 F300

G04 P2

B.4 Post-Processing

The post-processing was done by averaging the temperature for each thermocouple at each position and consolidating them into a text file as shown in Figure 474. Each line in the file corresponds to a measurement location with the circumferential position, radial position, and the average temperature of each thermocouple at that position listed.

The post-processing input file is then read into a MATLAB script that converts the data into a flooded contour map in polar coordinates so it looks like the exit plane

74_LLCB - Notepad

File Edit Format View Help

circumferential	radial	1	2	3	4
0	26.5	482.5722598	484.7438005	494.458418	526.1335623
0	36	486.432325	511.1466295	565.7192745	649.656236
10	26.5	484.8386558	497.9378345	526.9677685	582.455965
10	36	484.313608	516.8882624	583.6782423	657.0365995
20	26.5	484.105485	505.0504506	545.2565878	615.5709848
20	36	509.8703525	583.3380103	653.493925	693.48504
30	26.5	496.4648228	520.3853788	564.5615866	639.2490956
30	36	519.7875174	598.2310393	681.751879	721.9051644
40	26.5	510.4985975	537.394149	586.1510585	681.977272
40	36	519.885097	585.9853575	658.624914	709.951019
50	26.5	542.727727	563.3934623	594.0551568	648.0508973
50	36	541.9494063	578.8259913	611.807995	650.0389473
60	26.5	531.80986	545.5731458	563.6858343	575.2434763
60	36	525.4489225	542.1074928	587.332735	642.5172328
70	26.5	509.3707118	522.6502334	548.8106815	585.184344
70	36	505.5820831	536.5392223	586.2314951	637.2140869
80	26.5	500.6026185	522.3913663	562.7524623	617.4109535
80	36	517.4525703	581.492946	638.2446028	677.6197778

Figure 474. Thermocouple rake post-process input file

of the UCC. The MATLAB script is as follows:

```
% Create polar data:
% data in (r=radial position, t=theta measurement, temp=thermocouple)
display('Please Enter The File Name of the data excluding the file extension');
display('(File format should be a text file, .txt)');

datafile=input('Input Filename:  ','s');
display('Select the correct rake profile (Course=1, Half Step=2)');
mode=input('Rake Profile:  ');
fileName = sprintf('%s.txt',datafile);
data_raw = dlmread(fileName,'\t',1,0); %1 row offset so it doesn't read file data
L=length(data_raw(:,1));
%Data column format
        %column 1 = Circumferential (deg)
        %column 2 = Radial Position (mm)
        %column 3 = Thermal rake temp 1 K
        %column 4 = Thermal rake temp 2 K
        %column 5 = Thermal rake temp 3 K
        %column 6 = Thermal rake temp 4 K

offset=[2.794 7.62 12.446 17.272]; %Kiel head offset from probe tip (mm)
c=130; %plotting circumferential offset to plot in the quadrant data was taken
```

```
% Course
if mode==1;
    temp=zeros(L/2,4);
    t=zeros(L/2,4);
    r=zeros(L/2,4);
for i=1:2:L
    for j=3:6
        if i==1
       %(row,column)
    temp(i,j-2)=data_raw(i,j); %put temp into matrix
    t(i,j-2)=-data_raw(i,1)+c; %circumferential position
    r(i,j-2)=data_raw(i,2)+offset(j-2); %radial position
        else
            k=i/2+.5; %converts i steps to a 1,2,3,4... count
    temp(k,j-2)=data_raw(i,j); %put temp into matrix
    t(k,j-2)=-data_raw(i,1)+c; %circumferential position
    r(k,j-2)=data_raw(i,2)+offset(j-2); %radial position
        end
    end
    for j=5:6
        if i == 1
        %(row,column)
    temp(i,j)=data_raw(i+1,j); %put temp into matrix
    t(i,j)=-data_raw(i+1,1)+c; %circumferential position
    r(i,j)=data_raw(i+1,2)+offset(j-2); %radial position
        else
             k=i/2+.5;%converts i steps to a 1,2,3,4... count
    temp(k,j)=data_raw(i+1,j); %put temp into matrix
    t(k,j)=-data_raw(i+1,1)+c; %circumferential position
    r(k,j)=data_raw(i+1,2)+offset(j-2); %radial position
        end
    end
end

%%%%%%%%%%%%%%%%%%%%%%%%%%%%%%%%%%%%%%%%%%%%%%%%%%%%%%%%
% Half Step
elseif mode==2
    temp=zeros(L/4,11);
    t=zeros(L/4,11);
    r=zeros(L/4,11);
    q=[1 3 5 7]; %indexers
    q2=[9 11];
    for i=1:4:L
```

```
for j=3:6
    if i==1
   %(row,column)
temp(i,q(1,j-2))=data_raw(i,j); %put temp into matrix
t(i,q(1,j-2))=-data_raw(i,1)+c; %circumferential position
r(i,q(1,j-2))=data_raw(i,2)+offset(j-2); %radial position

temp(i,q(1,j-2)+1)=data_raw(i+1,j); %put temp into matrix
t(i,q(1,j-2)+1)=-data_raw(i+1,1)+c; %circumferential position
r(i,q(1,j-2)+1)=data_raw(i+1,2)+offset(j-2); %radial position
    else
        k=i/4+.75;%converts i steps to a 1,2,3,4... count
temp(k,q(1,j-2))=data_raw(i,j); %put temp into matrix
t(k,q(1,j-2))=-data_raw(i,1)+c; %circumferential position
r(k,q(1,j-2))=data_raw(i,2)+offset(j-2); %radial position

temp(k,q(1,j-2)+1)=data_raw(i+1,j); %put temp into matrix
t(k,q(1,j-2)+1)=-data_raw(i+1,1)+c; %circumferential position
r(k,q(1,j-2)+1)=data_raw(i+1,2)+offset(j-2); %radial position
    end
end

    if i == 1
    %(row,column)
temp(i,10)=data_raw(i+2,6); %put temp into matrix
t(i,10)=-data_raw(i+2,1)+c; %circumferential position
r(i,10)=data_raw(i+2,2)+offset(j-2); %radial position
    else
         k=i/4+.75;%converts i steps to a 1,2,3,4... count
temp(k,10)=data_raw(i+2,6); %put temp into matrix
t(k,10)=-data_raw(i+2,1)+c; %circumferential position
r(k,10)=data_raw(i+2,2)+offset(j-2); %radial position
    end

for j=5:6
    if i == 1
    %(row,column)
temp(i,q2(1,j-4))=data_raw(i+3,j); %put temp into matrix
t(i,q2(1,j-4))=-data_raw(i+2,1)+c; %circumferential position
r(i,q2(1,j-4))=data_raw(i+2,2)+offset(j-2); %radial position
    else
         k=i/4+.75;%converts i steps to a 1,2,3,4... count
temp(k,q2(1,j-4))=data_raw(i+3,j); %put temp into matrix
```

```
    t(k,q2(1,j-4))=-data_raw(i+3,1)+c; %circumferential position
    r(k,q2(1,j-4))=data_raw(i+3,2)+offset(j-2); %radial position
        end
    end
    end

%%%%%%%%%%%%%%%%%%%%%%%%%%%%%%%%%%%%%%%%%%%%%%%%%%%%%%%%%%%%
else display('Invalid thermocouple rake profile selection')
end
%%%%%%%%%%%%%%%%%%%%%%%%%%%%%%%%%%%%%%%%%%%%%%%%%%%%%%%%%%%%
% Convert rake data to Cartesian
x = r.*cosd(t);
y = r.*sind(t);
figure
hold on
%plots circles for radial steps of polar axis
silver=[.75 .75 .75];   %Polar axis line color
theta = linspace(0.83266,2.2993);%.87266,2.26893);
xi = 25.4*cos(theta) + 0;
yi = 25.4*sin(theta) + 0;
plot(xi,yi,'Color',silver,'LineWidth',1.5)
hold on
xo = 54.61*cos(theta) + 0;
yo = 54.61*sin(theta) + 0;
plot(xo,yo,'Color',silver,'LineWidth',1.5)
hold on
x25 = 32.7025*cos(theta) + 0;
y25 = 32.7025*sin(theta) + 0;
plot(x25,y25,'Color',silver,'LineWidth',1.5)
hold on
x5 = 40.005*cos(theta) + 0;
y5 = 40.005*sin(theta) + 0;
plot(x5,y5,'Color',silver,'LineWidth',1.5)
hold on
x75 = 47.3075*cos(theta) + 0;
y75 = 47.3075*sin(theta) + 0;
plot(x75,y75,'Color',silver,'LineWidth',1.5)
hold on
%Plot lines for circumferential steps of polar axis
for t=[50 70 90 110 130];   %angles of lines (deg)
    r1=25.4;
    x1 = r1*cosd(t);
    y1 = r1*sind(t);
```

```
    r2=56;
    x2 = r2*cosd(t);
    y2 = r2*sind(t);
    line([x1 x2],[y1 y2],'Color',silver,'LineWidth',1.5)
    hold on
end

%Plot rake data
contourf(x,y,temp, 'LineColor', 'none');

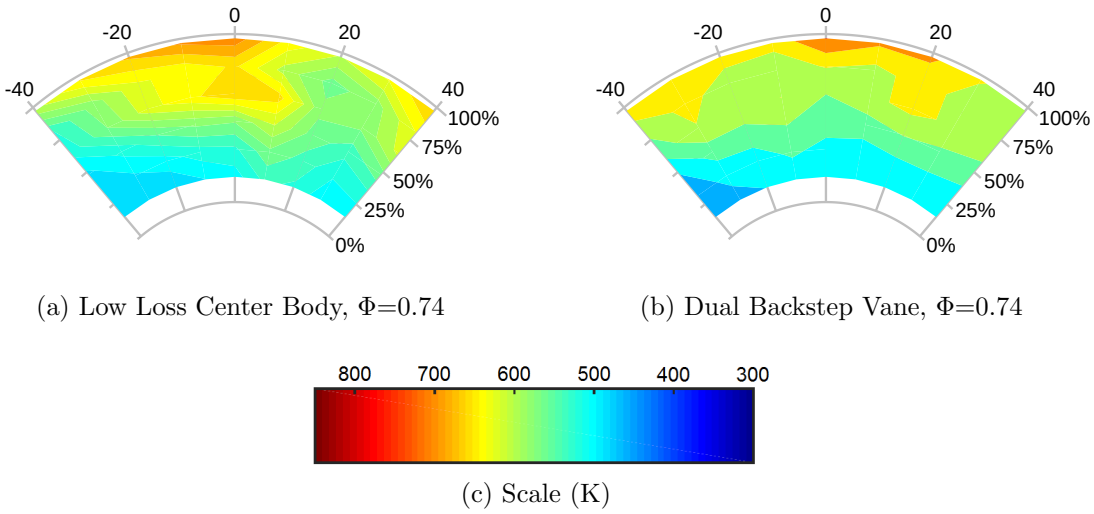
%Add polar axis labels
text(-40,45,'-40','FontName','Arial','FontSize',13);hold on
text(-23,55,'-20','FontName','Arial','FontSize',13);hold on
text(-1,58,'0','FontName','Arial','FontSize',13);hold on
text(18,55,'20','FontName','Arial','FontSize',13);hold on
text(36,45,'40','FontName','Arial','FontSize',13);hold on
text(17.5,18,'0%','FontName','Arial','FontSize',13);hold on
text(22.5,24,'25%','FontName','Arial','FontSize',13);hold on
text(27.5,29,'50%','FontName','Arial','FontSize',13);hold on
text(32.5,35,'75%','FontName','Arial','FontSize',13);hold on
text(37,40,'100%','FontName','Arial','FontSize',13);hold on

%Format Plot Window
axis([-41 47 15 60])
axis equal
axis off
colormap(jet)
caxis([300 850]);
% Comment the three lines below if you do not want a colorbar
     c=colorbar;
     c.Limits=[300 850];
     c.Label.String= '^oK';

%Save Figure as a Correctly Sized PDF
set(gcf,'Units','inches');
screenposition = get(gcf,'Position');
set(gcf,...
    'PaperOrientation','landscape',...
    'PaperSize',[5 2.5]);   %[5 2.5] w/o colorbar, [5 2.2] with colorbar
print('-dpdf', datafile)
```

End of MATLAB Script

A representative output from the MATLAB script is shown in Figure 475. These plots show the 80° circumferential measurement arc that is ±40° from top dead center, and the radial lines indicate the inner and outer diameter of the UCC exit passage. It can be seen in the figure that there is a gap in the data between the inner diameter and the start of the contours. This gap represents the distance from the inner diameter to the center of the first kiel head. Due to the hardware geometry, measurements could not be taken below that point. There is a smaller gap at the outer diameter. As shown in Figure 473, the center of the upper kiel head is closer to the outer diameter



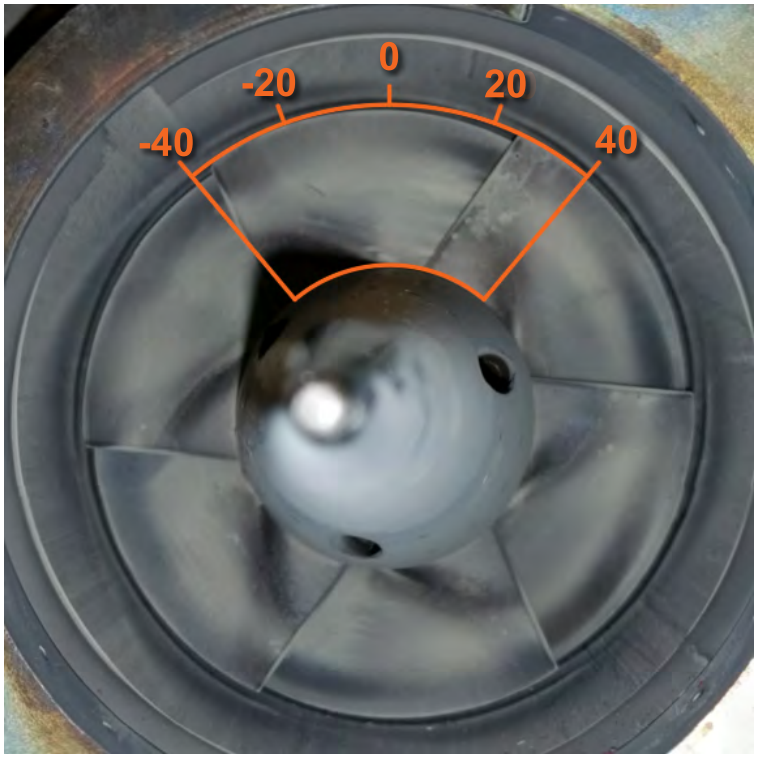
(a) Low Loss Center Body, Φ=0.74

(b) Dual Backstep Vane, Φ=0.74

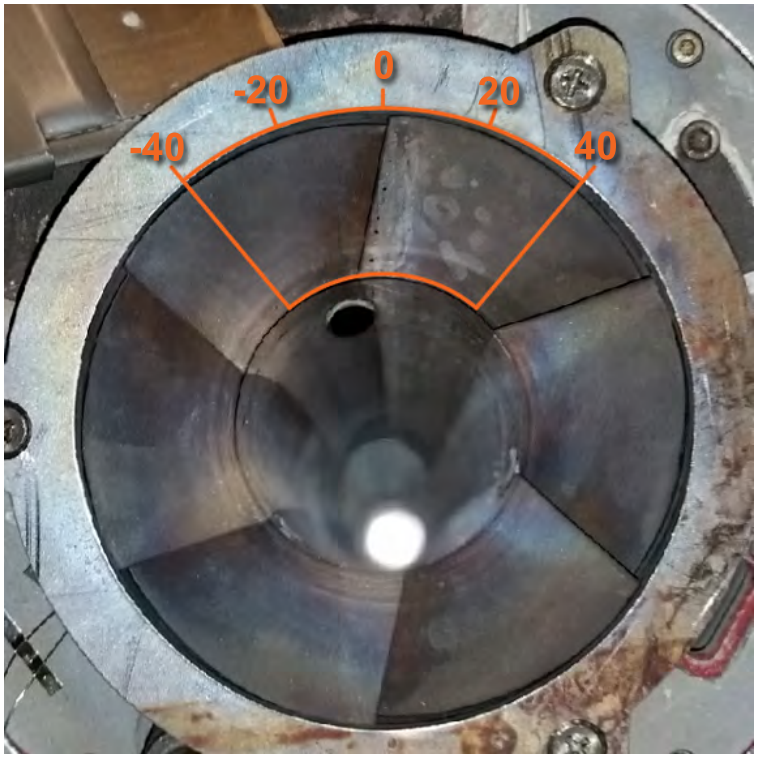
(c) Scale (K)

Figure 475. Example thermal contour plots using the low loss center body vane and the dual backstep vane with the course method and 10° circumferential spacing

The temperature contours in Figure 475 should be referenced to the relative measurement locations shown in Figure 476. In Figure 476 the measurement locations are shown with respect to the vane trailing edge for two hybrid guide vane variations. There is an approximate 20° offset between the trailing edge position of these two vanes. If differences in temperature profiles are observed, they may not be as different as the first appear when the 20° offset is applied back.



(a) Low Loss Center Body Vane



(b) Dual Backstep Vane

Figure 476. Thermocouple rake probe

Appendix C. 12-Step Combustor Operating Maps

This appendix holds the remainder of the collection of operating maps now shown in Section 6.3 for the 12-Step combustor at 0.060, 0.108, and 0.120 kg/s total air flow rates at all four levels of back wall fuel injection.

C.1 12-Step Combustor Operating Maps, $\dot{m}_{in} = 0.06 kg/s$

The ΔP map shown in Figure 477 is the same for all levels of back wall fuel injection.

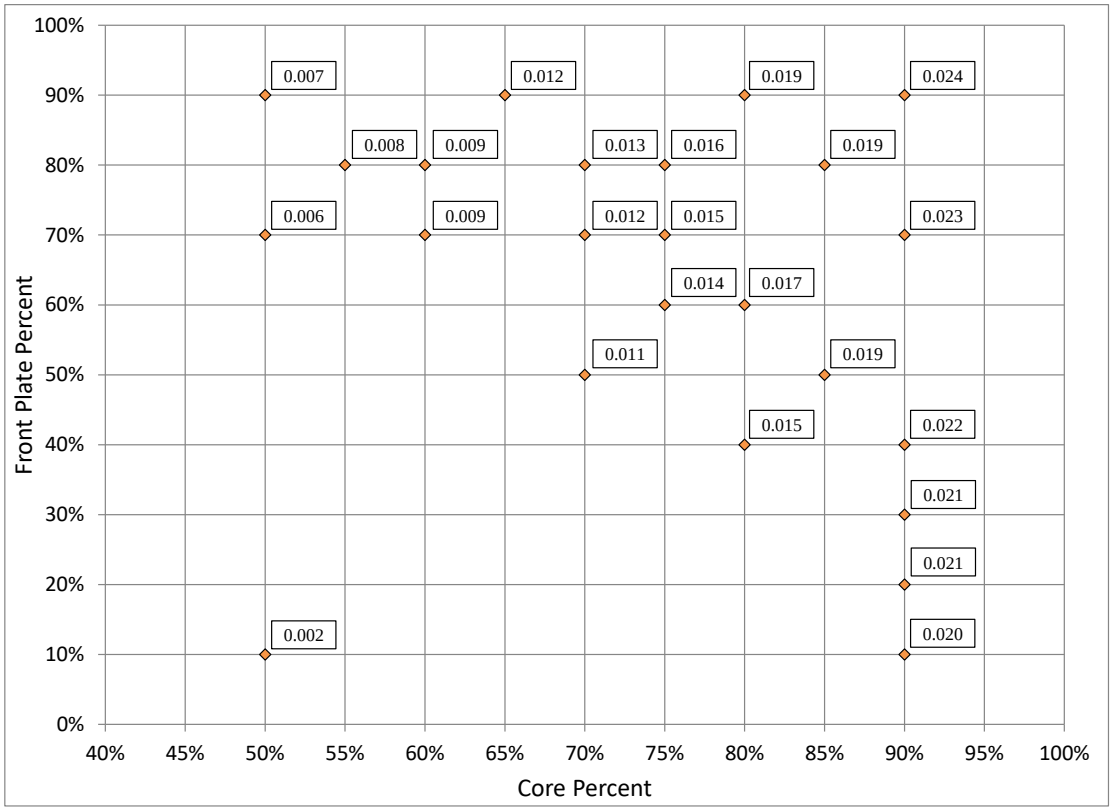


Figure 477. Required Diffuser Pressure Differential (ΔP) Map, $\dot{m}_{in} = 0.060 kg/s$

The remainder of this section shows the average exit temperature map, average cavity temperature map, and acoustic map at each successive back wall fuel injection level. The average exit temperature map at 0% back wall injection is shown in Figure 274. The acoustic plot at 0% back wall injection is shown in Figure 277.

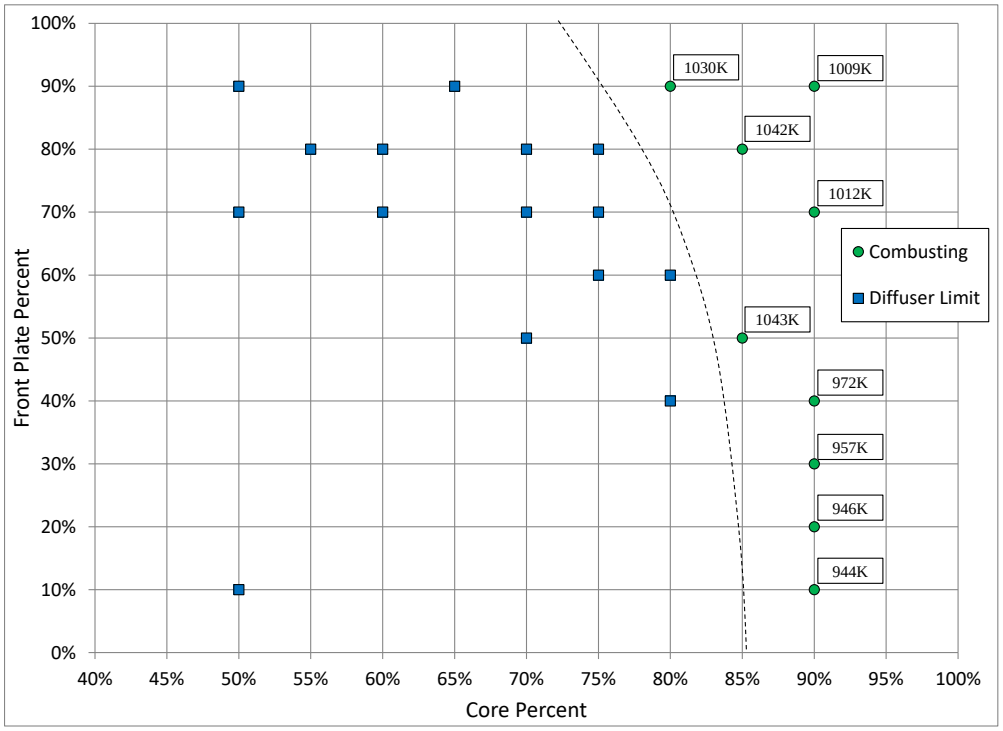


Figure 478. Average cavity temperature (K) operating map at $\dot{m}_{in} = 0.060kg/s$, 0% back wall fuel injection

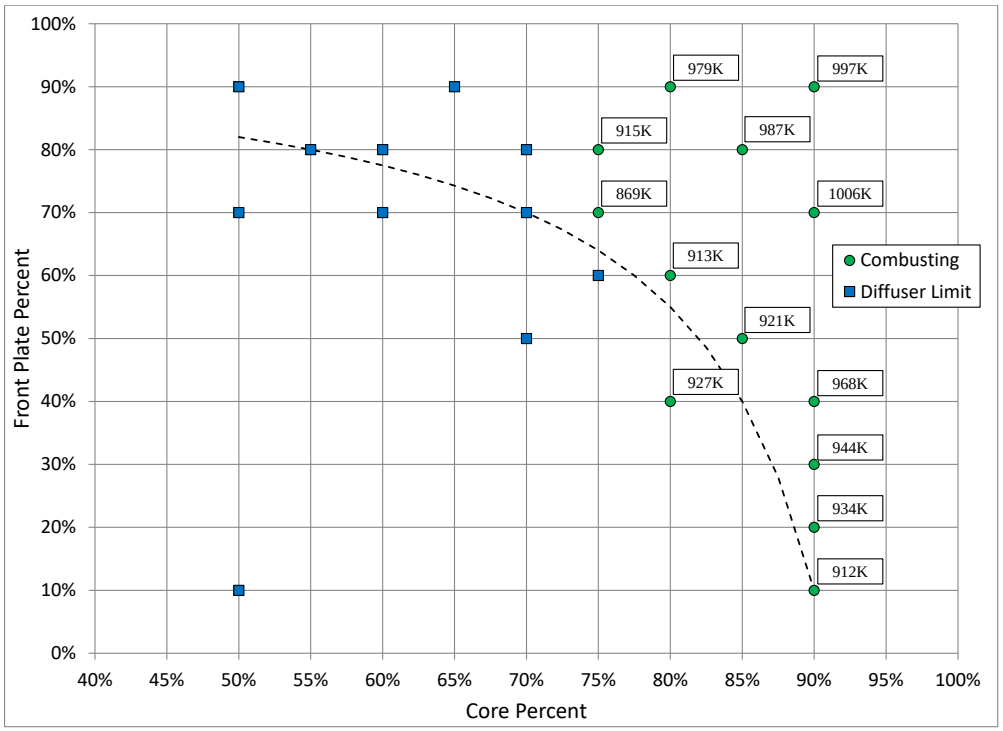


Figure 479. Average exit temperature (K) operating map at $\dot{m}_{in} = 0.060kg/s$, 10% back wall fuel injection

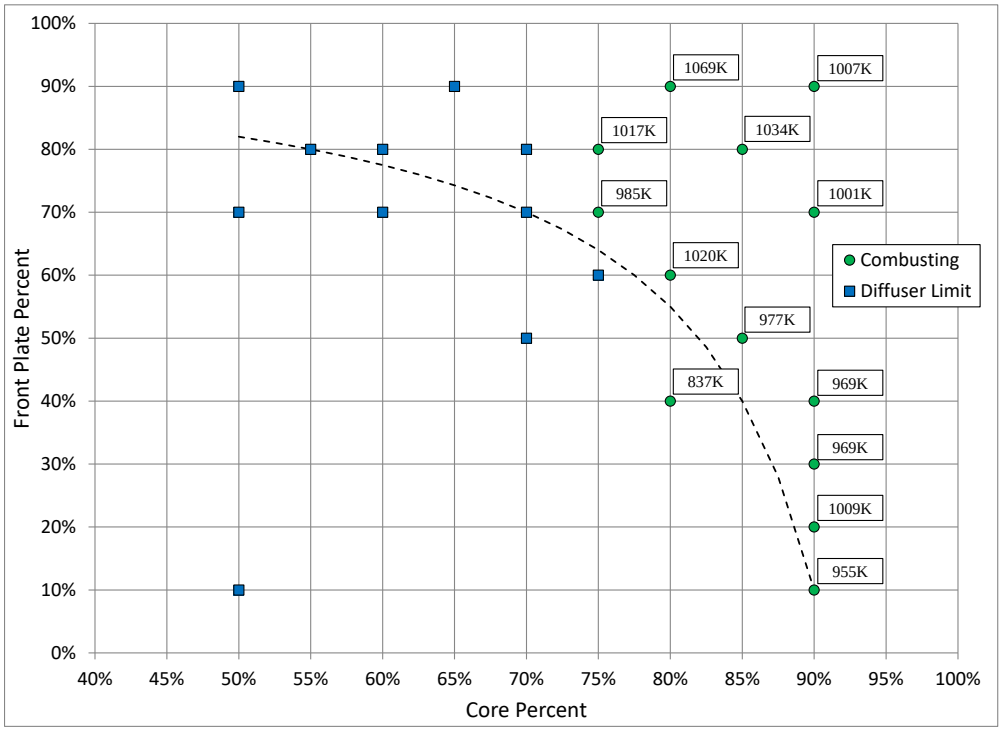


Figure 480. Average cavity temperature (K) operating map at $\dot{m}_{in} = 0.060kg/s$, 10% back wall fuel injection

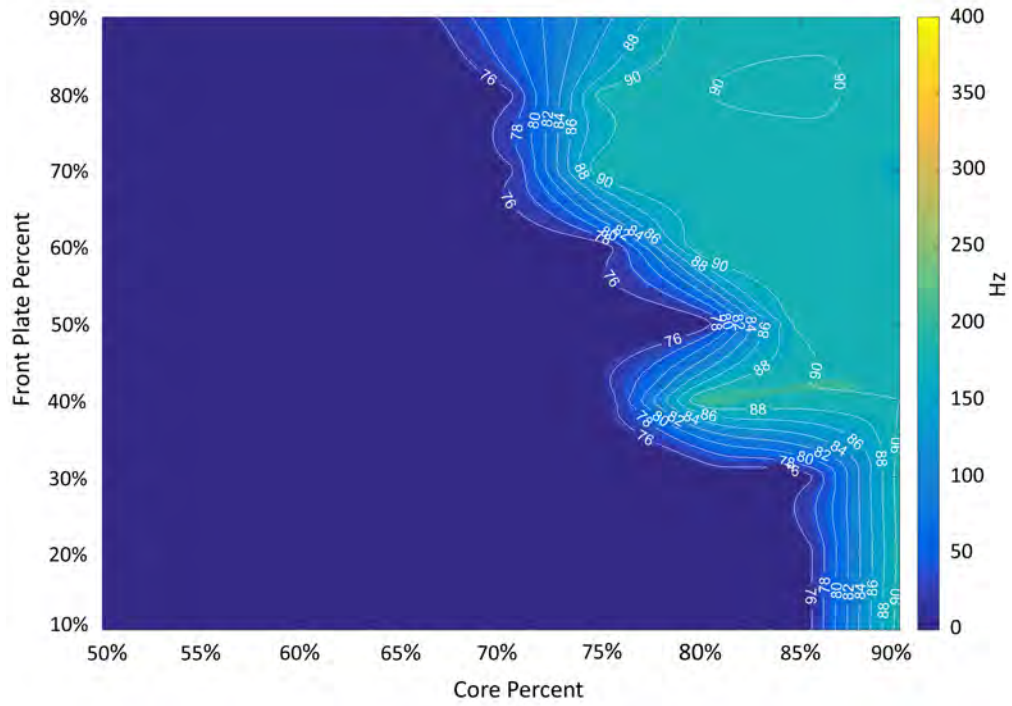


Figure 481. Flooded contours of dominant audible frequency (Hz) with overlaid line contours of sound pressure level (dB) at $\dot{m}_{in} = 0.060kg/s$, 10% back wall fuel injection

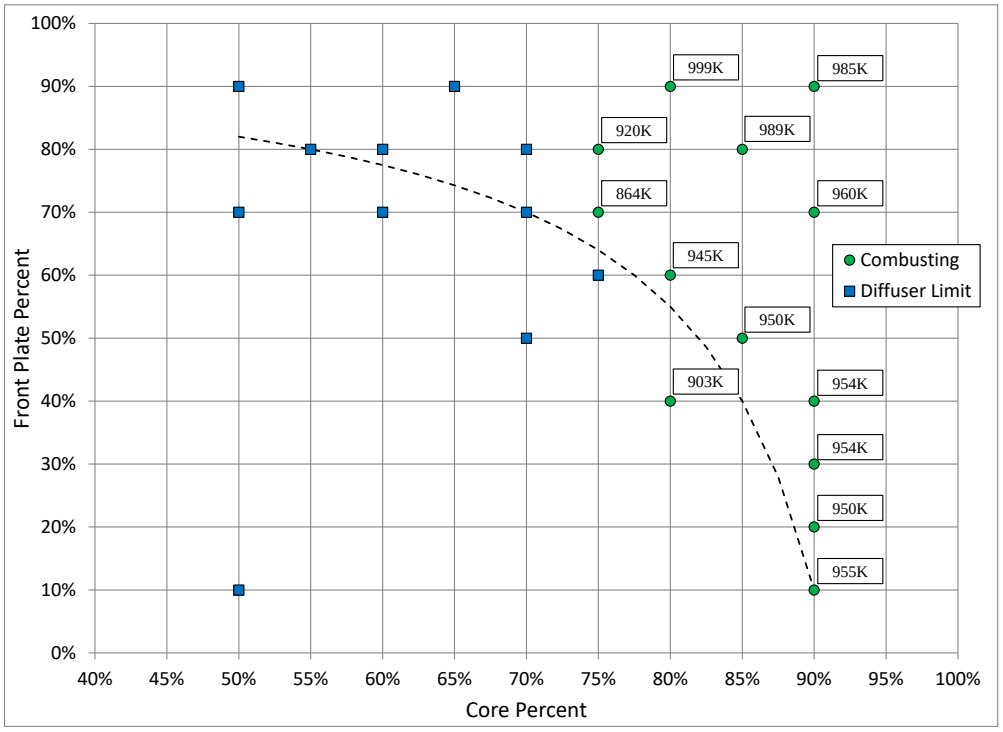


Figure 482. Average exit temperature (K) operating map at $\dot{m}_{in} = 0.060kg/s$, 20% back wall fuel injection

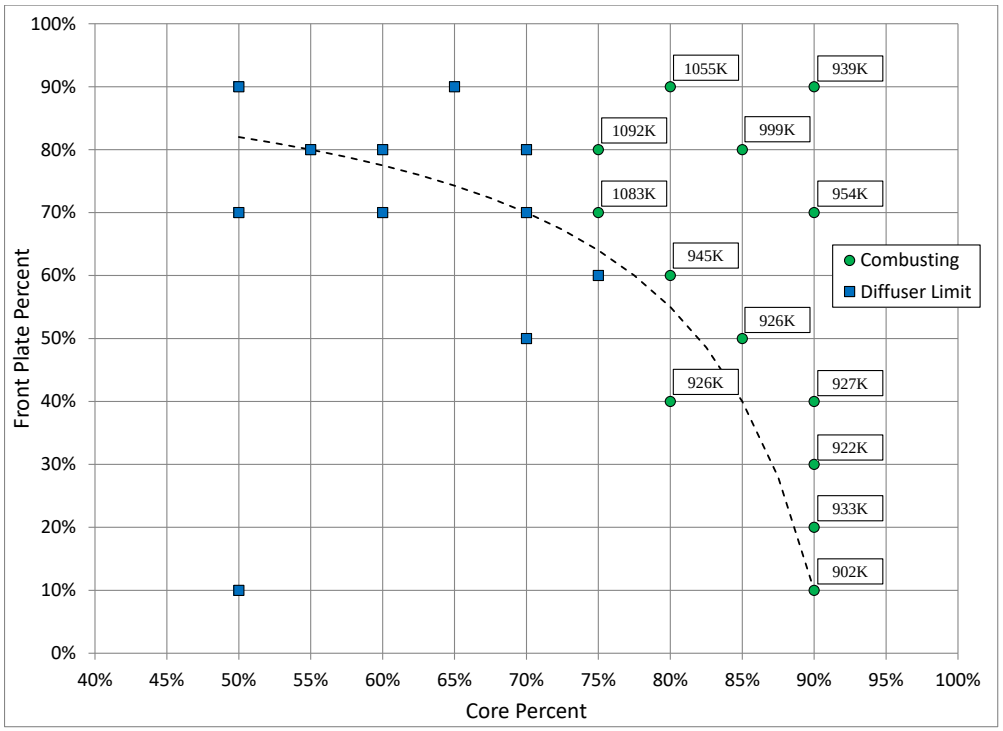


Figure 483. Average cavity temperature (K) operating map at $\dot{m}_{in} = 0.060kg/s$, 20% back wall fuel injection

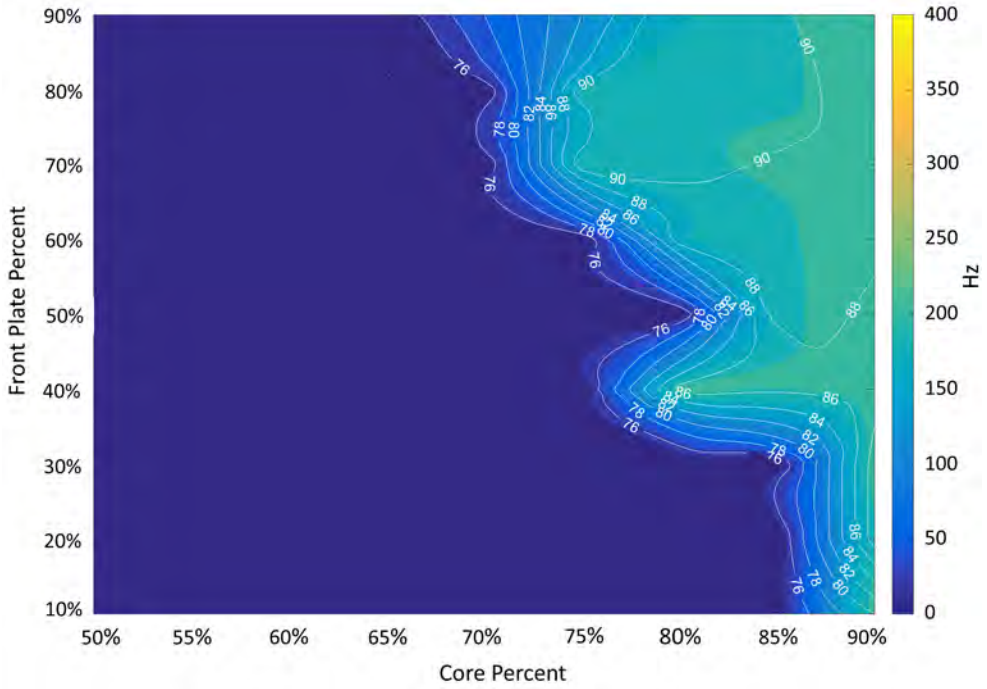


Figure 484. Flooded contours of dominant audible frequency (Hz) with overlaid line contours of sound pressure level (dB) at $\dot{m}_{in} = 0.060kg/s$, 20% back wall fuel injection

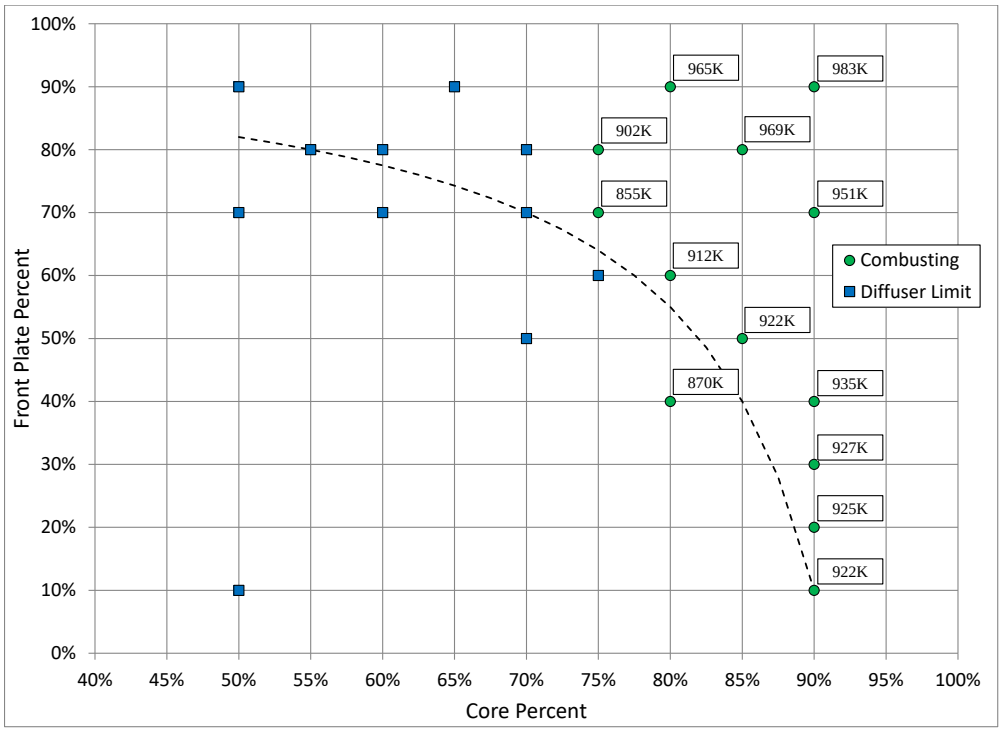


Figure 485. Average exit temperature (K) operating map at $\dot{m}_{in} = 0.060kg/s$, 30% back wall fuel injection

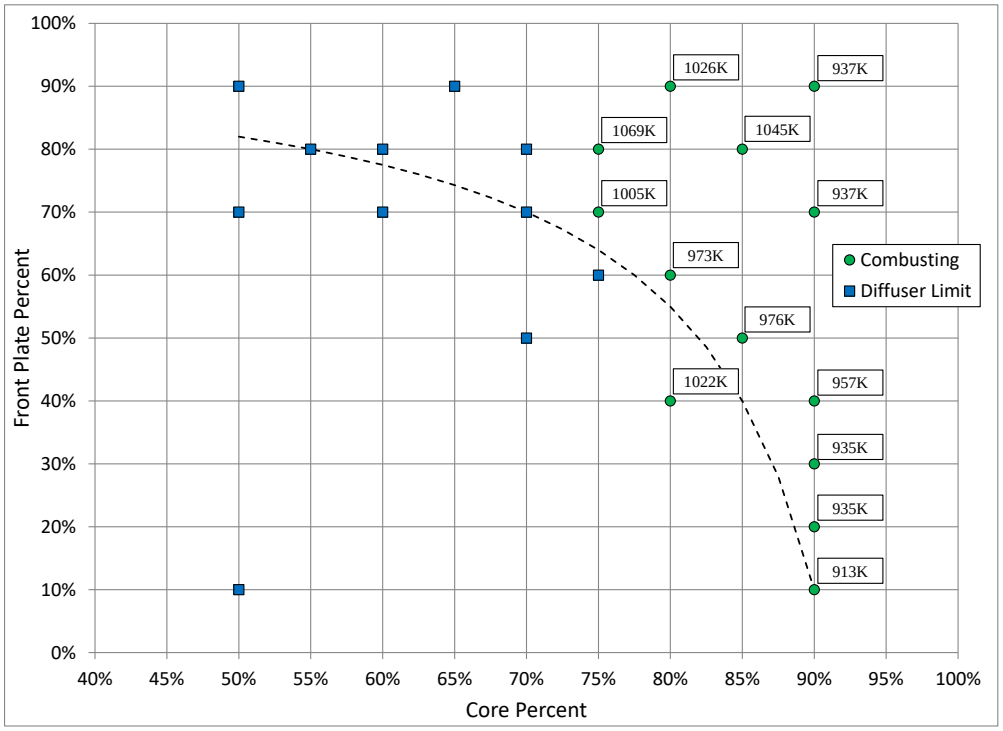


Figure 486. Average cavity temperature (K) operating map at $\dot{m}_{in} = 0.060kg/s$, 30% back wall fuel injection

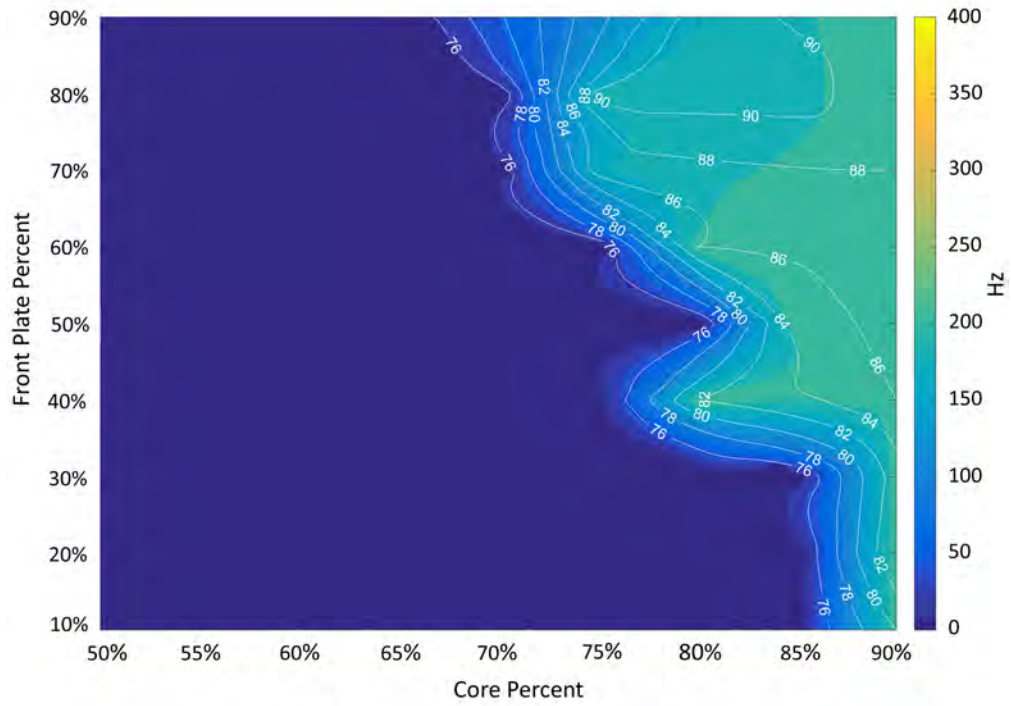


Figure 487. Flooded contours of dominant audible frequency (Hz) with overlaid line contours of sound pressure level (dB) at $\dot{m}_{in} = 0.060kg/s$, 30% back wall fuel injection

C.2 12-Step Combustor Operating Maps, $\dot{m}_{in} = 0.108kg/s$

The ΔP map shown in Figure 488 is the same for all levels of back wall fuel injection.

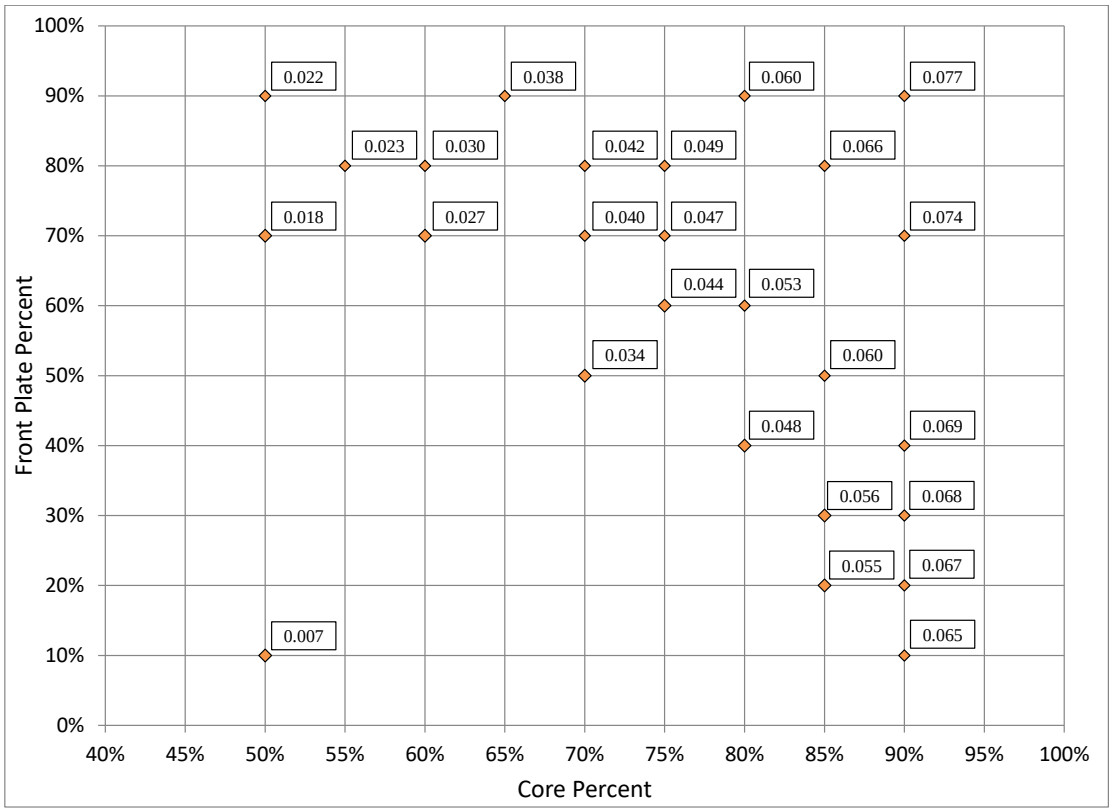


Figure 488. Required Diffuser Pressure Differential (ΔP) Map, $\dot{m}_{in} = 0.108kg/s$

The remainder of this section shows the average exit temperature map, average cavity temperature map, and acoustic map at each successive back wall fuel injection level. The average exit temperature map at 0% back wall injection is shown in Figure 273. The acoustic plot at 0% back wall injection is shown in Figure 276.

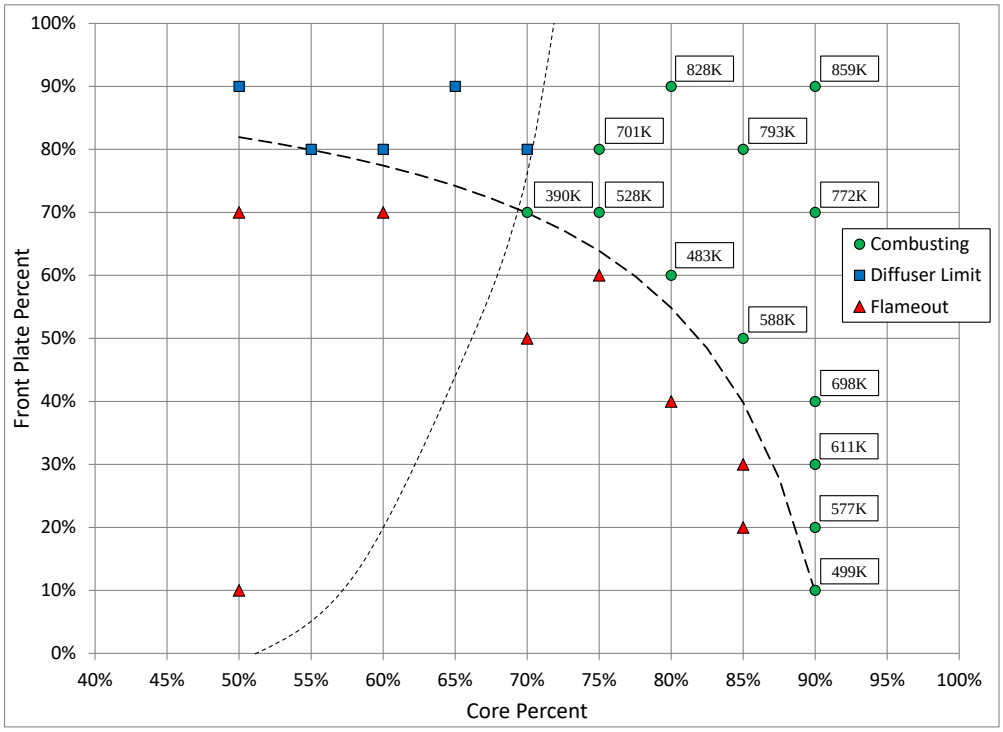


Figure 489. Average cavity temperature (K) operating map at $\dot{m}_{in} = 0.108kg/s$, 0% back wall fuel injection

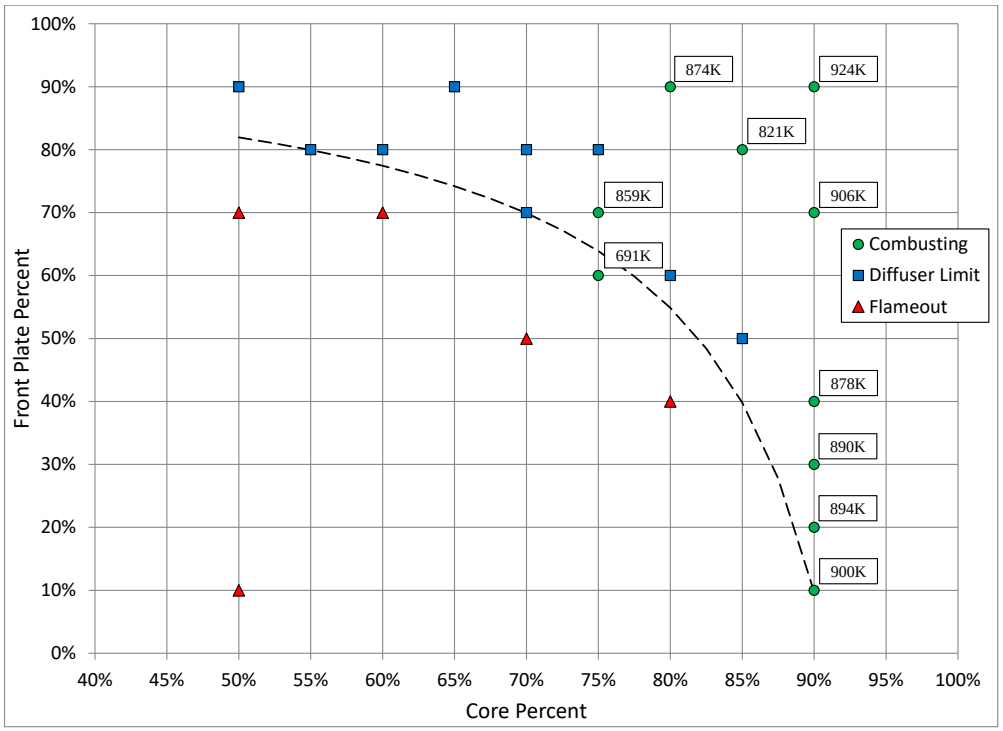


Figure 490. Average exit temperature (K) operating map at $\dot{m}_{in} = 0.108kg/s$, 10% back wall fuel injection

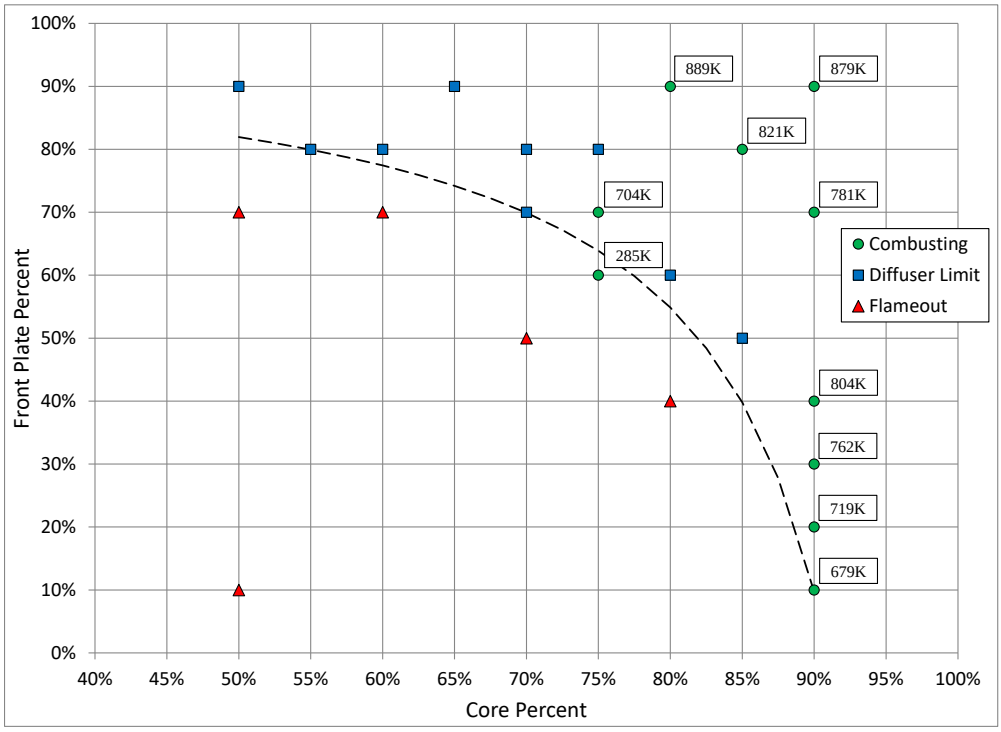


Figure 491. Average cavity temperature (K) operating map at $\dot{m}_{in} = 0.108kg/s$, 10% back wall fuel injection

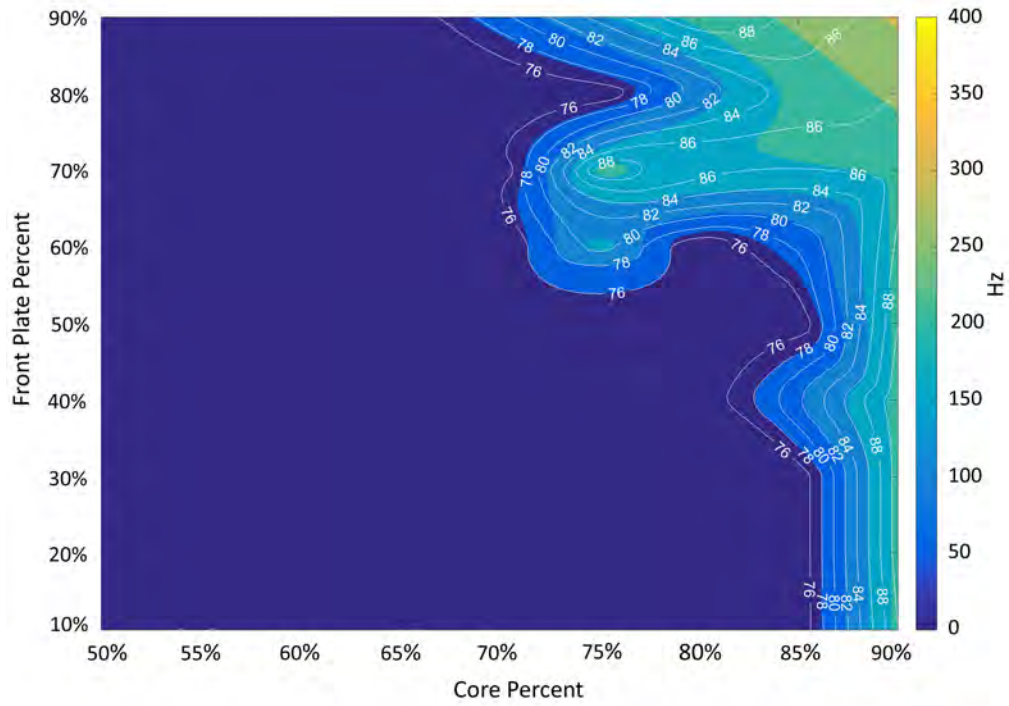


Figure 492. Flooded contours of dominant audible frequency (Hz) with overlaid line contours of sound pressure level (dB) at $\dot{m}_{in} = 0.108kg/s$, 10% back wall fuel injection

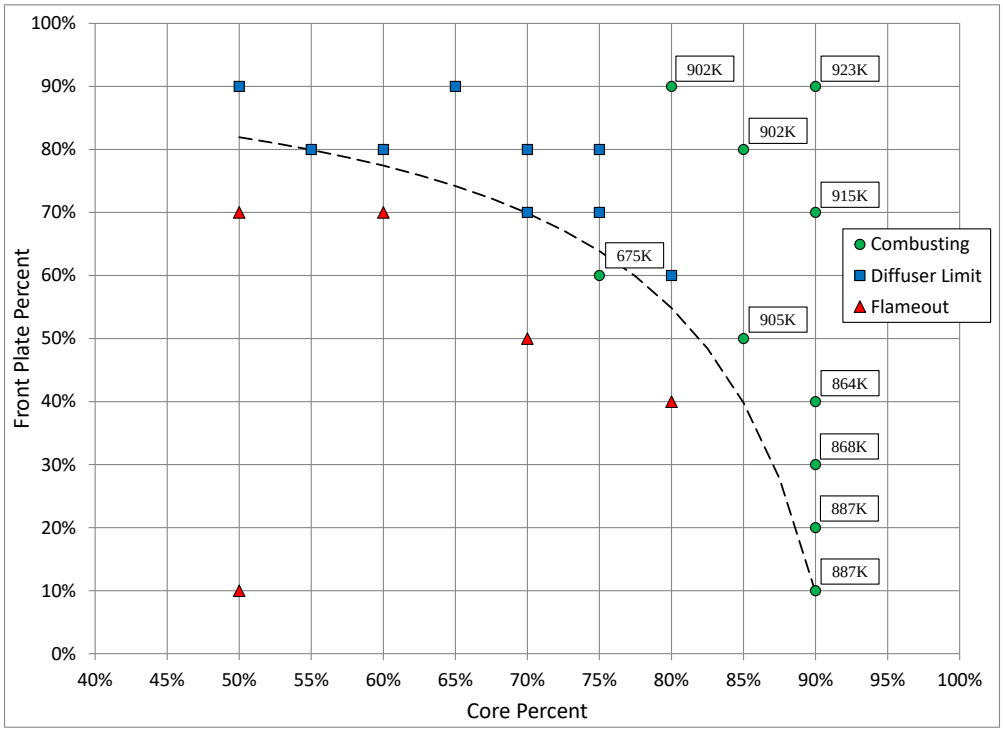


Figure 493. Average exit temperature (K) operating map at $\dot{m}_{in} = 0.108kg/s$, 20% back wall fuel injection

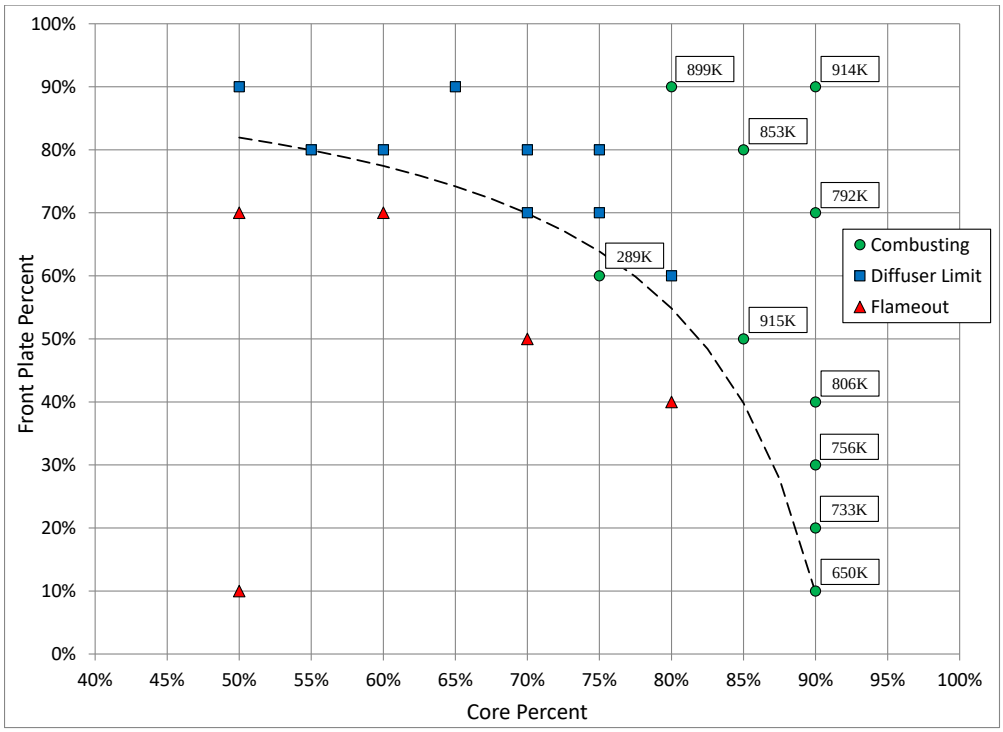


Figure 494. Average cavity temperature (K) operating map at $\dot{m}_{in} = 0.108kg/s$, 20% back wall fuel injection

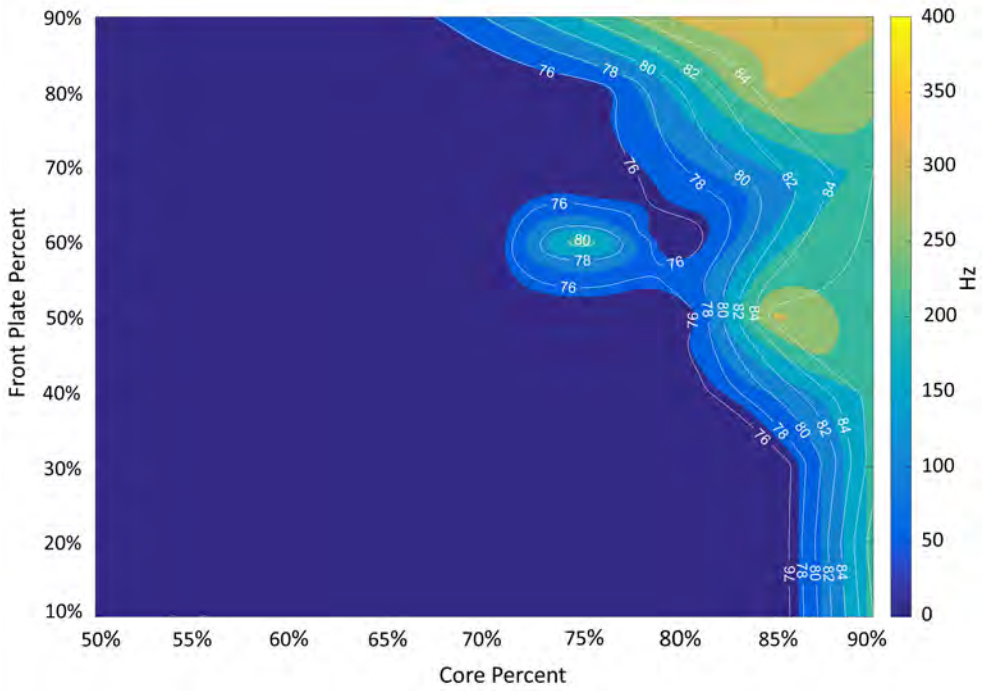


Figure 495. Flooded contours of dominant audible frequency (Hz) with overlaid line contours of sound pressure level (dB) at $\dot{m}_{in} = 0.108kg/s$, 20% back wall fuel injection

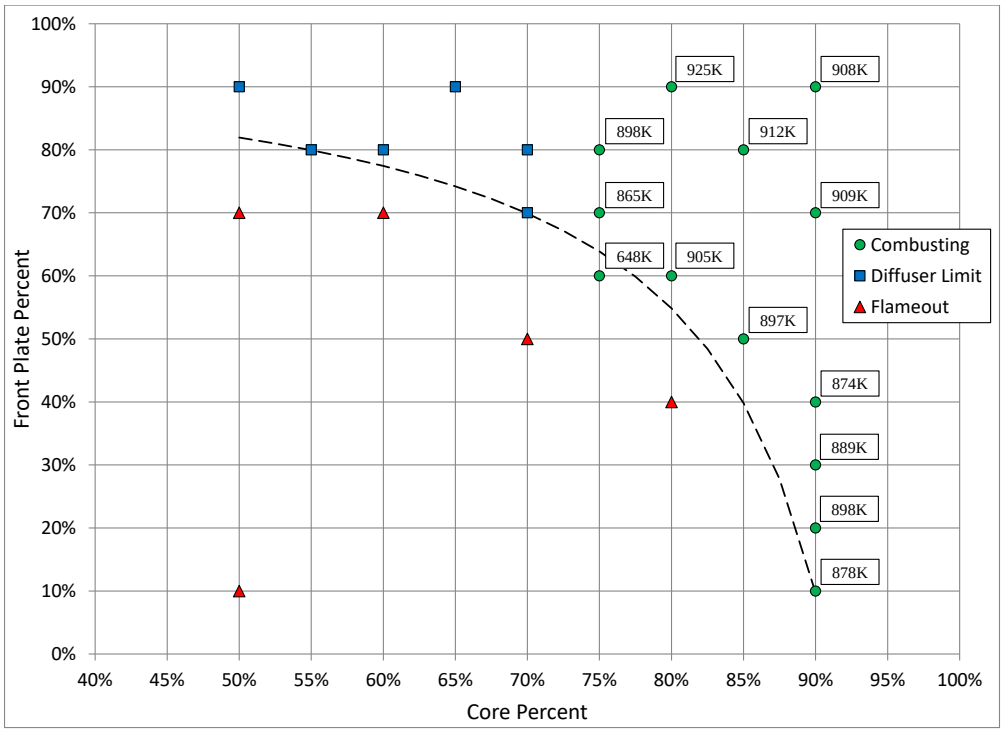


Figure 496. Average exit temperature (K) operating map at $\dot{m}_{in} = 0.108kg/s$, 30% back wall fuel injection

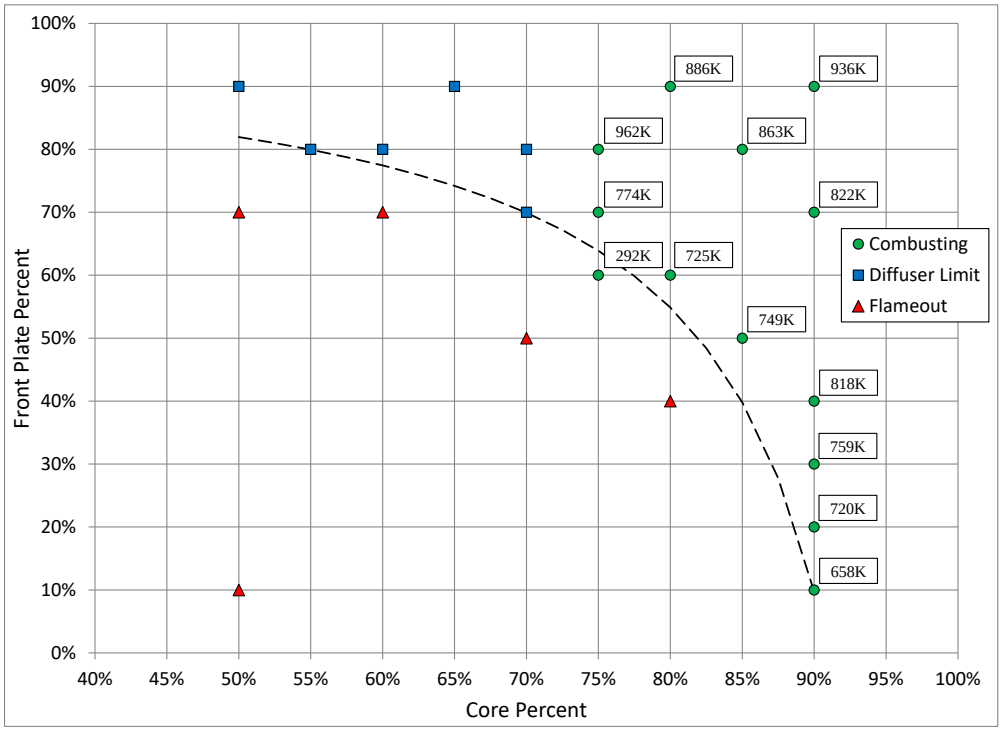


Figure 497. Average cavity temperature (K) operating map at $\dot{m}_{in} = 0.108kg/s$, 30% back wall fuel injection

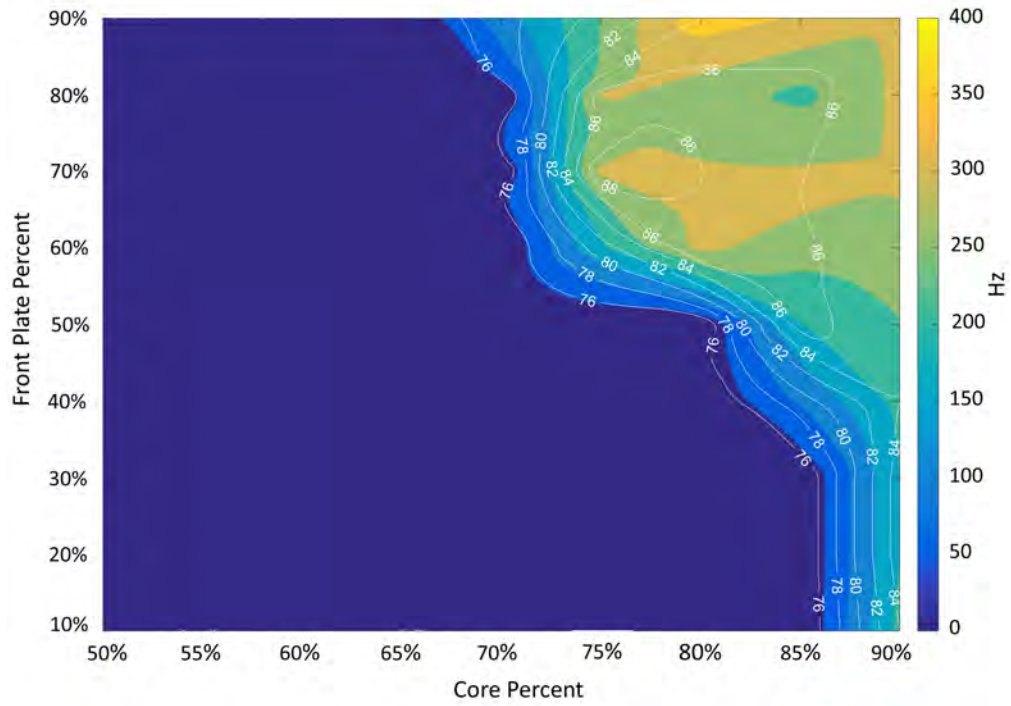


Figure 498. Flooded contours of dominant audible frequency (Hz) with overlaid line contours of sound pressure level (dB) at $\dot{m}_{in} = 0.108kg/s$, 30% back wall fuel injection

C.3 12-Step Combustor Operating Maps, $\dot{m}_{in} = 0.120kg/s$

The ΔP map shown in Figure 499 is the same for all levels of back wall fuel injection.

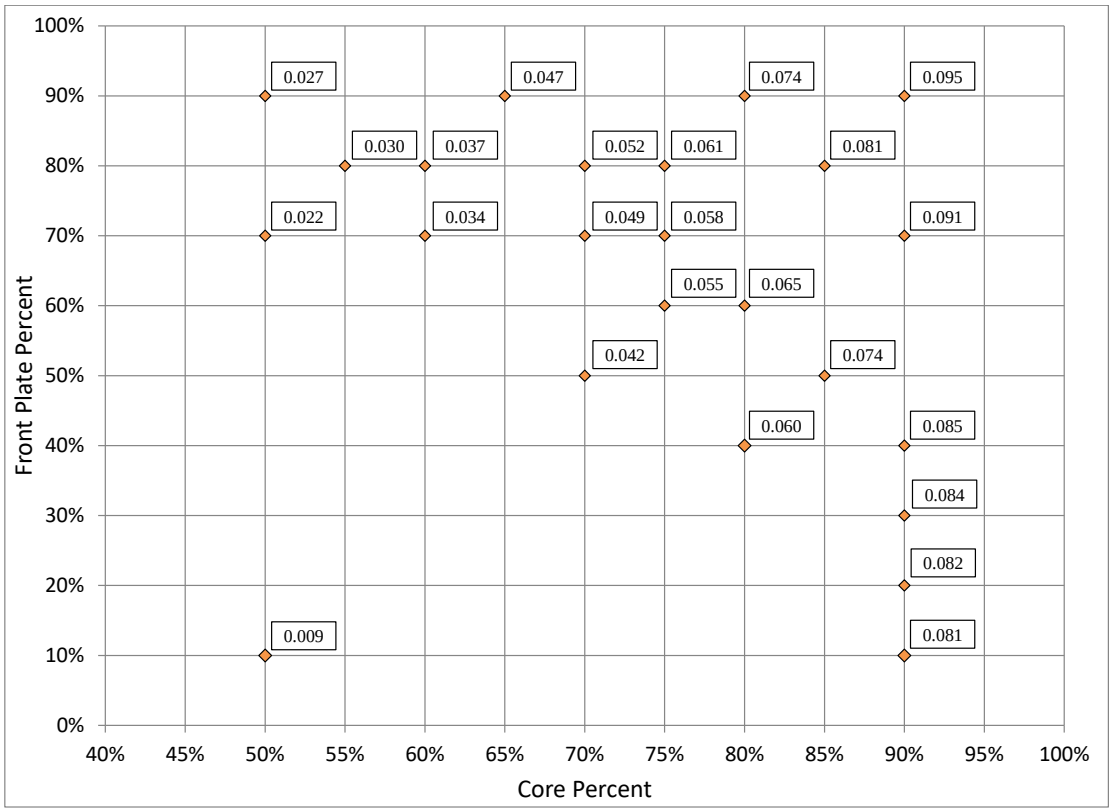


Figure 499. Required Diffuser Pressure Differential (ΔP) Map, $\dot{m}_{in} = 0.120kg/s$

The remainder of this section shows the average exit temperature map, average cavity temperature map, and acoustic map at each successive back wall fuel injection level. The average exit temperature map at 0% back wall injection is shown in Figure 275. The acoustic plot at 0% back wall injection is shown in Figure 278.

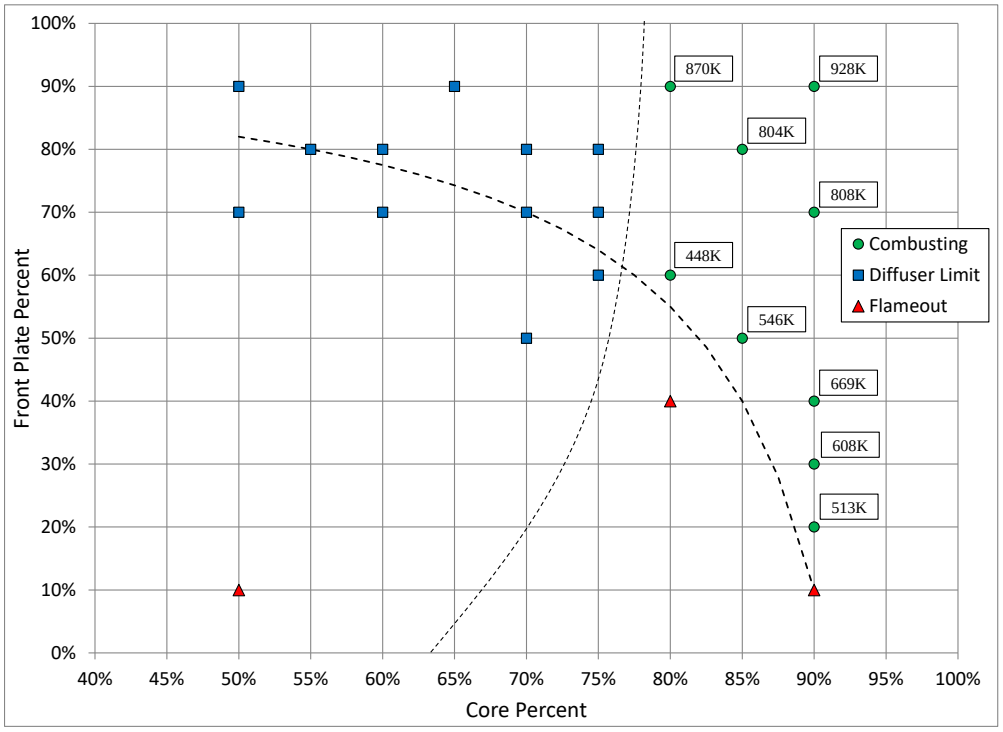


Figure 500. Average cavity temperature (K) operating map at $\dot{m}_{in} = 0.120kg/s$, 0% back wall fuel injection

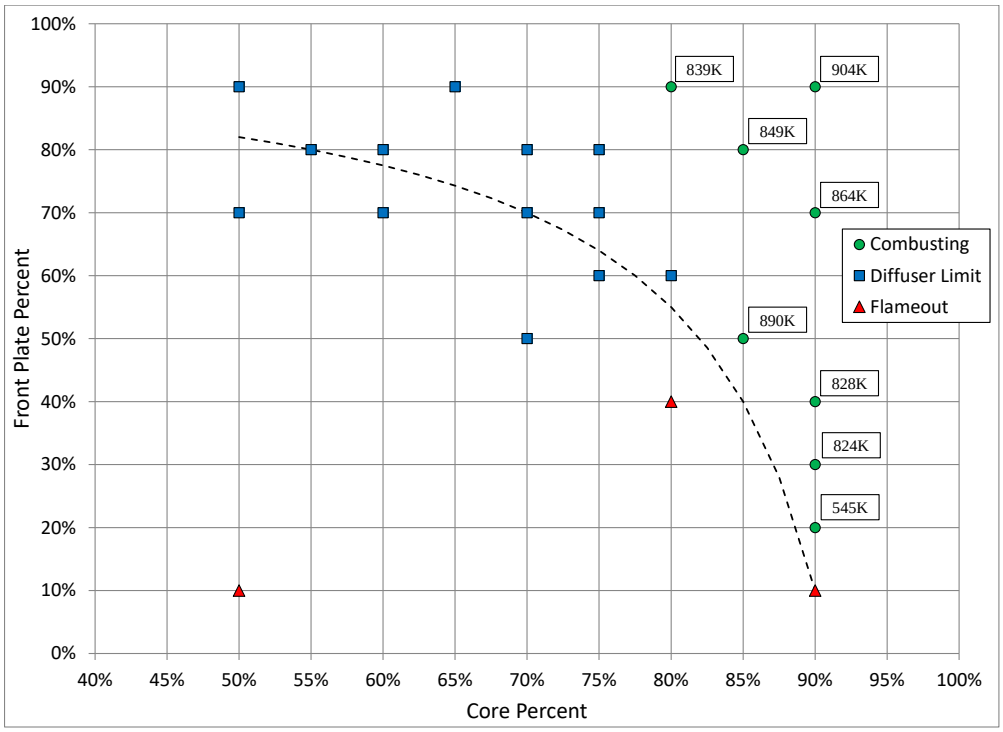


Figure 501. Average exit temperature (K) operating map at $\dot{m}_{in} = 0.120kg/s$, 10% back wall fuel injection

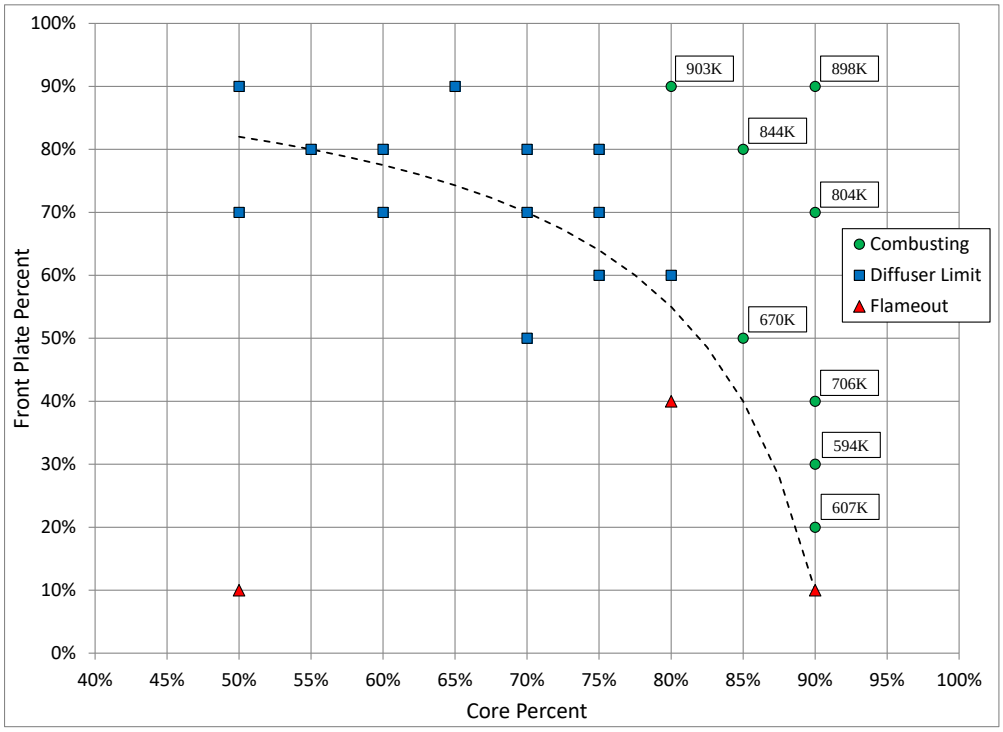


Figure 502. Average cavity temperature (K) operating map at $\dot{m}_{in} = 0.120kg/s$, 10% back wall fuel injection

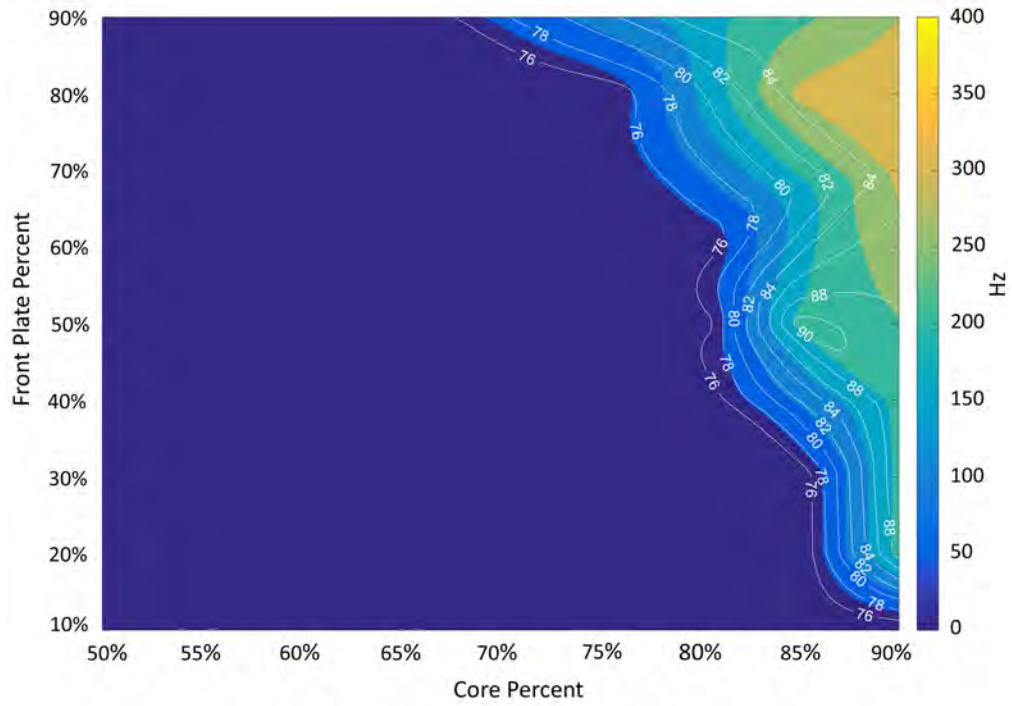


Figure 503. Flooded contours of dominant audible frequency (Hz) with overlaid line contours of sound pressure level (dB) at $\dot{m}_{in} = 0.120kg/s$, 10% back wall fuel injection

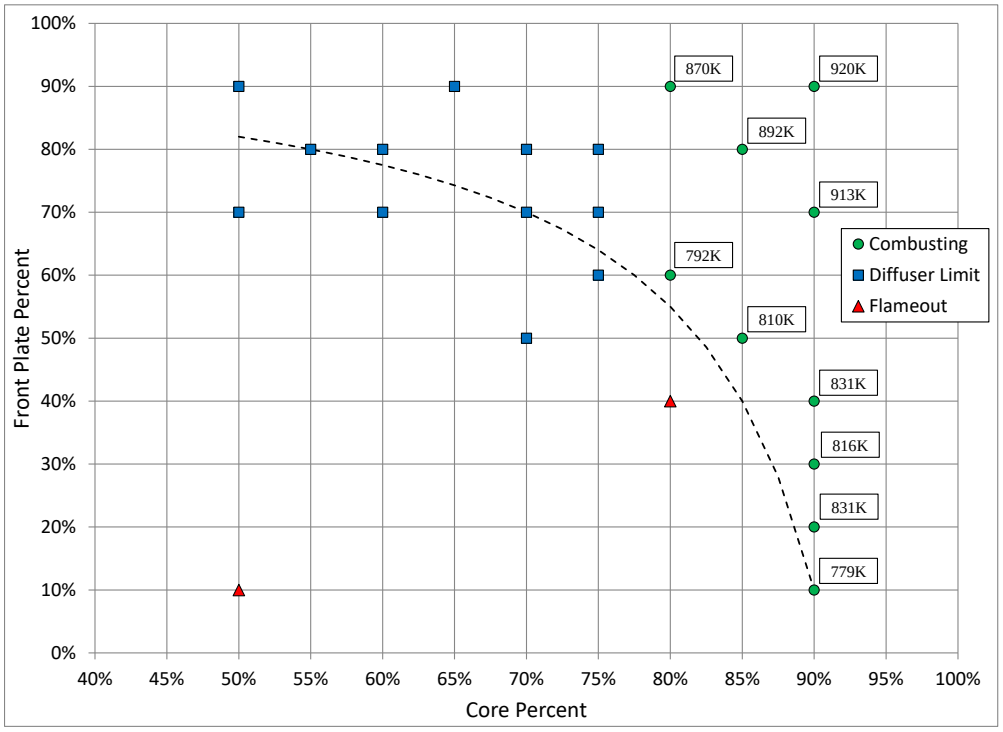


Figure 504. Average exit temperature (K) operating map at $\dot{m}_{in} = 0.120kg/s$, 20% back wall fuel injection

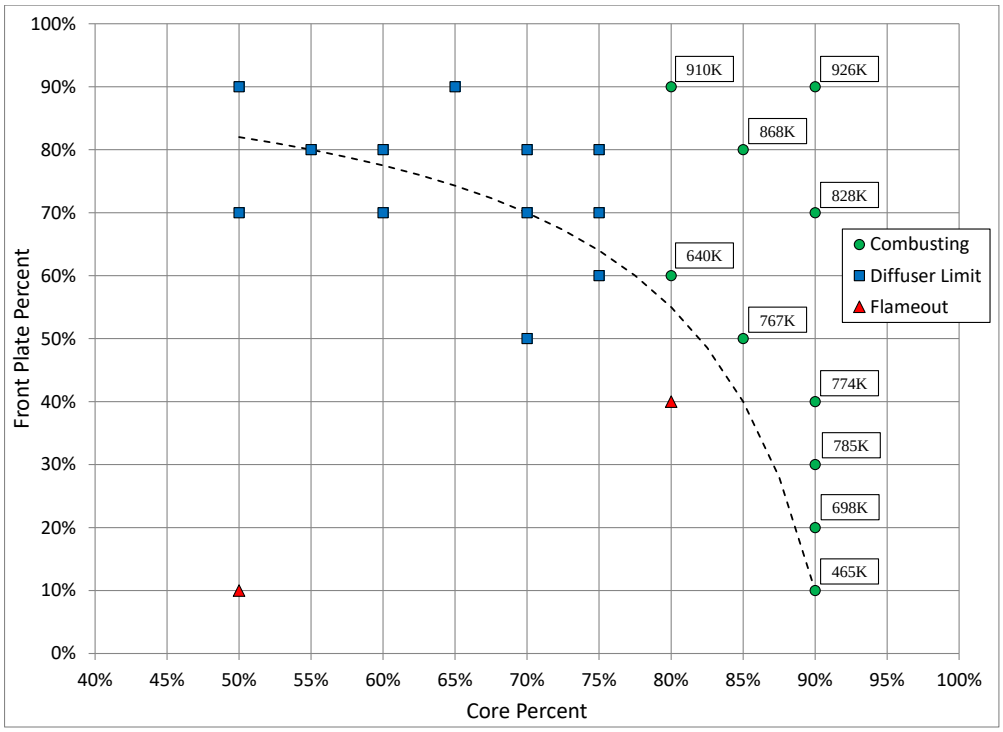


Figure 505. Average cavity temperature (K) operating map at $\dot{m}_{in} = 0.120kg/s$, 20% back wall fuel injection

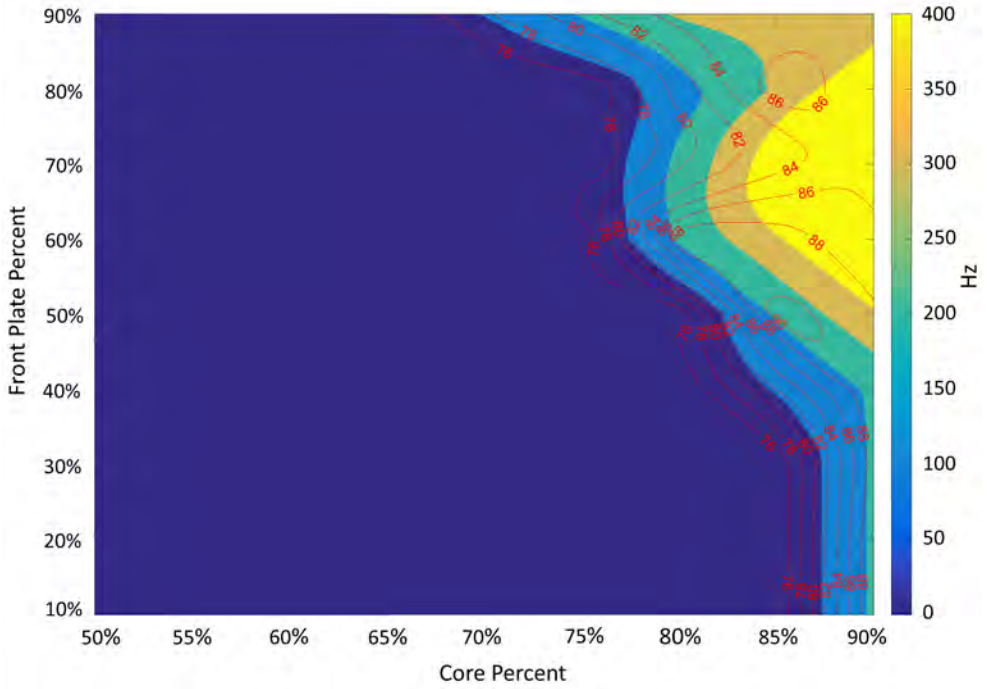


Figure 506. Flooded contours of dominant audible frequency (Hz) with overlaid line contours of sound pressure level (dB) at $\dot{m}_{in} = 0.120kg/s$, 20% back wall fuel injection

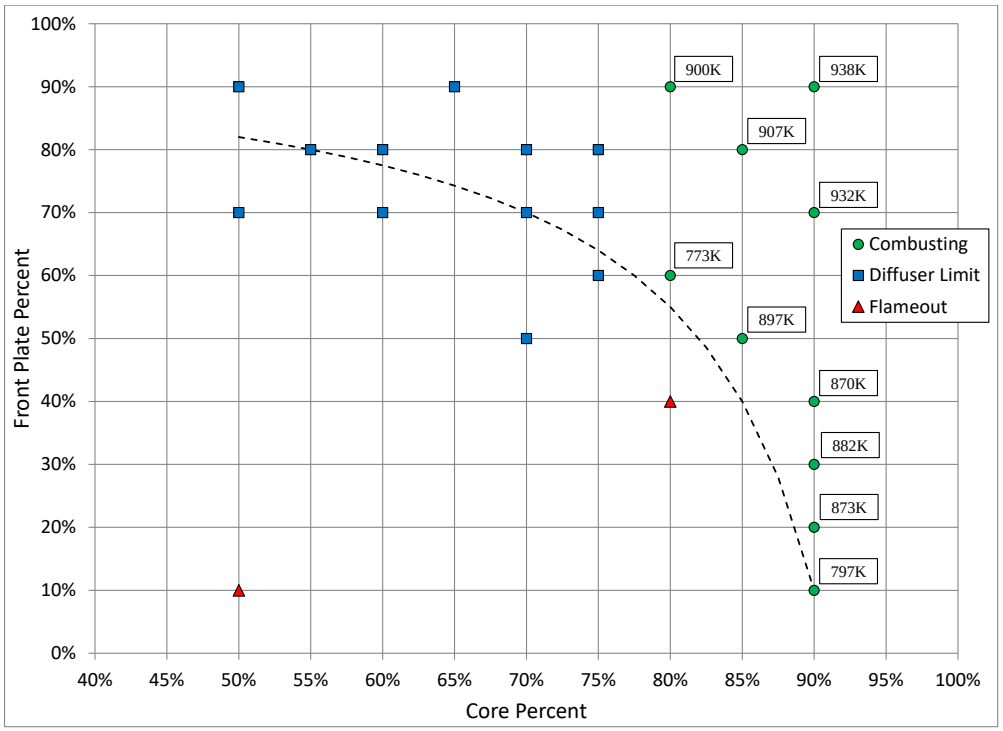


Figure 507. Average exit temperature (K) operating map at $\dot{m}_{in} = 0.120kg/s$, 30% back wall fuel injection

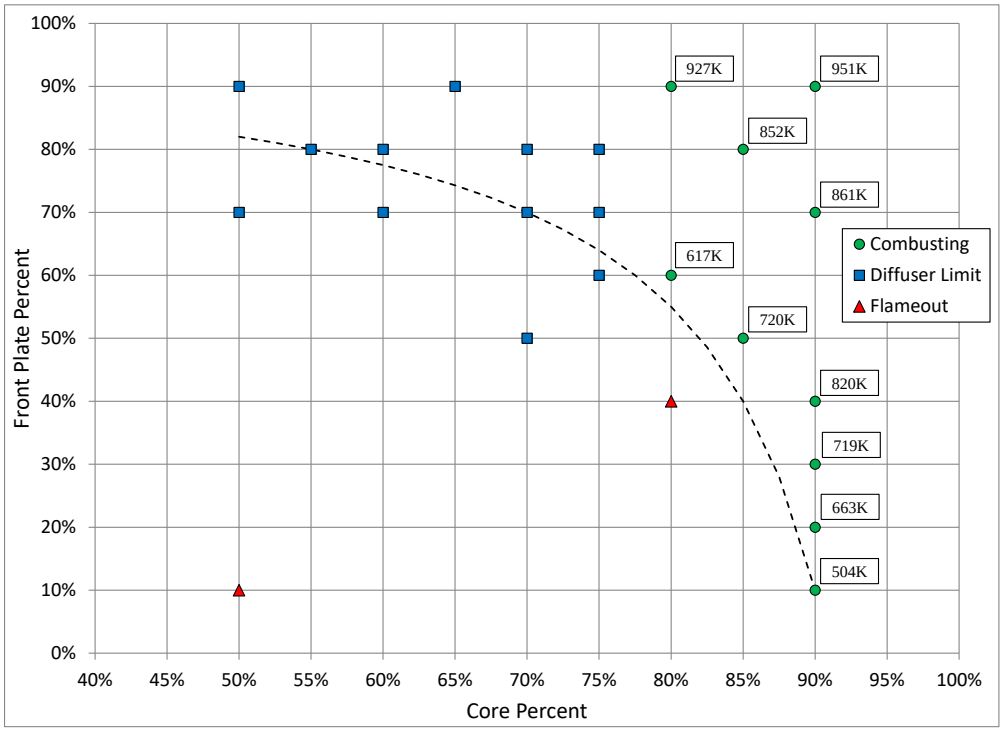


Figure 508. Average cavity temperature (K) operating map at $\dot{m}_{in} = 0.120kg/s$, 30% back wall fuel injection

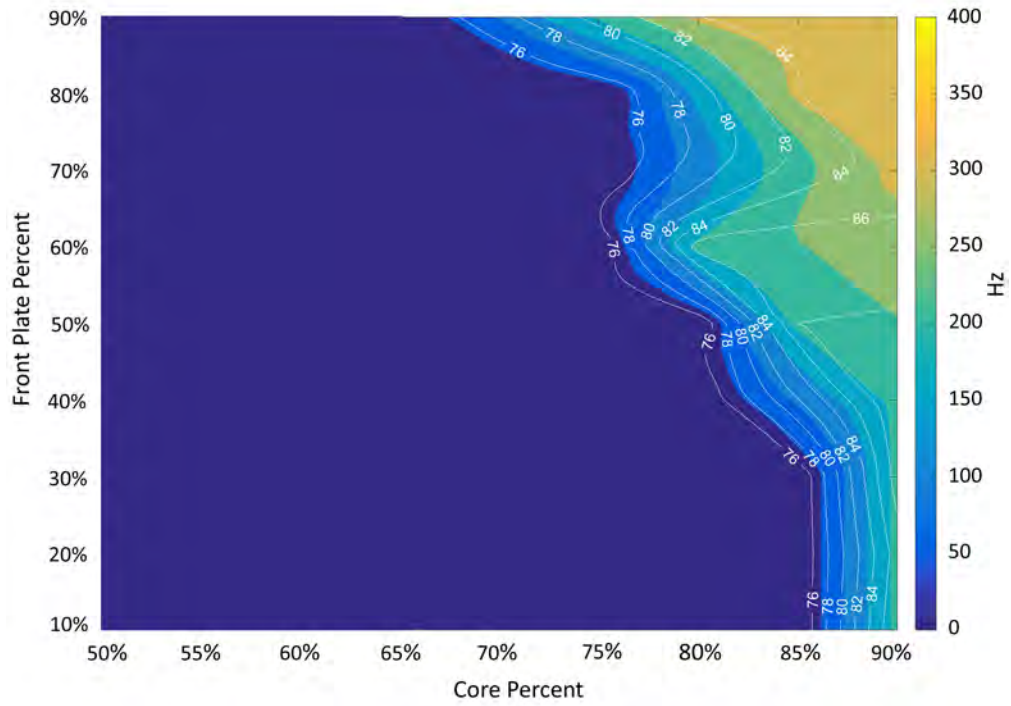


Figure 509. Flooded contours of dominant audible frequency (Hz) with overlaid line contours of sound pressure level (dB) at $\dot{m}_{in} = 0.120kg/s$, 30% back wall fuel injection

Appendix D. JetCat Electronics, Instrumentation, and Control

The electronics that came installed on the JetCat P90RXi were designed for closed loop analysis of the engine and active management of the engine operations with no need for outside interface. There was an option to connect the existing electronics to a computer to provide a readout of measured values, such as exhaust gas temperature (EGT) and RPM, using software integrated in the electronics themselves. There was no known way, however, to integrate LabView control of the engine and recording of engine performance without a redesign of the JetCat electrical system. Additionally, it was thought that the stock electronics had a means to measure the fuel flow of kerosene. Since the JetCat was modified to run on propane as the primary fuel for Objective 4 and 5 testing, kerosene was only used to lubricate the main shaft bearings. When only used for lubrication the flow rate of kerosene would be 1/7th the value the electronics would be expecting. This would result in the electronics shutting down the engine for what it would recognize as a system error. For all of the above mentioned reasons new electronics were developed that would provide the interface between engine hardware and a LabView control station.

The development of new JetCat electronics that would interface with LabView and the engine hardware began with an analysis of the stock circuit boards. A remote control (RC) 4-channel radio was connected to the electronics to power up the system and enable voltage measurements to be made at the input to the starter, fuel pump, and glow plug. When the system was powered off, resistance measurements were made across these components. By applying Ohm's law the current through each component was found. The current and voltage limits of the fuel pump motor were confirmed by researching the part number stamped on the motor. The current and voltage requirements of the installed glow plug were found in additional JetCat

documentation. The electrical values for these three stock components are listed in Table 67.

Table 67. Stock JetCat P90RXi Component Electrical Limits

Component	Voltage	Current
Starter Motor	6.5VDC	2.86A (Peaks to 3.6A at spool up (unloaded))
Fuel Pump	6.0VDC	0.85A
Glow Plug	6.0VDC	6.5A

The stock electronics consisted of two circuit boards. The first was a curved shaped board that wrapped around the compressor inlet as shown in Figure 510a, referred to as the engine board, and the second was an engine control module (ECM) that linked the RC receiver with the engine board, shown in Figure 510b, referred to as the ECM. This arrangement was maintained for the electronics redesign.



(a) Stock Engine Board (b) Stock ECM

Figure 510. Stock Electronics

A top-level diagram of the redesigned JetCat electronics, instrumentation, and control system as configured for LabView control and feedback is shown in Figure 511. All JetCat interactions with LabView were performed using all four modules in compact data acquisition 4 (CDAQ4). Module 1 was an NI9213 for receiving analog thermocouple voltages, Modules 2 and 3 were an NI9263 for producing analog signals,

and Module 4 was an NI9205 for receiving analog signals (voltages) from the ECM, pressure transducers, and thrust stand force sensor.

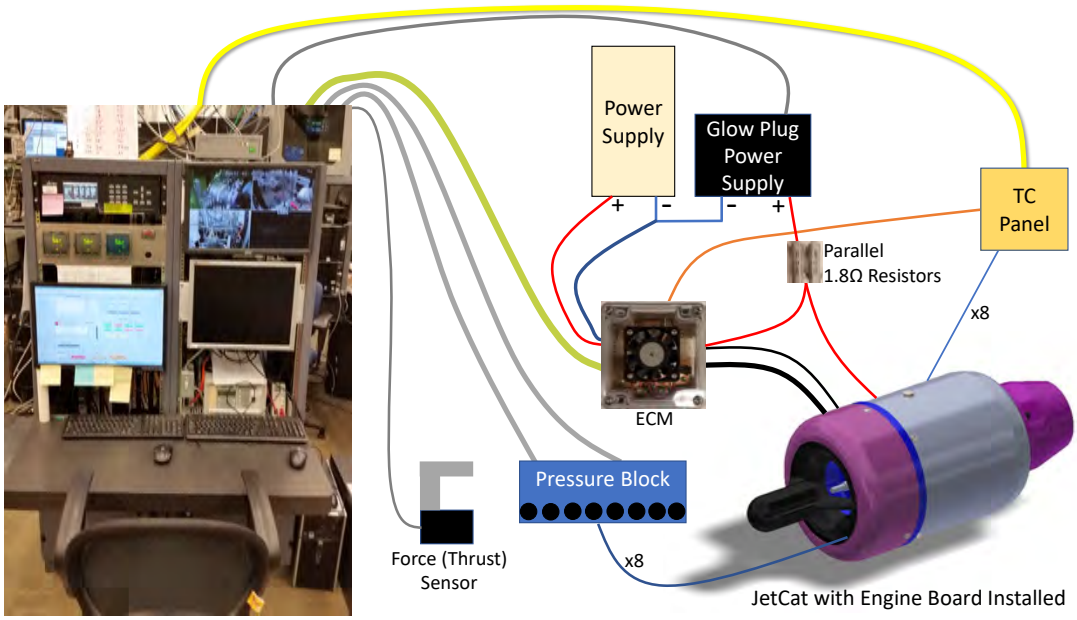


Figure 511. Redesigned JetCat electronics, instrumentation, and control system overview

D.1 Engine Control Module (ECM) Redesign

The ECM served as the central hub that linked the LabView control station, engine board, power supply, and thermocouple panel together. The thermocouple interface was only for a single on-board EGT measurement. All other temperature measurements in the JetCat linked to the thermocouple panel directly. The board features two power circuits to control the flow of electricity to the starter motor and the lubricant pump. There are additional pass through circuits to power the RPM sensor and to relay the EGT measurements, RPM signals, and control feedback signals back to LabView. The ECM included the components for glow plug control (F1, IC1, R1), however, after making the board it was determined that having LabView control a power supply would allow greater flexibility to adjust the voltage and current to

the glow plug as needed. This decision paid off when the stock glow plug failed to ignite the combustor used in Objectives 4 and 5, and a different glow plug was used which had a different power requirement. Future iterations of the ECM Board could remove these components and the associated traces from the board.

Figure 512 shows a schematic diagram of the Version 2 ECM board and Figure 513 shows the layout of the components. The schematic and board layout were generated in Eagle V8.2.2, a software package produced by Autodesk. The original design of the board made several assumptions about LabView's capabilities which turned out to be incorrect. As a result modifications were required to be made to the board to incorporate a transistor to the starter motor control circuit as a LabView commanded on/off switch, and to allow for the integration of a pulse-width modulation (PWM) generation board since LabView could not produce a PWM signal as planned. These modifications were incorporated in Figures 512 and 513. The board layout from the Eagle software was run through CircuitCAM 6.1 software to generate the necessary computer milling files to produce the board. The board was then drilled, milled, and cutout on a LPKF ProtoMat S62 CNC Router housed in B640, Rm274 at AFIT. Figures 514 and 515 show both sides of the manufactured board populated with components. Figure 516 shows the fully assembled ECM. Component reference numbers have been added to ECM board images and correspond to the components specified in Table 68.

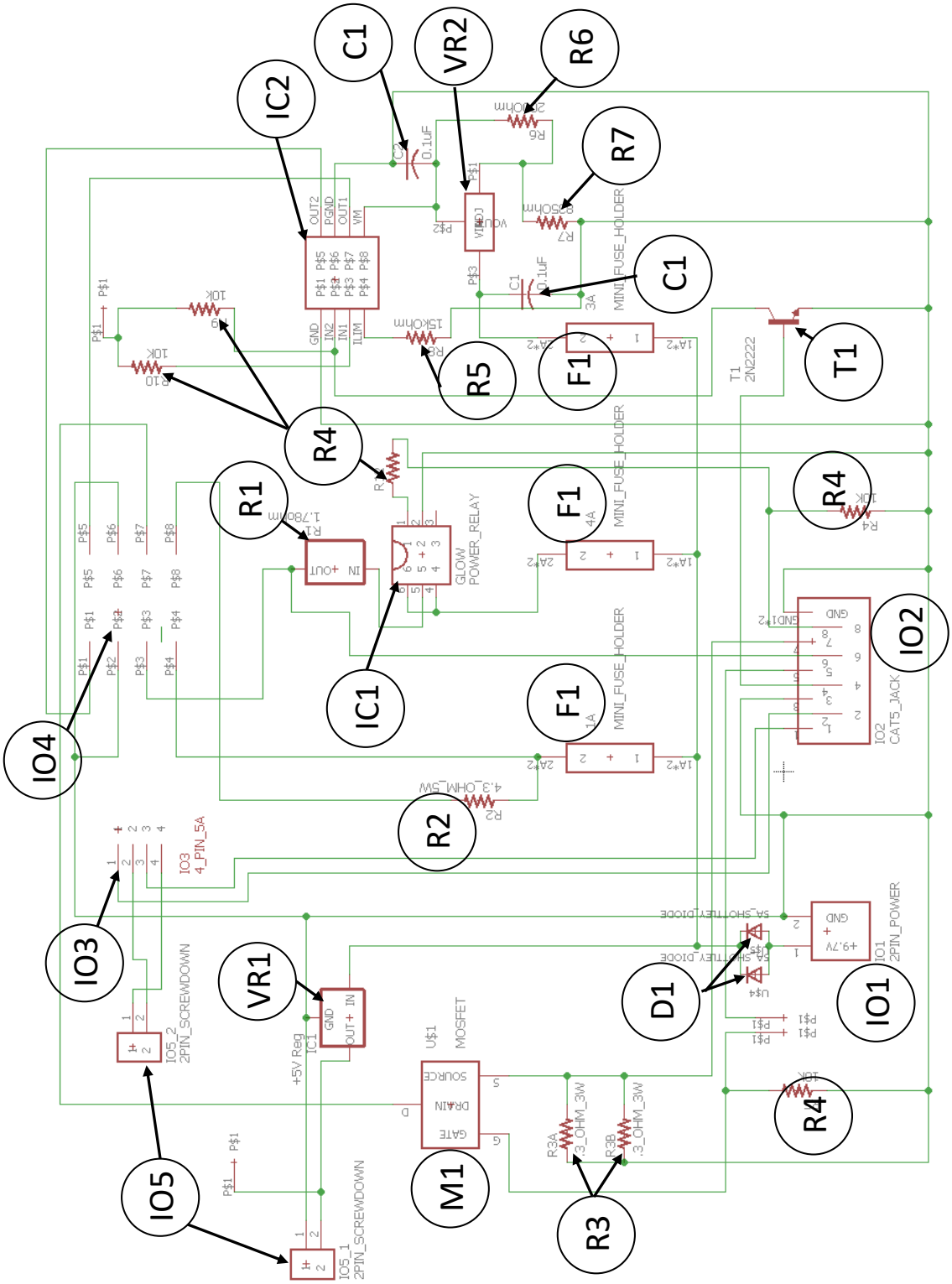
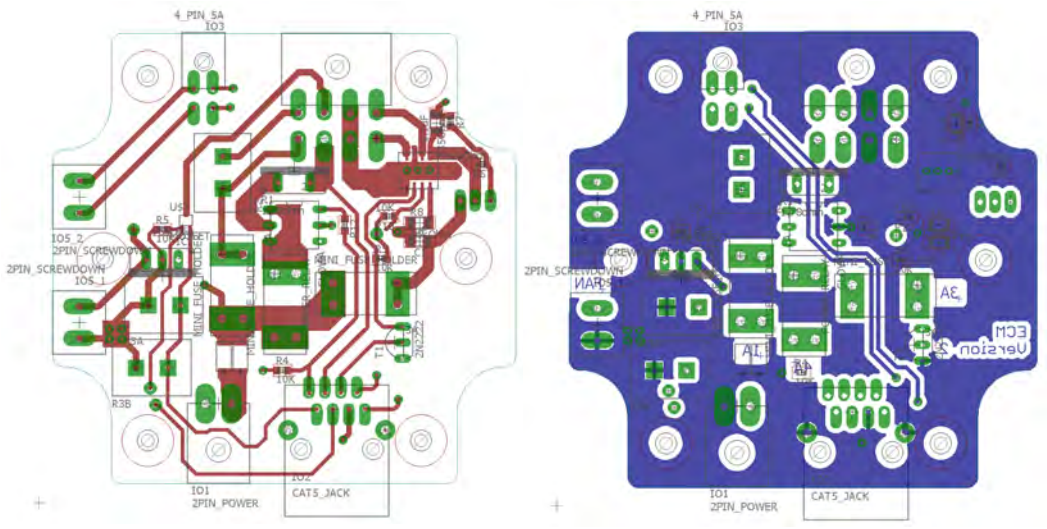


Figure 512. Redesigned ECM schematic diagram V2 Edited



Layer 1 (Red Traces), with Pads (Green)

Layer 16 (Blue Traces), with Pads (Green)

Figure 513. Redesigned ECM board layout, V2 Edited

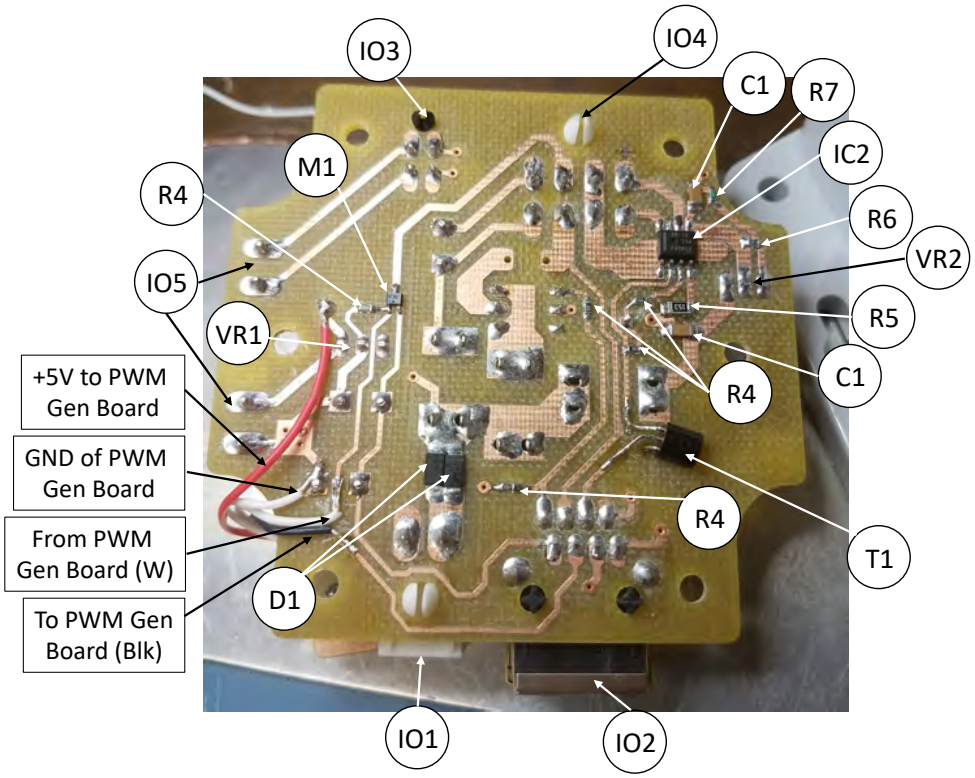


Figure 514. Redesigned ECM completed hardware layer 1, V2 Edited

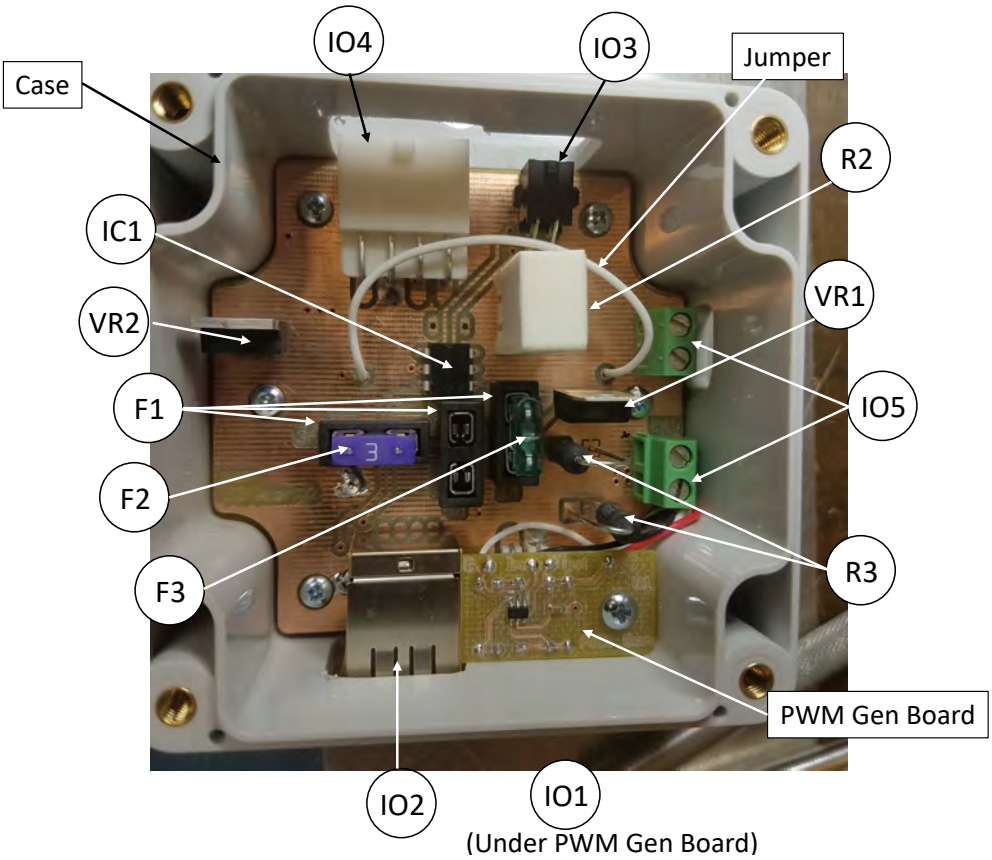


Figure 515. Redesigned ECM completed hardware layer 16, V2 Edited

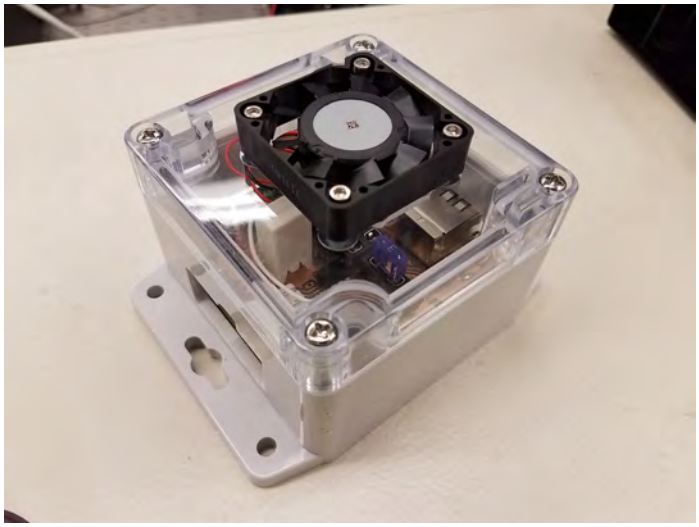


Figure 516. Fully assembled ECM

Table 68. ECM Board Component Specifications, V2 Edited

Label	Description	Manufacturer	Part Number	Qty
Case	ECM case	Polycase	WC-31F	1
C1	Capacitor, 0.1μF, 25V	Kemet	C1206F104K3RACTU	2
D1	Schottky Diode, 30V, 5A	Panasonic	DB2431200L	2
Fan	Cooling Fan, 5V	NMB	1604KL-01W-B30-B00	1
F1	Mini Blade Fuse Holder	Keystone	3568	3
F2	Mini Fuse, 3A	Eaton	BK/ATM-3	1
F3	Mini Fuse, 1A	225FWY	6930148976087	1
IC1	Power Relay, 4A	Infineon	PVG612APBF	1
IC2	Motor Driver, 3.86A	Texas Instr.	DRV8871DDARQ1	1
IO1	Connector, 2 pin	TE Connect.	1-770966-0	1
IO1M	IO1 Mate	TE Connect.	172165-1	1
IO2	Connector, Cat5e RJ45	TE Connect.	1-5406299-1	1
IO3	Connector, 4 pin	TE Connect.	3-794618-4	1
IO3M	IO3 Mate	TE Connect.	794617-4	1
IO4	Connector, 8 pin	TE Connect.	1-770970-1	1
IO4M	IO4 Mate	TE Connect.	770579-1	1
IO5	2-Position Terminal Block	Phoenix Contact	1985865	2
Pin-L	Large Connector Pins	TE Connect.	770986-1	10
Pin-S	Small Connector Pins	TE Connect.	1-794610-1	4
M1	MOSFET	ON	MCH3481-TL-H	1
R1	Resistor, 1.8Ω, 20W, TO-220	Arcol	AP821 1R8 J	1
R2	Resistor, 4.3Ω, 5W	Ohmite	TWW5J4R3E	1
R3	Resistor, 0.3Ω, 3W	Vishay	RS02BR3000FE70	2
R4	Resistor, 10kΩ, 0603	Panasonic	ERA-3AEB103V	4
R5	Resistor, 15kΩ, 1206	Panasonic	ERJ-8GEYJ153V	1
R6	Resistor, 200Ω, 0603	Panasonic	ERJ-3GEYJ201V	1
R7	Resistor, 835Ω, 0603	Vishay	TNPW0603835RBEEN	1
T1	Transistor, NPN, 40V	ON	2N3904G	1
VR1	Voltage Reg., 5V	STM Micro	L7805CV	1
VR2	Voltage Reg., Adj, 5A	Texas Instr.	LM338T/NOPB	1

D.1.1 Starter Motor Circuit.

The starter motor circuit is based around IC2, a 3.86A motor driver, with a typical connection shown in Figure 517. This driver has the ability to control a motor forward, backward, brake, and coast depending on the inputs to pins IN2 and

IN1. To activate the "Brake" condition, both pins IN1 and IN2 need to receive a digital high signal (5V) on the pin. To run the motor forward, the only direction the starter motor needs to turn, IN1 needs to remain high (5V), while IN2 needs to receive a digital low signal (or near ground). To accomplish this, 5V are supplied to both input pins through separate 10kΩ pull-up resistors. This configuration ensures the motor driver will keep the motor in "Brake" mode when no signals are received from LabView. Pin IN2 is connected to the collector leg of transistor T1. To turn the starter motor on, a 1V signal is sent from LabView to the base leg of transistor T1. This voltage allows current to flow through the transistor to the grounded emitter leg, thus pulling the input to IN2 to a low signal.

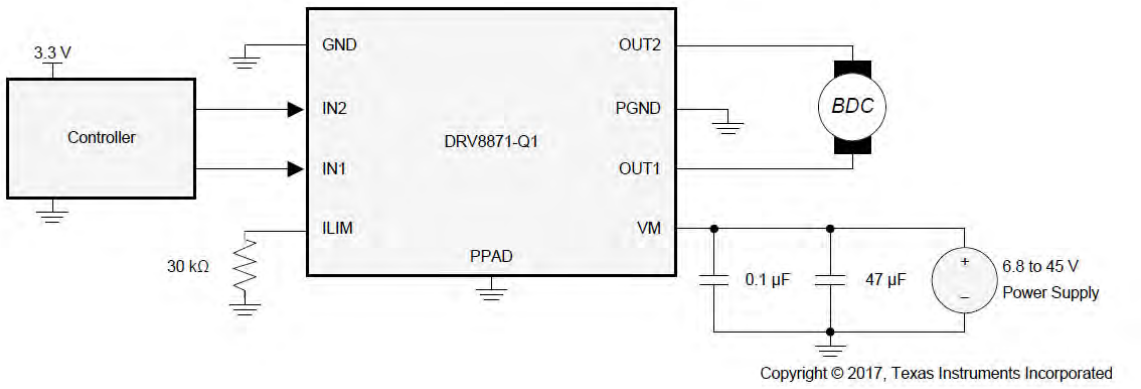


Figure 517. Typical connections of the DRV8871-Q1 TI motor driver [177]

This motor controller also has the ability to limit the maximum current output up to 3.86A no matter how much load torque is applied. The resistor connected to the ILIM leg controls the maximum current output through Equation 150 [177]; where I_{Ilim} is the current limit and R_{Ilim} is the resistor value in kΩ needed on the ILIM leg to achieve that current limit.

$$I_{Ilim}(A) = \frac{64kV}{R_{Ilim}(k\Omega)} \tag{150}$$

The startup torque on the starter motor during component testing required that a resistor value of 15kΩ be used to allow the full 3.86A to be supplied. During the component test the motor didn't pull an excess of 3.0A long enough to blow the 3A fuse, and after the initial startup the current draw dropped well below 3.0A.

The adjustable voltage regulator (VR2) had the ability to produce an output voltage between 1.2V and 32V at 5A depending on the resistor values connected to the "ADJ" leg shown in Figure 518. Resistors R1 and R2 in Figure 518 correspond to resistors R6 and R7 of the ECM Board, respectively. Equation 151 defines the relationship between R1 and R2 to produce the desired output voltage. This device controlled the voltage to the starter motor, so V_{out} needed to be 6.5V. The value of V_{Ref} was fixed by the chip at 1.25V. Using this reference voltage and assigning a value to R1 determined I_{adj}. Applying all of these values to Equation 151 produced a value of R1 = 200Ω and R2 = 835Ω, which match the values of R6 and R7 on the ECM Board.

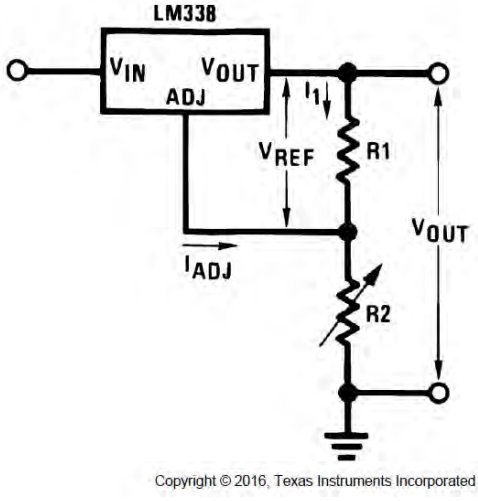


Figure 518. Typical connections of the LM338 TI adjustable voltage regulator [178]

$$V_{out} = V_{Ref}\left(1 + \frac{R2}{R1}\right) + I_{adj}R2 \tag{151}$$

D.1.2 Pump Circuit & Pulse-Width Modulation.

The preferred method to control the speed of a direct current (DC) motor is through pulse-width modulation PWM. Unlike other methods that generally rely on limiting the voltage supplied to the motor through a potentiometer, a PWM circuit allows the full voltage to be supplied to the motor, but it limits the duration that the voltage is supplied. The signal is sent on a square wave of constant frequency. The amount of time the voltage is supplied relative to the length of the square wave signal is called the duty cycle, measured in percent. A 50% duty cycle would then supply the motor with power for 50% of the square wave as shown in Figure 519. Since the supplied voltage is not limited while using a PWM signal, the motor outputs a peak torque whenever is receives power. Varying the duty cycle between 0% and 100% allows for motor speed control between off and maximum RPM, respectively.

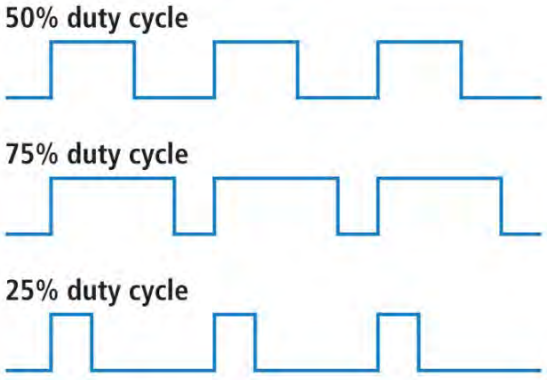


Figure 519. PWM duty cycle comparison [179]

An additional circuit board, referred to as the "PWM Gen" board, was jumpered into the ECM board to be able to use a PWM signal for pump speed control. The initial design plan was for LabView to output a PWM signal to the gate leg of MOSFET M1 on the ECM board. The MOSFET was positioned near the ground of the pump circuit. When the PWM signal was high, the MOSFET allowed current to flow from the drain leg to the source leg and the pump would run. When the PWM

signal was low, the MOSFET would not allow current to flow and the pump would stop. With the existing hardware in the COAL lab, LabView was not able to generate a PWM signal. To work around this limitation the PWM Gen board was created centered around the LTC6992CDCB-1 chip made by Linear Technologies. This chip receives an analog signal of 0-1V and converts that into a PWM signal with a duty cycle between 0% and 100% corresponding to the analog input voltage. Resistor values connected to the other legs of the chip control the square wave frequency. Figure 520 from the LTC6992CDCB-1 data sheet shows the connected resistor values needed to achieve a 2.6kHz square wave frequency.

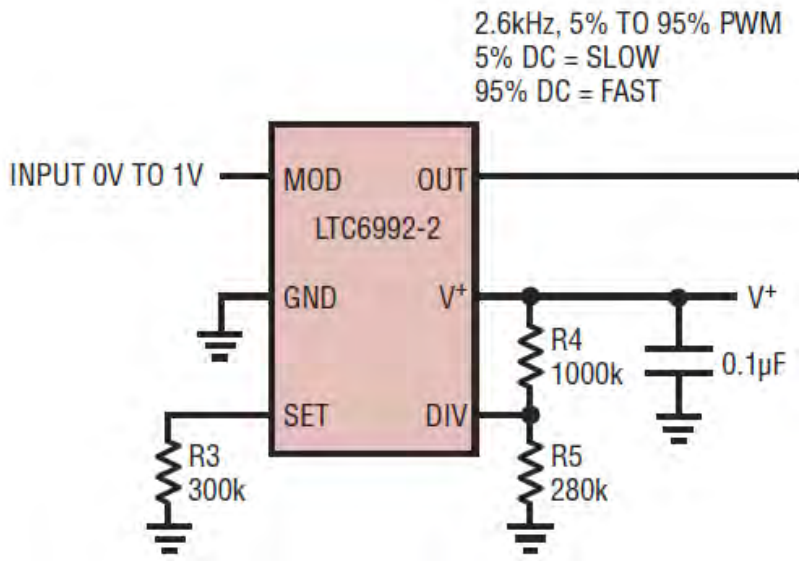


Figure 520. LTC6992CDCB-1 resistor requirements to achieve a 2.6kHz PWM output [180]

Figure 521 shows the schematic of the PWM Gen board with Figure 522 showing the layout diagrams. Large through hole resistors were used on this board because the necessary resistor values were readily available at AFIT. Like the ECM board, this board was drawn in Eagle V8.2.2 software, the router tool path was generated in CircuitCAM 6.1, and the board was made on the LPKF ProtoMat S62 CNC Router.

The populated manufactured board is shown in Figure 523. The PWM Gen board was mounted on a nylon stand-off over IO1 on the ECM board as shown in Figure 515 and was soldered onto the ECM board as indicated in Figure 514.

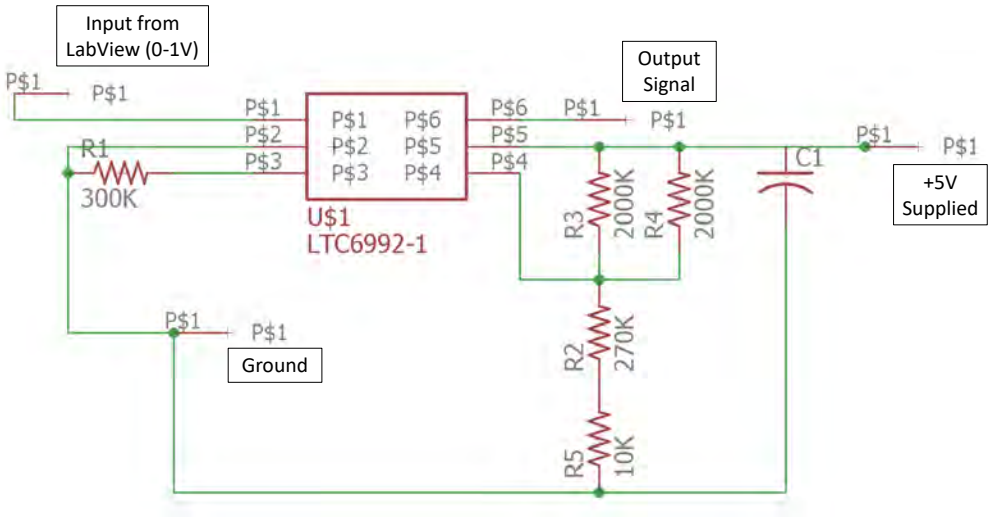
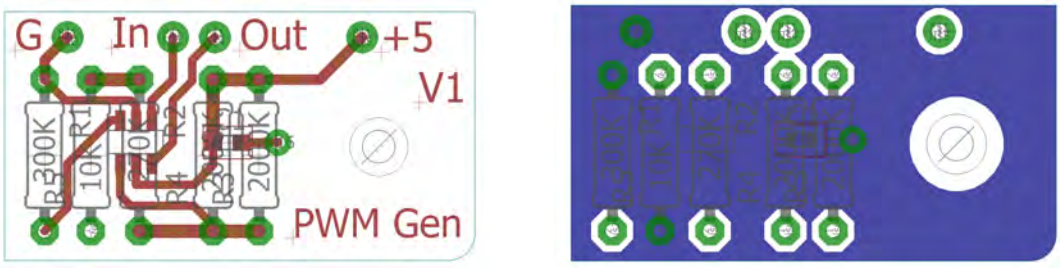


Figure 521. PWM Gen board schematic diagram



(a) PWM layout layer 1

(b) PWM layout layer 16

Figure 522. PWM Gen board layout diagram

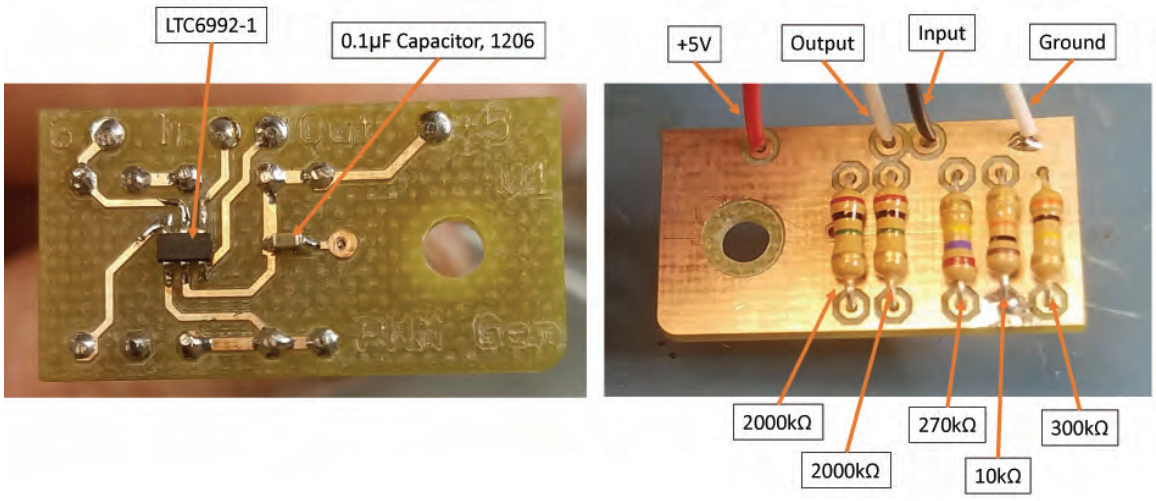


Figure 523. PWM Gen board manufactured hardware

D.1.3 Pass Through & Feedback Signals.

The ECM board featured two pass through signals and two feedback signals. The pass through circuits simply continued the conduction path from the engine board to the LabView interface cable through IO2 for the RPM hall effect sensor signals, and to a 2-pin, screw-type connector on the edge of the board (IO5) for the on-board EGT thermocouple sensor. A wire pair connected the thermocouple signal from IO5 to the thermocouple input panel (See Section D.4). An additional wire on the LabView interface cable was used to link the ECM board ground to the LabView DAQs.

Feedback signals were used to confirm LabView commanded operations did in fact take place and were at expected levels. The first feedback signal connected pin 2 of the LabView interface cable connected to IO2 to the pump circuit just prior to resistors R3. The PWM signal from the pump was read by LabView through the feedback channel to ensure the commanded PWM duty cycle was being achieved. Since the lubricant flow rate at each duty cycle was known (See Section D.7.2) this check confirmed that the correct amount of lubricant was provided to the JetCat for the given throttle setting. If the duty cycle measured through the pump feedback loop

didn't match the commanded duty cycle (within a tolerance band) a fault indicator was displayed on the LabView visual interface.

The second feedback signal measured the voltage after two parallel resistors connected to the positive terminal of the glow plug power supply, as shown in Figure 511. Each resistor was 1.8Ω (0.9Ω equivalent resistance since they were in parallel) and could dissipate 50 Watts each (TE Connectivity P/N THS501R8J). The voltage output of the power supply was increased greater than the required value needed by the glow plug to compensate for the voltage loss across the resistors. Using Ohm's law, a voltage measurement taken directly after resistors of known value, with a known input voltage, could directly determine the current out of the power supply. It was beneficial to confirm the current to the glow plug because it confirmed the plug would be at the correct temperature to light the combustor, but also because it confirmed continuity and that the filament wires of the plug were intact. If the current output from the power supply didn't match the expected value (within a tolerance band), a fault indicator was displayed on the LabView visual interface. The feedback signal was supplied to the ECM board through pin 2 of connector IO4. The signal was provided to LabView through pin 3 of IO2.

D.1.4 ECM Pin-Outs.

There are a total of five connectors (IO1 - IO5) that make external connections with the ECM board. The details of each connector are outline individually below. There are two parts labeled IO5 in Figure 515. They share the same part number because they are the same type of connector. One of these connectors makes an external connection for the pass through EGT thermocouple signal, the other is an internal connection to power an ECM case cooling fan (Fan). The fan is 40 x 40 mm and runs on 5V at 0.075A supplied by voltage regulator VR1. The red lead on the fan is positive, the black lead is negative. The word "FAN" is etched into the surface

of the ECM Board just above the fan connection block (IO5). The pin closest to the word “FAN” is the positive terminal. The first side of the ECM board contains connectors IO1 and IO2, as shown in Figure 524.

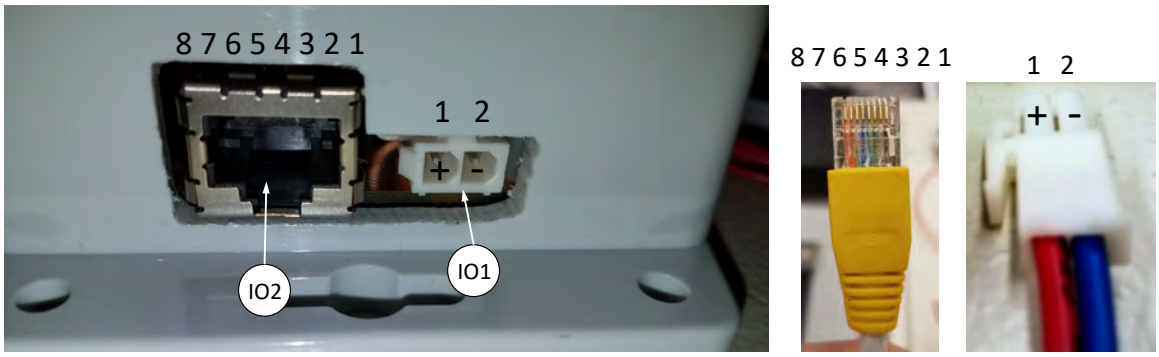


Figure 524. Pin numbering for connections IO1 and IO2

Connector IO1 serves as the main power connection to couple the ECM board to the primary power supply. There are two diodes, labeled D1 in Figure 514, that protect the power supply from a reversed current flow. These diodes should also protect the components on the board in the event the polarity was accidentally reversed on the input. The board was designed to run at 9V - 9.2V, so the power supply needed to be set to 9.2V - 9.4V to compensate for the 0.2V drop across the diodes. Table 69 provides the details for connector IO1.

Table 69. ECM Board connector IO1 specifications

Pin	Wire Color	Description	Other End Connection	Signal
1	Red	Power, +	Main power supply + terminal	9.4V
2	Blue	Power, -	Main power supply - terminal	GND

Connector IO2 served as the interface between the ECM Board and the LabView data acquisition (DAQ) modules. This connector is a standard 8 pin, RJ45 connector for Cat5e cables and was selected because it was compact. While standard ethernet cables will fit in the connector, the ECM is not compatible with routers or other

network hardware. The other end of the cable plugged in to connector IO2 was stripped and pig-tailed to plug into the necessary ports in the DAQ modules. Table 70 provides the details for connector IO2. At the DAQ end of the cable plugged into IO2, the ground wire (Green/White) was split to provide a common ground reference to Modules 2 and 3 and a differential ground reference to the Glow Plug Feedback, RPM 1 signal, and RPM 2 signal in Module 4.

Table 70. ECM Board connector IO2 specifications

Pin	Wire Color	Description	Other End Connection	Signal
1	Brown	Glow Plug Control	Legacy, No Connection	
2	Brown/White	Pump Feedback	CDAQ4, Module 4, ACH3	PWM 6V
3	Green	Glow Plug Feedback	CDAQ4, Module 4, ACH21	2V, 6V
4	Blue/White	Pump Control	CDAQ4, Module 3, AO2	0V - 1V
5	Blue	Starter Control	CDAQ4, Module 3, AO1	0V, 1V
6	Green/White	Ground	CDAQ4, Module 3 & 4	GND
7	Orange	RPM 1	CDAQ4, Module 4, ACH2	2V
8	Orange/White	RPM 2	CDAQ4, Module 4, ACH1	2V

The opposing side of the ECM board contains connectors IO3 and IO4 shown in Figure 525. These two connectors provide the linkage between the ECM Board and the Engine Board. They are divided by low power signals (IO3) and high power signals (IO4).

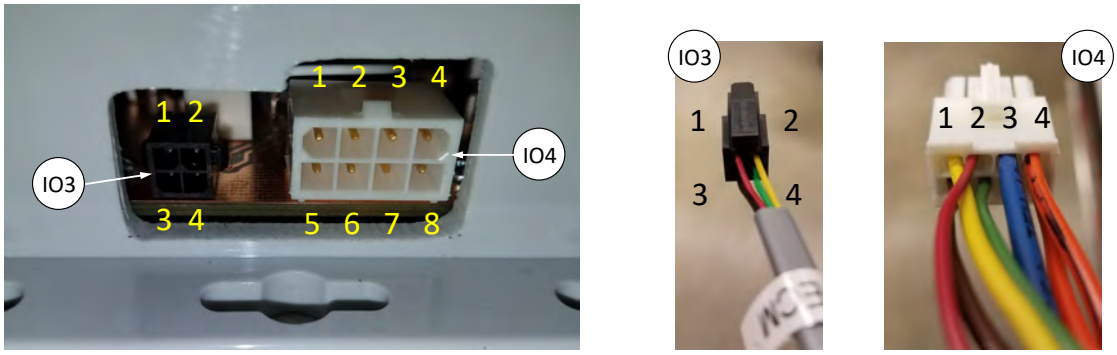


Figure 525. Pin numbering for connections IO3 and IO4

Connector IO3 accepts the low power inputs to the ECM Board for the pass through signals from the Engine Board. Table 71 provides the details for connector IO3. Note that the low power signal cable has the same connector types on both ends, yet the cable is not symmetric. Each end of the cable is labeled for "ECM" and "Engine" to ensure the correct connections.

Table 71. ECM Board connector IO3 specifications

Pin	Wire Color	Description	Other End Connection	Signal
1	Red	EGT Thermocouple 2	Engine Board IO3, Pin 3	mV
2	Yellow	RPM 1	Engine Board IO3, Pin 1	2V
3	Black	EGT Thermocouple 1	Engine Board IO3, Pin 4	mV
4	Green	RPM 2	Engine Board IO3, Pin 2	2V

Connector IO4 sends and receives higher voltage and/or higher current signals to and from the Engine Board. The one exception to the corresponding location of the connection to IO4 is the glow plug feedback connected into IO4 Pin 2. As previously discussed, this feedback signal originates just after the two 1.8Ω resistors connected to the positive terminal of the glow plug power supply. Table 72 provides the details for connector IO4. The high power signal cable is also not symmetric, however, there is only one 8-pin connection so it is easy to determine which end goes where.

Connector IO5 shown in Figure 526 is the final external ECM connection. This connector has two pins in a screw down terminal block to connect the pass through EGT thermocouple signal to the thermocouple panel. Table 73 provides the details for connector IO5.

D.2 Engine Board Redesign

The Engine Board served as the interface between the ECM Board and the JetCat hardware components. This structure allowed for consolidated input/output (I/O, IO) connectors, with the board distributing the signals to the hardware components.

Table 72. ECM Board connector IO4 specifications

Pin	Wire Color	Description	Other End Connection	Signal
1	Yellow	+9V supply to Engine	Engine Board IO6, Pin 3	+9V
2	Red	Glow Plug Feedback	Glow Plug Power Supply	2V, 6V
3	Blue	Ground	Engine Board Ground, IO7	GND
4	Orange/Black	Starter Motor -	Engine Board IO6, Pin 4	Return
5	Brown	Lubricant Pump +	Engine Board IO6, Pin 5	6V, 0.85A
6	Green	Lubricant Pump -	Engine Board IO6, Pin 6	Return
7	Empty	Redundant Ground	No Connection	
8	Orange	Starter Motor +	Engine Board IO6, Pin 1	6.3V, 3.86A

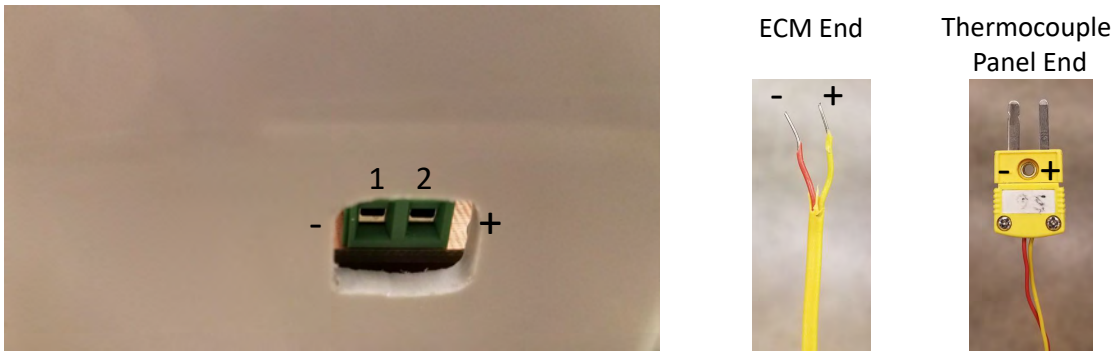


Figure 526. Pin numbering for connection IO5

Table 73. ECM Board connector IO5 specifications

Pin	Wire Color	Description	Other End Connection	Signal
1	Red	Thermocouple, -	Thermocouple Panel, Port 1	mV
2	Yellow	Thermocouple, +	Thermocouple Panel, Port 1	mV

When the internal glow plug was used with combustor Configuration 7, the Engine Board also interfaced with the glow plug power supply. The glow plug pins are not used with an external glow plug is tested. See Section D.3 for more information about glow plug power control. Figure 527 shows the schematic diagram of the Version 2 Engine Board and Figure 528 shows the layout of the components. The schematic and board layout were generated with Eagle V8.2.2 software. Version 2

incorporated a connector and traces for lubricant solenoid control, discussed in more detail later. Like the previous boards, the layout from the Eagle software was run through CircuitCAM 6.1 to generate the necessary computer milling files to produce the board. The board was then drilled, milled, and cutout on a LPKF ProtoMat S62 CNC Router housed in B640, Rm274 at AFIT. Figures 529 and 530 show both sides of the manufactured board populated with components. Component reference numbers have been added to Engine Board images and correspond to the components specified in Table 74. Several components were common between the Engine and ECM board. These components were given the same component reference numbers.

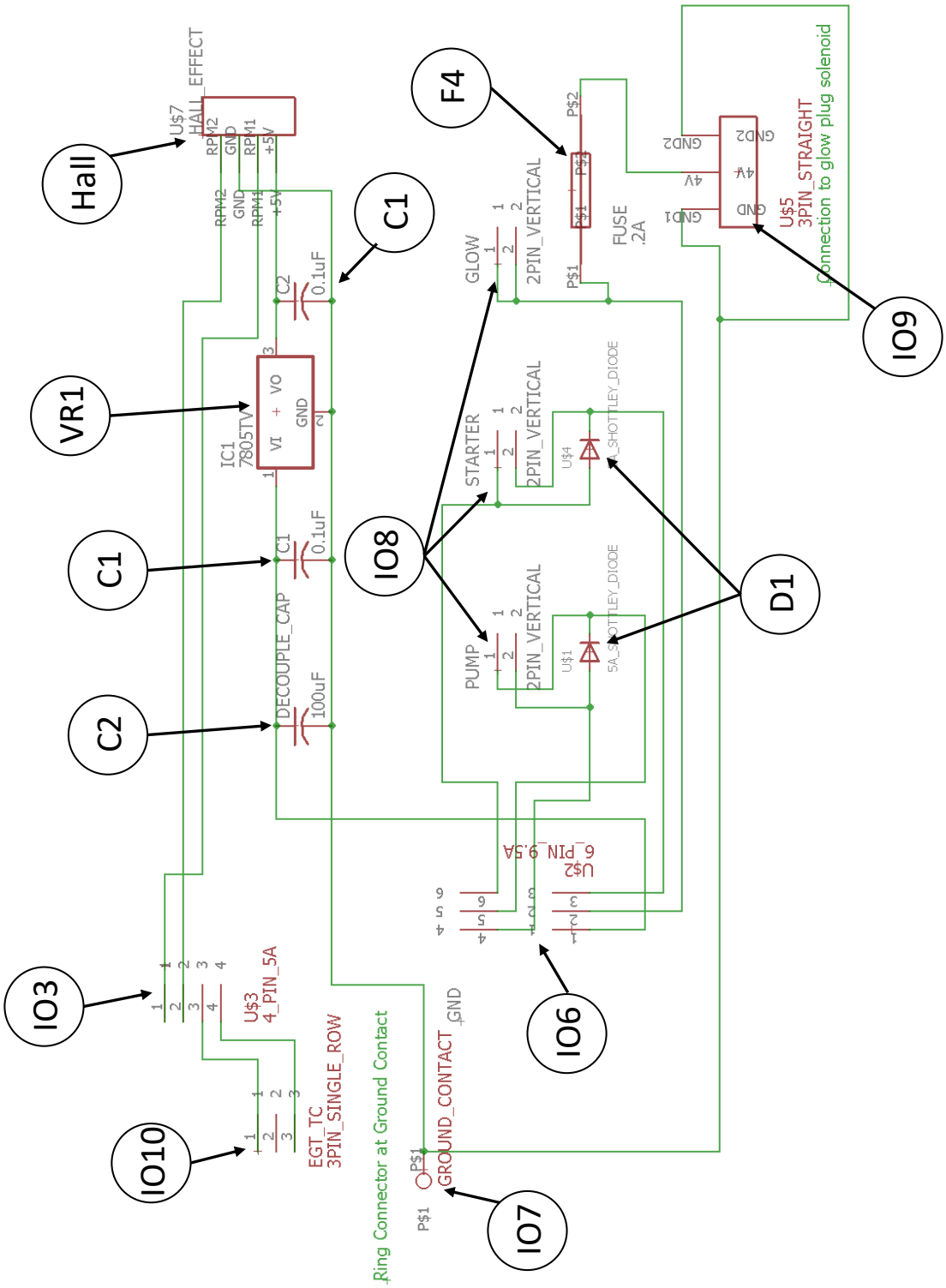


Figure 527. Redesigned Engine Board schematic diagram V2



Figure 528. Redesigned Engine Board layout, V2

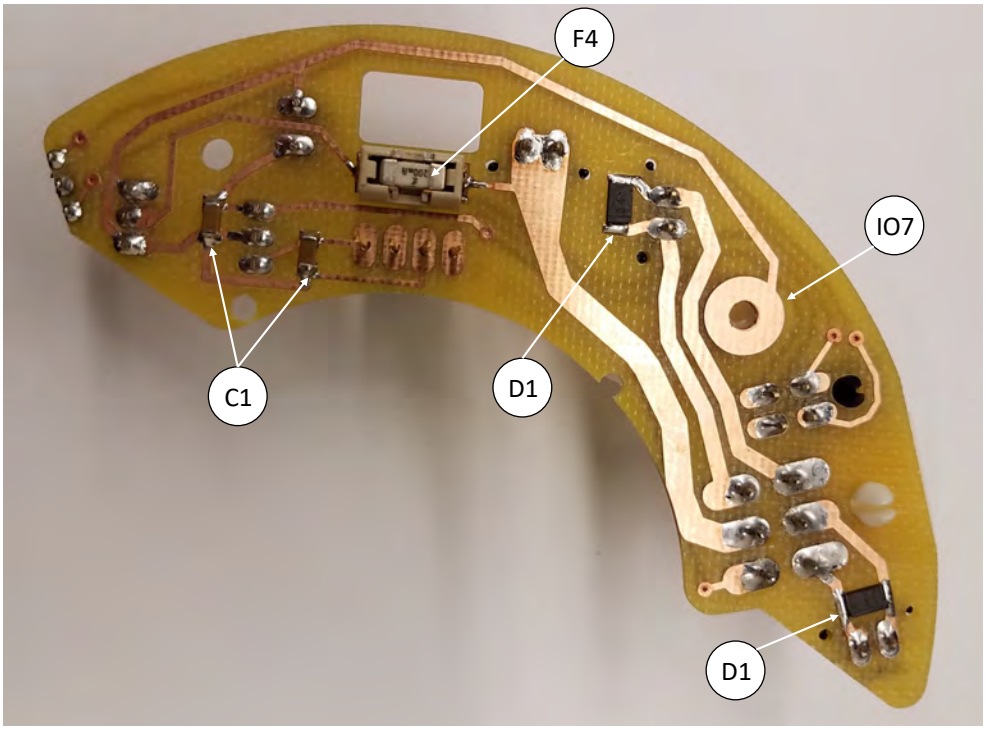


Figure 529. Redesigned Engine Board completed hardware layer 1, V2

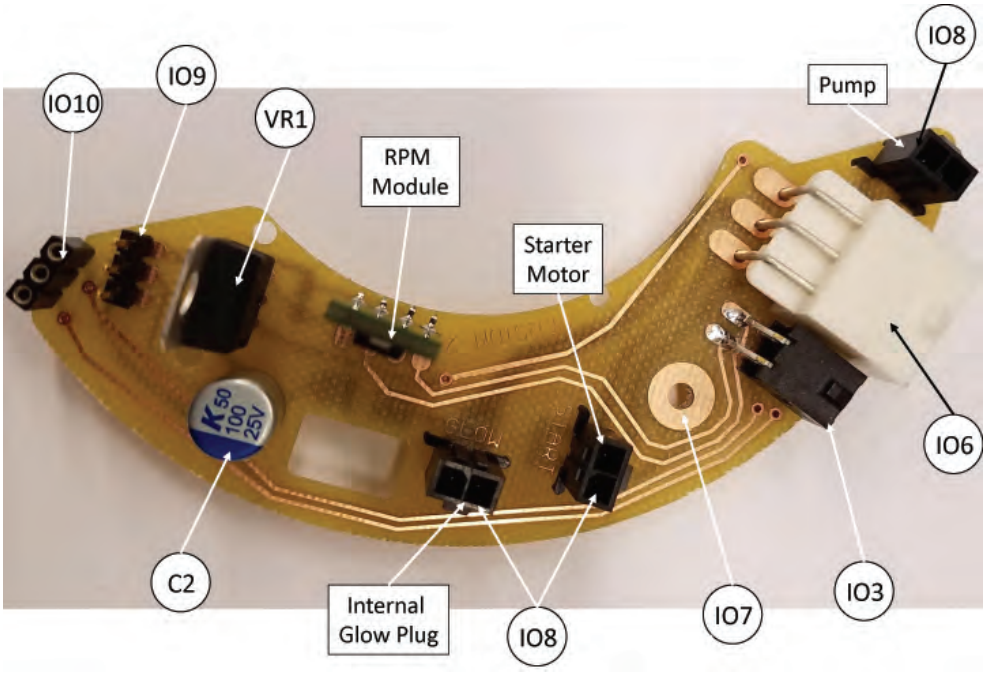


Figure 530. Redesigned Engine Board completed hardware layer 16, V2

Table 74. Engine Board Component Specifications, V2

Label	Description	Manufacturer	Part Number	Qty
C1	Capacitor, 0.1μF, 25V	Kemet	C1206F104K3RACTU	2
C2	Capacitor, 100μF, 25V	TE Connect.	A750KK107M1EAAE040	1
D1	Schottky Diode, 30V, 5A	Panasonic	DB2431200L	2
F4	0.2mA Surface Mount Fuse	Littelfuse	0154.200DR	1
IO3	Connector, 4 pin	TE Connect.	3-794618-4	1
IO3M	IO3 Mate	TE Connect.	794617-4	1
IO6	Connector, 6-Pin	TE Connect.	1-770969-1	1
IO6M	IO6 Mate	TE Connect.	172168-1	1
IO8	Connector, 2-Pin Vertical	TE Connect.	2-1445050-2	3
IO8M	IO8 Mate	TE Connect.	1445022-2	3
IO9	3-Pin header, vertical	Samtec Inc	TSW-103-07-G-S	1
IO10	3-Pin Socket, Vertical	Unknown	Unknown	1
Pin-L	Large Connector Pins	TE Connect.	770986-1	6
Pin-S	Small Connector Pins	TE Connect.	1-794610-1	10
VR1	Voltage Regulator, 5V	STM Micro	L7805CV	1

The connector labeled IO10 in Figure 530 was reused from the stock JetCat electronics so the manufacturer and part number are unknown. An attempt was made to purchase a replacement product but the sockets were too small to accept the larger diameter pins that were part of the EGT thermocouple assembly. The part labeled "RPM Module" in Figure 530 was also reused from the stock JetCat electronics for determining engine RPM. This part is discussed in greater detail in Section D.2.1.

With the exception of the circuit supporting the RPM Module circuit for RPM determination, the remainder of the circuits simply linked the connectors that interface with JetCat hardware to connectors IO3 and IO6. The starter motor and pump circuits included flyback diodes for circuit protection. Figure 531 shows how a flyback diode fits into an inductor (motor) circuit.

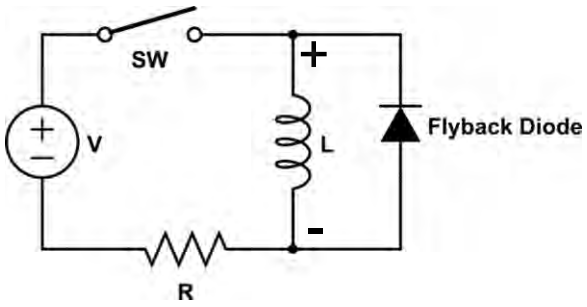


Figure 531. Simple inductor circuit with a flyback diode

When a motor or inductor (labeled "L" in Figure 531) is provided electricity a magnetic field is established and the motor begins to turn. When the switch (SW) is opened, the spinning inductor still has a magnetic field and continues to flow current. Since the source of the current was removed by opening the switch a large negative charge can build up at the positive end of the motor. The negative charge can be so strong that it can cause electricity to arc across the switch, potentially damaging components. When a flyback diode is installed parallel to the inductor, it prevents current from bypassing the inductor since diodes only allow current to flow in one

direction. However, when the switch is opened and a negative charge begins to build at the positive end of the inductor, the diode allows current to flow back to the positive end of the inductor to neutralize the charge. Current will continue to flow back up through the diode until the magnetic field in the inductor has dissipated.

The stock JetCat used a kerosene/oil blend for both lubrication and fuel. The new combustor tested in Objectives 4 and 5 switched to propane as the fuel, but the kerosene/oil blend was still required to lubricate the two main shaft bearings in the JetCat. The stock JetCat used two solenoid values to control the delivery of kerosene/oil to the internal glow plug and the fuel distribution plenum which also fed the bearing lubrication line. As shown previously in Figure 407 the solenoid that fed the fuel plenum and lubrication line was removed and replaced with a straight through lubricant fitting that could not be closed. This change ensured the bearings would always receive lubricant as long as the pump was operating. The solenoid that fed the glow plug line was maintained and an electrical connection was added to the Engine Board for solenoid operation.

The stock JetCat glow plug was designed vaporize and ignite kerosene to generate heat to then vaporize the main fuel supply without the use of a gaseous starter fuel. The solenoid connection on the Engine Board was directly connected to the glow plug positive lead. When the glow plug was energized from the engine board, a small amount of power was distributed to the solenoid through the board mounted fuse (F4) to allow the solenoid valve to open. No independent control of the solenoid was built into the board. When the glow plug was energized, the pump was commanded to speed up slightly to push a small amount of kerosene to the glow plug to flash off and ignite the main fuel. When the glow plug was switched off the solenoid would close stopping the flow of kerosene to the plug. When an external glow plug was used (installed through the engine casing from the outside), the glow plug connection on

the Engine Board was not energized and the solenoid would not open.

Also shown in Figure 407 are the M3 stainless steel screws with copper washers labeled "Closed Fuel Ports x6" that were installed to close off the stock fuel ports in the distribution plenum. The lubricant line was the only active fitting connected to the plenum.

The RPM Module circuit included a 5V voltage regulator (VR1), a decoupling capacitor (D2), and two smoothing capacitors (C1) to try and produce clean power to the RPM Module.

D.2.1 RPM Module.

The JetCat RPM measurement was determined by counting pulses from a sinusoidal wave produced by a hall effect sensor on the RPM Module. A small magnet installed under the engine spinner nut interacted with the hall effect sensor as it spun. The RPM module was reused from the stock JetCat electronics, however, the sensor chip was found to be a HAL401SF-K Linear Hall-Effect Sensor IC made by Micronas. The RPM module and typical application circuit for HAL401SF-K are shown in Figures 532 and 533, respectively. In Figure 533 the oscilloscope was replaced by LabView.

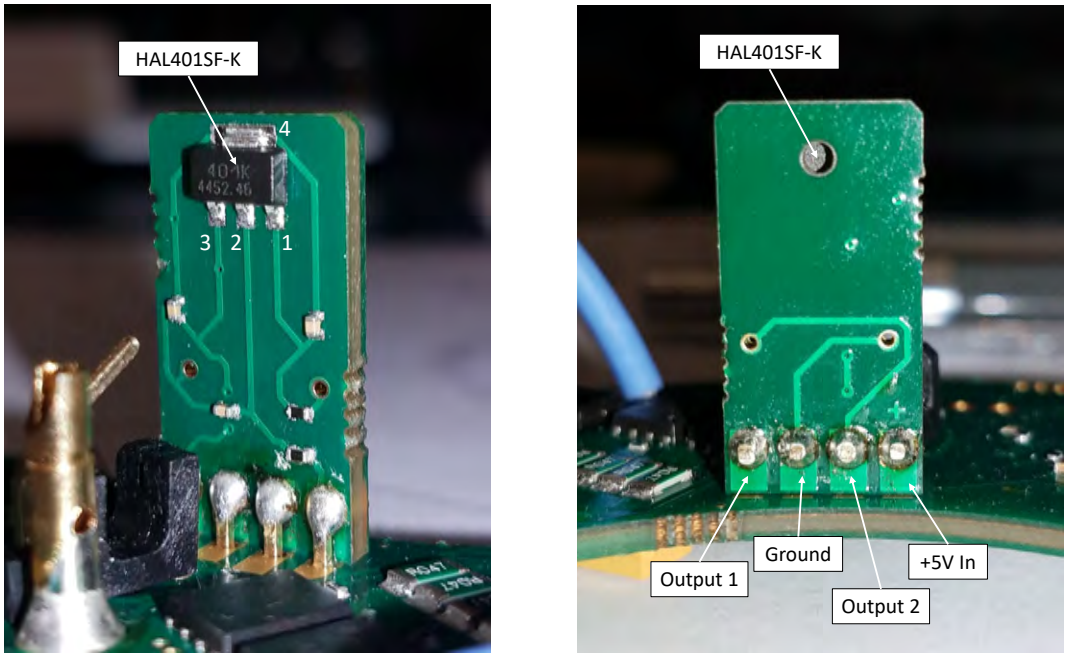


Figure 532. RPM module reused from stock JetCat P90RXi

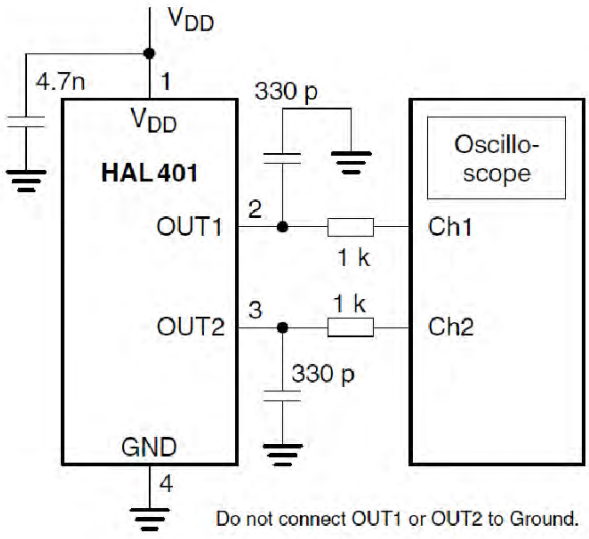


Figure 533. Typical application of the HAL401SF-K hall effect IC [181]

The HAL401SF-K chip is unique in that there are two hall effect sensors installed out of phase from each other that produce independent outputs. Figure 534 shows a voltage measurement from each output for different rotational positions of the

spinner nut. The initial attempt to have LabView calculate an RPM only used one of the outputs from the RPM module. As you can see in Figure 534 the fluctuation in voltage with spinner nut rotation was small. To make calculations even more difficult, the signal was noisy making it hard to find the output sine wave to count the frequency. However, once it was discovered that the two outputs were out of phase, the calculation became easier. Both outputs experienced the same electrical noise, so by subtracting the signal from output 1 from the signal from output 2, the noise was removed and a clean sine wave was produced. The LabView program was then able to treat the subtracted signal like a sound wave and calculate the frequency. The RPM calculated by LabView was compared to the RPM determined by an optical RPM sensor as the engine was turned with an electric motor. The LabView RPM value was found to be accurate.

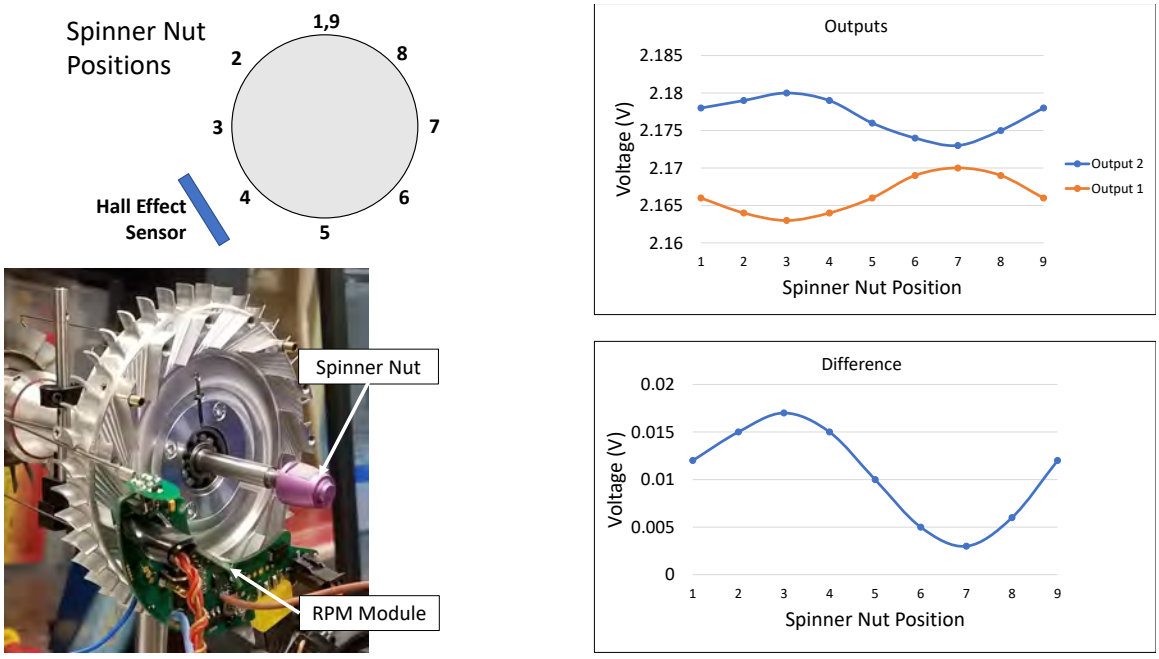


Figure 534. Output voltage measurements from RPM Module outputs 1 and 2

D.2.2 Engine Board Pin-Outs.

Connector IO3 on the Engine Board handled the low power signal transmission to the ECM. These signals included the RPM and EGT thermocouple voltages. Figure 535 shows connectors IO3, IO6, and IO7 on the engine board. These three connectors made up the extent of the external communications between the engine and the supporting systems. Table 75 provides the pin-out specifications for Engine Board IO3.

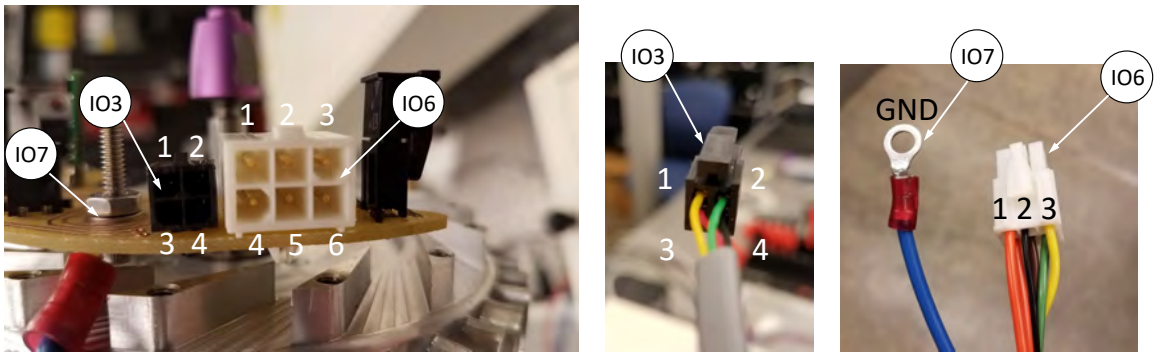


Figure 535. in numbering for Engine Board connection IO3, IO6, and IO7

Table 75. Engine Board connector IO3 specifications

Pin	Wire Color	Description	Other End Connection	Signal
1	Yellow	RPM 1	ECM Board IO3, Pin 2	2V
2	Green	RPM 2	ECM Board IO3, Pin 4	2V
3	Red	EGT Thermocouple 1	ECM Board IO3, Pin 1	mV
4	Black	EGT Thermocouple 2	ECM Board IO3, Pin3	mV

Connector IO6 was the high power connector on the Engine Board. The lubricant pump, starter motor, internal glow plug, and a 9V supply to VR1 to power the RPM module ran through this connector. Connector IO7 was a ground pad on the Engine Board. On Layer 1 this pad made contact with the engine chassis as a chassis ground. Both types of glow plugs were chassis grounded. While the ground pad was located on both sides of the board, the hole through the pads was not plated to connect both

sides together. A chassis mounting screw was needed to join the chassis and Layer 1 pad to the Layer 16 pad which connected to Connector IO7. Table 76 provides the pin-out specifications for IO6, and Table 77 provides the pin-out specifications for IO7.

Table 76. Engine Board connector IO6 specifications

Pin	Wire Color	Description	Other End Connection	Signal
1	Orange	Starter Motor +	ECM Board IO4, Pin 8	6.5V, 3.86A
2	Black	Int. Glow Plug +	Glow Plug Power Supply	See Table 84
3	Yellow	+9V Supply	ECM Board IO4, Pin 1	+9V
4	Orange/Black	Starter Motor -	ECM Board IO4, Pin 4	Return
5	Brown	Lubricant Pump +	ECM Board IO4, Pin 5	6V, 0.85A
6	Green	Lubricant Pump -	ECM Board IO4, Pin 6	Return

Table 77. Engine Board connector IO7 specifications

Pin	Wire Color	Description	Other End Connection	Signal
1	Blue	Ground	ECM Board IO4, Pin 3	GND

Connection IO8 included three 2-pin vertical connectors of the same type. The connectors went to the lubricant pump, starter motor, and internal glow plug. The lubricant pump and starter motor had a positive and negative pin, both pins on the internal glow plug connector were positive (the glow plug was chassis grounded). Figure 536 shows the pin specifications for connectors IO8. Tables 78, 79, and 80 list the details of the lubricant pump, starter motor, and internal glow plug connections, respectively.

Connectors IO9 and IO10 were the final two internal hardware connections to the internal glow plug solenoid and EGT thermocouple, respectively. Figure 537 shows the pin specifications for these two connectors with additional details provided in

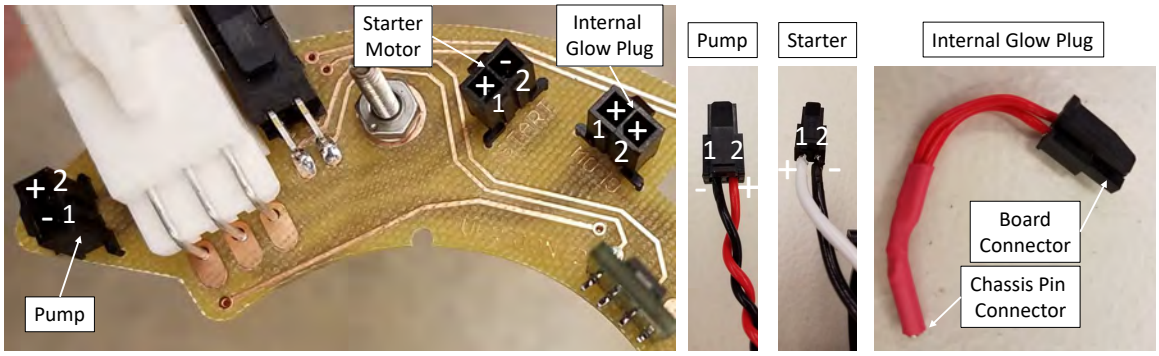


Figure 536. Pin numbering for connection IO8

Table 78. Engine Board connector IO8-lubricant pump specifications

Pin	Wire Color	Description	Other End Connection	Signal
1	Black	Lubricant Pump -	Lubricant Pump	Return
2	Red	Lubricant Pump +	Lubricant Pump	6V

Table 79. Engine Board connector IO8-starter motor specifications

Pin	Wire Color	Description	Other End Connection	Signal
1	White	Starter Motor +	Starter Motor	6.3V, 3.86A
2	Black	Starter Motor -	Starter Motor	Return

Table 80. Engine Board connector IO8-internal glow plug specifications

Pin	Wire Color	Description	Other End Connection	Signal
1	Red	Internal Glow Plug +	Chassis Pin	6V, 6.5A
2	Red	Internal Glow Plug +	Chassis Pin	6V, 6.5A

Tables 81 and 82. Pins 1 and 3 of Connector IO9 were both grounded, with Pin 2 providing a positive voltage. This configuration allowed the mating connector to be installed in either direction. Due to the placement on the board, the mating connector to IO10 could only be installed in one orientation.

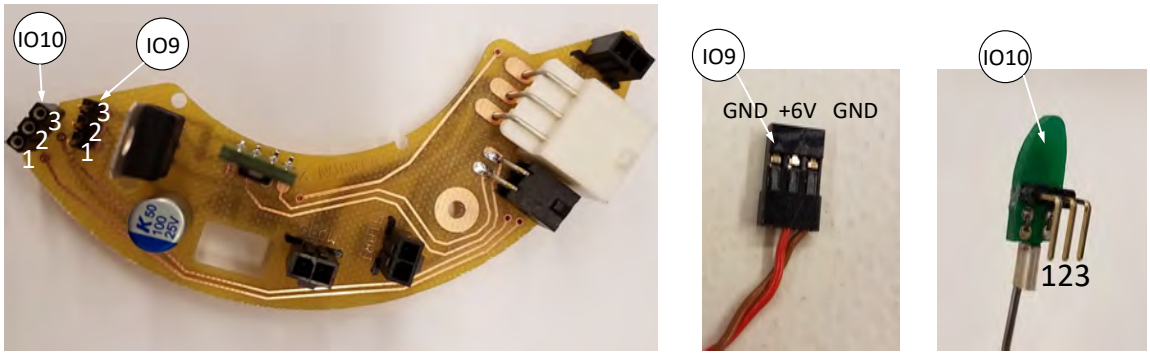


Figure 537. Pin numbering for connections IO9 and IO10

Table 81. Engine Board connector IO9 specifications

Pin	Wire Color	Description	Other End Connection	Signal
1	Orange	Solenoid ground	Lubricant Pump Solenoid	GND
2	Red	Solenoid +	Lubricant Pump Solenoid	+6V
3	Orange	Solenoid ground	Lubricant Pump Solenoid	GND

Table 82. Engine Board connector IO10 specifications

Pin	Wire Color	Description	Other End Connection	Signal
1	Header Pin	EGT Thermocouple +	EGT Thermocouple	mV
2	Header Pin	Unused	Unused	N/A
3	Header Pin	EGT Thermocouple -	EGT Thermocouple	mV

D.3 Glow Plug Power Control

To add greater control over the voltage and amperage supply to the glow plug, a switching mode power supply was used in place of a permanently configured circuit built into the ECM Board. The BK Precision Model 1688B power supply shown in Figure 538 had the ability to set the voltage and amperage remotely and turn the output on and off remotely through LabView. This power supply had an output range of 1 - 18V at 0 - 20A. To enable LabView control of the power supply, the power switch on the front of the unit must be on, and the mode switch on the back of the

unit must be set to “Remote Ctrl” with the remote control cable properly installed and configured.



(a) Glow plug power supply front



(b) Glow plug power supply back

Figure 538. BK Precision Model 1688B switching mode power supply (1-18V, 0-20A output) for glow plug power

The remote control connection was an 8-pin barrel connector, however, only four of the pins made connections with LabView. Figure 539 shows the pin-outs of the male wire connector and the female power supply connector with pins numbered. Table 83 provides the specifications on each pin.

The electronics could be configured to power an internal or external mounted glow plug as well as ceramic element and coil filament plugs to support current and future



Figure 539. BK Precision power supply remote control connector pins

Table 83. BK Precision power supply remote control connector pin specifications

Pin	Wire Color	Description	Other End Connection	Signal
1	Blue	Internal +5V	No Connection	+5V, <50mA
2	Brown	Voltage Adjust	CDAQ 4, Module 2, AO0	0-5V
3	Green	Current Adjust	CDAQ 4, Module 2, AO1	0-5V
4	White	Ground	CDAQ 4, Module 2, AO0/AO1/AO2 COM	GND
5	Red	Output Off	CDAQ 4, Module 2, AO2	Short to GND
6	Yellow	N/A	No Connection	N/A
7	Orange	N/A	No Connection	N/A
8	Black	N/A	No Connection	N/A

needs. The difference between the glow plug types are shown in Figure 540, where the ceramic element plug is the stock JetCat glow plug. Both of these plug configurations provided heat to the inside of the combustor to light the fuel and could be used as an external glow plug installed from outside of the engine and screwed in though the casing, or as an internal glow plug mounted fully inside the engine. Table 84 shows the power requirements for each glow plug as well as the required power supply voltage setting to produce the correct voltage to the glow plug after the voltage loss across the parallel resistors used for LabView feedback.



(a) Coil filament glow plug



(b) Ceramic element glow plug

Figure 540. Types of glow plugs used in Objectives 4 and 5

Table 84. Glow plug power requirements

Plug Type	Voltage	Current	Glow Plug Power Supply Voltage Setting
Coil Filament	2V	4.4A	6V
Ceramic Element	6V	6.5A	11.85

As mentioned in Section D.1.3, the output of the glow plug power supply was connected to two parallel 1.8Ω resistors that could dissipate 50 Watts each (TE Connectivity P/N THS501R8J), as shown in Figure 541. These resistors enabled a voltage measurement to be taken by LabView downstream of the resistors, which would confirm the current through the resistors. The current through the resistors would be the same as the current through the glow plug confirming continuity through the heating element and ensuring the correct heat level was reached for ignition. In the equation $V = I \times R$, V is the voltage drop across the resistors (V = Power Supply Voltage - Measured Voltage After Resistors), I is the current to be solved for, and R is 0.9Ω (equivalent resistance for parallel 1.8Ω resistors). If the current output from the power supply didn't match the expected value (within a tolerance band), a fault indicator was displayed on the LabView visual interface.

Figure 542 shows the glow plug power and feedback wire connections. After the 1.8Ω parallel resistors the wire was split to allow a plug-in fitting for the feedback

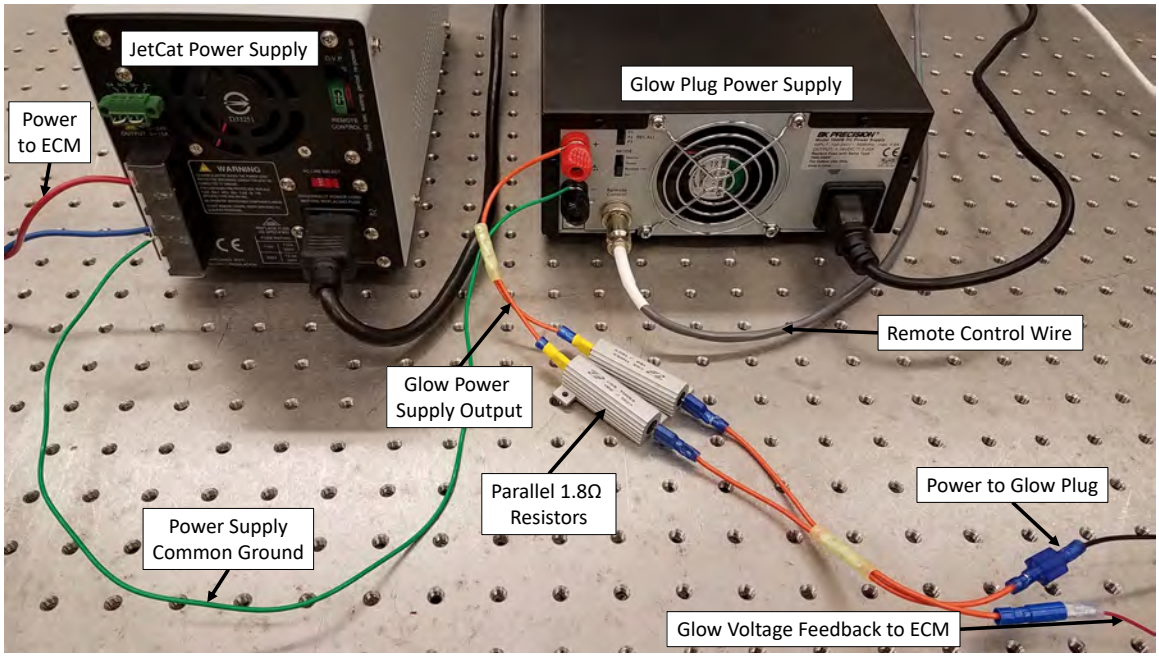


Figure 541. Glow plug power supply voltage feedback circuit

(round) and glow plug power (spade) connections. Since the internal glow plug was powered through the Engine Board, and the external glow plug was powered directly though an external fitting, the appropriate wire could be connected to the glow plug power connector from the power supply.

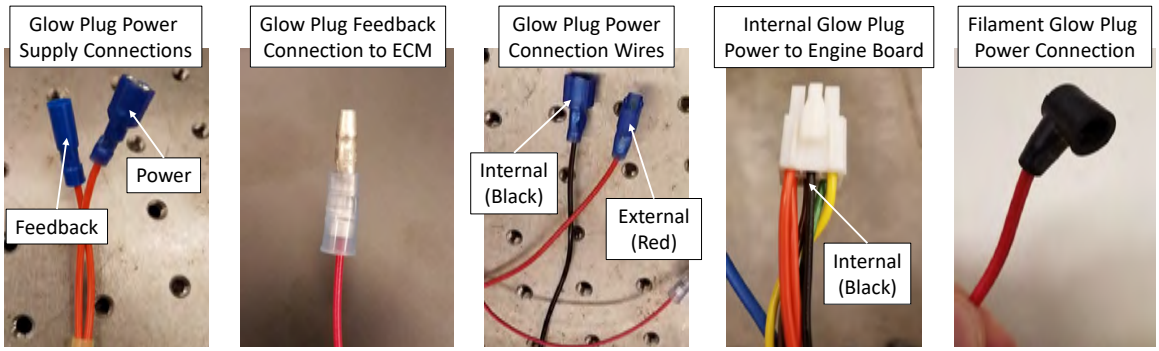


Figure 542. Glow plug power wire connectors

D.4 Temperature Measurements

Temperature measurements in the JetCat were made by Omega K-type thermocouples connected to a dedicated thermocouple panel shown in Figure 543. Each port in the panel was numbered from 1 to 24 and corresponded to the order they were connected to CDAQ4 Module 1, an NI 9213 high-density thermocouple module. The channel numbering in the module started at 0, so the module channel numbering was equal to the panel port number - 1. This DAQ module had 16 channels so only the first 16 ports in the panel were usable.

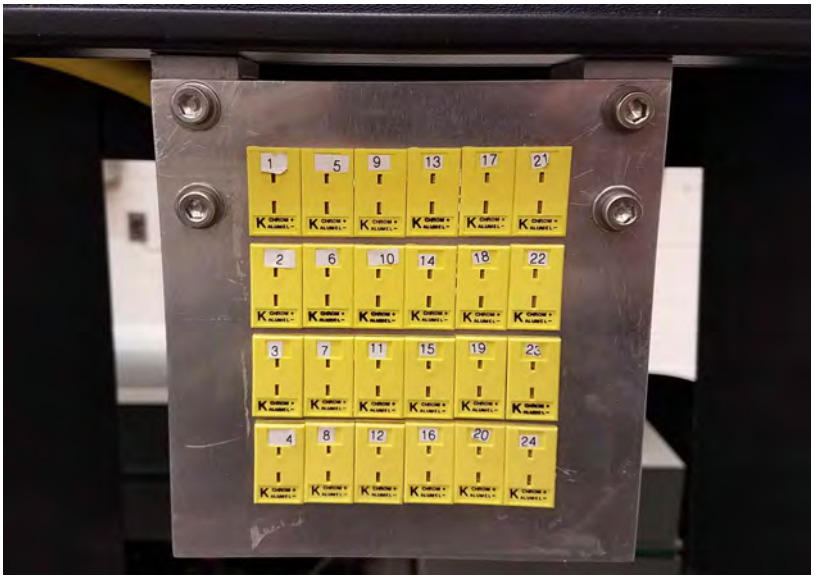


Figure 543. Dedicated JetCat thermocouple panel

D.5 Thrust Measurements

JetCat thrust measurements were made by an Interface Force Sensor Model SM-50 mounted between the laser table and the test stand engine mount as shown in Chapter IX. The sensor had a maximum excitation voltage of 15V and had a rated output of 3.0 mV per volt of excitation. A 10.0V excitation voltage was supplied from a power conditioning board mounted in the COAL Lab control station, as shown in

Figure 544. The conditioning boards were provided 14.0V from a Lambda Power Supply also located in the COAL Lab control station.

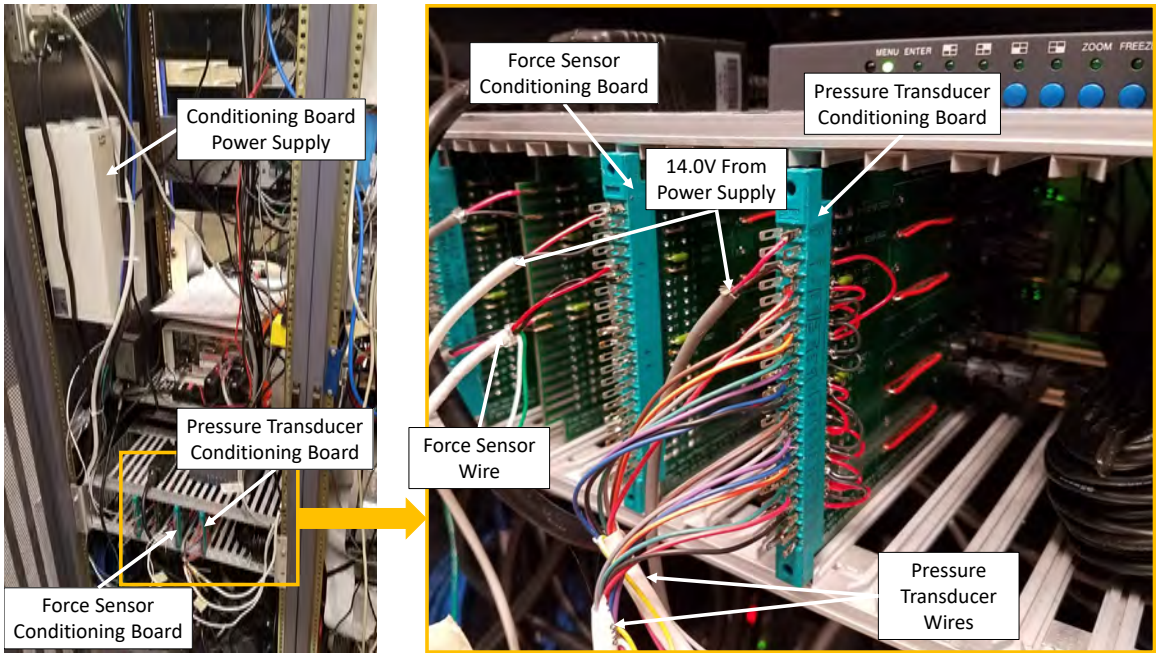


Figure 544. Thrust sensor and pressure transducer power conditioning boards

The Interface Force Sensor Model SM-50 had four wires; a positive and negative excitation, and a positive and negative output signal. A Molex connector was installed on the end of the force sensor wire to allow the sensor to be disconnected from the extension wire that connected back to the control station. Figure 545 shows the wire diagram for the Molex connection and Table 85 provides the sensor wire specifications. The + and - force sensor signals were connected to CDAQ 4, Module 4, Channel ACH4 in a differential mode so LabView could measure the difference between the inputs.

The force sensor needed to be calibrated in order for LabView to be able to convert a voltage output to a force. Since the force sensor was installed in the JetCat test stand, the calibration was performed in place. However, the sensor was installed horizontally, making it slightly more difficult to calibrate. A roller pulley was installed at the end of the table where the test stand was mounted. A cable was connected to

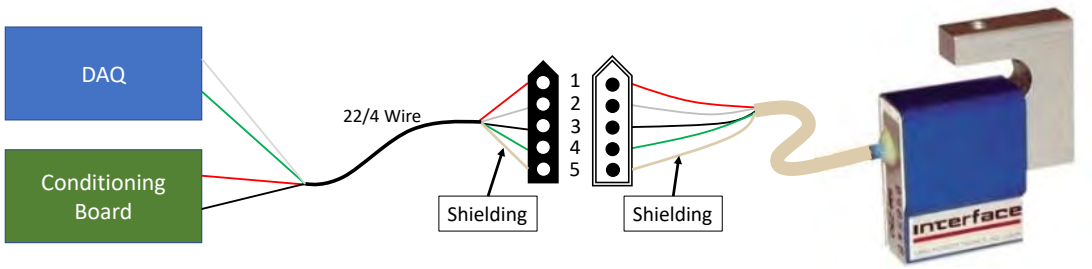


Figure 545. Thrust sensor - Interface Force S-Type, Model SM-50 wiring

Table 85. Interface Force Sensor Model SM-50 wire specifications

Pin	Wire Color	Description	Other End Connection	Signal
1	Red	Excitation +	Power conditioning board +	+10V
2	White	Signal -	CDAQ 4, Module 4, ACH4	mV
3	Black	Excitation -	Power conditioning board -	GND
4	Green	Signal +	CDAQ 4, Module 4, ACH4	mV
5	Shielding	Shielding	No Connection	N/A

the test stand engine mount and draped over the pulley and allowed to hang vertically. Calibrated weights were then hung from the cable. The pulley enabled the direction of force of the hanging weights to be shifted horizontal and thus apply the force to the engine mount. A series of increasing weights were applied to the hanging cable and the force sensor voltage output was measured for each increment. A plot of the force versus voltage (E) output is shown in Figure 546 along with the calibration equation.

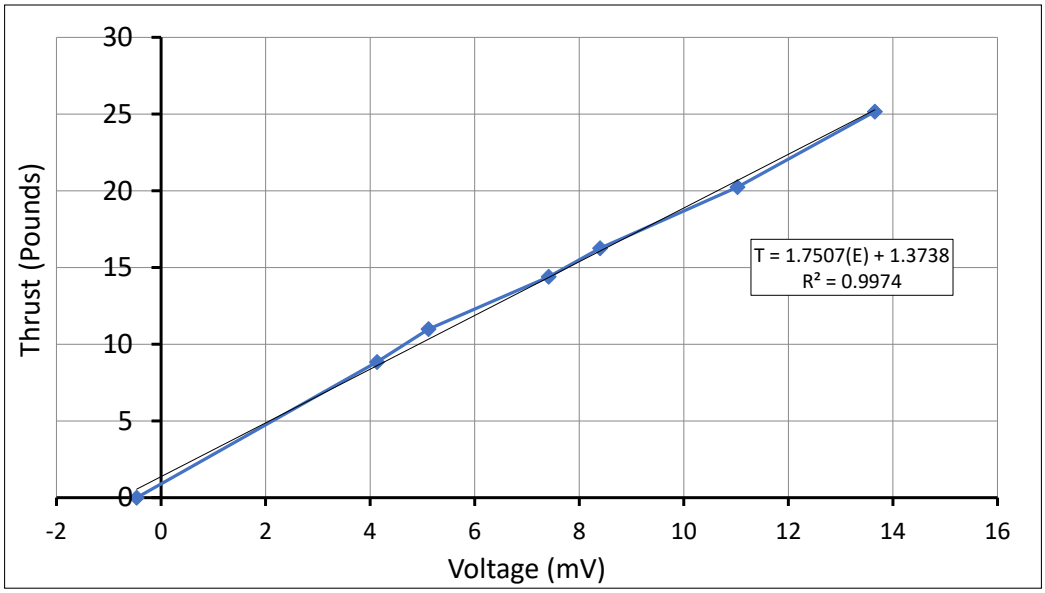


Figure 546. Engine thrust sensor calibration curve

D.6 Pressure Measurements

Pressures in the JetCat were measured using eight independent Omega High Performance Pressure Transducers. Three pressure measurement ranges were used including 0-5 psig (Model PX409-005G5V), 0-15 psig (Model PX409-015G5V), and 0-30 psig (Model PX409-030G5V). All of these transducers required a minimum of a 10V excitation to achieve an amplified 0 - 5V output signal. A 10V excitation was provided by the power conditioning boards as described in Section D.5 and shown in Figure 544. Because each of the pressure transducers only pulled 10mA, all of the pressure transducers could be powered by a single conditioning board without overloading the voltage regulators. Each transducer only had three wires; + excitation, signal output, and common ground. The common ground was connected back to the power conditioning board, but an additional wire was run from the conditioning board power supply ground terminal to each pressure transducer DAQ Module input (specified below) to ensure the differential measurement on each channel was referenced to the correct ground.

All eight pressure transducers were installed into a machined plastic block to allow for easy connection of the pressure feed lines and connection of the pressure transducer wires to extension wires through the use of screw terminal blocks. The extension wire was needed to get the signals between the JetCat test area and the COAL Lab control station. The pressure transducer assembly is shown in Figure 547. The threaded fittings on the pressure transducers were 1/4-18 NPT, while the Swagelok pressure feed line fittings were 1/16-27 NPT and accepted 1.59 mm (0.0625 inch) diameter tubing.

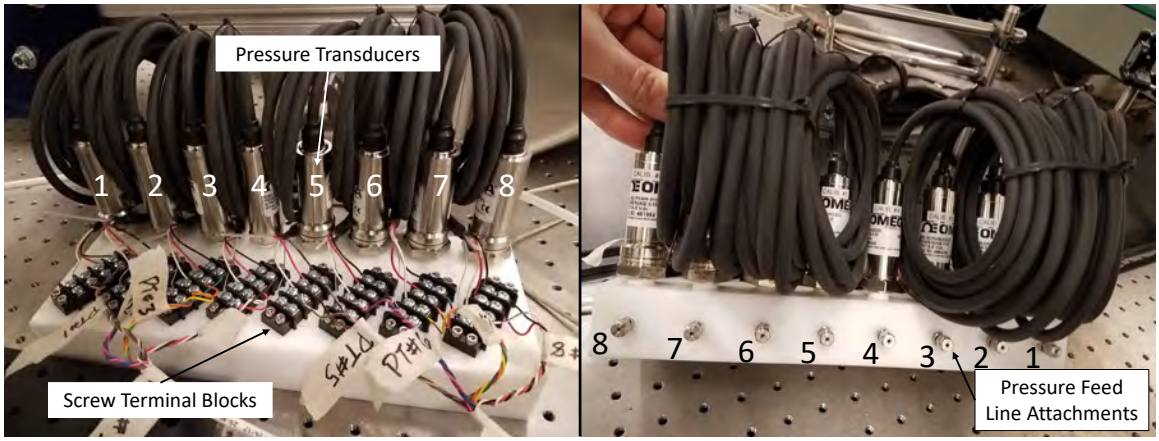


Figure 547. Pressure transducer block assembly and transducer numbering

Table 86 provides the pressure range of each transducer, the extension wire color pair to the transducer wire, wire description, the connection of the extension wire far end, and signal level, all arranged by the transducer numbers from Figure 547. The "Far End Connection" indicates the channel assignment in CDAQ 4, Module 4 for the specified transducer signal, or the positive or negative connection to the pressure transducer conditioning board. There were two 12-conductor wires used as extensions. Transducers 1 - 4 were connected to the first wire, while Transducers 5 - 8 were connected to the second wire. Black stripes were added to the individual conductors connected to Transducers 5 - 8 to distinguish them from the extensions of Transducers 1 - 4 which had all the same color wires.

Table 86. Pressure transducer pressure range and wire specifications

Transducer Number	Transducer Wire Color	Extension Wire Color	Description	Far End Connection	Signal
	White	Tan	Signal +	ACH5	0-5V
1	Red	Brown	Excitation +	+	+10V
(0-5 psig)	Black	Gray	Common GND	GND	GND
	White	Pink	Signal +	ACH6	0-5V
2	Red	Purple	Excitation +	+	+10V
(0-30 psig)	Black	Blue	Common GND	GND	GND
	White	Yellow	Signal +	ACH7	0-5V
3	Red	Orange	Excitation +	+	+10V
(0-30 psig)	Black	Green	Common GND	GND	GND
	White	White	Signal +	ACH16	0-5V
4	Red	Red	Excitation +	+	+10V
(0-30 psig)	Black	Black	Common GND	GND	GND
	White	Tan/Black	Signal +	ACH17	0-5V
5	Red	Brown/Black	Excitation +	+	+10V
(0-15 psig)	Black	Gray/Black	Common GND	GND	GND
	White	Pink/Black	Signal +	ACH18	0-5V
6	Red	Purple/Black	Excitation +	+	+10V
(0-15 psig)	Black	Blue/Black	Common GND	GND	GND
	White	Yellow/Black	Signal +	ACH19	0-5V
7	Red	Orange/Black	Excitation +	+	+10V
(0-15 psig)	Black	Green/Black	Common GND	GND	GND
	White	White/Black	Signal +	ACH20	0-5V
8	Red	Red/Black	Excitation +	+	+10V
(0-15 psig)	Black	Black/Black	Common GND	GND	GND

The transducers were calibrated at the factory with a 24V excitation voltage, meaning our 10V excitation voltage would produce a different response and a new calibration was required. The calibration curves, as well as the calibration equations, for all eight transducers with a 10V excitation are shown in Figure 548.

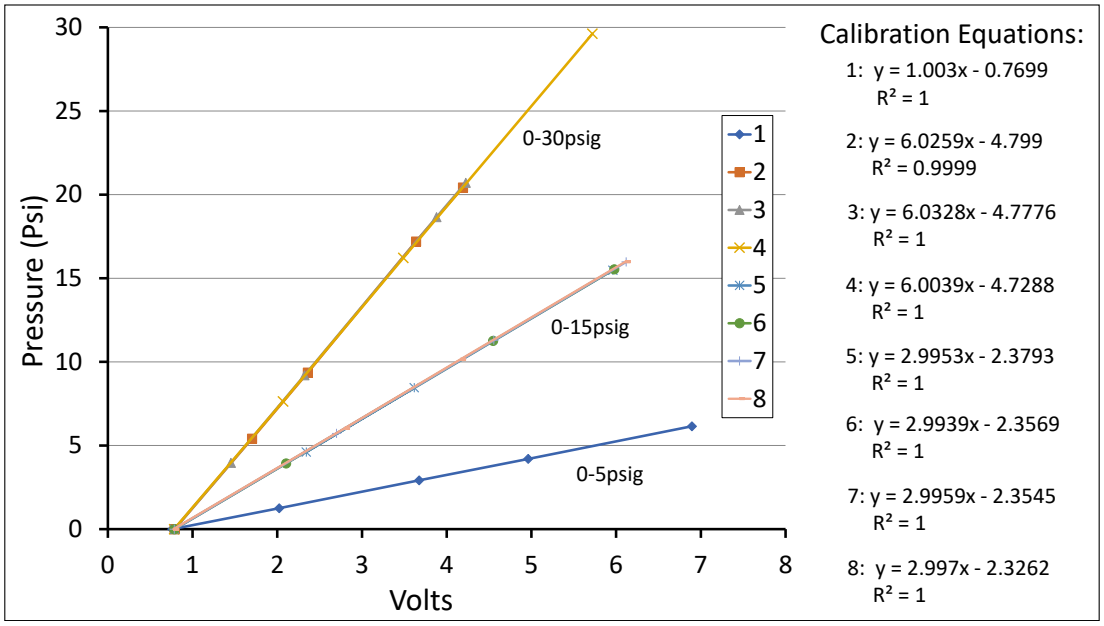


Figure 548. Pressure transducer calibration curves with 10V excitation

D.7 LabView Visual Interface

A custom built JetCat LabView Visual Interface served as a control and data acquisition system as shown in Figure 549. LabView enabled the automation of several functions including control of the engine bearing lubricant flow rate based on fuel flow rate, calculation of engine performance parameters, and an engine start sequence.

The VI layout was designed to look like a cockpit or dashboard in a car to provide the most important information in the easiest to digest formats. Warning lights were prominently displayed at the top of the screen with force and rotationally measured and controlled variables displayed on needle gauges on the left side of the screen. Input controls were localized at the top center and top right of the screen. All temperature, pressure, velocity, and calculated performance parameters took up the remainder of the screen centered around a cross-sectional diagram of the JetCat with indications of where each measurement was taken within the engine.

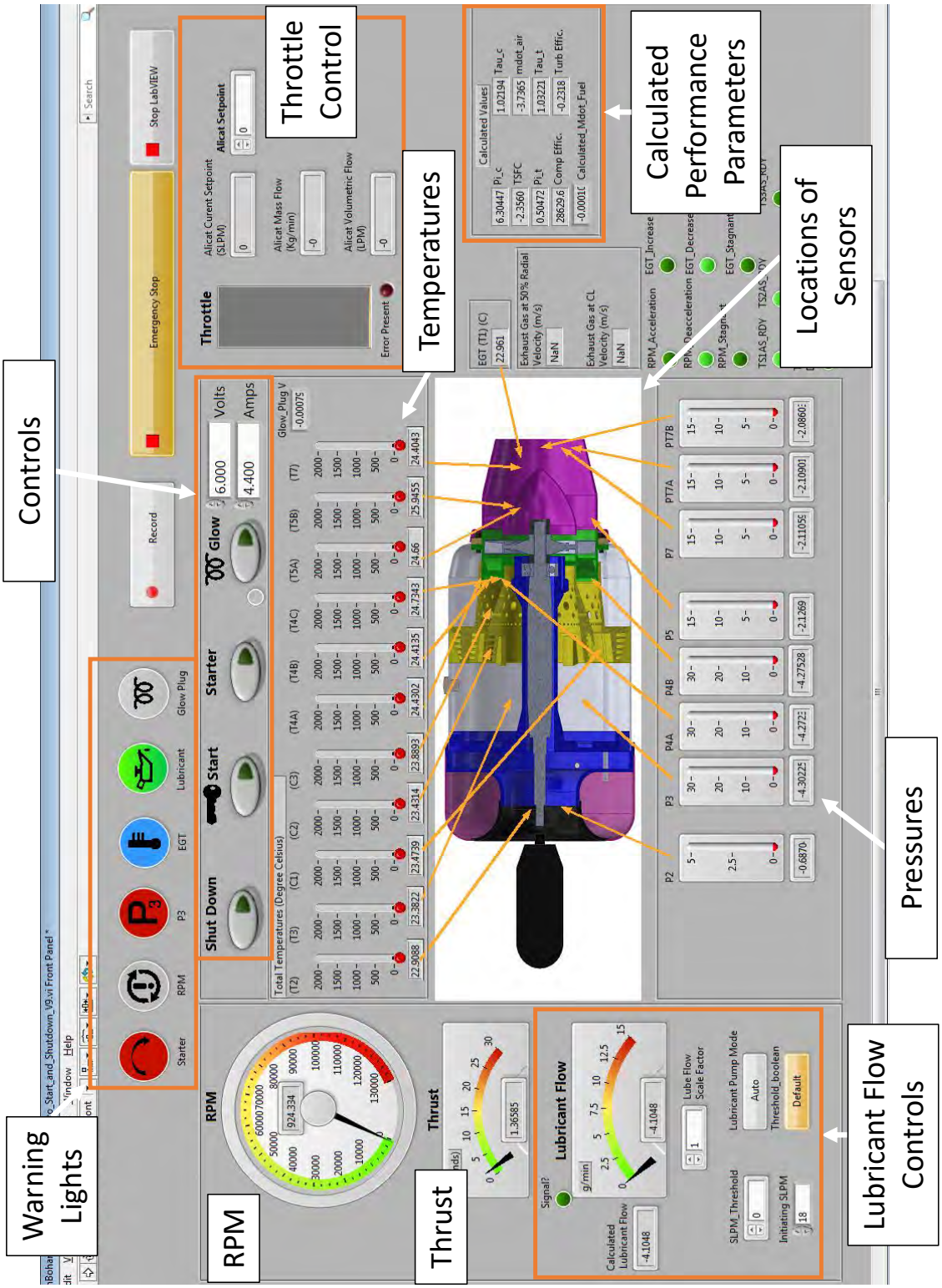


Figure 549. Custom JetCat LabView VI

D.7.1 Warning Lights.

Unlike the warning lights in a car which typically only illuminate when there is a problem, the warning lights in the JetCat Vi were always illuminated but changed color to provide real-time engine status. There was a warning light for starter operation, turbine rotor RPM, post-compressor pressure, engine EGT, lubricant flow rate, and glow plug conductivity. The specifications below provide threshold levels of when the warning lights change color is specific to the JetCat P90RXi cycle and hardware.

The starter warning light had three color levels. The light was gray when the starter was not active, green when the starter was activated and the RPM was increasing, and red if the starter was active but the RPM was not increasing. The turbine rotor RPM warning light had three color levels as well. The light would be green for RPM measurements between 30,000 and 100,000, yellow between 100,000 and 120,000, and red below 30,000 and above 120,000 indicating the RPM was below idle (approximately 35,000 RPM), or at or above maximum (130,000 RPM).

The post-compressor pressure (P_3) warning light had two color levels. The light was red below 1.5 psig (10,342.13 Pa), and changed to green above 1.5 psig (10,342.13 Pa). The level for color transition was selected because it is the pressure achieved at idle. When the light turns green there was sufficient pressure and a sufficient flow rate of air through the engine to sustain operation without starter assistance.

The engine exhaust gas temperature (EGT) light had three color levels and used the temperature measurement made by the EGT thermocouple connected to the Engine Board. The first color level was blue for measured temperatures below 200°C indicating cold flow and a lack of combustion. The second color indicator level was green for measured exhaust temperatures between 200°C and 690°C, the published upper bound JetCat P90RXi EGT. The final color indicator was red for EGT measurements greater than 690°C.

The lubricant flow indicator light had two color levels. The first was a green light if the lubricant flow feedback signal was received from the ECM. If the feedback signal was not received the warning light changed to red indicating that lubricant may not be flowing to the bearings. Finally, the glow plug warning light had three color levels. The first color was gray indicating that the glow plug was not in use. The second color level was green indicating that the measured glow plug feedback voltage was within 5% of 2V or 6V. If the voltage measurement was within this tolerance then the desired current from the power supply had been achieved. The third color level was red indicating that the voltage feedback measurement was outside the 5% tolerance while the plug was energized. The cause of an incorrect voltage reading could be due to an incorrect power supply voltage or current input setting, poor conduction through one of the connectors supporting the glow plug, or a broken heating filament in the glow plug.

D.7.2 Gauge Indicators & Lubricant Flow Control.

The JetCat VI included three gauge indicators for turbine rotor RPM, engine thrust, and lubricant flow rate. The turbine rotor RPM is the physical display of the signal processing of the hall effect sensor outputs. In addition to the dial display, there was a numerical readout on the dial providing the exact calculated RPM value.

The engine thrust gauge was a display of the conversion of strain gauge voltage from the force sensor into a force in units of pounds. The baseline JetCat was capable of producing 25 pounds (111 Newtons) of thrust, but the sensor was capable of measuring up to 50 pounds of force. Like the RPM dial, the thrust gauge also included a numerical readout of the measured thrust. The calibration of the force sensor was described in Section D.5.

The lubricant flow gauge displayed the lubricant flow value based on the commanded duty cycle. Since it was not measuring the actual flow rate, a check was in

place to ensure that the commanded signal resulted in pump operation. The check included a small indicator light directly above the lubricant flow rate gauge. This light illuminated anytime the pump feedback signal was received.

The propane flow rate threshold specifying when lubricant would begin flowing was user specified though an input on the VI front panel. Below the specified propane flow rate value the lubricant pump would remain off. The linear equation for the trendline through the lubricant flow data in Figure 411 was used to convert the commanded pump duty cycle to a lubricant flow rate in g/min to display on the VI gauge.

The JetCat VI also included a small numerical input labeled "Lube Flow Scale Factor" located below the lubricant flow rate gauge. This numeric value was set to 1 indicating that the amount of lubricant that would be used was pulled directly from the calibration curve. The Lube Flow Scale Factor was multiplied by the duty cycle output calculated by the calibration curve, thus a value of 1 would result in no change to the calibrated value. In the event that the calibrated value was found to be too much or too little lubricant, the Lube Flow Scale Factor could be changed slightly to increase or decrease the commanded duty cycle without having to reset the calibration curves for the pump operation in LabView. If a change was required to the lubricant flow, keep in mind that the scale factor was a direct multiplier of the duty cycle. A scale factor of 2 would be twice as much lubricant as the calibrated value, and a value of 0.5 would be half the lubricant.

D.7.3 User Controls.

There were several user controls built into the JetCat VI including starter motor on/off, glow plug on/off, glow plug current and voltage settings, throttle control, engine shut down, data record, emergency stop, stop program, and an automated startup sequence activation. The starter motor on/off and glow plug on/off buttons are self explanatory; when the button was toggled the respective system was turned on

or off. The glow plug current and voltage settings enabled the user to set the desired current and voltage output to the glow plug based on the type of glow plug used and the requirements specified in Table 84. The throttle control allowed the user to specify the fuel flow rate going to the engine through the AliCat mass flow controller. The user could provide an instantaneous throttle change, however, LabView regulated the rate of fuel addition or subtraction to or from the engine to ensure proper operation without flameout or damage to the hardware. If the user needed to shut down the engine for any reason the "Engine Shut Down" button could be pressed. This button commanded a fuel flow rate and lubricant flow rate of zero to ensure there would not be kerosene pooling in the engine housing as the RPMs reduced. When the RPMs dropped below 3,000 the system engaged the starter motor to run a cool down sequence where the starter turned the rotor to maintain airflow through the engine until the EGT measurement was less than 100°C. Once below 100°C the starter was stopped. If an emergency was encountered the "Emergency Stop" button could be pressed which stopped all fuel and lubricant flow and did not engage the starter.

The data record button enabled the user to save the data displayed on the screen to a text file at a 10 Hz rate. When the record button was toggled to the "on" position the data were written to the text file continuously until the button was toggled off. The "Stop LabView" button shutdown the entire VI and commanded all inputs back to their default values.

The final user control was an automated startup button that ran through a series of commands and system checks to bring the engine from not running to an idle setting. While the engine could be manually started by running through the same sequence of events as shown below, the automated startup simplified engine started and ensured the safety of engine hardware by performing all the necessary system checks between events that a human might miss. The startup sequence assumed that

all power supplies and support systems were powered on and standing by for LabView commands. The start up sequence was as follows:

1. Activate the starter
    (a) Verify engine RPM increase
        i. If the engine RPM does not increase, flash the RPM warning light, and abort the startup sequence
        ii. If engine RPM increases proceed to the next step
2. At 2,000 RPM, Activate the glow plug to begin heating
    (a) If the glow plug warning light is red, flash the glow plug warning light, and abort the startup sequence
    (b) Verify glow plug warning light is green, proceed to the next step
3. At 3,300 RPM, increment propane flow from zero at a rate of 1 SLPM every 0.5 seconds
    (a) Watch for the EGT light to turn green indicating engine combustion
    (b) If the EGT light does not turn green after 8 SLPM of propane is reached, stop fuel flow, flash the EGT warning light, and abort the startup sequence
    (c) If the EGT light turns green, disable the glow plug, ramp the fuel flow rate at a reduced rate of 1 SLPM per second. Proceed to the next step.
4. As fuel flow is increasing, verify RPM increase, EGT increase, and P_3 pressure increase
    (a) If rotor RPM, EGT, or P_3 pressure are not increasing, flash the appropriate warning light, shut off fuel flow, and abort the startup sequence

(b) If rotor RPM, EGT, and P_3 pressure are increasing, continue to ramp fuel flow at the same rate until idle RPM is achieved

5. When idle RPM is achieved, hold idle RPM fuel flow rate, exit startup sequence to return throttle control to the user

D.7.4 Calculated Performance Parameters.

LabView calculated real-time engine performance parameters including pressure ratios, temperature ratios, and efficiencies of the compressor and turbine. Global values of uninstalled thrust specific fuel consumption (TSFC), estimated air flow rate, and estimated fuel flow rate were also calculated. All of these parameters were calculated using temperature and pressure measurements from the engine.

The compressor parameters were defined in Equations 89 and 91 for the temperature and pressure ratios, respectively, and repeated below for ease of reference. The station numbering in the equations corresponds to the conventional numbering schemes shown in Figure 16a. The temperature and pressure values were taken with thermocouple and pressure taps that were perpendicular to the flow and likely measuring static values. These values were still applied to the equations below to approximate the required values as total measurements would be difficult inside the JetCat due to the small scale.

$$\tau_c = \frac{T_{t3}}{T_{t1}}$$

$$\pi_c = \frac{P_{t3}}{P_{t1}}$$

The compressor efficiency is defined in Equation 96 (repeated below for reference). This equation uses the pressure and temperature ratios from the equations above, and a constant value of $\gamma = 1.4$, to solve for the compressor efficiency.

$$\eta_c = \frac{(\pi_c)^{\frac{\gamma}{(\gamma-1)}} - 1}{\tau_c - 1}$$

The mass flow rate of air through the engine could be approximated through the use of Equation 95, repeated below. In this equation $R = 287$ J/(kg·K) and $\gamma = 1.4$. The temperature and pressure measurements were taken at Station 3, after the compressor exit guide vanes. The area at Station 3 was fixed at 0.00864 m^2.

$$\dot{m}_{air} = \frac{P_{t3}}{RT_{t3}} A_3 \sqrt{\gamma R T_{t3}}$$

The turbine temperature and pressure ratios were defined by Equations 97 and 98, respectively, and shown below with the station references adjusted to the global engine reference frame. Like the compressor measurements, the thermocouple and pressure taps around the turbine were directed into the flow. While this would yield a total pressure measurement, it only approximates a total temperature measurement as the fluid is likely not stagnating on the thermocouple bead. In the event that multiple temperature or pressure measurements were made at a station, the average value was used in the temperature or pressure ratio calculation.

$$\tau_t = \frac{T_{t5}}{T_{t4}}$$

$$\pi_t = \frac{P_{t5}}{P_{t4}}$$

The turbine efficiency was given in Equation 101 and shown below with the stage subscript, s, changed to a t representing the values across the single stage JetCat turbine. Due to the elevated temperature in the turbine section, γ typically has a value of 1.28.

$$\eta_t = \frac{1 - \tau_t}{1 - (\pi_t)^{\frac{(\gamma-1)}{\gamma}}}$$

Aside of using the mass flow rate of fuel directly from the fuel mass flow controller, the fuel flow rate could be calculated using Equation 99, repeated below. The mass flow rate of air was found above, c_p was the specific heat capacity of air at constant

pressure (1.130 kJ/kg·K at γ=1.34), the temperature difference across the burner shows the temperature rise due to the fuel combustion, and Q was the lower heating value of propane (46.4 MJ/kg).

$$\dot{m}_{fuel} = \frac{\dot{m}_{air} c_p (T_4 - T_3)}{Q}$$

The mass flow rate through the turbine is shown in Equation 100, and modified below to include the mass flow rate of lubricant since it also flows across the turbine in the JetCat. The total mass flow rate through the engine was simply the sum of the air, fuel, and lubricant.

$$\dot{m}_{total} = \dot{m}_{air} + \dot{m}_{fuel} + \dot{m}_{lubricant}$$

The uninstalled TSFC is defined in Equation 6, and simplified below as the ratio of the mass flow rate of fuel divided by the measured thrust. This result is a measure of how efficiently the engine converts fuel into thrust.

$$TSFC = \frac{\dot{m}_f}{F}$$

Finally, the exhaust velocity was calculated using the Bernoulli relationship combined with the ideal gas relationship as shown in Equation D.7.4. This relationship requires a total pressure, static pressure, and temperature measurement in the exhaust stream at the nozzle exit. The value of R = 287 J/(kg·K), and the other temperature and pressure measurements were taken as close to in-plane as possible.

$$U = \sqrt{\frac{2(P_t - P_s) \cdot R \cdot T}{P_s}}$$

Bibliography

1. Mattingly, J. D., Heiser, W. H., and Pratt, D., *Aircraft Engine Design*, AIAA, Reston, Virginia, 2nd ed., 2002.

2. Koff, B. L., "Gas Turbine Technology Evolution: A Designer's Perspective," *Journal of Propulsion and Power*, Vol. 20, 2004, pp. 577 – 595.

3. Zelina, J., Sturgess, G. J., and Shouse, D. T., "The Behavior of an Ultra-Compact Combustor (UCC) Based on Centrifugally-Enhanced Turbulent Burning Rates," *Proceedings of the 40th AIAA/ASME/SAE/ASEE Joint Propulsion Conference and Exhibit*, 2004, AIAA 2004-3541.

4. Lewis, G. D., "Swirling Flow Combustion - Fundamentals and Application," *Presented at AIAA/SAE 9th Propulsion Conference, Las Vegas, Nevada*, November 1973, AIAA Paper No. 73-1250.

5. Sirignano, W. A., Delplanque, J. P., and Liu, F., "Selected Challenges in Jet and Rocket Engine Combustion Research," *33rd AIAA/ASME/SAE/ASEE Joint Propulsion Conference, Seattle, WA*, 1997, AIAA-97-2701.

6. Bohan, B. T., *Analysis of Flow Migration in an Ultra Compact Combustor*, Master's thesis, Air Force Institute of Technology, WPAFB, OH, 2011, AFIT/GAE/ENY/11-M02.

7. Zelina, J., Shouse, D. T., Stutrud, J. S., Sturgess, G. J., and Roquemore, W. M., "Exploration of Compact Combustors for Reheat Cycle Aero Engine Applications," *Proceedings of ASME Turbo Expo 2006, Barcelona, Spain*, 2006, GT2006-90179.

8. Spytek, C. J., "Application of an Inter-Turbine Burner Using 100% Vitiated Air in a Gas Turbine Engine," *Proceedings of ASME Turbo Expo 2012, Copenhagen, Denmark*, 2012, GT2012-69333.

9. Bogard, D. G. and Thole, K. A., "Gas Turbine Film Cooling," *Journal of Propulsion and Power, Vol. 22, pp 249-269*, December 2005.

10. Lethander, A. T., *Assessment of Leading Edge Fillet for Decreasing Vane Endwall Temperatures in a Gas Turbine Engine*, Ph.D. thesis, Virginia Polytechnic Institute and State University, Blacksburg, Virginia, 2003.

11. Lukachko, S. P., Kirk, D. R., and Waitz, I. A., "Turbine Durability Impacts of High Fuel-Air Ratio Combustors, Part 1: Potential for Intra-Turbine Oxidation of Partially-Reacted Fuel," *Presented at ASME Turbo Expo 2002: Land, Sea and Air, Amsterdam, The Netherlands*, 2002, GT2002-30077.

12. Evans, D. S., *The Impact of Heat Release in Turbine Film Cooling*, Master's thesis, Air Force Institute of Technology, WPAFB, OH, 2008, AFIT/GAE/ENY/08-J02.

13. JetCat, "JetCat Americas," 2016, `http://www.jetcatamericas.com/`.

14. Mattingly, J. D., *Elements of Propulsion: Gas Turbines and Rockets*, AIAA, Reston, VA, 2006.

15. NASA, "General Thrust Equation," 2016, `https://www.grc.nasa.gov/www/k-12/airplane/thrsteq.html`.

16. Boyce, M. P., *Gas Turbine Engineering Handbook*, Butterworth-Heinemann, 3rd ed., 2011.

17. Hill, P. G. and Peterson, C. R., *Mechanics and Thermodynamics of Propulsion*, Addison Wesley, Reading, Massachusetts, 2nd ed., 1992.

18. Lefebvre, A. H. and Ballal, D. R., *Gas Turbine Combustion: Alternative Fuels and Emissions*, CRC Press, Boca Raton, FL, 3rd ed., 2010.

19. Baskaran Kala, "Introduction - An Early Combustion Chamber," 2011, Model Aircraft Blog, accessed from `http://aeromodelbasic.blogspot.com/2011/12/introduction-early-combustion-chamber.html` 3 Nov 2016.

20. Turns, S. R., *An Introduction to Combustion*, McGraw-Hill, Inc, New York, 1996, 2nd Edition.

21. Lu, F. K., Braun, E. M., Massa, L., and Wilson, D. R., "Rotating Detonation Wave Propulsion: Experimental Challenges, Modeling, and Engine Concepts," *Conference proceedings of Joint Propulsion Conference, San Diego, CA*, 2011, AIAA-2011-6043.

22. Law, C. K., *Combustion Physics*, Cambridge University Press, New York, NY, 2006.

23. Anthenien, R. and Zelina, J., "Experimental Results on the Turbulent Combustion Regimes within a Small-Scale Atmospheric Pressure High-g Combustor," *Spring Technical Meeting of the Central States Section: Combustion Institute*, 2006, Cleveland, OH.

24. Spalding, D., *Combustion and Mass Transfer*, Pergamon Press, Emsford, NY, 1979.

25. Anthenien, R., Mantz, R., and Roquemore, W. M., "Experimental Results for a Novel, High Swirl, Ultra Compact Combustor for Gas Turbine Engines," *2nd Joint Meeting of the U.S. Sections of the Combustion Institute*, 2001, Oakland, CA.

26. Steinfeld, J. I., Francisco, J. S., and Hase, W. L., *Chemical Kinetics and Dynamics*, Prentice Hall, Upper Saddle River, NJ, 2nd ed., 1999.

27. Erdmann, T. J., Blunck, D. L., Shouse, D. T., Neuroth, C., Lynch, A., Caswell, A. W., Richardson, D., and Briones, A. M., "Rayleigh Pressure Loss Analysis and Mitigation in Ultra-Compact Combustors," *Proceedings of the 51st AIAA Aerospace Sciences Meeting*, 2013, AIAA-2013-0873.

28. Samuelsen, S., "Conventional Type Combustion," *The Gas Turbine Handbook*, U.S. Department of Energy, Office of Fossil Energy, National Energy Technology Laboratory (NETL), DOE/NETL-2006-1230, Morgantown, WV, 2006.

29. Barringer, M. D., Thole, K. A., and Polanka, M. D., "Effects of Combustor Exit Profiles on High Pressure Turbine Vane Aerodynamics and Heat Transfer," *Proceedings of the ASME Turbo Expo 2006*, 2006, GT 2006-90277.

30. Barringer, M. D., Thole, K. A., and Polanka, M. D., "Experimental Evaluation of an Inlet Profile Generator for High Pressure Turbine Tests," *Journal of Turbomachinery*, Vol. 129, 2006.

31. Bahr, D. W., "Aircraft Turbine Engine NOx Emission Limits: Status and Trends," *Proceedings of ASME 1992 International Gas Turbine and Aeroengine Congress and Exposition*, 1992, Cologne, Germany, 92-GT-415.

32. Zelina, J., Shouse, D. T., and Hancock, R. D., "Ultra-Compact Combustors for Advanced Gas Turbine Engines," *Proceedings of ASME Turbo Expo 2004 Vienna, Austria*, June 2004, GT2004-53155.

33. Briones, A. M., Sekar, B., and Erdmann, T. J., "Effect of Centrifugal Force on Turbulent Premixed Flames," *Journal of Engineering for Gas Turbines and Power*, Vol. 137, 2015, GTP-14-13091.

34. Sirignano, W. A. and Liu, F., "Performance Increases for Gas-Turbine Engines Through Combustion Inside the Turbine," *Journal of Propulsion and Power*, Vol. 15, 1999.

35. Sirignano, W. A. and Kim, I., "Diffusion Flame in a Two-Dimensional Accelerating Mixing Layer," *Physics of Fluids*, Vol. 9, 1997.

36. Fang, X., Liu, F., and Sirignano, W. A., "Ignition and Flame Studies for an Accelerating Transonic Mixing Layer," *Journal of Propulsion and Power*, Vol. 17, No. 5, 2001.

37. Mehring, C., Liu, F., and Sirignano, W. A., "Ignition and Flame Studies for a Turbulent Acceleration Transonic Mixing Layer," *Proceedings of the 39th AIAA Aerospace Sciences Meeting, Reno, NV*, 2001.

38. Cheng, F., Liu, F., and Sirignano, W. A., "Reacting Mixing-Layer Computations in a Simulated Turbine-Stator Passage," *Journal of Propulsion and Power*, Vol. 25, No. 2, 2009.

39. Colcord, B., Sirignano, W. A., and Liu, F., "Turbine-Burner Model: Cavity Flameholding in a Converging, Turning Channel Flow," *Proceedings of the Joint Propulsion Conference, Atlanta, Georgia*, 2012, AIAA-2012-3778.

40. Roquemore, W. M., Shouse, D. T., Burrus, D., Johnson, A., Cooper, C., Duncan, B., Hsu, K. Y., Katta, V. R., Sturgess, G. J., and Vihinen, I., "Trapped Vortex Combustor Concept for Gas Turbine Engines," *Proceedings of the 39th AIAA Aerospace Sciences Meeting, Reno, NV*, 2001, AIAA-2001-0483.

41. Mair, W. A., "The Effect of a Rear-Mounted Disc on the Drag of a Blunt-Based Body of Revolution," *The Aeronautical Quarterly*, 1965.

42. Little, B. H. and R.Whipkey, R., "Locked Vortex Afterbodies," *Journal of Aircraft*, Vol. 16, No. 5, 1979, Article No. 78-1179.

43. Katta, V. R. and Roquemore, W. M., "Numerical Studies on Trapped-Vortex Concepts for Stable Combustion," *American Society of Mechanical Engineers Turbo Asia Conference, Jakarta, Indonesia*, 1996, 96-TA-19.

44. Erdmann, T. J., "Experimental Characterization of the Reaction Zone in an Ultra-Compact Combustor," *50th AIAA/ASME/SAE/ASEE Joint Propulsion Conference, Cleveland, OH*, 2014, AIAA-2014-3630.

45. Blunck, D. L., Shouse, D. T., Neuroth, C., Lynch, A., Erdmann, T. J., Burrus, D. L., Zelina, J., Richardson, D., and Caswell, A. W., "Experimental Studies of Cavity and Core Flow Interactions with Applications to Ultra Compact Combustors," *Journal of Engineering for Gas Turbines and Power*, Vol. 136, No. 1, 2014, GTP-13-1457.

46. Colcord, B. and Sirignano, W. A., "Combustion Model with Fuel Injection into and Air Flow Past a Cavity," *Proceedings of the Fall Meeting of the Western States Section of the Combustion Institute, Livermore, CA*, 2007.

47. Sirignano, W. A., Dunn-Rankin, D., Liu, F., Colcord, B., and Puranam, S. V., "Turbine Burners: Performance Improvement and Challenges of Flameholding," *AIAA Journal*, Vol. 50, No. 8, 2012.

48. Puranam, S. V., Arici, J., Sarzi-Amade, N., Dunn-Rankin, D., and Sirignano, W. A., "Turbulent Combustion in a Curving, Contracting Channel with a Cavity Stabilized Flame," *Proceedings of the Combustion Institute*, Vol. 32, 2009.

49. Chen, S., Chue, R., Yu, S., and Schluter, J. U., "Spinning Effects on a Trapped Vortex Combustor," *Journal of Propulsion and Power*, Vol. 32, No. 5, 2016.

50. Yonezawa, Y., Toh, H., Goto, S., and Obata, M., "Development of the Jet-Swirl High Loading Combustor," *26th AIAA/ASME/SAE/ASEE Joint Propulsion Conference, Orlando, FL*, 1990, AIAA-90-2451.

51. Dimonte, G., Young, D. L., Dimits, A., Weber, S., Marinak, M., Wunsch, S., Garasi, C., Robinson, A., Andrews, M. J., Ramaprabhu, P., Calder, A. C., Fryxall, B., Biello, J., Dursi, L., MacNeice, P., Olson, K., Ricker, P., Rosner, R., Timmes, R., Tufo, H., Young, Y. N., and Zingale, M., "A comparative study of the turbulent RayleighTaylor instability using high-resolution three-dimensional numerical simulations: The Alpha-Group collaboration," *Physics of Fluids*, Vol. 16, No. 5, May 2004.

52. Cook, A. and Zhou, Y., "Energy transfer in Rayleigh-Taylor instability," *Physical Review E*, September 2002, 026312.

53. Porter, D., Woodward, P., Stone, N., and Reddy, R., "Bursts of Stellar Turbulence," *Pittsburgh Supercomputing Center - Projects 2007*, 2007.

54. Cook, A. W. and Dimotakis, P. E., "Transition stages of Rayleigh-Taylor instability between miscible fluids," *Journal of Fluid Mechanics*, Vol. 443, 2001, pp. 69–99.

55. Li, S. and Li, H., "Parallel AMR Code for Compressible MHD or HD Equations," *University of California, operator of the Los Alamos National Laboratory under Contract No. W-7405-ENG-36 with the U.S. Department of Energy*, 2001.

56. Lapsa, A. P. and Dahm, W. J., "Hyperacceleration effects on turbulent combustion in premixed step-stabilized flames," *Proceedings of the Combustion Institute*, Vol. 32, 2009, pp. 1731–1738.

57. Anderson, W. S., Radtke, J. T., King, P. I., Thornburg, H. J., Zelina, J., and Sekar, B., "Effects of Main Swirl Direction on High-g Combustion," *Conference: 44th AIAA/ASME/SAE/ASEE Joint Propulsion Conference*, 2008, AIAA-2008-4954.

58. Presented at the Dayton-Cincinnati Aerospace Sciences Symposium (DCASS), *Analysis of Turning Vanes Designs for Flow Migration in an Ultra-Compact Combustor*, 2010, Brian T. Bohan.

59. Anderson, W. S., *Design, Construction, and Validation of the AFIT Small Scale Combustion Facility and Sectional Model of the Ultra-compact Combustor*, Master's thesis, Air Force Institute of Technology, WPAFB, OH, 2007, AFIT/GAE/ENY/07-M01.

60. Lebay, K. D., Drenth, A. C., Thomas, L. M., Polanka, M. D., Branam, R. D., and Schmidt, J. B., "Characterizing the Effects of G-Loading in an Ultra Compact Combustor via sectional models," *Proceedings of the ASME Turbo Expo 2010 Glaskow, UK*, 2010, GT2010-22723.

61. Lebay, K. D., Polanka, M. D., and Branam, R. D., "Characterizing the Effects of Radial Vane Height on Flame Migration in an Ultra Compact Combustor," *Proceedings of the ASME Turbo Expo 2011 Vancouver, Canada*, 2011, GT2011-45919.

62. LeBay, K. D., *Characterization of Centrifugally-Loaded Flame Migration for Ultra-Compact Combustors*, Ph.D. thesis, Air Force Institute of Technology, WPAFB, OH, 2011, AFIT/DS/ENY/11-22.

63. Bohan, B. T. and Polanka, M. D., "Analysis of Flow Migration in an Ultra-Compact Combustor," *Journal of Engineering for Gas Turbines and Power*, Vol. 135, 2013, GTP-11-1312.

64. Cottle, A. E., Gilbert, N. A., and Polanka, M. D., "Mechanisms for Enhanced Flow Migration from an Annular High-g Ultra Compact Combustor," *Presented at AIAA Sci Tech Conference, San Diego, CA*, 2016, AIAA-2016-1392.

65. Wilson, J. D., Damele, C. J., and Polanka, M. D., "Flame Structure Effects at High G-Loading," *Journal of Engineering for Gas Turbines and Power*, Vol. 136, 2013, GTP-14-1068.

66. Damele, C. J., *Operational Characteristics of an Ultra Compact Combustor*, Master's thesis, Air Force Institute of Technology, WPAFB, OH, 2013, AFIT/GAE/ENY/14-M-13.

67. Conrad, M. M., *Integration of an Inter Turbine Burner to a Jet Turbine Engine*, Master's thesis, Air Force Institute of Technology, WPAFB, OH, 2013, AFIT/GAE/ENY/13-M-06.

68. Miranda, J. L., *The Use of an Ultra-Compact Combustor as an Inter-Turbine Burner for Improved Engine Performance*, Master's thesis, Air Force Institute of Technology, WPAFB, OH, 2014, AFIT/GAE/ENY/14-M-38.

69. Cottle, A. E. and Polanka, M. D., "Optimization of Ultra Compact Combustor Flow Path Splits," *Proceedings of the 53rd AIAA Aerospace Sciences Meeting, AIAA SciTech*, 2015, AIAA-2015-0100.

70. Cottle, A. E. and Polanka, M. D., "Numerical and Experimental Results From a Common-Source High-G Ultra-Compact Combustor," *Proceedings of the ASME Turbo Expo 2016 Seoul, South Korea*, 2016, GT2016-56215.

71. Wilson, J. D. and Polanka, M. D., "Reduction of Rayleigh Losses in a High G-Loaded Ultra Compact Combustor," *Proceedings of the ASME Turbo Expo 2013 San Antonio, Texas*, 2013, GT2013-94795.

72. Radtke, J. T., *Efficiency and Pressure Loss Characteristics of an Ultra Compact Combustor*, Master's thesis, Air Force Institute of Technology, WPAFB, OH, 2007, AFIT/GAE/ENY/07-J18.

73. Johnson, D. D., *Cooling Requirements for the Ultra-Compact Combustor*, Master's thesis, Air Force Institute of Technology, WPAFB, OH, 2012, AFIT/GAE/ENY/12-M25.

74. Parks, A. K. and Polanka, M. D., "Quantifying Exhaust Emissions in an Ultra Compact Combustor," *Proceedings of the 50th AIAA Aerospace Sciences Meeting Nashville, TN*, 2012, AIAA-2012-0935.

75. Damele, C. J., Polanka, M. D., Wilson, J. D., and Rutledge, J. L., "Characterizing Thermal Exit Conditions for an Ultra Compact Combustor," *Proceedings of the 52nd AIAA Aerospace Sciences Meeting*, 2014, AIAA-2014-0456.

76. Gilbert, N. A., Cottle, A. E., Polanka, M. D., and Goss, L. P., "Enhancing Flow Migration and Reducing Emissions in Full Annular Ultra Compact Combustor," *Proceedings of the 54th AIAA Aerospace Sciences Meeting*, 2016, AIAA-2016-2122.

77. Mawid, M., Thornburg, H. J., Sekar, B., and Zelina, J., "Performance of an Inter-Turbine Burner (ITB) Concept with Three-Different Vane Cavity Shapes," *Proceedings of the 42nd Joint Propulsion Conference*, 2006, AIAA-2006-4740.

78. Cottle, A. E., *Flow Field Dynamics in a High-g Ultra-Compact Combustor*, Ph.D. thesis, Air Force Institute of Technology, WPAFB, OH, 2016, AFIT-ENY-DS-16-S-057.

79. Zelina, J., Ehret, J. A., Hancock, R. D., Shouse, D. T., Roquemore, W. M., and Sturgess, G. J., "Ultra-Compact Combustion Technology Using High Swirl for Enhanced Burning Rate," *38th AIAA/ASME/SAE/ASEE Joint Propulsion Conference, Indianapolis, IN*, 2002, AIAA-2002-3725.

80. Drenth, A. C., *Laser-Induced Fluorescence and Synthetic Jet Fuel Analysis in the Ultra-Compact Combustor*, Master's thesis, Air Force Institute of Technology, WPAFB, OH, 2009, AFIT/GAE/ENY/09-D03.

81. Katta, V. R., Blunck, D. L., and Roquemore, W. M., "Effect of Centrifugal Forces on Flame Stability in an Ultra-Compact Combustor," *Proceedings of the 51st AIAA Aerospace Sciences Meeting, Dallas, TX*, 2013, AIAA-2013-1046.

82. Brinker, A. J., Polanka, M. D., Richardson, D. R., Lynch, A., and Blunck, D. L., "Liquid Spray Characterization in Flow Fields with Centripetal Acceleration," *AIAA SciTech, National Harbour, MD*, 2014, AIAA-2014-1021.

83. Cottle, A. E., Polanka, M. D., Goss, L. P., and Goss, C. Z., "Investigation of Air Injection and Cavity Size Within a Circumferential Combustor to Increase G-Load and Residence Time," *Journal of Engineering for Gas Turbines and Power*, Vol. 140, 2016, GTP-17-1182.

84. Montfort, J. R., Stouffer, S. D., Hendershott, T. H., Wrzesinski, P. J., Foley, W. S., and Rein, K. D., "Evaluating Combustion Instability in a Swirl-Stabilized Combustor Using Simultaneous Pressure, Temperature, and Chemiluminescence Measurements at High Repetition Rates," *Proceedings of the 55th AIAA Aerospace Sciences Meeting, Grapevine, TX*, 2017, AIAA-2017-1101.

85. Boxx, I. G., Geigle, K. P., Carter, C. D., Lewalle, J., and Kumgeh, B. A., "Self-induced transition between stable and thermoacoustically excited states in a gas turbine combustor," *Proceedings of the 55th AIAA Aerospace Sciences Meeting, Grapevine, TX*, 2017, AIAA-2017-1102.

86. Dowling, A. P. and Mahmoudi, Y., "Combustion Noise," *Proceedings of the Combustion Institute*, Vol. 35, 2015, pp. 65–100.

87. Allison, P. M., Sidney, J. A. M., and Mastorakos, E., "Transient Behavior of Kerosene Flames in a Bluff-Body Stabilized Swirl Combustor," *Proceedings of the 55th AIAA Aerospace Sciences Meeting, Grapevine, TX*, 2017, AIAA-2017-1569.

88. Seebold, J. G., "Combustion-Driven Oscillations in Process Heaters," *IFRF Combustion Journal*, 2005, Article No. 200507.

89. Cai, J., Mohammad, B. S., Tambe, S. B., Kao, Y. H., and Jeng, S. M., "Gas Turbine Single Annular Combustor Sector: Combustion Dynamics," *Proceedings of the 48th AIAA Aerospace Sciences Meeting, Orlando, FL*, 2010, AIAA 2010-21.

90. He, Z. J. and Chang, C. T., "Combustion Dynamic Characteristics Identification in a 9-point LDI Combustor under Choked Outlet Boundary Conditions," *Proceedings of the 55th AIAA Aerospace Sciences Meeting, Grapevine, TX*, 2017, AIAA-2017-0779.

91. Samuelson, R., "Pneumatic Instrumentation Lines and their use in Measuring Rocket Nozzle Pressure," *Aerojet-General Corporation*, 1969, Report Number NR-DR-0124.

92. Langston, L. S., "Crossflows in a Turbine Cascade Passage," *Journal of Engineering for Power*, Vol. 102, 1980, pp. 866 – 874.

93. Sabatino, D. and Smith, C., "Boundary Layer Influence on the unsteady Horseshoe Vortex Flow and Surface Heat Transfer," *Proceedings of the ASME Turbo Expo 2007: Power by Land, Sea and Air*, 2007, GT2007-27633.

94. Hermanson, K. S. and Thole, K. A., "Effects of Mach Number on Secondary Flow Characteristics," *Journal of Turbo and Jet Engines*, Vol. 17, 2000, pp. 179 – 196.

95. Hermanson, K. S. and Thole, K. A., "Effects of Inlet Conditions on Endwall Secondary Flows," *Journal of Propulsion and Power*, Vol. 16, No. 2, March-April 2000, pp. 286 – 296.

96. M.Lei, V., Spakovszky, Z., and Greitzer, E. M., "A Criterion for Axial Compressor Hub-Corner Stall," *Journal of Turbomachinery*, Vol. 130, 2008.

97. Bailie, S., Hile, G. A., and Puterbaugh, S. L., "Initial Characterization of Three-Dimensional Flow Separation in a Compressor Stator," *Proceedings of the 44th Joint Propulsion Conference, Hartford, CT*, 2008, AIAA 2008-5064.

98. Gregory, J. W., Sullivan, J. P., Raman, G., and Raghu, S., "Characterization of the Microfluidic Oscillator," *AIAA Journal*, Vol. 45, No. 3, 2007, pp. 568–576.

99. Spyropoulos, C. E., "A Sonic Oscillator," *Proceedings of the Fluid Amplification Symposium*, Vol. 3, 1964, pp. 27–51.

100. Stouffer, R. D., "Oscillating Spray Device," 1979, United State Patent 4,151,955.

101. Hossain, M. A., Prenter, R., Lundgreen, R. K., Ameri, A., Gregory, J. W., and Bons, J. P., "Experimental and Numerical Investigation of Sweeping Jet Film Cooling," *Proceedings of ASME Turbo Expo 2017, Charlotte, North Carolina*, 2017, GT2017-64479.

102. Raman, G. and Rice, E. J., "Development of Phased Twin Flip-Flop Jets," *Journal of Vibration and Acoustics*, Vol. 116, 1994, pp. 263–268.

103. AL-Asady, A. and Razouqi, B., "Theoretical and Experimental Investigation of Fluidic Oscillator," *Journal of Engineering*, Vol. 19, No. 3, 2013, pp. 403–413.

104. Incropera, F. P., DeWitt, D. P., Bergman, T. L., and Lavine, A. S., *Fundamentals of Heat and Mass Transfer*, John Wiley and Sons, Inc, Hoboken, New Jersey, 2007, 6th Edition.

105. Hilbert, B. F. and Morris, S. C., "An Inverse Heat Conduction Problem Applied to the Rotor Casing of a Transonic Turbine," *Proceedings of the 52nd Joint Propulsion Conference, Salt Lake City, UT*, 2016, AIAA 2016-4859.

106. Smith, D., Bubb, J., Popp, O., Grabowski, H., Diller, T., Schetz, J., and Ng, W., "An Investigation of Heat Transfer in a Film Cooled Transonic Turbine Cascade, Part I: Steady Heat Transfer," *Proceedings of the ASME Turbo Expo 2000 Munich, Germany*, 2000, 2000-GT-0203.

107. Hyams, D. G. and Leylek, J. H., "A Detailed Analysis of Film-Cooling Physics: Part III - Streamwise Injection With Shaped Holes," *Journal of Turbomachinery*, Vol. 122, 2000, pp. 122 – 132.

108. Kays, W. M., Crawford, M. E., and Weigand, B., *Convective Heat and Mass Transfer*, McGraw Hill, Columbus, OH, 2004, 4th Edition.

109. Greiner, N. J., *Convective Heat Transfer with and without Film Cooling in High Temperature, Fuel Rich and Lean Environments*, Ph.D. thesis, Air Force Institute of Technology, WPAFB, OH, 2014, AFIT-ENY-DS-14-S-28.

110. Rutledge, J. L., Polanka, M. D., and Bogard, D. G., "The Delta Phi Method of Evaluating Overall Film Cooling Performance," *Proceedings of ASME Turbo Expo 2015, Montreal, Canada*, 2015, GT2015-43288.

111. Han, J. C., Dutta, S., and Ekkad, S., *Gas Turbine Heat Transfer and Cooling Technology*, CRC Press, Boca Raton, FL, 2nd ed., 2000.

112. Baldauf, S., Schulz, A., and Wittig, S., "High-Resolution Measurements of Local Effectiveness From Discrete Hole Film Cooling," *Journal of Turbomachinery*, Vol. 123, 2001, pp. 758–765.

113. Bogard, D. G. and Thole, K. A., "Gas Turbine Film Cooling," *Journal of Propulsion and Power*, Vol. 22, March-April 2006, pp. 249–270.

114. Thole, K. A., Sinha, A. K., Bogard, D. G., and Crawford, M. E., *Mean Temperature Measurements of Jets With a Crossflow for Gas Turbine Film Cooling Application*, Hemisphere, New York, 1992, Rotating Machinery Transport Phenomena.

115. Anderson, W. S., Polanka, M. D., Zelina, J., Evans, D. S., Stouffer, S. D., and Justinger, G. R., "Effects of a Reacting Cross-Stream on Turbine Film Cooling," *Journal of Engineering for Gas Turbines and Power*, Vol. 132, 2010.

116. Polanka, M. D., Zelina, J., Anderson, W. S., Sekar, B., Evans, D. S., Lin, C. X., and Stouffer, S. D., "Heat Release in Turbine Film Cooling, Part 1: Experimental and Computational Comparison of Three Geometries," *Journal of Propulsion and Power*, Vol. 27, 2010, pp. 257–268.

117. Lin, C. X., Holder, R. J., Polanka, M. D., Zelina, J., Sekar, B., Thornburg, H. J., and Briones, A. M., "Heat Release in Turbine Film Cooling, Part 2: Numerical Simulation of Shaped Hole Secondary Combustion Development and Location," *Journal of Propulsion and Power*, Vol. 27, 2010, pp. 269–281.

118. Katta, V. R. and Blunck, D. L., "Numerical Studies on Flames Established in Reacting Film-Cooling Experiment," *Proceedings of the ASME Turbo Expo 2014 Dusseldorf, Germany*, 2014, GT2014-25730.

119. Pohl, S., Frank, G., and Pfitzner, M., "Heat Transfer in Reacting Cooling Films: Influence and Validation of Combustion Modeling in Numerical Simulations," *Journal of Turbomachinery*, Vol. 137, 2015, Turbo-14-1284.

120. Bohan, B. T., Blunck, D. L., Polanka, M. D., Kostka, S., Jiang, N., and Stouffer, S. D., "Impact of an Upstream Film-Cooling Row on Mitigation of Secondary Combustion in a Fuel Rich Environment," *Journal of Turbomachinery*, Vol. 136, 2013, Turbo-13-1055.

121. DeLallo, M. R., Polanka, M. D., and Blunck, D. L., "Impact of Trench and Ramp Film Cooling Designs to Reduce Heat Release in a Reacting Flow," *Proceedings of the ASME Turbo Expo 2012 Copenhagen, Denmark*, 2012, GT2012-68311.

122. Shewhart, A. T., Polanka, M. D., Robertson, J. J., Greiner, N. J., and Rutledge, J. L., "Minimization of Heat Load Due to Secondary Reactions in Fuel Rich Environments," *Journal of Engineering for Gas Turbines and Power*, Vol. 137, 2015, GTP-15-1114.

123. Shewhart, A. T., Lynch, A. J., Greiner, N. J., Polanka, M. D., and Rutledge, J. L., "Mitigation of Heat Release from Film Cooling in Fuel Rich Environments," *Journal of Propulsion and Power*, Vol. 32, 2016, pp. 1454–1461.

124. Parks, A. K., *Desensitizing Flame Structure and Exhaust Emissions to Flow Parameters in an Ultra-Compact Combustor*, Master's thesis, Air Force Institute of Technology, WPAFB, OH, 2012, AFIT/GAE/ENY/12-M33.

125. Wurm, B., Schulz, A., Bauer, H. J., and Gerendas, M., "Impact of Swirl Flow on the Cooling Performance of and Effusion Cooled Combustor Liner," *Proceedings of ASME Turbo Expo 2012, Copenhagen, Denmark*, 2012, GT2012-68972.

126. Marosky, A., Seidel, V., Bless, S., Sattlemayer, T., and Magni, F., "Impact of Cooling Air Injection on the Primary Combustion Zone of a Swirl Burner," *Proceedings of ASME Turbo Expo 2012, Copenhagen, Denmark*, 2012, GT2012-68898.

127. Concepts NREC, "Turbines photo gallery," 2016, White River Junction, VT, accessed from `http://www.conceptsnrec.com/`.

128. Aungier, R. H., *Turbine Aerodynamics*, ASME Press, New York, NY, 2006.

129. Aguilar, F., Davis, R., and Clark, J. P., "Aerodynamic Simulation of Flows in a Highly Loaded Turbine," *Conference proceedings of AIAA Aerospace Sciences Meeting, Orlando, FL*, 2011, AIAA-2011-301.

130. Young, D. F., Munson, B. R., and Okiishi, T. H., *A Brief Introduction to Fluid Mechanics*, John Wiley & Sons, York, PA, 3rd ed., 2004.

131. Pope, S. B., *Turbulent Flow*, Cambridge University Press, Cambridge, UK, 2000.

132. ANSYS, Inc, *FLUENT 16.2 User's Guide*, 2016, Canonsburg, PA.

133. Batchelor, G. K., *An Introduction to Fluid Dynamics*, Cambridge University Press, Cambridge, UK, 1967.

134. Blazek, J., *Computational Fluid Dynamics: Principles and Applications*, Elsevier Publishing, Oxford, UK, 2005, 2nd Edition.

135. Menter, F. R. and Egorov, Y., "The scale-adaptive simulation method for unsteady turbulent flow predictions, Part 2: application to complex flows, journal=Flow Turbulence Combustion," Vol. 85, 2010, pp. 139–165.

136. Andreini, A., Bacci, T., Insinna, M., Mazzei, L., and Salvadori, S., "Hybrid RANS-LES Modeling of the Aero-Thermal Field in an Annular Hot Streak Generator for the Study of Combustor-Turbine Interaction," *Journal of Engineering For Gas Turbines and Power*, Vol. 139, 2016.

137. Law, W. P. and Gimbun, J., "Scale-Adaptive Simulation on the Reactive Turbulent Flow in a Partial Combustion Lance: Assessment of Thermal Insulators," *Applied Thermal Engineering*, Vol. 105, No. 3, 2016, pp. 887–893.

138. Mongia, H., "Recent Progress in Comprehensive Modeling of Gas Turbine Engine Combustion," *Proceedings of the 46th AIAA Aerospace Sciences Meeting, Reno, NV*, 2008, AIAA-2008-1445.

139. Ehret, J. A., *Design Optimization of a High-G Loaded Ultra-Compact Combustor*, Master's thesis, Wright State University, Dayton, OH, 2002.

140. Greenwood, R. T., *Numerical Analysis and Optimization of the Ultra Compact Combustor*, Master's thesis, Air Force Institute of Technology, WPAFB, OH, 2005, AFIT/GAE/ENY/05-M10.

141. Anisko, J., *Numerical Investigation of Cavity-Vane Interactions within the Ultra Compact Combustor*, Master's thesis, Air Force Institute of Technology, WPAFB, OH, 2005, AFIT/GAE/ENY/06-M01.

142. Mawid, M. A., Park, T. W., Thornburg, H. J., Sekar, B., and Zelina, J., "Numerical Analysis of Inter-Turbine Burner (ITB) Concepts for Improved Gas Turbine Engine Performance," *Proceedings of the 43rd AIAA Aerospace Sciences Meeting, Reno, NV*, 2005, AIAA 2005-1162.

143. Moenter, D. S., *Design and Numerical Simualtion of Two Dimensional Ultra Compact Combustor Model Sections for Experimental Observation of Cavity-Vane Flow Interactions*, Master's thesis, Air Force Institute of Technology, WPAFB, OH, 2006, AFIT/GAE/ENY/06-S07.

144. Mawid, M. A., Thornburg, H. J., Sekar, B., and Zelina, J., "Performance of an Inter-Turbine Burner (ITB) Concept with Three Different Vane Cavity Shapes," *Proceedings of the 42nd Joint Propulsion Conference, Sacramento, CA*, 2006.

145. Thornburg, H. J., Sekar, B., Zelina, J., and Greenwood, R. T., "Numerical Study of an Inter-Turbine Burner (ITB) Concept with Curved Radial Vane," *Proceedings of the 45th AIAA Aerospace Sciences Meeting, Reno, NV*, 2007, AIAA 2006-4740.

146. Briones, A. M., Sekar, B., Shouse, D. T., Blunck, D. L., Thornburg, H. J., and Erdmann, T. J., "Reacting Flows in Ultra-Compact Combustors with Combined-Diffuser Flameholder," *Journal of Propulsion and Power*, Vol. 31, 2015.

147. Bills, J. D., Crowe, D. S., Rutledge, J. L., and Coy, E. B., "Modeling Fuel Film Cooling on Rocket Engine Walls," *Proceedings of the 54th AIAA Aerospace Sciences Meeting, San Diego, CA*, 2016, AIAA 2016-2149.

148. Briones, A. M., Burrus, D. L., Erdmann, T. J., and Shouse, D. T., "Effect of Centrifugal Force on the Performance of High-G Ultra Compact Combustor," *Proceedings of ASME Turbo Expo, Montreal, Canada*, 2015, GT2015-43445.

149. Patankar, S. V., *Numerical Heat Transfer and Fluid Flow*, Hemisphere, 1980.

150. Lee, D. J., Thakur, S., Wright, J., Ihme, M., and Shyy, W., "Characterization of Flow Field Structure and Species Composition in a Shear Coaxial Rocket GH2/GO2 Injector: Modeling of Wall Heat Loss," *Proceedings of the 47th Joint Propulsion Conference, San Diego, CA*, 2011, AIAA-2011-6125.

151. Brown, T. L., LeMay, H. E., and Bursten, B. E., *Chemistry - The Central Science*, Prentice Hall, Upper Saddle River, NJ, eighth ed., 2000.

152. Gundermann, K.-D., "Luminescence Physics," *Encyclopedia Britannica*, Encyclopedia Britannica, inc., 2011, Accessed 8 March 2018.

153. Vincenti, W. G. and Kruger, C. H., *An Introduction to Physical Gas Dynamics*, Krieger Publishing Company, Malabar, Florida, 1965.

154. Jonassen, D. R., Settles, G. S., and Tronosky, M. D., "Schlieren "PIV" for Turbulent Flows," *Journal of Optics and Lasers Engineering*, Vol. 44, 2006, pp. 190–207.

155. Hargather, M. J., Lawson, M. J., Settles, G. S., and Weinstein, L. M., "Seedless Velocimetry Measurements by Schlieren Image Velocimetry," *AIAA Journal*, Vol. 49, 2011, pp. 611–620.

156. Hinds, W. C., *Aerosol technology: properties, behaviors, and measurements of airborne particles*, Wiley, New York, NY, 1999.

157. Reuter, M., Biasotti, S., Giorgi, D., Patane, G., and Spagnuolo, M., "Discrete Laplace-Beltrami Operators for Shape Analysis and Segmentation," *Computers and Graphics*, Vol. 33, No. 3, 2009, pp. 381–390.

158. Fisher, R., Perkins, S., Walker, A., and Wolfart, E., "Laplacian/Laplacian of Gaussian. [Online]," 2003, http://homepages.inf.ed.ac.uk/rbf/HIPR2/log.htm.

159. Adrian, R. J., "Twenty Years of Particle Image Velocimetry," *Experiments in Fluids*, Vol. 39, 2004, pp. 159–169.

160. Melling, A., "Tracer Particles and Seeding for Particle Image Velocimetry," *Measurement Science and Technology*, Vol. 8, No. 12, 1997, pp. 1406–1416.

161. DeMarco, K. J., *Control, Characterization, and Cooling of an Ultra Compact Combustor*, Master's thesis, Air Force Institute of Technology, WPAFB, OH, 2018, AFIT-ENY-MS-18-M-250.

162. Goss, L. P., Huelskamp, B., Belovich, V., Lynch, A., and Wang, G., "Thin-Filament-Pyrometry Temperature Measurements in a Split Air-Stream Bluff-Body Experimental Rig (SABER)," *Proceedings of the 9th U. S. National Combustion Meeting; Cincinnati, Ohio*, 2015, Paper No. 114DI-0097.

163. Martiny, M., Schiele, R., Gritsch, M., and Wittig, S., "In Situ Calibration for Quantitative Infrared Thermography," *Quantitative InfraRed Thermography Journal*, Vol. 96, June 1996, pp. 3–8, 99-GT-142.

164. Schulz, A., "Infrared Thermography as Applied to Film Cooling of Gas Turbine Components," *Measurement Science and Technology*, Vol. 11, February 2000, pp. 948–956.

165. Schmidt, B., "Schlieren Visualization," 2015, CalTech Laboratory Notes, http://shepherd.caltech.edu/T5/Ae104/Ae104b_handout2015.pdf, accessed 12 March 2018.

166. Hu, H., "Flow Visualization Techniques: Shadowgraph and Schlieren," 2018, Lecture 7 Notes, Iowa State University, Accessed 12 March 2018.

167. Settles, G., *Schlieren and Shadowgraph Techniques: Visualizing Phenomena in Transparent Media*, Springer, New York, NY, 2001.

168. Gilbert, N. A., *Enhanced Flow Migration in Full Annular Ultra Compact Combustor*, Master's thesis, Air Force Institute of Technology, WPAFB, OH, 2016, AFIT-ENY-MS-M-211.

169. Bogard, D. G., "Airfoil Film Cooling," *The Gas Turbine Handbook*, National Energy Technology Laboratory, Department of Energy, Morgantown, WV, 2006, Sect. 4.2.2.1.

170. Zhang, Y., Duda, T., Scobie, J. A., Sangan, C. M., Copeland, C. D., and Redwood, A., "Design of an Air-Cooled Radial Turbine Part 1: Experimental Measurements of Heat Transfer," *Proceedings of the ASME Turbo Expo 2018: Turbine Technical Conference & Exposition, Oslo, Norway*, 2018, GT2018-76384.

171. Zhang, Y., Duda, T., Scobie, J. A., Sangan, C. M., Copeland, C. D., and Redwood, A., "Design of an Air-Cooled Radial Turbine Part 2: Computational Modeling," *Proceedings of the ASME Turbo Expo 2018: Turbine Technical Conference & Exposition, Oslo, Norway*, 2018, GT2018-76378.

172. Barringer, M. D., Thole, K. A., and Polanka, M. D., "Effects of Combustor Exit Profiles on High Pressure Turbine Vane Aerodynamics and Heat Transfer," *Journal of Turbomachinery*, Vol. 131, April 2009, 021008-1.

173. Hornedo, E. A., Bohan, B. T., Cottle, A. E., Schmiedel, C., Polanka, M. D., and Goss, L. P., "Design Strategy for Product Migration from a Circumferential Combustion Cavity," *Conference proceedings of AIAA SciTech 2017, Grapevine, TX*, 2017, AIAA-2017-0390.

174. Wilson, J. D., *Characterizing G-Loading, Swirl Direction, and Rayleigh Losses in an Ultra Compact Combustor*, Master's thesis, Air Force Institute of Technology, WPAFB, OH, 2013, AFIT-ENY-13-S-02.

175. Bohan, B. T., Polanka, M. D., and Goss, L. P., "Development and Testing of a Variable Geometry Diffuser in an Ultra-Compact Combustor," *Proceedings of AIAA SciTech Forum, Grapevine, Texas*, 2017, AIAA-2017-0777.

176. Young, D. F., Munson, B. R., and Okiishi, T. H., *A Brief Introduction to Fluid Mechanics*, John Wiley & Sons, New Jersey, 3rd ed., 2004.

177. Texas-Instruments, "DRV8871-Q1 3.6-A Brushed DC Motor Driver With Internal Current Sense (PWM Control)," 2017, Component Technical Data Sheet.

178. Texas-Instruments, "LM138 and LM338 5-Amp Adjustable Regulators," 2016, Component Technical Data Sheet.

179. SparkFun, "Pulse Width Modulation," 2018, `https://learn.sparkfun.com/tutorials/pulse-width-modulation`, accessed 5 February 2018.

180. Linear-Technologies, "LTC6992-1/ LTC6992-2/ LTC6992-3/ LTC6992-4 TimerBlox: Voltage-Controlled Pulse Width Modulator (PWM)," 2010, Component Technical Data Sheet.

181. Micronas, "HAL 401 Linear Hall-Effect Sensor IC," 2008, Component Technical Data Sheet.

Vita

Major Brian T. Bohan graduated from Patchogue-Medford High School in Medford, New York. He entered undergraduate studies at Clarkson University where he graduated with a Bachelor of Science degree in Aeronautical Engineering in May 2005. He commissioned into the Air Force through the Air Force Reserve Officer Training Corps (AFROTC) also in May 2005.

Following a year of casual status and assorted in-residence trainings he was assigned to the 746th Test Squadron at Holloman AFB, NM. Duties included test management of GPS and inertial guidance system test programs, specifically in the areas of GPS vulnerabilities and electronic warfare. He was also the program manager for a state of the art simulator for a current navigation warfare threat. In June 2008 his duties were expanded to include deputy element chief/acting element chief of the avionics element.

In August 2009 he entered the Air Force Institute of Technology majoring in aeronautical engineering with concentrations in aerodynamics, air breathing propulsion, and computational fluid dynamics. During graduation in March 2011 he was awarded the Commandant's Award for the most exceptional master's thesis in the graduating class. Following graduation he was assigned to the Air Force Research Lab (AFRL), Air Vehicles Directorate, WPAFB, OH where he served as the deputy branch chief for the High and Low Speed Aerodynamic Configurations Branches.

In August 2012 he was assigned to the Advanced Programs Division of the Armament Directorate in the Air Force Life Cycle Management Center (AFLCMC), Eglin AFB, FL. In this position he served as the propulsion technology subject matter expert for highly classified weapon development programs and the Triple Target Terminator (T3) DARPA demonstrator program.

In August 2015 he returned to the Graduate School of Engineering and Management at the Air Force Institute of Technology to pursue a doctorate in aeronautical engineering with a focus in air-breathing propulsion. Upon graduation he is joining the faculty in the Department of Aeronautical and Astronautical Engineering at the Air Force Institute of Technology.

Major Bohan is married and has two daughters.

REPORT DOCUMENTATION PAGE

Form Approved
OMB No. 0704–0188

The public reporting burden for this collection of information is estimated to average 1 hour per response, including the time for reviewing instructions, searching existing data sources, gathering and maintaining the data needed, and completing and reviewing the collection of information. Send comments regarding this burden estimate or any other aspect of this collection of information, including suggestions for reducing this burden to Department of Defense, Washington Headquarters Services, Directorate for Information Operations and Reports (0704–0188), 1215 Jefferson Davis Highway, Suite 1204, Arlington, VA 22202–4302. Respondents should be aware that notwithstanding any other provision of law, no person shall be subject to any penalty for failing to comply with a collection of information if it does not display a currently valid OMB control number. **PLEASE DO NOT RETURN YOUR FORM TO THE ABOVE ADDRESS.**

1. REPORT DATE *(DD–MM–YYYY)*	2. REPORT TYPE	3. DATES COVERED *(From — To)*
27-08-2018	PhD Dissertation	1 September 2015 - 27 August 2018

4. TITLE AND SUBTITLE

COMBUSTION DYNAMICS AND HEAT TRANSFER IN AN ULTRA COMPACT COMBUSTOR

5a. CONTRACT NUMBER

5b. GRANT NUMBER

5c. PROGRAM ELEMENT NUMBER

6. AUTHOR(S)

Major Brian T. Bohan

5d. PROJECT NUMBER

5e. TASK NUMBER

5f. WORK UNIT NUMBER

7. PERFORMING ORGANIZATION NAME(S) AND ADDRESS(ES)

Air Force Institute of Technology
Graduate School of Engineering and Management (AFIT/EN)
2950 Hobson Way
WPAFB OH 45433-7765

8. PERFORMING ORGANIZATION REPORT NUMBER

AFIT-ENY-DS-18-S-057

9. SPONSORING / MONITORING AGENCY NAME(S) AND ADDRESS(ES)

Air Force Research Laboratory
Aerospace Systems Directorate, Combustion Branch
1950 Fifth Street, Building 490
WPAFB OH 45433-7251
POC: Dr. Andrew Caswell, Phone: 312-785-7098
Email: andrew.caswell.4@us.af.mil

10. SPONSOR/MONITOR'S ACRONYM(S)

AFRL/RQTC

11. SPONSOR/MONITOR'S REPORT NUMBER(S)

12. DISTRIBUTION / AVAILABILITY STATEMENT

DISTRIBUTION STATEMENT A:
APPROVED FOR PUBLIC RELEASE; DISTRIBUTION UNLIMITED.

13. SUPPLEMENTARY NOTES

14. ABSTRACT Engine designers are constantly working to increase the thrust-to-weight rating of their jet engines. A novel burner concept to help achieve this goal is the Ultra Compact Combustor (UCC). The UCC offers an axial length savings, and thus weight savings, in the combustion section by swirling the reactants in the circumferential direction inside an annulus. If the UCC can match the performance of the traditional burner it replaces, the engine can maintain thrust while reducing weight and thus improve the thrust-to-weight rating. In the present study four areas of UCC research were advanced including: cooling a UCC turbine vane, detailed computational modeling of UCC systems, development of a dynamic airflow split diffuser and characterization of combustion performance at different flow splits and additionally with a new 12-Step fuel injection system, and finally development and testing of a new UCC orientation that specifically addresses engine fit and turbine inlet temperature distribution issues that have been present in all other UCC configurations. The new UCC orientation was demonstrated to fit inside an engine casing and produced a desirable combustor exit temperature distribution.

15. SUBJECT TERMS

Ultra Compact Combustor, UCC, Turbines, Turbine Engine, Combustion, Jet Engine, JetCat, Heat Transfer, Film-Cooling, Fluidic Oscillators

16. SECURITY CLASSIFICATION OF:			17. LIMITATION OF ABSTRACT	18. NUMBER OF PAGES	19a. NAME OF RESPONSIBLE PERSON
a. REPORT	b. ABSTRACT	c. THIS PAGE			Dr. Marc Polanka, AFIT/ENY
U	U	U	U	844	19b. TELEPHONE NUMBER *(include area code)* (937) 255-3636, x4714; marc.polanka@afit.edu